AD-A091 010   HEBREW UNIV JERUSALEM (ISRAEL)   F/G 20/4
PROCEEDINGS OF THE INTERNATIONAL SYMPOSIUM ON SHOCK TUBES AND W--ETC(
FEB 80   A LIFSHITZ, J ROM   AFOSR-78-3679
UNCLASSIFIED   AFOSR-TR-80-1141   NL

1 of 8
AD
A091010

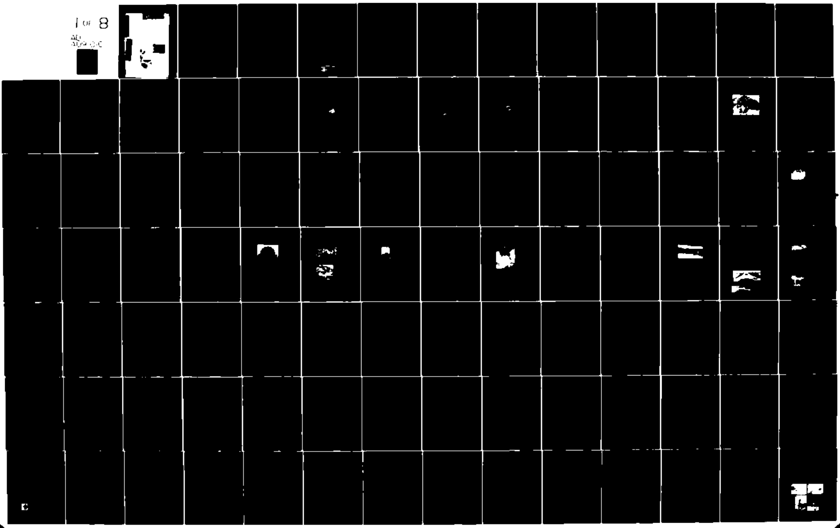

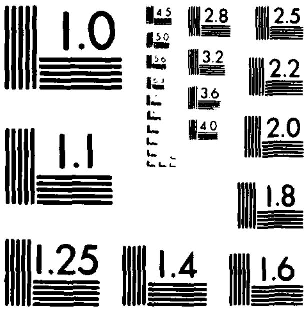

MICROCOPY RESOLUTION TEST CHART
NATIONAL BUREAU OF STANDARDS 1963 A

SHOCK TUBES AND WAVES

Proceedings of the 12th International Symposium
on Shock Tubes and Waves

Jerusalem, Israel, [illegible] 1979

Editors

ASSA LIFSHITZ
The Hebrew University of Jerusalem

JOSEF ROM
Israel Institute of Technology, Haifa

UNCLASSIFIED

SECURITY CLASSIFICATION OF THIS PAGE (When Data Entered)

(19) REPORT DOCUMENTATION PAGE

READ INSTRUCTIONS BEFORE COMPLETING FORM

1. ~~REPORT NUMBER~~ (18) AFOSR-TR-80-1141 ✓

2. GOVT ACCESSION NO. AD-A091010

3. RECIPIENT'S CATALOG NUMBER (9)

4. TITLE (and Subtitle) (6) Proceedings of the ~~TWELTH~~ INTERNATIONAL SYMPOSIUM ON SHOCK TUBES AND WAVES (12th) Held at Jerusalem on 16-19 July 1979.

5. TYPE OF ~~REPORT & PERIOD~~ COVERED FINAL rept. 30 Sep 78 - 31 Dec 79

6. ~~PERFORMING ORG. REPORT NUMBER~~

7. AUTHOR(s)
PROFESSOR ASSA LIFSHITZ
PROFESSOR JOSEF ROM (10) (15)

8. CONTRACT OR GRANT NUMBER(s) ✓ AFOSR-78-3679

9. PERFORMING ORGANIZATION NAME AND ADDRESS
THE HEBREW UNIVERSITY OF JERUSALEM
JERUSALEM 91190, ISRAEL (16)

10. PROGRAM ELEMENT, PROJECT, TASK AREA & WORK UNIT NUMBERS
2307/A1 (17) A1
61102F

11. CONTROLLING OFFICE NAME AND ADDRESS
AIR FORCE OFFICE OF SCIENTIFIC RESEARCH/NA
BUILDING 410
BOLLING AFB, DC 20332

12. ~~REPORT DATE~~ (11) Feb[redacted]

13. ~~NUMBER OF PAGES~~ 735

14. MONITORING AGENCY NAME & ADDRESS (if different from Controlling Office) (12) 746

15. SECURITY CLASS. (of this report) UNCLASSIFIED

15a. DECLASSIFICATION/DOWNGRADING SCHEDULE

16. DISTRIBUTION STATEMENT (of this Report)

Approved for public release; distribution unlimited.

17. DISTRIBUTION STATEMENT (of the abstract entered in Block 20, if different from Report)

18. SUPPLEMENTARY NOTES

Proceedings of the 12th International Symposium on SHOCK TUBES and WAVES Jerusalem, July 16-19, 1979
Feb, 1980

19. KEY WORDS (Continue on reverse side if necessary and identify by block number)

SHOCK TUBES
SHOCK WAVES
SHOCK INTERACTIONS
SHOCK REFLECTIONS
PLASMA FLOW
CHEMICAL RATE PROCESSES
DETONATIONS
LASERS

20. ABSTRACT (Continue on reverse side if necessary and identify by block number)

This volume contains seventy-four papers presented at the Twelth International Symposium on Shock Tubes and Waves which was held at the Van-Leer Foundation in Jerusalem, July 16-19, 1979. The papers in the volume are divided into three parts and arranged according to their presentation at the symposium. The first part contains the plenary lectures (sessions A) including the Paul Vieille (1A) and the Otto Laporte (7A) memorial lectures. The second part contains all the papers presented in sessions B and deals with the general field of shock waves and gasdynamics. Topics covered in these sessions included shock tube facilities,

DD FORM 1 JAN 73 1473 EDITION OF 1 NOV 65 IS OBSOLETE

165450 DM

UNCLASSIFIED

SECURITY CLASSIFICATION OF THIS PAGE (When Data Entered) shock flow computations, ionized gases in shock waves, instrumentation and experimental techniques, shock reflections and interactions, shock waves and jets, and plasma flow. The papers in the third part are those presented in sessions C. They describe work related to chemical and physical processes in shock waves. Topics covered were chemical rate processes, detonations, diagnostics and experimental methods, lasers and energy & waves. The plenary lectures (sessions A) were all invited. Papers in sessions B and C were selected from over one hundred submitted, on the basis of extended abstracts. The refereeing procedure consisted of initial screening by the executive committee (assisted by scientists and engineers from this country) and later, refereeing by reviewers from this country and abroad.

SHOCK TUBES AND WAVES

[redacted]

SHOCK TUBES AND WAVES

Proceedings of the 12th International Symposium
on Shock Tubes and Waves

ירושלים, כ״א—כ״ד בתמוז תשל״ט
Jerusalem, July 16–19, 1979

Edited by

ASSA LIFSHITZ
The Hebrew University of Jerusalem

JOSEF ROM
Israel Institute of Technology, Haifa

JERUSALEM 1980

THE MAGNES PRESS, THE HEBREW UNIVERSITY

Distributed by
The Magnes Press, The Hebrew University
Jerusalem

ISBN 965—223—350-1

Printed in Israel
Plates: Spotgraph
Printing: "Ahva" Co-op. Press

PREFACE

This volume contains seventy-four papers presented at the XIIth International Symposium on Shock Tubes and Waves which was held at the Van-Leer Foundation in Jerusalem, July 16-19, 1979. The papers in the volume are divided into three parts and arranged according to their presentation at the symposium. The first part contains the plenary lectures (sessions A) including the Paul Vieille (1A) and the Otto Laporte (7A) memorial lectures. The second part contains all the papers presented in sessions B and deals with the general field of shock waves and gasdynamics. Topics covered in these sessions included shock tube facilities, shock flow computations, ionized gases in shock waves, instrumentation and experimental techniques, shock reflections and interactions, shock waves and jets, and plasma flow. The papers in the third part are those presented in sessions C. They describe work related to chemical and physical processes in shock waves. Topics covered were chemical rate processes, detonations, diagnostics and experimental methods, lasers and energy & waves.

The plenary lectures (sessions A) were all invited. Papers in sessions B and C were selected from over one hundred submitted, on the basis of extended abstracts. The refereeing procedure consisted of initial screening by the executive committee (assisted by scientists and engineers from this country) and later, refereeing by reviewers from this country and abroad. The executive committee wishes to thank all those who helped with this procedure.

Participants from fourteen countries were welcomed at the opening session of the symposium by the Mayor of Jerusalem, Mr. Teddy Kollek and by Mr. Simcha Dinitz, Vice President of the Hebrew University of Jerusalem. Deputy Prime Minister of the State of Israel, Professor Yigal Yadin addressed the symposium participants and their accompanying guests at the farewell banquet, and presented an overview of the Israeli-Egyptian peace treaty and the current state of events in Israel. They have our sincere thanks.

Like its predecessors, the XIIth International Symposium on Shock Tubes and Waves has been sponsored by the U.S. AIR FORCE OFFICE OF SCIENTIFIC RESEARCH. Their support is highly appreciated.

Sincere thanks are also given to the following organisations for their support:

The Israel Academy for Sciences and Humanities; Dr. G. V. Bull, Aerospace Research Corporation Inc., Highwater P.Q. Canada; The Hebrew Univesrity of Jerusalem; The Technion, Haifa; Ben-Gurion University, Beer Sheva; The Ministry of Defense; The Israel Aircraft Industry.

Finally, the executive committee would like to thank Kenes-Organizers of Congresses and Special Events Ltd.,for their help and advice and Mrs. Miriam Achituv and Mrs. Eta Shushan for their help in organizing the symposium and publishing the proceedings.

ASSA LIFSHITZ, Jerusalem
JOSEF ROM, Haifa

February 1980 — שבט תש"ם

EXECUTIVE COMMITTEE

Assa Lifshitz (*co-chairman*)

Josef Rom (*co-chairman*)

INTERNATIONAL ADVISORY COMMITTEE

B. Ahlborn, Canada
T. Akamatsu, Japan
D. Baganoff, USA
S.H. Bauer, USA
T.V. Bazhenova, USSR
D. Bershader, USA
J.N. Bradley, England
R. Dannenberg, USA
L.Z. Dumitrescu, Rumania
R. Emrich, USA
R.G. Fiszdon, Poland
R.G. Fowler, USA
K. Fukuda, Japan
I.I. Glass, Canada
W. Griffith, USA
R. Gross, USA
A. Hertzberg, USA
H. Hornung, Australia
G. Kamimoto, Japan
A. Kantrowitz, USA
A. Lifshitz, Israel
L.G. Napolitano, Italy
R.W. Nicholls, Canada
H. Oguchi, Japan
A.K. Oppenheim, USA
S.S. Penner, USA
H. Reichenbach, Germany
B.E. Richards, Belgium
M. Rogers, USA
J. Rom, Israel
P. Rose, USA
D. Russell, USA
P. Savic, Canada
F. Schultz-Grunow, Germany
L.I. Sedov, USSR
R.I. Soloukhin, USSR
B. Sturtevant, USA
C. Treanor, USA
J. Valensi, France
U.V. Zhurin, USSR

LOCAL ORGANIZING COMMITTEE

Akiva Bar-Nun
Alexander Burcat
Harvey F. Carroll
Felix Dothan
Ozer Igra
Willi Low
Assa Lifshitz
Uri Openheim
Ornan Seginer
Josef Rom

THE SYMPOSIUM IS ENDORSED BY

The Israel Academy for Science and Humanities

The Israel Chemical Society

The American Physical Society.

CONTENTS

Part I. Plenary Lectures

Paul Vieille Memorial Lecture: POTENTIAL APPLICATIONS OF WAVE MACHINERY TO ENERGY AND CHEMICAL PROCESSES
P. H. Rose 3

THE REAL THING: BLAST WAVES FROM ATMOSPHERIC NUCLEAR EXPLOSIONS
H. L. Brode 31

DEVELOPMENTS IN LASER BASED DIAGNOSTIC TECHNIQUES
S. Lederman 48

WAVE PHENOMENA IN LASER-PLASMA INTERACTION
S. Eliezer and H. Zmora 66

REVIEW OF EXPERIMENTAL AND THEORETICAL STUDIES OF THE HARP SOLID PROPELLANT IGNITION AND COMBUSTION TUBE-LAUNCHER
G. V. Bull 82

RATE MEASUREMENT IN SHOCK WAVES WITH THE LASER-SCHLIEREN TECHNIQUE
J. H. Kiefer and J. C. Hajduk 97

Otto Laporte Memorial Lecture: REACTIONS AND RELAXATIONS IN GASEOUS SYSTEMS — THE INFORMATION THEORETIC APPROACH
R. D. Levine 111

Part II. Shock Waves and Gas Dynamics

TEST SECTION CONFIGURATION FOR AERODYNAMIC TESTING IN SHOCK TUBES
W. J. Cook, L. L. Presley and G. T. Chapman 127

A LARGE-SCALE AERODYNAMIC TEST FACILITY COMBINING THE SHOCK AND LUDWIEG TUBE CONCEPTS
L. Z. Dumitrescu 137

LUDWIEG TUBE FACILITY FOR STUDIES OF HIGH PRESSURE LOW TEMPERATURE SUPERSONIC FLOW TRANSITION LASERS
B. Forestier, B. Fontaine and J. Valensi 147

THE DOUBLE SHOCK WAVE TUBE: EXPERIMENTAL INVESTIGATION OF SHOCK-SHOCK REFLECTIONS
W. Garen and G. Lensch 155

ON THE MAXIMUM ATTAINABLE TEMPERATURE IN HARTMANN-SPRENGER TUBES
E. Brocher 161

PRESSURE WAVES RADIATED FROM BUBBLES COLLAPSING WITH PHASE CHANGE
S. Fujikawa and T. Akamatsu 169

SHOCK-TUBE FLOW COMPUTATION INCLUDING THE DIAPHRAGM AND BOUNDARY-LAYER EFFECTS
D. Zeitoun, R. Brun and M. J. Valetta 180

REFLECTION PROCESSES OF IONIZING SHOCKS IN ARGON ON AN END WALL OF A SHOCK TUBE
Y. Takano, S. Miyoshi and T. Akamatsu 187

IONIZATION RELAXATION IN SHOCK TUBES TAKING INTO ACCOUNT A NON-MAXWELLIAN ELECTRON VELOCITY DISTRIBUTION
R. Meyer-Prüssner and F. Demmig 197

ELECTRON VELOCITY DISTRIBUTION IN AN EXPANDING FLOW OF SHOCK HEATED IONIZED ARGON
H. J. Thor and H. Grönig 207

IONIZING SHOCK STRUCTURE FOR A STRONG SHOCK WAVE IN ARGON
H. Honma and H. Yoshida 215

EFFECT OF SHOCK-TUBE CLEANLINESS ON THE INITIAL IONIZATION RATE IN ARGON PLASMA
C. P. Schneider and G. Hahne 222

INTERACTIONS OF SHOCK STRUCTURE WITH SHOCK-INDUCED QUASI-STEADY LAMINAR SIDEWALL AND FLAT-PLATE BOUNDARY-LAYER FLOWS IN IONIZING ARGON
I. I. Glass, W. Shiun Liu, K. Takayama and P. I. Brimelow 232

PLASMA FLOW VELOCITY GAGE AT HIGH MAGNETIC REYNOLDS NUMBER
D. W. Baum, W. L. Shimmin and S. P. Gill 242

SHOCK PROPAGATION IN A TUBE WITH TRANSVERSE RIBS
J. E. Craig and K. A. Haines 248

RECENT RESULTS OF RESONANT REFRACTIVITY STUDIES FOR IMPROVED FLOW VISUALIZATION
G. Blendstrup, D. Bershader and P. Langhoff 258

MACH WAVE RADIATION OF HOT SUPERSONIC JETS INVESTIGATED BY MEANS OF THE SHOCK TUBE AND NEW OPTICAL TECHNIQUES
H. Oertel 266

A NEW TYPE OF FLAP VALVE FOR GENERATING SONIC BOOMS IN A PYRAMIDAL HORN
J. J. Gottlieb, W. Czerwinski, N. N. Wahba, and R. E. Gnoyke 276

DOMAINS AND BOUNDARIES OF NONSTATIONARY OBLIQUE SHOCK-WAVE REFLECTIONS IN PERFECT AND IMPERFECT MONATOMIC AND DIATOMIC GASES
G. Ben-Dor and I. I. Glass 288

THE INFLUENCE OF RELAXATION ON TRANSITION TO MACH REFLECTION IN PSEUDOSTEADY FLOW
J. Sandeman, A. Leitch and H. Hornung 298

EXPERIMENTS ON THE GROWTH OF THE MACH STEM FOR SHOCK REFLECTIONS IN A SHOCK TUBE
A. Lozzi 308

ON THE TRANSITION BETWEEN REGULAR AND MACH REFLECTION
S. Itoh and M. Itaya 314

STABILITY OF CYLINDRICAL CONVERGING SHOCK PERTURBED BY A BLEED APERTURE
J. H. T. Wu, T. S. H. Yu, R. A. Neemeh and P. P. Ostrowski 324

ON THE DIFFRACTION OF WEAK BLAST WAVES OVER CONCAVE CORNERS
L. F. Henderson and A. Siegenthaler 334

STABILITY OF NON-UNIFORM SHOCK WAVES
E. Marmor, Y. Kivity, A. Betser 341

THE DIFFRACTION OF THE BLAST WAVE EMERGING FROM A CONICAL NOZZLE DRIVEN BY COMPRESSED GAS
L. Pennelegion and J. F. Grimshaw 349

PROPAGATION OF SHOCK WAVES IN RANDOM MEDIA
B. Sturtevant, L. Hesselink, J-F. Haas 359

ELECTRIC AND MAGNETIC FIELDS OF SHOCK FRONTS
B. Ahlborn, J. Kwan and J. Pearson 366

INTERACTIONS BETWEEN AN E-BEAM SUSTAINED DISCHARGE AND SUPERSONIC FLOW
E. Margalith and W. H. Christiansen 376

FLOW ASPECTS OF HIGH POWER GASDYNAMIC LASERS
J. D. Anderson, E. Jones, K. N. Parthasarathy, G. Colasurdo, M. S.. Oggiano, and M. Onorato 386

SPHERICALLY CONVERGING SHOCK WAVES IN DENSE PLASMA RESEARCH
J. H. Lau, M. M. Kekez, G. D. Lougheed and P. Savic 396

Part III. Physical and Chemical Processes in Shock Waves

HOMOGENOUS NUCLEATION IN METAL VAPORS
VI. THE CONDENSATION OF SILICON
K. Tabayashi and S. H. Bauer 409

SHOCK-TUBE STUDIES OF RADIATIVE BASE HEATING OF JOVIAN PROBE
H. Shirai and C. Park 419

IN SITU OPTICAL MEASUREMENTS OF PARTICULATE GROWTH IN SOOTING ACETYLENE COMBUSTION
K. Bro, S. L. K. Wittig and D. W. Sweeney 429

SPONTANEOUS CONDENSATION OF AN AZEOTROPIC FLUID
S. L. K. Wittig, R. A. Zahoransky, S. S. Kim and D. E. Wurz 437

THE USE OF AN UNSTEADY WAVE CHEMICAL REACTOR AS A KEY ELEMENT IN THE PRODUCTION OF H_2 FOR USE IN SYNTHETIC FUEL PRODUCTION
E. L. Klosterman, R. T. Taussig, T. S. Vaidyanathan, P. Cassady, L. Steinhauer and M. Shirazian 446

ACEYLENE PYROLYSIS AND ITS OXIDATION BY WATER VAPOR BEHIND HIGH TEMPERATURE SHOCK-WAVES
A. Bar-Nun and J. E. Dove 457

SHOCK-TUBE STUDIES OF N_2O-DECOMPOSITION
K. G. P. Sulzmann, J. M. Kline and S. S. Penner 465

THERMAL DECOMPOSITION OF NH_3 IN SHOCK WAVES
T. R. Roose, R. K. Hanson, and C. H. Kruger 476

THERMAL DECOMPOSITION OF SO_2 MONITORED BY IR EMISSION
A. Grillo, R. Reed, and M. W. Slack 486

THE FORMATION OF OXIDES OF NITROGEN FROM CH_4-O_2-N_2 MIXTURES
M. J. Guinee, F. A. Hewitt, D. E. Fussey, B. E. Milton and T. F. Palmer 495

HIGH TEMPERATURE METHYL RADICAL REACTIONS WITH ATOMIC AND MOLECULAR OXYGEN
K. A. Bhaskaran, P. Frank and Th. Just 503

SHOCK TUBE IGNITION OF NITROCELLULOSE
A. Cohen and L. Decker 514

THE EFFECT OF REACTION EXOTHERMICITY ON SHOCK PROPAGATION
J. N. Bradley, W. D. Capey and F. Farajii 524

A SPECTROSCOPIC TEMPERATURE MEASUREMENT OF CONVERGING DETONATIONS
T. Sugimura and T. Fujiwara 533

ON THE DETONATION OF UNCONFINED ALUMINUM PARTICLES DISPERSED IN AIR
A. J. Tulis 539

TEMPERATURE MEASUREMENT IN DETONATION WAVES BY USING LIGHT EMISSION FROM SHOCK HEATED ARGON
K. Terao, K. Imamura and N. Takasu 548

LASER SCHLIEREN DEFLECTION IN INCIDENT SHOCK FLOW
T. Tanzawa, Y. Hidaka and W. C. Gardiner, Jr. 555

ION-MOLECULE REACTION MEASUREMENTS BY A SHOCK-TUBE PULSED-FLOW PULSED-AFTERGLOW TECHNIQUE
J. S. Chang, S. Joshi, G. L. Ogram and R. M. Hobson 562

PLASMA PROPERTIES IN A SHOCK HEATED ARGON ATOMIC BEAM
B. Evans, R. M. Hobson, J. S. Chang and K. Teshima 571

NOVEL LASER DOPPLER VELOCIMETER ENABLING FAST INSTANTANEOUS RECORDINGS
G. Smeets and A. George 579

MOLECULAR BEAMS FROM SHOCK HEATED SOURCE
K. Teshima and N. Takahashi 589

"GAIM" — GAS-ADDITION, IMPEDANCE-MATCHED ARC DRIVER
R. E. Dannenberg 599

THERMAL ISOMERIZATION REACTIONS OF SUBSTITUTED CYCLOHEPTATRIENES IN SHOCK WAVES
D. C. Astholz, J. Troe and W. Wieters 607

OXIDATION OF CYANOGEN III. SHOCK INITIATED IGNITION IN C_2N_2-O_2-H_2-Ar MIXTURES
A. Lifshitz and M. Bidani 612

THERMAL DECOMPOSITION OF CH_3
P. Roth, U. Barner and R. Löhr 621

RESONANCE ABSORPTION MEASUREMENTS OF ATOM CONCENTRATIONS IN REACTING GAS MIXTURES. 4. MEASUREMENTS OF H AND D ATOMS IN OXIDATION OF H_2, D_2 AND CD_4
C. C. Chiang and G. B. Skinner 629

SHOCK WAVES IN THE INTERSTELLAR SPACE
M. Elitzur 640

CO GASDYNAMIC LASER MEASUREMENTS IN A SHOCK TUNNEL
M. Tilleman, J. Stricker and A. Burcat 644

FLUID PROCESSES IN SUPERSONIC DIFFUSION LASERS
G. W. Butler and D. A. Russell 655

LASER-INDUCED-FUSION EXPERIMENTS AT KMS FUSION
S. B. Segall 664

PRESSURE WAVE ATTENUATION FOR REPETITIVELY PULSED FUSION LASERS
J. Shwartz, V. A. Kulkarny and D. R. Ausherman 675

ENERGY AND POWER REQUIREMENTS FOR DIRECT INITIATION OF SPRAY DETONATIONS
E. K. Dabora 685

MEASUREMENTS OF ENERGY DENSITY IN SHOCK AND BLAST WAVES
J. M. Dewey and D. J. McMillin 695

SHOCK WAVE GENERATION IN LIQUID BY A HIGH ENERGY CO_2 LASER PULSE
D. Dufresne, J. P. Caressa, P. Giovanneschi, M. Autric and Ph. Bournot 704

ENTRAINMENT OF DUST BY AN AIR SHOCK WAVE: INFLUENCE OF SHOCK DIFFRACTION AROUND AN OBSTACLE
K. Bracht and W. Merzkirch 712

THE FLUID DYNAMIC ASPECTS OF AN EFFICIENT POINT DESIGN ENERGY EXCHANGER
J. F. Zumdieck, T. S. Vaidyanathan, E. L. Klosterman, R. T. Taussig, P. E. Cassady, W. J. Thayer and W. H. Christiansen 720

Author Index 733

Part 1 : PLENARY LECTURES

POTENTIAL APPLICATIONS OF WAVE MACHINERY TO ENERGY AND CHEMICAL PROCESSES

P. H. Rose

Mathematical Sciences Northwest, Inc.
Bellevue, Washington 98009, USA

Wave machinery based on non steady gasdynamic processes, i.e., mechanizations of shock tubes to produce quasi-steady gas flows, have been suggested and applied to energy and chemical processes, since the invention of the "Comprex" by Seippel in 1942 and earlier. In the current critical period of energy shortages, the potential of this class of wave machinery is being investigated with renewed vigor and on a broader scale than before. It appears that if a wave machine can be developed, capable of operating over a temperature ratio of three with an available energy or work transfer efficiency of the order of 80 percent, a wide variety of applications will become practical.

Several applications of this technology are reviewed and their advantages and specific development problems identified. Among the applications discussed is the use of wave machinery in gas turbine topping cycles, in solar heat converters, as a high efficiency thermal conversion system for fusion reactors, and in chemical processing systems to produce fixed nitrogen and synthetic hydrocarbon fuels. The paper concludes with a description of the development program for this technology at MSNW.

INTRODUCTION

Wave machinery refers to the class of devices in which energy, pressure and/or temperature are transferred from one stream of a working fluid to another without mixing by means of non-steady gasdynamic wave processes. When the purpose of the device is to transfer the available work of expansion we call the concept an energy exchanger. When the objective is to transmit pressure, such as to supercharge, we call it a dynamic pressure exchanger. When the concept is used to produce a predetermined thermal pulse such as rapid heating, a steady bath and rapid quench, we call the device a wave reactor. They are all the same class of machinery, composed primarily of a large number of tubes exposed to pre-set reservoir conditions at timed intervals to produce a series of pressure and expansion waves.

Improvements in gasdynamic compression-expansion machinery components of thermal combustion cycles have always been sought. As early as 1900, but more intensely in the 1940s, the dynamic pressure exchanger was explored as a means of transferring pressure between fluids.[1] The genesis of the modern version of this class of machines probably lay with Seippel's inventions of that period, now generally referred to as the Comprex.[2] Although the gasdynamic and mechanical feasibility of this type of device has now been well established, practical and economically important applications of the Comprex have not been accomplished. From 1941 to 1943 Brown Boveri tested a pressure exchanger to serve as a high pressure stage of a locomotive gas turbine plant.[3] In the late 50s, the groups at Cornell University[4] as well as at Cornell Aeronautical Laboratory under Hertzberg actively investigated several different applications for wave machinery[5] built and used as a "wave superheater" to power a fluid mechanics test facility. In the early 60s, Power Jets Ltd. attempted to develop such a device as part of an air cycle refrigerator.[6] More recently Brown Boveri Company has been making a determined effort to introduce the pressure exchanger as a supercharger for truck and automotive diesel engines,[7] an application which had been pioneered by Berchtold.[8]

The realization of the current limitations of energy supplies and the resulting changed economics of energy technology have led some groups to revive this relatively dormant technology and look anew at the possible uses of wave machinery in the current era of costly and scarce energy. Can the wave chemical reactor compete with natural gas made from coal as a basic stock for nitrate fertilizer? Can the pressure wave supercharger help make the diesel with its potential fuel savings the engine of the 80s? Can an energy exchanger be an efficient thermal combustion cycle element and compete or out perform the high temperature turbine in an advanced power cycle?

In this paper I shall review the current state of this technology and share with you our group's thinking. It appears to us that wave machines have some important unique characteristics. First and foremost, they are direct work transfer devices and do not depend on heat transfer or thermal gradients for their operation. Consequently, they lend themselves very well to high temperatures, thus at least allowing the possibilities of higher cycle efficiencies due to the greater Carnot potential. Second, this high temperature operation is achieved without the need for high temperature materials due to the transient nature of the flow at any one fixed point in the system. Third, high component efficiency of a wave energy exchanger is at least possible even though losses and cycle imperfections are serious problems that need to be better understood. Fourth, these machines are basically high throughput machines and lend themselves well to large-scale processes such as are involved in the chemical and utility industry. Last, gasdynamic cooling by non-steady expansions allows very rapid cooling of a gas stream. The latter is a capability that has yet to be explored to any significant degree in the chemical processing industry.

In the analyses and applications that I will discuss, one or more of these characteristics have been explored. We are currently conducting a technology program under which we hope to extend the understanding of the performance of this type of device to the point where we can back up analyses with experimental data and modern fluid mechanical calculational techniques. We believe this is the combination needed to bring this type of machine into serious consideration.

BASIC OPERATING PRINCIPLES

Since the advent of shock tube technology, it has been well known that non-steady gasdynamic compression and expansion processes are a convenient and potentially efficient means for transferring pressure and even available energy from one fluid medium to another. Obviously, it is possible to compress and heat a static driven gas by transfer of wave energy from a higher pressure driver gas and to achieve a high temperature and pressure by such a process.

Although there is a long history of applications of wave mechanics to energy exchange in gases,[9] it was the clever invention of the "Comprex" by Seippel that essentially made a steady flow machine out of the shock tube. A wave-machine based on the Comprex principle is essentially a multiplicity of many shock tubes mounted on the periphery of a rotating drum. These "shock tubes" are rotated past a series of stationary nozzles which expose the gas to high pressure or driver gas for any desired period of time. The appearance of this high pressure reservoir is equivalent to the diaphragm break in the shock tube. A series of pressure waves or a shock wave propagates into the gas in the tube, accelerating, heating and compressing the driven gas, followed by the interface between the two gases. Figure 1 shows schematically the idea of a rotating wave machine and its relation to a shock tube.

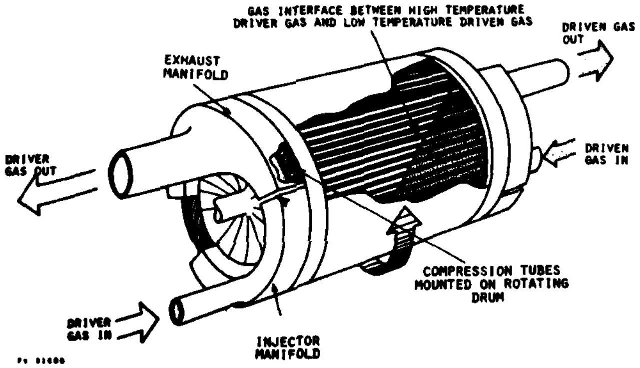

Figure 1. Schematic Diagram of a Typical Wave Machine.

The processes which can be made to occur in such a device can be completely generalized and a wide variety of transient pressure and thermal states can be generated in a highly controllable manner. One has control not only over timing but also pressure, velocity, temperature and composition of the two gas streams. Exposure to a high pressure reservoir is related to the bursting of a shock tube diaphragm; similarly, exposure to a low pressure or vacuum region can signal the start of an expansion and cooling process in the driven gas. By judicious choice of high and low pressure reservoirs, as well as solid walls or openings at either end of the drum, a series of waves can be generated that can create almost any heating or cooling cycle. In fact, as was done in the single pulse shock tube for chemical kinetic studies[10] a compressed and heated gas can be cooled or quenched by such a device in a highly controlled manner, leading directly to the several chemical processing applications to be discussed later.

Two more simple shock tube concepts which have been adopted into the wave machinery need to be discussed. Strong shock waves are a convenient but not efficient means of compressing a fluid, since there is a total available energy loss (entropy rise) across such a wave. If, however, a single strong wave is replaced by two or more weaker ones, the same compression ratio can be achieved at a considerably reduced loss (or smaller entropy rise) and consequently, at a higher compression efficiency. This effect is shown in Table I.

Table I. Adiabatic Static Compression Efficiency* (γ = 1.4)

Static Compression Ratio	One Shock	Two Equal Shocks	Three Equal Shocks	Four Equal Shocks
2	0.96	0.99	0.99	1.00
5	0.74	0.91	0.97	0.99
10	0.57	0.84	0.92	0.95
20	0.41	0.74	0.87	0.91
40	0.28	0.62	0.79	0.88

$$*\eta_c = \frac{\text{ISENTROPIC STATIC TEMPERATURE RISE}}{\text{SHOCK SYSTEM STATIC TEMPERATURE RISE}} = \frac{(T_2/T_1)_{\text{ISEN}}}{(T_2/T_1)_{\text{SHOCK}}}$$

The limit of the above suggestion is an isentropic, 100 percent efficient compression process. Also, it is clear that a small number of waves can achieve nearly isentropic compression over pressure ratios as large as 10 or 20.

Another important shock tube concept is impedence matching of the driver and driven gases, or the so-called tailored interface driver operation.[11] An impedence matched interface between two gases allows a sound or a shock wave to proceed from one gas into the other without any wave reflections at the interface. In terms of the gas conditions at the interface, this requirement means that the product of density and sound speed, i.e., the product ρa, as well as the specific heat ratio, γ, must be the same on each side of the interface. This condition allows the use of dissimilar gases under matched conditions where, in principle, wave energy can be transferred from one gas to another in an ideal manner; i.e., without any acoustic reflection losses at the interface.

Shock tube processes have historically been displayed as x-t diagrams, and such a diagram as shown in Figure 2a can be very useful again in visualizing the processes which occur in a wave machine, both within the tubes, in the reservoirs and at the tube ends. Figure 2b shows the locations of the various shock waves, S, contact interfaces, C, expansion waves, e, at nine key intervals during one cycle. In this diagram the driver gas enters at two pressure levels to produce a two-step compression process. In fact, the total compression process consists of three shock waves, the first one occurring when a solid end wall is imposed on the incoming driven gas, creating a hammer shock. The expansion process starts at point 3, as shown, and is timed so that it reverses the flow just as the interface reaches the tube end but never quite leaves the tube. The driven gas continues to exit the tubes up to point 5, after which a new charge of driven gas starts to re-enter the tube as the driver gas reverses its direction under the influence of the expansion. Points 6 through 9 are the scavenging cycle as the driver gas leaves the tubes and the new charge of driven gas flows into the tube to start a new cycle.

The following relatively simple wave diagram encompasses most of the concepts required for all the proposed applications. One of the key contributions of Hertzberg and Weatherston[12] was to point out the theoretical possibility of a perfect energy exchange process even across a large pressure or temperature ratio, by replacing the shock compression process with an isentropic compression and by impedence matching the two gases. Such a cycle is of course an idealized situation but helps to clarify the potential of these devices. Figure 3 shows the wave diagram for this ideal energy exchanger. Assuming no losses, it can be seen that this process can be 100 percent efficient and completely reversible. The key technology issue, which has never been faced experimentally, is to build a device approximating this performance.

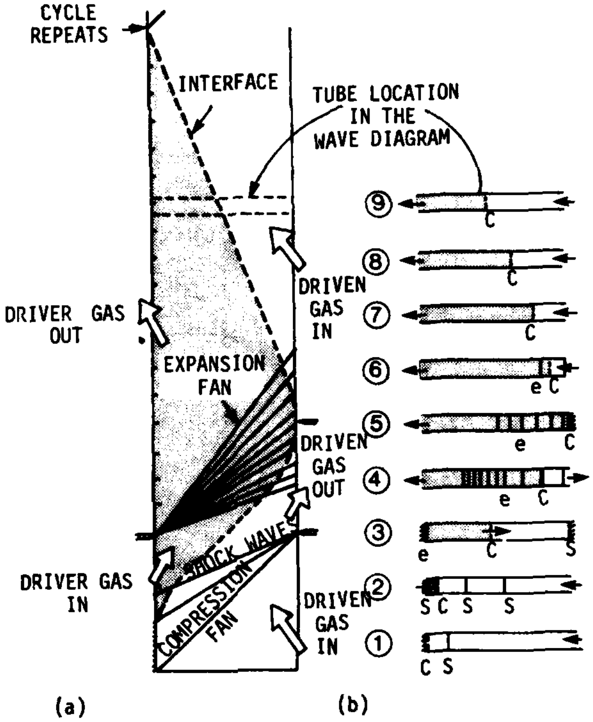

Figure 2(a) x-t Wave Diagram, (b) Schematic Snapshots of Process at Several Time Intervals.

The most important aspect of this ideal cycle is its potential to transfer all the available energy of expansion from the driver gas to the driven gas stream. That is not to say all the energy is transferred since the driver gas leaves with a thermal energy component. However, the change in available energy of the driver gas, i.e., $\Delta H - \Delta T_o S$, the maximum expansion work available in the driver stream when operating between the two given pressure levels can be transferred to the driven gas. This can be accomplished by substituting isentropic compressions for the less efficient shock processes and by impedence matching the interface gases so that no losses would occur in the energy transfer process either inside or outside of the machine. This of course reduced the total process to an ideal, isentropic, reversible one.

An important element had to be introduced into the wave diagram in order to prevent wave reflections at the tube ends to accomplish this ideal cycle, i.e., a circulating region of residual gases. These gases ideally circulate from one side of the machine to the other in a lossless manner. This circulating region is extremely difficult to implement in a real machine without incurring some losses.

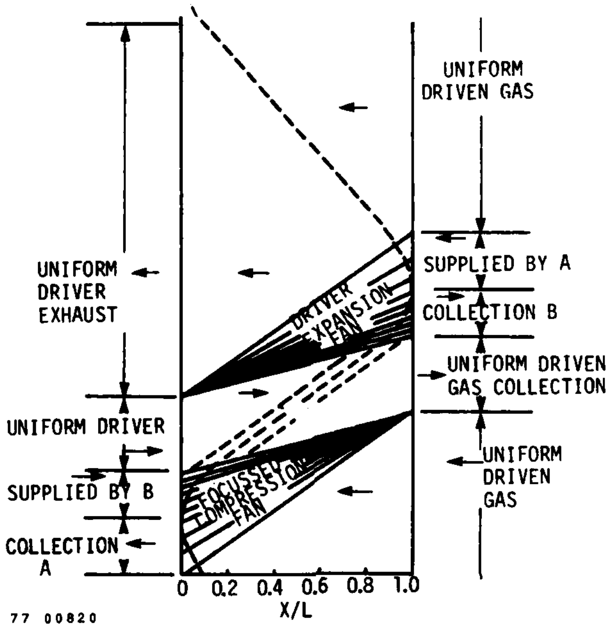

77 00820

Figure 3. x-t Diagram for an Ideal Energy Exchanger Cycle.

We believe the contribution of Hertzberg and Weatherston[12] to be the promise that efficient energy transfer devices can be considered which operate between two different fluids, thus allowing for the transfer of availability of work to a lower temperature gas. Previous investigators had always considered only a single fluid in their machines. In such a device the interface cannot be impedence matched if there is to be a temperature difference between the two streams. Consequently, by necessity, they accepted the losses generated by wave processes, whether they were created inside the device or in the manifolds. The more successful devices operated at modest pressure ratios where these losses were not very large. The two fluid machine can be made close to internally isentropic and the design challenge becomes the recovery of the maximum amount of the energy in the non-uniform flow in the ducting.

Converting an ideal cycle of this type into a machine is a development problem which has not been completely mastered as yet. Isentropic operation for both gases requires very careful attention to the wave structure to assure that all wave processes, such as reflections at the interface and the ends are minimized. This may and frequently can require the construction of a wave diagram much more complex than those shown in Figures 2 and 3. The design process is made doubly complex by the obvious requirement to close the cycle, i.e., the exiting driver gas must be compatible with an injection of a fresh supply of driven gas which must be identical to the initial charge.

Our group has attempted to generalize the problem of understanding such a wave diagram and generate some quantitative relationships with which the performance of these devices can be evaluated. Although we have been successful so far in only a limited case, the results demonstrate the physics of the process.

We have simplified the ideal reversible device of Hertzberg and Weatherston as shown in Figure 4 to make a tractable analysis. The extra ports on each side had to be added to allow closing of the cycle. This wave diagram is valid for both matched and mismatched gas streams and is composed of only simple regions which can be defined analytically. There are no waves crossing the contact surfaces. We had to introduce a second driver, in order to allow closing of the cycle, i.e., to match the velocity and pressure across the interface of the exiting uniform driver and the entering driven gas.

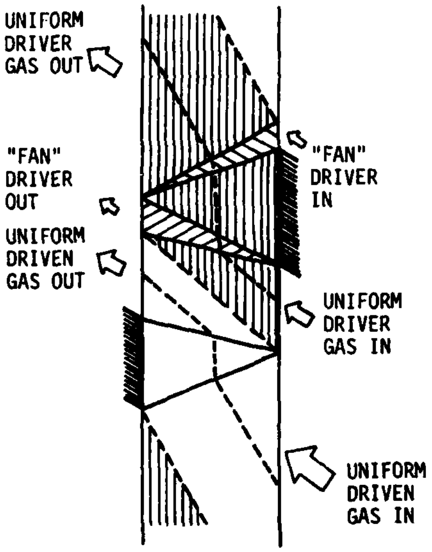

Figure 4. (left) Modified Wave Diagram Composed of Simple Analytic Regions.

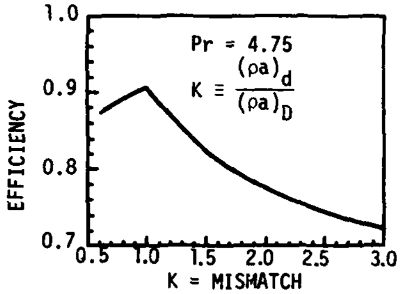

Figure 5. (above) Energy Exchanger Efficiency Calculated for Modified Wave Diagram of Figure 4.

From this wave diagram we can define an efficiency for this machine, represented by the ratio of the actual available energy transfer to the maximum possible available energy transfer for the fluid operating between the driver entrance conditions and the reference state. In order to close the cycle, some of this driver gas had to be introduced or ejected at intermediate pressures. This excess of energy in the fan driver is taken as a loss. Some of this energy could be recovered outside of the machine such as through a series of micro turbines to extract work from the non-uniform exhaust regions.

The results of the analysis are shown in Figure 5 for the case of $Pr = 4.75$. The maximum efficiency occurs when the impedances are matched. The efficiency curve changes curvature across the peak because for K less than one additional high pressure fluid must be injected to compress the gas, some of which escapes the machine before full expansion. Also the driver mass flow in the fan increases making the machine ineffectual due to choking at $K \sim 0.6$ for $Pr = 4.75$. The drop in efficiency for slight mismatching around the peak is not too great thus preserving efficient performance under real operating conditions.

This figure can be used to compare a single fluid machine like the BBC Comprex to our two fluid energy exchanger. In the Comprex, the cycle closing conditions require a complex series of shock waves to eventually equilibrate the driver gas. This process approximates the uniform condition we have assumed in our analysis. A single fluid comprex would operate at a mismatch parameter of about 2 in order to produce the same work as an impedence matched, K = 1, two fluid machine. The potential improvement due to impedence matching can thus be seen to be the order of 10 to 15 percent.

We will not dwell further with the difficulties of achieving an ideal energy exchanger design but rather will accept the degree of success that various investigators claim to have achieved and discuss their results. The technology program on wave machinery, in which our group is currently engaged, is designed to advance the state-of-the-art of this area. The problems of such a design are discussed in a companion paper by Zumdieck, et al.[13]

The previous discussions were based on ideal, inviscid fluids and the effects of interface mixing, finite tube opening times, boundary layers, and leakage were neglected. The magnitude of these effects depends strongly on the specific design under consideration, but an overall efficiency of about 85 percent appears achievable in a device operating with practical parameters. The accurate evaluation of these effects will have to await the development and verification of analytical techniques to calculate these effects.

Interface mixing should be minimized for the impedence matched case as such an interface is stable to Raleigh-Taylor instabilities,[14] i.e., no growth of disturbances should occur. A key question is how the interface behaves for non-impedence matched conditions, such as may be of interest for achieving larger temperature ratios for a given set of gases, or to allow specific non-ideal gas combinations to be used.

A primary source of interface mixing is the finite opening time of the individual tubes. As each tube rotates past the driver nozzle, the driver fluid will jet unsymmetrically into the tube. The depth of this penetration is related to the driver fluid velocity and the time interval required for the tube to open to a nozzle. It has generally been possible to restrict the affected zone to be only several percent of the tube length.

The mixing of the two gas streams can complicate the use of a wave machine in a practical cycle because of the requirement to separate the fluids for continuous closed cycle operation. Various concepts such as buffer gases have been suggested for minimizing this mixing. Although some containment of mixing can be achieved, all inhibition schemes represent added complexity and must be evaluated on an economic base for each application.

Boundary layers will affect the performance of the wave machine in the same manner as they do in non-ideal shock tube performance. Boundary layers interact with the interface due to differential action of the inviscid and boundary layer flow introducing vorticity at the interface, a phenomenon that has been thoroughly studied in shock tubes.[15,16] Boundary layer theory is complicated by the thermal cycling due to cyclic exposure to hot and cool gases. Standard boundary layer calculational techniques exist to estimate these processes, but the process can become complex for the non-steady flow problem.

Leakage at the ends of the drum between the nozzles and the tubes is another difficult design problem. This loss is very scale sensitive and although not expected to be a serious problem for utility or process application, it can be very serious for any small laboratory device. Solutions for minimizing leakages exist, such as drums made of low thermal expansion alloys,[17] rotating nozzles and a static drum, automatic control devices to compensate for thermal expansion,[18] hydrostatic pressure bearings to maintain a constant nozzle drum gap[19] as well as other innovative designs. A key unanswered question is the minimum size wave machine that can be designed without a dominant leakage loss.

In the following sections a variety of applications which have been considered will be discussed. No attempt will be made to generalize since the applications are varied and the design problems are very different. The first application, the Cornell Aeronautical Laboratory Wave Superheater, was one of the simplest and least demanding on device performance, however, it was a major achievement in device design and is still used as a landmark for proving the high temperature capabilities of the machines. We will complete the discussions by considering the most complex applications, those for chemical processing, which not only require high temperatures but also efficient energy transfer, minimized leakage and mixing, efficient energy recovery and in particular, careful attention to process economics.

FLUID MECHANICS TEST FACILITIES

The Cornell Aeronautical Laboratory (CAL) Wave Superheater

A direct application of the shock tube process to produce a flow of extremely hot gases for fluid mechanic testing purposes was the CAL Wave Superheater.[4,50] It was really the first two fluid comprex. Built in 1958 and utilized until its decommissioning in 1969, the wave superheater was an imaginative approach to supplying a "steady" stream of high temperature gases to an aerodynamic test facility. The efficiency of the device as a wave energy transfer machine was not too critical, except as it limited the ability to produce a high temperature (enthalpy) gas at a high pressure. The device was operated as an air open cycle and utilized shock heating with helium as the low molecular weight driver gas.

In the process of developing this facility the CAL group first built a smaller bench model, called "Little Rollo". Little Rollo achieved air temperatures of 1600 °K using a cold helium driver, in close agreement with simple shock tube theory.[21] In order to achieve the performance range desired for the wave superheater, a heated helium driver gas was used, preheated by pebble bed heaters. Air temperatures in excess of 4000 °K were achieved for run times as long as 15 seconds, and at stagnation pressures up to about 120 atmospheres. The practical limit on high temperature capability of this device proved to be the rotor tip speed. The design used broached tubes and proved to be exceptionally rugged and trouble-free. The research performed on Little Rollo proved to be invaluable in evaluating the imperfections, losses and deviation of the large machine from ideal theory. The accomplishments of that machine stand as strong support for predictable and practical design capability for this class of machines, being the first and only high temperature two fluid wave machine that has been built. Figure 6 is a photograph of the wave superheater drum.

TRANSPORTATION

Diesel Supercharger

Internal combustion engine performance can generally be boosted by increasing the total air throughput. Indicated power, brake power and mechanical efficiency, all go up and thus potentially increases the specific power and improve the fuel consumption of any given engine. In applying charge boosting to gasoline engines one very quickly runs into the limitations of knock and maximum cylinder pressures. Diesel engines, however, are not knock-limited and can benefit very directly from simple supercharging, usually from exhaust gas energy rather than by mechanical boosting. However, due to the need to provide a useful range of operating conditions and the effect of some unavoidable increased friction, decreased fuel consumption is not always achieved by supercharging.

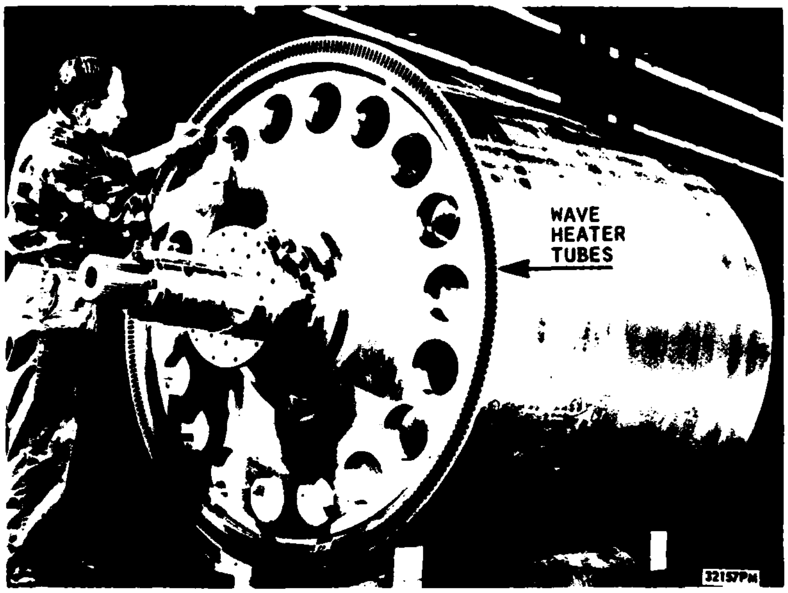

Figure 6. Photograph of the CAL Wave Superheater Drum.

Turbo superchargers are of course in wide use in the diesel industry, particularly in Europe. With small compressors and turbine efficiencies running between 70 and 80 percent, the turbo-supercharger efficiency is usually about 50 percent, falling off badly at both low and high speeds. It is difficult to obtain sufficient available energy from the exhaust to provide the required compressor work to give a turbo-supercharger efficient low speed boost. Also since the turbo-shaft speed is independent of the crank-shaft speed, there is a lag of as much as several seconds in the response of a turbo-supercharger.

The pressure wave supercharger, as typified by the Brown Boveri "Comprex", operates by transferring pressure energy directly from the engine exhaust to the intake air. Figure 7 is an isometric sketch of such a device. The multicell rotor is driven by a V belt from the crankshaft, usually at three to four times engine speed. High pressure exhaust gases flow into one end of the cells resulting in pressure waves which travel down the tube and compress the intake air. The compression waves are reflected from an expansion pocket and travel back down the cells allowing low pressure air to enter behind them.

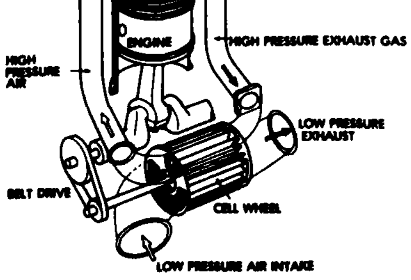

Figure 7. Schematic of the Brown-Boveri Company Comprex Dynamic Energy Exchanger Supercharger.

Table II. Comparative Performance.

Acceleration Times--Seconds

Speed Range km/h	Gears	Naturally Aspirated	Turbocharged	Comprex Boosted
0-100	All	23.0	14.0	12.5
50-90	3rd	10.0	7.0	5.9
90-100	4th	19.7	10.2	7.9

Gaseous Emissions--(g/mile)

Emission	Naturally Aspirated	Turbocharged	Comprex Boosted
HC	0.145	0.25	1.16
NO_x	0.99	1.24	0.66
CO	0.79	0.95	3.70

Fuel Economy--mile/gallon

Condition	Naturally Aspirated	Turbocharged	Comprex Boosted
Highway	35.8	33.7	33.1
Steady 50 km/h	49.3	43.3	42.0
Steady 90 km/h	32.7	30.5	33.0
Steady 120 km/h	19.6	18.0	23.2

This method of operation means that compression can be achieved whenever pressure wave energy can be obtained from the exhaust and effective boost can be obtained at very low speeds. The belt drive further gives the device excellent transient response, and excellent compression efficiencies of approximately 80 percent can be obtained at low speeds. The main drawbacks of the Comprex system appear to be their larger size, weight, and cost, and some problems with high frequency noise. The matching of a specific pressure wave supercharger to a particular diesel engine application involves careful selection of appropriate rotor size, siting of exhaust and intake manifolds, fitting of the bypass starting valve, the optimum rotor-crankcase speed ratio to give the desired performance.

A number of test programs have been performed with the BBC-Comprex pressure wave supercharger.[7,22] In one such program, a 1977 Opel Record 2100 D, was carefully monitored for naturally aspirated, turbo-supercharged and Comprex boosted operation.[23] Table II summarizes the results of that program.

The complexity of such a comparison should be emphasized. Whereas the naturally aspirated performance is the result of considerable optimization and experience, the problem of fitting and adjusting existing components or models to make such a direct comparison does not favor the superchargers. In each case very serious compromises needed to be made, as described in the detailed reports on that test program.[23]

The general conclusions are that supercharging enabled the diesel engine to achieve performance essentially equivalent to its gasoline equivalent, while extending its fuel consumption and emission advantages. The pressure wave supercharger in particular allowed satisfactory transient response to be achieved, and early problems of noise and installation have been overcome. The problem of cost, transient emission and transient fuel consumption still appear to require additional work, although the results of some other, more ideally matched tests have reported better results.[7]

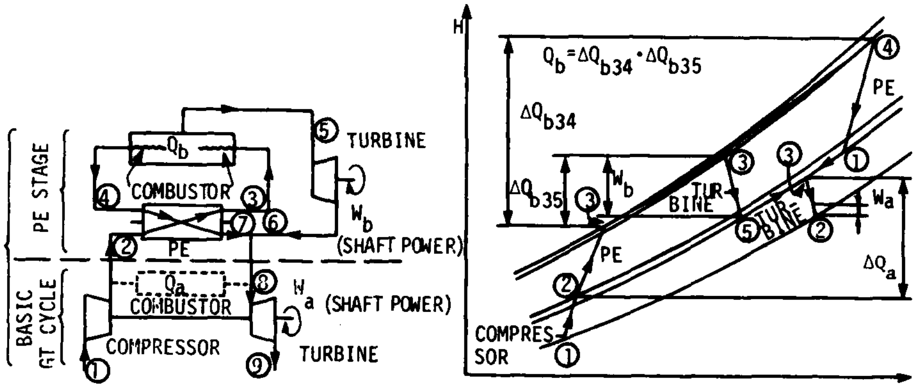

Figure 8. (a) Arrangement of a Throughflow Pressure Exchanger (PE) Gas Turbine (GT) Combination.

(b) Entropy-Enthalpy Diagram of Combined PE-GT Cycle.

Small Gas Turbine

The development of small gas turbines for passenger car and other applications has been held back by the difficulties of maintaining high overall efficiencies at sizes of 100 kW and smaller. Heat exchangers have been used with some success as a means of overcoming this disadvantage at a cost of compactness. A number of years ago, Berchtold and Lutz[24] suggested the pressure exchanger as an alternate means of overcoming this disadvantage.

The arrangement suggested by Berchtold is shown in Figure 8. The gas turbine cycle handles the air at lower pressure and the pressure exchanger (PE) at higher pressure. In this configuration the PE and a higher pressure combustor takes the place of the conventional combustor for the gas turbine cycle. Being a single fluid device it must split the combustor mass flow between the PE and a turbine. Both cycles produce shaft power as shown. The relative thermal efficiency gain, η_{tot}/η_{GT} of a combined system is shown in Figure 9 as a function of upper stage or pressure exchanger efficiency, η_{PE}. It can be seen that at the lower values of gas turbine cycle efficiency, the pressure exchanger can be very beneficial, for example, raising the total efficiency from 9 to 18 percent with a PE cycle efficiency of only 10 percent. Figure 9 shows clearly why this combined use is particularly attractive for improving the efficiency of small or low efficiency gas turbine cycles.

The key question of this application is the feasibility of achieving the desired efficiency for the pressure exchanger cycle. In this case the PE is operated in a parallel flow manner, i.e., the gases actually flow through the machine and exit on the opposite side, as opposed to the diesel crossflow system where there is essentially a hot and a cold flow side. The parallel flow is thought to have definite cooling advantages.

THERMAL POWER CYCLE APPLICATIONS

Some of the earliest applications of the Comprex concept involved improving the efficiency or output of thermodynamic machinery. In the 40s, Brown Boveri built a pressure exchanger to serve as the high pressure stage of a locomotive gas turbine for the British Railways based on the patent of Seippel[2,3]. It operated essentially on the same cycle as shown in Figure 8. So far as is known, the dynamic pressure exchanger worked satisfactorily, but did not give the anticipated performance. It was replaced by a heat exchanger which yielded a higher thermal efficiency. Some time later Power Jets, Ltd.[25]

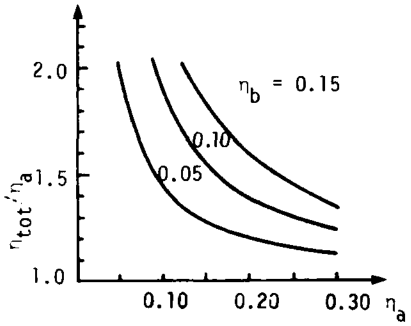

Figure 9. Total Efficiency Gain, η_{tot}/η_a of Combined PE/GT Cycle, Against Basic GT Cycle, η_a, and PE Efficiency, η_b.

Table III. Performance of Gas Turbine/Steam Combined-Cycle with Low Btu Gasifiers.

	Turbine Inlet Temp. °K		
	1365	1475	1645
Compressor pressure ratio	8	10	12
Percentage of compressor inlet flow used for turbine cooling	6.68	10.16	16.8
Gas-turbine efficiency, percent	26.8	29.2	31.7
Steam-turbine efficiency, percent	36.1	36.1	36.1
Overall energy efficiency, percent	37.0	39.3	42.0

experimented with the use of pressure exchangers as equalizers, a means of combining high and low pressure gas streams efficiently. Although their performance indicated improvements over competitive ejector performance, no data on further development is known to us.

Application of the ideas proposed by Hertzberg and Weatherston,[12] allowing new flexibility by the choice of suitable working fluids opens up the potential of more significant cycle improvements. In this age of critical energy supplies such a technology, potentially capable of increasing the efficiency of any energy conversion process by a significant factor, deserves a careful study. Consequently, our group has initiated studies to evaluate the benefits which could be achieved by applying wave machinery to several thermal cycle applications. The list of applications is by no means comprehensive; in fact, any thermal cycle which involves an energy source with working fluid temperature beyond those usually utilized in thermal conversion machinery is a good candidate for this technology.

High Temperature Gas Turbine Cycles

A low Btu coal gasifier combined with an open cycle gas turbine has been identified as a promising near-term alternative for electric power production.[26] The critical component of such a cycle is a turbine system capable of operating continuously at temperatures up to 2000 °K. If such development can be accomplished the open cycle, gas turbine, combined cycle promises to be an economical approach. Two major development programs are presently underway; one at the General Electric Company which utilizes water cooled blades and vanes, and the other at Curtiss-Wright Company which employs transpiration cooling. Both programs have demonstrated operation at 1800 °K on clean fuels. Both must overcome formidable technological obstacles to demonstrate safe, reliable operation on low Btu coal-derived fuels.

The energy exchanger offers a competitive alternative approach to achieving the same performance improvement.[27] For comparison purposes we have used a design study by the General Electric group in which system performance at three different turbine inlet conditions was investigated.[28] Their results are shown in Table III.

The energy exchanger cycle configuration we have chosen for this comparison is shown in Figure 10. The gasifier and main flow to the compressor have

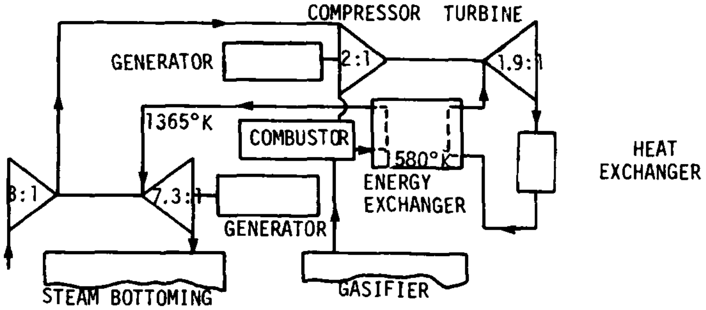

Figure 10. Schematic of Low Btu Gasifier Combined Cycle Gas Turbine System with Energy Exchanger.

been taken identical to the reference case. Since we are interested in near-term energy exchanger technology, a modest pressure ratio, 2:1, device with an energy exchanger inlet temperature of 1580 °K has been analyzed. We estimated 110 MWe output from the turbine power take off loop.

Our calculations indicate that 60 MW of high grade heat are rejected from the take off loop to the steam bottoming cycle. The three main sources of this heat are 1) non-ideal expansion in secondary loop turbine, 2) rejected heat from the energy exchanger rotor, and 3) throttled side streams to maintain the wave cycle operation. The exhaust from the driven stream is ducted at a pressure of 8 atm and 1365 °K to a turbine system equivalent in performance to the 1365 °K case used in the comparison.

A key element in the analysis of the energy exchanger cycle is an estimate of the losses of the system. Calculation of the losses of such a machine is as yet an imprecise process. Based on both steady and non-steady gasdynamic modelinging techniques, we have estimated the following losses, referred to percentages of the total energy input from the low Btu fuel. (See Table IV.)

Heat transfer from the hot gas to the cold gas via the intermediate temperature of the wall is a major loss accounting for a 0.55 percent loss in efficiency. Fluid friction losses due to unsteady opening, inlet and diffusion losses account for an additional 1 percent loss in overall efficiency. Leakage and shock losses were calculated to be negligible in this low pressure ratio machine.

A problem not treated was the mixing loss at the interface between the two fluids. For an impedence matched case, the density is equal for the two gases and no instabilities would be present. However, the opening and closing processes do introduce turbulence and could create a serious problem. Boundary layer mixing can also occur.

This application appears to us to be one of the most promising near-term applications of wave machinery. It is clear from this simple example that relatively modest energy exchanger technology has the potential of producing very significant performance gains. If we assume that the cost of the overall system is not significantly increased by the use of an energy exchanger, then the resultant effect of electricity cost is shown in Figure 11. This analysis was based on a simple, low pressure ratio energy exchanger, and it is expected that a higher pressure ratio system would challenge the performance potential of the highest temperature turbine technology presently under consideration.

Table IV. Loss Charged to Energy Exchangers in Pressure Ratio Two Reference Design

Loss Source	% Loss in Overall Efficiency $\frac{W_{loss}}{Q_{in}}$ 100
Power take off loop inefficiency	1.25
Heat transfer to tube walls	0.55
Throttling and heat transfer to energize auxiliary flows	0.45
Fluid friction to tube walls	0.70
Entrance and diffuser losses	0.50
Others, including: shock loss, windage, leakage	0.25

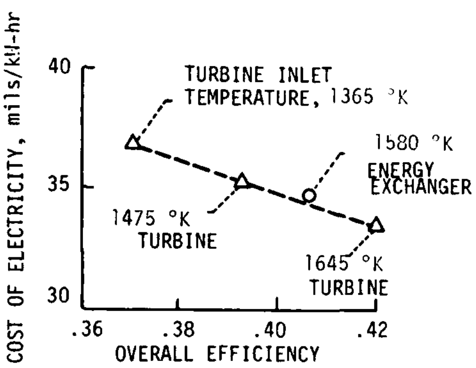

Figure 11. Effect of Turbine Inlet Temperature on Cost of Electricity of Gas Turbine/Steam Combined Cycles.

Fusion Power

Fusion processes leading to electric power generation have all the attributes to make them good partners for advanced energy conversion schemes. The system performance of fusion plants is very sensitive to the efficiency of the energy conversion process because of the need for a large amount of energy recirculation, increasing the useful output of the process strongly. This can easily be seen from consideration of the very simple process analyzed in Figure 12. The required yield of the plasma core defined as $H/L \equiv Q$, and the required fractional power recirculated, f, both strongly vary with the conversion efficiency, η_e. Since plasma Q is the parameter which measures the degree of confinement and consequently the "quality" of the fusion process, the significance of a high conversion efficiency to the fusion program, especially in its early stages where high values of Q are difficult to achieve, is great. A high efficiency conversion cycle could allow a low Q, near-term device to produce net saleable power.

A second characteristic of fusion power is that it is potentially a source of a very high temperature working fluid. Very energetic particles, 14 meV neutrons and in some cases γ rays or x-rays, are the source of energy. These high energy particles must be degraded in a converter or blanket region into a much lower quality heat, which eventually runs the power conversion system, i.e., steam turbines.

The Carnot efficiency of this secondary fluid loop sets the efficiency limits of the conversion system. In the process of degrading the energy from MeV to fractional eV values, the system is, of course, theoretically capable of producing far hotter secondary heat transfer streams. It is this high temperature potential of the fusion power reactor that can be exploited by the energy exchanger.

Present day fusion reactors are built to exploit the deuterium-tritium (D-T) reaction, since it has the lowest reaction cross section and produces a

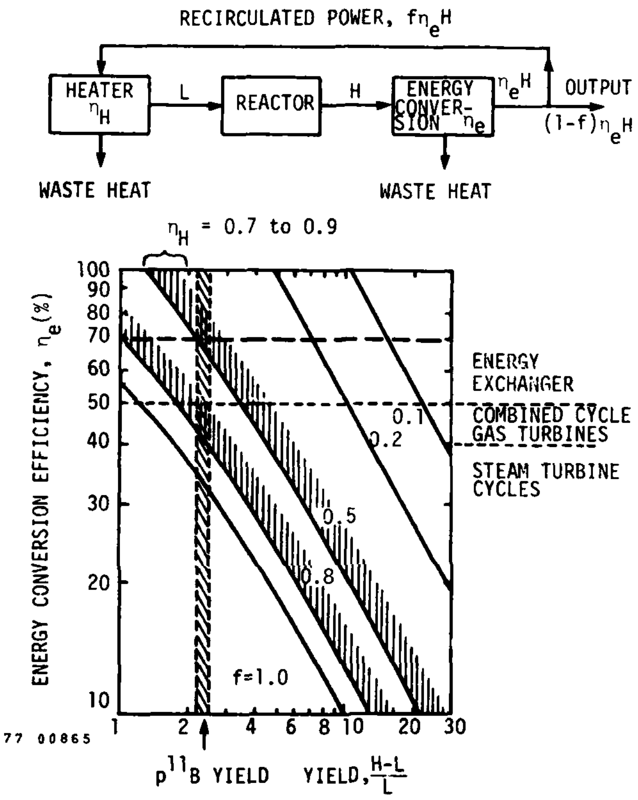

Figure 12. Energy Conversion Efficiency vs Thermonuclear Yield.

net energy gain at the least demanding level of plasma confinement. The current state-of-the-art is such that it is anticipated that a plasma with a $Q > 1$ will be achieved in the next generation of plasma experiments, exemplified by the Tokamak Fusion Test Reactor (TFTR) at Princeton, scheduled to be on line in the early 80s.[28] Concepts have been proposed whereby the neutron energy is captured in a high temperature ceramic blanket made of materials such as graphite, silicon carbide, tantalam or magnesium oxide.[29] A working fluid circulating through this blanket would be heated to a high temperature, the exact value depending on the material's precise capabilities. The heat transfer fluid might be an alkali vapor since alkali vapor binary cycles look favorable for achieving very high conversion efficiencies. The blanket or boiler of such a system would be a very difficult but, we believe, achievable technology.

If a high temperature, condensable vapor working fluid can be generated in such a blanket, then the conversion of this thermal energy to useful work in a binary Rankine cycle looks very promising. Figure 13 shows the schematic and T-S diagram of the cycle we have analyzed. Alternatively, a Brayton cycle, using a high temperature heavy noble gas, could be used, probably with similar results. The overall efficiency calculated for the cycle is given in Figure 14 Utilizing energy exchangers with pressure ratios of 3 to 4, overall cycle efficiencies for the binary system can be as high as 60-70 percent which, referring back to Figure 12, allows one to consider fusion reactor systems based on a low Q plasma source and still have circulating power fractions of less than 0.5.

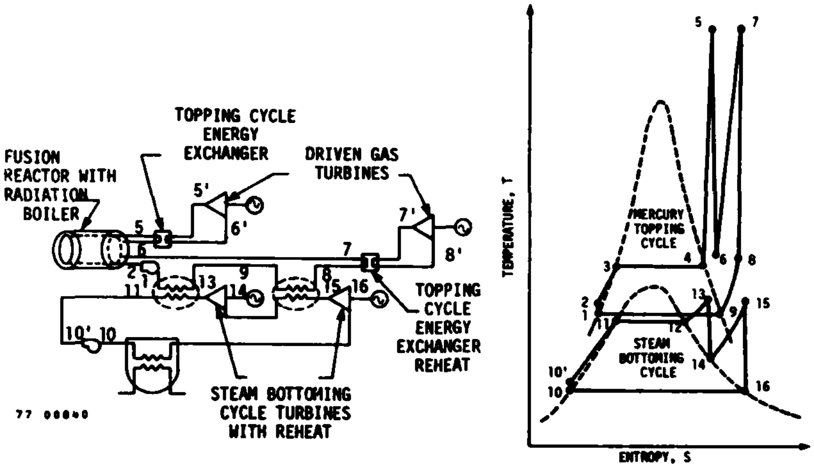

Figure 13. (a) System and (b) T-S Design for a Single Reheat Mercury Vapor Steam Combined Cycle Utilizing a Radiation Boiler and Two Energy Exchangers.

Plasma Qs of 3-5 appear very achievable within the next decade whereas plasma Qs of 10 or greater may require another 10 years of research.

An alternate and more futuristic use of the energy exchanger is in a more advanced, fusion reactor cycle.[30] Advanced fusion reactor cycles are those utilizing reactions which have smaller cross sections than D-T, but which have some special properties, mostly involving less neutron production. A particularly interesting one involves the reaction of a proton with boron-11, producing only x-rays and almost no neutrons (less than 0.1%).[31] This reaction has the potential of a nuclear system in which there is a minimum of activated radioactive material, which could operate in any environment without special safeguards.

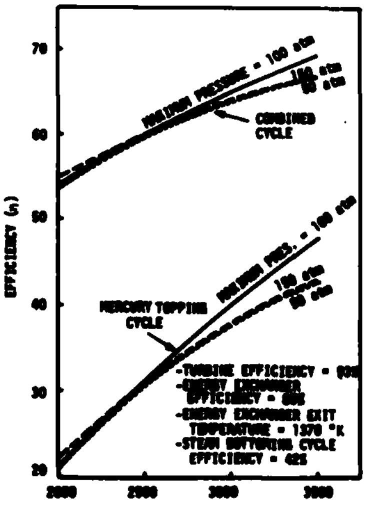

Figure 14. Cycle Efficiencies as a Function of Peak Cycle Temperature.

The $p^{11}B$ reaction has two characteristics that lend themselves to coupling to an energy exchanger. First, due to the nature of the output of the reaction, i.e., x-rays, it appears feasible to consider a unique, high temperature blanket or boiler concept based on volumetric absorption of the x-rays in a high Z gas or a noble gas seeded with high Z material to achieve the desired absorption. A second characteristic of this reaction is that it has a very limited yield potential, i.e., maximum of Q of only between 2 and 3, according to the latest calculations.[32] Such a low Q system needs a high conversion efficiency in order to be a viable candidate at all.

The new element which would make this type of cycle feasible is the x-ray radiation boiler.[33] The boiler must operate at relatively high pressures in order to make the total cycle efficient. The first wall between the plasma and boiler working fluid must be transparent to the x-rays and must simultaneously support the interior pressure of the working fluid. Hence a thin, high strength, low Z structural material is required. Further, the boiler cavity must be deep enough to allow absorption of the x-rays. The working fluid will probably also have to serve double duty and cool the first wall and support structure before absorbing too much energy. An initial look at potential materials indicated that berylium or carbon doped Be could meet the specified requirements.

Space Power Applications

Another application with many similar features is the space power application. Conversion efficiency plays a critical role here to reduce both the collector requirement and the waste heat radiator area. Obviously, any conversion efficiency increase has a major impact on system weight. There are two areas of energy exchanger application in this concept, i.e., the solar to electric energy conversion in space as studied by Hertzberg et al.[34] and the conversion of laser radiation into work on the ground in the case of a laser transmission link from space to ground. An overall study of the Space Laser Power System has been performed by Jones et al.[35] who have indicated a very critical role for the energy exchanger in such a system. This concept has been looked at by Taussig et al.[36] of our group.

Hertzberg et al.[34] have shown that very high gas temperatures are possible using concentrating solar collectors of special design. In order to attain high temperatures, efficient solar radiation absorption must be achieved at high pressures (100 atm) and high temperatures (4000 °K). Alkali metal vapors have the proper properties and potassium has been studied.[37] Absorption lengths of the order of 1 meter have been calculated for potassium at temperatures above 2000 °K and pressures of 10 atm or greater. One serious loss, i.e., the reradiation of the entrance window, can be minimized by the use of the incoming gas near the window to cool the window. Since radiation is deposited in depth, the radiation from the hotter gases will be partially absorbed or trapped by the cool gas near the window. This effect can have a major impact on the reradiation loss compared to a more usual black body loss. Figure 15 shows such a concept and its performance, which still falls off sharply near 4000 °K.

The performance of a potassium vapor binary cycle, similar to Figure 13 has been analyzed. To overcome the temperature limitations of conventional energy converters, the Rankine cycles analyzed utilized wave energy exchangers to transfer the available energy of the high temperature plasma to a cooler fluid for power extraction by conventional turbine. The system operates as a classical Rankine binary cycle utilizing a liquid metal for the high temperature topping cycle and a steam bottoming cycle. Figure 16 shows the variation of performance with condensing or radiator temperature and energy exchanger efficiency of a 2000 °K system. It is surprising that higher temperatures did not give a large increase in performance (69 to 73% at 85% energy exchanger

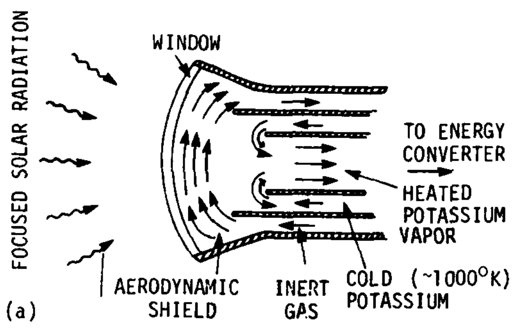

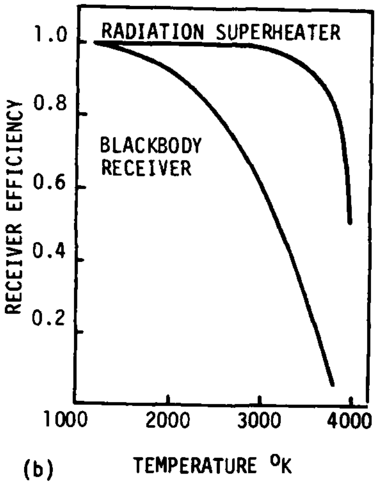

Figure 15. (a) Radiation Superheater Concept
(b) Solar Receiver Performance.

efficiency for 3500 °K). However, at 3500 °K the overall efficiency is still 71% for a 75% efficient energy exchanger, whereas at 2000 °K the performance has fallen to 62%. Combining the cycle performance with reradiation losses gives the result shown in Figure 17, indicating that operation beyond 3500 °K is unwarranted.

Jones[35] has integrated these concepts into a total laser based space power system. The several different concepts he evaluated always utilized a radiation boiler absorber/energy exchanger on the ground as the laser to electric energy converter. An energy exchanger was also utilized for all systems that

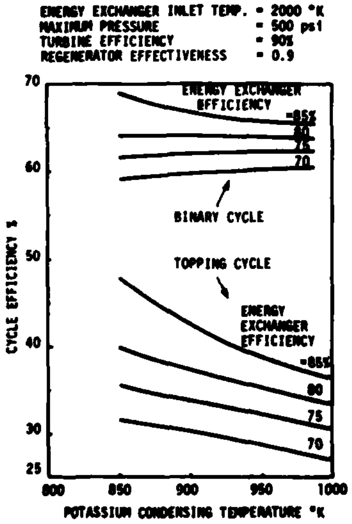

Figure 16. Potassium Vapor Binary Rankine Cycle Efficiency for Peak Energy Exchanger Temperature of 2000 °K.

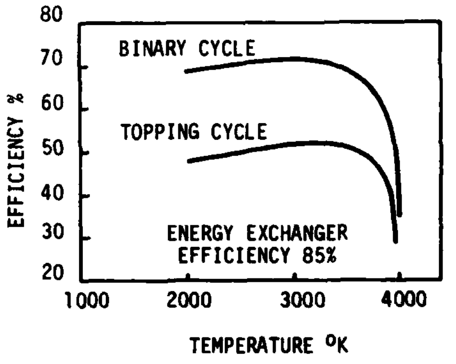

Figure 17. Overall Solar Collector-Efficiency.

converted solar energy to electricity in space prior to transmitting it back to earth. Consequently, he identified the energy exchanger as one of the key technology areas which required development in his plan for the Laser Space Power Satellite.

CHEMICAL PROCESSING

The use of non-steady gasdynamic techniques to heat a gas to high reaction temperatures to promote the formation of useful products and then to retain these products by extremely rapid cooling was suggested by Hertzberg and his colleagues in the early 50s.[38] Particular attention was given to the production of fixed nitrogen from air[39] as well as the conversion of butane to acetylene.[40] This group developed the single pulse shock tube,[10] a refinement of shock tube technology which could cycle a gas sample through a single controlled heating and cooling pulse for study of chemical kinetic behavior. The wave reactor for chemical processing is the steady flow analogue of the single pulse shock tube.

Nitrogen Fixation and Acetylene

The chemical process which has received the most attention is the fixation of nitrogen from air.[39, 41] It is well known that if air is heated under pressure (approximately 100 atm) to sufficiently high temperatures, nitrogen oxide will form in concentrations of 5 to 7 percent, sufficient for economic recovery. To retain the high NO concentrations, the hot air must be cooled very rapidly. A single pulse shock tube process is an ideal way to accomplish this under highly controllable conditions.

Hertzberg and colleagues sought commercial support for this concept from June 1956 to January 1958. Monsanto Chemical Company sponsored almost two years of research in this area.[42] The chemical kinetic data developed at CAL under Monsanto sponsorship indicated that acetylene could be formed in very high concentrations under shock tube conditions.[43] However, Monsanto's economic analysis did not warrant taking the concept into the pilot plant stage and Monsanto terminated the project relinquishing all rights to the data.

Data obtained under that program for butane diluted in argon, neon and water vapor, is shown in Figure 18.[43] Of particular interest was the fact that the water vapor did not yield the classic reactions as expected from the water gas system, and little CO appeared until the temperatures became very high.

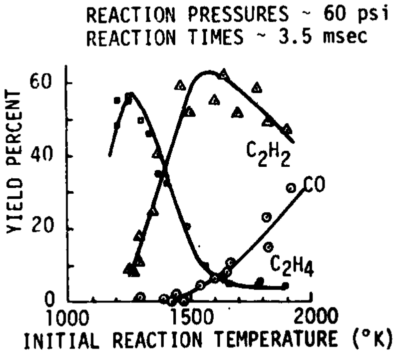

Figure 18. Carbon Conversion Efficiency to Ethylene and Acetylene (Reactant mixture of 0.75% C_4H_{10}, 16.7% H_2O and 82.3% (A+Ne)).

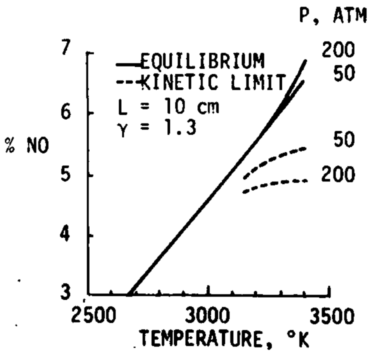

Figure 19. Nitric Oxide Yield.

The CAL success and the changed economic picture led our group to look anew at the nitrogen fixation process. The yield of NO as a function of temperature and pressure are shown in Figure 19, both for the equilibirum state and when followed by a fast (shock tube scale) gasdynamic cooling process. It is clear that concentrations as high as 6 percent are achievable. The kinetics of NO are relatively well known from early work of Zeldovich[49] as well as more recent shock tube measurements for individual key rates.[44,45] Consequently, the calculated yields are considered to be very realistic.

Our analysis of the CAL/Monsanto work indicated that a major weakness of their scheme was the excessive amount of peripheral equipment required in the gas streams. On the driver side, auxiliary power, a turbo compressor, heat exchanger and combustion chamber were required. A major innovation by our group was to completely eliminate the driver side auxiliary equipment by means of the "Flywheel Driver."[46] In this concept all the energy is supplied by the driven or reacting gas. A wave process energizes the driver gas and allows it to leave the machine at a higher total pressure than it entered. It can thus circulate back to the entrance, despite mixing and other losses, yet without any external power source. The flywheel driver significantly simplified the equipment requirements and allowed a new look at economic feasibility.

In our pursuit of this process we investigated various methods of incorporating the wave reactor into a commercially viable process, the production of nitric acid. Ammonia nitrate fertilizers are composed of approximately half nitric acid and ammonia. Currently, nitric acid is made from ammonia by the Haber process, utilizing methane as a feedstock. Our early investigations indicated the need to separate NO from air at low concentrations. Jackson Yu of Bechtel Corporation[47] made an ingenious observation that due to the anhydrous nature of the NO produced, a less complex stripping process was possible. This invention led to the development of the process flow chart as shown in Figure 20. The process used a fluidized bed reactor to deliver the process heat required.

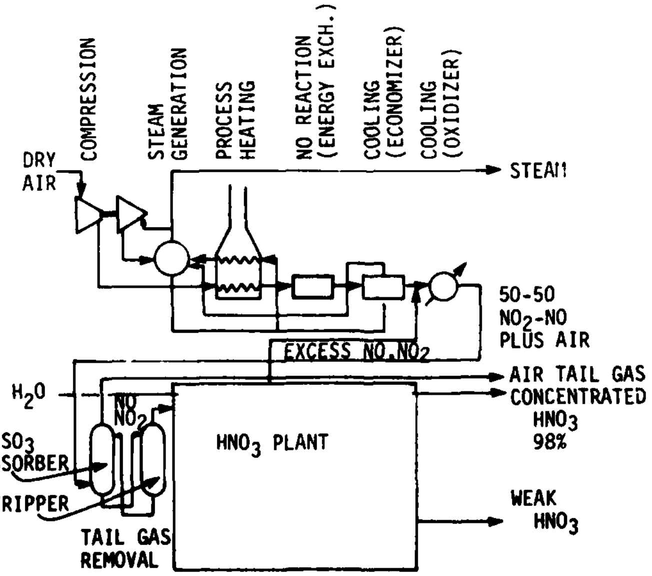

Figure 20. Conceptual Wave Reactor--Nitric Acid Process Flow Diagram.

An economic analysis of this process is shown in Figure 21. Comparison was made with a process based on the ammonia costing $124/ton, a cost roughly consistent with $2/MM Btu methane. Current methane cost is already beyond that level. It should be noted that our energy cost was assumed to be $1/MM Btu based on a coal fed fluidized bed process. This cost may also be too low in today's terms.

Basis: 500 T/day Nitric Acid, 100 percent basis. Product strength, 57 percent
300 Operating days per year
Capital Cost of Ammonia Oxidation Process - $11MM

Ammonia Oxidation Process			Wave Reactor Process		
Raw Materials	Unit Cost	$/ton		Unit Cost	$/ton
Ammonia 0.2845 ton/ton	$124/ton	35.28	Process water 242 gal/ton	0.1¢/gal	0.24
Utilities					
Electricity 15kwh/ton	2¢/Kwh	0.30	Fuel 13MM BTU/ton	$1/MMBTU	13.00
Cooling water 37,000 gal/ton	4¢/1000 gal	1.48	15 kwh/ton	2¢/kwh	0.30
Makeup water 173 gal/ton	0.1¢/gal	0.17	37,000 gal/ton	4¢/1000 gal	1.48
200 psi steam (-675 lb/ton)	$2/1000 lb	-1.35	236 gal/ton	0.1¢/gal	0.24
			300 psi steam (-1920 lb/ton)	$2/1000 gal	-3.84
Subtotal		$35.88			$11.42
Operating Labor and Materials	Annual Cost				
9 operators @ $15,800/year	$142,200	0.95			0.95
1 supervisor @ $19,000/year	19,000	.13			0.13
Operating Materials - 40% of operating labor		0.43			0.43
	Subtotal	1.51			1.51
Maintenance Labor & Materials (5% of $11MM)		3.67	ASSUMED TO BE THE SAME		3.67
Miscellaneous					
Indirect Plant Overhead - 80% of labor		2.04			2.04
Administration & General Corporate Expenses (2% of sales) (Assume $80/ton)		1.60			1.60
	Subtotal	7.31			7.31
Total Non-Capital Related Costs		44.70			20.24
Capital Related Fixed Costs					
(Insurance & Taxes 2.5% of Fixed Capital)		1.83			
Depreciation @ 10% per year straight line		7.34			
Return on Investment @ 25% before taxes		18.33			
	Subtotal	27.50	Available capital charges		51.96
TOTAL COST		$72.20			$72.20

Figure 21. Cost Estimate for Nitric Acid Process.

On the assumption of equal operating cost, the proposed wave reactor process has a 2:1 advantage in capital cost charges. At this stage of development that looks like a comfortable margin, but one that needs to be refined before the real economic viability can be established.

The wave reactor, for this process, ended up with an interesting design. In order to achieve the rapid quenching we had to minimize the scale of the device and thus ended up with a 4 mm dia. 10 cm long tube. 14,200 such tubes were aligned on a 1.2 m dia. drum operating at 3300 RPM. The rotor had a mass flow of 10 Kg/sec. Five rotors of this design were needed to produce 500 ton/day of HNO_3, which is roughly what a large ammonia nitrate plant would consume. Such an ammonia plant would cost $11 million. It is our position that building such a wave reactor is well within the technology of the turbine-compressor industry.

CO and Hydrogen Production

The combination of a high temperature gas source and the wave reactor allows the consideration of the production of hydrogen (H_2) from thermal decomposition of CO_2 for use in synthetic fuel production. This subject is the topic of another companion paper by Klosterman et al.[48] and will be summarized only briefly here.

The high temperature energy source studied was a fusion reactor; however, that is only incidental to the present purpose. The process considered was the production of carbon monoxide by thermal dissociation of CO_2. The CO produced is separated out and combined with steam in a standard water gas shift process to produce H_2 and to reform CO_2. Since the CO_2 is reformed, it circulates and the raw material is steam. The wave reactor enables the $CO+O_2+CO_2$ mixture to be quenched rapidly enough to freeze the CO concentration.

A simple flow chart for the process is shown in Figure 22. Other than the wave reactor and fusion source, standard commercial or development hardware has been considered in all areas. We have calculated a yield of CO at the wave reactor exit as shown in Figure 23. These data have been used to design a wave reactor which would be matched to the thermal output of a large fusion plant. The wave reactor would be similar to the NO reactor discussed above.

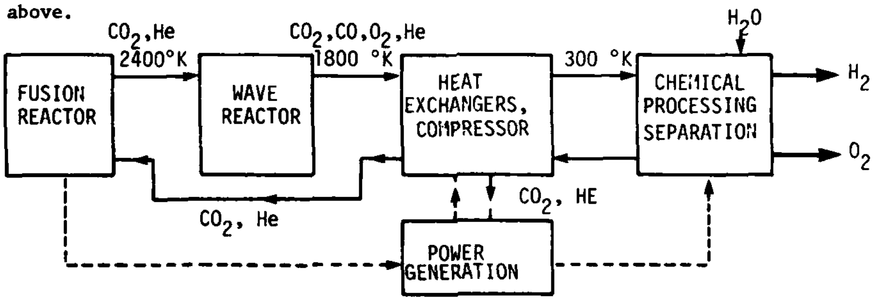

Figure 22. Schematic Diagram of Chemical Processing Cycle for H_2.

One interesting relationship which has been derived from that study is the dependence of the overall cycle efficiency on the wave reactor efficiency. For this purpose we have defined a wave reactor component efficiency as follows.

$$\eta_{\text{wave reactor}} = \frac{(h + \frac{1}{2}u^2)_{\text{out}} - \text{work output}}{(h + \frac{1}{2}u^2)_{\text{in}}}$$

The overall cycle efficiency is then defined as follows:

$$\eta_{\text{cycle}} = \frac{\Delta H_{\text{chem}} + \Sigma\, P_{\text{elec}}}{\text{Thermal Input}}$$

We have calculated the efficiency as shown in Table V for a 3000 °K temperature case.

Table V. Impact of Wave Reactor Efficiency on Overall Cycle Efficiency

Wave Reactor Efficiency(%)	Overall Cycle Efficiency(%)
90	34.0
80	23.3
70	12.6

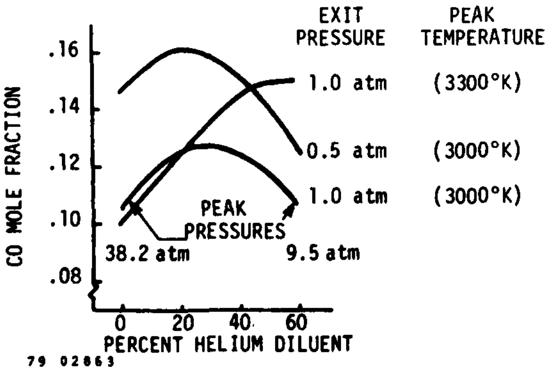

Figure 23. CO Yield at Wave Reactor Exit.

CURRENT DEVELOPMENT PROGRAM

In our attempts to find applications for wave machinery, we have been frustrated by our inability to convincingly demonstrate the performance of the wave machine itself. Chemical companies are not comfortable with such a novel technology. In thermal cycle applications the energy transfer efficiency is such a key question that it can make or break an application. Clearly what is needed is a technology demonstration which can produce the background data upon which studies of various applications can be based.

We have just completed the first year of a multi-year program to build such a technology demonstration device. To our knowledge this facility will be the first wave machine dedicated specifically to the purpose of upgrading the understanding of such machines. We intend to measure the efficiency of energy transfer, one of the really key parameters in many of the applications under consideration. The machine will operate with a modest pressure ratio and temperature in order to minimize the thermal design difficulties. The program also has a strong analytical component so that the results of the experiments can be compared with steady and non-steady analysis.

Figure 24 shows an isometric of the overall facility. Finally, Figure 25 is a photograph of the facility as it currently exists. The energy exchanger facility has the characteristics shown in Table VI.

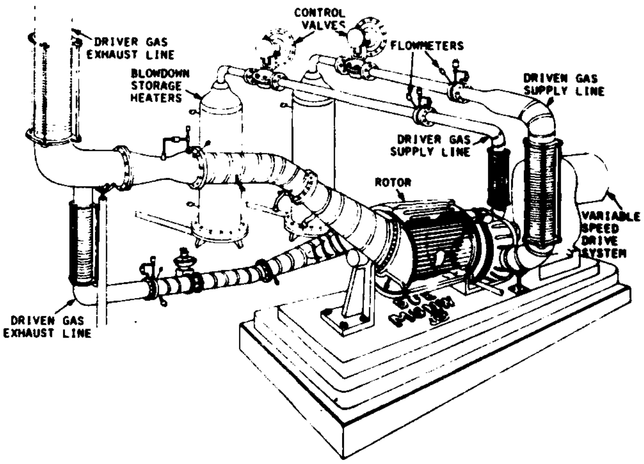

Figure 24. MSNW 100 kW Energy Exchanger Research Facility.

The objectives of this experiment are to verify the design point temperatures and pressures, measure mass and energy balances, and to measure the energy transfer efficiency and compare the results with analysis.

From this experiment, a combination of empirical, or validated analytical models for the behavior of these machines will be derived which will be useful in predicting the performance of a wide variety of wave machines. The facility to perform these measurements is not a trivial one. It has taken us over a year to complete the design, construction, and assembly of the system. Currently we are in the process of performing the very first gas flow shakedown experiments. We have to have some initial data at an early date.

Figure 25. Photograph of MSNW Energy Exchanger Research Facility.

Table VI. Energy Exchanger Parameters

Static Pressure Ratio	5.6
Driven Gas	80 Ar/20 He
Driver Gas	100 Ar
Mass Flow	2.7 kg/sec
Power Throughput	0.3 MW
Rotor Diameter	45 cm
Rotor Length	40 cm
Rotor Speed	4.6×10^3 cm/sec
Number of Tubes	100

CONCLUSIONS

Over the past 30 years the technology of wave machinery progressed steadily but as yet no significant commercial penetration has been made. The mechanical validity of the concept has, however, been firmly established. The CAL Wave Superheater demonstrated high temperature operation beyond any conceived application. The BBC Comprex pressure wave supercharger has clearly established wave machinery as a component in industrial machinery.

The pressure wave diesel supercharger is clearly furthest along the road to a practical application, and the Brown Boveri Company has made a major commitment to the success of this program. The gas turbine combined cycle utilizing low Btu gas made from coal appears to us to be a real candidate for a major development effort. The analysis on those applications indicates the ability to achieve significant performance improvements due to the utilization of higher gas temperatures. Additional and more detailed analysis is clearly warranted to assess the level of energy exchanger performance necessary to achieve significant gains.

It is in the areas of long-range energy solutions where wave machinery may well have its greatest impact. Both fusion and solar central thermal electric systems would benefit greatly from any increase in the conversion efficiency. Both are inherently very high temperature heat sources and consequently natural partners. However, the development of the high temperature, binary cycles necessary to take advantage of the high temperature represents a major technological challenge.

Finally, the chemical processing application appears to be another technology which offers great promise. Auxiliary technology such as ceramic heat exchangers and fluidized bed combustors may be required. The wave machinery for this application should be technologically feasible and should be pursued if the economics of the process continues to show promise.

ACKNOWLEDGEMENTS

The author wishes to acknowledge the hard work of many of his co-workers from whose original work he has freely drawn much of this paper. In particular he wishes to acknowledge Professor Abe Hertzberg's tireless efforts without which this area of technology would be quite dormant, Dr. Robert Taussig, who is leading the effort of our group in this technology and the several MSNW staff members, specifically Dr. Phil Cassady, Mr. Lee Klosterman, Dr. Bill Thayer, Dr. Nathan Vaidyanathan, and Mr. John Zumdieck, who are working on the difficult problems of this technology and who will be the ones to make it succeed. Support from the Department of Energy under contract numbers ER-78-C-06-1084 and ET-78-C-06-1095 is also gratefully acknowledged.

REFERENCES

1. P.H. Azoury, *An Introduction to the Dynamic Pressure Exchanger*. Proc. Inst. Mech. Eng. 180, (Pt. 1), 451-80 (1965-66).

2. C. Seippel, U.S. Patent No. 2 399394 (1946).

3. C. Seippel, U.S. Patent No. 2 461 186 (1949).

4. A. Kantrowitz, A. Hertzberg, E. McDonald, and E. Resler, Heat Engines Based on Wave Processes, Cornell University Graduate School of Aeronautical Engineering Report (1948).

5. R.C. Weatherston, W.E. Smith, A.L. Russo, and P.V. Marrone, *Gasdynamics of a Wave Superheater Facility for Hypersonic Research and Development*, CAL Report No. AD-118-A-1 (1959). Hertzberg, U.S. Patent No. 2836 665 and No. 2836 666 (1954).

6. D.B. Spalding, *Wave Effects in Pressure Exchanger, Part II*, Power Jets (Research and Development) Ltd., Rept. No. 2202/x 41 (1955).

7. Peter K. Doerfler, *"Comprex Supercharging of Vehicle Diesel Engines,"* Soc. of Automotive Engr. Paper 750335, Automotive Engr. Congress and Exposition, Detroit, Michigan (February 24-28, 1975).

8. M. Berchtold, *The Comprex diesel supercharger*, S.A.E. Paper No. 63A (1958).

9. A.F. Lebre, British Patent No. 290 669 (1928).

10. H.S. Glick, W. Squire, and A. Hertzberg, "A New Shock Tube Technique for the Study of High Temperature Gas Phase Reactions," from Fifth Symposium (International) on Combustion (1955).

11. C. Wittliff, M. Wilson, and A. Hertzberg, Journal of Aero Space Sciences, *26*, 4 (1959).

12. R.C. Weatherston, and A. Hertzberg, "The Energy Exchanger, A New Concept for High-Efficiency Gas Turbine Cycles," Journal of Engineering for Power (1966).

13. J. Zumdieck, et al. "The Fluid Dynamic Aspects of an Efficient Point Design, Energy Exchanger" to be presented at the XII International Symposium on Shock Tubes and Waves, Jerusalem, Israel (July 16-19, 1979).

14. G.I. Taylor, The Instability of Liquid Surfaces When Accelerated in a Direction Perpendicular to Their Planes, Proc. Roy. Soc. A201 (1950).

15. H. Mirels, AIAA Journal, *2*, 1 (1964).

16. H. Mark, "The Interaction of a Reflected Shock Wave with the Boundary Layer in a Shock Tube", TM 1418, NACA (1958).

17. Brown Boveri "Comprex" Supercharger.

18. A. Kantrowitz, An Automatic Control for Close Clearances in Rotating Machinery, ASME Paper No. 54-5 A-25 (1954).

19. W.B. Hansel, U.S. Patent No. 3 3841117 (1966).

20. Cornell Aeronautical Laboratory, Inc., Wave Superheater Hypersonic Tunnel, Description and Capabilities, Cornell University (1966).

21. William E. Smith and Roger C. Weatherston, Studies of a Prototype Wave Superheater Facility for Hypersonic Research, Cornell Aeronautical Laboratory, Report No. HF-1056-A-1 (1958).

22. M. Berchtold, and H.P. Gull, "Road performance of a Comprex supercharged diesel truck", S.A.E. Paper No. 118U (1959).

23. M.L. Monaghan, "Two Ways to Boost a Light Duty Diesel". Society of Automotive Engineers Inc. 0148-7191/7910226-0038 (1979).

24. M. Berchtold, T.W. Lutz, "A New Small Power Output Gas Turbine Concept", ASME Paper No. 74-GT-111 (1974).

25. D.B. Spalding, "A note on pressure equalizers and dividers", Power Jets (Research and Development) Ltd, Rept. No. 2251/Px 3 (1958).

26. J.C. Corman, "Energy Conversion Alternatives Study", ECAS, General Electric Phase I Final Report, Volume 1." Executive Summary (February, 1976).

27. J.F. Zumdieck, et al. "The Energy Exchanger in Advanced Power Cycle Systems" to be presented at the 14th Intersociety Energy Conversion Engineering Conference, Boston, Massachusetts, Paper No. 799427 (August 5-10, 1979).

28. M. Murakami and H.P. Enbank, Physics Today, *32*, 25 (1979).

29. A. Hertzberg, J. Dawson and P. Rose, *Near-Term Fusion Reactors Through Efficient Energy Conversion,* Mathematical Sciences Northwest, Inc., Preliminary Report (July, 1978).

30. J. Rand McNally, Jr., "Advanced Fusion Fuels", Proceedings of the Sixth Symposium Engr. Prob. Fusion Research, IEEE Pub. No. 75CH1097-5-NPS, p. 1012 (1975); and "Advanced Fuels for Nuclear Fusion Reactors", Nuclear Cross Sections and Technology, NBS-SP425, Vol. II, p. 683 (1975).

31. John M. Dawson, *Alternate Concepts in Controlled Fusion,* Part C: Fusion Reactor Using the P-^{11}B Reaction, EPRI Report ER-429-SR (May 1977).

32. G.H. Miley, H. Towner, and N. Ivich, *Fusion Cross Sections and Reactivities,* Report COO-2218-17, University of Illinois, Urbana, Illinois, (1974).

33. Mathematical Sciences Northwest, Inc., *High Thermal Efficiency, Radiation Based Advanced Fusion Reactors,* Report to EPRI. EPRI ER-544 (April 1977).

34. A.T. Mattick, A. Hertzberg, R. Decher and C.V. Lau, J. Energy *3*, 30 (1979).

35. Laser Power Conversion System Analysis, Lockheed Missile and Space Company NAS3-21132 (LRC) (1978).

36. R.T. Taussig, and J. Zumdieck, "Energy Exchanger Technology Applied to a Laser Heat Engine," Third NASA Conference on Radiation Energy Conversion, NASA - Ames Research Center, Moffett Field, Cal., Progress in Aeronautics and Astronautics, Vol. 61, K. Billman, ed. (Jan 26-28, 1978).

37. A. Hertzberg and C.V. Lau, "A High Temperature Rankine Binary Cycle for Ground and Space Solar Engine Applications," Third NASA Conference on Radiation Energy Conversion, NASA - Ames Research Center, Moffett Field, Cal., Progress in Aeronautics and Astronautics, Vol. 61, K. Billman, ed. (Jan. 26-28, 1978).

38. A. Hertzberg, H.S. Glick, W. Squire, and R.C. Weatherston, "Methods and Apparatus for Carrying Out Gas-Phase Reactions Which Require a High Temperature to Promote the Reaction and Rapid Cooling to Preserve the Reaction Product," U.S. Patent Numbers 2,832,665 and 2,832,666 (1958) and 2,902,337 (1959). Also: "The CAL Pressure Wave Chemical Reactor AFOSR TN 64-2530."

39. A. Hertzberg, "Nitrogen Fixation for Fertilizers by Gasdynamic Techniques," in Proceedings of the Tenth International Shock Tube Symposium, Kyoto International Conference Hall (1975).

40. A. Hertzberg and H.S. Glick, "Kinetics Studies in a Single-Pulse Shock Tube," Printed in AGARD, No. 41, Chapter IV D, 161-182 (1959).

41. Nathan Gilbert and Farrington Daniels, Industrial and Engineering Chemistry, *40*, No. 9:1719-1723 (September 1948).

42. CAL/Monsanto Acetylene Wave Reactor Study (1956-1958).

43. H.S. Glick, "Shock Tube Studies of Reaction Kinetics of Aliphatic Hydrocarbons," from Seventh Symposium (International) on Combustion (1959).

44. K.L. Wray and J.D. Teare, J. Chem Phys. *36*:2582-2596 (May 1962).

45. M. Camac, R.M. Feinberg, and J.D. Teare, *The Production of Nitric Oxide in Shock Heated Air*, AVCO Research Report 245, AVCO Everett Research Laboratory, Everett, Mass. (December 1966).

46. Mathematical Sciences Northwest, Inc., U.S. Patent No. 3,998,711 (December 21, 1976).

47. Jackson Yu, Private Communication.

48. E.K. Klosterman et al. "The Use of an Unsteady Wave Chemical Reactor as a Key Element in the Production of H_2 for Use in Synthetic Fuel Production", to be presented at the XII International Symposium on Shock Tubes and Waves. Jerusalem, Israel (July 16-19, 1979).

49. Ya Zeldovich and Yu Raizer, *Physics of Shock Waves and High Temperature Hydrodynamic Phenomena*, Academic Press, New York and London (1966).

50. J.J. Nainiger, and R.K. Burns, "Performance Potential of Combined Cycles Integrated with Low-Btu Gasifiers for Future Electric Utility Applications", NASA TM-73775 (December 2, 1976).

THE REAL THING:
BLAST WAVES FROM ATMOSPHERIC NUCLEAR EXPLOSIONS

HAROLD L. BRODE

Pacific-Sierra Research Corporation
1456 Cloverfield Blvd., Santa Monica, California 90404, USA

In the years between 1946 and 1963 (including a three year moratorium), the U.S. conducted over 200 nuclear tests in the earth's atmosphere. Since then, only underground tests have been carried out by the U.S. The possibility of a complete test ban prompts us to evaluate what was learned from the past atmospheric testing, and what is left to learn. This paper reviews the atmospheric test program relevant to blast phenomenology, identifies some problems remaining and suggests possible directions for further simulation and study.

Since the first nuclear explosion in 1945, much has been learned about such weapons of war, and as knowledge of the effects of nuclear weapons has grown, so has an appreciation of the importance of minimizing the devastation and risk to life in the event of their use accidentially or intentionally. From 1945 until 1963 (excluding a three-year moratorium) many nuclear explosive experiments were conducted in the atmosphere. Most of these shots were for the development of weapons; relatively few tests were exclusively conducted for studies of weapons effects. With the atmospheric test ban, came the end of easy and direct measures of blast or thermal or other atmospheric explosion phenomena. Since then, all U.S. testing has been done underground. A complete or comprehensive ban on all nuclear tests is now likely. What was learned in those years of atmospheric testing? What is left to discover or to figure out? What blast simulation methods are available to extend our knowledge in the absence of nuclear tests?

This paper provides a brief summary of the nuclear effects investigations of the past, with emphasis on physical effects, noting some omissions and failures in the previous test programs. The paper concludes with some suggestions for promising and potentially important programs of continued research.

TRINITY (Alamagordo, New Mexico) 1945

Even before the first nuclear explosion at Alamagordo, New Mexico, theory and experiment had contributed to the then fragmentary knowledge of air blast. These first predictions were quite elegant and sophisticated, e.g., Taylor (1950),[1] Bethe (1944).[2] Measurements on the TRINITY shot, however, were very limited. Everyone is familiar with the high-speed pictures of that very first earthly fireball from a nuclear detonation (Glasstone, 1962).[3] Those pictures, e.g., Fig. 1, prompts some questions, which have never been adequately answered. What causes the so-called "dirt cloud" ahead of the "Mach Front" which in turn precedes the strong fireball shock wave? What causes the bright puffs? What generates the violent, turbulent nature of the "dirt cloud?"

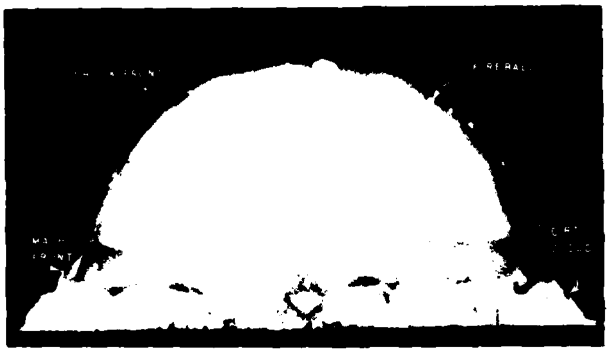

Fig. 1. TRINITY fireball (20 kt, 30 m height of burst) 10-20 msec after detonation.

HIROSHIMA/NAGASAKI (Japan) 1945

A few weeks after the TRINITY test, two bombs were dropped on Japanese cities. While the devastation was enormous, it represented less destruction than other WWII raids such as the fire bombing of Tokyo and Yokahama, which destroyed nearly two-thirds of the world's largest city. Observations of damage at Hiroshima and Nagasaki represent, today, our largest source of information about the effects of nuclear blast waves on urban and industrial targets. Extensive surveys of the damage in both cities[4,5] have helped to document the structural, as well as human consequences. Unfortunately, almost no direct measurements of the blast phenomena exist. Elaborate deductions from observations made more than a month later have lead to some estimates of the nature of the blast wave itself (Penny, Samuels, and Scorgie, 1970),[6] and one pressure record from a parachute-hung microphone gage dropped by the chase plane at Hiroshima gave a clear pressure-time trace (Fig. 2), but its interpretation is difficult (Brode, 1964).[7]

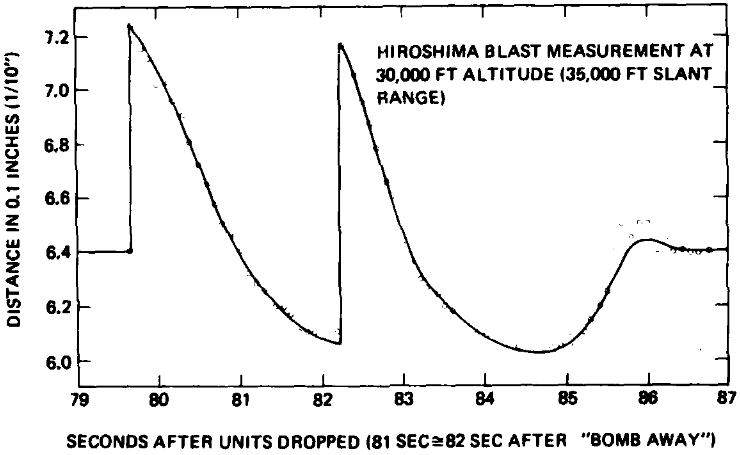

Fig. 2. Record trace from Hiroshima burst (∿ 14 kt, 567 m height of burst).

The relatively high burst height (567 m) and low yield (12-14 kt) of the HIROSHIMA bomb lead to peak overpressures on the ground directly under the burst of around 230 kPa (30 psi). This reflected pressure drops to less than half its peak value in about a tenth of a second. Figure 3 shows what that kind of a pressure pulse did to a massive reinforced building. (Note the smoke stack and antenna or lightning rod still standing on the far uncollapsed corner of the roof). This close to ground zero, the blast approaches the building almost vertically. This structure was also gutted by fire. At greater distances the blast winds drag down most projections above ground such as buildings, trees, street poles, and walls.

Fig. 3. Hiroshima (∿ 14 kt, 567 m HOB) Heavy reinforced concrete 3-story building near ground zero.

The damage at Nagasaki showed serious consequences to industrial buildings and equipment and considerable influence of hills and valleys. The burst height was a little lower (about 500 m) and the yield a bit higher (about 23 kt) than that at Hiroshima.

CROSSROADS (Bikini) 1946

In the following year, two more bombs were dropped in a test of naval vessels in the lagoon of Bikini Atoll. While the effects were duly noted, relatively few blast measurements were attempted. The spectacular water column of the underwater burst is a familiar picture (Fig. 4).

Fig. 4. Rising cloud, falling water column and spreading base surge from BIKINI BAKER shallow water detonation (20 kt).

SANDSTONE (Eniwetok) 1948

Less than three years after the first nuclear explosion, three nuclear development shots were fired from 61-m towers with yields around 20, 40, and 50 kt. Only the crudest of blast measurements were made on those faraway islands; one set being a string of crushable beer cans as indenter gauges. Good highspeed photographs of fireball growth, however, provided a wealth of information about the early blast wave.[8]

RANGER (Nevada) 1951

Five small-yield shots, all air dropped in Nevada, constituted the RANGER series. No extensive effects tests were included, but a number of used cars and other vehicles were exposed. Fire did extensive damage.

GREENHOUSE (Eniwetok) 1951

GREENHOUSE was the first series that included extensive effects programs. These shots were on 61- and 91-m towers, leading to relatively high overpressures on the ground. Some very hard bunkers, as well as conventional buildings, were exposed (Fig. 5).[9] Ground zero is to the left in Fig. 5. The building had openings (windows and doors) in the front wall, but none in the side walls, so that high reflected pressures inside the structure blew out the side walls. Many measurements of blast parameters were attempted; air density, temperature, and material velocities as functions of time, as well as overpressures and dy-

Fig. 5. GREENHOUSE-EASY structure (47 kt, 91 m HOB) 1353 m range (∿ 50 KPa), showing sidewall blow-out and debris pattern.

namic pressures, impulses, durations, and effects on buildings, vehicles, animals, and bunkers. In addition, an attempt was made to document the cloud physics and late fireball behavior. This test series marked the first extensive effort to conduct scientific measurement of nuclear explosion phenomena and their effects on structures.

BUSTER-JANGLE (Nevada) 1951

A series of seven shots (a tower shot, four air bursts, the first "surface" burst, and the first buried burst (5.2 m underground)) late in 1951 lead to some blast measurements which included studies of altitude effects and terrain effects. For the cratering burst (JANGLE-U), measurements included missile impacts, ground motions (accelerations, displacements, stresses), base-surge phenomena, and various structural responses, including buried structures. The surface burst was primarily a fallout test, and neither crater nor blast were well documented. In addition, much of the instrumentation was expedient and lacking in sophistication.[10,11]

On the air drops, a group of small shelters was exposed.[12] Unfortunately, instrumentation was exceedingly crude, and the results of individual shots were not documented, since all three shots (BAKER, CHARLIE, and DOG) occurred before examination. A communal shelter was also evaluated.[13]

TUMBLER-SNAPPER (Nevada) 1952

A few months later, a series of four air and four (90-m) tower shots was carried out in Nevada. A few of these shots were extensively instrumented for blast measurements, including studies of pre- and post-shock sound speed,[14] air temperature,[15] air and dust density,[16] and overpressure.[17] Various gauge types were cross-compared, surface effects were studied extensively,[18-21] and effects tests included minefields, trees,[22] aircraft, vehicles, and structures.

IVY (Eniwetok) 1952

Later that year, a return to the Pacific saw the first multimegaton nuclear explosion (10.4 MT) burst on an island in Eniwetok. A low air burst of high yield followed two weeks later. Considering the limited land area, fairly ambitious blast measurements were laid out. Measurements were attempted for air density, particle velocity, air temperature, and overpressure vs. time.

UPSHOT-KNOTHOLE (Nevada) 1953

The next Nevada series included an expanding effort to understand surface effects on air blast for low burst heights. UPSHOT-KNOTHOLE involved 11 shots, with blast projects on several of them. Seven were tower shots, three were air-dropped bombs, and one was an artillery shell fired from a 280-mm gun. Table I suggests the extensive investigations underway during this series.

Table I. UPSHOT-KNOTHOLE Programs

BLAST PHENOMENA	BLAST EFFECTS
Overpressure[23] and dynamic pressure[24]	Aircraft (in flight and parked)
Blast asymmetries	Ordnance, military vehicles, minefields
Soil stabilization for thermal and blast	Underground[27] and basement[28] shelters
	Field fortifications,[29] POL
Hill and dale influences[25]	Communication equipment
Smoke (black)	Railroad equipment
Preshock pressures and sound speeds	Animals and dummies[30,31]
Height of burst & height of target	Truss[32] and open-frame structures[33]
Precursors and thermal/blast effects	Wall & roof panels, 2-story homes[34]
Diffraction around shelters[26]	Trees (conifers)[35]
Negative phase	Field medical equipment

An example of the overpressures measured in a hill and dale experiment is illustrated in Fig. 6.[25] The low air burst pictured in Fig. 7 raised heavy dust clouds, but sucked only a small fraction of the dust up into the stem and cloud. All experiments were not complete successes, and measurements were frequently cut short or interrupted by physical damage from blast, debris impacts, dust clogging, thermal heating, nuclear radiation, or EMP interference.

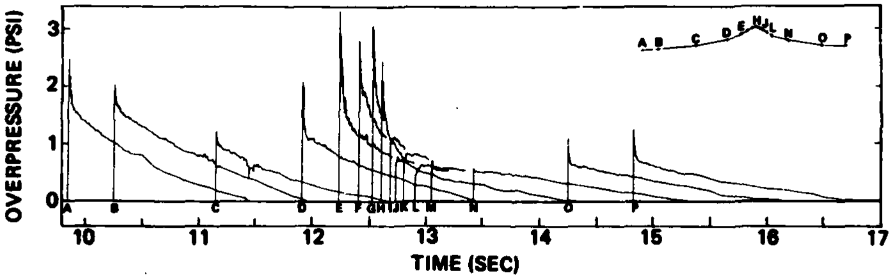

Fig. 6. UPSHOT-KNOTHOLE positive phases of pressure records across a hill.

CASTLE (Bikini/Eniwetok) 1954

In this series, six shots in the Pacific, including the largest U.S. test yield, CASTLE BRAVO (15 MT), made it possible to study long duration blasts and the slow and intense thermal pulses from large yields. Surface effects on overpressure and dynamic pressure were studied. Besides structural response observations, the effect of rain on blast waves, the use of jeeps as dynamic pressure gauges, and the effects of blast on tree stands[36] and vice versa were all studied.

TEAPOT (Nevada) 1955

By early 1955 the number of experiments that could be fielded had grown, as had the number of effects aspects recognized as worthy of investigation. A special test (3 KT) at high altitude (11.2 km) was carried out. Figure 8 shows the scaled pressure and ranges from airborne cannister measurements on this shot.[37] Modified Sachs scaling which seems to apply reasonably well to these results, assumes that the effect of the variable atmosphere can be handled by scaling everything to an homogeneous atmosphere at the pressure and density of the gauge, regardless of the altitude and ambient conditions at the source or explosion point or in-between.[39]

A set of specially prepared surfaces around a 122-m tower were exposed to a 22-KT shot to test the development of precursor action.[40,41] One surface was black asphalt, one was flooded with a few inches of water, and one was the usual dry desert (lakebed) surface. Another shot, 8 KT on a 150-m tower, had both asphalt and desert blast lines. Out of this experience came a classification of precursed blast wave-forms that tracks the growth and decay of the thermally distorted blast.[41] Figure 9 shows sketches of the overpressure wave forms along with example traces from the water, desert, and asphalt blast lines. Comparable dynamic pressure wave forms have been constructed.[41] In general, while the peak overpressures are eroded by precursor action, impulse and duration are if anything slightly enhanced. The dynamic pressures, due to higher dust densities and irregular flows, included upward gusts within the highly turbulent wake of the precursor, and exhibited much higher peak values (several times higher than near-ideal blast waves at the same scaled range or peak overpressure level).

Fig. 7. UPSHOT-KNOTHOLE low air burst torroidal fireball, entrainment vapors, and heavy dust clouds.

Table 2 is a partial list of projects fielded on this series, including those associated with a cratering burst.

WIGWAM (Pacific) 1955

One deep ocean underwater burst was studied for effects. A 30 KT nuclear depth charge was detonated at 600-m depth in deep water.[3] Bubble and surface phenomena were recorded; shock propagation and hull responses were measured; radioactivity spread was studied.

REDWING (Pacific) 1956

The Pacific atolls of Bikini and Eniwetok provided scant ground for mounting experiments, particularly for large yields, and so, some seemingly excellent opportunities to gather information about large nuclear bursts were passed or only lightly covered in the 13-shot REDWING series. Fairly extensive use was made of war surplus jeeps as the cheapest dynamic pressure indicator. Their drag behavior was quite predictable side-on and face-on. Again, a partial

Table II. Operation TEAPOT Programs

PHENOMENA	EFFECTS
Air Blast	Air Blast
Free air[37]	Airblast on underground structures[50]
High altitude[37-40]	Concrete panels[51]
Height of burst & surface effects[40-47]	Residences[52] and mobile homes[53]
Fireball effects	Earth-covered structures
Overpressure & dynamic pressure[41-44]	Noise in shelters[54]
Dust, temperature & sound velocity[45,46]	Canned goods, packaged beverages
Precursor drag loading[47-49]	Aircraft in flight
	LNG,[55] LPG,[56] POL, elect. Util.[57]
Cratering and Ground Shock	Biological systems
Airblast-induced ground shock	Industrial buildings
Crater dimensions[62] & induced motions	Communication equipment, machine tools[58]
Radiation	
Gamma dose rate, neutrons	Ground Shock
Fallout from underground burst[61]	Buried structures[59]
Cloud Physics	Radiation
	Radiological defense[64]
Thermal Radiation	Biological systems[65]
Direct and ground reflected	Contaminated aircraft[66]
Smoke-screen protection[62]	
Spectrometer measurements[63]	Thermal Radiation
High time resolution	Aircraft in flight
Fireball growth	Detonation locator

list of programs of measurement suggests the broad scope and challenging nature of the field experiments on REDWING (Table III).

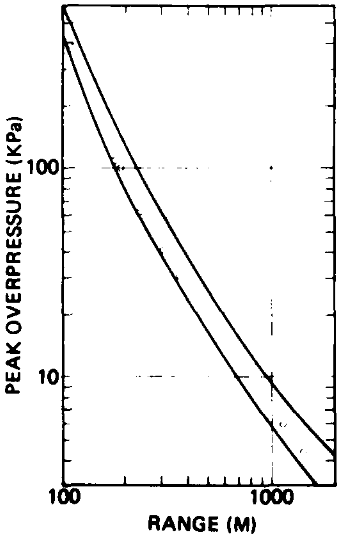

Fig. 8. TEAPOT-HA peak overpressure vs. slant range reduced to 1 KT sea level.

PLUMBBOB (Nevada) 1957

Meanwhile, back in Nevada, in 1957 the longest series yet (24 shots) allowed an ever widening diversity of investigations. While almost all of these shots were still weapons development tests, many opportunities existed to explore effects. Balloon-supported shots were tried for the first time. With a growing understanding of blast phenomena, it was no longer assumed that nothing could survive inside a fireball, and protective structures at high overpressures were designed, constructed, and tested. Further investigations of terrain effects were possible.[70] All sorts of equipment, from blimps and helicopters to bank vaults and air filters, were tested. The desert became populated with strange structures, contraptions, instruments, equipment, and experiments (Fig. 10). Precursed and non-ideal blast features were more completely examined, and hazards such as blast-driven debris and bodily transport by blast accelerations were studied. Further measurements helped determine that precursors in the desert from kiloton yields "cleaned up" below 70 KPa (10 psi). Contained underground nuclear detonations were first attempted, and the ground motions generated

Table III. REDWING Programs

Air Blast
- Ground surface measurements
- Free-air measurements
- Air burst (Mach reflection)
- Ground burst
- Blast over vegetated areas
- Positive phase and drag structures
- Aircraft in flight
- Ionospheric sound refraction

Fallout and Cloud Physics
- Activity in clouds, aerial surveys
- Shipboard radiological measures

Cratering and Ground Motion
- Geology and geophysics[67,68]
- Radii and depth[67,69]
- Ground shock

Thermal
- Chorioretinal burns
- Aircraft in flight
- Material response
- High resolution spectra

Nuclear Radiation
- Neutron and gamma flux and fluence
- Induced activity

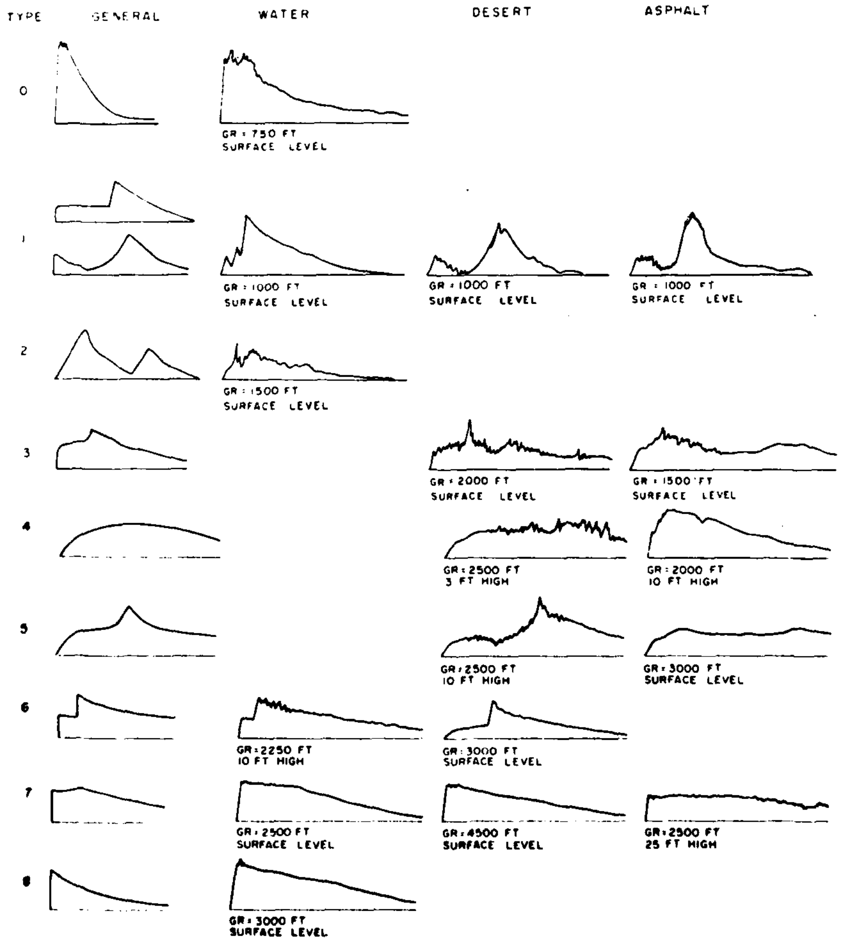

Fig. 9. Overpressure waveforms OPERATION TEAPOT shot MET.

Fig. 10. PLUMBBOB typical test instrumentation.

were the subject of study. Table 4 gives a partial list of PLUMBBOB program measurements.

Table IV. PLUMBBOB Programs

Air Blast
- Rough terrain[70]
- High-pressure blast, fireballs
- Above-ground structures[71,72]
- Aircraft, helicopter, blimp, missiles, rockets
- Shelters,[73,74] valuts, air filters[75]
- Blast-generated missiles[76]
- Precursors[71]
- Reinforcing & structural plates[77,78]

Thermal
- Eye protection[79]
- Aircraft, helicopter and blimp
- High-speed spectra
- Protection by clothes

Ground Motion
- Air-blast induced[80,81]
- Buried structure loading[73,74,78,82,83]
- Structure isolation[84]
- Spectra[85]
- Confined explosions[86-88]

Nuclear Radiation
- Soil activation
- Neutron, gamma-ray flux and fluence
- Gamma and neutron shielding
- Doses for aircrews
- Dosimetry instrumentation[89-91]
- Fallout[92,93]
- Foodstuff contamination[94]
- Plutonium monitoring

On the PRISCILLA shot (37 KT on a 213-m tethered balloon) fairly extensive blast measurements were made over the dry lakebed surface of Frenchman's Flat. Figure 11 shows peak dynamic pressures continuing to drop rapidly with increasing range, even at large distances.[71]

The largest structure exposed on shot PRISCILLA was a civil defense dual-purpose reinforced-concrete mass shelter,[73] which was at 488-m from ground zero. The surface peak overpressure was around 270 KPa. The below-grade shelter had a ramp entrance with an end wall at the bottom of the ramp where it turns to enter the shelter. The end wall, facing the shot, experienced 1300 KPa, and the end wall failed. Figure 12 shows this ramp and the failure of the end wall. Had the ramp continued up in the opposite direction (in place of the end wall) the high reflected pressures at the bottom of the ramp would have been eliminated, reducing the load on the shelter door, and avoiding the structural damage.

HARDTACK (Pacific/Nevada) 1958

The HARDTACK series had a Pacific phase (I) and a Nevada phase (II). The

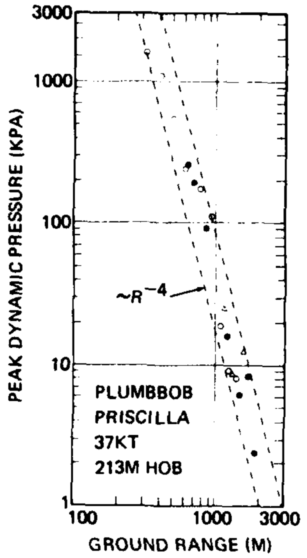

Fig. 11. PLUMBBOB PRISCILLA peak dynamic pressure vs. ground range.

Pacific phase had 31 shots, and the Nevada phase 18 tests. The Pacific phase included underwater shots and high-altitude shots as well as investigations of very high overpressure blast phenomena. The YUCCA test was on a free balloon at 26.2 km (86,000 ft). WAHOO and UMBRELLA were at 150-m and 46-m water depths, respectively. CACTUS and KOA were island shots (KOA was 1.3 MT in a water tank. The tank influenced the crater,[95,96] the ground motion,[97] the nuclear radiation and the EMP signals). A series of beams and slabs were tested at high levels on KOA, demonstrating survivability near 7600 KPa, but showing failure due to large footing displacements.[98] The whole structure and surrounding island sank two meters.[67] Figure 13 shows the closest beams, postshot. At overpressures from 540-1240 KPa, buried corrugated metal arches collapsed or showed heavy damage.[99,100] The structure at 1240 KPa is shown in Figure 14.

The remaining 24 shots were mounted on barges anchored in the lagoon, between islands, or in craters from previous shots. Two final shots in phase I (TEAK and ORANGE) were megaton-range rocket-borne shots at very high altitudes (76.8 and 43 km). Instrumentation for these shots was difficult, but excellent photographic coverage provided intriguing information.

The Nevada phase included some very small yield (subkiloton) shots[101] and some contained underground tests.[102-104] Ten tethered balloon shots

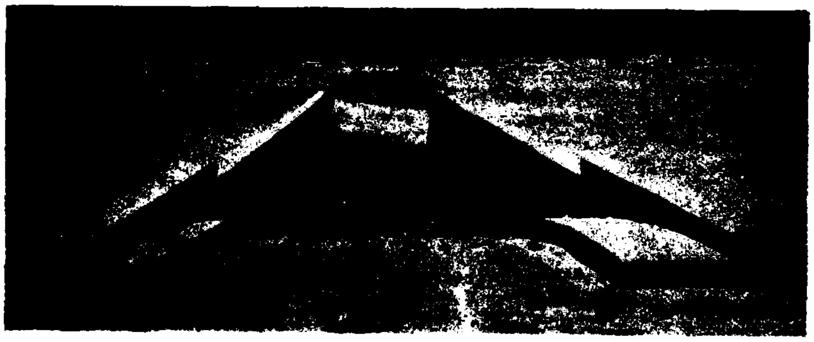

Fig. 12. PLUMBBOB PRISCILLA ramp to shelter (faced shot). Incident overpressure ≃ 270 KPa.

Fig. 13. HARDTACK-KOA (1.38 MT) deep beams (range 558-m) post shot ($\Delta P_s \simeq 7000$ KPa).

four contained underground tests, and four tower bursts made up phase II. Some structures tests were included.[105]

Fig. 14. HARDTACK-KOA (1.38 MT) Buried corrugated metal shelter, range 975-m, $\Delta P_s \simeq 1240$ KPa.

ARGUS (South Atlantic) 1958

Three shots in the kiloton range were fired above the atmosphere over the South Atlantic. Only modest photographic coverage and some ionospheric measurements were possible on these tests.

MORATORIUM (1958-1961)

From the end of October 1958 until mid-September 1961 the United States (and the Soviet Union) abstained from nuclear testing. In August 1961 the Soviets suddenly began atmospheric testing, more than 50 shots (as announced by the USAEC) before the end of 1961, and more than 40 in 1962.

DOMINIC, SUNBEAM (1961, 1962)

The United States began testing underground one month after the Soviet abrogation, but little preparation had been made for effects tests, and it was not until six months later that a small yield (0.42 KT) cratering test in hard rock (basalt) resulted in a 26-m deep, 81-m diameter crater (from depth of burial of 33.5-m).

More than nine months after resuming testing (June 1962) the tunnel shot (MARSHMALLOW) became the first of a series of vacuum-pipe experiments to study x-ray effects. Most of the rest of the Nevada test in 1961-1963 were underground weapon-development shots. However, four small near-surface shots were designed primarily for effects, SMALL BOY, JOHNNY BOY, and LITTLE FELLER I and II. SHOAL (about 12 KT) was shot in granite in Nevada in connection with research in the seismic detection of underground nuclear explosions. SEDAN, a PLOWSHARE test of 100 KT buried 194-m in alluvium produced the deepest crater (100-m deep, nearly 400-m diameter). A clump of dirt destroyed a massive structure 1 km away (Fig. 15).

Fig. 15. SEDAN. Ejecta impact on JANGLE structure about 1 km range.

Dominic, a Pacific series of less than 40 tests consisted mostly of air drops off Christmas Island. One shot was an operational test of a Polaris warhead fired from a submarine (FRIGATE BIRD),[3] and another was a proof test of the ASROC antisubmarine rocket (SWORDFISH).[3]

Several rocket-borne high-altitude shots concluded the U.S. atmospheric testing. STARFISH was a 1.4 MT detonation above the atmosphere (400 km). CHECKMATE, BLUEGILL, KINGFISH, and TIGHTROPE were all shot at tens of kilometers above Johnston Island. While microbarographs measured pressures on the ground, and some limited coverage by rocket-borne and aircraft-supported instruments was attempted, very little beyond photographic and electromagnetic observation was planned for these high-altitude shots.

ATMOSPHERIC TEST BAN

Observance of the atmospheric test ban treaty has meant the end of nuclear blast and thermal research experiments of a direct or simple nature. Certain measurements of nuclear source characteristics are possible underground, but even with heroic mining efforts, cavities sufficient to support meaningful blast experiments are impractical. It has proved more profitable to study simulation techniques based on a fairly complete understanding of the nuclear phenomena. Such indirect methods place great reliance on a full appreciation of the physics involved, and makes empirical observations or scaling dangerous and difficult.

What was overlooked or inadequately documented? Table 5 suggests a few areas in which further clarification or resolution may be useful. By the end of atmospheric testing, relatively few very high peak overpressure-time histories had been recorded, and only one on a megaton shot. The high-pressure loading and response of protective structures is still a very active subject of research.

Table V. Aspects of Nuclear Blast not Adequately Understood.

- High overpressure blast uncertainties
  - Near-ideal surfaces (dynamic pressures near double Mach peaks)
  - Non-ideal surfaces (enhanced drag?, impulses)
  - Structure interaction (loading, response, ablation rates, temperatures)
- Low overpressure blast uncertainties
  - Near-ideal surfaces (free air curves, surface normalization)
  - Non-ideal surfaces (dependence on yield and surface type)
  - Structure response (dynamics and material properties, hardening)
  - Height of target (aircraft in flight, Mach stems)
- Multiple burst interactions
  - Non-simultaneous (fire, debris, compound damage)
  - Simultaneous (blast reflection, enhancement)
  - Interactions (fire, dust, cloud rise, thermal)
- Blast/fire interaction
  - Blast suppression of incipient fires
  - Blast spreading of established fires (brands)
  - Glowing vs. flaming combustion (blast fanning?)
- Secondary impacts (disturbed blast)
  - Blast debris impact damage and injury
  - Blast bodily transported impacts, casualties
- Air-blast-induced ground motion
  - Dependence on geology and hydrology
  - Consequences of non-ideal blast loading

Table 6 identifies a few promising areas for simulation studies of nuclear air blast phenomena and effects.

Table VI. Some Nuclear Airblast Simulation Needs

- Aircraft in flight (drag, overpressure, thermal, combined)
- Structure response (structure interactions, duration and orientation)
- Blast/fire interactions (snuffing, fanning, spreading)
- Thermal influences on blast (precursors, preshock dust, smoke)
- Fireball physics (ablation, spallation, displacement)
- Height of burst and height of target (surface effects)
- Dust loading (preshock loading, postshock dynamics)

Simulation implies an incomplete reproduction of the phenomena or effect to be studied, and it is the essence of successful simulation to model those features necessary for the study of some important aspect or aspects without undue complexity or cost. The principal pitfalls lie in the demonstratability of relevance, i.e., that the proposed simulation experiments do faithfully reproduce some aspects of the phenomena to be studied, and that their isolated examination can be theoretically (or experimentally) justified.

For example, it is not enough to generate dust by intense thermal radiation pulses, if we are concerned about the dynamic properties of dust-laden shocks, nor is it obvious that mechanical means of dust loading can adequately represent the thermally-generated dust. Such simulation experiments place considerably more importance on an adequate (integrating) theoretical model for the overall phenomena.

REFERENCES

1. Sir G. Gaylor, "The Formation of a Blast Wave by a Very Intense Explosion," I and II, *Proc. Roy. Soc.*-Series A, Vol. 201 (1950).
2. H.A. Bethe, K. Fuchs, J. von Neumann, R. Peierls, W.G. Penny, *Shock Hydrodynamics and Blast Waves*, Los Alamos Scientific Lab., AECD-2860 (1944).
3. S. Glasstone (Ed.), *The Effects of Nuclear Weapons*, U.S. Dept. of Defense and Atomic Energy Commission (1957), revised (1962); [A subsequent revision with P.J. Dolan (Ed.) (1977) does not contain the list of nuclear tests.]
4. The Manhattan Engineer District, *The Atomic Bombings of Hiroshima and Nagasaki*, Los Alamos Scientific Laboratory (1946).
5. The United States Strategic Bombing Survey, *The Effects of the Atomic Bomb on Hiroshima and Nagasaki, Japan*, Report No. 92 & 93 (Vols. I-III), Physical Damage Division (1947).
6. Lord F.R.S. Penny, D.E.J. Samuels, G.C. Scorgie, *Phil. Trans. Roy. Soc. London*, Vol. 266, pp 357-424 (1970).
7. H.L. Brode, *Yield of the Hiroshima Bomb Derived from Pressure Record*, RM 4193-PR, The Rand Corp., Santa Monica, Ca. (1964).
8. R.A. Houghton, *Space Time Relationships Measured from the SANDSTONE Photography*, Los Alamos Scientific Lab, OS-28 (1950).
9. B.E. Pettitt, *U.S. Air Force Structures OPERATION GREENHOUSE Scientific Directors Report Annex 3.3*, (WT-29) Air Material Command USAF (1951), also Appendix I, Section II (WT-88) (1951).
10. S. Rankowitz, R.S. Chase, and J.B.H. Kuper, *OPERATION JANGLE Project 1.3 a Free Air Shock Arrival Times*, Brookhaven National Lab. (1952).
11. R.A. Eberhard, C.N. Kingery, W.F. Molesky, *OPERATION JANGLE Project 1.2a-1 Peak Air Blast Pressures from Shock Velocity Measurements Along the Ground*, WT-323, Ballistic Research Labs, Aberdeen Proving Ground, Md. (1952).
12. A.P. Flynn, *OPERATION BUSTER, Project 9.1a, FCDA Family Shelter Evaluation*, WT-359, Federal Civil Defense Administration (1952).
13. R.L. Corsbie, *OPERATION BUSTER, Project 9.1b, AEC Communal Shelter Evaluation*, WT 360, U.S. Atomic Energy Commission (1952).
14. R.C. McLoughlin, *Sound Velocity Changes Near Ground in the Vicinity of an Atomic Explosion*, TUMBLER Project 8.6, WT 546, USNEL (1953).
15. T.R. Broida, A. Broido, A.B. Willoughby, *OPERATION TUMBLER Project 8.2, Air Temperatures in the Vicinity of a Nuclear Detonation*, WT-542, USNRDL (1954).
16. E. Boulton, *et al*, *OPERATION TUMBLER*, *Pre Shock Dust Project*, 1.9, Army Chemical Center, WT-519 (1952).
17. N.A. Haskell and J.O. Vann, *OPERATION SNAPPER Project 1.1, The Measurement of Free Air Atomic Blast Pressures*, WT 511, AF Cambridge Res. Center (1953).
18. V. Salmon, *OPERATION TUMBLER, Project 1.2, Air Pressure vs. Time*, WT 512, Stanford Research Institute (1953).
19. G.W. Cook, V.E. Benjamin, *OPERATION TUMBLER, Project 1.13, Measurement of Air Blast Pressure vs. Time*, WT 521, David Taylor Model Basin (1953).
20. Ballistic Research Laboratory Staff, *OPERATION TUMBLER, Project 1.4, Air Blast Measurements*, WT 515, Aberdeen Proving Ground (1952).

21. F. Porzel, *OPERATION TUMBLER-SNAPPER, Project 19.2 a to f, Blast Measurements*, WT 556, Los Alamos Scientific Lab. (1952).
22. A.A. Brown, R.K. Arnold, W.L. Fons, F.M. Sauer, W.E. Reifsnyder, *OPERATION SNAPPER, Project 3.3, Blast Damage to Trees-Isolated Conifers*, WT-509, Div. of Fire Research, Forest Service, U.S. Dept. Agriculture (1953).
23. N.A. Haskell and R.M. Brubaker, *OPERATION UPSHOT-KNOTHILE, Project 1.3, Free Air Atomic Blast Pressure Measurements*, WT 715, AFCRC (1954).
24. C.D. Broyles, *OPERATION UPSHOT-KNOTHOLE, Project 1.1d, Dynamic Pressure vs. Time and Supporting Air Blast Measurements*, WT 714, Sandia Corp. (1954).
25. M.L. Merritt, *OPERATION UPSHOT-KNOTHOLE, Project 1.1c-2, Air Shock Pressures as Affected by Hills and Dales*, WT 713, Sandia Corp. (1954).
26. W.E. Morris, *OPERATION UPSHOT-KNOTHOLE, Shock Diffraction in the Vicinity of a Structure*, WT 786, Naval Ordnance Lab. (1959).
27. J. Meszaros, J. Randall, *OPERATION UPSHOT-KNOTHOLE, Project 3.28.1, Structures Instrumentation*, WT 738, Ballistic Research Lab. (1955).
28. E. Ruhl, *et al*, *OPERATION UPSHOT-KNOTHOLE, Project 24.3, AEC Shelter Instrumentation*, WT 790, Vitro Corp. of America (1953).
29. A.R. Fowler and D.R. Muller, *OPERATION UPSHOT-KNOTHOLE, Project 3.9, Field Fortifications*, WT 728, Engineer Res. and Devel. Labs., U.S.A. (1954).
30. R. Draeger and R. Lee, *OPERATION UPSHOT-KNOTHOLE, Project 4.2, Direct Air Blast Exposure Effects in Animals*, WT 744, Naval Medical Res. Inst. (1953).
31. J. Roberts, *et al*, *OPERATION UPSHOT-KNOTHOLE, Project 23.15, Effects of Overpressures in Group Shelters on Animals and Dummies*, WT 798, Lovelace Foundation (1953).
32. E. Sevin, *OPERATION UPSHOT-KNOTHOLE, Project 3.4, Tests on the Loading of Truss Systems Common to Open-Frame Structures*, WT 723, Wright-Patterson AFB Air Material Command (1955).
33. T.H. Schiffman and E.V. Gallagher, *OPERATION UPSHOT-KNOTHOLE, Tests on the Loading of Building and Equipment Shapes*, WT 721, Air Material Command, Wright-Patterson Air Force Base (1955).
34. J.B. Byrnes, *OPERATION UPSHOT-KNOTHOLE, Project 21.2, Effects of an Atomic Explosion on Two Typical Two-Story-and-Basement Wood-Frame Houses*, WT 792, Federal Civil Defense Admin. (1953).
35. F.M. Sauer and W.L. Fons, *OPERATION UPSHOT-KNOTHOLE, Project 3.19, Blast Damage to Coniferous Tree Stands by Atomic Explosions*, WT 731, Division of Fire Research, Forest SErvice, U.S. Dept. of Agriculture (1954).
36. W.L. Fons and T.G. Storey, *OPERATION CASTLE, Project 3.3, Blast Effects on Tree Stand*, WT 921, U.S. Dept. of Agriculture (1954).
37. N.A. Haskell, J.A. Fava, R.M. Brubaker, *OPERATION TEAPOT, Project 1.1, Measurement of Free Air Atomic Blast Pressures*, WT 1101, Air Force Cambridge Research Center (1958).
38. J.W. Reed, J.R. Banister, F.H. Shelton, *OPERATION TEAPOT, Project 1.3, Ground-Level Microbarographic Pressure Measurements from a High-Altitude Shot*, WT 1103, Sandia Corp. (1955).
39. H.L. Brode, "Review of Nuclear Weapons Effects," *Annual Review of Nuclear Science*, Vol. 18, pp 163-166, (1968).
40. J.F. Moulton, Jr., and E.R. Walthall, *OPERATION TEAPOT, Project 1.2, Shock Wave Photography*, WT 1102, U.S. Naval Ordnance Lab. (1958).
41. D.C. Sachs, L.M. Swift, F.M. Sauer, *OPERATION TEAPOT, Project 1.10, Air-blast Overpressure and Dynamic Pressure over Various Surfaces*, WT 1109, Stanford Research Institute (1957).
42. E.J. Bryant, N.H. Ethridge, J.H. Keefer, *OPERATION TEAPOT, Measurement of Air-Blast Phenomena with Self-Recording Gages*, WT 1155, BRL (1957.
43. M. Kornhauser and J. Petes, *OPERATION TEAPOT, Project 1.13, Drag Force Measurements*, WT 1111, U.S. Naval Ordnance Lab. (1958).
44. J.R. Banister and F.H. Shelton, *OPERATION TEAPOT, Project 1.11, Special Measurements of Dynamic Pressure vs. Time and Distance*, WT 1110, Sandia Corp. (1958).
45. R. McLaughlin, *OPERATION TEAPOT, Project 1.5, Preshock Sound Velocities Near the Ground in the Vicinity of an Atomic Explosion*, WT 1104, Navy Electronics Lab. (1957).

46. E.C.Y. Inn, *OPERATION TEAPOT, Project 8.4, Air Temperature Measurements over Several Surfaces,* WT 1149, U.S. Navy Radiological Defense Lab. (1957).
47. L.A. Schmidt, *OPERATION TEAPOT, Study of Drag Loading of Structures in the Precursor Zone,* WT 1124, Armour Research Foundation (1959).
48. L.J. Vortman, *OPERATION TEAPOT, Project 34.2, Effects of a Nonideal Shock Wave on Blast Loading of a Structure,* WT 1162, Sandia Corp. (1957).
49. G.K. Sinnamon, *et al, OPERATION TEAPOT, Project 3.7, Effect of Positive Phase Length of Blast on Drag and Semidrag Industrial Buildings,* WT 1129, Univ. of Illinois (1958).
50. R.E. Woodring, G.K. Sinnamon, N.M. Newmark, *OPERATION TEAPOT, Project 3.4, Air Blast Effects on Underground Structures,* WT 1127, University of Illinois (1957).
51. J.R. Allgood and W.A. Shaw, *OPERATION TEAPOT, Project 3.8, Teat of Concrete Panels,* WT 1130, Bureau of Yards and Docks (1957).
52. P.A. Randall, *OPERATION TEAPOT, Damage to Conventional and Special Types of Residences Exposed to Nuclear Effects,* WT 1194, Office of Civil Defense Mobilization (1961).
53. E. Shaw and F. McNea, *OPERATION TEAPOT, Project 36.1 and 36.2, Exposure of Mobile Homes and Emergency Vehicles to Nuclear Explosion,* WT 1181, Federal Civil Defense Agency (1957).
54. F. Hirsch, *et al, OPERATION TEAPOT, Project 33.2, The Effects of Noise in Blast-Resistant Shelters,* WT 1180, Sandia Corp. (1957).
55. G. Corfield, *OPERATION TEAPOT, Effects of a Nuclear Explosion on Typical Natural and Manufactured Gas Underground and Above-Ground Installations, Including Appliances in Houses,* WT 1176, American Gas Assoc. (1965).
56. P. Tucker and G. Webster, *OPERATION TEAPOT, Project 35.4a, Effects of a Nuclear Explosion on Typical Liquified Petroleum Gas (LP Gas) Installations and Facilities,* WT 1175, Federal Civil Defense Agency (1957).
57. R.V. Wood, *et al, OPERATION TEAPOT, Project 35.1, Effects of Atomic Weapons on Electric Utilities,* WT 1173, Edison Electric Inst. & FCDA (1965).
58. L. Sparks, *et al, OPERATION TEAPOT, Project 34.4, Nuclear Effects on Machine Tools,* WT 1184, AEC-Santa Fe Operations (1956).
59. G. Sinnamon, *et al, OPERATION TEAPOT, Project 3.32, Behavior of Underground Structure Subject to an Underground Explosion,* WT 1126, Univ. of Illinois (1957).
60. L.J. Vortman, "Craters from Surface Explosions and Scaling Laws," *Jour. of Geophys. Res.,* Vol. 73, No. 14 (1968).
61. L. Baurmash, Neal, Vance, Mork, Larson, *OPERATION TEAPOT, Distribution & Characterization of Fallout and Airborne Activity from 10 to 160 Miles from Ground Zero, Spring 1955,* WT 1178, UCLA School of Medicine (1958).
62. E. Enquist and J. Mahoney, *OPERATION TEAPOT, Project 8.3, Protection Afforded by Operational Smoke Screens Against Thermal Radiation,* WT 1144, Army Chemical Center (1956).
63. W.B. Plum and W.J. Parker, *OPERATION TEAPOT, Project 8.4d, Spectrometer Measurements,* WT 1148, Naval Radiological Defense Lab. (1958).
64. T. Petriken, *OPERATION TEAPOT, Project 6.1.1b, Evaluation of a Radiological Defense Warning System,* WT 1112, Signal Corp. Engineering Lab. (1957).
65. G.C. Imirie, Jr., and R. Sharp, *OPERATION TEAPOT, Radiation Enerby Absorbed by Human Phantoms in a Fission Fallout Field,* WT 1120, U.A. Naval Research Institute (195).
66. P.M. Crumley, J.L. Dick, K.C. Kaericher, W.J. Micholson, J.E. Banks, E.A. Pinson, *OPERATION TEAPOT, Project 2.8a, Contact Radiation Hazard Associated with Contaminated Aircraft,* WT 1122, Air Force Special Weapons Center (1957).
67. B.L. Ristvet, E.L. Tremba, R.F. Coud, Jr., J.A. Fetzer, E.R. Goter, D.R. Walter, V.P. Wendland, *Geologic and Geophysical Investigations of the Eniwetok Nuclear Craters,* AFWL-TR-77-242, Air Force Weapons Lab. (1978).
68. D.T. Griggs, F. Press, *Probing the Earth with Nuclear Explosions,* RM-2456-AEC, the Rand Corp. (1959).
69. L.J. Circeo and M.D. Mordyke, *Nuclear Cratering Experiences at the Pacific Proving Ground,* UCRL 12172, Lawrence Livermore Laboratory (1964).

70. E.J. Bryant, J.H. Keefer, L.M. Swift, *OPERATION PLUMBBOB, Project 1.8a, 1.8c, Effects of Rough and Sloping Terrain on Airblast Phenomena,* WT 1047 Ballistic Research Labs and Stanford Research Institute (1962).
71. J.R. Banister, L.J. Kortmary, *OPERATION PLUMBBOB, Effects of a Precursor Shock Wave on Blast Loading of a Structure,* WT 1472, Sandia Corp. (1961).
72. E.H. Bultmann, Jr., E. Sevin, T.H. Schiffman, *OPERATION PLUMBBOB, Blast Effects on Existing UPSHOT-KNOTHOLE and TEAPOT Structures,* WT 1423, Armour Research Foundation (1960).
73. E. Cohen, E. Laing, A. Bottenhofer, *OPERATION PLUMBBOB, Project 30.2, Response of Dual-Purpose Reinforced-Concrete Mass Structure,* WT 1449, Amman and Whitney, New York (1962).
74. E. Cohen and A. Buttenhofer, *OPERATION PLUMBBOB, Project 30.7, Test of German Underground Personnel Shelters,* WT 1454, Amman and Whitney (1960).
75. R. Dennis, C.E. Billings, L. Silverman, *OPERATION PLUMBBOB, Project 34.4, Blast Effects on an Air Cleaning System,* WT 1475, AEC Civil Effects Test Group (1962).
76. I.G. Bowen, R.V. Taborelli, and V.R. Clare, *OPERATION PLUMBBOB, Project 33.2, Secondary Missiles Generated by Nuclear-Produced Blast Waves,* WT 1468, Lovelace Foundation (1963).
77. R.H. Carlson, J.P. Martha, *OPERATION PLUMBBOB, Comparison Test of Reinforcing Steels,* WT 1473, Sandia Corporation (1960).
78. R.A. Williamson, P.H. Huff, *OPERATION PLUMBBOB, Test of Buried Structural-Plate Pipes Subjected to Blast Loading,* WT 1474, Holmes and Narver (1961).
79. W.E. Gulley, R.D. Metcalf, M.R. Wilson, J.A. Hirsch, *OPERATION PLUMBBOB, Project 4.2, Evaluation of Eye Protection Afforded by an Electromechanical Shutter,* WT 1429, Aero Med Lab., Wright Air Development Center (1960).
80. L.M. Swift, D.C. Sacks, F.M. Sauer, *OPERATION PLUMBBOB, Project 1.4, Ground Acceleration, Stress, and Strain at High Incident Overpressures,* WT 1404, Stanford Research Institute (1960).
81. W.R. Perret, *OPERATION PLUMBBOB, Project 1.5, Ground Motion Studies at High Incident Overpressure,* WT 1405, Sandia Corp. (1960).
82. G.H. Albright, E.J. Beck, J.C. LeDoux, R.A. Mitchell, *OPERATION PLUMBBOB, Evaluation of Buried Corrugated-Steel Arch Structures and Associated Components,* WT 1422, Bureau of Yards and Docks (1961).
83. E. Cohen, N. Dobbs, *OPERATION PLUMBBOB, Project 30.6, Test of French Underground Personnel Shelters,* WT 1453, Amman and Whitney, New York (1960).
84. R.B. Vaille, Jr., *OPERATION PLUMBBOB, Isolation of Structures from Ground Shock,* WT 1424, Stanford Research Institute (1960).
85. R.E. Grubaugh, L.E. Elliott, *Scaling of Ground Shock Spectra,* DASA 1921, United Aircraft Corp., El Segundo, California (1967).
86. L.M. Swift, D.C. Sachs, *OPERATION PLUMBBOB, Surface Motion from an Underground Detonation,* WT 1528, Stanford Research Institute (1960).
87. W.R. Perret, *OPERATION PLUMBBOB, Subsurface Motion from a Confined Underground Detonation,* WT 1529, Sandia Corp. (1961).
88. S.E. Warner, C.E. Violet, *RANIER, Properties of the Environment of Underground Nuclear Detonations at the Nevada Test Site,* UCRL 5542 RV, Univ. of California, Lawrence Livermore Laboratory (1961).
89. F.R. Rehm, *OPERATION PLUMBBOB, Aerial-Monitoring Operations Development,* WT 1485, Office of Civil Defense Mobilization (1962).
90. G.V. Tamplin, K.H. Malin, M.L. Griswold, *et al, OPERATION PLUMBBOB, Chemical Dosimetry of Prompt and Residual Radiation from Nuclear Detonations,* WT 1493, Univ. of California, Los Angeles (1961).
91. S. Sigoloff, H. Borlla, *OPERATION PLUMBBOB, Project 39.9, Remote Radiological Monitoring,* WT 1509, AEC Div. of Biology and Medicine (1959).
92. K. Larson, *et al, OPERATION PLUMBBOB, Projects 37.1, 37.2, 33.2a, 37.3, 37.6, Distribution, Characteristics, and Biotic Availability of Fallout,* WT 1485, Univ. of California, Los Angeles (1966).
93. C.F. Miller, *Some Properties of Radioactive Fallout - Balloon-Mounted Shot - PRISCILLA,* URS 757-4, URS Research Co. (1969).
94. H. McConnell, *OPERATION PLUMBBOB, Project 38.3, Measuring and Monitoring Training Exercise, Foodstuffs,* WT 1498, Food and Drug Admin. (1959).

95. L.J. Circeo, M.D. Nordyke, *Nuclear Cratering Experience at the Pacific Proving Ground*, UCRL-12172 Lawrence Livermore Laboratory (1964).
96. M.D. Nordyke, *On Cratering, A Brief History, Analysis, and Theory of Cratering*, UCRL-6578, Lawrence Livermore Laboratory (1961).
97. L.M. Swift, D.C. Sachs, W.M. Wells, *OPERATION HARDTACK, Earth Motion Measurements*, WT 1702, Stanford Research Institute (1961).
98. E.H. Bultmann, Jr., J.D. Hatiwanger, R.H. Wright III, and J.T. Hanley, *OPERATION HARDTACK, Project 3.6, Behavior of Deep Reinforced Concrete Slabs in High Overpressure Regions*, WT 1630, Univ. of Illinois (1961).
99. J.C. LeDouk, P.J. Rush, *OPERATION HARDTACK, Project 3.2, Response of Earth-Confined Flexible-Arch Structures in High-Overpressure Regions*, WT 1626, U.S. Naval Civil Engineering Lab. (1961).
100. R.A. Cameron, Jr., and P.H. Huff, *OPERATION HARDTACK, Project 34.1, Physical Damage Survey of AEC Test Structures*, WT 1701, Holmes & Narver (1962).
101. D.F. Seacord, *Fireball Calculations, RIO ARRIBA, OPERATION HARDTACK, Phase II, Project 15.1*, B-1947, (also B-1881, QUAY) Edgerton, Germershausen and Grier (1959).
102. R.H. Sievers, A.R. Stacy, *OPERATION HARDTACK, Structural Response and Permanent Displacement Measurements*, WT 1708, USAERDLAB (1960).
103. L.M. Swift, W.M. Wells, *OPERATION HARDTACK, Potshot Disturbances and Surface Motion*, WT 1740, Stanford Research Institute (1960).
104. W.K. Cloud, *et al*, *OPERATION HARDTACK, Surface Motions from Underground Explosions*, WT 1741, Coast and Geodetic Survey (1961).

DEVELOPMENTS IN LASER BASED DIAGNOSTIC TECHNIQUES

S. LEDERMAN

Aerodynamics Laboratories, Department of Mechanical and Aerospace Engineering
Polytechnic Institute of New York
Farmingdale, New York 11735, USA

Several laser based diagnostic techniques, applicable to fluid dynamic and combustion research consisting of the spontaneous Raman effect, coherent anti-Stokes Raman scattering, coherent Raman gain spectroscopy, laser induced fluorescence and the laser Doppler velocimeter are discussed. Characteristic features of each of these techniques are brought forth. It is shown that these modern, laser based diagnostic techniques are capable of measuring most of the variables of interest in fluid dynamics and combustion research. Among these are the temperature, species concentration, velocity, turbulent intensity temperature and concentration fluctuation as well as a number of correlation and crosscorrelation parameters. Practical examples of the applicability to flow fields and combustion diagnostics are presented.

INTRODUCTION

The appearance of the laser and its introduction into the field of spectroscopy was a turning point in the development of light scattering diagnostic techniques. In a relatively short period of time, laser based diagnostic techniques emerged as major investigative tools in a number of branches of the physical sciences. Since in this work the application of laser based diagnostic techniques to the investigations of flow fields and combustion systems are of interest, only some of the techniques which have been successfully applied, and which present some potential promise in the future for those investigations will be discussed.

Some of these techniques as mentioned previously are based on light scattering. A number of scattering processes have been considered for diagnostic purposes of flow fields and combustion systems. Among these the elastic scattering processes such as Rayleigh[1-3] and Mie[4] and the inelastic scattering processes represented by Raman,[5-17] near-resonant Raman[6,7] and fluorescence[18-20] have been extensively investigated. Other processes which could be utilized in combustion and flow field diagnostics are the absorption and nonlinear optical processes. The latter are represented by coherent anti-Stokes Raman[21-27] and stimulated Raman scattering.[28-30] From this list of potential diagnostic techniques applicable to flow fields and combustion, the Mie and spontaneous Raman scattering techniques are the most versatile. The Mie scattering phenomenon has been utilized in Laser Doppler Velocimetry[31-32] capable of providing non-intrusively velocity, turbulent intensity, and particle size distribution in flow fields. The spontaneous Raman effect can provide simultaneously, remotely and instantaneously species concentration and temperature of a flow field consisting of any number of species. When properly used it can provide, in addition, local turbulence properties, correlation and cross-correlation parameters and the so called mixedness parameters in reactive flows.[33] However, due to the very low equivalent scattering cross-section under certain conditions occurring in hydrocarbon turbulent combustors, difficulties may develop in securing reliable measurements. These difficulties are related to the very high noise level, generally attributable to carbon emissions. The signal to noise ratio under those conditions may become unacceptably low thus making the utilization of the spontaneous Raman technique very difficult. Here the coherent anti-Stokes Raman spectroscopy appears to fill the gap. The equivalent scattering cross-section in conjunction with the coherence of the radiation combine to provide signals 5 to 6 orders of magnitude higher than the spontaneous Raman effect. Its coherent character permits, in addition to the collection of the total generated signal, the simultaneous suppression of the collected interference signals, resulting in high signal to noise ratios in very hostile environments. One of the major drawbacks of CARS is its nonlinear character which may cause difficulties in a number of situations encountered.

A process which holds out great promise for flow field and combustion diagnostics has been recently demonstrated.[28] This process known as stimulated Raman spectroscopy, [SRS] has been known for over a decade[34-35] and applied in the first practical demonstration of a collinear CARS system. It has been used with high power pulsed lasers and CW low power lasers.[29] Being of a coherent nature, the SRS signals under certain conditions may exceed the signal strength of the CARS signals, with the added advantage of being linear and the fact that the technique is self-phase matched and thus requires no great effort in this respect.

In terms of high signal response, a technique which has been known for several decades is the fluorescent diagnostic method. Here the major interfering phenomenon of the spontaneous Raman technique is being utilized as a diagnostic technique. This technique, in spite of its very high signal levels, has not been until recently very successfully applied. The major obstacle being the strong collisional quenching process associated with fluorescence, which is competing with the radiative decays, and thus makes the measured fluorescent intensities ambiguous.

The cited possible nonintrusive diagnostic techniques are discussed at length in this work. A description and evaluation of these new techniques, the accomplishments to date and their potential applicability to flow fields and combustion systems is presented here.

THE RAMAN EFFECT

The Raman effect is the phenomenon of light scattering from a material medium, whereby the light undergoes a wavelength change and the scattering molecules undergo an energy change in the scattering process. The Raman scattered light has no phase relationship with the incident radiation. Based on quantum theoretical considerations, the incident photons collide elastically or inelastically with the molecules to give Rayleigh and Raman lines respectively with the inelastic process much less probable than the elastic. The process of light scattering can be visualized, as the process of absorption of an incident photon of energy E by a molecule of a given initial state, rising the molecule to a virtual state, from which it immediately returns to a final stationary state emitting a photon of the difference energy between the two stationary states and incident energy E. This is seen graphically in the schematic diagram of Fig. 1, where vibrational and rotational transitions are indicated corresponding to the appropriate vibrational and rotational selection rules which are $\Delta J = 0, \pm 2$ and $\Delta V = \pm 1$. Since the anti-Stokes lines must originate in molecules of higher energy level, which are less abundant at normal temperatures, the anti-Stokes lines would be expected to be much weaker than the Stokes lines. This qualitative description of the Raman effect is obviously very superficial. For a more rigorous and complete discussion of this effect one must consult the cited references.

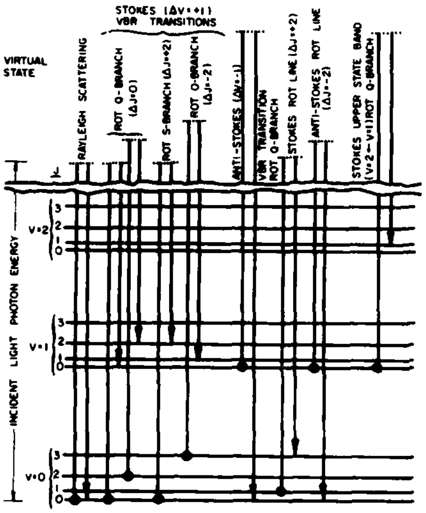

FIG. 1 SCHEMATIC DIAGRAM OF MOLECULAR TRANSITION[10]

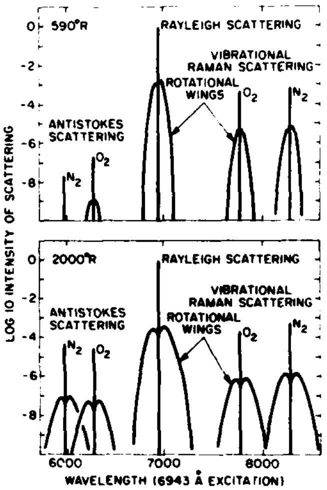

FIG 2 RAMAN AND RAYLEIGH SCATTERING FROM AIR[46]

An inspection of Fig. 1 reveals that the incidence of a photon on a molecule, if Raman active, may result in the exictation of vibrational as well as rotational transitions. Fig. 2 presents an approximate Raman and Rayleigh scattering response from air illuminated by a Ruby laser. It is evident that the Rayleigh as well as the vibrational spectra have closely associated rotational wings. Since, for our purposes, the vibrational scattering is of direct interest, it is worthwhile to examine the vibrational Raman response. It consists essentially of three branches: (1) the intense Q-branch for which $\Delta J = 0$, (2) the much weaker O-branch for which $\Delta J = -2$, and (3) the S-branch for which $\Delta J = +2$ of approximately the same intensity as the O-branch. The O and S branches are much weaker than the Q-branch and represent only about 1% of the intensity of the Q-branch. They are therefore of minor importance as far as the present applications to fluids are concerned. The Q-branch, if a high dispersive instrument is used, can be resolved into components corresponding to the energy levels characterized by the quantum numbers $v = 1,2,3$, etc. These of course will appear at elevated temperatures, and may be used to determine temperatures, Fig. 3. Since in fluids the orientation of the molecules cannot be fixed, the scattering will correspond to an average overall molecular orientation, and the vibrational Raman scattered intensity as derived using the Placzek polarizability theory may be expressed as

$$I_{S,A} = CNI_o \frac{(\nu_o \pm \nu)^4 f(\alpha',\gamma')}{(1-\exp[\frac{hc\nu}{kT}])}$$

and from the relative intensity of the Stokes and anti-Stokes lines, taking account of the Boltzmann factor, the temperature is given by

$$T = \frac{hc\nu}{k}\left[\ln\frac{I_s}{I_A} + 4\ln\left(\frac{\nu_o+\nu}{\nu_o-\nu}\right)\right]^{-1}$$

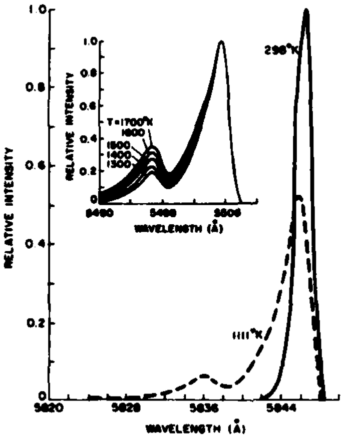

FIG. 3 THE RESOLVED Q-BRANCH[9]

It should be noted that the scattered intensity is proportional to the fourth power of the frequency and to the incident intensity and, of course, to the number density of a given species. It is well-known that the pure rotational Raman spectra appearing near the exciting radiation frequency can be quite intense. However the very small wavelength separation of the lines particularly in a mixture of gases makes the pure rotational spectra very difficult to use for diagnostic purposes as defined here in spite of its stronger signals. The weakness of the Raman scattering technique is its low scattering cross-section. Consequently, the signal obtainable is a major factor in determining the applicability of the technique to a given problem. The number of photoelectrons contributing to the signal, may be written

$$n_s = E_o N\sigma \ell \Omega \eta_o \eta_g E_p^{-1}$$

where E_p is the energy per photon, η_o is the optical efficiency of the collecting optics, and η_g is the quantum efficiency of the photocathode. The last equation may also be written in terms of an output voltage from a photomultiplier tube across a load R, with a gain G and laser pulse duration t,

$$V_s = E_o N\sigma\ell \cdot \Omega\eta_o\eta_g \cdot G \cdot eR \cdot (E_p \cdot t)^{-1}$$

where e is the electron charge in coulombs and V_s the signal voltage. The last two equations permit the evaluation of the achievable voltage signal or photon-count in a given situation, if not exactly, at least to a first reasonable approximation. (The laser pulse in the above approximation is assumed to have a rectangular shape whereas in actuality the laser pulse has generally a Gaussian distribution in intensity). The voltage signal or photon count must exceed the signals due to background noise or other disturbing signals, if the measurement is to be useful.

Some features of the Raman diagnostic technique

At this point it is clear that, in principle at least, instantaneous and simultaneous data for the determination of species concentration and temperature can formally be obtained. The former because the Raman transition takes place in a time of the order of fractions of picoseconds for most Raman active molecules, if illuminated by light in the visible range; and the second because one may record the Stokes and anti-Stokes intensity at the same time, the number of data points depending on the number of receiving channels one has available. The vibrational Raman system, which generally permits clear identification of species involved, is generally used. An obvious difficulty in performing Raman intensity measurements is the extremely small equivalent Raman scattering cross-section. Typically, this cross-section may vary between $10^{-29}cm^2$ and $10^{-31}cm^2$, depending on the molecule under investigation and the frequency of the primary light. Since the frequency dependence is of overriding importance here (fourth power), and is essentially the only parameter which is at the disposal of the experimentalist, one would tend to automatically chose the laser operating at the highest frequency. While this choice might be desirable in one respect, other aspects of this choice might be less favorable.

The line separation of the resulting Raman spectra is greater as a result of longer wavelength lasers, than shorter wavelength sources of primary radiation. This feature may become important in cases where several species are involved and their measurement and resolution are desired, in particular when narrow bandpass filters are contemplated. Figs. 4 and 5 illustrate this problem very clearly, both in terms of concentration measurements of a mixture of gases and the preference of using the ratio of the vibrational Stokes to anti-Stokes intensity for the determination of temperature, as opposed to the rotational spectra. It should also be pointed out that the use of a nitrogen laser at the conventional energy (1mj) levels available, requires the utilization of photon counting techniques and generally mean values of the measured variables are obtained, while with a Ruby laser, due to its much higher energy (4 joules) per pulse (several orders of magnitude), single pulse operation is possible and therefore instantaneous values can be obtained. The latter is also true for a doubled neodymium yag laser operating at 5320Å available at a repetition rate of 10pps at energy levels in excess of 0.5 joules.

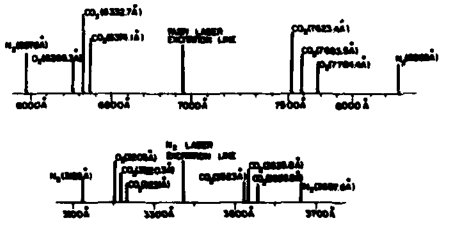

FIG. 4 VIBRATIONAL LINE DENSITY AS A FUNCTION OF 3 GASES

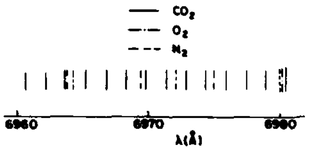

a) RUBY LASER EXCITATION

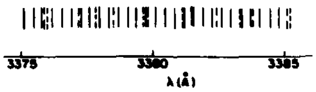

b) N$_2$ LASER EXCITATION

FIG. 5 ROTATIONAL LINE DENSITY OF A MIXTURE OF 3 GASES

In addition to these pulsed lasers, C-W lasers are being utilized to perform Raman measurements. In particular the argon ion laser operated at 5145Å or 4880Å is very useful in steady state systems where mean concentration and temperature are desired. C-W lasers would, of course, be ideal for time resolved Raman measurements of fluctuating flow fields and combustion systems. However, the available commercial lasers are of insufficient power to provide useful data concerning fluctuating systems.

It is therefore apparent from the above that spontaneous laser Raman scattering has all the desired features of an ideal probe. There are, however, problems associated with this diagnostic method.

In discussing the feasibility of diagnostics by means of monitoring the intensity of radiation, and particularly scattered radiation resulting from the Raman effect, one must consider the background radiation which may interfere with the desired signal and render it useless. There are a number of sources which may contribute to the undesired background radiation. In order of significance they are: Rayleigh scattering, scattering of the incident beam by viewing port windows, walls and large particles in the flow, gas particle and surface fluorescence, ambient light, detector dark current, electrical noise and detector shot noise.

The first two, being of the same frequency as the incident beam and thus spectrally separated from the desired signal, can be filtered out using proper interference filters or spectrographs used for the selection of the desired signals. The fluorescence problem can be a very serious problem. Careful selection of the materials and surface coatings may eliminate this problem. In some cases by proper choice of the primary laser this problem can be avoided. In this respect, the use of a Ruby laser has not caused any significant fluorescent problem in this laboratory. The detector dark current and electrical noise can generally be coped with by using photomultiplier coolers, which serve a dual purpose of decreasing the dark current and shielding the photomultiplier from electrical interferences. As far as the shot noise is concerned, this problem must be dealt with at the data processing level.

In general the larger the signal-to-noise ratio the better the system. As has been pointed out,[14] a very convenient parameter to assess the capability of a system is the "feasibility index". This index was defined as $X{=}NL\sigma_0\Omega e$ where N is the number density of the scatterers per cm^3, L is the length of the sample in the direction of the laser beam, σ_0 reference cross-section, and Ω and e the solid angle and optical efficiency, respectively. The minimum feasibility index for a 1 joule Ruby laser in a single pulse operation is approximately 10^{-15}. Thus, for a situation where this index is below 10^{-15} a 1 joule single pulse laser would not provide the desired information. An increase in the laser energy or any of the other factors may be necessary. There is, however, a limit on the laser energy one may apply. The laser energy density should be below the breakdown threshold which for Ruby and air appears to be around $10^{10} W/cm^2$.

The choice of the proper method of spectral analysis can be very important. There are basically three methods available. The standard monochromators, interference filters and Fabry-Perot interferometers. Each has a range of applicability and its positive as well as negative features. The interested reader may consult standard texts or some of the references cited.[10,15,24]

The detection of the scattered photons of interest is best accomplished by photomultipliers. They are the most sensitive low level light detectors available at present, applicable in the wavelength range from u.v. to near infrared or from about 3-10 thousand Angström wave length. The output of the photomultiplier may be used in one of several ways: a) as an input to a d.c. amplifier, b) as an input to a photon counter, c) as an input to a phase sensitive detector, or as a combination or modification of the above basic schemes.

In general photon counting is more accurate than a direct reading of the photomultiplier current. The reasons are: 1. the d.c. level caused by leakage currents of photomultiplier tubes cannot be detected by photon counters, 2. the statistically varying heights of the detector output pulses are replaced by standard height pulses, 3. the photon counting rate with proper care can be made insensitive to power supply voltage fluctuations. However, at high photon count rates photon counting may present some difficulties particularly if the detection rate exceeds about 10^7 counts sec^{-1}.

Recently a new detection system has been introduced. It offers a number of advantages over photomultiplier tubes. It is supposed to be capable of providing simultaneous measurements of the Raman scattering signals of a multiplicity of species at many spatial points, during a single laser pulse. It would therefore be capable in conjunction with proper computational facilities to provide in addition to concentration and temperature, data necessary for the determination of spacial correlation functions.

Two commerical versions are now on the market, the first and most known is the optical-multichannel analyser OMA and the more recent entree, the DAARS. Both claim a photon sensitivity as high as the best available photomultiplier. One claims one signal count for two detected photons, the other one count per photon. I have not been able to confirm that with either. Be it as it may, this kind of a detector represents a major advance in the laser scattering diagnostic technology. At this point it must be mentioned that, due to the simultaneous and instantaneous response of the spontaneous Raman signals, the correlation and crosscorrelation parameters defined in the following[32] can be obtained. Thus:

$$\overline{C'_\alpha C'_\beta} = \frac{1}{n}\sum_{i=1}^{k} fi(C_{\alpha i}-\bar{C}_\alpha)(C_{\beta i}-\bar{C}_\beta)$$

$$\overline{C'^{2}_\alpha C'_\beta} = \frac{1}{n}\sum_{i=1}^{k} fi(C_{\alpha_i}-\bar{C}_\alpha)^2(C_{\beta_i}-\bar{C}_\beta)$$

and

$$\overline{C'_\alpha\, C'^{2}_\beta} = \frac{1}{n}\sum_{i=1}^{k} fi(C_{\alpha i}-\bar{C}_\alpha)(C_{\beta i}-\bar{C}_\beta)^2$$

where fi is the frequency of occurrence of the joint values $C_{\alpha i}$ and $C_{\beta i}$, and $n=\sum_{i=1}^{k} fi$ and C_α and C_β are the concentrations of species α and β.

CARS

Coherent anti-Stokes Raman scattering has been receiving a great deal of attention since its introduction in 1973 by Regnier, Moya and Taran. It became popular among the researchers in the field of combustion and particularly combustion in systems with excessive soot. As discussed previously, the spontaneous Raman techniques cannot easily handle this type of flow field. It has been shown[21,23,24,33] that the coherent anti-Stokes Raman scattering system can provide signals several orders of magnitude higher than the Spontaneous Raman signals for the same initial driving laser intensity. In addition, the coherent character of the signal beam allows the collection of the total beam and at the same time minimize the collection of the interfering radiation.

Theory

When an incident photon of fixed frequency ω_1, interacts with a tunable photon ω_2 (Stokes photon of the given specie of interest) through the third order nonlinear Raman susceptibility it generates a polarization field which is responsible for coherent radiation of frequency $\omega_3 = 2\omega_1-\omega_2$. If $\omega_1-\omega_2$ is of or near a Raman resonance line the intensity of the coherent radiation becomes very large, in fact several orders of magnitude larger than the intensity of the spontaneous Raman radiation, and it occurs at the Raman anti-Stokes line with respect to the incident radiation ω_1. In Fig. 6 an energy level and the corresponding phase matching diagrams are shown, which are self-explanatory. The CARS radiated power for the case of collinear diffraction limited beams, can be shown to be:

$$P_3 = \left(\frac{\omega_1}{\pi d}\right)^2 \left(\frac{4\pi^2\omega_3}{c^2}\right)^2 P_1^2 P_2 |\chi|^2$$

where P_1, P_2 and P_3 are the incident, Stokes and anti-Stokes powers respectively and $|\chi|$ is the absolute Raman nonlinear susceptibility given by

$$\chi = K_j \Gamma_j (2\Delta\omega_j - i\Gamma_j)^{-1}$$

where $\Delta\omega_j = \omega_j - (\omega_1 - \omega_2)$ = the detuning frequency and

$$K_j = 4\pi C^4 (h\omega_2^4 \Gamma_j)^{-1} N \Delta_j g_j (\partial\sigma/\partial\Omega)$$

ω_j is the frequency of a particular possible transition from $V, J \rightarrow V', J'$, Δ_j = the normalized population difference between the levels involved in the transition, g_j = line strength factor equal to (V_j+1) when at resonance $\Delta\omega_j = 0$ and $|\chi| = K_j$ and Γ_j is Raman line width. The interaction of this type of a CARS system will occur in a beam diameter d of length ℓ given by:

$$d = 4\lambda f/\pi D \qquad \ell = \pi d^2/2\lambda$$

where f, λ and D are the focal length of the lens, the wavelength of the incident beam and the beam diameter at the lens respectively.

As is evident from the above, the CARS technique is a nonlinear technique, unlike the spontaneous Raman technique. It is a double ended technique. It is therefore necessary to traverse the sample and obtain the desired signal at the opposite side of the signal input to the sample. CARS can resolve only one specie at a time. The resolved specie corresponding to the applied Stokes beam. Spontaneous Raman as pointed out previously can resolve simultaneously as many species as there are in a mixture providing the acquisition system is capable of resolving the acquired spectra.

In applying CARS to a system, one must exert caution if the flowfield is very turbulent and extensive. Beam steering may cause difficulties in phase matching and relating the signals to actual concentrations and temperatures as obtained by this method.

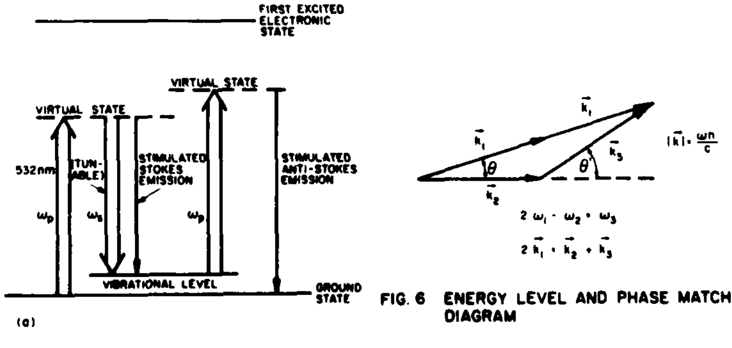

FIG. 6 ENERGY LEVEL AND PHASE MATCHING DIAGRAM

COHERENT RAMAN GAIN TECHNIQUE

A technique as old as CARS which provides a coherent signal beam of considerable strength has until recently been completely neglected as a diagnostic tool. This technique is based on stimulated Raman spectroscopy SRS. Recently it has been reported[28-30] that sensitivities comparable or exceeding those of CARS under similar conditions can be obtained. The added attraction of this new technique is the possible utilization of two low power C-W lasers, and the linear response of the technique.

Theory

The idea behind the direct SRS technique using C-W sources is as follows. A linearly polarized pump beam of a frequency ω_1 is -using an electro-optical modulator - modulated and combined coaxially through a dichroic mirror with a probe beam of frequency ω_2. The combined beam is focussed through the sample. The modulated pump beam produces a modulated Raman gain at the Stokes frequency or Raman loss at the anti-Stokes frequency which is then detected by the probe beam Fig. 7. If the probe and pump beams are focussed collinearly through the sample, it can be shown that the fractional power gain $\delta P(\omega_2)/P(\omega_2)$ at the probe frequency ω_2 induced by the pump beam of a frequency ω_1 is given approximately by[30]

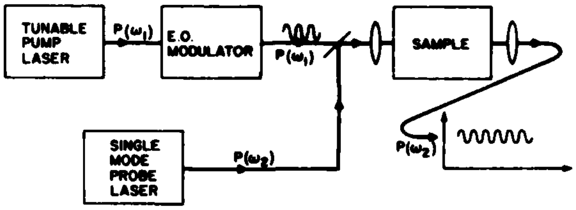

FIG. 7 S R S CONFIGURATION

$$G = \delta P(\omega_2)/P(\omega_2) = 384\pi^4\lambda^{-2}c^{-1}n^{-1}\mathrm{Im}\chi_3(-\omega_2,\omega_2,-\omega_1,\omega_1)\cdot P(\omega_1)$$

where n is the refractive index at frequency ω_2, $P(\omega_2)$ and $P(\omega_1)$ are the probe and pump powers respectively $\lambda^2 = (2\pi c)^2/\omega_1\omega_2$ and $I_m\chi_3$ is the imaginary part of the third order nonlinear susceptibility and is given by:

$$I_m\chi_3(-\omega_2,\omega_2,-\omega_1,\omega_1) = \pi Nc^3(24h\omega_2{}^4)^{-1}L(\omega_1-\omega_2)d\sigma/d\omega_1 d(1/\lambda)$$

where $L(\omega_1-\omega_2)$ is the line shape function equal to unity at the line center. Since both CARS and SRS depend on the nonlinear susceptibility χ_3 it is worth pointing out that SRS is linearly dependent on χ and the pump power $P(\omega_1)$, whereas CARS's dependence on these parameters is quadratic. One other property of SRS is the fact that the SRS technique is self-phase matched and therefore requires only an overlap of the two beams to proceed with the interaction, similar to the collinear CARS system. The technique is insensitive to slight depolarization of the beams, and offers high resolution.

As an example of the signal strength of SRS, Owyoung cites the following: the 992 cm^{-1} mode of liquid benzene for which $I_m\chi_3 = 15.9\cdot10^{-14}cm^3/erg$, a pump power of 100mw yields an SRS signal $\delta P(\omega_2)/(P(\omega_2) = 3.5\cdot10^{-5}$ which is about 6 orders of magnitude larger than that obtained at comparable power levels in CARS.

There are, however, certain problems associated with this diagnostic technique. The most serious of them being the required probe laser stability, and mode purity.

As of now, experimental data in liquids and dense media have been obtained. The application to gaseous media have been limited as of now to molecular hydrogen[29] at 1/4 to 14 atm. of pressure.

LASER INDUCED FLUORESCENCE

A technique which holds out great promise as a diagnostic tool in flames, combustors and combustion driven MHD generators is laser induced fluorescence. The great attraction of this technique is the relatively very high scattering cross-section, compared to any of the thus far discussed techniques. It is a very sensitive, spacially precise technique for determination of the species concentration in difficult environments. Fluorescence occurs when a light beam which is in resonance with a particular absorption line of an illuminated molecule, excites it into a higher energy level which, after a time delay of the order of 10^{-9} sec, radiatively decays to the original or intermediate energy level with the spontaneous emission of a corresponding photon. This process is illustrated in the simple energy level diagram Fig. 8. This process could therefore be used for diagnostic purposes, provided that this spontaneous emission is the only deexcitation process active. This however is not the case. Since at STP the collission rate is of the order of 10^{10} sec^{-1}, collisional deexcitation of the excited molecules may occur without radiative emission. This phenomenon known as collisional quenching is essentially a very complicated process depending on a number of properties of the gas under investigation such as density, temperature etc. Since those are the properties one is trying to measure, the computation of the quenching effects, effecting the measurement of some of those properties is generally very difficult.

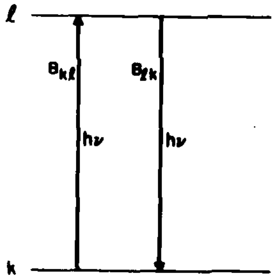

FIG. 8 ENERGY LEVEL DIAGRAM FLUORESCENCE

Theory

Recently, Daily[36] proposed a technique which may result in a very sensitive and useful method of obtaining concentrations. It is based on the so called saturation condition given by

$$N_\ell = N_k B_{k\ell}/B_{\ell k}$$

where N_ℓ and N_k are the upper and lower state number densities. This condition requires that:

$$B_{\ell k} I_\nu >> Q_\ell + A_\ell$$

where $B_{\ell k}$ and $B_{k\ell}$ are the Einstein coefficients for stimulated emission and absorption. A_ℓ is the total Einstein coefficient for spontaneous emissions summed over all transitions, Q_ℓ is the total quenching probability, and $I_\nu = P/A\Delta\nu$ is the laser beam energy density of the wavenumber interval $\Delta\nu$ and finally P and A are the incident power and crossectional area of the focal volume of the sample, respectively.

Assuming that the saturation condition is satisfied and N_ℓ is saturated, the fluorescent intensity can be written:

$$I_\ell = h\nu A_L (4\pi)^{-1} \Omega_c V_c N_k B_{k\ell}/B_{\ell k}$$

where Ω_c is the solid angle of the collecting optics and V_c is the excited volume. In the simplest case of a two level system N_o the total number density is given by

$$N_o = N_k + N_\ell = N_1 + N_2$$

$$I_\ell = I_2 = h\nu A_2 (4\pi)^{-1} \Omega_c V_c \cdot N_o (1+g_1/g_2)^{-1}$$

with $B_{k\ell}/B_{\ell k} = g_\ell/g_k = g_2/g_1$ resulting in the total number density

$$N_o = I_2 (g_2+g_1) 4\pi (h\nu A_2 \Omega_c V_c g_2)^{-1}$$

For multi-level system, assuming that the lines can be separated, similar expression for the total number density can be found. The complexity, however, increases greatly particularly the separation of the fluorescence spectrum of the various levels. In principle this technique requires the illumination of a gas volume with the intensity I_ν and the collection of the fluorescence radiation at 90° to the laser beam. From the last equation it is apparent that the concentration can be measured without any knowledge of the quenching probabilities when the saturation technique is used. However not all species are suitable for fluorescent diagnostics. First of all the specie must have its first excited electronic energy level located such that the absorption transitions are in a portion of the spectrum that can be covered with a laser. Second, the rotational spectrum must be sufficiently wide spaced such that the individual absorption and emission lines can be easily isolated. The last requirement might be difficult to satisfy with more complex molecules, whose rotational vibrational structure can be very complicated. It is therefore clear that while this technique can provide very strong signals in hostile environments, the range of applicability is limited to a selected group of species. In addition, only one specie at a time can be measured, with a given laser wavelength, in contrast to spontaneous Raman, where all the species present can be identified simultaneously using only one laser. In addition the temperature can be determined simultaneously with the concentration using spontaneous Raman, whereas the fluorescence technique cannot provide the temperature.

Laser Doppler Velocimeter

Laser Doppler Velocimetry is the best known laser based diagnostic technique. Mie scattering in conjunction with the Doppler effect provides the theoretical basis of the LDV. The laser Doppler velocimeter has been in use for over a decade. Its development has reached a point where most laboratories use it as a standard measuring device. The theoretical and operational background is described in References 31, 32 where most aspects of LDV technology have been treated and additional references can be found.

The operation of an LDV is predicated on the assumption that particles suspended in the flow, move with the same velocity as the fluid whose velocity one is attempting to measure. Furthermore, in the case of a turbulent flow, it is assumed that the frequency spectra of the scattering particles, provide the required information regarding the turbulent structure of the flow field. The latter is associated with particle dynamics. The effect of particle dynamics on the performance of LDV has been considered by a number of researchers.[38-41] They all came to the conclusion that the size of the scattering particle has an effect on the frequency resolution of the spectrum. This is shown in Fig. 9.

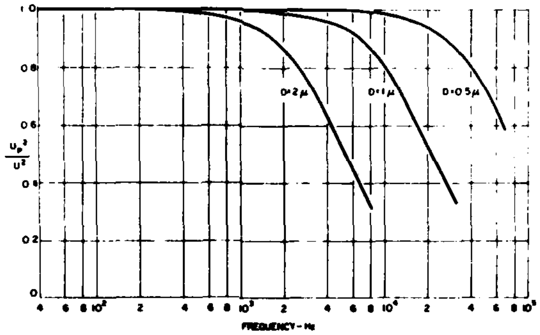

FIG. 9 RESPONSE OF ALUMINUM OXIDE PARTICLES TO TURBULENT FLUCTUATIONS

It is evident from the above, that the relationship of the frequency spectra from an LDV, to the turbulence spectra of a flow field is limited to the lower frequency region, that limitation being a function of the size of the majority of the scattering particles. This puts also a restriction on the use of naturally occurring particulates, because their sizes are generally unknown. The above suggests that for a more meaningful interpretation of the LDV measurements, a monitoring of the sizes of the particulates should be carried out and incorporated in the data reduction process. Careful choice, however, of the size and number of scatterers does permit one, within limits, to determine the velocity of the fluid and its turbulent intensity. The major problem in laser Doppler velocimetry is the acquisition, processing, and handling of the acquired data not the principle itself. Of the many optical arrangements possible, the one most frequently used is the dual scatter or sometimes known as the differential scatter systems. A schematic diagram of this type of an arrangement is shown in Fig. 10. The reason for its popularity is the fact that it can be operated in the forward as well as backward

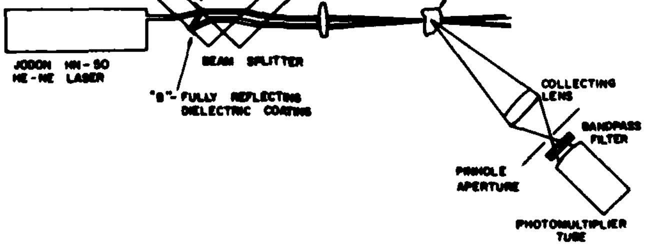

FIG. 10 SCHEMATIC DIAGRAM OF THE DUAL SCATTERER LDV SYSTEM

scatter mode. The acquired signals are independent of the angle of observation, and the alignment process is very simple. The translation of the signals into velocity and turbulent intensity of a one dimensional dual scatter LDV[33] is essentially reduced to the measurement of frequency. Since frequency can be measured with very high precision, extreme care is required in acquisition, processing, seeding and control of the LDV system to obtain precise velocity information.

At this point it should be mentioned that one of the very important parameters in combustion research is the droplet or particle size distribution in the flow field. Besides the standard sampling probe methods, optical methods based on the Mie scattering have been developed over the years. It has been found that for spheres the scattered light intensity is a complicated function of the scattering angle, of the size parameter $a = \pi d/\lambda$, the refractive index and the polarization. Durst[42] using two photomultipliers on both sides of optical axis of a forward scattering LDV was able to show that under certain conditions the phase difference between the two signals could be related to the particle size. Farmer[43] on the other hand, using fringe spacings larger than 100μm, was able to measure particles whose diameter was less than 100μm using the visibility concept. Youle et al[44] using a dual scatter LDV was able to measure particle sizes between 30-240μm. The particles had to be transparent, spherical and larger than the fringe spacing. They found that under those conditions, the peak LDV signal increased monotonically with the diameter of the particles. As of now there appears to be no satisfactory diagnostic technique based on Mie scattering, holography, or diffusion correlated spectroscopy capable of providing unambiguous measurements of size and concentration of particulates in a flow remotely and nonintrusively. Most of the techniques mentioned are under development and further research is needed to develop particle diagnostics for combustion flows.

Applications: Experimental Results

The previously discussed, laser based diagnostic techniques have been and are still being developed for the most part for a unique purpose. That is, to provide a reliable, nonintrusive, nondisturbing probe for the measurement of the relevant parameters of fluid dynamics and combustion. It is obvious that the spontaneous Raman and LDV techniques would fit that purpose completely if all the encountered practical systems would be ideal, that is, free from interfering radiation and noise. As has been pointed out previously, the equivalent scattering cross section of the spontaneous Raman technique is relatively very low and subsequently this technique is not universally applicable. However in systems where this technique can be applied, it, in conjunction with an LDV, presents a very unique diagnostic system. As an example, the system utilized in our laboratories and shown in Fig.11 is capable of providing simultaneous measurements of concentration of 4 species, or 2 species and their respective temperatures, the velocity, the turbulent intensity, the correlations and crosscorrelations of species and velocities and in reacting flows the mixedness parameters. In addition the probability density functions (PDF) which is of importance in combustion modeling can be obtained easily.

The system shown in Fig.11 is self-explanatory. The number of receivers is by no means limited to four. Any number required for a given system may be incorporated without affecting the system's performance. In the next several figures examples of measurements performed on turbulent diffusive flames are given. Thus Fig.12 shows the normalized axial velocity and temperature distribution in a flame with the corresponding turbulence intensity and temperature fluctuation. Fig.13 shows the normalized nitrogen, carbon dioxide and oxygen concentration distribution and the corresponding fluctuations in the same flame. Fig.14 represents the first and second order correlations between oxygen,nitrogen and carbon dioxide. Finally some histrograms of the N_2 specie in the flame are shown in Fig.15 at several points. It must be emphasized that all these data have been taken simultaneously with the apparatus shown in Fig.11.

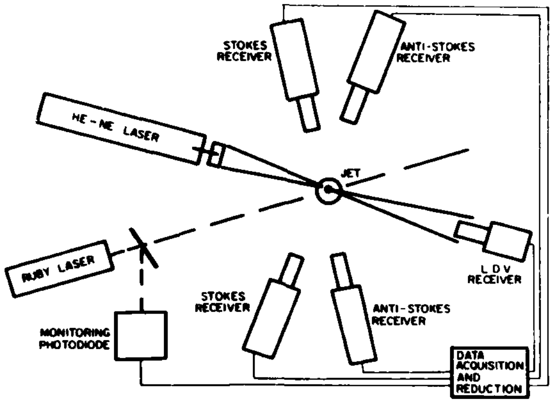

FIG. 11 BLOCK DIAGRAM OF EXPERIMENTAL APPARATUS

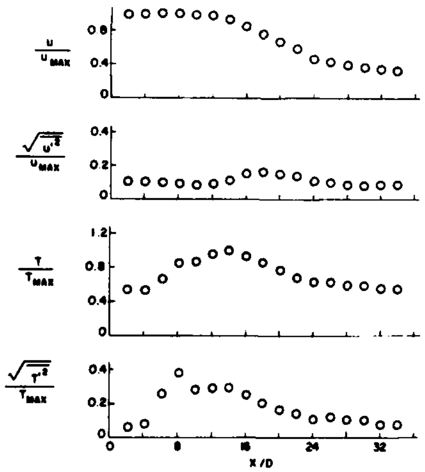

FIG. 12 VELOCITY AND TEMPERATURE, AXIAL PROFILES IN A FLAME

As discussed previously, under certain conditions the spontaneous Raman technique becomes inapplicable. Under those conditions, attempts have been made to utilize CARS. While CARS cannot replace spontaneous Raman, it is capable of providing information concerning density and temperature of a single specie in a hostile environment. There are essentially two types of optical arrangements utilized in CARS. They are both shown in Fig.16. The first one is the so called collinear one. The other is the so called "boxcars".[24] Both are essentially self-explanatory. The reason for the "boxcar" is the desire to improve the spacial resolutions, with a possible sacrifice in the anti-Stokes intensity. One should remark that the collinear type is self-phase matching, whereas the "boxcar" requires some delicate adjustments. The collinear system can be quite simple if one uses a stimulated Raman cell to generate the necessary Stokes line.[22,32]

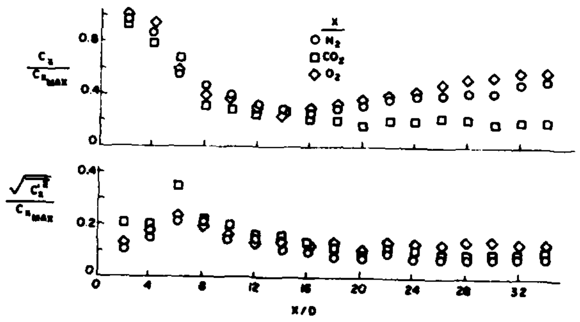

FIG. 13 CONCENTRATION, AXIAL PROFILES IN A FLAME

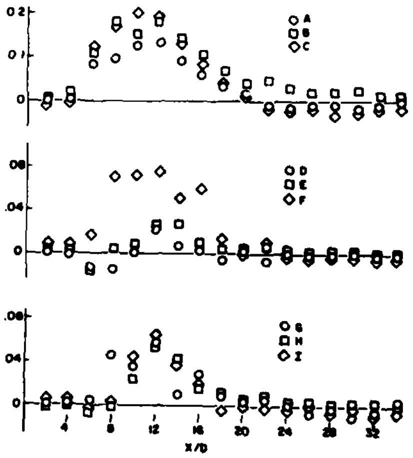

$$A = \frac{\overline{C_x' C_y'}}{\bar{C}_x \bar{C}_y} \qquad B = \frac{\overline{C_x' C_z'}}{\bar{C}_x \bar{D}_z} \qquad C = \frac{\overline{C_y' C_z'}}{\bar{C}_y \bar{C}_z}$$

$$D = \frac{\overline{C_x'^2 C_y'}}{\bar{C}_x^2 \bar{C}_y} \qquad E = \frac{\overline{C_x'^2 C_z'}}{\bar{C}_x^2 \bar{C}_z} \qquad F = \frac{\overline{C_y'^2 C_z'}}{\bar{C}_y^2 \bar{C}_z}$$

$$G = \frac{\overline{C_x' C_y'^2}}{\bar{C}_x \bar{C}_y^2} \qquad H = \frac{\overline{C_x' C_z'^2}}{\bar{C}_x \bar{C}_z^2} \qquad I = \frac{\overline{C_x' C_z'^2}}{\bar{C}_y \bar{C}_z^2}$$

FIG. 14 FIRST AND SECOND ORDER CORRELATION WITH $x = N_2$, $y = CO_2$, $z = O_2$

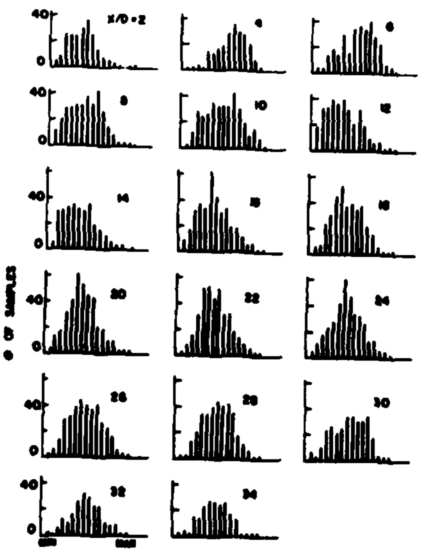

FIG. 15 HISTOGRAM OF N_2

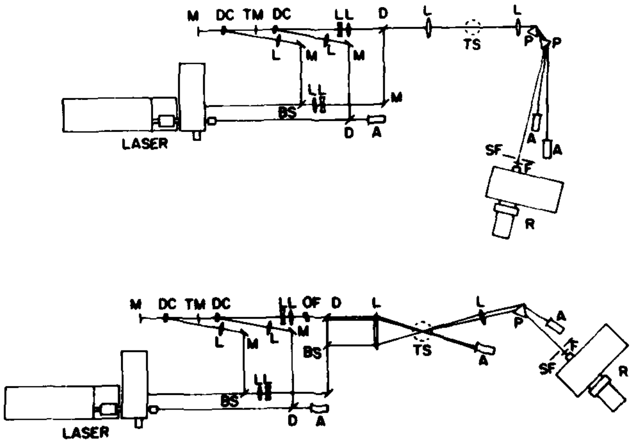

FIG. 16 COLLINEAR AND BOXCAR SCHEMATICS OF CARS

Some examples of data obtained using CARS are shown in the next few figures. Thus Fig.17 shows the concentration of unburned methane in a sooty flame, obtained with a collinear system and a stimulated cell,[32] while Fig.18 the radial temperature profiles in a laminar propane diffusion flame[25] obtained using the so called "boxcar" system. It would be emphasized again that CARS, unlike spontaneous Raman, can supply only temperature and concentration of one specie at a time with a given set of lasers. It is not generally applicable to provide fluctuation information or correlation parameters.

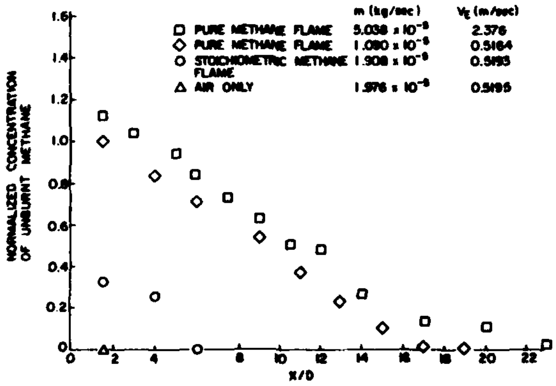

FIG. 17 CONCENTRATION OF UNBURNT METHANE

The practical application of laser fluorescence is still very limited.[37] The available data in the open literature are scarce and of limited scope. The same is true of the stimulated Raman technology. Both of these techniques as discussed previously hold out great promise for the future, by virtue of their great radiation transfer efficiency and their pointwise resolution capability. Both techniques need further development.

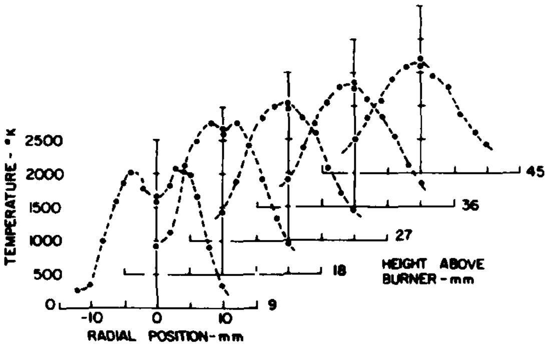

FIG. 18 TEMPERATURE PROFILE IN A PROPANE FLAME

TABLE I - SUMMARY

	Raman	CARS	SRS	Fluorescence	LDV
Specificity	Yes	Yes	Yes	Yes	X
Linearity	Yes	No	Yes	No	Yes
Independent Response	Yes	Yes	Yes	No	X
Spacial Resolution	Yes	Yes	Yes	Yes	Yes
Remoteness	Yes	Yes	Yes	Yes	Yes
Single Endedness	Yes	No	No	Yes	Yes
Instantaneity	Yes	Yes	Yes	Yes*	Yes*
Nonintrusiveness	Yes	Yes	Yes	Yes	Yes*
Simultaneity	Yes	No	No	No	Yes
General Applicability	Yes	Yes	No	No	Yes
Applicability to Fluctuation Meas.	Yes	No	No	No	Yes
Auto and Crosscorrelation	Yes	No	No	No	Yes*

*conditionally

ACKNOWLEDGEMENT

This research was sponsored by the Air Force Office of Scientific Research under Contract No. F-49620-78-C-0020, Project No. 2307-AI, the Department of Energy under Contract No. ET-78-C-01-3084 and the Office of Naval Research under Contract No. N00014-75-C-1143, Subcontract No. 8960-5.

REFERENCES

1. G. Placzek: Handb. Radial. Akademisebe Verlaqsqesellschaft VI (1939).
2. C.M. Sadowski and Y.E.H. Vanoverschelde, CARDE TN 1764167.
3. F. Robben: Project Squid ONR PU-R1-76 1975.
4. H.C. Van de Hulst: Light Scattering by Small Particles, Wiley N.Y. (1957).
5. G. Herzberg: Spectra of Diatomic Molecules, Van Nostrand, NY 1963.
6. H.A. Szymanski ed.: Raman Spectroscopy Theory and Practice, Plenum Press, 1967.
7. A. Anderson ed.: The Raman Effect, Bekker, N.Y. 1971.
8. B.P. Stoicherff: High Resolution Raman Spectroscopy, Adv. Spectr. I, pp. 91-174, Interscience (1959).
9. M. Lapp, C. Penny eds.: Laser Raman Gas Diagnostics, Plenum Press, NY, London 1974.

10. M. Lapp, C. Penny: Infr. and Raman Spectr., 3, p. 204 (1977).
11. G. Widhopf, S. Lederman: AIAA J., 9, 1971.
12. S. Lederman, M.H. Bloom, J. Bornstein, P.K. Khosla: Int. J. Heat and Mass Transfer, 17, p. 1479 (1974).
13. T. Yoshino, H.J. Bernstein: J. Mol. Spectr., 2, p. 213 (1958).
14. R. Goulard: Quant. Spectrosc. Rad Transfer, 14, p. 969 (1974).
15. S. Lederman: Prog. Energy Comb. Sci., Pergamon Press, 3, pp. 1 (1977).
16. S. Lederman: AIAA Paper No. 76-26 (1976).
17. S. Lederman: AIAA Paper No. 76-21 (1976).
18. E.L. Baardsen, R.W. Terhune: Appl. Phys. Lett., 21, p. 209 (1972).
19. A.G. Gaydon: The Spectroscopy of Flames, Chapman & Hall, London (1974).
20. A.P. Baranowski, J.R. McDonald: J. Chem. Phys, 66, p. 3300 (1977).
21. P.R. Regnier, J.P.E. Taran: Appl. Phys. Let., 23, p. 240 (1973).
22. P.R. Regnier, F. Moya and J.P.E. Taran: AIAA J., 12, 826 (1974).
23. A.B. Harvey, J.R. McDonald, W.M. Tolles: Progr. in Anal. Chem., 8, Plenum, (1976).
24. A.C. Eckbreth, P.A. Bomczyk, J.F. Verdieck: Appl. Spectr. Rev., 13, (1), 15 (1978).
25. J.W. Nibler, J.R. McDonald, A.B. Harvey: Opt. Comm., 18, 371 (1976).
26. J.J. Berret, R.F. Begley: Appl. Phys-Let., 27, p. 129 (1975).
27. A. Owyoung, E.D. Jones: Opt. Letl., 1, p. 152 (1977).
28. A. Owyoung: Opt. Let., 2, p. 91 (1978).
29. A. Owyoung: IEEE Journal of Quantum Electronics, QE, 14, 3, p. 192 (1978).
30. W.H. Stevenson, H.D. Thompson: Proceedings of a Workshop Project SQUID (1972).
31. H.D. Thompson, W.H. Stevenson: Proc. of a Workshop, 1, & 2, Proj. SQUID (1974).
32. S. Lederman, A. Celentano, J. Glaser: Phys. of Fluids, 22, 1965 (1979).
33. P. Lallesmand, P. Simova and G. Bret: Phys. Rev. Letters, 17, 1239 (1966).
34. W. Werncke, A. Lau, M. Pfeiffer, H.J. Weigmann, G. Hunsaly, K. Leur: Opt. Comm., 16, 128 (1976).
35. A.C. Eckbreth: AIAA, 79-0083, p. 9 (1979).
36. J.W. Daily: Applied Optics, 16, 3, p. 568 (1977).
37. P.A. Bonczyk, J.A. Shirley: Combustion and Flame, 34, p. 253 (1979).
38. F. Durst: Journal of Appl. Math. & Phys., 24, (1973).
39. W.J. Yantre: AIAA, 73-705 (1973).
40. S.L. Soo: Fluid Dyn. of Multiphase Systems, Blaisdell (1972).
41. P.K. Khosla, S. Lederman: PIBAL Rep. No. 73-22 (1973).
42. F. Durst and M. Zere: SFB 80-TM-63 U. Karlsruhe (1975).
43. W.M. Farmer: Appl. Opt., 13, p. 610 (1974).
44. A.J. Youle, N.A. Chigier, S. Atakan, A. Ungut: AIAA 77-214 (1977).
45. A.C. Eckbreth, R.J. Hall, J.A. Shirley: AIAA 79-0083 (1979).
46. M. Lapp, C.M. Penney, J.A. Asher: ARL 73-0045 (1973).

WAVE PHENOMENA IN LASER-PLASMA INTERACTION

SHALOM ELIEZER and HAGAI ZMORA

Plasma Physics Department
Soreq Nuclear Research Centre, Yavne, Israel

The basic phenomena of the interaction of high intensity laser radiation with matter are presented. The interaction physics between laser and matter leading to thermonuclear burn can be schematically summarized by the following sequence of events:

Light absorption → Energy transport → Compression → Nuclear fusion

The irradiated matter consists of a dense inner core surrounded by a less dense plasma corona. The laser radiation is mainly absorbed in the outer periphery of the plasma (at an electron density of 10^{21} cm^{-3} for a 1.06μm radiation). The energy is transported from there both inward to the ablation surface and outward into the expanding plasma. The onset of inward-going shock and heat waves results in the compression and heating of the core to a high density and temperature, adequate to meet the conditions needed for thermonuclear burn.

The various wave phenomena associated with these processes are described.

INTRODUCTION

The controlled thermonuclear fusion of hydrogen isotopes ($D + T \rightarrow \alpha + n + 17.6$ MeV) is potentially the best long term solution for the energy problem. In order to efficiently burn the thermonuclear fuel, certain conditions must be met, regardless of the heating and confinement method. First, ignition temperature (about 10 keV for DT fuel) must be reached. Second, the Lawson criterion, $n.\tau > 10^{14} cm^{-3}$ sec (where n is electron density and τ is the confinement time) must be met. In laser fusion, the Lawson criterion is met by maximizing n through the implosion and compression of the fusion fuel; 1000 fold compressions are expected. The confinement time τ is fixed by the intertia of the imploded material. The pellet compression is essential for a successful laser fusion scheme[1]. The confinement time of a 1mm pellet is about 200 psec, and the fusion reaction time is about 200 nsec. Consequently, only about 0.1 percent of the fuel will be burnt with no net gain. If on the other hand the pellet radius is reduced 10 fold, (the density would then increase 1000 fold), the confinement time would be reduced by a factor of 10, but the burn time would decrease by a factor of 1000, leading to a factor 100 increase in efficiency. An additional advantage of high core density is that the part of the reaction energy carried by the α particles (3.52 MeV per reaction) would be deposited within the pellet and propagate a thermonuclear burn wave. As a result, the needed ignition energy is reduced considerably (by a factor 100) since one would not have to bring the whole pellet to the ignition temperature.

The interaction physics between laser and matter, leading to thermonuclear burn, can be represented schematically by the following inter-correlated processes:

Light absorption → Energy transport → Compression → Nuclear fusion

The irradiated matter consists of a dense inner core, surrounded by a less dense corona. The laser radiation is mainly absorbed in the outer periphery of the plasma, up to a "critical density" n_c where the plasma frequency equals that of the laser light. The energy is transported from there both inward to the ablation surface and outward into the expanding plasma. The onset of inward going shock and heat waves results in the compression and heating of the core to a high density and temperature, adequate to meet the conditions needed for thermonuclear burn. These steps are inter-correlated. For instance, the transport of energy is influenced by the presence of turbulence in the plasma, which in turn, is generated in the absorption process. On the other hand, if the energy transport is inhibited, the density profile in the absorption region is steepened and the absorption mechanism is affected.

The concept of laser driven fusion has become a major research field during the last decade. Table 1 lists the main laser fusion facilities around the world. The basic parameters of the lasers used and the plasmas

TABLE I: Major Laser Produced Plasma Laboratories

Laboratory	Wavelength (μm)	Power(10^{12}W)	No. of beams
Livermore (USA)	1.06	30	20
Los Alamos (USA)	10.6	10	8
Lebedev (USSR)	1.06	10	12
Rochester (USA)	1.06	3	6
Osaka (Japan)	1.06	4	4
	10.6	1	2
Limeil (France)	1.06	2	8
Rutherford (England)	1.06	0.8	2
KMS (USA)	1.06	0.7	2
	0.53	0.2	2
NRL (USA)	1.06	0.5	2
NRC (Canada)	10.6	0.1	2
Palaisau (France)	1.06	0.1	1
Garching (Germany)	1.06	0.05	1
	1.3	1	1
Soreq (Israel)	1.06	0.05	1
ANL (Australia)	1.06	0.05	1
Bern (Switzerland)	1.06	0.05	1

TABLE II: Laser and Plasma Parameters

	Laser	Plasma
Wavelength	$\lambda=(0.53\div10.6)\mu m$	Size $\sim$ $100\mu m$
Irradiance	$I=(10^{13}\div10^{17})W/cm^2$	Duration $\sim$ 1 nsec
Electric field	$E=(6x10^7\div6x10^9)$Volt/cm	Expansion velocity$\sim10^7$cm/sec
Magnetic field	$B=(2x10^5\div2x10^7)$Gauss	Electron Density $n_e > 10^{18}cm^{-3}$
Light pressure	$P=(47x10^{-2}\div47)$Mbars	Electron temperature $T_e > 100$ eV
		Plasma frequency $\omega_p=1.8x10^{15}\{\frac{n_e}{10^{21}}\}^{\frac{1}{2}}\frac{rad}{sec}$
		Critical electron density $n_c=10^{21}\{\frac{1.06}{\lambda(\mu m)}\}^2 cm^{-3}$
		Collision mean free path $l \simeq 4,5x10^{12}\frac{T(eV)^2}{n}cm$

produced in laser fusion research are summarized in Table 2. One can distinguish between large, multibeam facilities and small, usually single beam systems. Although the physics of compressions of spherical targets with high neutron yields can be studied only with large, multibeam facilities, the physics of absorption and transport can conveniently be dealt with single beam, low power but high focussed intensity lasers and planar targets. Because of their simplicity and ease of operation and high repetition rates, these systems are often more advantageous for basic research. In contrast to high power TW lasers, focal spots of a few μm are easily achieved with small systems and thus the power density on target is still high (up to $10^{16}W/cm^2$).

The physics of laser-plasma interaction is based on hydrodynamics of one or more fluids, or alternatively, Boltzmann or Vlasov equations are used, together with Maxwell equations. This set of equations together with appropriate boundary conditions have all kinds of wave solutions: periodic waves, solitary waves or shock waves. These wave phenomena involved in the process of the interaction of the laser with the plasma are listed schematically in Figure 1. Although we shall try to discuss the main physical phenomena involved, no attempt has been made to cover all the vast theoretical and experimental work done in this field.

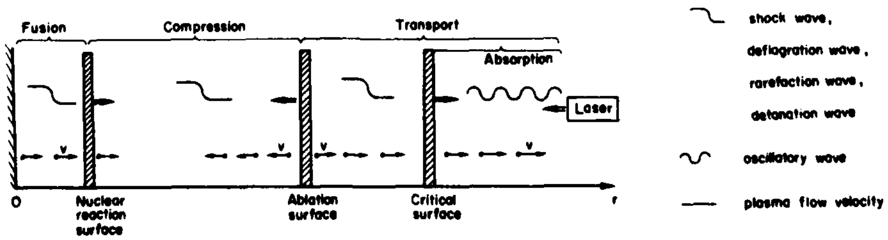

Figure 1. Wave phenomena in laser plasma interaction.

ABSORPTION OF THE LASER LIGHT

The problem of the laser light absorption in the plasma is one of the most important factors in the process of laser driven fusion. The two aspects of absorption which are of interest are:

a) What fraction of the incident laser light is absorbed, and b) What are the mechanisms responsible for the absorption.

The importance of the first question is self evident for an efficient coupling of energy into the plasma. The form by which energy is absorbed is also of importance because it affects energy transport into the dense material.

The laser light, incident on the target can penetrate the plasma up to a "critical density" n_c, given by $n_c = m\omega_o^2/4\pi e^2$ from which it will be totally reflected in much the same way as from a metal (ω_o is the laser light frequency, e and m are the electron charge and mass).

It is presently believed that the three main processes by which light can be absorbed by the plasma are: a) inverse Bremsstrahlung, b) resonant absorption and c) parametric instabilities.

The process of inverse Bremsstrahlung is of basic importance as a mechanism for laser light absorption in the plasma. In this process, an electron absorbs a photon as it moves from one free state to a more energetic one in the field of the ion. By simple considerations it can be shown that the attenuation of the light as it traverses the plasma (from the vacuum to the critical surface and back) is given by[2]

$$I_{abs} = I_o[1-\exp(-\frac{32}{15} k_o L \frac{\nu_c}{\omega_o})] \quad (1)$$

I_o and I_{abs} are the incident and absorbed light intensities respectively, ν_c is the collision frequency, ω_o is the frequency of the laser light and the scale length L is the distance over which the electron density changes from zero to n_c (assumed linear in Eq. 1).

ν_c goes down with temperature[3] ($\nu_c \sim T_e^{-3/2}$), and the plasma becomes collisionless, resulting in reduced absorption. I_{abs}/I_o is plotted as a function of laser intensity (for $\lambda_o = 1.06\mu m$) in Fig. 2. (a value of $100\lambda_o$ was assumed for L). As can be seen, classical heating ceases to be effective at about $10^{14} - 10^{15}$ W/cm^2 on target.

Collective process in the plasma can efficiently couple laser light into the plasma, by converting the light energy into electron plasma waves. The laser light can excite electron plasma waves, which then accelerate and heat the electrons. The generation of plasma waves is most efficient near the critical surface, where any spatial variation of the ion density will couple light into electron plasma waves.

The profile of the electron density in the vicinity of the critical surface n_c will effect the relative importance of each of the absorption mechanisms. In general, inverse Bremsstrahlung and instability heating will dominate in a plasma with a shallow density gradient. On the other hand, a steep density gradient will increase the efficiency of resonant absorption because the critical surface becomes more accessible to the on-coming laser light. Figure 3 shows a computation of inverse Bremsstrahlung and resonant absorption fractions as a function of the electron density scale-length L carried out for two selected rays impinging on a spherical target irradiated normally by a 1.06μm light.

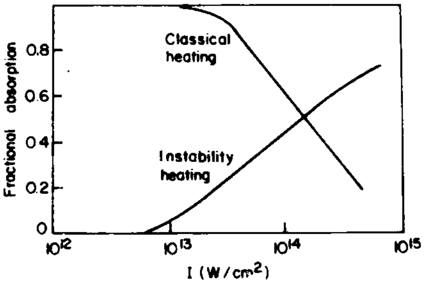

Figure 2. Fractional absorption as a function of laser intensity-theoretical (Ref. 4).

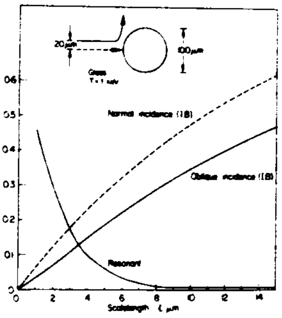

Figure 3. Classical and resonant absorption as a function of density gradient scale-length (Ref. 5).

The spatial variations of the density profile can be caused by a variety of mechanisms such as the pressure exerted by the laser light[6] on the otherwise freely expanding palsma (into the vacuum), transport inhibition of the energy flow from the absorption region to the ablation surface[7] or by stochastic fluctuations[8].

The electron density scale length has been measured experimentally by various methods. Holographic interferometry measurements of the electron density gradient have been carried out, using a frequency quadrupled laser light[9] . The results are shown in Fig. 4. In this particular measurement a 41μm glass microbaloon was irradiated with a 30 psec, 1.06μm laser light having an intensity of 10^{14} W/cm^2. The probing beam (0.266μm) was 15 psec long. The density profile shows a steepened region near n_c, for which a scale length of 1.5μm is inferred. Another type of measurement involves the mapping of the critical and quarter critical surfaces[10]. This is accomplished by imaging the source of the $2\omega_o$ and $3/2\ \omega_o$ light emitted from the plasma. Time resolved measurements yield the value of L as a function of time[11]. Typically, values of 10-30μm are obtained for 300 psec, Nd laser pulses. Finally, from space resolved X-ray spectroscopy[12], a value of 50μm was obtained for low intensity (10^{13} W/cm^2), relatively long pulse (500-700 psec) irradiation of slab aluminum targets.

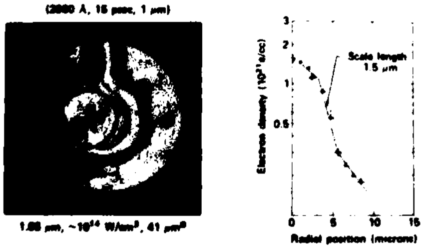

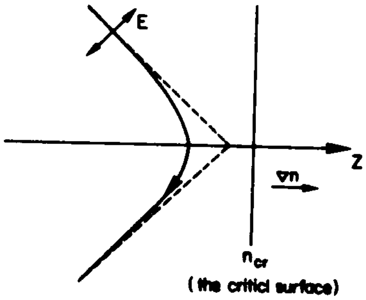

Figure 4. Holographic interferometry of a glass microbaloon (Ref. 9).

Figure 5. Geometry for resonant absorption.

It has been recently established that an absorption of 30-50% is achieved when a plane target is irradiated by short laser pulses (50 psec) from a Nd laser in focus, independent of intensity over more than four orders of magnitude, from 10^{13} to 10^{17} W/cm^2 [13,14]. Similar results were also obtained with 10.6μm CO_2 lasers[15]. Clearly, these experimental results cannot be explained by classical absorption only, and point out to the importance of collective processes in the plasma, such as resonant absorption or parametric instabilities.

Let us first discuss the phenomenon of resonant absorption. Assume that an obliquely incident electromagnetic wave having the electric field vector E lying in the plane of incidence (π polarization) is reflected from an inhomogeneous medium (see Fig. 5). There will exist a surface on which the electric field is along the density gradient. The electric field tunnels through the turning point to the critical density and an electrostatic wave is created there[16]. The electrons along the density gradient at the critical surface undergo resonantly driven electrostatic oscillations, which will finally damp and result in energy absorption by the plasma.

The importance of the resonant absorption mechanism has been demonstrated experimentally in various laboratories. In these experiments the laser light with power intensity ranging from 10^{13} to 10^{16} W/cm^2 and pulse length in the range of 30 psec, is obliquely incident on a plane target. Upon varying the angle of incidence, plasma parameters such as total light absorption[14], electron temperature[17,18] or momentum transfer to the plasma[19] show a definite maximum at about 20^o for π polarized light, whereas no such "resonance" is observed for σ polarization. The total light absorption is higher for π polarized with respect to the σ polarized light by about 35-50%, independent of laser light intensity. On the other hand, it has been shown experimentally[20] that for long laser pulses (2.5 nsec), this resonant behavior disappears, indicating that resonant absorption is less effective in this case.

Although resonant absorption seems to be less effective for larger pulse lengths, the total absorption efficiency remains quite high[21]. A value of 55% is obtained for 1.06μm pulses of 3 nsec duration and intensity of 7×10^{14} W/cm^2 on target. In this region, absorption by parametric instabilities[22,23] becomes an efficient mechanism. The term "parametric instability" stems from an analogy with parametric amplifiers, in which an external driving source at frequency ω_o excites natural oscillations of the system at frequencies ω_1 and ω_2 such that energy and momentum are conserved (i.e $\omega_o = \omega_1 + \omega_2$; $\underline{k}_o = \underline{k}_1 + \underline{k}_2$, where $\underline{k}$ is the wave vector). In our case, ω_o is the driving laser light ω_1 and ω_2 are either an ion acoustic wave (phonon) or an electron wave (plasmon) which are longitudinal waves, or another photon. The frequency of an ion acoustic wave is given by $\omega_i^2 = k^2(zT_e + \gamma_i T_i)/M$, and that of a plasmon wave by $\omega_e^2 = \omega_p^2 + 3k^2 T_e/m$. T_e and T_i are electron and ion temperatures (in energy units), k is the wave vector, M and m are the ion and electron mass respectively, γ_i is the ratio of specific heats (taken as 3 for a plane wave). ω_p is the plasma frequency. At the critical surface, $\omega_e \sim \omega_p$ while $\omega_i << \omega_p$.

The possible couplings between these waves are:

a) *photon → ion acoustic wave + photon (stimulated Brillouin).*
b) *photon → plasmon + photon (stimulated Raman).*
c) *photon → plasmon + ion acoustic wave (parametric decay instability).*
d) *photon → plasmon + plasmon (two plasmon instability).*

The first two mechanisms (and in particular Brillouin back scattering) lead to a reduced absorption, while the two other mechanisms add to the absorption efficiency. The parametric instabilities will occur at any amplitude of the driving force, unless there is a damping (collisional or Landau damping) which will limit the growth rate of the instability, or prevent it altogether if the pump wave is not strong enough[23,24]. For laser light normally incident on a plasma with an inhomogeneous density profile, the estimated absorption efficiency will roughly be given by[25] $I_{abs}/I_o \approx 2\Gamma k_o l/\omega_o$, where Γ is the effective energy damping rate of the instability and l is the size of the plasma effectively participating in the excitation of the instability (l is of the order of the scale-length L). This fraction is shown in Fig. 2 (*taken from* Ref. 4) *as a* function of laser intensity assuming $l = 100\lambda_o$.

Experimental phenomena related to parametric processes should exhibit threshold and intensity dependence as discussed above. The most direct evidence for the role of parametric instabilities in laser produced plasma has come from the observation of harmonic light emission from the plasma. As many as eight harmonics were observed in the backscattered light from a planar Al target irradiated by a 10^{14} W/cm^2 CO_2 laser[26]. By far the most intense emission of back reflected radiation from the plasma is due to stimulated Brillouin scattering. It has been found[27] that under certain conditions, as much as 50 percent of the incident light is being reflected from a plane target irradiated by a 1.06μm light. The problem of Brillouin scattering has been thoroughly investigated for both short pulse and long irradiation in many laboratories because of its paramount impact on the efficiency of light coupling into the plasma. It has been shown[28] that the back reflected light has a threshold at about 10^{13} W/cm^2, and its percentage increases with laser intensity. Finally, the spectrum of the back reflected light is red shifted, and the rays retrace the incident path[29]. All these phenomena are expected for Brillouin back reflection. The dependence of the back reflected light on the density scale length has been recently studied by the N.R.L. group[27]. In this experiment, polished CH and Al to planar targets were irradiated by a 75 psec, 1.06μm light with intensity of 10^{15}-10^{16} W/cm^2. The main pulse was preceded by a prepulse of variable energy, 2 nsec ahead of the main pulse. The density length produced by the prepulse at the time of arrival of the main pulse is of the order of 100μm, which is high enough for a high level of Brillouin growth. This experiment suggests that a significant back scattering may also occur with shaped pulses which are planned for laser fusion[1].

Emission of 3/2 ω_o radiation has been interpreted as an evidence for plasmons (Langmuir waves) generation at $n_e = 1/4 n_c$. Plasmons with frequency 0.5 ω_o created there (i.e. by the "two plasmon instability") can couple with the oncoming light wave ω_o to generate a 3/2 ω_o photon. The nature of this radiation has been studied among others, by H.C. Pant et al.[30]. It has been found that the onset of this radiation occurs at 2×10^{13} W/cm^2, in agreement with the predicted threshold calculated for their experimental conditions.

Reflected light at frequency $2\omega_o$ can also be explained on the basis of parametric instabilities. Plasmons generated near the critical density have a frequency close to ω_o. These longitudinal waves can couple with the oncoming light photon ω_o, or with another plasmon to give a photon at $2\omega_o$. This radiation should again exhibit threshold behavior and be red shifted compared with 2 ω_o.

Finally, the onset of parametric instabilities should be accompanied by the generation of fast, suprathermal electrons and ions in the plasma. Their existence has been proven directly by charge collectors measuring the energy spectrum of charged particles in the plasma blow-off and also by the X-ray continuum and line spectra emitted by the plasma. For high laser irradiances the continuum spectrum is usually composed of a thermal distribution together with a high energy tail which, if interpreted as a "temperature" T_H, yields a value of 1-20 keV depending on laser intensity. The line spectrum contains a line of K_α radiation from low ionization stages. It has been shown that this radiation comes as a result of energetic, non-thermal electrons impinging on the solid target behind the interaction zone[31].

To summarize, the possible absorption mechanisms and their predicted regions of occurance along the density profile are listed in Figure 6. In the low laser intensity regime, where electron temperature is low, collisional absorption dominates, whereas at higher laser intensities ($>10^{14}$ W/cm^2) collective effects take over. The type of collective effect that will dominate depends on the details of the plasma structure. If steep electron density gradients are produced, resonant absorption will be an important mechanism whereas shallow gradients will enhance the effectiveness of parametric instabilities.

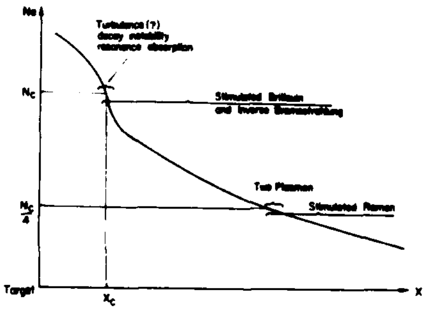

Figure 6. Topography of laser light absorption mechanisms.

HEAT TRANSPORT AND PLASMA FLOW

The heat transport from the critical surface inwards and the plasma flow from the ablation surface outwards is described schematically in Figure 7. At least three physical mechanisms have been suggested to dominate the heat and plasma transport: (a) the internally generated magnetic fields, (b) the ponderomotive forces and (c) turbulence.

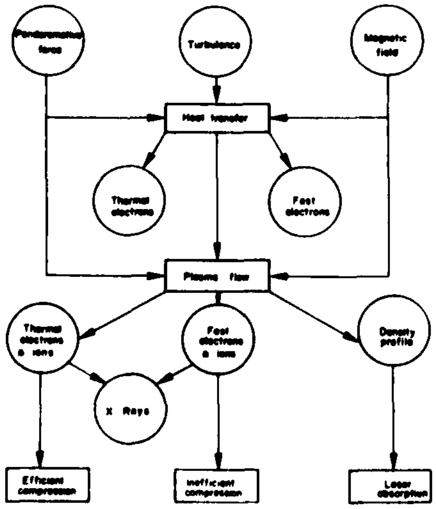

Figure 7. Flow chart of transport phenomena.

The theoretical importance and the experimental evidence of magnetic fields generated in laser produced plasma have been investigated by many authors[32-38]. These magnetic fields may be created from currents driven by electron pressure in non-uniform plasmas[32], which is proportional to $\nabla n_e x \nabla T_e$, where n_e and T_e are the electron density and temperature. These self-generated magnetic fields inhibit the electron heat transfer and can accelerate the ions through the JxB force, where J is the plasma current[35].

The ponderomotive force, which describes the radiation pressure in a plasma, may play a dominant role in the dynamics of laser-produced plasmas[6,39-44]. The time average Lorentz force on an electron in the electromagnetic field with frequency ω and electric field amplitude $|E|$ is given by the ponderomotive force

$$F_{p,e} = -\frac{e^2}{4m\omega^2}\nabla|E^2| \text{ (dyne)} \qquad (2)$$

The ponderomotive force of the laser radiation can sifnificantly influence the hydrodynamic behavior of the plasma near the critical density. The radiation pressure acts in addition to the hydrodynamic pressure and may modify the plasma density at the critical density and the flow velocity profile. The ponderomotive force may accelerate the ions in an indirect way by the generation of a charge separation electric field E_s,

$$F_{p,e} = eE_s \qquad (3)$$

such that an ion is accelerated by the force ZeE_s, where Z is the ion charge. The energetic ions cause an inefficient compression of the pellet. Most of the absorbed laser energy is converted into ion kinetic energy $W_i=\frac{1}{2}MV^2$ (M is the ablated mass and V is the average ion velocity). The momentum P_i transferred to the pellet due to the ablation effect is given by $P_i = 2W_i/V$. For a fixed value of W_i the momentum transferred to the pellet is increased with lower velocity of more ablated mass. Therefore, one can conclude that fast ions play a negative role in the quest for laser-fusion.

Laser light absorption and plasma transport physics may be influenced by the existence of turbulence in the laser-plasma interaction[45,46]. The phenomenon of inhibition of heat flow can be explained theoretically by ion acoustic turbulence with strong fluctuating electrostatic fields[46]. These random field structures scatter the electrons transporting energy into the target. However, more theoretical work and a better understanding of "turbulence physics" is needed in order to assess its importance in laser-plasma interaction.

The light absorption occurs in the underdense region of the plasma at densities $n_e<n_c$. The energy is transferred from the absorption region to the ablation surface by thermal conduction. In the region of the ablation surface,plasma is created and the core is compressed due to acceleration caused by the rocket reaction effect. Efficient transfer of energy from the absorption region to the compressed core of the pellet is needed in order to obtain efficient thermonuclear reactions. If, on the other hand, the heat flow would be inhibited by some mechanism, this would cause a high electron temperature which might lead to preheating of the core. In particular, a stringent inhibition of electron thermal conduction would significantly modify the design of fusion targets.

The thermal conductivity is described by the Fourier law

$$I_c = -K\nabla T \quad \text{erg cm}^{-2}\text{sec}^{-1} \tag{4}$$

where I_c is the classical energy flux and ∇T is the temperature gradient. For fully ionized plasma, the thermal conductivity coefficient K was calculated[3,47] to be proportional to $T_e^{5/2}$, where T_e is the electron temperature. The Fourier law, Eq. (4), does not imply any upper limit on the magnitude of the energy flux I_c. However, a finite number of flowing particles with a finite velocity cannot have an arbitrarily large energy flux. Since the collisional tranport, where the Fourier law is valid, cannot be faster than collisionless streaming, an upper bound on the energy flux can be obtained by calculating the free streaming[48,49] flux limit I_l. For a Maxwellian distribution of free streaming electrons the flux limit is given by

$$I_l = f n_e m^{-1/2} (kT_e)^{3/2} \tag{5}$$

where f=0.8 in cgs units[22]. Therefore, the electron thermal flux is given by

$$I = \min\{I_c, I_l\} \tag{6}$$

where I_c and I_l are defined in Eqs. (4) and (5).

It was found that when the laser flux exceeds 10^{14} W/cm^2, the value of f is reduced[7,50,51], implying a reduction in electron thermal conductivity. Transport reduction by factors up to 30 have been suggested[38]. By observing the percentage of laser light transmitted through thin polystyrene films, it was concluded[50] that the electron thermal conductivity is reduced only for laser fluxes larger than 10^{14} W/cm^2. The results of similar measurements[53,54] carried out at laser fluxes of about 2×10^{13} W/cm^2 can be explained by the classical mechanism (Eq. (4)).

The phenomenon of inhibition of heat flow can be explained theoretically by ion acoustic turbulence with strong fluctuating electrostatic fields[45,46]. Alternatively, the existence of self-generated magnetic fields can reduce the heat conduction[35,38].

In order to understand the plasma flow, we consider the expansion of ions of charge Z with a constant and uniform electron temperature. The mass and momentum conservation for the one dimensional expansion of ions, neglecting the ponderomotive force, are

$$\frac{\partial n}{\partial t} + \frac{\partial}{\partial x}(nv) = 0 \tag{7}$$

$$\frac{\partial}{\partial t}(nv) + \frac{\partial}{\partial x}(nv^2) = \frac{-ZkT_e}{Am_p}\frac{\partial}{\partial x} n \tag{8}$$

where n and v are respectively the ion density and velocity, Z is the ion charge and A is the atomic mass. The thermodynamic pressure is $ZnkT_e$ and the energy equation is replaced by the isothermal condition. The isothermal assumption applies if energetic electrons can move fast enough to heat the expanding plasma. In this case Eqs. (7) and (8) can be solved to yield the self similar solution[55,56].

$$n(x) = \begin{cases} n_o \exp\{-(x+ct)/ct\} & \text{for } x > -ct \\ n_o & \text{for } x < -ct \end{cases} \qquad (9)$$

where x is the distance from the target in the direction of the laser beam and c is the isothermal sound velocity.

$$c = (ZkT_e/Am_p)^{\frac{1}{2}} \qquad (10)$$

The spatial velocity is given by

$$v = c + x/t \qquad (11)$$

The plasma velocity distribution can be written as

$$(dN/dV)_{t=\tau} = (dN/dx)_{t=\tau} \cdot (dx/dV)_{t=\tau} \qquad (12)$$

where N is the total number of ions in the plasma and τ is the time when the pressure vanishes. From that time on the plasma drifts freely to the detector. It is generally assumed that τ is about equal to the laser pulse duration[57]. Using the relation $N(x) = n(x)Act$, where A is the area of the focal spot, together with Eqs. (9)-(12), one obtains

$$\frac{dN}{dV} = \frac{N}{c} \exp(-V/c) \qquad (13)$$

in agreement with the data taken by charge collectors[57].

Next, we consider the influence of the radiation pressure (i.e ponderomotive force) on the density and flow velocity profiles. One has to distinguish between two classes of models: (a) transient profile structures[58,59] induced by short laser pulses and (b) steady state profile induced by long laser pulses. The distinction between short and long pulses is given by the product $c\tau$, where c is the sound velocity and τ is the laser pulse duration. For long laser pulses one has $c\tau \gg \lambda$, λ being the laser wavelength. The importance of the plasma flow on the stationary density structure can be understood in a simple manner by using the "jump" conditions[39-41,60]. The "jump" conditions across the critical surface may be obtained by integrating the steady state equations of mass and momentum conservation from a point X_1 on one side of the critical surface to a point X_2 on the other side of the critical surface (see Fig. 8). If X_2 is chosen as the local maximum of the electric field E, one can write the jump conditions in a frame moving with the critical surface

$$\rho_1 V_1 = \rho_2 V_2 \qquad P_1 + \rho_1 V_1^2 = P_2 + \rho_2 V_2^2 + \Pi \qquad \Pi \equiv \frac{1}{16\pi} E^2_{max} \qquad (14)$$

The solution of Eq. (14) for M_2/M_1 as a function of Π and M_1, where M is the Mach number, M=v/c, with c the isothermal sound speed ($c^2=P/\rho$), is given for an isothermal flow (i.e $c_2^2 = P_2/\rho_2 = c_1^2$)

$$\frac{M_2}{M_1} = \frac{\rho_1}{\rho_2} = \frac{1 + M_1^2 - \Pi/\rho_1 c_1^2 \pm[(1 + M_1^2 - \Pi/\rho_1 c_1^2)^2 - 4M_1^2]^{\frac{1}{2}}}{2M_1^2} \qquad (15)$$

Using the fact that M_2/M_1 is real, one has

$$M_1 \geq M_R \equiv 1 + (\Pi/\rho_1 c_1^2)^{\frac{1}{2}} \text{ (R Type)} \qquad (16)$$

or

$$M_1 \leq M_D \equiv 1 - (\Pi/\rho_1 c_1^2)^{\frac{1}{2}} \text{ (D type)} \qquad (17)$$

Using Eq. (15) one obtains that "R type" solutions represent compressions (i.e. $\rho_1<\rho_2$,$M_1 > M_2$), whereas "D type" solutions describe rarefactions wave ($\rho_1 > \rho_2$, $M_1 < M_2$). The physical possible cases are described schematically in Fig. 9. The "D type" solution represent the familiar "density step" from plasma simulations.

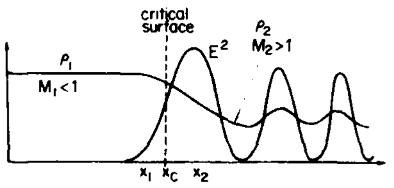

Figure 8 (see above). Transition of a subsonic flow (region 1) to a supersonic one (region 2) under the action of light pressure (Ref. 60).

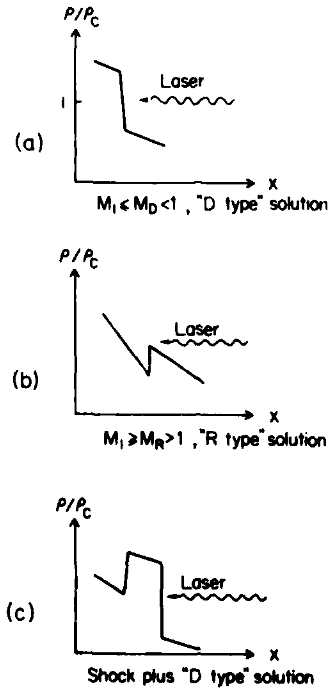

Figure 9 (see right). Schematic density profiles for (a) D type $M_1<M_D<1$,(b) R front $M_1\geq M_R>1$, (c) Shock (M>1) plus D front. (Ref. 41).

To conclude, in laser plasmas produced from dense targets, there is a region near the target where the flow is subsonic. Due to the free plasma expansion, the outflow becomes supersonic relative to the critical surface. These compressions and shock like structures may affect the light absorption and energy transport phenomena.

COMPRESSION

Due to the strong heating of matter in the absorption region, high pressure is exerted on the surrounding material which leads to the formation of an intense shock wave, travelling along the direction of the incoming laser beam, into the interior of the target. The momentum imparted to the compressed material behind the shock front is balanced by the momentum of the outflowing plasma. The thermal pressure together with the momentum of the ablated material drives the shock wave in the opposite direction of the ablated material. The idea of compressing the pellet by convergent compression waves has reduced the required laser energy needed to obtain a "breakeven" thermonuclear reaction. The required compression is of the order of $\rho R \sim 1$ gr/cm^2 (ρ is the fuel density and R is the core radius).

In 1974 the first direct observation of a laser driven shock wave was reported[61,62]. A planar solid hydrogen target was irradiated with a 10J, 5-nsec Nd laser pulse and the spatial development of the laser driven shock wave was measured using high speed photography. The planar interaction geometry approximates a small section of a pellet (until convergent effects dominate) and has the great advantage of theoretical simplicity, as well as, the possibility to diagnose the cold rear surface. The Hugoniot relations are used to determine the state of the compressed solid behind the shock front. For planar geometry the conservation of mass, momentum and energy for a steady state shock wave can be written as:

$$\rho_o V_s = \rho_1 (V_s - V_p) \ ; \quad \rho_o V_s^2 = \rho_1 (V_s - V_p)^2 + p_1 \tag{18}$$

$$\varepsilon_1(\rho_1, p_1) - \varepsilon_o(\rho_o, p_o) = \tfrac{1}{2} p_1 \left(\frac{1}{\rho_o} - \frac{1}{\rho_1}\right) \tag{19}$$

where the shock wave is moving with velocity V_s into the undisturbed solid, the subscript o and 1 describe the regions ahead and behind the shock front respectively, V_p is the particle velocity, ρ the density, p the pressure and ε is the specific internal energy. From these relations the state behind the shcok front can be determined if the equation of state $\varepsilon = \varepsilon(p, \rho)$ are known and the shock velocity is measured. The compression ratio and the pressure were estimated[62] to be about $\rho/\rho_o \simeq 4$ and $p_1 \simeq 2$ Mbars for the 10 Joules, 5 nsec Nd laser pulse interacting with a plane solid hydrogen. Using Eq. (18) together with the analysis of Caruso and Gratton[63] plasma pressures in the range of 1 to 10 Mbars and shock wave velocities between 10^6 to 3×10^6 cm/sec were estimated. These results are based on experiments done at Soreq[64] with Nd laser pulses with intensities $6\times10^{12} - 10^{14}$ Watts/cm^2, 0.5 nsec duration, interacting with thin foil aluminum targets.

For high laser irradiance and short pulse durations (<1 nsec) it was suggested[65] that the produced plasma might be hot enough and thus transparent to the laser light. In this case, the laser is absorbed at the surface of the dense region which moves into the target as a laser-heated deflagration wave preceded by a shock wave. This model was used to calculate the nuclear energy yield from a solid D-T target[66] as well as from high Z target materials[67].

To date, most compression experiments have been carried out with thin glass microbaloons, about 100μm in diameter and a few microns thick, filled with 10 atm. D-T gas. Short laser pulses of about 100 psec were used to illuminate the pellets as symmetrically as possible. The laser pulse duration is chosen such that most of the energy is deposited in the glass shell before an appreciable expansion has taken place. The glass shell then heats up rapidly and explodes both inwards and outwards. The inward going motion causes the D-T gas to compress and heat beyond the point where thermonuclear reactions start to take place. This type of target is called an "exploding pusher". Typically, yields of 10^9 neutrons were obtained with laser pulses of a few TW. The compression characteristics of the targets have been investigated experimentally by essentially two methods. First X-ray pinhole photographs of the pellet were taken which clearly show the compressed inner core[68]. Second, line broadenings of Ne X-ray spectra were analysed to yield the core density[57] (the Ne gas was introduced into the microbaloon instead or in addition to the D-T gas). Calculations show that it is impossible to obtain a net production of energy with this type of targets because although high temperatures are reached, the compression is too low.

The other types of targets are called "ablation compression" targets and are believed to lead to breakeven conditions. These have a thicker shell, and are usually of the multilayer type[69]. The thick shell prevents the high energy electrons from preheating the core. Moreover, the pulse length is chosen so that the laser energy is incident on the target during most of the implosion time, leading to a more efficient momentum transfer to the D-T fuel. If the incident laser energy is high enough, it is possible to attain higher gains, although the fuel temperature is low. Work on these types of targets has begun only recently, with the development of new multiterawatt laser systems. Since core temperature is expected to be lower than in exploding pusher type targets, diagnosing of the attained ρR causes a problem. A unique method of back lightening the imploding target with radiation from an external, laser produced X-ray source was recently developed[70]. Other proposed techniques employ the analysis of α particle emitted from the target, and ratio of nuclear reactions such as DT to DD[57].

THERMONUCLEAR BURN WAVES

Once the ablation driven implosion has led to the onset of thermonuclear reactions at the center of the pellet, a burn wave starts to propogate outwards from the center. Energy is transferred from the hot core to the adjacent cold layers by three mechanisms: a) thermal conduction, b) hydrodynamic expansion due to pressure buildup in the hot core and c) high energy, charged thermonuclear reaction products transport. Heating by neutrons is of significance only in the megajoule input energy range and for densities of the order of 1000 gr/cc. At electron temperatures above 15 keV and sufficiently high densities, heat conduction propagates at subsonic velocities, and the burn wave is therefore dominated by the supersonic charged particles[71].

Thermonuclear reaction waves differ from ordinary chemical wave reactions in that the temperature range is much higher (10^7-10^{10}°K) and hence the medium is completely ionized. Moreover, the thermonuclear reaction rate increases and then decreases with increasing plasma temperature. The energy content in the thermonuclear wave (taking into account α deposition only) is $Q=6.74 \times 10^{17}$ erg/gr which is orders of magnitude larger than in chemical reaction waves.

The structure and behavior of a reaction wave in a plasma can be described by five equations responsible for the change in density, degree of reaction, velocity, electron temperature and ion temperature[72,73]. This set of equations is basically similar to that describing the transport and the compression phenomena with the addition of the nuclear reactions. When the transport coefficients such as the thermal conductivity, the viscosity coefficient and the electron-ion collision time, approach zero these systems of equations have discontinuous solutions describing driven detonation wave in a one temperature gas. Therefore, the transport coefficients are broadening the mathematical shocks smearing out the discontinuities. The development, propagation and structure of the strong reaction wave were numerically studied assuming various initial and boundary conditions. The numerical solution of these equations indicate that a thermonuclear burn wave can actually be ignited with a net energy gain. This optimistic conclusion still remains to be realized experimentally.

ACKNOWLEDGEMENT

We would like to thank the members of the Plasma Physics Department in Soreq for their collaboration, and in particular Dr. S. Jackel for his valuable remarks and suggestions.

REFERENCES

1. J.L. Nuckolls, L.Wood, A. Thiessen and G. Zimmerman, Nature 239, 139 (1972).
2. J. Dawson, P. Kaw and B. Green, Phys. Fluids, 12, 875 (1969).
3. L. Spitzer, Physics of Fully Ionized Gases (Interscience, New York, 1956).
4. W.L. Kruer, Progress in Laser and Laser Fusion, ed. B. Kursunoglu et al., Plenum Press, 1976.
5. S. Jackel, Lab. for Laser Energetics, Rochester, N.Y. Report No. 68, 1977 (unpublished).
6. H. Hora, "Laser Interaction and Related Plasma Phenomena" ed. by H.J. Schwarz and H. Hora, Plenum Press, New York (1971).
7. F.C. Young et al., Appl. Phys. Lett. 30, 45 (1977).
8. S. Eliezer and Z. Schuss, Phys. Lett. 70A, 307 (1979).
9. D.T. Altwood, D.W. Sweeney, J.M. Auerbach and P.H.Y. Lee, Phys. Rev. Lett. 40, 184 (1978).
10. S. Jackel, J. Albritton and E. Goldman, Phys. Rev. Lett. 35, 514 (1975).
11. S. Jackel, B. Perry and M. Lubin, Phys. Rev. Lett. 37, 95 (1976).
12. A. Zigler, H. Zmora and Y. Komet, Phys. Lett. 60A, 319 (1977).
13. C.G .M. van Kessel et al., Z. Naturforsch 329, 1100 (1977).
14. H.G. Ahlstrom, Livermore Report, UCRL 79819 (1977).
15. V. Cottles and D. Giovanielli, LA-UR-77-763 and E.L. Lindman, Journal de Physique, 38, suppl. p. C6 (1977).
16. V.L. Ginzburg, "Propagation of Electromagnetic Waves in Plasma", pp. 364-402, Gordon and Breach (1961).
17. J.S. Pearlman and M.K. Matzen, Phys. Rev. Lett. 39, 140 (1977).
18. J.E. Balmer and T.P. Donaldson, Phys. Rev. Lett. 39, 1084 (1977).
19. B. Arad et al. (Soreq preprint).
20. S. Jackel et al., (Soreq preprint).
21. B.H. Ripin et al., NRL Report 3890.
22. D.F. Dubois and M.V. Goldman, Phys. Rev. 164, 207 (1967).
23. N.G. Basov et al., Sov. Phys. JETP 40, 61 (1874).
24. J.M. Dawson and A.T. Lin, Univ. of California LA Report PPG-191 (unpublished).
25. E. Valeo et al., Livermore Report, UCRL 78005.
26. N.H. Burnett, H.A. Baldis, M.C. Richardson and G.D. Enright, Appl. Phys. Lett. 31, 172 (1977).
27. B.H. Ripin et al., Phys. Rev. Lett. 39, 611 (1977); B.H. Ripin, NRL Report 3684 (1977).

28. B.H. Ripin et al., Phys. Rev. Lett. 33, 634 (1974).
29. K. Eidman and R. Sigel, in Laser Interaction and Related Plasma Phenomena, Vol. 3, p. 667 (1973), Plenum Press.
30. H.C. Pant et al., Optics Comm., 16, 396 (1976).
31. A. Zigler, H. Zmora and J.L. Schwob, Phys. Lett. 63A, 275 (1977); B. Yaakobi, I. Pelah and J. Hoose, Phys. Rev. Lett. 37, 836 (1976).
32. J.A. Stamper et al., Phys. Rev. Lett. 26, 1012 (1971).
33. J.A. Stamper and B.H. Ripin, Phys. Rev. Lett. 34, 138 (1975).
34. M.G. Drouet and R. Bolton, Phys. Rev. Lett. 36, 591 (1976).
35. R.S. Craxton and M.G. Haines, Phys. Rev. Lett. 35, 1336 (1975).
36. J.A. Stamper and D.A. Tidman, Phys. Fluids 16, 2024 (1973).
37. D.G. Colombant and N.K. Winsor, Phys. Rev. Lett. 38, 697 (1977).
38. B. Yaakobi and T. Bristow, Phys. Rev. Lett. 38, 350 (1977).
39. K. Lee et al., Phys. Fluids 20, 51 (1977).
40. P. Mulser and C. van Kessel, Phys. Rev. Lett. 38, 902 (1977).
41. C.E. Max and C.F. McKee, Phys. Rev. Lett. 39, 1336 (1977).
42. V.P. Silin, Sov. Phys. JETP Lett. 21, 152 (1975).
43. D. Baboneau et al., Phys. Lett. 57A, 247 (1976).
44. P. Mulser and C. van Kessel, Phys. Lett. 59A, 33 (1976).
45. R.J. Faehl and W.L. Kruer, Phys. Fluids 20, 55 (1977).
46. W.M. Manheimer, Phys. Fluids 20, 265 (1977).
47. R. Landshoff, Phys. Rev. 76, 904 (1949) and 82, 442 (1951).
48. R.L. Morse and C.W. Nielson, Phys. Fluids 16, 909 (1973).
49. S. Bodner, NRL Report 3591 (unpublished) 1977.
50. J.S. Pearlman and J.P. Anthes, Appl. Phys. Lett. 27, 581 (1975).
51. R.C. Malone, R.L. McCrory and R.L. Morse, Phys. Rev. Lett. 34, 721 (1975).
52. M.S. White, J.D. Kilkenny and A.E. Dangor, Phys. Rev. Lett. 35, 524 (1975)
53. A. Zigler, H. Zmora, Y. Paiss and J.L. Schwob, J. of Phys. D10,L159 (1977)
54. C. Yamanaka et al., Plasma Physics and Controlled Nuclear Fusion Research 1976, Vol. I, p. 147.
55. A.V. Gurevich, L.V. Pariiskaya and L.P. Pitaevskii, Sov. Phys. JETP 22, 449 (1966).
56. J.E. Allen and J.G. Andrews, J. Plasma Phys. 4, 187 (1970).
57. LLE Rochester Annual Report 1977, Vol. II.
58. H.H. Chen and C.S. Liu, Phys. Rev. Lett. 37, 693 (1976) and Phys. Fluids 21, 377 (1978).
59. H. Schamel and K. Elsässer, Plasma Phys. 20, 837 (1978).
60. P. Mulser and G. Spindler, Garching Preprint PLF 12 (1978).
61. C.G.M. van Kessel and R. Sigel, Phys. Rev. Lett. 33, 1020 (1974).
62. C.G.M. van Kessel, Z. Naturforsch 30a, 1581 (1975).
63. A. Caruso and R. Gratton, Plasma Phys. 11, 839 (1969).
64. B. Arad et al., J. Appl. Phys. (to be published).
65. C. Fauquignon and F. Floux, Phys. Fluids 13, 386 (1970).
66. J.L. Bobin, D. Colombant and G. Tonon, Nucl. Fusion 12, 445 (1972).
67. D. Colombant and G.F. Tonon, J. Appl. Phys. 44, 3524 (1973).
68. P.M. Campbell, G. Charatis and G.R. Montry, Phys. Rev. Lett. 34,74 (1975).
69. J. Nuckolls et al., Lawrence Livermore Lab. Laser Fusion Program, Annual Report 1976, UCRL 50021-76.
    J.D. Lindl, ibid. Rep. UCRL 79735.
70. M.H. Key et al., Phys. Rev. Lett. 41, 1467 (1978).
71. K.A. Brueckner and S. Jorna, Rev. Mod. Phys. 46, 325 (1974).
72. M.S. Chu, Phys. Fluids 15 , 413 (1972).
73. K. Nishihara et al., in "Laser Interaction and Related Plasma Phenomena", Vol. 4, ed. by H.J. Schwarz and H. Hora, Plenum Press, New York (1977).

REVIEW OF EXPERIMENTAL AND THEORETICAL STUDIES OF THE HARP SOLID PROPELLANT IGNITON AND COMBUSTON TUBE-LAUNCHER

GERALD V. BULL

Space Research Corporation (Quebec)
Highwater, P.Q., Canada

The H.A.R.P. program involved the ignition and burning of large quantities of solid propellant (up to 1300 lbs.) confined in a more or less cylindrical chamber of approximately 18 inches in diameter and some 190 inches in length. Varying shot travel and weights were studies, to achieve the highest muzzle velocities possible. A variety of grain configurations and web sizes, ignition devices (geometrical distribution and energy level) were used to overcome erratic burning, and ultimate catastrophic detonation problems.

This paper reviews the major problems, background theoretical studies and ultimate experimental solutions.

INTRODUCTION

Post World War II research in ordnance was conducted in a low-key manner and in the shadow of dominating, spectacular development in rocketry. During the decade 1950-1960 many investigations were begun, particularly at the Canadian Armaments Research and Development Laboratory at Valcartier, Quebec, which led ultimately to a relatively large program code named HARP and sponsored by the U.S. Army and Canadian Department of Defence. The program was centered at McGill University, with the major large scale firing range in Barbados, although other firing sites were used. The program was one of close collaboration between the Space Research Institute of McGill University, and the Free Flight Laboratory of the Ballistic Research Laboratories, U.S. Army, Aberdeen, Maryland. Any complete discussion of this program would be well beyond the scope of the present paper; extensive bibliographies covering the program are available, and the many names appearing therein are only partially reflective of those whose work was used in the preparation of this paper.

To provide background to the problem to be discussed in this paper, the HARP 16" firing facility in Barbados should be described, along with supporting ballistic test facilities in Highwater, Quebec. The geometry of the Barbados 16" gun is sketched in Figure 1A; the geometry of the Highwater 16" gun is sketched in Figure 1B, and the geometry of the propellant testing facility at Highwater, aptly named the HARP Flyer owing to its propensity to take-off in all directions in response to any technical error, is shown in Figure 1C.

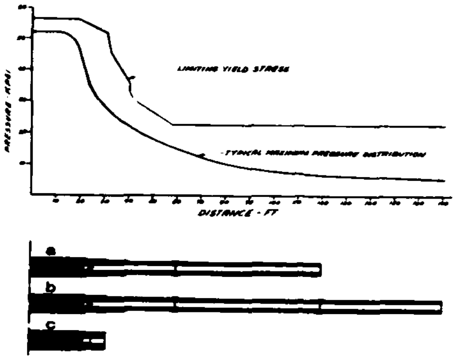

Figure 1. Geometry of the 16" Guns

a. The Barbados Gun. b. The Highwater Gun
c. The HARP Flyer.

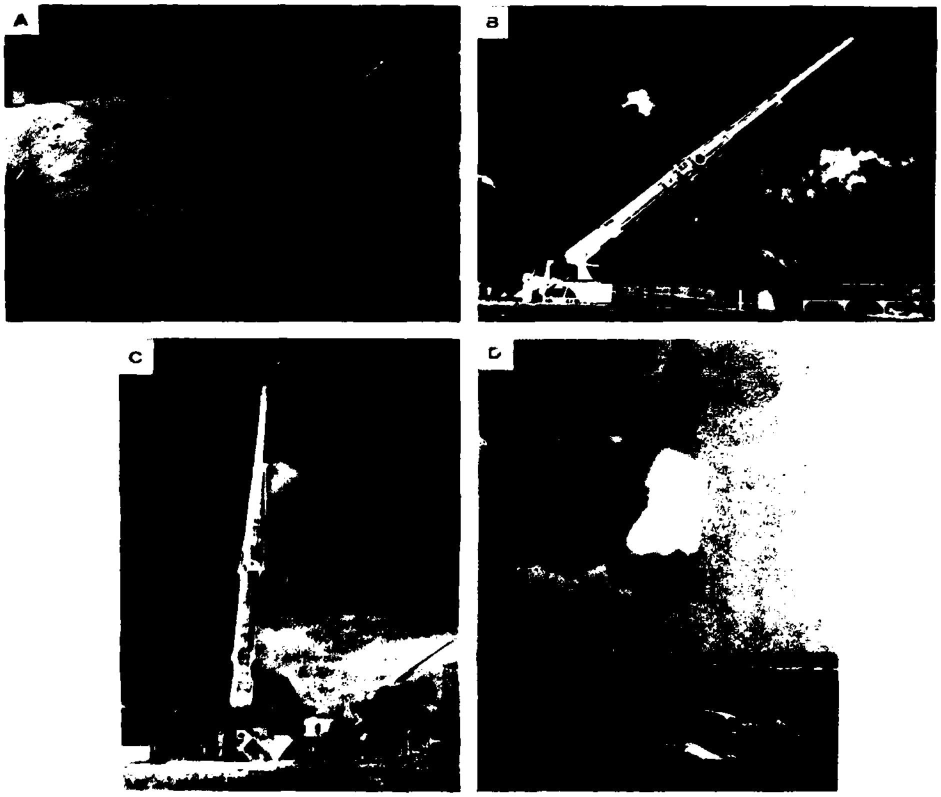

Figure 2. The Barbados Gun

A. Loaded Horizontally. B. In Mid Elevation

C. At Final Vertical Firing Angle. D. At Instant of Firing.

AD-A091 010 HEBREW UNIV JERUSALEM (ISRAEL) F/G 20/4
PROCEEDINGS OF THE INTERNATIONAL SYMPOSIUM ON SHOCK TUBES AND W--ETC
FEB 80 A LIFSHITZ, J ROM AFOSR-78-3679
UNCLASSIFIED AFOSR-TR-80-1141 NL

2 of 8

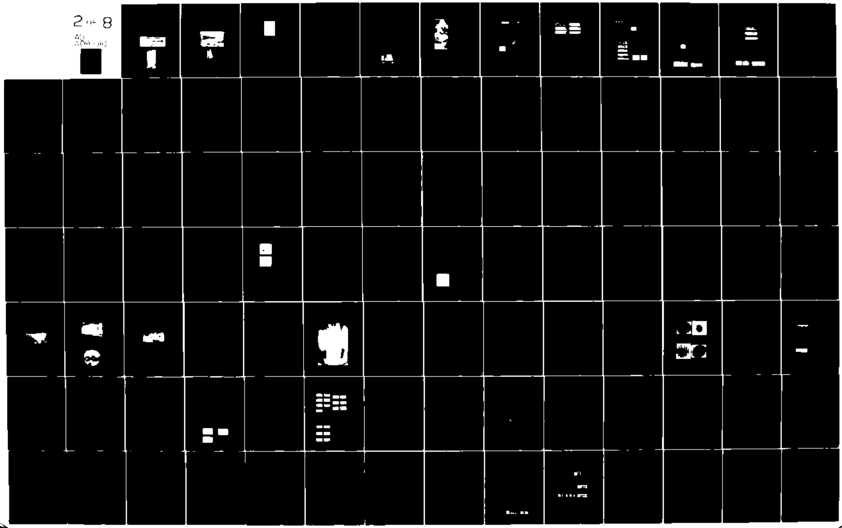

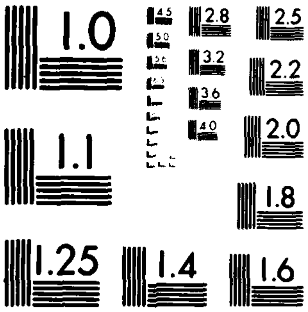

MICROCOPY RESOLUTION TEST CHART
NATIONAL BUREAU OF STANDARDS 1963 A

The Barbados gun is shown here in Figure 2. Loaded horizontally (Figure 2A), the gun is elevated (Figure 2B) to its final vertical firing angle 80 to 89 degrees, Figure 2C, and launches its projectile (Figure 2D) at muzzle velocities of up to 7,000 feet per second. The projectiles developed for this program were divided into two classes; those that received velocity only from the gun launch and through their large ballistic coefficient (5,000 pounds per square foot) glided to apogees of 200 kilometers (Martlet 2C and 2G, Figure 3), and those which were much heavier and carried rocket-boosters inside (Martlet 2G-1, Figure 3). The earliest developed, widely used vehicle was the Martlet 2C, shown here in Figure 4. This vehicle carried a heavy sabot, and none of the vehicle was exposed to the gun gas during launch. This feature was highly desirable in some experiments where no contamination of the vehicle surface was desired. Normally the vehicle carried a chemical payload in the rear and an electronic payload in the nose as illustrated in Figure 5A. The disadvantage of this type of vehicle is the heavy weight of the sabot. The use of a center-sabot, allowing the missile aft-end to extend into the powder chamber, allows a much larger vehicle as shown in Figure 3 (compare the 2C and 2G with approximately the same shot weight).

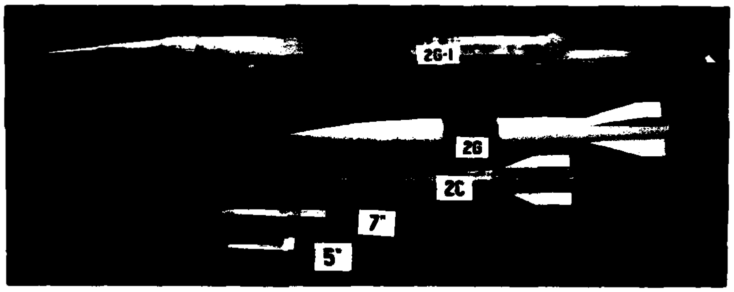

Figure 3. Martlet Vehicles

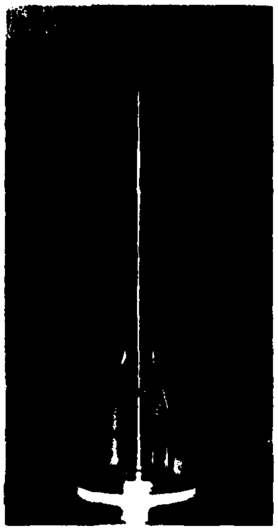

Figure 4. Martlet 2C

The vehicle, such as shown in Figure 5A, discards its sabot at the muzzle (Figure 5B) and starts towards apogee with a slow predetermined spin rate induced by bevelling the fin leading edges. A delay valve is used in the rear of the missile, allowing the TMA load to start being ejected at a fixed rate when the vehicle has attained an altitude of approximately 80 kilometers. At this altitude, the TMA reacts with the ozone in the atmosphere to produce a luminescent trail, which will extend up and over apogee back down to the cut-off altitude. The trail is thus over 100 kilometers in length (Figure 6) and visible for several hundred miles. Photo-theodolites, photographing against a star background, are located to supply adequate base leg triangulation for determination of a wind shear data[1].

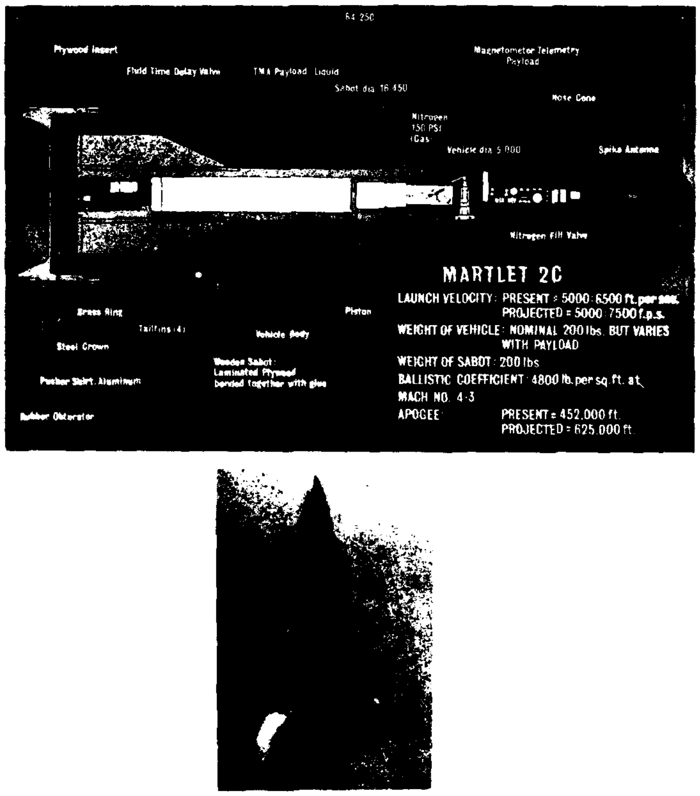

Figure 5. A) Martlet 2C with Chemical and Electronic Payloads

B) Smear Photograph of Martlet 2A Launch Showing Conditions 80' from Gun Muzzle Approximate Velocity 5500 FT/SEC

The optical data allows precise determination of vehicle apogee. However, the vehicle is also radar tracked from the muzzle. Muzzle velocity is usually measured by several other techniques, such as small doppler radars covering just the muzzle area, gauges located in the barrel close to the muzzle, etc. A gun, identical in all respects to the Barbados gun, was installed at the Yuma Proving Grounds, Yuma, Arizona. For the first time we present here in Figure 7 the apogee versus muzzle velocity summary of all Martlet 2C flights. It will be noted that the maximum apogee achieved was 581 kilo-feet, 110 miles or 177 kilometers.

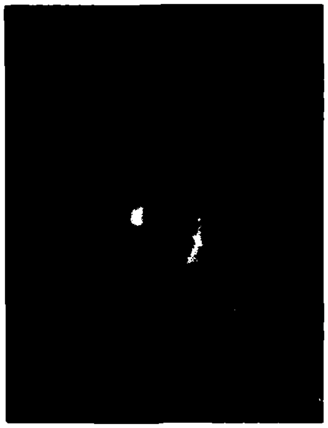

Figure 6. TMA Trail

The development of the HARP gun launching system led to long, large charges completely beyond previously utilized geometries and charge masses. Maximum muzzle velocity was the critical requirement to obtain useful apogees for atmospheric measuring experiments. The requirement then translated into the need to obtain successful ignition of the large powder charge, smooth burning and maximum shot base pressure profiles along the barrel within tube strength limits. As indicated by the opening remarks, we did achieve this successfully. The rest of this paper will review the painful progress towards that success through the highlights of the interior ballistics program conducted within the HARP program, more or less in historical order.

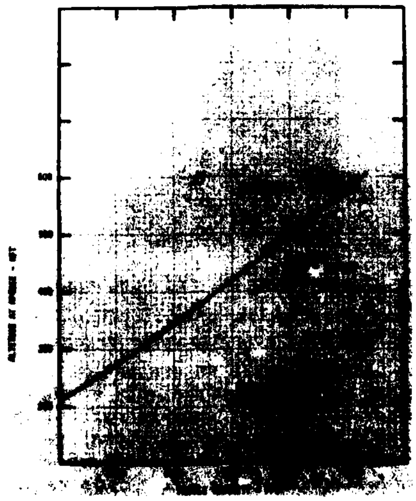

Figure 7. Apogee vs Muzzle Velocity

CONVENTIONAL INTERIOR BALLISTICS

Early Mathematical Work

Nineteenth century mathematicians concentrated extensively on solving the interior ballistics problem. The work of LaGrange, Le Duc, etc. is well covered and advanced in the classical textbook by Hunt and Hinds[2]. A less mathematical treatment of the problem may be found in Corner[3]. In all of these works, we might say a single phase approach is used; specifically, the model is one of gas generated uniformly in a chamber according to the classical burning law:

$$R = \beta P^{\alpha} \tag{1}$$

where R is the rate of conversion of solid into gas, represented by the reducing length of solid material, and β and α are constants determined by powder characteristics. Table 1 summarizes the chemical composition and thermophysical properties of the propellants subsequently of interest in this presentation.

Table I: Thermochemical Properties of 16 Inch Gun Propellants

	M8M	WNM	PYRO
Nitrocellulose	49.5	65.0	99.0
Nitroglycerine	44.0	29.5	-
Ethylcentralite	1.3	2.0	-
Diethylphthalate	5.0	-	-
Diphenylamine	-	-	1.0
Wax	0.2	-	-
Mineral Jelly	-	3.5	-
Density, LB/IN^3	.0573	.0575	.0578
Force Constant, FT-LB/LB X 10^{-3}	378	373	317
Isochcric Flame Temperature, ^{o}K	3400	3220	2570
Specific Heat Ratio	1.23	1.24	1.26
Covolume, IN^3/LB	27.7	25.5	27.0

The model generally used until large computer facilities became available, was that derived from the works referenced above, and often described after its well-known authors as the Hunt and Hinds method. Implicit in this model is the assumption of a uniform shot start pressure, initial burning on all surfaces and a pressure distribution which at any time is quasi-dynamic[4]. In this solution the amount of energy released by the burning propellant is determined from the burning rate law and thermophysical properties of the propellant, and taking into effect the covolume factor to determine the volume available for the gas, a space mean gas pressure is calculated. With surprising accuracy the motion of the shot down tube can be calculated by integrating the gas pressure acting on the base of the shot, according to the simple Le Duc formula:

$$P_{Base} = \frac{P_{Breech}}{1 + \frac{1C}{2M}} \tag{2}$$

where C is charge weight and M is total shot weight. The validity of this type of solution depends on the assumptions of smooth ignition and burning according to the simple model described. Furthermore C/M must be much less than unity, with deviation from the theoretical predictions increasing as this ratio increases.

Gough developed a much more sophisticated computer solution to the interior ballistics problem designated the Nova Code[5], wherein modelling of the ignition process is taken into account. Progressive work[6-11] advanced the modelling of chamber ignition processes. The code is based on a quasi-one-dimensional model of the axial two-phase flow in a gun, where in his most recent considerations, the effects of circumferential ullage, bag strength and mass exchange between the bag and the ullage are considered, along with obstruction of the flame front convective spreading.

The 16" Problem

With its extraordinary long chamber and large charge masses, the 16" HARP gun presented an extremely complex problem. The program proceeded essentially in a semi-empirical manner, with careful monitoring of breech pressure-time profiles, and study of among other effects:

i) Powder Distribution
ii) Ignition Energy Input, Both in Distribution and Strength
iii) Flame Front Propagation
iv) Mechanical Motion of the Solid Grains
v) Grain Geometry and Strength
vi) Grain Containment, Including Shot Start Pressure
vii) Packing Density, etc.

It is beyond the scope of this paper to attempt treating each of these items in any detail. Rather a few general remarks might be made on some of the areas, before proceeding to the solutions as they evolved.

The chemical and thermophysical properties of the propellants used are tabulated in Table 1. Various grain geometries were tried, shown here in Figure 8, in response to the need to match shot weights varying from 300 to 3,000 pounds. Many ignition techniques were used; commercially available squibs (CIL-S140) became the standard and most reliable, although they had large variations in ignition time (order of 1 or 2 milliseconds) and generally were low energy inputs. Attempts of reducing the jitter between squibs by using higher energy sources proved disastrous, as shown in Figures 9, 10 and 11. The combination which gave such spectacular results was that of high ignition source energy and relatively large packing density. Experiments using the strip propellant[12] were most promising on smaller scale guns, but disastrous on the larger chamber of the 16" gun.

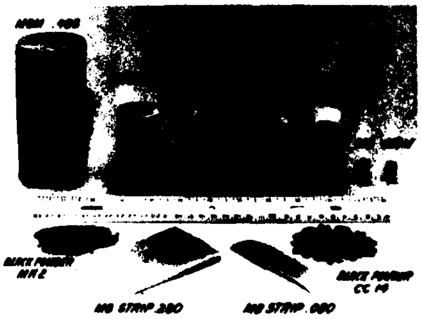

Figure 8. Propellant Grain Geometries

Figure 9, 10 and 11.
Ignition with High Energy Squibs

Examination of recovered polyethylene obturators showed heavy grain imprints in the case of base ignition of a contiguous charge. Clearly the flame front propagation and associated compression and shock waves accelerated unburnt grains down the chamber and into collision with the vehicle base. Evidence of fractured grains, leading to sporadic, uneven burning and large overpressures, were all encountered at the outset of the program. In some more or less logical sequence, the program can be divided into three phases, which really trace the time progression of the interior ballistics program of HARP.

Phase I: Single Point Base Ignition, Contiguous Charge:
January 1963 to November 1965

This paper will concentrate on the Martlet 2C problem where the shot weight was in the vicinity of 400 pounds and multiperforated grain geometry was used.

Figure 12 shows roughly the geometry of the chamber, charge, ignitor and projectile seating. A uniform shot start pressure was maintained by an interference fit between the tube and the rear portion of the sabot pusher plate. The vehicle was hydraulically rammed into place, with ramming pressure measured and maintained constant. Charge weights varied between 600 and 1,300 pounds dependant on powder energy and burning rate characteristics, the larger weights being associated with the low energy PYRO propellant.

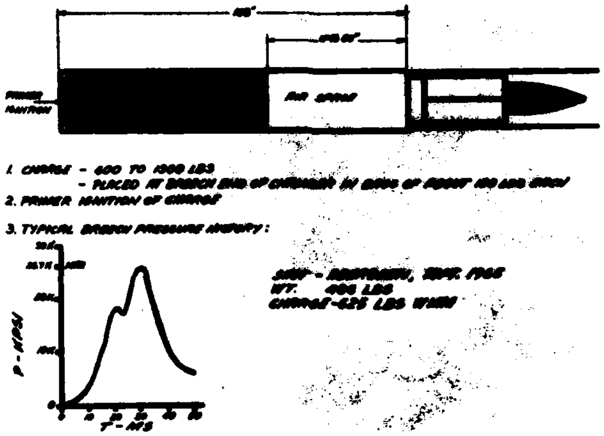

Figure 12. Schematic of Base Ignited, Contiguous Charge.
Phase 1, Jan. 63 - Nov. 65

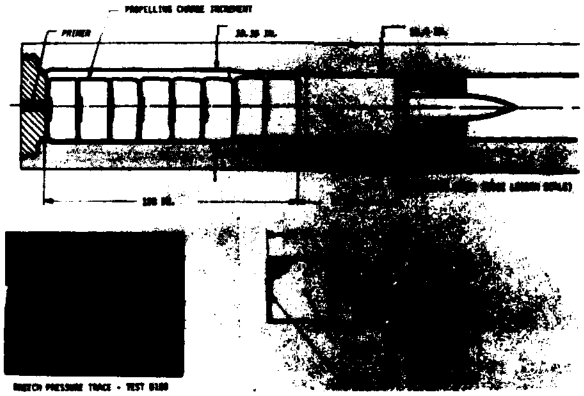

Figure 13. Detail of Base Ignited, Contingunous Charge

In Figure 12 a typical breech pressure time curve is shown with actual values. In Figure 13 typical dimensions are shown in detail for a specific charge, with a reproduction of the actual Kistler gauge record. It is to be noted that each powder bag weighed approximately 110 pounds and had a 350 gram grade A1 black powder ignitor pad on its base. The pressure time curve shows a smooth initial pressure rise, with a sudden step and then much more rapid rise in pressure to the maximum value. The physical model describing this ignition and burning process is illustrated in Figure 14. The flame front proceeds forward through the powder bags, at the same time the powder bags are being accelerated towards the projectile by chamber pressure build up from the rear face burning. The powder then collides with the projectile, causing unpredictable shock loads on the vehicle structure (a problem which proved serious to any instrumentation aboard the vehicle) and possible breaking of some of the grains hence altering grain geometry. A reflected wave proceeds rearwards as shown in the physical illustration of Figure 14 and, based on simple wave propagation calculations in the x-t diagram of Figure 15, reaches the barrel in approximately 20 ms. The reflected wave causes a sudden rise in breech pressure, and the associated steeper burning profile.

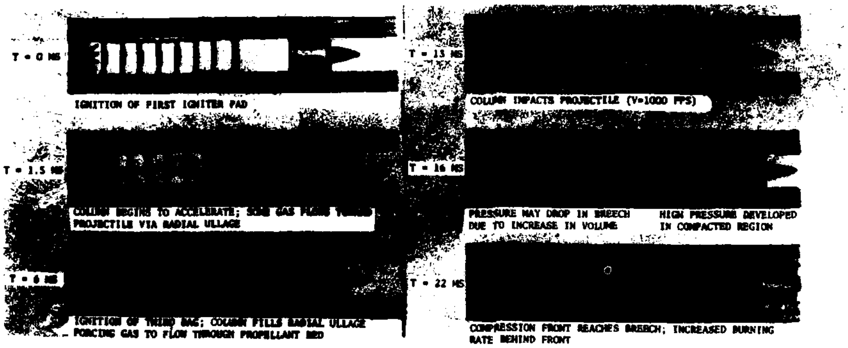

Figure 14. Physical Model Describing Ignition Process for Base Ignited, Contiguous Charge

Figure 15. Typical Wave Propagation Diagram

Phase II: Single Point Base Ignition, Spaced Charge:
November 1965 to September 1966

The powder charge arrangement was altered in the chamber to overcome the powder movement problem, still maintaining the standard service squib for single point base ignition. This is illustrated in Figures 16 & 17. Figure 16 shows schematically the arrangement where the powder bags were uniformly spaced along the chamber, and for a typical flight (nevis) shows the smooth breech pressure time curve obtained with numerical values plotted. Figure 17 shows the actual details of the charge spacing, where hollow wooden spacers were used to provide the bag-to-bag separation support. The typical Kistler gauge breech pressure time trace is reproduced in this figure, and shows the smooth profile. Figure 18 details the physical processes in this case. Recovery of obturator plates showed none of the large grain impact indentations of the non-spaced charge system. Figure 19 compares the traces and peak pressures for the two charge systems, and in addition to the smooth burning curve, it may be noted that the peak pressure at the breech is somewhat lower for the spaced charge case.

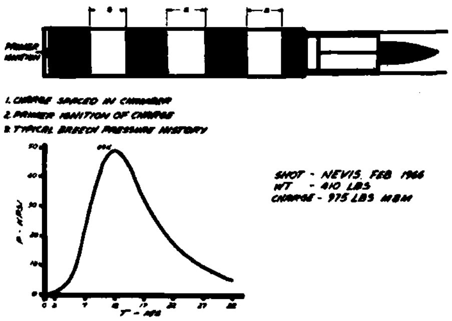

Figure 16. Schematic of Base Ignited, Spaced Charge.
Phase 2, Nov.65-Sept. 66

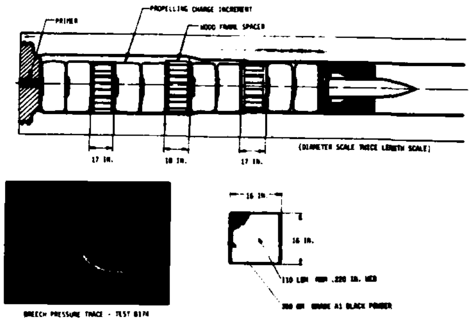

Figure 17. Detail of Base Ignited, Spaced Charge

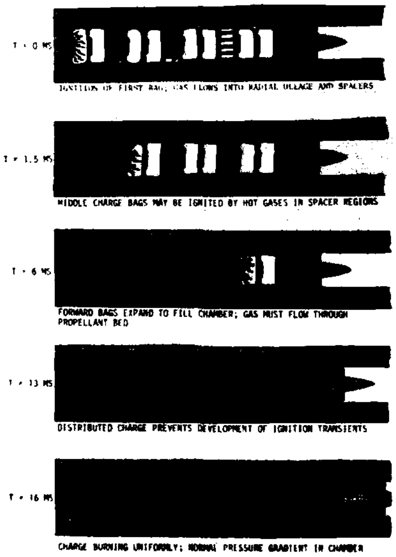

Figure 18. Physical Model Describing Ignition Process for the Base Ignited, Spaced Charge

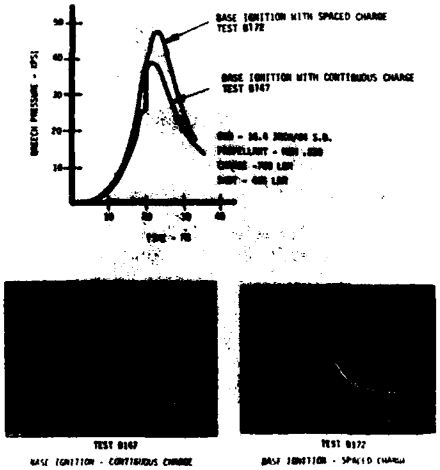

Figure 19. Comparison of Breech Pressures of Two Charge Systems

Phase III: Multi-Point Ignition and Spaced Charge

In such a long charge column, the ideal solution was to ignite the powder uniformly throughout the chamber. The manner in which this was accomplished is illustrated in detail with a typical successful breech pressure trace in Figure 20. In essence pyrotechnic squibs (reference 13) were placed on the black powder ignitor pad of virtually each bag. The essential requirement here was to achieve simultaneous ignition at each point along the charge axis. The inexpensive CIL-S140 low energy squibs used were found to have a spread of up to 2 milliseconds from the time of electrical impulse until ignition. More energetic squibs used in military systems were found to cut this jitter down by over an order of magnitude. However, they also were found to trigger some form of possible low order detonation in the long column. The solution finally adopted with success was to place a single S140 squib on each black powder bag, in a parallel electronic firing circuit. Two independent circuits were used for reliability, so that effectively each ignition point was with two squibs. The axial spacing of the ignition points was determined experimentally for the different powders. Figure 21 shows the typical pressure profiles obtained experimentally with PYRO as the number of axial ignition points were varied. In Test H44, axial simultaneous ignition occurred at larger than acceptable spacings, and the rough breech pressure trace obtained. In Test H45, axial simultaneous ignition at each bag occurred, and the smooth pressure profiles obtained. Similar results are shown for M8M propellant in Figure 22, where

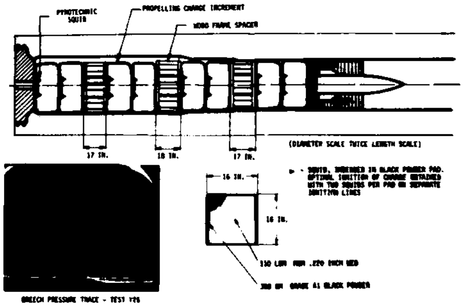

Figure 20. Schematic of Multi-point Ignited, Spaced Charges

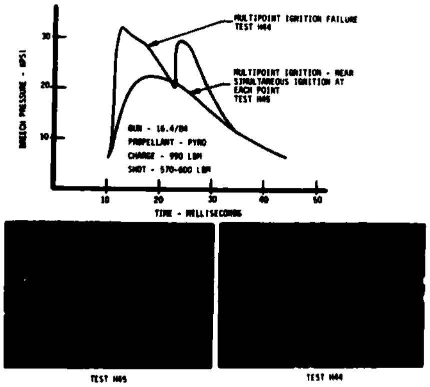

Figure 21. Typical Pressure Profiles Obtained Experimentally with PYRO

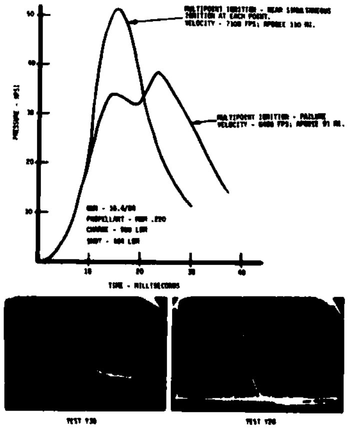

Figure 22. Typical Pressure Profiles Obtained Experimentally with M8M

the experimentally determined number of ignition points (10 points, 2 squibs at each station) functioned perfectly and smooth burning was obtained. Failure of simultaneous ignition resulted in the erratic curve, typically obtained during the early ignition experiments to optimize the ignition configuration. Figure 23 simply illustrates the uniform burning process achieved with multi-point ignition.

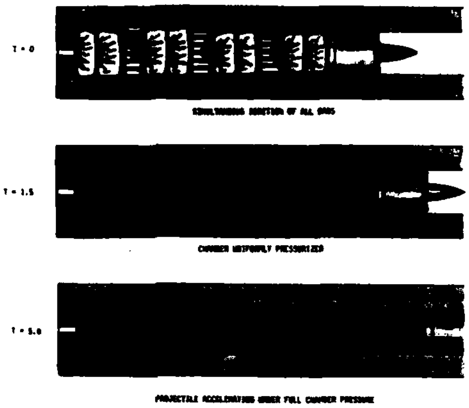

Figure 23. Illustration of Uniform (Multi-Point) Ignition Process

Comparison Results

Figure 24 shows typical traces comparing the simple base ignition, contiguous charge against the successful multi-point ignition with spaced charge. In addition to the much smoother pressure time curves, peak breech pressure for similar charges can be observed to decrease by over 30%. Similar comparison data is given in Figure 25 between single point and multipoint ignition with spaced charges.

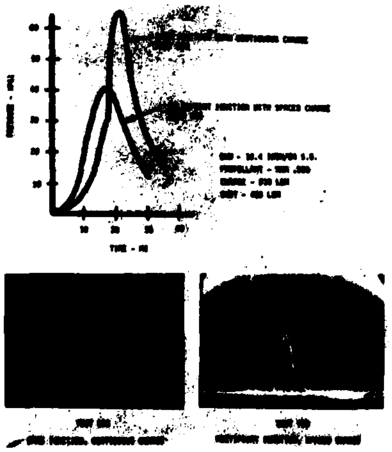

Figure 24. Comparison of Breech Pressures for Base Ignited, Contiguous Charge and Multi-Point Ignition with Spaced Charge

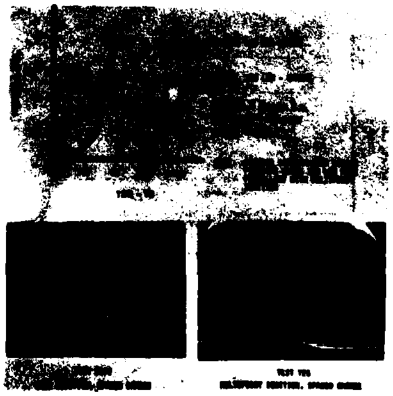

Figure 25. Comparison of Breech Pressures for Base Ignition and Multi-Point Ignition of Spaced Charges

The significant comparison data from the HARP Barbados gun is presented here in Figure 26, where the dramatic improvements in muzzle velocity and lower breech pressures are plotted from all the tests conducted. For the same peak pressure, increases of over 10% in muzzle velocity were achieved repetitively and in a reliable manner. The small note of caution here is the dependence on a reliable electronic firing circuit.

Table 2 summarizes the pertinent ballistic data tied to record flight data.

Table II. Record Test Data

Ignition Method	Base with Spaced Charge	Multipoint with Spaced Charge
Test	B173	Y28
Propellant	M8M .270	M8M .220
Charge Mass	915 LBM	960 LBM
Maximum Breech Pressure	49200 PSI	51300 PSI
Muzzle Velocity	6300 FPS	7100 FPS
Altitude at Apogee	467 KFT (142 KM)	581 KFT (177 KM)

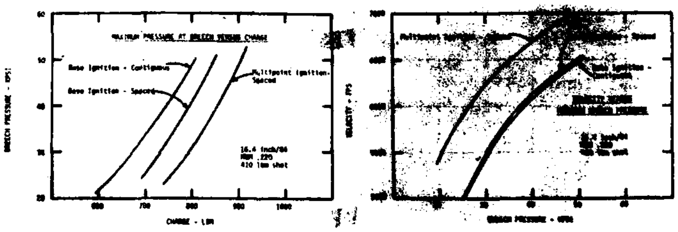

Figure 26. Comparison Data from HARP Barbados Gun

ACKNOWLEDGMENT

The HARP program involved many institutions and individuals in the period 1962-1967. The full bibliography of the program is available and covers the many aspects of the program, particularly the upper atmospheric (80 km to 160 km) modelling data measured over Barbados that are beyond the scope of a single paper. The interior ballistics program seemed a topic most appropriate to this Conference. The historical development of the ballistics program on such a large scale could be covered in a concentrated, if superficial manner. Yet the depth of the internal ballistics program and the necessity for better theoretical modelling could be illustrated, as well as the continuation of the work started during the program by reference to the Nova Codes development of P. Gough.

Specific acknowledgment must be made of Mr. D. Lyster for his help during the preparation of the present paper. Those who worked heavily on interior ballistics during the HARP program were Dr. O. Bain, Dr. George Gallagher Mr. D. Lyster and many of the interior ballistics group at the Ballistics Research Laboratory, Aberdeen Proving Ground. The major role of Dr. C.H. Murphy of BRL/APG as the chief US Army liason co-ordinator must be acknowledged, as well as his contributions to all other phases of the program.

REFERENCES

1. J.W. Wright, C.H. Murphy and G.V. Bull, Space Research VII, North Holland Publishing Company, Amsterdam (1967).
   J. Geophys. Res. *72*, No.5 (1967); *72*, No.13 (1967).
2. F.R.W. Hunt and G.H. Hinds, Published for the Ministry of Supply by His Majesty's Stationery Office, London (1951).
3. J. Corner, *Theory of the Interior Ballistics of Guns*, John Wiley & Son, Inc., New York (1950).
4. P.G. Baer and J.M. Frankle, BRL Report 1183, USA Ballistic Research Laboratories Aberdeen Proving Ground, Maryland (1962).
5. P.S. Gough, *The Flow of Compressible Gas Through an Aggregate of Mobile, Reacting Particles*, Ph. D. Thesis, McGill University, Montreal (1974).
6. P.S. Gough, and F.J. Zwarts, Final Report, Part II, Contract N00174-72-C-0223 USN, Naval Ordnance Station, Indian Head, Maryland (1972).
7. P.S. Gough, Final Report, Contract N00174-73-C-0501 USN, Naval Ordnance Station, Indian Head, Maryland (1974).
8. P.S. Gough, Final Report, Contract N00174-75-C-0131 USN, Naval Ordnance Station, Indian Head, Maryland (1975).
9. P.S. Gough, Final Report, Contract N00174-75-C-0259 USN, Naval Ordnance Station, Indian Head, Maryland (1977).
10. P.S. Gough, Final Report, Contract DAAK11-77-C-0028 USA, Edgewood Arsenal, Aberdeen, Maryland (1978).
11. P.S. Gough, Final Report, Contract DAAK11-78-C-0003 USA, Edgewood Arsenal, Aberdeen, Maryland (1979).
12. *Report on Propellant Testing Program of December 1965*, Internal SRC Memorandum (1966).
13. *Technical Description of S140 Squibs*, Letter Correspondence CIL to SRC (1969).

RATE MEASUREMENT IN SHOCK WAVES WITH THE LASER-SCHLIEREN TECHNIQUE

J. H. Kiefer and J. C. Hajduk

Department of Energy Engineering
University of Illinois at Chicago Circle, Chicago, Illinois 60680 USA

We discuss the laser-schlieren or narrow laser beam deflection technique in some detail, with particular reference to its application to very fast processes. The technique is first briefly reviewed together with selected previous applications. The optics of the beam-shock wave interaction is then examined using the scalar formulation of Huygens' principle (Kirchoff integral), with the shock density profile introduced as a transmission coefficient. The accuracy with which the signal generated by a differential detector will reproduce the variation of the refractive index gradient in a reactive shock is discussed in terms of this formulation. The response of such a detector to passage of a curved shock in a rare gas is also determined employing the shock-curvature theory of de Boer. These calculations are in good agreement with experiment and locate the "time origin" - coincidence of shock leading edge and beam center - on the "positive" portion of the signal near zero-crossing; an assignment which is in disagreement with the earlier calculations of Dove and Teitelbaum. This time origin shift and the averaging of initiation over a curved front can combine to generate a large correction of total density change measurements in relaxation experiments.

INTRODUCTION

Since its introduction in 1965(1), the laser-schlieren, or narrow laser beam deflection technique, has been used in the study of a broad range of kinetic phenomena in shock waves (2). Its virtues of simplicity, direct recording of rate, and excellent temporal/spatial resolution make it particularly suited to the observation of fast processes. It has accordingly been extensively employed in the study of relaxation in diatomics and polyatomics, the dissociation of diatomics, and the decomposition of a growing number of polyatomic species.

When the method is "pushed", as in the resolution of extremely rapid processes such as relaxation in H_2 (3) (4) (5), relaxation of many polyatomics (2), and the measurement of dissociation induction times (6), a very detailed analysis of the schlieren signal becomes imperative. The "time origin" must now be very accurately located; and since the characteristic length ($u\tau$) for such processes can become comparable to the axial extent of the curved shock

z_c, the axial "spread" of initiation over the curved front must also be taken into account.

Here we consider the above problems in some detail. In particular we present a rather rigorous treatment of the optics of the beam-shock interaction using the scalar formulation of Huygens' principle (Kirchoff integral) (7) (8). With this we are able to reproduce the signals generated by a rare-gas shock quite accurately. The analysis permits a decisive location of the coincidence of shock leading-edge and beam center, which is a starting point for the consideration of process initiation. We begin with a brief review of the technique.

I.) THE LASER-SCHLIEREN TECHNIQUE

A schematic of a typical modern set-up is shown in Fig. 1. The parallel beam from a He-Ne laser (6328Å) traverses the shock tube normal to the flow, and after some distance is intercepted by a differential detector (photodiode). Angular deflection of the beam produces a differential voltage which is recorded. The angular sensitivity may be calibrated by rotating the indicated mirror at a known speed. For small deflections the voltage-angular deflection relation is linear (23).

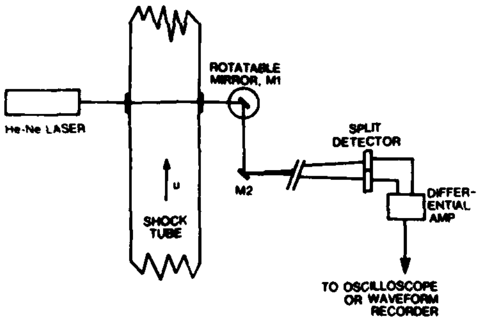

Fig. 1. Schematic of a "typical" modern laser-schlieren apparatus

The incident beam has the familiar Gaussian power distribution (7)

$$P(x,y) = P_0 \left(\frac{2}{\pi a^2}\right) \exp - \left(\frac{2(x^2 + y^2)}{a^2}\right) \qquad [1]$$

Where P_0 is the total beam power, and a_0 is the e^{-2} radius. Typical values are $0.2 < a_0 < 0.65$ mm and $P_0 = 1$-8 mw. As the beam traverses the system it retains its Gaussian form, but diffraction increases the radius. At distance D, the radius has grown to

$$a = a_0 \left(1 + \left(\frac{\lambda D}{\pi a_0^2}\right)^2 \right)^{1/2} \qquad [2]$$

The detector distance is usually large (3-10m) so the radius at the detector is 2-20 a_0.

When higher derivatives of the refractive index may be neglected (see below), the beam is simply deflected through an angle

$$\Theta = \int_{-W/2}^{W/2} \frac{dn}{dx}\, d\omega \qquad [3]$$

where W is the shock tube diameter and dn/dx the refractive index gradient along the tube axis. With a constant gradient across the tube as in a reactive but ideal plane shock, $\Theta = W(dn/dx)$; and if the gas refractivity is constant, the angular deflection is proportional to the density gradient $\Theta = KW\,(d\rho/dx)$. This gradient is directly proportional to the net rate of endothermic reaction in an ideal shock (2) (10), and the resulting proportionality of recorded signal and rate of reaction is a unique feature of the technique.

The narrow beam affords a high spatial resolution (0.1 mm is typical), and the large signal-to-noise ratio possible with modern detectors allows a commensurate speed of response while retaining a very high sensitivity to deflection. The useful resolution and sensitivity are usually limited only by shock nonideality, i.e., front curvature and early boundary layer.

II.) EXPERIMENTS

The advantages of the technique as well as its limitations are most easily delineated by consideration of a few selected experiments. Direct recording of rate and high spatial/temporal resolution allow the determination of "initial" rates for many reactions. There are some difficulties with the specification of an unambiguous initial rate for decomposition reactions (10) (11), but this does not appear too serious a problem in most cases. The usual advantages of initial rate determination - known composition and state, simpler mechanism - together with the improvement in precision which can result from direct rate measurement are nicely illustrated by the work of Breshears, Bird, and Kiefer (10) on O_2 dissociation. Their data for the dissociation rate coefficient in krypton diluent are shown in Fig. 2.

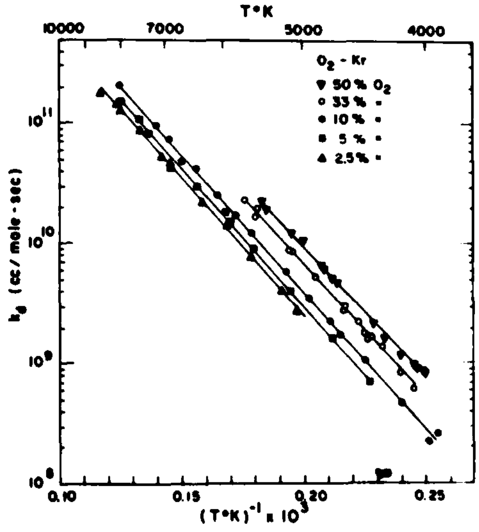

Fig. 2. Values of the effective dissociation rate coefficient k_d $[d(O_2)/dt = -k_d(O_2)(M)]$ obtained for mixtures of O_2 in Kr (10). The solid lines are independent least-squares fits of the Arrhenius expression, $k_d = A \exp(-E/RT)$, to the data for each mixture composition.

The technique is also useful in the extraction of primary dissociation rates in heteronuclear decomposition where fast secondary reactions often interfere. To illustrate we consider the decomposition of HCl as studied by Breshears and Bird (12). The mechanism is presumably

$HCl + M \rightarrow H + Cl + M$ (1)

$H + HCl \rightarrow H_2 + Cl$ (2)

$Cl + HCl \rightarrow Cl_2 + H$ (3)

$H_2 + M \rightarrow 2H + M$ (4)

$Cl_2 + M \rightarrow 2Cl + M$ (5)

If the rate is caught very early, only reactions (1) and (2) should be significant. But reaction (2) is nearly thermoneutral (∿1kcal exothermic) whereas the dissociation is 102.2 kcal endothermic. Since the schlieren signal is proportional to the net rate of endothermic reaction, reaction (2) has negligible effect regardless of its rate. This feature of fast but nearly thermoneutral secondary reaction is not uncommon in polyatomics and has been exploited in CH_4 (13) (14), CO_2 (15), SO_2 (16), and C_2H_6 (17).

The relaxation of H_2 (3) (4) (5) (18) (19) is perhaps the prime example of an extremely rapid process which requires maximum sensitivity and resolution. The very small relaxing heat capacity, low refractivity, and low molecular weight - which necessitates dilution with a heavy rare gas - prohibit slowing the relaxation with reduced pressure, as only when the process is very rapid is the gradient large enough to be discernable. An example oscillogram showing H_2 relaxation is given in Fig. 3, and a semilog plot of this signal is shown in Fig. 4. The slope of the latter provides the relaxation time. If the line is extrapolated to t = 0, giving an "initial" gradient ρ_i', the net density change for the process is $\Delta\rho_0 = u\tau\rho_i'$. Here τ is the (laboratory) relaxation time. The expected $\Delta\rho_v$ for pure vibrational relaxation is easily calculated and the ratio $\Delta\rho_0/\Delta\rho_v$ determined. In nearly every case this ratio is found to exceed unity (4) (18). In fact, Dove and Teitelbaum (4) obtained some ratios as large as 4. There is obviously a serious difficulty here which led these authors to suggest a strong rotational involvement in the relaxation (19) (4).

Of all the kinetic studies using the laser-schlieren technique, the work of Dove, Nip, and Teitelbaum (6) on N_2O pyrolysis most impressively illustrates its possibilities. From an extensive series of experiments covering the range 450 - 3590 K, these authors derived relaxation times, rates of primary dissociation, summed rates of two secondary reactions, and induction times for the primary dissociation. The measurements of induction time are unique; no such measurement has ever been reported for any other polyatomic species.

The major features of the N_2O pyrolysis mechanism were considered well-known by Dove et. al., although they ultimately did find indirect evidence suggesting one or more additional reactions may be occuring. The mechanism they employed is

$N_2O + M \rightarrow N_2 + O + M$ ($\Delta H \sim +38$ kcal/mole) (1)

$O + N_2O \rightarrow N_2 + O_2$ ($\Delta H \sim -79$) (2)

$$O + N_2O \rightarrow 2\ NO \quad (\Delta H \sim -36) \qquad \{3\}$$

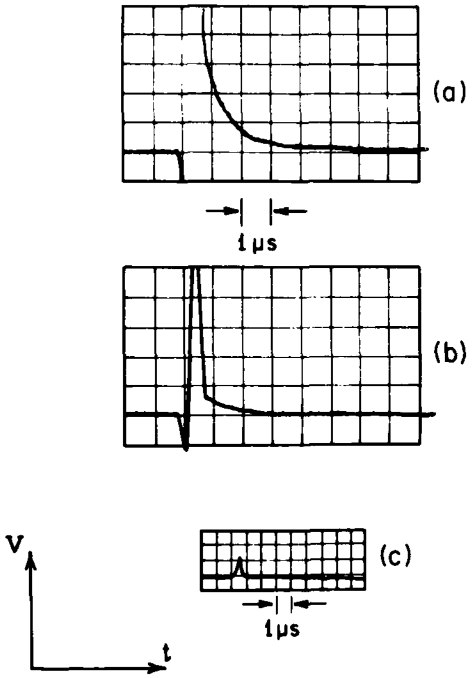

Fig. 3. Schlieren oscillogram tracings showing vibrational relaxation in a 30% H_2 - 70% Ar mixture (5). Horizontal axis is laboratory time and vertical axis is detector output voltage in each case. u = 1.989 mm/μsec, P_0 = 9.1 Torr, a_0 = 0.58 mm, D = 2m, and W = 7.62 cm. (a) Measure of axial density gradient showing exponentially decaying relaxation signal. $\Delta V/V_0P_0$ = 0.0231 per major division. (b) Less-amplified version of signal in (a) showing modulation due to shock front as well as the relaxation signal. $\Delta V/V_0P_0$ = 0.1153 per major division. (c) Measure of total laser power incident on photodiode as a function of time. The spike indicates that a significant portion of the light is deflected off the detector during passage of the shock front. $\Delta V/V_0P_0$ = 0.1774 per major division. (Courtesy J.E. Dove).

Example oscillograms showing pyrolysis are given in Fig. 5, where the temperature increases in the order of presentation. The first record (a), at 1950 K, shows relaxation followed by a very weak and slowly decaying dissociation gradient. Oscillogram (b) shows a (poorly resolved) relaxation followed by endothermic reaction (positive gradient), which finally tails into a weak exothermicity (negative gradient). In (c), relaxation is lost in the shock-front signal and the endothermic dissociation is quickly overwhelmed by a strong exothermicity. Finally, in (d) even the endothermic reaction {1} is nearly lost and, effectively, only the exothermic region appears. The complexity of such records should permit extraction of more than just the rate of {1}, and, recognizing this, Dove et. al. analyzed the entire gradient profile using both an approximate analytic solution of the kinetic equations for the above mechanism and a direct computer simulation. Consequently, they determined not only the rate of {1} but also the sum of the rates of {2} and {3}. The vibrational relaxation zone being of finite length, even though often unresolved, the onset of reaction is presumably delayed by an induction time. Such a delay was included in their analysis and its magnitude estimated.

The induction times determined by Dove, Nip, and Teitelbaum are very short, and thus very sensitive to time-origin location. In the H_2 relaxation experiments, the process is very rapid and the calculated $\Delta\rho_0$ is also very sensitive to time-origin location. For the interpretation of such experiments accurate assignment of this point is thus essential. Such an assignment

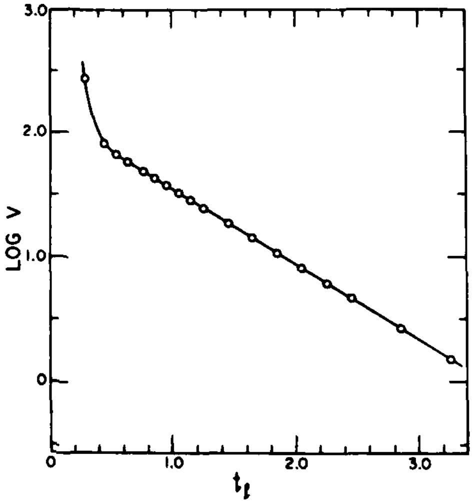

Fig. 4. Plot of logarithm of output voltage (mV) versus laboratory time (μsec) for the oscilloscope trace of Fig. 3. The plot is linear beyond the disturbance due to the shock front. (Courtesy J.E. Dove)

requires, among other things, a realistic treatment of the optics of the beam-shock wave interaction, which we now attempt.

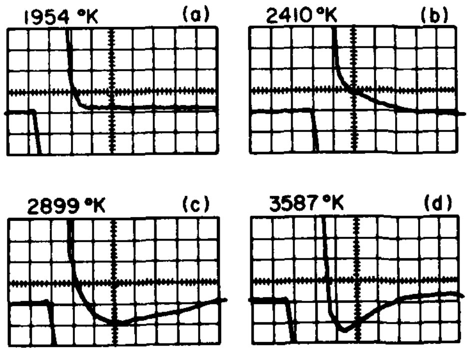

Fig. 5. Examples of schlieren signals from shock waves in 7.97% N_2O in Ar (6). Horizontal scale, 1 major division = 20 mV (corresponds to 2.04% modulation of laser signal). u = 1.435 mm/μsec, P_0 = 10.6 Torr, T = 1954 K; (b) u = 1.620 mm/μsec, P_0 = 10.1 Torr, T = 2410K; (c) u = 1.796 mm/μsec, P_0 = 9.6 Torr, T = 2891 K; (d) u = 2.022 mm/μsec, P_0 = 8.5 Torr, T = 3587 K (The origin for all measurements was taken to be the schlieren spike minimum measured from a less amplified trace of the same signal.) (Courtesy J.E. Dove)

III.) PHYSICAL OPTICS OF THE LASER-SHOCK WAVE INTERACTION

Although a real shock wave is three-dimensional, the narrow beam samples a plane section and a two-dimensional treatment is sufficient. Our coordinate system is shown in Fig. 6. Here t = 0 is again the coincidence of shock leading edge and beam center. The distance behind the front is z = x + ut, where x is fixed in the tube as shown and u is the (steady) shock velocity. *y* is fixed in the detector with origin at detector center and oriented so positive *y* corresponds to the usual "plus" voltage side of the detector. Then the differential signal for a rectangular detector of width 2r is

$$\Delta V = V_0 \int_{-r}^{r} \mathrm{sgn}(y)\ P(y)\ dy \qquad [4]$$

where V_0 is the signal for unit power, and P(y) is the power distribution in the detector plane.

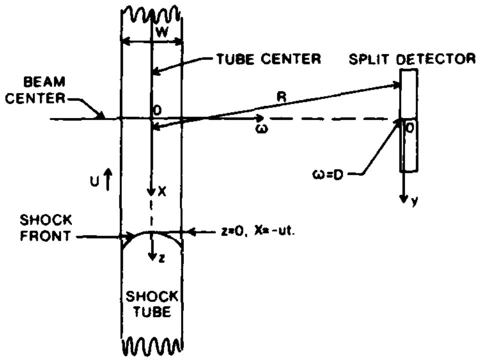

Fig. 6. Coordinate system for the laser beam-shock wave interaction.

The large detector distance effectively collapses the shock tube to a line from which D and R may be measured. That is, any ambiguity introduced by the finite width of the interaction region should be insignificant. We also assume the beam spread and any other distortion arising in passage through the shocked gas are negligible, i.e., the intensity distribution is constant for $|\omega| < W/2$. The integrated effect of the gas density on the beam may then be introduced at the source as a "transmission coefficient" T(z) (8).

We may now write the power at the detector in $y \rightarrow y + dy$ as (8)

$$P(y) = A \left| \int_{-\infty}^{\infty} T(z)\ E(x)\ \frac{\exp -\ (2\pi i R/\lambda)}{R}\ dx \right|^2 \qquad [5]$$

Here E(x) is the field at the shock tube, and A is a constant to be set below. The refractive index field of the shock wave appears in T(z) as

$$T(z) = |T(z)|\ \exp -\ \frac{2\pi i}{\lambda} \left[\int_{-W/2}^{W/2} n d\omega \right] \qquad [6]$$

Where the real factor |T(z)| is unity for a non-absorbing medium.

For large D we may expand R as

$$R = \left((y-x)^2 + D^2\right)^{1/2} \sim D\left(1 + \frac{(y-x)^2}{2D^2} + O(D^{-4})\right)$$

In the denominator R $\sim$ D is adequate. Cancelling phase factors, inserting $E(x) \alpha \exp - (x^2/a_0^2)$ and normalizing to the total beam power, we have

$$P(y) = P_0\left(\frac{2}{\pi(\lambda D a_0)^2}\right)^{1/2} \left| \int_{-\infty}^{\infty} T(z) \exp - \left[\frac{x^2}{a_0^2} + \frac{\pi i}{\lambda D}(x^2 - 2xy)\right] dx \right|^2 \qquad [7]$$

For T(z) = 1, we obtain the expected result

$$P(y) = P_0\left(\frac{2}{\pi a^2}\right)^{1/2} \exp - \left(\frac{2y^2}{a^2}\right) \qquad [8]$$

with a given by [2].

We begin the application of these equations to a consideration of the response to bulk density variations occuring after front passage, which might model that generated by reactive processes in an ideal shock wave. Here $z \gg 0$, $n(z, \omega) = n(z)$ and $|T(z)| = 1$. The power distribution at the detector is given by [6] and [7] as

$$P(y) = P_0\left(\frac{2}{\pi(\lambda D a_0)^2}\right)^{1/2} \int_{-\infty}^{\infty} d\alpha \int_{-\infty}^{\infty} d\beta \ \exp -(\alpha^2 + \beta^2)/a_0^2$$

$$X \exp - \frac{2\pi i}{\lambda D}\left[WD\left(n(\beta + ut) - n(\alpha + ut)\right) + \beta^2/2 - \beta y - \alpha^2/2 + \alpha y\right]$$

Define new variables through $\beta = \delta + \gamma/2$, $\alpha = \delta - \gamma/2$, and expand as

$$n(\beta + ut) - n(\alpha + ut) = n(\delta + ut + \gamma/2) - n(\delta + ut - \gamma/2)$$

$$= n'(\delta + ut)\gamma + n'''(\delta + ut)\gamma^3/24 + O(n^{v}\gamma^5)$$

Now $\Theta = Wn'$, so

$$P(y) = P_0\left(\frac{2}{\pi(\lambda D a_0)^2}\right)^{1/2} \int_{-\infty}^{\infty} d\delta \int_{-\infty}^{\infty} d\gamma \ \exp -(2\delta^2 + \gamma^2/2)/a_0^2$$

$$X \exp - \frac{2\pi i}{\lambda D}\left[\theta D\gamma + \theta'' D\gamma^3/24 + \ . \ . \ . + (\delta - y)\gamma\right] \qquad [9]$$

If we now assume linear detection, i.e., the magnitude of Θ and its derivatives is small, we may expand as

$$\exp - \frac{2\pi i}{\lambda D}\left[\theta D\gamma + \theta'' D\gamma^{3}/24 + \ldots\right] \sim 1 - \frac{2\pi i}{\lambda D}\left[\theta D\gamma + \theta'' D\gamma^{3}/24 + \ldots\right] \qquad [10]$$

For small θ the detector is effectively infinite. Then combining [10] with [9] and [4], and also expanding $\theta(\delta + ut)$, the integration may be done with the result

$$\Delta V = \frac{2\sqrt{2\pi}\, V_o P_o \theta a_o}{\lambda\phi}\left[1 + \frac{\theta'' a_o^2}{6\theta\phi^2} + \ldots\right] \qquad [11]$$

Where $\theta = \theta(ut)$ and $\phi = (1 + (\pi a_o^2/\lambda D)^2)^{1/2}$. This may be compared with the expression of Macdonald, Burns, and Boyd (9)

$$\Delta V = \frac{2\sqrt{2\pi}\, V_o P_o \theta a_o}{\lambda}\left[1 + \frac{\theta'' a_o^2}{8\theta} + \ldots\right] \qquad [12]$$

which may be obtained by setting $\phi = 1$ and neglecting the θ'' term in [10]. The latter constitutes neglect of diffraction by the refractive index field of the shock wave.

Actually the two expressions, [11] and [12], are almost numerically equivalent for the usual parameters, and either may be used to estimate the range over which a direct proportionality of signal and gradient will obtain. Clearly the requirements for this are linear detection, i.e., small deflections, and

$$\frac{\theta'' a_o^2}{8\theta} << 1 \qquad [13]$$

To check this inequality, consider an extremely rapid exponential variation $\Theta = \Theta_o \exp -(x + ut)/u\tau$, with $\tau = 0.2\mu\text{sec}$ (barely resolvable), $u = 2\text{mm}/\mu\text{sec}$, and $a_o = 0.3\text{mm}$. Then the lhs of [13] is 0.07. The small size of this term for such an extremely rapid process suggests that the proportionality of C and ΔV will be quite generally maintained. Equation [11] gives the same correction for $D = 77\text{cm}$.

If we neglect diffraction by the refractive index field, i.e., we drop all derivative terms in [9], then the power distribution is

$$P(y) = \frac{2P_o}{\lambda D}\int_{-\infty}^{\infty} \exp - \left(2x^2/a_o^2\right) \exp - \frac{1}{2}\left[\left(\frac{2\pi a_o}{\lambda D}\right)^2 (y-x-\theta D)^2\right] dx \qquad [14]$$

and this is simply a weighted superposition of Gaussians over the detector. The weighting, $\exp - (2x^2/a_o^2)$, is just the incident beam distribution; the detector Gaussians have a radius $\lambda D/\pi a_o$ and are centered at $y = x + \Theta D$. Thus each "ray" of the beam spreads to a radius $\lambda D/\pi a_o$ at the detector. This expanded ray is displaced from detector center by its initial position x and any deflection ΘD. In the absence of deflection, the beam is a parallel bundle of rays, but one in which each ray expands with distance. When D is very large, the usual case, we have $(x = 0(a_o))$

$$\frac{a_0(y - x - \Theta D)}{\lambda D} \rightarrow \frac{\pi a_0}{\lambda}\left(\frac{y}{D} - \Theta\right)$$

and the "memory" of initial ray location is lost.

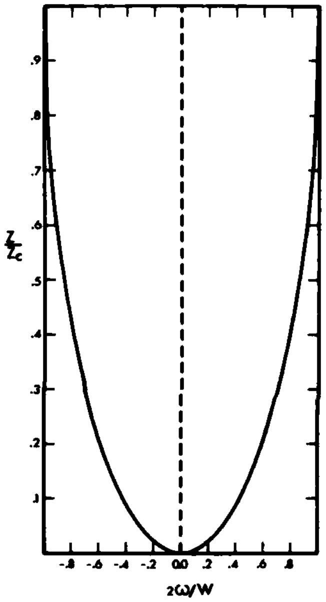

Fig. 7. Shock-front curvature. The line is the theory of de Boer (22) for parallel plane walls. His curve for cylindrical walls is very similar.

To model the signal generated by passage of a curved shock we assume the (rare gas) profile given by de Boer (22) for parallel plane walls, as shown in Fig. 7. We treat the shock as a discontinuity in density and refractive index.

Fig. 8. Calculated schlieren signals for the passage of a curved shock front. The vertical axis is fractional modulation ($\Delta V/V_0 P_0$) and the horizontal axis $\tau = ut/a_0$. On the left is the differential response and on the right the summed output of the detector. The shock thickness (axial extent) z_c is 0.39 mm and the detector width 3a, where a is the e^{-2} radius at the detector. Other parameters are as in Fig. 9.

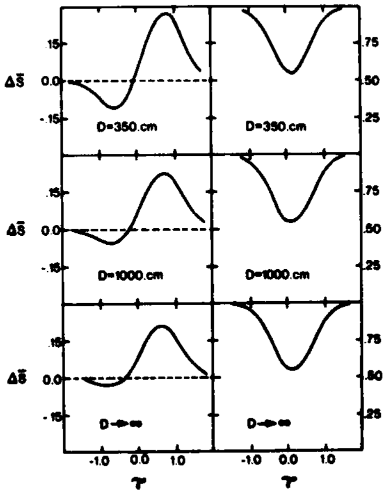

The necessary integrals were evaluated numerically, and the results for a rectangular detector at three distances are displayed in Fig. 8. For comparison the experimental signal generated by an argon shock with parameters similar to those of the D = 350cm simulation is shown in Fig. 9. The shape and magnitude of the simulation and the experiment are quite close, the only evident difference being a slightly larger negative maximum in the simulation.

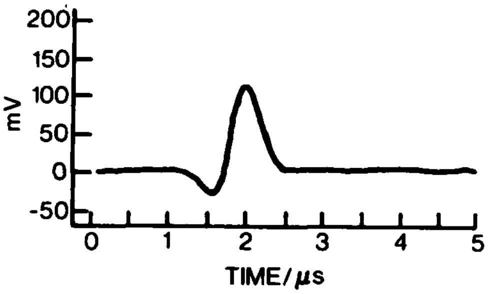

Fig. 9. Laser-schlieren signal generated by a shock in pure argon. The experiment involved detection using a differential photodiode with $u = 1.81$ mm/μsec, $P_0 \sim 10$ Torr, $a_0 = 0.65$ mm, D = 350 and W = 7.62 cm. The positive maximum corresponds to a modulation $(\Delta V/V_0 P_0)$ of 0.33. (courtesy T. Tanzawa and W.C. Gardiner, Jr.)

Here the ratio of negative to positive maximum is 0.4 whereas it is near 0.25 in the experiment. There could be any number of reasons for this discrepancy - the de Boer curve may be somewhat at fault, the assumed axial extent may be too small, or the negative maximum may be blunted slightly by inadequate response speed in the experiment - and it is impossible to establish a specific cause. Nonetheless the disagreement is minor and should not affect any qualitative conclusions. The time origin - here the coincidence of shock leading edge and beam center - is located on the positive rise near zero-crossing. As the detector distance increases, the negative signal fades and the time origin moves further onto the positive portion. The time from the "first break" in signal to the minimum is $\Delta\tau \sim 1$, or $\Delta t = a_0/u$, which is in agreement with the observations of Tanzawa and Gardiner (20) on argon shocks. Evidently the "first break" is not at radial distance from beam center.

Fig. 10. The power distribution in the detector plane at three characteristic times, the negative maximum, t = 0, and the positive maximum. The abscissa is y/a where a is given by equation [2]. The dashed lines indicate the limits of a detector with r = 1.5a (c.f. eq. [4]).

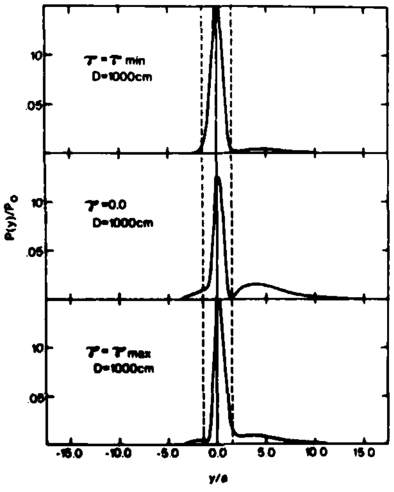

Consideration of the power distribution at various times (c.f. Fig. 10) shows the resulting signal is largely determined by a balance between small deflections from the "tail" of the curve and large deflections resulting in complete removal which are generated by the steep gradients near the leading edge. All deflection is to the positive side of the detector, and neglecting diffraction, a negative signal can only result from preferential removal of radiation initially located on the positive half. However, when the detector distance becomes large, each ray is spread almost equally over both halves and removal produces but small differential result - hence the very small negative signal at large distance (the residual negative signal for $D \rightarrow \infty$ arises from diffraction). The small deflections can then dominate even when the leading edge is at beam maximum thereby locating this point on the positive portion of the signal.

If the detector were to be placed very close to the shock tube, the situation would be quite different. There is then a one-to-one correspondence of radiation elements in the incident beam and on the detector. The large deflections which occur as the shock enters the beam now remove energy from the positive side exclusively, producing a large negative signal, and the negative maximum will then very nearly coincide with arrival of the leading edge at beam center. This situation corresponds to the "ray-tracing" model of Dove and Teitelbaum (21) presented at the last symposium. It ignores the diffractive nature of the beam spread and is not valid for the usual large detector distances.

One possible fault of the above analysis is neglect of reflection by the curved front. The reflectivity of the front is difficult to estimate and we have made no attempt to include such reflection. However, since the region likely to reflect strongly, that near the leading edge, produces complete removal through refraction in any case, this neglect is perhaps not serious. Our use of a rectangular detector is motivated by its simplicity. We have also calculated signals for a circular differential detector with results virtually identical to those of Fig. 8.

We now return to the H_2 relaxation (4) (5) and N_2O induction time (6) experiments cited earlier. We have mentioned two effects which can delay the time origin from the negative maximum, which is the origin assumed in both these studies. First there is the small shift from beam diffraction which will

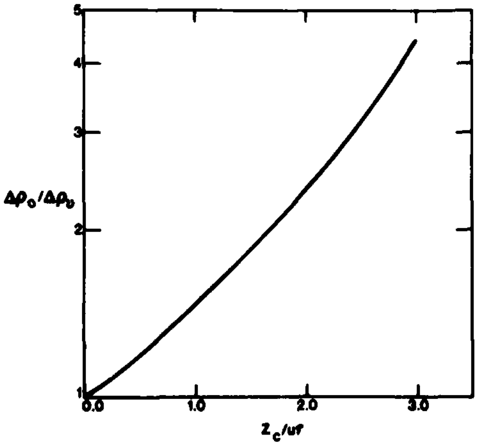

Fig. 11. The effect of shock-curvature averaging on the apparent $\Delta\rho$ for an exponential process. The ordinate is the multiplicative factor [15], the abscissa the ratio of shock axial extent z_c to the characteristic length $u\tau$ of the relaxation.

be 0.2 - 0.3μsec for the experimental conditions used. Second, there is a further delay arising from the axial spread of initiation over the curved shock. We can estimate the latter effect by averaging the amplitude at a later time ($t > z_c/u$), which gives an increase in $\Delta\rho$ by the factor

$$\frac{2}{W}\int_0^{W/2} \exp\,(z/u\tau)\; d\omega \qquad [15]$$

If we assume a parabolic profile, $z = z_c(2\omega/W)^2$, the integral may be easily performed (numerically) with the result shown in Fig. 11. The reason this ratio can be quite large is evidently the heavy weighting given delayed initiation with a rapid exponential decay. To illustrate the effect of the combined corrections we assume a rapid but resolvable relaxation with τ = 0.3μsec, and $u\tau \sim z_c$. Then the combination of delays predicts a $\Delta\rho_0/\Delta\rho_\nu$ of about 3. Although this is but a very crude estimate, it still suggests that a major portion of the experimental $\Delta\rho$ could be spurious. The induction time measurements in N_2O will also be seriously affected by time origin error. They are very short, less than 1 μsec in the laboratory frame, yet may well be too long.

IV.) CONCLUSIONS

The resolution and measurement of extremely rapid processes - processes having characteristic times in the submicrosecond range - is certainly feasible with the schlieren technique. But the interpretation of such experiments is complicated by shock curvature, boundary layer, and the non-geometrical nature of the laser optics. We have presented a rather rigorous formulation of the optical problem, but a more satisfactory treatment of initiation over the curved shock is clearly needed. Work on this problem is continuing and we hope to be able to present a more complete picture in the near future.

REFERENCES

1. J.H. Kiefer and R.W. Lutz, Phys. Fluids 8, 1393 (1965).
2. J.H. Kiefer in Shock Waves in Chemistry, A. Lifshitz Ed. (to be published by Marcel Dekker, N.Y.).
3. J.H. Kiefer and R.W. Lutz, J. Chem. Phys. 44, 668 (1966).
4. J.E. Dove, D.G. Jones, and H. Teitelbaum, 14th Symposium (International) on Combustion (The Combustion Institute, 1973) p. 177.
5. J.E. Dove and H. Teitelbaum, Chem. Phys. 6, 431 (1974).
6. J.E. Dove, W.S. Nip, and H. Teitelbaum, 15th Symposium (International) on Combustion (The Combustion Institute, 1974) p. 903.
7. O. Svelto, Principles of Lasers, (Plenum, N.Y., 1976).
8. M.V. Klein, Optics (Wiley, N.Y., 1970).
9. R.G. Macdonald, G. Burns, and R.K. Boyd, J. Chem. Phys. 66, 3598 (1977).
10. W.D. Breshears, P.F. Bird, and J.H. Kiefer, J. Chem. Phys. 55, 4017 (1971).

11. H. Teitelbaum, 14th Symposium (International) on Combustion (The Combustion Institute, 1973) p. 217.

12. W.D. Breshears and P.F. Bird, J. Chem. Phys. 56, 5347 (1972).

13. W.C. Gardiner, Jr., J.H. Owen, T.C. Clark, J.E. Dove, S.H. Bauer, J.A. Miller, and W.J. McLean, 15th Symposium (International) on Combustion (The Combustion Institute, 1974) p. 857.

14. K. Tabayashi and S.H. Bauer, Comb. Flame 34, 63 (1979).

15. J.H. Kiefer, J. Chem. Phys. 61, 244 (1974).

16. J.H. Kiefer, J. Chem. Phys. 62, 1354 (1975).

17. D.B. Olson, T. Tanzawa, and W.C. Gardiner, Jr., Int. J. Chem. Kin. 11, 23 (1979).

18. J.H. Kiefer and R.W. Lutz, J. Chem. Phys. 45, 3889 (1966).

19. J.E. Dove and H. Teitelbaum, Chem. Phys. (to be published).

20. T. Tanzawa and W.C. Gardiner, Jr., Private Communication.

21. J.E. Dove and H. Teitelbaum, Shock Tube and Shock Wave Research, Proceedings of the 11th Int'l. Symposium on shock tubes and waves, Seattle (1977) p. 474.

22. P.C.T. de Boer, Phys. Fluids 6, 962 (1963).

23. J.H. Kiefer and R.W. Lutz, J. Chem. Phys. 44, 658 (1966).

REACTIONS AND RELAXATIONS IN GASEOUS SYSTEMS THE INFORMATION THEORETIC APPROACH *

R. D. LEVINE

Department of Physical Chemistry
The Hebrew University, Jerusalem, Israel

An overview of the background, past applications and potential new directions of a thermodynamic-like approach to systems in disequilibrium is presented. The procedure of surprisal analysis is discussed for single collisions and for bulk macroscopic systems. The surprisal of a chemical reaction is related to its affinity and is shown to equal a linear combination of the surprisals of the species that participate in the reaction. We conclude on both theoretical and phenomenological grounds that the state of the system can be characterised as one of equilibrium subject to constraints.

INTRODUCTION

Otto Laporte was one of the pioneers in the application of the shock tube to the study of molecular relaxation processes and in the use of spectroscopic methods to probe shock heated gases. This overview considers some recent progress in our understanding of systems which have been displaced from equilibrium. The approach[1-3] will be a thermodynamic one, motivated by information theoretic considerations[4]. As will become obvious from the examples, spectroscopic methods have played a key role in obtaining the data.

In discussing the deviation of gaseous systems from equilibrium it is useful to note that different processes relax to equilibrium on different time scales. The slowest are usually chemical reactions which, at ordinary pressures, bring the system to equilibrium on a time scale of msec or longer. Many engines have a cycle time of a similar order of magnitude with the result, Figure 1, that the system is in chemical disequilibrium. The usual approach to the description of such systems is to list the main species and the major chemical reactions that they engage in and then solve the required set of (coupled) rate equations. The problems of such an approach are familiar: not all the required rate constants are necessarily known and not all the relevant species and reactions have necessarily been included. Another worry is that while one can start with a set of rate constants and solve for the time dependence of the concentrations the inverse process is much more difficult. It is hard to start from the experimental data and extract a unique set of rate constants for all the elementary reactions.

* Work supported by the US Air Force Office of Scientific Research, Grant AFOSR 77-3135.

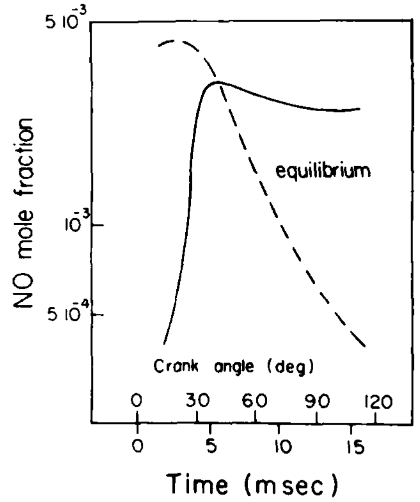

Figure 1.

Equilibrium (dashed line) and computed NO mole fraction in an internal combustion engine operated at 1200 rpm at an equivalence ratio of 1. (Results of M. Delichatsios and J.C. Keck. Private communication. See also ref. 5).

As one goes to shorter time scales the difficulties are compounded by the fact that the system may be in both chemical and thermal disequilibrium. The reason is that elementary chemical reactions if endothermic will typically deplete the vibrationally excited states of the reagents and if exothermic will specifically populate the vibrationally excited states of the products[1-3,6]. Engines operating on a time scale of μsecs are possible, the most notable example being the chemical laser. Here fast exothermic reactions, e.g., $F + H_2 \rightarrow HF + H$, selectively populate excited vibrational states of the products. Laser emission occurs on a time scale which is comparable to vibrational relaxation but which is typically slow compared to rotational relaxation[7]. Ordinary chemical lasers are therefore engines where work is extracted from a system which is in chemical and vibrational disequilibrium but is in rotational and translational equilibrium. More recently, chemical lasers which operate on pure rotational transitions have been reported. At the end of the scale, in the nsecs range at ordinary pressures, we come to systems in translational disequilibrium e.g., during the passage of a shock front.

In setting up the rate equations for systems in both chemical and thermal disequilibrium the number of coupled equations is much larger. The reason is that now each vibrational state of every molecule need be regarded as a species in its own right as its concentration is no longer just the Boltzmann fraction times the total concentration of the molecule. Rather, the concentration of every molecule in every vibrational state need be solved for. At shorter times one can no longer take rotational equilibrium for granted. Ultimately, even translational disequilibrium need be recognized, requiring the solution of transport equations for multicomponent systems.

Disequilibrium in a single collision.

Up to this point the relaxation time to equilibrium was determined by the time between collisions. To examine disequilibrium on shorter time scales we must recognise the finite duration of the collisions themselves. The slowest events on a molecular time scale are unimolecular dissociations where an energy rich molecule survives for very many periods of vibration and rotation before it falls apart. Direct bimolecular reactions typically last for less than a rotational period (about a psec). The 'system' in either case is a single, isolated, collision event. For such a system equilibrium is defined as: all quantum states at a given total energy (and other good quantum numbers) are equally probable.

The 'rate equations' that describe the time evolution during the collision are the equations of motion of mechanics (be it quantal or classical). To solve these equations we require as input the potential which governs the motion of the atoms during the collision. As was the case for rate constants which are the input for the macroscopic rate equations, the potential is seldom known and inversion from the experimental data to the potential is neither easy nor is always unique.

Experimental results and computational studies (using an assumed form of the potential) show[1-3,6] that the final states in a single collision are seldom in equilibrium, Figure 2.

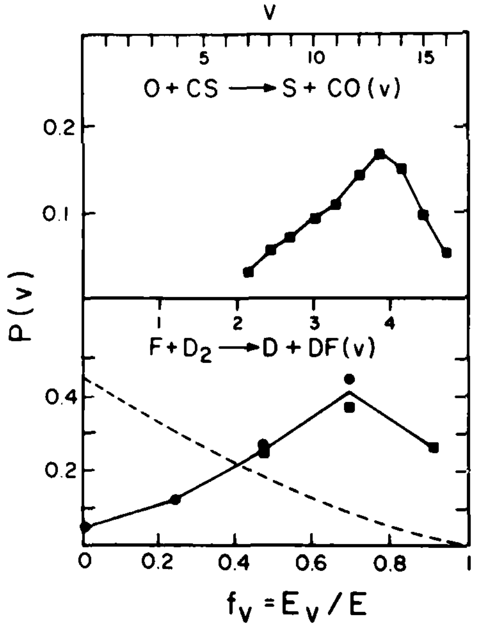

Figure 2.

The observed (solid symbols) and the equilibrium (all final states equally probable, dashed line) product vibrational distribution in two elementary reactions. The plot is vs. f_V, the fraction of the available energy in the product vibration since for such a plot the equilibrium (dashed line) distribution is essentially common to all A+BC reactions. The vibrational quantum numbers are shown in the top scale. See refs. 2 or 3 for the sources of experimenmental data and other details.

One can similarly consider collisions where the reactants are in well defined initial state and ask: at a given total energy, do all possible partitioning of this energy among the degrees of freedom of the reagents lead to the same reaction rate? The answer is often negative showing that reactions (and energy transfer processes) are selective in their energy reqiurements. As an example, endothermic reactions are usually faster when the required energy is supplied by the vibrational energy of the reagents rather than by their relative translational motion. In a macroscopic system this selectivity implies the preferential depletion of high reagents vibrational states by the reaction. Thermal equilibrium is thus perturbed due to the chemical disequilibrium. In a macroscopic system energy transfer collisions act so as to restore thermal equilibrium, and they can often do so on a time scale shorter than the relaxation time to chemical equilibrium. Hence selectivity of energy consumption is often not noticed for macroscopic systems in chemical disequilibrium unless the reactions are very endothermic (e.g. collision induced dissociation) when taking proper account of vibrational energy selectivity is inevitable in order to interpret the data[8], cf. figure 7 below.

Disequilibrium on the molecular level (i.e. the selectivity with respect to the initial states of the reagents and the specificity with respect to the final states of the products) is thus intimately related to disequilibrium on the macroscopic, bulk level. It is therefore not inappropriate to consider an approach that will treat both from a common point of view.

SURPRISAL ANALYSIS

To characterise the deviance of the system from equilibrium one needs a suitable measure. We have found it advantageous to use the surprisal defined by[1-3]: $I(n) = -\ln[P(n)/P^o(n)]$. Here $P(n)$ is the actual (observed or computed) probability of the species B_n and $P^o(n)$ is the probability at equilibrium. If the system is a single, isolated collision then $P(n)$ is the fraction of the collisions that lead to the formation of B_n. For example, in Figure 2, the different species are the diatomic product molecule in different vibrational states. In a macroscopic system $P(n)$ is the mole fraction of the species B_n.

The surprisal is a 'local' measure of disequilibrium since it assigns a separate number to each species in the system.

The empirical observation is that even for large deviances from equilibrium the structure of the surprisal may be simpler than that of the probabilities themselves. Figure 3 is an example for a single isolated collision.

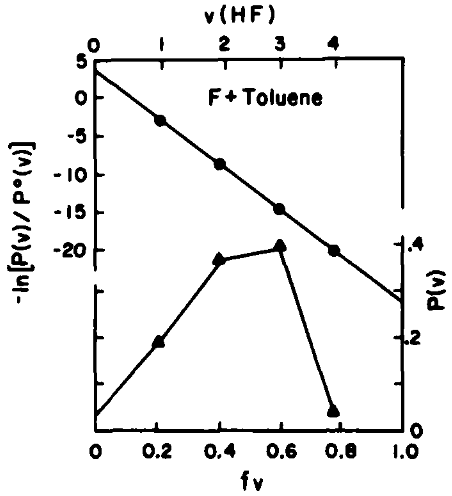

Figure 3.

The observed (bottom panel) HF vibrational state distribution resulting from the single collision of an F atom with toluene. Top panel: the surprisal vs. $f_V = E_V/E$. Adapted from D.J. Bogan and D.W. Setser, J. Chem. Phys. 64, 586 (1976).

The surprisal, while large is very well approximated as a linear function of the vibrational energy content of HF:

$$I(v) = \lambda_0 + \lambda_v(E_v/E) \qquad (I)$$

or

$$P(v) = P^0(v)\exp[-\lambda_0 - \lambda_v(E_v/E)]\,. \qquad (II)$$

Here λ_v is the slope of the straight line in Figure 3. λ_0, the intercept of the line, is not an independent parameter but is determined by the condition that the distribution (II) sums up to unity.

The linear representation (I) for the surprisal also obtains for other systems$^{1-3}$ e.g. those shown in figure 2. The role of reagent vibrational excitation can be similarly represented, figure 4.

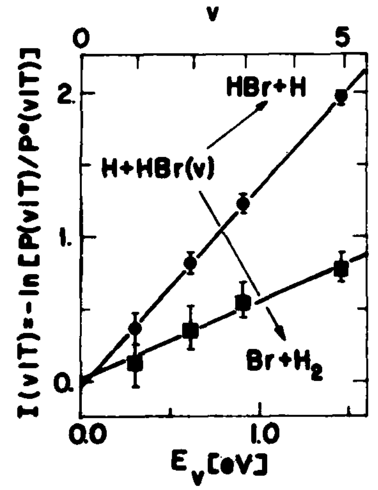

Figure 4.

Surprisal of the role of HBr vibrational excitation in the two possible reaction paths in the H + HBr(v) reaction. Note that the surprisal is different for the two reaction paths. Adapted from R.D. Levine and J. Manz, J. Chem. Phys. *63*, 4280 (1975).

The simple behavior of the surprisal is found also for macroscopic systems. Figure 5 shows an analysis of the results of a numerical solution of the rate ('master') equations for vibrational excitation. If one uses the Landau-Teller transition probabilities then one can show analytically that the functional form (II) is an exact solution of the rate equations[9]. Of course, and as is also obvious from figure 5, the value of λ_v does depend on time and tends to zero as the system approaches equilibrium.

THE CONSTRAINTS

As was argued in the introduction it is the slow processes that govern the approach to equilibrium. If these processes were frozen, the system would be in equilibrium. It is therefore reasonable to consider the following working hypothesis: At any point in time the system is at equilibrium subject however to constraints. The nature of these constraints is determined by the slow processes[5,10]. In this review we confine ourselves to showing that this hypothesis does account for the simpler structure of the surprisal and that it can be used as a predictive tool. Elsewhere[11] we have shown that this approach can indeed be justified as a rigorous implication of the equations of motion of mechanics.

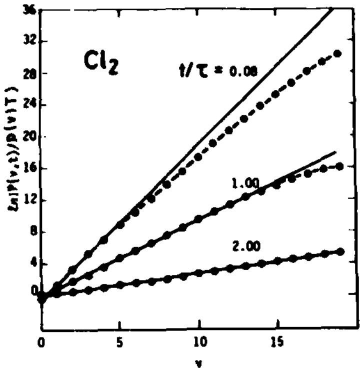

Figure 5.

Surprisal of the vibrational distribution of Cl_2 gas in thermal disequilibrium vs. the vibrational quantum number for three values of time (measured in units of the relaxation time of the mean vibrational energy). Adapted from I. Procaccia, Y. Shimoni and R.D. Levine, J. Chem. Phys. *65*, 3284 (1976).

In discussing the constraints we shall be guided here by physical considerations: the constraints reflect the 'bottleneck' processes but for which the system would be in equilibrium. For example, since three body recombination processes are slow, the total number of molecules in the system may be higher than at equilibrium. Or, since vibration to translation energy transfer is slow, the mean vibrational energy may be higher than at equilibrium. Indeed, Bethe and Teller suggested that it decays exponentially to its equilibrium value, $\langle E_{vib}\rangle^o$

$$-d\langle E_{vib}\rangle / dt = [\langle E_{vib}\rangle - \langle E_{vib}\rangle^o]/\tau \quad . \qquad \text{(III)}$$

For an isolated collision the constraints are due to the inertia (or 'adiabaticity') of the different degrees of freedom. Such constraints (reflected in the Franck Condon approximation of spectroscopy or the Landau-Teller adiabaticity factor) imply that a degree of freedom will come to equilibrium during a collision if it is perturbed on a time scale short compared to its natural period[6]. Electronic degrees of freedom are thus least perturbed and indeed are usually treated as adiabatic (the Born Oppenheimer approximation. Exceptions do occur if 'curve crossing'[6] is possible. Indeed, examples of collisions which lead to an equilibrium distribution among final electronic states are known[3]). Next in line come the vibrations, whose period is comparable to the duration of direct bimolecular collisions. Rotations are slower (except for hydrides) and hence products rotational distribution is seldom very deviant.

As has been noted in the introduction, disequilibrium for gaseous macroscopic systems is really a reflection of the elementary collisions taking place in the system. Hence one can forge a link from the microscopic to the macroscopic constraints. This has actually proved possible, e.g. in the case of macroscopic vibrational relaxation, the Bethe-Teller equation (III) can be related to a constraint on the rate constants of vibrational to translational energy transfer out of different initial vibrational states and into different final vibrational states[12]:

$$\sum_{v'} (E_{v'} - E_v)\, k\, (v \to v') = [\langle E_{vib}\rangle^o - E_v]/\tau \quad . \qquad \text{(IV)}$$

Here the primes denote the final vibrational states, and figure 6 below offers a concrete example.

THE ENTROPY DEFICIENCY

As a global measure of the deviance of the system from equilibrium we use the average value of the surprisal, termed 'the entropy deficiency' and defined by[2,3]

$$DS[P|P^o] = \sum_n P(n)\ln[P(n)/P^o(n)]. \qquad (V)$$

The following points are central to the discussion but are stated here without proof:

The entropy deficiency is non negative and vanishes if and only if the system is at equilibrium, i.e. if $P(n) = P^o(n)$ for all species B_n.

For an isolated system (e.g. a single collision) the entropy deficiency is the difference between the value of the entropy of the system at equilibrium and the entropy of its present state. Since $DS \gtrsim 0$, with equality only at equilibrium this property is equivalent to the second law of thermodynamics: the entropy of an isolated system can only increase. A proof of this important property is not available elsewhere and hence is provided in an appendix. It should be explicitly stated however that the proof and other statements to be made below are all based on the information theoretic definition of an entropy of a distribution[4],

$$S[P] = -\sum_n P(n)\ln[P(n)/g_n] \qquad (VI)$$

where g_n is the degeneracy of the species B_n. Classical thermodynamics does not define entropy outside of equilibrium. It is the adoption of the information theoretic definition (VI) that enables one to extend the language and methodology of classical thermodynamics to systems in disequilibrium.

For a system coupled to a heat bath at a temperature T, RTDS is the maximal work available from the system[2,13]. This result is valid whether the system is open or closed. In the special case that the system is only in chemical disequilibrium, RTDS is the affinity of the system as introduced by DeDonder[14]. In the special case that the system is only in thermal disequilibrium (and coupled to a heat bath)

$$-RTDS = \Delta E - T\Delta S \qquad (VII)$$

Here ΔE and ΔS have their usual thermodynamic significance, except of course that the entropy of the initial state, which is in disequilibrium, is defined by the information theoretic expression (VI).

The entropy deficiency is a measure of the 'thermodynamic weight' of the system as introduced by Boltzmann and Planck. In brief, given a system of N molecules which is at equilibrium. The probability P that due to a fluctuation it will be found with the composition $\{P(n)\}$ is given by $P = \exp\{-NDS[P|P^o]\}$. Hence the larger is DS, the less probable is the particular state of the system. Due to the factor N in front, large values of DS are strongly discriminated against.

Finally, $DS[P|P^o]$ has the information theoretic interpretation of the amount of information received when, if all we knew were the strictly concerved quantities (e.g. total energy, total number of atoms of each element), we are given the actual distribution $\{P(n)\}$.

The algorithm

Any one of the stated interpretations of DS can now be used to support the following technical version of the working hypothesis[15]: Consider all the compositions {P(n)} that are consistent with the constraints on the system. For example, all distributions over vibrational states that have the same value of the mean vibrational energy. Among those distributions choose the one that has the minimal value of DS. The (unique[16]) distribution chosen in this fashion is the one that is as much in equilibrium as possible consistently with the value of constraints. Minimising DS is the analogue of the classical thermodynamic prescription of minimising the free energy (or, for an isolated system of maximising the entropy). Minimising DS is the analogue of Boltzmann's approach of finding the most probably state of the system. Finally, minimising DS is, on information theoretic grounds[17], the most conservative inference. It is the lease biased or Ocam's rule description in that it is consistent with the constraints and otherwise provides as little information as possible. It should however be recognised that the procedure is an extension[15] rather than a part of classical thermodynamics. The two new features are, first, the choice of constraints. Equilibrium thermodynamics admits only such constraints that are strictly conserved and time-independent quantities. We have been able to show that the constraints required to rigorously describe systems in disequilibrium can also be regarded as constants of the motion[18]. However we shall not pursue this point here. The second non-classical feature is the definition (VI) of the entropy.

Getting down to business, the constraints are mean values of properties A_r, r = 0,1, ..., M,

$$\langle A_r\rangle = \sum_{n=1}^{n} A_r(n)P(n). \qquad \text{(VIII)}$$

$A_r(n)$ is the value of the property A_r (e.g. vibrational energy) for the species B_n. We reserve $A_0(n) = 1$. As long as the number of species (N) exceeds the number (M + 1) of constraints there will be more than one distribution {P(n)} which is consistent with the constraints. The particular (unique) one which is of minimal DS can be constructed by the method of Lagrange parameters[1,2,3]. The result is:

$$P(n) = P^0(n) \exp\,[-\sum_{r=0}^{M} \lambda_r A_r(n)] \,. \qquad \text{(IX)}$$

There are as many (Lagrange) parameters, λ_r's, in (IX) as there are constraints. Hence their values can be determined from the values of the constraints, and an efficient algorithm for doing so has been described[16].

SURPRISAL SYNTHESIS

The surprisal of the distribution which is maximally in equilibrium subject to constraints (cf. (IX)) is

$$I(n) = -\ln[P(n)/P^0(n)] = \sum_{r=0} \lambda_r A_r(n) \,. \qquad \text{(X)}$$

The whole point of surprisal analysis is thus to identify the constraints by an examination of the data. The pleasing observation, figures 3-5, is that typically very few constraints are required to provide an excellent approximation for the surprisal even for systems that are quite far from equilibrium. This suggests that the procedure be inverted. Rather than examine the distribution to identify the constraints, adopt a set of constraints and predict the surprisal and hence the distribution.

A concrete example of such a surprisal synthesis is shown in figure 6. The constraint is the so-called 'exponential gap rule' and the value of the Lagrange parameter is determined using equation (IV).

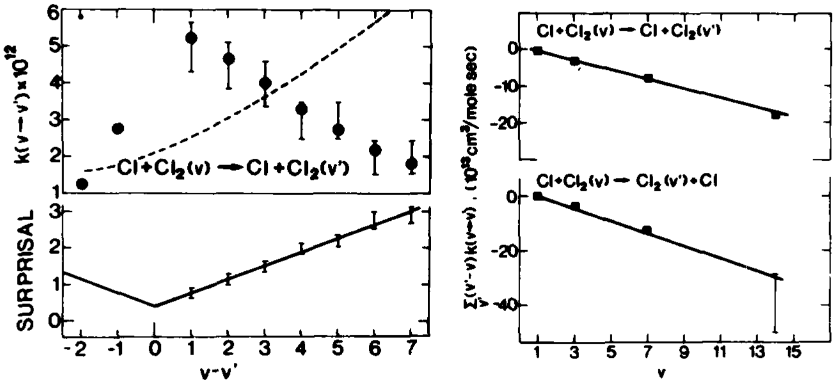

Figure 6.

Right panel: A plot of the left hand side of equation (IV) vs. E_v using rate constraints computed by the method of classical trajectories, for two different paths in a $Cl + Cl_2(v)$ collision at 1100K.

Left bottom panel: The surprisal of the trajectory computed distribution of Cl_2 final vibration states (bars) and the *predicted* surprisal (solid line) using (X) and a single constraint beside normalisation.

Left top panel: The trajectory computed (bars) and the surprisal synthesized (dots) Cl_2 final vibrational distribution. The equilibrium, P^0 (v) distribution is shown as a dashed line. Adapted from ref. 12.

An example relevant to shock tube kinetics is shown in figure 7. The problem is accounting for the low values of the activation energies for the dissociation of diatomic molecules in a shock heated monoatomic gas. Two types of rate constants are required for the solution of the kinetic equations. One is a set of rate constants for vibrational energy transfer. The other is the set of rate constants for collision induced dissociation of the diatomic molecule as a function of its vibrational state. The results shown in figure 7 are based on a linear surprisal representation for the role of the diatomic initial vibrational energy (cf. figure 4) in the collision induced dissociation process.

An application of surprisal synthesis to macroscopic disequilibrium was shown in figure 5. The straight lines are not fits to the surprisal of the distribution but an independent computation using $<E_{vib}>$ as a constraint, where the value of $<E_{vib}>$ is determined from equation (III). If both $<E_{vib}>$ and $<E^2_{vib}>$ are imposed as constraints the predicted surprisal (dashed line) is in excellent accord with the results of integrating the rate equations.

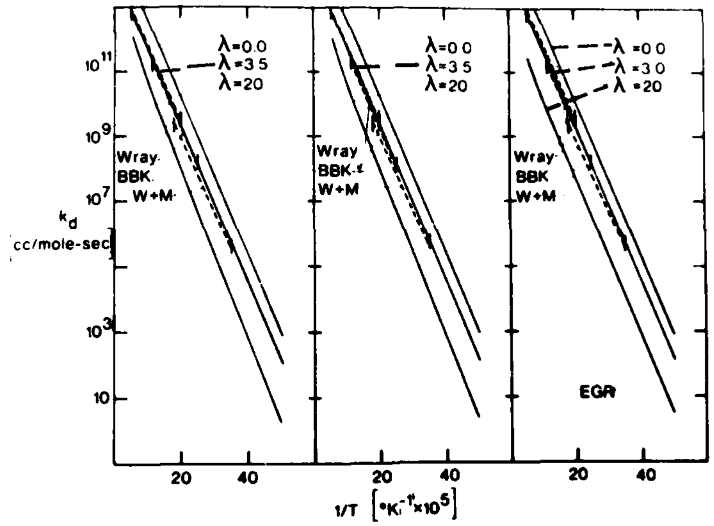

Figure 7.

Computed apparent dissociation rate constant for O_2 in Ar (solid lines). Adapted from ref. 8, where the sources of experimental data are identified. $-\lambda$ is the surprisal parameter for vibrational energy consumption (as in fig. 4) of the collision induced dissociation process. The panel on the right uses energy transfer rates of the exponential gap rule type. The other two panels are Landau-Teller type (near neighbour only) energy transfer rates.

THE AFFINITY

Consider a system in chemical disequilibrium. We have thus far discussed the surprisal of the concentrations of individual species or of the entire system (i.e. DS). A measure of deviance which is intermediate between the local and the global is the surprisal of a given elementary reaction. We shall show that it is a linear combination of the surprisal of the species that participate in the reaction and that it is equal to affinity of the reaction.

An elementary reaction can be schematically written as

$$\sum_n \nu_n^+ B_n \longleftrightarrow \sum_n \nu_n^- B_n$$

where the ν_n's are the stoichiometric coefficients and $\nu_n = \nu_n^- - \nu_n^+$. The affinity of the reaction is defined as[14]

$$A = -\sum_n \nu_n \mu_n \qquad \text{(XI)}$$

where the μ's are the chemical potentials. Since the affinity vanishes when the reaction is at equilibrium one can replace in (XI) μ_n by $\mu_n - \mu_n^e$ where μ_n^e is the chemical potential at equilibrium. Using the standard relation between chemical potential and mole fraction

$$\mathcal{A} = -RT\sum_n \nu_n \ln[P(n)/P^o(n)],$$

or using (X)

$$= RT\sum_r \lambda_r\Big(\sum_n \nu_n A_r(n)\Big) \equiv RT\sum_r \lambda_r C_r. \qquad \text{(XII)}$$

Here

$$C_r = \sum_n \nu_n A_r(n)$$

is the r'th constraint on the reaction.

A kinetic interpretation of this result is provided[5] by noting that e.g. the forward rate of the elementary reaction can be written as

$$R^+ = k^+\prod_n [NP(n)]^{\nu_n^+},$$

where k^+ is the rate constant. Writing the reversed rate in a similar way and using detailed balance in the form

$$k^+\prod_n [NP^o(n)]^{\nu_n^+} = k^-\prod_n [NP^o(n)]^{\nu_n^-}$$

we conclude that

$$\mathcal{A} = RT\ln(R^+/R^-). \qquad \text{(XIII)}$$

The affinity, which (up to RT) is the surprisal of the reaction is thus a measure of the deviance of the forward and reverse rates

$$-\ln(R^-/R^+) = \sum_r \lambda_r C_r\ . \qquad \text{(XIV)}$$

In summary, the surprisal of a reaction, $\mathcal{A}/RT$, has the kinetic interpretation of the deviance of the forward and reverse reaction rates, (XIII). The surprisal of the reaction vanishes only when the reaction is at equilibrium. It can be computed (cf. (XII)) as a linear combination of the surprisals of the species that participate in the reaction with weights that are the stoichoimetric coefficients. One can also express the surprisal (as in (XIV)) in terms of the constraints, C_r, on the reaction. These are linear combinations of the constraints on the species that participate in the reaction. As a simple example say that the temperature and pressure are not too high so that the three body collisions (dissociations and/or recombinations) are rate determining. Such collisions change the total number of species in the system. Hence the constraint is the total number of moles. Each species n gets counted with the same weight or $A_0(n) = 1$, where 0 is the 'total number of moles' constraint. For a particular dissociation process, e.g. $O_2 + Ar \rightleftharpoons O + O + Ar$, we have $C_0 = 2\nu_O - \nu_{O_2} = 1$. If A_0 is the only constraint, all collision induced dissociation processes have precisely the same surprisal, no matter how they differ in their individual rate constants.

OUTLOOK

Surprisal analysis has shown that deviance from equilibrium can often have a compact representation. This observation can be interpreted in terms of the constraints on the system. For example, the entire time evolution of a macroscopic system is described by the time dependence of the values of the constraints. Conversely, the measured time dependence of the concentrations of the different species is sufficient to determine the time rates of change of the constraints, but no more.

In the future we expect to see more attention paid to the identification of the constraints on macroscopic systems from the constraints on isolated single collisions. The link between the two is provided by the concept of the 'sum rule' of which equation (IV) is an example. On the one hand, the macroscopic result (III) is a direct implication of the sume rule (IV). On the other, one can show that sum rules identify the constraints on single collisions[11,18].

Another development which is yet to reach its maturity is the application of the thermodynamic-like nature of the approach. Work cycles for macroscopic systems in disequilibrium have already been discussed[2] and the required algorithms for adapting the JANAF thermochemical tables for state selected species have been noted[19]. It remains however to make full use of the thermodynamic point of view as a predictive tool.

APPENDIX

We show that for any isolated system DS is the entropy at equilibrium minus the entropy of the actual state of the system. The key step is to note that the equilibrium distribution, $P^o(n)$ is of the form[20]

$$P^o(n) = g_n \exp[-\sum_r \lambda_r^o B_r(n)] \qquad \text{(I)}$$

where the B_r's are strictly conserved properties. In other words, for any distribution $P(n)$

$$\sum_n P(n) B_r(n) = \sum_n P^o(n) B_r(n). \qquad \text{(II)}$$

This is not necessarily true if the system is not isolated or for the constraints used to characterise the non-equilibrium distribution $P(n)$. It follows from (I) and (II) that

$$-\sum_n P(n) \ln[P^o(n)/g_n] = -\sum_n P^o(n) \ln[P^o(n)/g_n]$$

and hence that (cf. (VI) and (V))

$$DS[P|P^o] = -S[P] - \sum_n P(n) \ln[P^o(n)/g_n] = S[P^o] - S[P], \text{ QED.}$$

Since $DS \geq 0$, with equality iff $P = P^o$, the entropy of an isolated system can only increase, unless it is already at equilibrium.

REFERENCES

1. R.D. Levine and R.B. Bernstein *in* Dynamics of Molecular Collisions, W.H. Miller editor (Plenum, N.Y., 1976). Vol B, p. 323.
2. R.D. Levine and A. Ben Shaul *in* Chemical and Biochemical Applications of Lasers, C.B. Moore editor (Academic Press, N.Y., 1977). Vol II, p. 145.
3. R.D. Levine, Ann Rev. Phys. Chem. *29*, 51 (1978).
4. R.D. Levine and M. Tribus, editors, The Maximum Entropy Formalism (MIT Press, Cambridge, 1979).
5. J.C. Keck in ref. 4, p. 219.
6. R.D. Levine and R.B. Bernstein, Molecular Reaction Dynamics (Clarendon Press, Oxford, 1974).
7. M.J. Berry *in* Molecular Energy Transfer, R.D. Levine and J. Jortner editors (Wiley, N.Y., 1976) p. 114.
8. J.H. Kiefer and J.C. Hajduk, Chem. Phys. *38*, 329 (1979).
9. I. Oppenheim, K.E. Shuler and G.H. Weiss, Adv. Mol. Relaxation Processes *1*, 13 (1967).
10. J.C. Keck and D. Gillespie, Combustion and Flame, *17*, 237 (1971).

11. Y. Alhassid and R.D. Levine, J. Chem. Phys. *67*, 4321 (1977).
12. I. Procaccia and R.D. Levine, J. Chem. Phys. *63*, 4261 (1975).
13. I. Procaccia and R.D. Levine, J. Chem. Phys. *65*, 3357 (1976).
14. Th. DeDonder and P. Van Rysselberghe, The Thermodynamic Theory of Affinity (Stanford University Press, 1936).
15. R.D. Levine, J. Chem. Phys. *65*, 3302 (1976).
16. Y. Alhassid, N. Agmon and R.D. Levine, Chem. Phys. Lett. *53*, 22 (1978). J. Comput. Phys. *30*, 250 (1979).
17. E.T. Jaynes, Phys. Rev. *106*, 620 (1957) and in ref. 4, p. 15.
18. Y. Alhassid and R.D. Levine, Phys. Rev. C. (1979).
19. W.C. Gardiner and R.D. Levine, J. Chem. Phys. *68*, 4524 (1978).
20. A. Katz, Principles of Statistical Mechanics: The Information Theory Approach (W.H. Freeman, San Francisco, 1967).

PRECEDING PAGE BLANK-NOT FILMED

Part II: SHOCK WAVES AND GAS DYNAMICS

TEST SECTION CONFIGURATION FOR AERODYNAMIC TESTING IN SHOCK TUBES

WILLIAM J. COOK

Mechanical Engineering Department, Iowa State University, Ames, Iowa, USA

LEROY L. PRESLEY and GARY T. CHAPMAN

NASA Ames Research Center, Moffett Field, California, USA

This paper presents results of a study of the test section configuration required to minimize or alleviate interference effects on model flow produced by the presence of test section walls in the aerodynamic testing of two dimensional transonic airfoils in a shock tube. Tests at a nominal Mach number of 0.85 and a chord Reynolds number of 2×10^6 were carried out by means of schlieren photography and pressure measurements for several symmetric airfoil profiles using shock tube test sections with unmodified straight walls, contoured walls, and slotted walls with adjacent chambers. Results were compared with corresponding results from conventional wind tunnel tests of the airfoils. Results for the straight wall tests show major airfoil flow distortions. Results from contoured wall tests and those performed using a slotted wall test section developed in this study exhibit essential agreement with wind tunnel results. The collective results show that test sections for aerodynamic testing can be designed for shock tubes that will alleviate wall interference effects.

INTRODUCTION

The shock tube is capable of generating flows with a wide range of Reynolds number that are potentially useful for experimental aerodynamic studies in the subsonic, transonic and low supersonic Mach number regimes. The high Reynolds number transonic flow regime is of current interest since certain advanced transonic aircraft undergo flight conditions that produce very high flow Reynolds numbers, e.g., Reynolds numbers based on airfoil chord length range to nearly 100 million.[1] Such Reynolds numbers exceed the performance capabilities of existing conventional wind tunnels by at least a factor of three. Although a cryogenic wind tunnel is presently under construction in the United States to provide high Reynolds number transonic testing capabilities,[2] there is a need for a smaller, less costly, high Reynolds number transonic test facility, particularly one in which research and testing of two-dimensional transonic airfoils can be carried out in order to provide fundamental flow data to augment analytical studies of transonic airfoil flows. As noted in Ref. 3., one device that shows promise in fulfilling these requirements is the shock tube. Among other considerations, it was shown that in theory transonic flows with very high Reynolds numbers can be generated, provided a shock tube of heavy construction is used.

Two major problems arise in relation to aerodynamic testing in shock tubes. These are first, the matter of model flow development time in relation to the inherently-short shock tube testing time, and second, the influence on facility walls or the flow about the model, a problem common to most aerodynamic test facilities. In the experimental phase of the study reported in Ref. 3, it was observed that steady two-dimensional transonic airfoil flows can be generated within the available testing time in shock tubes using models of reasonable size.

The matter of wall influence on model flow does, however, present a significant problem. Although there is a large body of literature[4] surrounding the design and performance for test sections intended to minimize or alleviate the wall interference effects in conventional wind tunnels, to the authors' knowledge there have been no studies reported that deal with the requirements for aerodynamic test sections for short duration flow facilities such as the shock tube. This paper presents the results of an investigation of the test section configuration required for the testing of two-dimensional transonic airfoils in a shock tube.

SHOCK TUBE DESCRIPTION

A diagram of the shock tube used in this study is shown in Fig. 1. The shock tube is gas driven and has a driven tube of rectangular cross section with a height $H = 15.2$ cm and a width $W = 7.6$ cm. The test section was located 8.5 m from the diaphragm and extended 0.18 m upstream and 0.28 m downstream of the midchord point of the airfoil. The test regime was the flow region behind the primary shock wave (Region 2 in Fig. 1). The nominal chord length c of the airfoil models used in this study was 7.6 cm, and the nominal value for the free-stream Mach number, M_2, of the flow relative to the airfoil was 0.85. All airfoils considered in this study exhibit transonic flows at this Mach number. The Reynolds number based on airfoil chord length, Re_c, was 2×10^6. The Reynolds number was limited by shock tube structural considerations. Although not in the high Reynolds number regime, $Re_c = 2 \times 10^6$ was large enough to produce turbulent boundary layers upstream of the shock wave boundary layer interaction on the airfoil and thus rendered results that could be compared with corresponding results from conventional wind tunnels. The airfoil profiles studied were symmetric profiles and, except as noted, the airfoils were mounted at zero angle of attack ($\alpha = 0$). The measured Region 2 testing time at $M_2 = 0.85$ was 3.5 ms. This was 40% of the ideal testing time t_i in Fig. 1.

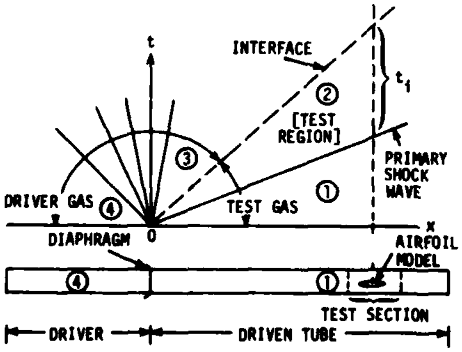

Figure 1. Diagram of shock tube and description of ideal shock tube flow.

TEST SECTION GEOMETRY

An important feature related to the performance of the test section is the size of the model in relation to the test section size. For two-dimensional flow, this is characterized by two ratios; the test section half-height to the airfoil chord length, H/2c, and the airfoil frontal area to the test section cross sectional area, A_f/A_{ts}, which is a measure of the test section blockage due to the presence of the airfoil. In order to accurately machine models and to provide internal space for instrumentation, the airfoil chord length must be greater than about 5 cm. This places the following limits on H/2c and A_f/A_{ts} for a typical 12% thick airfoil in the present test section: $(H/2c)_{max} \simeq 1.5$, and $(A_f/A_{ts})_{min} \simeq 0.040$. For the nominal 12% thick 7.6 cm chord airfoil models used in this study, $H/2c = 1.0$ and $A_f/A_{ts} = 0.06$. Transonic airfoil testing in most wind tunnels is carried out with much larger values of H/2c and significantly smaller values of A_f/A_{ts}.[4] Accordingly, more pronounced wall interference effects than those encountered in wind tunnels would be expected in the present test section. During the course of this investigation, test sections with three types of walls were investigated. These are listed in Table I.

STRAIGHT WALLS

At a Mach number of 0.85, test section blockage of 5% ($A_f/A_{ts} = 0.05$) would, on the basis of inviscid flow, cause choking to occur in the test section. Therefore, for a typical case of $A_f/A_{ts} = 0.06$ in the present study, distortions from the expected flows would be anticipated if a test section with straight unmodified test section walls was used. To examine the flow, tests were carried out by means of schlieren photography and pressure measurement instrumentation for a 7.6 cm chord length NACA 0012 airfoil (12% thick) in a test section with straight walls, designated as Configuration 1 in Table I. Pressure measurement instrumentation consisted of six Kulite pressure transducers imbedded in the airfoil.

Figure 2a shows a schlieren photo taken at $t' = 0.05$ ms of the primary shock wave passing over the airfoil and the reflected wave that forms and propagates upstream in the incoming subsonic flow ($t' = 0$ when the primary shock arrives at the airfoil leading edge). This wave, which is inherent to the flow starting processes in any test section, continues to propagate upstream in the straight wall test section, as evidenced by its appearance on the response record of a pressure transducer mounted flush with the side wall one chord length upstream of the airfoil leading edge. The response of this transducer for Configuration 1 is shown in Fig. 2b as

Table I. Shock Tube Test Section Configurations

Configuration Number	Type	Description					
1	Straight Walls	No wall modification					
2	Contoured Walls	Walls machined to match approximate stream surfaces					
		Dimensions, cm. See Fig. 5					
		x_a	x_b	y_a	n	A_s/A_w	d/s
3	Slotted Walls	15	43	4.8	3	0.13	7.9
4	Slotted Walls	3.8	11.4	0.5	4	0.17	5.9
5	Slotted Walls	9	15	0.5	4	0.17	5.9
6	Slotted Walls	9	15	0.5	5	0.21	4.8

a. $t' = 0.05$ ms

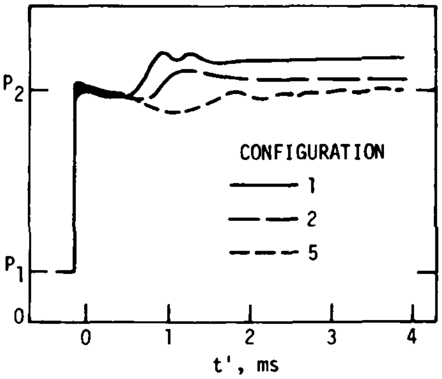

b. Sidewall pressure transducer response records. Kulite pressure transducer.

c. $t' = 2.6$ ms, Configuration 1.

Figure 2. Selected results from shock tube tests of the NACA 0012 airfoil profile.

the upper curve. The primary shock wave arrives at the transducer and, on its passage, the post shock pressure P_2 is registered. Subsequently, the reflected wave is detected by the transducer at $t' \simeq 0.6$ ms. This wave does not dissipate (as evidenced by the response of an additional wall pressure transducer further upstream) and, as a result, the flow arriving at the airfoil has a pressure significantly higher than P_2. (On the basis of inviscid flow, the free flight pressure one chord length upstream should be about 1.02 P_2 for the 0012 airfoil.) The resulting steady flow pattern observed at $t' = 2.6$ ms is shown in Fig. 2c. One basis for comparing this observed flow with the desired flow is the airfoil shock wave pattern. The airfoil shock wave patterns observed in a wind tunnel by Stivers[5] for transonic flows for the 0012 profile at Mach numbers ranging from 0.82 to 0.86 are shown as the solid lines in Fig. 3. From comparison of these shock wave profiles with the airfoil shock wave profiles in Fig. 2c, it is evident that the flow in Fig. 2c is incorrect. Hence, the need for test section wall modification to alleviate blockage is clearly established.

CONTOURED WALLS

One method of alleviating blockage is to employ contoured test section walls. The contoured wall test section is denoted as Configuration 2 in Table I. This method was used in the study reported in Ref. 3 for the circular arc airfoil and in a study of the NACA 0012 airfoil in the present investigation. In each case the stream surfaces one chord length above and below the airfoil were determined using an inviscid flow computer code and were machined into blocks that form the upper and lower walls of the test section. Different contours resulted for each airfoil. The stream surfaces of the 0012 airfoil were obtained by Arieli[6]. Schlieren photography and airfoil pressure measurements confirmed that the flows produced became steady for the contoured wall tests within the 3.5 ms testing time.

Evidence that blockage was significantly alleviated by use of contoured walls was provided by the observation that on arrival at the upstream pressure transducer, the reflected wave generated by interaction of the primary shock with the airfoil was diminished in strength when compared to the straight wall case. The response of the wall pressure transducer obtained for the 0012 airfoil tested in the contoured wall test section is shown as the middle curve in Fig. 2b. The gage response indicates constant pressure after $t' \simeq 2$ ms and registers a pressure value slightly higher than P_2 to yield $P/P_2 = 1.06$.

The steady flow results obtained for the 0012 airfoil in the test section with walls contoured for M = 0.85 flows compared favorably with those from corresponding wind tunnel tests. Results in terms of airfoil shock wave profiles and airfoil pressure distributions are shown in Figs. 3 and 4. The shock wave profiles in Fig. 3 for the shock tube tests are seen to lie somewhat downstream of the profiles observed in the wind tunnel at essentially the same flow conditions. Figure 4 shows the pressure coefficient $C_p = (P - P_\infty)/(\rho_\infty u_\infty^2/2)$ vs chord position x/c. The quantities with the subscript ∞ were taken as those computed for region 2 from measurements of primary shock speed, region 1 properties, and normal shock relations. The pressure values obtained in the shock tube tests show fair agreement with those measured in the wind tunnel. The differences in Figs. 3 and 4 between the shock tube and the wind tunnel results are attributed to the approximate wall contours used in the shock tube tests. Results from the contoured wall studies served to illustrate that very uniform airfoil flows are generated in the shock tube.

SLOTTED WALLS

The rather restrictive requirements of providing wall contours matched to each airfoil tested led to consideration of a self-regulating test section for the shock tube similar to those used in conventional wind tunnels. Desirable characteristics of such a test section are that it be of fixed geometry and that it provide automatic flow regulation to minimize wall

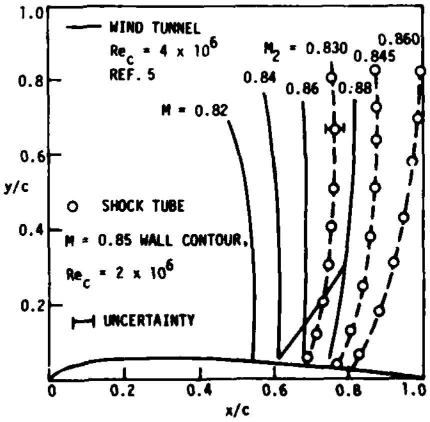

Figure 3. Comparison of shock wave profiles. NACA 0012 airfoil. Shock tube test section Configuration 2.

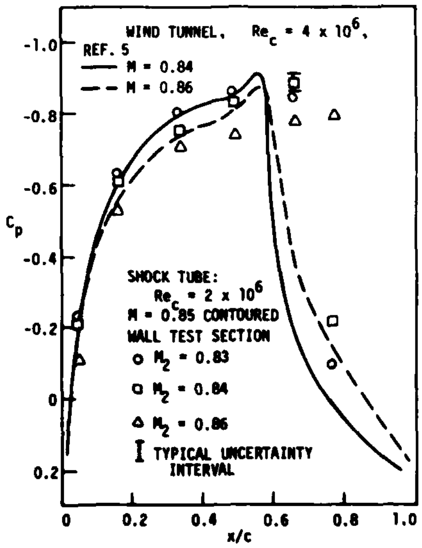

Figure 4. Pressure coefficients vs chord position. NACA 0012 airfoil. Shock tube test section Configuration 2.

effects regardless of the airfoil profile tested. Test sections for conventional wind tunnels typically consist of walls with open areas and relatively large adjacent chambers which, when properly designed in combination, produce test section flows around models very near to those that would exist in free flight. Generally, the slotted-wall test section is preferred for subsonic flows and flows with Mach numbers slightly above unity, and therefore was the type chosen for development for transonic airfoil testing in the shock tube. Important differences exist between transonic flows in slotted-wall wind tunnels and those produced in shock tubes. As a result, slotted-wall wind tunnel design features could be used only as guides in the present study.

Figure 5 shows the general configuration of the shock tube test section designed to accomplish these aims. The general configuration is patterned in part after slotted wall test sections typically used in transonic wind tunnels[4]. In addition to the ratios H/2c and A_f/A_{ts}, the slotted wall test section is characterized by the wall slot geometry and the chamber size and configuration. The latter factors influence the test section performance to a considerable extent. Centrifugal forces accompanying streamline curvature produced by the presence of the model produce flow through the slots into and out of the chambers and an associated regulating effect. It has been found for wind tunnels[4] that provided chamber size, slot spacing d/s, and the ratio of the slot area to the corresponding wall area A_s/A_w are chosen properly, the flow around the model will correspond to free flight flow, with departure from this flow being found to occur only in a narrow region adjacent to the wall, particularly in the vicinity of the slots. Values of A_s/A_w range up to 0.3 for various wind tunnels with slotted walls, and the number of slots varies according to the desired A_s/A_w and d/s. The slot width to the slotted-wall thickness is typically unity and larger. Chambers for wind tunnel test sections are usually relatively large (of the order of the test section volume). In view of the short testing time in the present study (3.5 ms), the chamber volume (characterized by x_b, y_a, and W is Fig. 5) must be of such size that steady flow is attained in both the test section and in the chambers well within the testing time. Due to the differences between transonic testing in the wind tunnel and the shock tube, the present test section was designed to permit different combinations of variables affecting test section performance to be studied.

Flows over various symmetric airfoils with a nominal Mach number of 0.85 and a chord Reynolds number of 2 x 10^6 were studied for several different slot and chamber geometries. Of the several slotted wall test section configurations studied, four will be discussed to provide a summary of the effect of configuration on the airfoil flow field. These are

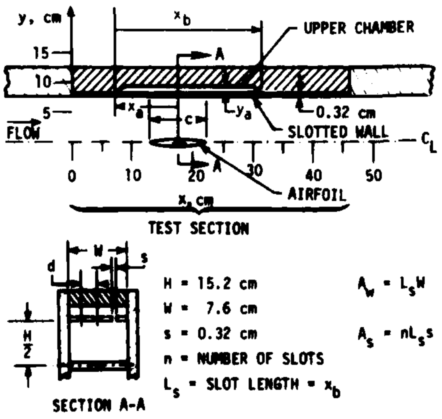

Figure 5. Shock tube slotted-wall test section.

designated as Configurations 3, 4, 5, and 6 in Table I. Configuration 3 was somewhat similar to configurations used in wind tunnels. It consisted of walls with three, 0.32 cm-wide slots (extending the length of the test section) and chambers with volumes each one-fourth of the test section volume. This configuration did not produce steady test section flows within the 3.5 ms testing time primarily because of unsteady shock waves produced in the chambers. Subsequent tests showed that significantly smaller chambers are required to produce steady test section flows about the airfoil. Configurations 4, 5 and 6 in Table I are configurations that produced steady airfoil flows. For these, each chamber volume ranged from about 1.3 to 2 times the volume of the airfoil tested. The nature of the steady flow fields produced by these configurations differs and was found to depend mainly on chamber volume, chamber position, and on the open area ratio, A_s/A_w.

Figure 6a shows a schlieren photo of the flow over a 7.6 cm chord NACA 64A010 airfoil obtained using Configuration 5. Similar photos were obtained for Configuration 4. Figure 6b shows a comparison of airfoil shock wave profiles observed in a wind tunnel with those obtained in Configurations 4 and 5. These two configurations differ only in the values for x_a and x_b. Configuration 5 produces results nearly identical to those from the wind tunnel while Configuration 4 causes the shock to form too far downstream. This is indicative of a test section that provides too much flow restriction. This behavior of Configuration 4 was confirmed by tests conducted on the circular arc airfoil. This is shown in Fig. 7 which presents pressure coefficients vs chord position obtained for the circular arc airfoil using slotted-wall test section Configurations 4 and 5. Also shown are results from the study reported in Ref. 3 for the circular arc airfoil tested in a contoured wall test section (Configuration 2). The results for configurations 2 and 5 are in close agreement while the results for Configuration 4 indicate lower values of pressure, suggesting that, as with the 64A010 airfoil, Configuration 4 unduly restricts the flow. Comparison of the dimensions of Configurations 4 and 5 in Table 1 shows that the difference in these two configurations is in the chamber dimensions x_a and x_b only. The smaller chambers in Configuration 4 limit the extent of flow regulation.

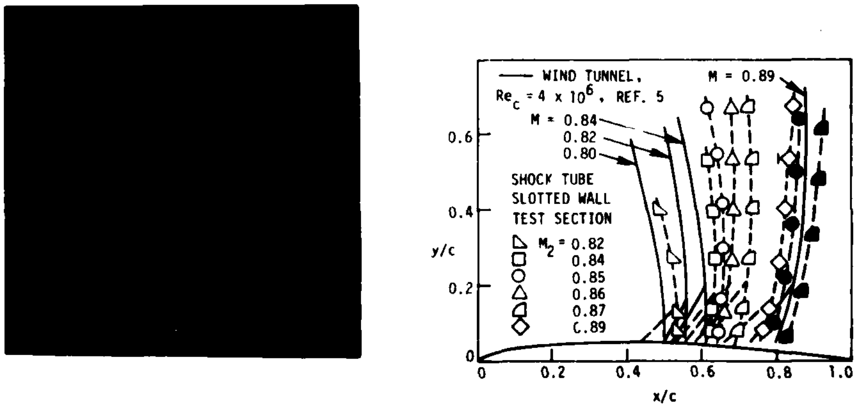

a. Schlieren photo, t' = 2.5 ms. M_2 = 0.87. Shock tube test section Configuration 5.

b. Shock wave profiles. Solid symbols: Configuration 4. Open symbols: Configuration 5.

Figure 6. Results for NACA 64A010 airfoil. Shock tube $Re_c = 2 \times 10^6$.

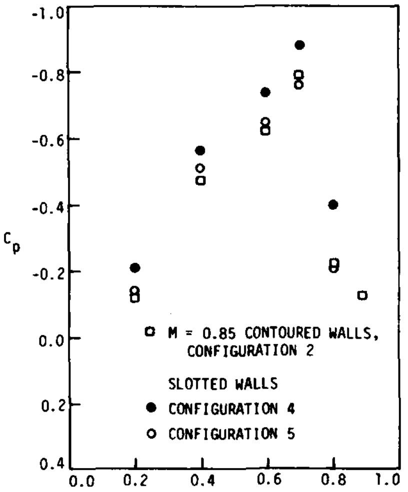

Figure 7. Comparison of pressure coefficients for the 12% thick circular arc airfoil. Shock tube $M_2 = 0.85$, $Re_c = 2x10^6$.

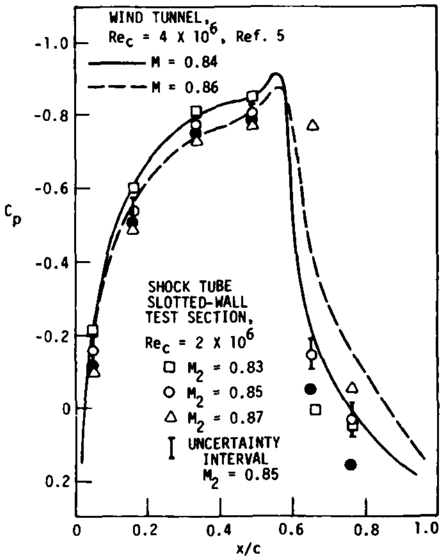

Figure 9. Pressure coefficients vs chord position. NACA 0012 airfoil. Open symbols: Configuration 5. Solid symbols: Configuration 6.

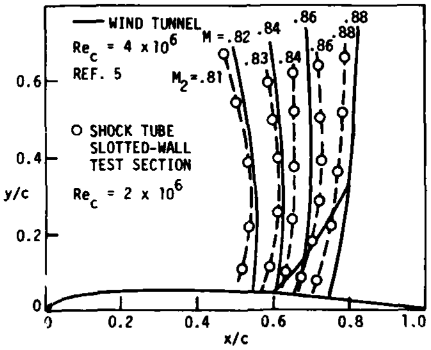

Figure 8. Shock wave profiles for the NACA 0012 airfoil. Shock tube test section Configuration 5.

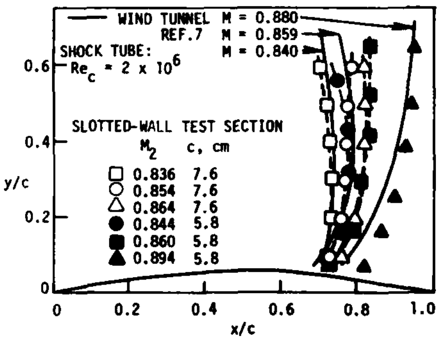

Figure 10. Comparison of shock wave profiles for the circular arc airfoil. Shock tube test section Configuration 5.

Figure 8 shows a comparison of airfoil shock wave profiles from wind tunnel tests of the 0012 airfoil and profiles obtained in the Configuration 5 test section. The agreement is good for the range of Mach number considered. Figure 9 compares wind tunnel pressure distributions for the 0012 airfoil with shock tube results obtained with Configurations 5 and 6. Table I shows that the only difference between these two configurations is that Configuration 5 has four slots (A_s/A_w=0.17) and Configuration 6 has five slots (A_s/A_w=0.21). The results in Fig. 9 suggest that Configuration 6 does not sufficiently confine the flow.

It is interesting to examine the response of the upstream wall pressure transducer for the case of the 0012 airfoil tested in Configuration 5. This is shown as the lower curve in Fig. 2b. After primary shock arrival a weak expansion wave appears at the transducer. At $t' \simeq 2$ ms the flow becomes essentially steady and exhibits a pressure very close to the computed value of P_2. This is an indication that the incoming flow relative to the airfoil is essentially correct.

The 12% thick circular arc airfoil profile was also tested in the Configuration 5 test section. Results for two values of chord length are shown in Fig. 10 in terms of airfoil shock wave profiles. The shock tube results are in good agreement with wind tunnel results and are independent of airfoil chord length.

It is seen from Figures 6 to 10 that Configuration 5 produces essentially correct flows for different airfoil profiles at zero angle of attack ($\alpha = 0$), i.e. for symmetric airfoil flows. To assess the performance of this configuration for non-symmetric flows, the 0012 airfoil was tested at $\alpha = 2°$. Comparisons of results in terms of airfoil shock profiles and pressure distributions shown in Figs. 11 and 12 demonstrate that Configuration 5 produces essentially correct results for non-symmetric flows also. The collective results obtained for the various airfoils tested using Configuration 5 indicate that this test section configuration exhibits the desired performance characteristics for test Mach numbers ranging from about 0.82 to 0.89.

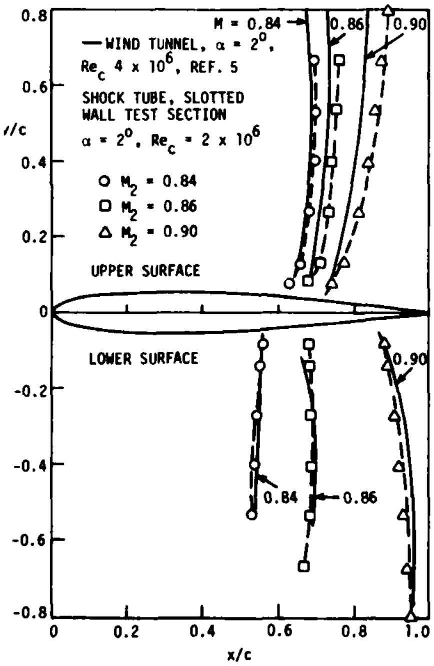

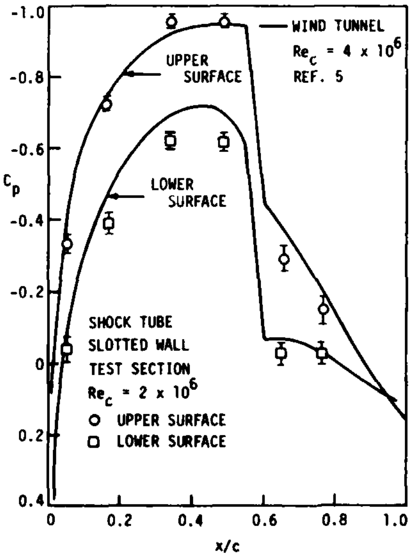

Figure 11. Comparison of shock wave profiles. NACA 0012 airfoil. $\alpha = 2°$. Shock tube test section Configuration 5.

Figure 12. Pressure coefficients vs chord position. NACA 0012 airfoil. $M = 0.842$, $\alpha = 2°$. Shock tube test section Configuration 5.

CONCLUDING REMARKS

The results of this study show that the wall interference problem in a shock tube test section intended for steady two-dimensional transonic airfoil testing can be successfully dealt with by use of either a contoured-wall test section or a properly-designed slotted-wall test section. Although the wall contouring method requires that contours be matched to each airfoil tested and may not produce flows that are in all respects correct, the method does have the advantage of producing test flows with known boundary conditions. Thus, the method can provide experimental results that are useful in analytical and numerical studies. The fixed-geometry slotted-wall test section developed in this study (Configuration 5, Table I) produces essentially correct airfoil flows for Mach numbers in the approximate range $0.82 \leq M_2 \leq 0.89$ at $Re_c = 2 \times 10^6$, and exhibits good testing flexibility, as evidenced by good agreement found for several cases between shock tube generated airfoil flows and corresponding airfoil flows observed in conventional wind tunnels. Although limited to test sections for transonic airfoil testing, the results reported here should provide a basis for future designs of test sections for aerodynamic testing in shock tubes and similar facilities with short flow times.

ACKNOWLEDGEMENTS

This study was supported by the Engineering Research Institute at Iowa State University under NASA-Ames Grant NSG-2152. The authors gratefully acknowledge the assistance rendered by Michael J. Chaney, an Iowa State University graduate student, in conducting the experimental work associated with this research.

REFERENCES

1. K. J. Orlik-Ruckemann, (Editor), AIAA Astronaut. & Aeronaut., 12, (6), 54 (1974).
2. E. C. Polhamus, R. A. Kilgore, J. B. Adcock, and E. J. Ray, AIAA Astronaut. & Aeronaut., 12, (10), 30 (1974).
3. W. J. Cook, L. L. Presley, and G. T. Chapman, Proceedings of the Tenth International Shock Tube Symposium, Kyoto, Japan, 472 (1975).
4. B. H. Goethert, Transonic wind tunnel testing, Pergamon Press, New York, (1961).
5. L. S. Stivers, Jr., NASA Ames Research Center, private communication.
6. R. Arieli, NASA Ames Research Center, private communication.
7. G. P. Wood and P. B. Gooderum, NACA TN2801, (1952).

A LARGE-SCALE AERODYNAMIC TEST FACILITY COMBINING THE SHOCK AND LUDWIEG TUBE CONCEPTS

LUCIAN Z. DUMITRESCU

National Institute for Scientific and Technical Creation — INCREST
Bucharest, Romania

A description is given of a large aerodynamic test facility, designed and built at the INCREST, which is capable of various modes of operation.
As a large shock tube, it has an 8oo mm square test section, with a 9oo mm ID, 17o m long main tube, and a 25o cu.m. vacuum tank. The maximum charging pressure is 2o atms, producing shocks with M_S=1.oo5-3.o, with test durations of 5o-1oo msecs. Shock loadings over 7 atms can be simulated on real scale structures.
For operation as a Ludwieg tube, a Laval nozzle and a supersonic test section, 8oo mm square, are inserted, for model testing in the range M=1.4-3,8 with flow duration o.7-o.8 secs.
Also, a 3oo x 8oo mm 2D transonic test section with perforated walls is used for airfoil tests at M=o.6-1.35;the Reynolds number range is 2.o-5o milion, with an extremaly low level of noise and disturbances.
A combined operating mode is also possible, simulating shock interactions with a preestablished flow.

INTRODUCTION

The facility described herein has been designed and put into operation at the National Institute for Scientific and Technical Creation. First, the basic aerodynamic configurations will be described, then some technical design features will be discussed. Finally, a few results of the preliminary operational tests will be presented.

BASIC AERODYNAMIC DESIGN AND PERFORMANCES

The main components of the facility are a 9oo mm ID, 17o m long tube, which can be charged with air at 2o atms, connected at the downstream end to a 25o cu.m vacuum tank, which may be evacuated to 2 torr abs. By using suitable inserts, several operating configurations may be set up (figure 1).

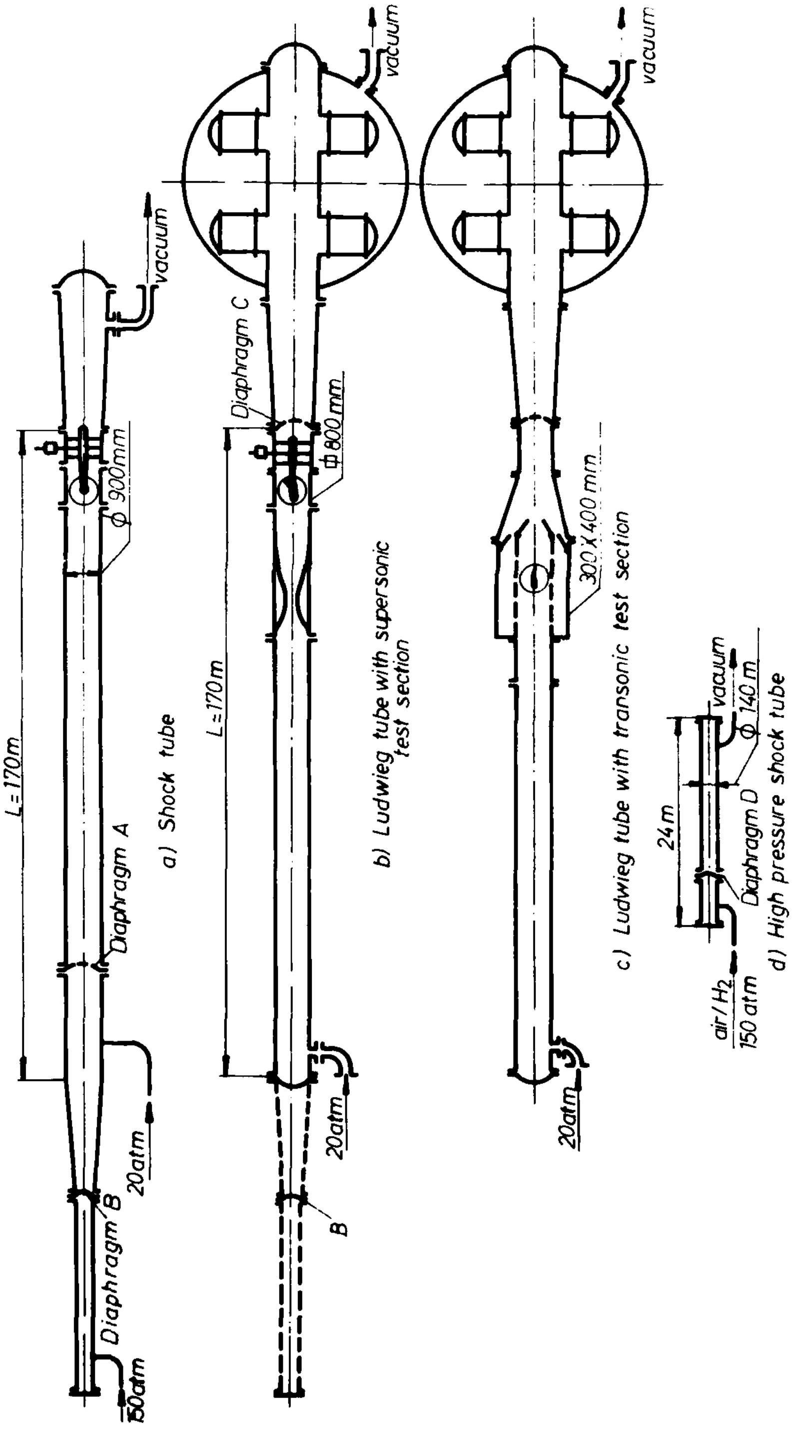

a) Shock tube

b) Ludwieg tube with supersonic test section

c) Ludwieg tube with transonic test section

d) High pressure shock tube

Figure 1. Possible configurations of the facility

1. Large shock tube

In this configuration, the first 15 m of the main tube may be used as a driver chamber;with scribed aluminium and/or steel diaphragms (station A, figure 1 a), shocks in the range M=1.oo5-3.o are produced in a test section 8oo mm square, with test durations of 5o-1oo msecs. The maximum shock loading for structural tests is over 7 atms.

For ease of operation an 14o mm ID, 24 m long driver tube has also been provided. A diaphragm station (B) may be fitted at its end, connected to the main tube by a conical transition piece. By charging this tube with air at 15o atms, or hydrogen, without the need to handle large diaphragms,similar results are obtained.

2. Supersonic Ludwieg tube

In the Ludwieg-tube mode of operation, the diaphragm has to be placed at the downstream end (station C, figure 1 b). For supersonic testing, a Laval nozzle insert, an 8oo mm square test chamber and a model support with 35 degs, pitch travel are fitted. Test Mach numbers are from 1.4 to 3.8, with clean flow durations of o.7-o.8 secs. The maximum stagnation pressure is limited by the charging pressure of the tube, 2o atms, and special operating techniques may be followed to reduce starting and stopping overloads on models.

3. Transonic Ludwieg tube

The Laval nozzle and test section may be replaced by a two-dimensional transonic test chamber, 3oo x 8oo mm (figure 1 c), with a variable porosity distribution on the upper and lower walls. The flow Mach number is in the range o.6-1.35, with durations of o.7-o.8 secs and a very low level of disturbances. A wide range of Reynolds numbers is attainable (2.o-5o.o milion for a 2oo mm chord model).

In the Ludwieg tube mode, the flow is discharged into the vacuum tank and, for ease of operation, a set of 12 fast-acting valves, 4oo mm ID, of special design, has heen mounted inside the tank, to replace the diaphragm. Very consistent results have been obtained with the valves, and this mode of operation is now standard.

4. Combined shock - and Ludwieg tube

A unique feature of the facility is its capability of combining the two modes of operation, i.e. after starting a conventional Ludwieg - tube flow (either transonic or supersonic), a secondary shock wave may be sent along the tube by controlled bursting of an upstream diaphragm at station B (figure 1 b). Thus, shock interaction phenomena with a preestablished flow may now be studied.

5. High pressure shock tube

Finally, it should be mentioned that the high-pressure driver tube may stand alone as a quite sizeable shock tube, 14o mm ID and up to 24 m long, if a diaphragm is placed at station D (figure 1 d). With hydrogen drive at 15o atms, shocks up to M=8.o may readily be produced, and the stainless-steel construction should prove useful for reducing contamination in chemical applications.

TECHNICAL DESIGN FEATURES

1. The main tube (figure 2)

To ease access for configuration changes and for maintenance, it is of segmented construction. A pair of hydraulic jacks permit manoeuvering, with an axial travel on rails, of 8oo mm. Two inserts are provided, with transition from 9oo mm ID to 8oo mm square.

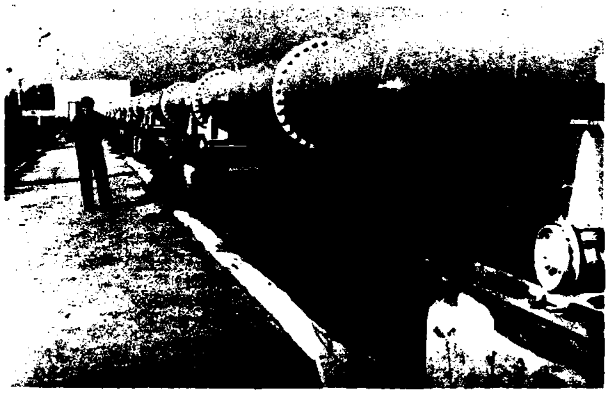

Fig.2. View of the main tube

2. The Laval nozzle

Specially designed plastic flexible plates are used, contoured by large number of screw jacks, which ensure an accurate profile setting (with the inconvenient of rather tedious adjustments).

3. The model support

The mechanical design uses a pair of spindles and a gear train to produce pitching of the model about a virtual center;the motion is hydraulically actuated, with a pitch sweep of 1o degrees during the run. An electrical drive sets this segment anywhere within the total pitch range of 35 degrees. Special care has been taken to ensure a high accuracy of pitch angle setting and measurement;we hope to have attained o.o1 - o.o2 degrees.

4. The transonic insert

This includes an upstream contraction, carefully machined to a theoretical contour derived after J.Rom & al.;this is followed by the test chamber proper. The upper and lower walls are perforated at 6o degrees, with an adjustable porosity distribution, obtained with a set of segmented sliding plates. At the downstream end, a diffuser section includes the flap system for Mach number control. For subsonic operation, a pair of flaps provide an adjustable

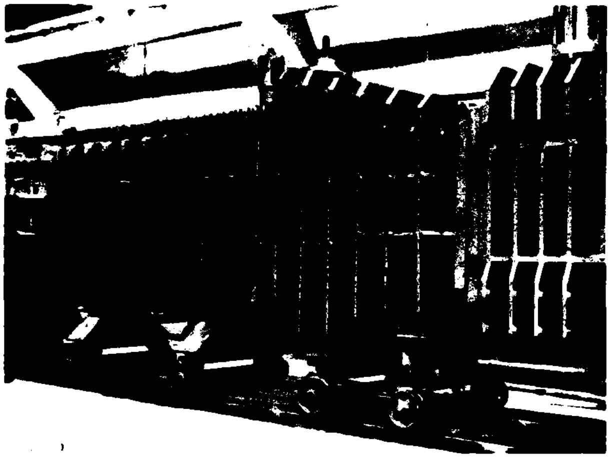

Fig.3. The transonic test chamber

downstream sonic throat. In the supersonic range, the Mach number is set by controlling, with a second pair of flaps, the outflow from the plenum chamber. For Mach numbers over 1.3o, a sonic throat may be installed at the entrance to the test chamber.

5. The fast - acting valves (figure 4)

These are of sliding sleeve type and pneumatically operated. By careful design and by exhaustive developement and testing, excellent performances have been attained:operating pressure up to 2o atms, actual opening time 125-5 msecs, triggering delay 17o-2o msecs.

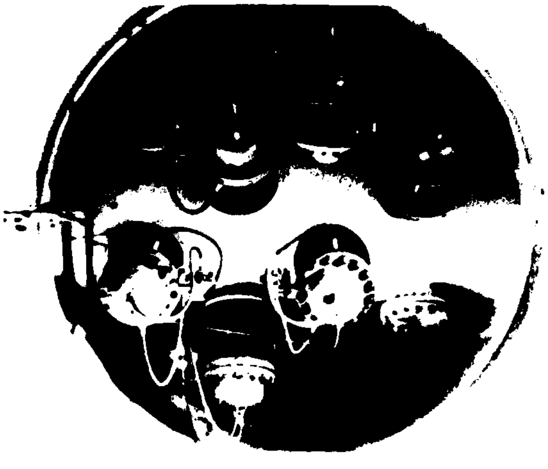

Fig.4. View of the valves installed inside the vacuum tank

It should be mentioned that such valves may also find other applications in the engineering field.

6. The vacuum tank (figure 5)

The capacity is 25o cu.m and the limit vacuum 2 torr abs, with a measured leak rate of 2 torr/24 h.

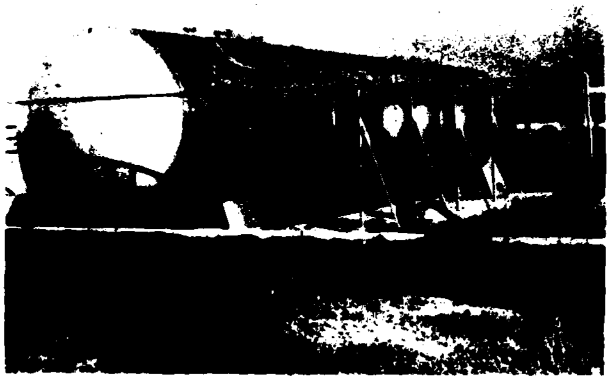

Figure 5. View of the vacuum tank

It should be mentioned that in the Ludwieg - tube mode of operation, evacuation of the tank is seldom needed;e.g. when exploring the lower Reynolds range. The maximum overpressure is 8 atms, dictated by emergency safety considerations.

7. The high-pressure shoock tube

This is also segmented, with a set of various lenghts of tubing and special inserts provided with instrumentation ports. For controlled bursting, the double-diaphragm technique may be used.

8. Ancillary equipement

The vacuum is produced by a 5o kW pumping station, while high pressure air is produced by a 15o atms compressor charging a battery of storage bottles. The main 2o atms supply is available from a large air plant, which delivers air having a very low oil and moisture content (dew point - 4o degs.C).

INSTRUMENTATION AND DATA AQUISITION

For operation in the shock - tube mode, the facility is equipped with the usual complement of pressure pick-ups, heat transfer gages, counter chronometers, oscilloscopes a.s.o. A 18o mm-field colour Schlieren, made by Rollab AG (Sweden) is also used.

For the Ludwieg - tube operation a complete data aquisition system has been designed and built (figure 6), comprising the following subsystems:

1.Blow - down sequence unit (BDS)

This takes care of the proper sequencing of the blow - down events (valve opening, scanivalve starting, schlieren spark triggering, computer starting a.s.o.). It provides also means for various checks, " dry " runs, a.s.o.

2. Model pitch control unit

This includes the controls for the pitch sweep, as well as an angle-of-attck indicator. The heart of this latter is a precision 15 turn potentiometer (POT) (made by Beckmann instruments) followed by a signal conditioning unit (SCU) and a buffer amplifier (BU). An analog instrument and a 4½ digit panel meter (DPM) display the pitch angle.

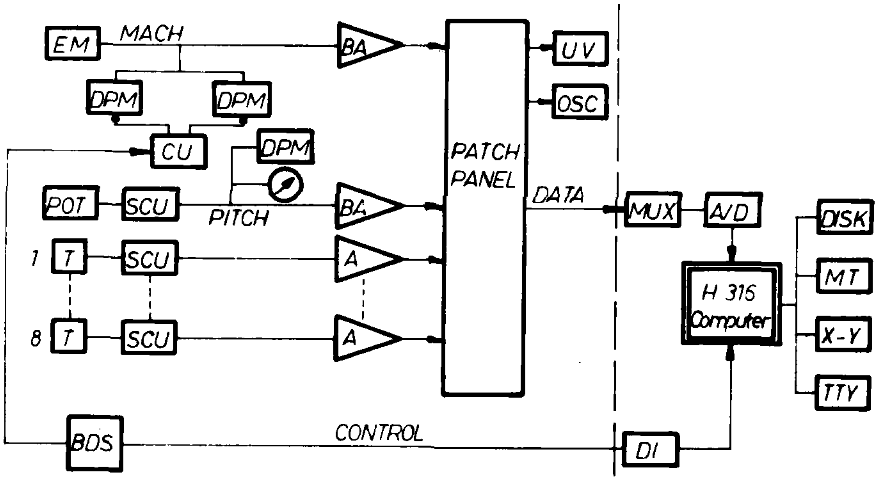

Figure 6. The data aquisition system

3. Mach number indicator

This uses to advantage the working principle of the Ludwieg tube, as follows:a precision electromanometer (EM) (type Bell & Howell), which may be checked periodically against a primary pressure calibration unit (Texas Instruments Co.) delivers continuously signals to a pair of digital panel meters (DPM). Coincident with the start of the blow-down sequence, by means of a control unit (CU), the first DPM indication is freezed, thus recording the charging pressure in the tube, just prior to the run. After a variable delay (o.3 - o.6 secs), the CU freezes also the second DPM, and the actual static pressure in the test chamber is recorded. The ratio of the two indications is a direct function of the Mach number.

4. Signal intake and conditioning

The measuring transducers (T), which may be pressure pick-ups (Kulite Co), scanivalves, strain gage model balances a.s.o., are fed by a set of 8 signal conditioning units (SCU) (Honeywell 1o5 Accudata), followed by precision DC amplifiers (Burr-Brown)

362o). The system is expandable to 16 channels. On line monitoring and analog recording is on memory osciloscopes (OSC) and UV recorders. Great care has been taken to ensure the highest quality of this low-level part of the data-handling system, since it is determinant for the overall measuring accuracy.

5. Digital aquisition and processing

The system is now being developed to share with another facility the use of a data aquisition system built around a Honeywell H 316 computer, having advanced performances:32 channel multiplesing (MUX), 16 bit word A/D conversion and storage, with 24 microsec. conversion time, disk buffering, off-line "quick-look " capability on an X-Y recorder for eight selected parameters, and final digital recording on high-speed magnetic tape (MT) for subsequent processing. The whole operation is controled from a teletype console (TTY). All analog and digital data from the tube will be transmitted at high level by cable to the aquisition unit, including Mach number and pitch angle indications The flexibility of the set-up permits further developements of the system.

PRELIMINARY TEST RESULTS

After completing all subassembly and mechanical testing, the facility has been put into operation. A few of the more interesting preliminary test results can be presented here.

In the shock - tube mode, a series of runs were carried out, with flow Mach numbers very close to unitary (M_S=1.o55-1.15o). The shock detachement distance in front of a 5o mm dia. sphere was measured, taking advantage of the large test chamber.

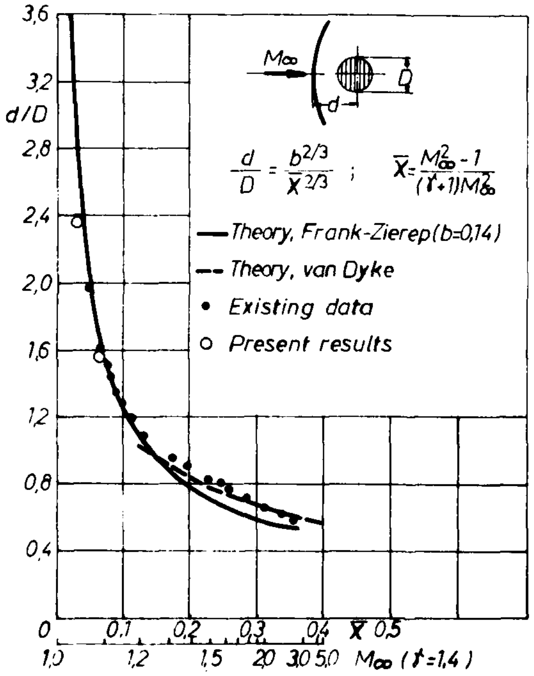

Figure 7.
Shock detachment distance in front of a sphere at transonic speeds

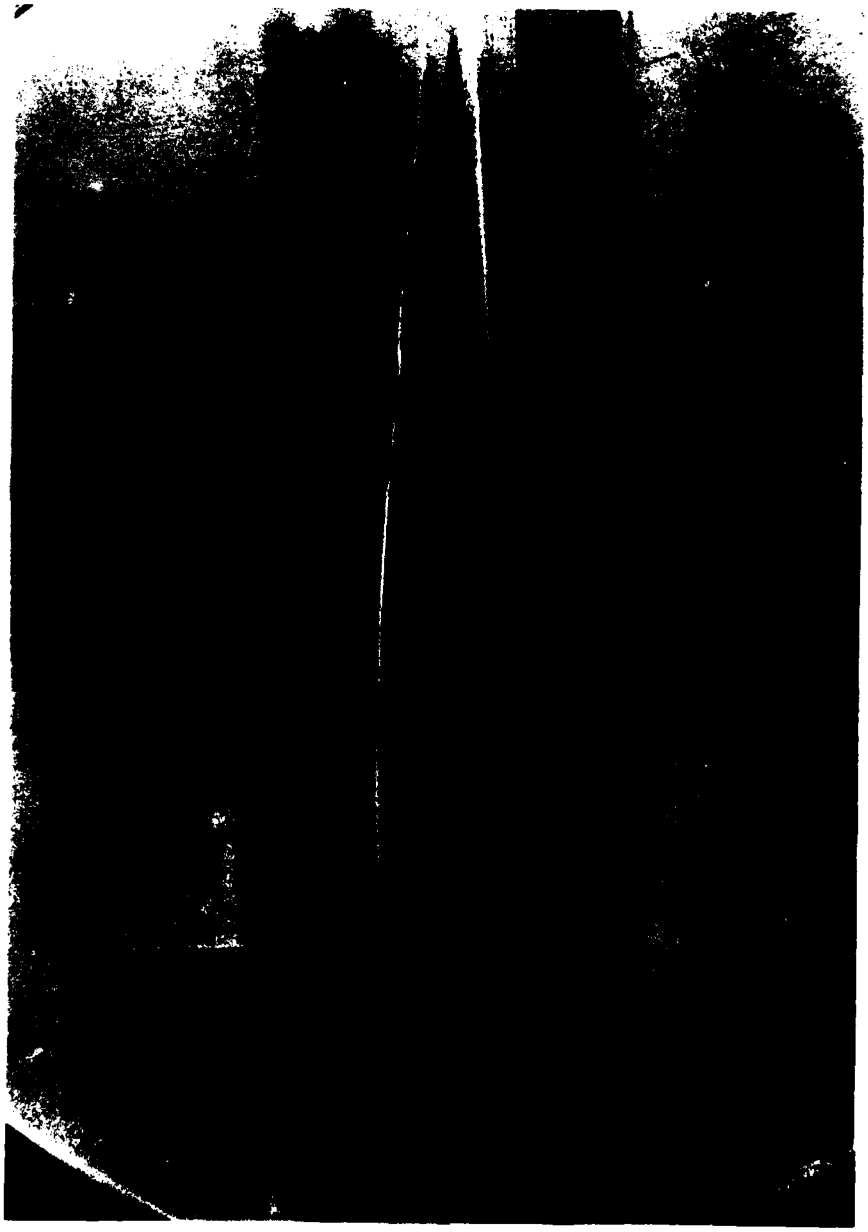

Figure 9. Transonic flow around a NACA airfoil (M=o.845)

Comparison with other results and with theory is quite satisfactory (figure 7).

For Ludwieg tube operation, of interest is a reproduction of a pressure recording (figure 8).

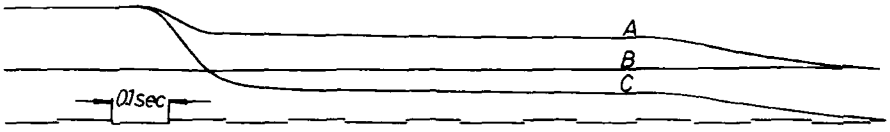

Fig.8. Pressure recording in the transonic test chamber. A-pressure in the main tube, ahead of the contraction; B-static pressure on wall (M=o.9);C-differential pressure between two points in the test chamber

It may be seen that the valves are opening sufficiently fast to produce a short initial transient, followed by a very flat pressure signal, with a drop, due to boundary-layer growth, under 1 percent. The low level of disturbances is evident, as well as the flow uniformity in the test chamber, shown by the trace of the differential pressure pick-up.

Finally, an early example of flow visualisation is given (figure 9). At the time, the air-drying plant was not operative and moisture condensation on the windows disturbed the picture, but also gave an indication of the flow pattern.

DISCUSSION AND PERSPECTIVES

The potentialities of such a facility are only now beginning to be explored and many interesting applications come to the mind, for scientific research and for industrial testing. The operating team will be happy to cooperate with other scientific organisations in developing these applications.

ACKNOWLEDGEMENTS

The author wishes to recall the encouragement and support received from the management of his institution (general director Dr.C.Teodorescu), which enabled him to start and pursue the project, and the help of all his colleagues in the institute and from the cooperating organisations, without whom it could not be succesfully completed. These are too numerous to cite individually;however, a special mention should be made of ing.I.Nedelescu and ing.C.Iordache, who led the mechanical design team, and whose seredipity produced a number of quite remarkable innovative solutions.

LUDWIEG TUBE FACILITY FOR STUDIES OF HIGH PRESSURE LOW TEMPERATURE SUPERSONIC FLOW TRANSITION LASERS

B. FORESTIER, B. FONTAINE and J. VALENSI

Institut de Mécanique des Fluides Université d'Aix-Marseille II
1, rue Honnorat, Marseille, 13003, France

The use of aerodynamic technics to achieve C.W. or high repetition rate ultraviolet or visible laser emissions through electronic transitions may play a leading part as in the well known infrared vibrational lasers. A Ludwieg tube facility associated to an electron gun device has been developed and has permitted to achieve several high power quasi C.W. ultraviolet or visible laser emission from an active medium in supersonic flow at very low temperature (80 or 120 K) and high density (up to 2 amagats). Some characteristics of these laser emissions will be given here as well as the first results of an interferometric study of flow field aerodynamic disturbances in the laser cavity which may lead to a large scattering of laser beam at so short wavelengths.

INTRODUCTION

The use of electronic transition molecular systems to achieve high efficiency high power short pulses laser emissions has been well improved these last years, moreover high pressure electron beam excited electronic transitions systems have recently allowed to achieve in room temperature experiments, quasi-continuous laser emissions in ultraviolet from molecular levels of rare gas halides[1,6]. At the Institut de Mécanique des Fluides de Marseille a study has been undertaken with the object of developping high average power or quasi continuous u.v. or visible lasers by means of an association of fluid dynamics technics and electron beam excitation capabilities in the same way as the well known infrared vibrational flow lasers[7,9].

In the case of electronic transition molecular lasers, and particularly with high pressure active medium, strong cooling of the working mixture may tend, on the one hand, to lower the quenching of excited species and absorbtion losses and, on the other hand, to increase the rate and the branching ratio of useful specific reactions. Cooling the gas by means of a supersonic expansion could, moreover, lead to C.W. or high repetition rate pulsed laser systems, as the heat and waste products are carried away by the supersonic flow.

The emphasis will be given here on the laser emissions which we have achieved from a high density supersonic flow and on the results of an interferometric study of flow field in laser cavity, it must be pointed out indeed, that the aerodynamic perturbations may play a leading part at such short wavelengths.

EXPERIMENTAL SET UP

The experimental apparatus which has been described in details previously[10] consists mainly of a small Ludwieg tube which feeds through a supersonic nozzle, a constant area channel (16 x 3 cm^2) associated with a cold cathode electron gun.

The Fig. 1 corresponds to a cross sectional view of the test section device. The characteristics of the flow in the test section depends on the nozzle design and the calculated steady flow parameters for an initial pressure in the high pressure tube equal to 7.5 Atm . of Argon are given on the following table :

Mach Number	$P_{(Atm)}$	$\rho\,(10^{19}cm^{-3})$	$T_{(K)}$	$U_{m\ s^{-1}}$
1.75	0.81	4.86	119.7	357.9
2.5	0.33	2.85	83.7	427.6
3	0.19	2.03	66.6	457.8

The home made electron gun was energized by a P.I. MX 31 Marx generator (300 kV, 1500 J). The e-beam current density could be varied between 2 A cm^{-2} for 5 µs and 20 A cm^{-2} for 0.5 µs. The e-beam fired when the flow is steady, excits the active mixture in supersonic flow through a 25 µm thick titanium foil (14 x 2 cm^2) flush mounted in the constant area channel. Particular care has been taken to ensure a good allignement between the different walls of the channel and the nozzle exit in order to minimize aerodynamic disturbances. Taking into account the little duration of the excitation in this demonstrative device the length and the volume of high pressure Ludwieg tube chamber, chosen as little as possible to minimize the consumption of expansive and corrosive gases, permit to achieve steady state flow conditions for about 2 ms, with Argon or Neon as diluant.

Provision is made on test section side walls for piezoelectric gauges, interferometric graded windows or hard coating MDL mirrors. Windows and mirrors are mounted slightly away from the walls, the cavity length being equal to 18 cm.

Experiments at room temperature, without flow, are also performed immediatly after a dynamic shot with the same sample of gas and the same excitation conditions, it is so possible to compare directly the effect of temperature on laser or fluorescence emissions.

Routine control diagnostics of the experiments consist essentially, for each shot, in a check of Marx generator voltage and total current intensity and in a measure of pressure time dependance of the supersonic flow.

It is also possible to record :

- Supersonic flow density map and its space and time variation following e-beam excitation by means of a Michelson interferometer using a pulsed ion laser source and streak or frame photographical records.
- Time variation of laser and fluorescence intensities by means of filtered

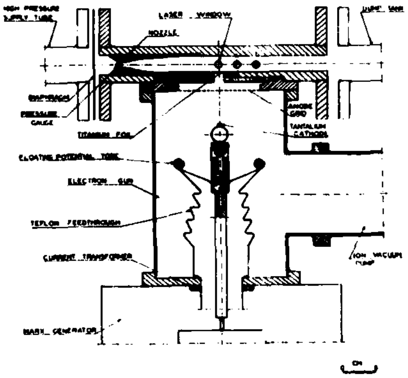

Fig.1 Cross sectional view of test section and electron gun

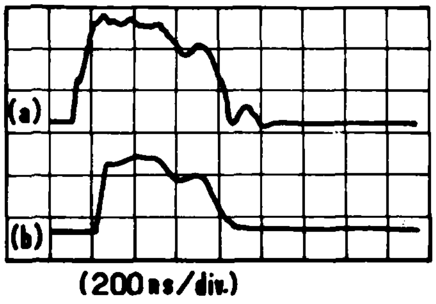

Fig.2 Electron beam current (a) and laser (b) waveforms. The peak current corresponds to a e-beam of 10 A cm^{-2} in laser cavity. Gas Ne/Xe/HCℓ;T=120K T_{mirror}=0.1 % and 5 %.

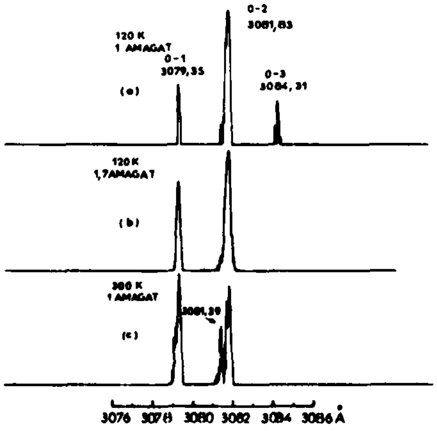

Fig. 3 Densitometer traces of XeCℓ laser spectra at various temperatures and densities (Gas : Ne/Xe/HCℓ 1000/17/7.5)

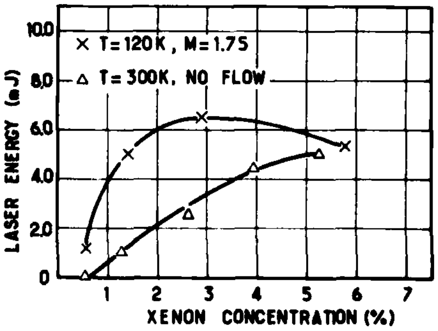

Fig. 4 Measured output laser energy as a function of Xe concentration for T = 120 and 300 K ; T_{mirror}=5 %, V_{gun}=240KV, $J_{e.b.}$=10 Acm^{-2}.

PMT or photodiodes.

- Time integrated spectral repartition of laser and fluorescence intensities by means of grating spectrographs.
- Total extracted optical energy by means of a Gen-Tech joulemeter.

EXPERIMENTAL RESULTS

A. Laser emissions

The described device has allowed the generation of several high power ultraviolet and visible laser emissions from excimers (XeF and XeCℓ) ionic (NeII) and atomic (FI) electronic transitions when mixtures or rare gases and fluored compounds in supersonic flow where e-beam excited at very low temperature.

- Strong lasing has been achieved near 350 nm on XeF^* when Ne-Xe-NF_3 mixtures, aerodynamically cooled to 120 K and at a density of 1 amagat, were excited by a 10 A cm^{-2} - 240 kV e-beam. About 1 millijoule of laser energy was obtained in a 400 ns FWHM pulse limited only by the e-beam pulse length[11,12]. It is noteworthy that the laser pulse length was much longer than the 17 ns radiative life time of the XeF (B-X) laser transition showing no bottlenecking for the lower laser level.

- Lasing was also achieved with the same device on NeII transitions at 3378,23 and 3481,95 Å when mixtures of Ne and a few part per thousand of NF_3 were cooled down to 80 K and excited by a 240 kV - 10 A cm^{-2} electron beam of 600 ns FWHM duration[13]. The two laser emissions have a 350 ns FWHM duration limited only by the e-beam lifetime. It is noteworthy that in our experimental conditions these two laser lines have never been generated at room temperature. The 3481Å laser line has never been obtained before at high density.

- Very strong lasing has also been achieved with the same device on FI transitions at 7130 and 7310 Å when mixtures of He and NF_3 were cooled down to 120 K and excited by an e-beam with a current density as low as a few A cm^{-2}.

More details are given below in the XeCℓ case, which has permitted to achieve, up to date, the best results in our device. Strong lasing was obtained on several XeCℓ bands near 308 nm at both very low temperature and room temperature with the present small amplification length device, when Ne : Xe : HCℓ mixtures were e-beam excited. These laser wavelengths are the shortest to have been generated up to date in a supersonic flow. Fig. 2 shows typical oscilloscope traces of e-beam current (Fig. 2a) and laser waveform (recorded with filtered PMT (Fig. 2b) for the case of supersonic flow XeCℓ laser experiments.

In all the experiments performed the laser pulse was much longer than the 11 ns XeCℓ upper level radiative life time[14] and was only limited by the electron beam pulse length.

Fig. 3 shows typical high resolution laser spectra recorded under three different conditions for the same working mixture, Ne : Xe : HCℓ (1000 : 27 : 7,5). Figures 2a and 2b correspond to the cases when active medium were aerodynamically cooled to 120 K, the densities being respectively equal to 1 and 1.7 amagat. The Fig. 3c corresponds to a room temperature experiment with the same active medium at 1 amagat density.

The recorded wavelengths measured in air λ = 3079, 35 ± 0.05 Å ;

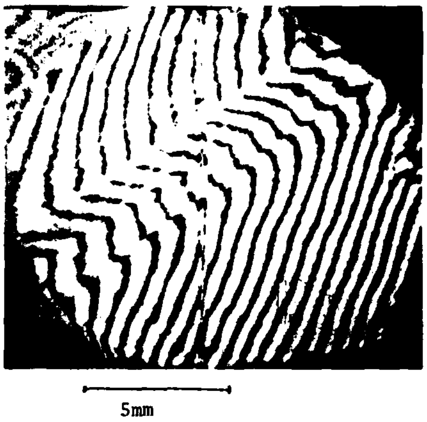

Fig. 5 Interferogram of a perturbated supersonic flow in test section. Gas: Néon, $M = 1.75$, $P = 4.5$ Atm, $\Delta\rho/\rho_{init.} = 2.1$ % per fringe.

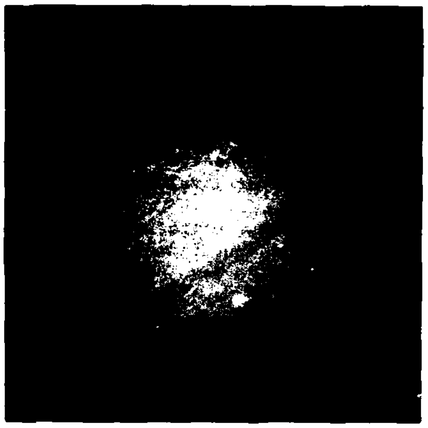

Fig. 6 Laser beam pattern with a perturbated supersonic flow corresponding to fig. 5 interferogram.
Gas : $Ne/Xe/NF_3$, $M = 1.75$, $P = 45$ Atm
$\lambda = 350$ nm

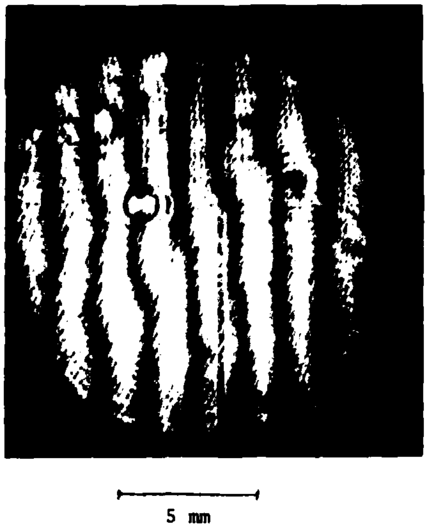

Fig. 7 Interferogram of a not perturbated supersonic flow. Gas : Helium, $M = 1.75$, $P = 4.5$ Atm, $\Delta\rho/\rho_{init.} = 4,3\%$ per fringe.

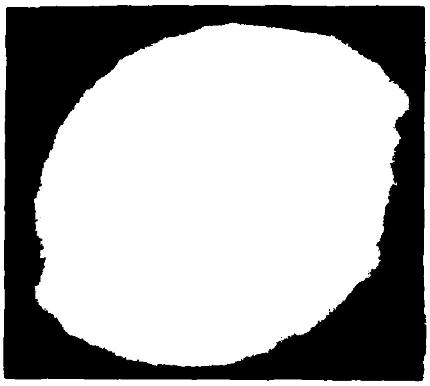

Fig. 8 Laser beam pattern with a not perturbated supersonic flow corresponding to fig. 7 interferogram. Gas He/NF_3, $M=1.75$, $P=4.5$ Atm. $\lambda = 730$ nm.

3081,83 Å and 3084,31 Å are respectively assigned following Tellinghuisen[15] to 0-1, 0-2 and 0-3 $Xe^{35}C\ell$ bands. The laser band at $\lambda = 3081{,}39$ Å has not been assigned. The comparison of the Fig. 3 spectra shows a strong modification of the ratio of 0-1, 0-2 and 0-3 Xe Cℓ band intensities with experimental conditions. At T = 120 K and $\rho = 1$ amagat the relative intensity of the 0-3 band is higher than the 0-1 band one in spite of the lower value of its Franck Condon factor[15]. This indicates that the XeCℓ lower level manifold is not fully relaxed. In spite of this the total laser energy is, as reported below, higher at low temperature than at room temperature. Whatever our experimental conditions we have observed only laser transitions from v' = 0 showing that the XeCℓ laser upper level is fully relaxed.

Fig. 4 plots the extracted optical energy of the XeCℓ laser for Ne/Xe/HCℓ mixtures as a function of Xe relative concentrations and that for temperatures equal to 120 and 300 K and a density equal to 1 amagat with an e-beam excitation of 240 kV and 10 A cm^{-2} during 600 ns (FWHM). The extracted energy for low Xe concentration is noticeably higher at T = 120 K, than at T = 300 K However for T = 120 K, when Xe concentration is increased a saturation process occurs which is faster for the low temperature case. The saturation at low temperature is probably due to the beginning of Xe liquefaction which would limit the available Xenon concentration and could lead to a scattering of the laser beam. The maximum output laser energy obtained with our device for T = 120 K and $\rho = 1.7$ amagat was equal to 15 millijoules on 0.5 μs pulses through a 5% transmission extracting mirror. This value corresponds to a specific extracted energy and power of 1 J/ℓ and 30 kW/cm^2 and has been achieved with a mixture (Ne - Xe - HCℓ , 1000 - 20 - 1).

The increase of extracted laser power and efficiency when cooling Ne/Xe/HCℓ mixtures is not induced by an increase of the upper laser level population as observed from fluorescence intensity at 308 Å which is not modified by cooling. The favorable effect of cooling is expected to be due to both an increase of the gain (spectral narrowing and optimum J number lowering) and a decrease of the absorption by Ne_2^+ and Xe_2^+ molecular ions at 308 mm as predicted by Wadt[16].

B. Aerodynamic flow field study

An interferometric study of the flow field in the test section has been undertaken to precise the contribution of aerodynamic perturbations to the losses in the laser cavity. The interferometer was of the Michelson type, the ionic laser light source permitts either to record a snapshot of the interferogram pattern with a 200 ns exposure time (Xenon laser) or to record and x,t diagram by means of a drum camera during about 1500 μs (Argon laser) and to check the Ludwieg tube starting process or the steady state flow in order to know the best time for the electron beam excitation of the flow and to measure the perturbations in laser cavity.

The interferogram of the Fig. 5 corresponds to a supersonic flow when a step in the electron gun window holder alignement lead to a strong perturbation of the flow. Even with such perturbations it has been possible to achieve laser emission down to wavelength as short as 350 mm. Moreover a photographical record of laser pattern shows (Fig. 6) the perturbations induced by aerodynamic density gradients.

A carefully alignement of the different parts of the channel permitted to achieve a quite good flow quality. The figures 7 and 8 correspond to an interferogram and a laser pattern obtained in such a configuration. Moreover it must be pointed out that the laser beam patterns recorded from an active medium in supersonic flow or without flow are similar.

The Figure 9 corresponds to an x,t diagram of the fringes when Helium

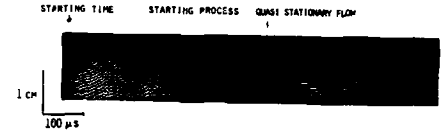

Fig. 9 X,t diagram of fringe.
gas : Helium, M = 1.75, P = 4.5 Atm
$\Delta\rho/\rho_{init.}$ = 4 % per fringe.

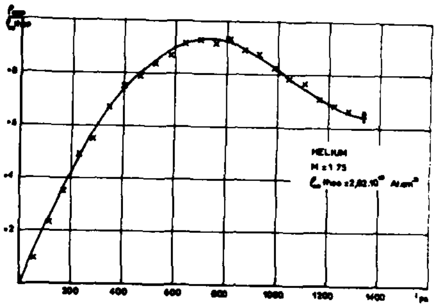

Fig. 10 Time density dependance in the test section ($\Delta\rho/\rho_{init}$) as calculated from fig.9 interferogram. Gas:Helium, M = 1.75, $\rho_{init.}$ = 2.8 $10^{19}cm^{-3}$

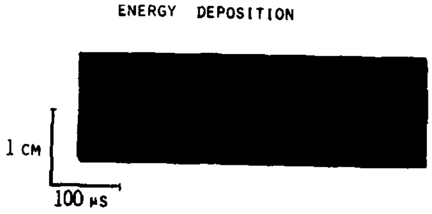

Fig. 11 X,t diagram of density perturbation induced by electron-beam energy deposition in a static gas Gas: Ar, P = 1 bar, T = 300 K, U = 0 m s^{-1} , $\Delta\rho/\rho_{init.}$=0.58% per fringe

is used in supply tube. The Ludwieg tube length being in these conditions too short to achieve quasi steady flow. The curve on Figure 10 shows the corresponding density time dependance of the flow in the constant area channel.

As an example and to illustrate the leading part of the supersonic flow in the frame of a high repetition rate or continuous laser, the Figure 11 shows a fringe pattern when e-beam energy is deposited in an active medium without flow. At the opposite no perturbations was recorded in the laser cavity when energy is deposited in a supersonic flow active medium.

The use of aerodynamic technics in laser physics has already permitted to achieve, in infrared wavelength range, high average power or continuous wave systems, similar technics in electronic transition systems could lead to a class of lasers whose applications are numerous.

REFERENCES

1. J.J. Ewing and C.A. Brau, Appl. Phys. lett. *27*, 350, 1975.

2. E.R. Ault, R.S. Bradford and M.L. Bhaumik, Appl. Phys. lett. *27*, 473 (1975).

3. J.A. Mangano, J.H. Jacob and J.B. Dodge, Appl. Phys. lett. *29*, 426 (1976).

4. L.F. Champagne, J.G. Eden, N.W. Harris, N.W. Djeu and S.K. Searles, Appl. Phys. lett. *30*, 160 (1977).

5. B. Fontaine and B. Forestier, Optics Communications *25*, 1978 (97).

6. M. Rokni, J.A. Mangano, J.H. Jacob and J.C. Hsia, I.E.E.E. J. Quant. Electr. *QE 14*, 464, 1978.

7. W.H. Christiansen, D.A. Russel and H. Hertzberg, Ann. Rev. Fluid Mech. *7*, 115 (1975).

8. M.M. Mann, A.I.A.A. J., *14*, 549 (1976).

9. R.I. Soloukhin, 11th International Symposium on shock tubes and waves, Seattle (July 1977). Proceedings p.629 (U. of Washington Press, 1978).

10. B. Forestier and B. Fontaine, Rev. Sci. Instrum. *50*, Mars 1979.

11. B. Forestier and B. Fontaine, Appl. Phys. lett. *32*, 569 (1978).

12. B. Fontaine and B. Forestier, 31th Annual Gaseous Electronics Conference, Buffalo (1978). Abstracts to be published in the Bulletin of the American Physical Society.

13. B. Fontaine and B. Forestier, Opt. Commun. *26*, 243 (1978).

14. P.J. Hay and T.H. Dunning, J. chem. Phys. *69*, 2209 (1978).

15. J. Tellinghuisen, J.M. Hoffman, G.C. Tisone and A.K. Hays, J. Chem. Phys., *64*, 2484 (1976).

16. W.R. Wadt, D.C. Cartwright and J.S. Cohen, Appl. Phys. lett. *31*, 672, (1977).

THE DOUBLE SHOCK WAVE TUBE: EXPERIMENTAL INVESTIGATION OF SHOCK-SHOCK REFLECTIONS

WALTER GAREN and GUENTER LENSCH

Fachhochschule Wedel, Germany

In a newly constructed shock wave tube, density and velocity of incident and reflected shock waves have been studied interferometrically. Shock waves are reflected from oncoming shock waves of equal strength instead of from an end-wall plate. The commonly used diaphragm has been replaced by a quickly opening pneumatic valve. In this paper we have investigated head-on collisions of identical shock waves for the gases Ar, Xe, CO_2 and CCl_2F_2 and for Mach numbers $1 \leq M_1 \leq 10$. Our present measurements can be summarized as follows: As to reflected shock waves, experimental and theoretical velocity results are in excellent agreement. The final state of the reflected shock wave has been found to be in equilibrium even at a distance of about ten mean free paths from the head-on collision point. As to large distances, the flow in the shock tube becomes quite complex due to the influence of the contact surface.

INTRODUCTION

A shock wave, passing through a gas, heats it rapidly and thus provides a useful experimental means of studying non-equilibrium processes. However, the gas influenced by a shock wave is set in motion and thereby complicates experimental measurements. Allowing the shock wave to reflect from an end-wall of a shock tube provides some advantages, but a serious problem is still the heat transfer to the end-wall[1,2]. In the absence of heat conduction, reflection from a plane wall is analogous to two equal shock waves of opposite directions interacting with each other[3]. Thus we have set up a double shock wave tube in which an incident shock wave is reflected from a shock of equal strength. This device, having an "ideal reflector" for incident shock waves could be useful in studying non-equilibrium rates of relaxing gases.

EXPERIMENTAL

Apparatus

Due to the behaviour of different bursting processes of diaphragms it is difficult to produce identical shock waves. Therefore we have replaced the commonly used diaphragm by a quickly opening valve[4], which produces equal shock waves for a chosen pressure ratio of driver and rest gas. This method has been successfully for several shock tube investigations[5,6,7]. Shock tube and high pressure chamber are separated by the pneumatic valve instead of a diaphragm.

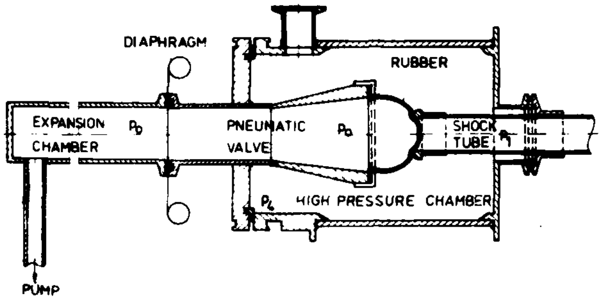

Fig 1. Principle of the pneumatic valve

The pneumatic valve consists of a cone and an expansion chamber. One side of the cone has been shut by a rubber disk of silicone with a thickness of 2 mm. Cone and expansion chamber are separated by a diaphragm, which is fixed by a magneto-electric shutter. By increasing the pressure p_o the initially plane rubber disk bulges and finally provides a vacuum tight seal for the shock tube. In order to open the shock tube rapidly one has to lower the pressure p_o suddenly. This can be done conveniently by lowering the pressure p_o in the expansion chamber by means of a mechanical vacuum pump until the diaphragm breaks. After rupture of the diaphragm, expansion waves travel into the cone and the rubber disk is pulled back. A shock wave is produced corresponding to the pressure ratio p_4/p_1. Slightly different behaviours of diaphragm ruptures have no effect on the opening process of the pneumatic valve, the reproduction of producing equal shocks is very good.
With the help of two identical valves at both ends of a shock tube we have constructed a so-called "double shock wave tube" (fig 2).

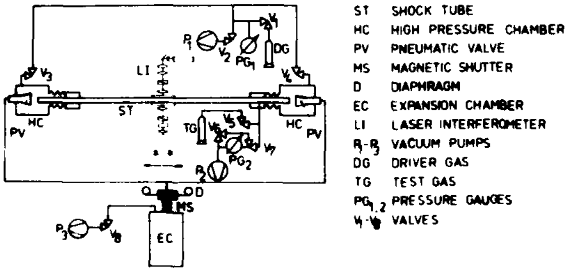

Fig 2. Schematic design of the double shock wave tube

It has a quadratic cross section of 40x40 mm and a length of 4300 mm. Both pneumatic valves (PV) are connected with one expansion chamber (EC). By lowering the pressure of the expansion chamber the diaphragm (D) ruptures and both pneumatic valves open simultaneously. Thus two identical shock waves are produced in the shock tube. By proper choice of pressures in the high pressure chambers and shock tube, it is possible of course to generate various shocks, two rarefaction waves or a shock wave and a rarefaction wave.

Measurement technique

Velocity and density change of the incident and the reflected shock wave have been measured by a laser interferometer[8, 9]. The interferometer (laser included) is mounted on a movable frame and can be moved within 200 mm in each direction of the middle of the shock tube. Thus the distance between the head-on collision point of both shock waves and the measuring position of the interferometer can be varied. Fig 3 shows the measuring arrangement.

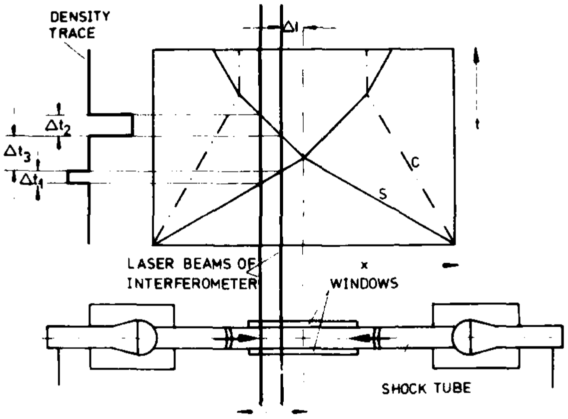

Fig 3. Measuring arrangement. Interferometer can be moved 200 mm out of the middle of the shock tube in both directions.
S:Shock wave
C:Contact surface

Both beams of the interferometer, separated by a distance of 5.3 mm, penetrate the shock tube perpendicularly to the tube axis. The incident shock (in this case coming from the left) triggers the scope. The movable interferometer has a distance Δ l from the head-on collision point. The first pulse of the schematic density trace belongs to the incident shock wave and the second one to the reflected shock wave. From the time intervals Δt_1 and Δt_2 the velocities of incident and reflected shock wave can be obtained. With these velocities and the measured time interval Δt_3 the distance Δl between the head-on collision point and the position of the interferometer has been calculated.

PRESENT RESULTS

Fig 4 shows typical density traces. Fig 4(a) is a result of two identical

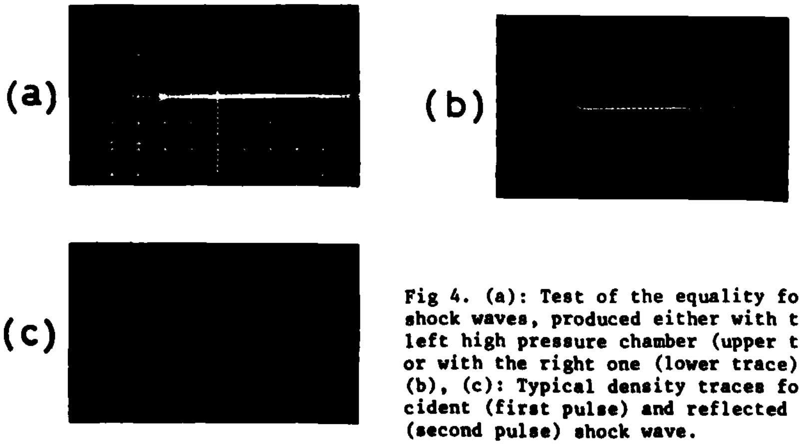

Fig 4. (a): Test of the equality for both shock waves, produced either with the left high pressure chamber (upper trace) or with the right one (lower trace). (b), (c): Typical density traces for incident (first pulse) and reflected (second pulse) shock wave.

shock waves which are produced one after the other first from the left (upper trace) and then from the right (lower trace) high pressure chamber. This is done periodically to check the equality of both shock waves. The following pictures are examples of density traces of interacting shock waves. The density pulse of the incident shock wave is followed directly by the density pulse of the reflected shock wave (fig 4 (b)). This shows that in this case the head-on collision point and one of the interferometer beams have the same position.

Fig 5 shows results of velocity measurements as a function of incident Mach number M_1. The velocities are normalized by the speed of sound a_1 ahead of the incident shock wave and by the incident shock velocity v_1 respectively.

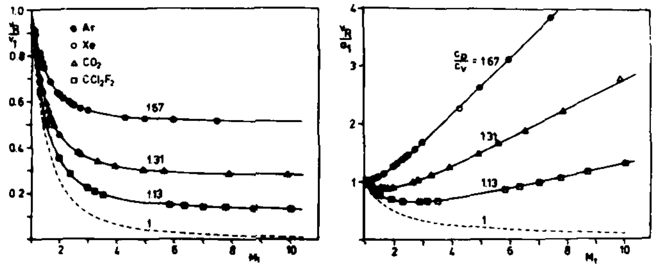

Fig 5. Velocity measurements of reflected shock waves vs. incident Mach number M_1. The velocities v_R are normalized either by the speed of sound a_1 or incident shock speed v_1. Curves are theoretical results for constant heat ratio c_p/c_v.

The curves are theoretical results of Glass[3] et. al. Excellent agreement has been found for all gases we have tested. These results have been obtained under the following conditions: The distance between head-on collision point and the position of the interferometer must be so small that the reflected shock wave arrives at the position of the interferometer earlier than the contact surface of the incident shock wave. For increasing distances there are remarkable deviations in the density profile of the reflected shock wave (fig 6).

If the distance between head-on collision point and position of the interferometer is larger than 20 mm, the shape of the reflected density pulse becomes more and more asymmetric. The shape in fig 6 (7) looks like an N-wave. This behaviour could be attributed to the influence of interactions of contact surface, rarefaction waves and shocks. For stronger shocks the contact surface becomes visible in the density trace. Fig 7 shows the deviation in the shape when the contact surface of the incident shock wave arrives earlier at the interferometer than the reflected shock wave (fig 7 (5), (6)). This tendency is similar for all gases we have tested.

Fig 8 shows a series of density traces in carbon dioxide. The density trace of CO_2 shows a slow change behind the incident and the reflected shock wave caused by the relaxation of the vibration process. The particle speed behind the reflected shock wave is zero due to boundary conditions. In the case of shock wave reflection by an equal shock wave there are no influences (energy exchange, heat conduction) of an end-wall plate. Thus relaxation processes can be exactly determined from density traces behind reflected shock waves (for instance fig 8 (1)).

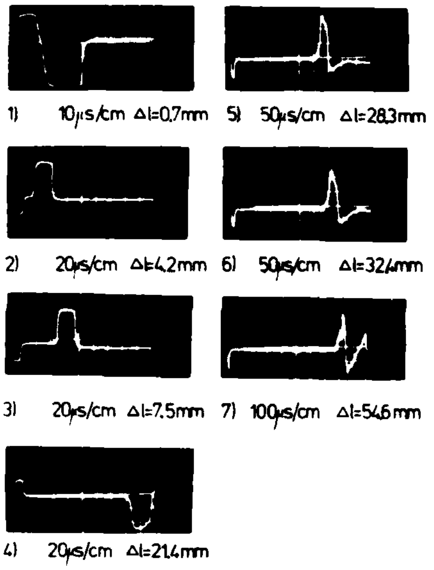

1) 10µs/cm Δl=0.7mm

2) 20µs/cm Δl=4.2mm

3) 20µs/cm Δl=7.5mm

4) 20µs/cm Δl=21.4mm

5) 50µs/cm Δl=28.3mm

6) 50µs/cm Δl=32.4mm

7) 100µs/cm Δl=54.6mm

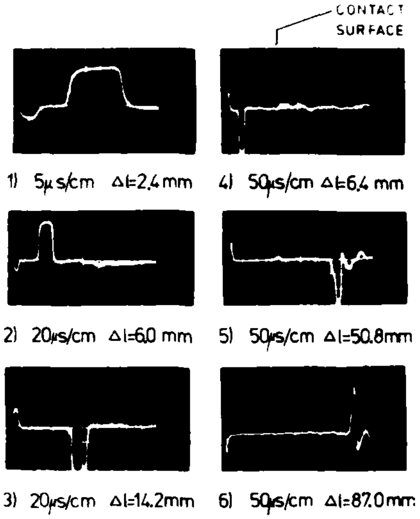

1) 5µs/cm Δl=2.4mm

2) 20µs/cm Δl=6.0 mm

3) 20µs/cm Δl=14.2mm

4) 50µs/cm Δl=6.4 mm

5) 50µs/cm Δl=50.8mm

6) 50µs/cm Δl=87.0mm

Fig 6. p_1 = 0.5 mbar

M_1 = 2.4

Fig 7. p_1 = 0.3 mbar (1, 2)

p_1 = 0.5 mbar (3, 4, 5, 6)

M_1 = 5.0

Density traces in Xenon for increasing distances Δl between head-on collision point and measuring position of the interferometer.

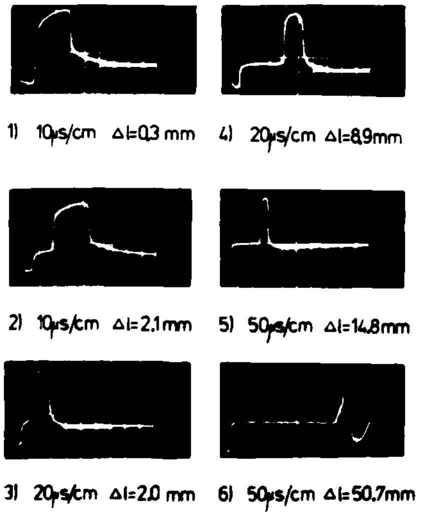

1) 10µs/cm Δl=0.3 mm

2) 10µs/cm Δl=2.1mm

3) 20µs/cm Δl=2.0 mm

4) 20µs/cm Δl=8.9mm

5) 50µs/cm Δl=14.8mm

6) 50µs/cm Δl=50.7mm

Fig 8. p_1 **= 1.0 mbar (1, 2, 3, 4)**

p_1 **= 1.5 mbar (5, 6)**

M_1 **= 1.8**

Density traces in carbon dioxide for increasing distances Δl between head-on collision point and measuring position of the interferometer.

CONCLUSION

Some preliminary experiments with this shock wave tube have shown the possibilities and advantages of this apparatus. With respect to the exact reproduction of gas states behind reflected shock wave (fig 5) by shock-shock reflections, this method provides a novel tool for experimental shock investigations:

(1) Determination of relaxation processes of gases without particle velocity and end-wall influences.
(2) Determination of end-wall influences on reflected shock waves and shock wave structure by energy exchange and heat transfer.
(3) Study of interaction processes between shocks, rarefaction waves and contact surfaces.

ACKNOWLEDGEMENTS

The authors wish to acknowledge the encouragement and support of Klaus Brudi in this investigation.
This research was supported by the Deutsche Forschungsgemeinschaft.

REFERENCES

1. C.M. Hung, R. Seebass, J. Fluid Mech. Vol 65, Part 2 (1974)
2. D. Hänel, Dissertation RWTH Aachen (1974)
3. I.I. Glass, G.N. Patterson, J. Aeron.Science, Vol 22, No 2 (1955)
4. W. Garen, R. Synofzik, A. Frohn, AIAA Journ. Vol 12, No 8 (1974)
5. W. Garen, R. Synofzik, G. Wortberg, A. Frohn, AIAA Vol 51, Part I (1976)
6. R. Synofzik, W. Garen, G. Wortberg, A. Frohn, AIAA Vol 51, Part II (1976)
7. D. Goebbels, W. Garen, R. Synofzik, G. Wortberg, A. Frohn, ed. in: XI. Int. Shock-Tube Symp., Seattle (1977)
8. G. Smeets, A. George, ISL-Report, 14, (1971)
9. G. Lensch, H. Grönig, ed. in: Int. Shock-Tube Symp., Seattle (1977).

ON THE MAXIMUM ATTAINABLE TEMPERATURE IN HARTMANN-SPRENGER TUBES

Eric Brocher

Institut de Mécanique des Fluides
Université d'Aix-Marseille II, Marseille, France

The Hartmann-Sprenger tube constitutes a repetitive shock tube in which shock waves travel up and down the tube at nearly the acoustic frequency. During each cycle, shock wave irreversibilities and frictional heating increase the mean temperature of the gas. If the tube material is a perfect insulator, the heat cannot escape from the gas, and the question arises up to which values the temperature of the gas will rise. For sufficiently long tubes, the compression waves produced by the penetration of the driving jet into the tube will in general coalesce to form a shock. However, if the temperature of the gas increases along the tube, the steepening distance will increase. So, as the temperature gradient of the gas increases, a smaller fraction of the compression waves will steepen and the shock strength will decrease at each cycle. The maximum temperature will be reached when this fraction tends to zero. The theory of E. Becker, which gives the steepening distance of a compression wave train in a gas with arbitrary temperature distribution ahead of the waves, is applied to the case of the Hartmann-Sprenger tube. Then, the maximum attainable gas temperature and the corresponding end wall temperature are derived. The agreement of experimental values with theoretical results is good when the conditions underlying the theory are met in the experiments.

INTRODUCTION

At the preceding Symposium on Shock Tubes and Waves, we presented a paper[1] on the heat transfer and equilibrium temperature near the end plate of a Hartmann-Sprenger tube.

Let us recall that the Hartmann-Sprenger tube (HS tube) is a repetitive shock tube in which shock waves travel up and down the tube at nearly the acoustic frequency. Fig. 1 shows a simplified wave diagram of a HS tube with the various flow fields. The nozzle of the driving jet is equiped with a needle so as to achieve a maximum pressure amplitude and, consequently, a maximum temperature rise, in the device[1]. If the pressure ratio is overcritical, the needle may be shaped so as to form a sonic throat and correctly expand the jet. During each cycle shock-wave irreversibilities and frictional heating increase the mean temperature of the gas. Near the end plate of the tube, the amplitude of the gas motion is very small so that in this region, dissipation by friction is negligeable and shock heating only needs to be taken into consideration.

In Ref. 1, we had studied the heat transfer to the tube wall that results from the shock heating. Now, if the tube material is a perfect insulator, the heat cannot escape from the gas and the question arises up to which value the temperature of the gas will rise. It is known from experiments that the wall temperature increases from the tube mouth to the end wall. From this, one may infer that the gas temperature has a similar temperature distribution. If the tube is sufficiently long, the compression waves produced by the penetration of the jet into the tube will in general coalesce to form a shock. But, if the temperature of the gas increases along the tube in field 1 (Fig. 1), each compression wave will accelerate as it moves down the tube and the steepening distance will increase. So, as the temperature of the gas increases a smaller fraction of the compression waves will steepen and the shock strength will decrease at each cycle. The maximum attainable temperature will be reached when this fraction tends to zero. Shapiro[2] was the first to consider this problem. Alhough his analysis is quite sound physically, his theoretical treatment is too crude to lead to satisfactory results.

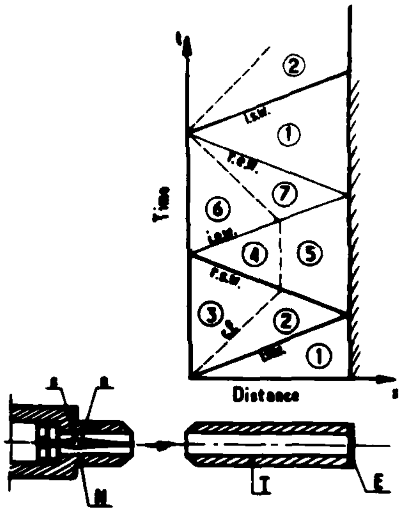

Figure 1. Simplified wave diagram of a H.S. Tube

i.s.w.: incident shock wave ; r.s.w.: reflected shock wave ; i.e.w.: incident expansion wave ; r.e.w.: reflected expansion wave ; c.f.: contact front

n = needle ; N = nozzle ; T = H.S. tube ;

E = end wall ; s = sonic throat

In this paper, we apply the theory of E. Becker[3] which enables one to calculate the steepening distance of a compression wave train in a gas with arbitrary temperature distribution ahead of the waves. The theory gives the maximum gas temperature in field 1, near the end plate. We then compute the corresponding maximum gas temperature in field 5. Finally, we estimate the resulting wall temperature in order to compare theoretical values with experimental ones.

BECKER'S THEORY

In Ref. 3, Becker derives a general theory on the steepening of compression waves. Among other things, the theory covers the case for which the entropy varies ahead of the waves. Becker approximates the continuous velocity distribution behind the front of the acceleration wave by a series of discontinuous Mach waves. The distance between the Mach wave fronts changes with the time and the waves are either damped or amplified.

The evolution of the acceleration $a = \partial u/\partial t$ at the wave front is found to obey the following differential equation

$$\dot{a} + \Omega_1 a - \Gamma_1 a^2 = 0 \qquad \text{I}$$

where $\dot{a}$ represents the time derivative of the acceleration. Ω_1 and Γ_1 are the values at the wave front*of the quantities Ω and Γ which are defined by

$$\Gamma = \frac{v^3}{2c^3} \left(\frac{\partial^2 p}{\partial v^2}\right)_{s=cst}$$

$$\Omega = \frac{1}{2\rho} \frac{d(\rho c)}{dx}$$

In these expressions v represents the specific volume, p the pressure, ρ the density, s the entropy, c the speed of the wave front and x the abscissa. For a perfect gas, it is easily shown that

$$\Gamma_1 = \frac{\gamma+1}{2c_1}$$

so that Eq. I takes the form

$$\dot{a} + \frac{1}{2\rho_1} \frac{d(\rho_1 c_1)}{dx} a - \frac{\gamma+1}{2c_1} a^2 = 0$$

Noting that $c = dx/dt$, this equation can be integrated and yields

$$\frac{1}{a} = \sqrt{\rho_1 c_1} \left\{ \left. \frac{1}{a\sqrt{\rho_1 c_1}} \right|_{x=0} - \frac{\gamma+1}{2} \int_0^x \frac{dx}{c_1^2 \sqrt{\rho_1 c_1}} \right\}$$

The steepening distance x_{st} corresponds to $a \to \infty$ and this condition leads to the following relation.

$$\int_0^{x_{st}} \frac{dx}{c_1^2 \sqrt{\rho_1 c_1}} = \frac{2}{\gamma+1} \left. \frac{1}{a\sqrt{\rho_1 c_1}} \right|_{x=0} \qquad \text{II}$$

APPLICATION OF BECKER'S THEORY TO THE H.S. TUBE

The oscillation frequency in a Hartmann-Sprenger tube is very close to the acoustic frequency $c_a/4L$, where the index a refers to ambiant conditions or, which is approximately the same, to conditions at the tube mouth. L is the length of the tube. Assuming that u varies sinusoidally with time at the tube mouth and that $c_{1_0} = c_{1_{(x=0)}} \simeq c_a$, the maximum value of the initial acceleration a_0 at x = 0 is given by

$$a_0 \simeq \pi M_j \frac{c_{1_0}^2}{2L} \qquad \text{III}$$

---

*We replace the index o used by Becker by the index 1,in accordance with the numerotation used in Fig. 1.

where M_j represents the jet Mach number. As mentioned in the introduction, the gas temperature is an increasing function of the distance x. We shall assume a temperature distribution ahead of the wave of the form

$$\frac{T}{T_{1_0}} = \frac{c_1^2}{c_{1_0}^2} = 1 + K\,\xi^n \qquad \text{IV}$$

where $\xi \equiv x/L$ and where K and n are constant.

If the pressure ahead of the wave is assumed to be constant

$$\frac{\rho_1}{\rho_{1_0}} = \frac{T_{1_0}}{T_1} = [1 + K\,\xi^n\,]^{-1} \qquad \text{V}$$

Introducing Eqs. III, IV and V into Eq. II and looking for the condition for which the steepening distance x_{st} is just equal to the tube length L we obtain

$$\int_0^1 \frac{d\xi}{[1 + K\,\xi^n\,]^{3/4}} = \frac{4}{(\gamma+1)\pi\,M_j} \qquad \text{VI}$$

Eq. IV can be integrated, assuming various values for the exponent n, and yields a relation between M_j and K.

For $n = 1$, this relation is

$$M_j = \frac{1}{\pi(\gamma+1)}\;\frac{K}{[(1+K)^{1/4} - 1]} \qquad \text{VII}$$

whereas for $n = 1/2$, it reads

$$M_j = \frac{1}{2\pi(\gamma+1)}\;\frac{K^2}{K\,(1+K)^{1/4} - \frac{4}{5}\,[\,(1+K)^{5/4} - 1]} \qquad \text{VIII}$$

For any value of n, making $K \to 0$ gives a minimum value of the Mach number

$$M_{j_{min}} = \frac{4}{\pi\,(\gamma+1)}$$

below which no shock steepening occurs. This is because the steepening length is larger than the tube length for $M_j < M_{j_{min}}$

TEMPERATURE BEHIND THE REFLECTED COMPRESSION WAVES

The temperature we have just computed is the maximum temperature attainable *ahead* of the compression wave train. This is not the maximum temperature of the cycle which occurs behind the compression waves reflected by the end plate of the tube. An estimate of the temperature ratio T_{5L}/T_{1L}, the index L referring to conditions near the end plate, may be obtained from our previous results on the limit cycle of a H.S. tube (Ref. 4, Eqs. 12 and 13).

$$\frac{T_{5_L}}{T_{1_L}} = \left[\frac{1 + \alpha^{1/2}\ f\ (M_j)}{1 - \alpha^{1/2}\ f\ (M_j)} \right]^2 \qquad \text{IX}$$

where α is a parameter which takes into account the heating of the driven gas ($1/\alpha$ = mean static temperature $\bar{T}_2$ of the driven gas in field 2 of Fig. 1/ stagnation temperature T_{tot_j} of the driver gas) and

$$f\ (M_j) = \frac{\frac{1}{2}\ (\gamma-1)\ M_j}{[1 + \frac{1}{2}\ (\gamma-1)\ M_j^2]^{1/2}}$$

We now seek a relation between α and K. The parameter α may be written as

$$\alpha^{-1} = \bar{T}_2/T_{tot_j}$$

$$= (\frac{\bar{T}_2}{\bar{T}_1})\ (\frac{\bar{T}_1}{T_{1_0}})\ (\frac{T_{1_0}}{T_{tot_j}}) \qquad \text{X}$$

where $\bar{T}_1$ represents the mean temperature of the gas in field 1 of Fig. 1.

Assuming that the pressure ratio across the compression wave train is independent of x, we have

$$\frac{\bar{T}_2}{\bar{T}_1} = (1 - \alpha^{1/2}\ f)^{-2} \qquad \text{XI}$$

The mean temperature $\bar{T}_1$ is found by integration of the temperature distribution (Eq. IV) :

$$\frac{\bar{T}_1}{T_{1_0}} = 1 + \frac{K}{n+1} \qquad \text{XII}$$

Near the entrance of the tube, the temperature of the driven gas is very close to T_{tot_j} , so that we may write

$$\frac{T_{1_0}}{T_{tot_j}} \cong \frac{T_{1_0}}{T_{2_0}}$$

$$= (1 - \alpha^{1/2}\ f)^2 \qquad \text{XIII}$$

Introducing Eqs. XI to XIII into Eq. X, we obtain

$$\alpha^{-1} = 1 + \frac{K}{n+1} \qquad \text{XIV}$$

The maximum attainable gas temperature is now written as

$$\frac{T_{5_L}}{T_{tot_j}} = \left(\frac{T_{5_L}}{T_{1_L}}\right) \left(\frac{T_{1_L}}{T_{1_o}}\right) \left(\frac{T_{1_o}}{T_{tot_j}}\right)$$

$$= (1+K)\ (1 + \alpha^{1/2}\ f)^2 \qquad \text{XV}$$

where K and α may be computed as functions of M_j with the help of Eqs. VII, VIII and XIV.

The temperature ratio T_{5_L}/T_{tot_j} given by Eq. XV is shown in Fig. 2. It is seen that this ratio becomes quite large when $M_j > 1$. For $M_j \cong 2$, T_{5_L} could be greater than 3000°K. It is also observed that the temperature ratio is larger for monoatomic gases than for diatomic gases. Although for different reasons, the equilibrium temperature of the driven gas when heat transfer is present has also been found higher for monoatomic gases[1] . Finally, it is seen that the exponent n of the temperature distribution has an influence on T_{5_L}. Since no measurement of the gas temperature has been made so far, we can only check the theory (and hopefully determine the adequate value of n) with measurements of the end wall temperature.

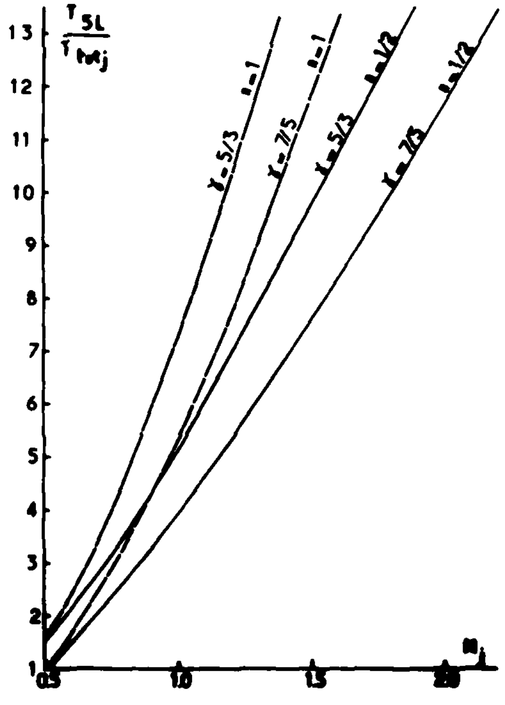

Figure 2. Maximum attainable temperature behind the reflected compression waves as a function of the jet Mach number

END WALL TEMPERATURE

Since the end wall is exposed approximately half-a-period to T_{5_L} and half-a-period to T_{1_L}, we may assume that its temperature T_w is close to the arithmetic average of T_{5_L} and T_{1_L}. With this assumption, it is easily verified that

$$\frac{T_w}{T_{tot_j}} \cong \frac{1}{2}\left(\frac{T_{5_L} + T_{1_L}}{T_{tot_j}}\right)$$

$$= (1+K)\ (1+\alpha\ f^2) \qquad \text{XVI}$$

The wall temperature given by Eq. XVI has been plotted on Fig. 3. It is seen that T_w could reach very high values when $M_j > 1$. For $M_j \simeq 2$, the

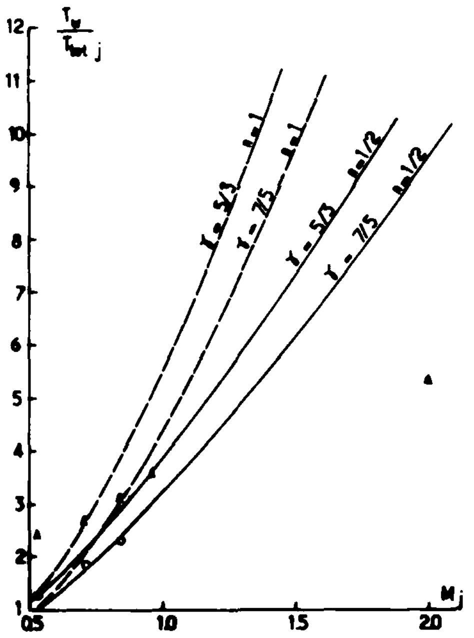

Figure 3. End wall temperature

Experiments : O tube material : wood ; gas : air (Ref. 5)
Δ tube material : Pt ; gas : He (Ref. 6)

theory indicates that T_w could be of the order of 3000°K. Until now, no such high temperatures have been reported. This is certainly because it is very difficult to achieve a sufficiently good insulation whereas it is assumed in the theory presented here that the tube is a perfect insulator. However, a few experiments have been run by Maresca[5] using wood as tube material and air as gas. The temperatures measured by this author are indicated on the figure. It is seen that the agreement between theory and experiments is fairly good over the small Mach number range tested (wood is an excellent insulator but burns at higher Mach number unfortunately !). At the lowest Mach number (M_j = 0,53) some heating is measured whereas none is predicted by the theory.

This is because frictional heating has not been considered in the theory. For higher Mach number (M_j = 0.71 and 0.84) experimental values appear to follow the theoretical curve obtained with n = 1/2. This temperature distribution corresponds to a sharp drop in temperature near the contact front between the driver and the driven gas. This drop can be explained by the mass exchange which occurs at this front through the boundary layer[5,7]. Also indicated on the figure are a few experimental points obtained by Albertini[6]. This author used a tube (10 cm in length, 3 mm in diameter) made of thin platinum sheet (1/10 mm). The tube was inserted into a sealed box in which vacuum was created and it was surrounded by a cylindrical reflector to decrease radiation losses. With Helium at M = 0.96 the agreement with the theoretical value (n = 1/2) is excellent whereas for lower M_j frictional heating is at the origin of higher experimental values. At M_j=2, the measured temperature (T_w = 1570°K) is substantially smaller than the predicted one ($\sim$3200°K) and this is certainly due to heat losses (especially radiation).

CONCLUSION

Considering the large values of the maximum attainable temperature predicted by the theory and the already available experimental values, it seems worthwhile to run experiments in which heat losses are minimised so as to approach the high temperatures predicted. The possibility of producing high temperature gases (3000°K) in a continuous way should offer interesting applications in high temperature physics and chemistry.

REFERENCES

1. E. Brocher, Proceedings of the 11th International Symposium on Shock Tubes and Waves, 66 (1978).

2. A. Shapiro, Journal of Aero/Space Sciences, *26*, 66 (1958).

3. E. Becker, Ingenieur Archiv, *33*, 302 (1970).

4. E. Brocher, C. Maresca and M.H. Bournay, J. Fluid Mech., *43*, part 2, 369 (1970).

5. E. Brocher and C. Maresca, Int. J. Heat Mass Transfer, *16*, 529 (1973).

6. M. Albertini, Effets thermiques dans un tube de Hartmann-Sprenger, Thèse de Doctorat de Spécialité, Université d'Aix-Marseille,(1973).

7. C. Maresca et E. Brocher, Journal de Mécanique, *12*, N°3, 24, (1973).

PRESSURE WAVES RADIATED FROM BUBBLES COLLAPSING WITH PHASE CHANGE

SHIGEO FUJIKAWA and TERUAKI AKAMATSU

Department of Mechanical Engineering
Kyoto University, Japan

This paper deals with, both theoretically and experimentally, the mechanisms by which the violent action of collapsing bubbles is brought to bear on solid boundaries. In the first part, are analysed the effects of nonequilibrium vapour condensation and heat conduction on the collapse of bubbles: (1) condensation coefficient, (2) presence of noncondensable gas, and (3) initial bubble radius. Numerical results indicate that these effects have a very strong influence on the dynamical behaviour of bubbles, and that purely vaporous bubbles produce strong pressure waves owing to the nonequilibrium behaviour of the contained vapour. In the second part, are described experimental observations of microjet formation and shock wave radiation from collapsing and subsequently rebounding bubbles near the surface of a photoelastic material. It is elucidated that the stress waves in a photoelastic specimen, due to the bubble collapse, are caused by the impact of the shock waves, not by the jets.

1. INTRODUCTION

Most of the theoretical and experimental efforts to explain the destructive action by cavitation have been spent in attempts to understand the collapse process of bubbles in the vicinity of solid boundaries. Two different mechanisms have been suggested as the primary source of cavitation damage: (1) shock waves emanated into the liquid at the instant of the bubble collapse, and (2) microjets induced on the bubble wall by the presence of solid boundaries.

Concerning the former shock wave radiation from the bubbles, a certain amount of work has been reported; Guth(1), Jones & Edwards(2), Kuttruff(3), Hickling & Plesset(4), and Fujikawa & Akamatsu(5). Kuttruff observed not only shock waves, but also flashes of sonoluminescence light from the ultrasonic cavitation. However, it had been believed that bubbles, very close to solid walls, cannot radiate shock waves accompanying the rebound(Plesset(6)); in such a situation spherical collapse or rebound cannot be expected to occur because of asymmetrical bubble shape distorted by wall effects. Under highly controlled conditions produced by a water shock tube, Fujikawa & Akamatsu observed shock waves emanating from bubbles in the neighbourhood of the solid boundaries and, furthermore, pointed out the possibility of shock wave radiation from purely vaporous bubbles owing to the nonequilibrium vapour condensation. If condensation rate is not high enough to keep up with the inward radial velocity of the bubble wall in the final stages, the contained vapour will behave like a noncondensable gas. One of the objects of the present study is to elucidate the behaviour of the spherically collapsing bubbles and the resulting shock waves. Theoretical and numerical analyses will be made taking account of the effects of evaporation, condensation at the interface, heat conduction inside and in the surrounding liquid, and liquid compressibility.

Liquid jet formation of collapsing bubble, on the other hand, also has been studied by numerous investigators; Kornfeld & Suvorov (7), Naudé & Ellis(8), Benjamin & Ellis(9), Plesset & Chapman(10), Kling & Hammitt(11), Lauterborn & Bolle(12), and Fujikawa & Akamatsu (13) The supposition that the destructive action on the solid boundary is caused by the impact of microjets has not been verified directly by experiments. Fujikawa & Akamatsu observed in greater detail the behaviour of collapsing bubbles; shock wave radiation, subsequent microjet formation and their impingement on the solid boundary. They found that the violent action was brought about by shock waves generated at the instant of the rebound. The other object of the present study is to give conclusive evidences for the authors' previous observations. They carried out experiments by using a high-modulus photoelastic material in order to distinguish the stress waves due to the shock waves from those due to the jets and the background noise.

2. NOMENCLATURE

c: sound speed
D: coefficient of thermal diffusivity
e: specific internal energy
E: internal energy
h: specific enthalpy
L: latent heat of evaporation or condensation
$\dot{m}$: rate of evaporation and condensation
p: pressure
P: Prandtle number
q: heat flux
r: radial distance from center of bubble
R: radius of bubble
$\dot{R}=dR/d\eta$
$\mathcal{R}$: gas constant
S: surface area
t: time
T: temperature
u: radial velocity
V: volume
α_M: evaporation and condensation coefficient
α_T: thermal accomodation coefficient
η: initial time on the outgoing characteristic
γ: ratio of specific heats
λ: coefficient of thermal conductivity
μ: coefficient of shear viscosity
ρ: density
σ: surface tension coefficient

Subscripts & superscripts

c: value at center
g: noncondensable gas
i: value at bubble wall
ℓ: liquid
m: mixture of vapour and noncondensable gas
v: vapour
o: initial value
∞: value at infinity
$*$: equilibrium value

3. COLLAPSE OF A SPHERICAL BUBBLE

3-1 *Statement of problem and basic equations*

A spherical bubble containing both vapour and noncondensable gas is located in an infinitely extended mass of liquid. The ambient pressure is increased instantaneously to a high state from an initial low state, and the collapse ensues, accompanied with phase change and heat conduction. The problem is to study these physical effects on the bubble collapse. Schematic diagram depicting a model is illustrated in figure 1.

In writing the basic equations, the following assumptions are made: (1) The bubble is spherically symmetric. (2) The pressure inside the bubble is uniform throughout. (3) The vapour and noncondensable gas are inviscid and obey the perfect gas law. (4) The temperatures of the vapour and noncondensable gas are equal. (5)The thermal boundary layers developing both inside and outside the bubble are thin enough compared with the bubble radius. (6) There is a thin but finite nonequilibrium region at the interphase. (7)The physical properties of liquid and gases are constant. The validity of these assumptions has been discussed elsewhere (14).

Then, the governing equations for the liquid and gases, and the boundary conditions may be expressed as follows:

Outside the bubble

CONTINUITY: $$\frac{\partial \rho_\ell}{\partial t} + u_\ell \frac{\partial \rho_\ell}{\partial r} + \rho_\ell \left(\frac{\partial u_\ell}{\partial r} + \frac{2u_\ell}{r}\right) = 0 \quad (1)$$

MOMENTUM: $$\frac{\partial u_\ell}{\partial t} + u_\ell \frac{\partial u_\ell}{\partial r} = -\frac{1}{\rho_\ell}\frac{\partial p_\ell}{\partial r} \quad (2)$$

ENERGY: $$\frac{\partial T_\ell}{\partial t} + u_\ell \frac{\partial T_\ell}{\partial r} = D\left(\frac{\partial^2 T_\ell}{\partial r^2} + \frac{2}{r}\frac{\partial T_\ell}{\partial r}\right) \quad (3)$$

EQUATION OF STATE: $$\frac{p_\ell + B}{p_\infty + B} = \left(\frac{\rho_\ell}{\rho_\infty}\right)^n \quad (4)$$

where B=3010 atm and n=7.15 for water.

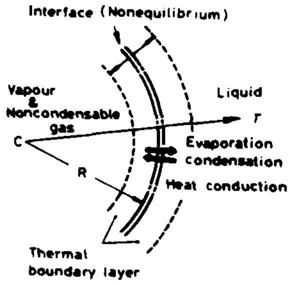

Fig.1 Model of a bubble

Inside the bubble

CONTINUITY: for the vapour $$\frac{d}{dt}\int_V \rho_v dV = \int_S \dot{m} dS \quad (5)$$

and for the noncondensable gas $$\frac{d}{dt}\int_V \rho_g dV = 0 \quad (6)$$

where the rate of evaporation and condensation $\dot{m}$ of the vapour is

$$\dot{m} = \frac{\alpha_M}{\sqrt{2\pi R_v}}\left(\frac{p_v^*}{\sqrt{T_{\ell i}}} - \Gamma\frac{p_v}{\sqrt{T_{mi}}}\right) \quad (7)$$

in which Γ is the correction factor approximately equal to unity.
ENERGY: for the thermal boundary layer near the interphase

$$\rho_m\left(\frac{\partial e_m}{\partial t} + u_m \frac{\partial e_m}{\partial r}\right) = -\frac{p_m}{J}\left(\frac{\partial u_m}{\partial r} + \frac{2u_m}{r}\right) - \left(\frac{\partial q_m}{\partial r} + \frac{2q_m}{r}\right) \quad (8)$$

and for the global contents within the bubble

$$\frac{dE_m}{dt} + \frac{p_m}{J}\frac{dV}{dt} + \int_V \nabla \cdot q_m dV - \int_S h_v \dot{m} dS = 0 \quad (9)$$

where q_m is

$$q_m = -\lambda_m \frac{\partial T_m}{\partial r}$$

EQUATION OF STATE: for the vapour $$p_v = \rho_v R_v T_m \quad (10)$$

for the noncondensable gas $$p_g = \rho_g R_g T_m \quad (11)$$

and for the vapour-gas mixture $p_m = \varrho_m R_m T_m$ (12)

At the interphase

CONTINUITY: for the liquid $[\varrho_\ell(u_\ell - \dot{R})]_R = -\dot{m}$ (13)

and for the vapour-gas mixture $[\varrho_m(u_m - \dot{R})]_R = -\dot{m}$ (14)

MOMENTUM:

$$p_{\ell,R} = -\frac{2\sigma}{R} + p_v + p_g + [\varrho_m(u_m - \dot{R})(u_m - u_\ell)]_R + \frac{4\mu_\ell}{3}\left(\frac{\partial u_\ell}{\partial r} - \frac{u_\ell}{r}\right)_R \quad (15)$$

ENERGY:

$$\lambda_\ell\left(\frac{\partial T_\ell}{\partial r}\right)_R = \lambda_m\left(\frac{\partial T_m}{\partial r}\right)_R + \dot{m}L \quad (16)$$

TEMPERATURE DISCONTINUITY:

$$T_{mi} - T_{\ell i} = -\frac{(2 - 0.827\alpha_T)\gamma_m\mu_m}{4(\gamma_m - 1)\varrho_m\alpha_T P_m}\left(\frac{2\pi}{R_m T_{\ell i}}\right)^{1/2}\left(\frac{\partial T_m}{\partial r}\right)_R \quad (17)$$

Finally, equilibrium(or saturated) vapour pressure can be estimated from Clausius-Clapeyron equation.

3-2 *Analysis*

The PLK coordinate-perturbation technique is applied, for the equations (1), (2), and (4), to derive the equation of motion of the liquid surrounding a collapsing bubble. Specific expansions for Φ,r, and t are taken in the following forms:

$$\Phi(r,\eta) = \phi_0(r,\eta) + \frac{1}{c_\infty}\phi_1(r,\eta) + \frac{1}{c_\infty^2}\phi_2(r,\eta) + \text{-----}$$
$$r = r \quad (18)$$
$$t = \eta + \frac{1}{c_\infty}t_1(r,\eta) + \frac{1}{c_\infty^2}t_2(r,\eta) + \text{-----}$$

where Φ is the velocity potential for the liquid. The boundary conditions are $\Phi=0$ as $r\to\infty$, and the equation (13). The resulting equations include all of the equations previously obtained,e.g., Rayleigh(15),Herring(16),and Tomita & Shima(17), as special cases.

In solving the energy equations (3), (8), and (9), the following Lagrangian coordinates are introduced:

$$\Psi_\ell(r,t) = (1/3)[r^3 - R(t)^3]$$
$$\Psi_m(r,t) = \int_0^r \xi^2 \varrho_m(\xi,t)d\xi \,/\, \int_0^R \xi^2 \varrho_m(\xi,t)d\xi \quad (19)$$
$$t = t$$

Approximate solutions are obtained, by the perturbation method, under the assumptions that appreciable temperature gradients are estimated only in thin layers both inside and outside the bubble. The initial and boundary conditions are $T_\ell(r,0)=T_m(r,0)=T_{\ell\infty}$, $T_\ell(r,t)=T_{\ell\infty}$ as $r \to \infty$, and the equations (14) and (16).

Finally, we can obtain the equations for vapour and gas pressures from the equations (5), (6), (10), (11), and (12).

3-3 *Numerical results and discussion*

3-3-1 Collapse of a vapour/gas bubble For comparison with our experimental data obtained by the water shock tube, the following conditions are chosen: $R_0=1.0$ mm, $T_{\ell\infty}=293.15$ °K, $p_{\ell\infty}=0.7025$ atm,

$p_{go}=7.025 \times 10^{-3}$ atm, $p_{vo}=0.02305$ atm, and $\alpha_T=1.0$. The numerical results are shown for condensation coefficient $\alpha_M=0.04$. The results are compared with the behaviour of the bubble containing air undergoing an adiabatic process and the saturated vapour, which is indicated by chained lines with one dot.

Figure 2 shows the time history of the bubble radius. In case in which the evaporation and condensation of water vapour and heat conduction take place at the bubble wall, the bubble contracts slowly in the final stages of the collapse in comparison with the adiabatic case. The damped ratio of the maximum radius R_{max} of the rebounding bubble to the initial radius R_o, $(|R_o-R_{max}|/R_o \times 100)$, is 19.4 % for the bubble with evaporation or condensation and heat conduction, and is 17.2 % for the adiabatic bubble.

Figure 3 shows the time histories of the temperatures of the bubble contents (a) and the liquid (b). The maximum temperatures at the center and at the interface of the bubble are 6700 °K and 3413 °K, respectively. These temperatures are much lower than those in the adiabatic collapse(8786 °K). The temperature throughout the bubble contents is not uniform because of heat conduction at the interface. The interfacial temperature of the bubble falls to 292.4 °K at a time 2 μsec after the first rebound, because the bubble rapidly expands. The temperature at the bubble center, on the other hand, decreases adiabatically during 11.4 μsec after the rebound, and then it is maintained at about 870 °K. The maximum interfacial temperature of the liquid is 474 °K. The temperature discontinuity at the interface increases as the bubble collapse proceeds.

Figure 4 shows the time history of the vapour pressure within the bubble. The maximum vapour pressure p_{vmax} is 144 atm, while the maximum equilibrium vapour pressure p^*_{vmax} is 15.6 atm. The actual vapour pressure deviates from the equilibrium pressure in the final stages of collapse.

Figures 5(a) and (b) show the pressure distributions in liquid before and after the collapse of the bubble. Dotted lines indicate the pressure at the bubble wall, and dashed lines represent the locus of the instantaneous peak pressure. The time $\tau(=t\sqrt{p_{g\infty}/\rho_\ell}/R_o)$ is taken from the start of the collapse. The comparison of the present result with the adiabatic collapse is made for the nearly same bubble radii.

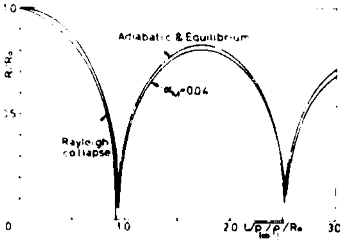

Fig.2 The time history of the bubble radius

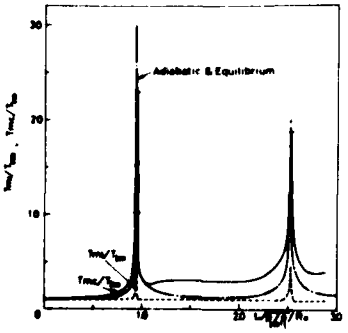

(a)

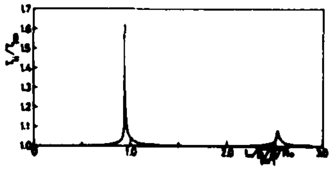

(b)

Fig.3 The time histories of the temperatures of the bubble contents(a), and liquid(b)

In the early stages of the collapse the pressure in liquid is slightly higher than that in the adiabatic case, but in the final stages becomes lower than it. The attained maximum impulsive pressures are 991 atm for the present calculation and 1033 atm for the adiabatic collapse. The pressure in liquid attenuates by the effect of liquid compressibility and, at the instant when the bubble attains to its minimum radius, the pressure, at the position $r/R_o=1$, is 13 atm(the same value as in the adiabatic case). Figure (b) shows that the pressure wave forms and travels outwards into the liquid after the rebound. The pressure front gradually steepens, but the wave attenuates approximately in proportion to 1/r through the liquid. The peak pressure is lower than that in the adiabatic collapse and, at the position $r/R_o=1$, 58 atm(in the adiabatic case 63 atm). As a whole, present calculations support the earlier work (Hickling & Plesset$^{(4)}$, Tomita & Shima$^{(17)}$) both in the order-of-magnitude of the peak pressures and the pressure wave attenuation in inverse proportion to distance.

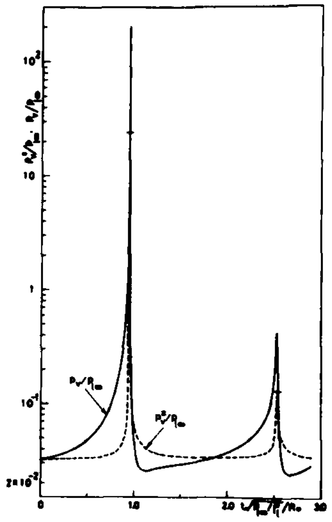

Fig.4 The time history of the vapour pressure

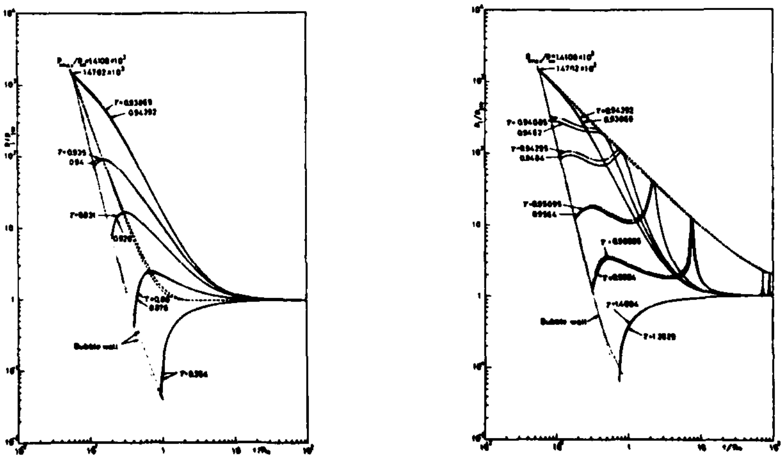

(a) Before the collapse (b) After the collapse

Fig.5 The pressure distributions in liquid before and after the collapse of a vapour/gas bubble with initial radius R_o =1.0 mm

3-3-2 Collapse of a vapour bubble Figure 6 shows the pressure distributions after the collapse of a bubble containing only the water vapour; initial conditions are the same as those in figures 2-5. The maximum impulsive pressure $p_{\ell max}$ is 8340 atm. The pressure at the instant when the bubble reaches its minimum radius is 10 atm at the position $r/R_o=1$. Meanwhile, the greatest pressure at the same position after the collapse is 218 atm. Here, even a

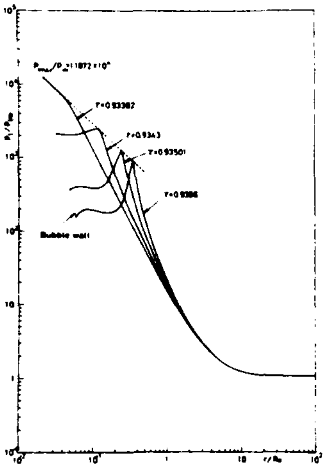

Fig.6 The pressure distributions after the collapse of a vapour bubble with initial radius R_o=1.0 mm

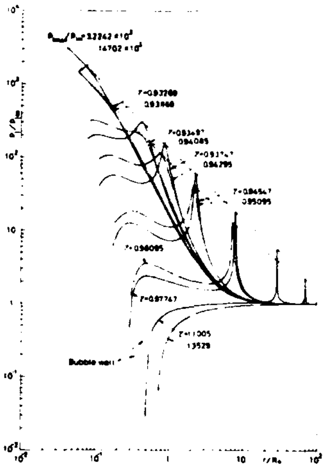

Fig.7 The pressure distributions after the collapse of a vapour/gas bubble with initial radius R_o=0.1 mm

purely vaporous bubble proves to produce a pressure wave at the instant of the rebound. The mechanism can be explained as follows; at the initial stages of the collapse the vapour condenses back into the liquid, so that the vapour pressure in the bubble remains equal to a saturated vapour pressure. However, at the final stages the collapse takes place so rapidly that most of the vapour does not have enough time to condense. This remnant of vapour may then be compressed to a high pressure, which will eventually become large enough to halt the inrushing liquid. Then, the bubble rebounds and the pressure wave radiates into the liquid.

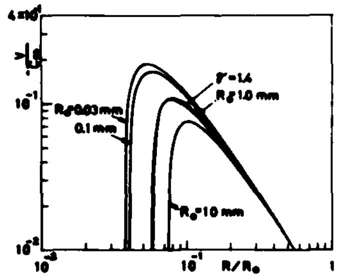

Fig.8 The effect of the bubble radius on the bubble collapse

3-3-3 Effect of the bubble size on the collapse of bubble Figure 7 shows the pressure distributions in liquid after the collapse of a bubble with initial radius R_o=0.1 mm; initial conditions are the same as those in figures 2-6. The present bubble collapses to a much smaller radius in comparison with the adiabatic collapse, because the smaller bubbles show increased effects of heat conduction ;the thermal diffusion length δ within bubbles will be proportional to $R_o^{1/2}$, and the ratio δ/R_o will vary as $R_o^{-1/2}$. This results in a high collapse speed and a more violent collapse. The attained maximum impulsive pressure and gas temperature at the bubble center are 2265 atm and 4151 °K, respectively. The pressure is about twice higher than that in the adiabatic collapse, whilst the temperature is about one-half lower than it. During rebound, a stronger pressure wave emanates into the liquid and its front steepens when compared with the adiabatic case. Figure 8 shows the effect of the bubble radius on the collapse speeds. The smaller are the radii of bubbles,at the higher speeds the bubbles collapse, and consequently the stronger pressure waves may be emanated into the liquid.

4. EXPERIMENTS

4-1 *Apparatus*

The authors already gave a detailed description of their water shock tube in their papers(5),(13). So that, they will explain only the present experimental method. In the water-filled shock tube, bubbles expand to maximum radii under the action of expansion waves, and then collapse under successive compression waves. The collapse and rebound of bubbles situated at various distances from the solid boundary of a photoelastic material are observed by means of dynamic photoelasticity.

Figure 9 shows the configuration of a photoelastic specimen relative to a bubble and a pressure gauge. The specimen is fabricated with 12 mm x 8 mm x 6 mm-thick epoxy regin(photoelastic sensitivity: 1.00 mm/k_g) of stress wave velocity 2600 m/sec. The pressure gauge with high responsibility is flush mounted with the tube wall opposite to the photoelastic specimen and is used to detect the instant of arrival of the shock wave radiated from the bubble. It takes just 10.57 μsec for the shock wave emanated from the bubble to reach the pressure gauge.

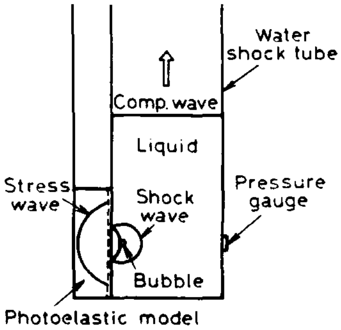

Fig.9 The configuration of the photoelastic specimen relative to the bubble and the pressure gauge

4-2 *Experimental results and discussion*

4-2-1 Microjet formation and shock wave radiation Figure 10 shows typical high-speed photographs of a spherical bubble collapsing close to a solid boundary. The bubble is produced at a distance L=1.80 mm from the boundary and reaches a maximum radius R_0=0.95 mm; the ratio L/R_0=1.89. The time elapsed from the start of collapse is marked under each of the frames. During collapse, the bubble loses spherical symmetry by flattening and forming an inward moving jet on the bubble wall opposite to the solid boundary. In our pictures the jet, inside the bubble, is invisible because these frames are shadow pictures taken by a Cranz-Shardin camera. However, as a result of a higher collapse speed of the upper bubble wall, the jet can be expected to be produced, penetrating the bubble towards the rigid wall. The funnel-shaped protrusion, visible as a fine dark line, is a secondary effect produced by the jet impingement on the lower bubble wall. This is called " tip " and distinguished from " true jet "(12). Whether the true jet and the tip can produce impulsive pressures will be clarified in the next section.

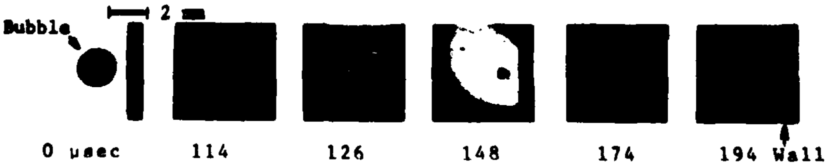

Fig.10 Microjet formation from the bubble in the neighbourhood of the solid boundary

Figures 11(a) and (b) show representative pictures of shock waves radiated from bubbles (a) close to, or (b) in contact with, the solid boundary. These results clearly indicate that the presence of a solid wall does not inhibit the bubble rebound and the resulting shock wave radiation.

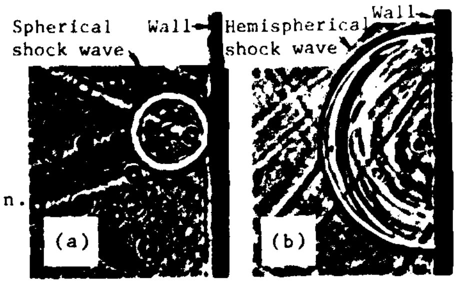

Fig.11 The photographs of the shock waves emanated from the bubbles (a) close to, or (b) in contact with the solid boundary

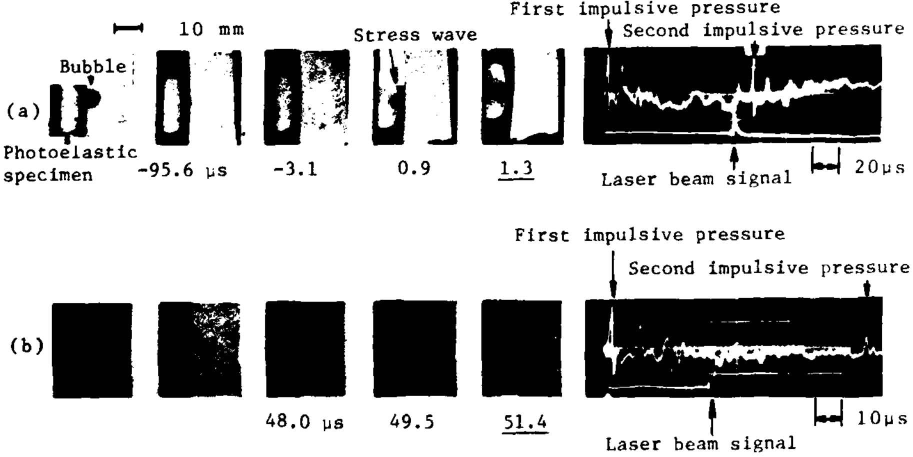

Fig.12 The isochromatic fringe patterns in photoelastic specimen due to the stress waves originated by the bubbles collapsing, (a)in contact with, and (b) in the neighbourhood of, the specimen surface. The time elapsed from the instant of shock wave generation is taken as positive.

4-2-2 Stress fringes, in the photoelastic material, caused by the bubble collapse   Figures 12(a) and (b) show typical high-speed photographs of bubbles in contact with, or close to, the solid boundary. The picture marked with the underlined time index was just taken by the timed laser emission. The impulsive pressure due to the bubble collapse and the signal of laser emission both are recorded on each oscillogram.

The isochromatic fringe patterns in the specimen due to the stress wave, as shown in figure 12(a), are originated by the second rebound of the bubble initially in contact with the solid boundary. The signal of the impulsive pressure due to the first rebound of the bubble triggers, through a variable delay unit,a laser flash lamp so that the stress waves due to the second rebound of the bubble are photographed at any stage of their propagation. In particular, the fifth frame shows that the stress wave propagate 3.5 mm after its appearance on the specimen. The wave velocity being 2600 m/sec in epoxy resin, the present stress wave had been generated on the surface of the photoelastic specimen, 1.34 μsec before this photograph was taken. On the contrary, the corresponding oscillogram shows that the laser light was emitted at the instant that 1.31μsec elapsed after the shock wave(second impulsive pressure) radiated from the bubble; the time difference between the laser signal and the second impulsive pressure is 9.26 μsec and it takes 10.57 μsec for the shock wave to reach the pressure gauge (figure 9) situated on the opposite wall. Therefore, the present stress wave in the specimen proves to be caused by the shock wave emanated at the instant of the bubble rebound. It must be noted here that no isochromatic fringe patterns are recognized in the specimen before the bubble rebound(second and third frames) although the bubble collapses in such a situation that the jet is expected to directly impinge on the boundary. Therefore, the strength of the jet may be infered to be much less than the shock intensity. The spatial resolution of the photoelastic specimen may be sufficient to detect the impact of the jet , judging from the fact that the stress wave caused by a shock wave emanated at the minute bubble size(<0.1 mm in radius) can be clearly observed.

The behaviour of a bubble in the vicinity of the boundary is shown in the figure 12(b). The bubble is produced at a distance L=3.20 mm from the boundary and reaches a maximum radius R_o=2.76 mm ; the ratio L/R_o=1.16. Even in the present situation very close to the solid boundary the jet, on the upper bubble wall, does not strike directly the boundary. During rebound, the bubble approaches the boundary forming the tip and finally attaches to the solid surface. The second frame indicates that the fringes are caused in the specimen before the tip reaches the surface. These fringes are originated by the impact of shock wave radiated at the instant of bubble rebound. The shock intensity on the boundary is of the order of 10^2 atm, from the results of the theoretical part in the present paper, provided that the bubble collapses in spherical form.

4-3-3 Effect of the bubble size on the instability of bubble wall

The authors as well as the previous investigators used large bubbles in their experiments because the use of small bubbles made it extremely difficult to observe the transient behaviour of cavitation bubble collapse; Naudé & Ellis(8), Lauterborn & Bolle(12), and the authors used bubbles of 6.2 mm, 5.2 mm, 2.0-5.6 mm in diameter respectively. Real cavitation bubbles seem to be usually of the order of 0.1 mm in diameter. According to the experiments by Efimov et al(18), the bubble size has an influence not only on the impulsive pressure,but also the instability of bubble wall;the former has been theoretically clarified in Chapter 3. Let us here discuss the effect of the bubble size on the instability of bubble wall, which leads to microjet formation. We consider the spherical interface r=R(t) disturbed to the shape r_s=R + aY_m, where Y_m is a spherical harmonic of degree m and a is a small quantity. For the sake of simplicity, we use the Rayleigh equation as the equation of bubble motion as follows:

$$R\ddot{R} + \frac{3}{2}\dot{R}^2 = \frac{p_g - p_{\ell\infty}}{\rho_\ell} \qquad (20)$$

The stability condition(19) is given by

$$\ddot{a} + \frac{3\dot{R}}{R}\dot{a} - \frac{(m-1)\ddot{R}}{R}a = 0 \qquad (21)$$

If we consider a collapsing bubble and suppose that the pressure difference, $p_g - p_{\ell\infty}$, remains constant as R decreases, we obtain the following equation from the equations (20) and (21):

$$\frac{a}{R_0} \sim \frac{R_0^{1/2}}{R^{1/4}} \exp\left[\pm i b m^{1/2} \int^{t} \frac{dt'}{R^{5/2}}\right], \qquad (R \rightarrow 0) \qquad (22)$$

where b is positive, being proportional to $p_g - p_{\ell\infty}$. We can conclude, from the present analysis, that a collapsing bubble is unstable, i.e., $a/R_o \rightarrow \infty$ as $R \rightarrow 0$, and the larger is the initial size of bubble, the more unstable is the bubble. This conclusion was experimentally verified by Efimov et al; bubbles smaller than 0.1 mm in diameter collapse in spherical form even close to a solid boundary and produce shock waves in liquid at the instants of rebound.

5. CONCLUSIONS

Numerical analyses have been made of the effects of nonequilibrium vapour condensation and heat conduction on the collapse of bubbles in water. It has been found that the temperature gradient develops inside the bubble owing to heat conduction through the interface, and that the combination of the condensing water vapour and noncondensable gas has a very strong influence on the behaviour of collapsing bubble and the radiated pressure wave. The calculations indicate further that a purely vaporous bubble may produce a strong pressure wave in the liquid at the instant of the rebound.

The stress wave both in a solid and a liquid due to the collapse of a single bubble has been observed in detail by means of the dynamic photoelasticity. The present experimental evidences also support our previous observations that the impulsive pressure accompanying the bubble collapse is caused by the shock wave emanated into the liquid from the bubble, and that the microjet impingement does not produce any detectable effects.

Continuation of the present numerical calculations will reveal the effects of the liquid temperature and applied ambient pressure in the liquid on the collapse of the cavitation bubble. This research was carried out partly with the Grants in Aid for Scientific Research of the Ministry of Education in Japan in 1976, 1978, and 1979. The authors wish to express their gratitude for these Grants.

6. REFERENCES

1. W.Guth, Acustica 6, 526(1956).
2. I.R.Jones and D.H.Edwards, J.Fluid Mech. 7, 596(1960).
3. H.Kuttruff, Acustica 6, 526(1962).
4. R.Hickling and M.S.Plesset, Phys.Fluids 7, 7(1964).
5. S.Fujikawa and T.Akamatsu, Proc.10th Intern.Shock Tube Sympo., 174(1975).
6. M.S.Plesset, Phil.Trans.Roy.Soc. 260, 241(1966).
7. M.Kornfeld and L.Sovorov, J.Appli.Phys. 15, 495(1944).
8. C.F.Naudé and A.T.Ellis, Trans.ASME 83, 648(1961).
9. T.B.Benjamin and A.T.Ellis, Phil.Trans.Roy.Soc. 260, 221(1966).
10. M.S.Plesset and R.B.Chapman, J.Fluid Mech. 47, 283(1971).
11. C.L.Kling and F.G.Hammitt, Trans.ASME 94, 825(1972).
12. W.Lauterborn and H.Bolle, J.Fluid Mech. 72, 391(1975).
13. S.Fujikawa and T.Akamatsu, Bull.JSME 21, 223(1978).
14. S.Fujikawa and T.Akamatsu, J.Fluid Mech., (to be published).
15. Lord.Rayleigh, Phil.Mag. 34, 94(1917).
16. C.Herring, OSRD Report 236, (1941).
17. Y.Tomita and A.Shima, Bull.JSME 20, 1453(1977).
18. A.V.Efimov, G.A.Vorob'ev, Yu.I.Filenko, and K.N.Petrov, Proc. IAHR Sympo., 159(1976).
19. M.S.Plesset and T.P.Mitchell, Q.Appli.Math. 13, 419(1956).

SHOCK-TUBE FLOW COMPUTATION INCLUDING THE DIAPHRAGM AND BOUNDARY-LAYER EFFECTS

DAVID ZEITOUN, RAYMOND BRUN and MARIE-JOSEE VALETTA

Laboratoire de Dynamique et Thermophysique des Fluides
Université de Provence, centre St Jérôme, 13397 MARSEILLE cedex 4, France

The flow regime in shock-tubes is computed, taking account simultaneously of the finite duration of the diaphragm opening and of the hot gas boundary-layer. The computation is performed by a classical method of characteristics with the aid of simplifying hypotheses the most important of which are the prior knowledge of the mechanical opening process of the diaphragm (some models are examined), the one-dimensional behavior of the flow and the neglect of the cold gas boundary-layer. On the other hand, the unsteadiness of the boundary-layer, its interaction with the core flow and the perturbations coming from the progressive opening of the diaphragm are taken into account. The spatial and temporal evolution of the flow is deduced, particularly this one of the shock wave and the usual phases of acceleration and deceleration may be observed in the chosen examples. In spite of the rarity of experiments allowing a direct comparison (the initial conditions are generally not given in the literature) some ones which might be used show a good agreement with the results of the computation about the shock wave evolution.

INTRODUCTION

To our knowledge, no complete computation of shock-tube flows has been carried out up to now, taking account simultaneously of the influence of the wall boundary-layer and of the finite duration of the diaphragm opening. The aim of the present paper is to contribute to the resolution of this problem. Many previous studies have been devoted to partial aspects, so rough models of the influence of the diaphragm opening have been proposed in the past. Thus, White's model[1] is an approximation of the formation process ; in the x,t diaphragm, compression waves are assumed to coalesce in a single point where the shock possesses its final and constant value, but the acceleration process is not taken into account. More recently, the "multistage" model[2] may be considered as an improvement of White's model but it is still a discontinuous model.

In the same way, more or less sophisticated opening processes have also been suggested[3 4 5] and experimental verifications have been carried out [5 6]. However, it does not seem that any connection has been established between the opening process itself and the resulting aerodynamic flow. This has been done in a recent study[7] in which a flow model is described in connection with an opening process. The boundary-layer effects are however neglected.

These effects are taken into account in the now classical studies of Mirels[8 9] which, however, treat only of quantities like the incident shock evolution and hot flow duration. More refined models of the interaction inviscid flow-boundary layer have been developed more recently[10 11] which enable one to compute the spatial and temporal evolution of the inviscid flow quantities up to the limiting steady regime, with however the restrictive hypothesis of the steadiness of the boundary-layer with respect to the shock. Finally, this hypothesis has been also suppressed in a still more recent study[12] and now it can be considered that the interaction studies are at their final stage, but they do not take account of the diaphragm opening. This is precisely the aim of the present work.

MODEL ANALYSIS

The principle of the present computation is the following : the inviscid flow, assumed one-dimensional, is determined by a method of characteristics with constant temporal steps. The equations of the flow are coupled with those of the boundary-layer by a non-simplified mass loss term $\dot{m}$, with

$$-\frac{R}{2}\dot{m} = \frac{\partial}{\partial t}\int_{o}^{\delta}(\rho-\rho_e)(1-\frac{Y}{R})dY + \frac{\partial}{\partial x}\int_{o}^{\delta}(\rho u-\rho_e u_e)(1-\frac{Y}{R})dY$$

where R is the tube radius, Y the distance from the wall, ρ the specific mass, u the absolute velocity, δ a characteristic boundary-layer thichness and where the subscript e refers to the local inviscid flow quantities.

The boundary-layer assumed laminar, axisymmetrical and unsteady, is simultaneously computed at each step and takes into account the spatial and temporal variations of the core flow. The boundary-layer is taken into consideration only in the hot flow region. From a numerical point of view, the system of the boundary-layer equations is solved by a procedure using a Crank-Nicolson scheme, a Newton-Ralphson linearization and a simultaneous resolution of the mass and momentum equations.

The mechanical opening process itself is assumed known and determined only by the initial conditions. Among the models tested experimentally, two models have been retained here and compared[4 5]. These models give the time dependent ratio of the aperture area to the tube area. The first one[4] (Simpson et al) assumes a newtonian form for the pressure acting on the breaking diaphragm $(P_4-P_1)\cos^2\theta$, where P_4 and P_1 are respectively the initial pressures in the driver and driven sections and $\theta(t)$ is the variable angle made by the petals and the initial diaphragm plane. The second pressure law used here[5] (Hickman et al) takes into account the time evolution of the local pressures on both sides of the opening diaphragm during the expansion. Finally, these processesgive results which are not very different and for copper diaphragms, the agreement with experiments[6] is relatively good (fig.1), but the first law is easier to use in the computations because it can be put under the form :

$$t/t_{ouv} = f(\theta)$$

where t_{ouv} is the total opening duration depending only on the initial conditions including the characteristics of the diaphragm. The second law needs iterations in order to know the pressures given by the aerodynamic model at each instant.

AD-A091 010   HEBREW UNIV JERUSALEM (ISRAEL)   F/G 20/4
PROCEEDINGS OF THE INTERNATIONAL SYMPOSIUM ON SHOCK TUBES AND W--ETC(
FEB 80   A LIFSHITZ, J ROM   AFOSR-78-3679
UNCLASSIFIED   AFOSR-TR-80-1141   NL

3 of 8
AD
A091010

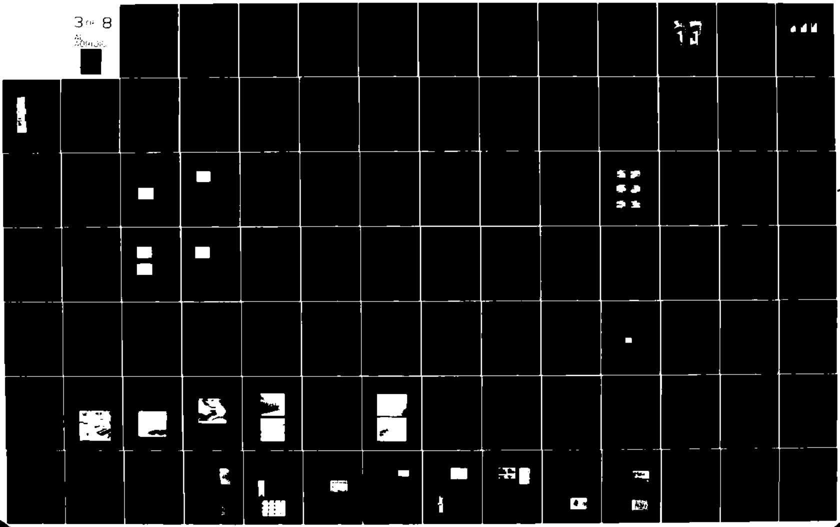

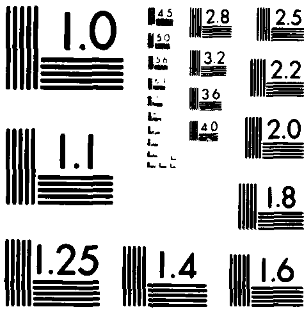

MICROCOPY RESOLUTION TEST CHART
NATIONAL BUREAU OF STANDARDS 1963 A

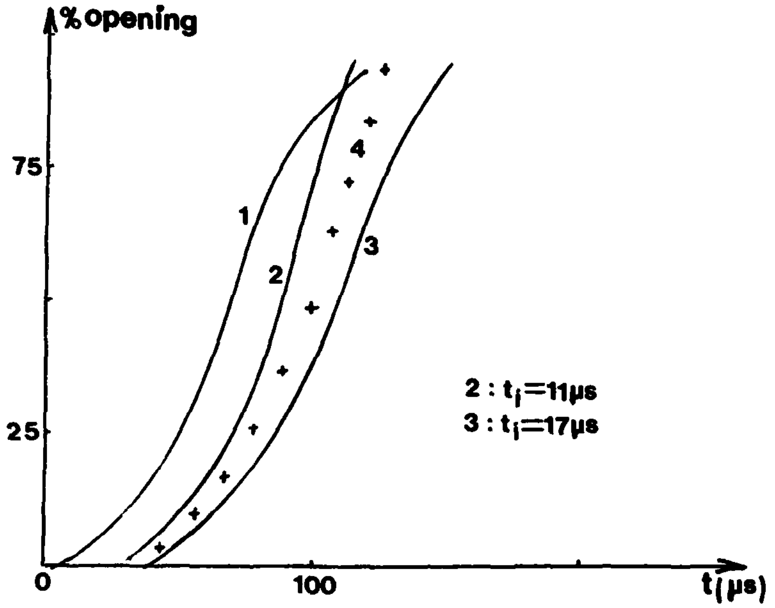

FIGURE 1

Example of opening processes (0,3mm Copper diaphragm)
1. Experimental (Ref.6)
2. Variable pressure (Ref.5)
3. Constant pressure with computed t_{ouv} (Ref.4)
+ 4. " " " experimental t_{ouv} (Ref.4)

This aerodynamic opening model is the following (fig.2) : At the abscissa of the diaphragm a steady flow is assumed and the driver gas is isentropically expanded (3a-3b) through the variable orifice of the breaking diaphragm and recompressed by a standing shock (3c). Thus, at each instant, the driver gas quantities are related to the aperture area, assuming a simple wave regime in the high pressure chamber. This scheme is qualitatively analogous to the experimental observations[13] and takes the non-isentropic behavior into consideration but the initial three-dimensional effects are neglected. The flow quantities behind this steady shock are used as boundary conditions for the computation in the x,t diagram and are a source of compression waves during the opening.

The numerical procedure needs an initial scheme at $t=t_i$ called "initial instant". At t_i, the flow is assumed to have the same character as at the further instants : the problem is to determine the corresponding aperture so that at t_i, the previously described steady flow is compatible with this one generated by a moving shock-wave followed by an interface. This problem has a unique solution[14]. Thus, knowing the opening process, the gas combination and the initial pressure ratio, t_i can be determined as well as the corresponding properties of the flow. As an example, with an air/air combination, an aluminum diaphragm of 1mm thick (total opening duration : 620μs) and an initial pressure ratio of 2.300 (Ideal Mach number : 3,4), the initial instant t_i is equal to 95μs. It is much larger for lighter driver gases but the major part of the acceleration phase can be determined with the model.

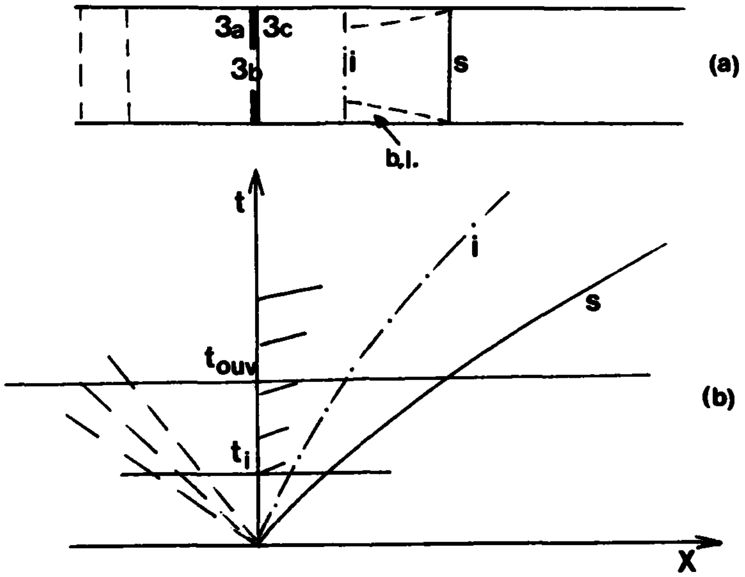

FIGURE 2

Flow model in tube (a) and in the x,t diagram (b)

DISCUSSION OF THE MODEL

It is well known that Simpson's or Hickman's opening model is idealized because, even if the breaking with petals is assured, the origin of time is very difficult to know and also because the diaphragm swells before the breaking. This is particularly marked for aluminum diaphragms. However, as far as the total opening time can be determined either theoretically or experimentally, the previous laws are satisfying and sufficiently simple to be used easily.

. The aim of the present model is not to represent the initial three-dimensional flow process following the very initiation of the rupture[15]. This is not indeed a disadvantage because of the rapid formation of a plane shock-wave[15] [16] and the confinement of these phenomena at the rear part of the hot flow at the usual measuring stations.

In the same way, the steady shock-wave of the model may represent to some extent the initial dissipative phenomena.

. As for the initial data line, it is a sort of summary of the complex events occured at the very beginning of the opening. Other choices are of course possible[14] [15] and a moving shock instead of a steady shock has been imagined : the results are not really different but the computations are more complex and arbitrariness remains in the initial position of this secondary shock (t_i is also changed).

. Taking account of the unsteadiness of the hot gas boundary-layer improves the previous results. However, neglecting the cold gas boundary-layer does not allow a correct representation of this flow. In fact, this is a minor drawback because the interest is of course in the hot gas and the influence of this boundary-layer on the hot gas flow is small as it has been shown assuming an approximate form[17] for the cold boundary-layer and including the corresponding mass gain term in the previously described computation.

. The real gas and relaxation effects could also be easily included[18] as well in the inviscid flow as in the boundary-layer, but it would be time-consuming.

RESULTS. CONCLUSION

A systematic study of the separate influence of each effect has been previously made[7 12] and only the principal features are presented here. First, it is well known that the boundary-layer effects are responsible of a monotonous decrease of the shock velocity up to a constant value (limiting regime). The influence of the diaphragm opening manifests itself by a strong acceleration followed by a slow deceleration, the final regime being the ideal regime. The simultaneous consideration of both effects obviously represents the superposition of these types of evolution, the preponderance of the one or of the other effect depending on the experimental conditions.

The influence of the diaphragm on the flow is completely determined with the present hypotheses if the initial pressure ratio P_{41} and the total opening time t_{ouv} are known. This time, as previously said, depends on all initial conditions (pressures, tube diameter, characteristics of the diaphragm). On fig.3, this influence on the shock evolution is summarized. With the acceleration and deceleration already noted, it may be seen that the abscissa of the maximum is proportional to the opening time which has been verified experimentally[19]. Moreover, this abscissa increases with the initial pressure ratio and decreases with the sound velocity of the driver gas. A direct comparison with experimental results[20] is shown on fig.4a and the agreement is reasonable except in the decreasing zone where, obviously, the boundary-layer effects neglected in this first calculation are responsible of the disagreement. A second comparison is shown on fig.4b where both effects have been taken into account in the calculation. In the same way, the profiles of all flow quantities have been obtained by the computation but they have not been represented here.

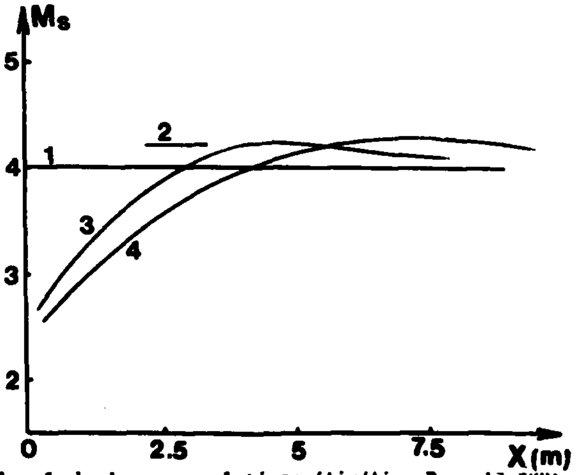

FIGURE 3 - Example of shock-wave evolutions (Air/Air, P_{41}= 17.739)
1. Ideal ; 2. White (Ref.1)
3. Present computation (without boundary-layer t_{ouv}= 300 μs)
4. " " (" " " t_{ouv}= 600 μs)

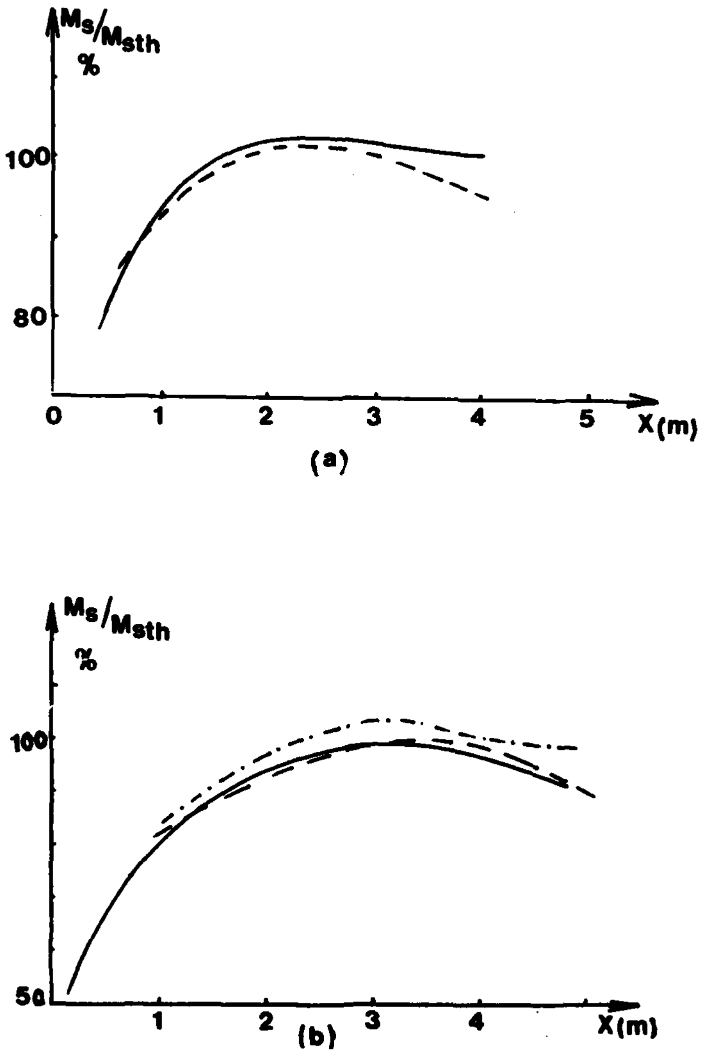

FIGURE 4

Comparison of computation and experiments (Ref.20)

(a) : Air/Air, P_{41}= 554, P_1= 8mm Hg, t_{ouv}= 574μs

----- Experiments — Computation without boundary-layer

(b) : Air/Air, P_{41}= 2.134, P_1= 4mm Hg, t_{ouv}= 618μs

--- Experiments -·-·- Computation without boundary-layer

— " with " "

In conclusion, when the uncertainties concerning the total opening time are removed, the model seems to give satisfying results.

REFERENCES

1. D. White - J. Fluid. Mech. 4, 585 (1958)
2. T. Ikui, K. Matsuo and N. Nagai - J. Soc. Mech. Eng.(part 2) 12, 52, 783 (1969)
3. J. Drewry and Z. Walenta - Inst. Aero. Rep.90, Univ. Toronto (1965)
4. C. Simpson, T. Chandler and K. Bridgman - Phys. Fluids 10, 1894 (1967)
5. R. Hickman and J. Kyser - AIAA J. 11, 961, (1973)
6. E. Rothkopf and W. Low - Phys. Fluids 17, 1169 (1974)
7. R. Brun and R. Reboh - AIAA J. 15, 1344 (1977)
8. H. Mirels - Phys. Fluids 6, 1201 (1963)
9. H. Mirels - 8th Int. Shock-Tube Symp. London (1971)
10. L. Dumitrescu, R. Brun and J. Sides - 9th Int. Shock-Tube Symp. Stanford (1973)
11. R. Brun and M. Imbert - 10th Int. Shock-Tube Symp. Kyoto (1975)
12. D. Zeitoun and M. Imbert - J. Mecanique, 16, 1 (1977) and AIAA J. (to be published)
13. R. Hickman, J. Farrar and J. Kyser - Phys. Fluids, 18, 1249 (1975)
14. H. Oertel - Stossrohre, Springer, 618 (1966)
15. E. Outa, K. Tajima and K. Hayakawa - 10th Int. Shock-Tube Symp. Kyoto (1975)
16. I. Glass and G. Patterson - J. Aeronaut. Sci. 22, 73 (1955)
17. K. Tong and D. Russel - AIAA J. 15, 1763 (1977)
18. D. Zeitoun - Acta Astronautica 2, 879 (1975)
19. E. Rothkopf and W. Low - Phys. Fluids 19, 1885 (1976)
20. K. Tajima, E. Outa and G. Nakada - J. Soc. Mech. Eng. 11, 116 (1968)

REFLECTION PROCESSES OF IONIZING SHOCKS IN ARGON ON AN END WALL OF A SHOCK TUBE

Y. TAKANO, S. MIYOSHI and T. AKAMATSU

Department of Mechanical Engineering
Kyoto University, Kyoto, Japan

Shock-reflection processes in ionizing argon on the end wall of a shock tube were investigated theoretically and experimentally. The Lax-Wendroff scheme, a finite-difference method, were applied to calculate the reflected-shock flowfields at the condition of the incident-shock Mach-number Ms = 14 and the initial pressure p_1 = 3 torr for two cases which include and exclude radiative cooling effects, respectively. The results of computations reveal unsteady nature of shock-reflection process and influences of radiative cooling on flowfields. The trajectories of reflected-shock were visualized by use of a streak schlieren technique. The experimentally-determined distance-time diagrams confirm the unsteady nature of shock-reflection process. The reflected-shock flowfields were visualized taking a series of snap-shot photographs in a schlieren and a shadow arrangement. The developments of bifurcations in reflected shocks were observed to occure as a result of interaction between reflected shock and ionization relaxation.

INTRODUCTION

The stationary ionized monatomic gases heated by reflection of an incident shock at the end wall of a shock tube have been often used for experimental studies of the thermal conductivity, the heat transfer rate on the end wall, and the ionization relaxation time. These experimental investigations have indicated that reflected-shock flowfields are complicated by interactions between ionization relaxation processes and shocks. Camac & Feinberg[1] measured the convective heat transfer on the end wall from ionizing argon behind a reflected shock by use of an infra-red heat transfer gauge. Their measurements showed that the reflected-shock flowfields were characterized by two ionization times of incident and reflected shocks. Friedman & Fay[2] also used an infra-red heat transfer gauge to measure the convective heat transfer from argon and xenon gases to the end wall of a shock tube. Smith[3] made the measurements in ionizing xenon, using a fast-rise pressure gauge mounted in the end wall of a shock tube. He proposed a distance-time diagram of shock-reflection process, considering a model which consisted of complicated series of shocks, rarefaction waves and contact surfaces, in order to explain the pressure histories at the end wall. Kuiper & Bershader[4] visualized reflected-shock flowfields in ionizing argon by means of streak interferometry, and obtained the experimentally-determined distance-time diagrams. They pointed out bifurcations of reflected shock, unexpected in non-ionizing argon, causing associated with ionization behind an incident shock and also suggested the radiative cooling affecting reflected-shock flowfields. Takano & Akamatsu[5,6] made numerical analyses of shock-reflection process in ionizing argon, solving the time-dependent one-dimensional inviscid flow problem by use of a finite difference method. The distance-time diagrams of numerically-obtained flowfields were more drastic than had ever described; for example, an ionizing shock, reflecting away from the end wall, does not only decelerate, but also rebounds to the end wall. Recently, Ezumi[7] studied shock reflection process in ionizing krypton theoretically and experimentally. He used an interferometer technique to measure the electron density in reflected-shock flowfields and also made numerical analyses taking account of the side-wall boundary-layer effects.

The present paper studies theoretically and experimentally reflection process of ionizing shock in argon on the end wall of a shock tube. The influence of radiative cooling on the reflected-shock flowfield is investigated applying the Lax-Wendroff scheme, a finite difference method, to time-dependent one-dimensional ionizing inviscid-flow problems which include and exclude the radiative cooling term, respectively. Experimental studies are performed using the free-piston shock-tube. In order to verify experimentally the unsteady nature of shock-reflection process in ionizing gas as was predicted theoretically, the trajectories of reflected shocks are visualized by use of a streak schlieren technique. The developments of bifurcations in reflected shocks are observed by taking a series of snap-shot photographs of reflected-shock flowfields in a schlieren and a shadow method with a pulsed dye-laser as a light source.

NUMERICAL ANALYSES

Governing Equations

Numerical simulations on shock-reflection processes in ionizing argon were attempted by Takano & Akamatsu[5] using a finite-difference scheme, whose analyses did not include the radiative cooling effects. However, as pointed out by Kuiper & Bershader[4] the radiative cooling is expected to cause severe effects in real reflected-shock region of a shock tube. In this numerical analyses, we extend the numerical scheme to consider effects of radiative cooling on reflected-shock flowfields.

In investigating the shock-reflection process in ionizing argon, the effects of viscosity, diffusion between species and thermal conduction are neglected. Hence, the governing equations can be written as follows:

$$\frac{\partial \rho}{\partial t} + \frac{\partial (\rho u)}{\partial x} = 0 \,, \qquad \text{I}$$

$$\frac{\partial (\rho u)}{\partial t} + \frac{\partial (\rho u^2 + p)}{\partial x} = 0 \,, \qquad \text{II}$$

$$\frac{\partial}{\partial t}\{\rho (e + \frac{u^2}{2})\} + \frac{\partial}{\partial x}\{\rho u (e + \frac{u^2}{2} + \frac{p}{\rho})\} = - q_R \,, \qquad \text{III}$$

$$\frac{\partial (\rho \alpha)}{\partial t} + \frac{\partial (\rho \alpha u)}{\partial x} = \rho \dot{\alpha} \,, \qquad \text{IV}$$

$$\frac{\partial}{\partial t}(\frac{3}{2} n_e k T_e) + \frac{\partial}{\partial x}(\frac{3}{2} n_e k T_e u) + n_e k T_e \frac{\partial u}{\partial x} = q_{el} - q_{inel} - q_B \,, \qquad \text{V}$$

$$p = \rho R (T + \alpha T_e), \qquad R = k/m_h \,, \qquad \text{VI}$$

$$e = \frac{1}{\gamma - 1}\frac{p}{\rho} + \frac{E_I}{m_h} + W \,. \qquad \text{VII}$$

where t is the time, x is the distance, being measured from the end wall, ρ, u, p and e are the density, the velocity, the pressure and the energy of the plasma, α the degree of ionization, $\dot{\alpha}$ the net production-rate of ionization degree, T and T_e the temperatures of heavy particles and electrons, respectively, n_e the electron density, q_B the rate of energy loss of the electrons due to bremsstrahlung, q_{el} the rate at which thermal energy is given to electron gas by elastic collisions, q_{inel} the inelastic energy-transfer rate, k the Boltzmann constant, m_h the mass of a heavy particle, γ the specific ratio, E_I the ionization energy, and W denotes the electronic energy of excited atoms.

The ionization relaxation of shock-heated monatomic gas has been well described by considering the two-step process where the excited-state populations are assumed in local thermodynamic equilibrium with free electrons. As collisional transitions dominate radiative transitions even in the equilibrium region behind incident and reflected shocks where the radiative transitions are important, the following expressions for net production rate of ionization degree, formulated by Hoffert & Lien[8] considering the two-step model for ionization, are applied:

$$\dot{\alpha} = \dot{\alpha}_a(T) + \dot{\alpha}_e(T_e) \ , \qquad \text{VIII}$$

where $\dot{\alpha}_a$ and $\dot{\alpha}_e$ are the production rates of ionization degree due to atom-atom inelastic collisions and due to atom-electron inelastic collisions, respectively. In the present calculations, we use the atom-atom collisional-ionization cross-section obtained by McLaren & Hobson[9] the atom-electron collisional-ionization cross-section given by Petchek & Byron[10]

The elastic energy transfer rate can be written as

$$q_{el} = 3\,\frac{m_e}{m_h}\,k(T - T_e)\nu_{eh} \ , \qquad \text{IX}$$

where m_e is the mass of an electron, and ν_{eh} is the elastic collisional frequency between electrons and heavy particles whose expression is given by Liu & Glass[11]

In no radiative cooling case, with the assumption of local equilibrium in excited levels with free electrons, the rate of energy loss of electrons due to inelastic collisions is expressed as

$$q_{inel} = \rho\dot{\alpha}_e E_I/m_h \ . \qquad \text{X}$$

In the equilibrium region where the radiative cooling is severe, nevertheless collisional processes dominate radiative processes, and free-bound transitions and bound-bound transitions in the excited levels may be promptly compensated by inelastic transitions due to electron impacts. Therefore, the inelastic energy loss of electrons due to free-bound transitions and due to bound-bound transitions should be considered:

$$q_{inel} + q_B = \rho\dot{\alpha}_e E_I/m_h + q_R \ . \qquad \text{XI}$$

The total radiative energy loss q_R is the sum of the continuum radiation q_C due to free-bound transitions and due to free-free transitions (bremsstrahlung), and line radiation q_L due to bound-bound transitions. The rate of energy loss by continuum radiation was given by Oettinger & Bershader[12] as follows

$$q_C = \frac{64e^6\pi^{3/2}}{3(6)^{1/2}m_e^{3/2}k^{1/2}c^3}\left(\frac{\alpha\rho}{m_h}\right)^2\left(\nu_c + \frac{kT_e}{h}\right)\frac{Z_{eff}^2}{T_e^{1/2}} \ . \qquad \text{XII}$$

In the present calculations, we do not include rate of energy loss due to line radiation which is assumed to be small compared to that of continuum radiation. The estimations for the rate of line-radiation loss was made using the formula given by Horn[13] and recent data of Stark broadening for argon[14] and the result is that the portion of continuum radiation in the total radiation is about 65%

in the equilibrium region behind an incident shock and over 80% in the equilibrium region behind an reflected shock for the present conditions.

The local steady-state approximation being applied for electron temperature, the differential equation (V) reduces to such an algebraic equation as

$$T - T_e = \frac{1}{3(m_e/m_h)\nu_{eh}}\left(\frac{\dot{\alpha}_e}{\alpha}\frac{E_I}{k} + \frac{q_{R/k}}{\rho\alpha/m_h}\right) . \qquad \text{XIII}$$

Finite Difference Method

As the basic equations (I - IV) are of a conservation form of

$$\frac{\partial U}{\partial t} + \frac{\partial F(U)}{\partial x} = G(U) , \qquad \text{XIV}$$

the two-step Lax-Wendroff scheme proposed by Rubin & Berstein[15] is employed, which was used in our previous work. In the present calculations, Tyler's artificial viscosity term (see Roache[16]) is added to the pressure term in order to damp vibrations in shocks.

Results and Discussions

Calculations are made at the conditions of the incident-shock Mach-number 14 and the initial pressure 3 torr for two cases which respectively include and exclude the radiative cooling effects. Figure 1 shows the density profiles and the pressure profiles in the reflected-shock flowfields for the radiative cooling case which are plotted one above another with the value shifting at every 30 computational steps. Figure 2 shows the distance-time diagram for the radiative-cooling case where the reflected-shock trajectory of no radiative cooling case are present for comparisons. We shall explain the reflection process briefly because the detailed descriptions were reported in our previous paper[5] The incident shock reflects on the end wall at the frozen speed of reflection. Expansion waves are caused by rapid ionization in the reflected-shock flowfields and follow after the reflected shock. The reflected shock is attenuated not only by the expansion waves, but also by the density increase of the ionization front upstream of the reflected shock. Owing to the combined effects, the reflected shock rebounds to the end wall. Then, the pressure and temperature at the ionization front behind the reflected shock grow high and compression waves are generated. One propagates to the end wall as the interaction wave and the other moves to the reflected shock. The collision of the compression wave with the reflected-shock causes a weak expansion wave, a contact surface and a transmitted reflected-shock. The interaction wave reflects at the end wall and catch up with the transmitted reflected-shock. This collision gives a rise of a weak expansion wave, a contact surface and a coalesced reflected-shock.

As shown in figure 2, the radiative cooling has no influence on the primary reflected-shock, but affects the transmitted and the coalesced reflected-shock attenuate. Figure 3 shows the end wall histories of the pressure, the temperatures, the density and the degree of ionization after reflection of the incident shock. The end wall histories are characterized by two ionization times behind the incident and the reflected shocks. The first jumps of the pressure, the density and temperature are due to the reflection of the incident shock. The second jumps are caused by the reflection of the interaction wave, relating to the ionization behind the incident shock. Then, the radiative cooling begins to have more influences on the reflected-shock flowfields. The density grows higher and the degree of ionization decays much affected by the radiative cooling. However, the pressure and the temperature are not so much affected by the radiative cooling.

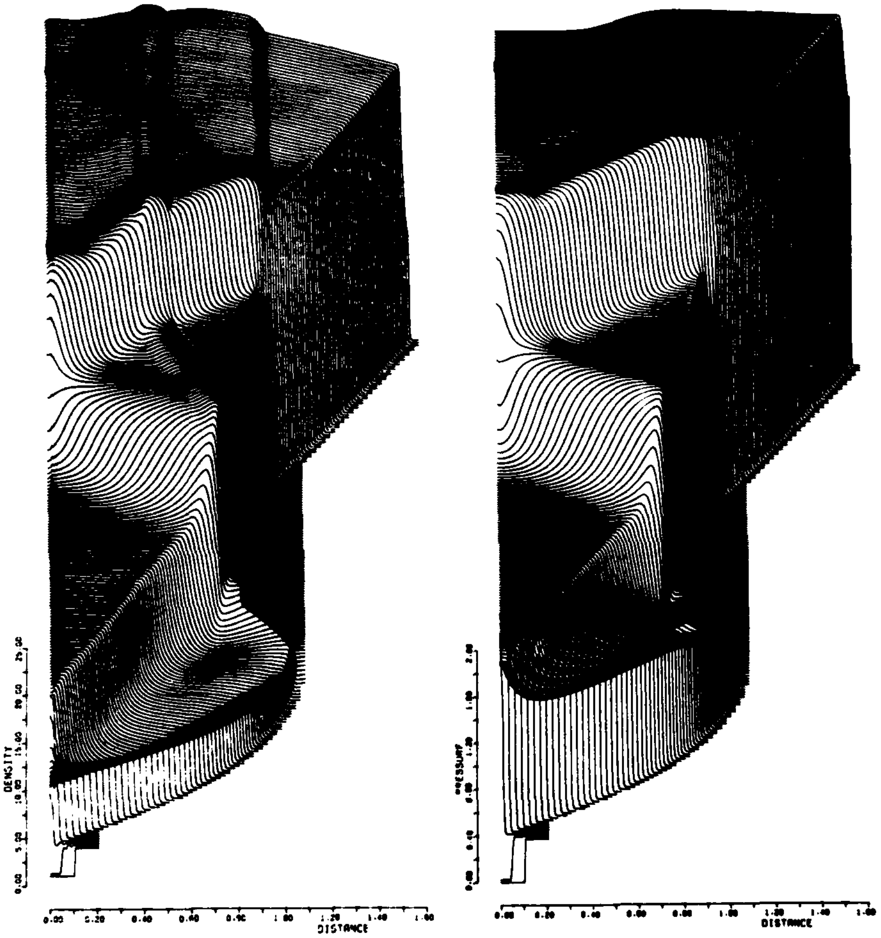

(a) density profiles (b) pressure profiles

Figure 1. Density and pressure profiles of reflected-shock flowfields for radiative cooling case.

EXPERIMENTS

Experimental Equipment and Methods

The shock tube used in the present experiments is a free-piston shock-tube consisting of a high pressure air tank (60 cm in length and 30 cm in diameter), a piston cylinder in which a free piston, driven by high pressure air, compresses a driver gas (2.5 m in length and 8 cm in diameter) and a driven section (15 cm in length and 4 cm in diameter). The 28.2 mm square, 13 cm long, test section with a pair of 45 mm diameter glass window and an end piece, was attached to the driven section through a 12 cm long square inlet. In this experimental study, we filled the high pressure tank with air of 5 atm and the piston cylinder with helium gas of 125 torr which was compressed to be about

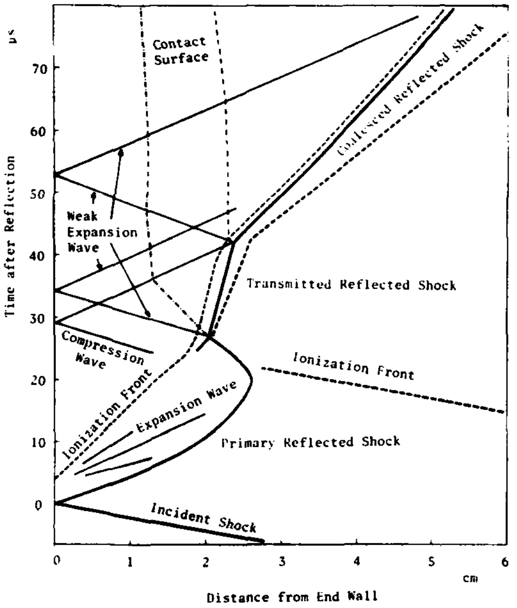

Figure 2. Distance-time diagram of reflection processes for radiative-cooling case at $M_s = 14$ and $p_1 = 3$ torr. Trajectories of reflected shock for no radiative-cooling case are plotted as dotted lines.

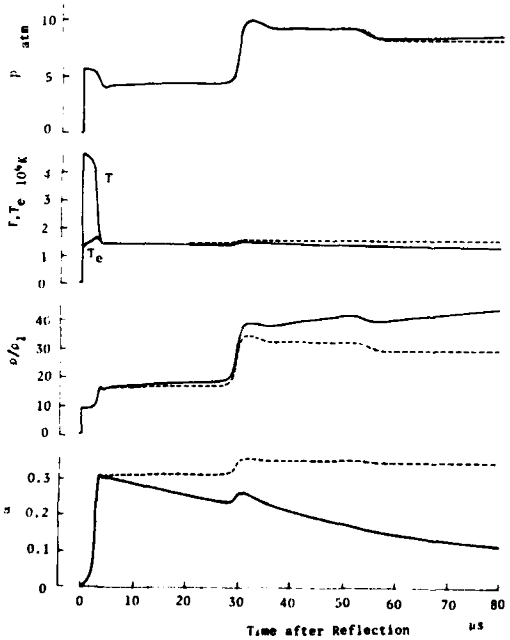

Figure 3. End-wall histories of the pressure (p), the temperature of heavy particles (T), the electron temperature (T_e), the density (ρ) and the degree of ionization (α) after reflection of incident shock at $M_s = 14$ and $p_1 = 3$ torr. ——, radiative-cooling case, ---, no radiative cooling case.

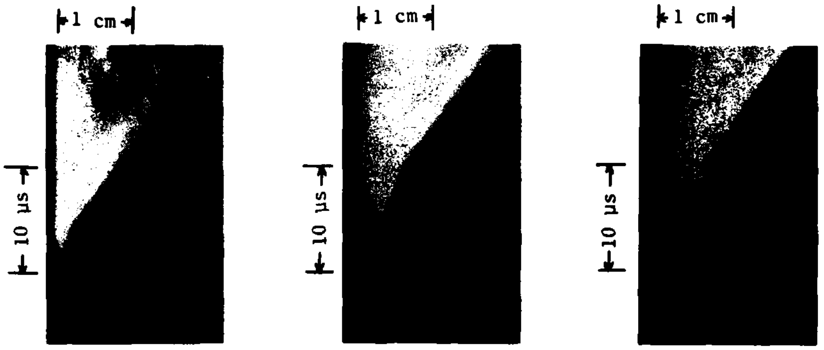

(a) (b) (c)

Figure 4. Experimentally-determined distance-time diagrams.
(a) $M_s = 14.4$, $p_1 = 1$ torr (b) $M_s = 11.4$, $p_1 = 3$ torr
(c) $M_s = 10.8$, $p_1 = 5$ torr

70 atm by the free piston.

The visualization of shock-reflection process was conducted by using a streak schlieren technique. The schlieren system consists of a light source, a collimating lense of focal length of 20 cm and a focusing lense of focal length of 80 cm. The light source used here is a strobotron for cameras. For streak photography, a 0.5 mm wide slit was placed parallel to the side wall of the test section and Beckman & Whitley high-speed camera (Dynafax Model 350) was used as a drum camera by stopping the rotation of mirror.

The observation of reflected-shock flowfields were performed by taking a series of snap-shot photographs in a schlieren and a shadow method. A pulsed dye laser (Chromabeam 1050 system, Synergetics Research Inc.) with a lasing mediem of Rodamin 6G, provided 0.3 μs-duration, continuous spectra, light source. The collimation of laser light was achieved by use of a 2 cm focal-length lense and a 80 cm focal-length lense. For schlieren photography, a 80 cm focal-length lense was used to bring a paralell beam of light passing through the test section to a focus on a knife edge. For shadowgraph, this lense was also used and a pin hole of diameter 2 mm was placed in the focal point to cut off emission from the test section.

Visualization of Shock-Reflection Process

The reflected-shock trajectories have been visualized using a streak schlieren technique. Figure 4 shows typical streak pictures of shock-reflection process in ionizing argon. In these pictures, shocks and ionization fronts can be observed but interaction waves and contact surfaces are not distinguishable because of strong radiation from the equilibrium regions behind reflected shocks. In the present experiments, the ionization relaxation times of incident and reflected shocks are much shorter than those in the numerical calculations owing to several effects such as an impurity of test gas[17] and a side-wall boundary-layer[18]

From these pictures, it can be seen that a reflected shock consists of three characteristic parts of a primary, a transmitted and a coalesced reflected-shock. In figure 4(a), the rebound of the primary reflected-shock is seen. In figure 4(b) and 4(c), the rebounds are not so clear, but it is obvious these primary reflected-shocks come to rest. It is no wonder that a qualitaive agreement is good between theoretical and experimental results of the shock reflection process as long as the one-dimensional relation can be applied in the reflected-shock flowfields.

In the present experiments, the traces of bifurcation in reflected-shocks

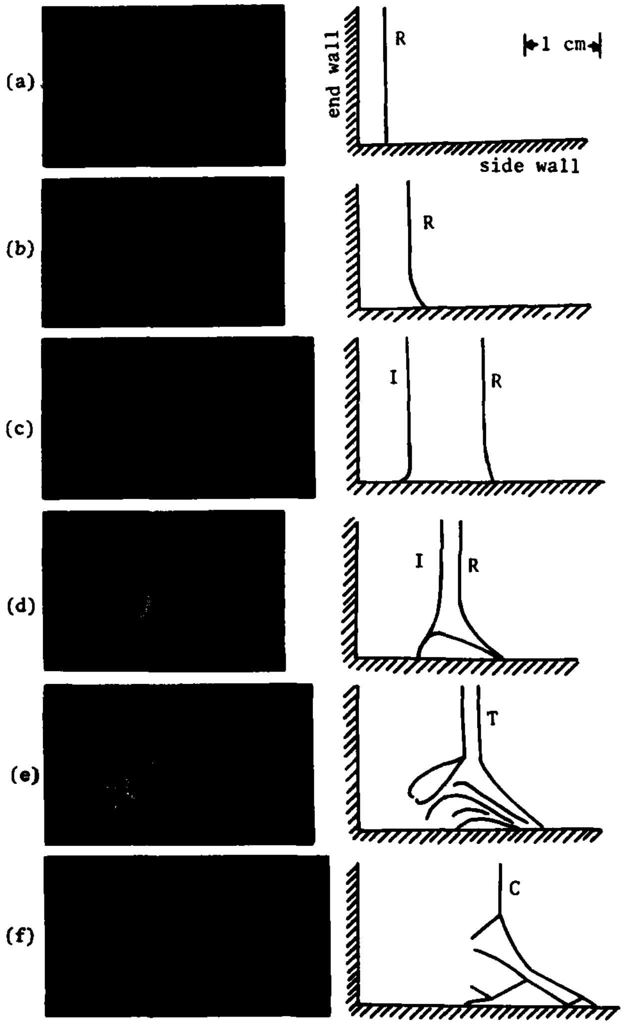

Figure 5. Reflected-shock flowfields. $M_s = 11 - 12$, $p_1 = 3$ torr.

R: Reflected-shock front
I: Ionization front
T: Transmitted reflected-shock
C: Coalesced reflected-shock

are found to develop associated with the interaction between reflected-shocks and incident ionization-fronts as were pointed out by Kuiper & Bershader[4].

Observation of Reflected-Shock Flowfields

The bifurcation of reflected shocks, caused by the interaction between reflected shocks and incident side-wall boundary-layers, were investigated by several authors. Mark[19] proposed a criterion that the bifurcation of reflected shock occurs when the stagnation pressure of the boundary layer is less than the normal reflected-shock pressure. Strehlow & Cohen[20] observed the reflected shock bifurcations in polyatomic gases under certain conditions, but they did not observed the bifurcated reflected-shocks in monatomic gases such as helium and argon under no ionizing conditions. Davies & Wilson[21] investigated the formation of the bifurcated reflected-shock.

Figure 5 shows snap-shot photographs of reflected-shock flowfields at the incident-shock Mach-number $M_s = 11 - 12$ in argon with the initial pressure $p_1 = 3$ torr. We took plates (a) and (b) of figure 5 in the schlieren method and plates (c) - (f) in the shadow method. In the schlieren technique, the visualization was good for reflected shocks, but not for ionization fronts because ionization fronts did not have enough discontinuity of the density.

Immediately after reflection, the reflected shock behaves like an ideal plane shock as shown in figure 5(a). Figure 5(b) shows that the reflected shock is curved near the side wall. It is well known that the incident-shock front is not plane but convex due to the side-wall boundary-layer acting as a suction on the side wall which causes a secondary free-stream behind the incident shock.[22] The curvature in a reflected shock is thought to be caused by this secondary flow ahead of the reflected shock. Consequently, the reflected-shock flowfield is not strictly one-dimensional but slightly perturbed. According to the results of numerical computations, in a relaxation time after reflection of the incident shock on the end wall. the sudden onset of equilibration beginning at the end wall due to rapid ionization, an ionization front is generated from the end wall and expansion waves are caused following after the reflected shock. Figure 5(c) shows a shock front and an ionization front in the reflected-shock region. In this plate, a fluid moves from right to left in the nonequilibrium region between the reflected-shock front and the ionization front, and it comes to rest in the equilibrium region, behind the ionization front, where the pressure and the density are much higher as shown in figure 1. Hitherto flowfields are essentially one-dimensional, however, hitherafter flowfields turn to possese two-dimensional structure. Figure 5(d) shows that the reflected shock front make a bent near the side wall, and the boundary layer, becoming a free shear layer or a slip line, seperates away from the side wall. The criterion of reflected-shock bifurcation propsed by Mark[19] is that the occurance of bifurcation is due to the inability of the boundary layer fluid to pass through the normal reflected shock and therefore the boundary layer fluid is trapped and carried along at the foot of the shock. This basic idea of the formation of bifurcation may be applied to the present bifurcation.

For a shock-fixed coordinate as shown in figure 6, the Mach number in the boundary layer M_{bl} is defined by the velocity of reflected shock-wave U_R and the sound velocity in the boundary layer fluid at room temperature a_1

$$M_{bl} = U_R/a_1 \, . \qquad \text{XV}$$

The stagnation pressure of the boundary layer flow $P_{bl,stg}$ is given by the following isentropic relation

$$\frac{p_{bl,stg}}{p_2} = \left(1 + \frac{\gamma - 1}{2} M_{bl}^2\right)^{\frac{\gamma}{\gamma-1}} \, . \qquad \text{XVI}$$

As well known, for monatomic gases,($\gamma = 5/3$), the pressure $P_{bl,stg}$ is always larger than the pressure behind the reflected shock P_5 for Ms > 2.8. There-

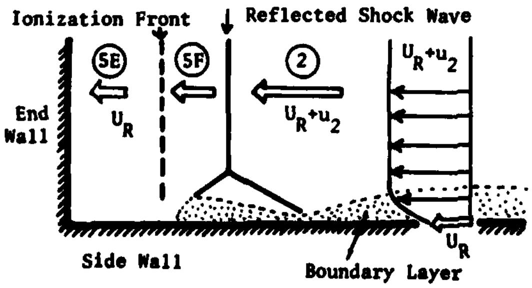

Figure 6
Bifurcated-shock flow diagram for shock-fixed coordinate

fore, the fluids in the boundary layer can pass through the reflected shock without bifurcation. However, in the present case that the reflected shock is retarded by the ionization-induced expansion waves, M_{bl} is much reduced even to null. Hence, from equation (XVI),

$$p_{bl,stg} < p_5 \ . \qquad \text{XVII}$$

This relation shows the possibility that the boundary layer fluid is trapped and carried along the foot of the reflected shock. Moreover, the higher pressure at the ionization front impose the steep adverse pressure gradient on the boundary layer fluid, and it forces the more severe bifurcation.

Figure 5(e) shows the transmitted reflected-shock which has several complicated limbs. From figure 5(f), the coalesced reflected-shock is seen to have an unique configuration. The forward limb bifurcates from the normal reflected shock and another triple-shock configuration is observed to exist behind the forward limb.

CONCLUSIONS

Numerical analyses of shock-reflection process in ionizing argon on the end wall of a shock tube have been made by use of the two-step Lax-Wendroff scheme. It is shown the reflected shock consists of three characteristic parts of a primary, a transmitted and a coalesced reflected-shock as a result of gasdynamic interaction with ionization relaxation. The radiative cooling affects reflected-shock flowfields after equilibration, and it results in the attenuation of the reflected shock, the increase in the density and the decay of the ionization degree.

Experimental studies of reflection process of ionizing shock in argon have been performed using the free-piston shock-tube. The distance-time diagrams, determined experimentally in a streak schlieren method, verify that the reflected-shock trajectories consist of three characteristic parts as predicted theoretically. The reflected-shock flowfields have been visualized by taking a series of snap-shot photographs in a schlieren and a shadow method. The development of bifurcation in the reflected shock is observed to occure associated with interactions between reflected shocks and ionization front.

REFERENCES

1. M. Camac & R.M. Feinberg, J. Fluid Mech. 21, 1965.
2. H.S. Friedman & J.A. Fay, Phys. Fluids 8, 1965.
3. J.A. Smith, Phys. Fluids, 11, 1968.
4. R.A. Kuiper & D. Bershader, AIAA J. 7, 1969.
5. Y. Takano & T. Akamatsu, Z. Naturforsch. 32a, 1977.
6. Y. Takano, Y. Shimomura & T. Akamatsu, Proc. 11th Int. Sym. Shock Tube,1977
7. H. Ezumi, J. Phys. Soc. Japan 46, 1979.
8. M.I. Hoffert & H. Lien, Phys. Fluids 10, 1967.
9. T.I. McLaren & R.M. Hobson, Phys. Fluids 8, 1967.
10. H. Petschek & S. Byron, Ann. Phys. 1, 1957.
11. I.I. Glass & W.S. Liu, J. Fluid Mech. 84, 1978.
12. P.E. Oettinger & D. Bershader, AIAA J. 5, 1967.
13. K.P. Horn, Stanford Univ. Rep. SUDAAR 268, 1966.
14. H.R. Griem, Spectral Line Broadening by Plasma, Academic press, 1974.
15. E.L. Rubin & S.Z. Burstein, J. Comp. Phys. 2, 1967.
16. P.J. Roache, Computational Fluid Dynamics, Hermosa pub., 1972.
17. G. Kamimoto & K. Teshima, Dep. Aero. Eng. Kyoto Univ. C.P. 32, 1972.
18. Y. Enomoto, J. Phys. Soc. Japan 35, 1973.
19. H. Mark, NACA TM 1418, 1958.
20. R.A. Strehlow & A. Cohen, J. Chem. Phys. 30, 1959.
21. L. Davies & J.L. Wilson, Phys. Fluids 13,1969.
22. E.W. Hubbard & P.C.T. de Boer, Phys. Fluids 12, 1969.

IONIZATION RELAXATION IN SHOCK TUBES TAKING INTO ACCOUNT A NON-MAXWELLIAN ELECTRON VELOCITY DISTRIBUTION

R. MEYER-PRUESSNER and F. DEMMIG

Institut für Plasmaphysik
Universität Hannover, Hannover, Germany

The two step model of ionization relaxation is extended to allow for a non-Maxwellian electron velocity distribution. In the initial stage of relaxation (small ionization degree) the electron-electron and the superelastic collisions are too infrequent to replenish the high energy tail of the distribution that is depleted by inelastic electron collisions leading to excitation/ionization. To investigate the non-Maxwell effects we utilized the electron velocity distribution of J.F. Shaw, M. Mitchner, and C.H. Kruger. Our computations, taking also into account the influence of boundary layers and shock attenuation, yield smaller population and electron densities, a qualitatively different variation of the electron temperature, and a relaxation time of the order of 10 % larger as compared to the Maxwell case.

The evaluation of relaxation measurements for the determination of cross section constants on the basis of a Maxwellian electron velocity distribution can result in considerable errors. Our results underline the necessity to include inelastic collision processes in the derivation of the velocity distribution function.

INTRODUCTION

While studying ionization relaxation of rare gases in shock tubes at Mach numbers about 9 one is confronted with the question whether or not the velocity distribution of the electrons is Maxwellian.[1,2,3] For plasmas with low ionization degree a deviation of the electron velocity distribution from a Maxwellian has been confirmed.[4-8] We deal with the same situation in the initial stage of relaxation where the collision frequency for electron-electron (e-e) collisions are too small to replenish the Maxwell-tail depleted by the inelastic electron collisions leading to excitation/ionization. Further, de-exciting collisions producing superelastic electrons will be infrequent in the initial stage characterized by small electron densities n_e since the corresponding rate is proportional to the product $n_e n_1$. As a result, the electron velocity distribution will be underpopulated in the high energy tail as compared to the Maxwellian.

In this case the rate coefficients have to be calculated with the non-Maxwellian electron velocity distribution function (NMEVD) yielding smaller rates and hence smaller population densities. The deviation from the Maxwellian will of course disappear towards the end of the relaxation zone where equilibrium is attained, but as a whole the relaxation time is larger as in the case of an entirely Maxwellian distribution function (MEVD).

NON-MAXWELLIAN ELECTRON VELOCITY DISTRIBUTION FUNCTION

The actual velocity distribution function of the electrons contained in a fluid particle travelling through the plug of a shock wave has to be determined by solving the Boltzmann equation. Since the non-equilibrium flow is computed taking into account the influence of shock tube boundary layers and the (weak) instationarity of the shock front,[9,10] the solution of the Boltzmann equation at each time step would have posed serious computation time problems. Thus we decided to make use of an approximate analytic solution of the Boltzmann equation derived by J.F. Shaw, M. Mitchner, and C.H. Kruger.[7] This distribution function is determined by the interplay of elastic *e-e*, *e-a*, *e-i*, *and inelastic e-a* collisions[*] and shows the aforementioned depression of the high energy electron population. In the derivation of the Shaw-Mitchner-Kruger distribution function only collisional transitions between the ground level *0* and the first excited level *1* for electron energies $E \geq E_1$ have been taken into account. This assumption is valid for the krypton shock waves in question since the first step of excitation with E_1 = 10.18 *eV* is rate controlling.

Instead of reproducing the rather complicated formulae we refer to figs. 1 and 2 which show this depression of the NMEVD f^0 relative to the Maxwellian f_{Max} depending on the parameters C_0 and P_2.

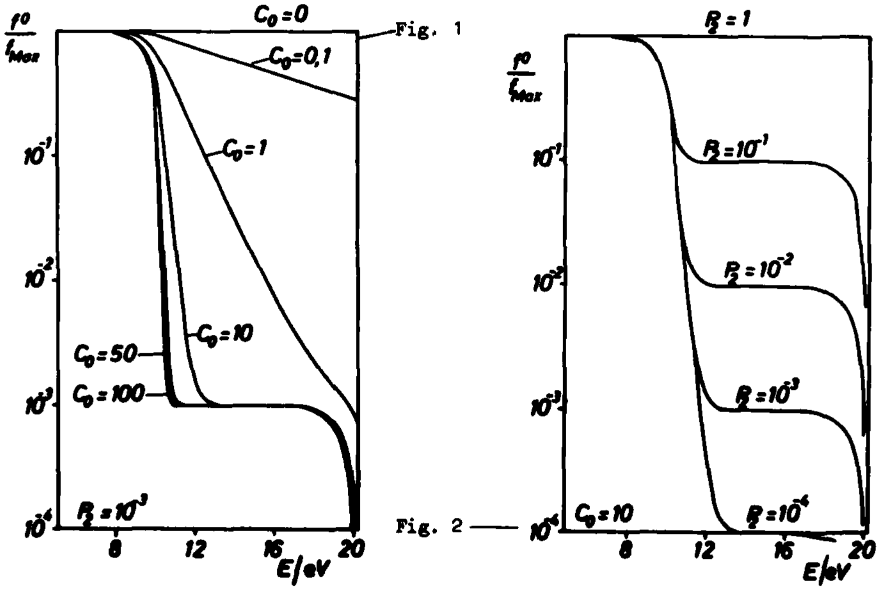
Fig. 1

Fig. 2

Values of the non-Maxwell electron velocity distribution f^0 relative to a Maxwellian f_{Max} for krypton (T_e = 9000 *K*).

---

[*] a: atom, e: electron, h: heavy, i: ion

The parameters C_0 and P_2 are given by

$$C_0 = \frac{kT_e}{E_1 + kT_e} \; \frac{\nu_{01}(E_1 + kT_e)}{\sum\limits_h \frac{2\, m_e}{m_h} \; \nu_{eh}(E_1 + kT_e) + 3\; \nu_{ee}(E_1 + kT_e)} \tag{1}$$

$$P_2 = \frac{n_1/n_0}{(n_1/n_0)^*} \quad \text{with} \quad (n_1/n_0)^* = \frac{g_1}{g_0} \; exp\left(- \frac{E_1}{kT_e}\right) \tag{2}$$

C_0 determines the influence of the energy consuming inelastic collisions (frequency ν_{01}) relative to all elastic collisions (ν_{eh}, ν_{ee}). The corresponding momentum transfer cross sections (needed only in the small energy range E_1+kT_e) have been taken from L.S. Frost and A.V. Phelps[11], $Q_{ea}^{(m)} = 2 \cdot 10^{-19}\; m^2$, and M. Mitchner and C.H. Kruger[12] (p 59, p 259, see also ref. 7, formulae (22) and (23)). Following G. Meinhold and W. Schöpper[13] the coulomb cross section has to be multiplied by a factor of 2 in order to achieve a better agreement of theoretical and experimental values of the electron densities in krypton shock waves. For the inelastic cross section Q_{01}^{ea} we made the usual assumption: $Q_{01}^{ea} = S_{01}^{a}\; (E - E_1)$.

In the initial zone of relaxation we find $C_0 >> 1$ since n_e and ν_{ee} are very small. With increasing electron density n_e and increasing e-e collision frequency ν_{ee} the value of C_0 approaches 0, i.e. f^0 approaches a Maxwellian (see figs. 3 and 4).

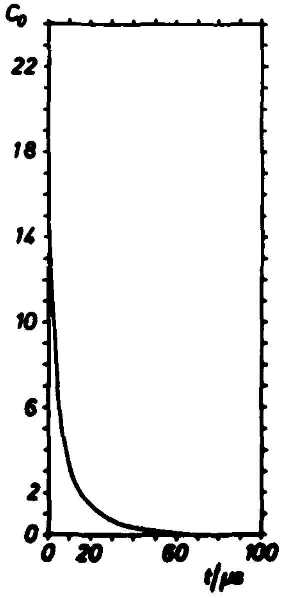

Fig. 3

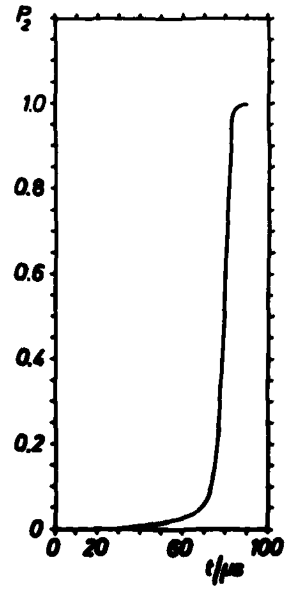

Fig. 4

Variation of the non-Maxwell parameters C_0 and P_2 with time at a fixed location of measurement at the shock tube.

The second parameter determining the shape of the electron velocity distribution function, P_2, expresses the deviation of the actual relative population density n_1/n_0 from the corresponding equilibrium value $(n_1/n_0)^*$ calculated with the electron temperature T_e. In the case $P_2 < 1$ the high energy region of the electron population drained by inelastic collisions $0 \rightarrow 1$ cannot be filled by superelastic electrons for which the rate is proportional to $n_e n_1$. For $P_2 = 1$ the electron velocity distribution will be Maxwellian since then the de-excitation collisions balance the excitation collisions.

Fig. 4 shows the variation of the parameter P_2 in the relaxation zone beginning with time $t = 0$ at the shock front. Since, according to figs. 3 and 4, C_0 takes large values and P_2 small values in the initial relaxation zone one concludes that in this region the electron velocity distribution f^0 will deviate significantly from the Maxwellian f_{Max} (compare figs. 1 and 2). At the end of the relaxation zone, which is attained after 80 µs, f^0 is of course Maxwellian.

At thermal electron energies the NMEVD shows virtually no deviation from the MEVD such that the concept of an electron temperature T_e has still a meaning, which otherwise simplifies the formulation of the electron energy equation and of the backward rates. J.F. Shaw, M. Mitchner, and C.H. Kruger derived their NMEVD for $kT_e \ll E_1$. This condition is fulfilled for our rare gas shock waves with Mach numbers about 9 or temperatures about 0.8 eV as compared to $E_1 \approx 10$ eV.

TWO-STEP MODEL AND CALCULATION OF RATE COEFFICIENTS

To study at first a simple and thus more transparent case we used the well known two step model with ionization energy E_{ion} and only one intermediate level E_1 which allows for the following reactions:

$$\mathrm{M + A \rightleftharpoons M + A^*; \qquad M + A^* \rightleftharpoons M + A^+ + e} \tag{3}$$

The collision partner M can be an atom A or an electron e, giving rise to the rates

$$\dot{n}_{1(a)} = k^a_{01}\, n_0^2 + k^a_{+1}\, n_0 n_e^2 - k^a_{1+}\, n_0 n_1 - k^a_{10}\, n_0 n_1 \tag{4}$$

$$\dot{n}_{e(a)} = k^a_{1+}\, n_0 n_1 - k^a_{+1}\, n_0 n_e^2 \tag{5}$$

$$\dot{n}_{1(e)} = k^e_{01}\, n_e n_0 + k^e_{+1}\, n_e^3 - k^e_{1+}\, n_e n_1 - k^e_{10}\, n_e n_1 \tag{6}$$

$$\dot{n}_{e(e)} = k^e_{1+}\, n_e n_1 - k^e_{+1}\, n_e^3 \tag{7}$$

where the coefficients k are the rate coefficients for excitation/ionization resp. de-excitation/recombination. The super- (sub-) scripts a and e denote atom and electron collisions, respectively. The subscripts 0, 1, and $+$ relate to the ground, intermediate, and ionization level.

In principle every rate coefficient k^e has to be calculated using the NMEVD. Since this function is practically identical with the Maxwellian in the range below $0.8 \times E_1$ containing the overwhelming majority of de-exciting and recombining electrons, the rate coefficients k^e_{10} and k^e_{+1} can be calculated on the basis of a MEVD in the usual manner via the principle of detailed balancing.[14,15] For the forward rate coefficients k^e_{01} and k^e_{1+} analytical expressions[15] have been obtained by integration over the Shaw-Mitchner-Kruger distribution function under the usual assumption of a linear cross section law. These two rate coefficients are much more complicated in form than in the MEVD case and are now dependent on the particle densities, too.

The rate coefficients k^a have the usual form determined under the assumption of a Maxwellian velocity distribution for the heavy particles with $T_a = T_i = T_h$. It goes without saying that a fluid particle travelling through the relaxation zone experiences a different temperature history in the NMEVD case as compared to the MEVD case (see fig. 6 and the following section). Consequently, the rate coefficients for atom-atom collisions k^a at a specific point of the relaxation zone will be different, too.

NONEQUILIBRIUM FLOW EQUATIONS AND ELECTRON ENERGY EQUATION

The non-equilibrium gas dynamical equations describing the (weakly) unsteady shock tube flow read[9,10],

$$\frac{D_0\rho}{Dt} + \rho\frac{\partial u}{\partial x} = R \tag{8}$$

$$\rho\frac{D_0 u}{Dt} + \frac{\partial p}{\partial x} = 0 \tag{9}$$

$$\rho\frac{D_0 h}{Dt} - \frac{D_0 p}{Dt} = 0 \tag{10}$$

$$\rho\frac{D_0(n_j/\rho)}{Dt} = \dot{n}_j(n_j,\ \rho,\ T_a,\ T_e) \qquad j = 1,\ e \tag{11}$$

where R is a mass loss term due to the boundary layer and $\dot{n}_j$ $(j = 1,\ e)$ the total rate for excitation/ionization. ρ denotes the mass density, u the flow velocity, p the pressure and h the specific enthalpy.

This set of equations has to be completed by the electron energy equation,

$$\frac{3k}{2}\frac{D_0 T_e}{Dt} + kT_e\frac{\partial u}{\partial x} = 3\frac{m_e}{m_a}(\bar{\nu}_{ea} + \bar{\nu}_{ei})\ k(T_h - T_e) - \frac{1}{n_e}\left(\dot{n}_{1(e)}\ E_1 + \dot{n}_{e(e)}\ E_{ion}\right) \tag{12}$$

The first term at the right hand side gives the energy gain of the electron gas by elastic collisions with all heavy particles while the second term represents the energy loss by inelastic electron-atom collisions leading to excitation/ionization. Comparing the Maxwell and the non-Maxwell case one concludes that on behalf of the differently evaluated rates $\dot{n}_{1(e)}$ and $\dot{n}_{e(e)}$ the values of the electron temperature T_e determined from this energy balance will differ. Strictly speaking, there is a more complicated interdependence since the collision frequencies ν_{ea} and ν_{ei} depend on T_e.

To find the energy weighted average of the momentum transfer collision frequency

$$\bar{\nu}_{ej} = n_j\ \bar{C}\ \bar{Q}_{ej}^{(m)} \qquad j = i,\ a \tag{13}$$

one has to calculate the average momentum transfer cross section $\bar{Q}_{ej}^{(m)}$ and the mean electron velocity $\bar{C}$. Since the value of the integral

$$\bar{C} = \int_{-\infty}^{+\infty} C\ f(C)\ d^3C \tag{14}$$

virtually is not influenced by the high velocity tail of the distribution function $f(C)$, i.e. where the NMEVD deviates substantially from the MEVD (see figs. 1 and 2), this integral can be evaluated with a Maxwellian to give

$$\bar{C} = \left(\frac{8\,kT_e}{\pi m_e}\right)^{1/2} \tag{15}$$

For $\bar{Q}_{ea}^{(m)}$ we used a polynomial approximation to the data given by R.S.Devoto.[16]

RESULTS

The values of the parameters C_0 and P_2 for krypton shock waves with Mach numbers in the range of 9 indicate a distinct deviation of the electron velocity distribution from a Maxwellian in the initial relaxation zone. To show the influence of the NMEVD in more detail figs. 5 and 6 reproduce the theoretical

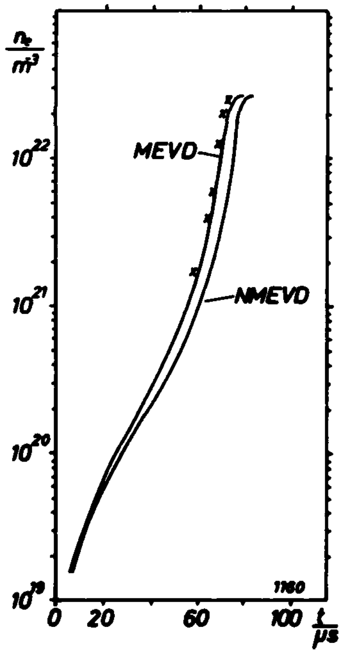

Fig. 5

Electron density profiles in the relaxation zone of a krypton shock wave with average Mach number of 10.44. Solid curves computed on the basis of the non-Maxwellian NMEVD and the Maxwellian MEVD, respectively. Crosses: experimental n_e values (P_1 = 7.92 Torr, T_1 = 302.7 K).

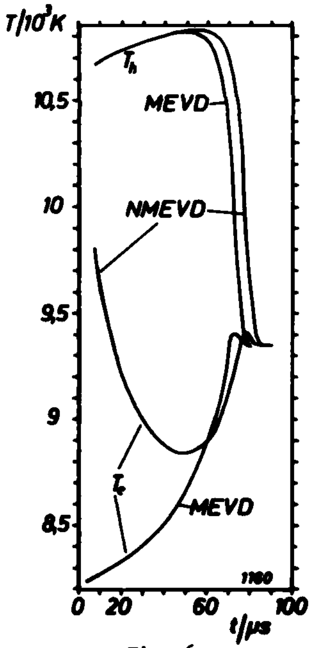

Fig. 6

Computed T_h and T_e profiles referring to the conditions of fig. 5.

values of n_e, the gas temperature T_h, and the electron temperature T_e computed on the basis of a NMEVD resp. MEVD at a fixed location using the *same set* of cross section constants ($S^a_{01} = 1.5 \cdot 10^{-5}$, $S^a_{1+} = 0.5$, $S^e_{01} = 1.1 \cdot 10^{-2}$, $S^e_{1+} = 4\ m^2/Ws$). The most prominent difference between these two cases is a relaxation time approximately 15 % longer for the NMEVD case. The electron density n_e (NMEVD) is smaller than n_e (MEVD) since the collisions able to fill the excited level are much less frequent in view of the strong drain of high energy electrons from the tail of the distribution. Also, there is a striking difference in the behaviour of T_e in the initial relaxation zone; T_e (NMEVD) there is clearly higher than T_e (MEVD). The flow velocity u does not differ very much for the NMEVD and MEVD (see fig. 7). This is an integral effect since the flow is strongly influenced by the ionization processes only in the final relaxation zone where the ionization enthalpy becomes important (maximum ionization degree about 2 %).

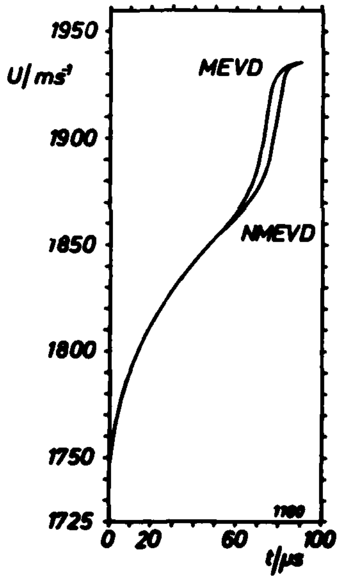

Fig. 7

Flow velocity profiles referring to the conditions of fig. 5.

In contrast to the above shock wave with an average Mach number of 10.44 a weaker shock wave with average Mach number 8.28 does not lead to equilibrium though the time scale of fig. 8 extends to 250 μs, i.e. 0.44 m downstream. Again, the electron density n_e (NMEVD) is smaller than n_e (MEVD). Similar to n_e the density n_1 of excited atoms reflects the difference between the NMEVD and the MEVD case, which amounts to 100 % after 130 μs (see fig. 9). T_h (NMEVD) is virtually identical with T_h (MEVD) since the ionization degree is smaller than 10^{-4} such that the flow acts like a heat bath. However, as T_e (NMEVD) initially follows closely T_h, T_e (MEVD) is apparently less than T_h because immediately behind the shock front the inelastic Maxwellian rate $\dot{n}_{1(e)}$ is greater than the corresponding non-Maxwellian one and hence the electron gas is cooled more effectively (compare fig. 10).

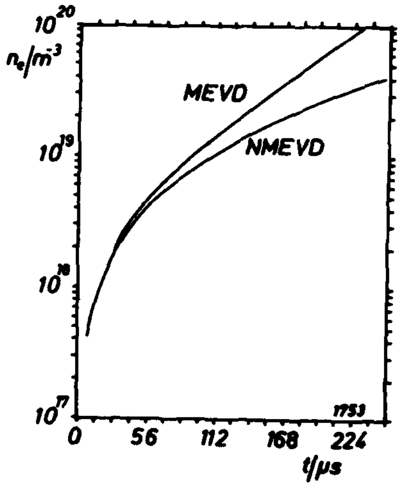

Fig. 8

Electron density profiles in the relaxation zone of a krypton shock wave with average Mach number of 8.28 based on a non-Maxwellian NMEVD and a Maxwellian MEVD, respectively. Equilibrium is not attained (P_1 = *40.1 Torr*, T_1 = *294.2 K*).

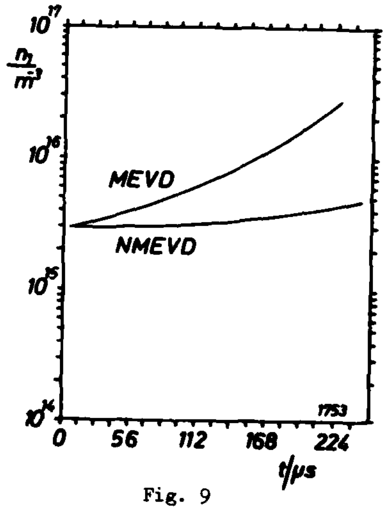

Fig. 9

Profiles of excited particle density n_1 referring to the conditions of Fig. 8. The initial increase of n_1 within a fraction of a microsecond is not displayed.

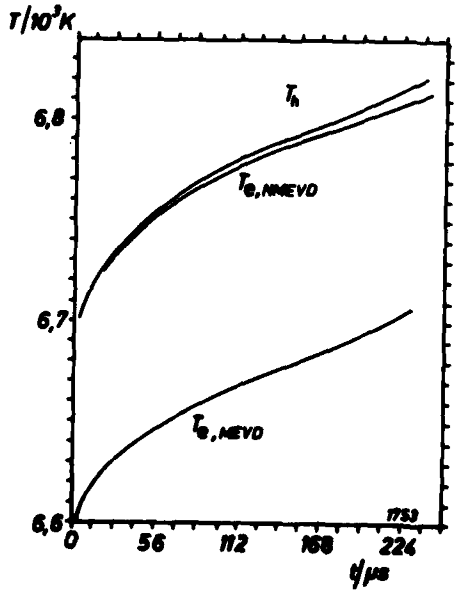

Fig. 10

Temperature profiles referring to the conditions of Fig. 8. The gas temperature profiles based on the MEVD and the NMEVD are virtually identical.

DISCUSSION

To discuss an important implication of our findings we assume for the moment that the values of the boundary layer parameter[9,10] and all relevant cross sections are reliably known. Only the cross section constant S^a_{01} is to be determined by comparison of experimental and theoretical n_e values as shown in fig. 5. As stated above, a value of $S^a_{01} = 1.5 \cdot 10^{-5}$ chosen to fit the *Maxwell* n_e*-curve* to the experimental points (crosses) leads to a distinctly deviating non-Maxwell n_e-curve. Since there is a clear theoretical evidence for a deviation from the Maxwellian electron velocity distribution at small ionization degrees, which has also been experimentally confirmed in glow discharges, one concludes that this value of S^a_{01} has to be corrected. Hence the evaluation of relaxation measurements on the basis of a Maxwellian can result in considerable systematic errors.

If one interpretes the experimental n_e-curve of fig. 5 on the basis of a NMEVD then an additional computation shows that the cross section constant S^a_{01} has to be enlarged from $1.5 \cdot 10^{-5}$ *to* $2.0 \cdot 10^{-5}\ m^2/Ws$ in order to fit the *NMEVD* n_e*-curve* to the experimental points. We obtained a similar result evaluating the n_e values of experiments at lower Mach numbers in the range of 8. The theoretical NMEVD-curve seems to fit the experimental one tendentially better in some experiments. However, the present experimental material is not yet sufficient to give an additional support to the evidence of a NMEVD since, in contrast to the clear-cut assumption made above, the values of the boundary layer parameter and the cross sections are known only to within fairly large error limits.

The measurements at low electron densities ($n_e \leq 3 \cdot 10^{19}\ m^{-3}$) have been performed by 70 GHz microwave interferometry.[17] Measurements with a HCN-laser interferometer are in preparation in order to reach a n_e-region where the non-Maxwellian effects are more pronounced (see fig. 8). Also, our shock tube group plans to perform absorption experiments to determine the electron collision frequency which should be suited too to discriminate between the non-Maxwell and the Maxwell case in the initial relaxation zone.

ACKNOWLEDGMENTS

We thank Mr. J. Meißner for carrying out the computations and Mr. W. Bötticher and the shock tube group of our institute for numerous stimulating discussions.

REFERENCES

1. L.M. Biberman, V.S. Vorob'ev, I.T. Yakubov, Soviet Physics JETP 29, 1070 (1969).
2. L.M. Biberman, A. Kh. Mnatsakanyan, and I.T. Yakubov, Soviet Physics USPEKHI 13, 728 (1971).
3. H. Dreicer, Phys. Rev. 117, 343 (1960).
4. J. Oxenius, Z. Naturforsch. 25 a, 101 and 1302 (1970).
5. H.W. Drawin, Pure & Appl. Chem. 48, 133 (1976).
6. S. Suckewer, Z. Physik 247, 354 (1971).
7. J.F. Shaw, M. Mitchner, C.H. Kruger, Phys. Fluids 13, 325 (1970).
8. E.C. Shoub, Astrophys. J. Suppl. 34, 259 and 277 (1977).
9. F. Demmig, Shock tube and shock wave research, 11. Shock tube symposium, 119, Seattle (1977).
10. F. Demmig, Computer Phys. Commun. 14, 7 (1978).
11. L.S. Frost and A.V. Phelps, Phys. Rev. 136, A 1538 (1964).
12. M. Mitchner and Ch. H. Kruger, Partially ionized gases, New York (1973).

13. G. Meinhold, W. Schöpper, Shock tube and shock wave research, 11. Shock tube symposium, 115, Seattle (1977).
14. L. Bergmann, F. Demmig, Z. Naturforsch. 32 a, 1245 (1977).
15. R. Meyer-Prüßner, Diplomarbeit, Universität Hannover (1978).
16. R.S. Devoto, AIAA J. 7, 199 (1969).
17. Th. Reese, E. Scholle, unpublished report, Institut für Plasmaphysik, Universität Hannover (1978).

ELECTRON VELOCITY DISTRIBUTION IN AN EXPANDING FLOW OF SHOCK HEATED IONIZED ARGON

HEINZ J. THOR and HANS GRÖNIG

Stosswellenlabor, Institut für Luft- und Raumfahrt
Rheinisch-Westfälische Technische Hochschule, Aachen, Germany

A diagnostic technique for measuring the velocity distribution of electrons in an ionized argon flow has been developed. The argon plasma is generated by the reflected shock in a hydrogen driven shock tube ($7<M_S<10$; $5<p_1/\text{mbar}<26$, i.d. 14 cm) and expanded through a nozzle (dia. 1-1.5 mm) in the end wall. The centerline of the expansion flow is sampled by a movable skimmer which forms a molecular beam. The velocity distribution of the electrons in this beam is registered by a magnetic analyzer with an electron multiplier attached to it. The magnetic field of the analyzer is swept during the test time and the whole velocity distribution function, i.e. the electron current distribution, is scanned. The diameters of the nozzle and skimmer together with the characteristics of the analyzer allow to neglect the divergence of the electron flow. Under these assumptions the parameters of the distribution are evaluated. The comparison of the evaluated electron temperatures for different values of the nozzle-skimmer distance shows good agreement with a theoretically predicted temperature decay in the expansion flow. Constant reservoir conditions are terminated by the effects of interation between the reflected shock and contact surface. During the test time the influence of the thermal wall boundary layer is negligible.

INTRODUCTION

The knowledge of the electron velocity distribution promises better understanding of ionization processes and phenomena of ionized gas flow. By the development of a magnetic analyzer it was possible to measure directly the precursor electron distribution in front of electromagnetically driven strong shocks[1]. During each run of these experiments the magnetic field was kept constant and only one point of the distribution could be obtained. For the experiments described in this paper, however, a different approach was chosen. Within the test time (600-700μsec)

the magnetic field was varied and the velocity distribution was registered by counting the electrons leaving the analyzer.

EXPERIMENTAL EQUIPMENT AND MEASURING TECHNIQUE

The experiments were conducted using the region behind the reflected shock as plasma source. A conventional, pressure driven shock tube (i.d. 14 cm) with a double diaphragm chamber was employed. Hydrogen was used as driver gas. Incident shock Mach numbers varied from 7 to 10, using argon as working gas with pressures from 5 to 26 mbar. Piezo-electric pressure probes together with 10 MHz-counters were applied for registering shock speeds.

Attached to the end wall of the shock tube is the molecular beam apparatus. Figure 1 shows a schematic diagram of the device.

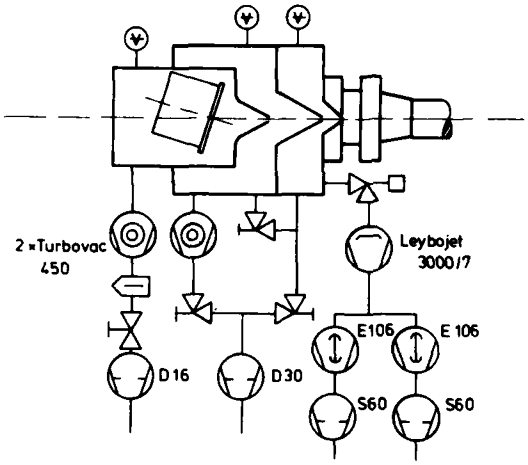

Fig. 1
Schematic diagram of molecular beam apparatus with pumping system

The skimmer in the first stage adjacent to the end wall is movable on the axis of the system. The diameters of the nozzle throat, the skimmer and collimator inlets were calculated to match the pumping capacity available for these experiments[2]. The first stage was pumped by a 3000 l/s diffusion pump, the second and third by two 450 l/s turbomolecular pumps. With a nozzle throat diameter of 1.5 mm and a pressure in the shock tube of $p_1=26$ mbar the first stage was kept at a level of about $2\cdot 10^{-3}$ mbar. The first stage was buffered by a dump tank not shown in the diagram of approximately 300 l to reduce the pressure rise during the test time after the shock reflection. The skimmer inlet diameter was 3 mm, the inlet to the analyzer chamber 4 mm. The pressure in this chamber was about $5\cdot 10^{-6}$ mbar. The orifice in the end wall is closed after each run by a solenoid valve.

The magnetic analyzer utilizes the properties of a homogeneous magnetic field to focus electrons onto the exit aperture of the device[3]. Figure 2a shows the trajectory of an electron that enters the magnetic field through the entrance aperture. The exit of the analyzer (on the right-hand side of Fig. 2b) is located where the trajectory with entrance angle α crosses the axis. The housing of the analyzer is built as a cage of μ-metal bars to shield disturbing fields. The field coil is wound on a hollow cylinder of Teflon whose wall is also perforated to ease evacuation of the system.

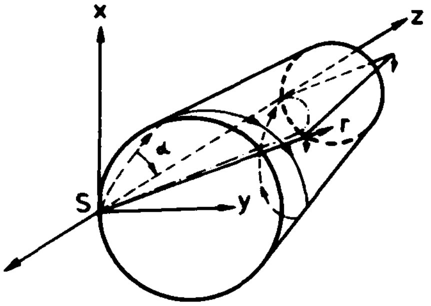

Fig. 2a. Electron trajectory

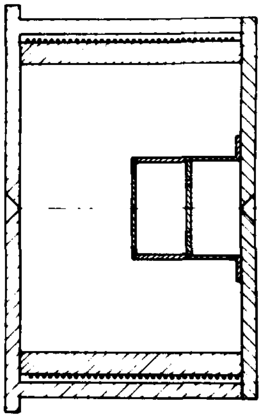

Fig. 2b. Analyzer housing with field coil

The electron crosses the axis for a value of z_0 given by the expression[3]

$$z_0 = \pi \cdot D \cdot \cos\alpha \qquad \text{I}$$

with

$$D = \frac{2mv}{eB} \qquad \text{II}$$

With the exit aperture at a fixed distance z_0 from the inlet and for a given mass/charge ratio m/e only those electrons can reach the exit whose velocity v satisfies Eq. II for a given value of the magnetic field B. The deviation $d\alpha$ of the entrance angle is limited by two annular slits. These slits also exclude electrons with multiple revolutions. The resolution obtained with this configuration is $v/\Delta v = 225$.

By variation of the magnetic field, i.e. the current in the field coil, the whole velocity distribution of the electrons at the entrance of the analyzer can be scanned. The electrons leaving the exit aperture are accelerated by a potential of 300 V to hit the entrance of the electron multiplier. In this energy range the multiplier has its highest detection efficiency.

In order to test the whole system a glow discharge as stationary electron source was used (Fig. 3). The distribution of the electron current dj together with the coil current I is shown in Fig. 4. The curve of dj is obtained by a frequency to voltage conversion of the counted electrons per unit time.
A different way to display the distribution had to be developed for the experiments carried out with the shock tube. Because of the necessary fast changing of the magnetic field the μ-metal cage caused nonlinearities and a time delay in the variation of

the field vs. the coil current. Therefore the field was measured by an induction coil with a subsequent RC-integration. The output of the integrator is proportional to the magnetic field. This signal was used for the vertical deflection of the oscilloscope.

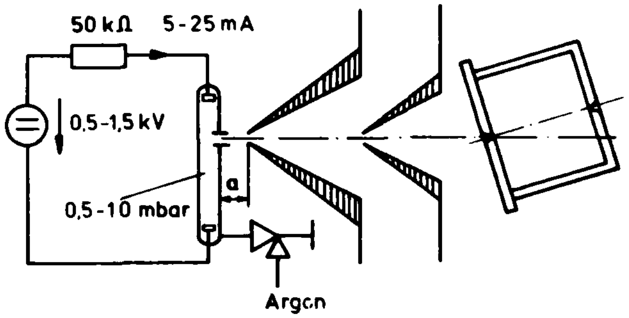

Fig. 3
Schematic arrangement of measurements with a continuous glow discharge

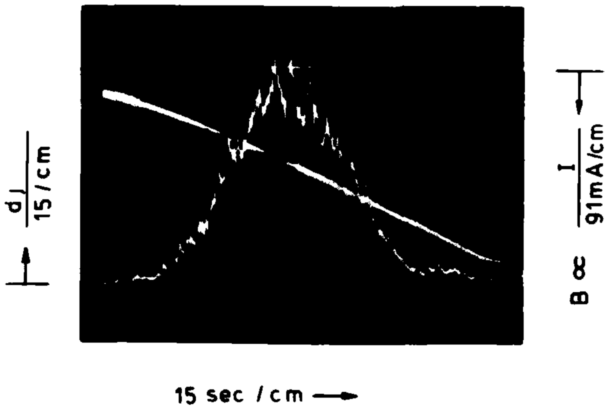

Fig. 4
Measurement of electron current distribution and coil current vs. time

The output of the electron multiplier is amplified and fed to the z-input of the oscilloscope. Thus the beam of the scope is intensity-modulated for each registered electron by a light dot. In this way the electron density is displayed vs. the magnetic field, i.e. the electron velocity (Fig. 5).

To facilitate the evaluation of the display obtained in this manner the time dependence of the magnetic field should be linear in the section that corresponds to the velocity range under examination. By biassing the magnetic field with an appropriate current a suitable part of the transient response is adjusted to cover this range. The marker in Fig. 5 shows the point where the magnetic field is zero. With alternating triggering of the two channels of a dual beam oscilloscope (Tektronix 556) it is possible to stretch the time scale of the display and obtain a high resolution.

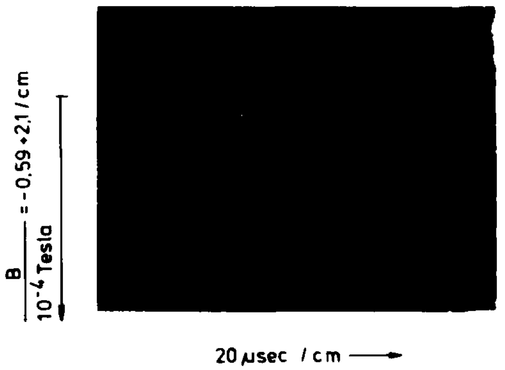

Fig. 5
Display of the electron current distribution. Registered electrons shown as intensity modulation of the magnetic field signal (M_S= 9.15, p_1 = 7 mbar) Δ:B = 0

MEASUREMENTS AND RESULTS

Under the assumption of a Maxwellian velocity distribution of the electrons at the entrance of the skimmer, the measured electron current distribution component in x-direction, the axis of the system, is given by

$$dj(v_x) = n \cdot \sqrt{\frac{m}{2\pi kT}} \cdot v_x \cdot e^{-\frac{m}{2kT}(v_x - v_D)^2} \cdot dv_x \qquad \text{III}$$

with the number density n, mass m, temperature T, velocity v_x and superposed drift velocity v_D. This represents the measured current density if one can consider the sampled electron beam as one-dimensional. The geometry of the skimmer-collimator configuration together with the characteristics of the analyzer allow only electrons moving almost parallel to the axis of the skimmer to reach the multiplier; thus the divergence is negligible.

For the determination of the parameters by the method of least squares Eq. III is developed into a first order power series. The set of linear equations obtained in this manner is solved by matrix inversion. The diagonal elements of this matrix allow to calculate the inherent errors in the parameters due to data scattering[4].

The curves in Fig. 6 show the best fit to measurements of the electron velocity displayed in this case as energy distribution obtained from the glow discharge. Distributions at different distances from the orifice are plotted to prove the applicability of the experimental set up and the numerical evaluation procedure.

An example of the evaluation of the shock reflection experiment shown in Fig. 5 presents Fig. 7. Due to the low number of electrons counted per unit time, in the order of 5 to 10 per 20 μsec, the deviation from the best fit is larger than in the measurements carried out with the stationary discharge.

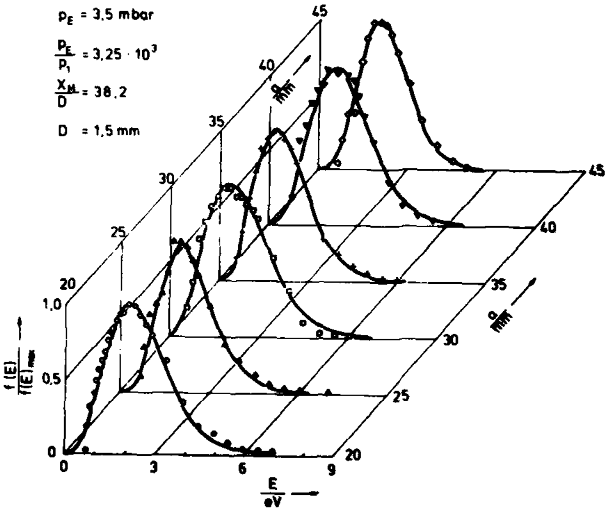

Fig. 6
Electron energy distribution in expansion flow from a glow discharge.
p_E-discharge pressure
D-orifice diameter
$\frac{x_M}{D}$ = location of Mach disk

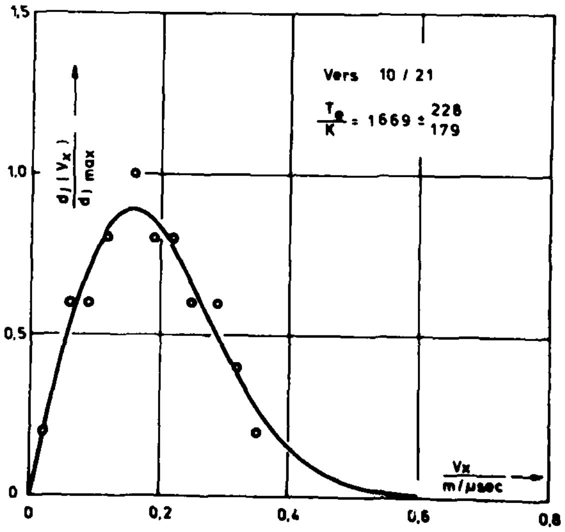

Fig. 7
Electron current density distribution measurements with curve of best fit

During this experiment the shock heated. partially ionized gas expands through the end wall orifice into the molecular beam system. This situation is a typical example of a decaying plasma. In a plasma at rest with adequate density the dominating recombination process is composed of triple collisions between electrons and ions which convert ions to excited atoms:

$$A^{*} + e \leftarrow A^{+} + e + e \qquad (1)$$

The ground state is then reached by collisions or emission of radiation:

$$A + e \leftarrow A^{*} + e \qquad (2)$$

$$A + h\nu \leftarrow A^{*} \qquad (3)$$

The energy transferred to the electrons by the process in Eq. 2 causes the temperature of the electron gas to remain higher than the neutral gas temperature. The loss of energy due to radiation depends on the optical thickness of the plasma. In the optically thick case the radiation is absorbed within the plasma, whereas it is lost in the optically thin case.

Based on this model of a decaying plasma at rest the influence of the flow on the recombination parameters in a nozzle and a free jet expansion was studied by Talbot et al.[5,6]. Flow parameters for the axis of the free jet were calculated with the model of orifice flow[6].

These calculations for an expanding plasma flow show a slower decrease of the temperature of the electrons than that of the atoms and ions. There is no observable difference in the components of electron temperature parallel and normal to the flow direction, since the collision frequency of electrons is high enough to maintain equipartition. Differences can be observed in ion- and atom temperature. This difference is influenced by the collision frequency in the flow source. By high collision frequencies the deviation from equipartition is reduced.

The results of the shock tube measurements were compared with the calculations of Chou and Talbot[6] carried out for an argon source flow expansion of a partially ionized gas in the limits of optically thick and thin plasma (Fig. 8).

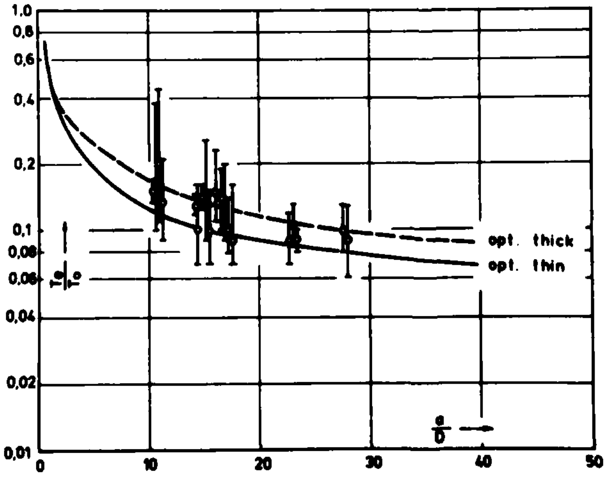

Fig. 8
Measured electron temperatures in expanding argon plasma compared to theory[6]

The evaluated electron temperatures were related to the reservoir temperature T_0, i.e. the temperature behind the reflected shock. This temperature was calculated as a function of the incident Mach number assuming thermal equilibrium[7]. The agreement of the measurements with theory is satisfying within the error bars which are due to the low count rates.

The plasma jet leaving the orifice in the end wall is influenced by the temperature boundary layer that develops there. The heated gas is cooled down by the wall which remains at room temperature. Assuming that the outflowing gas sample comes from a hemisphere with its center at the orifice, the center stream line will become influenced by the growing temperature boundary layer when its thickness gets equal or larger than the radius of the hemisphere. A comparison of the layer thickness[8] with the radius of the gas volume [9,10] shows that, during the test time, this can be neglected.

The presented measuring method shows the possibility to sample the electron velocity distribution in a flowing plasma. Difficulties that are inherent with electro-static probes are avoided.

ACKNOWLEDGMENT

The authors acknowledge the support provided for this project by the "Deutsche Forschungsgemeinschaft".

REFERENCES

1. W. Limberg: Magnetischer Energieanalysator für langsame Elektronen am inversen Pinch. Dissertation, RWTH Aachen, (1974)
2. B.W. Schumacher: Dynamic Pressure Stages for High-Pressure/High-Vacuum Systems. 1961 Trans. 8th Vac. Symp. and 2nd Int. Congress. Pergamon Press, Oxford, (1962)
3. T. R. Gerholm: Beta-Ray Spectroscopes, in Handbuch der Physik, Bd. 33, Korpuskularoptik, Hrsg. : S. Flügge, Springer-Verlag, Berlin, (1956)
4. R. Zurmühl: Praktische Mathematik für Ingenieure und Physiker. Springer-Verlag, Berlin, 323 (1965)
5. L. Talbot, Y. S. Chou, F. Robben: Expansion of a Partially-Ionized Gas Through a Supersonic Nozzle. Rept. AS-65-14 (1965), Univ. of California, Berkely, Calif.
6. Y. S. Chou, L. Talbot: Source Flow Expansion of a Partially Ionized Gas into a Vacuum. AIAA Journ., 5, 2166 (1967)
7. W. A. Menard, T. E. Horton: Shock-Tube Thermochemistry Tables for High-Temperature Gases. Techn. Rep. 32-1408, Vol. III, Calif. Inst. of Techn., Pasadena (1970)
8. H. Oertel: Stoßrohre, Springer-Verlag, Wien, 488 (1966)
9. J. B. Anderson: Molecular Beams from Nozzle Sources in: Molecular Beams and Low Density Gasdynamics. Ed.: P. P. Wegener, M. Dekker, New York, (1974)
10. K. R. Fritz: Zeitaufgelöste massenspektrometrische Untersuchungen der Kinetik schneller homogener Reaktionen hinter reflektierten Stoßwellen. Dissertation, RWTH Aachen, (1976)

IONIZING SHOCK STRUCTURE FOR A STRONG SHOCK WAVE IN ARGON

HIROKI HONMA and HIRO YOSHIDA

Department of Mechanical Engineering
Chiba University, Chiba, Japan

The effects of the charged particles on the internal structure of the shock front are investigated for 10-13 km/s shock waves in argon for the initial pressure p_1 = 10 and 20 Pa. A free piston double diaphragm shock tube is used to produce strong shock waves. The time characteristics for the ion probe current, the continuum and spectrum emission of light, and the pressure are compared with each other. The rise time t_0 of the probe current and the photo-emission is measured to be 0.1-0.5 μsec, and the corresponding shock thickness may be considered as 2-5 mm, which is the same order of magnitude as the estimated thickness of the neutral shocks. The value of $p_1 t_0$ is found to decrease with increase of the shock speed. The internal structure of the front may be considered as affected by the charged particles

INTRODUCTION

This paper discusses some features of ionizing shock structure for a strong shock wave in argon. As well known, for comparatively weak shocks (for the shock speed below 6-7 km/s in argon), the shock front structure is controlled by the dissipative processes of neutral atoms, and then most ionization reaction processes occur in the relaxation zone formed behind the shock front[1~4].

With increase of the shock strength, the number density of the charged particles increases within the front due to the effects of precursor ionization , electron thermal conduction, diffusion, radiation heating, and so on. Furthermore, for extremely strong shocks, the gas ahead of the shock becomes considerably ionized due to thermal radiation effects, and therefore, the shock front structure becomes controlled by the dissipative processes of the charged particles[5].

In the intermediate case, it may be expected that the internal structure of a shock wave changes from the atom-controlled structure to the ion-controlled structure with increase of the shock speed. This transitional behaviour of the shock structure is a matter of our primary concern.

In the present report, the effects of the charged particles on the internal structure of the shock front are investigated for 10-13 km/s shock waves. An experimental study is made, using a free piston double diaphragm shock tube. The time characteristics of the ion probe current and the photo-emission at the front are investigated.

EXPERIMENTAL APPARATUS AND INSTRUMENTATION

The free piston double diaphragm shock tube has been used as a powerful device for producing strong shocks[6,7]. Figure 1 shows a schematic diagram of our shock tube. It consists of the high-pressure chamber of 100 mm internal diameter and one meter long, the compression chamber of 61.8 mm internal diameter and 3 meters long, the buffer chamber of 50 mm internal diameter and 1.5 meters long and the low-pressure chamber of 40x40 mm and 3.5 meters long. The compression chamber has been used as a piston tube for NO kinetics and laser research[8,9].

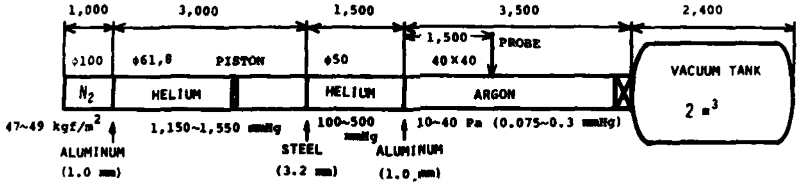

Figure 1. Schematic diagram of the shock tube.

The bottled nitrogen gas is supplied to the high-pressure chamber, and gives a natural bursting of the unscribed alminum diaphragm of 1 mm in thickness at the pressure of 47-49 kgf/cm^2. The high-pressure nitrogen gas drives the free piston along the tube. The piston is made of stainless steel, and has piston rings which are made of copper resined teflon. It is 119 mm in length and 2.36 kgf in weight, and has a hemisphere nose, which protects the piston from its deformation at the clash against the end of the tube. The initial pressure of the helium gas in the compression chamber is chosen to minimize the impact on the end wall between 1,150 and 1,550 mmHg. The cross scribed steel diaphragm of 3.2 mm in thickness is installed between the compression and buffer chambers, and burst at the pressure of about 680 kgf/cm^2 by the compressed helium.

The maximum shock Mach number measured at the end of the buffer chamber is about 6.1 for the initial pressure of 100 mmHg in helium[10]. The cross scribed aluminum diaphragm of 1 or 1.5 mm in thickness is installed between the buffer and low-pressure chambers. The preliminary study[10] shows that the maximum and constant shock speed can be attained at a distance of about 1.5 m from the diaphragm. Therefore, we choose this place as a test section.

Schematic diagrams of the test section are shown in Figures 2 (a) and (b) , which correspond to two series of experiment. In the first, the plastic optical fiber (0.5 mm O.D., 30 cm long), the single probe and the piezoelectric transducer (PCB 1124A) are installed at the test section. The photo-emission of the high temperature argon is guided to the photomultiplier (TOSHIBA MS-9S) through the optical fiber and the optical filter (TOSHIBA V-VIA), which transmits the light between 3,800 and 4,500 Å in wave length. The response time of the system is measured by use of the light pulse of the discharge tube, and found to be less than 10 nsec.

The electrode of the probe is a tungsten wire with 0.3 mm O.D. and 2.7 mm long, and settled at the center of the test section, perpendicular to the flow. The probe circuit is a simple one, as shown Figure 1 (a). The side wall of the shock tube is grounded. The applied voltage is kept constant (5 V), while the load resistance is changed (1Ω - 50KΩ). The response time of the system of the circuit is measured to be 20-50 nsec for a step input of the voltage.

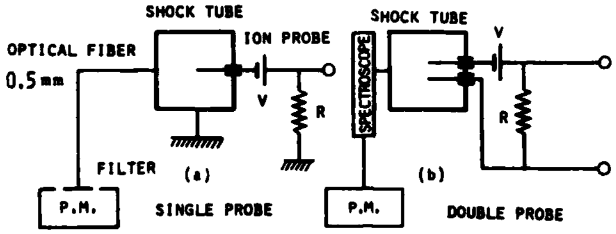

Figure 2. Schematic diagrams of instrumentation at the test section.

In the second series, the glass window of the aperture of 3 mm is installed on the side wall, and the monocromatic emission of light is observed by use of a plane grating spectrometer (RIKO MC-30). The width of the incident slit is 50 μm. The double probe is also installed at the section. The electrodes of the probe are also tungsten wires with 0.3 mm O.D. and 2.7 mm long, and their spacing is about 1 mm.

EXPERIMENTAL RESULTS AND DISCUSSION

Figure 3 shows the output signals of the ion probe, the photomultiplier and the pressure transducer. All signals are once memorized by the 2-channel transient recorder (BIOMATION 8100, sampling time: 1-ch, 10 nsec; 2-ch, 100 nsec), and displayed on the oscilloscope.

(*a*) *Two Ion Probes*: Two single probes are installed at the same time in the test section. The load resistances are chosen as 50 KΩ and 5 Ω, respectively. For case of high R, the precursor ionization can be observed, and the output signal reaches an uppermost limit after the arrival of the shock wave. For case of low R, pulse signal can be seen at the front. The pulse width is about 2 μsec. It can be estimated that the raising and falling portions of the pulse correspond to the shock front and the contact surface, respectively. It should also be noted that the raising behaviour of the signal for 5 Ω is the same as that for 50 KΩ. Both signals raise up at the same time regardless of the load resistance. This suggests that the probes primarily respond to the generated electric field at the shock front, while they respond to the ion number density in the other region.

(*b*) *Pressure and Ion Probe*: The characteristic response time of the pressure probe is estimated to be one μsec. The pressure response starts at the peak of the ion probe output. This correspondance also suggests that the raising portion of the probe signal corresponds to the shock front.

(*c*) *Ion Probe and Photo-emission*: The trace of the photo-emission pulse is very similar to the trace of the ion probe pulse near by the front. These behaviours of both signals seem to illustrate that the ion density rapidly increases at the raising portion of the pulse, and then decreases at the falling portion due to the fast radiation cooling.

(*d*) *Ion Probe (Single)*: This is a fine time-resolving record to observe the details of the raising portion of the pulse. The same record is displayed in three time scales.

(*e*) *Photo-emission (Continuum)*: This is a fine time-resolving record

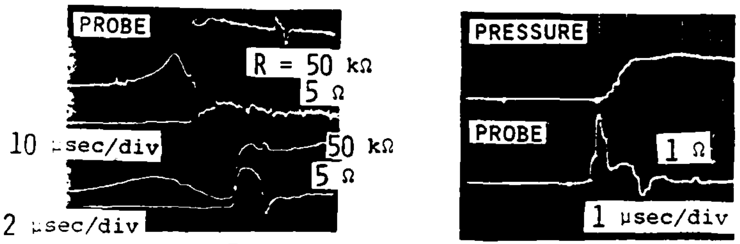

(a) SINGLE 5 V
P_1 = 11.6 P_a
U_s = 10.9 km/sec

(b) SINGLE 5 V
P_1 = 11.1 P_a
U_s = 11.0 km/sec

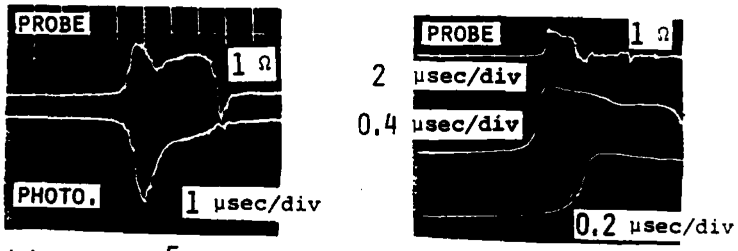

(c) SINGLE 5 V
P_1 = 10.0 P_a
U_s = 12.5 km/sec

(d) SINGLE 5 V
P_1 = 23.2 P_a
U_s = 12.0 km/sec
t_0 = 0.135 μsec

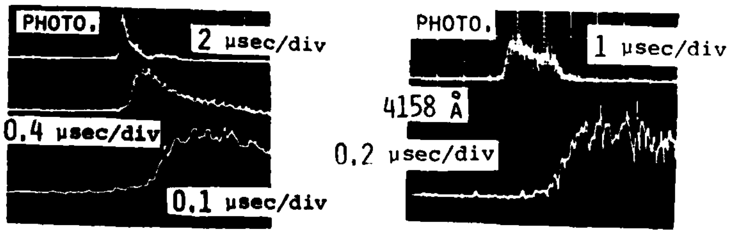

(e) P_1 = 20.0 P_a
U_s = 12.2 km/sec
t_0 = 0.135 μsec

(f) P_1 = 19.6 P_a
U_s = 11.5 km/sec
t_0 = 0.23 μsec

Fig. 3 Output signals of the ion probe, the photomaltiplier and the pressure transducer. P_1 initial pressure, U_s shock speed.

for photo-emission for a case of continuum observation.

(f) *Photo-emission (4158 Å)*: This is a case of monocromatic observation at 4158 Å (Ar I). The essential difference cannot be observed for both cases of photo-emission signals.

For the raising portion of the output signals of the ion probes and the photomaltiplier, we define the characteristic rise time t_0 as shown in Figure 4. The digital data stored in the transient recorder are used for plotting. The values of t_0 thus obtained are shown in Figures (d), (e) and (f).

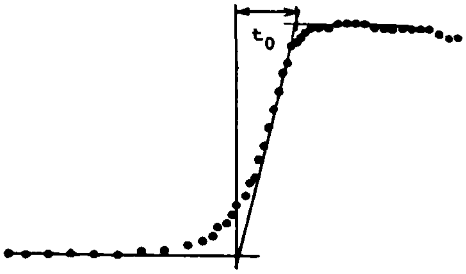

Fig. 4 The definition of the rise time t_0.

In Figure 5, the rise time of the probe current (single probe) is plotted against the shock speed Us for the initial pressure of 10 and 20 Pa. The solid lines L = 2 mm and 5 mm denotes the curves for the time required for the passage of the length L. Therefore, if the raising portion of the probe signal corresponds to the passage of the shock front, the shock thickness may be considered to be measured as 2-5 mm. As shown in Figure 5, the rise time t_0 decreases with increase of the shock speed, and can be grouped in accordance with the initial pressure as shown by the broken lines.

Figure 6 shows a plot of p_1t_0 as a function of the shock speed for all cases of the probe current and the photo-emission. The solid lines denote the curves for $\lambda_1/\delta s$ = const., where λ_1 is the mean free path of the neutral atoms ahead of the shock wave and δs is the shock thickness. According to the existing results for the strong neutral shocks[11 13], we have $\lambda_1/\delta s \simeq 0.2$. That is, the measured thickness of the front is the same order of magnitude as the thickness of the neutral shock. Furthermore, the measured thickness can also be estimated to be the same order of magnitude as a fully ionized shock[14]. The value of p_1t_0 tends to decrease with increase of the shock speed, though the data are scattered.

In summary, the raising portion of the probe current and the photo-emission can be considered as shock front. Their time characteristics seem to show that the internal structure of the front is considerably affected by the charged particles, though the extended experimental works should be done to assure the results described above.

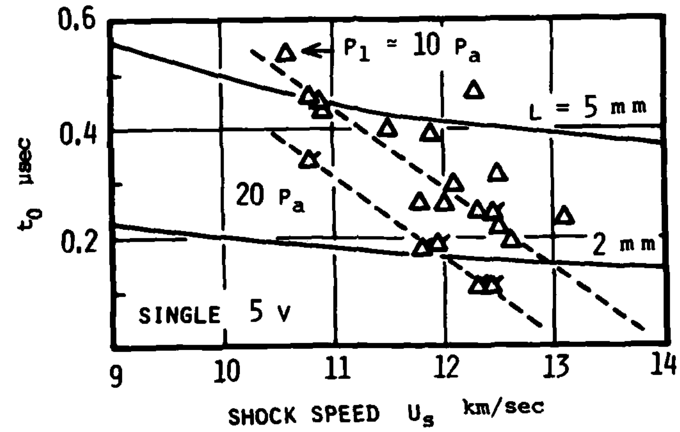

Fig. 5 The rise time t_0 of the probe current(single) as a function of the shock speed U_s. [△ 10 Pa, △̸ 20 Pa.]

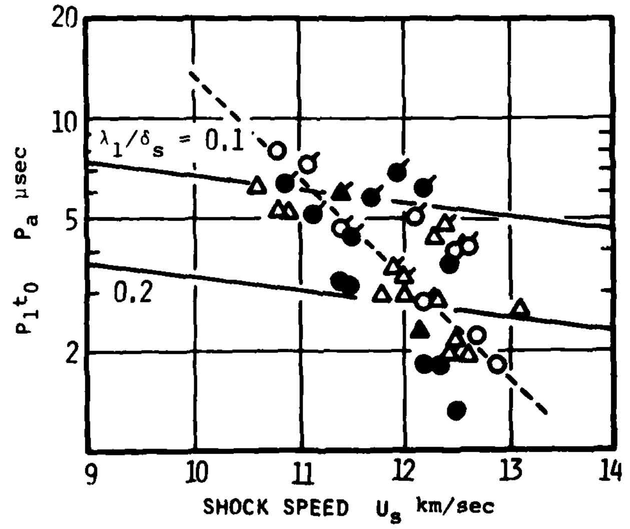

Fig. 6 $P_1 t_0$ vs. U_s for the probe current and the photo-emission. [Single probe; △ 10 Pa, △̸ 20 Pa. Double probe; ▲ 10 Pa, ▲̸ 20 Pa. Continuum; ○ 10 Pa, ○̸ 20 Pa. 4158 Å; ● 10 Pa, ●̸ 20 Pa.]

REFERENCES

1. H. Petschek and S. Byron, Ann. Physics *1*, 270 [1957].
2. H. Wong and D. Bershader, J. Fluid Mech. *26*, 459 [1966].
3. G. Kamimoto and K. Teshima, Trans. Japan Soc. Aero. Space Sci. *15*, 141 [1972].
4. D. Bershader, Proc. 10th ISTS, 3 [1975].
5. Ya. B. Zel'dovich and Yu. P. Raizer, "Physics of Shock Waves and High-Temperature Hydrodynamic Phenomena, Vol. II", 526 [1967].
6. R.J. Stalker and H.G. Hornung, Proc. 7th ISTS, 242 [1970].
7. R.J. Sandeman and G.H. Allen, Proc. 8th ISTS, No. 52 [1971].
8. H. Honma, Proc. 10th ISTS, 236 [1975].
9. H. Honma, K. Misegawa and H. Usuba, Proc. 11th ISTS, 534 [1977].
10. H. Honma, Jour. Fac. Engg. Chiba Univ. *28*, 199 [1977].
11. M. Camac, Rarefied Gas Dynamics, 4th Symp. *1*, 240 [1965].
12. F. Schultz-Grunow and A. Frohn, ibid., 240 [1965].
13. D. A. Russell, ibid., 265 [1965].
14. K. Abe, Physics of Fluids *18*, 1125 [1975].

EFFECT OF SHOCK-TUBE CLEANLINESS ON THE INITIAL IONIZATION RATE IN ARGON PLASMA

C. P. Schneider

Messerschmitt-Boelkow-Blohm GmbH
Ottobrunn, W. Germany

G. Hahne

Fachibereich Luft- und Raumfahrttechnik
Hochschule der Bundeswehr München, W. Germany

The investigation described herein consisted of two parts. The first part was an exploration of methods of obtaining a very clean shock-tube. The cleaning method decided upon comprised glass bead peening of the shock-tube walls, followed by multiple flushing of the tube; this method, however, left a practically irreducible and non-negligible residue of sodium chloride vapor in the tube. The second part of the investigation, accordingly, consisted of the theoretical simulation of the observed time dependence of the electron density, the electron temperature, and the emitted sodium D light, in shock-heated argon contaminated by a small amount of sodium chloride vapor.

It was found that accounting for the effects of contaminants required important revisions in rate constants for pure argon from previously determined values.

INTRODUCTION

The fact that low ionization potential contaminants can influence ionization rate experiments is known, as is the fact that shock-tubes should be cleaned before attempting kinetics - particulary electron kinetics - experiments /1,2,3 7. The first objective of this investigation was to find a cleaning method to remove the residue (produced by an electric arc driver) from the interior shock-tube walls. As it is a non-destructive cleaning method, glass bead peening was chosen over other methods. After cleaning, the investigation took an unexpected turn with tne discovery that the cleaning method was not perfectly effective and introduced new contaminants with non-negligible effects on the argon ionization. Fortunately, the nature of the contaminants was determinable. Their content could be reduced to a level much lower than that obtainable before cleaning the walls. Nevertheless, the level could not be reduced below the point where their presence could be neglected, and we were accordingly forced to incorporate their effect in our simulation program. Temperature dependent changes of previously given reaction rate constants for pure argon [2,4,5] were needed to simulate the measured data. This suggests that the reaction rate constants for pure argon inferred from previous shock-tube experiments contain important errors, in that their corresponding data analyses failed to account for the non-negligible influence of impurities on the evolution of the gas behind the shock.

TUBE CLEANING

Prior to this investigation, the electric discharge driver was replaced by a cold helium driver in combination with double diaphragm operation, as a pressure driver is known to cause relatively low contamination. Before the cleaning, combustion and ablation products from the arc chamber - e.g. of the tungsten wire for arc initiation or of the silicon rubber insulation - settled in the driven tube. They appeared in the forms of a fine black powder and of a harder residue layer strongly bonded to the metal surface. The powder was easily wiped off with the aid of solvents such as alcohol or acetone. The bonded layer could not be removed this easily, but had to be scraped off the wall. The testing of the powder and scraped-off smudge with hydrochloric acid solutions gave evidence mostly of iron [6]. As a cleaning method for the removal of the bonded layer, glass bead peening with beads of 0.05 to 0.1 mm diameter was preferred over sand-blasting, or hand or machine honing, because this method does not damage the metal surface. After peening, the hard residue was completely removed. However, ionization experiments in argon revealed that peening did not remove the expected "clean" gas condition immediately The beads contain at least 12% of Na_2O, 8% CaO and 1% Al_2O_3, i.e. molecules with low dissociation energies. Dissociation of these molecules produces molecules or atoms with ionization energies much lower than that of argon. Apparently, the peening process left a residue of the constituents of the glass beads on the walls of the shock tube* . After repeated testing in argon, including cleaning, pumping, and flushing after each of approximately 100 runs with the cold helium driver, the tube was sufficiently clean to permit the study of electron kinetics with inert gases, provided that a simulation program accounting for impurity effects was incorporated into the data reduction.

Diagnostics

The electron density of the argon plasma behind a shock was determined with microwave diagnostics and an electric wire probe both before and after peening. Microwaves of the frequency $f = 35.0$ GHz were transmitted across windows mounted in the shock-tube walls. Before the cleaning, and before a well-matched wide-aperture test section could be utilized, the microwaves were sent through a preliminary set-up with quartz glass windows framed by the shock-tube's portholes of 25 mm diameter. Since the transmission of waves is strongly influenced by refraction when aperture (25 mm) and wave length (8 mm) are of the same order of magnitude, measurement of the attenuation of waves in the plasma could not in practice be evaluated. The phase shift, however, was less affected by refraction as may be expected from previous experiments [8] where a microwave section was mismatched deliberately in order to produce a phase shift in the reflexion signal. An oscillogram typical for the 35 GHz phase shift and amplitude attenuation obtained with the preliminary test section is shown in fig. 1. The upper beam represents the phase shift signal, the lower beam the attenuation, both on a time base of 100 μs/division. For constrast, phase shift and attenuation for approximately the same test conditions measured with a matched

---

* In addition, sodium chloride molecules contained in the air will be adsorbed on the inner wall of the shock tube driven section, when the tube is opened for the purpose of installing a new diaphragm. While the driven tube section is being filled with the required test gas, vapor molecules will desorb and remain in the test gas [7].

section /‾9/ are displayed in fig. 2.

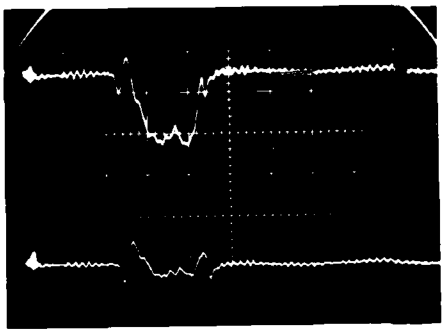

Fig. 1 Microwave signals of transmission phase shift (upper beam) and attenuation (lower beam) by refraction. Time scale 100 μs/division, sensitivity: upper beam 2 mV/division, lower beam 5 mV/division. Test condition: u_s = 2.99 mm/μs p_1 = 2.9 Torr argon, f = 25 GHz

For the interpretation of the phase shift in fig. 1, additional information from the other diagnostics is needed, on account of the superimposed high frequency oscillation. The narrow portholes may act as side port feeding horns. They refract and scatter a portion of the transmitted waves and feed them in the direction parallel to the longitudinal shock tube axis. Signals due to interactions of the scattered waves with the moving ionized flow "piston" add to the phase shift. In order to separate the signals, the source of the unwanted oscillation and the onset of the phase signal had to be determined. The latter was accomplished by time coordination of the phase signal with the trace of the ionization probe /10/ in fig. 3, which measures qualitatively the conductivity of the ionized flow. The main sources of the stray signals are Doppler shift, beats, and standing waves in the tube. Additional tests which reveal that beats by interaction of waves with various ionized layers cause the stray signals, are explained in ref. /‾31 /.

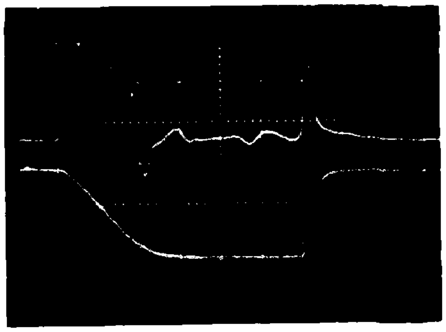

Fig. 2 Microwave signals of transmission phase shift (upper beam) and attenuation (lower beam) unaffected by refraction. Time scale 100 μs/division, sensitivity: upper beam 10 mV/division, lower beam 5 mV/division. Test condition: u_s = 3.02 mm/μs p_1 = 3.0 Torr Argon, f = 35 GHz

For the purpose of identifying the contaminant, the intensity of the sodium D doublet, located at 5889.95 anf 5895.92 Å, was measured along with the microwave signals. A detailed description of the D line evaluation is given in ref. /‾7 /. In order to confirm that sodium was the only significant impurity, the radiation from iron atoms, which were considered to be the second important contaminant that may contribute to ionization in the shocked gas, was also measured in separate runs in the spectral region around 3735 Å.

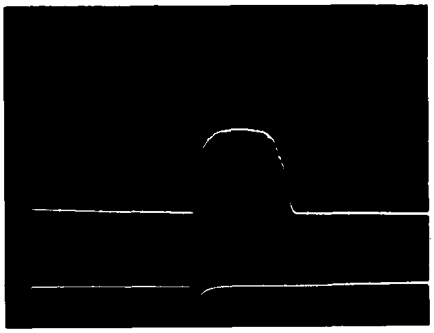

Fig.3 Signal of an electric wire probe taken simultaneously with fig.1. Advance time with respect to fig. 1: 200 μs. Time scale 100 μs/div., sensitivity 20 V/div. Test cond. see fig. 1

In addition, mass spectrograms were taken from the shock tube gas both under evacuation and under pressure /7/ . These studies indicated that the impurity level in research grade argon was less than 1 ppm and that contaminants detected by this method consisted of 40% H_2O, 50% N_2, 5% CO_2 and 5% hydrocarbons (mostly CH_4) by volume to within ± 20% of the mean. Oxygen content was below the measurable limit. Attempts to detect sodium and iron by mass spectrometry failed.

Experimental results

Both microwave signals in figs. 1 and 2 were recorded after the cleaning. The electron density and electron temperature extracted from the measured oscilloscope traces by means of an evaluation program /9/ relating the plasma properties (electron density and electron collision frequency) to the transmission attenuation and phase shift of the microwaves. The electron density, taken from figs. 1 and 2, as function of the laboratory time, is compared with the density obtained in a test before the glass bead peening and in a test (with 33 GHz waves) in another (aluminum) shock tube /11/ at test conditions very close to those of the experiments above, i.e. at a shock speed of ~3 mm/μs in 3 Torr argon. From fig. 4, one sees that the initial electron density gradients before and after peening do not differ appreciably. This outcome derives mainly from the fact that the components of the silica glass beads /12/ (which are listed above) participate in the ionization reaction. After approximately 100 test runs, including cleaning and flushing with nitrogen, the contamintion level was significant lower. Then the initial argon ionization rate approaches the experimental result of McLaren and Hobson /3/, a rate four times lower than the one previously measured by Kelly /2/ which has so far been considered to present the best data for the least contaminated argon(i.e., argon with an impurity level of 1 ppm from outgassing materials of an approximate composition of 60% H_2O, 10% Na_2 and 30% hydrocarbons).

ANALYTICAL SIMULATION

For analytical simulation, which was based on a computer program in refs. /13,14/, the experimental results of two tests runs with different impurity levels were chosen. The measured time dependent data for these runs, identified as test nos. 128 and 140, consist of the electron density, the electron temperature, and the concentration of excited sodium. The simulation of the electron density and its time derivative includes the following collisional and radiative processes.

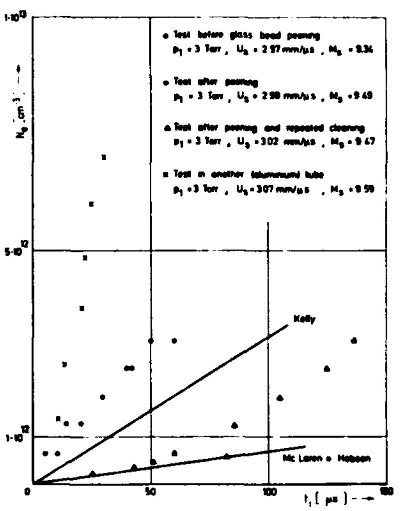

Fig.4 Electron number density as function of the laboratory time. Comparison of tests before and after peening with results in another (aluminum) tube and with data by Kelly and McLaren and Hobson

Collisional processes:

1 $Ar + Ar + 15.76\ eV \rightarrow Ar + Ar^+ + e$
2 $Ar + e + 15.76\ eV \rightarrow Ar^+ + e + e$
3 $Ar + NaCl + 4.27\ eV \rightarrow Ar + Na^o + Cl$
4 $Ar + NaCl + 5.8\ eV \rightarrow Ar + Na^+ + Cl^-$
5 $Ar + NaCl + 6.37\ eV \rightarrow Ar + Na^* + Cl$
6 $Ar + Cl^- + 3.61\ eV \rightarrow Ar + Cl + e$
7 $e + Cl^- + 3.61\ eV \rightarrow e + Cl + e$
8 $Ar + Na^o + 2.1\ eV \rightarrow Ar + Na^*$
9 $e + Na^o + 2.1\ eV \rightarrow e + Na^*$
10 $Ar + Na^* + 3.04\ eV \rightarrow Ar + Na^+ + e$
11 $e + Na^* + 3.04\ eV \rightarrow e + Na^+ + e$
12 $Ar + Na^o + 5.14\ eV \rightarrow Ar + Na^+ + e$
13 $e + Na^o + 5.14\ eV \rightarrow e + Na^+ + e$
14 $Na^o + Cl + 1.53\ eV \rightarrow Na^+ + Cl^-$

Radiative processes

15 $Ar^+ + e \rightarrow Ar + h\nu$
16 $Na^+ + e \rightarrow Na^* + h\nu$
17 $Na^+ + e \rightarrow Na^o + h\nu$
18 $Cl^- + e \rightarrow Cl + h\nu$
19 $Na^* \rightarrow Na + h\nu$.

The reaction rates and equilibrium constants are taken from the literature sources indicated in the brackets following each reaction. The reverse reaction rate k_{-12} results from a curve fit to the experimental data in ref.[15], and the rate of reaction 3 is linearly extrapolated from measured data of ref.[16]

Reaction rates

1 $k_{r_1} = 2.5 \cdot 10^{-33} \, (10^{-4} T)^{-6.5}$ [2]

2 $k_{r_2} = 4.1 \cdot 10^{-28} \, (10^{-4} T_e)^{-17.4}$ [4,15]

3 $k_{r_3} = 4.1 \cdot 10^{-37} \exp\left(\frac{11160}{T}\right)$ [16,17]

4 $k_{r_4} = 3.8 \cdot 10^{-36} \, (10^{-4} T)^{-3.6}$ [7]

5 $k_{r_5} = 5.1 \cdot 10^{-41} \, (10^{-4} T)^{-13.8} \exp\left(\frac{8550}{T}\right)$ [7]

6 $k_{r_6} = 1.27 \cdot 10^{-32} \, (10^{-4} T)^{-1.5}$ [16]

7 $k_{r_7} = 2.1 \cdot 10^{-31} \, (10^{-4} T_e)^{-5.4}$ [7]

8 $k_{r_8} = 2.28 \cdot 10^{-15} \, T^{0.5} \left(1 + \frac{2T}{24413}\right)$ [18]

9 $k_{r_9} = 2 \cdot 10^{-7}$ [19]

10 $k_{r_{10}} = 4.12 \cdot 10^{-30} \, T^{-1.0} \left(1 + \frac{2T}{35214}\right)$ [18]

11 $k_{r_{11}} = 6.2 \cdot 10^{-23} \, T_e^{-1.5}$ [20]

12 $k_{r_{12}} = 1.83 \cdot 10^{-30} T^{-1.0} \left(1 + \frac{2T}{59650}\right)$ [18]

13 $k_{r_{13}} = 2.07 \cdot 10^{-23} \, (1 + 3 \exp\left(\frac{-24413}{T_e}\right) \, T_e^{-1.5}$ [20]

14 $k_{r_{14}} = 2.88 \cdot 10^{-13} \exp\left(\frac{17750}{T}\right)$ [21]

15 $\alpha_{15} = 2.17 \cdot 10^{-11} \, T_e^{-0.5}$ [22]

16 $\alpha_{16} = 9.9 \cdot 10^{-13} \, (10^{3} T_e^{-1})^{0.728}$ [23]

17 $\alpha_{17} = 1.36 \cdot 10^{-17} \, (10^{-4} T_e)^{1.5} \left(2 - \frac{59638}{T_e} + \left(\frac{59638}{T_e}\right)^2\right)$ [23]

18 $\alpha_{18} = \alpha_{16} - \alpha_{17}$ [24]

19 $A = 6.28 \cdot 10^{7}$ (Einstein factor)

Equilibrium constants

1 $K_1 = 2.656 \cdot 10^{16} T^{1.5} \exp\left(\frac{-183100}{T}\right)$ [2]

2 $K_2 = 2.656 \cdot 10^{16} T_e^{-1.5} \exp\left(\frac{-183100}{T_e}\right)$ [2]

3 $K_3 = 1.71 \cdot 10^{27} \exp\left(\frac{-51450}{T}\right)$ [25]

4 $K_4 = 1.2 \cdot 10^{26} \exp\left(\frac{-68270}{T}\right)$ [25]

5 $K_5 = 5.13 \cdot 10^{27} \exp\left(\frac{-75860}{T}\right)$ [25,26]

6 $K_6 = 4.83 \cdot 10^{15} \left(4 + 2 \exp\left(\frac{-1270}{T}\right)\right) T^{1.5} \exp\left(\frac{-41900}{T}\right)$ [27,28]

7 $K_7 = 4.83 \cdot 10^{15} \left(4 + 2 \exp\left(\frac{-1270}{T_e}\right)\right) T_e^{1.5} \exp\left(\frac{-41900}{T_e}\right)$ [27,28]

8 $K_8 = 3 \exp\left(\frac{-24413}{T}\right)$ [26,28]

9 $K_9 = 3 \exp\left(\frac{-24413}{T_e}\right)$ [26,28]

10 $K_{10} = 8.05 \cdot 10^{14}\, T^{1.5} \exp\left(\frac{-35214}{T}\right)$ [19,27]

11 $K_{11} = 8.05 \cdot 10^{14}\, T_e^{\,1.5} \exp\left(\frac{-35214}{T_e}\right)$ [19,27]

12 $K_{12} = 2.415 \cdot 10^{15} T^{1.5} \exp\left(\frac{-59650}{T}\right)$ [26]

13 $K_{13} = 2.415 \cdot 10^{15} T_e^{\,1.5} \exp\left(\frac{-59650}{T_e}\right)$ [26]

14 $K_{14} = K_{12}/K_6$.

As will be discussed in a following section, the simulation required changes of the listed reaction rate constants.

Discussion of the simulation

The experimentally determined electron densities in figs. 5 and 9 reveal plateaus which begin at 90 µs for run 128 (fig. 5), where a shock propagates at $M_s = 8.98$ into argon at $p_1 = 5$ Torr, and at approximately 100 µs for run 140 (fig. 9) with $M_s = 7.55$ and $p_1 = 10$ Torr. Within the time period where the plateau occurs the rate of increase of electron density drops to values much lower than at any time after the shock begins. This one sees in figs. 6 and 10 where the rates of increase of electron density of runs 128 and 140, respectively, are plotted versus the laboratory time.

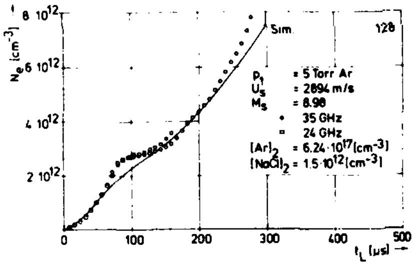

Fig.5 Electron number density as function of laboratory time. Comparison of experimental and analytical results. Run 128

The tendency towards a plateau is weakly present in Kelly's data [2], fig.[5] as well; the weakness here is associated with a very strong shock ($M_s = 9.55$) where the argon ionization quickly covers the effects of any impurity. It proves impossible to simulate the plateau with only argon reactions for the following reasons: the electron density rate from reaction 1 is constant in time while the rate resulting from reaction 2 is monotonically increasing with time. Therefore, no bump, such as clearly present in the rate data from run 128, is possible in pure argon. Moreover, the minimum value that the measured electron density rate takes at approximately 120 µs (fig. 6), is less than the rate of increase of electron density one would predict from Kelly's rate for reaction 1, if this were the only source of electrons at $t_L \approx 120$ µs. Therefore, the rate of reaction 1 of ref. [2] is untenable despite the claim that an effective activation energy of ∿ 11.6 eV - inferred from an Arrhenius plot of the initial rate data - indicates that initial ionization occurs by two successive atom-atom collisions involving an intermediate excited state A* which is rate controlling [2, 29]. With strong shocks, the collisional rate between electrons and argon, which also may involve the intermediate state A^* strongly influences the early ionization period (fig. 6) and thus can explain the mentioned observation.

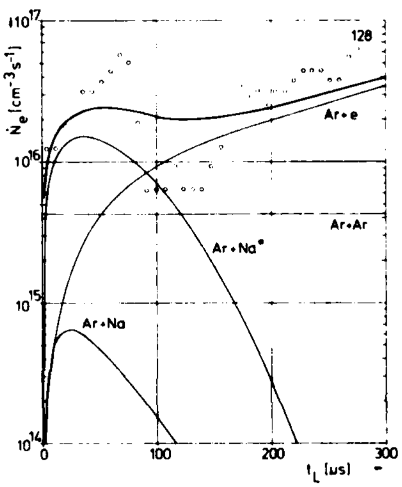

Fig.6 Electron density gradient in time as function of laboratory time. Experimental result in comparison to the sum of the simulated gradients of the dominant reactions; Run 128

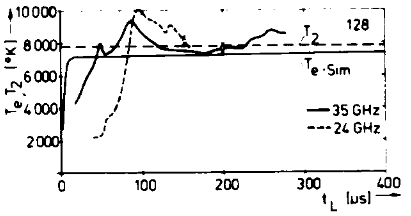

Fig.8 Electron temperature as function of lab. time. Comparison of exper. data of 24 and 35 GHz to the heavy particle temp. T_2 and to the simulated T_e; Run 128

In our case, the minimum value of the measured reaction rate at $t_L \simeq 120$ μs is not significantly greater than the rate inferred from the measurement of McLaren and Hobson [3] for reaction 1. As mentioned, Kelly's measured electron density has an inflexion point which we infer to mean the presence of similar reactions in Kelly's shock tube experiment as in ours. Kelly, however, did not account for the presence of impurities in his simulation. Our program does include the impurity reactions 3 to 14, and as a result of our analysis we were forced to conclude that the rate constant for reaction 1 given by McLaren and Hobson should be preferred to the one proposed by Kelly. It may be seen from figs. 5 and 6 that our simulation only roughly approximates the experimental data of run 128. The source of discrepancy is yet to be found. However, our conclusion concerning rate constants is supported by the approximate simulation of sodium D light behind the shock shown in fig. 7. The agreement that we have obtained in simulating the time dependence of the electron temperature (fig. 8) offers only indirect support of the reaction scheme, for as explained elsewhere [30], the electron temperature behavior is not sensitive to sodium chloride impurity at a density less than about 10^{13} cm^{-3}; the agreement between simulation and experimental data only confirms the accuracy of the microwave measurement.

Run 140 is a case for which the NaCl concentration was about 10 times lower than in run 128. We have attempted to simulate run 140 with the assumption of $[\mathrm{NaCl}] = 1\cdot10^{11}$ cm^{-3} (A=1) and $[\mathrm{NaCl}] = 2\cdot10^{11}$ cm^{-3} (A=2). The impurity level A = 2 seems to be the better fit to the electron density inferred from the 24 GHz measurement (fig. 9), which we consider the more reliable data in this run. Note that the predicted long time electron production rate (fig. 10), which results overwhelmingly from reaction 2, is approximately proportional to the assumed NaCl concentration despite the latter's smallness. It is therefore practically unavoidable to account for the presence of NaCl in the simulation of the reactions in even slightly contaminated argon. As in run 128, the emitted sodium D light was successfully, albeit roughly, modelled with A = 2 (ref. [31]).

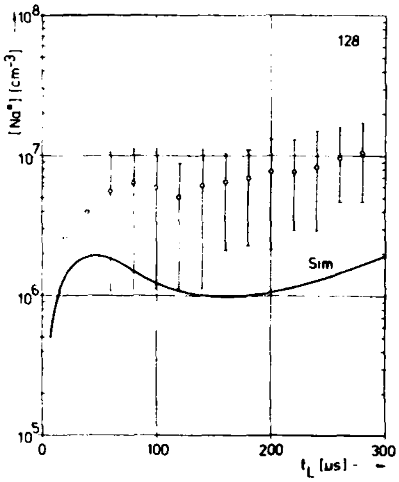

Fig.7 Number density of sodium in the excited state (sodium D line) as function of the laboratory time. Comparison of experimental and simulated results; Run 128

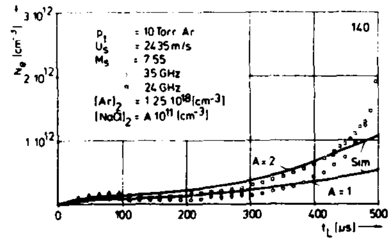

Fig.9 Electron number density as function of laboratory time. Comparison of experimental and analytical results; Run 140

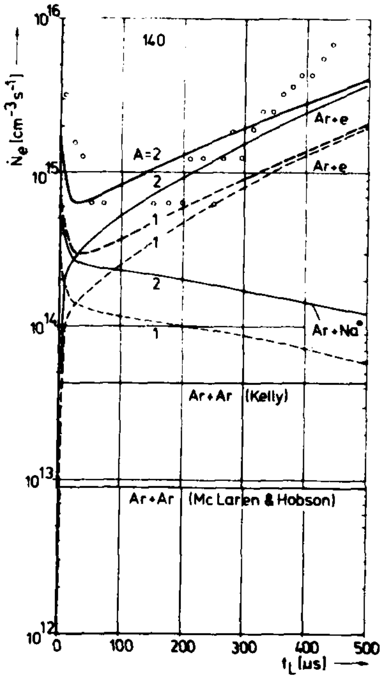

Fig.10 Electron density gradient in time as function of lab. time. Experimental result in comparison to the sum of the simulated gradients of the dominant reactions; Run 140

A large number of other experiments were made with the range of shock speeds ($2450 \leq U_s \leq 3050$ m/s), argon densities ($3 \leq p_1 \leq 10$ Torr) and NaCl concentrations (as inferred from the approximate simulation of the intensity of the Na D light). For several of these runs, which so far have been evaluated with the simulation program, we achieved a similar degree of success in modelling the three quantities (electron density, electron temperature and sodium D light) as in run 128 and 140. In every case it was necessary to change the reaction rate constants from previously accepted values sometimes by factors as large as 10. In run 140 for instance, the factors of the rate constants 1-14 are as follows: $C_1 = 0.2$, $C_2 = 10$, $C_3 = 0.1$, $C_4 = 10^{-4}$, $C_5 = 0.1$, $C_6 = 1$, $C_7 = 1$, $C_8 = 0.1$, $C_9 = 0.1$, $C_{10} = 10$, $C_{11} = 1$, $C_{12} = 1$, $C_{13} = 1$, $C_{14} = 1$. An exception is factor C_4, which is set 10^{-4} in accordance with a suggestion of Gait [21], that NaCl dissociates to atoms via reaction 3 rather than to ions (reaction 4), which could be verified in this investigation. The other changes which we considered were necessary always consistent in direction and showed a smooth temperature dependence.

CONCLUSION

Previous investigators have sometimes unjustifiably neglected the influence of low ionization potential contaminants on the reaction rates in shock-heated argon. Our simulation gives a qualitative and only semi-quantative approximation to the experimental data. In particular, we were not able to simulate in detail the very pronounced peak and valley in the time rate of change of the electron density. But the reaction models of other investigators assuming pure argon reactions are far more seriously at variance from experimental findings than the model we propose here. We believe, therefore, that our calculations show that temperature dependent changes of the reaction rate constants (1), (2), (3), (4), (5), (8), (9), and (10) are necessary to simulate the electron density evolution in shock-heated argon.

REFERENCES

1. E.J. MORGAN and R.D. MORRISON: Phys. Fluids 8, 1608, (1965)
2. A.J. KELLY: J. Chem. Phys. 45, 1723, (1966)
3. T.I. McLAREN and R.N. HOBSON: Phys. Fluids 11, 2162,(1968)
4. S.V. DESAI and W.H. CORCORAN: J. Quant. Spectrosc. Radiat. Transfer 9, 1371, (1969)
5. H.E. PETSCHEK and S. BYRON: Ann Phys. (N.Y.) 1, 270, (1957)
6. Private Communication, Testing and Controls Inc., Mountain View, Cal. 94040
7. C.P. SCHNEIDER and C. PARK: Phys. Fluids 18, 969,(1975)
8. R.G. JAHN: Phys. Fluids 5, 678, (1962)
9. C.P. SCHNEIDER: J. Plasma Physics 19, 15, (1878)
10. R.E. DANNENBERG and D.E. HUMPHREY: Rev. Sci. Instr. 39, 1692, (1968)
11. C.P. SCHNEIDER and H. GRÖNIG: Z. Naturforschung, 27a, 1717, (1972)
12. W.A. WEYL and E.C. MARBOE: The Constitution of Glasses; Vol. II, Part 2 Interscience Publishers, New York, London, Sydney (1967)
13. S.W. BOWEN: Univ. Michigan, College of Engineering TR 033390-2-T, (1971)
14. H. LOMAX: NASA TN D-4703, (1968)
15. M.I. HOFFERT and H. LIEN: Phys. Fluids 10, 1769 (1967)
16. R. HARTIG, H.A. OLSCHEWSKI, J. TROE and H.G. WAGNER: Ber. Bunsen Gesellsch. 72, 1016, (1968)
17. K. LUTHER, J. TROE, H.F. WAGNER: Ber. Bunsen Gesellsch. 76,53, (1972)
18. H.W. DRAWIN and F. EMARD: Z. Physik 254, 202, (1972)
19. C. PARK: J. Quant. Spectrosc. Radiat. Transfer 11, 7, (1971)
20. W. LOTZ: Z. Physik 216, 241, (1968)
21. P.D. GAIT: Phys. Fluids 20, 1962, (1977)
22. D.R. BATES, A.E. KINGSTON and R.W.P. WHIRTER: Proc. R. Soc. A 267, 297, (1962)
23. H.W. DRAWIN: Z. Physik 225, 483, (1969)
24. G. PEACH: Mem. R. Astron. Soc. 72, (1970)
25. JANAF: NSRDS-NBS 27, (1971)
26. W.L. WIESE, M.W. SMITH and B.M. MILES: NSRDS-NBS 22, (1969)
27. J.W. BOND, K.M. WATSON and J.A. WELCH: Atomic Theory of Gas Dynamics, Addison-Wesley, (1965)
28. W.G. VINCENTI and C.H. KRUGER: Introduction to Physical Gas Dynamics, J. Wiley and Sons, (1965)
29. K.E. HARWELL and R.G. JAHN: Phys. Fluids 7, 214, (1964)
30. C.P. SCHNEIDER: MBB-Bericht Nr. UA-471-790, (1979)
31. C.P. SCHNEIDER: MBB-Bericht Nr. UA-498-790, (1979)

INTERACTIONS OF SHOCK STRUCTURE WITH SHOCK-INDUCED QUASI-STEADY LAMINAR SIDEWALL AND FLAT-PLATE BOUNDARY-LAYER FLOWS IN IONIZING ARGON

IRVINE ISRAEL GLASS, WILLIAM SHIUN LIU*,
KAZUYOSHI TAKAYAMA** and PETER IRVING BRIMELOW†

Institute for Aerospace Studies
University of Toronto, Toronto, Canada

A combined experimental and theoretical investigation was conducted on the interactions of shock-wave structure with shock-induced quasi-steady flat-plate and shock-tube sidewall laminar boundary-layer flows in ionizing argon. Dual-wavelength interferometric shock-structure and induced flat-plate and sidewall boundary-layer flow data were obtained by using a 23-cm dia Mach-Zehnder interferometer with the UTIAS 10 cm x 18 cm Hypervelocity Shock Tube at initial shock Mach numbers $M_s \sim 13$ and 16 moving into argon at a pressure $p_0 \sim 5$ torr and temperature $T_0 \sim 300$ K. The plasma density and electron-number density in the shock structure and boundary layers were measured from the dual-frequency laser interferograms ($\lambda_1 = 6943$Å, $\lambda_2 = 3471.5$Å) and compared with analytical-numerical profiles. The present study deals basically with four parts: (1) effects of hydrogen impurities on shock structure and stability in ionizing argon, (2) effects of sidewall boundary-layer growth on shock structure, (3) shock-tube sidewall boundary-layer flows, and (4) quasi-steady flat-plate laminar boundary-layer flows.

INTRODUCTION

Experimental and analytical researches on ionizing shock-wave structure and induced laminar sidewall and flat-plate boundary-layer flows were initiated several years ago at UTIAS.[1-10] This work is not only of interest in determining fundamental physical quantities such as species refractive indices and atom-atom collision cross-sections, for example, but is of importance in providing an understanding of the coupled chemical-kinetic and gasdynamics processes occurring in such complex flows. In turn, such information can be applied to practical problems in reentry physics and hypersonic flows.

Considerable work has been done already on ionizing shock-wave structure and boundary-layer flows during the past decade (see Refs. 4 and 6 for details). Most of these analyses treated in isolation the problems of shock-structure and boundary-layer flows. As shown by Glass and Patterson[11] and

---

* Present address: Thermalhydraulics Research Branch, Whiteshell Nuclear Research Establishment, AECL, Pinawa, Manitoba, Canada, ROE 1LO.

** Institute of High Speed Mechanics, Tohoku University, Sendai, Japan.

† We dedicate this paper to the memory of our young colleague and friend, Peter Irving Brimelow, who died of bone cancer on May 16, 1978.

Mirels[12] the flows between shock waves and contact surfaces in an actual shock tube is nonuniform owing to the existence of a sidewall boundary layer. The gross features of a shock-wave structure in an ionizing gas are altered by the sidewall boundary layer. Consequently, the induced ionizing boundary layer on a flat plate in the so-called quasi-uniform flow between the shock wave and the contact region is also affected by these mutual interactions.

The most important effects of the sidewall-boundary-layer growth on the freestream flow are the induced wall shearing stress and heat transfer and their consequent nonuniformities in the flow. In order to take into account the effects of the flow nonuniformities in a shock tube, Mirels[12] obtained correlation formulae for a perfect gas. These relations are based on similarity solutions of the boundary-layer equations and the simplified quasi-one-dimensional flow equations. Local-similarity assumptions cannot be applied to cases where variations of freestream flow quantities are significant. It was shown[6,7] that a similarity assumption is not valid for the electron-temperature and electron-number-density profiles for the sidewall boundary layer where ionizing nonequilibrium occurs in the freestream flow. The validity of Mirels' correlation formulae in ionizing gas flows needs further investigation. Nevertheless, Mirels' correlation was used by several investigators[13-15] in their studies of shock structure in ionizing gases. Demmig[16] examined the ionization relaxation in a shock tube under the influence of a weakly unsteady shock front and wall boundary-layer effects.

Enomoto[13] studied the sidewall boundary-layer effects on ionizing shock structure in argon. He applied Mirels' perfect-gas correlation formulae[12] to flow nonuniformities generated by the plasma-mass mixture. He obtained the important result that the relaxation length was significantly reduced by the growth of the sidewall boundary layer.

The present investigation provides a comprehensive analytical and experimental study of shock-wave structure and laminar boundary-layer flows in ionizing argon. In addition, the complex coupled interactions between the inviscid freestream and viscous sidewall boundary-layer flows also are investigated. The plasma density and electron-number-density in the shock structure, sidewall and flat-plate boundary layer flows were measured and compared with analytical-numerical profiles.

EXPERIMENTAL ASPECTS

The present experiments were conducted in the UTIAS combustion-driven 10 cm x 18 cm Hypervelocity Shock Tube. A Mach-Zehnder interferometer with a 23-cm dia field of view, equipped with a dual-frequency (λ_1 = 6943Å, λ_2 = 3471.5Å) giant-pulse (30 ns) ruby-laser light-source, was used as the main diagnostic instrument. From the two simultaneous interferograms it was possible to determine the electron-number density n_e, and the total plasma density ρ, throughout the flow. In turn, the degree of ionization α is obtained from ρ and n_e. The details are described in Refs. 1-7.

THEORETICAL ASPECTS

The effective quasi-one-dimensional flow equations for an ionizing gas in a shock tube can be obtained[10] by applying the flow area-average on the local instantaneous macroscopic balance equations. The governing equations for a steady one-dimensional flow for an ionizing gas are:

$$\frac{d}{dx}\rho u(A - \delta^* L) = 0 \qquad \text{I}$$

$$\frac{d}{dx}\rho u^2(A - \delta_m L) + A\frac{dp}{dx} = -L\left(\mu\frac{\partial u}{\partial y}\right)_w \qquad \text{II}$$

$$\frac{5}{2}\frac{d}{dx}\,pu(A-\delta_u L)+RT_I\frac{d}{dx}\,\rho u\alpha(A-\delta_\alpha L)+\frac{1}{2}\frac{d}{dx}\,\rho u^3(A-\delta_e L)$$

$$=-Q_R(A-\delta_R L)-L\left(\mu u\,\frac{\partial u}{\partial y}\right)_w-L(q_d+q_c)_w \qquad \text{III}$$

$$\frac{d}{dx}\,\rho u\alpha(A-\delta_\alpha L)=m_a\dot{n}_e(A-\delta_{\dot{n}_e}L)-L\left(\rho D_a\,\frac{\partial\alpha}{\partial y}\right)_w \qquad \text{IV}$$

$$\frac{3}{2}\frac{d}{dx}\,\rho u\alpha RT_I(A-\delta_{T_e}L)+\rho\alpha RT_e(A-\delta_{n_e}L)\,\frac{d}{dx}\,u(A-\delta_u L)$$

$$=-L(q_{ce}+q_{de})_w+(Q_{el}+Q_{inel})(A-\delta_Q L) \qquad \text{V}$$

where the second-order terms in the momentum and energy equations are negligible compared with the wall-dissipation terms. Here ρ is the plasma density; u the velocity; A the shock-tube cross-section area; L the shock-tube perimeter length; p the plasma pressure; μ the plasma viscosity coefficient; T the temperature; α the degree of ionization; Q_R the radiation energy loss; q_c and q_d the plasma-heat conduction and diffusive-energy fluxes, respectively; $\dot{n}_e$ the electron production rate; D_a the ambipolar-diffusion coefficient; R the plasma gas constant; Q_{el} and Q_{inel} are the elastic and inelastic energy-transfer rates to electrons, respectively; subscripts w, I, e denote wall, ionization and electrons, respectively. The following boundary-layer thicknesses are defined:

$$\begin{array}{llll}
(a) & \delta^* =\int\left(1-\dfrac{\rho u}{\rho_\delta u_\delta}\right)dy & (f) & \delta_m =\int\left(1-\dfrac{\rho u^2}{\rho_\delta u_\delta^{\,2}}\right)dy \\
(b) & \delta u =\int\left(1-\dfrac{u}{u_\delta}\right)dy & (g) & \delta_\alpha =\int\left(1-\dfrac{\rho u\alpha}{\rho_\delta u_\delta \alpha_\delta}\right)dy \\
(c) & \delta_e =\int\left(1-\dfrac{\rho u^3}{\rho_\delta u_\delta^{\,3}}\right)dy & (h) & \delta_R =\int\left(1-\dfrac{Q_R}{Q_{R\delta}}\right)dy \qquad \text{VI} \\
(d) & \delta_{\dot{n}_e} =\int\left(1-\dfrac{\dot{n}_e}{\dot{n}_{e\delta}}\right)dy & (i) & \delta_Q =\int\left(1-\dfrac{Q}{Q_\delta}\right)dy \\
(e) & \delta_{T_e} =\int\left(1-\dfrac{\rho u\alpha T_e}{\rho_\delta u_\delta \alpha_\delta T_{e\delta}}\right)dy & (j) & \delta_{n_e} =\int\left(1-\dfrac{n_e}{n_{e\delta}}\right)dy
\end{array}$$

where $Q = Q_{el} + Q_{inel}$; y is the coordinate normal to the wall; subscript δ denotes the edge of the boundary layer.

The governing equations for a quasi-one-dimensional ionizing-gas flow applied by Enomoto[13] based on Mirels' method can be obtained from Eqs. I-V by letting all δ's, except δ^*, equal to zero and neglecting all wall-dissipation terms.

Equations I-V were solved[4,5] for shock-wave structure in ionizing argon and krypton without considering the boundary-layer effects and the wall-dissipation terms. The results were compared with our interferometric data in some detail. The δ's and their derivatives with respect to the flow direction x in Eqs. I-V can be obtained by solving the two-dimensional boundary-layer equations for an ionizing gas. The details of an implicit six-point finite-difference method for solving the two-temperature nonequilibrium boundary-layer equations for ionizing argon are given in Refs. 6 and 9. Details of the derivation of Eqs. I-V can be found in Ref. 10.

EFFECTS OF HYDROGEN IMPURITY ON SHOCK STRUCTURE

The shock-wave structure in ionizing argon without considering the mutual interactions between freestream and sidewall boundary-layer flows was examined in Ref. 4. In the study of shock structure, it was found that the translational shock front developed sinusoidal instabilities which affect the entire shock structure including the ionization-relaxation region, the electron-cascade front and the final quasi-equilibrium state. By adding a small amount of hydrogen (0.5% of the initial pressure), the entire flow was stabilized. However, the relaxation length for ionization was drastically reduced to about one-third of its pure-gas value. Using the familiar two-step collisional model coupled with radiation-energy losses and the appropriate chemical reactions, it was possible to deduce from interferometric measurements a precise value for the argon atom-atom collisional excitational cross-section constant to be 1.0×10^{-19} cm^2/eV with or without the presence of a hydrogen impurity. The reason for the success of hydrogen, and not other gases, in bringing about stabilized shock waves, is not clear yet.

It was also found that the electron-cascade front approached the translational shock front near the shock-tube wall. This effect appears to be independent of the wall materials and is not affected by the evolution of adsorbed water-vapour from the walls or by water-vapour added deliberately to the test gas. The effects of this phenomenon on the shock-tube sidewall boundary-layer-flow profiles are more pronounced for the stronger shock waves. Here as well, the reasons for the near-merging of the cascade front with the translational shock wave are not understood as yet.

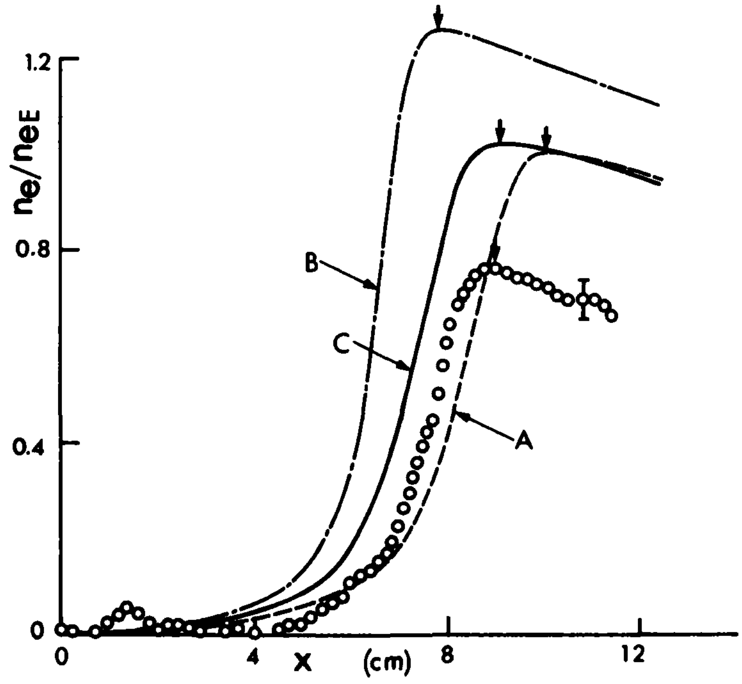

Figure 1. Variations of n_e/n_{eE} with distance x for M_s = 13.1, p_O = 5.16 torr, T_O = 300 K and n_{eE} = 0.566 x 10^{17}/cm^3. Subscript E denotes quasi-equilibrium value. A: first order result; B: Enomoto's model; C: the present result. Arrows show termination of relaxation.

EFFECTS OF SIDEWALL BOUNDARY LAYER ON SHOCK STRUCTURE

Figure 1 shows a comparison between the various analyses and the experimental data for the electron-number-density profiles for a lower shock-Mach-number case of $M_s = 13.1$, $p_o = 5.16$ torr and $T_o = 300$ K. Curve A is the first-order result without taking into account the effects of the sidewall boundary layer. Curve B is obtained from Enomoto's model. Curve C is the present result where the boundary-layer equations were solved by an implicit finite-difference scheme.

It is seen that the difference between the present model (curve C) and Enomoto's model (curve B) is significant for this lower Mach-number case. The electron-number density at the electron-cascade front from Enomoto's model is much higher than from the present model. The relaxation length, x_E is very much reduced in Enomoto's model ($x_E = 7.8$ cm). The first-order result for x_E is about 10 cm, while the present theory predicts an x_E of 8.9 cm, which is in close agreement with the experimental value.

In order to investigate the effects of shock-tube diameter on shock structure, different cross-sections are used in the calculations. It is shown that the relaxation length decreases and the electron-number density increases at the cascade front as the shock-tube diameter decreases. A smaller shock-tube diameter means a more pronounced sidewall-boundary layer effect.

For the higher Mach-number case $M_s = 15.9$, $p_o = 5.1$ torr, and $T_o = 298$ K, the difference between the present model and Enomoto's model is much smaller. This is due to the fact that the relaxation length for the higher Mach-number case is much shorter (see Fig. 2). Here, the effect of shock-tube diameter on shock-wave structure is also much smaller. In this case, the relaxation length is reduced only by 6% due to the sidewall-boundary-layer effects.

From the previous comparisons between analyses and experimental data, we conclude that: (1) our value[4] of the argon-argon collisional cross-section constant of 1.0×10^{-19} eV/cm^2 is accurate; (2) the relaxation length is

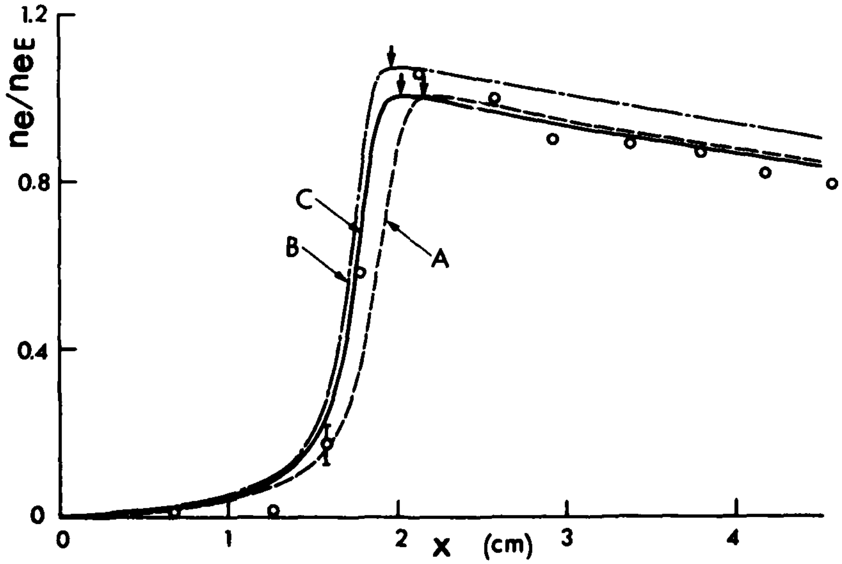

Figure 2. Variations of n_e/n_{eE} with distance x for $M_s = 15.9$, $p_o = 5.10$ torr, $T_o = 298$ K and $n_{eE} = 0.168 \times 10^{18}/\text{cm}^3$. For other notations see Figure 1.

significantly reduced for a weak shock wave owing to the growth of the sidewall boundary layer; (3) Enomoto's model which neglected the momentum and energy nonuniformities and the wall dissipations, exaggerates the effects of boundary-layer growth on shock structure for lower shock Mach numbers; (4) the effects of the sidewall boundary layer on the shock structure are more pronounced for shock tubes of small diameters. For further details see Ref. 10.

SHOCK-TUBE SIDEWALL BOUNDARY-LAYER FLOWS

Shock-tube sidewall boundary-layer flows in ionizing argon without mutual interactions effects between the inviscid and the viscous flows were analyzed and compared with dual-wavelength interferometric data in Ref. 1. Satisfactory agreement was obtained for the lower shock-Mach number case of $M_s = 13.1$. The experimental results lie between the frozen and nonequilibrium solutions. However, it was found that two-dimensional effects were significant for the higher Mach-number case of $M_s = 15.9$.

The present sidewall boundary-layer results were obtained by using the shock-structure solutions described previously as the edge conditions of the boundary-layer equations. The difference between the previous[7] and the present results arises from the variations of the freestream-flow quantities. As expected, a change in the freestream conditions will induce some changes in the boundary-layer structure.

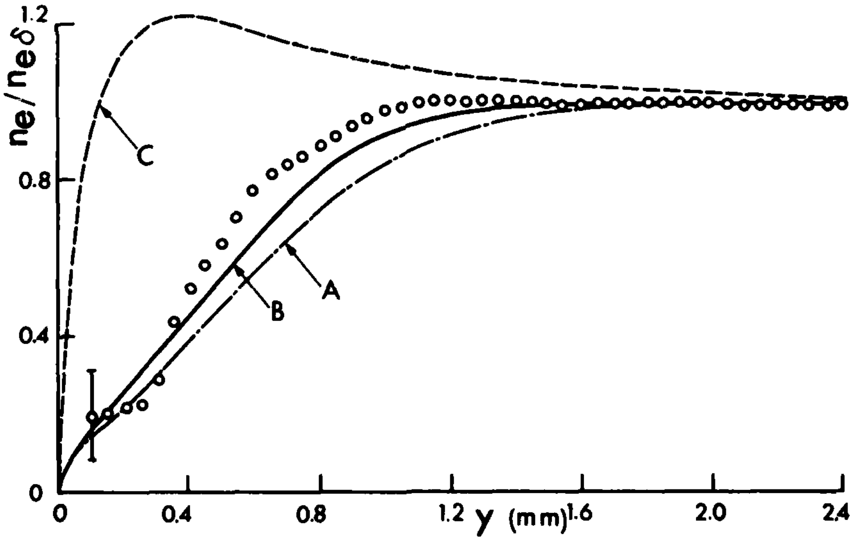

Figure 3. Comparison of analytical and experimental normalized electron-number-density profiles with distance y in the sidewall boundary layer at $x = 9.5$ cm, $M_s = 13.1$, $p_0 = 5.16$ torr, $T_0 = 300$ K and $n_{e\delta} = 0.570 \times 10^{17}/\text{cm}^3$. A: first-order result; B: the present result; C: first-order frozen result.

Figure 3 shows the results with and without coupled interactions for $M_s = 13.1$, $p_0 = 5.16$ torr and $T_0 = 300$ K together with the experimental data for the electron-number-density profiles. It is evident that the present results agree better with the experimental data than the first-order analysis.

The thickness of the electron thermal layer is much thinner than predicted by Honma and Komuro.[17] They indicated a thickness almost an order greater than the present result. It is shown that the thickness of the electron thermal layer is of the same order as the thickness of the viscous layer for the sidewall and flat-plate cases. A similar result was found by Hutten Mansfeld[18] for a thermal Rayleigh boundary layer.

For the higher Mach number case, $M_S = 15.9$, $p_O = 5.1$ torr and $T_O = 298$ K, the agreement with the experimental data is worse using the mutual-interaction analysis, as shown in Fig. 4. The reasons for the discrepancy are as follows. The measuring station for this higher Mach number is 18 cm behind the shock front and is located in the radiation-cooling region. The radiation process affects both the inviscid and viscous flows when the distance between the measuring station and the shock front is greater than 2 cm. It has been shown[8] that the flow is nonuniform. In the experiment, the electron-number density kept on increasing with distance from the wall and did not reach its asymptotic value.

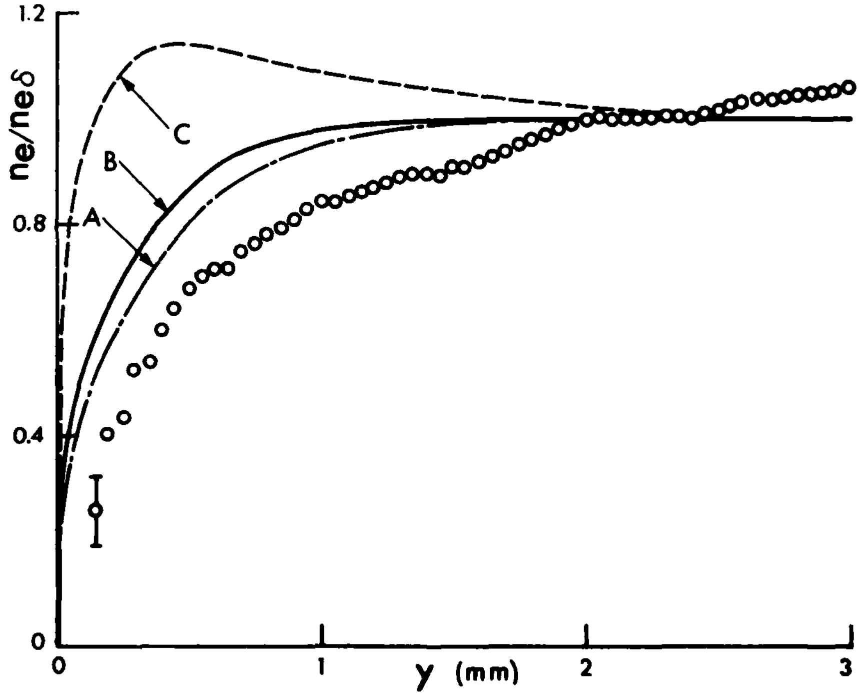

Figure 4. Comparison of analytical and experimental normalized electron-number-density profiles with distance y in the sidewall boundary layer at $x = 18$ cm, $M_S = 15.9$, $p_O = 5.10$ torr, $T_O = 298$ K and $n_{e\delta} = 0.620 \times 10^{17}/cm^3$. For other notations see Figure 3.

FLAT-PLATE BOUNDARY-LAYER FLOWS

Owing to radiation-energy losses and the changes in flow properties caused by the growing sidewall boundary layer, the flat-plate boundary layer generated by a stronger shock wave can no longer be considered as being generated in a quasi-steady flow.[6] The quasi-steady flat-plate boundary layer was first analyzed without taking into account these unsteady effects.[6] The analysis was compared with experimental results which had significant bumps in the electron-number-density profiles for the cases studied at M_S =

16.6, p_O = 4.81 torr, T_O = 296 K, and M_s = 12.8, p_O = 5.01 torr, T_O = 297 K. Quite good agreement was obtained for the measured plasma-density profiles. However, rather poor agreement was obtained using a first-order analysis for the electron-number-density profiles in a frozen or nonequilibrium flow for M_s = 16.6. Much better agreement was found for the electron-number-density profiles for M_s = 12.8, where the experimental results lie between the analytical nonequilibrium and frozen-flow profiles. The disagreement between first-order theory and experiment for the electron-number-density profile is discussed in detail in Ref. 6.

The effects of the mutual interactions on the flat-plate boundary layer are small compared with the sidewall case. As explained in Ref. 6, the main discrepancy between analyses and experiment arises from the unsteady-flow effects, which were neglected in the analyses.

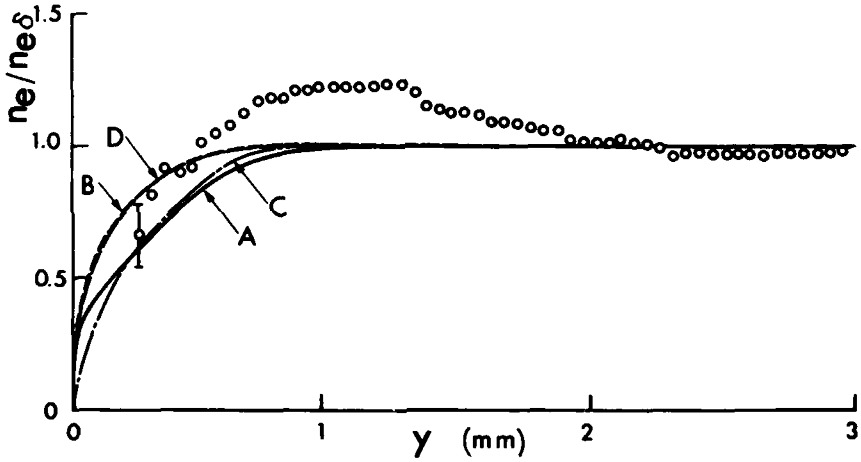

Figure 5. Comparison of analytical and experimental normalized electron-number-density profiles with distance y in the flat-plate boundary layer at x = 14 cm, M_s = 16.6, p_O = 4.81 torr, T_O = 296 K and $n_{e\delta}$ = 0.378 x $10^{17}/cm^3$. A: the present nonequilibrium profile; B: the present frozen profile; C: first-order nonequilibrium profile; D: first-order frozen profile.

Comparisons of various analyses with experimental results for M_s = 16.6 and p_O = 4.81 torr are shown in Figure 5 for the electron-number density. The experimental data show a significant bump, which was not observed in the sidewall n_e-profile. This is not predicted by either the nonequilibrium or the frozen-flow analysis. A similar bump does appear in the experimental degree of ionization profile.

For the second case, M_s = 12.8 and p_O = 5.01 torr, the analytical results for the n_e profile are plotted in Figure 6 together with the experimental data. Unlike the high Mach-number case, the experimental results for n_e lie between the analytical nonequilibrium and frozen-flow profiles. The two-temperature frozen-flow solution predicts a larger bump than that obtained from the experiment, while no bump occurs in the nonequilibrium profiles. The differences between the first-order and the present analysis are small. Some improvements do occur using the present theory.

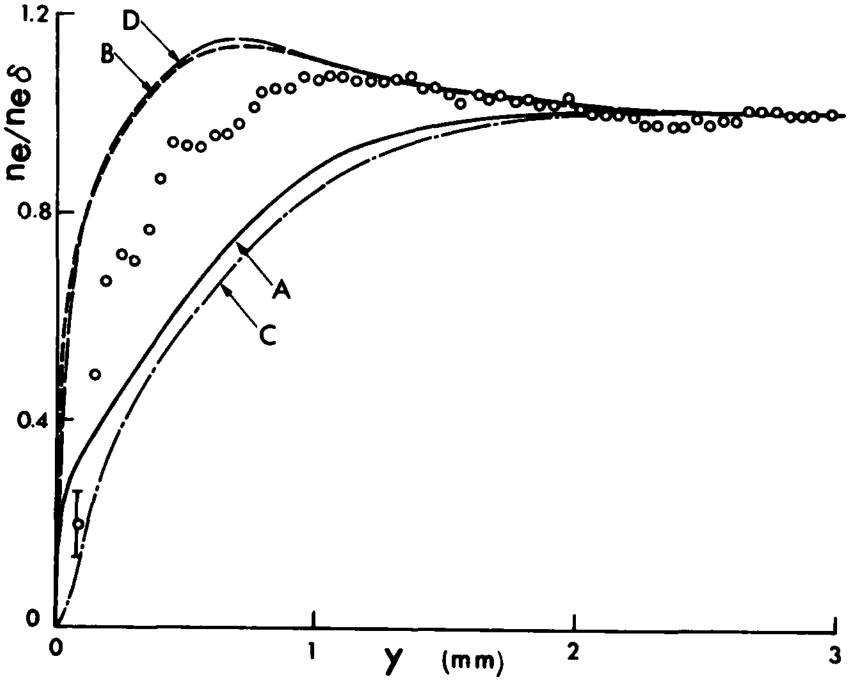

Figure 6. Comparison of analytical and experimental normalized electron-number-density in the flat-plate boundary layer at $x = 14$ cm, $M_s = 12.8$, $p_0 = 5.01$ torr, $T_0 = 297$ K and $n_{e\delta} = 0.297 \times 10^{17}/\text{cm}^3$. For other notations see Figure 5.

CONCLUSIONS

A comprehensive investigation was presented on ionizing shock-wave structure and its interaction with the induced laminar sidewall boundary layer. Their combined influence on flat-plate boundary-layer flows was also considered. The quasi-one-dimensional shock-structure model was based on a flow area-average concept. The analytical results are compared with our interferometric data.

The agreement between the analyses and the experimental results for the electron number-density and total plasma-density profiles are fair to excellent. The experimental data for the flat-plate boundary layers show bumps in the n_e profiles. These were not observed in the sidewall boundary-layer cases.

The interactions between the inviscid freestream and viscous sidewall boundary-layer flows were investigated. It is shown that the relaxation length is significantly reduced by the growth of the sidewall boundary layer. This reduction of the relaxation length is more pronounced at lower shock Mach number where long relaxation lengths exist. However, the effects of the mutual interactions on the flat-plate boundary layer are small.

These investigations of shock structure, sidewall and flat-plate boundary layers and their mutual interactions are of particular interest since they were done under nearly-identical initial conditions in ionizing-argon shock-tube flows. Further discussions of their differences and similarities can be found in Refs. 4 to 10.

ACKNOWLEDGEMENTS

The financial assistance received from the National Research Council of Canada and the U.S. Air Force Office of Scientific Research under Grant AF-AFOSR 77-3303 is acknowledged with thanks. The assistance in evaluating some of the interferometric data which we received from Mr. B. T. Whitten and Mr. F. C. Tang is acknowledged with thanks.

REFERENCES

1. M. P. F. Bristow, UTIAS Report No. 158 (1971).
2. M. P. F. Bristow and I. I. Glass, Phys. Fluids 15, 2066 (1972).
3. P. I. Brimelow, UTIAS Technical Note No. 187 (1974).
4. I. I. Glass and W. S. Liu, J. Fluid Mech. 84, 55 (1978).
5. I. I. Glass, W. S. Liu and F. C. Tang, Can. J. Phys. 56, 1269 (1977).
6. W. S. Liu, B. T. Whitten and I. I. Glass, J. Fluid Mech. 87, 609 (1978).
7. W. S. Liu and I. I. Glass, J. Fluid Mech. (to be published, 1979).
8. I. I. Glass, W. S. Liu and F. C. Tang, submitted to Phys. Fluids (1979).
9. W. S. Liu, UTIAS Report No. 226 (1979).
10. K. Takayama and W. S. Liu, UTIAS Report No. 233 (1979).
11. I. I. Glass and G. N. Patterson, J. Aeronaut. Sci. 22, 73 (1955).
12. H. Mirels, Phys. Fluids 9, 1907 (1966).
13. Y. Enomoto, J. Phys. Soc. Japan 35, 1228 (1973).
14. T. I. McLaren and R. M. Hobson, Phys. Fluids 9, 2162 (1978).
15. T. A. Brabbs and F. E. Belles, in Proc. 8th Inter. Shock Tube Symp., London (1971).
16. F. Demmig, in Proc. 11th Inter. Shock Tube Symp., Seattle (1977).
17. H. Honma and H. Komuro, AIAA J. 14, 981 (1976).
18. C. B. L. Hutten Mansfeld, Ph.D. Thesis, Eindhoven Univ. of Technology, Eindhoven, The Netherlands (1976).

PLASMA FLOW VELOCITY GAGE AT HIGH MAGNETIC REYNOLDS NUMBER*

DENNIS W. BAUM, W. LEE SHIMMIN and STEPHEN P. GILL

Artec Associates Incorporated
Hayward, California, USA

A plasma flow velocity gage based on the principle of a Faraday generator has been developed for use in a shock tube at extreme conditions of pressure, temperature, and flow velocity. Barium ferrite permanent magnets provided a magnetic field transverse to the plasma flow and orthogonal with a pair of brass electrodes mounted nearly flush with the shock tube wall. The output voltage measured at the electrodes was proportional to the axial plasma flow speed and provided a velocity-time history independent of the pressure, temperature and electrical conductivity in the plasma. A laboratory mock-up with a spring-driven aluminum rod was used to simulate the plasma flow for calibration of the averaged, or effective, magnetic field strength and to verify the linearity of gage output at high magnetic Reynolds number. The gage output was found to be linear with flow velocity, and hence unperturbed by eddy currents, at magnetic Reynolds number up to 8.2. The velocity gage has been used successfully to measure plasma flow speed at pressures up to 1 GPa, temperatures of 50 kK, and flow speeds of 28 km/s.

INTRODUCTION

This paper reports on a plasma flow velocity gage developed for use in a shock tube at high temperature (10-50 kK), high pressure (1 MPa-1GPa), high flow velocity (10-40 km/s), and high magnetic Reynolds number ($R_m \lesssim 40$). At these extreme conditions of plasma flow it is difficult to measure the properties of the plasma, and therefore it is fortunate that a simple MHD velocity gage can be adapted to furnish such a useful quantity as the axial flow speed history.

The velocity gage output has the advantage of being independent of both pressure and temperature, the upper limit on both being imposed by structural integrity of the shock tube. The gage output is also independent of plasma conductivity over several decades of conductivity. The low conductivity limitation relates to the measuring circuit impedance; for a 50Ω readout the plasma interelectrode resistance should be less than 1Ω to provide an open circuit measurement. For sufficiently high conductivity and/or flow velocity eddy current effects can limit the accuracy of the measurement if there are nearby magnetic field gradients.

The gage measures a bulk property of the plasma without intruding significantly into the flow. The gage is also self-activating, in that a transverse magnetic field having been provided, the plasma itself generates the voltage to be measured. Thus there is no need for an externally generated voltage source, and the gage can be provided with an absolute calibration beforehand. A simple static calibration of the gage is also possible by measuring the magnetic field strength between the electrodes.

The gage has been used successfully over the following range of conditions:

Flow Speed: 8.5 km/s to 28 km/s
Conductivity: 400 S/m to 26 kS/m
Temperature: 16 kK to 51 kK
Pressure: 2.4 MPa to 1.0 GPa

PRINCIPLES OF OPERATION

The velocity gage is based on the principle of a Faraday generator, shown schematically in Figure 1. When a conducting gas (a plasma) passes through a transverse magnetic field, a voltage is produced. When the flow velocity, magnetic field, and pickup electrodes are mutually orthogonal, the open circuit voltage (zero current) is given by

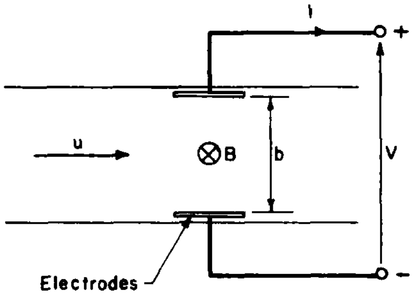

Figure 1.
Simplified schematic of Faraday generator.

$$V = buB \qquad \text{I}$$

where b is the interelectrode distance in meters, u is the velocity in m/sec, and B is the magnetic field in tesla. With a known magnetic field and known electrode spacing the measured voltage provides the plasma velocity history by

$$u(t) = V(t)/bB \qquad \text{II}$$

The voltage is reduced when a current is flowing by resistive losses in the plasma:

$$V = buB - IR \qquad \text{III}$$

where the resistance is related to gas conductivity, σ, by

$$R = \beta/\sigma d \qquad \text{IV}$$

Here d is the shock tube diameter, and β is a geometric factor related to electrode configuration. Typically β≃ 1.2.

If the impedance of the measuring circuit is much greater than the generator resistance, the open circuit voltage of Equation I is measured, providing an exact absolute measurement of the flow velocity. If the plasma resistance is too high in comparison with the input impedance of the measuring circuit, then the IR loss dominates, and generator voltage is diminished by a factor depending on conductivity.

DESCRIPTION OF GAGE

In the work described here the driven section of the shock tube consisted of a Lexan tube with an inner diameter of 25 mm and a wall thickness of 3 mm. Inertial confinement of the shock tube was provided by casting the tube in Hydrostone (a high density plaster, $\rho = 1.76\ Mg/m^3$). The transverse magnetic field was provided by a pair of barium ferrite magnets placed on either side of the tube and cast in Hydrostone along with the tube. Figure 2 shows a cross-section of the velocity gage assembly. The magnet pieces were 25 mm thick and 51 mm high and extended at least 76 mm upstream and downstream of the electrodes.

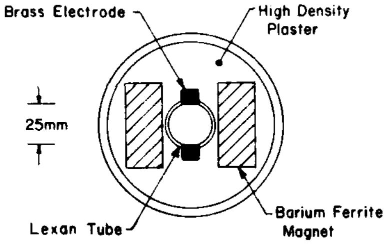

Figure 2.
Cross-section of velocity gage.

The electrodes, shown in Figure 3, consisted of 13 mm diameter threaded brass rods screwed into the Lexan tube and bonded and sealed in place with epoxy. The electrode surfaces protruded into the flow with a 10° taper, while the leading edge was recessed 0.2 mm to minimize perturbation of the flow. The portion of the electrodes outside the tube had 16 mm by 38 mm brass plates soldered to them to act as ballast in preventing the electrodes from being pushed out of the tube during the flow.

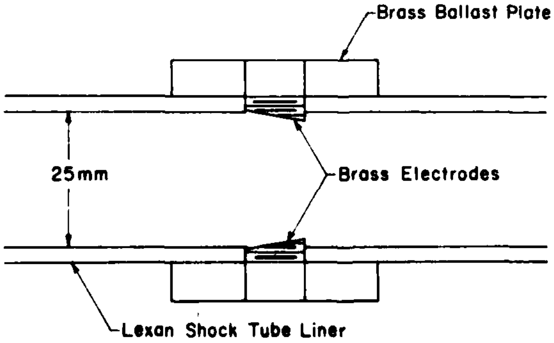

Figure 3.
Cross-section showing velocity gage electrodes.

The electrodes were connected to a 50Ω coaxial cable and were terminated with 50Ω at an oscilloscope. Since the plasma interelectrode resistance was less than 10mΩ, the 50Ω termination was essentially an open circuit. A wide-band isolation transformer was used in the line to provide DC isolation of the ground lead since there were generally other sets of diagnostics with electrodes in contact with the plasma. When pairs of electrodes at different axial locations have different net voltages, connecting two of them together via a common external ground will result in current flow in the plasma to equalize the potential. The net result will be misleading voltage readouts at both axial locations. The transformers used were North Hill Electronics Type 0017-CC with a band width of 10 Hz to 5 MHz.

CALIBRATION OF GAGE

The velocity gage was calibrated in the laboratory by propelling a spring-driven aluminum rod through a mock-up of the velocity gage configuration. A dummy Lexan or glass tube served as the channel with the proper magnets positioned as on the shock tube. As the conductive aluminum rod passed through the magnetic field, a voltage was generated across the rod, proportional to the rod velocity, rod diameter and effective magnetic field. Copper braid brush contacts were used to contact the rod and pick up the generated voltage.

Precautions were taken in these calibration tests that were not necessary for the shock tube tests. For example, the tube was swabbed with anti-static compound before each test to eliminate electrostatic signals arising from charge buildup on the tube. This reduced the noise level on the voltage records well below the level of the generated rod voltage.

The aluminum rod speed was monitored on each test using a collimated light source and a photodiode to record the arrival and departure of the rod at a given axial location. The rod deceleration was monitored using a pair of such setups at different locations. The measured deceleration of 35 m/s^2 amounted at most to a 2.5 percent correction to the measured average rod speed.

The calibrations were performed at rod speeds ranging from 6 to 10 m/s and are shown in Figure 4. The magnetic field strengths calculated from the measured output voltages were 1 to 3 percent greater than the measured on-axis B-field. The effective B-field was determined to be 96 mT for the location whose calibration is shown in Figure 4. The calibration is accurate to within 5 percent, the greatest source of uncertainty being the effective electrode

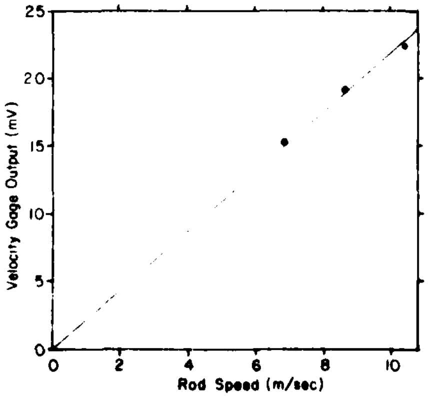

Figure 4.
Velocity gage calibration plot showing velocity gage output versus rod speed.

spacing. This is due to the fact that broad copper braid contacts were used which partially wrapped around the rod.

The aluminum rod conductivity was 25 MS/m, and the corresponding magnetic Reynolds number at the highest rod speed was $R_m = 8.2$. The magnetic Reynolds number is a dimensionless parameter which indicates the magnitude of eddy currents effects. It is defined as

$$R_m = \mu_0 \sigma u d \qquad \text{V}$$

where μ_0 is the permeability of free space ($\mu_0 = 1.257 \times 10^{-6}$ H/m), σ is the conductivity in S/m, u is the velocity in m/s, and d is the tube diameter in meters. The output voltage was linear with rod speed in this range and proportional to the measured B-field, indicating that the measurements were not significantly affected by an eddy currents or skin depth problems. Detailed theoretical analysis of magnetic field perturbation and gage response at high magnetic Reynolds number has been undertaken (Reference 1) and is consistent with laboratory calibration experiments.

RESULTS OF MEASUREMENTS

An example of a shock tube velocity gage measurement is shown in Figure 5.

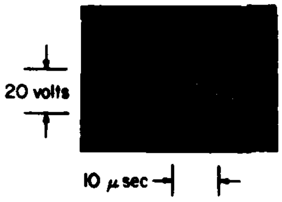

Figure 5.
Oscilloscope record of velocity gage output versus time.

This record was obtained on an explosively driven shock tube using xenon gas. The initial flow velocity was 18.5 km/s.

Since there were several diagnostic stations on the shock tube, the shock times-of-arrival provided a measure of the shock speed, and for the above example the shock speed was 19.7 km/s. The initial axial flow speed can be obtained from the shock speed by the strong shock relation,

$$U = \tfrac{1}{2}(\gamma + 1)u \qquad \text{VI}$$

where U is the shock speed, u is the flow speed, and γ is the isentropic exponent. The initial pressure of the driven gas (air) was 4.0 kPa, and for the conditions obtained here $\gamma \approx 1.2$. Thus the calculated initial axial flow speed based on the observed shock velocity was 18.0 km/s. The difference between this calculated flow velocity and the measured value is within the calibration error limits of the velocity gage.

This same basic type of velocity gage has been used successfully for several years in measuring high magnetic Reynolds number flow velocity histories. The dynamic calibration procedure described above has shown that the velocity gage response can be linear in velocity for a magnetic Reynolds number of more than 30. Future experiments using a compressed air gun will extend the range of calibration to $R_m = 100$ or greater.

REFERENCES

1. S.P. Gill, "MHD Phenomena at High Magnetic Reynolds Number," Second International Conference on Megagauss Magnetic Field Generation and Related Topics, Washington, D.C., 29 May - 1 June 1979.

*This work was supported by the Office of Naval Research.

SHOCK PROPAGATION IN A TUBE WITH TRANSVERSE RIBS

JAMES E. CRAIG and KENNETH A. HAINES

Science Applications, Inc.
Santa Ana, California, USA

The propagation of strong shock waves in tubes with transvere ribs has been investigated in the NASA/Ames Electric Arc Shock Tube (East). Using holographic techniques, a pictoral description of the wave and flow structure as well as measurements of the density fields have been compiled for various times after shock arrival. Attention was directed at two features of the flowfield; 1) shock wave diffraction about the equally spaced ribs, and 2) viscous effects which may cause rapid boundary layer growth on the very rough wall. Laser shadowgrams of the main shock region revealed a multiple shock structure behind the leading shock. Offset fringe holographic interferometry was used to obtain a vertical fringe interferogram of the shock wave, revealing a strong compression process with the wall density exceeding twice the centerline density. A holographic interferogram of the late time flow shows separating and reattaching regions about the ribs; however, comparison with Mirels theory for the growth of turbulent boundary layers on smooth walls reveals that transverse ribs do not significantly increase the boundary layer growth rate in these short duration flows.

INTRODUCTION

This investigation was motivated by numerical calculations of airblast propagation in tunnels with transverse ribs. Two types of calculations were being performed in an attempt to predict shock strength decay. Two-dimensional finite difference calculations were being performed by Needham[1] at the Air Force Weapons Laboratory, and one-dimensional calculations which modeled viscous effects were being performed by Kuhl[2] at TRW. A complicated flow structure due to shock interaction with the ribs was predicted by inviscid two-dimensional calculations, but the effects of viscosity or boundary layer growth were absent from the calculations. One-dimensional calculations neglected the shock/rib interactions but did attempt to model viscous effects by invoking wall friction and heat transfer models. A physical description of the shock propagation was lacking from the calculations making their interpretation difficult, and a program[3] was conducted to provide experimental data. Two experiments were configured, one in which shockwave attenuation was determined from the pressure waveforms measured at several points along a 50 diameter section of shocktube with tranverse ribs, and the other in which the shock/rib interaction flow field was observed optically in a square test section with ribs on the top and bottom walls. The optical investigation is described in this paper.

EXPERIMENTAL

Apparatus

A square test section (Figure 1) was constructed to accomodate optical measurements of the shock wave and boundary layer interactions with the ribs. To avoid complicated geometrical transistions from the cylindrical NASA shock tube, a cookie cutter was used, thus limiting the internal dimension of the test section to 5 cm. The test section was installed 90 diameters from the diaphragm. The transverse ribs were machined into the top and bottom walls over a 1 meter portion of the test section. A plexiglass optical port mounted flush with the side walls (Figure 2) was located 67 cm from the first rib.

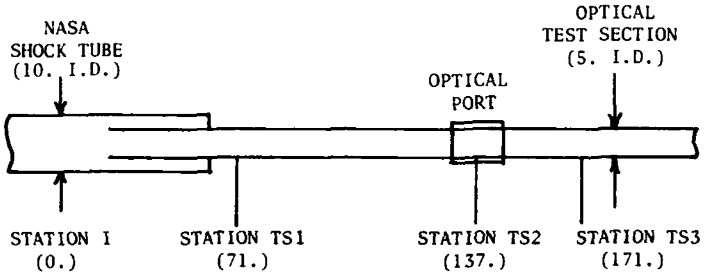

FIGURE 1 OPTICAL TEST SECTION INSTALLATION AT 90 DIAMETER STATION IN NASA SHOCK TUBE (DIMENSIONS IN CENTIMETERS)

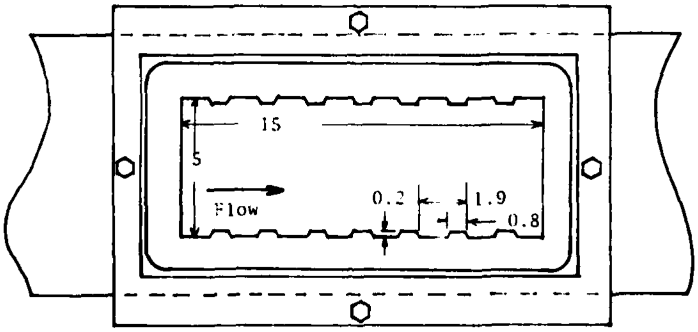

FIGURE 2 OPTICAL PORT IN TEST SECTION (DIMENSIONS IN CENTIMETERS)

Shock wave arrival time was measured every ten diameters in the NASA tube and at stations TS1, TS2, and TS3 in the test section. The laser was fired by a signal indicating shock wave arrival at Station I, using an appropriate delay to allow the shock to reach the optical port. The actual firing time was verified by a detector placed within the laser beam.

Optics

A custom built laser holography system was used to record several types of flowfield images including laser shadowgraphy, conventional inline and off-axis holography, and holographic interferometry. For this system, the source of coherent illumination was a Nd:YAG frequency doubled laser emitting 30 millijoules of 5320 A light in 20 nanosecond pulses.

The optical system is shown schematically in Figure 3. The holographic camera has the capability of focusing the image of the center of the test section into the hologram plane when laser shadowgraphy is employed; or option-

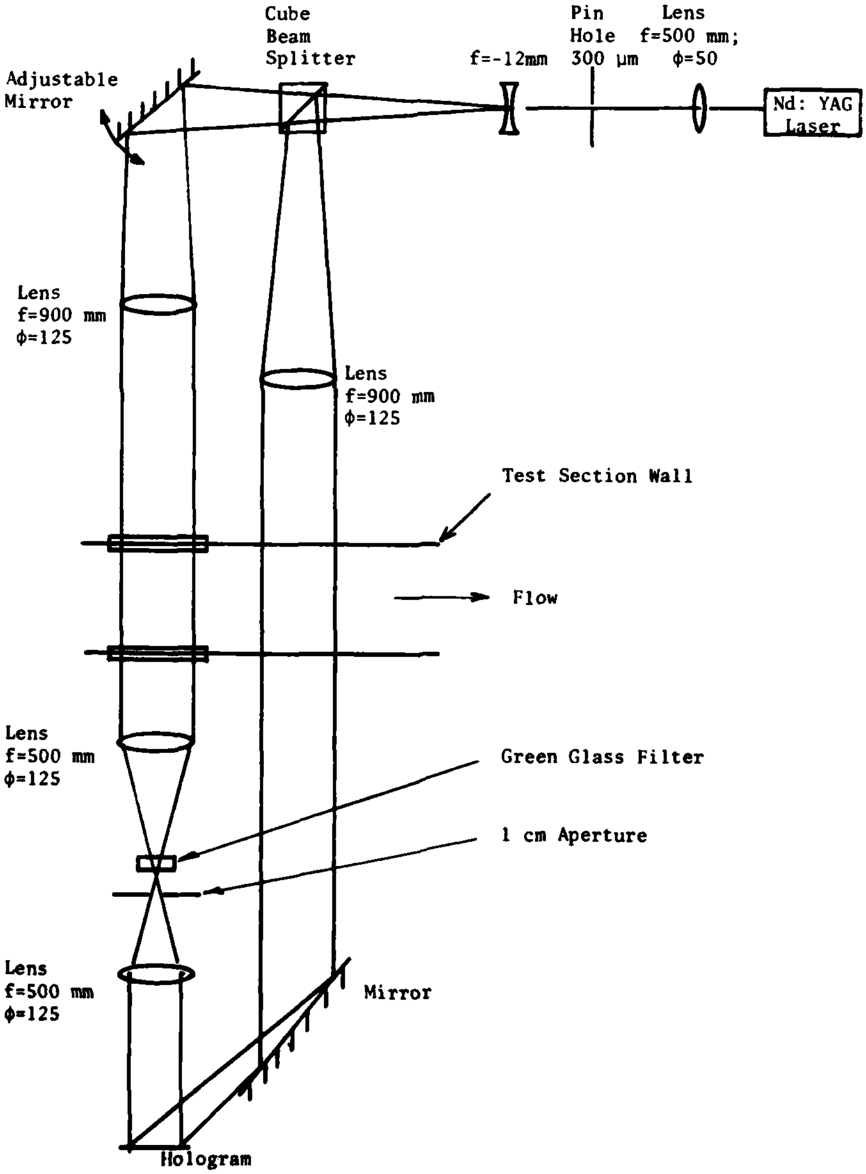

FIGURE 3 LASER HOLOGRAPHY SYSTEM

ally focusing the image into a place upstream from the holograph plane when off-axis holography is employed. An optional off-axis reference beam provided the capabilities to perform off-axis holography. The laser was externally spatially filtered to provide a smooth beam, and the entire laser train was rail mounted for stability.

Holograms constructed with this system contain records of both the amplitude and phase of the object wave (the essence of holography), and the reconstructed image waves can be allowed to interfere with a reference wave to create interference fringes. The fringe structure contains information from which can be extracted details about the density for all points within the flow field. A second method of interferometry was implemented which has both advantages and disadvantages over this post event method. This second method requires that one record two exposures on the single photographic plate. One of the exposures represents the reference, and thus, the interferometric structure is contained within the single holographic image. An obvious disadvantage of the method is that the interferometric fringe structure is frozen and cannot be altered during the reconstruction and interrogation steps. An advantage is that the effects of the distortions and aberrations caused by the optics in the construction apparatus are automatically cancelled from the resulting fringe structure. The optical system and test section were installed in the EAST facility (Figure 4).

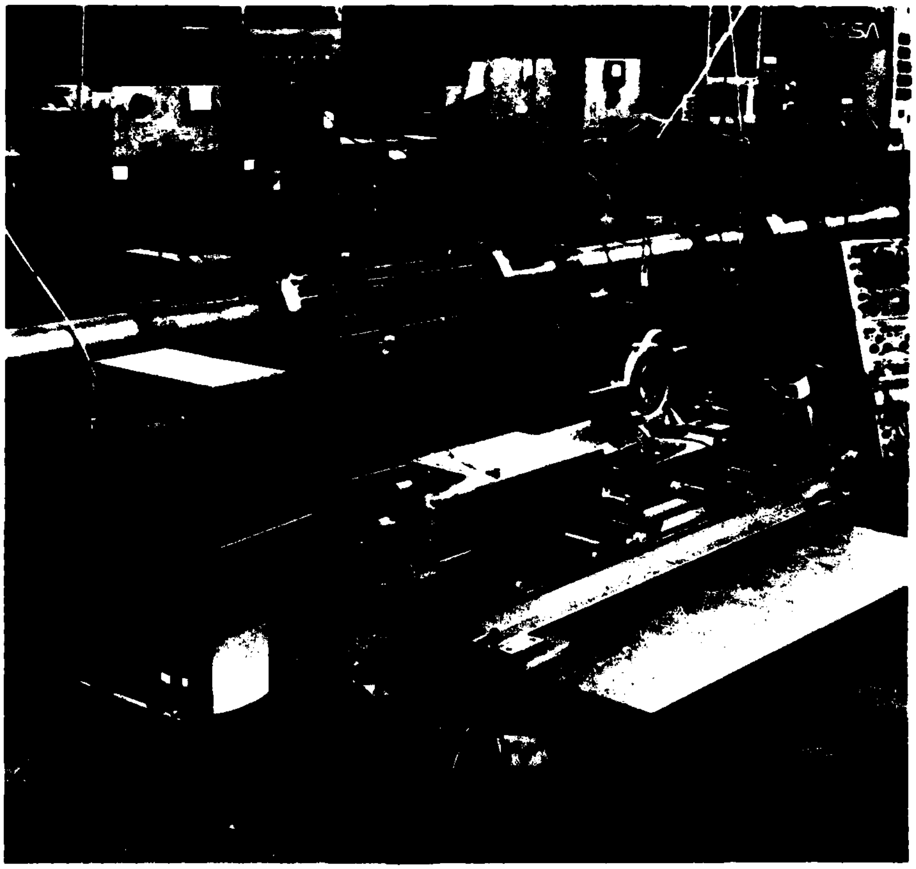

FIGURE 4. HOLOGRAPHY SYSTEM AND TEST SECTION IN NASA SHOCK TUBE FACILITY

RESULTS

The shock tube was operated with air in the driven tube at an initial pressure of 0.1 atmospheres, and a preset driver condition sufficient to produce a shock speed of 2.5 km/sec at the test section. As the shock passes over the ribs, the resultant interaction attenuates the shock which decreases its propagation velocity to 2.3 km/sec between stations TS1 and TS2 and to 2.1 km/sec between stations TS2 and TS3.

Laser shadowgrams of the main shock region (Figure 5) confirm the existence of a multiple reflected shock structure predicted in the two-dimensional calculations of Needham. The source of the multiple shock structure is the reflection of the main shock off the ribs. Each shock/rib interaction generates a reflected shock, one end of which propagates along the main shock and the other end remains essentially stationary in the cavity between two ribs. The main shock moves about two tunnel heights before the reflected shock reaches the opposite side of the tunnel. By this time, most of the reflected wave has become stationary with a diagonal orientation across the tunnel. If the wave orientation is interpreted as the local Mach angle (30°) then the local Mach number is two.

FIGURE 5. LASER SHADOWGRAM OF SHOCK/RIB INTERACTION

The main features observed in the flow are the reflected shock interactions with the main shock (i.e., triple shock intersections) and the reflected shock interactions with the turbulent cavity flow.

An off-axis hologram of the main shock region was used to produce the reconstructed image shown in Figure 6. The photograph is interesting in that it shows how well a duplication of the shock phenomena of Figure 5 is achieved.

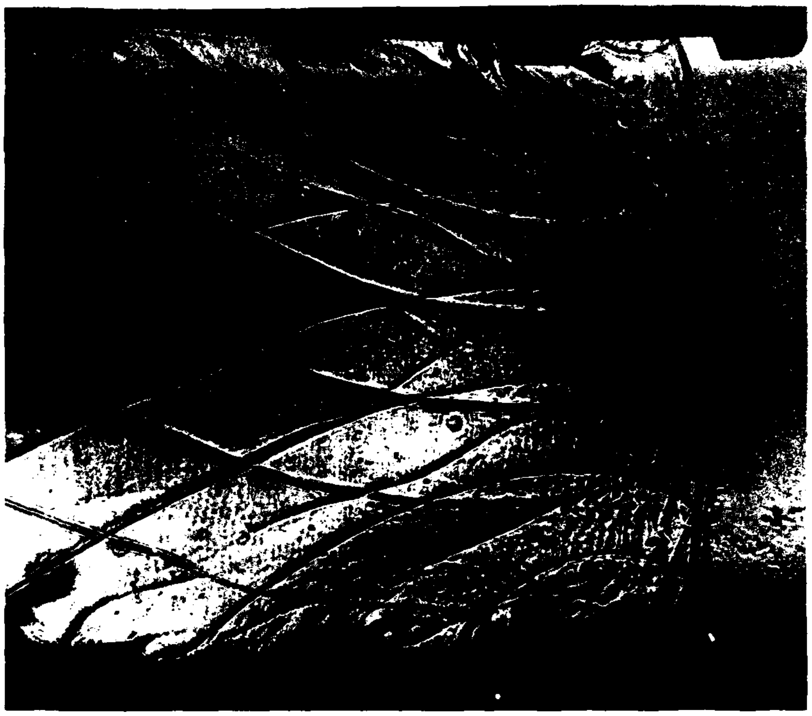

FIGURE 6. LASER HOLOGRAM OF SHOCK/RIB INTERACTION

An example of holographic interferometry with zero offset is shown in Figure 7 in which the first exposure occurred prior to shock propagation and the second exposure occurred with the shock in the optical port. This image of the main shock region is quite different in detail from the images shown in Figures 5 and 6. However, the fringe structure is of such a nature that interpretation is difficult, if not impossible, because with infinite fringe interferometry the sign of the density change between adjacent fringes is ambiguous.

To overcome this problem, the direction of the test section illumination wave (or alternatively the hologram construction reference wave) is slightly altered so that a residual linear fringe structure overlays the holographic image and reduces the ambiguities. The degree of directional change determines the residual fringe spacing; too great a tilt causes fringes which are too fine to be useful while not enough tilt contributes little to reducing ambiguities. This technique is sometimes denoted as offset fringe holographic interferometry. An example of the results of this technique is shown in Figure 8 in which the image is a vertical fringe interferogram of the main shock wave region. A comparison of Figures 6 and 8 is interesting in that it reveals how the complex details of flow phenomena become evident with interferometry.

FIGURE 7. DOUBLE PULSE LASER HOLOGRAM WITH ZERO OFFSET OF SHOCK/RIB INTERACTION

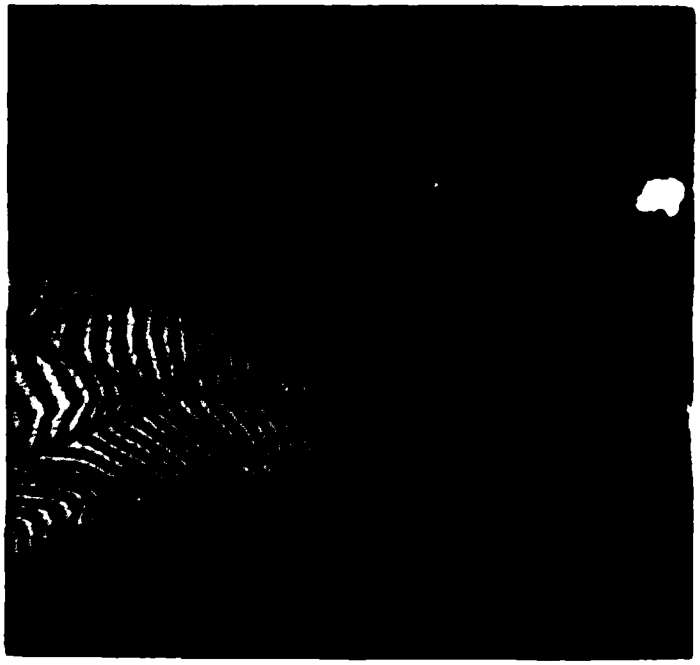

FIGURE 8. DOUBLE PULSE LASER HOLOGRAM WITH FINITE OFFSET OF SHOCK/RIB INTERACTION

Density profiles are determined from the fringe structure by relating fringe shift to index of refraction changes (which for gases is related to the density change). For these experiments the absolute density change, $\Delta\delta$, required to produce one fringe shift is

$$\Delta\rho = k^{-1}\lambda/D = 4.71 \times 10^{-5} \frac{\text{gm/cm}^3}{\text{fringe}}$$

where the Gladstone-Dale constant for air (k=0.23 cm^3/gm), the wavelength of the laser radiation (λ=5320A), and the tunnel width (D=5.0 cm), were used to calculate the interferometer sensitivity. Density profiles were obtained by counting fringes outwards from the centerline of the test section. The absolute centerline density was estimated from the shock speed (C_s = 2.2 km/sec) and the initial density (ρ_1 = 1.28 x 10^{-4} gm/cm^3, air) to be 9.03 x 10^{-4}gm/cm^3. The The density profile one rib spacing behind the shock (Figure 9) reveals a strong compression process with the wall density exceeding twice the centerline density. This increased density was presumably a result of the reflection of the main shock off the ribs.

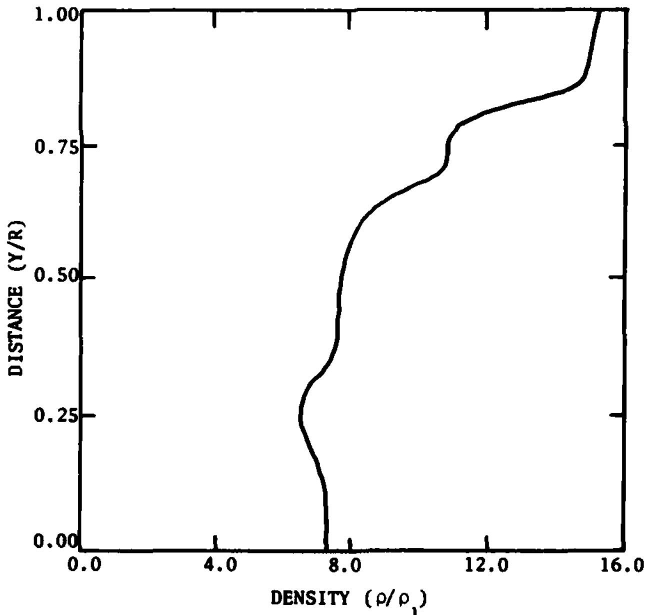

FIGURE 9. DENSITY PLOTTED AGAINST DISTANCE FROM TUNNEL CENTERLINE AT A POSITION ONE RIB SPACING BEHIND SHOCK.

A laser shadowgram and a holographic interferogram of the flow field recorded when the shock was 30 cm beyond the optical port are shown in Figures 10 and 11. The shadowgram indicates that most of the flow field perturbations have decayed, as only weak shocks are apparent in the freestream and turbulence can be observed between the ribs. However, the interferogram shows that the flow symmetry still persists in the freestream; and in addition, some details of the separating and the reattaching flows about the ribs are more clearly illustrated. Interesting, Mirels[4] turbulent boundary layer theory predicts a smooth wall boundary layer thickness of two rib heights which agrees qualitatively with the observed fringe shifts near the wall, and which indicates that the transverse ribs do not increase the boundary layer growth rate in these short duration flows.

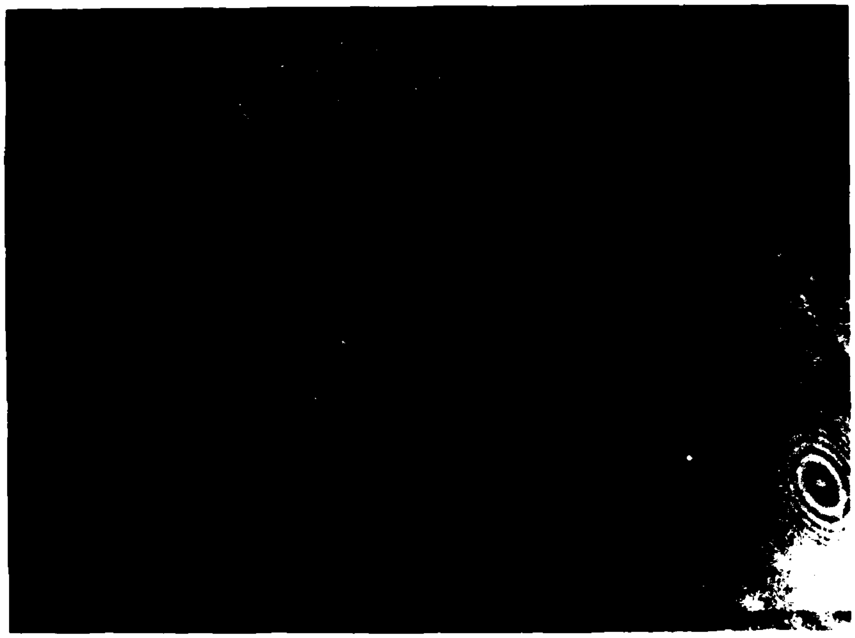

FIGURE 10. LASER SHADOWGRAM OF QUASI-STEADY FLOW

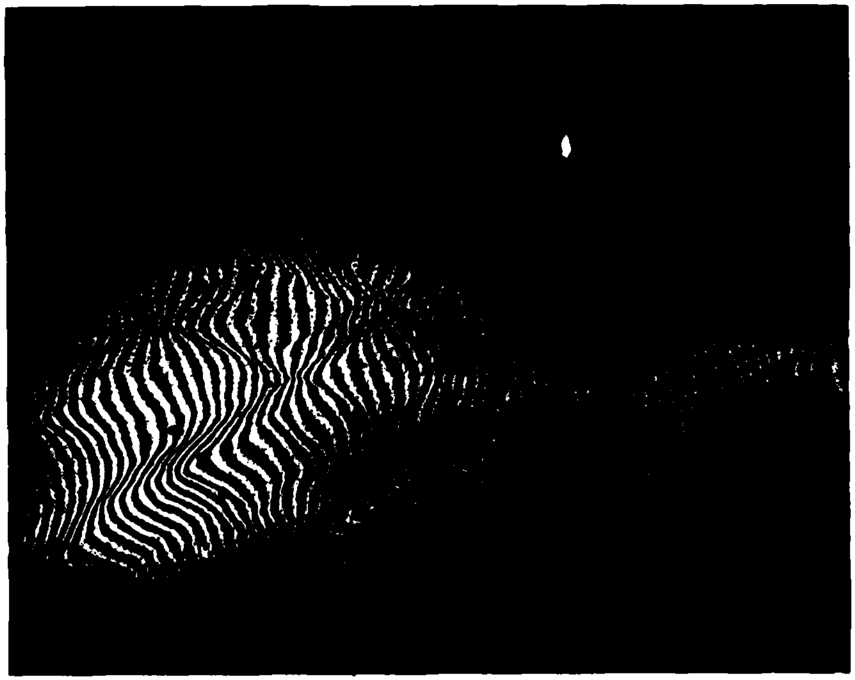

FIGURE 11. DOUBLE PULSE LASER HOLOGRAM WITH FINITE OFFSET OF QUASI-STEADY FLOW

SUMMARY

Strongly two-dimensional flow fields have been observed near the shock wave propagating in a tube with transverse ribs. Shadowgrams of the shock revealed a complicated but symmetric wave structure composed of a perturbed main shock and reflected shocks originating at each rib. Farther behind the shock, quasi-steady bow shocks are observed emanating from each rib. The major viscous effects are observed in the separation and reattachment regions about the ribs, which apparently do not promote the initial boundary layer growth.

ACKNOWLEDGMENTS

This work has been supported at Science Applications, Inc. by the Defense Nuclear Agency (DNA001-77-C-0280). We are greatful to Dr. George Ullrich, the Defense Nuclear Agencies Project Officer and to Dr. Robert E. Dannenberg of Ames Research Center for their cooperation and suggestions.

REFERENCES

1. C.E. Needham and C. Westmorland, "Airblast Calculations for Advanced Missile System (MX) Support", AFWL-TR-75-297, February 1976.

2. A.L. Kuhl, "Numerical Calculations of Shock Decay in Rib Walled Ducts", TRW Report No. 78. 4735.9-14, September 1978.

3. D.T. Hove and J.E. Craig, "Airblast Attenuation Experiments for the MX Trench", Draft report submitted to DNA.

4. H. Mirels, "Estimates of Turbulent Boundary Layer Behind a Shock Wave Moving With Uniform Velocity", Report SAMSO-TR-77-166, December 1977.

RECENT RESULTS OF RESONANT REFRACTIVITY STUDIES FOR IMPROVED FLOW VISUALIZATION

G. Blendstrup

McKinsey & Co., Düsseldorf, Germany

D. Bershader

Dept. of Aeronautics & Astronautics, Stanford Univ., California, USA

P. Langhoff

Dept. of Chemistry, Indiana University, USA

Objective of this work is to achieve a two-order-of magnitude increase in the sensitivity of refractive-type optical flow diagnostic techniques, e.g., interferometry, schlieren methods and shadowgraphy. Useful applications would include visualization of audio-frequency sound waves at moderate levels, vortices and other disturbances in nearly-incompressible flow, turbulent structure in shear layers and other flows, and boundaries of rocket exhaust and plume flows where the refractivity variations are marginal. The method makes use of sodium vapor whose specific refractivity in the D-line region (589 nm) is several orders of magnitude higher than that of air or combustion gases. Injection of the vapor into a flow facility in highly diluted proportions (around $1{:}10^3$ - $1{:}10^4$, depending on flow conditions) would achieve the desired result. A tunable dye laser is required as the light source to provide the wavelength control and resolution needed in the resonant region. By now the calibration measurements of resonant dispersion have been completed together with an analytic study of the effects of Doppler and collisional line broadening on the shape of the refractivity profile near resonance. The results confirm a successful tradeoff between enhanced refraction and manageable absorption in the "near" region (several Å off resonance), a feature which makes the technique feasible.

INTRODUCTION

The sensitivity of nearly all refractive-type flow visualization studies to date has been limited by the value of the specific refractivity parameter (Dale-Gladstone constant) of diatomic gases. That quantity, K_o, relates the refractive index n and mass density ρ in the well-known constitutive relation[1]

$$n - 1 = K_o\rho \qquad \text{I}$$

For air K_o is relatively constant over the visible portion of the spectrum, equal to $2.3 \times 10^{-4} m^3/kg$. Physically, K_o represents the volume density of dipole moment induced in the atomic or molecular gas by the electric field associated with the traversing light waves. This polarizability is not highly dispersive, except near electronic ground-state transition frequencies, where its value increases by some orders of magnitude. Unfortunately, these resonances for air lie in the far vacuum ultra-violet. Indeed, such transitions in the visible spectrum are not easy to come by. The yellow-orange D_2-line of sodium vapor (wavelength λ = 588.9963 nm) was chosen after consideration of the possibilities. It turns out that the non-resonant refractivity for sodium, $K_{o,Na}$ is 4.05 m^3/kg , 17.6 times that of air, so there is already an initial advantage. At about 8Å off resonance this ratio increases to approximately 4,000. However, the latter figure is for so-called homogeneous line broadening as determined by Na-Na collisions. Line broadening for sodium highly diluted by a carrier gas X is of the heterogeneous type, controlled by Na-X collisions. For carrier gases of interest, the latter is another favorable factor: for example, the collision line width for sodium in argon is about 25 times smaller than for self-broadening in pure sodium vapor, which yields an additional factor of about 5 for the specific refractivity enhancement.

The calibration phase of the work consists of a combined experimental-analytical effort whose description forms the essence of the present paper. An experimental configuration was designed and constructed which measured the near-resonant dispersion of a sodium vapor column by interferometry. The analysis yielded a theoretical dispersion curve with which to compare the experiments. The theoretical basis starts with the Lorentzian analysis of electromagnetic wave dispersion by molecular dipoles, with the addition of Doppler and collisional line broadening features (Voigt profile). The formulation was done in terms of the Kramers-Kronig integral transforms relating refractive and absorptive dispersion, resulting in a computer output of both sets of profiles over the resonant region.

EXPERIMENT

The idea is illustrated in the schematic diagram of Figure 1. We see a

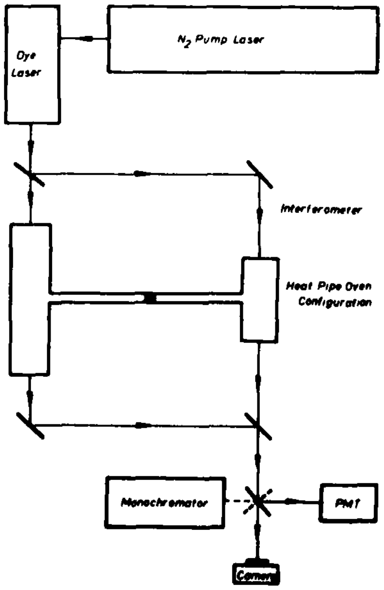

Figure 1. Overall schematic diagram for sodium resonant dispersion calibration.

double heat-pipe oven configuration occupying both arms of a Mach-Zehnder interferometer[2], with a dye laser as the light source and various output devices used in different parts of the experiment. A few words are warranted about some of the components.

The heat-pipe oven is a relatively new concept[3] for containing a uniform, steady-state column of metal vapor in a defined volume, buffered by an inert gas. Briefly, the steady-state behavior includes vaporization of sodium in the central portion of the tube surrounded by a clam-shell heater, occupation by the vapor of the heated volume at a pressure determined by the metal's vapor pressure-temperature curve, condensation of the vapor at the boundary of the heated and cooled regions, and transport of the condensate back to the center of the tube by capillary action along a stainless steel mesh lining the inside walls of the oven. The use of a double oven of different column lengths allows cancellation of boundary and end effects on the optical path difference measured by interferometry. For reference, we note that the vapor pressure of sodium (torr) is related to temperature (°K) by

$$\ell n P = 10.864 - 5619/T + (3.45 \times 10^{-6})\, T - 1.041\, \ell n T$$

The tunable dye-laser light source designed and built by us for the purpose, is the component which makes resonant refractive work possible in the first place. It is shown schematically in Figure 2. The cavity is defined by a high-resolution blazed grating with micrometer angular control and an output window having a very small wedge angle. The dye cell (Molectron Co. No. D1051) contains rhodamine 6G and is magnetically stirred. Activation is supplied by a pulsed nitrogen laser (Molectron UV300) at 3371 Å, with a repetition rate of 10 pps and a pulse duration of about 10 nsec and a peak power of 300 kw. Fluorescence emitted by the dye solution lies between 5680 Å and 6050 Å with a maximum around 5790 Å, enabling convenient tuning to the D-line wavelength at 5890 Å with the rotatable grating. The laser cavity is about 50cm long; thus a 10 nsec pulse allows for only a few light passes, helping to ensure a suitably high power output combined with a reasonably narrow band width. Specifications of the dye laser are given in Table I. The listed bandwidth of 0.24 Å was satisfactory for present purposes.

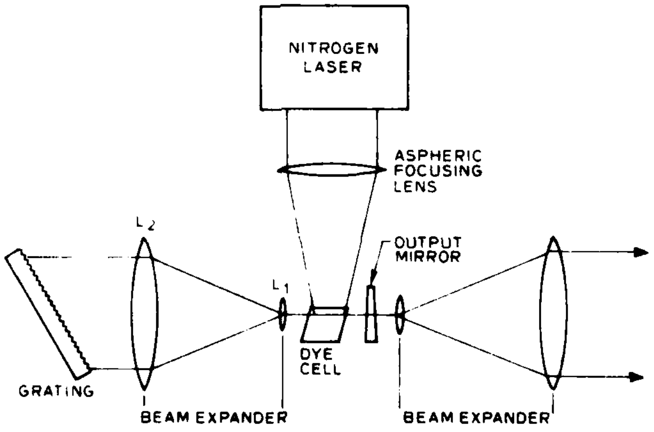

Figure 2. Schematic of Dye Laser Configuration

TABLE I

Specifications of Dye-Laser

Dye Solution	Rhodamine 6G
Tuning Range	5860 - 6050 Å
Bandwidth (FWHM) at 5890 Å	0.24 Å
Wavelength Accuracy	< 0.1 Å
Wavelength Reproducibility	< 0.1 Å
Wavelength Stability	< 0.1 Å
Output Peak Power at 5890 Å	31 kW
Output Pulse Energy at 5890 Å	155 μJ
Repetition Rate	10 pps
Pulse Duration	5 ns

Sharpening the wavelength spread with a Fabry-Perot etalon would have resulted in a significant loss of output power, a feature we wished to avoid.

Wavelength accuracy, reproducibility and stability were determined with a McPherson 1-meter scanning monochromator (Model 2051) with a minimum instrumental line width of < 0.1 Å. It turned out that wavelength shifts due to temperature changes or other causes were smaller than this tolerance. Wavelength calibration was performed before each run, with the help of a sodium spectral lamp.[4]

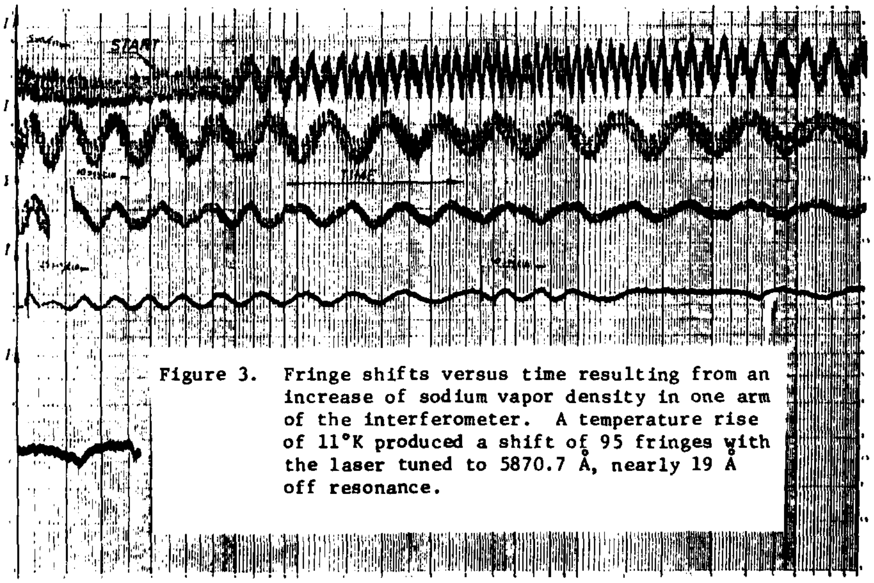

Figure 3. Fringe shifts versus time resulting from an increase of sodium vapor density in one arm of the interferometer. A temperature rise of 11°K produced a shift of 95 fringes with the laser tuned to 5870.7 Å, nearly 19 Å off resonance.

The basic experiment consisted of measurement of shifts of the Mach-Zehnder fringes associated with a change in sodium vapor concentration; data was obtained at several wavelengths in the near-resonance region as described later in this paper. The shifting fringes traversed a 0.5 mm pinhole in front of a type RC5 C31000F photomultiplier tube cooled to -30°C to increase signal to noise ratio by a factor of 10. Output was recorded with an x-y plotter (Hewlett-Packard Type 7004B). Figure 3 shows the type of data obtained. Fringe shifts were considered to be precise to 0.1 fringes.

THEORETICAL CONSIDERATIONS

Both collision and doppler broadening produce marked changes in the dispersion profiles near resonance for the conditions of the present calibration experiment, or in a typical flow application. Collision broadening is essentially Lorentzian, i.e., the functional form is $\Delta\nu/(A+(\Delta\nu)^2)$, where $\Delta\nu$ is the frequency separation from resonance, with A a constant. Doppler broadening, on the other hand, is characterized by the exponential functional factor $e^{-B(\Delta\nu)^2}$, where B is also a constant; that factor stems from the random (Maxwellian)velocity distribution of the molecular dipoles. The combined collision-doppler phenomenon gives a convoluted Lorentzian-doppler shape termed a Voigt profile. The latter is represented by the following expressions for the refractive index $n(\nu)$ and absorption coefficient $\mu(\nu)$ as functions of the frequency ν :

$$n_r(\nu)-1 = \frac{\sqrt{\ell n 2}}{8\pi^2\sqrt{\pi}} \frac{e^2 N f_r}{m\varepsilon_o \gamma_D \nu_r} \int_{-\infty}^{\infty} \frac{\varepsilon - \nu}{(\varepsilon-\nu)^2+\gamma_L^2/4}\, e^{-4\ell n 2(\varepsilon-\nu_r)^2/\gamma_D^2}\, d\varepsilon \qquad \text{II}$$

$$\mu_r(\nu) = \frac{\sqrt{\ell n 2}}{4\pi\sqrt{\pi}} \frac{e^2 N f_r \gamma_L}{mc\,\varepsilon_o \gamma_D} \int_{-\infty}^{\infty} \frac{1}{(\varepsilon-\nu)^2+\gamma_L^2/4}\, e^{-4\ell n 2(\varepsilon-\nu_r)^2/\gamma_D^2}\, d\varepsilon \qquad \text{III}$$

where the usual symbols are used for well-known physical constants, and where f is the oscillator strength for the transition, N the atomic number density and γ_D and γ_L the characteristic doppler and Lorentzian spectral widths, respectively, given by

$$\gamma_D = \frac{4\pi\nu_r}{c}\sqrt{\frac{2kT\ell n 2}{M}} \qquad \text{IV}$$

and

$$\gamma_L = 2C_r N \qquad \text{V}$$

with C_r a proportionality constant obtained from collision theory[7] . Note also that M represents the atomic mass and ν_r the resonant frequency. Table II gives some basic numerical data for the sodium D-lines. The calibration studies were performed on the high-frequency side of the D_2-lines. When expressed in suitable nondimensional form, the integrals in equations II and III can be treated as the imaginary and real parts, respectively, of the function

$$W(z) = e^{-z^2} \operatorname{erfc}(-iz) \;, \; z = u + ia \qquad \text{VI}$$

TABLE II

Resonant Parameters for Sodium D-Lines. Subscript r Represents Resonant Frequency. C_r is the Parameter Which Determines Collision Broadening of the Lines.

	λ_r[Å]	$\nu_r[10^{14}$/sec]	f#	$C_r[10^{15} m^3$/sec]
D_1	5895.930	5.083345	0.327	7.32
D_2	5889.963	5.088500	0.655	8.59

where erfc represents the complementary error function and u is a non-dimensional doppler width given by $u = 2 \ \ell n2 \ (\nu - \nu_r)/\gamma_D$; while a , the so-called Voigt parameter, is essentially a Lorentzian-doppler width ratio: $a = \gamma_L \ \ell n2/\gamma_D$. This formulation was used for the computer program. Results for the dispersion are shown as the solid line in Figure 4, based on results obtained in .01Å intervals.

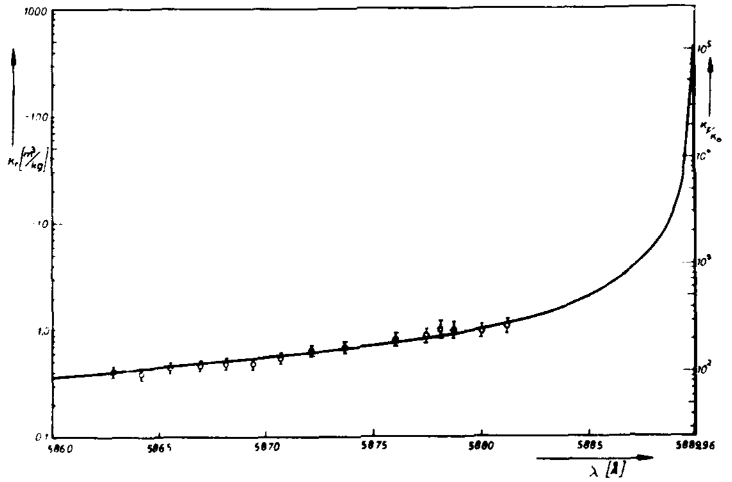

Figure 4. Wavelength dependence of refractivity parameter K(=(n-1)/ρ) on high frequency side of sodium D_2 line. Solid curve is the theoretical prediction on which are superimposed measured points. Right-hand ordinate gives ratio to the non-refractive value for sodium. Ratio to nonrefractive value for air would be about 20 times larger.

FURTHER DISCUSSION

The refractivity peaks occur at the frequencies of half-maximum absorption which, in practice, are of order of 10^{-2} Å away from resonance. This spread stems from both collision and doppler broadening which, in turn, modify appreciably the predicted peak refractivity enhancement. For typical conditions in the present experiment, namely an atomic density of around 10^{21}/met^3 at a temperature in the range near 750°K, peak refractive amplification lies somewhat under 10^5. In practice high absorption at or very near the refractivity maximum requires one to utilize the "near region" which is of the order of a few Å away from resonance. This trade-off between absorption and dispersion works because the spectral region of highly enhanced refractivity is considerably broader than the absorption region. As seen in Figure 4, the calibration experiments were performed at wavelengths where the refractive constant for the sodium vapor is around 10^2 times its nonresonant value. Experimental points superimposed on the theoretical curve show good agreement between the two, establishing good confidence in the predicted dispersion. Vertical uncertainty segments on the measured points stem largely from a corresponding uncertainty in the effective length of the sodium vapor column in the heat-pipe oven. Further work is required for more accurate determination of the position and shape of the diffusion boundary between the condensing sodium vapor and the argon buffer gas. Another limitation is the degradation of signal to noise ratio when the increased absorption near resonance lowers the transmitted wavelength intensity relative to the broad band noise background associated with the pulsed dye-laser arrangement. For example, at 7Å away from resonance with $T = 465°C$, the absorption coefficient $\kappa \sim 7$ (met)$^{-1}$, and fringe shift measurement becomes difficult.[5] However, this problem becomes less severe with a more powerful light source, or in an aerodynamic application when sodium is diluted in a carrier gas, as described below.

In assessing the practical application of the resonant refractive method, one (1) needs to confirm the technology for injecting sodium vapor, say in atomic concentrations of 10^{-3}, with a laboratory flow, (2) apply the trade-off between enhanced refractivity and absorption to the flow parameters of the particular experiment and (3) decide on the objective, the latter determining which particular refractive diagnostic method will be used. Note that Fig. 4 also shows an ordinate which gives K in ratio to the nonresonant value for sodium K_o, and we note further that $K_{o\,Na} = 4.031 \times 10^{-3}$ met^3/kg while a typical value for $K_{air} \approx 2.3 \times 10^{-4}$met^3/kg. Thus, with sodium seeded into a flow of nitrogen, for example, the ordinate ratios are increased by about a factor of 18. The corresponding total refractivity enhancement reaches a value of 2.5×10^3 .

Another favorable factor relates to the change of Lorentzian line width for the case of heterogeneous broadening (sodium in a bath of buffer gas such as nitrogen or argon) as compared with self-broadening in pure sodium vapor, as was the case in these calibration experiments. A sensitivity analysis of the parameters indicates that the magnitude of the absorption in the wings of its profile is proportional to γ_L whereas the refractivity line shape is relatively insensitive to this same parameter. Thus a decrease of γ_L would permit closer approach to the resonance wavelength with corresponding considerable increase in refractive enhancement. Recent calculations indicate that the collision line width is much smaller in the heterogeneous case, and this result, in turn, indicates an additional factor of 5 in refractive amplification compared to the case of sodium self-broadening. A sample calculation for flow visualization of sound waves is performed in another paper.[6]

Injection of small amounts of sodium vapor from an oven into a flow has been a technique used by research chemists and others, but needs further development in aerodynamic applications. For quantitative interferometric studies, the absolute concentration of sodium vapor will have to be known, but that would not be the case for schlieren and shadow-type studies. All features considered, it looks quite feasible to improve sensitivities of these methods surely by one and possibly up to two orders of magnitude by suitable experimental design. The method also offers a quasi-localized diagnostic [illegible] resulting from localized injection of the seed vapor. The results of the present calibration study and related analysis warrant development of a pilot facility designed to utilize the resonant refractive technique.

REFERENCES

1. (a) M. Born and E. Wolf, Principles of Optics, 5th edition, p. 88, Pergamon Press, 1975.
   (b) D. Bershader, "Some Aspects of the Refractive Behavior of Gases" in Modern Optical Methods in Gas Dynamic Research, D. Dosanjh (Ed.), pp. 65-83, Plenum Press (1971)
2. R. Ladenburg and D. Bershader, "Interferometry," in Physical Measurements in Gas Dynamics and Combustion, Princeton University Press, 1954.
3. C.R. Vidal and J.J. Cooper, J. Appl. Physics 40, 3370 (1969).
4. G.H. Blendstrup, Resonance Refractivity Studies of Sodium Vapor for Enhanced Flow Visualization, Doctoral Thesis, Department of Aeronautics and Astronautics, Stanford University, December 1978.
5. G. Blendstrup, D. Bershader and P. Langhoff, A.I.A.A. Journ. 16, pp. 1106-1108, October 1978.
6. D. Bershader, G. Prakash and G. Huhn, "Improved Flow Visualization by Use of Resonance Refractivity", Experimental Diagnostics in Gas Phase Combustion Systems, (B.T. Zinn, Ed.), pp. 595-609, American Inst. of Aeronautics and Astronautics, New York, 1977.
7. K. Niemax and G. Pichler, J. Physics, B8, Feb. 1975, p. 179.

ACKNOWLEDGEMENT

We acknowledge support for this work from the U.S. Air Force Office of Scientific Research, Department of Defense, Grant AFOSR 74-2670.

MACH WAVE RADIATION OF HOT SUPERSONIC JETS INVESTIGATED BY MEANS OF THE SHOCK TUBE AND NEW OPTICAL TECHNIQUES

HERBERT OERTEL

Institut franco-allemand de recherches de Saint-Louis
Saint-Louis, France

The supersonic jet emits Mach waves which are rather regular ones. Likewise inside the jet besides the well known stationary Mach waves also moving ones do exist. The kinematics of these Mach waves has been investigated by means of double exposure interferograms, high speed movies, double exposure streak records and immobilisations on moving film. A laser microphone has been used for studying the dynamics outside the jet. Two different methods of producing the jet by means of the high pressure shock tube have been applied which allowed for varying the data of both the jet and ambient gas within very wide limits.

The experimental results can be represented by unpredicted simple relations. The Mach waves do accompany coherent mixing layer structures propagating downstream at three preferred speeds. The Mach angles depend on the jet Mach number and the ratio of sound velocities inside and outside the jet. No dependence on any length ratio or Reynolds number has been detected. Outside the jet strong and long Mach waves are conically spreading shock waves. The mean shock distances λ are linearly increasing with the production coordinate ξ and independent of the propagation coordinate η. The maximum shock compressions turned out to be determined by λ/η and an initial shock compression which is independent of ξ, the jet velocity and the jet diameter. The shock waves are so strong that theories based on acoustic approximations are considered to be inadequate.

The Mach waves can be suppressed by means of an appropriate subsonic envelope. For studying the waves inside the envelope a new method of simultaneous jet and envelope production by means of the shock tube has been developed.

INTRODUCTION

Supersonic jets emit Mach waves like those visualized in Fig. 1. In the case of about equal pressures at the nozzle exit and outside the jet these Mach waves are rather regular ones. They have been assumed to originate from turbulence or from coherent mixing layer structures of different kind[1,2,3,4]. Previous experimental investigations [5,6] did not definitely answer the question whether the one or the other or none of these assumptions correspond to reality. More experiments with jet data varied within wider limits were needed. At the 10th Shock Tube Symposium [7] the high pressure shock tube and double exposure interferometry were shown to be useful tools for doing the parametric investigation. This investigation has been continued.

Not only supersonic jets but also subsonic envelopes surrounding such jets have been produced by means of the shock tube. Once more new optical techniques have been applied. The kinematics of the Mach waves has been investigated using high speed movies, double exposure streak records and immobilisations on moving film. The dynamics has been studied by means of a laser microphone. The experimental results can be represented by simple formulae which have not been predicted.

Fig. 1 - Mach waves

FACILITY

The ISL-high pressure shock tubes [8,9,10] were used. Its length 2o m, diameter 1o cm and nitrogen or hydrogen driver pressures up to 8oo bars allowed for varying the jet data within very wide limits. Inside the test chamber connected to the end of the tube the ambient gas data could be varied as well. From the five possible methods of supersonic jet production presented on the 1oth Shock Tube Symposium the two ones scetched in Fig. 2 have been preferred. The well known reflected shock tunnel method offers the advantage that the exit and ambient pressure equality can be obtained without exit diaphragm and at high Mach numbers. The non reflected shock method was used for producing very hot jets at moderate Mach numbers without complicating real gas effects and with the possibility of varying the exit boundary layer thickness by simply changing the length of the inserted tube. Fig. 3 presents the method used for simultaneous supersonic jet and subsonic envelope production. The numerous small supersonic jets join and transform into the subsonic flow. This method is restricted to equal gases having equal stagnation enthalpy. Cold helium envelopes covering hot nitrogen jets have been produced by conventional blow down out of an annular slit. The blow-down method was also used for producing some cold supersonic as well as subsonic air jets for comparison. Most of the experiments have been done with axial nozzles. A few experiments have also been accomplished with plane nozzles. All nozzles were contoured for giving parallel outflow.

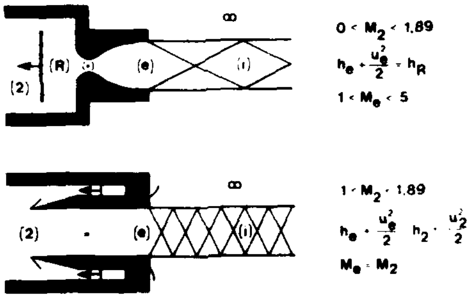

Fig. 2 - Supersonic jet production

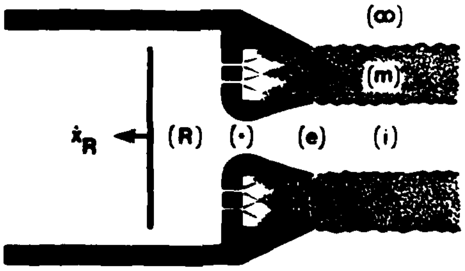

Fig. 3 - Subsonic envelope production

OPTICS

Different versions of the well known [11,12] differential interferometer working with polarized light and Wollaston prisms have been used for visualizing the

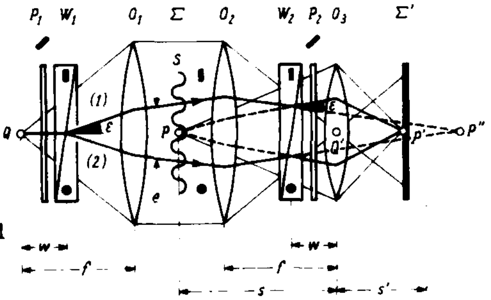

Fig. 4 - Differential interferometer

jet and its Mach waves. The basic instrument shown in Fig. 4 was adjusted to infinite fringe spacing and then employed for taking series of pictures each exposed by one single spark. At large aperture a λ/2 plate was used for improving the picture quality by 9o° - turning the directions of polarization behind the prism W1. In some cases stationary or slowly moving phase objects had to be suppressed by complementary double exposure. This has been obtained by the two methods [13,14] scetched in Fig. 5. That using two sparks jumping at points Q1 and Q2 with some time interval 1 < Δt/μs < 1o was applied for taking pictures like that shown in Fig. 1. The other one using a single continuous light source and a third prism W3 served for taking streak records like that presented in Fig. 6. High speed movies have been

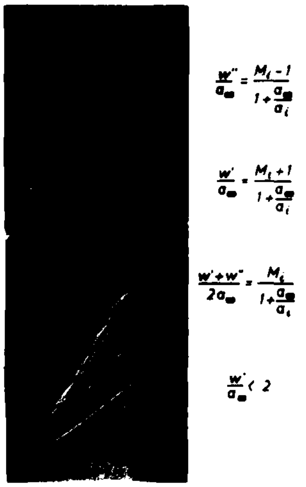

Fig. 6 - Streak record

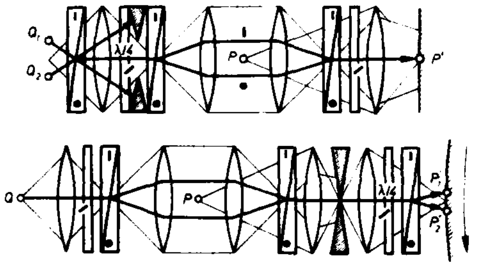

Fig. 5 - Complementary double exposure

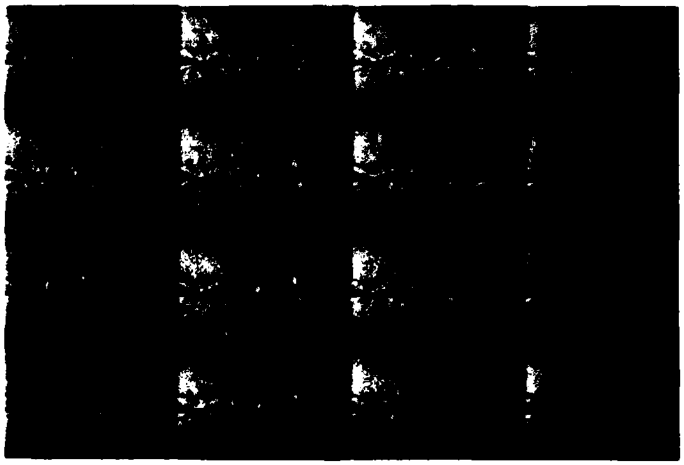

Fig. 7 - Pictures selected from a movie

obtained by three different methods: The Cranz-Schardin-camera, the Früngel-drum-camera and the Cordin-rotating-mirror-framing-camera. The 16 pictures shown in Fig. 7 are selected from 8o pictures taken with the Cordin camera at 2μs-interval. The informations given in the pictures turned out to be highly dependent of the visualization optics and its adjustment as well as on the duration and interval of the exposures. This is due to the coexistence of different families of ordered waves outside and inside the jet as well as different families of coherent structures within the mixing layer which are modulated by turbulence. The light phase shifts produced by all these phase objects are integrated. Finally immobilisations on appropriately moving film have been found to be the most useful tool for separate visualization of objects travelling at different velocities. Fig. 8 compares the method to that of streak records with the slit set perpendicular to the jet axis. Fig. 9 presents three immobilisations taken from the same jet at three different speeds w'' < w < w'.

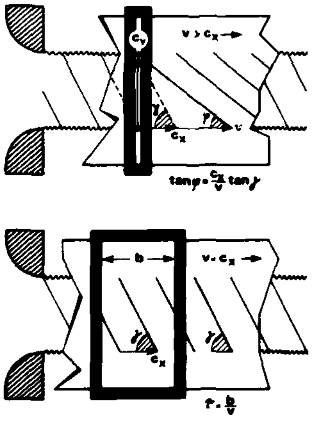

Fig. 8 - Method of immobilisation

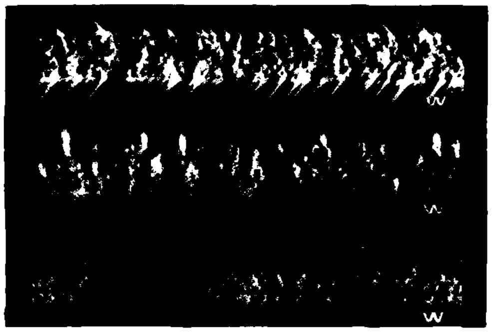

Fig. 9 - Immobilisations

The dynamics of the Mach waves outside the jet was investigated by means of the laser microphone [15] presented in Fig. 1o. The adjustment of the Mach-Zehnder-set up is stabilized by means of the piezo-translator. In order to get local data both beams are shielded except of a short sensitive length between small windows closing capillaries. Shock fronts being exactly parallel to the sensitive length have been recorded with about o,5 μs rise time. Signals like that shown in Fig. 11 were digitized, stored, transmitted to the computer and finally submitted to various statistical evaluations.

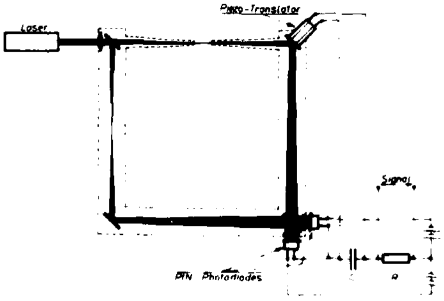

Fig. 1o - Laser microphone

KINEMATICS

The kinematics of the Mach waves has been investigated with the jet data varied within the following limits: $1,3 < d/\text{mm} < 1oo$; $o,1 < p_\infty/\text{bar} < 5,5$; $3oo < u_i/\frac{m}{s} < 35oo$; $1 < M_i < 4,4$; $o,5 < a_i/a_\infty < 3,2$.

d = diameter of the nozzle exit. p_∞ = ambient pressure. u_i = jet flow velocity.

M_i = jet flow Mach number. Sound velocities a_i inside and a_∞ outside the jet. Air, nitrogen, helium and different mixtures of these gases were used as jet gases and ambient gases.

Two families of strong Mach waves outside the jet as well as two families inside exist. They do accompany coherent mixing layer structures propagating downstream at three preferred speeds $w'' < w < w'$. The 327 experimental points in Fig. 12 can be fitted by the following Mach number equations:

$$\frac{w}{a_\infty} = \frac{u_i - w}{a_i} \pm \delta \qquad (1)$$

$$\frac{w'}{a_\infty} = \frac{u_i - w'}{a_i} + 1 \pm \delta' \qquad (2)$$

$$\frac{w''}{a_\infty} = \frac{u_i - w''}{a_i} - 1 \pm \delta'' \qquad (3)$$

The standard deviations are:
$\delta = 0{,}064$, $\delta' = 0{,}081$, $\delta'' = 0{,}068$.

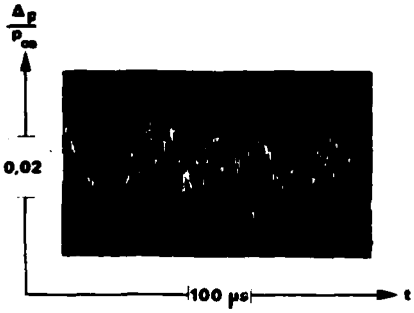

Fig. 11 - Density oscillations

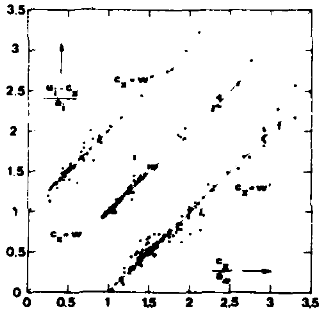

Fig. 12 - Mach numbers

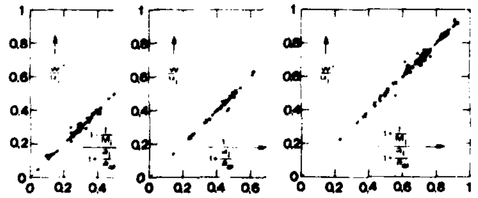

Fig. 13 - Velocity ratios

The velocity ratios presented in Fig. 13 as well as the Mach angles do solely depend on M_i and a_i/a_∞:

$$\frac{1}{\sin\gamma} = \frac{w}{a_\infty} = \frac{u_i - w}{a_i} = \frac{M_i}{1+\frac{a_\infty}{a_i}} \qquad (4)$$

$$\frac{1}{\sin\gamma'} = \frac{w'}{a_\infty} = \frac{M_i + 1}{1+\frac{a_\infty}{a_i}} \; ; \qquad \frac{1}{\sin\gamma''} = \frac{u_i - w''}{a_i} = \frac{M_i + \frac{a_\infty}{a_i}}{1+\frac{a_\infty}{a_i}} \qquad (5)\;;\;(6)$$

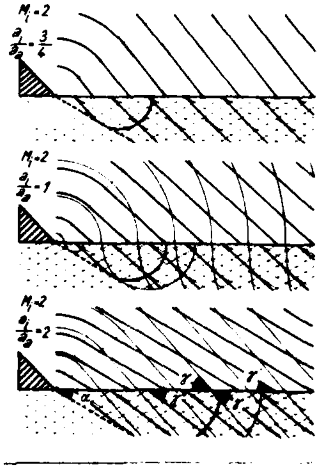

Fig. 14 - Mach waves

No dependence on any length ratio or Reynolds number has been detected.

Fig. 15 - Mach waves

The γ'-Mach waves outside the jet are most easily recognized and are those which have already been visualized in the past. They appear at $u_i > a_\infty$. The proof of existence of the γ''-Mach waves inside the jet has been given by immobilisations like that shown in Fig. 9. They appear at $u_i > a_i$. The γ-Mach waves can only exist at high $u_i > a_i + a_\infty$. They are much shorter than the other ones because their angle is much larger. This fact is illustrated in Fig. 14 and 15. The proof of existence inside the jet could not be given because they have equal angles inside and outside provided they exist. But there is no reason for assuming the existence at one side without the coexistence at the other side of the mixing layer.

STRUCTURES

The structures accompanied by strong Mach waves are more or less annular ones. High speed movies have given the impression that they are rapidly deforming themselves. But this may be an optical effect due to turbulence. On the other side the behaviour of the Mach waves as well as the appearence of the structures on immobilisations support the statement that they are coherent in the sense of having much longer life and more lateral extent than the random turbulence. Some of them could be identified from the beginning down to the transonic portion of the jet. This statement does not imply any answer to the question about the physical nature of the structures. They may be vortices, vortex sheet deformations or pressure waves, and they may be cause or effect of the pressure waves outside the mixing layer.

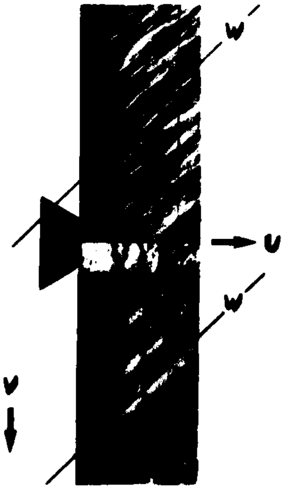

Fig. 16 - Subsonic w-structures

Coherent and obviously growing structures travelling at speed w have also been detected at the beginning of subsonic jets. There they are accompanied by strong and quasistationary pressure fields which are vanishing with increasing distance from the jet. This can be seen from Fig. 16. Besides these rather big structures always numerous fine and nearly parallel filaments have become visible on pictures and immobilisations of supersonic as well as subsonic jets. They prefer angles about 3o° and 6o° and are convected with all velocities up to u_i. Pictures like that presented in Fig. 17 and 18 suggest that such filaments are due to vortex stretching. The contribution to the jet noise is unknown.

DYNAMICS

The dynamics of the Mach waves outside the jet has been investigated with the jet data varied within the following limits:

$3{,}75 < d/\mathrm{mm} < 2o$; $52o < u_i/\frac{m}{s} < 212o$

$1 < M_i < 4$; $o{,}75 < a_i/a_\infty < 1{,}53$

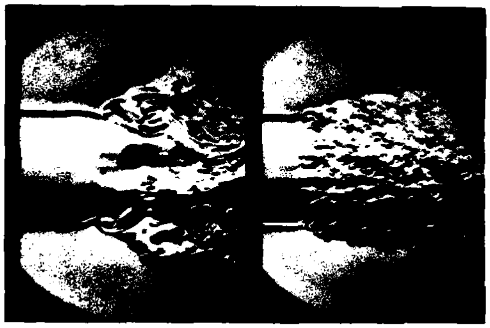

Fig. 17 - Vortex stretching

Air has been used as the jet gas and air or mixture of nitrogen and helium as the ambient gas the pressure of which was always atmospheric. The sensitive length of the optical microphone was placed at the following distances x from the exit plane and distances y from the jet:

Fig. 18 - Filaments

$o{,}5 < x/d < 11; \quad o{,}5 < y/d < 7{,}5$

The strong Mach waves are shock waves. The following considerations are restricted to those having shock compressions higher than the local rms-value $\Delta\tilde{p}$ of the pressure fluctuations and recorded with rise times shorter than 3μs. By this restriction shock fronts crossing at angles above $1o^{o}$ have been excluded. The mean shock compressions $\Delta\overline{p}$ of such shock waves turned out to be about twice and the maximum shock compressions $\Delta\hat{p}$ four to seven times $\Delta\tilde{p}$. Such shocks are not rare events, but are the dominant contribution to the near field noise.

The mean shock distance λ was found to grow with increasing production coordinate $\xi = x - y \tan\gamma'$ and to be practically independent of the propagation coordinate $\eta = y/\cos\gamma'$. The experimental points presented in Fig. 19 can be approximated by the following relation:

$$\lambda - \lambda_0 = A \left(\frac{a_\infty}{w''} - \frac{a_\infty}{w'}\right)(\xi - \xi_0) \qquad (7)$$

$$\xi_0 = \frac{w}{a_\infty} \lambda_* \qquad (8)$$

$$\lambda_0 = \left(\frac{w}{a_\infty} + 1\right) \lambda_* \qquad (9)$$

With constant $A = 1/11$ and $\lambda_* = 1{,}2$ mm the standard deviation $\delta = o{,}16$ is smaller than the scatter at equal experimental conditions. The Mach waves appear beyond some small ξ_0

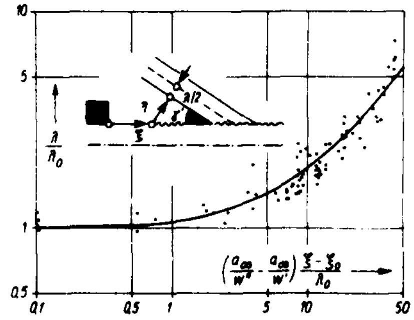

Fig. 19 - Mean shock distance

The influence of ξ_0 on λ decreases with increasing ξ. The growth of λ with increasing ξ seems to be due to some loss of w'-structures by interaction with w''-structures. The mean shock frequencies a_∞/λ were higher than the 16ooo cps-limit of audibility. But extrapolation suggests that they become audible if the supersonic portion of the jet is longer than a certain critical length which for instance in the case $M_i = 2$ and $a_i = a_\infty$ is about 16o mm.

The mean shock compression $\Delta\overline{p}$ grows with increasing λ/η in a manner which seems to be weakly dependent of the jet diameter d. On the other side no dependence of the maximum shock compression $\Delta\hat{p}$ on d has been detected. The experimental points presented in Fig. 2o can be approximated by the relation:

$$\frac{\Delta\hat{p}}{p} = \frac{B\cdot\frac{\lambda/2}{\eta+\lambda/2}}{1+C\sqrt{\frac{\lambda/2}{\eta+\lambda/2}}} \qquad (1o)$$

$$B = \frac{2+f_\infty}{1+f_\infty}\ ; \quad f_\infty = \frac{2}{c_{p_\infty}/c_{v_\infty}-1} \qquad (11)$$

$$C = B\,\frac{p_\infty}{\Delta\bar{p}_0} - 1 \qquad (12)$$

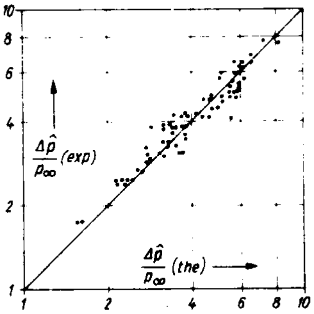

Fig. 2o - Maximum shock compression

Once more the standard deviation δ = o,1o is smaller than the scatter at equal experimental conditions. No experimental constant at all does appear explicitely in this relation which has been established from the hypothesis of conically spreading sawtooth-waves. The initial shock compression $\Delta\hat{p}_0$ at η = o has been assumed to be independent of u_i, d and ξ:

$$\frac{\Delta\hat{p}_0}{p_\infty} = \frac{\Delta\hat{p}}{p_\infty}\ (y = o) = \frac{2+f_\infty}{2f_\infty}\left(\frac{w'-w}{a_\infty}\right)^2 = \frac{2+f_\infty}{2f_\infty}\left(1+\frac{a_\infty}{a_i}\right)^{-2} \qquad (13)$$

This initial shock compression which in the case $f_\infty = 5$, $a_\infty = a_i$ and p_∞ = 1 bar amounts to $\Delta\hat{p}_0$ = 175 mbar is as high as that of the bow wave of a 7,5 mm-9oom/s -bullet at propagation distance η = 3o mm from the trajectory[16,17].

ENVELOPES

The formula for w' suggests the prediction that a subsonic envelope having flow velocity u_m and sound velocity a_m rises the structure speed from w' to w'_m fulfilling the following condition:

$$\frac{w'_m - u_m}{a_m} = \frac{u_i - w'_m}{a_i} + 1 \qquad (14)$$

If this is allright, then w'_m/a_∞ is higher and $(w'-u_m)/a_m$ is smaller than w'/a_∞. The Mach waves will perhaps disappear at $w'_m < u_m + a_m$ which is obtained at $u_m + a_m > u_i$.

The results of some preliminary experiments support these suggestions. With thin helium envelopes the beginning of Mach wave emission is shifted downstream to a certain point where the helium is nearly completely swallowed by the mixing layer. This may be seen from Fig. 21.

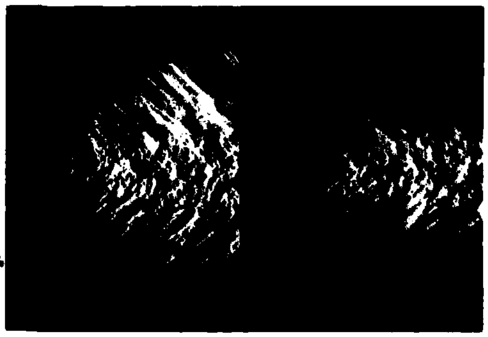

Fig. 21 - Thin helium envelope

Within the shifted beam of Mach waves the λ are about the same as without envelope. The $\Delta\hat{p}$ are reduced. With thick and hot nitrogen envelopes having $u_m + a_m > u_i$ it has been demonstrated that the strong Mach waves can actually be completely suppressed. Immobilisations like that presented in Fig. 22 have shown, that within thick envelopes having $u_m + a_m < u_j$ the Mach waves are refracted from angles above to angles below γ' as expected. But because of the uncertainty of the a_m-profile calculated from the measured u_m-profile the w'_m-relation cannot yet be considered to be verified.

CONCLUSIONS

The results as a whole have shown that the strong and long Mach waves are not due to random turbulence but do accompany coherent mixing layer structures. The physical nature of these structures is still unknown. But whatever this nature may be, the Mach number relations suggest that the reason for the preferred speeds may not be found inside, but outside the mixing layer. They may be due to the coupling of shock waves coexisting on both sides.

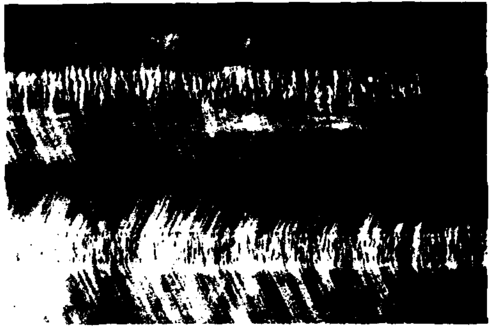

Fig. 22 - Refraction within thick envelope

These shock waves are so strong that theories using acoustic approximations are considered to be inadequate. Outside the jet the shock compressions are mainly determined by the deformation of conically spreading expansion waves between the shocks. It seems that also the initial shock compression and the shock distances do not depend on mixing layer characteristics. But this needs verification by future experiments. The physical meaning of the two constants entering into the similarity laws has not yet been found. This problem is now attacked inside the mixing layer by means of a special continuously recording laser anemometer [18].

The formulae have led to the proposal of Mach wave suppression by means of an optimized subsonic envelope. The method works. Moreover measurements inside the envelope are hoped to give additional insight into the mechanism of Mach wave production. The Mach waves are, of course, only one of various contributions to the supersonic jet noise. But another important contribution coming out of the transonic zone seems also to be due to the same structures. This can be seen from Fig. 23 where the jet exit diameter 1,9 mm has been chosen such that the transonic zone was within the viewing field. Studying the transonic zone will be our next step.

Most results would not have been obtained without varying the jet data within wide limits. Once more the shock tube has proven to be a valuable tool for doing such parametric investigations. The new optical measuring techniques developed for these investigations can also be applied to other fields of research. The combination of interferometry and immobilisation is especially well suited for visualizing waves and persistant vortices in turbulent flows. The laser microphone offers capabilities far beyond that of mechanical ones.

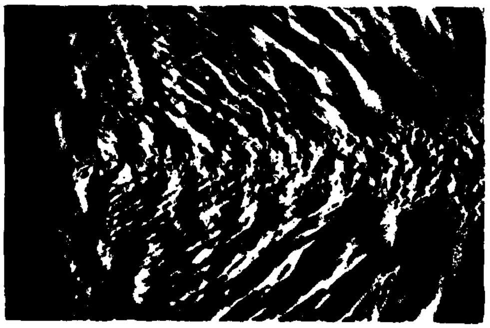

Fig. 23 - 1,9 mm - Jet noise

AKNOWLEDGEMENTS

The optical instruments have been prepared and most of the microphone measure-

ments have been done by Dr. G. Smeets and G. George. Most of the pictures, streak records and immobilisations have been taken by A. Sanner. The envelope investigations have been done by Dr. G. Patz and the subsonic jet investigations by M. Fiechter. Computations have been programmed by F. Gatau.

REFERENCES

(1) J.E. Ffowcs Williams, G. Maidanik. J. Fluid Mech. 21,4 (1965) 641-657

(2) C.K.W. Tam. J. Fluid Mech., 46,4 (1971), 757-768

(3) H. Michalke. DLR-FB-7o-51

(4) H. Gropengießer. DLR-FB-69-25

(5) M.V. Lowson, J.B. Ollerhead. J. Acoust. Soc. Am. 44,2 (1968) 624-53o

(6) J. Laufer, R. Schlinker, R.E. Kaplan. AIAA J. 14,4 (1976) 489-497

(7) H. Oertel. Proc. 1oth Int. Shock Tube Symp. Kyoto 1975

(8) H. Oertel. Stoßrohre - Shock Tubes - Tubes à choc. Springer Wien - New York, 1966

(9) H. Oertel. Tubes à choc in "Chocs et ondes de choc", p. 347-512 A.L. Jaumotte Ed., Masson & Cie, Paris, 1973

(1o) G. Patz. ISL-N 3o/7o, N 27/71, N 28/71, N 29/71

(11) H. Oertel. Proc. 4th Shock Tube Symp. 1961, BRL-Rept. 116o (1962)

(12) H. Oertel. Messungen im Hyperschallstoßrohr in "Kurzzeitphysik", K. Vollrath - G. Thomer Ed. Springer Wien - New York, 1967, p. 759-848

(13) H. Oertel. ISL-Bericht N 19/74

(14) G. Smeets, A. George. ISL-Bericht 39/72

(15) G. Smeets. JASA 63,3 (1977) 872-75

(16) H. Oertel. DEFA. LRBA - 23/49

(17) H. Oertel. Zs. Angew. Physik 4,5 (1952) 177-183

(18) G. Smeets, A. George. Rev. Sci. Instr. 49, 11 (1978) 1549-56

A NEW TYPE OF FLAP VALVE FOR GENERATING SONIC BOOMS IN A PYRAMIDAL HORN

J. J. GOTTLIEB*, W. CZERWINSKI, N. N. WAHBA and R. E. GNOYKE

Institute for Aerospace Studies
University of Toronto, Toronto, Ontario, Canada

The design, operation and performance of a sonic-boom simulator, featuring a radically new dual-flap valve and electromechanical control system, are described. This new flap valve with its large maximum throat area (160 cm^2) was designed to regulate the air flow from a low-pressure reservoir (up to 1.2 atm) into the apex of a large pyramidal horn (25 m long, 3 by 3 m base), where the incoming low-speed air flow (up to 150 m/s) produces a travelling simulated sonic boom or N-wave with little superposed high-frequency flow noise. As a consequence the N-wave has minimal jet noise superposed on its signature, a major advance over past work with such horn-type simulators. The simulated sonic boom is full scale, having an N-wave duration from 100 to 300 ms and longer, a peak amplitude up to 600 N/m^2 and higher, and a suitable rise time of 5 to 15 ms. Additionally, an advanced gasdynamic and acoustic analysis is presented to predict the characteristics of the simulated sonic boom (waveform, amplitude, duration and rise time). The gasdynamic part of the analysis describes the time varying reservoir conditions and the mass flow rate of air through the flap valve. The mass flow rate is then used in the acoustic part of the analysis to predict the simulated sonic boom in the pyramidal horn. Predicted and measured overpressure signatures at the test section are shown to be in excellent agreement.

INTRODUCTION

In order to successfully simulate a sonic boom from a supersonic transport (SST) or military aircraft, a simulation facility should have the capability of producing an N-shaped wave (Fig. 1) having the correct peak overpressure, rise time and duration. Typical values of the peak overpressure, duration and rise time are 100 N/m^2, 300 ms and 5 ms respectively for a current SST (Concorde, TU-144) and a large military bomber (B-58). In the case of a shorter supersonic fighter aircraft (F-16) only the duration is significantly different, being correspondingly shorter at about 100 ms. In the late 1960s and early 1970s many different types of sonic-boom simulators were constructed and tested.[1-3] Most of these simulators were only partially successful (i.e., they produced an N-wave having the correct peak overpressure and possibly rise time but not duration), and only a few met all of the desired requirements adequately.[4-9]

*Now at the Defence Research Establishment Suffield, Ralston, Alberta, Canada

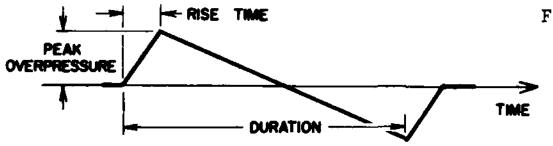

Fig. 1. Idealized overpressure signature of a sonic boom.

Of interest in the present paper is one type of successful simulator in the form of a pyramidal horn, which has a fast-acting control valve at the apex to regulate the release of air from a high-pressure reservoir into the horn, where the incoming air flow produces the simulated sonic boom. The first horn-type simulator which was developed at the General Applied Science Laboratories (GASL) had a large concrete pyramidal horn (31 m long, 2.5 by 2.5 m base).[5,6] This simulator used a high-pressure reservoir (up to 75 atm) and a small plug valve (maximum flow area of 6.5 cm^2) to produce a full-scale simulated sonic boom. A major problem was the very intense high-frequency jet noise superposed on the N-wave. This jet noise was generated by the high-speed air flow at the plug valve.

The second horn-type simulator developed at the University of Toronto's Institute for Aerospace Studies (UTIAS) benefitted from a knowledge of the jet-noise problem.[9] A similar facility was designed with a larger plug valve (maximum flow area of 35 cm^2) and a lower reservoir pressure (up to 10 atm), in order to reduce the air-flow speed at the plug valve and thus the jet-noise intensity. Additionally, a low-pass acoustic absorber was designed for the horn interior. Without the acoustic absorber the jet noise superposed on the N-wave was less severe than that for the GASL facility, but it was still very intense. With the acoustic absorber, however, the jet noise was markedly less intense, but it was still a problem. It essentially limited the performance of the UTIAS Travelling-Wave Horn to N-waves having a peak overpressure less than 200 N/m^2 and a duration shorter than 150 ms.

In order to further reduce the jet noise and markedly improve the performance of the UTIAS Travelling-Wave Horn, a dual-flap valve with a much larger throat area (up to 200 cm^2) was designed. By virtue of its large throat area the reservoir pressure requirement decreased substantially (to less than 1.5 atm), and thus both the flow speed through the flap valve and the jet noise from this flow were significantly reduced. The slow speed air flow through the large throat area still produces the high mass flow rate required to generate a full-scale simulated sonic boom. In the next two sections the design, operation and performance of the new dual-flap valve and its electro-mechanical control system are described. Then, in a following section, an advanced gasdynamic and acoustic analysis is presented to predict the mass flow rate of air from the reservoir into the horn and the resulting simulated sonic boom in the horn interior.

DESCRIPTION OF THE TRAVELLING-WAVE HORN

A plan view of the UTIAS Sonic-Boom Laboratory and Travelling-Wave Horn is shown in Fig. 2. The pyramidal horn with a total divergence angle of 7.2 degrees is 25 m long and has a square base which is 3 m on each side. The horn is made mainly of steel-reinforced concrete (20 cm thick), in order to minimize wave-energy losses and the resulting waveform distortion as the simulated sonic boom propagates from the small to the large end of the horn. The air reservoir system consists of a large cylindrical tank (3.4 m^3) located inside the control room, two additional cylindrical tanks (3.4 m^3 each) outside the control room, and an air compressor with a small high-pressure reservoir (0.025 m^3). Their combined volume is sufficient to maintain a reasonably constant reservoir pressure during the generation of a simulated sonic boom.

The mass flow valve with its dual flaps in the valve housing, three-bar linkage, cam, clutch, flywheel and electric-motor drive are shown schematically in Fig. 3. The primary function of this flap valve is to release in a controlled manner higher pressure air from the reservoir into the horn, where the air

AD-A091 010   HEBREW UNIV JERUSALEM (ISRAEL)   F/G 20/4
PROCEEDINGS OF THE INTERNATIONAL SYMPOSIUM ON SHOCK TUBES AND W--ETC(U)
FEB 80   A LIFSHITZ, J ROM   AFOSR-78-3679
UNCLASSIFIED   AFOSR-TR-80-1141   NL

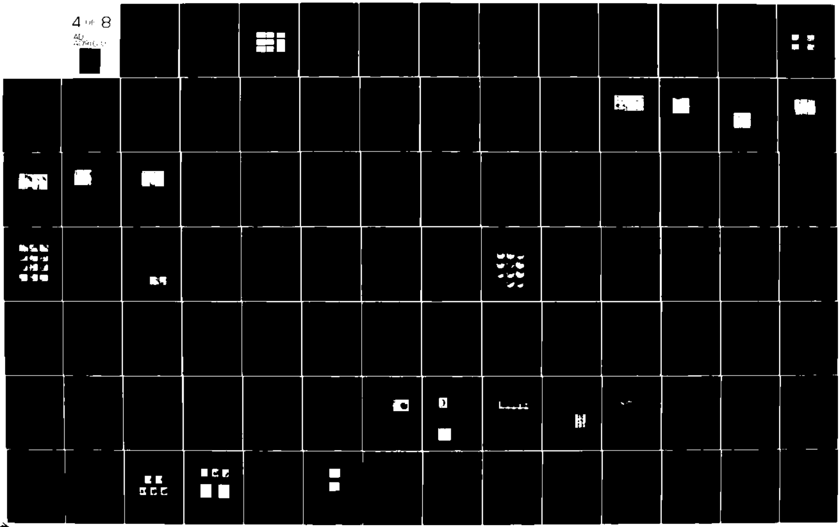

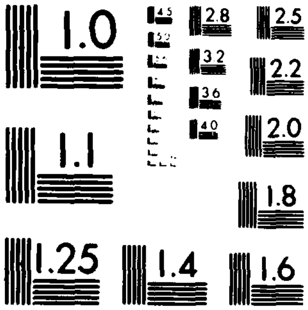

MICROCOPY RESOLUTION TEST CHART
NATIONAL BUREAU OF STANDARDS-1963-A

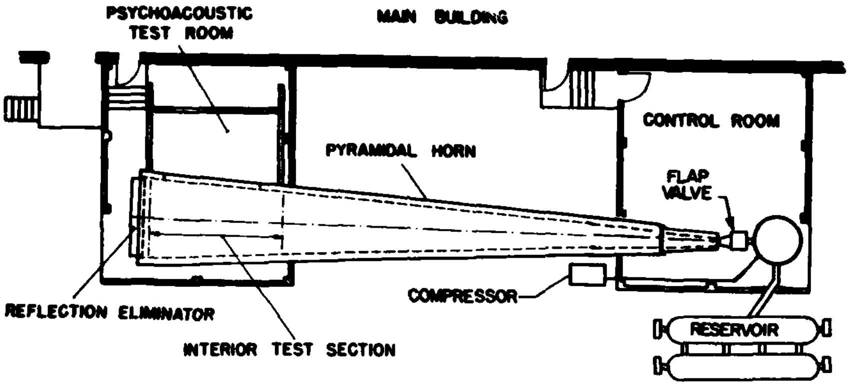

Fig. 2. Plan view of the Travelling-Wave Horn

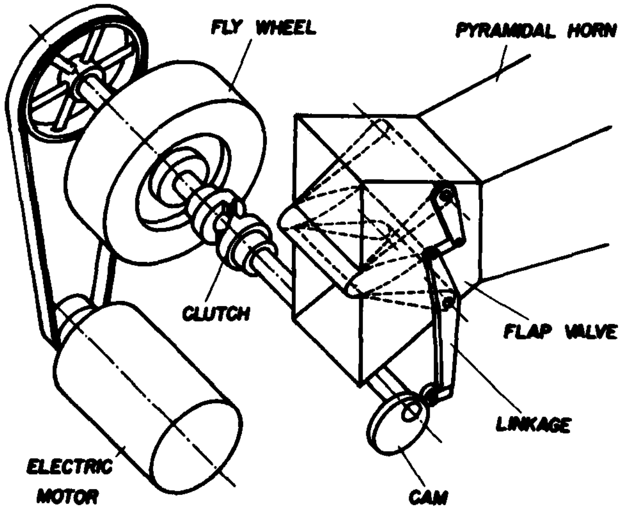

Fig. 3. Diagram of the dual-flap valve and electro-mechanical control system.

flow generates the simulated sonic boom. To achieve this simulation each valve flap must execute a one-cycle, oscillatory rotational motion such that the valve-throat area is approximately a parabolic function of time. For essentially constant reservoir conditions the mass flow rate of air through the flap valve has the same parabolic profile. This particular mass-flow-rate distribution, from zero to a maximum and back to zero again, produces the N-shaped overpressure signature of the simulated sonic boom.[5,9]

When the valve flaps are in their normally closed state, as shown in Fig. 3, the higher pressure reservoir air is prevented from flowing into the horn. Although the electric motor rotates the flywheel and the nearest part of the disengaged clutch at constant speed, the cam and the valve flaps are motionless. To actuate the valve the stationary half of the clutch is allowed to move axially toward the rotating half and engage it, causing the cam shaft and cam to suddenly rotate at constant speed. The rotating cam forces the three-bar linkage to synchronously rotate the flaps, first outward to increase the throat area and mass flow rate and then inward to decrease them. After one cam-shaft revolution the clutch disengages automatically and also suddenly stops the cam and cam-shaft rotation. The flaps have now returned to their original positions and the one-cycle operation has been completed.

A more detailed drawing of the flap valve and its central fairing is given in Fig. 4. During most of the valve opening and closing stages, as shown, the central fairing is aerodynamically shaped to minimize flow turbulence and thus jet noise. Although the central-fairing plates are shown in their outermost position, they also have an innermost postion when the valve is closed, allowing the closed flaps to be recessed in the central fairing. During the initial outward motion of the flaps, the fairing plates are forced by the compression spring to follow the flaps and maintain an air seal. When the flaps move beyond the central fairing the fairing plates suddenly stop. Consequently a rapid transition from no flow to flow through the valve occurs when the plates stop, which is necessary to achieve a short rise time for the first shock of the N-wave. When the flaps return and re-establish contact with the fairing plates, a rapid transition from flow to no flow helps to produce a short rise time on the second shock of the N-wave.

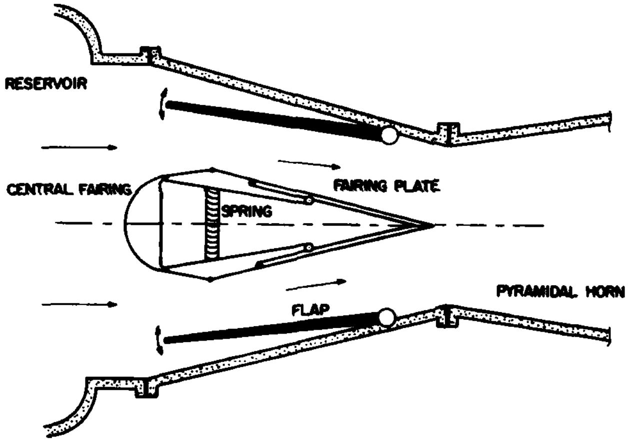

Fig. 4. Dual-flap valve showing the central fairing.

The two valve flaps are 28 cm long and 20 cm wide, and their pivot shafts are 22 cm apart. Although the cam shaft which dictates the desired flap rotation has to be made quite precise, this is not a major difficulty. The present cam shape is designed to give a maximum valve-throat area of 156 cm^2. This value could be as high as 200 cm^2 for a larger cam.

The open base of the pyramidal horn is covered by a specially designed reflection eliminator (Fig. 2), which is in the form of a recoiling porous piston. This device adequately minimizes the undesirable reflection and its subsequent echoes. It is worth mentioning that many more design details of the UTIAS Travelling-Wave Horn with its dual-flap valve and electro-mechanical drive system can be found in Refs. 9 and 10.

PERFORMANCE OF THE TRAVELLING-WAVE HORN

The Travelling-Wave Horn with the dual-flap valve has proven to be a practical facility for the simulation of a sonic boom from either a SST or supersonic military aircraft. The N-wave duration requirements are more than sufficiently satisfied because the easily adjusted motor speed can be set to give valve open-to-close times and thus durations from 100 to 300 ms and even longer. Owing to the flexibility of setting the reservoir pressure from as low as 1 atm (absolute) to as high as 2 atm, the facility has the capability of producing an N-wave having a lower, equivalent or higher amplitude than that of an actual sonic boom. Peak overpressures as high as 1200, 600 and 400 N/m^2 can be easily achieved for N-wave durations of 100, 200 and 300 ms respectively. The rise times of the front and rear shocks of the simulated sonic booms are not constant but depend very weakly on N-wave amplitude and more strongly on duration. For example, a typical rise time of the front shock, defined as 1.25 times the time for the overpressure to rise from 10 to 90% of its peak value, is about 6, 8 and 10 ms for corresponging durations of 100, 200 and 300 ms. The rise time of the rear shock is always somewhat longer (10 to 25%).

The capability of the Travelling-Wave Horn for generating both different amplitude and duration simulated sonic booms having a good N-shaped signature is aptly demonstrated by the measured overpressure signatures shown in Fig. 5. These signatures show that low-amplitude and short-duration booms are virtually free of jet noise, and that significant jet noise only occurs superposed on infrequently used booms having a high amplitude and long duration. The precursor noise (ahead of the front shock) in only the 100-ms duration N-waves is due to mechanical banging of clutch parts during the fast clutch engaging process.

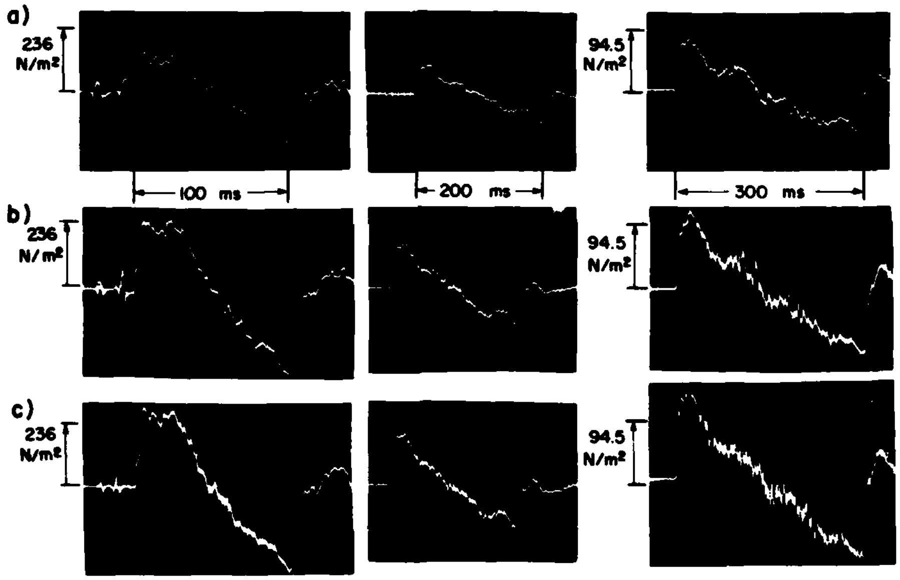

Fig. 5. Simulated sonic booms measured in the test section of the Travelling-Wave Horn (Reservoir pressures for Rows a, b and c of 1.068, 1.136 and 1.204 atm respectively).

The simulated sonic booms produced by the Travelling-Wave Horn have the correct N-wave shape and duration, adequate rise time for both shocks, and more than sufficient amplitude to perform structural response, fatigue and damage tests. This is, in fact, the main function of the facility. Furthermore, the facility has the capability of producing repeatable booms at a high repetition rate (1 to 10 or more booms per minute) to facilitate such structural response investigations. Owing to the rather long rise times (6 to 10 ms and longer) of the two shocks, the simulated sonic booms can be used for only limited human and animal response studies.

ANALYSIS FOR THE TRAVELLING-WAVE HORN

A combination of gasdynamic and acoustic theory is used to successfully predict the main features of the simulated sonic boom. Gasdynamic theory is used first to describe the time varying conditions in the reservoir and the mass flow rate of air out of the reservoir through the flap valve into the pyramidal horn. Acoustic theory is then used to describe the resulting wave motion in the horn. Because of certain assumptions made in the gasdynamic analysis, the mass-flow rate of air out of the reservoir can be determined without solving for the wave motion in the horn, and it thus serves as a convenient boundary condition for the separate acoustic analysis. Although this type of analysis is based on work given originally in Refs. 5 and 6 and much more completely in Ref. 9, the present analysis features not only a new interesting method of solution but also new results.

Gasdynamic Analysis of the Reservoir

The properties of the air in the finite-volume reservoir are not fixed with time but vary continuously as the air discharges out through the flap valve. In order to predict the reservoir conditions, the state properties are assumed to be spatially uniform and all changes with time are taken to be adiabatic and reversible. Then the following isentropic expressions can be used to relate the time-dependent reservoir temperature $T_0(t)$, sound speed $a_0(t)$, pressure $p_0(t)$ and density $\rho_0(t)$ to their initial values which are denoted by an overhead bar.

$$\frac{T_0(t)}{\overline{T}_0} = \left[\frac{a_0(t)}{\overline{a}_0}\right]^2 = \left[\frac{p_0(t)}{\overline{p}_0}\right]^{\gamma-1/\gamma} = \left[\frac{\rho_0(t)}{\overline{\rho}_0}\right]^{\gamma-1} \qquad \text{I}$$

Now assume that the air flow from the reservoir through the flap valve, which is essentially a convergent-divergent duct flow with a slowly varying throat area, is not only adiabatic and reversible but also one-dimensional and quasisteady. Isentropic expressions given below then relate the time-dependent properties of the reservoir air to those at the valve throat (denoted by a subscript *) and also to the flow Mach number $M_*(T)$.

$$\frac{T_0(t)}{T_*(t)} = \left[\frac{a_0(t)}{a_*(t)}\right]^2 = \left[\frac{p_0(t)}{p_*(t)}\right]^{\gamma-1/\gamma} = \left[\frac{\rho_0(t)}{\rho_*(t)}\right]^{\gamma-1} = 1 + \frac{\gamma-1}{2}M_*^2(t) \qquad \text{II}$$

The mass flow rate of air per unit area at the valve throat $m_*(t)$ can be expressed as follows as a function of the Mach number $M_*(t)$ which is simply the ratio of the flow speed $u_*(t)$ and sound speed $a_*(t)$.

$$m_*(t) = \rho_*(t)\, a_*(t)\, M_*(t) \qquad \text{III}$$

If the flow-area variation $A_*(t)$ at the valve throat is expressed as $\overline{A}_*N_*(t)$, where $\overline{A}_*$ is the maximum throat area and $N_*(t)$ describes the area variation, then the mass flow rate is $m_*(t)\overline{A}_*N_*(t)$ or $\rho_*(t)a_*(t)M_*(t)\overline{A}_*N_*(t)$. For this mass flow rate of air out of the reservoir having a volume V, the resulting rate of decrease of reservoir-air mass is simply $V\rho_0'(t)$, where the prime denotes differentiation with respect to the variable in the following brackets. The reservoir density is thus governed by the following differential equation.

$$\rho_0'(t) + \rho_*(t)\, a_*(t)\, M_*(t)\, \overline{A}_*\, N_*(t)/V = 0 \qquad \text{IV}$$

In order to solve this equation in conjunction with previous expressions, an equation of state ($p = \rho RT$) and a sound-speed relation ($a^2 = \gamma RT$), one needs to specify a boundary condition for the flow at the valve throat.

In the case of choked flow at the valve throat this boundary condition is simply $M_*(t)$ equal to unity.[9] However, in the present case the flow is always unchoked or subsonic at the valve throat. For this case a reasonable boundary condition is to take the static pressure $p_*(t)$ at the throat as being constant and equal to atmospheric pressure $\overline{p}_*$. An immediate consequence which follows from Eqs. I and II is that all other throat conditions such as $T_*(t)$, $a_*(t)$ and $\rho_*(t)$ are also constant. By using the previous assumption and Eqs. I and II, the differential equation for the density (Eq. IV) can be recast in terms of only one unknown $M_*(t)$, as given below.

$$\left[1 + (\gamma-1)M_*^2(t)/2\right]^{2-\gamma/\gamma-1} M_*'(t) + \overline{a}_*\, \overline{A}_*\, N_*(t)/V = 0 \qquad \text{V}$$

Although an exact implicit solution can be derived for $M_*(t)$ for certain values of the specific heat ratio (e.g., 5/3, 3/2, 7/5),[10] a much simpler approximate solution, which is accurate, explicit for $M_*(t)$, and good for all relevant values of γ, can be obtained. If $M_*(t)$ is first expressed in the form of a suitable series, starting with its initial value $\bar{M}_*$, and then substitued into Eq. V, the following third-order perturbation solution can be derived.

$$M_*(t) = \bar{M}_* + a_1 \alpha I(t) + a_2 \alpha^2 I^2(t) + a_3 \alpha^3 I^3(t) \qquad \text{VI}$$

$$\alpha = \bar{a}_* \bar{A}_* t_0/V, \qquad I(t) = \frac{3}{2}\int_0^{t/t_0} N_*(y)\, dy$$

$$\bar{M}_*^2 = \frac{2}{\gamma-1}\left[\left(\frac{\bar{p}_0}{\bar{p}}\right)^{\gamma-1/\gamma} - 1\right], \qquad \bar{a}_* = a_0\left[\frac{\bar{p}}{\bar{p}_0}\right]^{\gamma-1/2\gamma}$$

$$a_1 = -4 / 3\{2 + (2-\gamma)\bar{M}_*^2\}$$

$$a_2 = -16(2-\gamma) / 9\{2 + (2-\gamma)\bar{M}_*^2\}^3$$

$$a_3 = 64(2-\gamma)\{2 - 5(2-\gamma)\bar{M}_*^2\} / 81\{2 + (2-\gamma)\bar{M}_*^2\}^5$$

The symbol t_0 denotes the flow duration, and $\bar{p}_0$ is the initial reservoir pressure. Note that $\alpha I(t)$ is the small parameter in the perturbation solution.

The normalized function $N_*(t)$ for the throat-area variation has thus far been left in a general form. At this stage, however, it is worthwhile to introduce the ideal parabolic form for $N_*(t)$, which is given below.

$$N_*(t) = \begin{cases} 0 & t < 0, \quad t > t_0 \\ 4(1 - t/t_0)\, t/t_0 & 0 < t < t_0 \end{cases} \qquad \text{VII}$$

As mentioned earlier, the cam-shaft and valve-flap rotation are designed to produce this parabolic throat-area variation, in order to generate a good simulated sonic boom.

Once $M_*(t)$ has been determined by using Eqs. VI and VII for a fixed initial reservoir pressure $\bar{p}_0$ and sound speed $\bar{a}_0$, the time-varying reservoir conditions and the mass flow rate follow from Eqs. I and II. For example, the expressions for the mass flow rate per unit area and the reservoir pressure are given below.

$$\frac{m_*(t)}{\bar{\rho}\,\bar{a}} = \frac{\bar{a}}{\bar{a}_0}\left[\frac{\bar{p}_0}{\bar{p}}\right]^{\gamma-1/2\gamma} M_*(t) \qquad \text{VIII}$$

$$\frac{p_0(t)}{\bar{p}_0} = \frac{p}{\bar{p}_0}\left[1 + \frac{\gamma-1}{2} M_*^2(t)\right]^{\gamma/\gamma-1} \qquad \text{IX}$$

Although it may not be readily apparent from Eqs. VI, VII, VIII and IX, the initial reservoir pressure $\bar{p}_0$ and the nondimensional parameter α or $\bar{a}_*\bar{A}_*t_0/V$ in the solution of $M_*(t)$, $m_*(t)$ and $p_0(t)$ determines how fast the reservoir conditions and mass flow rate per unit area change with time. The changes are more rapid for a low initial reservoir pressure ($\bar{p}_0$), small reservoir (V), large valve ($\bar{A}_*$), and long valve open-to-close time (t_0).

The time histories of the mass flow rate and the reservoir overpressure are illustrated in Fig. 6, for one typical α or $\bar{a}_*\bar{A}_*t_0/V$ value of 0.10. The distortion in the mass-flow-rate profile, as compared to the ideal one (dotted line), and the change in the reservoir overpressure are not small and insignificant. For larger values of $\bar{a}_*\bar{A}_*t_0/V$ the effects are similar but proportionally larger. Note that many more graphical illustrations of the flow Mach number, mass flow rate, pressure, temperature, and density are given in Ref. 10.

Acoustic Analysis of the Simulated Sonic Boom

The well-known spherical wave equation given on the following page is employed to describe the acoustic wave motion in the pyramidal horn. In this equation the symbols Φ and r respectively denote the velocity potential and the

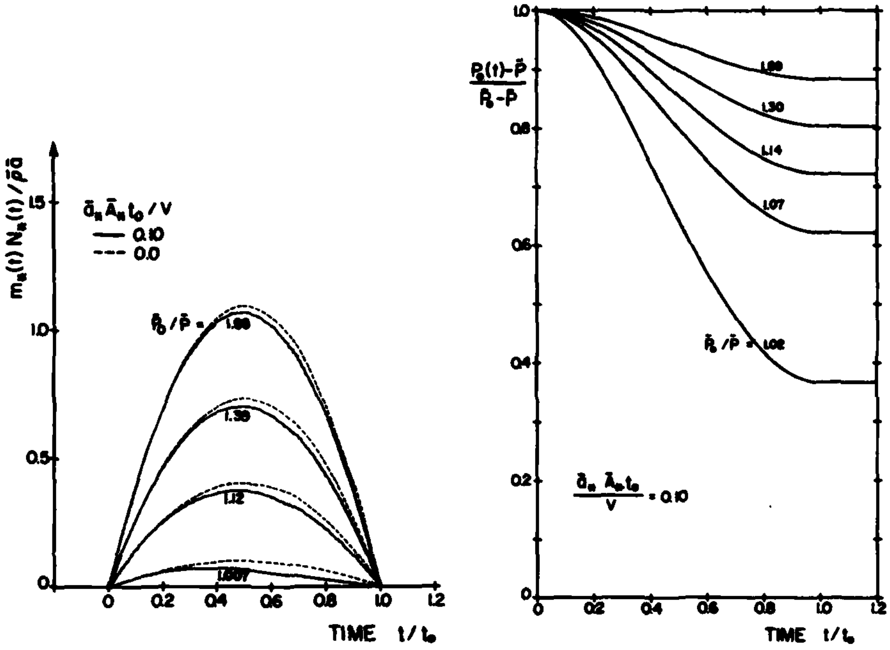

Fig. 6. Mass-flow-rate and reservoir overpressure variation with time.

radial distance measured from the horn apex. Because only an outward moving

$$\frac{\partial^2(r\phi)}{\partial t^2} = \bar{a}^2\,\frac{\partial^2(r\phi)}{\partial r^2} \qquad \text{X}$$

wave is generated by the air entering the horn and the reflection of this wave at the reflection eliminator is neglected, the general solution to the wave equation can be expressed simply as shown.

$$\phi = f(\tau)/r, \qquad \tau = t - (r-r_0)/\bar{a} \qquad \mathit{XI}$$

The symbol r_0 denotes the radial distance at which the flap valve is joined to the pyramidal horn (1.58 m), and τ is a retarded time having an initial value of zero at the wave front.

The overpressure Δp and the particle velocity Δu of the wave in the horn are related to the velocity potential ϕ, and also to the general function $f(\tau)$ which describes the wave signature, as illustrated below.

$$\Delta p = -\bar{\rho}\,\partial\phi/\partial t = -\bar{\rho}\,f'(\tau)/r \qquad \text{XII}$$

$$\Delta u = \partial\phi/\partial r = -f'(\tau)/\bar{a}r - f(\tau)/r^2 \qquad \text{XIII}$$

It is worth noting that the overpressure is directly proportional to the derivative of $f(\tau)$ and decays with distance like $1/r$. The particle velocity, however, is essentially directly proportional to $f(\tau)$ at small radii (near-field) and diminishes like $1/r^2$, whereas at large radii (far-field) it is directly proportional to $f'(\tau)$ and decays like $1/r$. Hence, the overpressure and particle velocity signatures have the same shape only in the far-field.

In order to determine the function $f(\tau)$ and thus the overpressure of the simulated sonic boom, the mass flow rate at the valve throat from the gasdynamic analysis $m_s(t)\bar{A}_s N_s(t)$ is used as the boundary condition for the acoustic analysis. Firstly, it is assumed that the flow is quasisteady from the valve throat to the downstream location where the flap valve is joined to the horn. This location is designated by radius r_0 and area $\bar{A}_0$. The mass flow rate at this location is $m_*(t)\bar{A}_0$ or $\bar{\rho}\bar{A}_0\Delta u$ to first order. Then, this mass flow rate can be equated to $m_*(t)\ \bar{A}_*\ N_*(t)$ from the gasdynamic analysis, and Δu can be eliminated from the resulting expression by using Eq. XIII, to give the following differential equation for $f(\tau)$.

$$f'(\tau) + \frac{\bar{a}}{r_0} f(\tau) = -\frac{\bar{a}r_0}{\bar{\rho}} \frac{\bar{A}_*}{\bar{A}_0} m_*(\tau)\ N_*(\tau) \qquad \text{XIV}$$

This equation can be solved in general form to give explicit integral expressions for both $f(\tau)$ and $f'(\tau)$.

From the explicit results of $f'(\tau)$ and Eq. XII, the general solution for the overpressure is given below.

$$\Delta p(\tau) = \begin{cases} \dfrac{\bar{a}r_0\bar{A}_*}{r\,\bar{A}_0} exp(-\bar{a}\tau/r_0) \int_0^\tau \{m_*(y)N_*'(y)+m_*'(y)N_*(y)\}exp(\bar{a}y/r_0)\ dy & 0<\tau<\tau_0 \\ \Delta p(\tau_0)\ exp\{-\bar{a}(\tau - \tau_0)/r_0\} & \tau > \tau_0 \end{cases} \qquad \text{XV}$$

To obtain more specific results let the mass flow rate per unit area and the throat-area variation be given by Eqs. VI, VII and VIII. After these expressions are substituted into Eq. XV the integrals can be evaluated analytically. The procedure is not unduly difficult, but it is rather tedious. The final results for the overpressure signature are summarized below.

$$\begin{aligned} \Delta p(T) = \overline{\Delta p}\, \big[& 1 - 2T + 2\beta - (1+2\beta)exp(-T/\beta) + a_1\alpha\{10T^4 - 20T^3 + 9T^2\} \\ & + a_1\alpha\beta\{-40T^3 + 60T^2 - 18T\} + a_2\alpha^2\{-32T^7 + 112T^6 - 126T^5 + 45T^4\} \\ & + a_1\alpha\beta^2\{120T^2 - 120T + 18(1 - exp(-T/\beta))\} + a_2\alpha^2\beta\{224T^6 - 672T^5 \\ & + 630T^4 - 180T^3\} + a_3\alpha^3\{88T^{10} - 440T^9 + 810T^8 - 648T^7 + 189T^6\}\big] \\ & \qquad \qquad if\ 0 < \tau < \tau_0 \\ \Delta p(T) = \Delta p(1)\ & exp\{-(T - 1)/\beta\} \quad if\ T > 1 \qquad \text{XVI} \\ T = \tau/\tau_0, \quad & \alpha = \bar{a}_*\ \bar{A}_*\ \tau_0/V, \quad \beta = r_0/\bar{a}\tau_0 \\ \overline{\Delta p} = 4\ & r_0^2\ \bar{m}_*\ \bar{A}_*\ /\ r\ \tau_0\ \bar{A}_0 \end{aligned}$$

Note that both α and β are small parameters, and that the solution is accurate to third order in these parameters.

The characteristic amplitude $\overline{\Delta p}$ in Eq. XVI can be expressed in a more convenient form. Firstly, $\bar{A}_*/\bar{A}_0$ can be replaced by r_*^2/r_0^2, where r_* is an equivalent radius corresponding to the maximum throat area $\bar{A}_*$. For example, if $\bar{A}_*$ is 156 cm² for the UTIAS facility, the r_* equals 1.0 m. Secondly, the initial mass flow rate per unit area $\bar{m}_*$ and the initial flow Mach number $\bar{M}_*$ can be expressed in terms of the initial reservoir pressure $\bar{p}_0$. After some rearrangement the desired expression for $\overline{\Delta p}$ is given below.

$$\overline{\Delta p} = 4\gamma\bar{p}\,\frac{r_*}{r}\,\frac{r_*}{\bar{a}_0\tau_0}\left[\frac{2}{\gamma-1}\left(\frac{\bar{p}_0}{\bar{p}}\right)^{\gamma-1/\gamma}\left\{\left(\frac{\bar{p}_0}{\bar{p}}\right)^{\gamma-1/\gamma} - 1\right\}\right]^{1/2} \qquad \text{XVII}$$

Hence, the result is expressed in terms of the initial reservoir pressure $\bar{p}_0$ and sound speed $\bar{a}_0$, atmospheric pressure $\bar{p}$, flow or N-wave duration τ_0 and the equivalent radius r_*.

The expression for the particle-velocity signature can be derived in a similar manner. However, now that the results for the overpressure are known, it is much simpler to use these in the following equation to obtain the particle-velocity signature.

$$\Delta u(T) = \frac{\Delta p(T)}{\bar{\rho}\,\bar{a}} + \frac{\tau_0}{\bar{\rho}\,r}\int_0^T \Delta p(y)\ dy \qquad \text{XVIII}$$

Because the integration can be done rather easily to obtain the final results for Δu, these lengthy results are not presented. Note that Eq. XVIII can be obtained directly from Eqs. XII and XIII.

To illustrate some interesting and important features of the overpressure signature, consider the following simplified case. Let α or $\bar{a}_*\bar{A}_*\tau_0/V$ be zero, which corresponds to the case of a reservoir having an infinite volume. Hence, the reservoir conditions are constant during the generation of a simulated sonic boom. Also, let β or $r_0/\bar{a}\tau_0$ be zero. This corresponds to the case of a point source for which the reservoir air enters the horn at its apex ($r_0 = 0$). Then the overpressure $\Delta p(T)$, from Eq. XVI, is given simply by $\overline{\Delta p}(1 - 2T)$. The signature is N shaped (Fig. 1) with two equal-amplitude shocks having instantaneous rise times.

More interesting features of the overpressure signature can be illustrated by letting β or $r_0/\bar{a}\tau_0$ be zero as in the previous case, but now letting α or $\bar{a}_*\bar{A}_*\tau_0/V$ be nonzero in Eq. XVI. Two sets of graphical results for different reservoir pressure ratios of 1.007 and 1.015 are shown in Fig. 7. It can be seen that the distortion in the signatures from the ideal N shape becomes worse with diminishing values of the reservoir pressure ($\bar{p}_0$) and increasing values of $\bar{a}_*\bar{A}_*\tau_0/V$ (larger valve, longer duration, smaller reservoir). These results illustrate that, if a long-duration simulated sonic boom having a good N-shaped signature is to be generated with a simulator having a large valve, then the reservoir volume (V) must be sufficiently large to offset large values of the throat area ($\bar{A}_*$) and duration (τ_0). The parameter $\bar{a}_*\bar{A}_*\tau_0/V$ should therefore have a value which is less than 0.1.

Further interesting and important features of the overpressure signature can be illustrated by letting β or $r_0/\bar{a}\tau_0$ be nonzero (finite source) and α or $\bar{a}_*\bar{A}_*\tau_0/V$ be zero (infinite reservoir) in Eq. XVI. The effects of nonzero values of β are illustrated graphically in Fig. 8. The essential result of a nonzero

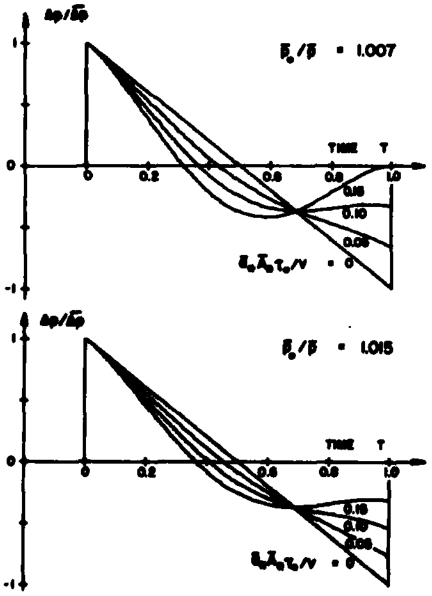

Fig. 7. Effects of the reservoir pressure ratio $\bar{p}_0/\bar{p}$ and parameter $\bar{a}_*\bar{A}_*\tau_0/V$ on the overpressure profile.

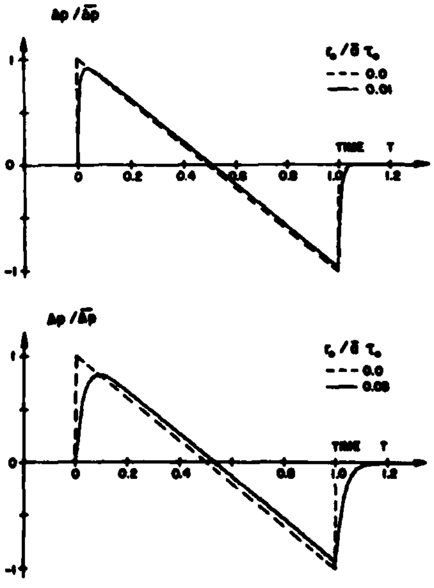

Fig. 8. Comparison of instantaneous and finite rise times of N-shaped signatures.

β value is that the front and rear shocks of the profile both have a finite rise time. It can be seen that the two rise times become longer relative to the N-wave duration as the value of $r_0/\bar{a}\tau_0$ increases. Hence, a larger valve which is joined to the horn at a larger r_0 value results in a simulated sonic boom with a longer rise time. On the other hand, for a simulator with a fixed value of r_c, the predicted rise time of each shock is more or less constant.[10] For the UTIAS simulator the predicted rise time is roughly $2r_0/\bar{a}$ or 9 ms.

Comparison of Predicted and Measured Results

Three overpressure signatures having nominal durations of 100, 200 and 300 ms were traced from the oscillograms in Fig. 5 (Row b) and are reproduced in Fig. 9a, 9b and 9c. It can readily be seen that the predicted and measured signatures are in good agreement. In general the overpressure signatures measured in the Travelling-Wave Horn can be predicted successfully by the analysis given earlier in this section.

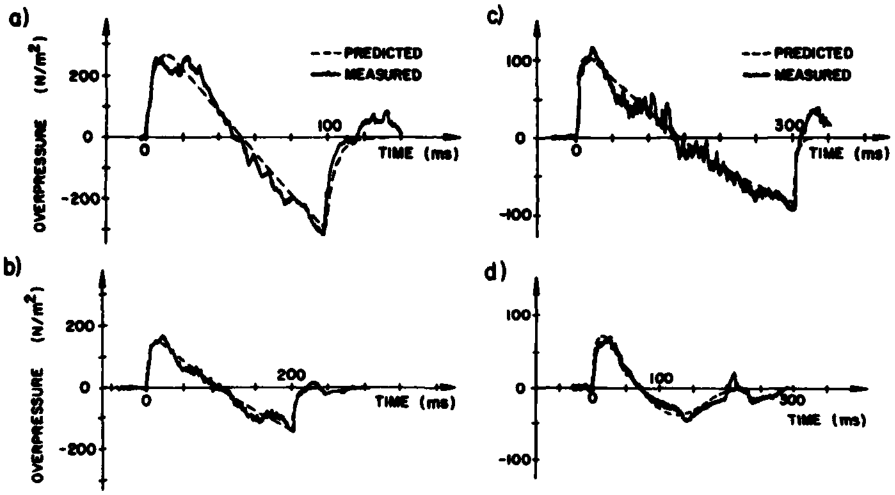

Fig. 9. Comparison of measured and predicted overpressure signatures.

An additional measured overpressure signature having a nominal duration of 200 ms is shown in Fig. 9d. For this case the reservoir pressure was 1.034 atm and the reservoir volume was reduced to one-third from 10.2 to 3.4 m^3. Included in the figure is the corresponding predicted profile, which is again in good agreement with the measured signature. Note that both the measured and predicted results differ fairly markedly from the desired N shape required for a good simulation of a sonic boom, owing to an inadequate reservoir volume. Such a result illustrates the importance of having a reservoir with sufficient volume.

DISCUSSION AND CONCLUSIONS

The UTIAS Travelling-Wave Horn has proved to be a practical facility for the simulation of a full-scale sonic boom. Owing to both the large flap valve and air reservoir, it has the desired capability of producing a good N-shaped overpressure signature with little superposed jet noise. The N-wave amplitude and duration can be controlled individually to be less than, equal to, or more than that of an actual sonic boom. Repeatable booms at a high repetition rate (1 to 10 booms per minute) can be produced to facilitate structural response, fatigue and damage studies, which are the primary objective of the facility.

The combined gasdynamic and acoustic analysis successfully describe the wave motion in the pyramidal horn. The gasdynamic analysis has the capability of predicting the pressure, temperature and other reservoir properties as well as the mass flow rate and the flow Mach number of the air discharging through the flap valve. The acoustic analysis is able to predict the overpressure and particle-velocity signatures of the simulated sonic boom, including the peak overpressure, duration and rise time. One important result of the analysis is a suitable criterion of how large the reservoir volume must be, in order that the overpressure signature is not significantly distorted from the N shape. The nondimensional parameter $\overline{a}_*\overline{A}_*\tau_0/V$ should be less than 0.05, 0.10 and 0.15 to avoid significant distortion in an N-wave having a duration of 100, 200 and 300 ms respectively.

It is worth mentioning that a compromise has to normally be made when a mass flow valve is designed for a sonic-boom simulator. On one hand, a large valve is required to reduce the flow speed at the valve and thus minimize jet noise superposed on the N-wave. On the other hand, the analysis indicates that a small valve joined to the horn at a small radius (r_0) is necessary to achieve short rise times on the two shocks of the N-wave. Instead of compromising for these two effects, the trick is to design a large valve which functions like a small valve during the initial opening and final closing stages, in order to achieve rapid transitions from no flow to flow initially and from flow to no flow finally. In past work a specially designed central fairing with more responsive, rapidly moving fairing plates gave a rapid transition, and the rise time of the front shock was as low as 1 ms.[10] This central fairing is not normally used in the present flap valve because it frequently jammed and failed mechanically. However, the short rise time obtained from its use illustrates that a flap valve can be designed to produce a simulated sonic boom with a fast rise time of the order of 1 ms.

ACKNOWLEDGEMENTS

The authors would like to express their gratitude to Dr. I.I. Glass for his helpful advice, friendly encouragement and continued interest in the work. One of the authors (J.J. Gottlieb) is grateful to the Defence Research Establishment Suffield, Ralston, Alberta, for granting special educational leave so that the paper could be presented at the symposium. The financial assistance provided by the Canadian Transportation Development Centre, Ministry of Transport, the National Research Council of Canada, and the United States Air Force Office of Scientific Research (Grant No. AF-AFOSR-77-3303) are acknowledged with thanks.

REFERENCES

1. I.R. Schwartz, Aircraft Engine Noise and Sonic Boom Section, AGARD, No. 29, May 1969.
2. P.M. Edge and H.H Hubbard, J. Acoust. Soc. Amer. *51*, 722-728, 1972.
3. J.J. Gottlieb and I.I. Glass, Can. J. Phys. *52*, 207-218, 1974.
4. L.J. Shepherd and W.W. Sutherland, NASA CR-1192, 1968.
5. R. Tamboulian, General Applied Science Laboratories Report GASL TR No. 713, 1968.
6. R. Tamboulian and W. Peschke, NASA CR-1696, 1970.
7. C. Thery, A. Peter and F. Schlosser, Rapport 15/71 of the Institut Franco-Allemand de Recherches de St. Louis, 1971.
8. A. Falkiewicz, M.A.Sc. Thesis, Institute for Aerospace Studies, University of Toronto, 1972.
9. J.J. Gottlieb, Prog. Aerospace Sci. *17*, 1-66, 1976. (Also, UTIAS Report No. 196, July 1974.)
10. J.J. Gottlieb, W. Czerwinski, N.N. Wahba and R.E. Gnoyke, UTIAS Report No. 208, Oct. 1978.

DOMAINS AND BOUNDARIES OF NONSTATIONARY OBLIQUE SHOCK-WAVE REFLECTIONS IN PERFECT AND IMPERFECT MONATOMIC AND DIATOMIC GASES

GABI BEN-DOR* and IRVINE ISRAEL GLASS

Institute for Aerospace Studies
University of Toronto, Toronto, Ontario, Canada

The reflection of oblique shock waves in nonstationary flows of monatomic and diatomic gases was investigated analytically and experimentally. It is shown analytically that seven different diffraction domains exist in nitrogen and six in argon in the range $1 < M_s < 10$. The diffractions (Figure 1) consist of the four well-known regular reflection (RR), single-Mach reflection (SMR), complex-Mach reflection (CMR) and double-Mach reflection (DMR). All the transition boundaries were established analytically for both perfect and imperfect monatomic and diatomic gases in thermodynamic equilibrium. It was shown that real-gas effects significantly affect the transition boundaries between different reflections as well as the size of each domain. The analysis was substantiated by over 100 experiments performed in the 10 cm x 18 cm Hypervelocity Shock Tube in nitrogen and argon at initial temperatures of nearly 300 K and pressures of 15 torr. The shock-Mach-number range covered was $2 \leq M_s \leq 8$ over a series of wedge angles in the range $2° \leq \theta_w \leq 60°$. The nonstationary process was recorded using the UTIAS 23-cm dia field of view Mach-Zehnder interferometer, equipped with a dual-wavelength ($\lambda_1 = 6943Å$, $\lambda_2 = 3471.5Å$), giant-pulse ruby laser. In addition to our numerous results, the available data for nitrogen, oxygen, air, argon and helium obtained by various investigators over the last three decades were also utilized. The experimental data from all sources substantiate the present analysis.

INTRODUCTION

When a planar incident shock wave encounters a sharp compressive corner in a shock tube, two different processes take place simultaneously. The incident shock wave itself is reflected by the wedge surface, whereas the shock-induced nonstationary flow behind it is deflected by the wedge corner. The former process is called shock-wave reflection, the latter flow-deflection and the overall phenomenon is known as shock-wave diffraction.

It is well known that the reflection process depends on the combination

---

*Now, Lecturer, Department of Mechanical Engineering, Ben-Gurion University of the Negev, Beer-Sheva, Israel.

of the incident shock-wave Mach number M_S, and the wedge angle θ_W. However, we have shown[1,2,3] that real-gas effects have a significant influence on shifting the boundary lines between the domains of different types of reflection processes. Consequently, the reflection process depends additionally on the thermodynamic state of the gas ahead of the incident shock wave, i.e., the initial pressure P_0 and temperature T_0.

The shock-wave-reflection process can be either one of the four well-known (Figure 1) regular, single-Mach, complex-Mach or double-Mach reflections. The shock-induced flow can negotiate the corner through either an attached or a detached bow shock wave. Since the shock-wave-diffraction process results from the interaction of these two processes, it is theoretically possible to have eight different configurations of oblique-shock-wave diffraction.

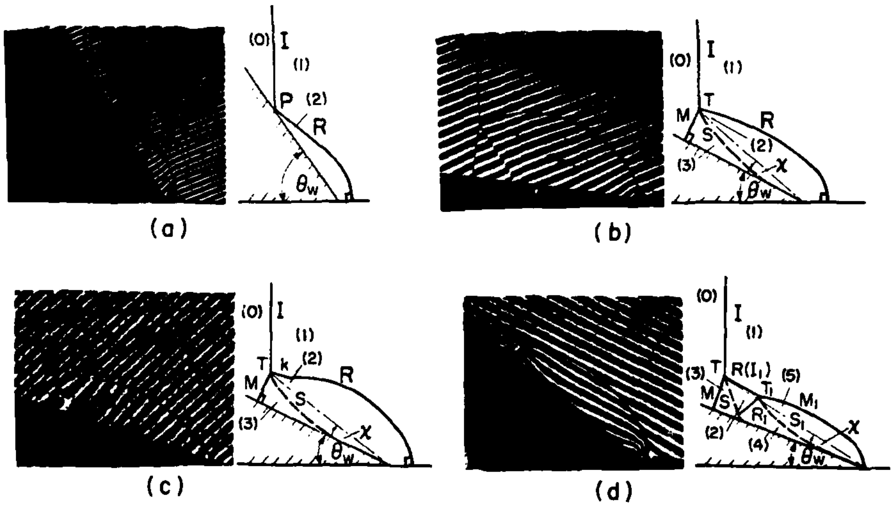

(a) (b) (c) (d)

Figure 1. Illustration of four possible oblique shock-wave reflections (interferograms are on the left and explanatory sketches on the right). The interferograms ($\lambda = 6943Å$) were taken with the 23-cm dia Mach-Zehnder interferometer of the UTIAS 10 cm x 18 cm Hypervelocity Shock Tube in argon at initial pressure $P_0 \sim 15$ torr and temperature $T_0 \sim 300$ K. I, I_1 - incident shock waves; R, R_1 - reflected shock waves; M, M_1 - Mach stems; S, S_1 - slipstreams; T, T_1 - triple points; χ, χ' - triple-point-path angles; K - kink; (0) to (5) - thermodynamic states; θ_w - actual wedge angle; θ_w' - effective wedge angle; M_s - shock-wave Mach number. (a) regular reflection (RR), $\theta_w = 60°$, $M_s = 2.03$; (b) single-Mach reflection (SMR), $\theta_w = 20°$, $M_s = 2.82$; (c) complex-Mach reflection (CMR), $\theta_w = 30°$, $M_s = 5.29$; (d) double-Mach reflection (DMR), $\theta_w = 50°$, $M_s = 7.03$.

During our investigation,[1,2,3] all the formation and termination criteria for the different types of reflection were established analytically in the (M_s, θ_w') and (M_s, θ_w)-planes for the first time. The analytical results were then substantiated by the present experiments as well as those from other available sources.

ANALYSIS

In analyzing the shock-wave reflection problem, two major difficulties were overcome: the nonlinearity of the oblique-shock-wave equations that describe the various reflections and the inclusion of real-gas effects. Consequently, the fourteen nonlinear oblique-shock-wave equations (with fourteen unknowns) describing the first triple point of SMR, CMR and DMR and the nine equations (with nine unknowns) for the reflection point of a RR, were solved for the first time for imperfect gases.

The imperfect-gas model takes into account the excitation of internal degrees of freedom such as rotation-vibration coupling, vibration and dissociation in nitrogen and electronic excitation and ionization in argon. It was found that real-gas effects significantly influence the transition boundaries between various reflections and diffractions as well as the size of their domains.

In a frame of reference attached to the reflection point P (Fig. 1a) of a RR the incident and reflected shock wave (I and R, respectively) can be treated using a steady-flow analysis. Treating I and R separately, and making use of the equations of motion across an oblique shock wave[4] one obtains for a RR:

for I:

$$\rho_o \tan\phi_o = \rho_1 \tan(\phi_o - \theta_1) \tag{I}$$

$$\rho_o U_o \sin\phi_o = \rho_1 U_1 \sin(\phi_o - \theta_1) \tag{II}$$

$$P_o + \rho_o U_o^2 \sin^2\phi_o = P_1 + \rho_1 U_1^2 \sin^2(\phi_o - \theta_1) \tag{III}$$

$$h_o + \frac{1}{2} U_o^2 \sin^2\phi_o = h_1 + \frac{1}{2} U_1^2 \sin^2(\phi_o - \theta_1) \tag{IV}$$

for R:

$$\rho_1 \tan\phi_1 = \rho_2 \tan(\phi_1 - \theta_2) \tag{V}$$

$$\rho_1 U_1 \sin\phi_1 = \rho_2 U_2 \sin(\phi_1 - \theta_2) \tag{VI}$$

$$P_1 + \rho_1 U_1^2 \sin^2\phi_1 = P_2 + \rho_2 U_2^2 \sin^2(\phi_1 - \theta_2) \tag{VII}$$

$$h_1 + \frac{1}{2} U_1^2 \sin^2\phi_1 = h_2 + \frac{1}{2} U_2^2 \sin^2(\phi_1 - \theta_2) \tag{VIII}$$

where the boundary condition is:

$$\theta_2 = -\theta_1 \tag{IX}$$

If thermodynamic equilibrium is assumed, two thermodynamic properties are sufficient to define a thermodynamic state, i.e., the flow density and enthalpy are expressed as functions of P and T, or $\rho = \rho(P, T)$ and $h = h(P, T)$. Consequently, the above equations have only thirteen independent variables, namely P_o, P_1, P_2, T_o, T_1, T_2, U_o, U_1, U_2, ϕ_o, ϕ_1, θ_1 and θ_2. Thus if four of them are known the remaining nine can in principle be determined. The four known parameters are usually the pressure P_o and temperature T_o of the flow ahead of the initial shock wave, the flow velocity $U_o = U_s \sec\theta_w$ and its angle of incidence with the incident shock wave $\phi_o = 90° - \theta_w$.

In the case of SMR, CMR and DMR the frame of reference is attached to the first triple point (Fig. 1b, c and d). Again the incident and reflected shock waves and the Mach stem (I, R and M, respectively) are treated separately to obtain the appropriate set of oblique shock-wave equations. The equations are:

for I:

$$\rho_o \tan\phi_o = \rho_1 \tan(\phi_o - \theta_1) \tag{X}$$

$$\rho_o U_o \sin\phi_o = \rho_1 U_1 \sin(\phi_o - \theta_1) \tag{XI}$$

$$P_o + \rho_o U_o^2 \sin^2\phi_o = P_1 + \rho_1 U_1^2 \sin^2(\phi_o - \theta_1) \tag{XII}$$

$$h_o + \frac{1}{2} U_o^2 sin^2\phi_o = h_1 + \frac{1}{2} U_1^2 sin^2(\phi_o - \theta_1) \qquad \text{XIII}$$

for R:

$$\rho_1 tan\phi_1 = \rho_2 tan(\phi_1 - \theta_2) \qquad \text{XIV}$$

$$\rho_1 U_1 sin\phi_1 = \rho_2 U_2 sin(\phi_1 - \theta_2) \qquad \text{XV}$$

$$P_1 + \rho_1 U_1^2 sin^2\phi_1 = P_2 + \rho_2 U_2^2 sin^2(\phi_1 - \theta_2) \qquad \text{XVI}$$

$$h_1 + \frac{1}{2} U_1^2 sin^2\phi_1 = h_2 + \frac{1}{2} U_2^2 sin^2(\phi_1 - \theta_2) \qquad \text{XVII}$$

for M:

$$\rho_o tan\phi_3 = \rho_3 tan(\phi_3 - \theta_3) \qquad \text{XVIII}$$

$$\rho_o U_o sin\phi_3 = \rho_3 U_3 sin(\phi_3 - \theta_3) \qquad \text{XIX}$$

$$P_o + \rho_o U_o^2 sin^2\phi_3 = P_3 + \rho_3 U_3^2 sin^2(\phi_3 - \theta_3) \qquad \text{XX}$$

$$h_o + \frac{1}{2} U_o^2 sin^2\phi_3 = h_3 + \frac{1}{2} U_3^2 sin^2(\phi_3 - \theta_3) \qquad \text{XXI}$$

where the boundary conditions are:

$$P_2 = P_3 \qquad \text{XXII}$$

$$\theta_3 = \theta_1 \pm \theta_2 \qquad \text{XXIII}$$

If thermodynamic equilibrium is assumed, the above fourteen equations have eighteen unknowns, namely, P_o, P_1, P_2 P_3 T_o, T_1, T_2, T_3, U_o, U_1, U_2, U_3, ϕ_o, ϕ_1, ϕ_3, θ_1, θ_2 and θ_3. Consequently, if four of them are defined the remaining fourteen can in principle be calculated. The four chosen quantities are again P_o, T_o, $U_o = U_s sec\theta_w'$ and $\phi_o = 90° - \theta_w'$, where $\theta_w' = \theta_w + \chi$ and χ is the first triple-point-trajectory angle. Unfortunately, unlike the case of RR the known quantities, namely, P_o, T_o, M_s and θ_w are not sufficient to define them since θ_w' involves an additional unknown, χ.

One way of overcoming this problem was suggested by Law and Glass[5] who assumed a straight Mach stem perpendicular to the wall. Consequently, they introduced an additional independent geometrical relation:

$$\phi_3 = 90° - \chi \qquad \text{XXIV}$$

Equation XXIV together with Eqs. X to XXIII are solvable in principle since they have only fifteen unknowns.

Since the reasons for the formation and termination of the various reflections were published recently[1,2,3] only a brief discussion is given. The criterion for the termination of RR makes use of the boundary condition that the flow downstream of the reflection point must be parallel to the wall, i.e., $\theta_1 + \theta_2 = 0$ (Eq. IX). When this is violated, i.e., θ_w decreases to a point where it forces θ_1 to exceed in magnitude the maximum deflection angle θ_{2_m}, RR terminates. Therefore, the termination criterion of RR is:

$$\theta_1 + \theta_{2_m} = 0 \qquad \text{XXV}$$

When RR terminates, three different types of reflection, SMR, CMR or DMR can occur depending on the Mach number of the flow behind the reflected shock wave R. As long as this flow is subsonic with respect to the first triple point T, SMR occurs. When this flow becomes supersonic with respect to T, a kink K develops in the reflected shock wave R, SMR terminates and CMR forms. Therefore, the SMR ⇄ CMR transition criterion is:

$$M_{2T} = 1 \qquad \text{XXVI}$$

where M_{2T} is the flow Mach number in state (2) behind R with respect to T.

When the flow behind R becomes supersonic with respect to the kink K, a second triple point T_1 develops at K, CMR terminates and DMR forms. Thus, the CMR DMR transition criterion is:

$$M_{2K} = 1 \qquad \text{XXVII}$$

where M_{2K} is the flow Mach number behind R with respect to K of CMR or T_1 of DMR. The value of M_{2K} can be found from:[1]

$$M_{2K} = M_{2T}\left[\, 1 + \left(\frac{V_{T_1T}}{U_2}\right)^2 - 2\left(\frac{V_{T_1T}}{U_2}\right) \cos(\phi_1 - \theta_2) \right]^{\frac{1}{2}} \qquad \text{XXVIII}$$

where V_{T_1T}, the velocity of the second triple point (or kink) with respect to the first triple point is given by:[1]

$$V_{T_1T} = U_1 \frac{\sin\phi_o}{\sin(\phi_1 + \phi_o - \theta_1)} \qquad \text{XXIX}$$

Note that all the variables in Eqs. XXVIII and XXIX are known once Eqs. X to XXIII are solved.

The domains of different types of reflections in the (M_S, θ_w')-plane, for both nitrogen and argon are shown in Figures 2(a) and (b), respectively. The solid boundary lines are for an imperfect-gas with four different initial pressures (P_O = 1, 10, 100 and 1000 torr) at a constant initial temperature (T_O = 300 K). The dashed boundary lines are for a perfect gas.

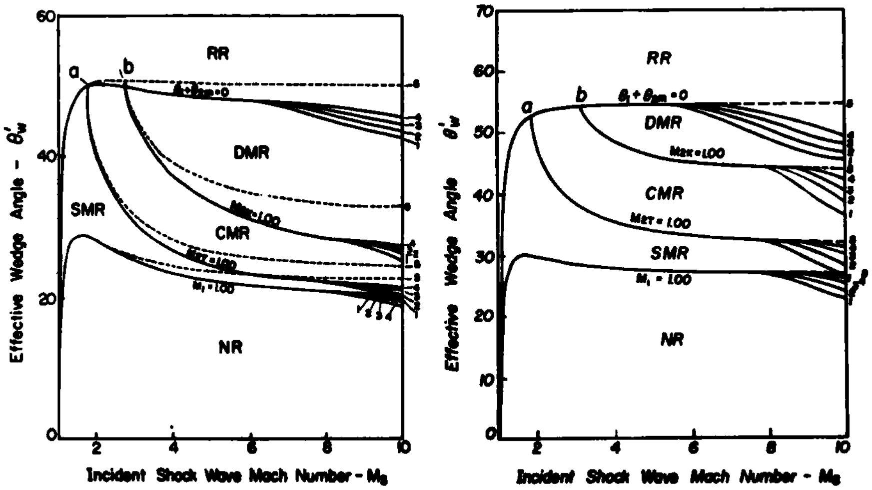

(a) (b)

Figure 2. Regions of different oblique shock-wave reflections in (M_S, θ_w')-plane. Lines (1) to (4) are for imperfect gas with P_O = 1, 10, 100 and 1000 torr, respectively, and T_O = 300 K. Line (5) is for a perfect gas, (a) nitrogen, (b) argon.

The domains of different types of flow-deflection in the (M_S, θ_w)-plane, for nitrogen and argon are shown in Figures 3(a) and (b), respectively. Again the dashed lines are for a perfect gas while the solid lines account for real-gas effects.

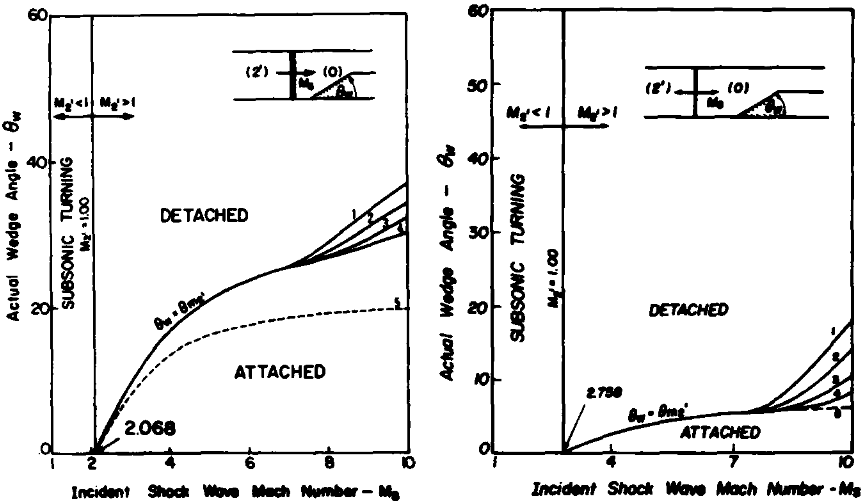

(a) (b)

Figure 3. Deflection processes of shock-induced quasi-steady flow (2') as a function of M_s and θ_w. Lines (1) to (4) are for imperfect gas, T_0 = 300 K and P_0 = 1, 10, 100 and 1000 torr, respectively. Line (5) is for a perfect gas, (a) nitrogen, (b) argon.

The overall phenomenon can be obtained by superimposing Figures 2 and 3, respectively. However, the vertical axis of Figure 2, θ_w', is different from that of Figure 3, θ_w. They are related through the triple-point-trajectory angle χ, i.e., $\theta_w' = \theta_w + \chi$. Therefore, the reflection process should be transformed from the (M_s, θ_w') to the (M_s, θ_w)-plane, by subtracting χ from the appropriate boundary lines of Figure 2, prior to any superposition. An analytical version of the graphical method of Law and Glass[5] was developed[1] to obtain a better prediction of χ as a function of M_s, θ_w, P_0 and T_0. The reflection process was then transformed from the (M_s, θ_w') to the (M_s, θ_w)-plane. The reflection process in the (M_s, θ_w)-plane for nitrogen and argon is shown in Figures 4(a) and (b), respectively. Only lines corresponding to imperfect nitrogen and argon at P_0 = 15 torr and T_0 = 300 K are reproduced.

The reflection process in the (M_s, θ_w)-plane (Figure 4) was then superimposed with the flow-deflection process in the (M_s, θ_w)-plane (Figure 3), to provide the overall shock-wave diffraction in the (M_s, θ_w)-plane. The overall diffraction process is shown in Figures 5(a) and (b) for nitrogen and argon, respectively. (The experimental data points will be discussed subsequently.)

Out of the maximum of eight possible shock-wave diffractions only seven are obtained in nitrogen (Figure 5a) and six in argon (Figure 5b) in the range $1 < M_s < 10$. The seven different shock-wave diffractions in nitrogen are RR with a detached shock wave (region 1), detached SMR (region 2), attached SMR (region 3), detached CMR (region 4), attached CMR (region 5), detached DMR (region 6) and attached DMR (region 7). The unobtainable diffraction is an attached RR. If, however, the line $\theta_1 + \theta_{2m} = 0$ and the attached/detached-line are extrapolated beyond M_s = 10, or the initial pressure is reduced, these two lines might intersect, resulting in a RR with an attached shock wave at the wedge corner.

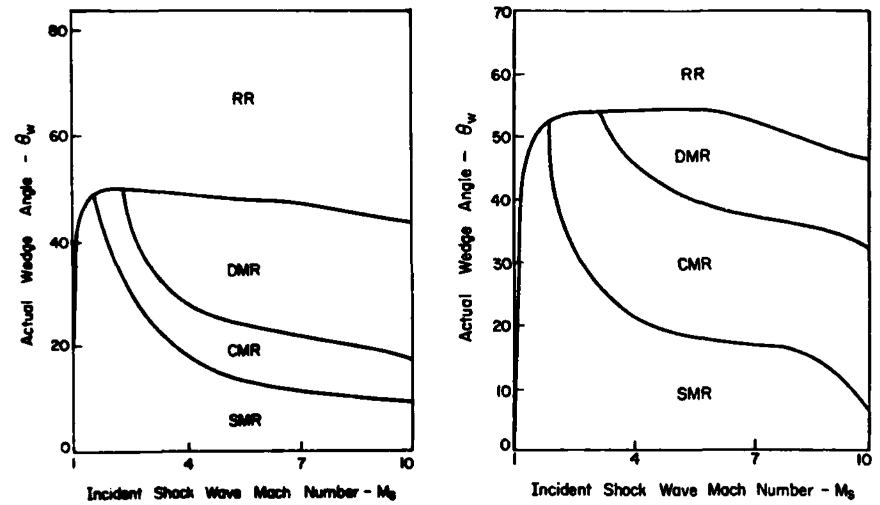

(a) (b)

Figure 4. Regions of different oblique-shock-wave reflections in (M_s, θ_w)-plane. All boundary lines are for imperfect gas with P_0 = 15 torr and T_0 = 300 K, (a) nitrogen, (b) argon.

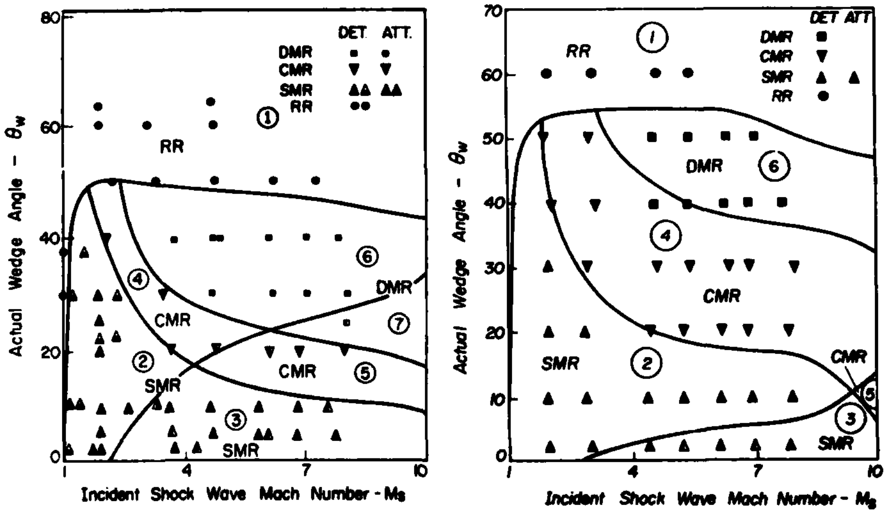

(a) (b)

Figure 5. Domains of different oblique-shock-wave diffractions in (M_s, θ_w)-plane and experimental verification. All boundary lines are for imperfect gas with P_0 = 15 torr and T_0 = 300 K. Regions: 1 - detached RR, 2 - detached SMR, 3 - attached SMR, 4 - detached CMR, 5 - attached CMR, 6 - detached DMR, and 7 - attached DMR.

(a) nitrogen, experimental data: air - White[8] ▲●▲; nitrogen - present ■□▼▼▲▲● (b) argon, experimental data: argon present. (For data from References 9 and 10, see our References 1, 2 and 3.)

In the case of argon, both an attached RR and an attached DMR are not possible in the range $1 < M_S < 10$. However, if the line $\theta_1 + \theta_{2_m} = 0$, $M_{2K} = 1$ and the attached/detached-line are extrapolated beyond $M_S = 10$, or the initial pressure is reduced, the former two lines might intersect the latter one, resulting in the missing two diffractions.

EXPERIMENTAL RESULTS

Over 100 experiments were performed in the 10 cm x 18 cm UTIAS Hypervelocity Shock Tube in both nitrogen and argon, at initial pressures of about 15 torr and temperatures of 300 K. The incident shock-Mach-number range was $2 \leq M_S \leq 8$ over a series of wedge angles $2° \leq \theta_W \leq 60°$. Dual-wavelength ($\lambda_1 = 6943Å$, $\lambda_2 = 3471.5Å$) laser interferograms were obtained using a 23-cm dia field of view Mach-Zehnder interferometer.

Our experimental results[1,6] as well as those from many other sources[7-10] are shown in Figure 5. It is seen that in the case of nitrogen (Figure 5a) all the data points fall inside their predicted regions. Consequently, one can conclude that the present analysis of the shock-wave-diffraction process in nonstationary diatomic gases is substantiated, and the seven types of diffraction are all valid. In the case of argon, only one experimental point ($M_S = 4.44$, $\theta_W = 40°$) that corresponds to a DMR lies outside its predicted domain, in the CMR region. This we believe is due to the assumptions used in calculating the CMR/DMR boundary line[1] ($M_{2K} = 1$) that were found by Law and Glass[5] and Bazhenova et al[10] to be in good agreement with experimental results only in the range $\theta_W \leq 40°$. For the range $\theta_W > 40°$ the agreement becomes progressively worse. All the other experimental points lie inside their predicted domains. Unfortunately, out of the six different diffractions predicted by the present analysis in argon, only five were observed experimentally. The remaining CMR with an attached shock wave at the wedge corner (region 5 in Figure 5b) was not observed. This domain starts at $M_S = 9.4$ and extends beyond the safe upper limit of incident shock wave ($M_S = 8$) which can be used without damaging the high-quality optical test-section windows of the shock tube. However, in light of the verification of five regions out of six shown in Figure 5(b) it can be concluded that the present analysis for the diffraction of oblique shock waves in nonstationary monatomic flows is substantiated and that six different types of shock-wave diffraction exist in the range $1 \leq M_S \leq 10$.

DENSITY FIELDS

In order to have a deeper understanding of the overall shock-wave diffraction process, the density fields, as well as the density distribution along the wedge surfaces, of the various diffractions were deduced from the corresponding interferograms. The interferograms were evaluated using a new approach to interferometry which was developed recently by Whitten at UTIAS.[11] The results were then used to understand the similarities and differences between the various diffractions[1,2,3] and compare them with numerical predictions.[12]

A typical example of an attached CMR in nitrogen and a detached CMR in argon are shown in Figures 6(a) and (b), respectively. It is seen that when the shock wave at the wedge is detached (Figure 6b) the constant-density lines (isopycnics) tend to run along the shock wave, while for an attached shock wave (Figure 6a) the isopycnics run across this direction. All our results revealed the same difference between attached and detached reflections. It is worthwhile to note that our results for the density field of CMR verified the hypothesis of Henderson and Lozzi[13] who advanced the idea that a compression wave should exist at the kink of a CMR. Figure 6 indicates that a compression wave does indeed emanate from K. The strength (density jump) of the compression waves in Figures 6(a) and (b) are approximately 1.17

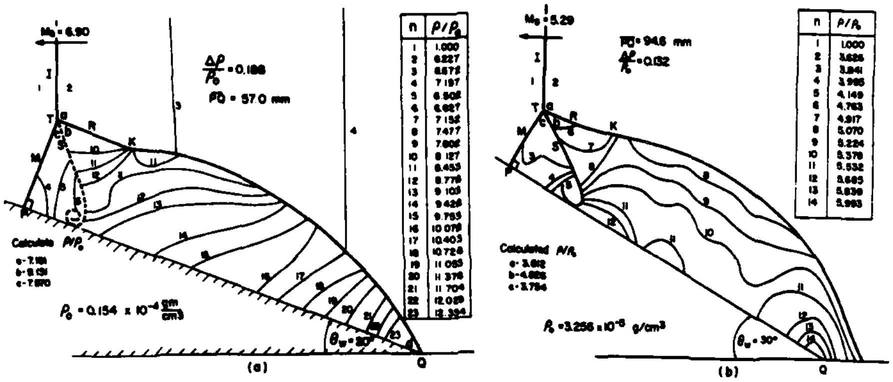

Figure 6. Actual flow isopycnics corresponding to: (a) an attached CMR (region 5, Figure 5a) in nitrogen; (b) a detached CMR (region 4, Figure 5b) in argon.

(8.127/7.477) and 1.03 (5.070/4.917), respectively. It was further found[1,2,3] that the stronger the incident shock wave the stronger is the compression wave, and in turn the sharper is the kink.

Our comparison of actual with numerical experiments[12] revealed that the existing computer codes for RR and SMR are capable of predicting the shock shapes of the diffraction process. However, they fail to predict the location and values of the isopycnics. Unfortunately, no computer codes exist for CMR and DMR. Undoubtedly numerical codes that will reliably predict RR, SMR, CMR and DMR in real-gases will evolve in the future. Our interferometric data for all these cases then should provide a solid base for comparison.

CONCLUSION

The present analysis and experiments have brought order and clarity to the problem of oblique-shock-wave reflections in nonstationary flows. The domains and transition boundaries of the various types of oblique-shock-wave diffractions have been established analytically for perfect and imperfect monatomic and diatomic gases. The analysis is substantiated by our numerous data as well as results from other sources.

Our very comprehensive isopycnic data are the first since the pioneering work of White.[8] Our results provide an important base for testing available and future computational codes for such complex flows.

ACKNOWLEDGEMENT

The financial support received from the National Research Council of Canada and the U.S. Air Force under grant AF-AFOSR 77-3303 is acknowledged with thanks.

REFERENCES

1. G. Ben-Dor, UTIAS Report No. 232 (1978).
2. G. Ben-Dor and I. I. Glass, J. Fluid Mech., 92, 3, 459 (1979).
3. G. Ben-Dor and I. I. Glass, submitted to J. Fluid Mech. (1979).
4. H. W. Liepmann and A. Roshko, John Wiley & Sons, Inc., New York (1957).
5. C. K. Law and I. I. Glass, CASI Trans., 4, 1, 2 (1971).
6. G. Ben-Dor, UTIAS Report No. 237 (1978).
7. L. G. Smith, OSRD Report 6271 or NDRC Report A-350 (1945).

8. D. R. White, Tech. Report II-10, Dept. of Phys., Princeton Univ. (1951).
9. L. G. Gvozdeva, T. V. Bazhenova, O. A. Predvoditeleva and V. P. Fokeev, Astronautica Acta, 14, 503 (1969).
10. T. V. Bazhenova, V. P. Fokeev and L. G. Gvozdeva, Acta Astronautica, 3, 131 (1976).
11. G. Ben-Dor, B. T. Whitten and I. I. Glass, J. of Heat and Fluid Flow (to be published, 1979).
12. G. Ben-Dor and I. I. Glass, AIAA Journal, 16, 11, 1146 (1978).
13. L. F. Henderson and A. Lozzi, J. Fluid Mech., 68, 1, 139 (1975).

THE INFLUENCE OF RELAXATION ON TRANSITION TO MACH REFLECTION IN PSEUDOSTEADY FLOW

JOHN SANDEMAN, ALISON LEITCH and HANS HORNUNG

Department of Physics
Australian National University, Canberra, Australia

Attempts to find relaxation effects in the transition to Mach reflexion have been unsuccessful in the past, the equilibrium transition condition being observed throughout. In this paper we report on experimental results in ionizing argon and dissociating nitrogen which show significant qualitative and quantitative relaxation effects. The most important of these is that the shock angle at transition in relaxing argon flow lies between the equilibrium and frozen values which are separated by more than 10°. While the expected double Mach reflexion is observed in nitrogen, it does not occur in argon flows where weak complex Mach reflexion is observed. In both cases the reflected shock shows distinct curvature due to relaxation. The experiments use the free piston shock tube with Mach-Zehnder interferometry. A nitrogen laser pumped dye laser, incorporating a fibre optic beam expander and a tuning interference filter provides an excellent 5 ns light source for such work.

INTRODUCTION

In real gas dynamics it is important to distinguish between situations in which the gas may be considered to be in thermodynamic equilibrium and those in which the relaxation times are not negligible compared with the time scale of the flow. The former - equilibrium flows - differ from perfect gas flows only in their more complex equation of state. In the latter - relaxing flows - at least one new dimensionless parameter is introduced, i.e. the ratio of relaxation time to the flow time scale.

The influence of equilibrium real gas effects on the transition to Mach reflexion of shock waves has recently been examined in some detail by Ben-Dor and Glass[1], who considered the pseudosteady situation of a plane shock impinging on a stationary wedge at an angle α. They mapped out the regions in which simple, double and complex Mach reflexion occurs by numerical calculations for nitrogen and argon up to shock Mach number, $M_s = 10$. They used the term complex Mach reflexion for the situation when the reflected shock of a simple Mach reflexion is not monotonically curved but has a concave kink. They supported their calculations with experimental results in both gases up to $M_s = 8$, with generally good agreement. No relaxation effects seem to have been observed.

An attempt to discover relaxation effects on the transition condition in both pseudosteady and steady flow was made by Hornung, Oertel jr. and Sandeman[2]. Although the relaxation length after the primary shock in pseudosteady nitrogen flow was comparable to the model dimension, no relaxation effect could be observed. The measurements agreed best with the calculated transition condition for frozen incident and equilibrium reflected shock (I_f, R_e). Both in argon (M_s up to 9) and nitrogen (M_s up to 13) double Mach reflexion was observed, in agreement with Ben-Dor and Glass[1].

In this paper we address ourselves to the problem of how relaxation after the primary shock affects transition to Mach reflexion in pseudosteady flow. The important length scale in pseudosteady flow is the distance from the wedge tip to the intersection of the shock and wedge, w, which increases linearly with time, see figure 1. It is clear that at a sufficiently small time after the shock encounters the wedge tip, w is smaller than the incident shock relaxation length, ℓ_I. At later times, w becomes larger than ℓ_I. In the limiting cases $w \ll \ell$ and $w \gg \ell$ there is no doubt that the frozen and equilibrium conditions respectively must apply. The observation of Hornung et al.[2] for nitrogen, that the transition condition agrees best with (I_f, R_e), is consistent with this in view of the relaxation lengths after the incident and reflected shocks in their experiments. However, the difference between the calculated transition angles, α_{tr}, for (I_f, R_e) and (I_e, R_e) is smaller than the resolution limit of their experiment.

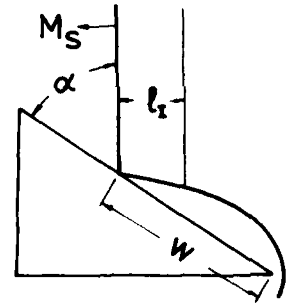

Fig. 1 Sketch of regular reflexion in pseudosteady flow.

In order to be able to ascribe a more clearly defined relaxation length to the experimental data it was decided to examine argon flows. The sudden onset of ionization at a clearly measurable distance from the shock waves makes this possible. A pilot experiment was therefore set up in which a shock at $M_s = 15$ into 10 Torr argon (relaxation length = 4 mm) was photographed with a Mach-Zehnder interferometer and an image converter camera at 2×10^6 frames s^{-1}. An example of the results is given in figure 2, which shows a set of infinite fringe interferograms. The end of the relaxation zone (onset of ionization) is clearly visible as a dark fringe resulting from the negative fringe shift due to the increase of the electron density. This and finite fringe photographs like it show what appears to be double Mach reflexion, as expected from Ben-Dor and Glass[1] calculations. They also seem to indicate that the growth of the shock configuration is not self-similar, the distance between the first and second Mach stem remaining constant and

Fig. 2 Infinite fringe interferograms taken with the image converter camera at 2 × 10^6 frames/sec. Argon, $M_S = 15$, $p_1 = 10$ Torr, $\alpha = 60°$.

being apparently controlled by the relaxation length after the primary shock. However, the image converter camera does not give very sharp definition (8 line pairs per mm, with a frame size of 15 mm). It was therefore decided to use a different camera, which could obtain better definition but could only take one frame per shot, in order to resolve the detail of the small region near the Mach stems. It was also decided to examine a second condition in argon at $M_S = 12$, $p_1 = 30$ Torr, at which the relaxation length ℓ_I is 11 mm, as well as one in nitrogen at $M_S = 15$, $p_1 = 10$ Torr giving $\ell_I = 3$ mm. The two important differences between argon and nitrogen relaxation are, firstly, that nitrogen relaxes with a rapidly decaying rate, while argon ionizes suddenly after a delay during which no significant ionization occurs, and secondly that the ratio, ℓ_I/ℓ_R, of the relaxation lengths associated with the incident and reflected shocks is very large in nitrogen and of order one for argon at the chosen conditions.

EXPERIMENT

The facility used in the experiments was the large free piston shock tube known as T3, described in more detail by Hornung and Stalker[3]. The free piston technique is particularly suitable for this work because its driver condition flexibility makes it possible to obtain a given shock speed at a variety of initial pressures, p_1, merely by adjusting the appropriate pressures in the free piston compressor. In this manner, the relaxation lengths may be adjusted at constant shock speed. The free piston machine is also able to produce shocks at high Mach number with very small attenuation. Typical values for shock attenuation are 5% per m at 4 km s^{-1} falling to 2% per m at 8 km s^{-1}. However, these may be reduced even to negative values by changing the piston trajectory, at the expense of the service life of the buffers which absorb the excess energy of the piston after diaphragm rupture. The shock tube is 7 m long and has a diameter of 7.6 cm.

The Carl Zeiss Mach-Zehnder interferometer was used together with a home-made dye laser light source. The dye cell is pumped by a home-made nitrogen laser with an exposure time of 5 ns. The cell is located in a cavity of 25 cm length, the rear and front mirrors being 100% and 40% reflecting respectively. Initially, the dye laser beam was expanded by a microscope objective with spatial filter pinhole. While this gives an ideal light source for our purpose in some respects, its transverse spatial coherence causes the image of every sharp edge to have an associated diffraction pattern around it. An example of the picture quality achievable with this system is shown in figure 3a. While better definition is obtained with this than with the image converter camera, the diffraction patterns sometimes lead to misinterpretation of the gasdynamic features shown in the interferograms. This problem was solved by replacing the beam expander system with a fibre optic. One end of the fibre optic was placed in the dye laser beam, the other at the focus of the input lens of the interferometer. Not only does this expand the beam to a suitable angle, but it also destroys its spatial coherence, so that the diffraction patterns are eliminated. Furthermore, the tiresome necessity of aligning the nitrogen laser, dye laser and interferometer accurately relative to each other is obviated, the flexible fibre optic allowing the interferometer to be separated from the light source. To show the improvement in the picture quality, figure 3b presents the same conditions as figure 3a photographed with the modified system. A sketch of the experimental setup is shown in figure 4.

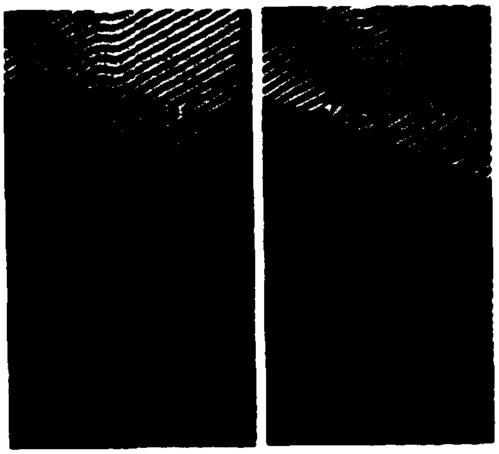

Fig. 3 Finite fringe interferograms, $M_S = 15$, $p_1 = 10$ Torr, argon, $\alpha = 69°$.

a) Dye laser beam expanded by microscope objective and spatial filter.

b) Dye laser beam expanded by fibre optic.

A second difficulty arose from the high self-luminosity encountered in the high speed argon experiments. Most of this comes from the steady flow over the wedge after the primary shock. The steady flow lasts for approximately 50 μs compared with the laser flash of 5 ns. While it is a simple matter to change the relative intensity of self-luminosity and laser light on the photographic plate by means of a stop placed at the output focus of the interferometer, this also reduces the quality of the definition. With the $M_S = 15$ argon flow the stop size had to be reduced to such an extent that the picture quality was not much better than with the image converter camera, even though an interference filter of 10 nm bandwidth passing only the wavelengths of the laser light had been used. This problem was successfully overcome by inserting a tuning interference filter of 0.8 nm bandwidth in the dye laser cavity, thus concentrating more of the laser power into this narrow wavelength range. A second filter passing the same wavelengths was inserted near the focus of the output lens of the interferometer. This reduced the relative intensities of luminosity and laser light at the photographic plate approximately by a factor of 4. An example of the improvement is shown in figures 5a and 5b. Note that although figure 5b was taken with a much larger stop size, the self-luminosity is not any worse. As can be seen in figure 5b speckle is introduced in the photograph because of the reduced bandwidth.

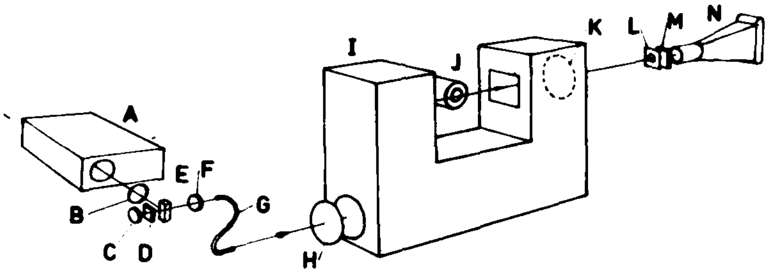

Fig. 4 Experimental setup. A, nitrogen laser; B, cylindrical lens; C, 100% reflecting mirror; D, interference filter; E, dye cell; F, 40% reflecting mirror; G, fibre optic; H, collimating lens; I, interferometer; J, shock tube; K, output lens; L, aperture stop; M, interference filter; N, camera.

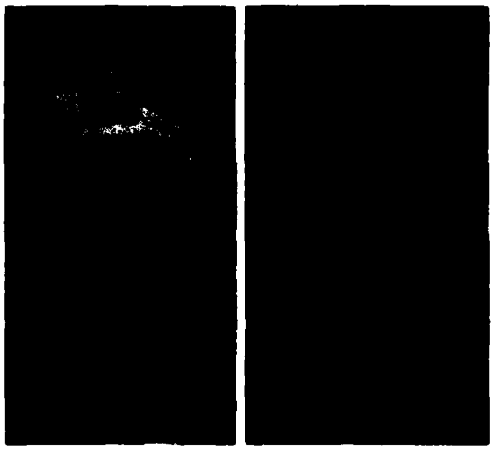

Fig. 5 Interferograms of complex Mach reflexion in relaxing argon flow. $M_S = 11.8$, $p_1 = 30$ Torr, $\alpha = 58°$, $\ell_I = 11$mm.

a) Without interference filter D, with interference filter M at 10 nm bandwidth, stop diameter = 3 mm

b) Interference filters D and M both at 1 nm bandwidth, stop diameter = 7 mm. Note improvement in definition without worsening of self-luminosity.

Note bend of reflected shock at end of relaxation region. Also note slight concavity in the middle of the relaxation zone indicating complex Mach reflexion.

With the technique adopted, i.e. one photograph per shot, the experimental procedure becomes extremely laborious if a sequence of photographs is desired at each experimental condition. It was therefore decided to take one interferogram with the shock near the wedge tip and one with the shock far from the wedge tip at each condition, and to adjust the wedge angle until the transition condition is ascertained to an accuracy of ± 1°.

RESULTS AND DISCUSSION

Relaxation after the primary shock

It is necessary to begin with to verify the fringe shift observed in the various relaxation regions against previously measured dissociation and ionization rates. To show that the qualitative behaviour is as expected, figure 6 shows finite fringe interferograms of the shock in the three chosen conditions. The argon flows (6a,b) show the characteristic initial positive fringe shift followed, after a small delay, by the negative fringe shift due

Fig. 6a,b Finite fringe interferograms of shock waves into argon just outside the shock tube.

a) $M_s = 15$, $p_1 = 10$ Torr, $\ell_I = 4$ mm. Note the initial positive fringe shift followed after some delay by the negative fringe shift due to the ionization.

b) $M_s = 11.8$, $p_1 = 30$ Torr, $\ell_I = 11$ mm. Similar features as in a).

c) Finite fringe interferogram of double Mach reflexion in nitrogen. $M_s = 15$, $p_1 = 10$ Torr, $\alpha = 60°$, $\ell_I = 3$ mm. Note: fringe shift is positive downward.

to the onset of ionization. Calculations made with the model of Wong and Bershader[4] give good agreement with the measured fringe shift. In the case of nitrogen (6b), the relaxation length is more difficult to define because of the asymptotic approach of the fringes to their equilibrium value. However, calculations made using the rates measured by Kewley and Hornung[5] again give good agreement with the measured fringe shift, except where the experiment is not able to resolve the initial fringe shift across the frozen shock.

ARGON, $M_s = 15$

Figure 7 shows a sequence of infinite fringe interferograms of shocks at $M_s = 15$ into 10 Torr argon. From these it is immediately clear that what we had interpreted as double Mach reflexion in the experiments with the image converter photographs, is in fact just the fringe shift due to the onset of ionization after the Mach stem. Actually, simple Mach reflexion is observed. The reflected shock shows up only weakly and could not be resolved by the image converter photograph of figure 2. This is contrary to the expectation that double Mach reflexion should be observed at this condition in equilibrium flow (Ben-Dor and Glass[1]), and is possibly a relaxation effect. A large number of photographs were taken at this condition in an attempt to discover whether the self similarity of the shock configuration is destroyed by the fixed relaxation length. However, to be able to test this, photographs have to be taken with the shock near the tip, $w = O(\ell)$. At the tip the self-luminosity is most intense, especially when $\alpha \to \alpha_{tr}$, so that, even with the tuning filter, the stop size on the camera has to be reduced to such an extent that it is not

Fig. 7 Infinite fringe interferograms of argon flows $M_s = 15$, $p_1 = 10$ Torr, $\ell_I = 4$ mm.
a) $\alpha = 68°$, instrumentation as in fig. 5a, stopsize = 5 mm.
b) $\alpha = 60°$, instrumentation as in fig. 5a, stopsize = 3 mm.
c) $\alpha = 53°$, instrumentation as in fig. 5b, stopsize = 10 mm.
d) $\alpha = 50°$, instrumentation as in fig. 5b, stopsize = 5 mm.
Note that in 7a)-c) the simple Mach reflexion is almost obscured by the dominant fringe shift accompanying the rise of electron density. The weak reflected shock is relatively obscure.

possible to resolve the very small shock configuration. In the regions examined no departure of the triple point trajectory from self-similarity could be detected.

ARGON $M_s = 11.8$

The most striking features of the shock configuration in this case are that complex Mach reflexion is observed and that the reflected shock shows a definite change in slope at the end of the relaxation region after the primary shock. This is clearly brought out by figure 5b. The feature emanating from the junction of the "slip-line" with the wedge is clearly the fringe shift due to the onset of ionization, which occurs even further upstream behind the Mach stem.

These features can be seen, though much less definitely in figure 8b at an angle close to α_{tr}. Note that, though the Mach stem is considerably shorter, the relaxation length is fixed and the reflection configuration is considerably narrower. This change in the aspect ratio is another clear manifestation of a relaxation effect. Although the relaxation length is larger here than at $M_s = 15$, and a large number of pictures were again taken both with $w = O(\ell_I)$ and $w > \ell_I$, no departure could be detected from self-similarity of the triple point trajectory. Figure 8a is taken at similar conditions to 5b but with $w \approx \ell_I$. The configuration is more obviously complex Mach reflexion. Again there is a change of slope of the reflected shock at the end of the relaxation region, this time occurring on a more strongly curved part of the shock. Thus the relaxation destroys the self-similarity of the overall shock configuration.

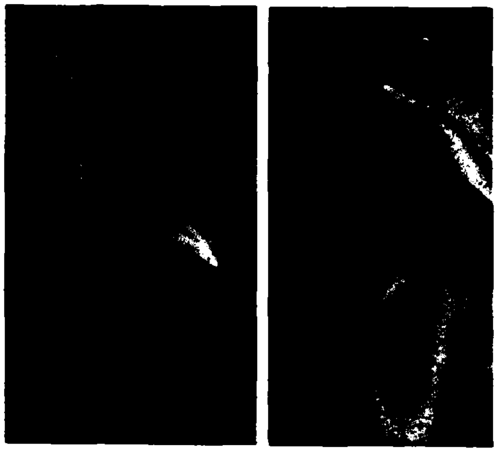

Fig. 8 Infinite fringe interferograms of argon flows at M_S = 11.8, p_1 = 30 Torr and ℓ_I = 11 mm. Compare with figure 5.
a) $w \approx \ell_I = 11\text{mm}$, $\alpha = 58°$. Note the clearly evident complex Mach reflexion and the bend in the shock at the end of the relaxation zone, near the wedge tip.
b) $w > \ell_I$, $\alpha = 54°$. Note that the size of the features governed by the relaxation does not change significantly, though the Mach stem is much reduced relative to figure 5b. Result is a changed aspect ratio of the configuration.

NITROGEN, M_S = 15

In contrast with the argon flows, the relaxation length after the reflected shock in nitrogen is so much smaller than that after the incident shock that it is not resolvable. This is shown in the regular reflexion of figure 9a. Figures 9b and c show that in the nitrogen flow the double Mach reflexion expected from Ben-Dor and Glass[1] calculations clearly does occur. The relatively lower self-luminosity of the gas permits a larger stop size to be used, with consequent improvement of the definition, allowing even small reflexion configurations such as that in figure 9b to be resolved in detail. Again, no significant departure of the first triple point trajectory from self-similarity can be measured. However, as the double Mach reflexion configuration increases to a size larger than the relaxation length, ℓ_I, it becomes possible to detect a convex curvature in the first reflected shock (see figure 9c). The bulge in the Mach stem of figure 9c is repeatable, and we cannot explain it.

TRANSITION CONDITIONS

The transition conditions are determined to an accuracy of ± 1.0° by extrapolating the dimensionless Mach stem length, s/w to zero. This is shown in figure 10 for the case of argon (M_S = 11.8, p_1 = 30 Torr) giving α_{tr} = 42.2 ± 1.0°. Similar plots of the argon M_S = 15 and nitrogen results yield the values given in table I which also gives the calculated transition conditions for various cases (I,R). The slope of the best straight line through the experimental points in the plot of s/w versus α turns out to be the same in both argon flows (0.46/radian) but for nitrogen is larger (0.74/radian).

Table I

Gas	M_s	$\frac{p_1}{\text{Torr}}$	$\frac{\ell_I}{\text{mm}}$	α_{tr}/deg.			
				(I_f, R_e)	(I_e, R_e)	(I_f, R_f)	measured
Ar	11.8	30	11	46.7	44.0	35.5	42.2 ± 1.0
Ar	15.0	10	4	49.4	45.0	35.5	47 ± 1
N_2	15.0	10	3	49.3	48.7	40.0	51.5 ± 1.0

In order to put these results into context with the previous measurements of Hornung et al.[2] and with calculated conditions, figure 11 shows plots of

Fig. 9 Interferograms of nitrogen flows. $M_s = 15$, $p_1 = 10$ Torr, $\ell_I = 3$mm.
a) $\alpha = 50°$, regular reflexion, note small ℓ_R.
b) $\alpha = 57°$, double Mach reflexion, with s = 1 mm.
c) $\alpha = 60°$, double Mach reflexion. Note curvature of reflected shock.

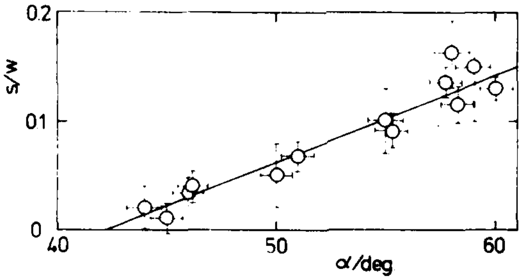

Fig. 10 Determination of transition angle by extrapolating dimensionless Mach stem length to zero. ———, straight line of best fit.

α_{tr} versus M_s. Figure 11a, giving the nitrogen data, shows that the increase to $M_s = 15$ does not alter the relative position of the experimental and theoretical values. The points lie consistently above the curve for (I_f, R_e), which is appropriate for the nitrogen experiment in view of the relative magnitude of the relaxation lengths ℓ_I and ℓ_R. This is explained by Hornung et al.[2] as a viscous boundary layer effect.

The viscous effect is even more strongly evident in the previous results for argon at $M_s = 7$ and 9, shown in figure 11b, the measured α_{tr} being again larger than the most appropriate theoretical value (I_f, R_e). However, in the new results at $M_s = 11.8$ and 15, where the relaxation lengths are comparable with the scale of the reflexion configuration, the experimental points fall below the (I_f, R_e) curve. Since the viscous effect can only raise the experimental result for α_{tr} above the appropriate theoretical curve, we interpret the fact that both points lie between the frozen and equilibrium theory as an effect due to finite relaxation length. This is substantiated by the fact that the discrepancy between experiment and (I_f, R_e) increases with relaxation length. The fact that only the argon and not the nitrogen flows show such a relaxation effect is due to the larger ℓ_R in the argon case.

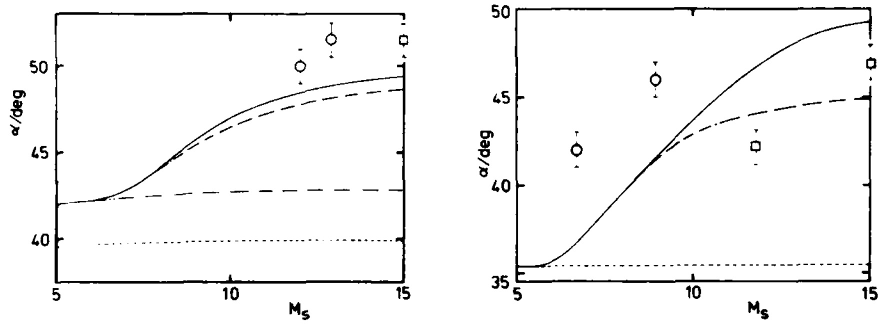

Fig. 11 Transition angle versus M_s. ○ , Hornung et al.[2] □ , present results.
a) Nitrogen. Calculated values with equilibrium vibration for p_1 = 10 Torr: ——, (I_f,R_e); —·—, (I_e,R_e); —··—, (I_f,R_f). Calculated values with frozen vibration: ----, i.e. perfect gas.
b) Argon. Calculated values for p_1 = 10 Torr: ——, (I_f,Re); —·—, (I_e,R_e). Note: The calculations for p_1 = 30 Torr differ insignificantly from these. -----, perfect gas, i.e. (I_f,R_f).

CONCLUSIONS

1. Two important qualitative effects of relaxation on pseudosteady Mach reflexion have been demonstrated for the first time in argon at M_s = 11.8 and 15 and in nitrogen at M_s = 15:

a) The double Mach reflexion expected from equilibrium calculations[1] does not occur in argon, but it does occur in nitrogen. This is explained in terms of the relaxation lengths after the incident and reflected shock.

b) The reflected shock shows a distinct bend at the end of the relaxation zone in argon and a convex curvature in nitrogen flows. The self-similarity of the overall shock configuration is lost because of relaxation, though the triple point trajectory follows a straight line.

2. A significant quantitative effect due to relaxation is the reduction of the shock angle at transition in the case of argon. As might have been expected, this reduction increases with relaxation length. It does not occur in nitrogen at the conditions tested, because the relaxation length after the reflected shock is too small to be resolvable.

3. The nitrogen laser pumped dye laser has been made into a high quality light source for very short exposure Mach-Zehnder interferometry by incorporating in it a fibre optic to expand the beam and to destroy transverse spatial coherence. This allows the image quality to be considerably improved over image converter photography. The latter led to a serious misinterpretation which was easily detected in the better quality "one per shot" interferograms.

ACKNOWLEDGEMENTS

This project was financially supported by the Australian Research Grants Committee. Vic Adams and Ken Smith contributed significantly with technical support.

REFERENCES

1. G. Ben-Dor and I.I. Glass, J. Fluid Mech. (1979) to appear. See also UTIAS Reports 232, 237.
2. H.G. Hornung, H. Oertel jr. and R.J. Sandeman, J. Fluid Mech. *90*, 541 (1979)
3. H.G. Hornung and R.J. Stalker, in Applied Fluid Mechanics, H. Oertel jr. ed., Karlsruhe 1978.
4. H. Wong and D. Bershader, J. Fluid Mech. *26*, 459 (1966).
5. D.J. Kewley and H.G. Hornung, Chem. Phys. Lett. *25*, 531 (1974).

EXPERIMENTS ON THE GROWTH OF THE MACH STEM FOR SHOCK REFLECTIONS IN A SHOCK TUBE

A. Lozzi

Department of Mechanical Engineering
The University of Sydney, Sydney N.S.W. 2006, Australia

The growth of the Mach stem is examined for shock reflections generated by two types of experimental configurations in a shock tube. It is found that at the onset of Mach reflection the Mach stem grows very rapidly and from the vicinity of the 'extreme angle concition'. On the other hand for reflections free of solid boundaries, between symmetric shock waves near the centre of the shock tube, the onset of Mach reflection takes place smoothly and close to the 'normal Mach stem' condition. This last experimental configuration gives results which are in agreement with data obtained from wind tunnel experiments, but on the basis presented here comparisons cannot be readily made with wind tunnel results. For reflections free of solid boundaries in a shock tube no Mach stem is detected until χ, the extended angle of the Mach stem to the origin of the reflection, becomes 0.5° or larger. A difference in wave angle of this magnitude appears to be the absolute limit of resolution of our wave angle measurements technique. A model is suggested here for the physical conditions which may govern the growth of the Mach stem in shock tube reflections. Viewing the reflection in side elevation, it is proposed that the gas initially contained in the volume swept by the Mach stem is relocated in the new volume bounded by the slip line, the Mach stem and by the solid boundary. The ratio of these two volumes is then to be in the same ratio as the density jump across the Mach stem. It is then this density jump which controls the required Mach stem height. This model is reasonably successful in predicting the Mach stem height.

INTRODUCTION

There are two principal types of reflections which take place when a plane shock wave meets a solid boundary: these are of course the regular (RR) and the Mach reflection (MR). The understanding of the flow parameters which determine the transition between these two reflections was substantially established by von Neumann (ref. 4). Theoretically the condition for transition can be one of three possibilities, and it has been left to experimental evidence to establish which of these actually apply. Unfortunately the available data has not been unequivocal in favour of a single criterion. The three criteria described in terms of the incident wave angle ω_0 are: (1) the normal Mach stem condition: ω_N; (2) downstream sonic flow condition: ω_o*; and (3) the extreme deflection condition for the reflection wave: ω_e.

In the work published by Henderson and Lozzi (ref. 2) essentially it was reported that of the four different experimental configurations investigated, in only one did the transition occur near the then normally accepted criterion of the extreme wave angle: ω_e. The other three configurations all indicated ω_N as the most likely transition point, and perhaps significantly by a closer margin than did the one exception. Of the four configuration referred to above, two produced stationary flow conditions in a wind tunnel, and two pseudo-stationary conditions in a shock tube. The configuration which gave the anomalous result was that of the plane compression corner type as used in shock tubes, and as it is probably the one which is most commonly studied it's special properties are therefore very important.

It is the purpose of this paper to examine the growth of the Mach stem at a plane compression corner in a shock tube, to compare it to the growth in the other configuration in a shock tube and to suggest a mechanism which may govern its development.

EXPERIMENTS

There is a considerable amount of evidence to indicate that in shock tube experiments the flow behind the Mach stem may be trapped or contained by the slip line, the Mach stem and the wall. Interferograms (such as Figure 14a of Law and Glass's paper ref. 1) clearly indicate that the Mach stem flow has very little space between the vortex sheet and the wall to propagate into its surrounds. Although the diffusion rate across the vortex sheet must be high, the time available is correspondingly short, and it will be assumed here that the effects of this diffusion are negligible. White (ref. 6) states that, for sufficiently strong waves, the slipstream will curl under itself at the boundary, and from there it will join the reflected wave with a new wave.

On Figure A1 of Weynants' report (ref. 5), we can see that this trend becomes more pronounced as the incident shock Mach number is increased. The new shock now moves away from the wall and up the slip line. The slip line itself becomes a spiral, and an abnormally high pressure in the Mach stem flow is evident from the forward bulge of the Mach stem itself.

In search for a mechanism which may explain the apparently spurious growth of the Mach stem (or persistence of regular reflection), the above observations suggested the model detailed on Figure 1, in which the slip line and the shock

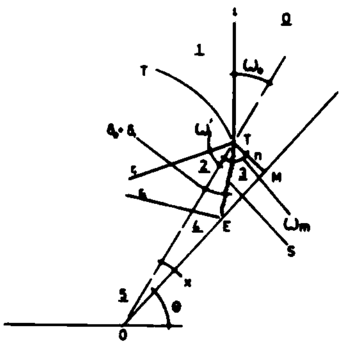

Figure 1. Model of Mach reflection at a plane compression corner in a shock tube, showing straight shock waves and slip lines.

— —	Triple point path
i	incident shock
n	Mach stem
r_1	reflected shock
r_2	recompression shock
S	slip line
T	Triple point
ω_o	incident wave angle
ω_m	= 90 - χ
χ	= Triple point angle

waves are assumed to be adequately represented by straight lines. The Mach stem flow is trapped where the vortex sheet is joined at the wall by the additional shock wave (or compression waves). The wave is produced where the supersonic flow above the slip line is caused by the wall to rotate to a direction parallel to it. The gas originally contained in triangle TOM is now contained in TEM. The Mach stem is assumed to have a constant pressure ratio equal to that expected at the triple point. From these geometric and mass continuity considerations, the relationship between the angle χ and the density ratio across the Mach stem is given by

$$\tan \chi = \frac{(\eta - 1) - (\eta^2 - 2\eta + 1 - 4\eta\tau)^{\frac{1}{2}}}{2\eta\tau} \qquad \mathrm{I}$$

where:

$\eta = \rho_3/\rho_0$ the density ratio across the Mach stem

$\tau = \tan \delta_m$ the tan of the deflection at the triple point

$(\gamma = 1.402$ ratio of specific heats.)

For given conditions at the triple point, χ may therefore be calculated. Law and Glass (ref. 1) assumed that:

$$\chi = 90° - \omega_m$$

where ω_m is the wave angle of the Mach stem at the triple point. Law and Glass pointed out that this assumption is equivalent to the Mach stem's being perpendicular to the boundary at the triple point, but that is does not require the stem to be straight between there and the boundary. They showed that for wedge angles (θ) close to the transition, the above equation gave a good approximation to the actual value of χ. Within 5% for $\chi \sim 4°$, for more developed Mach reflection, $\chi \sim 11°$, the error grew to approximately 10%. It is of interest to note that, if the Mach stem is straight, the size of χ will be larger than if it is of the normally assumed shape.

Figures 2 and 3 show the development of the incident wave angle ω_0 at a plane compression corner (shown on Figure 1 here and Figure 1d of ref. 2) in a shock tube, near the transition condition RR $\rightleftarrows$ MR. These experiments were carried out at an incident Mach number of 4.0 in air and are the same experiments as those shown in Figure 6 of Henderson and Lozzi's paper (ref. 2). As shown in Figure 1, the wave angle ω_0 is given by:

$$\omega_0 = 90° - (\theta - \chi)$$

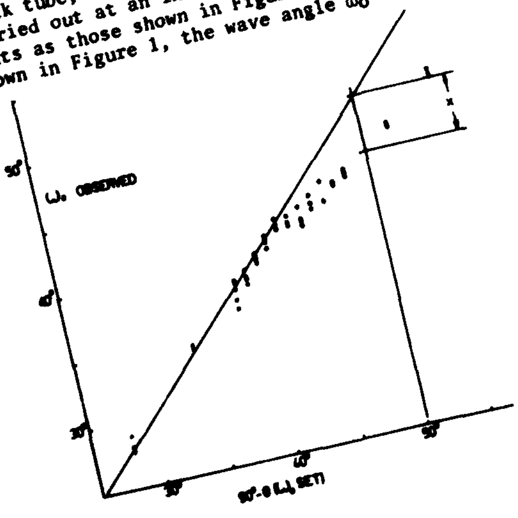

Figure 2. Experimental value of ω_0 plotted against 'ω_0 set' showing the development of the Triple point angle χ. Triple point Mach No. of 4.0, at a plane compression corner.
• Experimental point.

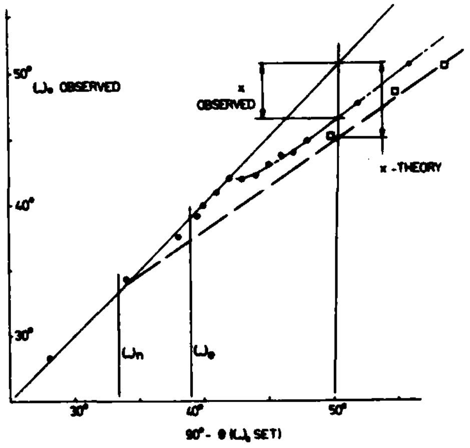

Figure 3. Experimental value of ω_o, as for Figure 2 except:

- • Average value of ω_o from Figure 2, for experiment repeated with the same initial condition.
- □ Data derived from Law and Glass (ref. 4).
- — — Value of χ calculated with equation 1.
- —·— Estimated curve of best fit.
- ——— Plot for regular reflection.

the wedge angle θ may be set very accurately for each experiment and ω_o is the wave angle which may be measured most precisely on the negatives. Therefore, in a plot of ω_o against (90 - θ), any deviation from equality will be due to development of χ (the triple point trajectory angle). Figure 2 shows all the experimental data, while 3 gives the average ω_o for those with common θ. This last figure gives a convincing demonstration of the almost instantaneous growth of χ, at an incident wave angle well past the normal shock criterion ω_N, but also past the extreme angle ω_e condition as well.

Working from data shown in ref. 1 Figure 10, the present author interpolated into Smith's results (ref. 3), to determine values for a constant incident Mach number of 4.0. These are shown on Figure 3, together with magnitude of χ calculated using the present author's model. Smith's results fall closer to the theory than the present author's results, but the difference may be insignificant, considering the difficulties of working with Figure 10 of ref. 1.

Figure 4 shows the growth of ω_o for a constant incident Mach number of 3.0, again a rapid growth of χ is observed. Figure 5 shows the development of the Triple point angle χ as the incident wave angle ω_o is increased, for the configuration shown of Figure 1d of ref. 2. In that experimental configuration the reflection takes place between symmetrically disposed shock waves, in the

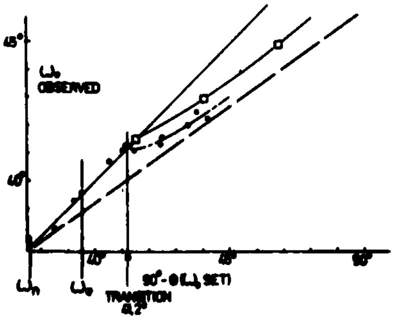

Figure 4. Experimental values of ω_o plotted for a constant Triple point Mach number of 3.0 at a plane compression corner. For symbols see the caption to Figure 3.

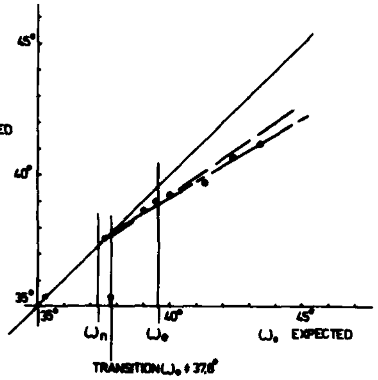

Figure 5. Experimental values of ω_0 plotted a constant Triple point Mach number of 3.0, between two similar shock waves free of any solid boundary in a shock tube. For symbols see captions of Figure 3.

centre of the shock tube, free of any solid boundary. This was the only other configuration which readily allows χ to be measured, and is presented here to highlight the singular nature of the transition between regular and Mach reflection at a plane compression corner. Figure 5 shows a finite and constant growth of χ with ω_0 beginning within 0.5° from the normal Mach stem condition: ω_N. Figure 4 on the other hand shows the very fast growth of χ with ω_0 at transition, 1.8° from the extreme deflection condition: ω_e. Figure 6 gives the results of L.G. Smith, together with the value of χ, calculated by the present authors for an incident Mach number of 5.0.

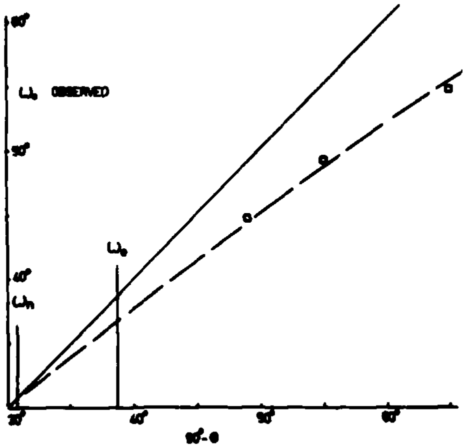

Figure 6. Experimental values of ω_0 for a constant Triple point Mach no. of 5.0: For symbols see caption of figure 3.

CONCLUSIONS

For shock wave reflections at a plane compression corner, it appears reasonable to conclude that the rapid growth of the Mach stem and the related persistence of regular reflections are valid. These features are not normally observed in other types of experimental configurations. In particular, from the experimental data presented here, for shock reflections free of solid boundaries in a shock tube, transition occured smoothly at the normal Mach stem condition with no significant persistence of regular reflection.

The model suggested here to describe the development of the Mach stem appears useful particularly away from the transition conditions, and in all cases indicated an onset of Mach reflection near the ω_N condition and not the ω_e one. The almost instantaneous growth of the Mach stem at transition for a plane compression corner belies the smooth transition predicted by any of the transition theories, and implies that some kind of suppressing mechanism is at work.

REFERENCES

1. C.K. Law and I.I. Glass, C.A.S.I. Transactions *4*, No. 1, 1 (1971).
2. L.F. Henderson and A. Lozzi, Journal of Fluid Mechanics *68*, pt. 1, 139 (1975).
3. L.G. Smith, O.S.R.D. Report No. 6271 (1945).
4. Von Neumann, Collected Works, Ed. A.H. Taub, *VI* (1961).
5. R.R. Weynants, U.T.I.A.S. Technical Note No. 126 (1968).
6. D.R. White, Second Midwestern Conference on Fluid Mechanics, 253 (1952).

ON THE TRANSITION BETWEEN REGULAR AND MACH REFLECTION

SHIGERU ITOH and MATSUKI ITAYA

Department of Mechanical Engineering
Kyushu Sangyo University, Japan

The transition between regular and Mach reflection were investigated by both experiments and theory.
We indicate that the transition process is much affected by the wall curvature.
In the case of the transition from regular to Mach reflection ,we construct the theoretical treatment concerning to the critical angle defined by the incident angle at the onset of Mach reflection applying Ray shock theory. We see that this theory well predicts the experimental results. However,in a case of the transition from Mach to regular reflection,we see that this theory cannot predict the transition between them. In a concaved curved wall boundary case,we consider the length of Mach-stem and construct its theory,and we see that this theory well predicts the experimental results. Using this theory,we estimate the transition from Mach to regular reflection. We see that this theory well estimate the experimental results besides a weak shock strength case.

INTRODUCTION

As is well known when a travelling normal shock strikes a solid boundary it reflectes in one of two configurations,regular R.R ,or Mach reflection,M.R. If a shock interacts with a convexed or concaved wall boundary,the transition between R.R and M.R occurs as a transmitted shock propagating towards downstream (ref.1 - 3). These transition processes were investigated,usually,by Two shock theory(ref.4) ,or Three shock theory(ref.5). Henderson(ref.6) investigated in cases of curved wall,he concluded that this process was obeyed by Three shock theory.

We investigated the transition process between R.R and M.R at a convexed or a concaved curved wall boundary using an usual pressure driven shock tube with 50mm x 70mm rectangular duct. We,also,constructed a theoretical treatment for the transition from R.R to M.R by applying Ray shock theory developed by Whitham(ref.7). We see that this theory well predicts the transition from R.R to M.R,but it cannot estimate the critical angle defined by the onset of regular reflection in a case of concaved curved wall boundary. We construct the theoretical treatment concernig a length of Mach stem in this case,and this theory well predicts the experimental results besides a small incident angle. Moreover we modify this theory and we estimate the critical angle in the case of a concaved wall boundary. We see that this theory comparatively well predicts the experimental results except a weak shock strength.

THEORY

We,first show a theoretical treatment for the transition from R.R to M.R. The shock wave system in the vicinity of a transition point is shown in Fig.1. From its geometry,we get following relations;

$$\begin{aligned} L &= Mo\ ao\ dt \\ S &= M_1\ ao\ dt \\ L' &= S\ Sin(\alpha crit) \end{aligned} \qquad (1)$$

,where ao is a sonic velocity at undisturbed region ahead of a transmitted shock,and dt is an infitesimal time, and Mo and M_1 are Mach number of an incident and a Mach stem,respectively.

If L' becomes to be greater than L,we recognize the onset of Mach reflection,so that we define the critical angle which is the incident angle at the onset of Mach reflection,as following;

$$L' = L + 0,\text{that is } M_1/Mo\ Sin(\theta crit) = Tan(\theta crit) \qquad (2)$$

,where $\theta crit = \pi/2 - \alpha crit$. As taking $dt \rightarrow 0, M_1$ is well estimated by Ray shock theory with appling as a wedge wall boundary case. The relation between the wall angle θw and the strength of Mach stem is given as following;

$$\theta w = \int_{Mo}^{M_1} \frac{\sqrt{2}\ dM}{\{(M^2 - 1)K(M)\}^{1/2}} \qquad (3)$$

,where $K(M)$ is called as Chester's function and it takes $0.5\ (M \rightarrow 1)$ and $0.3941\ (M \rightarrow \infty)$. If we suppose that $K(M)$ is constant and equals to n,the integration of eq.(3) is very easy to next equation;

$$\frac{M_1}{Mo} = \frac{1}{2Mo}[\{(\sqrt{Mo^2-1} + Mo)exp(\sqrt{\frac{n}{2}}\ \theta w)\} + \{(\sqrt{Mo^2-1} + Mo)exp(\sqrt{\frac{n}{2}}\ \theta w)\}^{-1}]. \qquad (4)$$

First,supposing n is no ,then we calculate M_1 using eq.(4) and $Mmean = (Mo + M_1)/2$ and $n = K(Mmean)$. We repeat these procedures untill n coinsides with no,iteratively,to get a solution.

In the extream case of $Mo \rightarrow 1$,eq.(4) becomes to next equation;

$$\frac{M_1}{Mo} = Cosh(\frac{1}{2}\theta w). \qquad (5)$$

Developing eq.(5) by θw ,we get a equation for weak shock case as following;

$$\frac{M_1}{Mo} = 1 + \frac{1}{8}\theta w^2 . \qquad (6)$$

In the extream case of $Mo \rightarrow \infty$,we get next equation;

$$\frac{M_1}{Mo} = exp(\sqrt{\frac{n}{2}}\ \theta w). \qquad (7)$$

Combining eq.(4) with eq.(2),we get next equation;

$$\frac{1}{2Mo}[(\sqrt{Mo^2-1} + Mo)exp(\sqrt{\frac{n}{2}}\ \theta w) + \{(\sqrt{Mo^2-1} + Mo)exp(\sqrt{\frac{n}{2}}\ \theta w)\}^{-1}]\ Sin\ \theta w = Tan\ \theta w. \qquad (8)$$

Supposing a suitable value of θw,then using eq.(4),we obtain M_1. We put this value into eq.(8) in order to get the critical angle of $\theta crit$ after a few of iterations.

The results obtained by eq.(8) are shown in Fig.2. In this figure,the intersection of a straight line with a slope of unity and each of curved line indicates the theoretical critical angle.

In the case of concaved curved wall boundary,we construct the theoretical treatment for a length of Mach stem using a model as seen in Fig.3. We suppose that the Mach stem is straight and normal to the tangent of curved wall,then the strength of Mach stem is uniformly at any point on it. In this figure, θo is an initial angle of concaved curved wall boundary,and λ is a nondimensional length of Mach stem. From its geometry,we get following equations;

$$A = \lambda$$

$$Ao = Cos\theta o - (1 - \lambda)Cos(\theta o + \phi) \qquad (9)$$

$$1 - (\lambda + d\lambda)Sin(\theta o + \phi + d\phi) - (1 - \lambda)\,Sin(\theta o + \phi) = L \qquad (10)$$

,where A is a ray tube of area and Ao is the undisturbed ray tube of area,and $L = Mo\ d\alpha_1$,and $d\alpha_1$ is a shock position at any time dt and it equals to $ao\ dt_1$. If we suppose that $d\lambda \ll 1$,and $d\phi \ll 1$,we get next relation;

$$\frac{d\lambda}{d\phi} = \frac{1 - \lambda}{Tan(\theta o + \phi)} - \frac{Mo}{Sin(\theta o + \phi)}\left(\frac{d\alpha_1}{d\phi}\right). \qquad (11)$$

Following Bryson & Gross,$d\alpha_1/d\phi$ is obtained as following;

$$\frac{d\alpha_1}{d\phi} = (1 - \lambda/2)\,\frac{1}{M}. \qquad (12)$$

Finally,combining eq.(12) with eq.(11),we get next equation;

$$\frac{d\lambda}{d\phi} = \frac{1 - \lambda}{Tan(\theta o + \phi)} - \frac{1 - \lambda/2}{Sin(\theta o + \phi)}\left(\frac{Mo}{M}\right) \qquad (13)$$

In an extream case of $Mo \rightarrow \infty$,we get a next relationship between A and M ;

$$\frac{A}{Ao} = \left(\frac{Mo}{M}\right)^{\nu} \qquad (14)$$

,where ν is $2/K(\infty) = 5.0743$.

From eq.(8),(13) and (14),we obtain a relationshop between λ and ϕ .

$$\frac{d\lambda}{d\phi} = \frac{1 - \lambda}{Tan(\theta o + \phi)} - \frac{1 - \lambda/2}{Sin(\theta o + \phi)}\left(\frac{\lambda}{Cos\,\theta o - (1 - \lambda)Cos(\theta o + \phi)}\right)^{1/\nu} \qquad (15)$$

Eq.(15) cannot to be solved analytically but numerically with a suitable initial value. The numerical result in a case of Mo of infinity and θo of $0°$ is shown in Fig.4. The initial value of λ is given by the distance between the straight line with a slope of $Tan(m)$ and a concaved curved wall at ϕ of $0.5°$. The term of m indicates a characteristic angle given by next equation;

$$Tan(m) = \left(\frac{(M^2 - 1)K(M)}{2M^2}\right)^{1/2} \qquad (16)$$

The critical angle which is defined by the incident angle at the onset of regular reflection is obtained as the incident angle at which the length of Mach stem equals to 0.

RESULTS AND DISCUSSION

Typical Schlieren records are shown in Fig.5. We see that in a case of convexed curved wall boundary,Mach stem is much curved by the effects of disturbancies occured at a rear part of Mach stem. However,we recognize that a

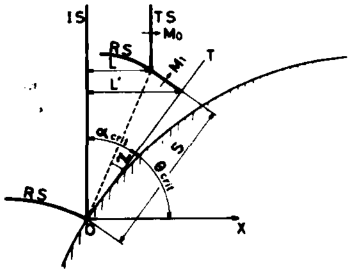

Fig.1 Shock wave system in the vicinity of a transition point(O). χ indicates a shock-shock angle. IS and RS are a incident shock and a reflected shock,respectively. MS is Mach stem and TS is a transmitted shock. T is the tangent at point O on curved wall.

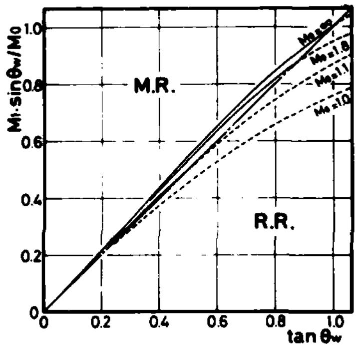

Fig.2. Numerical results obtained by eq.(8). The intersection of a straight line with a slope of unity and each of curved line indicates the critical angle. M.R. and R.R correspond to the region of Mach reflection and of regular reflection ,respectively.

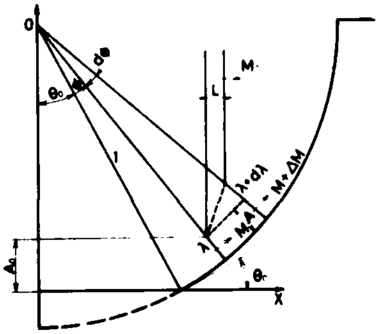

Fig.3. Theoretical model for a length of Mach stem in a case of concaved curved wall boundary. λ is a nondimensional length of Mach stem,*θo* is an initial angle of concaved curved wall. *A* is a ray tube of area .

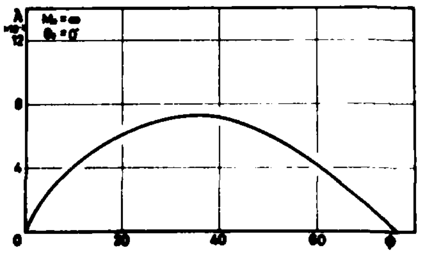

Fig.4 Theoretical result for the length of Mach stem in a case of *Mo* of infinity and *θo* of *0°*.

$\tau = 7.85$ μsec $\quad$ $\tau = 24.43$ μsec $\quad$ $\tau = 50.01$ μsec

(a) In a case of convexed curved wall.

$\tau = 25.53$ μsec $\quad$ $\tau = 38.66$ μsec $\quad$ $\tau = 46.29$ μsec

(b) In a case of concaved curved wall θ_o of 0°.

$\tau = 10.31$ μsec $\quad$ $\tau = 21.43$ μsec $\quad$ $\tau = 28.85$ μsec

(c) In a case of concaved curved wall θ_o of 10°.

$\tau = 10.10$ μsec $\quad$ $\tau = 18.93$ μsec $\quad$ $\tau = 26.61$ μsec

(d) In a case of concaved curved wall θ_o of 20°.

Fig. 5 Typical Schlieren records in each case of curved wall boundary and of a initial angle. τ indicates the time after striking a normal shock with a tip of curved wall boundary.

Mach stem is almost straight and normal to a tangent of concaved curved wall. We also see that a reflected shock is very weak at θo of 0°, and it becomes to be stronger as θo increases.

The critical angle of the transition from regular to Mach reflection against the pressure ratio ahead to rear of the incident shock, ξ, are shown in Fig.6. In this figure,Heilig's and Henderson's results are also seen for comparison. We see that the theoretical treatment of $\alpha crit$ given by eq.(8) well predict the experimental results.

The locus of triple point which is the intersection of a reflected and a transmitted shock and Mach stem are shown in Fig.7. The solid line started from α_{Ray} corresponds with a theoretical locus obtained by a method of characteristic(ref.2) with an initial value of α_{Ray} which is a critical angle obtained by eq.(8). Another solid line is a same theoretical locus of triple point started from a critical angle obtained by Two shock theory. We see that the locus of triple point are well estimated by the method of characteristic with a critical angle obtained by eq.(8) as an initial value. In a case of Mo of 1.8,the locus of triple point at both concaved and convexed curved wall boundaries are shown in Fig.8. In this figure,a solid line indicates the theoretical locus obtained by the method of characteristic,and a chain dotted line indicates a straight line with a slope of $Tan(m)$ given by eq.(16). We see that in the neighbourfood of a tip of a concaved curved wall,this straight line well predicts the experimental result.

The Schlieren records obtained at the same incident angle in both cases of convexed and concaved curved wall boundaries are shown in Fig.9. We see that there are much difference between them. This may be caused by the effects of disturbancies occured at the region rear of Mach stem.

Figure 10 shows the locus of triple point obtained at a concaved curved wall boundary at each case of θo. Each of straight line indicates the locus of shock-shock at wall angle of θo and Mo. This shock-shock angle is given by next equation;

$$Tan\chi = \frac{A1}{Ao}\left(\frac{1-(Mo/M1)^2}{1-(A1/Ao)^2} \right)^{1/2} \qquad (17)$$

,where χ is shock-shock angle. As seen in Fig.10 ,in the neighbourfood of a tip of the curved wall,this shock-shock angle well predicts the locus of triple point.

By considering above results,we use a distance between a straight line with a slope of $Tan(\chi + \theta o)$ or $Tan(m)$ and a curved wall at intial vale of ϕo as an initial length of Mach stem, in each case of any θo and θo of $0°$,respectively. Figure 11 shows the results of length of Mach stem at θo of $0°$. We see that the theoretical value indicated by solid line well predicts the experimental result in each case of Mo besides a large value of ϕ . It seems that,at a large value of ϕ ,an effect of disturbance is so remarkable that the descrepancy between them is appeared. This descrepancy between them may be increased as θo increases (see Fig.12). These descrepancies may be caused by a lacking of the effects of the disturbancies and a reflected shock in estimating of M.

We modify the theory of the length of Mach stem by using A - M relation proposed by Milton(ref.8). This is given by following equation;

$$\frac{dA}{A} = \frac{-2MdM}{(M^2-1)K(M)} + \frac{-\eta dM}{M} , \qquad (18)$$

$$\eta = 0.546\left(1-\frac{Mo^2}{M^2}\right) + \frac{1}{2} ln\left(\frac{Ao}{A}\right). \qquad (19)$$

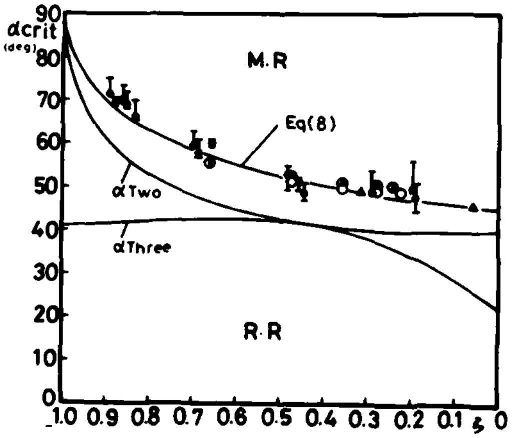

Fig.6 Critical angle for each of incident shock strength. ξ indicates the pressure ratio ahead to rear of the incident shock. Φ are after Heilig and ▲ are after Henderson. Eq.(8) indicates the theoretical critical angle obtained by eq.(8).α_{Two} and α_{Three} indicate the theoretical critical angle obtained by Two shock and Three shock theory,respectively.

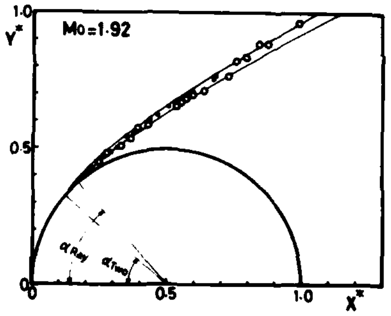

Fig.7 The locus of triple shock point. α_{Ray} indicates the theoretical critical angle obtained by eq.(8),and α_{Two} is the theoretical critical angle obtained by Two shock theory. o are after Heilig. The solid lines indicate the theoretical locus of triple point obtained by a method of characteristic.

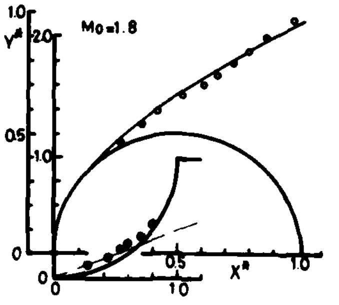

Fig.8 The locus of triple point at both convexed and concaved curved wall boundaries. A solid line indicates the theoretical locus obtained by a method of characteristic. A chain dotted line is a straight line with a slope of *Tan(m)*.

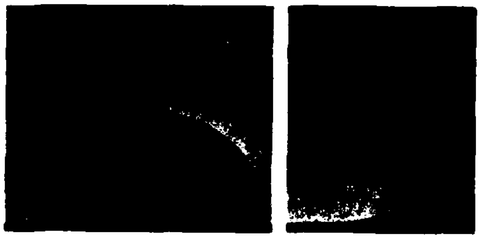

Fig.9 Schlieren records obtained at same incident angle in both cases of convexed and concaved curved wall boundaries.

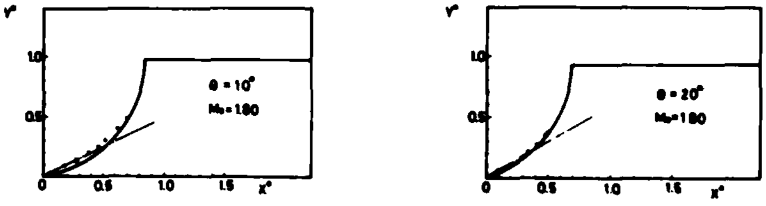

Fig.10 The locus of triple point at concaved curved wall boundary with any initial angle. The straight lines indicate the locus of shock-shock angle at θ_0.

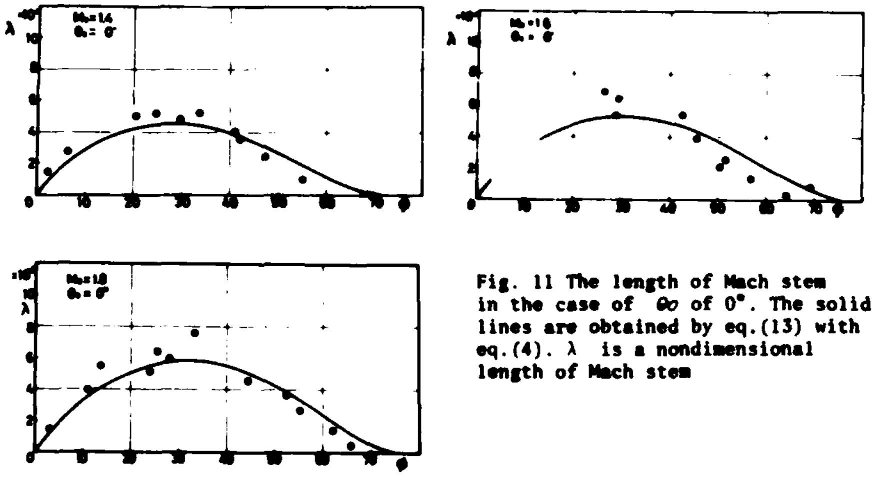

Fig. 11 The length of Mach stem in the case of θ_0 of 0°. The solid lines are obtained by eq.(13) with eq.(4). λ is a nondimensional length of Mach stem

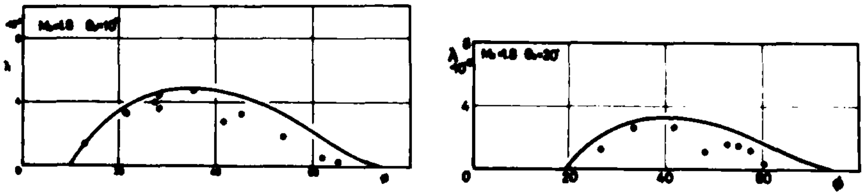

Fig. 12 The length of Mach stem in a case of concaved curved wall boundary with an initial angle. The solid lines indicate the the theoretical value obtained by eq.(13) with eq.(4).

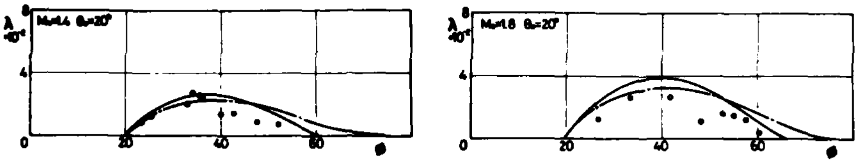

Fig. 13 The length of Mach stem in a case of concaved curved wall boundary with θ_0 of 20°. Solid lines indicate the theoretical length obtained by eq.(13) with a modified A - M relation. Another lines are same as in the case of in Fig.12.

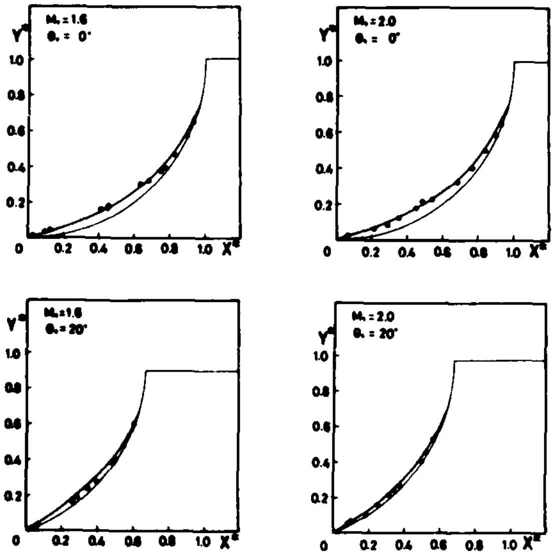

Fig. 14 The theoretical locus of triple point in the case of concaved curved wall boundary. Solid lines indicate the theoretical locus of triple point.

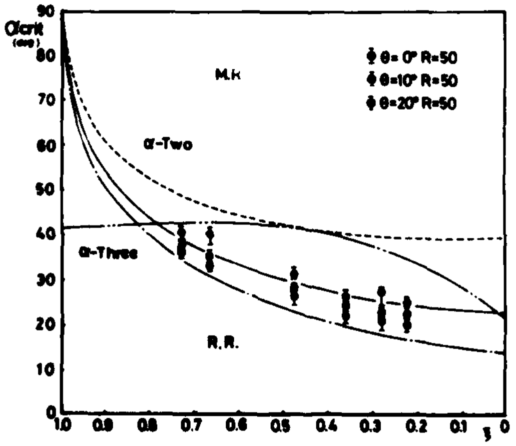

Fig. 15 Critical angle for each of incident shock strength in the case of concaved curved wall boundary. Solid line is obtained by eq.(13) with a modified A-M relation. A chain dotted line is obtained by eq.(13) with eq.(4). α_{Two} and α_{Three} are the theoretical critical angle obtained by Two and Three shock theory,respectively.

Using a modified A - M relation,we estimate the theoretical length of Mach stem. The results for θo of 20° are shown in Fig.13. We see that at large value of ϕ ,the theoretical value used a modified A-M relation indicated by solid line well predicts the experimental results,but at smaller of ϕ ,it is appeared a descrepancy between them. This may be caused by the manner of modifications. We used a strong shock case of modifications. However,as pointed out by Milton,using an exact solution for them is too complex to calculate in view of the accuracy of the results.

The locus of a triple point are shown in Fig.14. Each of solid line indicates the theoretical locus obtained by eq.(13) with a modified A-M relation. We see that the experimental results are well agreement with theory in each case of Mo and θo.

Theoretical critical angle for the transition from M.R to R.R against the initial shock strength of ξ,are shown in Fig.15. In this figure,α_{Two} and α_{Three} indicate the theoretical critical angle obtained by Two and Three shock theory,respectively. The theoretical critical angle obtained by eq.(13) with a modified A-M relation are comparatively well predicts the experimental results besides the weak shock strength (see solid line in this figure). However,a fully discussion concerning with the transition from M.R to R.R is one of the subject to be cleared.

CONCLUSION

Shock reflexion at convexed and concaved curved wall boundaries were investigated by both experiments and theory applying Ray shock theory. We conclude as following;

The theoretical treatment for the transition from R.R to M.R. well predicts the experimental results. However in a case of the transition from M.R to R.R,we see that this theory cannot predict the experimental results. In the case of convexed curved wall,the locus of triple point are well estimated by the method of characteristic with an initial angle obtained eq.(8). We,also construct the theoretical treatment for the length of Mach stem in the case of concaved curved wall boundary ,and we see that this theory well predicts the experimental results besides a smaller of incident angle which equals to a larger of ϕ. We,moreover,modify this theory considering the effects of disturbancies occured at the region rear of Mach stem and a reflected shock. We see this modified theory comparatively well predicts the experimental results in the case of smaller of incident angle.

The theoretical treatment for the transition from M.R to R.R are comparatively well predicts the experimental results besides the weak shock case. For a weak shock strength,a more suitable modifications for theory may be neccessary.

REFERENCE

1. W.Heilig, Shock tube symp. Pys. of Fluids supp.I,p.I-154,1969
2. A.E.Bryson & R.W.Gross, J. Fluid Mech.,vol.10,1,p.1,1961
3. L.F.Henderson & A.Lozzi, J. Fluid Mech.,vol.68,1,p.139,1975
4. J.Von Neuman, Collected works,vol.6.Pergamon,1963
5. W.Bleakney & A.H.Taub, Rev. Mod. Phys.,vol.21,p.584,1949
6. L.F.Henderson & A.Lozzi, Mod. Develop. in Shock Tube Res.,p.363,1975
7. G.B.Whitham, J.Fluid Mech.,vol.2,p.145,1957
8. B.E.Milton, A.I.A.A. J. vol.13,p.1531,1975.

STABILITY OF CYLINDRICAL CONVERGING SHOCK PERTURBED BY A BLEED APERTURE

J. H. T. WU, T. S. H. YU, R. A. NEEMEH† and P. P. OSTROWSKI*

Department of Mechanical Engineering
McGill University, Montreal, Canada

The stability of a converging cylindrical shock wave to the disturbances produced by interference with a small circular aperture is investigated experimentally in an annular air to air shock tube. This interference is characterized by shock diffraction and Mach reflection processes which result in the appearance of a pair of expansion fans and secondary shock waves sweeping around the collapsing shock front. Measurements from spark-schlieren photographs indicate that the initial shock front perturbation, shock shape and angular variation are reasonably well predicated by simple theoretical models based on Whitham's ray-shock theory. It is noted that the disturbance is fairly well tolerated by the collapsing shock in the sense that the relative size of the perturbations tends to decrease somewhat at large shock radii. However, at smaller radii, an eventual instability is manifest by the appearance of Mach reflection, a rapid growth in the relative size of the shock front perturbations, and the presence of binary vortices behind the expanding shock which follows the implosion process. The experiment results are in good agreement with Butler's square root amplification law for cylindrical converging shock waves.

INTRODUCTION

Recent interest in black holes by astronomers promotes further studies of converging shock waves. A black hole may become a singularity which is created by the collapsing of gravitational waves which overcome the radiation force of an exhausted star. The hole has a volume which diminishes sufficiently rapidly that its density approaches infinitely large values. The existence of such phenomena in the universe can be detected by X-radiation and is suggested by the observation of gases swirling around like giant vortex-pairs surrounding regions of enormous gravitational forces. Such phenomena are similar to the collapsing of imploding shock waves in gasdynamics, especially with regard to the appearance of mathematical singularities, binary vortices and instability. The instability of a collapsing shock is known to be the source of later vortex generation.

† Present address: Department of Mech. Eng., Concordia Univ., Montreal, Canada.
* Present address: Naval Ordance Station, Indian Head, Maryland, U. S. A.

In addition to black hole studies, several recent investigations have sought to take advantage of the high enthalpy gas which may be produced behind strong converging shock waves. These include controlled thermonuclear fusion[1], the production of diamonds from graphite[2], a cylindrical analog of the Hartmann-Sprenger tube[3], and detonation coating of materials[4]. For cylindrical converging waves, significant shock amplification occurs only at relatively small radii, hence the maintenance of shock front symmetry is one factor which controls the ultimate gas states which may be achieved. Since the inherent instability of converging cylindrical shock is well established[5], it is worthwhile to determine which type of disturbance is best tolerated by such shock.

The present study investigates the stability of a converging cylindrical shock which is perturbed by bleed effects resulting from its passage over a small circular aperture. The net effect of this interference is a local attenuation of the shock owing to a loss of mass, momentum and energy through the opening. Within the aperture, this is initially manifest by shock diffraction and then Mach reflection which are somewhat similar to that observed in shock-slot interactions[6]. The interaction between Mach reflection and the converging shock results in angular and circular pertubations which are measured to determine the converging shock stability.

EXPERIMENTAL APPARATUS

All tests were conducted in an annular air to air shock tube in which a cylindrical implosion chamber is formed by the circular end plates of a 10.2cm inner tube and a 15.2cm outer tube, as described previously in Reference 7. The test section is fitted with three successive conical contractions which turn and transform a plane annular incident shock into a cylindrical imploding wave. For schlieren viewing, the implosion chamber contains a mirrored inner wall and a plate glass window in the outer wall. The window exposes 6.9cm diameter field of view, and the chamber wall spacing (h) is variable. For the tests, a single aperture of diameter (d) equal to 6.4mm is drilled in the window at a distance 2.45cm from the geometric center of chamber. A single-pulsed spark, controlled by a time delayed circuit, is employed to produce a single schlieren photograph for each firing of the shock tube. Pressure measurements are accomplished by replacing the window with an aluminum plate containing peizoelectric transducers.

RESULTS AND DISCUSSION

Spark schlieren photographs showing the shock-aperture bleed effect on a converging cylindrical shock wave are presented in Figure 1 for a test chamber spacing h = 2.5mm and h/d = 0.39. According to pressure measurements, the reference shock Mach number is $M_o = 2.10$ at $R_o = 2.45$cm. The edge of the aperture appears dark and irregular due to over-stressing of the window resulting from drilling. The photographs clearly show that the flow through the aperture causes expansion waves which accompany diffraction of the incident shock wave. Although the expansion-head wave is seen to remain perpendicular as it sweeps around the converging cylindrical shock front, the latter curiously appears to be largely unaffected until after it has traveled some distance away from the aperture. Then, a pair of secondary shocks and associated contact discontinuities suddenly appear as shown in photographs (b) to (e). In photograph (e), these are seen to stretch back to the aperture where they merge with the jet which is discharging through the aperture. Photographs (c) to (e) show that imploding shocks become quite distorted at small radii. This breakdown in shock front curvature[7] which is shown in photograph (f) is known to be responsible for the formation of a pair of clockwise and counter-clockwise rotating vortices observed behind the reflected exploding cylindrical shock in photographs (g) to (ℓ). It is noted that these binary vortices do not spread out with time but remain close to the centre of the cylindrical chamber.

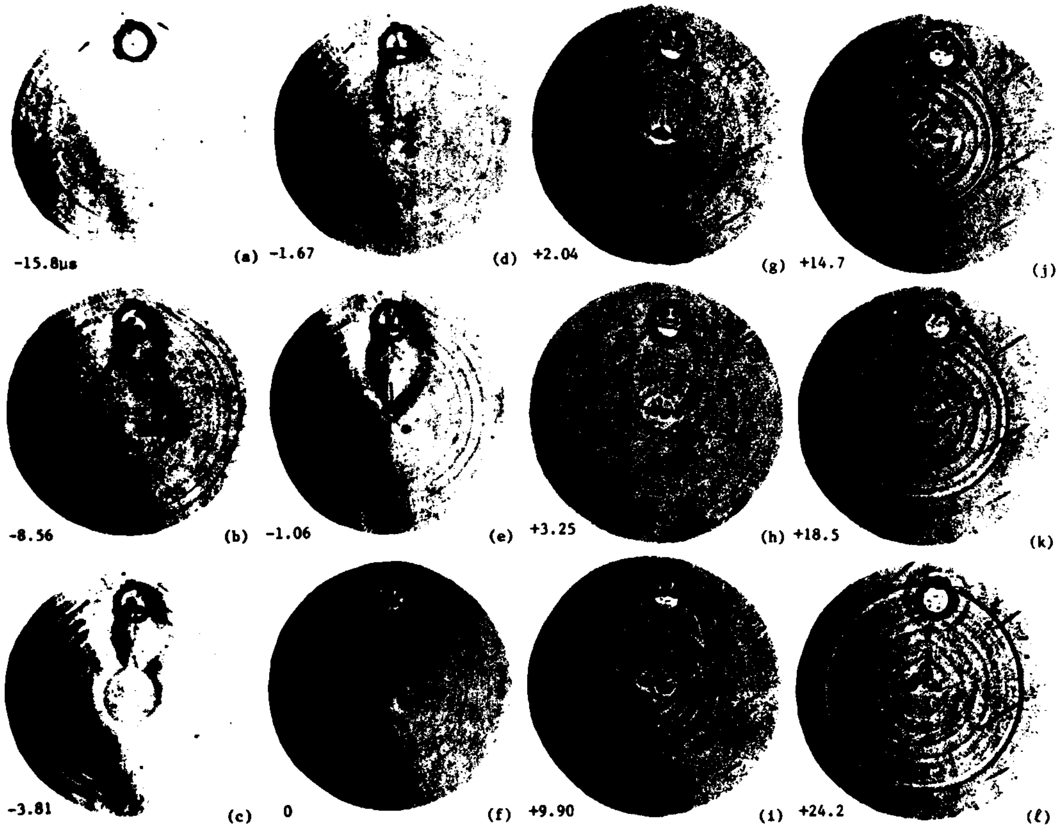

Figure 1. Schlieren photographs showing bleed effects. $M_O = 2.10$, $R_O = 2.45$cm, $h = 2.5$mm, $d = 6.4$mm, $h/d = 0.39$, & scale: viewing diameter = 6.9cm.

In general, the shock-aperture interaction is obviously complex, and a complete description should include the spreading of disturbances in the direction tangential to the collapsing shock front and normal to the walls. Analytically, however, these effects can be treated in an approximate manner. For h/d << 1, the transverse waves on the converging wave front experience repeated reflection between the chamber walls. Then, as the implosion process continues, these disturbances become more diffuse so that the shock strength may be regarded as essentially uniform across the chamber width. Therefore, if the converging shock is considered to be locally planar, the tangential propagation of disturbances can be treated by Whitham's theory[8]. Within this two dimensional assumption, the disturbances carried by the characteristics (kinematic waves) can propagate outside the circular boundary representing the aperture. It is postulated that all characteristics on the boundary are tangent to the boundary. Clearly, the characteristics form a simple wave so that the Mach number and ray angle are constant on each. With this information, the shock shape and Mach number distribution can be determined by interation. However, as the shock propagates away from the aperture, a transition from regular to Mach reflection occurs so that a triple point, or break, appears on the transmitted shock front. Then, the initial perturbation may be difined as $\xi_0 = \Delta/R_s$ where Δ is the transition distance[9] measured from the downstream edge of the aperture. For the experimentally observed conditions: $M_0 = 2.10$, $R_0 = 2.45$cm, d = 6.4mm and h = 0.5mm, the present theory gives $\xi_0 = 0.198$ calculated from $\Delta = 0.55$d and $R_s = R_0 - \Delta - d/2$, but the measurement from a schlieren photograph yields $\xi_0 = 0.164$. Thus, despite the rather approximate nature of analyses, the experimental value tends to be rather close to the theoretical one.

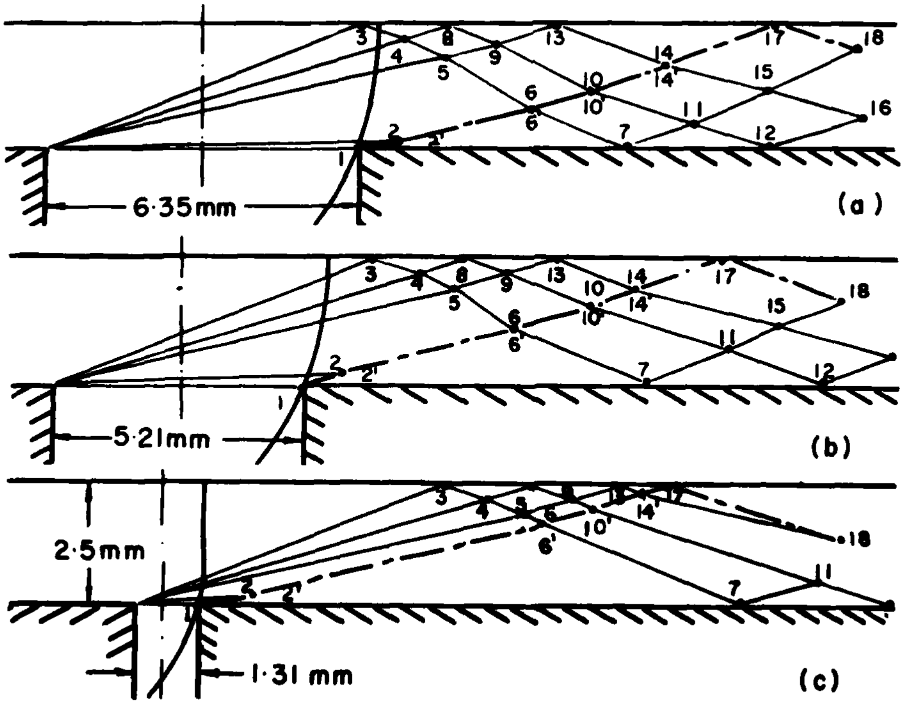

Figure 2. Sample of wave diagrams for shock-aperture interaction. $M_0 = 2.10$, h = 2.5mm & h/d = 0.39. ———— , shock wave; —— — —— , shock-shock; ———— , kinematic wave.

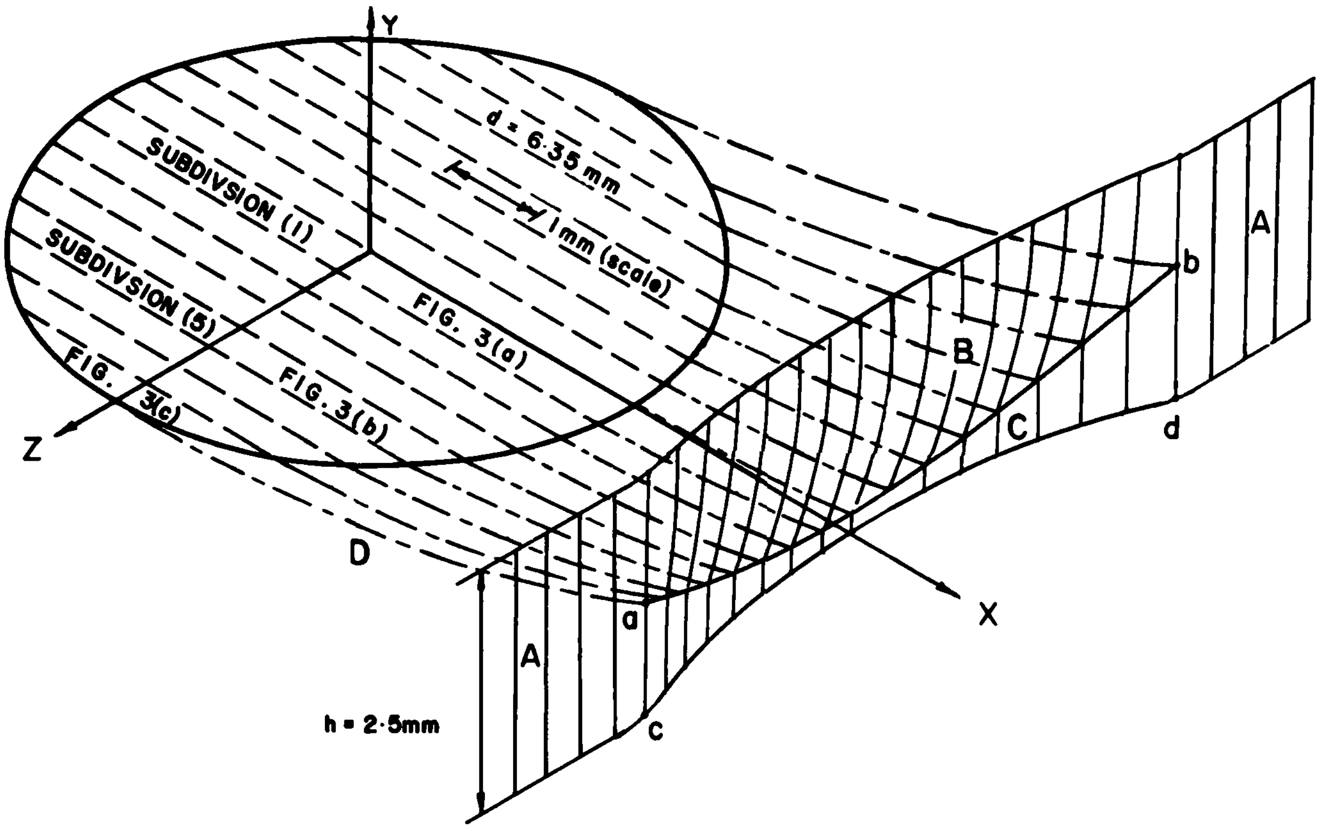

Figure 3. Isometric view of perturbed shock shape. A, initial shock of $M_0 = 2.10$; B, diffracted shock; C, Mach stem; D, shock-shock; a-b, line between B and C; c-d, curved shock on the wall.

Another feature of the shock-aperture interaction can be described by the ray-shock theory[8] in the following approximate fashion. This is accomplished by subdividing the aperture into 16 narrow slots and treating the flow as two-dimensional in each. The individual solutions may then be joined as a somewhat approximate estimate of the true shock shape. For example, the wave diagrams constructed for $M_0 = 2.10$ and $h/d = 0.39$ are shown in Figure 2. Here, for brevity, only the diagrams for the first, fifth, and eighth subdivisions are illustrated. Each is constructed for a unit chamber width and according to the techniques for plane shock-slot interactions[6]. Diffraction of the incident shock is descirbed by a family of simple kinematic waves centered at the upstream edge of each slot. In the inner subdivisiona, as in Fig. 2(a), a relatively large portion of the incident shock is affected, as compared with 2(c). It can be seen that at the downstream edge of each slot, the diffracted shock experiences Mach reflection, and the shock-shock[8] trajectory is shown as a dashed line on the diagrams. Downstream of the aperture, the transmitted shock front is then repeatedly traversed by shock and expansion waves which experience multiple reflections from the walls. Consequently, the shock front perturbation varies in a cyclic fashion with decreasing amplitude.

The synthesized shock shape downstream of the aperture as obtained from the wave diagrams is shown in an isometric view in Fig. 3. It is observed that the shock surface consists of three main parts: an un-disturbed region (A), a diffracted, curved portion (B), and a Mach stem portion (C). Line a-b separates the latter two portions and the dash-dotted lines represent a shock-shock surface (D). Line c-d on the lower chamber-wall represents a distorted concave shock whose curvature increases with distance traveled. This is so because the shock-shocks in the outer segments of the aperture have already suffered multiple reflections from the chamber walls so that the transmitted shock front is relatively planar there. Thus, the greatest shock front curvature occurs in the inner regions, and Fig. 3 demontrates that the bleed effect of the aperture on the converging shock can be illustrated by applying Whitham's ray-shock theory.

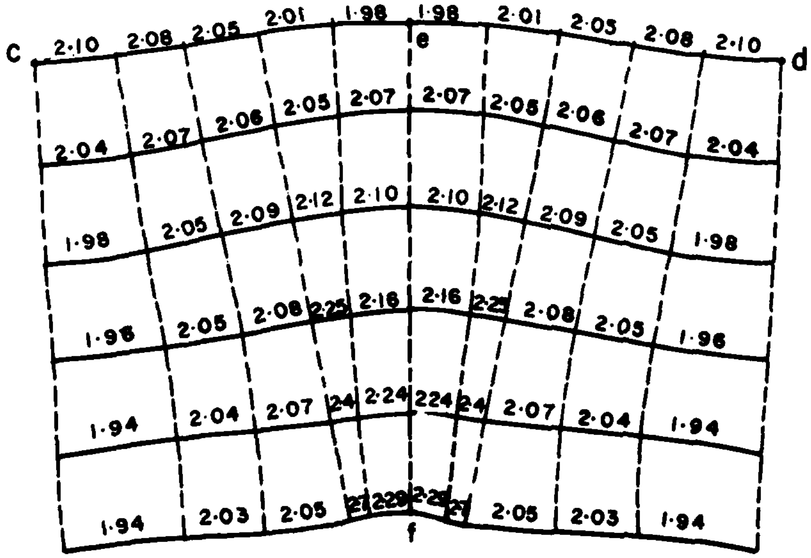

Figure 4. Propagation of curved shock. ———— , shock wave; — — — , ray; number, Mach number; scale: line e-f = 2.64mm.

As shown in Figure 3, line c-d is a distorted concave shock. While propagating downstream, the shock curvature increases with distance as illustrated in Figure 4 which is marked with local Mach numbers as calculated based on Whitham's theory[8]. It is known that through the shock focusing process[10], Mach reflection is eventually formed and a Mach stem is attached to the converging cylindrical shock. The experimental evidence can be clearly shown in the photographs of Figure 1.

By measuring the reference shock Mach number M_o at radius R_o, the theoretical shock Mach number at radius R_s can be calculated from[8]

$$f(M_s) = f(M_o) * (R_s/R_o) \tag{1}$$

$$f(M) = \mathrm{EXP}\ \{ - \int_1^M \lambda(M)\ [\ M / (M^2 - 1)\ ]\ dM \tag{2}$$

Plotting theoretical and experimental shock Mach numbers versus R_s/R_o where $M_o = 2.10$ at $R_o = 2.45$cm as noted before yields very close agreement as shown in Figure 5, excepting those close to the imploding center.

Although it is difficult to completely describe the shock-aperture interaction by existing theory, another important feature may be treated by analytic methods using the Mach-number-area rule[8], following a method originally developed to descirbe the propagation of disturbances on imploding detonation waves[11]. If θ is the angle swept by the expansion heads on the converging shock as shown in Figure 5, θ may be calculated for shock waves of moderate to strong strength by noting that the expansion head traverses the shock front at the local sound speed a_1. The shock Mach number M_s at radius R_s is V_s/a_o where a_o is the sound speed ahead of the collapsing shock. The swept angle θ can then be derived from

$$a_1 = R_s \frac{d\theta}{dt} = R_s \frac{dR_s}{dt} \frac{d\theta}{dR_s} = R_s M_s a_o \frac{d\theta}{dR_s} \tag{3}$$

$$d\theta = (a_1/a_o)\ (1/M_s)\ d(\ln R_s) \tag{4}$$

Applying Equations (1) and (2) for Equation (4) and then integrating

$$\theta = \int_{M_o}^{M_s} (a_1/a_o)\ [\ R_o/f(M_o)\ ]\ [\ \lambda(M)/(M^2 - 1)\ ]\ dM \tag{5}$$

$$a_1/a_o = [\ 2\gamma M^2 - (\gamma - 1)\ ]\ [\ (\gamma - 1)M^2 + 2\ ]\ /\ [\ (\gamma + 1)^2 M^2\ ] \tag{6}$$

$$\lambda(M) = \{\ 1 + [\ 2\ (1 - \mu^2)\ /\ (\gamma\mu + \mu)\ ]\ \}\ [1 + 2\mu + M^{-2}] \tag{7}$$

$$\mu^2 = [\ (\gamma - 1)\ M^2 + 2\ ]\ /\ [\ 2\gamma M^2 - (\gamma - 1)\ ] \tag{8}$$

Photographic measurements of the disturbed arc length (θR_s) are presented in Figure 5 which shows very reasonable agreement with Equation (5). It is noted that the stability of a converging cylindrical shock perturbed by a rod[7] has a large discrepancy between theoretical and experimental values of (θR_s). This is due to the fact that the rod-induced shocks do not traverse the converging shock front at the speed a_1 and they are not normal to the converging shock.

To indicate the converging shock stability, photographic measurements of the shock front perturbations (ε) due to the aperture bleed-effect at different shock radii (R_s) are presented in Figure 6 for the same reference M_o and R_o and for h/d varying from 0.08 to 0.39. First, it is seen that at a constant R_s/R_o, decreasing h/d leads to larger ε/R_s, owing to a different degree of initial disturbances. Secondly, for a fixed h/d, in the early stages of the imploding process, ε/R_s decreases as R_s/R_o decreases. This finding means that the converging shocks are stable at large shock radii. It is apparently due to the fact that the initial disturbances are dominated by expansion waves to enable the converging shock to stabilize somewhat as demonstrated by Figures 1(b) and 1(c) that the appearance of Mach reflection is delayed. Figure 6 shows that in this situation the shock perturbation is in proportion of $[(R_s/R_o) * * (0.6)]$ where R_s/R_o can be transformed in time (t) by the same derivation as Equation (14). Then the converging shock waves follow a one-half-power decay law which becomes the same as a planar wave[12]. Finally, however, as implosion proceeds, ε is observed to increase at smaller shock radius and to rise steeply as R_s/R_o approaches zero, indicating that the collapsing shock eventually becomes unstable to the disturbances. For R_s/R_o approximately less than 0.5, the experimental results for h/d = 0.39 can be expressed as

$$\varepsilon/R_s = 0.072\ (R_s/R_o) * * (-0.6) \tag{9}$$

Equation (9) gives that the shock radius has to be less than half that of the aperture, and the value (0.072) is only applied for h/d = 0.39 but the power factor (-0.6) is the same for those h/d as employed.

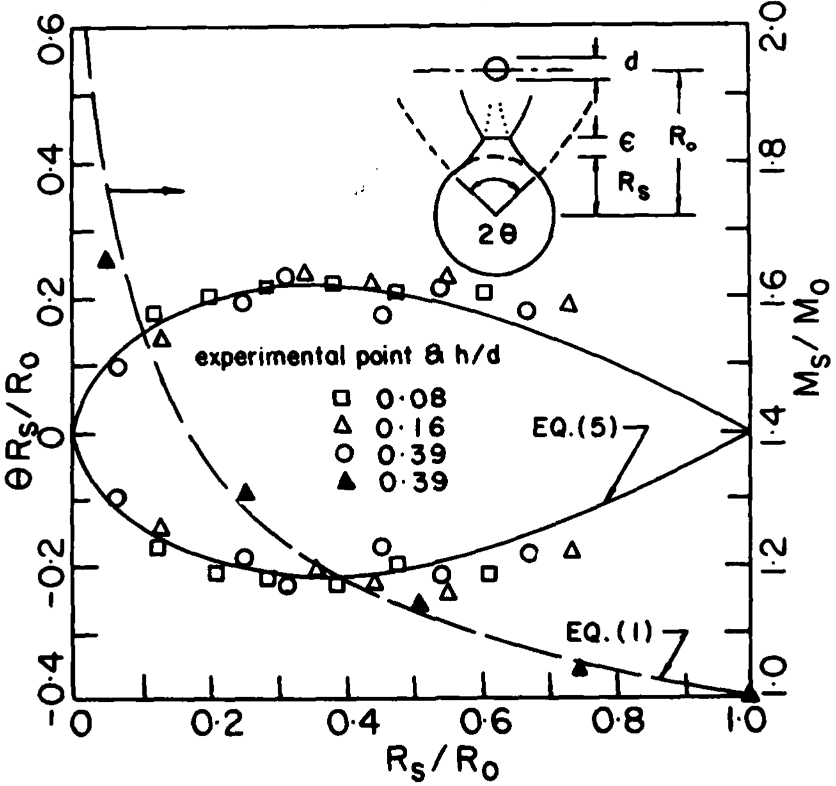

Figure 5. Shock Mach number and perturbed arc length vs. shock radius.

Butler[13] showed that for the converging cylindrical shock waves the perterturbations ε/R_S are a function of shock radius R_S/R_O

$$\varepsilon/R_S = (\text{experimental constant}) * (R_S/R_O) ** (-0.5987) \quad (10)$$

Comparing Eq. (9) to (10) yields that the experimental constant is 0.072 for h/d = 0.39, and the respective shock amplification rates are in good agreement. Since the motion of converging cylindrical shocks for $\gamma = 1.4$ can be written[14]

$$R_S = \text{constant} * (-t) ** (0.8352) \quad (11)$$

differentiating Equation (11) and satisfying the reference conditions yield

$$V_S = 0.8352\ R_S/(-t) \quad (12)$$

$$(-t_O) = 0.8352\ R_O/(a_O M_O) \quad (13)$$

$$(R_S/R_O) = [\ a_O\ M_O\ (-t)\ /\ (0.8352\ R_O)\ ] ** (0.8352) \quad (14)$$

Combining Eqs. (10) and (14) and having $M_O = 2.10$, $R_O = 2.45\text{cm}$, $a_O = 333.4$ m/s and experimental constant = 0.072, one obtains

$$\varepsilon/R_S = 389 * 10^{-6} * (-t) ** (-1/2) \quad (15)$$

Equation (15) demonstrates that Butler's one-half-power shock amplification law for converging cylindrical shock is true in the region close to the collapsing center for the present investigation.

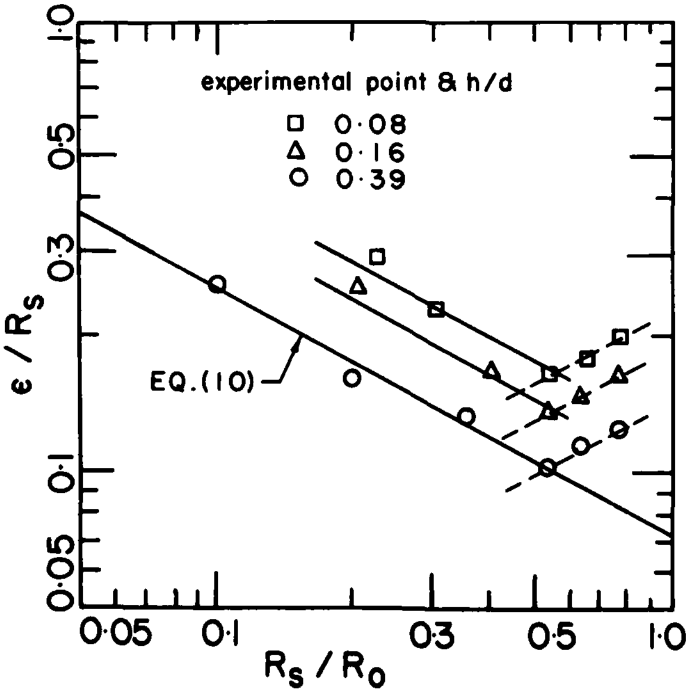

Figure 6. Perturbation of the collapsing shock front.

CONCLUSIONS

It is concluded that simple theoretical models based on Whitham's ray-shock theory has been successfully employed to approximate some features of the interference of a converging cylindrical shock with a small, circular bleed-aperture. Diffraction of the incident wave within the aperture and tangential spreading of the accompanying expansion wave are found to be responsible for a relatively large initial shock front perturbation. Experiments have shown that the size of the perturbation with respect to the shock radius first decreases but then begins to rapidly increases at a radius about half that at which the disturbance is introduced. Thus, although instability is ultimately observed, it appears that this type of disturbance is more tolerable at large radius than that produced by solid obstables such as a circular rod. In addition, for the present case, the perturbed arc lengths are observed to be in good agreement with those predicted by Whitham's theory since the disturbance tends to be more diffuse owing to its expansive character. At smaller radii, the measured perturbations are found to obey Butler's square root amplification law for cylindrical converging shock waves.

ACKNOWLEGEMENT

This work was supported by the National Research Council of Canada, under Grant number A-1255 (Wu), A-4206 (Neemeh) and General Research Board of the University of Maryland (Ostrowski), and assisted by N. Elabdin, O. Mueling and J. Kelly. One of the authors (Wu, during his sabbatical leave at Caltech) wishes to express his gratitude to Prof. B. Sturtevant for his consideration and generosity.

REFERENCES

1. Clark, J.S., Fisher, H.N. & Manson, R.J., Laser Driven Implosion DT Targets to Thermonuclear Burn Conditions, Physics Review Letter, Vol. 30, 1973.
2. Glass, I.I. and Sharma, S.P., Production of Diamonds from Graphite Using Explosion-Driven Implosion, AIAA Journal, Vol. 14, 1976.
3. Wu, J.H.T., Ostrowski, P.P., Neemeh, R.A. and Lee, P.H.W., Experimental Study of a Cylindrical Resonator, AIAA Journal, Vol. 12, 1974.
4. Donato, M., Bergeron, M. & Lee, J.H.S., Use of Detonation for surface Coating, Proceedings of Eleventh International Symposium of Shock Tubes & Waves, 1977.
5. Perry, R.W. and Kantrowitz, A., The Production and Stability of Converging Shock Waves, Journal of Applied Physics, Vol. 22, 1951.
6. Lee, J.H.S., Ostrowski, P.P. and Wu, J.H.T., Shock Attenuation by a Single Transverse Slit, JFM, Vol. 76, 1976.
7. Wu, J.H.T., Neemeh, R.A., Ostrowski, P.P. and Elabdin, M.N., Production of Converging Cylindrical Shock Wave by Finite Element Conical Contractions, Proceedings of 11th International Symposium of Shock Tubes and Waves, 1977.
8. Whitham, G.B., A New Approach to Problems of Shock Dynamics, Part 1, Two-Dimensional Problems, JFM, Vol. 2, 1957.
9. Smith, L.G., Photographic Investigation of the Reflection of Plane Shocks in Air, Office of Sciences for Research & Development Report No. 6271,1945.
10. Sturtevant, B. and Kulkarny, V.A., The focusing of Weak Shock Waves, JFM. Vol. 73, 1976.
11. Knystautas, R. & Lee, J.H.S., Experiments on the Stability of Converging Cylindrical Detonations, Combustion & Flame, Vol. 16, 1971.
12. Moorhem, W.K.V. & George, A.R., On the Stability of Plane Shocks, JFM, Vol. 69, 1975.
13. Butler, D.S., The Stability of Converging Spherical & Cylindrical Shock Waves, Armament Research & Development Establishment, Report B18/56, 1956.
14. Butler, D.S., Converging Spherical & Cylindrical Shock, Armament Research & Development Establishment, Report 54/54, 1954.

ON THE DIFFRACTION OF WEAK BLAST WAVES OVER CONCAVE CORNERS

L. F. HENDERSON and A. SIEGENTHALER

Department of Mechanical Engineering
The University of Sydney, N.S.W., 2006, Australia

Shock tube experiments were done with weak shocks $\xi_i > 0.433$ diffracting over single concave corners, the inverse shock strengths were $\xi_i = 0.905 \pm 0.005$, $\xi_i = 0.83 \pm 0.01$, and $\xi_i = 0.49 \pm 0.01$. It is shown that for weak shocks the corner signal always catches up with a Mach reflexion MR so the MR is always partly attenuated. The well known von Neumann three shock theory fails for weak MR because it does not take the attenuation into account. Experiment suggests that the true transition condition between regular RR and Mach reflexion MR is where the Mach stem is a normal shock. This is consistent with what Henderson and Lozzi found for strong diffraction.

INTRODUCTION

The classic theory of regular RR and Mach reflexion MR is due to von Neumann (1943). He defined the incident shock to be *weak* or *strong* by means of a polynomial equation of eighth degree - the variable was the Mach number downstream of *i*. If $\xi_i \equiv P_o/P_1$ is the inverse strength of *i*, where P is the pressure and the subscripts o,1 refer to conditions upstream and downstream of *i* then for air the boundary between the weak and the strong types is at $\xi_i = 0.433$. Hence *i* is weak when $\xi_i > 0.433$ and strong when $\xi_i < 0.433$. Kawamura and Saito (1956) gave essentially the same classification more conveniently in terms of the polar diagram, figure 1.

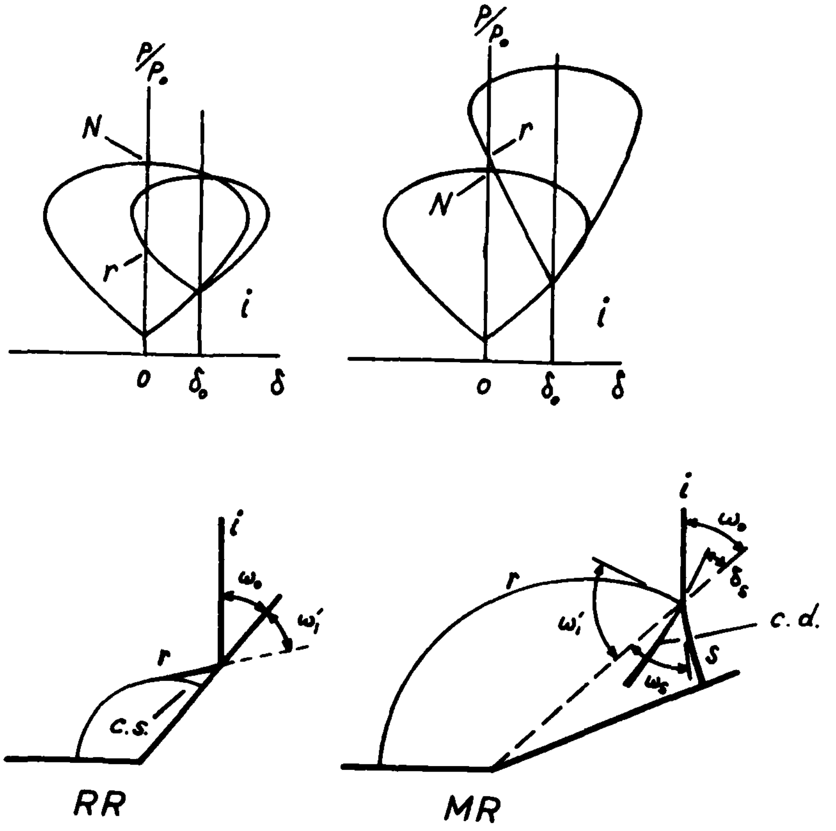

Figure 1. Nomenclature for diffracting blast waves. i, incident shock; r, reflected shock; s, Mach shock; c.s., corner signal; cd, contact discontinuity; ω_0, angle of incidence; ω_i', measured angle of reflexion; ω_s, wave angle of Mach shock; δ_s, streamline deflexion through Mach stock; δ, streamline deflexion; P, pressure.

It has been known since the pioneering experiments of Smith (1945) and the discussion by Bleakney and Taub (1949) that the von Neumann theory of weak MR is an apparent failure. This was a surprising result because the same theory was found to succeed brilliantly for strong MR, except occasionally near transition to RR, denoted here by RR $\rightleftharpoons$ MR, or when there were significant variations in the specific heats. For RR, the theory succeeded for both weak and strong i except for the conditions just mentioned. These conclusions were substantially confirmed by Kawamura and Saito and by Henderson and Lozzi (1975).

The data is usually presented as a plot of the measured angle of reflexion ω_i' of the reflected shock r against the angle of incidence ω_0 of i, figure 1, with ξ_i held constant, but Henderson and Lozzi gave their data for constant free stream Mach number M_0 upstream of i. One finds that for given ω_0 that ω_i' is sensitive to variations in ξ_i and the 1945 and 1956 data is open to the criticism that no information was published on the variation of ξ_i from its nominal values, namely $\xi_i = 0.9$, 0.8 and 0.5.† Furthermore when the $\xi_i = 0.8$ data of Smith is compared with that of Kawamura and Saito there is some discrepancy between them.

In this paper data is presented with a prescribed tolerance on the variation of ξ_i. Then the conditions for the corner signal to catch up with i are examined and it is found that this occurs *before* transition to MR. It is also found that even the von Neumann theory of RR becomes increasingly inadequate as transition is approached. Some of the experimental data suggests that at transition the Mach stem s is very nearly a normal shock, this is consistent with what Henderson and Lozzi found for a variety of strong shock transitions - but not for all. Finally although the von Neumann theory of weak MR has so far failed to agree with experiment, we demonstrate that in principle it can be reconstructed to agree with some of the data presented here. In all of this work there is no evidence of imperfect gas effects having any significant effect on the results.

EXPERIMENTS

The experiments were done in a conventional shock tube by diffracting weak plane shock waves in air over single concave corners, figure 1. Two methods were used to obtain ξ_i; firstly with a Kistler 603B transducer which measures (P_1-P_0) from which $\xi_i = \left[1 + \dfrac{P_1-P_0}{P_0}\right]^{-1}$, and secondly with three Atlantic Research Corp. LC71 transducers which were spaced a known distance along the tube. From then we obtained two measurements of the shock speed and by measuring the undisturbed gas temperature we could calculate the shock Mach number M_i and hence two values of ξ_i. These were combined with the Kistler value to obtain a mean ξ_i. Typically the variations between the three values were less that ±1%. The diffracting shocks were photographed with the aid of a Zeiss schlieren system with off-axis parabolic mirrors accurate to about 1/12 wavelength, and 20 cm aperture, the camera lenses were Haseblad. The wave angles were measured by enlarging the photographs by a factor of about 10 on a Nikon profile projector which could measure to about 1 min. of arc, but the resolution of our photographs seldom allowed this accuracy. In the RR range the experimental errors were estimated to be ±0.2° for both ω_0 and ω_1', while in the MR range we estimated ±0.2 for ω_0, ±1.5° for ω_1', and ±2.0° for ω_s.

RESULTS AND DISCUSSION

Our data for $\xi_i = 0.9$, 0.8, and 0.5 are presented in figures 2, 3, and 4 respectively, and it will be seen that there are prescribed limits on the variation of ξ_i, these are a maximum of about ±2% from the nominal value. In the RR range all the figures show that the von Neumann perfect gas theory agrees very closely with the data provided that ω_0 is not too close to the extreme angle $\omega_0 = \omega_e$ beyond which there are no real solutions for RR. For these circumstances it is concluded that the theory is correct and that there are no significant imperfect gas effects due to viscosity or variation of the specific heats. However as $\omega_0 \to \omega_e$ some discrepancy does develop, especially for the $\xi_i = 0.9$ data, but the range of ω_0 for which the discrepancy is evident becomes smaller as ξ_i approaches the strong shock boundary, thus compare figure 4 with 2. In all the figures the data displays the well known persistence of RR into the MR range, that is RR still exists for some $\omega_0 > \omega_e$. The measured angle at transition RR $\rightleftharpoons$ MR is denoted by $\omega_0 = \omega_t$. For $\omega_0 > \omega_e$ the von Neumann

---

† Henderson and Lozzi gave the variation in their data in terms of $\pm\Delta M_0$.

theory of MR apparently either fails completely as for $\xi_i = 0.9$ and 0.8, or is inaccurate as for $\xi_i = 0.5$. Our $\xi_i = 0.8$ data disagrees in some places with the earlier data, but we found best agreement with Kawamura and Saito. The Smith data disagrees significantly both with our data and that of Kawamura and Saito for $\omega_0 \approx 60°$.

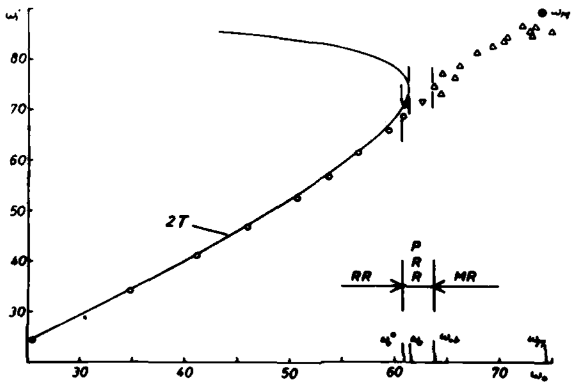

Figure 2. Comparison of experimental data with the von Neumann two-shock theory 2T for $\xi_i = 0{\cdot}905 \pm 0{\cdot}050$. ○, RR data; ▽, PRR data; △,MR data; —, 2T theory; ⊗, ω_M point, i.e. (ω_M, ω_{iM}') point.

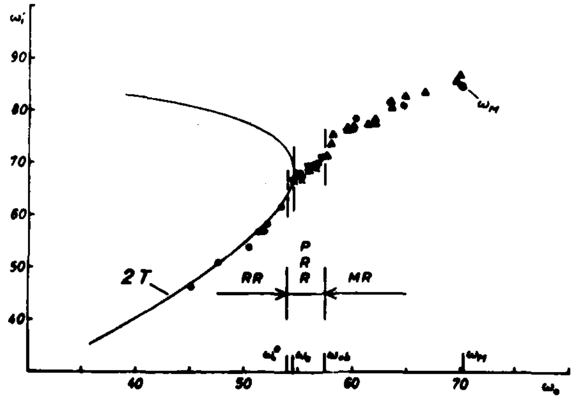

Figure 3. Comparison of experimental data with the von Neumann two-shock theory 2T, for $\xi_i = 0.83 \pm 0.01$. ○, RR data; ▽, PRR data; △,MR data; ●, theoretical point in the MR range, calculated from the measurements of $(\gamma,\ \xi_i,\ \omega_0\ \beta_1)$, note that two of the points coincide; X, theoretical point in the PRR range calculated from the measurements of $(\gamma, \xi_i, \omega_0, \beta_1)$, with the assumption that $\beta_1 = \omega_i'$.

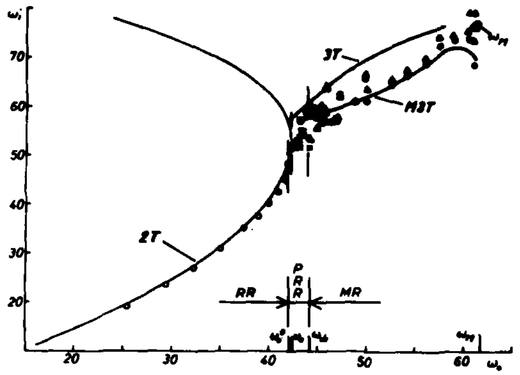

Figure 4. Comparison of experimental data with the von Neumann two-shock 2T, and three-shock 3T theory, and with the modified M3T theory for $\xi_i = 0.49 \pm 0.01$. The following symbols are the same as for the caption in Figure 3, ○, ▽, △, ●, X.

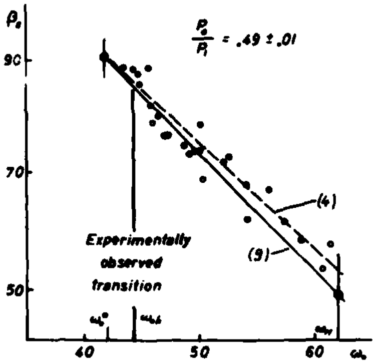

Figure 5. Wave angle of the Mach shock β_s versus angle of incidence ω_0 for a weak diffracting blast wave, $\xi_i = 0.49 \pm 0.01$. $\beta_s = \omega_s - \delta_s$; ——, linear regression line obtained from three shock theory; ----, linear regression line through experimental data. Estimated experimental error for β_s is ±3.2°.

With the help of the Nikon Projector we measured the so-called catch-up condition at which the corner signal first reached the foot of i. As far as we could determine this occurred close to the sonic point $\omega_0 = \omega_0^*$ of the RR theory, that is where the Mach number of the flow downstream of r is sonic $M_2 = 1$. This means that catch-up takes place *before* transition $\omega_0^* < \omega_t$, and it follows that weak Mach reflexion is always compounded with the corner signal expansion wave. As a consequence both the reflected r, and Mach s shocks are partly attenuated.

A STEP TOWARDS THE RECONSTRUCTION OF THE VON NEUMANN THEORY FOR WEAK MACH REFLEXION

Here we attempt to reconstruct the theory so that it will fit the data in the MR range. In our experiments it was always possible to measure ξ_i, ω_0, and

ω_1', and sometimes for MR we could in addition measure for wave angle ω_s and the streamline deflexion angle δ_s of the Mach stem, figure 1. Actually it was more convenient to measure the equivalent set ξ_i, ω_0, ω_1', β_1, and β_s, where β_1, β_s are the angles between r and the contact discontinuity cd, and between s and cd. Any four of these quantities are sufficient to define a three shock confluence completely, given only that the shocks must satisfy the shock wave equations and the well known compatibility equations, namely

$$\delta_0 + \delta_1 = \delta_s \quad , \qquad \text{I}$$

$$\xi_i \;\; \xi_r = \xi_s \quad , \qquad \text{II}$$

where $\delta_{0,1,s}$, are the streamline deflexions across i, r and s, respectively. We took a set of the four quantities ξ_i, ω_0, ω_1', and β_1 whose numerical values we had measured and substituted them into the shock wave and compatibility equations and calculated a value of β_s, which could then be compared to the experimental value of β_s. The quantity β_s was singled out for this purpose because the experimental error was larger for it than any of the other quantities. The equations are too lengthy to be given here, but the results for $\xi_i = 0.5$ are shown in figure 5. The linear regression line for the experimental data is,

$$\underset{\text{experimental}}{\beta_s} = 170 - 1.92\omega_0 \quad , \qquad \text{III}$$

with a coefficient of determination of 0.93, while for the calculated values we obtained,

$$\underset{\text{calculated}}{\beta_s} = 181 - 2.18\omega_0 \quad , \qquad \text{IV}$$

with a coefficient also of 0.93. The maximum discrepancy between theory and experiment occurs at $\omega_0 \simeq 60°$, and is about 3.5° which is about our estimated error. It seems therefore that it is possible to construct a three shock confluence which satisfies the shock wave and compatibility equations for weak Mach reflexions. However the method used here is not yet sufficient to enable the solution to be obtained from a convenient set of assumptions. This will require further study to obtain a better understanding of the wave geometry.

It is interesting to notice that in figure 5, $\beta_s \rightarrow 90°$ as ω_0 approaches the transition condition from the MR side, MR→RR. It is tempting to conclude that the Mach stem becomes normal to the flow at transition, and furthermore we find that when $\beta_s = 90°$ then $\omega_0 = 42.0°$ which is the corner signal catch-up point! *Hence for* $\xi_i = 0.5$ *the normal shock point coincides with the sonic point* $\omega_0 = \omega_0^* = 42.0°$. It is tempting to conclude that this is the true transition condition, and if so it would mean that the Mach stem although of zero length would be normal to the flow, and in addition there would be sonic speed of the gas $M_2 = 1$ downstream of the reflected shock. The normal shock condition would be consistent with what Henderson and Lozzi found for many, but not all strong shock transitions. However $\xi_i = 0.5$ is close to the strong shock limit $\xi = 0.433$ and this may be the dominant effect. Unfortunately the von Neumann theory provides no solution for MR when $\xi_i = 0.8$ or 0.9, and it is difficult to measure β_s because the contact discontinuity is often faint or invisible. Therefore we have no evidence of the effect for these values of ξ_i.

CONCLUSIONS

(i) The discrepancy between the data of previous researchers appears to be due to variation in ξ_i.

(ii) The catch-up condition takes place near the sonic point of regular reflexion, that is where the flow downstream of the reflected shock moves at the speed of sound. This means that catch-up always occurs *before* the onset of transition and therefore that weak Mach reflexion is always partly attenuated by the corner signal.

(iii) It is possible to construct a three shock wave confluence for weak Mach reflexion which satisfies the shock wave and compatibility equations and which agrees with the data presented here within the limits of experimental error.

(iv) If the regression line through the β_s data for $\xi_i = 0.5$ is extrapolated to $\beta_s = 90°$ then $\omega_0 = 42.0°$ which is the catch-up condition (sonic) of the corner signal. Simultaneously the flow downstream of the reflected shock is sonic, and the Mach stem (if it exists) will be of zero length and normal to the flow. It is not known if this circumstance is valid for other values of ξ_i in the weak shock range.

REFERENCES

1. W. Bleakney and A.H. Taub, Rev. Mod. Phys. 21, 584 (1949).
2. L.F. Henderson and A. Lozzi, J. Fluid Mech. 68, 139 (1975).
3. R. Kawamura and H. Saito, J. Phys. Soc. of Japan 11, 584 (1956).
4. J. von Neumann, Collected Works, Vol. 6, Pergamon (1963).
5. L.G. Smith, Photographic investigations of the reflection of plane shocks in air, O.S.R.D. Rep. 6271 (1945).

ACKNOWLEDGEMENT

This work is supported by the Australian Research Grants Committee.

STABILITY OF NON-UNIFORM SHOCK WAVES

E. MARMOR, Y. KIVITY and A. BETSER

Department of Aeronautical Engineering
Technion, Haifa, Israel

The stability of plane shock waves, moving in ideal gases and having non-constant velocity, is studied using numerical methods. The shock waves are generated by: (a) moving a corrugated piston into the fluid, and (b) prescribing the boundary pressure pulse on the corrugated fluid surface. A small perturbation solution is obtained assuming that the amplitude of corrugations is small compared to their wavelength. Linearization of the two-dimensional flow equations about the one-dimensional, non-uniform wave solution yields a set of partial differential equations with variable coefficients. Using Fourier series expansion of the perturbations with respect to the lateral coordinate, the perturbation equations are reduced to a set of one-dimensional hyperbolic equations. Numerical integration by the method of characteristics is employed for both the perturbation equations and the basic one-dimensional equations. Results of calculations show that the shock front is stable for both the piston-driven and the pressure-driven shocks. For the case of an applied pressure, however, the fluid surface is found to be unstable, and its corrugations acquire a constant rate of growth, asymptotically.

INTRODUCTION

The inherent stability of plane shock waves forms the basis for shock tube operation. The actual bursting of a diaphragm is far from being simultaneous, and consequently the shock wave is initially non-planar. Due to the stability of the shock, however, deviations from planarity are smoothed our rapidly, and the shock front becomes planar after travelling a short distance.

Freeman[1] was the first to analyze the stability of a plane shock wave, formed by moving a corrugated piston into an ideal gas. He obtained an analytic expression for the behavior of shock front perturbations, and showed that the perturbations decay asymptotically like $t^{-3/2}$. Richtmyer[2] found a similar behavior for the transmitted and reflected shock waves generated when a plane incident shock wave crosses a corrugated interface between two ideal gases.

In the present work, we are interested in studying two effects which were not considered by previous investigators: (1) the effect of shock acceleration on its stability, and (2) the effect of various boundary conditions on the shock front behavior. Two types of boundary conditions are studied in this work: (a) a corrugated piston and (b) a pressure pulse applied at the fluid surface.

The shock waves generated in this manner have non-uniform velocity; the acceleration or deceleration level of the shock may be controlled by the rate of change of the piston velocity or the boundary pressure.

EQUATIONS OF FLOW

The equations governing two-dimensional unsteady flow of an inviscid incompressible fluid are:

$$\begin{aligned} &\rho_t + (\rho u)_x + (\rho v)_y = 0 \\ &u_t + uu_x + vu_y + p_x/\rho = 0 \\ &v_t + uv_x + vv_y + p_y/\rho = 0 \qquad (1) \\ &s_t + us_x + vs_y = 0 \\ &p = f(\rho,s) \end{aligned}$$

Here t denotes the time, (x,y) are Cartesian coordinates, (u,v) are the velocity components in (x,y)-directions, p, ρ and s are the pressure, density and specific entropy, respectively. The last relation is the equation of state of the fluid. The x-axis is assumed to be alligned with the basic one-dimensional flow.

Considering two-dimensional perturbations, we let any flow variable q be represented as:

$$q(x,y,t) = q^1(x,t) + \tilde{q}(x,y,t)$$

Assuming that the perturbations are small, the flow equations are linearized, yielding a set of partial differential equations for $\tilde{q}$. The variable coefficients in the linearized equations are functions of the one-dimensional flow, i.e., are functions of (x,t) only. This allows the following Fourier expansion:

$$\tilde{q}(x,y,t) = \sum \bar{q}_i\,(x,t)\,\cos(k_i y + \varphi_i)$$

The Fourier coefficients $\bar{q}_i$ are governed by the following first-order, linear partial differential equations:

$$\begin{aligned} &\bar{\rho}_t + u^1\bar{\rho}_x + \rho^1\bar{u}_x + \rho^1_x\bar{u} + u^1_x\bar{\rho} - \rho^1 k^2\,\bar{v} = 0 \\ &\bar{u}_t + u^1\bar{u}_x + u^1_x\bar{u} + \bar{p}_x/\rho^1 - p^1_x/(\rho^1)^2\bar{\rho} = 0 \\ &\bar{v}_t + u^1\bar{v}_x + \bar{p}/\rho^1 = 0 \\ &\bar{s}_t + u^1\bar{s}_x + s^1_x\bar{u} = 0 \\ &\bar{p} = f_\rho(\rho^1,s^1)\bar{\rho} + f_s(\rho^1,s^1)\bar{s} \end{aligned}$$

The process of linearization and Fourier expansion is applied also to the boundary conditions on the fluid perturbed surface and the perturbed shock front, yielding the necessary boundary conditions for the $\bar{q}$ variables.

NUMERICAL SOLUTION

The two sets of equations for the $q^1(x,t)$ and the $\bar{q}(x,t)$ variables are integrated numerically using the method of characteristics. The following features of the numerical solution are worth mentioning:

(1) Continuous rezoning of the mesh. At every time-step the zone between the shock front and the fluid surface is divided into equally spaced net

points, thus avoiding irregular mesh segments with small segments near the boundaries.

(2) Monitoring of the total energy coservation in the numerical solution, for both the one-dimensional and the perturbation flow. This helps to trace errors or inaccuracies due to inappropriate time-steps.

(3) Use of integration time-steps larger than those imposed by the Courant-Friedrichs-Lewy condition (Kot[3]). This procedure requires additional interpolations, but reduces the total computing time considerably.

RESULTS AND DISCUSSION

Calculations were carried out for two types of boundary conditions on the fluid surface: (a) a piston moving into the fluid with a prescribed velocity time history and (b) a pressure pulse applied at the fluid surface. In each case the time variation of the prescribed function was given by an exponential decay or growth:

$$F(t) = F_0(M)\ e^{-\beta t}$$

where F is the piston velocity (for case (a)) or the pressure difference at the surface (for case (b)), M is the initial shock Mach number, and β is an acceleration or deceleration parameter.

For simplicity in presenting the results, non-dimensional quantities are used. As the unit of length we choose the perturbations wavelength $1/k$, and as a unit of time $1/c_0 k$, c_0 being the speed of sound in the quiescent region ahead of the shock.

Before proceeding to summarize the results of calculations, a definition of shock stability is necessary. We have adopted Freeman's definition, namely: a shock of Mach number M_1, is defined to be less stable than a shock of Mach number M_2 if the amplitude of perturbations A_1 is greater than the amplitude A_2 after the shocks have traversed the same distance. (In this comparison the sinusoidal variation is disregarded).

The results of calculations are shown in Figs. 1-7 for a variety of initial Mach numbers M and acceleration parameters β. Fig. 1 shows a piston-driven shock with $\beta = 0$, i.e., a uniform velocity piston. This is actually the case treated by Freeman. Detailed comparison between the present numerical solution and the analytical solution of Freeman (evaluated using a digital computer) showed agreement to at least four significant figures, thus validating the computer program developed in this work. (The differences between the numerical and analytical solution cannot be resolved on the scale of Fig. 1).

Effect of Deceleration

Before proceeding to the discussion of results, one basic conclusion regarding the relative stability of uniform shocks must be stressed, namely: for uniform shocks, stability decreases with Mach number (for M above a critical value of about 1.1). This behavior is depicted in Fig. 1.

The effect of deceleration on the shock stability is shown in Fig. 2 for moderate decelerations, and in Fig. 3 for strong decelerations. It can be concluded from these results that a decelerating shock wave is more stable than a uniform one. However, the enhanced stability of the decelerating shock could be explained also by the fact that after some deceleration, the shock becomes slower, and therefore more stable. To clarify this point, we refer to Fig. 4, where the amplitude of shock perturbation for three combinations of initial Mach number M and deceleration β, is plotted vs. the local (instantaneous) Mach number, M_l. It is clear from this plot that the stability of the different shocks is determined mainly by the local conditions of the flow, and much less

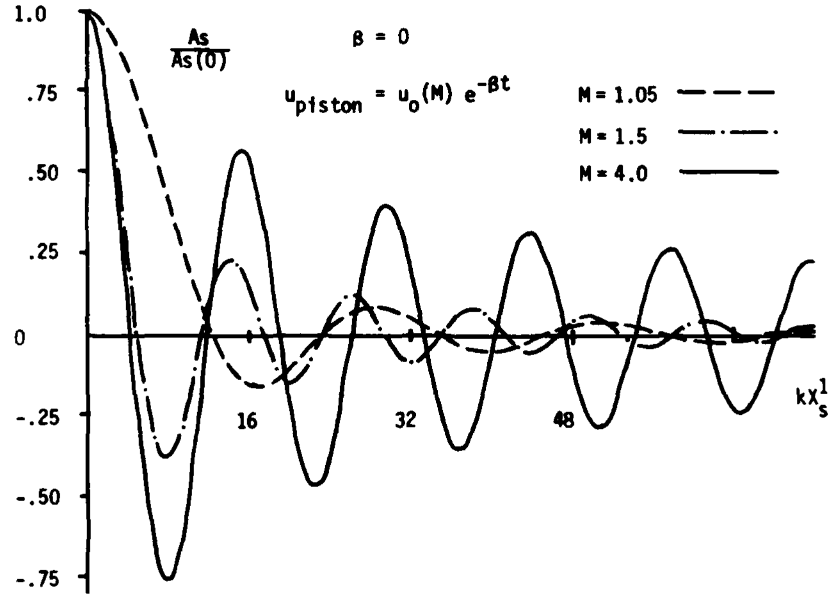

Fig. 1. Amplitude of Shock Front Perturbation vs. Distance Uniform Piston Velocity.

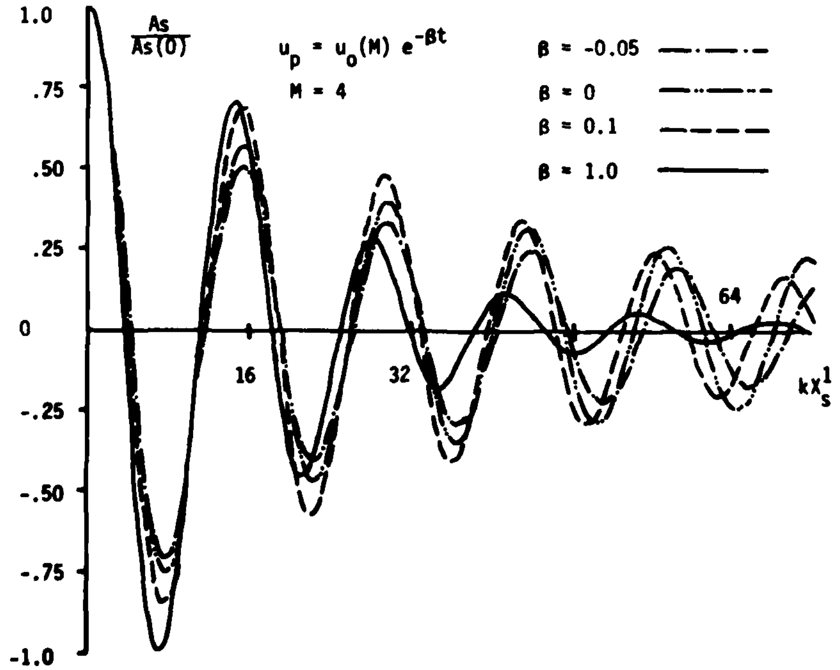

Fig. 2. Amplitude of Shock Front Perturbation vs. Distance for $M = 4$ and Various Decelerations.

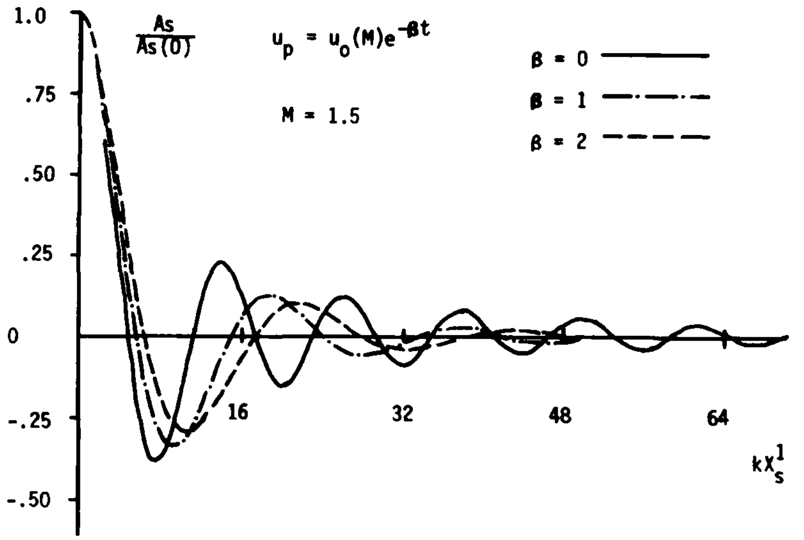

Fig. 3. Amplitude of Shock Front Perturbation vs. Distance, for *M* = 1.5 and Various Decelerations.

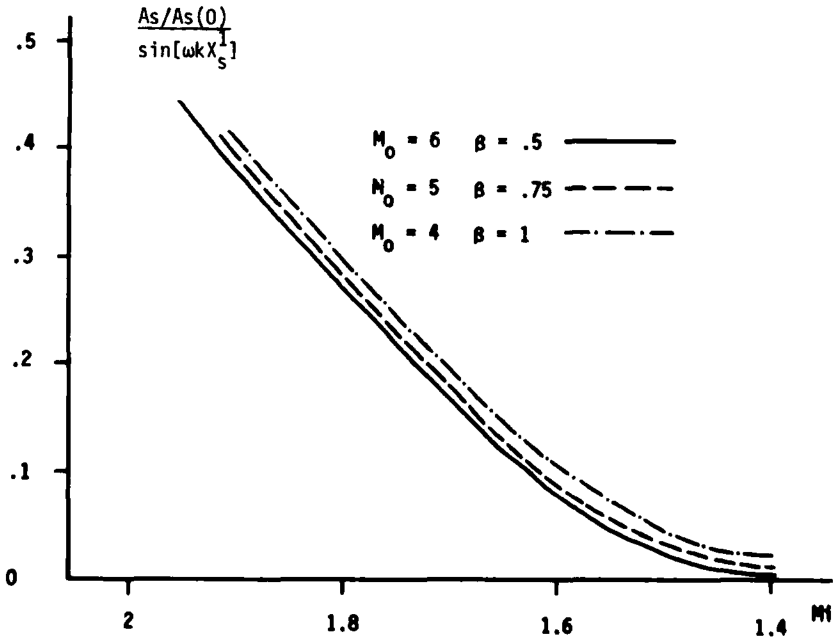

Fig. 4. Rate of Decay of the Shock Front Perturbation as Function of Instantaneous Mach Number.

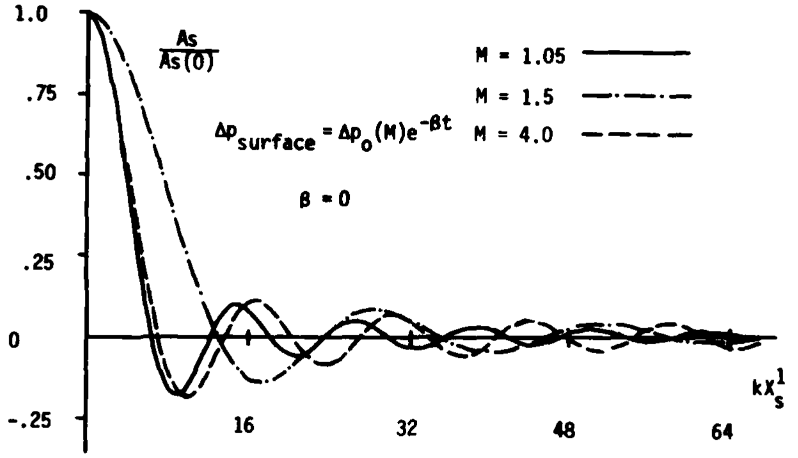

Fig. 5. Amplitude of Shock Front Perturbation vs. Distance for a Step Pressure Pulse Applied at the Surface.

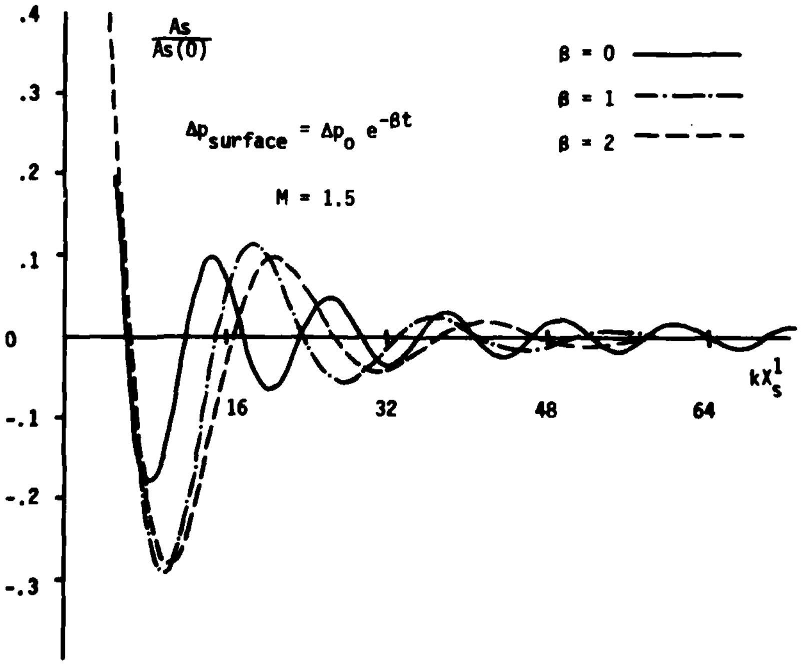

Fig. 6. Amplitude of Shock Front Perturbation vs. Distance for an Applied Pressure Pulse with $M = 1.5$ and Various Decelerations.

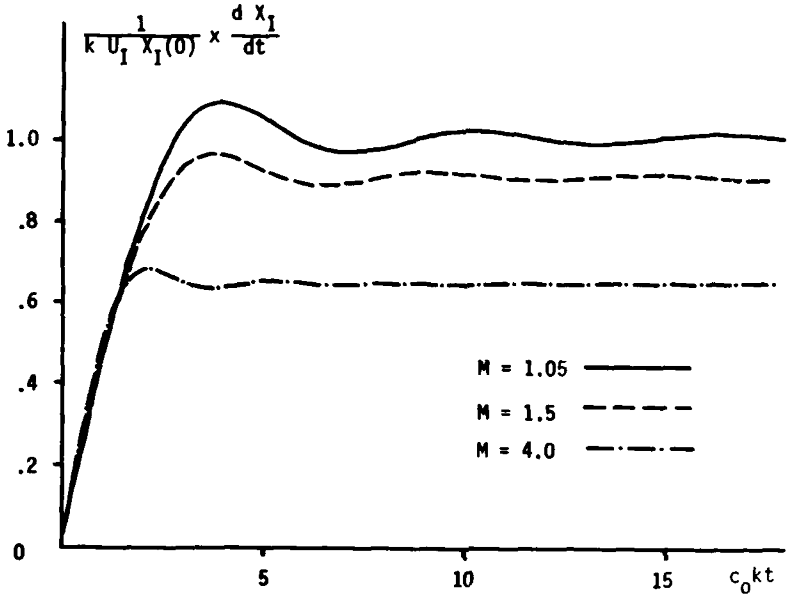

Fig. 7. Rate of Growth of Surface Perturbation vs. Time. Step Pressure Applied at the Surface.

by the initial conditions. Consequently, we may conclude that the effect of deceleration is itself small. It affects the shock stability indirectly by lowering its speed.

Effect of Boundary Condition

Figs. 5-7 give the results of calculations for the shock wave generated by applying a pressure pulse at the fluid surface.

Fig. 5 shows the amplitude of shock perturbation vs. distance for a step pulse ($\beta = 0$) and various initial Mach numbers. These results are the analog of the uniform velocity piston case shown in Fig. 1. It is observed that the shocks of Fig. 5 decay much faster. Since in an actual shock tube the boundary condition may be regarded as an intermediate state between the two cases considered here (prescribed velocity and prescribed pressure), it may be expected that the stability of the shock wave in a shock tube would be bounded by these two extremes.

Fig. 6 shows the effect of deceleration on stability for the applied pressure case. Considering the difference in scale between Fig. 5 and Fig. 6, it may be concluded that the deceleration adds little to the already very stable shock.

Fig. 7 gives the rate of growth of the fluid surface perturbation. The surface is unstable, and acquires a constant rate of growth, asymptotically. The instability of the surface is expected on the basis of the incompressible theory (Taylor instability) for impulsive acceleration (Richtmyer[2]). However, the asymptotic values of the growth rate do not agree with Richtmyer's formula very well. A closer agreement is found with results of Kivity[4] for the interface instability in a shock tube configuration.

ACKNOWLEDGEMENT

The authors wish to thank Prof. M. Hanin for very useful suggestions concerning the interpretation of the results.

REFERENCES

1. N.C. Freeman, *Proc. Roy. Soc.* (London) A228, p. 341 (1955).
2. R.D. Richtmyer, *Comm. Pure Appl. Math. XIII*, p. 297 (1960).
3. C.A. Kot, *Proc. 3rd Int. Conf. Numerical Methods in Fluid Dynamics*, Paris (1970). Springer-Verlag, Edt. Vol. I, p. 30.
4. Y. Kivity, *Stability of Unsteady Two-Dimensional Flow with Small Lateral Perturbations*, D.Sc. Thesis, Department of Aeronautical Engineering, Technion - Israel Institute of Technology (1971).

THE DIFFRACTION OF THE BLAST WAVE EMERGING FROM A CONICAL NOZZLE DRIVEN BY COMPRESSED GAS

LEONARD PENNELEGION

Department of Mathematics and Ballistics

JOHN F. GRIMSHAW

Department of Mechanical Engineering
The Royal Military College of Science, Shrivenham, England

The blast field emerging from a gun muzzle or from a rocket venturi eventually reaches the gunner and may cause him discomfort or permanent physiological damage. This paper presents some of the results from a wider study in which compressed gases are used to simulate weapon blast with the aim of predicting and controlling the growth of blast pressure.

Single, dual and multiple spark techniques were used to record flow development and blast wave velocity and displacement. An array of miniature piezoelectric transducers was used to record time of blast arrival and overpressure.

The blast field due to helium, air and carbon dioxide source gas was examined optically out to 8 calibres, and with side-on pressure transducers from 2 to 67 calibres. Variations in blast velocity due to these gases was apparent only in the near field of a nozzle, though a given nozzle and gas exhibited differences in the azimuth plane. Measurements of the quasi-steady shock bottle development are presented and compared with that due to a rifle. Reasonable correlation of Mach disc location is achieved.

INTRODUCTION

The blast field emerging from a gun muzzle or from a rocket motor venturi grows three dimensionally; expanding not only in the outward direction of the main axis of the muzzle or nozzle because of the directed momentum but in a sphere-like manner about the point of emergence. Comparative studies[1] have been made of certain weapons which showed that the expanding blast field can be quite different for each weapon and moreover in the case of tube launchers and recoilless guns can comprise a mixture of the impulsive flows from both the muzzle and venturi. (Fig. 1).

A detailed study of the way this blast wave develops around full scale weapons is difficult to accomplish, both from the hazard of live ammunition and the difficulty of separately controlling relevant parameters. In addition measurements of blast overpressure around existing guns and rockets to sufficient depth to predict confidently the overpressure for a new gun or rocket motor are expensive. Centre line measurements are not normally possible due to the hostile environment.

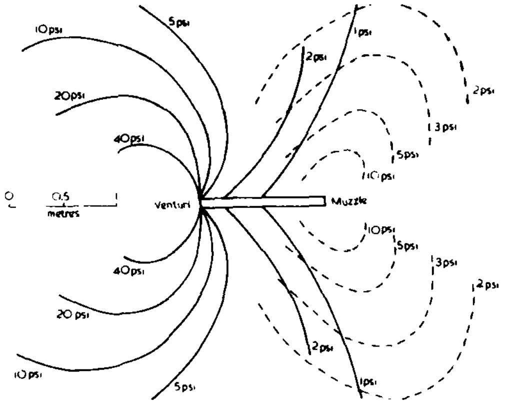

Fig. 1 A typical distribution of peak blast overpressure around an 84mm calibre Carl Gustav rocket launcher[1]. Following firing of the weapon, venturi outflow occurs first and on this is superposed muzzle outflow as the rocket emerges.

Despite the strength and propagation characteristics of blast waves from explosions being well documented and scaling laws established, when the energy source of the blast is the emerging propellant gas the resultant blast cannot be predicted with any confidence.

AIM

The establishment and validation of scaling laws for gun blast would be achieved more conveniently if instead of a weapon firing a projectile, a blast simulator could be used. Compressed gas being impulsively released from a tube or nozzle is an obvious possibility. Clearly, equivalent pressure magnitudes can be generated though in this work environmental and safety factors limited the maximum pressure to 30 bar, but a principal difficulty arises when endeavouring to provide a compressed gas which at ambient temperature has gas properties similar to propellant gas. One seeks a gas of specific heat ratio $\gamma = 1.24$ and speed of sound $a = 970$ m/s. In available gases at ambient temperature these properties cannot be obtained in the same gas e.g. helium $\gamma = 1.66$ $a = 965$ m/s, carbon dioxide $\gamma = 1.3$, $a = 256$ m/s. Some research has therefore been done using different gases and examining the effect on resulting blast strength and profile of specific heat ratio and speed of sound. The effect of conical nozzle angle was also examined although the parallel nozzle was of most interest.

EARLIER WORK

Simulation of a spherically growing blast wave (as from a point charge of explosive) has been superbly demonstrated by Glass[2] using frangible glass spheres pressurised with gases such as helium, air and sulphur hexafluoride. Esparza and Baker[3] subsequently used the same technique to measure static pressure distributions and showed that the characteristic blast profile obtained for compressed gas differed significantly from explosive. The simulation of weapon blast requires both cylindrical and spherical symmetry, indeed Nettleton[4] using a circular shock tube to study the decay of an expanding shock wave at an abrupt area change computes the wall shock attenuation assuming cylindrical symmetry, a necessary stage in the study of diffraction of the blast around a muzzle or nozzle. Skews [5,6] identifies the fluid disturbances resulting from a range of abrupt convex corners, but following Whitham[7] only considers two dimensional area expansions.

BLAST GENERATOR AND FLOW FIELD SENSORS

Generator

Blast waves were produced in the laboratory by pressurising a small cylinder with gases up to a pressure of 28 bar and bursting a Mylar diaphragm (0.025 mm) with a manually operated spike. The gas was released through a nozzle into the atmosphere: for this study conical nozzles of constant throat diameter of 15 mm and semi-cone angle α ranging from 0 to 11° were used.

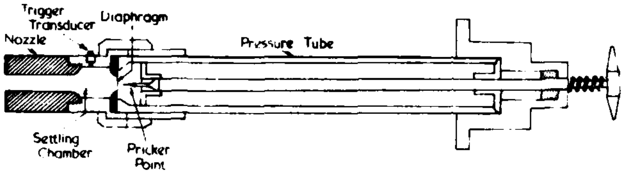

Fig. 2 shows the blast generator fitted with a parallel nozzle.

Flow field sensors

The study was divided into two types of measurement: the use of *optical* techniques for blast wave location, velocity and flow development, and the use of *pressure* transducers for blast overpressure and time of arrival.

The temporal growth of the blast wave emerging from the nozzles was recorded by single, dual and multiple-spark light-sources in a parallel focussed schlieren system comprising a pair of 2.44 m (8.0 ft) focal length 0.305 m (12 in) diameter concave mirrors in the conventional 'Z' layout. Triggering for the spark light sources was derived from a piezo-resistive transducer in the plenum chamber. The spark light sources were argon-stabilised and used with a vertical graded filter or knife edge as appropriate. A multiple-spark light source[8] (Hartley Measurements) having a capacity of 10 sparks firing across a single gap (with a minimum time between sparks of 70 μs) was used to follow the diffracted blast wave through the parallel optical beam.

The transient rise in side-on pressure above atmospheric as the blast wave arrived at a given radial location was measured by an array of four one-eighth scaled models of the internationally known 'pancake' blast gauge (variously called AWRE B12, RARDE H3C and USBRL). These Meclec gauges represented the smallest size of 'pancake' gauge of similar profile to the RARDE H3C that could be made with available quartz discs yet generate sufficient output charge to measure pressure steps of about 0.1 psi. The pressure sensitivities that were obtained in a low pressure shock tube were typically 0.8 pC/psi. More promising for gun blast overpressures appears to be the H1 or 'hatchet' gauge developed by RARDE for explosive testing but used at RMCS for measuring side-on pressures close to the muzzle of a 7.62 mm gun. The charge outputs of the transducers were processed by charge amplifiers (Meclec M142/Kistler 5001) and stored in a Physical Data 515A 6-channel digital transient recorder (10 bit word accuracy, 2 MHz maximum sampling rate).

BLAST FIELD DEVELOPMENT

The sudden release of energy can give rise to local step changes of pressure, density and temperature and this is evidenced by the propagation of blast and rarefaction waves. The strength and velocity of propagation are found to depend upon the rate of release of energy, explosive for example giving an almost instantaneous release, and propellant[9] and compressed gases[3] being progressively less efficient. Since we are using compressed gases to simulate the blast field from propellant gas, comparisons are made with gun blast fields where appropriate.

Specifically our simulation has to model the flow emerging from a gun or venturi tube, i.e. a flow field comprising axial symmetry close to the tube and having spherical symmetry at larger distances. Thus in the near-field conventional Hopkinson scaling has been to little effect. This paper reports only times of arrival, velocity and overpressure at various calibres distant from our simulator since a satisfactory method of scaling has not yet been found. The penultimate chapter discusses some approaches.

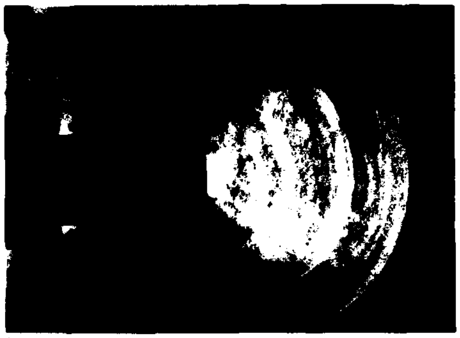

Fig. 3 showing the blast wave propagating from a parallel nozzle due to helium gas. The time between each spark is 70 μs.

In order that the blast wave growth around each nozzle could be followed for each blast a multiple spark light source was used (Fig. 3). Analysis shows that the forward-going blast velocity greatly exceeds those at 90° and rearward along the muzzle wall. Displacements measured from multiple spark photographs are compared in Fig. 4 with dual-spark and image-converter photographs at different times and for separate blasts. The same trends are shown and as expected the scatter is reduced when the multiple spark source or framing image converter camera is used.

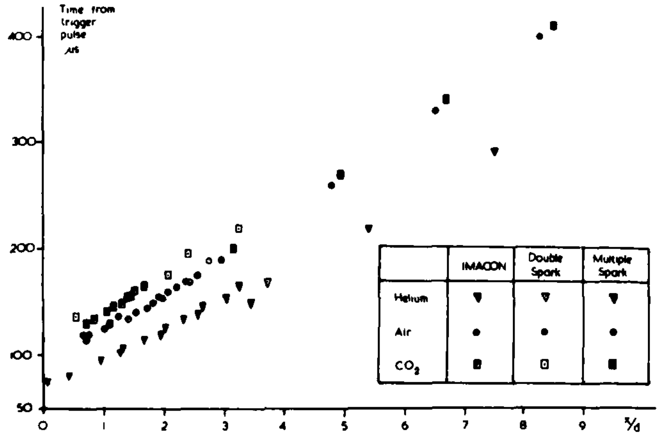

Fig. 4 compares the use of 3 photographic techniques to measure blast trajectories for 3 gases from a parallel nozzle.

Differentiating the *x*-*t* curve of a blast wave is an inaccurate method for deducing its velocity. Far more applicable is to use a dual-spark light source[8]. Fig. 5a was obtained by using two in-line individual spark sources, one focussed into the plane of the other, and a delay of approximately 5 μs between them. The actual time interval is monitored by a fast photo-diode which switches a 0.1 μs chronometer. Some blast wave velocity measurements made in this way are shown in Fig. 5b. These show both the significant increase in blast wave velocity on the centre line when helium gas is used, and then for these reservoir pressures, the velocity falls rapidly towards the ambient speed of sound in air (341 m/s) within a few calibres. Simultaneous measurements of

blast wave velocity can of course be made at any angle around the nozzle and this is an attractive aspect of the technique especially for nozzle-like flows since unlike centred static explosions the outflows have axially directed momentum.

Fig. 5a Dual spark photo of helium emerging from parallel nozzle.

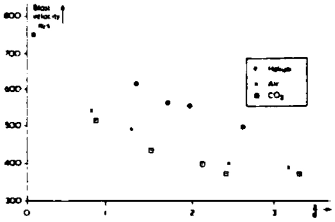

Fig. 5b Blast wave velocities on centre line of parallel nozzle.

These directed flows are jet-like (Fig. 6a) and usually supersonic. Certain similarities with steady jet theory are discussed in the next section.

MACH DISC DEVELOPMENT

The characteristic structure of a highly under-expanded supersonic jet is a jet plume that contains one or more enclosed 3 dimensional shock wave cells. Above a certain pressure ratio the barrel shock terminates in a triple point Mach disc configuration (Fig. 6b), beyond which there is a region of subsonic flow bounded by a slipstream emanating from the triple point. In steady state flows the distance of this disc from the exit of the nozzle has been adequately correlated[10,11,12] as $\frac{x}{d} \sim M_e\left(\frac{\gamma_e p_e}{p_\infty}\right)^{\frac{1}{2}}$ where M_e is the exit flow Mach number, γ_e and p_e/p_∞ are the specific heat ratio of the nozzle gas and exit static pressure ratio respectively. Thus the Mach disc distance is strongly dependent upon nozzle pressure ratio, and if this is time-dependent then the characteristics of the supersonic plume will change accordingly[13].

Fig. 6a Single spark photo of air emerging from parallel jet.

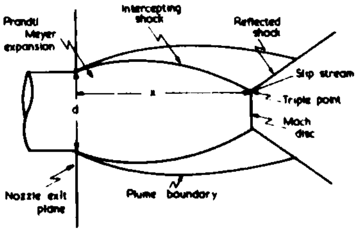

Fig. 6b Idealised steady jet structure.

The sequence of spark schlieren photos in Fig. 7 confirms the temporal growth of the shock bottle from the RMCS simulator and shows that it has a quasi-steady structure. The exit plane of the nozzle was radially extended for these measurements so that the blast field expanded in half space and generated no other waves. It should be noted that though the blast wave continues to expand radially the distance of the Mach disc from the nozzle passes through a maximum value.

Fig. 7 The developing shock bottle from a parallel nozzle due to air at 34 μs, 95 μs, 145 μs, 195 μs and 245 μs from blast emergence.

The time-dependence of the Mach disc location in the RMCS simulator and in a 5.56 mm gun[14] is shown in Figs. 8a and b. The abscissa on Fig. 8a has been magnified in order to show that the value of x/d has a maximum value in a similar time to that of the gun. The different maximum values obtained in Fig. 8a and b reflect the relative magnitudes of the nozzle/muzzle gas pressure ratio. Schmidt[14] furthermore showed that the establishment of the Mach disc location in the muzzle blast flow field, though initially delayed by the bullet, is determined by the momentary muzzle pressure of the propellant gas.

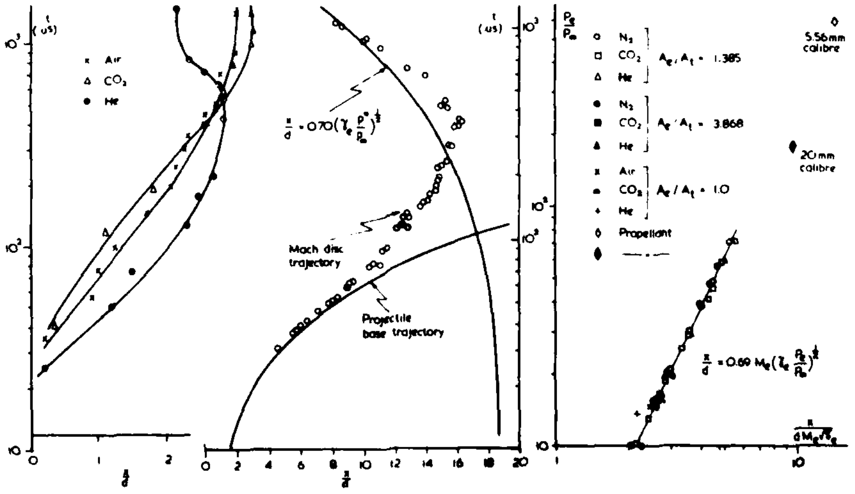

Fig. 8 a) RMCS simulator, b) 5.56 mm gun Mach disc trajectories c) Mach disc distance correlation

Lewis and Carlson[11] presented data on Mach disc location due to helium, nitrogen and carbon-dioxide gases emerging from conical nozzles ($\alpha = 15°$) for two different area ratios. Their facility was a blow-down tunnel (i.e. quasi-steady flow) operating at a nominal reservoir pressure of 6 bar. Superimposed on some of their data in Fig. 8c are our data for a parallel nozzle with a reservoir pressure of 28 bar but with a flow duration of a few milliseconds. The measured maximum value of x/d has been used in the correlation. Fig. 7 shows a typical sequence of Mach disc and blast wave displacements for compressed air from a parallel nozzle. Additionally in Fig. 8c are plotted values extracted from measurements by Schmidt for two different calibre guns[14,15] showing that *the same correlation exists for short duration as well as nominally steady state flows.*

CHARACTERISTICS OF NOZZLE FLOWS

The single spark photos in Fig. 9 were taken at a time when the retreating blast wave had reached a fixed pressure transducer in the shadow of the nozzle on the 150° radial. The similarity in the arrival time for each of the three gases at this point means that each photo has occurred at a similar time from blast emergence. A discernible structure for each gas is evident; the blast wave shape is similar for CO_2 and Air but much 'fuller' for helium, and whereas the shock bottle and Mach disc are clearly visible for $0 < \alpha < 8^\circ$ they are not discernible for $\alpha = 11^\circ$. This may be due to the fact that an increase in the exit diameter of the nozzle requires more time for the flow field to establish. As expected the stronger blast wave due to helium results in a steeper density gradient across the blast wave. Expansion waves from the corner of the nozzle structure can be seen, particularly in Fig. 5a.

Nozzle semi-angle	Exit dia. (mm)	M_{exit}		
		CO_2	Air	He
0	15	1.0	1.0	1.0
4	22	2.205	2.29	2.52
8	30	2.76	2.94	3.44
11	38	3.14	3.41	4.17

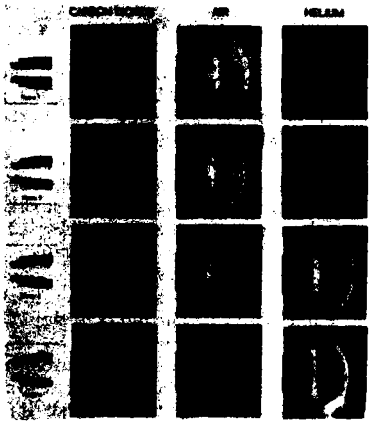

Fig. 9 shows characteristic near-blast-field for each nozzle and gas.

PEAK BLAST OVERPRESSURE DISTRIBUTION

From Smith[16] it is known that the directed momentum of the propellant gas from a gun results in a downstream motion of the effective blast source. Overpressure measurements should therefore be made with omni-directional transducers and if near-field then the dimensions of the transducer should be comparable with or smaller than the dimensions of the blast source. These criteria were satisfied by using the Meclec miniature transducers (25.4 mm dia) rather than the large H3C 'pancake' gauge (216 mm dia) or the H1 'hatchet' gauge which is directional (Fig. 10a). The response of each of these 3 gauges to a 7.62 mm rifle firing standard L2A2 ammunition when positioned at 0.3 m (this was the nearest reasonable location for the larger gauge) on the 90° azimuth radial is shown in Fig. 10b. The small initial pulse is known as the *'precursor'* blast and is due to the supersonic expulsion of the air resident in the gun barrel prior to propellant ignition.

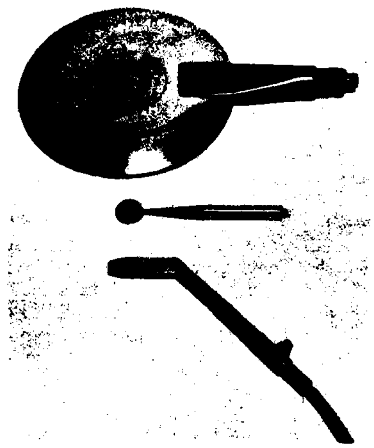

Fig. 10a RARDE H3C 'pancake' gauge (1502 pC/bar), Meclec miniature gauge (11.6 pC/bar), and RARDE H1 'hatchet' gauge (2871 pC/bar).

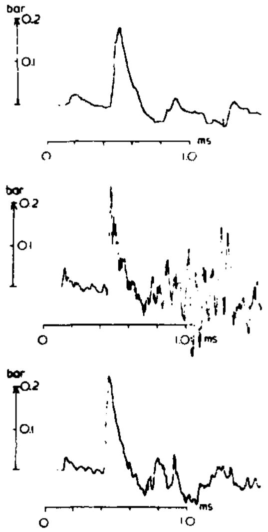

Fig. 10b Corresponding side-on overpressure response to gun blast.

The propellant blast has the characteristics of a Friedlander wave and though each of the traces was from a separate firing the similarity is evident as far as peak overpressure is concerned, though the frequency response can be seen to be best for the Meclec gauge. The fluctuations in the signal following the blast wave are compounded from unsteady flow fields and induced resonance in the gauge supports. No electronic filtering, other than the 180 kHz band pass of the charge amplifiers, has been employed.

Peak blast overpressure ratios measured around each of the 4 nozzles are plotted in Fig. 11 for various calibre radii and azimuth angles. On studying these results, certain trends and differences become apparent: *(a)* The overall level of overpressure is significantly higher for helium driven blasts than for air or carbon dioxide. In addition, those for air are higher than those for carbon dioxide. *(b)* The variation in overpressures from 0° to 150° azimuth angle for a given distance from the nozzle exit increases from carbon dioxide to air and from air to helium. *(c)* The variation in overpressure from 0° to 150° azimuth angle for a given distance from the nozzle decreases with increasing nozzle angle, as the flow tends more and more towards a spherical blast from a small compressed gas source of a type investigated by Esparza and Baker[3]. *(d)* The pressures measured on nozzle centreline (0°) for helium show a more rapid decay with radius than those for the other two gases. This is also noticeable on the 30° and 60° radials but only closer to the nozzle exit. In all cases it is apparent that the blasts have become weak by the time they have travelled a distance of 1 metre. *(e)* The overpressures measured along the 90°, 120° and 150° radials rise with increasing nozzle angle for all gases.

In an attempt to find a normalising factor to relate overpressures for varying driver gases, several methods have been considered. In order to minimise the effects of forward momentum of the issuing gas (and, in the case

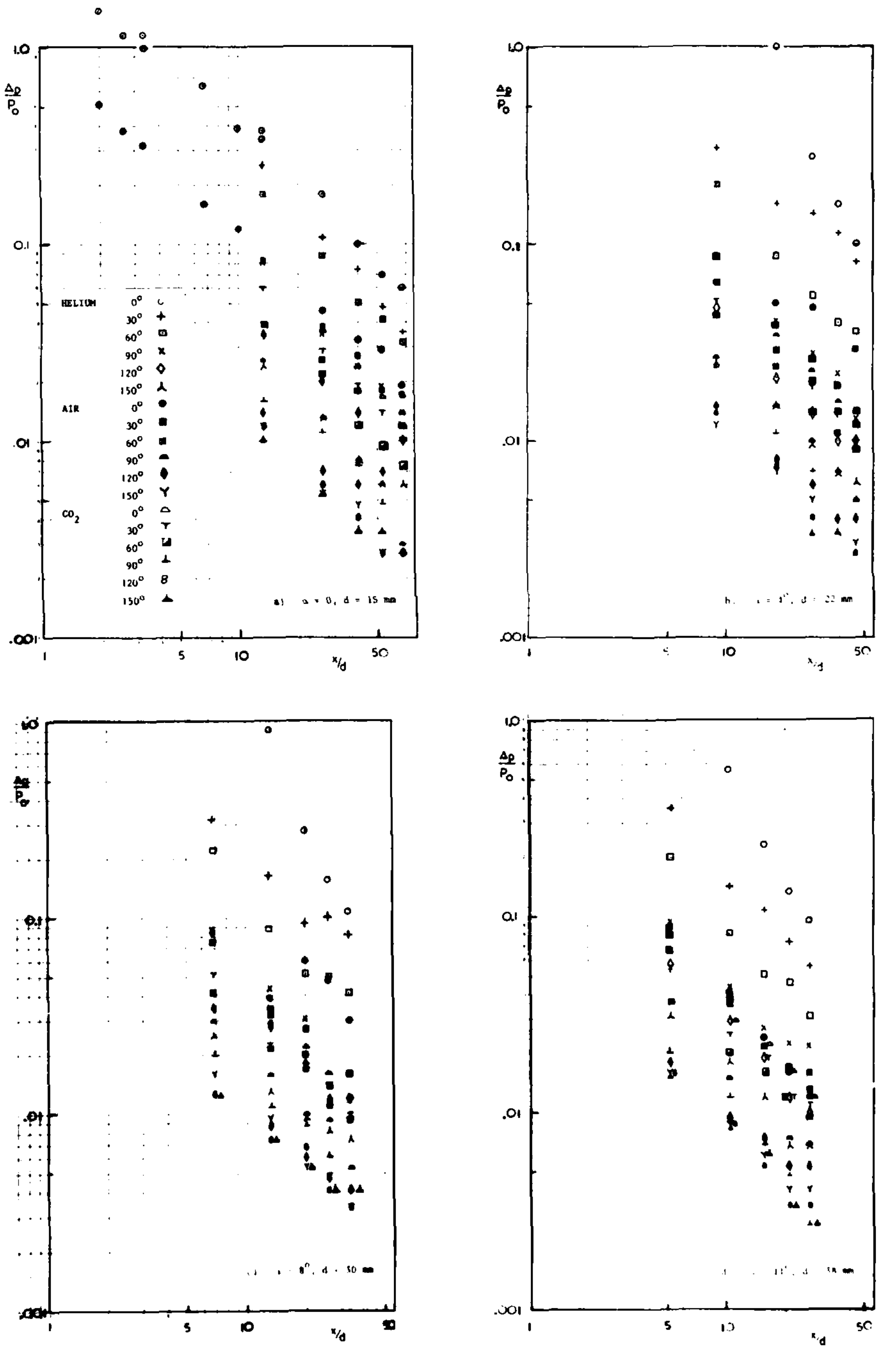

Fig. 11 Azimuthal pressure distributions for
4 nozzles and 3 gases.

of the parallel-sided nozzle, eliminate them), results along the 90° radial have been considered. This procedure has been suggested by Smith[16] in distinguishing between the effects of spherical growth and forward momentum and has been utilised by Westine[17] to correlate successfully results from a number of service weapons. Glass et al[18] in the context of acoustic waves reported that the rate of change of mass flow rate is a valuable parameter for normalising weak blast overpressures. In an earlier paper Grimshaw and Pennelegion[19] demonstrated that if the overpressures on the 90° azimuth were normalised by the mass flow rate through the nozzle, the pressure distributions from three different gases could be closely correlated. This correlation resulted from an error in calculations and unfortunately cannot be substantiated.

DISCUSSION OF CURRENT AND FUTURE STUDIES

The purpose of this research is i) to study the establishment and structure of the initial blast field from a gun or rocket nozzle, and ii) to apply the understanding to devising ways of protecting the gunner from harmful blast overpressures. Currently we have developed suitable techniques to quantify laboratory scale blast fields. The chief constraint of this study was that the physical size of the miniature transducers prevented close-field measurements with nozzles of these calibres. For future studies the 3D diffraction process will be examined more closely by generating stronger blast waves from larger nozzles. In this way higher mass flow rates result and the existing transducers may be used at closer scaled distances to the nozzle exit without significantly perturbing the flow.

ACKNOWLEDGEMENTS

The authors are very pleased to acknowledge the interest and assistance of Frank Winkfield and Kevin Dawson of RMCS, the enthusiastic support of John Bowman of RARDE, and the loan of the RARDE H1 and H3C blast transducers by Ken Jarvis of RARDE. The research reported in this paper is financed by MOD Research Agreement AT/2160/036/RARDE.

REFERENCES

1. W.A. Clayden and A. Hillman, 4th Int. Symp. Ballistics (1978).
2. I.I. Glass, Canadian Aeronautical Jnl. Vol. 7, *3*, 109 (1961).
3. E.D. Esparza and W.E. Baker, NASA CR 2843 (1977).
4. S.A. Sloan and M.A. Nettleton, J. Fluid Mech. Vol. 88, *2*, 259 (1978).
5. B.W. Skews, J. Fluid Mech. Vol. 29, *2*, 297 (1967).
6. B.W. Skews, J. Fluid Mech. Vol. 29, *4*, 705 (1967).
7. G.B. Whitham, J. Fluid Mech. Vol. 2, *2*, 145 (1957).
8. J.F. Grimshaw and L. Pennelegion, 6th Int. Symp. on Military Applications of Blast Simulation, 1.14, (1979).
9. S. Tuokko, 6th Int. Symp. on Military Applications of Blast Simulation, 1.5, (1979).
10. K. Bier and B. Schmidt, Zeitschrift für angewandte Physik *11*, 34 (1961).
11. C.H. Lewis Jnr. and D.J. Carlson, AIAA Jnl. Vol. 2, *4*, 776 (1964).
12. J.H. Fox, AIAA Jnl. Vol. 12, *1*, 105 (1974).
13. J.I. Erdos and P.D. Del Guidice, AIAA Jnl. Vol. 13, *8*, 1045 (1975).
14. E.M. Schmidt and D.D. Shear, AIAA Jnl. Vol. 13, *8*, 1086 (1975).
15. E.M. Schmidt, E.J. Gion and K.S. Fansler, 4th Int. Symp. Ballistics, (1978).
16. F. Smith, RARDE Memo 17/74 (1974).
17. P.S. Westine, Shock and Vibration Digest Bulletin, *6*, 139 (1969).
18. I.I. Glass, H.S. Ribner and J.J. Gottlieb, Canadian Aeronautics and Space Journal, 18, *8*, 241 (1972).
19. J.F. Grimshaw and L. Pennelegion, 4th Int. Symp. Ballistics (1978).

PROPAGATION OF SHOCK WAVES IN RANDOM MEDIA

B. STURTEVANT, L. HESSELINK, J-F. HAAS

Graduate Aeronautical Laboratories
California Institute of Technology, Pasadena, California, USA

Recent studies of the scattering of shock waves by continuous and discrete scatterers in random media are described. The effect on shock waves of fluid nonuniformities and, conversely, the flow field generated by passage of shocks through nonuniform media are studied. Two sets of experiments have been conducted, one in a 43 cm dia shock tube to study shock propagation through a continuous random medium, and the other in a 15 cm dia shock tube in which interaction with a random array of discrete scatterers has been studied. In the first experiment, the random medium consists of imcompletely mixed helium and Freon, in which the initial rms fluctuation of sound speed is approximately 6%. High-speed motion pictures have been made using both schlieren photography and speckle interferometry to visualize the motion in the flow field. Individual frames are analyzed to study the changes that take place with time. In the second experiment preliminary observations of the interaction of shock waves with a random array of small helium-filled soap bubbles have been made with shadow photography.

INTRODUCTION

This paper reports recent progress in a research program to study the interactions which occur when shock waves propagate through nonuniform random media, originally described two years ago at the XIth Shock Tube Symposium. In reference 1 the problem and some preliminary results were described in general terms and in reference 2 further details were presented. Of central interest in this research is the nonlinear interaction between shock-wave propagation and turbulence, that is, the way in which fluid nonuniformities affect shock propagation, and, conversely, the effect the shock wave has on the nonuniformities. This coupling, or 'feedback', is particularly important in flows in which the shocks are relatively strong and the nonuniformities large; typically high speed and high energy turbulent flows. In this situation the basic nonlinearity of fluid mechanics is important both in the wave propagation and in the motion of the turbulent fluid, so nonlinear interactions are the most complex. So far in the present work, only relatively weak shocks (up to $M_s = 1.3$) and weak 'turbulence' have been studied.

Consider an initially plane shock wave incident upon a volume of fluid in which initially there exist random fluctuations of, say, sound speed (e.g., entropy). The propagation speed of the wave varies from point to point in the fluid so the wave front distorts and no longer remains plane. In general, when the direction of the wave propagation is not parallel to the initial gradient of sound speed, slip streams or vortex sheets are generated in the fluid because of the differential acceleration of fluid of varying properties. As the vortex sheets subsequently roll up due to Helmholtz instability, the entropy gradients are intensified by stretching. Furthermore, the portions of the wave front that are concave in the direction of propagation tend to focus, generating localized regions of intense vorticity[3]. A field of scattered waves develops behind the shock, and transverse waves propagate back and forth along the front. This is the problem studied in the present work. In this paper recent results obtained from two experiments, one in which the shock wave interacts with a continuous random medium and the other in which the interaction is with discrete scatterers, are described.

EXPERIMENTS AND RESULTS

Continuous Random Medium

This experiment is carried out at atmospheric pressure in the GALCIT 17" diameter shock tube. As illustrated schematically in figure 1, a 25 cm square by 35 cm long rectangular volume of randomly inhomogeneous gas is generated in an apparatus which consists of two two-dimensional 7 × 8 arrays of fine jets alternately of helium and Freon-12 located on opposite sides of a box behind coarse grids. Just before shock arrival, the grids retract to cover the jet orifices and make the side walls of the box smooth. The two other side walls of the box are fitted with 15 cm dia optical windows for diagnostics. The upstream and downstream faces of the box are fitted with shutters which can be opened rapidly just before firing the shock tube. The gas mixture is made neutrally buoyant in and with the same average acoustic impedance as air, so the mean interface between the scattering region and the uniform air in the shock tube remains parallel to the incoming wave, and has minimum effect on the wave propagation. It is important that, on the scale of the experimental apparatus, the fluctuations in the random medium are homogeneous and isotropic, so large-scale perturbations of the shock wave that might overshadow the effects of scattering are avoided. All these characteristics are demonstrated by measurement with a special density probe[4] and also by demonstrating (figure 4, reference 2) that when the random medium is allowed to mix for a long time (2.5 sec) before shock arrival it becomes uniform, and essentially no perturbation of the shock wave is caused. The rms sound-speed

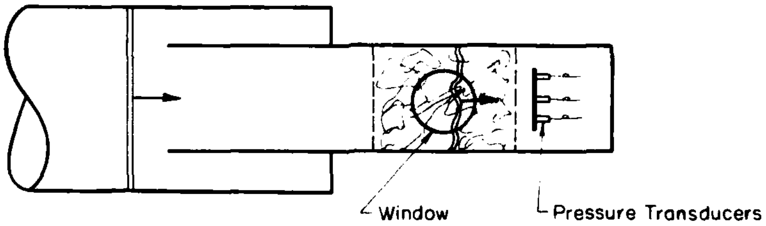

Figure 1. Schematic diagram of scattering experiment.

fluctuation prior to shock arrival is measured with the density probe to be 6%.

Recent research has concentrated on obtaining photographic records using two different types of optical diagnostics; schlieren photography and speckle interferometry. The optical setup is shown in figure 2.

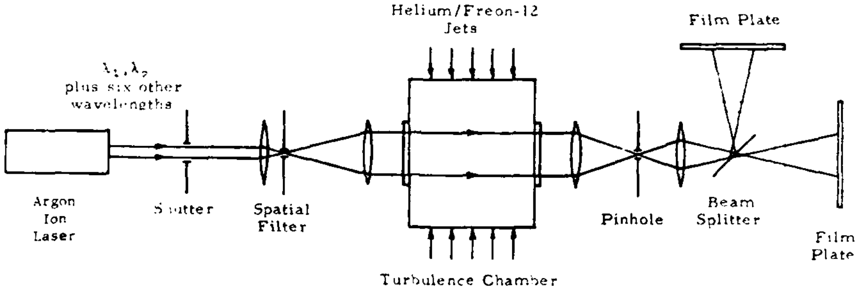

Figure 2. Schematic diagram of optical setup.

With a pinhole (or dot) of order 1 mm dia at the back focal plane of the schlieren mirrors, a light field (or dark field) schlieren image of the test section is formed in the image plane (designated 'film plate' in the figure). On the other hand, the random diffraction pattern generated by propagation of the coherent optical radiation from the laser source through the random medium can be enhanced by introducing a very small pinhole (low-pass filter) at the same location. If the pinhole is small enough that the resolution cell of the optical system is larger than the largest scale of the object being illuminated (in this case the random medium and the shock wave) then the diffraction pattern (speckle) will be dominant in the image. The scale δ of the speckle pattern is given by the diameter d of the pinhole, the focal length f of the imaging system, and the wavelength λ of the incident radiation,

$$\delta \approx \frac{f\lambda}{d}, \qquad (1)$$

and in the present experiments, with $d = 200\ \mu m$, is a few mm. Therefore, the size distribution of the speckle pattern is not among the properties that can be used for quantitative diagnostic measurements of the random medium because it is determined primarily by the characteristics of the optical system. However, the motion of the speckle pattern, which can be used to measure velocity[5], the time required for the pattern to decorrelate, which is a measure of a 'mixing time', or the wavelength-dependence of the speckle pattern, which is related to the fluctuations of the phase of the optical radiation[6] and, therefore, to the fluctuations of index of refraction and their correlation length in the random medium, are useful for quantitative measurements. Use of the wavelength dependence to measure fluctuation amplitude has been reported previously[7]. The purpose of the present discussion of speckle is to introduce a high-speed motion picture, shown during the presentation at the Symposium, to illustrate the motion of the speckle pattern before, during and after passage of the shock wave through the scattering medium.

As indicated schematically in figure 2, two recording instruments have been used in these experiments; a high-speed photodetector resolving a small portion of the image field for quantitative pointwise measurements, and a high-speed rotating-drum framing camera which in these experiments is operated at 15,000 frames per second.

Figure 3 shows a sequence of five consecutive frames of the shock wave propagating from left to right through the scattering volume. When

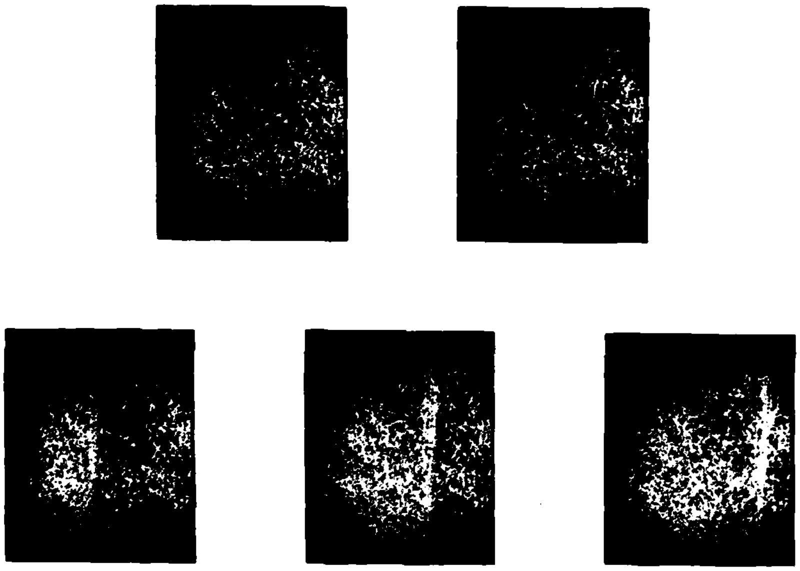

Figure 3. Sequence of frames showing motion of incident shock wave. Time increases left to right, top to bottom. Time interval between frames 67 μsec.

the shock enters the field of view it has propagated 10 cm through the nonuniform medium and, as can be seen, has *already been considerably* dispersed by scattering. It can be seen from the appearance of the random medium in the first and last frames that considerable change is caused by passage of the shock wave. This is further illustrated in figure 4, which shows three frames, one taken immediately before shock arrival, one just after shock departure, and the third sometime later. One of the goals of the present research is to quantify and explain the considerable differences that exist between these three frames. On the other hand, speckle patterns (figure 5), in contrast to the behavior of the schlieren images, show no significant change of scale with time, as explained above.

Images from frames similar to those shown in figure 4 have been read and digitized using a microdensitometer, and preliminary analysis of the data has been made. Figure 6 shows the power spectrum (arbitrary scale) of the spatial distribution of photographic density on

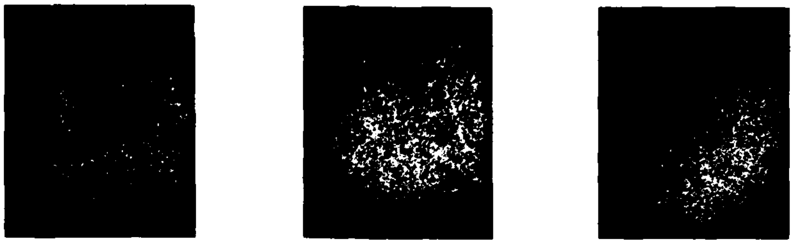

Pre - shock **Post - shock** **1.7 ms. later**

Figure 4. Three frames showing increasing predominance of small scales with time.

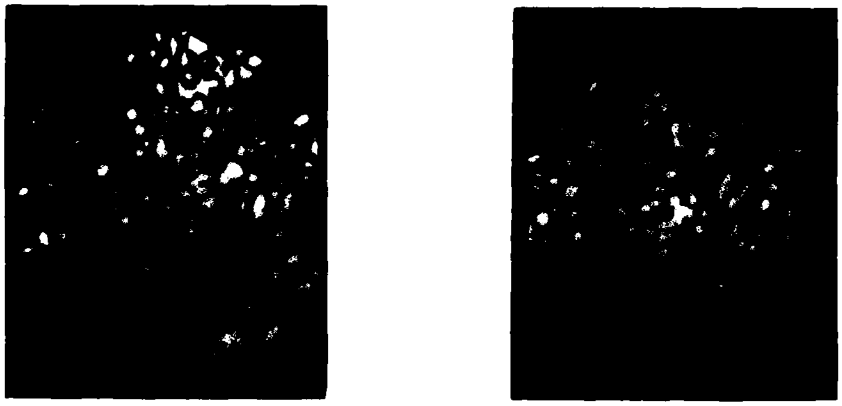

a. Pre-shock b. Post-shock

Figure 5. Speckle pattern before shock passage and 1.5 msec after.

two different frames, one just before shock arrival and the other 2.5 msec later. The spectra were obtained by averaging data from several widely spaced horizontal sweeps across each frame. The straight lines drawn on the spectra are to emphasize the qualitative behavior. They exhibit the effect already pointed out in the discussion of figure 4, namely that as time (and mixing) increases the radiation intensity at large scales decreases and high frequencies become relatively more important than low. Comparative analysis of digitized data from different frames promises to yield important information about the behavior of this flow field and considerably more analysis and image processing will be carried out in future work. Slow-motion films made up of 100 frames from the high-speed schlieren motion pictures, projected at the Symposium at speeds 2,000 and 10,000 times less than real time, show the violent mixing that occurs after shock-processing of the random medium.

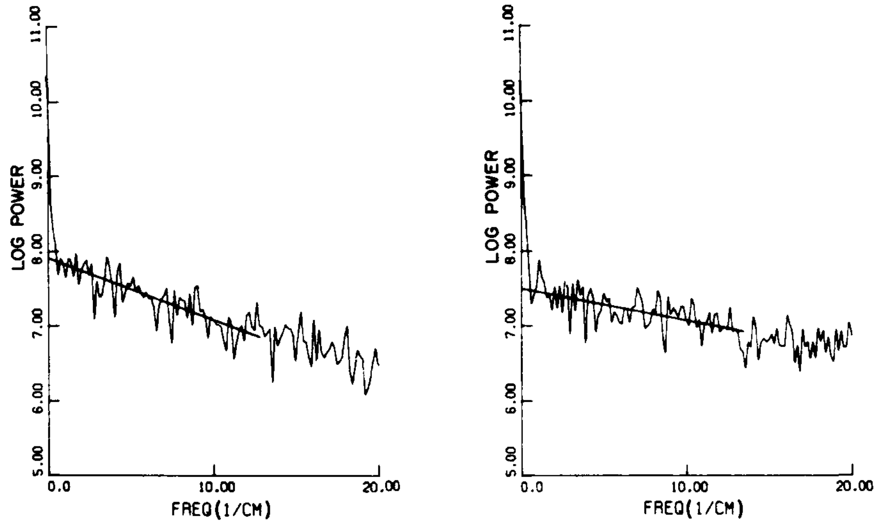

a. Pre-shock

b. Post-shock

Figure 6. Mean spatial power spectrum in the horizontal direction of the schlieren images in two frames of a high-speed movie.

Discrete Scatterers

Another series of experiments to study the interaction of a shock wave with a random array of discrete scatterers has been initiated in a 15 cm diameter shock tube. In this case the scatterers are neutrally buoyant, helium-filled soap bubbles of approximately 2 mm dia. The bubbles are generated at the downstream end of a 9 cm square test section in the shock tube and, just before the experiment, occupy approximately the last 40 cm of the test section. Figure 7 shows shadowgraphs of shock waves of two different strengths interacting with the bubbles. The magnitude of the difference between sound speeds inside and outside the bubbles is not yet known with certainty, but apparently conditions are such that the scatterers have little effect on the shock wave (though in some photographs weak reflected waves can be seen around some bubbles near the shock). On the other hand, dramatic changes in the random medium caused by the shock wave are easily seen. In particular, a 'relaxation time' for the response of the bubbles to shock excitation, of approximately 70 μs for the weak shock and 25 μsec for the strong shock, is observed. Rather complete mixing behind the stronger shock is seen after only 100 - 200 μs. Future work will concentrate on maximizing the difference in sound speed between the gas in the bubbles and the ambient medium in order to increase the interaction between shock wave and scatterers.

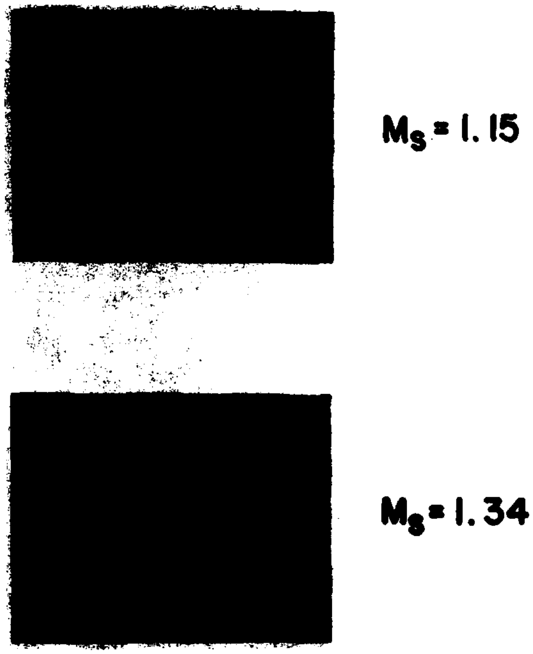

Figure 7. Shadowgraphs of shock waves interacting with helium-filled bubbles.

ACKNOWLEDGMENTS

This research was supported by the National Science Foundation under Grant No. ENG 78-22089 and by the Air Force Office of Scientific Research, Air Force Systems Command, USAF, under Contract No. F49620-77-C-1107.

REFERENCES

1. B. Sturtevant in "Shock Tube and Shock Wave Research" (ed. B. Ahlborn, A. Hertzberg, D. Russell), Univ. Wash. Press (1978), p. 12.
2. L. Hesselink, ibid., p. 82.
3. B. Sturtevant and V. A. Kulkarny, J. Fluid Mech. 73, 651 (1976).
4. G. L. Brown and M. R. Rebollo, AIAA Jour. 10, 649 (1972).
5. T. D. Dudderar and P. G. Simpkins, Nature 270, 45 (1977).
6. George, N. and Jain, A., Appl. Phys. 4, 201 (1974).
7. L. Hesselink, Paper TuB4-1 in Topical Meeting on Meteorological Optics: Keystone, Colo., August, 1978.

ELECTRIC AND MAGNETIC FIELDS OF SHOCK FRONTS

BOYE AHLBORN, JOE KWAN and JOHN PEARSON

Department of Physics
University of British Columbia, Vancouver, Canada

University of British Columbia, Vancouver, Canada

The strong charge carrier gradients in ionizing shock waves produce electromotive forces (emf) which are responsible for space charge fields, electrical currents and magnetic fields. We have attempted to measure the magnetic field, and have studied the open circuit electric field and the current under load in standing shock fronts. Voltages were obtained using as working fluid either argon gas or the reaction products of acetylene oxygen detonations. The plasma of the shock front acts like the hot electrode in a thermionic convertor or a thermocouple. The supersonic flow provides the power to maintain the configuration and prevents heating of the cold electrode. Electrical power generation with the emf produced in standing shock waves can therefore be considered as an alternate principle for direct energy conversion from high temperature supersonic flow fields, in a temperature range where so far only MHD generators may be applied.

INTRODUCTION

This paper attempts to provoke discussions about an aspect of shock waves - namely electric and magnetic effects - which has received little attention but which may have implications for fields which are as far apart as the formation of stars and direct energy conversion. We have started to look into this subject in a series of experiments and model discussions but we are fully aware that some of our calculations should be considered as order of magnitude estimates and some of our measurements are only of qualitative or preliminary nature. However, it is hoped that they will illustrate the potential for interesting investigations in this area of shock tube research.

It has been known for some time that an electric field E can exist inside an ionizing shock front[1,2]. This electric field is caused by space charge separation due to the diffusion of electrons away from the regions of high concentration in the direction parallel to the propagation of the shock wave. In the frame of the moving shock front this space charge field is constant, but in the laboratory frame the space charge profile is moving with the shock speed so that a spontaneous magnetic field B must be produced. Tidman[3] has discussed such magnetic fields, and large magnetic fields have been observed in laser blowoff plasmas[4,5], which contain shock fronts.

The transport of charged particles may be described by the generalized ohms law[6] written for steady state condition

$$\vec{J}\{n_i\varepsilon_{ie}(\varepsilon_{io}+\varepsilon_{eo})+n_o\varepsilon_{io}\varepsilon_{eo}\}= e(\varepsilon_{io}-\varepsilon_{eo})\,grad\ p_e+ n_i(\varepsilon_{io}+\varepsilon_{eo})e^2\vec{E} + e^2(grad\ p_0 \times \vec{B})/(n_i+n_0) - e\{\varepsilon_{io}- \frac{n_o\varepsilon_{eo}}{n_i+n_o}\}\vec{J}\times\vec{B} \qquad \text{(I)}$$

where J is the current density, p_e the electron pressure and $\varepsilon_{k\ell}$ are the friction coefficients defined as

$$\varepsilon_{kl}= \frac{4}{3}\sqrt{\{}\ \frac{8}{\pi}\ kT\,\frac{m_k m_l}{m_k+m_l}\ \}\ \sigma_{kl}$$

and n_i, n_e, n_o are the number densities and $\sigma_{k\ell}$ is the collision cross section. If no external electric and magnetic fields are present the above equation may be simplified as

$$\vec{J}= \sigma_o\{\ \vec{E} + \frac{1}{e\rho}\ (m_i grad\ p_e - m_e grad\ p_i)\} \qquad \text{(II)}$$

where σ_o is the DC conductivity of the plasma. It is defined in terms of the collisional frequency ν_{ei} as

$$\sigma_o = n_e e^2/(m_e\nu_{ei})$$

Equation (II) shows that a current must flow if a pressure gradient is present. A strong gradient for the electron pressure is always generated in an ionizing shock front. Consider a volume element which has just been reached by a shock so that an electron density gradient has been set up. There will be an initial current described by (II), however, the current must quickly built up a space charge which in turn creates an electric field that stops the current. The structure of an ionizing shock front is shown in Fig.1. The spatial distance of the charge separation must be of the order of the Debye length δ_x

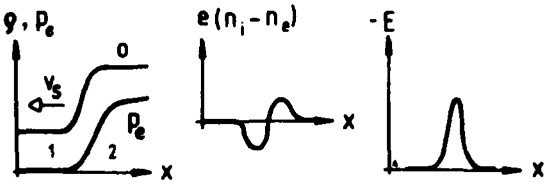

Figure 1. Structure of an ionizing shock front

If the development of the space charge is prevented by short circuiting the plasma externally, a continuous current can be maintained. This situation may be achieved in a standing shock produced by inserting a conducting obstacle into a supersonic flow field, Fig. 2.

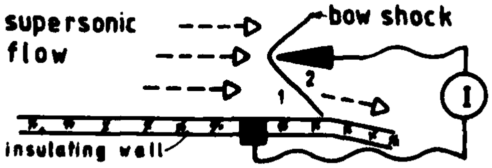

Figure 2. Bow shock in a supersonic flow and electrical circuit to short the space charge field.

THE SPONTANEOUS MAGNETIC FIELD

The spontaneous magnetic field of a shock observed in the lab frame of reference can be estimated from the special relativity transformations of E and B fields. In the frame of a free running shock the magnetic field is absent and the electric field due to the space charge separation is constant. The electric field is of course only present within the charge separation layer, and it points in the direction of the shock propagation (except in cases where the planar geometry of the charge layers is not maintained, namely near the boundary layer of a shock in a shock tube and in situations as described by Tidman[3]. The transformation equations are

$$B'_y = \gamma(B_y + \frac{v}{c^2} E_z) \quad \text{(III)}; \qquad B'_z = \gamma(B_z + \frac{v}{c^2} E_y) \quad \text{(IV)}$$

where

$$\gamma = 1/\{\ 1 - (v/c)^2\ \}^{1/2}$$

For most cases the shock velocity is small compared with the speed of light, c. The magnetic field is therefore of the magnitude E v_s/c^2. Since the electric field is approximately given as $E \sim kT/e\ \delta x$ (see below), the magnetic field can be approximately given as

$$B \approx (v_s/c^2)\frac{kT}{e\delta x} \qquad \text{(V)}$$

A similar result is obtained if one calculates the magnetic field of a positive and a negatively charged disc separated by a distance δx and travelling together at a velocity v_s. If the abrupt electron density discontinuity in the boundary layer of the shock front is replaced by a gradual changing distribution, the magnetic field is obtained from a term $B \sim \nabla n_e \times \nabla T$ as in ref. 3. The approximate relation (V) yields a magnetic field of about 10^{-5} Gauss for the temperature step and debye length found in a Mach 11 shock wave travelling through the test gas argon of 5 torr initial pressure. The direction of the magnetic field is indicated in Fig. 3. The field is only expected at the edge of the shock front.

We attempted to measure this magnetic field (unfortunately before estimating its magnitude) of a free running Mach 11 shock with a Rogowski coil wound around the shock tube, Fig.3.

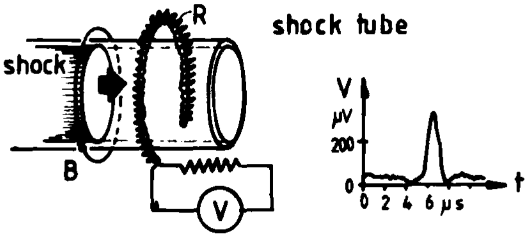

Figure 3. Shock tube with Rogowski coil R for measurement of the magnetic field B. Insert: typical signal obtained.

The tube diameter is 2.5 cm and the minor and major diameters of the coil are 0.17 cm and 2.84 cm respectively. The coil has 113 turns per cm for a total of 920 turns. A typical obtained signal is shown in Fig.3b. Unfortunately this signal does not reverse its polarity when the coil is flipped around. Hence it cannot be the wanted signal of the magnetic field but must be a capacitatively induced signal associated with the shock front. This capacitive signal unfortunately masks any signal of the magnetic field which we tried to measure.

MAGNETIC FIELDS NEAR INTERSTELLAR SHOCK FRONTS

Shock are some times produced at the edges of HII region in the interstellar space. (HII regions are regions of hydrogen plasma in the vicinity of hot young stars. The hydrogen is photoionized by the intense ultraviolet radiation). The shock always propagates ahead of a radiation front into the surrounding neutral gas. Often this background gas is not uniformly distributed but condensed into clouds of typically 1 solar mass. Therefore the ionization and shock front is interrupted. Space charge discs will then be set up and spontaneous magnetic fields be produced at their edges, as indicated in Fig.4. The magnetic field would produce a Zeeman splitting of the spectral lines emitted in this region and such Zeeman splitting has indeed been measured for instance in the Crab nebula[7] which indicates a direction of the magnetic field as predicted by this spontaneous field generation mechanism. Hence it is possible that all or part of the magnetic field near interstellar shock fronts is spontaneously created by moving space charge discs.

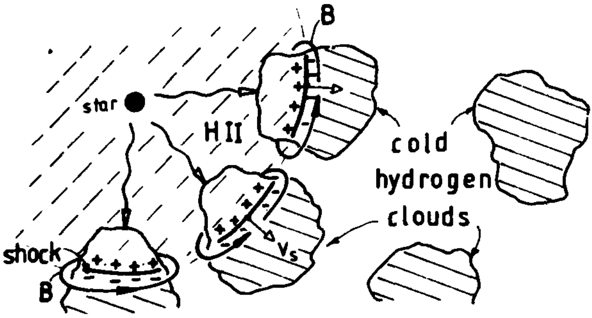

Figure 4. Shock fronts near the edge of interstellar HII region penetrating through clouds of cold hydrogen, and magnetic fields produced at the edge of the space charge discs.

It has been argued[8], that stars are formed out of these hydrogen clouds. The initial acceleration of matters is due to the gravitational collapse and it is triggered by the passage of the shock waves which are generated at the edge of the HII region of a nearby star. It is then quite likely that the self generated magnetic fields which surround the shock discs accelerate the gravitational collapse. This arises because the density is so low that the interstellar matter is essentially frozen to the field lines. The tension along the field lines (which makes them shrink like stretched rubber rings) contracts the shock front and thereby adds to the compression of matter in the hydrogen clouds.

CURRENTS AND ELECTRIC FIELDS

In order to estimate the electric field of a shock in open circuit configuration, we return to Ohms law (II) and assume that no current is flowing (J=0). Also taking $m_e \ll m_i$ we have

$$\vec{E} = \frac{-1}{en_e}\, grad\; p_e \qquad \text{(VI)}$$

The potential difference across the electron density step is obtained by integration of (VI) from the conditions 1 to the state 2.

$$V = \int \frac{kT}{e}\left(\frac{\partial}{\partial x}\ln\, n_e\right)dx + \int \frac{k}{e}\,\frac{\partial}{\partial x}(\;T_e)dx \qquad \text{(VII)}$$

$$= T_2'\,\ln(n_{e2}/n_{e1}) + \Delta T'$$

where $T' = kT/e$ is the electron temperature expressed in electron volts. In general the potential is of the order of the temperature step $\frac{k}{e}(T_2-T_1)$. This means physically that the potential difference across a shock is proportional to the jump of internal energy. Typical values for a Mach 10 shock travelling through 5 torr argon of room temperature are $E \sim 10^5$ volt/m and $V \cong 0.8$ volt.

Potential differences across free running shocks have been measured previously[1,10]. We have performed similar measurements in standing shocks. Such measurements are of course relatively convenient because the reference frame is stationary in the laboratory, while it is moving with respect to the lab in free running shocks. If a steady supersonic flow of plasma is available, one can obtain the steady electric field for as long as the flow lasts. More importantly the potential of a standing shock can be used to drive currents through external circuits which are connected to the plasma on both sides of the shock front. It is then possible to extract electrical energy with a "bow shock generator" out of a supersonic gas flow of high temperature in a regime which is otherwise only accessible to MHD generators. A bow shock generator differs, however, fundamentally from an MHD generator since a different electromotive force is used, and since no magnetic field is required. (The emf of the bow shock generator is the grad p_e term whereas the emf of an MHD generator is the $v \times B$ term in Ohms law). Bow shock diodes also carry certain similarities with thermocouples or thermionic convertors.

The experiments with bow shocks require a partially ionized supersonic flow which can be produced in a shock tube. The column of shocked test gas travels supersonically in the lab frame but subsonically with respect to the moving shock front. We are interested here only in the shocked gas which is steady for some test time. The conditions in this test gas can be calculated for instance by using a computer code[11] (which has been verified by many experiments) if the shock velocity and the initial fill gas conditions are given.

Our experiments were performed with a shock tube of about 1 m length and a cross section of 6.3 cm^2. The initial pressure in the test gas argon ranged from 5 to 10 torr at room temperature. The test time is slightly longer than 20 μsec. The shock tube has a gaseous detonation driver[9], which is operated with an acetylene oxygen misture of 150 to 250 torr. A detonation wave is ignited by a spark plug at one end of the driver chamber. The detonation pressure is slightly amplified by area convergence before reaching the membrane between the driver and the test gas, so that shock Mach numbers of $M=11$ can be easily achieved in this apparatus. The velocity of the shock wave was measured with a smear camera and from the delay between two pressure probe signals mounted at different positions in the shock tube. The shock velocity is of course needed to obtain the pressure, temperature and flow velocity of the plasma slug behind the shock wave, which is the working medium for the bow shock experiments. The obstacle to create the standing shock is mounted at a distance of 1 m from the shock tube membrane. The experimental set up is shown in Fig.5.

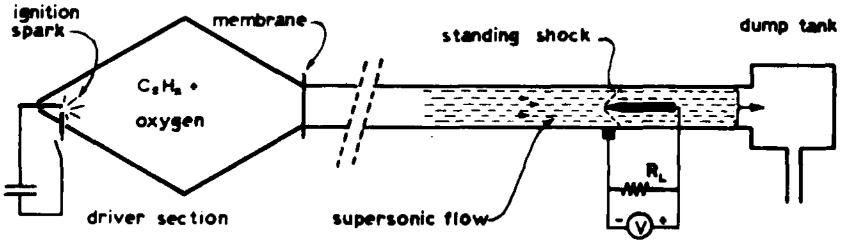

Figure 5. Shock tube facility to generate a supersonic flow field for current and voltage measurements at standing shock fronts. R_L load resistance

The experiments were initially carried out in a tube with cylindrical test section using a cone shaped bow shock obstacle mounted on axis. Comparison with model calculations is, however, difficult for this geometry since one cannot treat the flow around the cone as a 2-dimensional oblique shock. We have therefore lately converted the apparatus to a test section with square cross section, where a wedge shaped obstacle is employed, Fig.5. The flow field may now be treated as a 2-dimensional oblique shock. The shock tube is fabricated out of lucite, planar wedges with various angles of attack and conducting surfaces can be mounted in the tube. They serve as the downstream electrode. The other electrode is mounted flush with the wall at a place behind which the oblique shock is produced while the slug of (shock heated and shock accelerated) test gas passes by. Fig.6 shows how the bow shock voltage is expected to vary with flow mach number and angle of attack. For instance for a wedge with 13° apex angle and the flow created by a Mach 10 shock wave one expects a bow shock potential drop of 0.6 volts. (The Mach 10 shock creates a plasma of about 9000 K with 0.8% ionization, a pressure jump of 125, a density jump of 4 and a flow Mach number with respect to the wedge of M 1.4). The measured voltage signal includes a potential drop at the anode and the cathode (plasma sheath potential) which is proportional to the electron temperature of the nearby plasma. We have not yet found a method to quantitatively determine the magnitude of the sheath potential so that quantitative comparison between measurements and the calculated bow shock potential has not yet been carried out. Nevertheless, the two sheath potentials at different electrodes tend to cancel each other and the measured signal give a voltage quite close to our expected value with the sheath potentials neglected. Typical voltage signals of the bow shock diode are shown in Fig.7. The initial negative spike is due to the shock

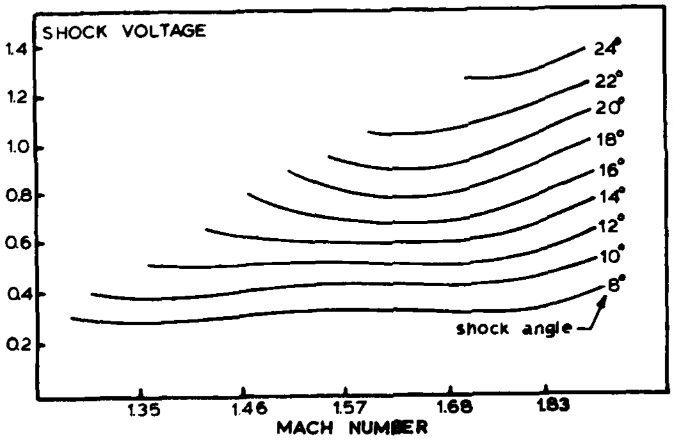

Fig. 6
Calculated oblique shock potential as a function of flow Mach numbers and wedge angle.

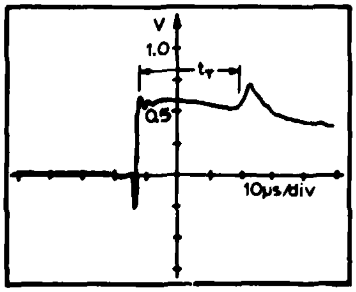

Fig. 7 Typical signal of bow shock diodes. Wedge angle=12°, flow Mach number=1.5 and R_L = 100Ω. The test time is only 30 μsec long.

wave that generates the supersonic plasma slug. The test time is slightly longer than 25 μsec. If one wants to develop such a bow shock diode into a power conversion system, one must know the current and power extraction characteristics under load. Therefore the load resistance R_L and the current and voltage was measured. Fig.8 shows the current voltage characteristics and the extracted power for a 12^c wedge obstacle. The flow is generated by a Mach 11 shock. The output power peaks at a load resistance of 0.6 ohm. The bow shock diode has properties of a low voltage high current device. The voltage is limited by (VII), and the current density by (II), but the total current can be increased by increasing the surface area of the standing shock. (see later).

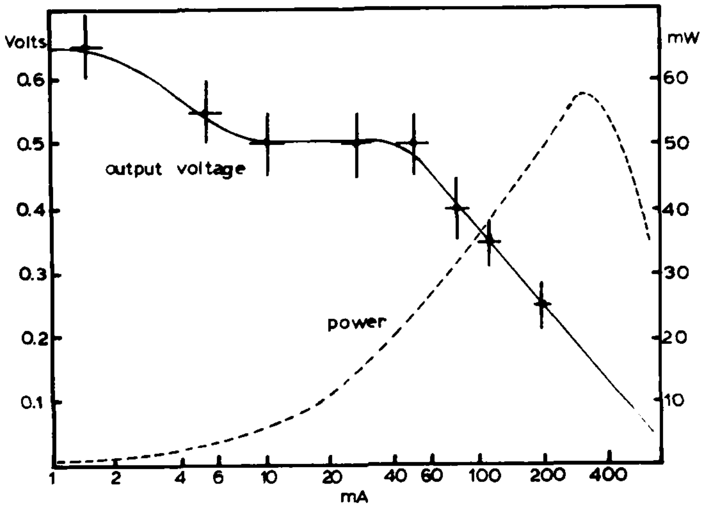

Fig. 8
Current and Voltage characteristic and output power of a 12° wedge in a Mach 1.5 flow field.

SUPERSONIC FLOW PRODUCED WITH COMBUSTION PRODUCTS

We have wondered whether one could produce currents and voltages in a similar fashion from supersonic flow fields which are produced with combustion products in Laval nozzles. This should be possible in a flow which contains charged radicals rather than atomic ions and electrons if there is a significant difference in the mobility between positive and negative charge carriers. The first preliminary experiment to the test this concept was carried out with the products of an acetylene oxygen detonation exhausted into a Laval nozzle, Fig.9, a device which has been used for other purposes.[12] Since the detonation is ignited in one end of the chamber and oscillating motion is set up in the reaction chamber which leads to a nonsteady flow in the nozzle. Pressure gauges

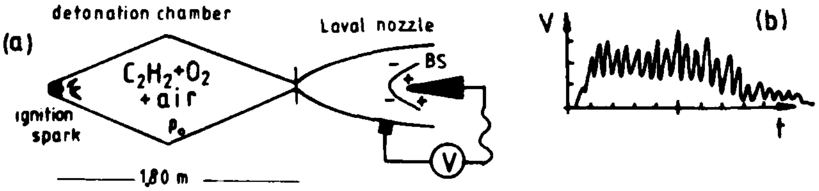

Figure 9. (a) Bow shock generator in Laval nozzle with products of C_2H_2 plus oxygen as working fluid. (b) Signal observed. 0.1V/div, 5 msec/div.

mounted upstream and downstream of the nozzle throat show large pressure oscillations with a period of 1 msec. A conical bow shock obstacle mounted in the laval nozzle produces (open circuit) voltage signals with the same frequency. The magnitude of the signals is consistent with (VII). We consider these experiments as proof of principle, but felt that we did not understand the reaction kinetics sufficiently to interprete the results in a quantitative manner. Therefore we have abandoned this experiment. Recently a second set of experiments has been initiated, in which an acetylene oxygen combustion is produced at high pressure and exhausted into a Laval nozzle. The first crude system operated at a pressure greater than 2 atm and it exhausted directly into ambient pressure. The hot gas was blown onto a graphite obstacle. A steady electrical signal of about 0.1 volt was obtained. No detailed analysis of the flow field in this crude device was possible, instead the construction of a versatile and controllable test facility has begun.

POWER OUTPUT AND EFFICIENCY

In order to judge the potential of bow shock generators for power conversion, one would like to estimate the efficiency of the device. An upper limit for the power extraction can be obtained by multiplying the open circuit voltage by the short circuit current. The short circuit current can be estimated from (II). We assume $\varepsilon_{io} \gg \varepsilon_{eo}$ and treat the case of strong ionization, where $n_i \varepsilon_{ie} \gg n_o \varepsilon_{eo}$. Then one finds

$$\vec{J}_m \cong \frac{e\,\mathrm{grad}\,p_e}{n_o \varepsilon_{eo}} = \frac{e}{n_o}\frac{3}{4}\sqrt{\left(\frac{\pi}{8kTm_e}\right)}\,\frac{1}{\sigma_{eo}}\,\frac{\Delta(n_e kT)}{\Delta x} \qquad \text{(VIII)}$$

If one approximates $\Delta(n_e kT) \sim kT\Delta n_e$ and estimates the scale length $\Delta x = 1/n_e\sigma_{io}$, the short circuit current becomes

$$J_m = e\frac{3}{4}\sqrt{\left(\frac{\pi kT}{8m_e}\right)}\,\frac{\sigma_{io}}{\sigma_{eo}}\,\Delta n_e \qquad \text{(IX)}$$

The open circuit voltage was derived above as $V \approx \Delta kT/e \approx kT_2/e$. Hence an upper limit of the power density is $w_m = V_o J_m$ (watt/m^2)

$$w_m = \frac{kT_2}{e} \times e\frac{3}{4}\sqrt{\left(\frac{\pi}{8}\right)}a_{e2}\,\frac{\sigma_{io}}{\sigma_{eo}}\,\Delta n_e \qquad \text{(X)}$$

where $a_{e2} = (kT_2/m_e)^{1/2}$ is approximately the acoustic speed of the electrons on the hot side of the standing shock. For typical values of the collision cross sections σ_{io} and σ_{en} one has

$$w_m = 0.05\, kT_2 a_{e2}\Delta n_e \qquad \text{(XI)}$$

and for a total surface area A_s one has the power output

$$W_m = w_m A = kT_2\, 0.05\, a_{e2} n_2 A_s$$

The efficiency of the bow shock generator in a Laval nozzle may be estimated with reference to Fig. 10. The power flux through the throat of the Laval

AD-A091 010 HEBREW UNIV JERUSALEM (ISRAEL) F/G 20/4
PROCEEDINGS OF THE INTERNATIONAL SYMPOSIUM ON SHOCK TUBES AND W--ETC
FEB 80 A LIFSHITZ, J ROM AFOSR-78-3679
UNCLASSIFIED AFOSR-TR-80-1141 NL

5 OF 8
AD
A091 010

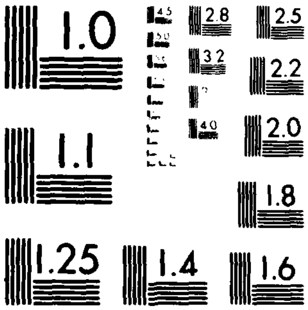

MICROCOPY RESOLUTION TEST CHART
NATIONAL BUREAU OF STANDARDS 1963 A

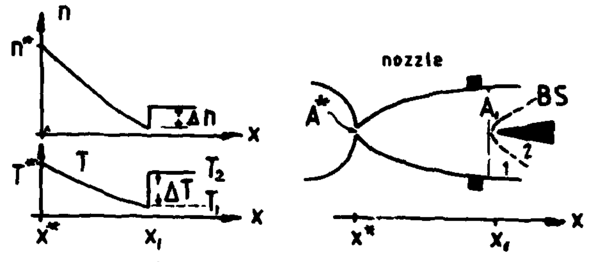

Figure 10. Fluid parameters T and n in supersonic nozzle with wedge and standing shock BS. A_1 is the area of the nozzle at position X_1.

nozzle containing a fully ionized gas is approximately

$$P = v^* \, 2n_e^* kT^* \, A^* \qquad \text{(XII)}$$

where A* is the throat area, and the flow velocity v* equals the speed of sound a* in the nozzle. The generator efficiency is then

$$\eta_m \leq \frac{W_m}{P} = \frac{0.05}{2M_1} \frac{T_2}{T^*} \frac{\Delta n_e}{n_{e1}} \frac{a_{e2}}{a_1} \frac{A_s}{A_1} \qquad \text{(XIII)}$$

where we have used the condition $n_1^* a^* A^* = v_1 n_{e1} A_1 = M_1 a_1 n_{e1} A_1$. The Mach number in the nozzle ahead of the standing shock, M_1, is of the same order as the compression ratio $\Delta n_e/n_{e1}$ across the shock. If the temperature T_2 rises in the shock compressed region to about the same value as T^* the efficiency can be approximated as

$$\eta_m \lessapprox 0.02 \frac{a_{e2}}{a_1} \frac{A_s}{A_1} \qquad \text{(XIV)}$$

It depends not only on the ratio of the hot electron sound speed a_{e2} to the cold ion sound speed a_1 but also on the ratio of the bow shock area A_s to the nozzle area A_1 at the position 1. Clearly the estimate (XIV) is an upper limit and we do not place too much confidence in the value of the numerical constant, but it appears that one could obtain efficiencies of a few percent if a reasonable fill factor A_s/A_1 can be achieved. Such an efficiency may be significant if a bow shock generator is used (similar as an MHD generator) as a topping device of a conventional thermal power plant.

Equation (XIV) points to the importance of covering large areas of a flow field with bow shock diodes and at the same time keeping the current paths through the plasma short (to minimize the internal resistance). We believe that both ends can be met with arrays of parallel bow shock generators, as shown in Fig. 11. We have set into operation a second shock tube with larger cross section (3x3 cm) which is capable of accomodating several wedges. One design has the two electrodes mounted on opposite side of the wedge body, so that series and parallel circuits can be tried.

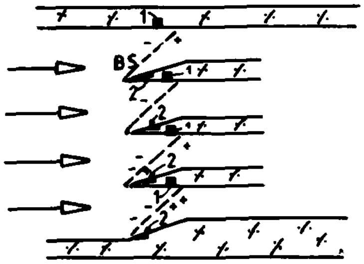

Figure 11. Array of wedges to produce several standing shocks across a supersonic flow field. The electrodes 1 and 2 connected to the fluid ahead of and behind the standing shocks are mounted in insulating material.

REFERENCES

1. Petchek and Byron, Annals of Phys. *1*,270 (1957).
2. M.Y. Jaffrin, Phys. of Fluids *8*, 606 (1965).
3. D.A. Tidman and L.L. Burton, Phys. Rev. Lett. *37*, 1397 (1976).
4. J.A. Stamper, E.A. McLean and B.H. Ripin, Phys. Rev. Lett. *40*, 1177 (1978).
5. A. Raven, O. Willi and P.T. Rumsby, Phys. Rev. Lett. *41*, 554 (1978).
6. R. Wienecke, Zeitsch. Naturforschung *18a*, 1151 (1963).
7. S.A. Kaplan, Interstellar Gas Dynamics, 2nd ed., Pergamon Press, 20 (1966).
8. B. Elmegreen and C. Lada, private communication, (1976)
9. P. Redfern and B. Ahlborn, Can. J. Phys. *50*, 1771 (1973).
10. J.B. Heywood, MIT Fluid Mechanics Laboratory, Publ. No. 65-1 (1965).
11. T.E. Horton and W.A. Menard, Jet Propulsion Laboratory Technical Report 32-1350 (1969).
12. B. Armstrong, B. Ahlborn, S. Mikoshiba and J. Tulip Can. J. Phys. *56*, 17 (1978).

INTERACTIONS BETWEEN AN E-BEAM SUSTAINED DISCHARGE AND SUPERSONIC FLOW

E. MARGALITH and WALTER H. CHRISTIANSEN

University of Washington, Seattle, Washington, USA

Two problem areas which result from the interaction of electrical discharges in supersonic flow are experimentally investigated. The first is the effect of the flow on the transition from glow to arc. Static discharges are also observed and compared to the transition of a discharge in flow. A large difference in the performance limits between the two cases is shown. Second, density disturbances which result from the nonuniform heat release in the cathode fall are studied. The resulting thermal layer near the cathode surface was carefully examined in static discharges. The measured thickness of the layer cannot be accounted for by gas kinetic values of the diffusivity. Based on observations, a model for the phenomena is suggested which correlates with the measurements. The important role of the boundary layer in determining glow to arc transition of the discharge is emphasized experimentally. By removing the cathode surface from the existing boundary layer into the core flow, the power loading per unit volume is found to increase by a factor of two.

INTRODUCTION

High pressure, large volume glow discharges have become an important topic in recent years due to the development of high power electric lasers. Supersonic flows are often used in the discharge region of these lasers to provide cyrogenic temperatures for operation and to remove waste heat.[1-6] The theoretical performance of these systems using a combination of electric discharge and supersonic flow are very attractive. But problems have been encountered experimentally which affect the performance and efficiency of the laser system. It is known, for example, that the energy per unit mass that can be deposited in the gas by the discharge is much lower than predicted, due to early glow to arc transition. Additionally, enhanced boundary layer growth in the region of the discharge reduces useful volume of the test section as well as causes undesirable density disturbances in the core flow. While there is considerable published material in the field of laser performance, little of it has been devoted to the basic interaction of the flow and discharge physics in closed channels.

A small scale experiment was designed and built to simulate a continuous e-beam controlled discharge in steady supersonic flow in order to investigate some of the problems. Quasi-steady flow is provided by a Ludwieg tube. A plasma-diode electron-beam gun is adopted and used for the first time in a supersonic system for the ionization source. The high current density of this gun results in high power loading in the sustained discharge which enables the small scale experiment to simulate larger thermionic systems. In order to determine the effect of flow on the transition from glow to arc, the characteristics of discharges without an external flow were observed and compared to discharges with flow. The transition to arc in static discharges was also observed and compared to discharge breakdown in flow. Based on observations, a correlation was developed between the time lag for breakdown and the electrical energy deposited in the gas prior to the arc.

Density disturbances, resulting from the heat release in the cathode fall, were carefully observed in the static experiments using laser interferometry. The acoustic wave originating at the cathode at the initiation of the discharge has been previously investigated by others[7,8] for different conditions; however, the thick thermal layer which follows the wave was omitted from their discussions. This layer was examined carefully in the present research. The measured thickness of the disturbance cannot be accounted for by gas kinetic values of diffusivity. A model is proposed which suggests that heat transfer occurs by convectively enhanced diffusion. The results obtained in static experiments are used to help explain the interaction of the flow boundary layer with the discharge.

THE EXPERIMENTAL SETUP

The experimental setup is composed of three main systems which can be controlled independently: the flow system, the electron-beam gun, and the main discharge. The flow is provided by a Ludweig tube and nozzle arrangement. Premixed gas is expanded to $M = 3.2$ via a contoured 2-D nozzle to temperatures and pressures on the order of 80°K and 100 Torr, respectively. In this apparatus, following a starting process of 1.5 milliseconds, quasi-steady flow is obtained for approximately 8 milliseconds. As the duration of the discharge is only on the order of 0.5 milliseconds, it is easy to synchronize it and operate it during the steady flow conditions. The Mach number, flow quality, and boundary layer thickness were examined by laser holographic interferometry and pressure measurements and found to be within the nominal design requirements.

An electron-beam gun, which is located above the test section, is used as an external source of electrons that preionizes the gas and provides the necessary conditions to sustain the discharge. A plasma diode e-beam gun, as described by O'Brien,[9] is adopted and used for its high current density emission and the simplicity of its operation. It can operate with current density outputs more than one order of magnitude greater than that of thermionic guns. The cross section of the gun is shown in Fig. 1. The discharge takes place in a pyrex cylinder (1) filled with ultra pure He at pressures from 20 to 70 millitorr. An aluminum cathode (2) is centered in the pyrex cylinder with about 0.12 cm gap around the walls. The edges of the cathode were carefully rounded. The cathode is typically placed about 17.8 cm above the anode (3) which has a rectangular opening corresponding to the size of the discharge in the test section. The e-beam chamber is separated from the test section by a 1 mil Kapton foil, through which high energy electrons can penetrate to the test section. Complete details can be found in Ref. 10. Power was supplied from a capacitor bank charged to a voltage of

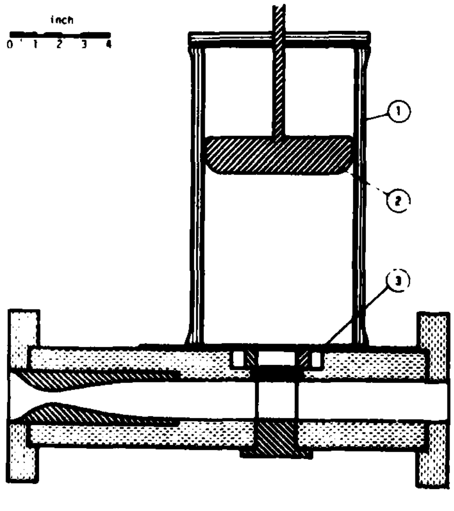

Fig. 1 Cross Section of the Test Section

135 kV. Even at the highest current setting the resulting voltage drop on the capacitor bank was only 10% for a 1/2 millisecond run time, thus simulating nearly constant voltage during the experiment.

The main discharge is applied across two electrodes in the test section. The power for this discharge is supplied by a separate capacitor bank with large energy storage. The initiation and termination of the discharge is done separately from the e-beam. The flow test section is 4 cm in height and 20 cm wide with the electrode spacing equal to the test section height. The discharge dimensions are 4 cm in the flow direction and 14 cm transverse to it, thus giving a 4 cm insulating region on each side of the discharge to prevent interaction with the side wall boundary layer.

DISCHARGE CHARACTERISTICS AND BREAKDOWN

Measurements of the sustainer discharge characteristics in N_2 were carried out first. A typical oscilloscope trace from which the discharge characteristics were obtained is presented in Fig. 2. The e-beam discharge is turned on first (upper trace) and the sustainer voltage is applied 100 μsec later (center and lower traces) to allow the e-beam current to reach steady state. Over the entire range of experiments (100 Torr to 400 Torr), the discharge is found to be recombination dominated[10] and the current density, J_s, is given by

$$J_s = n_e v_d e = fn(E/N) \sqrt{J_{eb} N} \qquad (1)$$

where n_e is the electron number density, v_d is their drift velocity, J_{eb} is the e-beam current density, and E/N is the ratio of sustainer field strength to gas number density. These results from the static experiments may be put into one curve by plotting $J_s/\sqrt{J_{eb}N}$ versus E/N, as shown in Fig. 3. The points show almost linear dependence of the two parameters in a wide range of experimental conditions. Similar current-voltage measurements were also performed in flow with N_2 as the test medium. The discharge was also found to be recombination dominated, as in the static case. The presentation of the data in the case of the flow experiments is based on the computed free stream density. As in the static case, the electrical field strength is taken to be equal to the ratio of the applied voltage divided by the electrode gap. These data fall along the curve established by the static measurements. The slope agrees very well with the static

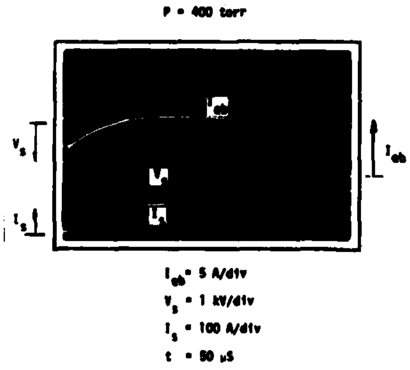

Fig. 2 Voltage and Current Traces

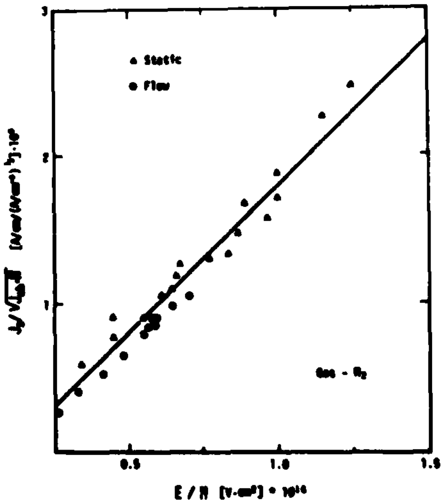

Fig. 3 Unified Discharge Characteristics

cases. This correlation shows that the free-stream density controls the current-voltage characteristics in flow situations. Similar experiments were performed in mixtures of N_2 and Ar and similar correlation was found between the flow and static discharge parameters.

Discharge breakdown experiments were intentionally performed in the sustainer to determine the upper voltage limits of its performance. The experiments were conducted in a mixtures of 90% Ar and 10% N_2 rather than in pure N_2 because of the lower voltages required to initiate an arc in Ar mixtures. Thus, high energy release by the arc and subsequent possible damage to the sustainer are avoided. Arcs are observed to occur in both flow and static experiments at different times after the initiation of the discharge. Since the time that a molecule stays in the discharge in flow varies from 80 μsec approximately in the free stream to infinity at the test section walls, it is suggested that the transitions from the glow to arc with times less than 80 μsec are subject for comparison.

It is observed that the time required for an arc to develop depends on many discharge parameters. Based on preliminary experiments, it was found that the best correlation of data was the time to arc versus power loading of the discharge. Additional experiments were carried out and the time to arc, t_{arc}, was plotted as a function of $E/N \cdot J_s$ and is presented in Fig. 4. Each point on the graph corresponds to the average power introduced to the gas in the time interval prior to the arc. In other words, each point determines the energy deposited per unit mass during the glow discharge stage of the process. The curve of constant energy is an hyperbola, one of which at 350 J/gram, is shown in the figure. The somewhat sparse and scattered data makes it difficult to state that t_{arc} is directly related to the energy deposition, but a trend is observed. The results from flow experiments (N based on the free-stream density) are contained in the same figure for comparison. It is easily seen that the electrical power input for a given time to arc is considerably smaller by a factor of at least 3 to 4 in the discharges with flow than in the static case. While the ratio of field strength to the free-stream density was used successfully to compare the current-voltage characteristics of the discharge between the static and the flow experiments, the correct value of E/N for comparison between the discharge breakdown characteristics is more in doubt. From measurements of the electrical field strength distribution done elsewhere,[6] it can be assumed that the electric field distribution is independent of the gas conditions and nearly represented by the average field strength E. But the gas density varies from the free stream value to less than a quarter of it in the boundary layers of the flow situation as the temperature varies from 70°K to 300°K. If E/N was computed on the basis of the density at the wall rather than at the free stream value, the results of the two experiments would fall more closely together. This observation implies that if the energy deposition is the parameter controlling the arc, the presence of the boundary layers is a cause for the breakdown in the flow.

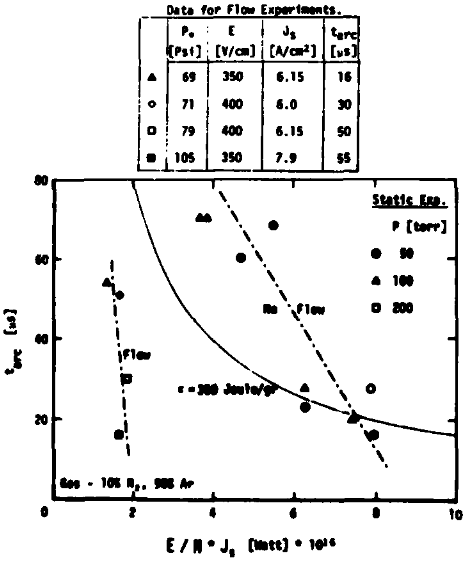
Data for Flow Experiments.

	P_o [Psi]	E [V/cm]	J_s [A/cm²]	t_{arc} [μs]
▲	69	350	6.15	16
○	71	400	6.0	30
□	79	400	6.15	50
■	105	350	7.9	55

Fig. 4 t_{arc} as Function of the Power Input.

THE EFFECT OF THE SUSTAINED GLOW DISCHARGE ON THE FLOW BOUNDARY LAYERS

(a) The Interaction Mechanisms

The primary interaction between the electric discharge and the flow is through heating of the gas. Measurements have shown that approximately 5% to 10% of the discharge energy shows up as heat in the supersonic core flow region.[8,10] The turbulent boundary layers are affected by the discharge because of an adverse pressure gradient due to volumetric heat release in the confined supersonic core flow.[11] The boundary layers are also subject to volumetric heat addition, but, due to density variations in the boundary layer, the heat deposition process is non-uniform. The trend of this process has been evaluated[10] and it can be shown that the heat deposition per unit mass, ε, is proportional to $\rho^{-a}t_{bl}$, where a varies between 0 and 1, depending on the gas, and ρ, the density within the boundary layer varies, of course. The parameter, t_{bl}, is the time at which a fluid element is exposed to the discharge within the boundary layer and is equal to $\int_0^\ell u^{-1}dx$. Very near the cathode this result is no longer valid as the plasma is not neutral. In this region the volumetric heat release is orders of magnitude larger than in the rest of the boundary layer and core flow. The region is very thin, being on the order of 10^{-3} cm thick[12], so that this heat release may be treated as a surface heating phenomenon. The gas at the wall expands drastically and moves away from the cathode, causing streamline deflections in the boundary layer. In supersonic flow, a stationary oblique compression wave is developed at the cathode leading edge through which the flow is turned.[12]

The first two processes are independent of the discharge polarity and are as effective on the anode side of the boundary layer as on the cathode side. The latter process is related only to the cathode as it stems from the cathode fall region. From interferograms in various discharge and flow conditions it is observed that the boundary layer on the cathode side exhibits much higher growth rates than the one on the anode side. This points out that the adverse pressure gradient and volumetric heating influence on boundary layer growth is less than the cathode surface heating phenomena.

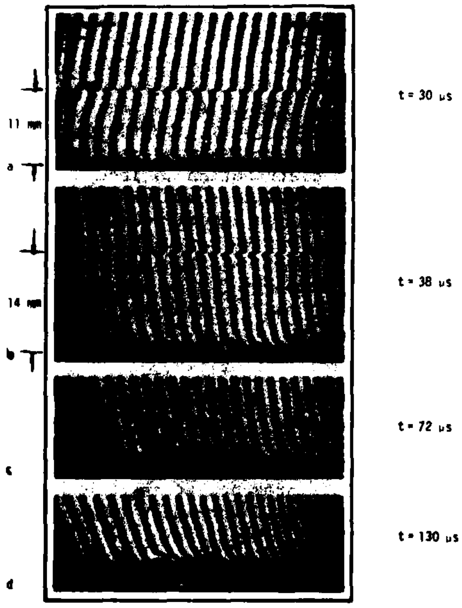

ρ = 300 torr N_2.

Fig. 5 Interferograms of the Density Disturbances at the Cathode in a Static Discharge, $\frac{\Delta\rho}{\rho_\infty} \approx 4.2\%$/fringe shift

(b) Static Discharge Investigation

The cathode fall thickness is thought to be on the order of 10^{-3} cm, whereas the boundary layer thickness is measured on the order of 1 cm. Thus, the flow speed is small in the region of the cathode fall. Experiments were therefore carried out under static conditions in order to observe more easily the details of the cathode phenomena. Density disturbances resulting from the heat release in the cathode fall were carefully observed. Fig. 5 presents interferograms of a series of static discharge experiments which were performed in N_2 at 300 Torr. The sensitivity, $\Delta\rho/\rho_\infty$ = 4.2% per fringe, is based on the cathode width of 14 cm. The local increase of the density variation at the cathode edges is neglected. The interferograms are taken at times specified on each picture. In all these experiments, the e-beam current was 14 amps at 110 kV ($J_{eb} = 15$ ma/cm^2). At a sustainer voltage of 3 kV, the resulting sustainer current was nearly constant at 260 amps. The light from a laser interferometer is separately recorded in order to determine the time at which the hologram is taken. The times indicated in the figure are measured from the initiation of the sustainer discharge.

A wave, which propagates away from the cathode, is seen in the first two pictures. The source of this wave is the density disturbance associated with the layer due to cathode fall heating. Very little disturbance and no wave were seen on the anode side of the discharge. From the position of the wave and the time indicated, the average wave speed is calculated to be 360 meters per second, or within a few percent of the sound speed in unheated N_2. The density variation across the wave is on the order of 1/2 fringe shift. The corresponding velocity behind the wave can be estimated from acoustics[13] to be

$$v_\delta = a_\infty \frac{\Delta\rho}{\rho_\infty} = 360(1/2)(0.042) \approx 7.5 \text{ m/sec} \qquad (2)$$

where $\Delta\rho$ is the density variation, a_∞ and ρ_∞ are the sound speed and a density of the undisturbed gas.

Another phenomenon on the interferograms is the relatively thick density variation adjacent to the cathode. The growth rate of the layer at the cathode, as measured from subsequent pictures, is on the order of 40 m/sec. The gas velocity, computed above, cannot account for it, nor can the thickness be explained on the basis of ordinary thermal diffusion. In fact, the gas-kinetic diffusivity is from two to three orders of magnitude too small to explain the observation. Other possible mechanisms, such as higher heat conductivity due to the partially ionized gas or non-uniform electron density that could enhance a non-uniform heating rate, were eliminated on the basis of other measurements.

A closer look at the details of the density variations unveils non-uniformities in the density profiles. The fact that the interferogram is averaged along the whole cathode width implies that there are areas where the gas withstands higher heating and the density is much lower than is seen on the hologram. To verify this observation, photographs of the cathode were taken during a 20 μsec discharge pulse. These are shown in Fig. 6. These photographs show a large non-uniformity in illumination over the cathode surface, thus implying a non-uniform current distribution and heat release at the cathode surface. This observation suggests that the discharge current is confined to small areas rather than covering the entire cathode surface, which is a phenomena of the normal glow discharge. From these pictures and interferograms a model is proposed where local heating gives rise to a small scale flow with an apparent heat conductivity orders of magnitude greater than the gas kinetic value. To evaluate this idea, a detailed study of the interferograms is necessary.

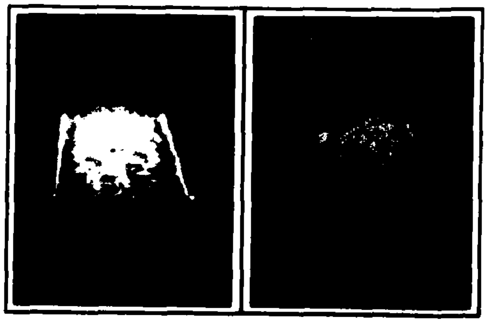
P = 100 torr

P = 300 torr

$t_{pulse} = 20$ μs

Fig. 6 Open Shutter Photographs of the Cathode Glow.

Fig. 7 shows the density profiles as measured from the holograms in Fig. 5. These curves are results from measurements at a few horizontal locations on each hologram and averaged to eliminate the small scale density fluctuation. The profiles can be represented by a single curve using the following transformations. Define $\eta \equiv y/\delta$, $\bar{\rho} = \rho/\rho_\infty$, $\bar{\rho}_w = \rho_w/\rho_\infty$ where δ is the layer thickness and the subscript w refers to the wall. Forming a dimensionless group by $\hat{\rho} = (1-\bar{\rho})(1-\bar{\rho}_w)^{-1}$, the reduced density is plotted vs. η and shown in Fig. 8. The analytic expression

$$\hat{\rho} = (1 - \eta)^{1.5} \tag{3}$$

well approximates the data. Using this result with the one dimensional form of the continuity equation

$$\frac{\partial\rho}{\partial t} + \frac{\partial}{\partial y}(\rho v) = 0 \tag{4}$$

the velocity distribution in the layer may be obtained. Integrating Eqn. 4 with respect to y gives

$$v = \frac{\rho_\infty}{\rho}\int_0^y \frac{\partial}{\partial t}\left(\frac{\rho_\infty-\rho}{\rho_\infty}\right) dy' \tag{5}$$

treating ρ_∞ as a constant. Introducing Eqn. 3 and carrying out the integration gives

$$v = \frac{1}{\bar{\rho}}\left\{v_\delta + 1.5(1-\bar{\rho}_w)\frac{d\delta}{dt}\left[\frac{(1-\eta)^{2.5}}{2.5} - \frac{(1-\eta)^{1.5}}{1.5}\right] + \delta\frac{d\bar{\rho}}{dt}\frac{(1-\eta)^{2.5}}{2.5}\right\} \tag{6}$$

The velocity at the edge of the layer is given by

$$v_\delta = 0.4\frac{\partial}{\partial t}\left[\delta(1 - \bar{\rho}_w)\right] \tag{7}$$

The product $\delta(1-\bar{\rho}_w)$ can be obtained from the profiles in Fig. 7 and is shown as a function of time in Fig. 9. The slope of this curve is nearly constant after 20 μsec. Using Eqn. 7, these results give a speed equal to 8.5 m/sec. The result is in rough agreement with the previous estimate of the flow behind the acoustic wave. The velocity distribution within the cathode layer is shown in Fig. 10 at 50 μsec by the solid line.

Integrating the inviscid 1-D momentum equation shows that the pressure change across the layer is on the order of $\rho_\infty v_\delta^2$. For the current experiments, this is less than 1 torr and can be neglected. Thus, from the equation of

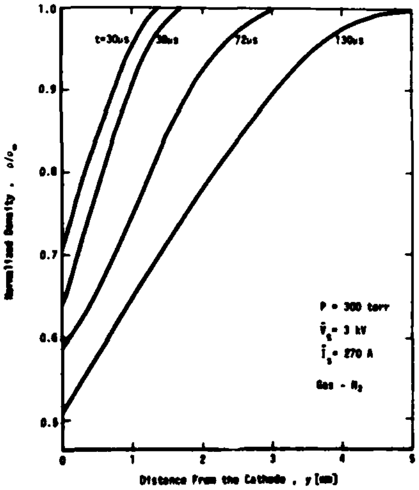

Fig. 7 Density Profiles behind the Cathode Wave

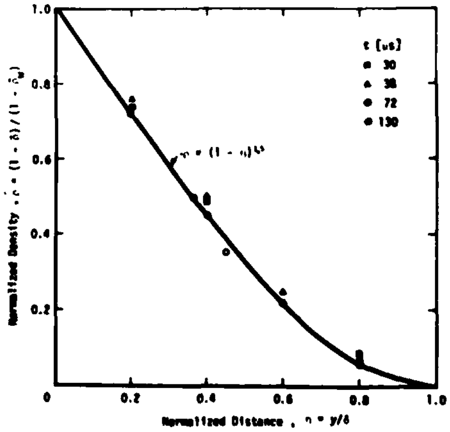

Fig. 8 Normalized Density Profile

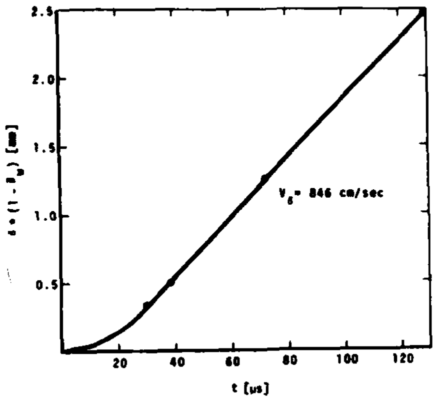

Fig. 9 The Product $\delta \cdot (1-\bar{\rho}_w)$ as a Function of Time

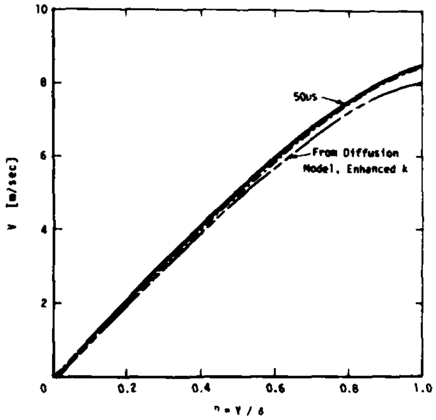

Fig. 10 The Velocity Distribution in the Thermal Layer

state of a perfect gas, the relation between temperature and density is

$$T/T_\infty = \rho_\infty/\rho \tag{8}$$

The temperature profiles deduced from the density curves are shown in Fig. 11.

The temperature distribution described by the results of Fig. 11 may be analyzed by using the enthalpy equation outside the cathode fall region. Neglecting body forces, dissipation, and taking the pressure to be uniform in space gives

$$\frac{\partial \rho h}{\partial t} + \frac{\partial \rho v h}{\partial y} = \frac{\partial p}{\partial t} + \frac{\partial}{\partial y}\left(k\frac{\partial T}{\partial y}\right) + J\cdot E_{eff} \tag{9}$$

where h is enthalpy and k is the thermal conductivity. Near the cathode fall, it is estimated that $\frac{\partial}{\partial y}(k\frac{\partial T}{\partial y}) >> J \cdot E_{eff}$ giving

$$\frac{\partial \rho h}{\partial t} + \frac{\partial \rho v h}{\partial y} = \frac{\partial}{\partial y}\left(k\frac{\partial T}{\partial y}\right) + \frac{\partial p}{\partial t} \tag{10}$$

If pressure variations are neglected (ρh = const, $\frac{\partial p}{\partial t} = 0$), Eqn. 10 can be integrated to give the velocity at the edge of the layer as

$$v_\delta = \frac{\gamma-1}{\gamma}\frac{q_w}{p} = -\frac{\gamma-1}{\gamma}\frac{k\,\partial T/\partial y|_w}{p} \tag{11}$$

where q_w is the heat transfer to the gas at the wall from the cathode fall (at $y=\delta$, $q=0$). Using $v_\delta = 8.5$ m/sec, q_w is calculated to be 114 w/cm^2 for the conditions of Fig. 5. This value is much smaller than the heat released in the cathode fall. Assuming a cathode fall voltage of 200 volts[6] and current density of 4.62 amp/cm^2, the heat release is 920 w/cm^2. Thus, most of the heat is conducted into the wall and little is conducted into the gas, as may be expected[8].

The temperature distribution can also be obtained using Eqns. 10 and 4. That is

$$\rho\frac{\partial h}{\partial t} + \rho v\frac{\partial h}{\partial y} = \frac{\partial}{\partial y}\left(k\frac{\partial T}{\partial y}\right) \tag{12}$$

Neglecting the convection term (estimated to be less than 10% of the first term) gives the ordinary heat diffusion equation for variable density. It is emphasized that k in this equation is as yet not known. Assuming the usual boundary layer assumptions that Pr = constant, $\rho\mu$ = constant, and using the transformation of the y coordinate as $\xi = \int_0^y (\frac{\rho}{\rho_\infty})dy'$, Eqn. 12 is reduced to

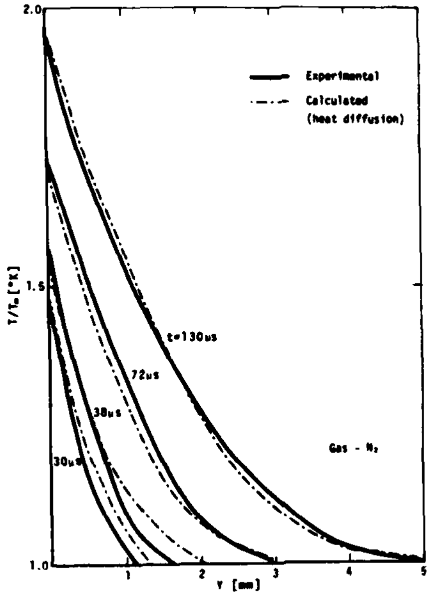

Fig. 11 Temperature Profiles

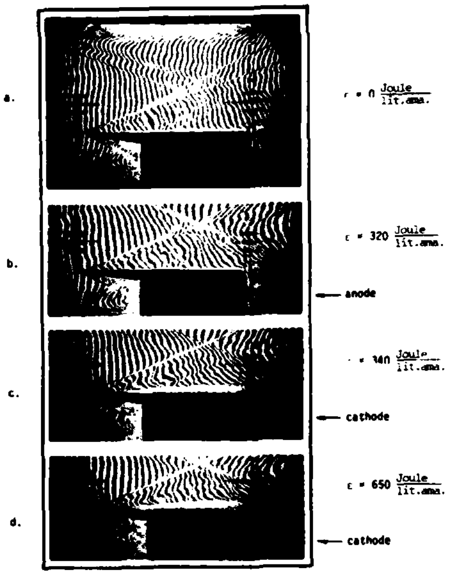

Fig. 12 Interferograms of the Raised Cathode

$$\frac{\partial h}{\partial t} = \alpha_\infty \frac{\partial^2 h}{\partial \S^2} \tag{13}$$

where α_∞ is the diffusivity $= \frac{k}{\rho c_p}$. The diffusion equation was solved for constant heat flux at the wall and found to be

$$h = h_\infty + \frac{q_w}{\rho_\infty \alpha_\infty \eta} \text{ ierfc } (\eta_\infty \S) \tag{14}$$

where $\eta = 1/2\sqrt{\alpha_\infty t}$. Assuming c_p is a constant, the temperature at the wall is

$$T_W = T_\infty + \frac{1.1284\ q_w\sqrt{t}}{\rho_\infty c_p \sqrt{\alpha_\infty}} \tag{15}$$

This functional dependence is in agreement with the temperature results @ y=0 shown in Fig. 11. Using $q_w = 114$ w/cm^2, the apparent heat diffusivity can be obtained from each of the curves in Fig. 11. On the average α_∞ is nearly a constant and equal to 88 cm^2/sec, a value 150 times the gas kinetic value. Using this result in Eqn. 14 yields the temperature variations as a function of space and time. The calculated values are shown in Fig. 11 for comparison. Using Eqn. 14, the result for v can be shown to be

$$v = v_\delta \text{ erf } (\S/2\sqrt{\alpha_\infty t}\ ) \tag{16}$$

This velocity relation is shown in Fig. 10 by the dashed line. Similar experiments were performed at different pressures and discharge conditions. However, the value of α_∞ was always larger than the gas kinetic value with the discrepancy getting larger at lower pressures. For example, α_∞ is about 450 times the gas kinetic value at p=100 torr.

(c) The Effect of Heat Release at the Cathode in Supersonic Flow

The contribution of the cathode phenomena to the boundary layer's growth can be separated experimentally from that due to volumetric heat addition. The effect of the cathode on the boundary layer is well shown in Fig. 12. A flat plate having the same planform as the cathode surface is placed above the wall boundary layer to serve as a sustainer electrode. Fig. 12a shows the density disturbances due to the presence of the plate in the supersonic flow without a discharge. A very thin boundary layer is observed as would be expected because of the nearness of the leading edge. There is not much change in this boundary layer when the discharge is applied, if the plate serves as the anode. When an equal voltage with opposite polarity is applied, the boundary layer thickness triples (Fig. 12c). Increasing the power to the discharge results in an even thicker layer (Fig. 12d). The oblique wave at the leading edge is clearly enhanced by the discharge in Figs. 12c and 12d. The relative density jump across the wave changes from 5 to 15 percent when sufficient power is applied.

This disturbance level can be estimated on the basis of the static results by the analogy between one-dimensional non-steady motion and two-dimensional supersonic flow[13]. When supersonic flow is superimposed on the discharge, the stream will deflect by the perpendicular outflow producted by excessive heating from the cathode side. It was found in static experiments that v_δ is constant with time, and from theory, it is only a function of the heat flux at the wall and the static pressure. The result for v_δ obtained from the static experiments can be applied to estimate the free stream deflection angle θ. By the principle of superposition, this angle is v_δ/U_∞. An oblique wave is then developed in the flow, with its origin at the cathode leading edge. The density ratio across the wave can be calculated from weak shock theory[13] as

$$\frac{\rho_2}{\rho_1} \simeq 1 + \frac{M^2}{\sqrt{M^2-1}}\,\theta \tag{17}$$

Applying the results for v_δ from the static experiments gives an estimate for θ which in turn is in qualitative agreement with the density changes measured across the wave.

In removing the cathode from the existing boundary layer as shown in Fig.12, the power loading per unit volume can be increased by a factor of two before arcing occurs. Energy input reached 1000 J/lit.ama. corresponding to 5000 w/cm^3 before the arc was developed after one flow time. This is a significant improvement in the flowing gas case and suggests that additional gains are possible when boundary phenomena in discharges are fully understood.

ACKNOWLEDGEMENT

This work was supported by the Department of the Air Force, Air Force Office of Scientific Research.

REFERENCES

1. W.H. Christiansen, D.W. Russell and A. Hertzberg, "Flow Lasers," Annual Reviews of Fluid Mechanics 7, 115 (1975).
2. E. Vallach et al, Appl. Phys. Lett. 10, 10,(1972).
3. J.H. Blom and R.K. Hanson, Appl. Phys. Lett. 26, 4, (1975).
4. J.W. Rich, R.C. Bergmann and J.A. Lord, AIAA Journal 13, 1, (1975).
5. M.J. Plummer, J.L. Wagner and W.J. Glowacki, IEEE J. of Quan.Elec.11,(1975).
6. E.L. Klosterman, S.R. Byron and D.C. Quimby, "Supersonic cw CO Parametric Investigation," Mathematical Sciences NW 76-1048-1, November (1976).
7. E.R. Pugh et al, Appl. Optics 13, 11, (1974).
8. F.E. Culick, P.I. Shen and W.S. Griffin, IEEE J.Quan. Elec.QE-12, 10, (1976).
9. B.B. O'Brien, Appl. Phys. Lett. 22, 503, (1973).
10. E. Margalith, "The Interaction between E-Beam Sustained Discharge and Supersonic Flow," Ph.D. Thesis, University of Washington, (1978).
11. A.H. Shapiro, The Dynamics and Thermodynamics of Compressible Fluid Flow, Vol. 1, Ronald Press Co., (1953).
12. C.G. Parazzoli, AIAA J. 15, 6, June (1977).
13. H.W. Liepmann and A. Roshko, Elements of Gasdynamics, John Wiley & Sons, Inc., London, (1957).

FLOW ASPECTS OF HIGH POWER GASDYNAMIC LASERS

J. D. ANDERSON, E. JONES, K. N. PARTHASARATHY

University of Maryland, USA

G. COLASURDO, M. S. OGGIANO, M. ONORATO

Politecnico di Torino, Italy

Some recent theoretical results on high power gasdynamic lasers obtained at the University of Maryland and at the Polytechnic of Torino are reviewed in this paper. Moreover new results concerning both premixed gasdynamic lasers and downstream mixing gasdynamic lasers are presented. These results refer to the effect of a multireflected shock wave on a lasing medium and to the influence of initial flow conditions on the mixing downstream of the nozzles exit.

INTRODUCTION

Since the suggestion of Hurle and Hertzberg[1] in 1965 that a lasing medium could be created in the rapid, nonequilibrium expansion of an initially hot gas through a supersonic nozzle, it was evident that the development of such lasers would involve the solution of complex fluidmechanical problems. The laser power output and the beam quality are strictly connected with the behaviour of the flow in the nozzle and in the cavity. Later on, with the advent of the concept of the downstream mixing gasdynamic lasers in 1970 [2], many and more complicated fluidmechanical problems arose.

The theoretical analysis of such flows has required the development of complete and sophisticated numerical methods, owing to their complexity and to the interaction between fluidmechanics and reaction rates.

The goal of this paper is to review some recent results obtained by means of numerical procedures at the University of Maryland and at the Polytechnic of Torino for the prediction of the performance of CO_2-N_2-H_2O gasdynamic lasers and to present new results concerning both premixed gasdynamic lasers and downstream mixing gasdynamic lasers.

PHYSICAL PROBLEMS AND METHODS OF ANALYSIS

a) Premixed Gasdynamic Lasers

In a conventional CO_2-N_2-H_2O premixed gasdynamic laser, the mixture of hot and high pressure gases is expanded very rapidly through a supersonic nozzle. Due to the rapid cooling, the mixture becomes a lasing medium and a beam of laser energy may be extracted from the cavity.

The nozzles are very short, generally minimum length nozzles, and the area ratio very high; the flow Reynolds number is generally low, particularly for the case of combustion driven gasdynamic lasers. Complex fluid mechanical phenomena occur, in which the viscosity may play an important role. Moreover, even if the molecular vibrational energy of the gas is a small amount of the total energy of the mixture, the phenomena related to molecular reactions are strictly coupled with fluidmechanical phenomena.

In order to study such internal flows, a sophisticated numerical analysis has been developed [3,4]. The reacting, nonequilibrium flow field into the nozzle is considered inviscid everywhere except in that region close to the wall where a viscous boundary layer develops. The coupling between the inviscid core and the viscous boundary layer is achieved by means of an iterative procedure. The flow in the inviscid core is considered two-dimensional and shock waves are allowed to develop.

The boundary layer is assumed as laminar. As far as the vibrational energy is concerned, the two extreme cases of fully catalytic and non catalytic wall are considered.

Following the kinetic model of Anderson [5] the vibrational relaxation of the mixture is described by two vibrational temperatures, T_{vib_1} for the ν_1 and ν_2 modes of the CO_2 and T_{vib_2} for the ν_3 mode of the CO_2 and the $v = 1$ level of N_2.

The vibrational energies are assumed as frozen through the shock.

b) Downstream Mixing Gasdynamic Lasers

In the downstream mixing gasdynamic laser, vibrationally excited N_2 is expanded through a supersonic nozzle and mixed with CO_2 and H_2O downstream of the nozzle exit. The transfer of energy from the N_2 to the CO_2 in the mixing region creates the lasing medium.

Two advantages are evident with respect to the convenctional premixed gasdynamic laser:

i) The reservoir temperature of N_2 can exceed 4000°K and then more vibrational energy in the gas is available for lasing with respect to the premixed configuration. For this one, there is an upper limit of 2300°K, because the CO_2 starts to dissociate above this temperature and the laser performance detiorates.

ii) More efficient freezing of the N_2 vibrational energy is obtained during the expansion, because of the absence of CO_2 and H_2O, which act as a contaminants on the N_2.

It is evident that the performance of the laser depends strictly on the behaviour of the flow in the mixing region and on the local interaction between reaction rates and fluid mechanics. Prediction methods must include all physical effects related to the mixing of reacting gases; this requires the development of reliable physical models and very complex computational methods.

Some results of a very precise and complete numerical analysis [6] will be shown here, where two-dimensional Navier-Stokes equations, fully coupled with the finite-rate vibrational rate equations, are solved. This analysis allows the direct calculation of axial and transverse pressure gradients as well as the temperature and gain profiles in the mixing region.

The analysis is refered to the case of very small nozzles and very low pressures, leading to Reynolds numbers on the order of 10^3. Hence, the mixing is assumed laminar.

Due to the low cavity pressures considered, the Anderson model for the vibrational energy is not appropriate for this study, because the assumption of instantaneous equilibrium between the ν_3 mode of CO_2 and the $v = 1$ level of N_2 leads to an overestimation of the gain. Hence, the three-vibrational temperatures model of Munjee [7] has been assumed.

RESULTS AND COMMENTS

The results shown in Figs.1 ÷ 12 refer to the case of premixed gasdynamic lasers, the results in Figs.13 ÷ 30 refer to the case of downstream mixing gasdynamic lasers.

For more detailed comments on Figs.1 ÷ 7 and on Figs.14 ÷ 22 the reader may refer to [4] and [6].

Promising results may be expected from the C_6H_6-Air combustion-driven gasdynamic laser. The optimal characteristics of this laser are [8]: the area ratio, $C_e/C^* = 72$; the throat hight, $C^* = 0.15$ mm; the mixture composition, $X_{CO_2} = 0.138$ $X_{N_2} = 0.788$, $X_{H_2O} = 0.074$; the pressure and temperature in the reservoir $p_o =$ $= 30$ atm, $T_o = 1955$°K. Few results are here shown related to the performance of this laser. Figs.1 ÷ 7 refer to a contoured nozzle. In Fig.1 isobares along the inviscid core are reported; the details of the two-dimensional expansion through the nozzle are clearly shown. In Fig.2 the pattern of the resulting small signal gain G_o (m^{-1}) is shown. In Figs.3,4 and 5 curves of constant static temperature T/T_o and constant vibrational temperatures T_{vib_1}/T_o and T_{vib_2}/T_o are reported. Results of the boundary layer calculations are shown in Fig.6 and 7 , where temperature profiles and the small signal gain G_o are displayed.

The wall temperature T_w is supposed to vary linearly from the value in the reservoir down to 300°K at the throat and then it remains constant. Results are shown for catalytic and noncatalytic wall. The similar type nondimensional coordinate η is defined as,

$$\eta = \left(\frac{u_e}{\rho_o \mu_o x} \right)^{\frac{1}{2}} \int_0^y \rho \, dy$$

where u_e is the velocity at the edge of the boundary layer, ρ_o and μ_o are the density and the coefficient of viscosity of the gas mixture in the reservoir, x is the curvilinear coordinate along the wall, y the transverse coordinate.

The boundary layer thickness at the exit station is $\delta(u = 0.99\ u_e) = 0.66$ mm, the displacement thickness is $\delta^* = 0.36$ mm (the nozzle length is shown in Figs. 1 ÷ 5).

In some configurations of practical interest, multireflected shock waves may occur in the cavity, downstream of the nozzle array exit or inside the nozzles, if these are not contoured. An example showing how a lasing medium may be affected by a multireflected shock wave inside the nozzle is reported in the next five figures. This refers to a gas mixture having the optimal characteristics[8] for a CO and N_2O combustion driven gasdynamic laser. The mixture composition is, $X_{CO_2} = 0.158$, $X_{N_2} = 0.831$, $X_{H_2O} = 0.011$; the pressure and temperature in the reservoir are, $p_o = 34$ atm and $T_o = 1862$°K. The nozzle area ratio is $C_e/C^* = 80$, the throat hight is $C^* = 0.15$ mm. The geometry of the nozzle is a 15.5 degrees wedge matched with a constant cross-sectional area duct.

The boundary layer has been neglected. Details of the shock development and of his downstream propagation are reported in Fig.8. In the wedge shaped portion of the nozzle, the pressure is about constant at each axial location; a shock originates downstream from the wall.

The results in Fig.9 must be observed in comparison with those in Fig.2. For the contoured geometry, the gain G_o increases continuously along the nozzle up to a value of about 1.5 at the exit section, where it shows a variation of about 7% going from the axis to the wall. The picture in Fig.9 is quite different , the small signal gain G_o decreases steeply through the shock, owing to the growth of static temperature and then starts to increase again downstream. It seems from Figs.11 and 12 that the vibrational energies are not greatly affected by the shock wave. The variation of G_o , from the axis to the wall, at the last section shown in the figure is about 17%.

All the following figures refer to results concerning the downstream mixing gasdynamic laser. Fig.13 illustrates the physical set-up of these lasers. Here, a supersonic stream of N_2 is mixed with a supersonic stream of CO_2 and H_2O. Typical dimensions of the nozzles considered are reported in the picture. The conditions of the two streams at the cavity inlet are tabulated in Table 1.

These conditions refer to results from Fig.14 to Fig.19. Nozzle wall boundary layers have been here neglected, the results refer to the fluid dynamics of the laminar mixing between two initially uniform, parallel streams. The velocity profiles at various x/h locations along the cavity are shown in Fig.14; at $x/h = 0$ the velocity ratio between the two streams is $u_1/u_2 = 0.5$, at $x/h = 200$, an almost uniform velocity is achieved across the complete flow-field. Static temperature profiles are displayed in Fig.15, where an increase of temperature is shown along the cavity, due to the viscous dissipation and to the collisional deactivation of vibrational energy to translational energy. Fig.16 is a plot of the N_2 mass-fraction profiles. The vibrational energy distributions in modes (12) and (3) of CO_2 are indicated in Figs.17 and 18. The small signal gain G_o

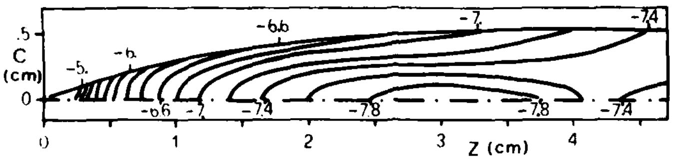

Fig.1
Contoured nozzle
$\ln\left(\frac{p}{p_0}\right)$ = const.curves

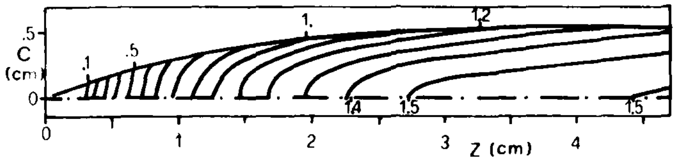

Fig.2
Contoured nozzle
G_0/m = const.curves

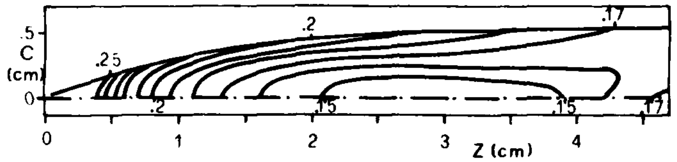

Fig.3
Contoured nozzle
$\frac{T}{T_0}$ = const.curves

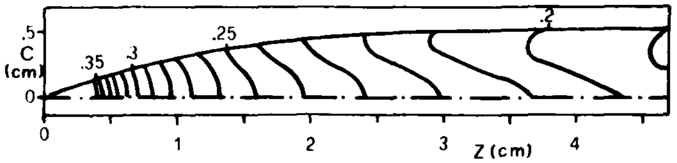

Fig.4
Contoured nozzle
$\frac{T_{vib1}}{T_0}$ = const.curves

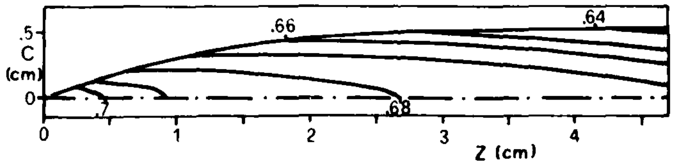

Fig.5
Contoured nozzle
$\frac{T_{vib2}}{T_0}$ = const.curves

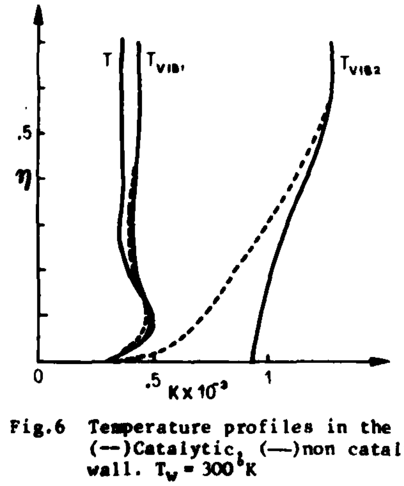

Fig.6 Temperature profiles in the B.L. (--)Catalytic, (—)non catalytic wall. T_w = 300°K

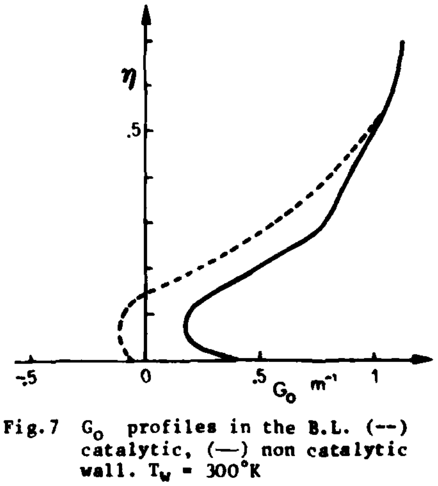

Fig.7 G_0 profiles in the B.L. (--) catalytic, (—) non catalytic wall. T_w = 300°K

Fig.8 $\mathrm{Ln}\left(\frac{P}{P_o}\right)$ = const. curves

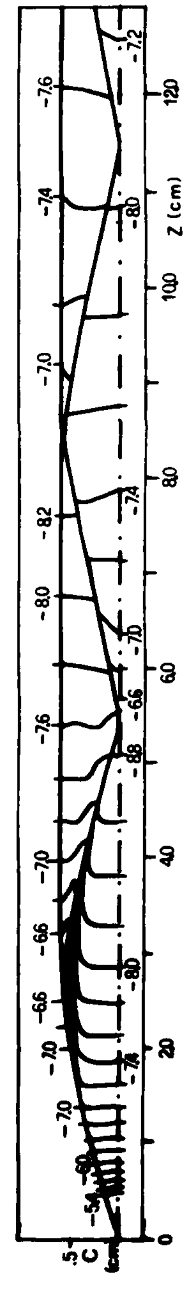

Fig.9 G_o/m = const. curves

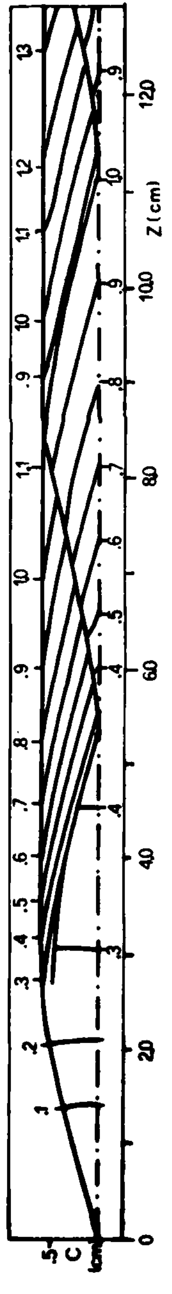

Fig.10 $\frac{T}{T_o}$ = const. curves

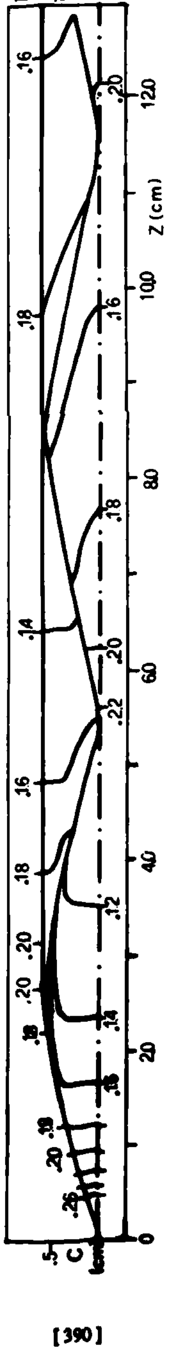

Fig.11 $\frac{T_{vib1}}{T_o}$ = const. curves

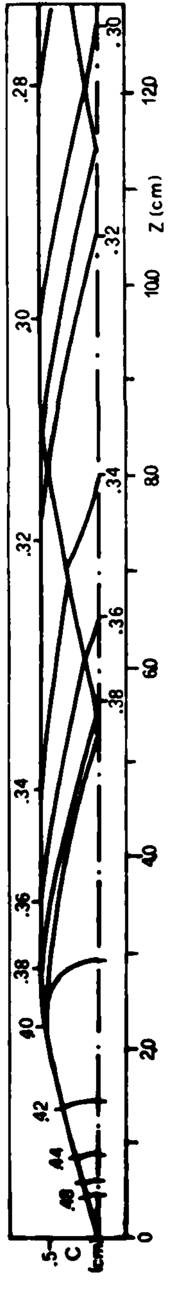

Fig.12 $\frac{T_{vib2}}{T_o}$ = const. curves

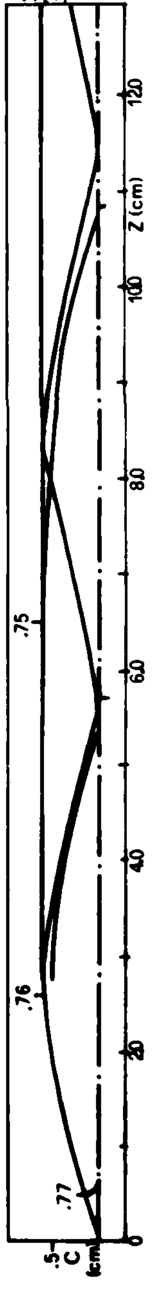

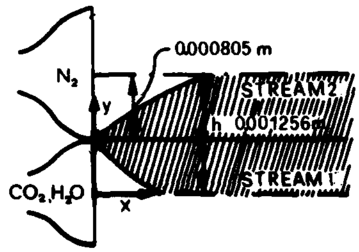

Fig.13 Nozzle configuration

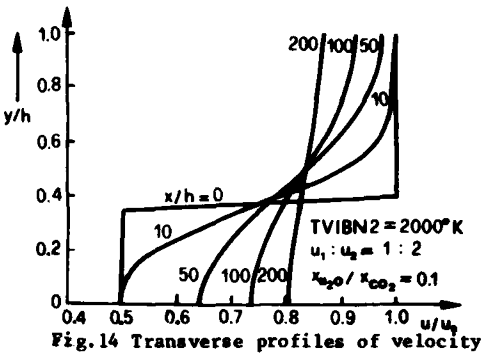

Fig.14 Transverse profiles of velocity at various axial locations in the cavity.

Table 1

	STREAM 1	STREAM 2
p n/m^2	656	656
T °K	300	300
ϱ kg/m^3	1.094×10^{-2}	7.36×10^{-3}
ϱ_{CO_2} Kg/m^3	1.051×10^{-2}	-
ϱ_{H_2O} Kg/m^3	4.280×10^{-4}	-
Mach No	3.3	5.3
T_{VIB} °K	300	2000

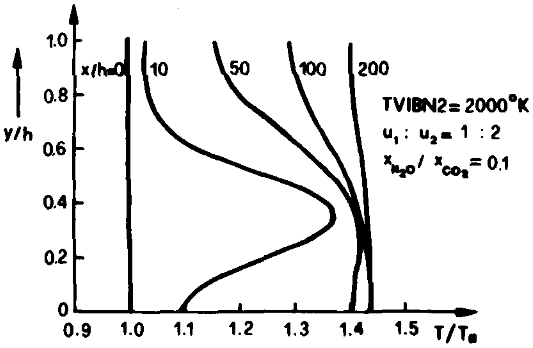

Fig.15 Transverse profiles of static temperature at various axial locations in the cavity.

Table 2

	STREAM 1	STREAM 2
p n/m^2	740	720
T °K	306	308
X_{CO_2}	0.96	-
X_{H_2O}	0.04	-
Mach No	2.94	5.22
T_{VIBN2} °K	-	1985
T_{VIB12} °K	524	-
T_{VIB3} °K	634	-

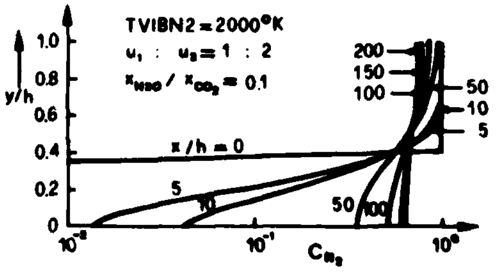

Fig.16 N_2 mass-fraction profiles.

profiles are shown in Fig.19, where values of G_0 at least a factor of two higher than a conventional premixed gasdynamic laser (with the same reservoir temperature) are demonstrated. In Figs.20, 21 and 22 the values of the gain, integrated with respect to y/h, are displayed along the mixing region.

The results in Fig.20 assess the influence of the initial velocity ratio of the two streams. It is shown that the one-to-one velocity ratio gives higher gain ; this is due to the fact that in this case the mixing is totally obtained by diffusion; the viscous dissipation is minimized and consequently the static temperature in the mixing region is kept lower than in Fig.15. The influence of the H_2O content on the integrated gain is shown in Fig.21; the best gain is obtained with no H_2O in the mixture (notice that a small amount of H_2O is required for power extraction). Fig.22 demonstrates the effect of increasing the vibrational temperature of the N_2 stream up to 4000°K; very high gains are obtained showing clearly the substantial improvements of the downstream mixing gasdynamic laser over the convectional premixed configuration.

Owing to the low Reynolds number involved, thick boundary layers will be originated within the nozzles. To study the effect of such boundary layers on the downstream mixing, calculations have been performed inside the nozzles, starting from the reservoir, in order to obtain the real gas conditions of the two streams at exit section. The nozzle wall temperatures, from the throat down to the exit section, have been considered constant and equal to 300°K. The case of noncatalytic wall has been considered. For the gas conditions of Table 1, boundary layers fill a large part of the nozzles; for both, the N_2 nozzle and the CO_2-H_2O nozzle the displacement thickness at the exit is about 20% of the section semi-heigth. Displacement thickness have been taken into account for the nozzle contours. The gas conditions at the nozzle exits, in the inviscid core, are tabulated in Table 2. Profiles of quantities in the boundary layers may be deduced from the diagrams describing the mixing region, for $x/h = 0$. In Fig. 23 profiles of velocity along the cavity are shown. Even if they are initially affected by the inlet velocity distributions, they become relatively uniform beyond $x/h = 150$; that is, the boundary layer structure does not persist for large distances from the nozzle exit. The same conclusions as above apply to the static temperature profiles displayed in Fig.24. However, the viscous dissipation is stronger than in the case of initially uniform profiles, leading to higher static temperature at large distances downstream from the nozzle exit.

This increase in static temperature tends to reduce the gain, as it will be shown. Fig.25 reports the N_2 mass-fraction profiles at various x/h locations. The vibrational energy distributions in modes (12) and (3) and in N_2 are indicated in Figs.26,27 and 28. Owing to the increased static temperature higher values of $e_{vib_{12}}$ are observed when compared with those in Fig.17.

Moreover e_{vib_3} and e_{vibN_2} result decreased at the lower centerline with respect to the case of initially uniform profiles, because the boundary layer profiles tend to inhibit the mixing and the diffusion of N_2 into the CO_2 stream (see Fig.25). As a consequence the small signal gain behaves as it is shown in Fig.29. The peak in the mixing region near the nozzle exit depends on the fact that the CO_2, H_2O and the N_2 molecules have a residence time in the boundary-layer mixing region longer than in the uniform profiles case. The negative gain in the regions near the lower centerline depends on the local behaviour of e_{vib_3} and $e_{vib_{12}}$.

Finally in Fig.30, the integrated values of G_0, obtained starting the mixing calculations with real initial conditions, are compared with the results obtained assuming uniform inlet profiles. The main result is that the peak small-signal gain, integrated across the duct, turns out to be about one half with respect to the case where nozzle boundary layers have been neglected.

ACKNOWLEDGMENT

The authors wish to acknowledge Miss Claudia Masotti for typing the manuscript with characteristic care.

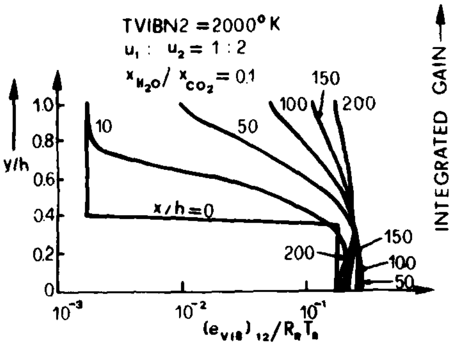

Fig.17 Profiles of vibrational energy in mode (12).

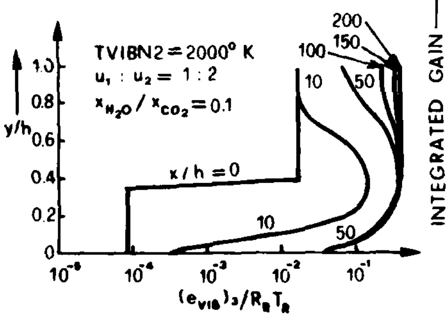

Fig.18 Profiles of vibrational energy in mode (3).

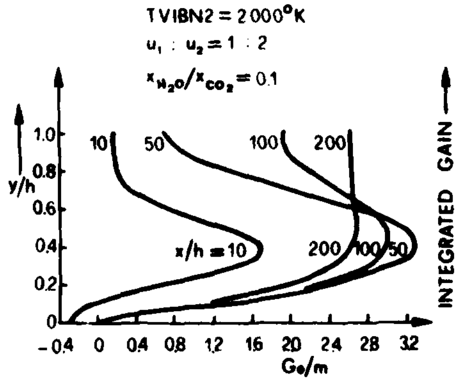

Fig.19 Transverse profiles of G_0 at various axial locations in the cavity.

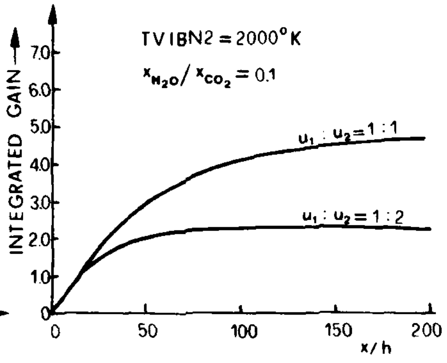

Fig.20 Variation of integrated gain with distance along the flow; comparison between different velocity ratios.

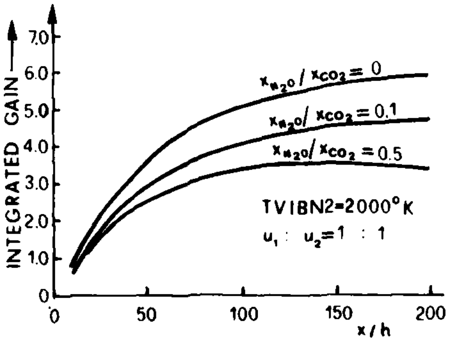

Fig.21 Variation of integrated gain with distance along the flow; comparison between different H_2O contents.

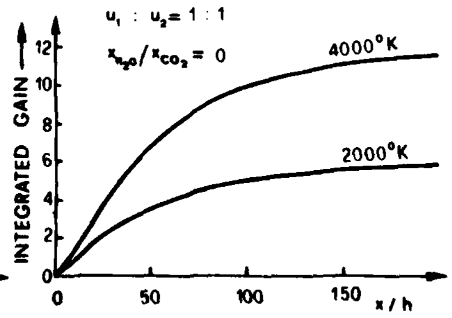

Fig.22 Variation of integrated gain with distance along the flow; comparison between different N_2 vibrational temperatures.

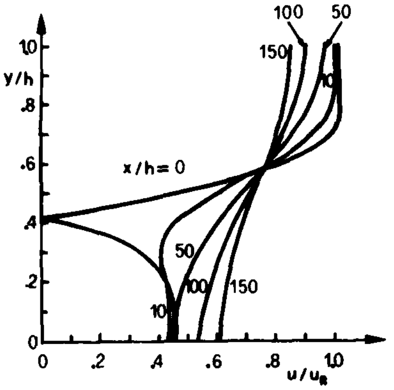

Fig.23 Transverse profiles of velocity at various axial locations in the cavity

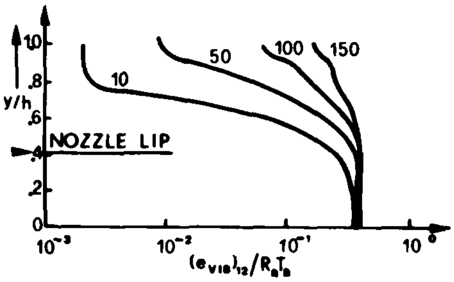

Fig.26 Profiles of vibrational energy in mode (12).

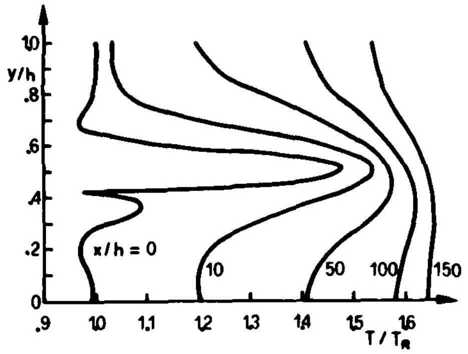

Fig.24 Transverse profiles of static temperature at various axial locations in the cavity.

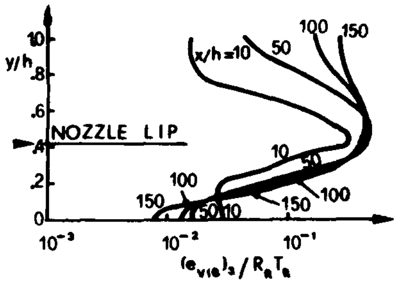

Fig.27 Profiles of vibrational energy in mode (3)

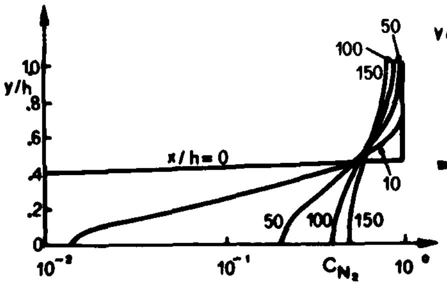

Fig.25 N_2 mass-fraction profiles

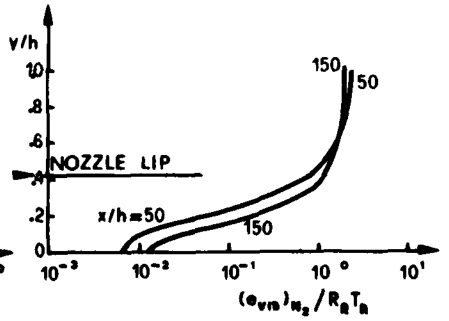

Fig.28 Profiles of vibrational energy in N_2

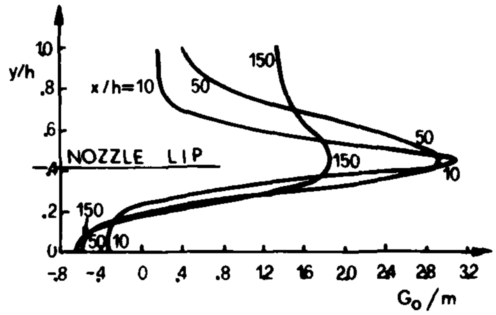

Fig.29 Transverse profiles of G_0 at various axial locations in the cavity.

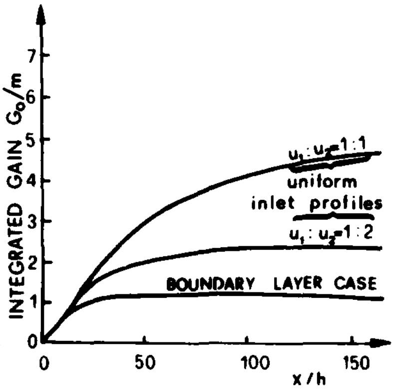

Fig.30 Variation of integrated gain with distance along the flow; comparison between the case of uniform inlet profiles and real inlet profiles.

REFERENCES

1. I.R.Hurle and A.Hertzberg, The Physics of Fluids, *8* , No.9 (1965)
2. B.R.Bronfin, L.R.Boedeker and Cheyer, Applied Physics Letters,*16*,No.5,(1970)
3. M.S.Oggiano, M.Onorato and M.Pandolfi, Proceedings of the Int.Symp.on Gasdynamic and Chemical Lasers, Köln, DFVLR-Press (1976)
4. G.Colasurdo, M.S.Oggiano and M.Onorato, Proceedings of the 2nd Int.Symp.on Gas-Flow and Chemical Lasers, Rhode-St-Génèse. Hemisphere Publ.Corp.(1978)
5. J.D.Anderson Jr., The Physics of Fluids,*13*, No.8, (1970)
6. K.N.Parthasarathy, J.D.Anderson Jr. and E.Jones, AIAA Paper No.79-0207,New Orleans, La.(1979)
7. S.A.Munjee, The Physics of Fluids, *15* , No.3 (1972)
8. R.C.Saunders III, L.J.Otten III, Proceedings of the Int.Symp.on Gasdynamic and Chemical Lasers, Köln, DFVLR-Press (1976)

SPHERICALLY CONVERGING SHOCK WAVES IN DENSE PLASMA RESEARCH

J. H. LAU, M. M. KEKEZ, G. D. LOUGHEED and P. SAVIC

Division of Mechanical Engineering
National Research Council, Ottawa, Canada

The collision of microscopic particles at high velocities (10^8 cm/sec) offers, in principle, the possibility of attaining plasmas of very high density and temperature. A study was made of the entrainment of such particles behind spherically converging shock waves. Analytical and numerical calculations show that submicron particles can be accelerated to a significant fraction of the gas velocity. A discharge chamber with shaped side walls was constructed to generate spherically converging shocks. Results to-date indicate that imploding speeds of about 10^7 cm/sec can be achieved. An approximate analysis suggests the use of a novel type of "laser beam plasma confinement" scheme, for which analytical expressions are derived.

INTRODUCTION

The use of spherically imploding shock and compression waves as a means of heating, compressing, as well as inertially confining plasmas, has recently received much attention in connection with laser pellet fusion. In this case the implosion is generated by surface ablation of a pellet by a converging optical beam. The use of shaped side walls of a shock tube in order to generate an imploding shock has been suggested by Milton and Archer[1]. Spherically convergent shocks were produced by Lau[2] from electromagnetically driven plane and cylindrical shocks. Lui[3] obtained toroidal focusing of a shock in a coaxial electromagnetic shock tube by using a suitably shaped end wall. The three methods are diagrammatically depicted in Fig. 1,a-c. The common feature in these approaches is the use of Whitham's theory[4] to calculate the appropriate shape of the end or side wall to generate the imploding shock. The requisite profile depends on the geometry chosen; starting with a plane shock, the convergence will, in general, produce a focus lying in the shaped wall (Fig. 1,a,c). However, if the initial shock is cylindrical (Fig. 1,b) the appropriate side walls end in cusps, hence the collapsing shock wave will generate a focus well away from any material surface. The effect of the side walls on the heat loss from and contamination of the plasma is therefore likely to be a minimum in the case of the cylindrical wave. For this reason, the latter geometry was chosen in our case.

WALL PROFILE CALCULATIONS

Whitham's[4] "ray-shock theory" is based on two partial differential

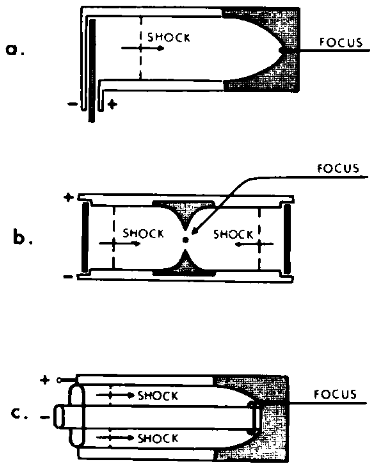

Fig. 1 Schematic diagrams of method of wall shape shock convergence.

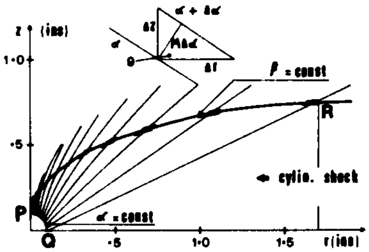

Fig. 2 Wall shape construction.

equations of hyperbolic type. If the cylindrical net (r,z) with the polar angle θ is chosen, the equations can be written in characteristic form thus:

$$d\theta + \frac{1}{\tan m}\frac{dM}{M} +$$

$$\frac{\tan m}{1-\tan\theta.\tan m}\cdot\frac{dr}{r} = 0$$

$$\text{along } \frac{dz}{dr} = \tan(\theta+m)$$

$$d\theta - \frac{1}{\tan m}\frac{dM}{M} -$$

$$\frac{\tan m}{1+\tan\theta.\tan m}\cdot\frac{dr}{r} = 0$$

$$\text{along } \frac{dz}{dr} = \tan(\theta-m)$$

$$\text{where: } \tan m = \frac{A}{M}\frac{d\beta}{d\alpha} = \frac{A.C}{M}$$

$$= .4746$$

where α = constant denotes the shock position, β that of a ray, M the shock Mach number, A the area between successive rays. The characteristic net is now constructed as in Fig. 2 with the condition that PQ (α = const.) is a quadrant of a circle and QR (straight line, $\theta = 0$) is the first characteristic due to wall curvature. The values of θ along the positive characteristic are then computed and the wall shape PR is faired in starting from P, where θ = 90°.

EXPERIMENTAL REALISATION

Small-diameter, converging cylindrical shock waves are comparatively easily realisable by means of Z- or theta pinches. Larger diameter shocks tend to exhibit local irregularities due to "holes" in the driving current sheets. This has been overcome using the arrangement shown in Fig. 3. A cylindrical conducting box is divided horizontally by a conducting disc on a cylinder which is insulated from the box by a glass bushing. When a high potential is applied between the box (ground) and the disc, the gas breaks down in a ring close to the bushing as in an "inverse pinch", whereby the magnetic pressure inside the current sheet quickly forces it outward towards the rim of the disc. There, it "folds over" and becomes a regular Z-pinch in the upper part of the chamber. This configuration has the added advantage that the initial breakdown region lies in the "shadow" of the converging current sheet and its strong UV radiation, thus preventing unwanted restrikes. The inner portion of the disc and part of the upper surface of the chamber contains the cusped sections of the shaped side walls. These are made of non-conducting material.

The discharge chamber was electrically switched to a Marx-connected

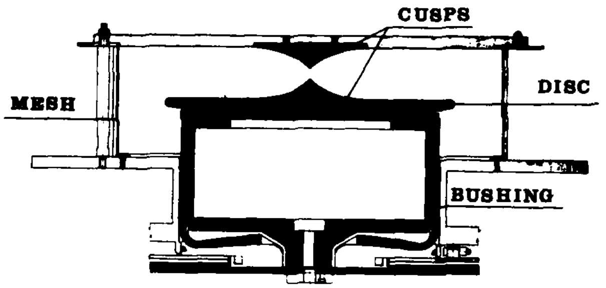

Fig. 3 Discharge chamber

condenser bank with a maximum energy of 100 kJ and a bank voltage up to 100 kV. Diagnostics included image converter photography of the luminous phenomena, magnetic probes and soft x-ray emission monitors. A small nebulizer has been designed which can generate a spray of liquid deuterium droplets in the desired size range. This will be incorporated in the future.

RESULTS

If it is assumed that the current sheet is not "leaky" and that it drives a shock wave ahead of itself in the manner of an impermeable piston, equilibrium temperatures behind the shock can be readily estimated from the tables of Miller and Wilder[5]. It then appears that the temperature corresponding to a shock speed of 10^7 cm/sec should be 12 eV. Treating the shock as one-dimensional, the temperature on reflection will be 30 eV. Lui[3] has shown that the convergence process may increase the shock temperature by another factor of eight, hence the ion temperature may be close to 240 eV. It must be realised that the duration of the maximum compression phase is very short, making it unlikely that the electron temperature will be of the same order as the ion temperature. It is therefore to be expected that the electron temperature as determined by soft x-ray emission may be somewhat lower.

The image converter camera and the magnetic probes register a current sheet velocity of 5×10^6 to 10^7 cm/sec in the lower chamber, whereas velocities of 10^7 cm/sec have been observed in the upper chamber. In Fig. 4 the convergence process is shown in pictures 1-5. In H_2, convergence was obtained at 1 torr pressure and less, and there are indications of spherical shock implosions at higher pressures. Unlike the plasma focus device, the maximum convergence occurs when the current is at or near zero. The x-ray pulse is coincident with the maximum compression on the image converter records and indicates electron temperatures of the order of those of the ions.

COLLISION OF MICROSCOPIC PARTICLES

Although very high temperatures and pressures can be achieved in the focus of converging spherical shock waves, it is unlikely that true thermonuclear conditions can be attained in this manner. The reason for this lies in the fact that the density increase across a plane shock wave reaches a limit for infinite shock strength. Some increase beyond this may be expected due to convergence, but not sufficient to make up for the extremely short inertial containment time given by reflection at the convergence centre. It was therefore decided to launch a preliminary study into the possibility of generating a very dense, hot plasma by means of collision of microscopic particles suspended in the gas behind converging shock waves. Harrison[6] has shown that if particles of solid deuterium were made to collide with a relative velocity of 10^8 cm/sec, close to thermonuclear conditions can be expected to be obtained. According to Guderley[7], the velocity of a spherically

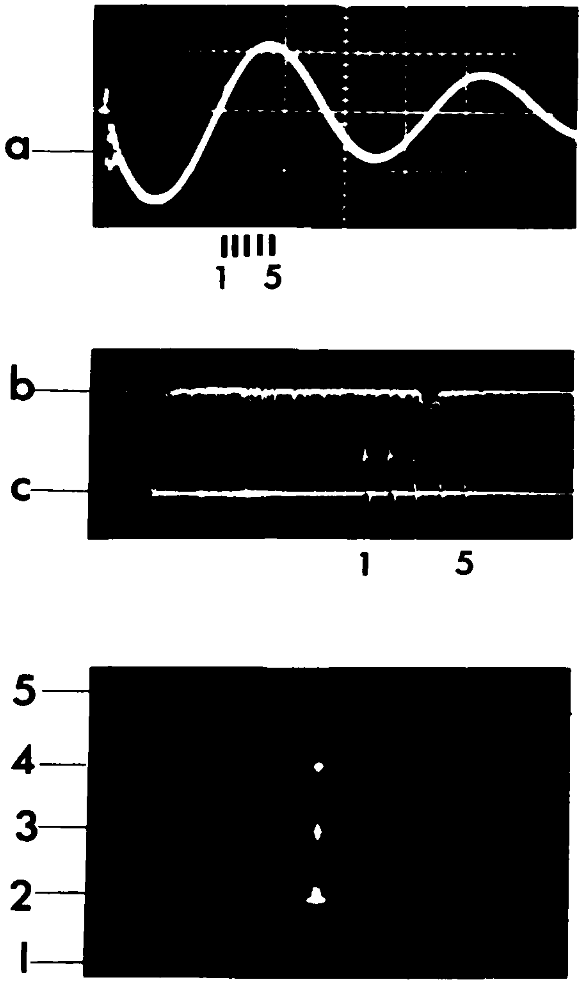

Fig. 4 Experimental results for p_0 = 0.5 torr H_2; a - current waveform (350 kA/div; 5 μs/div); b - x-ray pulse (.2 volts div; 2 μs/div); c - image converter camera monitor (2 μs/div; time markings also presented on current waveform); image converter framing pictures (50 ns exposure) at times shown by c.

converging shock wave increases as $x^{-.453}$ where x is the distance from the convergence focus. If the velocity at a distance x_0 is 10^7 cm/sec, at $x_0/161$ it will be 10^8 cm/sec. Thus, it is possible to create particle velocities of the right order of magnitude, provided the particles can be made to attain a high enough proportion of the gas velocity in which they are suspended.

A simplified theory will be presented in the following which permits calculation of the time-dependent acceleration of the particles after they have been enveloped by the incident and reflected shock waves. To simplify the problem and make it analytically tractable, Guderley's exact theory of converging shock waves is replaced by the asymptotic approximation of Stanyukovich[8]. In addition, we confine ourselves to consideration of a gas with $\gamma = 5/3$, which is reasonable, as in the high-temperature limit, our gas (H_2 or D_2) will certainly be fully dissociated and ionized.

The equation of motion of a particle of mass m imbedded in a gas of velocity u is:

$$mx'' = a(u - x')$$

where primes denote differentiation with respect to time and a is related to the Stokes drag. (The particle is assumed small enough to be always in the Stokes regime of flow of the gas.) Since x' is always smaller than u, we shall neglect the former relative to the latter and write:

$$mx'' = au \tag{I}$$

From Stanyukovich[8] we find:

$$u = -bx^{(d-1)/d} \tag{II}$$

where for a monatomic gas in spherical convergence, d = .688 and b is a constant depending on the initial conditions. Substituting (II) in (I), we find that the resulting equation is not integrable in finite terms unless we approximate d by 2/3. The error is about 3% and is unlikely to change the physical behaviour radically. Adopting this compromise and solving (I) with the initial conditions

$$x' = 0 \text{ when } x = x_o \text{ and } t = t_o$$

we find that the solution is the positive root of the cubic:

$$R^3 - \frac{3R.(x_o)^{1/2}}{(3/4)(v-v_o)^{2/3}} + 2 = 0 \tag{III}$$

where $v = t(ab/m)^{1/2}$ and

$$R = \frac{((x_o)^{1/2} - (x)^{1/2})^{1/2}}{(3/4(v-v_o))^{1/3}}$$

To change to non-dimensional representation, we assume that we are given the shock Mach number M_o at a distance x_1 and time $t = 0$ in a gas of sound velocity c, then the shock trajectory is:

$$x_o/x_1 = (1 - T_o)^d, \text{ where } T_o = t_o cM_o/dx_1).$$

Equation (III) is written:

$$R^3 - 3Rp + 2 = 0 \tag{IV}$$

where

$$R = \frac{((x_o/x_1)^{1/2} - (x/x_1)^{1/2})^{1/2}}{((3/4)(2abd^2x_1)^{1/2}(\gamma+1)mM_oc)^{-1/2}(T-T_o))^{1/3}}$$

and

$$p = \frac{(x_o/x_1)^{1/2}}{((3/4)(2abd^2x_1)^{1/2}((\gamma+1)mM_oc)^{-1/2}\,(T-T_o))^{2/3}}$$

The relevant root of (IV) can be expressed by:

$$R = 2p^{1/2}\,cos((\pi/3) + 3^{-1}cos^{-1}p^{-3/2}\,)$$

If it is assumed that the particle is also overtaken by the shock reflected from the centre, we first must calculate the latter's trajectory. If x_2 is its position coordinate and we assume that the gas velocity behind it must vanish, we have:

$$x_2' = (\gamma-1)u/2 = (\gamma-1)(\gamma+1)^{-1}M_oc(x_1/x_2)^{(1-d)/d}$$

Therefore, by integration we have:

$$x_2/x_1 = ((\gamma-1)(\gamma+1)^{-1}(T_o-1))^d \tag{V}$$

Since the particle now finds itself in an approximately stationary gas, its equation of motion is:

$$mx'' = -abx' \tag{VI}$$

with the initial conditions $x = x_2$, $x' = x_2'$, when $t = t_2$, where t_2 is the time of arrival of the particle at the reflected shock. Integration of (VI) gives:

$$x/x_1 = x_2/x_1 + (v/N)(1 - exp.(-N(T-T_2)) \tag{VII}$$

where $N = abdx_1/(mcM_o)$ and

$$v = \frac{d(x/x_1)}{dT} = -2(2Nd/(\gamma+1))^{1/2}\,((x_o/x_1)^{1/2} - (x/X_1)^{1/2}\,)^{1/2}$$

With eq. (IV) and (VII) the whole history of the particle motion under the action of incident and reflected shock is given. Shock and particle trajectories are depicted in Fig. 5. The figure must be thought of as the

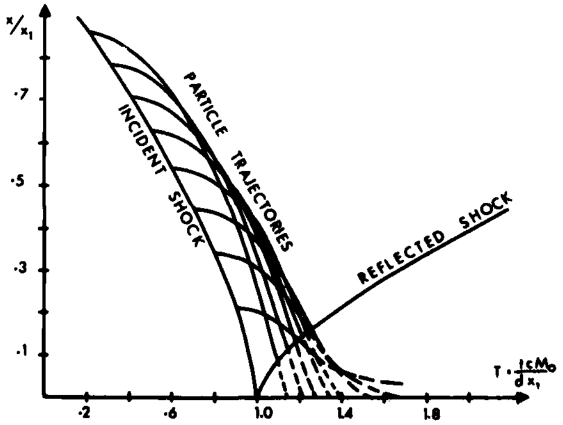

Fig. 5 Analytical results - trajectories of micro-particles

upper half of a symmetric representation with the T-axis as line of symmetry. Particles originating on either side of this line can collide if their trajectories intersect. It will be seen that some particles starting too close to the centre, not only cannot pick up enough speed from the gas to collide with the necessary velocity, but may not even reach the centre at all. It must be remembered that in the part of the motion before arrival of the reflected shock, the particle is not accelerated indefinitely, but reaches at most the speed of the gas behind the shock.

Another interesting graph is obtained when the particle velocity u_p is plotted as a function of the distance from the convergence focus (Fig. 6). A different curve is obtained for each time after launching of the shock wave from the periphery of the chamber. We see that from a certain time onward, the curves become double-valued, hence, in principle, collision between particles travelling at different speeds can occur even before the centre is reached. However, this is found to be physically unreal, when the gas velocity u_g is drawn into the graph. It will then be seen that in the upper branch, the particle velocity is higher than the gas velocity (due to neglect of the x'-term in (I)) which is, of course, impossible. As will be seen in the following, in practice the particles will travel with a velocity well below that of the gas behind the shock. In any case, the upper branch in Fig. 6 must be ignored.

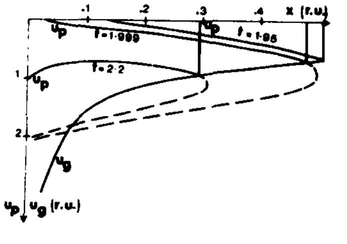

Fig. 6 Particle speed vs x

NUMERICAL CALCULATIONS

The foregoing treatment is only approximate and was supplemented by a more realistic numerical approach. The following assumptions have been adopted in the calculations:

- the gas follows the perfect gas laws
- the flow is one-dimensional
- the particles are uniformly distributed
- the particles occupy negligible volume and contribute no partial pressure
- there is no interparticle interaction
- the particles do not change shape and remain solid or liquid.

While in the analysis the momentum exchange was considered to proceed in one direction only, i.e. from the gas to the particles, in the numerical work, the gas flow is also affected by the presence of the particles. This is important in the case of high particle density. The momentum exchange is given by a free-molecular drag coefficient, also used by vom Stein and Pfeifer[9]. The justification for this lies in the fact that the Knudsen number (ratio of mean free path to particle diameter) is in all cases of practical interest, quite large. A one-dimensional hydrodynamic code was drawn up in which the starting values were obtained from the Stanyukovich profiles[8] and the Rankine-Hugoniot relations across the shock waves were applied. The latter supplied the proportionality constants necessary to evaluate the Stanyukovich profiles.

Some of the results obtained are depicted in Fig. 7. The gas and particle speeds are made non-dimensional by division by the gas sound velocity c. Both graphs, 7.a and 7.b are plotted against the numerical cell number, a quantity proportional to the distance from the convergence centre. The curves in Fig. 7a will be found to be only little different from the classical results

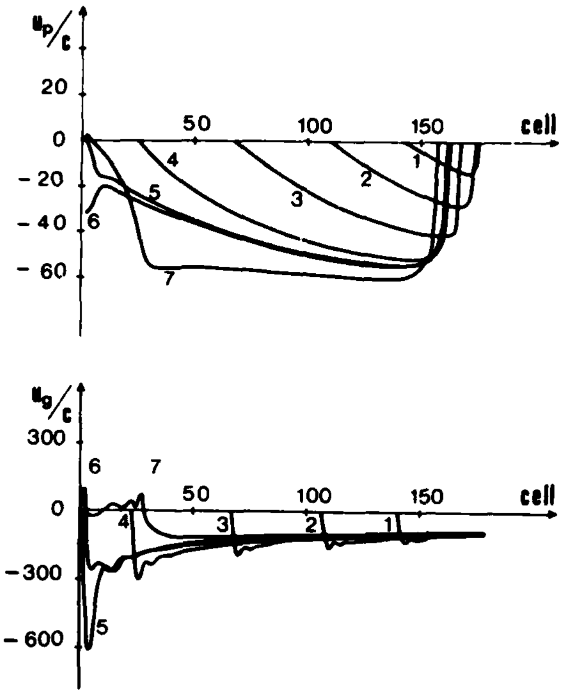

Fig. 7 Numerical results for initial gas pressure = 1 Torr in D_2, particle diameter = .1 μm and initial shock Mach number = 150 at radius r = 1 cm; graph a - particle velocity u_p, graph b - gas velocity u_g (c = sound velocity). Times given by: 1 - 13.10 ns, 2 - 23.10 ns, 3 - 33.10 ns, 4 - 41.25 ns, 5 - 43.47 ns, 6 - 43.68 ns, 7 - 47.95 ns.

of converging shock theory, except that the absolute values of the ordinates are very slightly smaller due to the deceleration of the gas by the particles. Figure 7b shows the particle speeds as a function of radial distance with time after launching of the shock wave as a parameter. It can be seen that behaviour near the origin - where most of the interparticle collisions can be expected to occur - depends critically on the time of shock wave launching. This is due to the fact that, while the particle must spend a sufficient time immersed in the gas flow behind the shock in order to pick up enough speed, too long a time will cause it to be overtaken by the shock reflected in the focus, behind which the flow speed is very small and of the wrong sign! It follows that only particles associated with curve 6 have any hope of interacting with their opposite numbers coming from a direction beyond the focus. Even here, the particle Mach number is only about 30, a small proportion of initial shock Mach number of 150. The main source of this deficiency appears to be the reflected shock, as can be seen from curve 7 in Fig. 7b. If it were not for the cutoff due to this wave, the curve would continue to rise towards the origin, probably reaching values of over Mach 60.

Studies are currently underway to determine means to suppress the reflected wave. The pressure rise at the focus causing the appearance of this wave can be minimised, for example, by introducing near the focus a small venting duct. This is best done by splitting the upper chamber of the discharge vessel in two by the introduction of a solid horizontal plane containing a hole near the focus. An investigation along these lines will be initiated.

AUGMENTATION OF CONTAINMENT TIME BY MEANS OF A LASER BEAM

It is well known that in order for a fusion device to be effective, the product of plasma density and containment time must exceed a certain limit. In the foregoing we discussed means of increasing the density without thought of affecting the containment time. As an alternative, it has been suggested that a powerful converging laser beam be employed to irradiate the plasma ahead of the shock reflected from the focus. This spherical plasma takes the place, in some sense, of the pellet in conventional laser fusion experiments. The effect of the laser beam can be thought of as twofold: (a) as a means of stopping the outward flow of the plasma from behind the reflected shock, thereby providing some sort of "containment", and (b) recompressing the plasma by another inward going wave. As the laser beam interacts with a plasma, rather than with a solid surface, we cannot, in our case, think of the interaction as an ablation process. Instead, we consider the interaction to be mediated by a laser-supported detonation[10]. As in the immediate neighbourhood of the interaction point the wave system can be looked upon as plane, the wave diagram can be drawn as in Fig. 8 and the relavant transition relations for plane waves employed. The original outward going shock S_1 is at time t_0 augmented by an optical detonation wave D. Self-consistency demands that in addition, a centered expansion fan E, a contact surface C and a second shock S_2 be inserted. The calculations are rather involved, though elementary, as simultaneous algebraic equations of larger than fourth order are to be solved, hence generally valid relations cannot be obtained explicitly. However, a few expressions valid in the strong shock limit are readily derivable. For instance, once it is realised that "containment" in the above sense is established if the contact surface C is parallel to the time axis, the ratio of Mach numbers of the detonation M_D to incident shock wave M_s is in the limit of strong shocks:

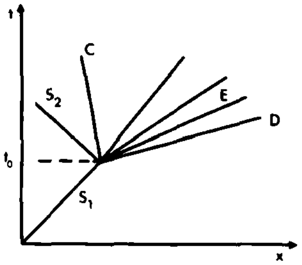

Fig. 8 Wave diagram of laser beam-plasma containment mechanism.

$$M_D/M_s = \sqrt{2 + 2\frac{\gamma-1}{\gamma+1}\gamma((\gamma-1)/2\gamma)^{1/2}\,(\frac{\gamma-1}{4}((\gamma-1)/2\gamma)^{1/2} + \sqrt{1+\frac{(\gamma-1)^3}{32\gamma}})}.$$

For physically realistic values of γ, this expression varies around the value 1.5 by approximately ±5%. Similarly, one can calculate the density ratio on either side of the contact surface in the strong shock limit as:

$$\rho_2/\rho_3 = (\frac{\gamma+1}{\gamma-1})^2 \frac{\gamma}{\gamma+1} (\frac{\gamma+1}{2})^{2/(\gamma-1)}$$

For the monatomic value $\gamma = 5/3$, this expression assumes a value of almost 24. Thus, although the plasma is not contained in a vacuum - which should ideally be the case - it is surrounded by a gas of a density considerably lower than its own. Moreover, the surrounding gas is of the same species as its own, therefore contamination of the plasma is ruled out.

To calculate the containment time, one would require to find the time the shock S_2 needs to collapse on the centre and re-emerge to interact with the contact surface C. This has not been attempted yet, as it would require taking into consideration spherical flow effects and hence numerical computations.

CONCLUSIONS

It is shown theoretically and experimentally that by suitably shaping the side walls of a cylindrical pinch, it is possible to obtain spherically symmetric collapsing shock waves in hydrogen. A theoretical study on the feasibility of using such a device to effect high-speed collision between microparticles has yielded promising results, as have calculations on the use of laser beams to augment the containment time of the plasma behind the shock reflected from the centre.

ACKNOWLEDGEMENTS

We gratefully acknowledge the valuable assistance given by G. Boult, A. Shewchuck, A. Prini, and W. Michie. Also, it is a pleasure to acknowledge the interest shown by Dr. D.C. MacPhail and Mr. R.A. Tyler.

REFERENCES

1. Milton, B.E. and Archer, R.D., AIAA J. Vol. 7, No. 4, p. 779 (1969).
2. Lau, J., CASI Trans Vol. 4, No. 1, p. 13 (1971).
3. Lui, H.C., "Numerical Studies of Shock Focusing in a Coaxial Electromagnetic Shock Tube". Thesis, Columbia U. Plasma L. (1973).
4. Whitham, G.B., J. Fluid Mech. Vol. 4, p. 337 (1958).
5. Miller, C.G. and Wilder, S.E., NASA Rep. SP 3087 (1976).
6. Harrison, E.R., Phys. Rev. Lett. Vol. 11, No. 12, p. 535 (1963).
7. Guderley, G., Luftfahrtforsch. Vol. 19, p. 302 (1942).
8. Stanyukovich, K.P., "Unsteady Motion of Continuous Media", p. 524, (1960) (Pergamon Press - Oxford).
9. vom Stein, H.D. and Pfeifer, H.J., Proc. 9th Intern. Symp. Shock Tubes (1973), p. 804.
10. Ramsden, S.A. and Savic, P., Nature, Vol. 203, p. 1217 (1964).

Part III: PHYSICAL AND CHEMICAL PROCESSES IN SHOCK WAVES

HOMOGENEOUS NUCLEATION IN METAL VAPORS. VI. THE CONDENSATION OF SILICON

KIYOHIKO TABAYASHI and SIMON H. BAUER

Cornell University, Department of Chemistry, Baker Laboratory,
Ithaca, New York 14853, USA

The shock tube technique for preparing controlled levels of supersaturated vapors of refractory materials has been extended to the condensation of silicon. Silane, with impurity levels of $O_2 < 5$ ppm and $H_2O < 2$ ppm, was the precursor substance; the desired concentrations of silicon vapor were generated by shock heating 1.0-0.05% of SiH_4 in Ar carrier; $1500 < T^{o}K < 2800$. Experiments were made both with incident and reflected shock heated samples. The turbidity and the intensity of light scattered at 90° were recorded, with a time resolution of $\approx 1\ \mu s$. The laser beam passed along a diameter normal to the shock tube axis, near its terminus. The transmitted beam was incident onto a phototube, located 150 cm from the exit window. The light scattered from the tube center passed through a side window and was focused onto the entrance slit of a grating monochromator. Critical pressures for the onset of condensation, on the time scale of our measurements, were deduced from the scattered light intensities. As for Fe, Pb, and Bi the dependence of the critical supersaturation on temperature is an exponential function: $\ln \mathscr{S}_c = 392.5 \exp(-2.260 \times 10^{-3}\ T)$. A number of measurements were also made of cluster growth rates, wherein we monitored both the scattered light and turbidity, in the incident shock regime. Mean radii were deduced as a function of time. The growth sequence for Si is similar to the growth curves we found for Pb vapor.

INTRODUCTION

A shock tube technique for preparing controlled levels of supersaturated metal vapors was first described by Kung and Bauer[1], and subsequently applied to Fe, Pb, and Bi. The onset of avalanche condensation can be ascertained either from light scattering or increased turbidity. In this manner, the temperature dependence of the critical supersaturation for these metals was determined.[1,2] The growth rates for Pb clusters[3] were estimated from the scattered intensity and turbidity which are coupled through their cross-section. In this report we extended our experimental approach to the condensation of Si. The homogeneous nucleation of Si is of interest in such diverse areas as the preparation of solar cell devices and the mechanism of formation of iron silicide and silicate particles in stellar atmospheres and protostellar nebulae, the latter being the subject of several recent papers[4,5].

For generating a specified level of supersaturated Si vapor, we select SiH_4 as a source of silicon atoms. There are extensive reports on the rates of thermal decomposition of SiH_4.[6] Purnell and Walsh[7] investigated the pyrolysis of silane in a static system, over the temperature range 648~703°K: $k_{uni} = 10^{15.18} \exp(-55,900/RT) \times [SiH_4]^{1/2}$ sec^{-1}. Recently, Newman et al.[8] subjected SiH_4 to shock heating in argon mixtures, over the temperature range $1204 \leq T°K \leq 1304$ and found: $k^{\infty}_{uni} = 10^{13.7} \exp(-56,100/RT)$ sec^{-1}. They also observed that under their condition the fragmentation stoichiometry is: $SiH_4 \rightarrow 0.7Si + 0.3SiH + 1.85H_2$. By extrapolating the above rate expressions, one can estimate the time for 90% decomposition at 1500 and 1800°K, $t_{90\%} = \ell n 10/k_{uni}$, = 2.4~6.9 μs and 0.1~0.3 μs, respectively. If the first elimination of H or H_2 is the rate limiting step for the subsequent stripping of H atoms, Si atoms would be produced within a few microseconds after passage of the shock front. On the other hand, the present experiments showed that at moderate supersaturations the time for complete condensation of Si vapor was the order of 300 μs.

The equilibrium concentrations of the product species were computed using the NASA "equilibrium shock" program.[9] The species considered were: SiH_4, SiH_3, SiH_2, SiH, Si, Si_2H_6 and Ar. For each of these the thermochemical data were introduced as a polynomial in T with coefficients fitted to the tabulated JANAF values.[10] For species not listed in JANAF, we estimated the necessary terms from mass spectroscopic data,[11] and computed partition functions.[10] At typical shock conditions, 1% SiH_4 in Ar at T_2 = 1500°K and P_2 = 1 atm (total), the calculated equilibrium composition, per mole of silane, is: $SiH_4 \rightarrow 0.54 Si + 0.25 SiH_3 + 0.18 SiH + 0.02 SiH_2 + 1.5 H_2$. The mole fraction of disilane is less than 10^{-4}. Based on Newman's rate data, we conclude that silane is a good source of silicon atoms for temperatures greater than 1500°K.

EXPERIMENTAL

The silane impurity levels (manufacturer's specifications) were $O_2 < 5$ ppm and $H_2O < 2$ ppm. The desired concentrations of silicon vapor were generated by shock heating 0.05-1.0% of SiH_4 in Ar carrier (99.999%); $1550 < T°K < 2800$. Observations were made both on incident and reflected shock heated samples. The turbidity and the intensity of light scattered at 90° were recorded, with a time resolution of ≈1 μs. Generally the light source was a Lexel, model 96 Ar-ion laser, tuned to $\lambda = 514.5$ nm, operated at power levels 50-500 mW; a He-Ne laser (632.8 nm) was also used at a power of 50 mW. The laser beam passed along a diameter normal to the shock tube, near its terminus. The beam was weakly focused at the tube center, and its radiation was polarized parallel to the shock tube axis. The transmitted light passed through neutral density and narrow band filters and was incident onto an EMI 9634 phototube, located 150 cm from the exit window.

The light scattered from the tube center passed through a side window and was focused (with a collimating lens) onto the entrance slit of a SPEX Minimate (model 1670) grating monochromator. The slits were set to isolate either the 514.5 ± 1 or 632.8 ± 1 nm line. The Rayleigh scattered intensity was measured with an EMI-9558 phototube. Both signals were recorded with a dual beam tektronix 551 oscilloscope. Since there was some radiative emission from samples at the higher temperatures (when the data were taken from reflected shocks) the laser beam was mechanically chopped at 5 x 10^3 Hz to provide estimates for the background correction. Optical alignment and absolute calibration of the scattered light signals were made by filling the tube with $CHF_2C\ell$ to 800 torr. Prior to introducing the test gas the driven section was purged with argon to minimize residual impurities. After each filling it was pumped down to less than 0.2 milliTorr. The leak and outgassing rates were less than 0.2 mTorr/min.

Special precautions were taken to minimize possible contaminations of the test section. We found that a residual trace of $CHF_2C\ell$ initiated laser-induced dissociation of SiH_4 within a few seconds, prior to shock initiation. By purging with Ar we essentially eliminated the photoinduced decomposition. Laser powers as high as 500 mW were safe for our operation. Other contaminations may be due to a very slight leak and outgassing of the shock tube. An elapse time of less than 2 min was allowed between sample charging and diaphragm rupture; this could introduce an air contamination of less than 0.4 x 10^{-3} torr. Since typical initial pressures were $P_1 \sim 50$ torr, with ~0.5% SiH_4, the maximum O_2/SiH_4 ratio was 3 x 10^{-4}.

CRITICAL SUPERSATURATION RATIOS

Critical pressures for the onset of condensation, on the time scale of our measurements, were deduced from the scattered light intensities. The light scattered by the Si clusters was almost completely polarized, as was previously observed for Pb clusters.[3] This implies that initially these clusters are liquid-like, with viscosities which are not particularly high. As indicated above, radiative emission from the gas was observed throughout the reflected zone and decayed soon after the arrival of the cooling fan from the expansion wave. The corrected scattered light signal was extrapolated to the base line. The conditions in the expansion wave at that instant were calculated from the recorded pressure trace. The resulting data are summarized in Table I, and a plot of $\ell n \mathcal{J}_c$ vs T(°K) is shown in Figure 1. For Si, as for Fe, Pb, and Bi, the dependence of the critical supersaturation on temperature is an exponential function: $\ell n \mathcal{J}_c = 392.5 \exp(-2{,}260 \times 10^{-3}\ T)$, obtained by least-squares fitting of the experimental points.

The error bars were estimated by assigning the maximum uncertainty to the width of the chopping pulse, for reading the critical point on the record. A chopping rate of 5 x 10^3 Hz corresponds to an uncertainty ~ ± 100 μs, which leads to ~ ± 100°K for the critical temperature. Because of the steepness in T dependence of the equilibrium vapor pressure, the data points at low temperatures, T < 1900°K, show a larger uncertainty in $\ell n \mathcal{J}_c \approx \pm 1.7$. The points for Runs # 8152, 8162, and 8181 were measured only in the reflected zone, where the largest source of error is the uncertainty in the shock speed. This introduced ± 50°K in temperature, and ± 0.45 in $\ell n \mathcal{J}_c$. Consideration of these errors lead us to the conclusion that above 1900°K the stated T-dependence of $\ell n \mathcal{J}_c$ is good within an uncertainty of ± 1 in $\ell n \mathcal{J}_c$.

One may now compare the experimental results with theoretical predictions. A series of curves calculated from classical nucleation theory[12] for assumed magnitudes of J^{ss}, the steady state condensation flux, are superposed on the experimental points in Fig. 1. In Table II we listed the physical parameters used in computing these curves. The observed steep T-dependence cannot be fitted with a single value of J^{ss}; our data span the range from 10^{12} and 10^{18} cm^{-3} sec^{-1}. The Lothe-Pound theory[13] predicts nucleation rates greater than classical, often by a factor of 10^{17}; a sample calculation for our conditions ($P_{Si} = 0.001$ atm, T = 2000°K, and $n \sim 100$) gave $J^{ss} \approx 5 \times 10^{21}$. It is therefore evident that the LP theory also cannot be fitted to our data, for any reasonable nucleation current. We conclude that the

Table I. Critical Supersaturation Ratios for Silicon; Reflected Shock Regime

Run No.	SiH_4 (%)	P_{ex} (P_5) (atm)	T_{ex} (T_5) (°K)	$\ln \mathcal{S}_c$
7241	0.5	2.748	2307	2.909
7222	0.5	4.647	2593	1.120
7212	0.5	4.532	2643	(0.765)*
7221	0.5	4.748	2693	(0.519)*
7202	0.5	4.354	2703	(0.333)*
7201	0.5	5.484	2734	(0.347)*
7231	0.5	6.090	2756	(0.305)*
8142	0.2	3.167	2071	4.492
8161	0.2	5.732	2385	2.022
8152	0.2	5.886	2452	1.521
8162	0.2	5.712	2464	1.390
8261	0.1	2.251	1633	9.733
8182	0.1	2.579	1723	8.210
8262	0.1	4.696	2161	3.232
8181	0.1	5.842	2317	1.959
9091	0.05	2.314	1547	10.928
9101	0.05	4.056	1960	4.668
9092	0.05	4.707	2100	3.204
9071	0.05	5.958	2310	1.367

* Give negative $\log(\ln \mathcal{S}_c)$ values and introduce large errors in $\log(\ln \mathcal{S}_c)$ plot; these runs were excluded from the least-square evaluation.

experimental temperature dependence is steeper than that predicted by either theory, but lies closer to the classical values.

The dependence of $\ln \mathcal{S}_c$ for Si on temperature appears to be steeper than that for iron. The corresponding curve for Fe was also included in Fig. 1. It is interesting to note that the extrapolated curve for iron (over the temperature range 2200-2800°K) intersects the curve for silicon at about 2400°K, but these may be equal, within our experimental error limits. In Table III are calculated the critical pressures for the onset of condensation for elementary silicon and iron, over the temperature range 1700-2600°K. Thus, while $\mathcal{S}_c$ for Si exceeds that for Fe at low temperatures, because of its lower equilibrium pressure the critical pressure for onset of homogeneous condensation for silicon is considerably lower than that for iron. This is of particular interest with respect to the sequence of condensation of materials under highly reducing protostellar conditions.

The determination of $\mathcal{S}_c$ for Si presented technical difficulties associated with a substance whose equilibrium vapor pressure is very small. Note that P_e(Si) is about an order of magnitude smaller than P_e(Fe). For comparable levels of $\mathcal{S}_c$, one must experiment with a corresponding lower initial concentration of the sample. Here we are limited by the minimum particle density required to obtain reliable scattered light intensities, and by losses due to possible adsorption of SiH_4 on the shock tube walls. Empirically, it has been observed that in very dilute mixtures (< 0.1%) of H containing gases [such as H_2O, NH_3, and HCN], the bulk concentration

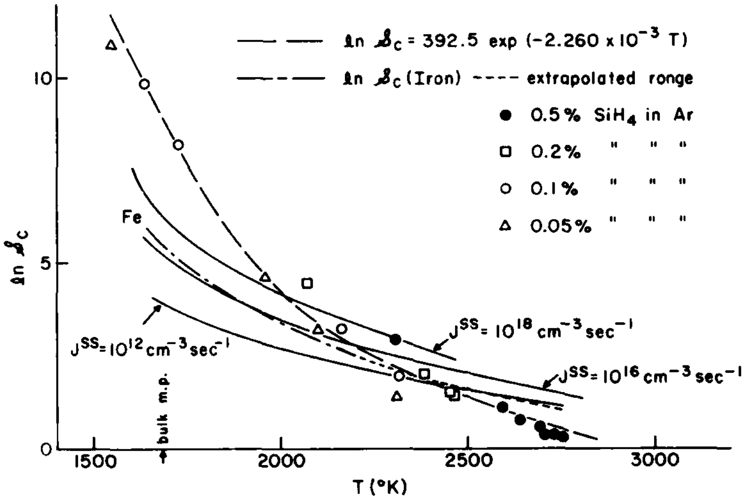

Figure 1. Dependence of critical supersaturation ratio on temperature, for Si and Fe. The three full curves were calculated for Si from classical nucleation theory using the parameters listed in Table II.

Table II. Physical Parameters used in Classical Nucleation Theory Calculations

Physical Parameter	Si	Ref.
Surface tension (erg cm^{-2})	$\sigma(T) = 1083.8 - 0.13T$ (°K)	a
Liquid density ($g \cdot cm^{-3}$)	$\rho(T) = 3.049 - 3.2 \times 10^{-4}T$ (°K)	a
Melting point - Boiling point (°K)	1685 - 3543	a
Crystal structure	fc - cubic	b
ΔH_{vap} (kcal/mole)	71.	c

a) C. J. Smithells ed., "Metals Reference Book", 5th ed., Butterworth, London and Boston, 1976.

b) R. Hultgren, et. al., "Selected Values of Thermodynamic Properties of Metals and Alloys", Wiley, New York, 1963.

c) R. C. West, ed., "CRC Handbook of Chemistry and Physics", 55th ed., CRC Press, Cleveland, Ohio, 1974.

introduced in the shock tube is appreciably reduced prior to shock initiation. Finally, it did not prove possible to obtain quantitative data from the turbidity measurements for many of these runs due to significant accumulation of Si on the window after the arrival of reflected shock.

Table III. Comparison of P_c for Si and Fe

Si

	$\ln \mathcal{S}_c$	$\mathcal{S}_c$	P_e (torr)	P_c (torr)
1700°K	8.423	4550.3	3.420×10^{-4}	1.556
2000°K	4.276	71.952	0.02333	1.679
2300°K	2.171	8.765	0.5180	4.540
2600°K	1.102	3.010	5.7152	17.202

Fe

	$\ln \mathcal{S}_c$	$\mathcal{S}_c$	P_e (torr)	P_c (torr)
1700°K	5.399	221.1	4.841×10^{-3}	1.070
2000°K	3.371	29.10	0.2812	8.183
2300°K	2.105	8.205	4.743	38.92
2600°K	1.314	3.721	46.132	171.7

CLUSTER GROWTH RATES

A. Data Reduction

In analyzing the kinetic behavior of Si condensation from both scattering and turbidity signals, we followed the method of Frurip and Bauer[3]. The necessary refractive index was derived from the complex dielectric constant, $\epsilon(\omega) = \epsilon_1 + i\epsilon_2$. The real and imaginary components are given by the Drude free electron formula,[14]

$$\epsilon_1 = 1 - \frac{4\pi N_c e^2 \tau^2/m}{(1 + \omega^2 \tau^2)} \qquad \text{I}$$

$$\epsilon_2 = 4\pi N_c e^2 \tau / m\omega (1 + \omega^2 \tau^2) \qquad \text{II}$$

where ω, N_c, and τ are (respectively) the angular frequency, the density of conduction electrons, and their relaxation time. Optical measurements of the dielectric constant for the liquid metal gave values for N_c which were close to the density of valence electrons (N); $N_c e^2 \tau/m$ is close to the measured d.c. conductivity ($\sigma_{d.c.}$). At present, no direct measurements of the optical properties of liquid Si are available; we estimated them from the d.c. conductivity of the liquid (1683 ~ 1873°K).[15] Small discrepancies generally appear between optically and electrically determined values. These were minimized by introducing "reduced" parameters. For the 4-valent liquid metals [Ge, Sn and Pb] the average ratios $N_c/N \approx 1.14$, and $\sigma(\omega=0)/\sigma(\text{d.c.}) = 0.912$. However, this correction for the optical parameters was found to have an essentially negligible effect on the calculated $\langle r \rangle$ values over the temperature range: $1550 \le T°K \le 1930$. We then assumed that both $\sigma(\omega=0) = N_c e^2 \tau/m$, and τ were linear with the temperature, and calculated refractive indices for the Ar+ and He/Ne wavelengths.

B. Results

Cluster growth rates were measured in the incident shock regime. The total pressure in the shock heated gases ranged from 0.65 to 1.4 atm. The temperature span was set at the upper limit by significant radiative emission; at the lower end, our expression for the complex refractive index led to physically inadmissible limits. Generally, the turbidity signal showed an exponential relaxation to a steady state level; this rate increased as the temperature rose. On the other hand, the scattered light showed an initial gradual rise, followed by an accelerated growth.

Mean radii reduced from the records are plotted in Fig. 2. These are the representative for our temperature range and supersaturation ratios (8 x 10^2 to 2 x 10^5). The experimental conditions are summarized in Table IV. The scattered intensities were corrected for emission, recorded for runs made under identical conditions, with the laser off. During the first 50 μs after shock arrival, the scattered signal could not be adequately resolved from the background noise and the weak emission at the higher temperatures. Thereafter, the mean cluster radii rose to a constant level, $\langle r \rangle_{max}$. As expected, the value of $\langle r \rangle_{max}$ decreased when the level of supersaturation increased.

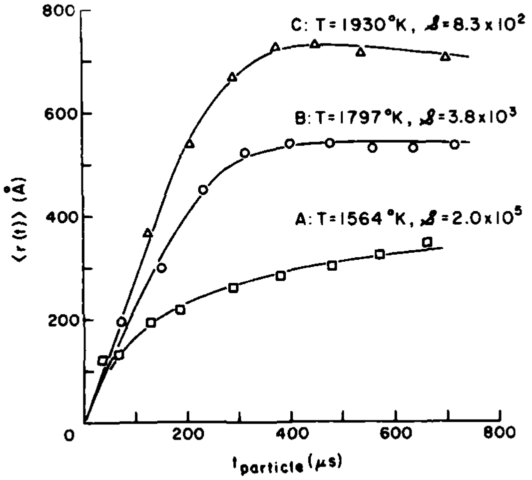

Figure 2. Growth curves for the three runs listed in Table IV.

Table IV. Experimental Conditions for Cluster Growth Runs

Run	n(%)	λ(nm)	T_2(°K)	P_2(atm)	P_e(Si)/Torr	$\langle r \rangle_{max}$(Å)	$\mathcal{S}$
A	1.01	514.5	1564	1.09	2.25×10^{-5}	350.	1.96×10^{5}
B	1.15	623.8	1797	0.84	1.57×10^{-3}	540.	3.81×10^{3}
C	1.15	623.8	1930	1.08	9.75×10^{-3}	730.	8.3×10^{2}

The growth rate during early times (up to ~ 70 μsec) is linear and exhibits a slight increase with temperature. At T ≈ 1800°K the initial slope is

$$\frac{d\langle r\rangle}{dt} \approx 2.2 \times 10^{-2}\ \mathrm{cm\cdot s^{-1}}$$

This compares with the value 9.4×10^{-3} cm s^{-1} we found for Pb vapor at 1100°K[3]. In terms of a gas kinetic binary-collision model, the rate of addition of atoms onto the n-mer is

$$\frac{d\langle n\rangle}{dt} = 4\pi \langle r\rangle_n^2 \rho_n \left(\frac{d\langle r\rangle_n}{dt}\right) = \alpha\, 4\pi \langle r\rangle_n^2 N_1 \bar{c}_1/4 \qquad \mathrm{III}$$

where ρ_n is the monomer density in the n-mer, α is a sticking coefficient, and $\bar{c}_1$ is the mean velocity of the monomers. If ρ_n is taken as the bulk density (5.32×10^{22} cm^{-3}), $N_1 = 3.2 \times 10^{+16}$ and T = 1800°K, we deduced $\alpha = 1.2$. However, ρ_n is clearly less than ρ_{bulk}. We conclude that the collisions are very sticky ($\alpha \approx 1$) within the approximations of a hard-sphere collision model.

Figure 3 is a plot of mean cluster density <u>vs</u> particle time for the three runs shown in Fig. 2. In Run A, relatively precise measurements of the scattered signal were obtained at early times. As for Pb vapor, the density peaked at about 50 μs and then decreased monotonically. In runs B and C, however, there was a slight rise after 300 μs and the mean density leveled off at about 1/5 of the peak value; for run A, $N_{t=\infty}/N_{max} \approx 0.07$. A decrease in mean n-mer density is expected due to coagulation of the clusters. The distribution in cluster sizes is probably log-normal, based on many empirical observations, and justified by a stochastic analysis.[16]

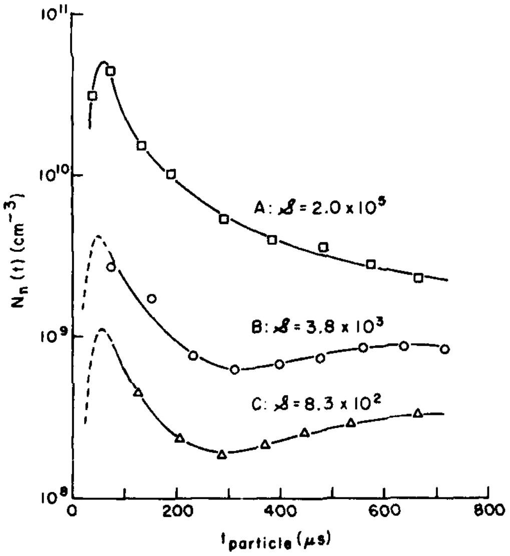

Figure 3. Time variation of the cluster density (mean size) for runs A, B, C.

The fraction of monomer, $\chi(t)$, which enters the condensed phase can be calculated from $N_n(t)$ and $\langle r\rangle$

$$\chi(t) = N_n(t)\, \langle n\rangle / N_1^o = \frac{4}{3}\pi \langle r\rangle^3 \rho_n N_n(t)/N_1^o \qquad \mathrm{IV}$$

The dependence of $\chi(t)$ on particle time is shown in Figure 4. The higher the supersaturation the greater the fraction condensed at a given time, more rapidly approaching complete condensation. For all runs [illegible] $\infty) > 0.6$. Note that this plot is not comparable to Fig. 15, ref. 3 for Pb which showed the dependence of $\chi(t)$ on supersaturation ($\mathcal{S} = 30 \rightarrow 94$) at a constant temperature ($1150 \pm 30°K$). For $(Si)_n$, very high levels of supersaturation are generated, but $\langle r \rangle_{max}$ are also comparatively large.

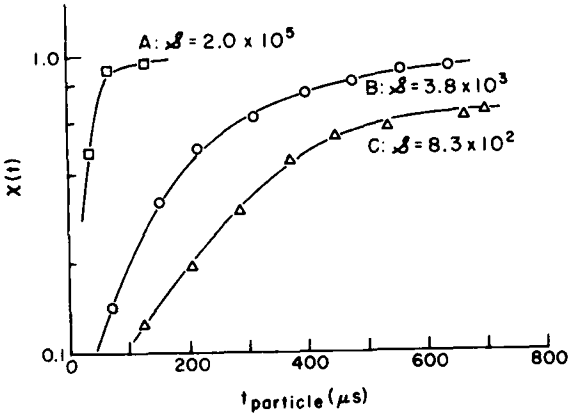

Figure 4. The fraction of monomers condensed, vs particle time.

SIGNIFICANCE OF THESE CONDENSATION DATA

There are two current problems for which knowledge of the critical pressures for homogeneous nucleation and condensation of silicon vapor may facilitate their solution. The first pertains to a process for the production of thin wafers of silicon for solar cell devices, by reacting sodium vapor with silicon tetrachloride at elevated temperatures [$4Na + SiCl_4 \rightarrow \underline{Si} + 4NaCl$]. The two gases are mixed and allowed to flow down a heated tube. Flow rates and temperatures are adjusted so that elementary silicon deposits on the tube walls, whereas the sodium chloride condenses homogeneously from the vapor phase, and its crystallites are trapped downstream from the reaction chamber. Clearly, for optimum operation, the homogeneous condensation of Si should be avoided, while that of NaCl should be favored; the total throughput should be maximized. Conditions should be adjusted so that the operating vapor pressure of Si is just below its critical level for the onset of homogeneous condensation as measured in this investigation. Unfortunately, our low temperature data show considerable scatter, so that on the basis of these results extrapolation to still lower temperatures is problematic.

A mechanism of condensation of solid grains is necessary for computing the thermal valance in stellar atmospheres. The condensation of grains is believed to be one of the most important chemical differentiation processes that occur during the formation of solar systems. Over 90% by mass of the condensable elements in our sun is comprised of C, O, Mg, Fe, Si, and S. At high temperatures (> 2000°K), at which all of the abundant elements are in the gas phase, Fe occurs predominantly as a monoatomic element, while Si is present as the oxides: $SiO_{(g)}$ and $SiO_{2(g)}$. When the temperature falls, were the system in thermodynamic equilibrium, reduced iron should condense as the metal; then the oxides of Mg and Si should condense at still lower temperatures. However, in meteorites, which may contain a record of processes that occurred during the formation of the solar system, one finds the reduced phases Fe_xSi_y and Mg-Fe silicates, such as olivine $(Mg, Fe)_2SiO_4$. Much effort has been expended to elucidate the mode of formation of these phases and their subsequent history. Knowledge of the kinetic limitations of the condensation process which may have produced these phases would also allow us to infer the conditions which prevailed during the formation of the solar system. Unfortunately, the development of a theory for the early condensation processes is hampered by the lack of experimental data on these refractory phases. Further shock tube experiments of naturally abundant elements under well controlled conditions would greatly aid our understanding of the condensation mechanism from complex gas systems.

ACKNOWLEDGMENT

This work was supported by the National Science Foundation under Grant No. DMR-78-10307. We thank Dr. J. Stephens for comments on the astrophysical significance of these experiments.

REFERENCES

1. R. T. V. Kung and S. H. Bauer, "Shock Tube Research", 8th International Shock Tube Symposium, Chapman and Hall, London, 1971, (Part I).
2. D. J. Frurip and S. H. Bauer, J. Phys. Chem. 81, 1001 (1977), (Part III).
3. D. J. Frurip and S. H. Bauer, J. Phys. Chem. 81, 1007 (1977), (Part IV).
4. J. R. Stephens and B. K. Kothari, The Moon and the Planets, 19, 139 (1978).
5. J. R. Stephens and R. W. Russell, Astrophys. J. 228, 780 (1979).
6. For a review; L.K. Praturi, L. Lutwack and G. Hsu, LSSA Project Task Report, 77-38, (1977).
7. J. H. Purnell and R. Walsh, Proc. Royl Soc. Ser. A, 293, 543 (1966).
8. C. G. Newman, M. A. Ring and H. E. O'Neal, J. Am. Chem. Soc. 100, 5945 (1978).
9. S. Gordon and B. McBride, NASA Spec. Publ., No. 273 (1971).
10. D. R. Stull and H. Prophet, Ed., "JANAF Thermochemical Tables, 2nd ed.", Dow Chemical Co., Midland, Michigan, 1970.
11. P. Potzinger and F. W. Lampe, J. Phys. Chem. 73, 3912 (1969).
12. F. F. Abraham, "Homogeneous Nucleation Theory", Academic Press, Inc., New York, 1974.
13. J. Lothe and G. M. Pound, J. Chem. Phys. 36, 2080 (1962).
14. T. E. Faber, "An Introduction to the Theory of Liquid Metals", Cambridge University Press, 1972.
15. C. J. Smithells, Ed., "Metals Reference Book, 5th ed.", Butterworths, London and Boston, 1976.
16. C. F. Wilcox, Jr., S. Russo, and S. H. Bauer, J. Phys. Chem. 83, 897 (1979).

SHOCK-TUBE STUDIES OF RADIATIVE BASE HEATING OF JOVIAN PROBE

HIROYUKI SHIRAI and CHUL PARK

Entry Technology Branch
Ames Research Center, NASA
Moffett Field, California, USA

A 6.4-cm-diameter scale model of the Jovian entry vehicle is tested in an electric-arc-driven shock tube and a 5-cm-diameter sphere model is tested in a combustion-driven shock tube and in an electric-arc-driven shock tunnel. The radiative heat-transfer rate and pressure on the front and the base regions are measured in the absence of ablation with sensors imbedded in the models in a stream consisting of 10% hydrogen in a bath of either neon or argon. The measured radiative heat-transfer rates and pressures range to about 22 kW/cm^2 and 12 atm, respectively, at the front stagnation point. The ratio of the radiative heat-transfer rate at the base stagnation point to that at the front stagnation point is found to be about 1/4 for the sphere at Mach 1.8, about 1/30 for the sphere at Mach 4.8, and about 1/6 for the scale model at Mach 1.7. The present experimental results agree well with the theoretical predictions of Park, thus indicating that Park's theory is valid.

INTRODUCTION

The United States of America is planning to send a probe vehicle into the atmosphere of the planet Jupiter in the early 1980's. The probe will enter the Jovian atmosphere at a speed in excess of 50 km/sec. A number of theoretical studies have been made[1,2] to predict probe heating and to determine an optimum probe configuration. Until now, however, the research efforts have been focused mainly on the front region of the probe. The problem of heat transfer to the base region has been given little attention, although at such speeds, radiative heat transfer to the base region of the probe is also expected to be severe.

In the Jovian flight, ionized hydrogen in the front shock layer flows downstream along the surface of the probe with increasing flow velocity. The flow then separates from the body surface at the frustum edge and expands rapidly to form a shoulder-expansion region. The region is expected to be in thermodynamic nonequilibrium because of the rapid expansion. A portion of the flow decelerates and reattaches at the flow axis, thereby forming a recompression region. The region between the reattachment point and the rear surface of the body is a recirculation region. In the recirculation region, the flow moves slowly and hence it is likely to be in equilibrium. Behind the reattachment point, a neck region forms. Temperature and pressure in the recompression/neck region are high enough for radiation to be significant.

Recently, Park[3] carried out parametric calculations of radiative base heating rates by adopting the above flow model, and obtained a scaling law. The scaling law gives a relation between the ratio of the radiative heat flux at the base stagnation point to that at the front stagnation point and the following parameters: the ratio of the pressure at the base stagnation point to that at the front stagnation point, the ratio of shock standoff distance to frustum diameter of the model, and the ratios of position and diameter of the neck region to the frustum diameter. When these parameters are known, the scaling law provides the means of calculating radiative heat flux to the base stagnation point.

The purpose of the present work is to measure the radiative heat-transfer rates to the base stagnation point in the flows that simulate Jovian entry environments and to verify the validity of Park's theoretical scaling law. Experiments are conducted in shock tubes, using mixtures of hydrogen in a bath of neon or argon as the test gas, with two types of models. Radiative heat-transfer rates are measured with radiometers imbedded in the models. The flows produced in the facilities are in the ionizing regime. The shock tubes are used for the tests because, although limited in Mach number, they offer the advantage that models large enough to accommodate radiometers can be tested.

EXPERIMENTS

Facilities

Experiments are performed in three different shock tubes: an arc-driven shock tube, 60-cm i.d.; a combustion-driven, constant-area shock tube, 16.8-cm i.d.; and an arc-driven shock tunnel with a driven section, 10-cm i.d., and a test section, 10-cm i.d. The three facilities are shown schematically in Fig. 1. The combustion-driven shock tube is described in Ref. 4. The two arc-driven shock tubes are driven by the same capacitor discharge system described in Ref. 5.

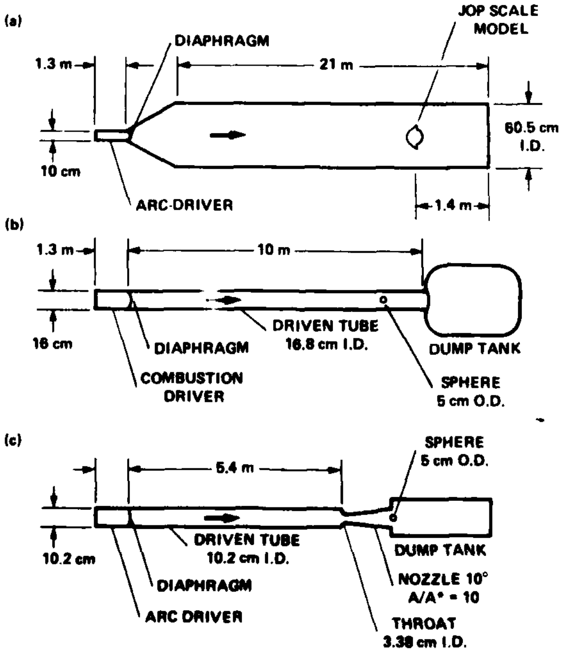

Figure 1. Schematic of shock-tube facilities.

The 60-cm-i.d. arc-driven shock tube provides relatively long test times and the largest test-section to model-diameter ratio. Hence, the experiments performed in this facility are least likely to suffer from the imperfections of the shock-tube flow such as transient phenomena during establishment of the base flow, mixing of driver gas with driven gas at the interface, and boundary-layer growth over the shock-tube wall. A scale model of the Jovian entry vehicle, i.e., Galileo probe, is used as the model for the tests. Time-resolved luminosity photographs and time-resolved spectra are obtained simultaneously with pressure and radiation intensity measurements. The combustion-driven shock tube offers the highest pressures and temperatures among the three facilities used in the present work. In both the 60-cm and the combustion-driven facilities, flow Mach number is limited to less than 2 because of the intrinsic limitation of a shock-tube flow. The shock tunnel, equipped to produce a frozen-flow Mach number of 4.8, is used here to test the effect of high Mach number. The drawbacks of this facility are that the flow-establishment time is relatively long and the thermodynamic conditions are difficult to determine. The typical flow conditions produced by the three facilities are shown in Table I. In Table II, the total number of runs, the number of successful runs, the main purpose of the tests in the facility, and the types of measurements made are given for each facility.

Models and Instruments

Two types of models are used in the experiments: a 5-cm-diam sphere and a scale model of the Jovian probe (JOP Model) with a frustum diameter of 6.4 cm. These models, made of stainless steel, are mounted in the shock tubes on supports having double-wedge cross sections with 20° total angle at the leading and trailing edges. The models are equipped with two voltage-mode piezoelectric pressure transducers, one in the front and the other in the base region. The spherical model has four pyroelectric radiometers, two each on the

Table I. Typical (Calculated) Experimental Flow Conditions

Arc-driven shock tube	
Test gas:	10% H_2 + 90% Ar
Initial pressure:	3 Torr
Shock speed:	4.0 km/sec
Conditions behind primary shock wave	
Temperature:	9900 K
Pressure:	0.75 atm
Density:	2.8×10^{-5} g/cm^3
Mach number (frozen):	1.58
Conditions behind standing shock wave	
Temperature:	13,300 K
Pressure	1.8 atm
Density:	4.5×10^{-5} g/cm^3
Electron density:	1.6×10^{17} cm^{-3}
Conditions at stagnation point	
Temperature:	13,800 K
Pressure:	2.4 atm
Density:	5.8×10^{-5} g/cm^3
Electron density:	2.2×10^{17} cm^{-3}
Combustion-driven shock tube	
Test gas:	10% H_2 + 90% Ne
Initial pressure:	8 Torr
Shock speed:	6 km/sec
Conditions behind primary shock wave	
Temperature:	10,700 K
Pressure:	2.5 atm
Density:	4.7×10^{-5} g/cm^3
Mach number (frozen):	1.69
Conditions behind standing shock wave	
Temperature:	14,200 K
Pressure:	9.8 atm
Density:	1.4×10^{-4} g/cm
Electron density:	2.0×10^{17} cm^{-3}
Conditions at stagnation point	
Temperature:	14,700 K
Pressure:	13.8 atm
Density:	1.8×10^{-4} g/cm
Electron density:	2.9×10^{17} cm^{-3}
Arc-driven shock tunnel	
Test gas:	10% H_2 + 90% Ne
Initial pressure in driven tube:	10 Torr
Shock speed:	7.5 km/sec
Conditions behind reflected shock	
Temperature:	20,900 K
Pressure:	32.4 atm
Density:	2.8×10^{-4} g/cm^3
Electron density:	2.0×10^{18} cm^{-3}
Conditions in test section	
Area ratio:	10
Temperature:	2430 K
Pressure:	0.14 atm
Density:	1.1×10^{-5} g/cm^3
Velocity:	7.1 km/sec
Mach number (frozen):	4.8
Conditions behind standing shock wave	
Temperature:	17,900 K
Pressure:	4.0 atm
Density:	3.9×10^{-4} g/cm^3
Electron density:	2.1×10^{17} cm^{-3}

Table II. Summary of Runs

	Model	Successful run / Total run	Main purpose	Type of measurements
Arc-driven shock tube	JOP	6/6	Long test time Free from wall effect	Radiative q Pressure Time-resolved flow-field photograph Time-resolved spectra
Combustion-driven shock tube	Sphere	6/11	High shock speed High radiative q	Radiative q Pressure Time-integrated flow-field photograph Time-integrated spectra
Arc-driven shock tunnel	Sphere	3/5	High Mach number	Radiative q Time-resolved spectra

front and base sides; the JOP model has three radiometers, two on the front and one on the base side. The shapes of the models and the positions of the pressure transducers and radiometers are shown in Fig. 2. The radiometers have a constant spectral sensitivity over a wavelength range of 0.2 to 50 μ. The nominal response time is 1.2 μsec. Two layers of sapphire windows, each 1.5-mm thick and 9.5-mm diam, protect the radiation sensors. The windows limit

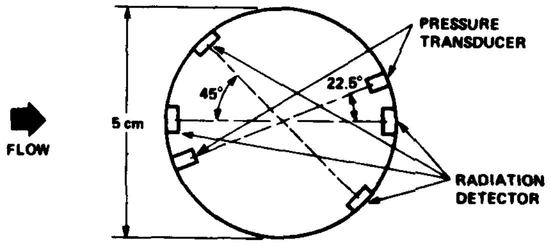

SPHERICAL MODEL

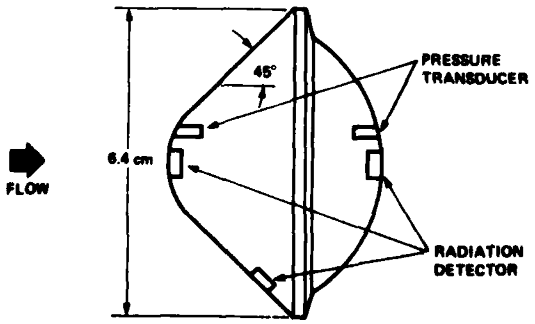

JOP MODEL

Figure 2. Geometry of models and positions of pressure transducers and radiation detectors.

the passband of radiation from about 0.2 to 6 μ. The radiation from ionized hydrogen reaching the wall of the entry vehicle contains most of its radiation energy in the wavelength range from 0.3 to 3 μ (see Refs. 1 and 2) and hence the detectors and windows are adequate for the present work.

To obtain information on the position and diameter of the neck region and the general behavior of the base flow, luminosity photographs are taken with a high-speed framing camera and still cameras. The high-speed camera is used in the tests with the arc-driven shock tube at a framing rate of about 30,000, i.e., a frame at every 33-μsec interval. The open period of the shutter is 3.3 μsec at the framing rate. Several still cameras are used in the tests with the combustion-driven shock tube. The shutters of the still cameras remain open during a test so that the time-integrated luminosity is recorded on the film. Color photographs are taken in all cases. In some cases, an interference filter is placed in front of the still camera to admit only the H-alpha line of hydrogen at 656.3 nm.

Spectra of the flow are recorded with both a time-resolved streak spectrograph and still spectrograph. The streak spectrograph, which has a spectral dispersion of 81 A/mm with a nominal aperture of f/5 and a focal length of 0.4 m, is used in the tests with the arc-driven shock tube and the shock tunnel. The still spectrograph is a Jarrell-Ash 0.75-m, f/8 Czerney-Turner spectrograph. The spectrograph shutter is left open during a run to obtain the time-integrated spectral intensities.

The absolute sensitivity of the radiometers, i.e., the voltage output for known radiation intensity, is calibrated by the manufacturer for a ray normal to the sensor surface. For a ray that reaches the sensor surface at an oblique angle, the sensitivity varies with angle: not only does the sensor surface reflect a portion of incoming radiation, but the sapphire windows, which protect the detectors, block radiation to an extent that varies with angle of incidence of the radiation. Therefore, the sensitivity of the detector-window combinations was calibrated against incidence angle in the present work. The sensitivity decreases rapidly at a large angle and falls to zero at about 45°. The effective viewing solid angles of the detectors are about 1.9 sr as opposed to 6.28 sr for an ideal radiation flux detector. Details of the radiometer calibration are given in Ref. 6.

RESULTS

General Behavior of Flow

In Fig. 3, time-resolved luminosity photographs of the flow field around the Jovian probe model are shown. These photographs are taken in the arc-driven

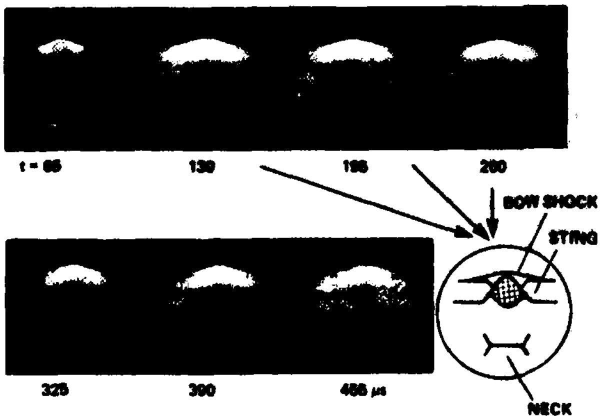

Figure 3. High-speed luminosity photographs of flow field taken in the 60-cm arc-driven shock tube with JOP model.

shock tube by means of the high-speed framing camera. The figure indicates the times measured from the moment of arrival of the primary shock wave at the test section. At $t = 0$, no luminosity was observed and hence the frame is not shown here. After the last frame shown, the luminosity decays rapidly to a very weak intensity. The figures show the bright stagnation region of the shock layer and a fairly bright recompression/neck region behind the model from $t = 130$ to 260 μsec. After 325 μsec, the flow pattern behind the model changes and the neck region disappears. The useful test time is judged from these photographs to be from about 100 to 300 μsec, i.e., over a period of about 200 μsec. As seen from the photographs, the distance between the model frustum and the neck is $x/D \cong 1.5$, and the approximate width of the neck is $W/D \cong 1$, where D is the model (frustum) diameter. Time-resolved spectrograms (not shown) are taken in the four regions of interest, i.e., the front stagnation region, near-recirculation region, far-recirculation region, and neck region in the arc-driven shock tube. The spectra consist mostly of hydrogen lines H-alpha, H-beta, H-gamma, and H-delta, superimposed on impurity radiation. The impurity lines are identified to belong mostly to those of neutral iron.

In experiments with the combustion-driven shock tube, luminosity photographs of the sphere model are taken with a still camera. The shutter is left open from the beginning of a run. The pictures show qualitatively the same features as those in Fig. 3: the front stagnation region and the neck region are the brightest. The distance between the center of the model and the neck region is $x/D \cong 1.2$ in this case as opposed to 1.5 for the JOP model. The difference is probably due to the fact that the flow separation point on a sphere is downstream of the shoulder. The width of the neck region is $W/D \simeq 1$ as it is with the JOP model. The time-integrated spectra taken for the tests in the combustion-driven shock tube are virtually identical to those obtained in the arc-driven shock tube. The time-resolved spectrograms are taken for the tests in the arc-driven shock tunnel. The results indicate that unlike in the other two facilities, radiation emanates mostly from impurities rather than from hydrogen.

Radiative Heat Flux

The measured values of radiative heat flux q_m are tabulated in Table III for each facility. As shown, the measured values of the heat flux to the base stagnation point are significant fractions of those to the front stagnation region. The raw data presented in Table III do not represent the total radiative heat flux because the viewing solid angle of the radiometers is about 1/3 that of an ideal heat flux sensor. To infer the true heat flux from the measured flux q_m, q_m must be multiplied by a correction factor (5.16 for the front-mounted radiometers and 3.13 for the base-mounted radiometers; see Ref. 6). The inferred radiative flux values, denoted by q, obtained by multiplying these factors, are plotted in Fig. 4.

In Fig. 4, the radiative heat flux values are plotted as a function of shock speed. The maximum radiative flux to the front stagnation point obtained from a test in the combustion-driven shock tube is $q_s = 22.1$ kW/cm^2. The base heat flux at the same shock speed is $q_b = 4.7$ kW/cm^2, or 21% of that to the front stagnation point. For the sphere model, the front stagnation point receives twice as much radiative heat flux as does the front 45° point. This is understandable: existing theories predict a difference of such a magnitude between the two points[1,2]. For the JOP model, the front stagnation point and the front 45° point receive about the same heat flux, possibly because of the low Mach number of the flow prevailing in the test facility. As evident from the photographs in Fig. 3, the shock-layer thickness is large over the conical portion of the model due to the low Mach number. Between the two base-mounted radiometers on the sphere model, the 45° point receives about 15% more radiation than the base stagnation point.

Table III. Measured Radiative Heat Flux and Base Pressure (Uncorrected for Radiometer Response)

Run	Initial pressure (Torr)	Shock speed (km/sec)	Heat flux q_m (kW/cm^2)				Pressure (atm)	
			Front stag-nation point	Front 45° point	Base stag-nation point	Base 45° point	Base stagnation point	Front stagnation point
A. 60-cm arc-driven shock tube with Jovian probe model								
15	3	3.8		0.49	0.14			
16	3	3.9	0.49	.44	.14			
17	3	4.1	.70	.71	.21			
18	3	4.1	.64	.57	.19		0.20	
19	2	4.7	.72	.85	.22		.16	
20	4	3.8	.39	.38	.12		.23	
B. Combustion-driven shock tube with sphere model								
3	8.0	6.0	1.50	0.78	0.70			
5	8.9	5.3		.13	.12	0.14		
6	9.0	6.0		.87	.83	.95		
7	6.3	6.5		1.23	1.00	1.12	0.70	10.9
8	5.1	7.0		1.34	1.20	1.33	.53	11.0
9	5.0	7.2	4.28	2.11	1.50		.62	12.0
C. Arc-driven shock tunnel with sphere model								
30	9.9	7.1	3.49	1.47	0.185	0.22		
31	5.0	7.7	1.60	0.64	.079	0.086		
32	7.3	7.5	3.63		.172	0.186		

The ratios of the heat fluxes at the front stagnation point, front 45° point, and base 45° point to that at the base stagnation point are plotted in Fig. 5. The outstanding feature of the result is that all the ratios are nearly independent of shock speed. The ratios are affected significantly, however, by the facility used and by the shape of the model. The data taken in the arc-driven shock tunnel give the highest ratio of front-to-base stagnation point radiative-heat-flux values. This is probably due to the high Mach number attained in the shock tunnel. Between the tests made in the two shock tubes, the tests in the arc-driven shock tube show higher ratios. This difference is attributable to the difference in the model configuration.

Comparison with Theoretical Predictions of Park

According to the theory of Park[3], the ratio of the radiative heat flux at the base stagnation point to that at the front stagnation point, in the absence of ablation, can be written approximately as

$$q_b/q_s = 0.041 f_1(p_b/p_s) f_2(W/D) f_3(x/D) f_4(d/D)$$

and

$$f_1 = [(p_b/p_s)/0.023]^2$$

$$f_2 = [(W/D)/0.667]^2$$

$$f_3 = 1.5/(x/D)$$

$$f_4 = 0.0185/(d/D)$$

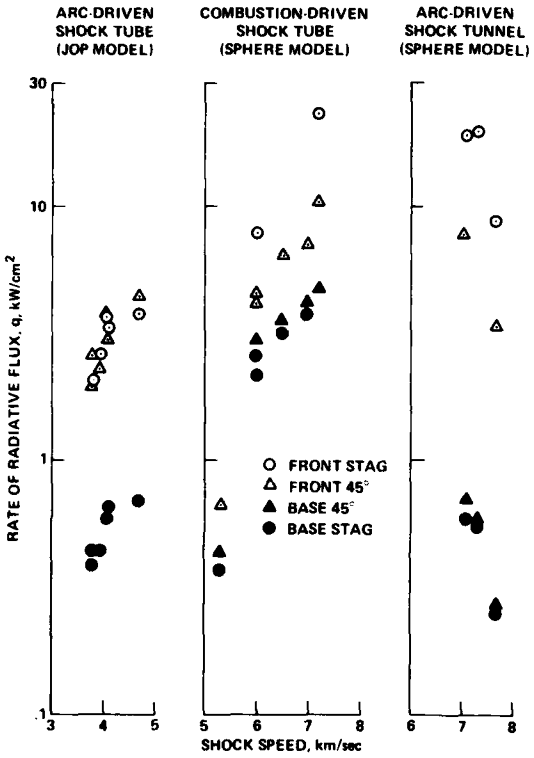

Figure 4. Measured radiative heat fluxes.

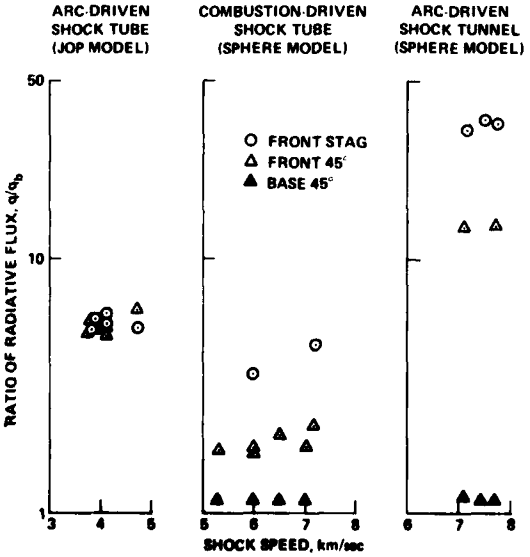

Figure 5. Ratio of radiative heat fluxes at front stagnation point, front 45° point, and base 45° point to that at the base stagnation point.

where q_b is the radiative heat flux to the base stagnation point, q_s the radiative heat flux to the front stagnation point, p_b the base stagnation point pressure, p_s the front stagnation point pressure, W the diameter of the neck region, D the frustum diameter, x the position of the neck region measured from the frustum of the body, and d the shock standoff distance.

In the experiments made in the 60-cm arc-driven shock tube and the combustion-driven shock tube, parameters p_b, W/D, and x/D have been determined experimentally (see above subsection on general behavior of flow and Table III). The front stagnation point pressure p_s is calculable from the charging pressure and the shock velocity. The shock standoff distance d is determined using the formula[7]

$$\frac{d}{R + d} = \frac{k}{1 + \sqrt{k}}$$

where R is the nose radius and k is the density ratio across the bow shock, i.e., the ratio of the density ahead of the shock to the average density in the stagnation region shock layer. The density ratio k is, in turn, calculated assuming equilibrium. For the tests conducted in the arc-driven shock tunnel, the parameters p_b/p_s, W/D, and x/D are unknown; only parameter d/D can be determined using the above equation. Hence, for the tests in the shock tunnel $f_1 = f_2 = f_3 = 1$ is assumed in the comparison between the present data and the theoretical predictions of Park.

The experimental values of q_b/q_s are compared with the theoretical ones of Park in Fig. 6. Here, the data are plotted in the form of q_b vs q_s. Figure 6 shows good agreement between the experimental data and the theory of Park for the tests conducted in the arc-driven shock tube and the combustion-driven shock tube. The experimental data obtained in the shock tunnel show q_b/q_s of about 3% compared to the theoretical value of about 1%. This difference can be attributable to any of the three unknown factors, f_1 through f_3 being different from unity. For instance, if the ratio of the pressure at the base stagnation point to that at the front stagnation point, p_b/p_s, is 0.04 instead of the 0.023 assumed implicitly in the present plots, then the experimental data agree closely with the theory. The value of $p_b/p_s = 0.04$ is not unreasonable, considering the fact that the model in this case was a sphere and the Mach number was only 4.8 instead of 50 in the flight case.

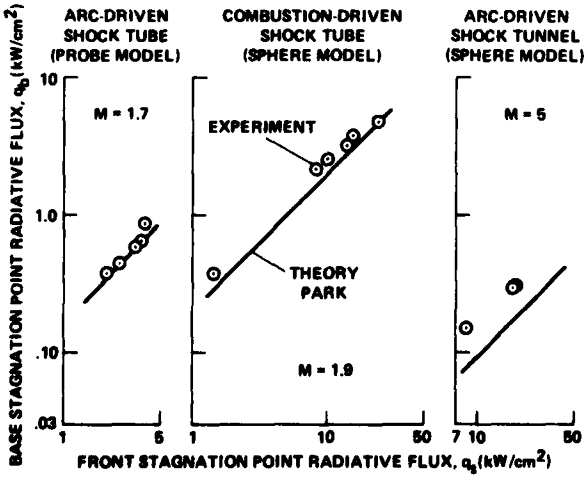

Figure 6. Comparison between the present experimental heat-flux data and the theoretical predictions of Park.

CONCLUSIONS

Within the base flow region, the neck region is the most luminous. The ratio of the radiative heat flux at the base stagnation point to that at the front stagnation point is approximately independent of thermodynamic conditions. With a spherical model, the ratio is about 1/4 at $M \approx 1.8$ and about 1/30 at $M \approx 4.8$. The ratio is about 1/6 for a scale model of the Jovian probe vehicle at $M \approx 1.7$. The present experimental results agree well with the theoretical predictions of Park and hence confirm the validity of the theory.

REFERENCES

1. M. J. Green and W. E. Nicolet, AIAA Paper 78-186, (1978).
2. J. N. Moss, J. J. Jones, and A. L. Simonds, AIAA Paper 78-908, (1978).
3. C. Park, AIAA Paper 79-39, (1979).
4. D. M. Cooper, Absolute Measurements of the Electronic Transition Moment of Seven Band Systems of the C_2 Molecule. Ph.D. Dissertation, York Univ., Canada, (1974).
5. R. E. Dannenberg, Proceedings of the 11th International Symposium on Shock Tubes and Waves, 416 (1978).
6. H. Shirai and C. Park, AIAA Paper 79-38, (1979).
7. W. D. Hays and R. F. Probstein, Hypersonic Flow Theory, Academic Press, New York, 160 (1959).

IN SITU OPTICAL MEASUREMENTS OF PARTICULATE GROWTH IN SOOTING ACETYLENE COMBUSTION

K. Bro*, S. L. K. Wittig** and D. W. Sweeney

The Combustion Laboratory, School of Mechanical Engineering
Purdue University, West Lafayette, Indiana 47907, USA

Particulate growth in shock-induced rich acetylene combustion is studied using the improved dispersion quotient method. The exact Lorenz-Mie equations are solved to compute the extinction cross section for individual particles. Multiple scattering effects and the deviation of the particle shape from the spherical form are analyzed. A constant total soot volume is observed in the later stages of the reaction with growing particle size indicating agglomeration. The spherical shape is largely retained with a relatively narrow size distribution. Soot is formed in the temperature range from 1600 K to 2100 K with a significant increase due to rising reactant pressure.

INTRODUCTION

Efficiency and performance considerations as well as environmental concern increasingly have focused new attention on the formation of particulates and especially soot from various technical applications such as the new generation of high performance gas turbine combustors, Diesel engines and furnaces. Although the nucleation of soot from gaseous hydrocarbon combustion has been of longstanding fundamental interest as shown in the literature review by Lahaye and Prado[1], Lester and Wittig[2,3], Palmer and Cullis[4] and others, many questions still remain to be solved. D'Alessio et al.[5] recently have raised new questions and initiated extensive discussions.

The majority of experimental studies has been performed in flames. Pagni and Bard[6], for example, investigated in their latest study particulate behaviour in diffusion flames. Temperature, concentration and velocity gradients, however, strongly

---

Present adress: * Kildedalen 110, DK-3400 Hillerød/Denmark

** Institut für Thermische Strömungsmaschinen, Universität Karlsruhe (T.H.), Kaiserstraße 12, D-7500 Karlsruhe 1/West Germany effect the measurements in flames. In an earlier study, Lester and Wittig[7] have shown that the shock tube is uniquely suited for an experimental observation of the early stages of soot formation. By applying the optical dispersion quotient technique, soot formation from rich methane combustion was followed in the reflected shock core flow region which provides a homogeneous reaction environment largely void of property gradients.

The purpose of the present investigation was to extend the earlier studies[7] based on the improved dispersion quotient technique. Of primary importance was the soot formation from acetylene combustion as acetylenic species may play a dominant role in the soot formation route[2,3].

EXPERIMENTAL

The experimental apparatus, i.e. the shock tube and peripheral instrumentation, have been described by Wittig, Lester et al.[2,3,7]. Various improvements, however, were added to the conventional shock tube and the optical light extinction technique described below. Extreme care was taken to verify the fuel to air ratio of the premixed gases. Samples were analyzed spectrometrically. As with previous experiments, measurements were made in the reflected shock region.

The light sources were a 3 mW He-Ne laser and a 5 W Argon-Ion laser. The red He-Ne line (6328 A) was used to give the long wavelength reference line whereas the Ar-Ion laser was tuned to give all lines in the visible range with filters of 100 A band width separating the green λ = 5145 A line and the blue 4880 A line. The alignment was such that all beams were colinear within the shock tube test region. The laser intensity was kept relatively high to minimize the significance of emission from the combustion. Furthermore, several apertures and diffusing screens eliminated any remaining influence from stray light and emissions.

The detectors (photomultipliers and photodiodes) were checked for both response and linearity. The uncertainty originating from the laser noise was less than ± 0,5 per cent.

The theoretical basis for determining the mean-volume-radius and the number density of the soot particulates is the two-wavelength turbidity ratio method as described by Lester and Wittig[7]. The dispersion quotient is obtained from

$$DQ(r, \lambda_1, \lambda_2, m) = \frac{\ln(\frac{I}{I_o})_{\lambda_1}}{\ln(\frac{I}{I_o})_{\lambda_2}} = \frac{C_{ext_{\lambda_1}}}{C_{ext_{\lambda_2}}}$$

with

$r \triangleq$ particle radius
$m \triangleq$ complex index of refraction
$I \triangleq$ intensity
$C_{ext} \triangleq$ extinction cross section

By assuming that the particles are spherical in shape the dispersion quotient can be computed by applying the exact Lorenz-Mie relations. Figure 1 shows the relation between the particle size and the dispersion quotient for three different indices of refraction, under the assumption that the refractive index is constant with wavelength.

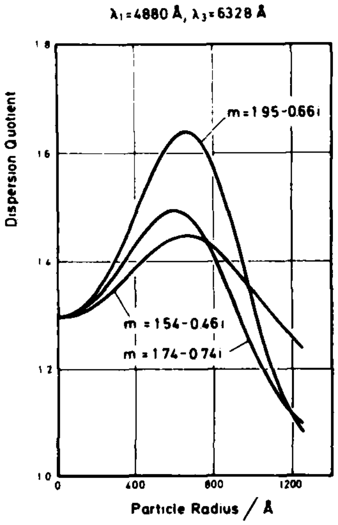

Figure 1. Dispersion quotient computed from exact solution to Lorenz-Mie theory.

It is obvious that the method is sensitive to refractive index variations. A detailed analysis is presented in References 3 and 8. The most conspicuous problem, however, is the ambignity to particle size as shown in Figure 1. To solve this problem it is necessary to introduce a third wavelength giving two independent sizing curves. Figure 2 shows the dispersion quotient for two different wavelength pairs: the convenient laser lines 4880 A, 5145 A and 6328 A. If a dispersion quotient as shown by line A is measured utilizing the wavelengths 5145 A and 6328 A, the size is seen to be either approximately 400 A or 750 A. However, a coincidence check as shown in Figure 2 using an additional wavelength provides a unique solution.

The discussion so far has assumed the particles to be of spherical shape. However, electron microscopy of larger particles from flames indicates that particles can and often do agglomerate into odd shaped clusters. Computation of the dispersion quotient of arbitrary shaped particles is extremly difficult, but the dispersion quotient for randomly oriented cylinders can be computed for representation of strongly elongated particles. Figure 3 shows this dispersion quotient together with that of spheres. It is obvious that there is a marked difference indicating the necessity for knowing the characteristic shape. On the other hand, if the particles during transient growth show a dispersion quotient with a definite high maximum it can be concluded that the particles are not elongated.

Analysis of the method shows that measurement errors have the least influence if I/I_0 is in the vicinity of 0.37. For

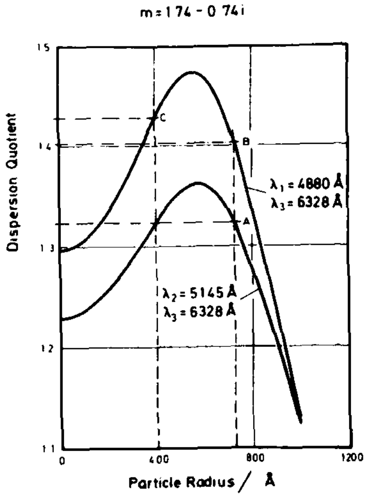

Figure 2. Dual ratio sizing curves.

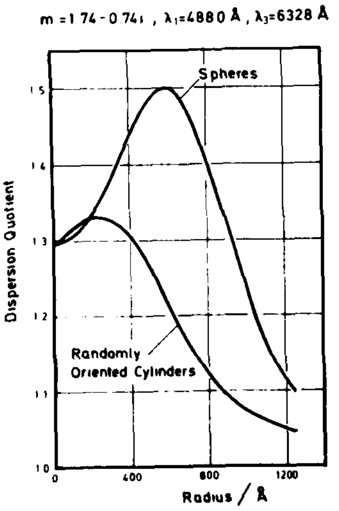

Figure 3. Dispersion quotient for spheres and cylinders.

small I/I_0 multiple scatterings effects will be of importance in conflict with the assumptions of Beer's law.

A thorough investigation[8] shows that with carbon heavily absorbing, the error induced will not exceed 1 per cent for I/I_0 down to approximately 0.37.

A final question concerns the size distribution of the growing particles. Measurements in flames by Wersborg et al.[9] show that the particles have a narrow relative Gaussian size distribution. A relative standard deviation of s = 0.2 for the smallest particles and in extreme cases s = 0.5 was measured. For larger particles the size distribution becomes logarithmic. Studies by Lahaye and Prado[1] advocate that the particles are monodisperse in size in a time resolved system and that measurements in flames, which are spatially resolved, show Gaussian distribution because of sampling from different volume elements, and not because of spatial distribution. Figure 4 shows that there is a decrease of the maximum attainable value of the dispersion quotient with increased standard deviation. It, therefore, follows that a high maximum dispersion quotient is an indication for a narrow size distribution.

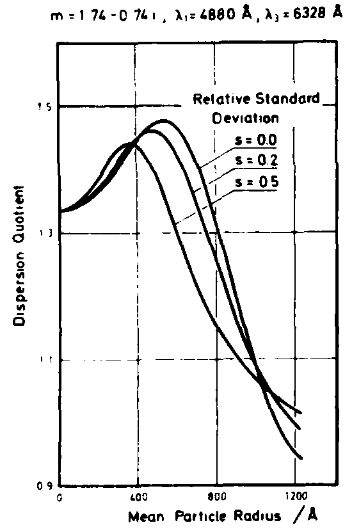

Figure 4. Dispersion quotient as a function of the standard deviation of the Gaussian size distribution.

In summarizing, the lower limit of the particle size that the method is capable of measuring was found to be approximately 150 A. However, the method is still capable of determining the particle volume for all particles below this limit. The upper limit, depending on the optical system, is typically above 1000 A. A calibratioh of the technique was obtained for the upper size range.

EXPERIMENTAL RESULTS

Experiments were made in argon diluted rich methane and acetylene combustion. We were able to reproduce the sooting limits of Radcliff and Appleton[10].

The experiments clearly show a maximum particle formation at temperatures around 1850 K for equivalence ratios above the sooting limit. For methane the formation was found to disappear at temperatures below approximately 1600 K and to be very weak above 2100 K at an equivalence ratio of Ø = 5.0, while no formation was measured below Ø = 5.0. For acetylene nearly the same pattern was found for equivalence ratios above Ø = 3.0. At Ø = 5.0 the formation appeared with very short induction time at temperatures around 1600 K and with strongly increasing induction time for increasing temperatures.

Figure 5 shows an extinction trace for acetylene at T = 1840 K (the 5145 A trace is inverted). The extinction is seen to have several plateau's indicating changes in the formation pattern or optical effects. Figure 6 shows the related dispersion quotients for the two wavelength pairs 4880 A, 6328 A and 5145 A, 6328 A. The dispersion quotients determined are too high by 10 to 15 per cent when compared to be sizing curves. The reason for this is not fully understood. It could be caused by the influence of large hydrocarbons or droplets. However, as the particle agglomeration may not be fully compact it is more likely to be due to changes in the index of refraction. A very important fact about this maximum, however, is the indication that the particles must be spherical in shape and of relative narrow size distribution. As shown in the previous section, the maximum value for randomly distributed cylinders is significantly smaller than for spheres. Hence, it would not be possible to reach the maximum value shown in Figure 6 for acetylene combustion if the particles were elongated. It could be argued that the particles were large molecules of low absorptivity resulting in high dispersion quotients[8]. This, however, is not credible, as these particles would have to be formed from absorbing (soot) particles present earlier as indicated by a small dispersion quotient.

Using the criterion to be derived from Figure 2 that the size is approximately 600 A for maximum dispersion quotient we arrive at the sizes plotted in Figure 7. The figure also shows the particle number density and carbon concentration. It is seen that the carbon concentration in this experiment is constant in the time interval where the dispersion quotient could be measured. Furthermore, it is seen that the size is increasing, which means that the particles are growing by agglomeration and not by formation of carbon. As the particles are spherical and agglomerating it follows that the soot particulates remain spherical in shape during agglomeration in a largely homogeneous system such as the reflected core zone of the shock tube. In comparison to methane, the particle size is considerably larger at comparable reaction times.

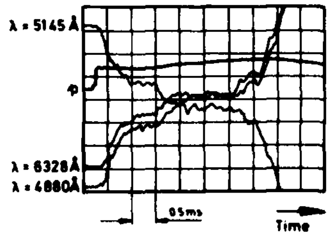

Figure 5. Light extinction in rich acetylene combustion (Ø = 5.0; T = 1840 K; p = 0.49 bar).

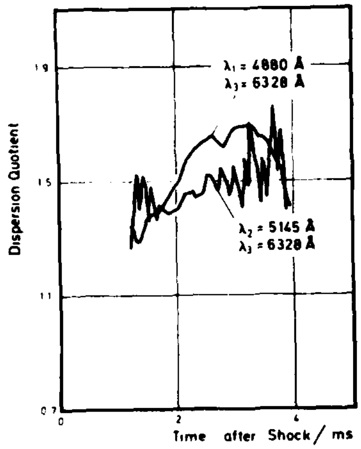

Figure 6. Dispersion quotient with time after shock arrival (Ø = 5.0; T = 1840 K; p = 0.49 bar)

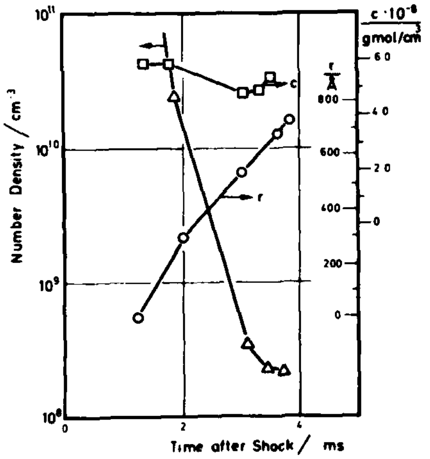

Figure 7. Particle number density, carbon concentration and particle size (Ø = 5.0; T = 1840 K; p = 0.49 bar)

CONCLUSIONS

The extended analysis of the dispersion quotient method provides detailed information on the soot formation process during hydrocarbon combustion and specifically in acetylene combustion in the reflected core region of a shock tube. In the later stages of the reaction a constant total soot volume is observed and from sizes of approximately r = 200 A the particulates grow by agglomeration. Up to r = 800 A the particles largely retain a spherical shape and a narrow relative size distribution.

A comparison of the improved measurements with methane combustion indicates that particle radii in acetylene are considerably larger. In both cases it was found that no soot was formed at temperatures below 1600 K and above 2100 K with a maximum formation at intermediate temperatures (approximately 1850 K). Rising reactant pressures produced a significant increase in the soot volume.

ACKNOWLEDGEMENT

The authors are grateful to the American Chemical Society and the Danish Research Council for the financial support of this work.

REFERENCES

1. Lahaye, J. and Prado, G., Petroleum Derived Carbons, M.L.Deviney and T.M.O'Grady, Eds., ACS Symposium, Series 21, American Chemical Society, Washington, D.C., 335 (1976)
2. Lester, T.W. and Wittig, S.L.K., Sixteenth Symp.(Intl.) on Combustion, The Combustion Institute, 671 (1976)
3. Wittig, S.L.K. and Lester, T.W. in Advances in Chemistry Series, No.166, J.T.Zung Ed., 167 ff.(1978)
4. Palmer, H.B. and Cullis, C.F., The Chemistry and Physics of Carbon, Vol.1, P.P.Walker Jr., Ed., Marcel Dekker 265 (1965)
5. D'Alessio, A., DiLorenzo, A., Borghese, A., Beretta, F. and Masi, S., Sixteenth Symposium (Intl.) on Combustion, The Combustion Institute, 695 (1976)
6. Pagni, P.J. and Bard, S., Particulate Volume Fractions in Diffusion Flames, paper presented at the 17th Symposium (Intl.) on Combustion, Leeds (1978), to be published
7. Lester, T.W. and Wittig, S.L.K., in Modern Developments in Shock Tube Research, G.Kamimoto Ed., Kyoto University, 632 (1975)
8. Bro, K., The Optical Dispersion Quotient Method for Sizing of Soot in Shock Induced Combustion, Ph.D.Thesis, Purdue University (1978)
9. Wersborg, B.L., Howard, J.B. and Williams, G.C., Fourteenth Symposium (Intl.) on Combustion, The Combustion Institute, 929 (1972)
10. Radcliffe, S.W. and Appleton, J.P., Comb.Sci.Tech. 3, 255 (1971)

SPONTANEOUS CONDENSATION OF AN AZEOTROPIC FLUID

S. L. K. Wittig, R. A. Zahoransky, S. S. Kim and D. E. Wurz

Institut für Thermische Strömungsmaschinen
Universität Karlsruhe (T.H.), D-7500 Karlsruhe-1, West-Germany

The homogeneous condensation of an alcohol/water azeotrop (MWA) has been studied utilizing the expansion fan of a shock tube combined with light extinction measurements. The study has been performed in the temperature range of 340 K to 420 K at pressures up to 5 x 10^5 N/m^2. The thermodynamic data obtained from parallel measurements of the speed of sound are comparable with those of water/steam. The analysis of the experimental data reveals new phenomena. Predominantly, condensation occured at low subcooling. The effects of the expansion rate were of minor importance. The results are of practical importance to power plant design.

INTRODUCTION

The homogeneous condensation of initially saturated or superheated vapors during rapid expansion has been of longstanding theoretical interest. In technical applications, its importance especially in the area of energy conversion increasingly has attracted attention in recent years with the growth of the power plants. One of the most important examples is found in low pressure ends of steam turbines. Their design depends on the knowledge of the Wilson region which defines the states of condensation occurance. The majority of studies, therefore, can be found on steam condensation. Almost no information, though, is available for binary vapor mixtures and specifically azeotrops. Especially with interest growing in solar energy utilization, waste heat recovery and other applications, these fluids have attracted considerable attention. The present study is directed towards the condensation characteristics of an alcohol/water azeotrop (MWA). Originally, i.e. prior to this investigation and associated studies, the fluid was considered to be well qualified to be used in a modified power plant where MWA was to be utilized as fluid in a bottoming cycle with major advantages with respect to turbine size and cooling tower application[1,2,3].

As shown in Figure 1, the phase diagram of the binary methoxypropanol/water mixture of the present study deviates con-

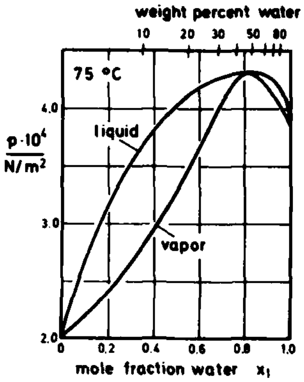

Figure 1. p,x-diagram water-methoxypropanol

siderably from an ideal mixture. At a certain composition the vapor pressure will show a maximum value at constant temperature forming an azeotropic mixture with the liquid and vapor phase of the same composition. Thus, a separation of the components by distillation is impossible and azeotropic fluids generally can be described as one-component systems. In the case of the methoxypropanol/water mixture of this study it was indicated by the manufacturer that the azeotropic mixture composition is practically independent of temperature in the range of interest from 340 K to 420 K. Please note that the azeotropic mixture consists of approximately 50 percent water by weight. As thermodynamic data were scarce, we derived a shortened virial equation for determination of the thermodynamic states of the following form:

$$pv = RT + B(T)p \qquad \text{for } 340\ \text{K} < T < 420\ \text{K} \qquad \text{I}$$

with

$$B(T) = b_o + \frac{b_1}{T} \exp\left(\frac{b_2}{b_3 + T^2}\right) \qquad \text{II}$$

$b_o = 0.115\ \text{m}^3\text{kg}^{-1}$

$b_1 = -26.3\ \text{m}^3\text{K kg}^{-1}$

$b_2 = 1.33 \times 10^7\ \text{K}^2$

$b_3 = 1.6 \times 10^7\ \text{K}^2$

This form was chosen as it has been shown to be quite accurate for water vapor close to the saturation line and in the metastable state[4,5]. Furthermore, MWA is quite similar to water with respect to density and vapor pressure. The virial coefficient of equation II was determined by matching speed of sound measurements made in a parallel study. With additional information on the vapor pressure[6] and the specific heat[7] we were able to determine the properties of interest assuming that the mixture is azeotropic. The saturation line in the T,s- or h,s-diagram thus determined deviates from the data obtained from the supplier of MWA with interesting consequences as will be described in the following.

EXPERIMENTAL

To avoid the difficulties associated with a continuous cycle operation, the studies were performed in the expansion fan of a shock tube.

The main components of the experimental setup are shown in Figure 2.

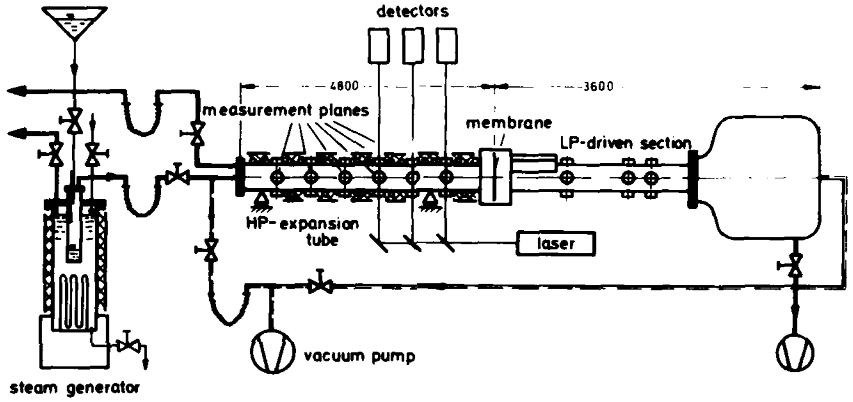

Figure 2. Schematic of expansion tube

To avoid local excessive superheating, the test fluid was indirectly heated in a water bath within the steam generator. The expansion tube was connected by insulated tubing with the steam generator. The high pressure (expansion) section - 4.8 m in length, 0.089 m in diameter and insulated - is heated by several independently controlled heating coils. Temperature deviations were carefully determined and found to be within ± 1 K.

The condensation was observed by simultaneous pressure and light extinction measurements[8]. For this reason, six measurement planes were used in the expansion tube each equipped with four taps for pressure transducer and window mounting. The response time of the piezoelectric pressure transducers was determined to be 8 μs. The onset of condensation was observed by light extinction. A He-Ne laser was used as light source with a photodiode detector. The response time of the photodiode was comparable to that of the pressure transducer - well within the required value. The initial state within the tube was determined by static pressure transducers and several thermocouples along the tube.

All components in contact with the fluid were of stainless steel. The vacuum system and other associated equipment were of conventional design. Up to temperatures of 370 K we used cellophane as diaphragm material. With rising pressures and temperatures, hostaphan was chosen.

MEASUREMENTS AND ANALYSIS

For calibration purposes, measurements were made with argon, nitrogen, air and steam. In contrast to several other studies[9,10], no major deviations from the centered rarefaction fan were observed. All experimental results with non-condensable gases could be described with sufficient accuracy by assuming an ideal, centered expansion fan without correction for boundary layer and non-ideal opening effects of the diaphragm. An experimental series with steam in the reflected rarefaction wave shows excellent agreement with previous measurements as shown in Figure 3[11,12,17].

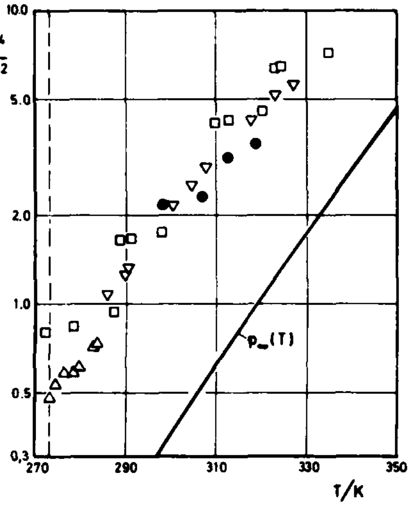

Figure 3. Wilson region of steam

- ☐ Gyarmathy and Meyer[11]
- ▽ Barschdorff[17]
- △ Barschdorff[12]
- ● Present study

The speed of expansion $\dot{p} = -1/p \; dp/dt$ in our experiments was approximately $10^2 \; s^{-1}$ and thus by one or two orders of magnitude lower than those reported in reference[11,12,17].

With condensation within the expansion fan, the assumption of simple isentropic flow is invalidated. Figure 4 shows a typical oscillogram of moist air. It can be seen that pressure pulses originate within the expansion fan approximately at the same time condensation begins. In contrast to the analysis of the experiments with gases, it is impossible to determine the state and the speed of expansion under these conditions.

Heat addition yields a higher local speed of sound and the slopes of the left-running characteristics are changing as qualitatively shown in Figure 5.

As reported by Heybey and others[9,10,14,15,16] this will lead to "weak detonations". The sudden heat addition initiates a pressure rise in the subsonic flowfield of the expansion fan. Qualitatively this may be explained by the fact that the onset of homogeneous condensation depends on the speed of expansion. At high speeds of expansion higher supersaturation will be obtained than at low expansion rates. Therefore, the condensation front intersects the leftrunning characteristics thus leading to supersonic speed of the fluid particles relative to the condensation front. From Figure 5 it can be seen for a leftrunning characteristic ($x/t = u-a$) crossing the condensation front ($x/t = c_c < 0$):

$$u - c_c > a \qquad \text{III}$$

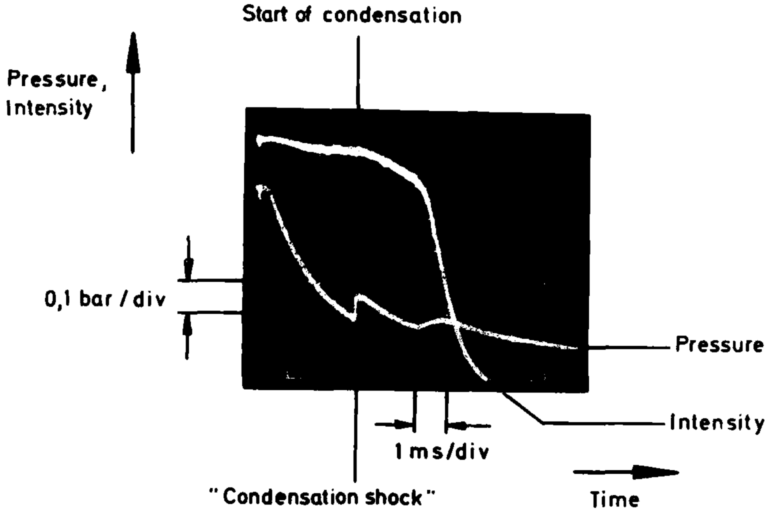

Figure 4. Expansion of moist air

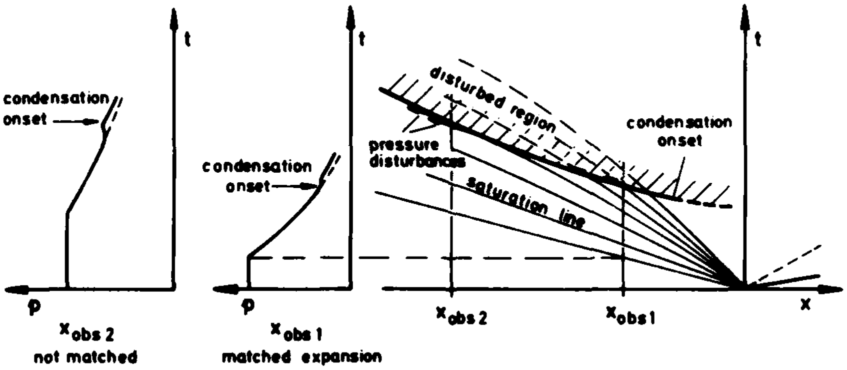

Figure 5. Expansion fan with heat addition by condensation

This may explain the local pressure rise observed. It should be noted, however, that the onset of condensation generally is not identical with the "condensation shock". With proper choice of the initial pressure ratio across the diaphragm it is possible to avoid the occurance of the pressure rise prior to condensation. By using this technique, known as "matched expansion", isentropic relations can be applied up to condensation[17].

With reliable and reproducible performance of the facility assured, measurements were made with MWA. Figure 6 shows a typical "matched expansion" with MWA vapor. The condensation begins before a deviation from the isentropic expansion occurs. In general, no "condensation shocks" were observed with pure MWA and pure steam. However, in comparison with isentropic expansion, a pressure rise was always observed (Figure 7).

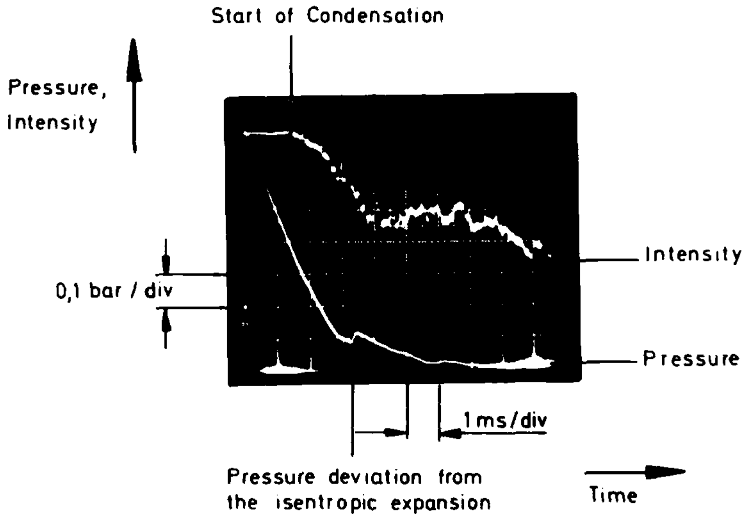

Figure 6. Matched expansion of MWA-vapor

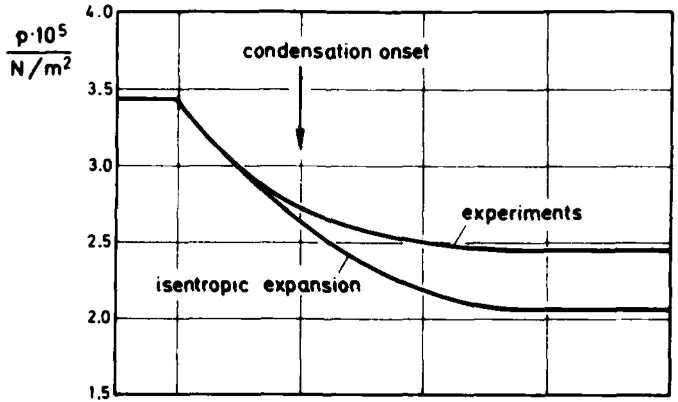

Figure 7. Influence of condensation on pressure history (not matched)

Figures 8 and 9 show the Wilson-points for MWA-vapor. MWA was treated as a real gas using equation I. At the beginning of the expansions the states of the vapor were very near to the satu-

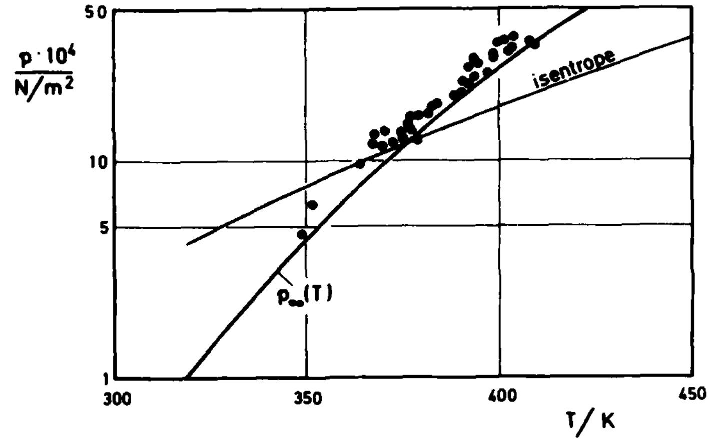

Figure 8. Wilson-region of MWA-vapor (p,T-diagram)

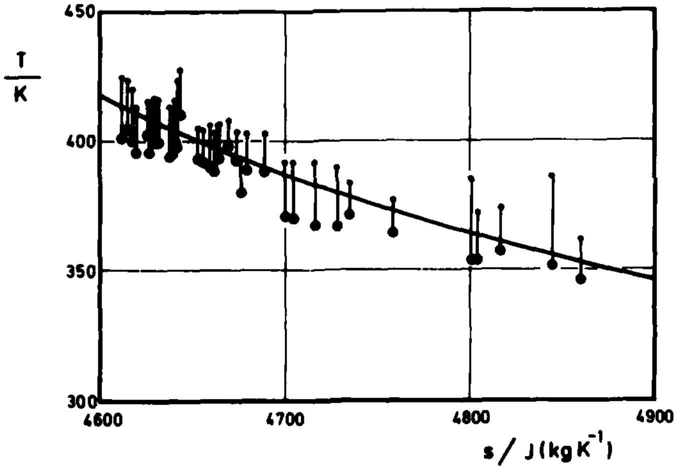

Figure 9. Wilson-region of MWA-vapor (T,s-diagram)

ration conditions, while the vapor temperature was varied between 340 K and 420 K. The temperature/pressure range was chosen because of its importance to practical applications. The speed of expansion was varied from 10^2 s^{-1} to $3x10^2$ s^{-1}. A strong influence of the expansion rate was not observed. It can be seen that considerable lower subcooling rates were achieved with MWA than with steam under similar conditions (6 °C vs 30 °C respectively), i.e. condensation starts "earlier" with MWA, an effect highly undesirable for a number of practical applications. Furthermore, considerable variations and scattering of the data was observed, considerably outside the measurement uncertainties.

DISCUSSIONS AND CONCLUSIONS

Besides the "early" condensation with its technical consequences, a remarkable observation during the present study is a relatively wide scattering of the Wilson-points in MWA which is in contrast to our results with steam. Figures 8 and 9 even show onset of condensation above the saturation line. An explanation may be found by consulting the p,T-diagram (see also Fig.1). The vapor pressure of MWA is the highest in comparison with water and pure methoxypropanol. If deviations from the azeotropic point occur, a condensation onset at higher temperatures can be explained as discussed by Reiss[18]. In this event, a simple thermodynamic description of the binary mixture as a one-component system is impossible.

Qualitatively, the theory of condensation of binary mixtures is well established[18]. The majority of studies has been performed utilizing the ethanol/water mixture[19-22] without specific consideration of the azeotropic point. A theoretical analysis of MWA, however, poses extreme difficulties, as phase equilibria and surface tension data are not available with reliable accuracy. An additional difficulty is introduced with binary mixtures. Besides the often discussed dependence of the surface tension on the radius of curvature of the surface, Mirabel and Katz[23] pointed out an additional difficulty:

The surface tension of a binary mixture, determined for a plane surface as a function of the mixture composition, generally cannot be used for the analysis of the fast process of homogeneous condensation. The binary fluid will be enriched with that component which reduces the surface tension. This, however, is impossible during the fast process of condensation. Consequently, the surface tension will be higher during condensation. This phenomenon certainly will be of greater importance with these mixtures which have a strong dependence of the surface tension on composition.

Because of the difficulties and uncertainties described a detailed theoretical analysis of the condensation of MWA presently seems not to be appropriate. For engineering applications, though, the present experimental study reveals sufficient information for a design analysis.

REFERENCES

1. A.Buch, Energie 3, 91 (1978)
2. J.Heeren, Energie 4, 135 (1978)
3. M.A.N., Energie 3, 74 (1978)
4. A.Ludwig, Diss.Univ.Karlsruhe (TH)(1975)
5. G.Hausmann, Diss.Univ.Karlsruhe (TH)(1976)
6. Maschinenfabrik Augsburg-Nürnberg AG (MAN), private communication
7. Institut für Technische Thermodynamik, Univ.Karlsruhe (TH) private communication
8. K.Bro, S.L.K.Wittig and D.K.Sweeney, This Symposium (1979)
9. H.Kawada and Y.Mori, Bull.of the JSME 16/97, 1053 (1973)
10. I.I.Glass, S.P.Kalra and J.P.Sislian, AIAA-J. 15/5, 686 (1977)
11. G.Gyarmathy and H.Meyer, VDI Forschungsheft 508 (1965)
12. D.Barschdorff, Forsch.Ing.-Wes. 37/5, 146 (1971)
13. P.P.Wegener and A.A.Pouring, Phys.Fluids 7, 352 (1964)

14. W.H.Heybey and S.G.Reed jr., J.Appl.Phys. 26/8, 969 (1955)
15. J.P.Sislian and I.I.Glass, AIAA-J. 14/12, 1731 (1976)
16. P.P.Wegener, Gasdynamics 1, Nonequilibrium Flows, Marcel Dekker, N.Y. (1976)
17. D.Barschdorff, Phys.Fluids 18/5, 529 (1975)
18. H.Reiss, J.Chem.Phys. 18, 840 (1950)
19. H.Flood, Z.Phys.Chem. A 170, 286 (1934)
20. A.Kaser, ZAMM 53, 39 (1973)
21. G.Wilemski, J.Chem.Phys. 62/9, 3763 (1975)
22. P.P.Wegener and B.J.C.Wu, Faraday Disc.Chem.Soc.61, 77 (1976)
23. P.Mirabel and J.L.Katz, J.Chem.Phys. 67/4, 1697 (1977)

THE USE OF AN UNSTEADY WAVE CHEMICAL REACTOR AS A KEY ELEMENT IN THE PRODUCTION OF H_2 FOR USE IN SYNTHETIC FUEL PRODUCTION

E. L. KLOSTERMAN, R. T. TAUSSIG, T. S. VAIDYANATHAN
P. CASSADY, L. STEINHAUER and M. SHIRAZIAN

Mathematical Sciences Northwest, Inc.
Bellevue, Washington USA

Recently we have studied the use of an unsteady wave chemical reactor in the production of H_2 for use in synthetic fuel production. In the hydrogen production process studied, the wave reactor performs the important function of cooling a gas stream containing dissociated CO_2 sufficiently fast that the recombination reaction is quenched.

The paper describes the gas dynamics and chemical kinetics of the CO_2-diluent stream in the wave reactor. Low specific heat ratios of the gas mixture ($\gamma \sim 1.3$) and large compression-expansion ratios lead to high gas flow speeds and increased aerodynamic losses. Specific unsteady wave processes which minimize these losses are described. Results are presented giving the dependence of CO yield on pressure, temperature, and diluent gas fraction. Realistic estimates of losses and the effect of wave reactor operation on overall cycle efficiency are also discussed.

INTRODUCTION

The use of unsteady wave machines for various applications originated with the pressure exchanger patented by Seippel in 1942.[1] Such machines make use of unsteady waves (shocks and expansion waves) to process a gas stream (or streams) in a specified manner. An early application of unsteady wave machinery developed by the Brown Boveri Company[2] was to supercharge diesel engines. Other important applications including the use of unsteady wave machinery to produce high stagnation temperature flows for hypersonic wind tunnel research,[3] applications in the chemical processing field,[4] and, more recently, applications in the energy field[5,6] have been identified. These and other applications are summarized in the Paul Veille paper of this conference.[7] The present paper describes an application of the unsteady wave machine to the production of hydrogen (H_2) for use in synthetic fuel production (e.g., CH_4, gasoline, methanol).

Unsteady wave machines consist basically of an array of shock tubes attached to the circumference of a rotating drum as shown in Figure 1. As the drum rotates, each individual tube will experience a gas dynamic cycle determined by the placement of stationary manifolds at each end of the drum which allow gas to be fed or exhausted from the tubes. In addition, solid end walls are used to stop the flow at strategic points in the cycle and reflect waves. To generate compression waves the tubes are exposed to a high pressure manifold of an auxiliary driver gas which enters the tubes and compresses the gas within

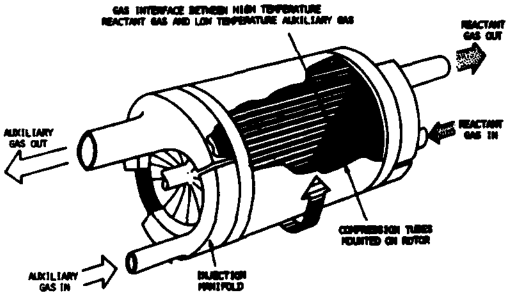

Figure 1. Sketch Showing the Basic Geometry of an Unsteady Wave Chemical Reactor.

it. To generate expansion waves the tubes are exposed to low pressure manifolds and the gas in the tubes flows out. By properly timing the exposure of the tubes to the different manifolds, the gas in each tube will undergo the desired pressure and temperature history required by a particular chemical process (e.g., see Reference 8). By using a large number of tubes on the rotating drum, the pulsed process occurring in a single shock tube is converted to a continuous process.

H_2 PRODUCTION PROCESS

The production of H_2 can be accomplished in several ways.[9,10,11] The method described here is based upon the thermal dissociation of CO_2 into CO and O_2. The CO so produced is separated out and reacted with steam to form H_2 and CO_2. The wave reactor is used in conjunction with the CO_2 dissociation.

A simplified schematic of the process is shown in Figure 2. A stream of CO_2 and He diluent is used to cool the blanket of a fusion reactor where the high energy neutrons originating from the fusion reactions deposit their energy in the form of heat. In particular, the blanket must reach temperatures of greater than 2000 °K. The necessity for high temperature is based on maximizing the amount of CO_2 dissociation which occurs. For the blanket materials (CaO, MgO, ZrO_2) considered, temperatures of 2400 °K maximum appear feasible in a stress-relieving design. To achieve CO_2 dissociation levels greater than the 3 to 6 percent consistent with 2400 °K, higher temperatures are required. These are achieved by injecting the CO_2-He coolant into a wave reactor where it is heated and compressed to 3000 °K or more. At these temperatures equilibrium CO_2 dissociation yields range from 15 to 25 percent depending on the partial pressure of CO_2. Unsteady gas dynamic expansion (the key feature of the wave

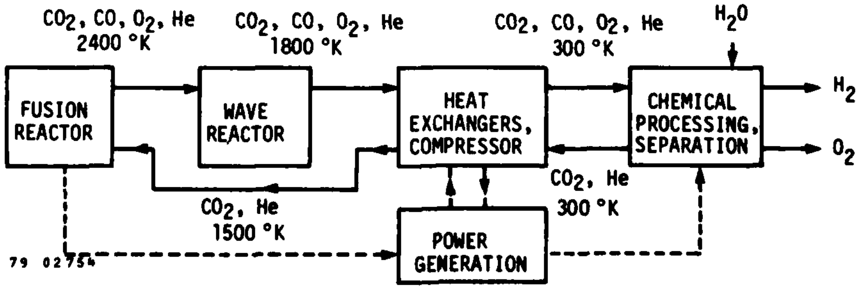

Figure 2. Schematic Diagram of H_2 Chemical Processing Cycle

reactor) is used to rapidly cool the mixture ($dT/dt > 10^6$ °K/sec) from 3000 °K to below 2000 °K to prevent significant recombination of the CO and O_2. The unsteady expansion process in the wave reactor is the only viable means to achieve such rapid cooling rates and is central to the achievement of high CO (hence H_2) yield.

Once cooled to below 2000 °K, further cooling to ambient conditions is necessary. High temperature ceramic heat exchangers with gas cooling rates as high as 10^5 °K/sec have been developed. Some of the heat rejected in the heat exchangers is used to preheat the coolant stream entering the fusion reactor blanket and some is used for generation of electric power to operate the chemical plant. Once cooled to ambient conditions, the CO_2, CO, O_2, He mixture enters the chemical plant where the CO is separated out and injected along with steam into a "water gas shift" reactor.[12] About 98 percent conversion to H_2 and CO_2 is accomplished in the reaction $CO + H_2O \rightarrow H_2 + CO_2$. The product stream is then separated into H_2, the desired end product, and CO_2 which is recycled along with the previously separated CO_2 and He as fusion blanket coolant. The stream is compressed when leaving the chemical plant to allow for pressure drops which occur in the system.

The discussion in this paper assumes a total fusion power of 4000 MW thermal with 50 percent of this power extracted by the high temperature blanket coolant reactant stream. This results in a coolant mass flow rate of 900 Kg/sec with 60 percent of the coolant He and the balance CO_2 and its dissociation products.

CHEMICAL KINETICS

Two computer codes have been developed to follow the chemical kinetics through the wave reactor. The first code is a chemical kinetics code used to determine the CO yield when given a gas temperature and pressure history based on ideal gas dynamics. A second code which couples the unsteady gas dynamics and chemical kinetics was also developed. This code uses a flux corrected transport[13] method of numerical calculation and has been adopted specifically for application to the processes occurring in the wave reactor. This code allows the inclusion of heat transfer and wall friction effects in addition to those of chemical heat release. For most cases of interest the results from the simpler code are sufficiently accurate and are used in this paper.

The major high temperature chemical reactions included in the codes are listed in Table I; the rate data were taken from shock tube data in References 14 through 16. Additional chemical reactions which include the impact of trace amounts of water impurity have also been included. Water is known to significantly impact the rate of CO-O_2 recombination.[17,18] (Water impurities may be introduced by the CO_2 originating from the water gas shift reactor.) The gas temperature should be dropped by at least 1000 °K in the expansion to ensure

Table I. Key High Temperature Reactions

Primary Reactions	Forward Rate Constant @ 3000 °K
$CO + O_2 \rightleftarrows CO_2 + O$	$k \sim 10^{-15}$ cm³/sec
$CO + O + M \rightleftarrows CO_2 + M$	$k \sim 10^{-34}$ cm⁶/sec
$O + O + M \rightleftarrows O_2 + M$	$k \sim 10^{-34}$ cm⁶/sec
Impurity Reactions	
$CO + OH \rightleftarrows CO_2 + H$	$k \sim 10^{-12}$ cm³/sec
$O_2 + H \rightleftarrows OH + O$	$k \sim 10^{-11}$ cm³/sec

adequate quenching of the $CO-O_2$ recombination. Rate coefficients at 3000 °K for the key reactions are indicated in Table I. For pressures of 10 atmospheres at 3000 °K the characteristic CO/O_2 recombination time is about 1 msec so that cooling rates of 10^6 °K/sec or more are required in the wave reactor. The results of the chemical kinetic calculations are given later in the paper.

GAS DYNAMIC CONSIDERATIONS

Shock wave compression is used to heat the gas to peak temperature and pressure. After a short time delay to allow chemical equilibration, a centered expansion wave rapidly cools the gas. The paragraphs below describe the compression and expansion processes used in the wave reactor to approximate the ideal single pulse shock tube temperature and pressure histories given in Figure 3.

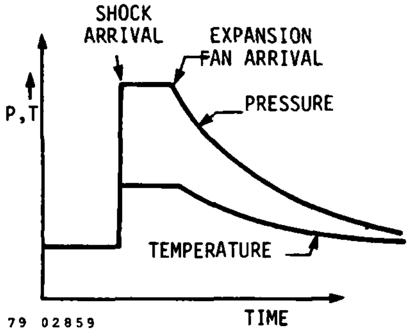

Figure 3. Idealized Temperature and Pressure Time History of a Gas at the Endwall of a Single Pulse Shock Tube. The cycle in the chemical wave reactor approximates these time histories.

Compression

As mentioned above, the incoming reactant gas stream from the fusion reactor must first be heated from ~ 2400 °K to 3000 °K in the wave reactor and then cooled from 3000 °K to less than 2000 °K as it exhausts from the wave reactor. For pure CO_2 gas streams, these changes in temperature lead to large pressure ratios (30 to 1) due to the low specific heat ratio, γ, of CO_2 at high temperatures ($\gamma \sim 1.16$). For a stream pressure of 1 atmosphere at the wave reactor exit, which is consistent with the requirements of the heat exchangers and chemical processing plant, peak pressures of 30 to 40 atmospheres are required. These pressures require cooling rates even faster than previously indicated to prevent $CO-O_2$ recombination. However, if a monatomic diluent such as He is added, the required peak pressures will drop and acceptable pressure ratios on the order of 10 can be obtained.

To compress through a pressure ratio of 10 relatively strong shocks are required. With strong shocks high flow velocities are present and aerodynamic losses (which are proportional to M^2) will be high. To minimize flow velocities multi-shock compression is used as shown in Figure 4. The incoming reactant gas (CO_2, CO, O_2, He) is first stagnated at the far end of the tube by an endplate coming into position at the proper time. This is accomplished by rotation of the tube past a solid wall. Once this "hammer" shock reaches the near end of the tube, the near end is exposed to an even higher pressure auxiliary reservoir causing a second shock to propagate down the tube. The auxiliary gas (He has been chosen) enters the tube and an interface between the dissimilar gases moves as indicated by the dashed line. This second shock encounters a solid endplate at the far end of the tube (zero velocity boundary) and reflects. Once the reflected shock reaches the near end (point a), compression of the CO_2 gas stream is complete. By using multiple shock compression the entropy rise is reduced and the compression efficiency is improved. After a short

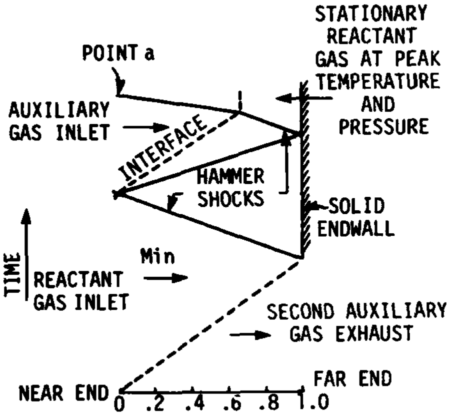

Figure 4. Wave (x-t) Diagram for the Compression Process which is used in the chemical wave reactor.

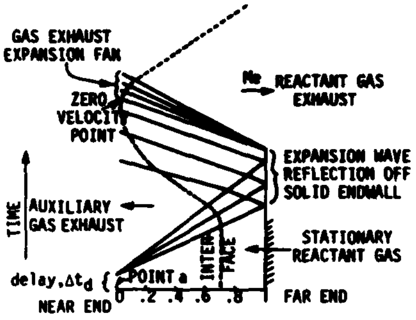

Figure 5. Wave (x-t) Diagram Depicting the Expansion Process which is used in the chemical wave reactor.

delay in time (Δt_d, shown in Figure 5) which ensures chemical equilibrium behind the final shock, the expansion process begins.

The amount of volume compression which occurs in the compression process is seen by the final position of the interface between the driver and reactant gases. In the case shown, the volume compression is roughly 3 to 1. This number depends weakly upon the reactant gas inlet flow velocity and more strongly on the ratio of peak reactant gas temperature to reactant gas inlet temperature. The lower the inlet temperature or lower the inlet velocity, the greater the volume compression. The amount of volume compression impacts the expansion process as described below.

Expansion

Adding He diluent also reduces the flow velocities inside the tube during the unsteady expansion process. In ideal unsteady gas expansion, the relationship between flow velocity and gas temperature during the expansion process is given[19]

$$\frac{2}{\gamma-1}\, a + u = \text{const}$$

where "a" is the sound speed in the gas ($a^2 = \gamma RT$) and "u" the gas velocity. As γ is decreased the flow velocity change for a given change in "a" (or T) is increased. Added diluent (larger γ) reduces Mach numbers in the tubes and therefore reduces friction pressure drop.

One finds that even with 60 percent helium diluent added to the reactant gas, the flow velocity which would arise from a single centered expansion fan cooling the gas from 3000 °K to 2000 °K is supersonic. The centered expansion fan must therefore be "broken up" into smaller portions. One effective way to do this is to allow the expansion fan to reflect off an endwall as depicted in Figure 5. Here the total cooling accomplished by the reflected fan is about twice that by the initial centered portion of the fan; however, because of the zero velocity boundary condition at the endwall, the gas flow velocity after the fan has passed is zero. Additional expansion fans could be sent in from the near end and reflected as necessary. Once sufficient cooling is achieved by these reflected expansion fans, a final centered fan can be used to exhaust the gas.

The amount of cooling that can be obtained from the reflected expansion fans is limited by the amount of expansion which brings the interface between the auxiliary gas and reactant gas to rest at the near end as indicated in the figure. If the interface were allowed to leave the tube before expansion cooling was complete, not all of the reactant gas would be completely cooled. Clearly, the amount of volume compression occurring during the compression process will determine how much expansion cooling can be completed by the reflected fans. With less volume compression, less cooling is accomplished by the reflected fans and the exit velocity of the reactant gas will be higher for fixed exit temperature (~1800 °K). To illustrate this effect, temperatures at the point where the interface has zero velocity at the near end are given in Table II. Also given are the gas exit Mach numbers which result from the final centered expansion fan when cooling the rest of the way down to 1800 °K. The exit Mach numbers become large for relatively small changes in volume fraction. As discussed earlier the amount of volume compression is primarily a function of inlet temperature (also indicated in Table II) so that there is essentially a unique relationship between inlet temperature and exit Mach number through the amount of volume compression (assuming fixed peak and exit temperatures).

Table II. Effect of Volume Compression on Exit Mach Number

Volume Compression	Temperature at Zero Velocity	Exit Mach Number, Me	Inlet Temperature ($M_{in} = 0.5$)
2 to 1	2447 °K	1.129	2550 °K
3 to 1	2171 °K	.668	2410 °K
4 to 1	1996 °K	.361	2290 °K
5 to 1	1869 °K	.129	2165 °K

To determine the cooling rates achievable in a single pulse shock tube an analytic expression given originally by Poggi[20] for the temperature history at the tube endwall for a reflected centered expansion fan is used. He gave:

$$\frac{dT}{dt} = -4\,\frac{\gamma-1}{\gamma+1}\,\frac{a_i T_i}{L}\left(\frac{T}{T_i}\right)^{\frac{\gamma}{\gamma-1}}$$

where T is the gas temperature at time t, a_i the uncooled sound speed in the gas, T_i the uncooled temperature and L the tube length (more specifically, the distance of the expansion wave origin from the end wall). For fixed peak temperatures, higher γ mixtures or shorter tube lengths will give higher cooling rates so that the expansion quenching of the expansion process should be more efficient with more diluent. For 60 percent He diluent, the initial cooling rate for a 20 cm long tube is 10^7 °K/sec (here $\gamma = 1.294$, $T/T_i = 1$ and $a_i = 1.32 \times 10^5$ cm/sec).

Wave Diagram for Full Cycle

Shown in Figure 6 is an idealized full cycle wave diagram incorporating the wave systems discussed above. Appropriate temperatures and pressures are indicated. An added feature of the composite wave diagram is that an additional wave appears after the exhaust expansion wave. This additional wave is termed a "matching" wave and is used to match pressure and velocity between the exiting reactant gas stream and the reactant gas stream entering for the next cycle. The inlet and exit velocities and inlet and exit pressures are generally not equal respectively because of the unique relationship between inlet and exit conditions; the matching wave is required to ensure cyclic operation of the wave reactor. The temperature and molecular weight of the second auxiliary gas can be adjusted to give the proper conditions across a single wave. Argon at ~500 °K has been chosen as the second auxiliary stream. If it is allowed to flow for a longer period of time than shown, it helps to cool the wave

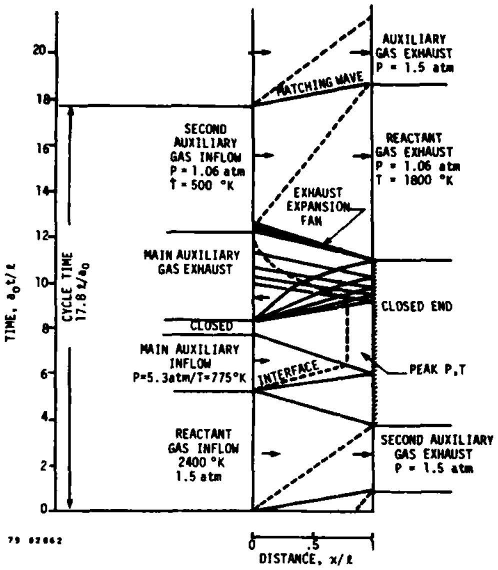

Figure 6. Wave (x-t) Diagram Depicting a Complete Cycle in the Chemical Wave Reactor. Diagram incorporates the wave systems given in Figures 4 and 5.

reactor walls to the required temperatures. The inlet temperature of the main auxiliary gas has been chosen to ensure proper acoustic impedance (ρa) matching across the interface at the point where the final shock in the compression process crosses the interface, i.e., no shock reflection occurs at the interface. Helium has been chosen as the driver gas because of its low molecular weight and hence low temperature (~800 °K) for impedance matching.

The time to complete a full gas dynamic cycle can be obtained from the full diagram. For the case shown the total cycle time is 17.8 ℓ/a_0 (ℓ = tube length, a_0 = reactant gas peak sound speed). The reactant inflow time is about 5.2 ℓ/a_0 or 29 percent of the total time. Using the inflow times the amount of reactant gas and auxiliary gas (both main and second) mass flow per cycle can be determined. For the case depicted, the main auxiliary mass flow is 30 percent higher than that of the reactant gas flow and the second auxiliary gas mass flow is about 50 percent of the reactant gas mass flow.

WAVE REACTOR PERFORMANCE

Chemical Yield

Figure 7 gives the quenched CO yield (in the absence of water impurity) at the wave reactor exit as a function of helium diluent fraction, peak temperature, and exit pressure. The exit temperature is fixed at 1800 °K and the tube length is 20 cm. The yield first increases with helium fraction due to improved quenching. A peak is reached when the impact of helium dilution outweighs the improvement in quenching of the recombination reaction. As expected, lower exit pressures which relate to lower peak pressures give higher yields at lower diluent fractions. Increased peak temperatures give higher yields at the highest diluent fractions. The trend towards higher diluent fractions at increased temperatures is a result of the fact that the quenching must be more efficient (faster) because of both the increased peak pressures (higher pressure ratio across the expansion fan going from 3300 to 1800 °K) and faster recombination rates at the higher temperatures. CO yields up to approximately

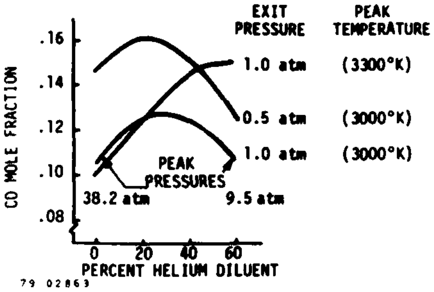

Figure 7. Frozen CO Yield at the Wave Reactor Exit vs % Helium Diluent.

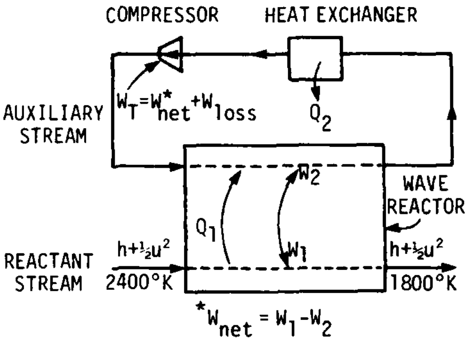

Figure 8. Idealized Power Flow in Chemical Wave Reactor.

13 percent are achievable with a 3000 °K peak temperature, 1 atmosphere exit pressure and 30 percent helium diluent.

Wave Reactor Efficiency

A simplified model of the wave reactor is shown in Figure 8 where the reactor is shown as a black box with two streams entering and two streams leaving. The reactant stream enters with a total enthalpy of $h_1 + \frac{1}{2} u_1^2$ and leaves with total enthalpy $h_2 + \frac{1}{2} u_2^2$. Here h includes both thermal and dissociation enthalpy. Inside the black box work, W_1 is transferred from the auxiliary to the reactant stream during compression and W_2 is transferred in reverse during expansion. Heat transfer, Q_1, occurs between the reactant stream and the auxiliary stream via the wave reactor walls. In the external auxiliary stream loop, heat Q_2 is rejected and compression work W_T is put into the stream. Work W_T includes the difference between W_1 and W_2, plus any work requirements due to losses. Given this information the wave reactor thermal efficiency is calculated as

$$\eta = \frac{h_2 + \frac{1}{2} u_2^2 - W_T}{h_1 + \frac{1}{2} u_1^2}$$

For a wave reactor with a 90 Kg/sec flow of 60 percent helium diluent reactant gas, and for the temperatures given in Figure 8, $h_1 + \frac{1}{2} u_1^2$ is 428 MW (megawatts), $h_2 + \frac{1}{2} u_2^2$ is 420 MW and W_T is estimated to be 69 MW. The value calculated for η is 82 percent. This number is quite sensitive to the losses included in W_T.

Parasitic Losses

Parasitic losses for the wave reactor include, but are not limited to, those due to friction pressure drop, heat transfer losses, mixing losses at the interfaces between the dissimilar gases, windage in rotating the reactor, and leakage of gas in the region between the manifolds and rotating drum. Additional discussion of the different losses in these machines is given in a companion paper presented at this symposium.[21] Some of these losses are difficult to estimate. The largest uncertainty lies in the estimate of the heat transfer losses which may also represent the largest single loss in the wave reactor. The average wall temperatures must be kept down to around 1100 °K for materials reasons and large temperature differences between the gas and wall temperature exist. The value for the losses used in the calculation above of efficiency incorporates a value of heat loss, 45 MW, midway between a worst estimate and the case of no heat loss. Other losses are estimated to be as follows: a friction pressure loss of 14 MW, a mixing loss of 5 MW, and a windage and leakage loss of 5 MW. The total estimated loss is 69 MW. Since both flow speeds and wave strengths tend to increase with decreased diluent, parasitic losses are expected to increase with decreasing diluent. This trend in parasitic losses will favor higher diluent fractions.

The parasitic losses, cooling rate requirements, mass flow requirements and other considerations will impact the sizing of a wave reactor. The primary parasitic losses (friction and heat transfer losses) are primarily a function of tube length (ℓ) to diameter (d) ratio. The lowest losses are obtained with low ℓ/d. Cooling rate is proportional to ℓ^{-1} so for maximum cooling rates minimum tube length is required. The diameter, D, of a wave reactor drum will be determined primarily by the total mass flow and the number of drums desired in the system. A reasonable maximum diameter will be that of gas turbines which range in diameter up to 6 m. Drum tip speed will be limited by windage losses and mechanical stress in the rotor. Table III gives a summary of the key sizing constraints and preliminary sizing. The mass flow rate, $\dot{m}$, is that of the reactant gas per wave reactor unit.

Table III. Wave Reactor Sizing

CONSTRAINTS:		PRELIMINARY SIZE:
$\frac{dT}{dt} > 10^6$ °K/Sec	$\frac{dT}{dt} \sim \frac{1}{\ell}$	$L = 80$ cm
		$L/d = 12$
$\frac{\Delta p}{P} \leq 10\%$	$\frac{\Delta p}{P} \sim \frac{\ell}{d^{1.25}}$	$V_T = 21800$ cm/sec
		$D = 350$ cm
$D < 600$ cm	$D \sim \frac{\dot{m}}{\alpha}$	$\dot{m} = 9 \times 10^4$ g/sec
$\alpha \lesssim 10$ rotors		$\alpha = 10$ rotors
$V_T < 24000$ cm/sec	$V_T \sim \frac{D}{rn}$	

Impact of Wave Reactor Performance on Overall Cycle Efficiency

The impact of wave reactor performance on overall cycle efficiency can be measured in terms of 1) the quenched CO yield at the wave reactor exit, and 2) the parasitic losses. For most cases of interest (i.e., moderate diluent fractions) the quenched CO yield is sufficiently close to the peak dissociation yields that the peak temperature achievable is the primary determinant. Since higher peak temperatures will also lead to higher heat transfer losses, an optimum peak temperature may exist. Parasitic losses also have a significant effect. Table IV gives an indication of the sensitivity of overall cycle efficiency to wave reactor losses (wave reactor component efficiency). In all cases the total H_2 chemical power is 1420 MW. The efficiency for the overall cycle is

$$\eta_{cycle} = \frac{\Delta\hat{H}_{chem} + \Sigma P_{elec}}{P_{fusion}}$$

where ΔH_{chem} is equal to the rate of heat release in burning the H_2 produced at 300 °K (68,000 Kcal/mole), ΣP_{elec} is the net sum of electrical power required

Table IV. Impact of Wave Reactor Efficiency on Overall Cycle Efficiency

Wave Reactor Efficiency(%)	Overall Cycle Efficiency (%)
90	34.0
80	23.3
70	12.6

in the system and P_{fusion} is equal to 4000 MW thermal. Table IV shows that wave reactor component efficiencies have a strong influence on overall cycle efficiency and should be as high as possible. An optimization analysis needs to be completed to find the operating point where the overall cycle efficiency is maximized. Additional details of the overall cycle efficiency calculation are found in Reference 22.

SUMMARY

The gas dynamic aspects of applying an unsteady chemical wave reactor to CO/H_2 production have been described in detail. Detailed analysis of the compression and expansion processes has shown that multiple wave processes are useful in minimizing flow velocities and therefore friction losses. Similarly, significant amounts of helium diluent (30 to 60 percent) are necessary to minimize these same losses and at the same time retain high CO/H_2 yields. Efficient freezing of the chemical reaction products at the high peak temperatures appears possible with CO yields of up to 13 percent predicted. High overall cycle efficiencies (34 percent) appear possible with efficient (90 percent) wave reactor performance.

ACKNOWLEDGEMENTS

The authors would like to acknowledge the support of other individuals at Mathematical Sciences Northwest, Inc. who made contributions to the study from which this paper was derived. Support of the study by the U.S. Department of Energy under contract number ET-78-C-06-1095 is gratefully acknowledged.

REFERENCES

1. C. Seippel, "Pressure Exchanger," U.S. Patent No. 2,399,394, 1946.
2. P.K. Doerifler, "Comprex Supercharging of Vehicle Diesel Engines," Society of Automotive Engineering Paper 750335, Automotive Eng. Congress and Exposition, Detroit, Michigan, February 24-28, 1975.
3. R.C. Weatherston, W.E. Smith, A.L. Russo and P.V. Marrone, *Gas Dynamics of A Wave Superheater Facility for Hypersonic Research and Development*, Cornell Aeronautical Laboratory, Inc. Report No. AD-118-A-1, Cornell University, Ithaca, New York, February, 1959.
4. A. Hertzberg, "Nitrogen Fixation for Fertilizers by Gas Dynamic Techniques," IN Proceedings of the Tenth International Shock Tube Symposium, Kyoto International Conference Hall, Kyoto, Japan, 1975.
5. R.C. Weatherston and A. Hertzberg, "The Energy Exchanger, A New Concept for High Efficiency Gas Turbine Cycles," *Journal of Engineering for Power*, 1966.
6. J.F. Zumdieck, W.J. Thayer, P.E. Cassady and R.T. Taussig, "The Energy Exchanger in Advanced Power Cycle Systems," to be presented at 14th Intersociety Energy Conversion Engineering Conference, Boston, Massachusetts, August, 1979.
7. P.H. Rose, "Potential Applications of Wave Machinery to Energy and Chemical Processes," Presented at 12th International Symposium on Shock Tubes and Waves, Jerusalem, Israel, July 16-19, 1979.

8. A. Hertzberg and H.S. Glick, AGARD 41, Chapter IV-D, p. 161, 1959.
9. N. Biederman, K. Danow, Jr. and A. Konopha, "Utilization of Off Peak Power to Produce Industrial Hydrogen," Prepared by the Institute of Gas Technology for the Electric Power Research Institute, EPRI Report No. EPRI 320-1,1975.
10. F.J. Salzano, S. Srinivason, Editors, Draft Summaries of the International Energy Agency Water Electrolysis Workshop, Brookhaven National Laboratory, Upton, New York, September, 1975.
11. R.H. Wentdorf, Jr. and R.E. Hanneman, Science *185*, p. 311, 1974.
12. R.M. Stephenson, *Introduction to the Chemical Process Industries,* Reinhold Publishing Company, New York, 1966.
13. J. P. Boris, "Flux Corrected Transport Modules for Solving Generalized Continuity Equations," NRL Memorandum Report No. 3237, Naval Research Laboratory, Washington, D.C., March, 1976.
14. B.F. Meyers, K.G.P. Sulzmann, and E.R. Bartle, Journal of Chemical Physics *42*: 3969, 1965.
15. R. S. Brokaw, "Ignition Kinetics of the Carbon Monoxide-Oxygen Reaction," Proceedings of the Eleventh International Combustion Symposium, 1966.
16. N.A. Ebrahim and R.J. Sanderman, Journal of Chemical Physics *65*: 3446, 1976.
17. B.F. Meyers, K.G.P. Sulzmann and E.R. Bartle, Journal of Chemical Physics *43:* 1220, 1965.
18. T.A. Brabbs, F.E. Belles and R.S. Brokaw, "Shock Tube Measurements of Specific Reaction Rates in the Branched-Chain H_2-CO-O_2 System," Proceedings of the 13th International Combustion Symposium, 1970.
19. G. Rudinger, *Nonsteady Duct Flow,* Dover Publications, New York, 1969.
20. L. Poggi, Journal of Aeronautical Sciences *17:* 813, 1950.
21. J.F. Zumdieck et al., "The Fluid Dynamic Aspects of an Efficient Point Design Energy Exchanger," Presented at the 12th International Symposium on Shock Tubes and Waves, Jerusalem, Israel, July 16-19, 1979.
22. E.L. Klosterman et al., "CO/H_2 Production Using Fusion Reactor Heat," to be presented at the 14th Intersociety Energy Conversion Engineering Conference, Boston, Massachusetts, August, 1979.

ACETYLENE PYROLYSIS AND ITS OXIDATION BY WATER VAPOR BEHIND HIGH TEMPERATURE SHOCK-WAVES

AKIVA BAR-NUN*

Department of Geophysics and Planetary Sciences,
Tel-Aviv University, Tel-Aviv, Israel

JOHN E. DOVE

Department of Chemistry, University of Toronto,
Toronto, Ontario, Canada

The oxidation of acetylene by water vapor and its pyrolysis at 2650K were studied by a shock-tube coupled to a time of flight mass spectrometer. Acetylene polymers are formed in the pyrolysis, with C_4H_2 and C_6H_2 as the initial products. The rate constant of acetylene disappearance, $k = 3.3 \times 10^{-14}$ cm^3 $molec^{-1}$ sec^{-1}, is very close to the rate constant of diacetylene formation. Evidence for the reversibility of the polymerisation reaction is presented.

Hydrogen atoms, which are generated during the polymerisation of acetylene, are consumed in the reaction: $H + H_2O \rightleftarrows OH + H_2$ which is the main producer of OH radicals. The direct reaction of OH with C_2H_2 is: $OH + C_2H_2 \rightarrow C_2H_2O + H$, and its rate constant is $5.8 \times 10^{-12} \exp(-2155/RT)$ cm^3 $molec^{-1}$ sec^{-1}. The C_2H_2O decomposes rapidly to CO and CH_2.

INTRODUCTION

The oxidation of hydrocarbons by water vapor, in the temperature range 1300-2600 K, was studied recently by Shaviv and Bar-Nun[1] using the single pulse shock-tube technique. The experimental results suggested that methane is converted to acetylene prior to its oxidation to carbon monoxide. The temperature dependent product distribution in acetylene oxidation, after dwell times which ranged from 0.5 to 0.7 msec, was simulated by a rather complex set of reactions. The kinetic scheme involved three major processes: (1) Production of hydrogen atoms by the sequence of reactions which lead from acetylene to carbon, according to the scheme which was proposed by Gay et al[2]. (2) Production of OH radicals, mainly by the reaction $H + H_2O \rightarrow OH + H_2$ and rapid reshuffling of the oxygen between the various O/H species; and (3) oxidation of the acetylene and other C/H species by the available oxidants in the system. Very good fits between the experimentally obtained temperature dependent profiles of CO, C_2H_2, H_2 and polymers and the computed ones were achieved which, however, does not guarantee the correctness of the proposed mechanism. Therefore, a time dependent study of the same reaction was carried out, using a time of flight mass spectrometer (TOFMS) coupled to a shock-tube.

In addition to its kinetic interest, water being a much milder oxidizing agent than oxygen, this mode of oxidation is probably one of the major pathways

---

*The experimental part of this work was done at the Dept. of Chemistry, University of Toronto, while A. B-N was on a leave of absence from Tel Aviv University.

by which the hydrocarbons in the Earth's primitive reducing atmosphere were converted to carbon monoxide and eventually to carbon dioxide by the action of lightning produced shock-waves[3,4]. Yet another aspect of hydrocarbon pyrolysis and oxidation by water vapor at high temperatures was confirmed by the recent detection of lightning activity on Jupiter[5], which was predicted by Bar-Nun[6,7]. In the Jovian atmosphere, methane and water have mixing ratios in hydrogen of the order of 10^{-3} and that of acetylene[8] is about 10^{-8}. The methane can be pyrolized to acetylene despite the large excess of hydrogen, at the high temperatures behind lightning produced shock-waves[6,7]. The hydrocarbons can also be oxidized by water vapor under the same high temperature conditions to carbon monoxide, which was detected in the Jovian atmosphere by Beer[9].

EXPERIMENTAL

Acetylene (Matheson Purified Grade, 99.6% pure) was further cleaned by 4 bulb to bulb distillations. Double distilled water was degassed 4 times at 5×10^{-5} Torr, with alternating freezing and thawing. Argon and neon (Matheson Research Grade) were used without further purification. A reaction mixture consisting of 1.0% C_2H_2, 2.0% H_2O and 0.23% Ar in Ne was stored in a stainless steel container, which was constantly heated to 45°C. The shock-tube was also heated to this temperature and no depletion of the water vapor was observed when samples were introduced either directly to the TOFMS or via the driven section of the shock-tube. In the pyrolysis study, a mixture of 1.0% C_2H_2 and 0.23% Ar in Ne was run.

After evacuating the stainless steel 2.54 cm I.D. and 570 cm long driven section to 2×10^{-5} Torr, the reaction mixture at a pressure of $\sim$ 13 Torr was introduced. Hydrogen at a pressure of 6 psi was then introduced into the driver section and an aluminium diaphragm was punctured, thus initiating the shock. The incident shock velocity was measured by 5 to 7 gold thin-film resistance thermometers, having a rise time of 0.5 μsec. Their signals were used to obtain the incident shock speed and to trigger the data recording system.

A Bendix model 12 TOFMS, with model 14-101 "fast reaction" ion source was connected to the shock-tube in such a way that the end wall of the shock tube also formed the base plate of the mass spectrometer ion source. The shock heated gas was sampled into the mass spectrometer through a 3×10^{-4} cm diameter orifice located centrally on the end wall, forming a jet of expanding gas, which was co-axial with the flight tube of the TOFMS. On arrival of the reflected shock wave, a number of successive mass spectra of the sampled gas (5, 10 or 20 μsec apart) were automatically photographed from 4 oscilloscopes. This equipment, and its use to study fast reactions by mass spectra produced internally in the conventional way, has been described in detail previously by Barton et al[10] and by Barton and Dove[11].

The relative peak heights in the TOFMS for the various stable species (C_2H_2, C_4H_2, C_2H_4, CO and H_2O) were determined by running mixtures containing these species under weak shock conditions where no decomposition occurred. The peak heights of the various species at 28 ev, relative to that of Ar ($m/e = 40$), are: 0.83 for CO (at $m/e = 28$) 0.55 for H_2O (at $m/e = 18$), 2.35 for C_2H_2 (at $m/e = 26$), 3.1 for C_4H_2 (at $m/e = 50$) and 2.4 for C_2H_4 (at $m/e = 28$). The value of 4.6 for C_6H_2 (at $m/e = 74$) was estimated from the increase in peak height from C_2H_2 to C_4H_2. Because of the rather low signal to noise ratio for the products, the results of 18 runs in each series, at the temperature range 2600 to [illegible], were averaged and the standard deviation at each point was determined.

RESULTS AND DISCUSSION

The time dependent profiles of C_2H_2, C_4H_2, C_6H_2, C_2H_4, H_2O and CO at [illegible] and a total density behind the reflected shock of 5×10^{-6} [illegible] mole cm^{-3}, are shown in Figures 1 and 2.

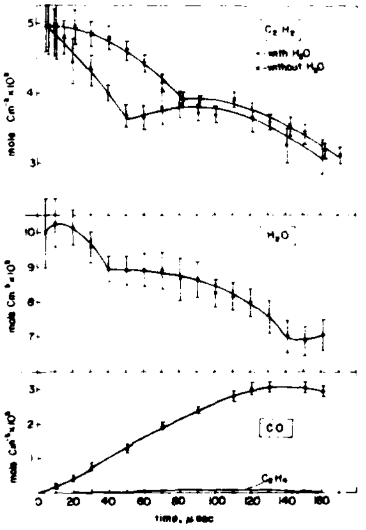

Figure 1: Time-dependent profiles of C_2H_2, H_2O, CO and C_2H_4, at 2650K. Concentrations are in units of 10^{-8} moles cm^{-3}.

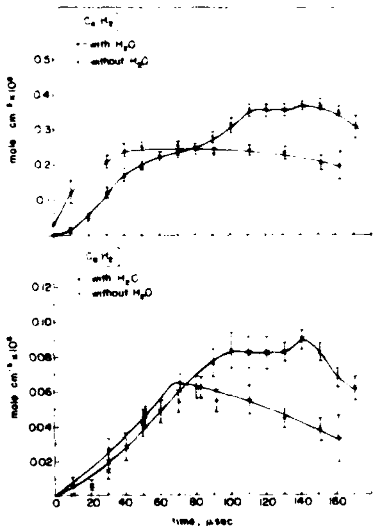

Figure 2: Time-dependent profiles of C_4H_2 and C_6H_2, at 2650K.concentrations are in units of 10^{-8} moles cm^{-3}.

Vertical lines represent the standard deviation.

Acetylene pyrolysis

In the absence of water vapor, the major products are diacetylene (C_4H_2) and triacetylene (C_6H_2), as reported by Gay et al[2]. The rate constant of acetylene consumption (Fig. 1) as measured during the first 40 μsecs at 2650K is 3.3×10^{-14} cm^3 $molec^{-1}$ sec^{-1}. This value agrees well with the rate constant for diacetylene formation (Fig. 2) of 2.8×10^{-14} cm^3 $molec^{-1}$ sec^{-1}, and the rate constant of 3.5×10^{-14} cm^3 $molec^{-1}$ sec^{-1} which was measured for diacetylene formation by Gay et al[2]. Hence, it seems that the initial step in acetylene disappearance is the formation of diacetylene (C_4H_2), with the liberation of hydrogen, as proposed by Gay et al[2]. The formation of C_4H_4, as was suggested by Bradley and Kistiakowsky[12], stemmed probably from a mistaken identification of the products masses, as no peak at m/e = 52 was observed by us. In some oscilloscope traces a minute peak of C_4H_3 could be identified, but in most traces it was completely absent.

A detailed mechanism of acetylene polymerization cannot be based upon the present data. Yet, the agreement with the results of Gay et al[2] regarding the formation of di and triacetylene lends credence to the mechanism which was proposed by them. However, unlike in their mechanism and in apparent agreement with the suggestion of Bradley and Kistiakowsky[12] the polymerization reaction seems to be reversible. As seen in Fig. 1, a plateau in the acetylene profile starts after about 80 μsec. This plateau lasts for ∿30 μsec, after which the acetylene resumes its initial rate of decrease. No other mechanism seems to explain the plateau in the acetylene profile and further evidence for the reversible nature of the polymerization will be discussed in the next chapter. Unlike in the mechanism which was proposed by Bradley and Kistiakowsky[12], the initial polymerization product is C_4H_2 and not C_4H_4. Hence, the depolymerization should involve H-atoms and not simple dissociation of the dimers.

Thus, the mechanism of acetylene polymerization can be constructed, after Gay et al[2] with the addition of reversible steps, as suggested by Bradley and Kistiakowsky[12].

(a) $C_2H_2 + C_2H_2 \rightleftarrows C_4H_3 + H$

(b) $C_4H_3 + M \rightleftarrows C_4H_2 + H + M$

(c) $C_4H_2 + C_2H_2 \rightleftarrows C_6H_3 + H$

(d) $C_6H_3 + M \rightleftarrows C_6H_2 + H + M$

.

.

.

(n) $C_nH_2 \rightarrow \text{carbon} + 2H$

Reactions (b) and (d) should be fast under the experimental conditions, so that the steady state concentration of C_4H_3 and C_6H_3 would be below the limit of detection in the present experiments.

According to the yet unpublished work of Just et al (personal communication in this symposium), part of the acetylene would decompose at 2650K to C_2H and H. The C_2H radicals could be even better than C_2H_2 in polymerization reactions, which would proceed according to: $C_nH_2 + C_2H \rightleftarrows C_{n+2}H_2 + H$. In this case, the intermediate C_nH_3 would not be formed, in agreement with its absence from among the observed reaction products.

Acetylene oxidation

As seen in Fig. 1, the rate of acetylene consumption increases considerably in the presence of water vapor. This is accompanied by the consumption of water and the production of CO. The ethylene which has the same m/e ratio as CO, is much smaller than the CO and could not affect its observed concentration considerably, unless in the presence of water vapor the ethylene reaches a much higher concentration, which is rather unlikely.

In the runs with water, the initial rates of production of di and triacetylene are considerably higher than in the runs without water (Fig. 2). Since hydrogen atoms are consumed by the water in the fast reaction: $H + H_2O \rightleftarrows H_2 + OH$, less hydrogen atoms are left for depolymerization and hence the initial increase in the polymers concentrations. Once enough di and triacetylene are produced, they consume most of the hydrogen atoms and the water reaches a steady state (Fig. 2). The coincidence between the plateau of acetylene, water vapor and diacetylene is thus explained. It whould be pointed out, however, that this explanation is only tentative. Yet, the ability of this mechanism to explain all the experimental observations makes it quite plausible.

MODELLING

In order to avoid the complex reversible part of acetylene polymerization, in which higher polymers and possibly nucleation processes are involved, the computer modelling was carried out only for the initial 50 μsec of the reaction. The kinetic scheme which describes best the experimental observations is shown in Table. 1.

Table 1. A Kinetic scheme for the oxidation of acetylene by water vapor.

Group	No.	Reaction	Rate Constant cm^3 mole^{-1} sec^{-1}		Ref.
			A^a	E_a cal mole^{-1}	
1	1	$2C_2H_2 \rightleftarrows C_4H_2+2H$	6.0+13	41,000	Gay et al[2] and this study
	2	$C_2H_2+C_4H_2 \rightleftarrows C_6H_2+2H$	1.5+14	34,000	b
	3	$C_2H_2+C_6H_2 \rightleftarrows C_8H_2+2H$	2.5+14	30,500	b
	4	$C_8H_2+M \rightleftarrows C_8+2H+M$	2.0+14	45,000	b
11	5	$H_2O+M \rightarrow H+OH+M$	5.01+14	105,000	Olschewski et al[13]
	6	$H_2O+H \rightarrow H_2+OH$	8.4+13	20,000	Baulch et al[14]
	7	$H_2+M \rightarrow 2H+M$	2.23+12 $T^{1/2}$	92,600	Mayerson and Watt[15]
111	8	$C_2H_2+OH \rightarrow [C_2H_2O] +H \rightarrow CH_2+CO+H$	3.5+12	2,155	This study and Davis et al[16]
	9	$CH_2+OH \rightarrow CHO+H_2$	3.0+13		Browne et al[17]
	10	$OCH+M \rightarrow CO+H+M$	7.0+13	15,000	Browne et al[17]

a 6.0 + 13 denotes 6.0×10^{13}.

b The rate constants for reactions 2 and 3 were chosen in such a way that the experimental profiles of C_4H_2 and C_6H_2 were reproduced. The hypothetical reaction (4) describes polymer or carbon formation.

As in the previous study[1], the intermediates C_4H_3 and C_6H_3 were omitted from the scheme. This is justifiable in view of the agreement between the measured rates of acetylene disappearance and diacetylene formation, which suggest a fast conversion of C_4H_3 to C_4H_2 and of C_6H_3 to C_6H_2. The polymerization of acetylene leads eventually to the formation of carbon and reaction (4) describes this process schematically.

The polymerization is accompanied by the production of hydrogen atoms and these are used in the production of OH radicals from water by reaction (6). This reaction is the major OH producer, since the direct dissocation of water (reaction 5) cannot furnish enough OH radicals to account for the observed rate of CO production. The direct reaction between OH and C_2H_2 was studied in two corssed molecular beam experiments by Gehring et al,[18] and by Kanofsky et al,[19] and by flash photolysis-resonance fluorescence technique by Davis et al.[16] Four other studies are listed by the last authors. While Gehring et al[18] suggest that the initial reaction is:

(e) $C_2H_2 + OH \rightarrow CO + CH_3$

Kanofsky et al[19] propose the following reaction:

(f) $C_2H_2 + OH \rightarrow C_2H_2O + H$

based on the detection of C_2H_2O as the only reaction product. Reaction (f) is proposed also by Davis et al[16] as the main channel of the reaction of OH with C_2H_2. Davis et al[16] measured the rate constant of reaction (f) and suggest $k = (1.61 \pm 0.17) \times 10^{-13}$ cm^3 molec^{-1} sec^{-1} at 300K. From the difference between the rates of acetylene disappearance with and without water vapor, after the initial 40 μsec (Fig. 1), the rate constant of reaction (f) can be determined, provided that the concentration of OH radicals is known. This could not be measured experimentally, because of the dissociation of water in the ion source. The OH radical concentration can be calculated, however, from reaction (6) which is the main contributor to OH formation. At 2650K, after 20 μsec, the OH concentration is 9.5×10^{14} molec. cm^{-3} and the rate constant of reaction (f) at this temperature is 3.0×10^{-12} cm^3 molec^{-1} sec^{-1}. From the values of the rate constants at 300 and 2650K, the activation energy of reaction (f) is 2155 cal mole^{-1} and the rate constant is

$$k = 5.8 \times 10^{-12} \exp(-2155/RT) \text{ cm}^3 \text{ molec}^{-1} \text{ sec}^{-1}$$

This rate constant was used in the model for the reaction of OH with C_2H_2. The absence of a peak at m/e = 42 of C_2H_2O points to its fast dissociation into CO and CH_2. If a steady state for C_2H_2O is reached rapidly, like for C_4H_3 and C_6H_3 which could not be detected as well, the reaction can be represented by reaction (8) in Table 1:

$$C_2H_2 + OH \rightarrow [C_2H_2O] + H \rightarrow CH_2 + CO + H$$

for which the rate constant of reaction (f) was used.

The CH_2 which is produced in this reaction could react, according to Browne et al[17], with OH to form CHO (reaction 9 in Table 1). At lower temperatures this species could lead to formaldehyde, but at high temperatures it decomposes to CO and H. CH_2 could participate in four alternative reactions, with C_2H_2 and H_2O, which are more abundant than OH by factors of ~13 and ~30 respectively.

(g) $CH_2 + C_2H_2 + M \rightarrow CH_3 - C \equiv CH + M$

(h) $CH_2 + C_2H_2 + M \rightarrow CH_2 = C = CH_2 + M$

(i) $CH_2 + C_2H_2 \rightarrow C_3H_3 + H$

(j) $CH_2 + H_2O + M \rightarrow CH_3OH + M$

Methanol formation (j) can be ruled out by the absence of peaks at m/e = 32 and 31. The peak of C_3H_4 at m/e = 40 is masked by the argon, but a peak at m/e = 39 is seen to be growing with time. However, since it is comparable in height to that of the peak at m/e = 40, its source cannot be C_3H_4. Alternatively, reaction (i) could take place to produce C_3H_3 (m/e = 39). If this is the main channel for CH_2 consumption and not the reaction with OH (reaction 8 in Table 1) the rate constant of reaction (8) should be larger by about 25 per cent in order to account for the observed CO profile. The reactions which described in the previous study[1] the reshuffling of oxygen between the various O/H species were omitted from the present scheme, as they changed the rate of CO production by less that 10%. The experimental results up to 50 μsec, together with the computer generated profiles, are shown in Figure 3.

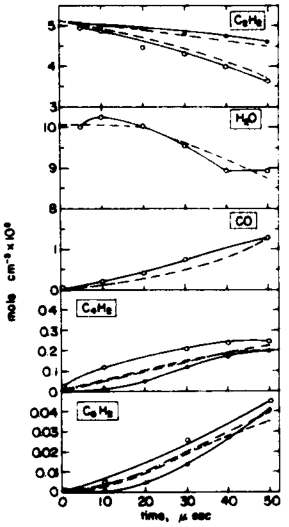

Fig. 3. Comparison between the experimental time-dependent profiles of C_2H_2, H_2O, CO, C_4H_2 and C_6H_2 and the computed ones at 2650K, for the initial 50 µsec. Concentrations are in units of 10^{-8} mole cm^{-3}. Experimental points: • - without water, ○ - with water, ——— experimental profiles. Computed profiles: —.—.— without water, – – – – – with water.

CONCLUSION

The processes of acetylene pyrolysis and oxidation by water vapor which emerge from this study are as follows: Acetylene polymerizes reversibly to form C_4H_2, C_6H_2 etc., with the liberation of H-atoms. These react with water vapor to produce OH radicals. The direct reaction of OH with C_2H_2leads to the formation of C_2H_2O, which decomposes rapidly to CO and CH_2. Computer modelling, using available rate data, reproduces successfully the time dependent profiles of the various species during the initial 50 µsec, after which the polymerization of acetylene begins to reverse itself.

REFERENCES

1. A Shaviv and A. Bar-Nun, Int. J. Chem. Kinetics 7, 661 (1975).
2. I.D. Gay, G.B. Kistiakowsky, J.V. Michael and H. Niki, J. Chem. Phys. *43*, 1720 (1965).
3. A. Bar-Nun and Shaviv, Icarus *24*, 197 (1975).
4. A. Bar-Nun and M.E. Tauber, Space Life Sci., *3*, 254, (1972).
5. F.L. Scarf, D.A. Gurnett and W.S. Kurth, Science *204*, 991 (1979).
6. A. Bar-Nun, Icarus, *24*, *86* (1975).
7. A. Bar-Nun, Icarus, *38*, 180 (1979).
8. A. Tokunaga, R.F. Knacke and T. Owne, Astrophys. J. *209*, 294 (1976).
9. R. Beer, Astrophys. J. *200*, L167 (1975).
10. S.C. Barton, M.A.Di Valentin and J.E. Dove, Proc. 5th Int. Shock-Tube Symp. Am. Phys. Soc. 1965 p. 739.
11. S.C. Barton and J.E. Dove, Can. J. Chem. *47*, 521 (1969).
12. J.N. Bradley and G.B. Kistiakowsky, J. Chem. Phys. *35*, 264 (1961).
13. H.A. Olschewski, J. Troe and H. Gg. Wagner, Proc. 11th (Internat.) Symp. on Combustion, 1967, p. 155.
14. D.L. Baulch, D.D. Drysdale and A.C. Lloyd, High Temperature Reaction Rate Data, Leeds University, England (1968).
15. A.L. Mayerson, and W.S. Watt, J. Chem. Phys. *49*, 425 (1968).
16. D.D. Davis, S. Fischer, R. Schiff, R,T. Watson and W. Bollinger, J. Chem. Phys. *63*, 1707 (1975).

17. W.G. Browne, R.P. Porter, J.D. Verlin and A.H. Clark, Proc. 12th (Internat.) Symp. on Combustion, 1968, p. 1035.
18. N. Gehring, K. Hoyermann, H. Gg. Wagner and J. Wolfrum, Z. Naturforsch. A. *25*, 675 (1970).
19. J.R. Kanofsky, D. Lucas, F. Pruss and D. Gutman, J. Phys. Chem. *78*, 311 (1974).

SHOCK-TUBE STUDIES OF N_2O-DECOMPOSITION*

K. G. P. SULZMANN, J. M. KLINE and S. S. PENNER

Energy Center and Department of Applied Mechanics and Engineering Sciences
University of California/ San Diego, La Jolla, California 92093, USA

The thermal decomposition of nitrous oxide has been studied behind reflected shock waves for $1685 \leq T$, $°K \leq 2560$ and $1.7 \leq p$, atm ≤ 4.6 in Ar-N_2O mixtures containing 2% N_2O. Concentration-time histories have been determined for N_2O from emission at 4.52 μ ($\Delta\lambda = 0.083$ μ) and for NO by correlation spectroscopy at 2259 A ($\Delta\lambda = 39$ A). Needed spectral absorption coefficients were obtained by the use of semi-empirical procedures.

There is some delay before the O-atom concentrations attain steady-state values at low temperatures, for which the initial N_2O-decomposition is governed by the binary decomposition reaction $N_2O + M \rightarrow N_2 + O + M$ with the rate coefficient k_1. At higher temperatures, the reactions $N_2O + O \rightarrow 2NO$ and $N_2O + O \rightarrow N_2 + O_2$ (with rate coefficients k_2 and k_3, respectively) occur so rapidly that the O-atoms attain steady-state concentrations (within the experimentally achieved time resolution) immediately after reflected shock-heating. When a steady state obtains for the O-atom concentrations, the effective rate of N_2O-decomposition is double ($2k_1$) that for the one-step binary decomposition step. We find that $k_1 = (3.71 \pm 2.74) \times 10^{14} \exp[-(27{,}660 \pm 1{,}445)°K/T]\,cm^3$/mole-sec and $k_3/k_2 \approx 1.09 \pm 0.10$ for $1685 \leq T$, $°K \leq 2560$. For $1685 \leq T$, $°K \leq 2000$, $k_2 + k_3$ was measured directly and yielded $k_2 = (4.07 \pm 3.26) \times 10^{13} \times \exp[-(12{,}350 \pm 2{,}380)°K/T]$ and $k_3 = (4.43 \pm 3.97) \times 10^{13} \times \exp[-(12{,}350 \pm 2{,}380)°K/T]\,cm^3$/mole-sec.

INTRODUCTION

The decomposition of nitrous oxide has been studied extensively in static systems[1-9] and behind incident and reflected shock waves.[10-27] For $830 \leq T$, $°K \leq 3360$ at $p \approx 1$ atm, the pyrolysis of N_2O is initiated[28] by the endothermic bimolecular step

$$N_2O + M \rightarrow N_2 + O + M + 39.95, \qquad (1)$$

which is followed by the two exothermic steps

---

* This research was supported under U.S. Office of Naval Research Contract No. N00014-75-C-0261 (monitored by Lt. Richard S. Miller).

$$N_2O + O \rightarrow 2NO - 36.01 \tag{2}$$

and

$$N_2O + O \rightarrow N_2 + O_2 - 79.17, \tag{3}$$

where the numbers are heats of reaction in kcal/mole under standard conditions. Subsequent reaction steps are[27,28]

$$N_2 + O \rightarrow NO + N + 75.02, \tag{4}$$

$$NO + O \rightarrow N + O_2 + 31.86, \tag{5}$$

$$O + O + M \rightarrow O_2 + M - 119.12, \tag{6}$$

$$NO + O + M \rightarrow NO_2 + M - 73.23, \tag{7}$$

$$NO_2 + O \rightarrow NO + O_2 - 45.89, \tag{8}$$

$$N_2O + NO \rightarrow N_2 + NO_2 - 33.28, \tag{9}$$

$$N_2O + NO_2 \rightarrow N_2 + O_2 + NO - 5.94. \tag{10}$$

Reactions (4) through (10) are unimportant at $p \approx 1$ atm during the first 30-150 μsec at all values of T considered.[12,16,27] The initial N_2O decomposition is described by

$$(\dot{N_2O}) = - k_1(M)(N_2O) - (k_2 + k_3)(N_2O)(O), \tag{I}$$

$$(\dot{O}) = k_1(M)(N_2O) - (k_2 + k_3)(N_2O)(O), \tag{II}$$

$$(\dot{NO}) = 2k_2(N_2O)(O). \tag{III}$$

These relations have been used[21,28] with a steady-state assumption for O-atoms,

$$(O)_{ss} = k_1(M)/(k_2 + k_3), \tag{IV}$$

in order to determine k_1 and the ratio k_3/k_2 from

$$(N_2O) = (N_2O)_o \exp[- 2k_1(M)t] \text{ for } (O)_{ss} \tag{V}$$

and

$$\begin{aligned}(NO) &= [(k_3/k_2) + 1]^{-1}[(N_2O)_o - (N_2O)] \\ &= [(k_3/k_2) + 1]^{-1}(N_2O)_o\{1 - \exp[- 2k_1(M)t]\} \text{ for } (O)_{ss},\end{aligned} \tag{VI}$$

where the subscript o refers to the initial concentration. Experimental data for k_1 and k_3/k_2 show considerable scatter. Baulch et al.[28] adopted for k_1 the expression[16]

$$k_1 = 5 \times 10^{14} \exp(- 29{,}187^\circ K/T) cm^3/mole\text{-}sec. \tag{VII}$$

Actually, $0.67 \leq k_3/k_2 \leq 3.0$, but this ratio was set equal to unity in the cited review[28] as well as by others,[24-27] who used computer codes to find k_1 and $k_2 = k_3$ as functions of T and obtained[24-27]

$$k_1 = 1.42 \times 10^{14} \exp(- 25{,}805^\circ K/T) cm^3/mole\text{-}sec \tag{VIII}$$

for $1815 \leq T/^\circ K \leq 3360$.

Since the rate of N_2O-removal was[27] sensitive to $k_2 = k_3$ for $T \leqslant 2000^\circ K$, we conclude that a steady-state did not obtain for (O). For $T \geqslant 2200^\circ K$, (O) is at the steady state and the rate of N_2O disappearance depends[27] on k_1 but is insensitive to $k_2 = k_3$. Our measurements and conclusions are at variance with the discussions given in Ref. 28.

EXPERIMENTAL PROCEDURE

Studies were conducted behind reflected shock-waves[29-32] with 2% N_2O in argon, $1685 \leq T$, $^\circ K \leq 2560$, $1.70 \leq p$, atm < 4.55. We measured emission-intensity vs. time histories (with an LiF-prism monochromator and an InSb-detector) for N_2O at $\lambda = 4.52\ \mu$ ($\Delta\lambda = 0.083\ \mu$) and NO γ-band absorption at $\lambda = 2259$ A ($\Delta\lambda = 39$ A) using a 50-cm vacuum-u.v. monochromator with a concave (Seya-Namioka type) grating of 600 line/mm at a reciprocal dispersion of 37 A/mm. The instrument was equipped with an EMI-6255 B, S-13-response photomultiplier and associated circuitry with an electronic rise time of about 0.5 μsec. A Hinteregger-type, hollow-cathode discharge lamp served as light source with a modified DC-power supply which was adapted from an HeNe-laser. The lamp was flushed at ∿ 5 torr with a mixture of ∿ 0.9% NO and 39 ppm NO_2 in N_2 to produce emission lines of the NO γ-band system. The entrance slit of the ultraviolet monochromator was imaged by a spherical mirror onto the discharge of the hollow-cathode lamp; the light rays passed through two LiF windows. Determinations of absorption coefficients are described elsewhere.[33,34] The time resolution achieved by us was 5-10 μsec.

EXPERIMENTAL OBSERVATIONS AND RESULTS

Concentration-time histories of N_2O and NO were obtained for $1685 \leq T$, $^\circ K \leq 1900$ and $2215 \leq T$, $^\circ K \leq 2560$. At lower T, the N_2O-removal rate increased only slightly with time, as was previously found by Jost et al.[12] for $T \leqslant 1750^\circ K$. At higher T, (N_2O) decreased at first exponentially with t, as was observed also by Monat et al.[27] for $T \geqslant 2200^\circ K$; (NO) increased rapidly for 20-50 μsec and then increased linearly with t (cf. Fig. 2 of Ref. 27).

A rate-coefficient for the initial N_2O-removal was obtained (see Table 1) from

$$k_{exp} = \lim_{t \to 0} \left[\frac{-1}{(M)} \frac{d}{dt} \ln (N_2O) \right] \qquad \text{IX}$$

for various values of the initial temperatures (T_5) and pressures (p_5) behind the reflected shock-wave. A least-squares fit to our data yields

$$k_{exp} = (5.90 \pm 4.22) \times 10^{15} \exp[-(32{,}710 \pm 1{,}470)^\circ K/T] \mathrm{cm}^3/\mathrm{mole\text{-}sec} \qquad \text{X}$$

Table 1. Measured rate coefficient, k_{exp}, for N_2O-decomposition in a mixture containing 2% N_2O in Ar.

T_5, $^\circ K$	p_5, atm	$k_{exp} \times 10^{-8}$, cm^3/mole-sec
1720	2.171	0.307 ± 0.023
1855	2.162	2.359 ± 0.013
1860	2.155	1.362 ± 0.100
1899	2.231	1.171 ± 0.100
1980	1.901	3.649 ± 0.959
2215	2.060	17.68 ± 0.47
2276	1.802	44.19 ± 1.91
2290	1.829	37.31 ± 0.47
2382	4.547	68.37 ± 0.95
2554	1.702	154.6 ± 5.8

for $1720 \leq T$, $^{o}K \leq 2555$ with correlation coefficient $r^2 = 0.980$. Our experimental data (which agree within a factor of 1.5 with those of Refs. 12, 16, and 28), and those from Refs. 11, 12, 16, and 28 are shown in Fig. 1; k_{exp} for Ref. 28 was obtained by multiplying the given value for k_1 by two.

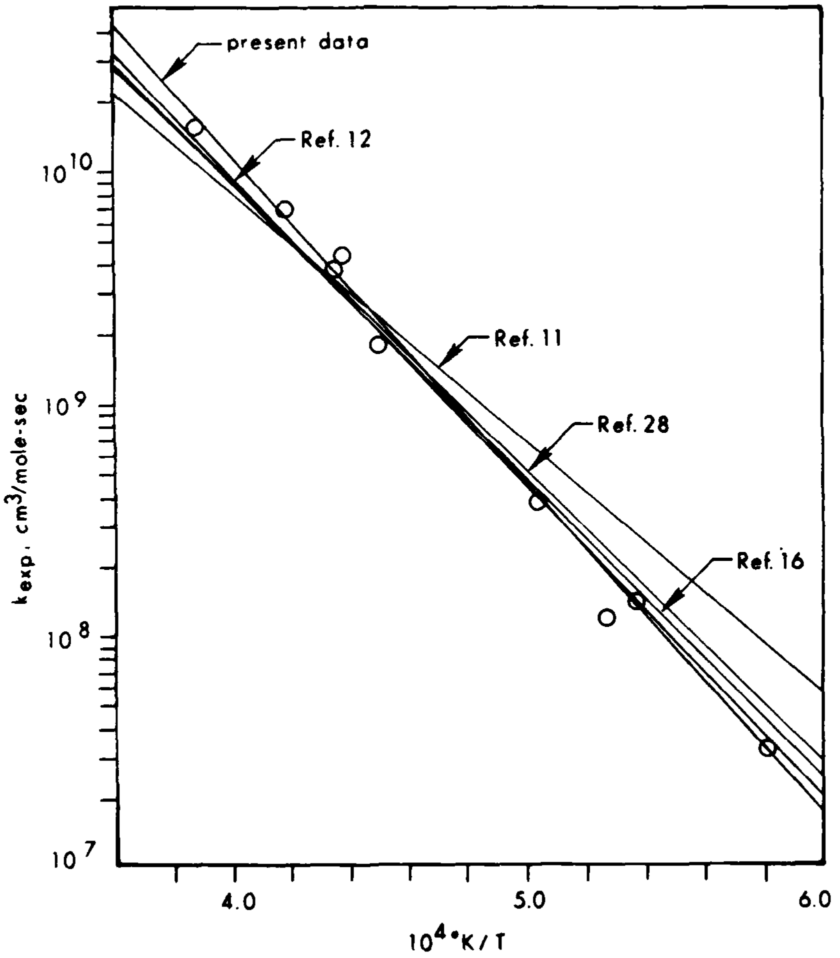

Fig. 1. Experimentally determined best fits to k_{exp} in mixtures containing N_2O in Ar. Our experimental data are shown as open circles. They approach our values of k_1 and $2k_1$ at low and high temperatures, respectively.

DATA INTERPRETATION

Subtraction of Eq. (I) from Eq. (II) and integration yield

$$(O) = 2k_1(M)\int_0^t (N_2O)dt' - [(N_2O)_o - (N_2O)] . \qquad XI$$

Addition of Eqs. (I)-(II), use of Eq. (III), and integration yields

$$(O) = [(N_2O)_o - (N_2O)] - \left(\frac{k_3}{k_2} + 1\right)(NO). \qquad \text{XII}$$

Subtracting Eq. (XII) from Eq. (XI), we find

$$\frac{k_3}{k_2} + 1 = \frac{2[(N_2O)_o - (N_2O)] - 2k_1(M)\int_0^t (N_2O)dt'}{(NO)}. \qquad \text{XIII}$$

For $(O)_{ss}$, Eq. (V) applies for (N_2O) and Eq. (XIII) reduces to Eq. (VI). Equation (XIII) shows that k_3/k_2 may be determined from measurements of (N_2O) and (NO) as functions of t, except at very early times.

Direct integration of Eq. (II) leads to

$$(O) = \frac{k_1(M)}{(k_2 + k_3)}\left\{1 - \exp\left[- (k_2 + k_3)\int_0^t (N_2O)dt'\right]\right\}, \qquad \text{XIV}$$

which shows that (O) reaches a steady state for $t > t_s$ with

$$1 \simeq (k_2 + k_3)(N_2O)_o t_s. \qquad \text{XV}$$

With $k_2 = k_3$ from Refs. 26 and 27, $t_s \simeq$ 20-35 μsec at the lower values of T and $t_s \simeq$ 9-12 μsec at the higher values of T used. For our time resolution (∿ 5-10 μsec), $(O) \neq (O)_{ss}$ initially, especially for the smaller values of T.

Replacing (O) in Eq. (I) by using Eq. (XIV) and rearranging leads to

$$k_2 + k_3 = \left[\ln \frac{k_1(M)(N_2O)}{(N_2^{\circ}O) + 2k_1(M)(N_2O)}\right] \bigg/ \int_0^t (N_2O)dt', \qquad \text{XVI}$$

which shows that $k_2 + k_3$ may be determined from time-dependent measurements of (N_2O) for known k_1 provided $(O) \neq (O)_{ss}$ [compare Eqs. (V) and (VI)].

Equations (XI) and (XIV) lead to

$$(N_2O)_o - (N_2O) = \frac{k_1(M)}{(k_2 + k_3)}\left\{2(k_2 + k_3)\int_0^t (N_2O)dt' - \left\{1 - \left[\exp - (k_2 + k_3)\int_0^t (N_2O)dt'\right]\right\}\right\}, \qquad \text{XVII}$$

i.e., (N_2O) as a function of $x \equiv \int_0^t (N_2O)dt'$ decreases initially (for $t \to 0$) according to

$$d[(N_2O)_o - (N_2O)]/dx\Big|_{x\to 0} = k_1(M), \qquad \text{XVIII}$$

whereas, after the induction period for which

$$x_{i,N_2O} = \int_0^{t_{i,N_2O}} (N_2O)dt' \underset{=}{\sim} \tfrac{1}{2}(k_2 + k_3)^{-1}, \ldots \qquad \text{XIX}$$

it decreases for $t \gg t_i$ according to the relation

$$2k_1(M) = [(N_2O)_o - (N_2O)] / \int_{t_i}^{t} (N_2O)dt' \text{ for } t \gg t_i = t_{i,N_2O}. \qquad \text{XX}$$

The induction time $t_i = \frac{1}{2}t_s$ when $(O) = (O)_{ss}$ [compare Eqs. (XIX) and (XV)]. Thus, k_1 may be determined either from Eq. (XVIII) when $(O) \neq (O)_{ss}$ or from Eq. (V) for $(O) = (O)_{ss}$. Also, for $(O) \neq (O)_{ss}$ and $t_i \neq 0$, $k_2 + k_3$ may be found from Eq. (XIX). Equation (XVII) is usually easier to use than Eq. (XVI) since it does not involve $(N_{\dot{2}}O)$; it may also be used to ascertain if $(O) = (O)_{ss}$ initially and, if not ($t_i \neq 0$), when the steady state is reached.

The observed time histories of (NO) show when $(O) \simeq (O)_{ss}$. By eliminating (O) from Eqs. (III) and (XIV), we find that

$$\begin{aligned}(\dot{NO}) &= \frac{2k_1(M)(N_2O)}{[(k_3/k_2) + 1]} \left\{1 - \left[\exp - (k_2 + k_3) \int_0^t (N_2O)dt'\right]\right\} \\ &= \frac{2k_1(M)(N_2O)}{[(k_3/k_2) + 1]} + \frac{2k_1(M)}{k_2[(k_3/k_2) + 1]^2} \frac{d}{dt} \exp\left[- (k_2 + k_3) \int_0^t (N_2O)dt'\right],\end{aligned} \qquad \text{XXI}$$

which may be integrated to

$$(NO) = \frac{2k_1k_2(M)}{(k_2 + k_3)^2} \left\{(k_2 + k_3) \int_0^t (N_2O)dt' - \left\{1 - \left[\exp - (k_2 + k_3) \int_0^t (N_2O)dt'\right]\right\}\right\}. \qquad \text{XXII}$$

According to Eq. (XXII), (NO) increases linearly with x for

$$x > x_{i,NO} = \int_0^{t_{i,NO}} (N_2O)dt' \underset{=}{\sim} (k_2 + k_3)^{-1}; \qquad \text{XXIII}$$

x_i corresponds to t_s ($\simeq t_i$) when $(O) \simeq (O)_{ss}$ [compare Eqs. (XXII) and (XIV)], and

$$\frac{k_3}{k_2} + 1 = 2k_1(M)\left[\int_{t_i}^{t} (N_2O)dt'\right] \Big/ (NO)_t \text{ for } t \gg t_i = t_{i,NO}. \qquad \text{XXIV}$$

For $(O) \simeq (O)_{ss}$ immediately behind the reflected shock-wave, $x = \int_0^t (N_2O)dt' \ll 1$ in Eqs. (XIV), (XVII) and (XXII) for times short compared with the experimentally achieved time resolution; also, $(k_2 + k_3)x \gg 1$ and $t_i \simeq 0$ in Eqs. (XX) and (XXIV). This situation holds for T > 2000°K. For $(O) \neq (O)_{ss}$ initially, (NO) has a zero initial slope as a function of x while $(N_2O)_o - (N_2O)$ as a function of x shows an initial slope of $k_1(M)$. The sum $k_2 + k_3$

may then be determined from Eqs. (XIX) and (XXIII); this behavior has been observed for $T \leqslant 2000°K$.

Determination of k_1

We conclude that $(O) \simeq (O)_{ss}$ immediately after shock-heating only for our high-temperature data; for lower T, (N_2^*O) is governed by reaction (1) and $(O) \simeq (O)_{ss}$ is attained later. Consequently, k_1 could be determined independently from Eqs. (XVIII) and (XX) for $T_5 < 2000°K$, whereas it could be derived only from Eq. (XX) for $T_5 > 2000°K$. The experimental data are displayed [circles for Eq. (XX) and squares for Eq. (XVIII)] as functions of 1/T in Fig. 2 and yield

$$k_1 = (3.71 \pm 2.74) \times 10^{14} \exp[-(27,660 \pm 1,445)°K/T] cm^3/mole\text{-}sec \qquad XXV$$

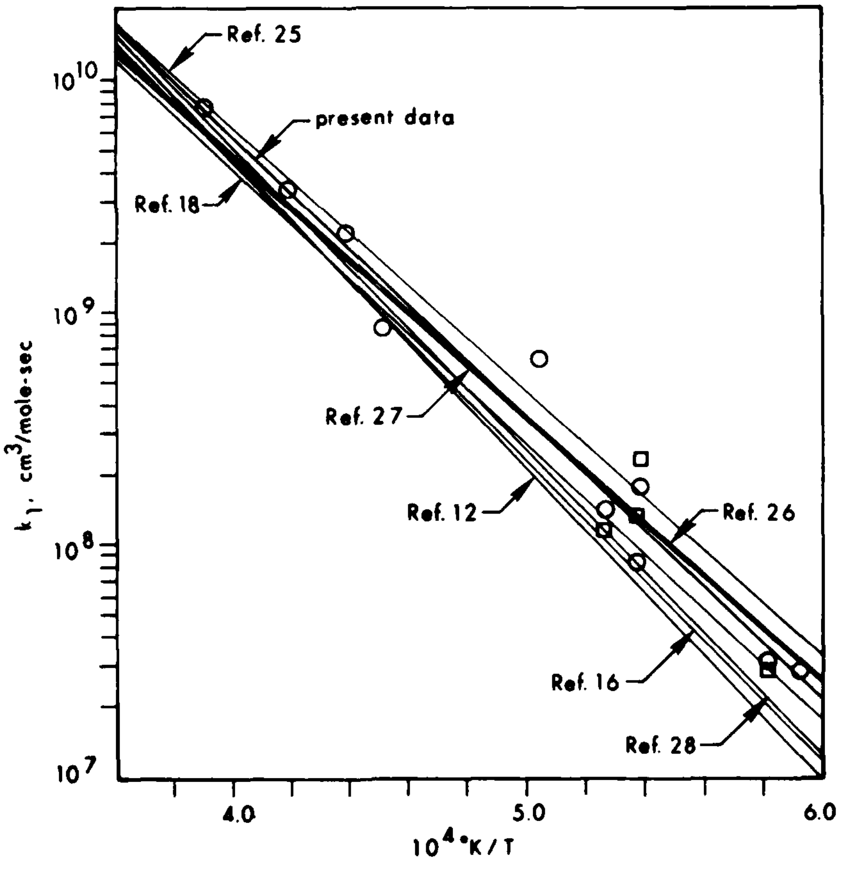

Fig. 2. Rate coefficients for the reaction $N_2O + M \rightarrow N_2 + O + M$ as functions of 1/T. The symbols ○ and □ refer to data obtained from Eqs. (XX) and (XVIII), respectively. Also displayed are expressions derived in Refs. 12, 16, 18, and 25-28.

AD-A091 010 HEBREW UNIV JERUSALEM (ISRAEL) F/G 20/4
PROCEEDINGS OF THE INTERNATIONAL SYMPOSIUM ON SHOCK TUBES AND W--ETC(
FEB 80 A LIFSHITZ, J ROM AFOSR-78-3679
UNCLASSIFIED AFOSR-TR-80-1141 NL

6 of 8

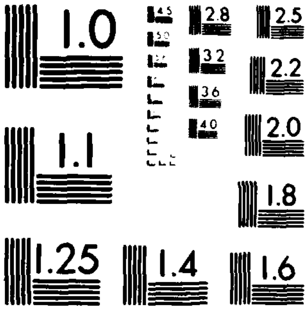
1.0
4.5
5.0
2.8
2.5
3.2
2.2
3.6
4.0
2.0
1.1
1.8
1.25
1.4
1.6

for $1685 \leq T, {}^{o}K \leq 2560$ with correlation coefficient $r^2 = 0.961$. Also shown in Fig. 2 are literature data.[12,16,18,25-28] The present results show only a slightly larger activation energy than the numerical fits to shock-tube data described in Refs. 26 and 27. Our values for k_1 are ∿ 30% larger for large T and ∿ 20% smaller for small T than the results given in Refs. 26 and 27; for small T, k_1 lies ∿ 80% and, for high T, ∿ 35% above the values of Ref. 16 for $(O)_{ss}$; our data show practically the same activation energy as those of Borisov[18] while k_1 is about 30% larger than Borisov's values.

Determinations of k_3/k_2 and $k_2 + k_3$

The ratio k_3/k_2 was determined graphically from Eq. (XXIV) after plotting (NO) vs. $x = \int_0^t (N_2O)dt'$ according to Eq. (XXII). The results are displayed in Fig. 3 (circles) as functions of 1/T. Application of Eq. (XIII) yielded one usable point, which is shown as a square in Fig. 3. The data in Fig. 3 show that

$$k_3/k_2 = 1.09 \pm 0.10. \qquad \text{XXVI}$$

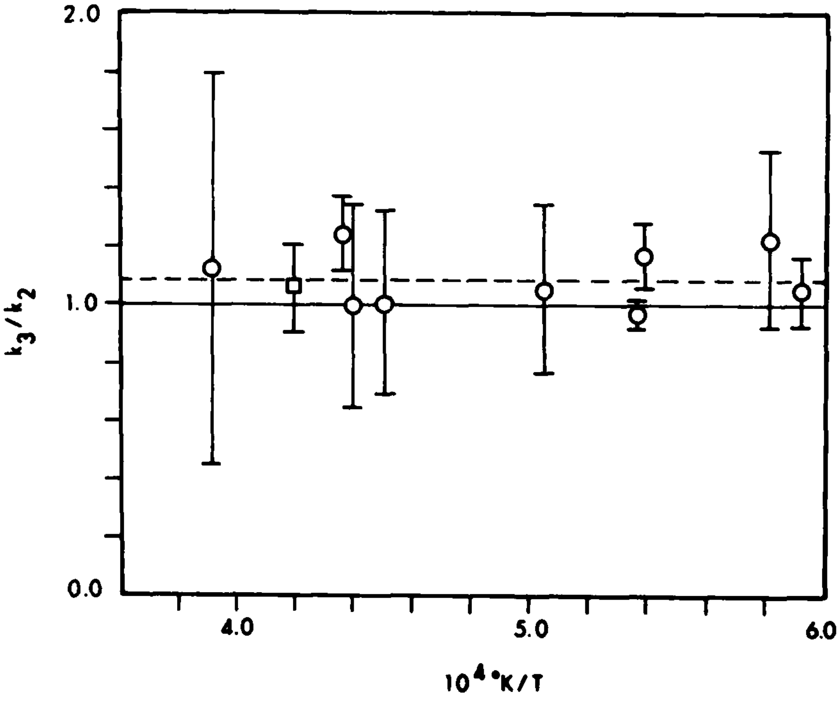

Fig. 3. Experimental values of k_3/k_2 as functions of 1/T; ○: data obtained from Eq. (XXIV); □: data obtained from Eq. (XIII). The error bars refer to the accuracy of the data reduction.

The result $k_2 = k_3$ agrees with Baulch et al.[28] but is at variance with other data.[7,12,14,22]

Values for $k_2 + k_3$ were obtained for $T \leq 2000$°K from Eqs. (XIX) and (XXIII) after plotting $(N_2O)_o - (N_2O)$ and (NO) as functions of $x = \int_0^t (N_2O)dt'$ according to Eqs. (XVII) and (XXII). The results are displayed in Fig. 4 [circles for Eq. (XVII) and squares for Eq. (XXII)] and yield

$$k_2 + k_3 = (8.50 \pm 6.38) \times 10^{13} \exp[-(12{,}350 \pm 2{,}380)°K/T]\,cm^3 mole\text{-}sec \qquad XXVII$$

for $1685 \leq T$, °K ≤ 1980 with $r^2 = 0.749$. Also shown in Fig. 4 are data from Refs. 11, 18, 26-28. Equation (XXVII) shows E = 24.5 kcal/mole, which is practically the same as the values given in Refs. 11, 18, 21, and 27. Around 2000°K, our results for $k_2 + k_3$ agree with and, around 2680°K, are only about 18% lower than the expression in Ref. 28 which has an activation energy of 28.0 kcal/mole.

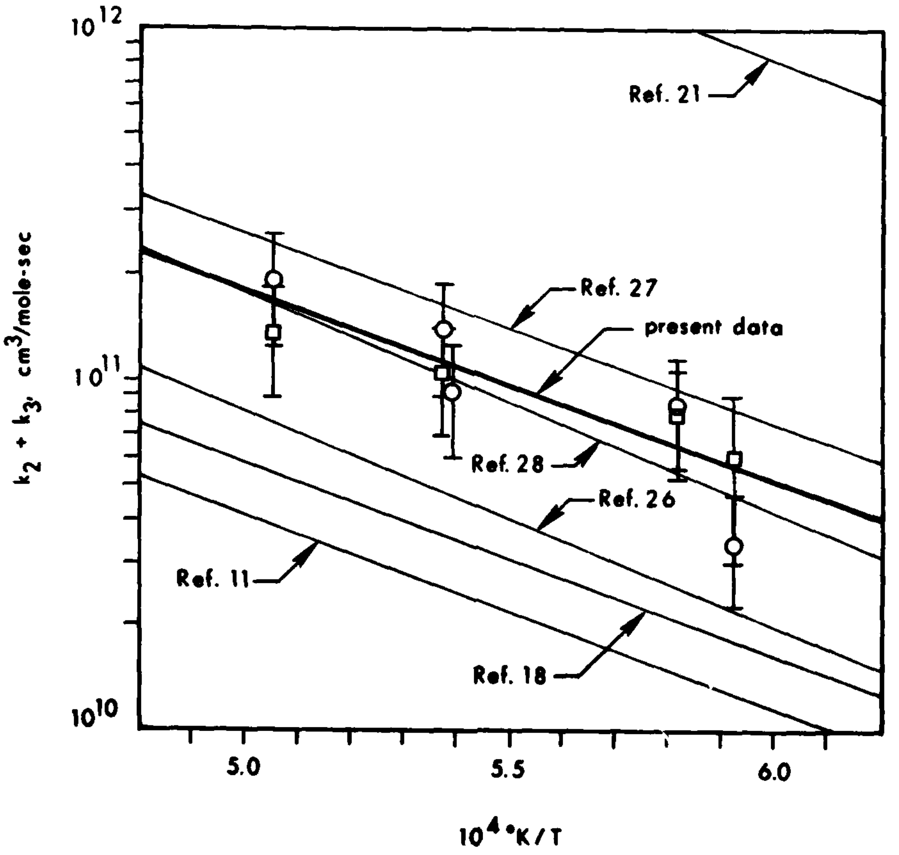

Fig. 4. Experimental values for $k_2 + k_3$ as functions of $10^4/T$; ○: data obtained from Eq. (XIX); □: data obtained from Eq. (XXIII). Also displayed are the expressions derived in Refs. 11 and 26-28.

Using $k_3/k_2 = 1.09 \pm 0.10$, we find from Eq. (XXVII) that

$$k_2 = (4.07 \pm 3.26) \times 10^{13} \exp[-(12{,}350 \pm 2{,}380)^{\circ}\mathrm{K}/T]\,\mathrm{cm}^3/\mathrm{mole\text{-}sec} \qquad \mathrm{XXVIII}$$

and

$$k_3 = (4.43 \pm 3.97) \times 10^{13} \exp[-(12{,}350 \pm 2{,}380)^{\circ}\mathrm{K}/T]\,\mathrm{cm}^3/\mathrm{mole\text{-}sec} \qquad \mathrm{XXIX}$$

for $1685 \leq T, {}^{\circ}\mathrm{K} \leq 2000$.

CONCLUDING REMARKS

We have shown that k_1, k_3/k_2 and $k_2 + k_3$ are determined independently and uniquely from the (N_2O) and (NO) time-histories.

ACKNOWLEDGEMENTS

We are indebted to Messrs. Larry Cady and Denduluri Seshadri for help with the data reduction and related calculations.

REFERENCES

1. M. Volmer and H. Kummer, Z. Physik. Chem. *B9*, 141 (1930).
2. N. Nagasako, Z. Physik. Chem. *B11*, 420 (1931).
3. M. Volmer and H. Froelich, Z. Physik. Chem. *B19*, 89 (1932).
4. M. Volmer and M. Bogdan, Z. Physik. Chem. *B21*, 257 (1933).
5. R. M. Lewis and L. N. Hinshelwood, Proc. Roy. Soc. *A168*, 441 (1938).
6. F. J. Lindars and C. N. Hinshelwood, Proc. Roy. Soc. *A231*, 162 (1955), *ibid.*, *A231*, 178 (1955).
7. F. Kaufman, N. J. Gerri and R. E. Bowman, J. Chem. Phys. *25*, 106 (1956).
8. T. N. Bell, P. L. Robinson and A. B. Trenwith, J. Chem. Soc., 1474 (1957).
9. R. J. Coleman, M. G. Holliday and B. B. Reuben, *First Gas Kinetics Symposium*, p. 429, University of Szeged, Szeged, Hungary, 1969.
10. J. N. Bradley and G. B. Kistiakowski, J. Chem. Phys. *35*, 256 (1961).
11. E. S. Fishburne and R. Edse, J. Chem. Phys. *41*, 1297 (1964).
12. W. Jost, K. W. Michel, J. Troe, and H. Gg. Wagner, Z. Naturforsch. *19a*, 59 (1964).
13. I. D. Gay, G. B. Kistiakowski, J. V. Michael, and H. Niki, J. Chem. Phys. *43*, 1720 (1965).
14. D. Gutman, R. L. Belford, A. J. Hay, and R. Pancirov, J. Phys. Chem. *70*, 450 (1966).
15. A. Martinengo, J. Troe and H. Gg. Wagner, Z. Physik. Chem. *51*, 104 (1966).
16. H. A. Olschewski, J. Troe and H. Gg. Wagner, Ber. Bunsenges. Physik. Chem. *70*, 450 (1966).
17. L. J. Drummond and S. W. Hiscock, Austral. J. Chem. *20*, 815 (1967).
18. A. A. Borisov, Kin. i. Kat. *9*, 482 (1968); English translation: Kinetics and Catalysis *9*, 399 (1968).
19. S. C. Barton and J. E. Dove, Can. J. Chem. *47*, 521 (1969).
20. S. H. Garnet, G. B. Kistiakowski and B. V. O'Grady, J. Chem. Phys. *51*, 84 (1969).
21. H. Henrici and S. H. Bauer, J. Chem. Phys. *50*, 1333 (1969).
22. W. H. Lipkea, D. Milks and R. Matula, Comb. Sc. & Tech. *6*, 257 (1973).
23. Q. Le Trung, D. Mackay, A. Hirata, and O. Trass, Comb. Sc. & Tech. *10*, 155 (1975).
24. S. C. Baber and A. M. Dean, Int. J. Chem. Kinet. *7*, 381 (1975).
25. A. M. Dean, Int. J. Chem. Kinet. *8*, 459 (1976).
26. A. M. Dean, D. C. Steiner and E. E. Wang, "A Shock Tube Study of the H_2/O_2/CO/Ar and H_2/N_2O/CO/Ar System," Project Squid Technical Report No. UMO-2-PU, Purdue University, West Lafayette, Ind., 1977; Combustion and Flame *32*, 73 (1978).
27. J. P. Monat, R. K. Hanson and C. H. Kruger, Comb. Sc. & Tech. *16*, 21 (1977).

28. D. Baulch, D. D. Drysdale, D. G. Horne, and A. C. Lloyd, *Evaluated Kinetic Data for High-Temperature Reactions, Vol. 2, Homogeneous Gas Phase Reactions of the* H_2*-*N_2*-*O_2 *System*, p. 69, Butterworths & Co., Ltd. London, 1973.
29. M. L. Price, K. G. P. Sulzmann and S. S. Penner, JQSRT *11*, 427 (1971).
30. A. Gilbert, K. G. P. Sulzmann and S. S. Penner, JQSRT *14*, 455 (1974).
31. K. G. P. Sulzmann, JQSRT *15*, 313 (1975).
32. W. M. Heffington, G. E. Parks, K. G. P. Sulzmann, and S. S. Penner, *Sixteenth Symposium (International) on Combustion*, pp. 997-1011, The Combustion Institute, Pittsburgh, Pa., 1977.
33. K. G. P. Sulzmann, J. M. Kline and S. S. Penner, "Empirical Determinations of the Effective Absorption Coefficients for the NO γ-Band at 2259 A and the ν_3-Fundamental of N_2O at 4.52 μ," JQSRT, *21*, 475 (1979).
34. K. G. P. Sulzmann, "Expressions for the Local Spectral Absorption Coefficient for Correlation Absorption Spectroscopy," JQSRT, in press (1979).

THERMAL DECOMPOSITION OF NH_3 IN SHOCK WAVES

T. R. Roose, R. K. Hanson and C. H. Kruger

Department of Mechanical Engineering
Stanford University, Stanford, California 94305, USA

Shock tube kinetics experiments have been conducted with NH_3 in argon to determine the rates of the initial thermal decomposition reactions

$$NH_3 + M \xrightarrow{k_1} NH_2 + H + M$$

and

$$NH_3 + M \xrightarrow{k_2} NH + H_2 + M \ .$$

The temperature range of the experiments was 2200 to 3450 K. Species concentrations were monitored behind incident shock waves using emission techniques: NH_3 at 3 and 10.5 μm, NH_2 at 5380 Å and NH at 3360 Å. A computer simulation of the experiments was used to infer k_1 and k_2 with the following best-fit results:

$$k_1 = 2.52 \times 10^{16} \exp(-47200/T) \ cm^3/mole\text{-}s$$

and

$$k_2/k_1 \lesssim 0.01$$

with

$$k_2 = 3.4 \times 10^6 \ cm^3/mole\text{-}s \quad \text{at } 2798 \ K.$$

INTRODUCTION

The objective of the present work was to determine the initial thermal decomposition rate of NH_3 and to assess the relative importance of the initial decomposition reactions

$$NH_3 + M \xrightarrow{k_1} NH_2 + H + M \qquad (1)$$

and

$$NH_3 + M \xrightarrow{k_2} NH + H_2 + M \ . \qquad (2)$$

This work is important to the development of a detailed kinetic model of the overall NH_3 pyrolysis process, which in turn is relevant to the kinetics of fuel-nitrogen NO_x and to flue gas removal of NO_x by selective reactions with NH_3.

There have been a number of previous shock tube studies of NH_3 pyrolysis.[1-7] On the basis of these studies it is clear that the overall kinetic mechanism is complex and that failure to recognize these complexities has led to some erroneous determinations of k_1. Only two of these previous studies[1,2] have recognized that sufficiently low initial mole fractions of NH_3 must be used to minimize the influence of subsequent reactions on the determination of k_1. Questions regarding the kinetic models employed (including new evidence for the possible importance of reaction 2), together with discrepancies between the reported values of k_1, suggested that another study with different diagnostics was warranted.

As a means of studying the initial NH_3 decomposition reactions, we have shock-heated mixtures of NH_3 and argon. The species NH_3, NH_2 and NH have been monitored using emission techniques. At the low NH_3 concentrations required to minimize the effect of subsequent reactions, interferences in the NH_3 record prohibited its use for the determination of the initial NH_3 decomposition rate. Calibrations for NH_2 and NH were obtained in separate experiments at higher NH_3 concentrations. A computer simulation was utilized to fit the NH_2 time histories and infer a best-fit value for k_1. The NH time histories were utilized to extract upper-bound values for k_2 along with a computer simulation of one experimental record resulting in a determination of k_2 at 2798 K.

EXPERIMENTS

The experiments were conducted behind incident shock waves in a conventional, pressure-driven shock tube (15.2 cm internal diameter). Incident shock speeds varied from 1.5 to 1.8 mm/μsec, producing frozen-chemistry temperatures of 2200 to 3450 K and postshock pressures of 0.14 - 0.6 atm. Shock speed attenuation was typically 0.6% per meter. The mixtures of NH_3 (200-1200 ppm for kinetics runs and 0.1 - 1.0% for calibrations) and the inert gas argon were prepared immediately before each run in a stainless steel mixing tank with an externally driven stirring rod. Helium was used as the driver gas. Since NH_3 has been observed to adsorb on stainless steel, the mixing tank and shock tube were flushed with pure NH_3 at low pressure before each experiment. Independent tests confirmed that effects due to adsorption were negligible in the rate coefficient determinations.

The concentrations of NH_3, NH_2 and NH were monitored with emission techniques. The detection systems are shown schematically in Figure 1. The spatial resolution and circuit frequency bandpass of each system were chosen

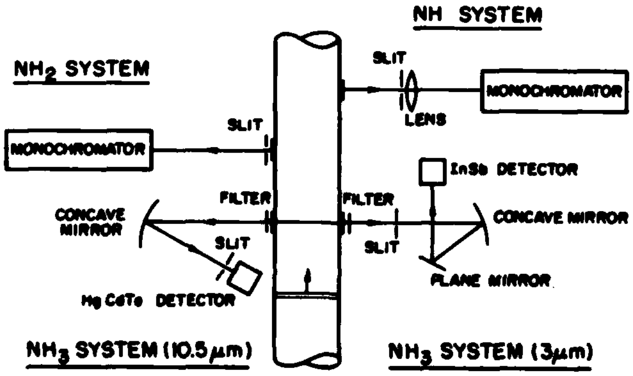

Figure 1. Schematic of the detection systems.

to be consistent with the reaction time of each experiment. The outputs of the various emission systems were recorded on both analog and digital oscilloscopes, the latter being equipped with disk storage capability.

The 3 μm NH_3 detection system, monitoring the 2.9 and 3.0 μm bands of NH_3, employed a configuration with a variable-width vertical slit between the mirror and shock tube. The 1 × 3 mm InSb detector (77 K) was imaged at the near shock tube window with a magnification of 1.5. The spatial resolution at the far wall was determined by the vertical slit width. The spectral bandpass of the system was determined by a 3.1 μm long-wavepass filter and the long-wavelength cutoff of the detector (5.5 μm).

The 10.5 μm NH_3 detection system employed an alternate configuration in which the spatial resolution was defined by a variable-width vertical slit located between the detector and the concave mirror. The 2 × 2 mm HgCdTe detector (77 K) was imaged with a magnification of 2 at the near shock tube window. The vertical slit was imaged at the far window. The spectral bandpass of the system was determined by a 9.5 μm long-wavepass filter and the long-wavelength cutoff of the detector (12.1 μm).

The NH and NH_2 detection systems employed 1/4-meter monochromators and photomultipliers (Dumont 6292 for NH_2 and Dumont 7664 for NH). The spatial resolution in each system was determined by a variable-width vertical slit and the monochromator entrance slit. The spectral regions monitored were centered at 5380 Å (NH_2) and 3360 Å (NH), each system utilizing a total bandpass of 400 Å.

RESULTS

The rate of the dominant initial decomposition reaction

$$NH_3 + M \xrightarrow{k_1} NH_2 + H + M \qquad (1)$$

was determined in the temperature range of 2250 to 3050 K by monitoring the early-time rate of formation of NH_2 in highly dilute NH_3-argon mixtures. Mixtures of 0.02 - 0.12% NH_3 in argon at total gas densities of about 1.5×10^{-6} mole/cm^3 were used to minimize and delay the effect of subsequent reactions. The rate coefficients inferred in 14 separate experiments are listed in Table 1. These rate coefficients were obtained by fitting the early-time NH_2 data using a 24-reaction mechanism (including both forward and reverse reactions) with 10 species. For the experimental times under consideration only the 8 reactions listed in Table 2 are important. Boundary layer effects are expected to be negligible at early times for our test conditions and large tube diameter and hence no boundary layer correction was applied.

Typical results for measured and computed NH_2 time histories are shown in Figures 2 and 3. Immediately after the shock arrival, the NH_2 signal is seen to rise linearly with respect to time. This linear rise is an indication that secondary reactions are not yet influencing the NH_2 formation rate. Figure 3 illustrates the following two points. First, by examining the $k_1 = 1.5\ k_1^+$ and $k_1 = k_1^+/2$ curves (k_1^+ = best-fit k_1), it is observed that the NH_2 concentration scales linearly with respect to k_1. Second, the relative insensitivity to secondary reactions, for the low NH_3 concentrations considered in this study, is illustrated by increasing the rate of the most important secondary reaction, reaction (3), by a factor of 5 ($k_3 = 5\ k_3^+$). This change in k_3 would cause only an 8% variation in the inferred value for k_1.

The absolute calibration of the NH_2 detection system was an important step in these experiments. This calibration was accomplished by shock heating mixtures of NH_3 and argon under conditions where the decomposition of NH_3 could be measured and related directly to the formation of NH_2, i.e., where $\Delta NH_2 = -F \Delta NH_3$, with F a factor near 1 determined by kinetic modeling. To obtain good quality NH_3 records, it was necessary to utilize initial mole fractions of 0.1 - 1.0%, somewhat higher than desired for determining k_1; temperature ranged from 2200–2950 K. This calibration was an iterative procedure in that an initial NH_2 calibration was used to obtain a calibration for NH, which in turn was used together with several NH emission time histories to show that $k_2/k_1 << 1$. This latter result was employed in detailed kinetic calculations, using the 24-reaction mechanism, to determine the F values for each experiment, i.e., the fractional conversion of NH_3 to NH_2 at early times. The time region typically used was from about 1/3 the time-to-peak to about 2/3 the time-to-peak

Table 1. Summary of Experimental Data for the Determination of k_1.

Run	T(K)	P(atm)	% NH_3	k_1
1	2266	.479	.106	2.43×10^7
2	2403	.477	.059	6.91×10^7
3	2565	.340	.074	2.63×10^8
4	2600	.344	.104	3.24×10^8
5	2653	.301	.077	4.71×10^8
6	2746	.269	.053	9.06×10^8
7	2746	.274	.021	1.05×10^9
8	2786	.274	.0953	9.39×10^8
9	2798	.243	.024	1.34×10^9
10	2852	.277	.023	1.46×10^9
11	2862	.248	.023	1.75×10^9
12	2913	.256	.062	2.53×10^9
13	2920	.257	.113	2.26×10^9
14	3048	.237	.065	4.93×10^9

Table 2. NH_3 Early Time Kinetic Mechanism
(cm^3-$mole^{-1}$-sec^{-1} units)

No.	Reaction	Rate	Direction	Reference
1	$NH_3 + M \rightleftarrows NH_2 + H + M$	$2.52 \times 10^{16} \exp(-47200/T)$	Forward	This Study
2	$NH_3 + M \rightleftarrows NH + H_2 + M$	$k_2 \lesssim .01\ k_1$	Forward	This Study
3	$NH_3 + H \rightleftarrows NH_2 + H_2$	$2.75 \times 10^{13} \exp(-8760/T)$	Forward	8
4	$NH_2 + H \rightleftarrows NH + H_2$	$3.0 \times 10^{13} \exp(-4300/T)$	Forward	Estimate
5	$NH_2 + NH_2 \rightleftarrows NH_3 + NH$	$6.0 \times 10^{12} \exp(-5030/T)$	Forward	9
6	$NH_2 + M \rightleftarrows NH + H + M$	$2.0 \times 10^{16}\ T^{-.5}$	Reverse	10
7	$NH + H \rightleftarrows N + H_2$	$1.0 \times 10^{13} \exp(-3200/T)$	Forward	Estimate
8	$NH + M \rightleftarrows N + H + M$	$3.0 \times 10^{16}\ T^{-.5}$	Reverse	10

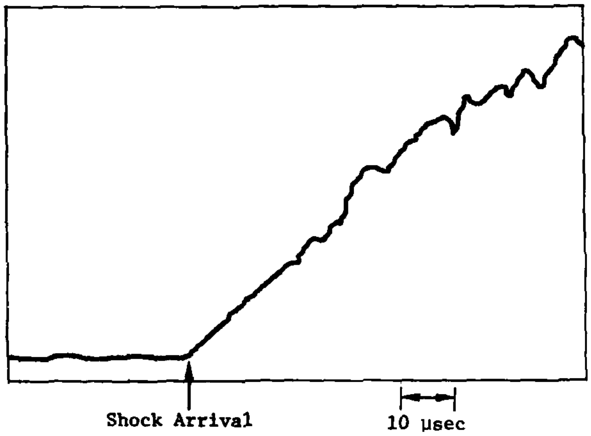

Figure 2. NH_2 experimental record for an initial mixture of 526 ppm NH_3 in argon at conditions of T = 2746 K and P = .269 atm.

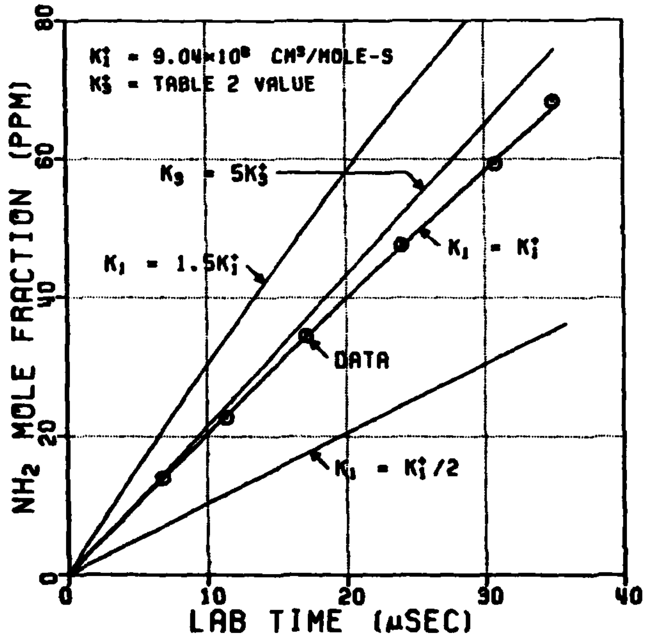

Figure 3. Comparison of experiment and theory for an initial mixture of 526 ppm NH_3 in argon at conditions of T = 2746 K and P = .269 atm.

of the NH_2 signal. In this region the NH_3 concentration is well defined and the rise in the NH_2 signal is still essentially linear. F values ranged from about 0.66 at 2200 K to about 0.88 at 2950 K. At the higher NH_3 concentrations employed for calibration, reactions other than 1 play a larger role in controlling the rate of conversion of NH_3 to NH_2, but variations in the important rate coefficients do not substantially change the value of F. Thus uncertainties in the kinetic mechanism and rate coefficients do not cause a large uncertainty in an NH_2 calibration determined at early times. A conservative estimate of the uncertainty in the NH_2 calibration ranges from ± 40% at 2200 K to ± 15% at 2950 K.

The present results for k_1 are compared with previous work in Figure 4. Our best-fit expression is in excellent agreement with Nip's work,[2] while falling a factor of 1.7 below the results of Henrici[1] and 2.1-4.2 below those of Michel and Wagner.[3]

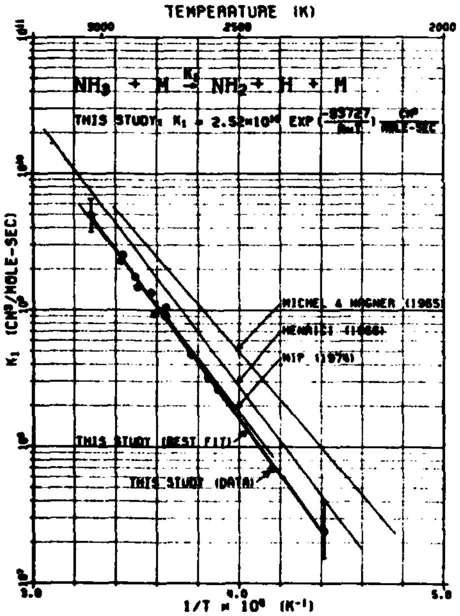

Figure 4. Arrhenius diagram for k_1 showing data of this study and a least-squares best-fit to the data. Also shown are k_1 determinations of Michel and Wagner[3] and Henrici,[1] along with the coefficient for the initial NH_3 decomposition rate reported by Nip.[2]

Michel and Wagner followed the decay of uv absorption of NH_3 formed from shock-heated hydrazine. However, little information is given about the mechanism of the reaction, so their measured rate coefficient cannot be correlated directly with either initiating reaction 1 or 2. The activation energy of 79.5 kcal/mole as determined by Michel and Wagner is also significantly below the heat of reaction for both reaction 1 (106 kcal/mole at 2500 K) and reaction 2 (103 kcal/mole at 2500 K), suggesting an early acceleration in the NH_3 decomposition due to a chain reaction. Henrici recognized that consecutive reactions may have influenced earlier k_1 determinations and accordingly sought to minimize these effects by extending the measurements to higher temperatures and by utilizing very low NH_3 concentrations in the lower temperature regime. In his experiments, NH_3 was monitored by uv absorption over the temperature range 2165-3275 K. At low temperatures, between 2165 and 2400 K, Henrici used mixtures in the range of 0.03 - 0.07% NH_3 in argon at total gas densities of about 3×10^{-5} mole/cm³. The NH_3 decay was observed to accelerate to a value corresponding to Michel and Wagner's rate at long times. The activation energy determined by Henrici, 91 kcal/mole, compares more favorably with the heats of reaction for reactions 1 and 2. We believe, however, that Henrici did not completely account for secondary reactions, in particular the reaction

$$NH_3 + H \longrightarrow NH_2 + H_2 \ . \tag{3}$$

Nip studied NH_3 decomposition by means of time-of-flight mass spectrometry over the temperature range of 2400 to 3100 K.[2] Nip's mixtures consisted of 0.14% and 6% NH_3 in argon at total gas densities of about 1.7×10^{-6} mole/cm^3. Nip's study also showed the importance of using low initial NH_3 concentrations to minimize the effect of secondary reactions. In particular, Nip recognized the influence of reaction (3) and separately determined a rate for that reaction.[2,9] In his thesis,[2] he reported a rate expression for the initial NH_3 decomposition reaction

$$NH_3 + M \longrightarrow \text{products}$$

with an activation energy of 89.5 kcal/mole based on his 0.14% experiments. (This is the curve labelled "Nip" in Figure 4.) Although Nip attempted to assess the relative importance of reactions 1 and 2 by analyzing his high concentration (6% NH_3 in argon) experiments, his expression for k_2/k_1 was strongly mechanism dependent, varying over several orders of magnitude. We have chosen to regard his value for the initial decomposition of NH_3 as a determination of k_1.

In the second part of this study, we have investigated the NH_3 decomposition reaction

$$NH_3 + M \xrightarrow{k_2} NH + H_2 + M \tag{2}$$

in the temperature range 2200 to 3450 K by monitoring the early-time rate of formation of NH in highly diluted NH_3-argon mixtures. Some preliminary evidence for the importance of this reaction has recently been obtained.[8] With a few exceptions, these are the same experiments used to infer k_1, resulting in 15 separate upper-bound determinations of k_2. A rate coefficient at 2798 K was determined by fitting the early-time NH data using the 24-reaction mechanism. As noted previously in connection with the NH_2 records, for the experimental times considered only the 8 reactions listed in Table 2 are important.

Figures 5 and 6 illustrate a typical NH-time history and computer predictions. Immediately after the shock arrival, the NH signal is seen to rise linearly with respect to time. However, after a relatively short time (~ 20 μsec), it becomes apparent that the rate of NH formation is accelerating. This is due to the influence of other reactions. In particular, the reaction

$$NH_2 + H \longrightarrow NH + H_2 \tag{4}$$

is becoming increasingly important until it becomes the dominant NH formation reaction after about 40 μsec.

Figure 6 illustrates the method employed to infer the k_2 rate coefficient, as well as the method by which upper-bound values were determined. At times longer than 40 μsec, reaction 4 is the dominant NH formation reaction, and k_4 could be adjusted to fit the data with $k_2 = 0$. This result clearly did not match the early time data. In order to match these data while retaining agreement at longer times, k_2 was increased and k_4 slightly decreased, i.e.,

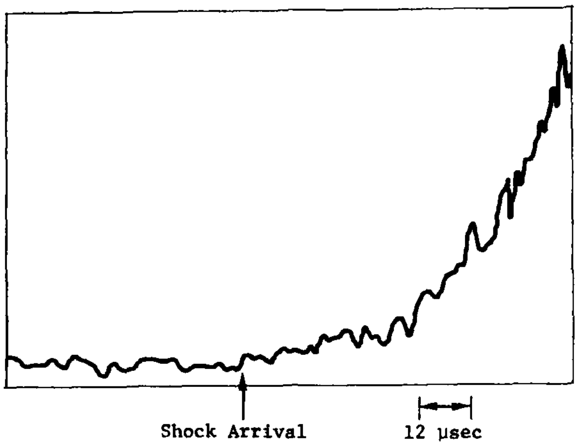

Figure 5. NH experimental record for an initial mixture of 237 ppm NH_3 in argon at conditions of T = 2798 K and P = .243 atm.

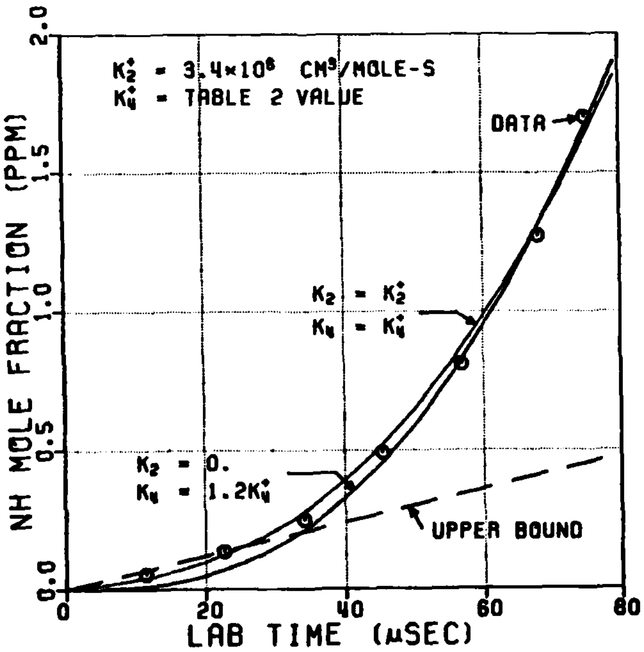

Figure 6. **Comparison of experiment and theory for an initial mixture of 237 ppm NH_3 in argon at conditions of T = 2798 K and P = .243 atm.**

$k_2 = k_2^+$ and $k_4 = k_4^+$, resulting in the best-fit plot shown. We thus have inferred a value of $k_2 = 3.4 \times 10^6$ cm^3/mole-s at 2798 K. In order to obtain an upper bound on k_2, a straight line was drawn through a data point at an early time when the NH signal could be accurately determined, in this case at about 20 μsec. The upper-bound value indicated by the dashed line in Figure 6 corresponds to a value of 1.8 k_2^+.

An essential step in the determination of k_2 was the absolute calibration of the NH detection system. These calibrations were carried out in the same NH_3-argon experiments used to calibrate the NH_2 system. The calibration was based on data for NH_3, NH_2 and NH recorded just after the peak concentration for NH has occurred (the peak NH concentration always occurs after the peak NH_2 concentration). At these times a partial equilibrium between NH_3, NH_2 and NH exists. This partial equilibrium condition is also predicted by the 24-reaction kinetic mechanism and is characterized by the reaction

$$NH_2 + NH_2 \rightleftharpoons NH_3 + NH \ . \qquad (5)$$

(Insensitivity of this partial equilibrium to rate coefficients was demonstrated.) The calibration procedure consisted of selecting a time just after the peak NH concentration where the measured NH_2 and NH_3 concentrations and the equilibrium constant K_{5eq} could be used to solve for NH, i.e., $(NH) = K_{5eq} (NH_2)^2/(NH_3)$. The estimated uncertainty in the NH calibration, including uncertainty in the kinetic model, is less than a factor of 2 in the temperature range investigated.

Upper-bound values for k_2 along with the rate determination at 2798 K are shown in Figure 7. Also shown is a plot of k_1 (as determined in this study) divided by 100. For temperatures above 2600 K, all upper-bound values

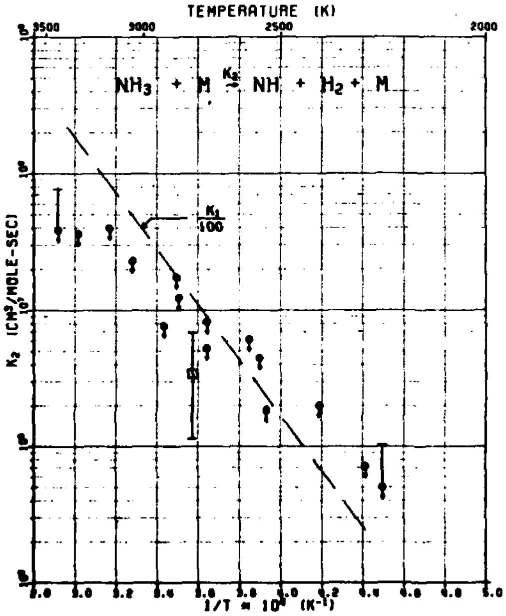

Figure 7. Arrhenius diagram for k_2 showing upper-bound data and a rate coefficient determination at 2798 K. Also shown is the k_1 rate determination of this study divided by 100.

indicate that $k_2/k_1 \lesssim 0.01$. The upper-bound values for temperatures less than 2600 K are less likely to be directly representative of k_2 for the following reasons. First, as the temperature was lowered, larger initial NH_3 concentrations were required to produce acceptable NH signal levels. Second, at lower temperatures the decomposition reaction

$$NH_3 + M \xrightarrow{k_2} NH + H_2 + M \qquad (2)$$

becomes much slower than subsequent reactions. Both effects increase the relative influence of other reactions on the NH profile, even at early times, and thereby lead to an increased difference between the value obtained for the upper-bound on k_2 and the actual value of k_2. Also, we do not expect the activation energy of reaction (2) to be greatly different from that of reaction 1. We therefore believe that $k_2 \lesssim 0.01\ k_1$ represents a more reasonable upper-bound for k_2.

CONCLUSION

In summary, we have assessed the relative importance of the initial NH_3 decomposition reactions

$$NH_3 + M \xrightarrow{k_1} NH_2 + H + M \qquad (1)$$

and

$$NH_3 + M \xrightarrow{k_2} NH + H + M \qquad (2)$$

and found that k_1 is the dominant reaction. By monitoring NH_2 emission, we have inferred a rate constant for reaction (1) of

$$k_1 = 2.52 \times 10^{16} \exp(-47200/T)\ cm^3/mole\text{-}s$$

over the temperature range 2250 to 3050 K. By monitoring NH emission, we have determined that $k_2/k_1 \lesssim 0.01$ over the temperature range 2200 to 3450 K and have inferred a rate of $k_2 = 3.4 \times 10^6\ cm^3/mole\text{-}s$ at 2798 K.

ACKNOWLEDGEMENTS

This work was supported by the National Science Foundation under Grant ENG-76-08279.

REFERENCES

1. M. Henrici, Ph.D. Thesis, Göttingen, 1966.
2. W. S. Nip, Ph.D. Thesis, University of Toronto, 1974.
3. K. W. Michel and H. Gg. Wagner, Tenth Symposium (International) on Combustion, p. 353, The Combustion Institute, 1965.
4. D. L. Baulch, D. D. Drysdale, D. G. Horne, and A. C. Lloyd, Evaluated Kinetic Data for High Temperature Reactions, Vol. 2, 1973.
5. J. N. Bradley, R. N. Butlin, and D. Lewis, Trans. Faraday Society, 63, p. 2962, 1967.
6. T. A. Jacobs, J. Phys. Chem., 67, p. 665, 1963.
7. A. P. Genich, A. Z. Zhirnov, and G. B. Manelis, translated from Kinetikai Kataliz, 16, No. 4, p. 841, 1975.
8. T. Just, Private communication.
9. J. E. Dove and W. S. Nip, Can. J. Chem., 50, p. 777, 1974.
10. K. W. Michel, Tenth Symposium (International) on Combustion, p. 351, The Combustion Institute, 1965.
11. G. S. Bahn, Reaction Rate Compilation for the N-O-H System, Gordon and Breach, 1968.

THERMAL DECOMPOSITION OF SO_2 MONITORED BY IR EMISSION

A. GRILLO, R. REED and M. W. SLACK

Research Department, Grumman Aerospace Corporation, Bethpage, New York 11714, USA

Thermal decomposition rates of sulfur dioxide dilute in argon have been measured and yielded a rate coefficient

$$k_1 = 8\ (\pm\ 2) \times 10^{15} \exp(-108{,}000/RT)\ cm^3 mole^{-1} sec^{-1}$$

for the reaction $SO_2 + M = SO + O + M$ in the temperature range 2800 to 3880°K. A critical assessment of earlier measurements of k_1 is presented and the combined data base yields a recommended k_1 between 2500 and 5200°K. From additional measurements in SO_2 - N_2O - argon mixtures, rate coefficients for $SO_2 + O = SO + O_2$ were determined as

$$k_2 = 4\ (\pm\ .4) \times 10^{12} \exp(-18{,}300/RT)\ cm^3 mole^{-1} sec^{-1}$$

in the temperature range 2630 to 3570°K.

INTRODUCTION

Rate coefficients for the thermal decomposition of sulfur dioxide

$$SO_2 + M = SO + O + M \qquad 1$$

measured in previous investigations[1-6] are inconsistent. The two most recent papers[1,2] presented at the 11th Shock Tube Symposium differed by about a factor of 20. Because of this uncertainty, we have investigated the thermal decomposition of shock heated SO_2 dilute in argon, using infrared emission from the SO_2 ν_3 fundamental to monitor the reactant decay rate. Furthermore, we have measured SO_2 decay rates in mixtures of SO_2-N_2O-argon and related these results to the kinetics of the reaction

$$SO_2 + O = SO + O_2 \qquad 2$$

which is a secondary pathway in the decomposition of SO_2. This paper presents our measured rate coefficients for Reactions 1 and 2, and reviews earlier investigations.

EXPERIMENTAL TECHNIQUE

SO_2 - argon mixtures were heated behind reflected shock waves in a conventional 3.81 cm i.d. stainless steel shock tube. This facility has been previously described.[7,8]

IR emission from the ν_3 fundamental centered at 7.347 μ was transmitted through barium fluoride windows, focussed by an IRTRAN 2 lens, isolated by an interference filter (peak transmission = 7.362 μ; half-power points 7.256 and 7.469), and monitored by a liquid nitrogen cooled HgCdTe detector. At a given temperature the IR emission was proportional to the SO_2 concentration. Fig. 1 shows typical oscillograms of IR emission and of the output from a static pressure transducer. Both IR emission and pressure rise at the incident and reflected shock fronts.

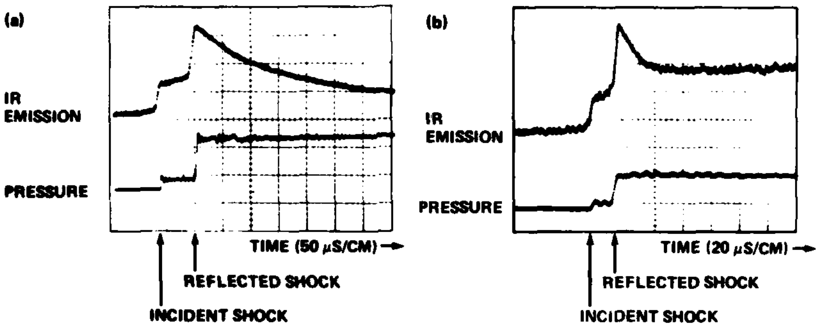

Figure 1. Representative Oscillograms of SO_2 IR Emission (λ=7.36 μ) and Static Pressure. (a) 0.13% SO_2 and 99.87% Ar; Reflected shock parameters 6.47 atm, 3135°K. (b) 0.75% SO_2, 2.5% N_2O and 96.75% Ar; Reflected shock parameters 2·12 atm, 2870°K.

The SO_2 (anhydrous grade) was 99.98% pure with a maximum water vapor impurity of $\leq$ 50 ppm. The argon diluent was 99.999% pure with a maximum water vapor content of 3 ppm based on dew point. A primary mixture of 0.527% SO_2 in argon was prepared, from which 0.26% and 0.13% SO_2 mixtures were obtained by further dilution. In the experiments with added nitrous oxide, the N_2O was 99.99% pure and mixtures with 0.75% SO_2 + 2.50% N_2O, and 0.75% SO_2 + 1.25% N_2O were prepared, and the balance being argon. The shock tube was periodically baked out at temperatures up to 100°C. Prior to a run the tube was flushed with the argon-SO_2 mixture, evacuated to about 6×10^{-6} Torr and then refilled. Outgassing and leaks contributed a foreign gas partial pressure of 10^{-4} Torr. Initial pressures of the test gas ranged from 20 to 60 Torr.

Reflected shock temperatures (frozen chemistry) were computed[9] from the measured incident shock wave velocity, reactant mole fractions, and JANAF thermodynamic data. Temperature uncertainties were conservatively estimated as ± 30°K at 3000°K.

RESULTS

Thermal Decomposition

SO_2 decay rates (derived from the IR emission records) for the SO_2-Ar mixtures were first order with respect to SO_2 and argon. Rate coefficients k_1 determined from

$$-d[SO_2]/dt = k_1 \cdot [SO_2] \cdot [Ar] \qquad \text{I}$$

are presented in Fig. 2 and yielded an Arrhenius expression

$$k_1 = 8\ (\pm 2)\ \times 10^{15}\ exp(-108{,}000/RT) cm^3 mole^{-1} sec^{-1} \qquad \text{II}$$

over the temperature range 2800-3880°K and concentration range $0.8\text{-}3.4 \times 10^{-5}$

mole/cm^3. A systematic dependence of k_1 on the SO_2 percentage was not evident in Fig. 2. The activation energy in Eq. II is 25.0 kcal/mole below the heat of reaction (133.0 kcal/mole) at 3000°K.

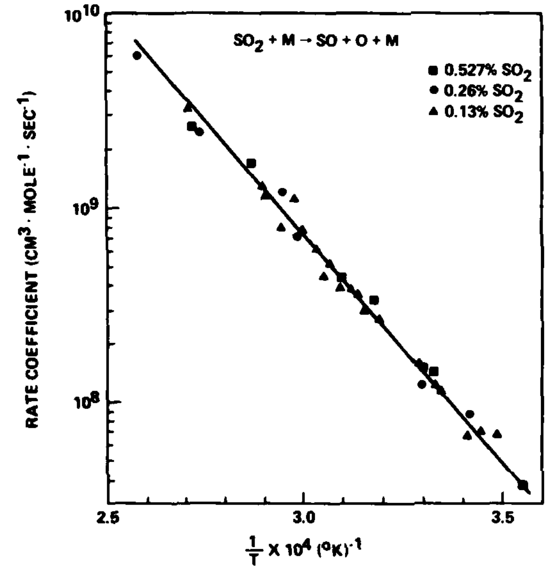

Figure 2. Measured Rate Coefficients for the Decomposition of Sulfur Dioxide.

Influence of N_2O on SO_2 Decay Rates

Initial IR decay rates for the tests with added N_2O were significantly faster below 4000°K than the thermal decomposition rate measured previously; compare Fig. 1a and 1b. As an initial convenience in data reduction we determined apparent SO_2 dissociation rate coefficients from this data, assuming the relationship in Eq. I, and the results are shown in Fig. 3 where the tem-

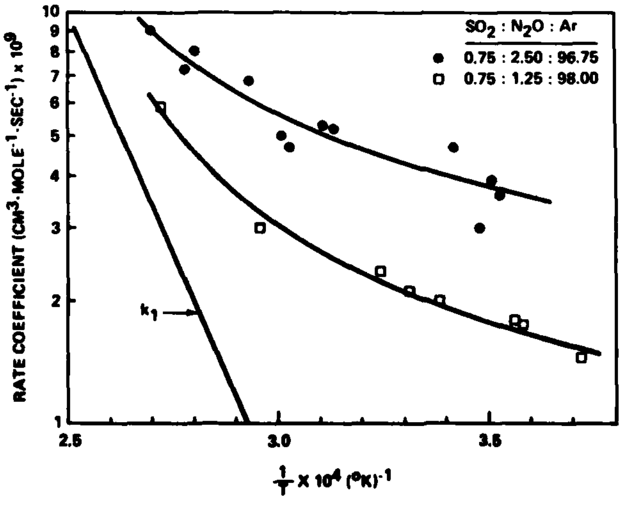

Figure 3. Apparent SO_2 Dissociation Rate Coefficient in the Presence of N_2O.

perature is the frozen reflected shock temperature. The apparent rate coefficients in Fig. 3 were all greater than k_1, assymptotically approach k_1 at high temperatures, were orders of magnitude greater than k_1 below 3000°K, and at low temperatures were proportional to the N_2O concentration.

The N_2O dissociates rapidly behind the reflected shock wave to yield atomic oxygen and N_2. Therefore we interpret the data in Fig. 3 in terms of Reactions 1 and 2 with the decay rate given by

$$-d[SO_2]/dt = k_1 \cdot [SO_2] \cdot [M] + k_2 \cdot [SO_2] \cdot [O] \qquad \text{III}$$

where M is any third body and back reactions have been neglected. From Eq. III the apparent rate coefficient k in Fig. 3 is related to k_2 by

$$k = k_1 + k_2 \; [O]/[M] \qquad \text{IV}$$

This equation is readily solved for k_2 using the known k_1 and assuming an initial O-atom concentration equal to the N_2O concentration. Fig. 4 presents the resulting rate coefficients for Reaction 2. The temperatures in Fig. 4 were corrected for the temperature drop associated with the N_2O decomposition. The data in Fig. 4 yields the Arrhenius expression

$$k_2 = 4\ (\pm.4)\ X\ 10^{12}\ exp(-18{,}300/RT)\ cm^3 mole^{-1} sec^{-1} \qquad \text{V}$$

over the temperature range 2630 to 3570°K, with an activation energy only 7.73 kcal/mole greater than the heat of reaction at 3000°K.

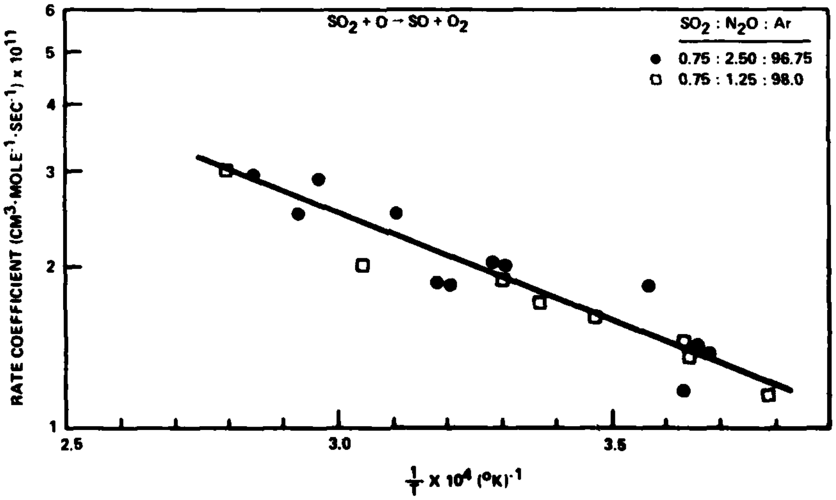

Figure 4. Rate Coefficients for Reaction 2 Derived from Data in Figure 3.

DISCUSSION

SO_2 Thermal Decomposition

A comparison of the present rate coefficients with earlier results is shown in Fig. 5. The present k_1 is in excellent agreement with both the results of Just and Rimpel[1] (JR) and of Kiefer[3], but falls well above the results of Olschewski, Troe and Wagner[5] (OTW) and of Astholz, Glanzer and Troe[2] (AGT). Data at high SO_2 mole fractions[4,6] was not included in Fig. 5 and will be discussed separately.

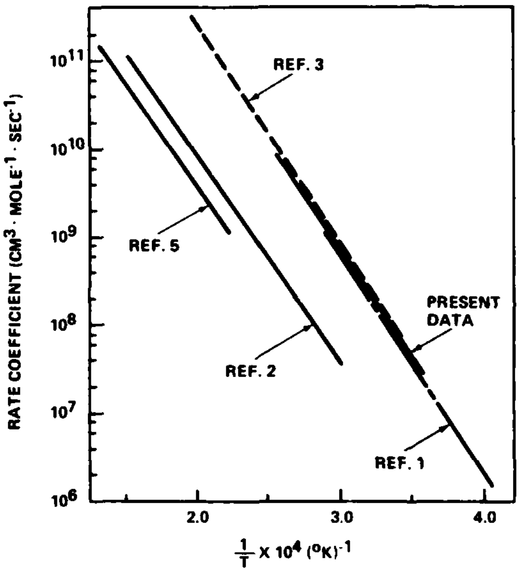

Figure 5. Comparison of Present SO_2 Decomposition Rate Coefficients with the Previous Work of Just and Rimpel[1], Astholz et al.[2], Kiefer[3], and Olschewski et al.[5]

The agreement between our k_1 and the results of JR (see Fig. 5) is considered significant because while we monitored the decay rate of SO_2, JR monitored the spectroscopy at 1305 Å, in SO_2 - Ar mixtures with 20 to 200 ppm SO_2. Their detection system was calibrated by dissociating N_2O, and the overall apparatus checked by a measurement of the established O_2 dissociation rate. Furthermore, JR present evidence that neither secondary pathways nor reactions with H-atoms (a minor impurity) influence the measured O-atom profiles. JR also measured the formation rate of SO (monitoring SO in absorption at 1469 Å) during SO_2 decomposition at 2950 °K and obtained results[1,11] in agreement with their O-atom formation rates.

Kiefer[3] derived k_1 from laser beam schlieren deflection densitometry measurements conducted in mixtures containing 3% to 30% SO_2 in Kr, and secondary reaction pathways such as Reaction 2 will be significant. However, Kiefer argues that the influence of Reaction 2 upon the initial density gradient will be negligible because of the low heat of reaction relative to Reaction 1. As a test of the validity of Kiefer's rate coefficients, we have computed the density changes behind an incident shock wave in SO_2-Kr mixtures using first the single reaction pathway Reaction 1 and secondly the six reaction mechanism of Table 1. Computations were conducted with the NASA General Chemical Kinetics code[10] using the rate coefficients listed in Table 1. The influence of the five secondary reactions upon the initial rate of change of density was found to be negligible for the 3% mixture; typically $d\rho/dt$ increased by

2% when the full mechanism was used instead of Reaction 1 alone. Since Kiefer corrected his 10% and 30% data down to the k_1 obtained with 3% SO_2, we conclude that his reported k_1 was essentially unaffected by secondary pathways.

Table I. Mechanism and Recommended Rate Coefficients for SO_2 Decomposition

Reaction	Rate coefficient[a]	Source
$SO_2 + M = SO + O + M$	$1.5 \times 10^{16} \exp(-112000/RT)$	Eq. VIII
$SO_2 + O = SO + O_2$	$4.2 \times 10^{12} \exp(-19500/RT)$	Eq. VI
$SO + M = S + O + M$	$1.0 \times 10^{15} \exp(-111000/RT)$	Ref. 1[b]
$S + SO_2 = SO + SO$	$1.0 \times 10^{14} \exp(-7150/RT)$	Ref. 1[b]
$S + O_2 = SO + O$	1.4×10^{12}	Ref. 12
$O_2 + M = O + O + M$	$1.8 \times 10^{18}\ T^{-1} \exp(-118000/RT)$	Ref. 12

[a] Units of $cm^3 mole^{-1} sec^{-1}$.

[b] Estimated.

Since the recent data of AGT superseded those of OTW in the same laboratory, we will limit our discussion to the former. In that investigation[2], SO_2 decay rates were monitored primarily via UV absorption (2270 and 2340, and 2385 Å) with additional data obtained in both UV emission (2750 and 3165 A) and IR emission (7.25 μ). The mixtures of SO_2-Ar ranged from 100 to 2000 ppm SO_2, which overlap the present and JR's experimental conditions. The discrepancy between AGT's rate coefficient k_1 and the results of Kiefer, JR and the present investigation (see Fig. 5) is puzzling, particularly since the IR emission monitoring technique used in some experiments by AGT is identical with the present experimental technique. One possible explanation for the discrepancy has been suggested by JR. In addition to monitoring O-atom formation from SO_2 decomposition, JR also measured SO concentrations via absorption at 1469 Å and obtained[1,11] a rate coefficient for SO dissociation in close agreement with the k_1 of OTW and AGT. Therefore JR suggest that AGT measured not the decomposition rate of SO_2 but the slower dissociation of SO, and suggest that this may have occurred because of complex interference of SO_2 and SO UV absorption.

Gaydon et al.[6] report rate coefficients for Reaction 1 based on the observed rate of formation of SO in shock heated SO_2 - Ar mixtures with high SO_2 mole percentage (4 to 32%). Their results shown in Fig. 6 have an activation energy of 56 kcal/mole, considerably below the activation energy of the present data. For high SO_2 percentages, secondary reaction pathways will contribute to the SO_2 decay rate and with falling temperature will increasingly elevate this rate above that for Reaction 1 alone, thereby yielding a low apparent activation energy unless secondary pathways are corrected for in the data analysis. No corrections for secondary reactions were made by Gaydon et al. Their data in Fig. 6 agrees (both in magnitude and temperature dependence) with our k_1 in the temperature range 3400 to 4000°K their data lies above our k_1. We have computed[10] apparent rate coefficients k' for a 16% SO_2 mixture with the mechanism and rates of Table 1. These k', shown in Fig. 6, lie increasingly above our k_1 with falling temperature, and are in better agreement with Gaydon's data. It is possible that additional secondary reactions with hydrogenous impurities further increased the low temperature rates measured by Gaydon et al., since the argon was only 99.8% pure and the SO_2 purity is not specified. We conclude that Gaydon's data supports the present results and that the apparent low activation energy is a consequence of secondary reaction pathways in high SO_2 percentage mixtures.

A dissociation mechanism involving the triplet state of SO_2 was suggested by Gaydon et al. to account for the low activation energy of their rate coefficients. This suggestion was speculative and, as the preceding discussion has shown, not necessary to account for the low activation energy.

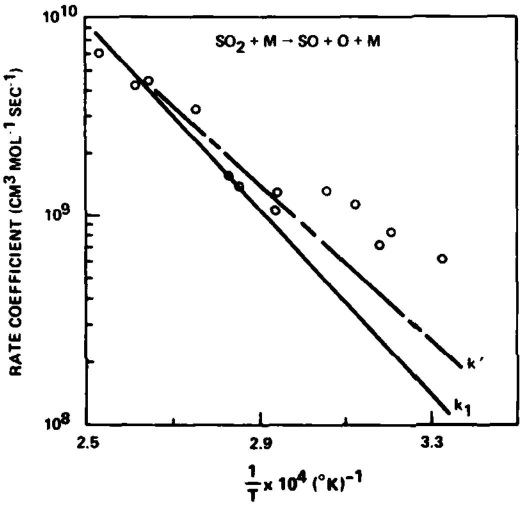

Figure 6. Data from Gaydon et al.[6] Compared with k_1 and k'

Furthermore, Gaydon et al. underestimated the temperature drop accompanying the decomposition by assuming the stoichiometry $2SO_2 \rightarrow 2SO + O_2$ which requires less energy than the net pathways given in Table 1. This underestimation was greatest at the higher temperatures (and at higher concentrations). The data in Fig. 6 has been corrected to more realistic temperatures based on computations using the mechanism of Table 1.

Levitt and Sheen[4] measured SO_2 visible emission decays at 4360 Å and reduced these decays to a dissociation rate. The SO_2 mole percentages in their study ranged from 1 to 40. We have computed the effective SO_2 decay rate for the 20% SO_2 case using the mechanism of Table 1, and find that the decay rate is doubled because of Reaction (2). Figure 7 compares the rate coefficients obtained by Levitt and Sheen at $M = 2.0 \times 10^{-6}$ mole/cm^3 with $2k_1$, where k_1 is from Eq. II. The agreement in magnitude is generally better than a factor of 2 but the slope of the data is lower than that of k_1. Quantitative agreement is best at the higher temperatures (3100 - 3450°K). At lower temperatures the equilibrium dissociation fractions are less than 0.15 at $M = 2 \times 10^{-6}$ and mole fractions ≥ 0.20, and the measurement of such small changes over characteristic times of 2.5×10^{-3} sec will be most challenging and will be influenced by boundary layer growth and other nonidealities within the shock tube. Taking this into account, the agreement in Fig. 7 is reasonable and the data of Levitt and Sheen is judged consistent with the present measurement of k_1.

Rate Coefficient for $SO_2 + O \rightarrow SO + O_2$

We are restricted to comparing our measured k_2 with data on the back reaction k_{-2}, since Baulch et al[12] reported no measurements of k_2 and we are unaware of any other recent measurements. Fig. 8 presents high temperature k_{-2}

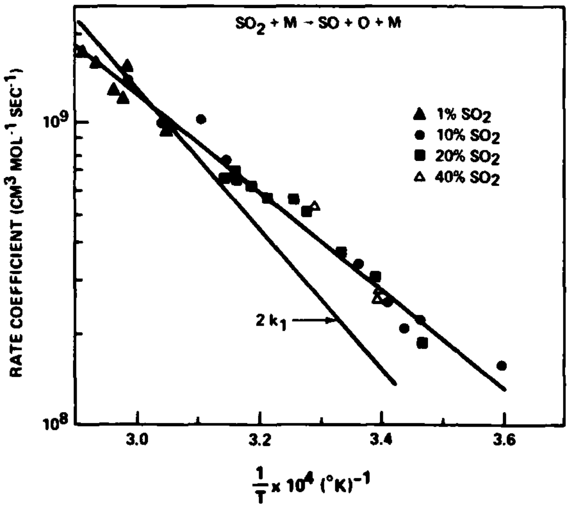

Figure 7. Data of Levitt and Sheen[4] Compared with $2k_1$

data[13-16] and our measured rate coefficient for Reaction 2 converted via the equilibrium relationship. Our data is in good agreement with the measurements of Homann et al.[13] and Williams[14], and helps to clarify the temperature dependence. From the data in Fig. 8 and the equilibrium relationship we obtain a combined rate coefficient

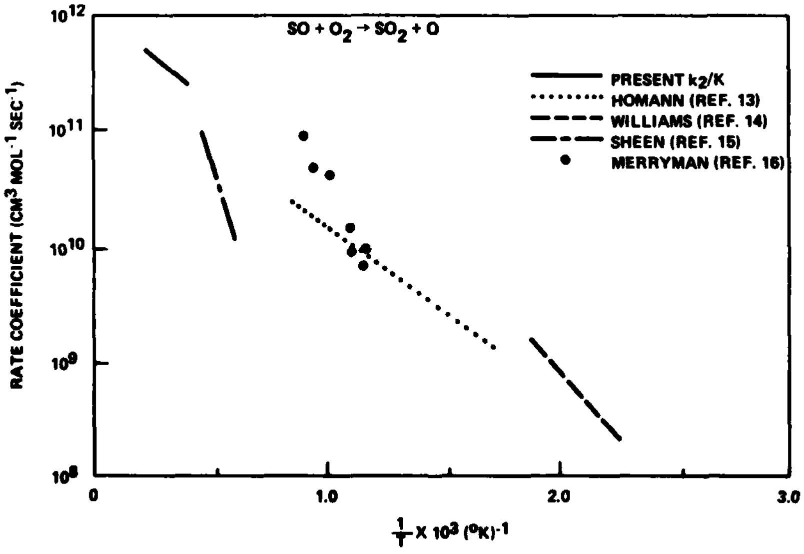

Figure 8. Rate Coefficients for $SO+O_2 \rightarrow SO_2+O$ Compared with Present k_2/K

$$k_2 = 4.2(\pm 1) \times 10^{12} \exp(-19{,}500/RT)\ cm^3 mole^{-1} sec^{-1} \qquad \text{VI}$$

over the temperature range 440 to 3570°K, which agrees well with our individual result in Eq. V and with Wagner's assessment[17] which yielded

$$k_2 = 5 \times 10^{12} \exp(-19{,}500/RT)\ cm^3 mole^{-1} sec^{-1} \qquad \text{VII}$$

Our measurements of k_2 in Fig. 4 do not represent a thorough test of the reaction mechanism since only the oxygen atom concentration was varied. We plan to conduct additional measurements to check the assumption that the SO_2 decay rate is first order in SO_2 concentration and zero order in argon concentration.

CONCLUSIONS

The combined measurements of Kiefer, Just and Rimple, and the present investigation yield a rate coefficient for the thermal decomposition of SO_2 of

$$k_1 = 1.5 \times 10^{16} \exp(-112{,}000/RT)\ cm^3 mole^{-1} sec^{-1} \qquad \text{VIII}$$

over the temperature range 2500-5200°K. This rate coefficient results from independent observations of the SO_2 decay rate (present work), the production rate of O-atoms and SO,[1] and the overall rate of change of density accompanying the reaction,[3] and is consistent with the data of Gaydon et al.[6] and Levitt and Sheen[4].

Rate coefficients for $SO_2 + O \rightarrow SO + O_2$ have been measured (see Eq. V), are in good agreement with lower temperature data on the reverse reaction (converted via the equilibrium relationship), and yield the recommended rate coefficient in Eq. VI for the temperature range 440 to 3750°K.

REFERENCES

1. T. Just and G. Rimpel, Proceedings of the 11th International Symposium on Shock Tubes and Shock Waves (University of Washington, Seattle 1977) p. 226.
2. D. Astholz, K. Glanser, and J. Troe, Proceedings of the 11th International Symposium on Shock Tubes and Shock Waves (University of Washington, Seattle 1977), p. 232.
3. J. H. Kiefer, J. Chem. Phys. *62*, 1354 (1975).
4. B. P. Levitt and D. B. Sheen, Trans. Faraday Soc. *63*, 2955 (1967).
5. H. A. Olschewski, T. Troe, and H. Gg. Wagner, Z., Phys. Chem. *44*, 173 (1965).
6. A. G. Gaydon, G. H. Kimbell, and H. B. Palmer, Proc. Soc. London Ser. *A276*, 461 (1963).
7. M. W. Slack, J. Chem. Phys. *64*, 228 (1976).
8. M. W. Slack, Combust. Flame *28*, 241 (1977).
9. S. Gordon and B. McBride, NASA SP0273 (1971).
10. D. A. Bittker and V. J. Sculling, NASA Tech. Note TND-6586 (1972).
11. T. Just, private communication, DFVLR 7000 Stuttgart 80, German Federal Republic, May, 1978.
12. D. L. Baulch et al., Evaluated Kinetic Data for High Temperature Reactions, Vol. 3 (Butterworths, London 1976).
13. K. Homann et al., Ber Bunsenges. Physik. Chem. *72*, 998 (1968).
14. D. Williams, Combust. Flame, *12*, 165 (1968).
15. D. B. Sheen, J. Chem. Phys. *52*, 648 (1970).
16. E. L. Merryman and A. Levy, APCA J., *17*, 800 (1967).
17. H. Gg. Wagner, 14th Combust. Sym., 27 (1973).

THE FORMATION OF OXIDES OF NITROGEN FROM $CH_4/O_2/N_2$ MIXTURES

M. J. GUINEE†, F. A. HEWITT†, D. F. FUSSEY*,
B. E. MILTON** and T. F. PALMER††

Departments of Mechanical Engineering and Chemistry
University of Nottingham, University Park, Nottingham NG7 2RD, U.K.

The formation of nitric oxide has been studied at temperatures around 2200 and 3100 K; a cold hydrogen driven, reflected-wave shock tube was used for the 3100 K measurements and a combustion-driven incident-wave tube for the lower temperature. The concentrations of nitric oxide and hydroxyl radical were monitored by ultraviolet absorption spectrophotometry. Post-shock temperature profiles were obtained for the reflected-wave tube by means of an infra-red emission/absorption method. The initial post-shock temperatures measured were found to compare well with ideal calculations, but fell more rapidly than predicted. Concentration measurements were obtained at 3100 K for times up to 600μs after reflected shock arrival for methane/oxygen molar ratios from 0.4 to 0.7. At 2200 K, however, the quantity of nitric oxide formed was found not to exceed the limit of detectability within the time available (800μs).

INTRODUCTION

Earlier studies of nitric oxide formation in shock tubes using $CH_4/O_2/N_2/Ar$ mixtures[1] have been extended in this work to include a wider range of temperatures and mixtures. In the process, several developments of established shock tube and spectroscopic techniques have been made. This paper describes the developments and the experimental results are compared with values predicted by a chemical kinetic reaction scheme and rate data from the previous work.

---

† now at Rolls-Royce Ltd., Derby, U.K.

* now at Papua New Guinea University of Technology, Lae, P.N.G.

** on leave from University of New South Wales, Sydney, Australia.

†† Department of Chemistry, University of Nottingham.

EXPERIMENTAL

A reflected-wave shock tube was used to produce temperatures around 3100 K at pressures of approximately 10 bars absolute, in gas mixtures containing 90% argon. A ball-valve and buffer gas (pure argon) were used in the tube to increase available observation times.[2] The shock wave velocity was measured by timing the pulses produced as the shock traversed four piezoelectric pressure transducers. Accuracy of timing was such as to allow calculation of temperatures behind the reflected shock wave to ± 50 K at 3100 K. An incident-wave shock tube was used to produce temperatures around 2200 K, and pressures around 12 bars absolute. This tube was combustion driven, using hydrogen/oxygen or hydrogen/oxygen/argon mixtures,[3] in a constant volume mode, and the accuracy of velocity measurement allowed temperature calculation to ± 20 K at 2200 K. In both tubes the pressure prior to filling was $\leqslant$ 0.1Pa, and the leakage rates were both < 0.3Pa per minute.

NO concentrations were measured by ultraviolet spectrophotometry of the NO γ bands. The main problem encountered was continuum absorption by other reaction components. The solution to this problem at 3100 K was measurement of absorbances at two wavelengths: 236.18 nm in the γ (0,1) band, and 240.0 nm where the absorbance due to NO is very small. Calibration experiments were carried out using shock-heated mixtures of NO in argon, to allow the accurate determination of NO concentration from the experimental measurements. At 2200 K the interfering absorption was no longer a continuum, requiring measurement of NO absorption in the stronger γ (0,0) band, further calibration experiments, and multiple measurements to ensure a statistically accurate result. The additional time requirement limited the 2200 K measurements to one methane/oxygen ratio only. No experimental calibration was possible for the OH radical concentrations. Measurements of absorption were carried out at the ($A^2\Sigma^+ - x^2\pi$) bandhead, 306.35 nm, where there were no interference problems, and a high signal/noise ratio was achieved. A calibration process based on partial equilibrium theory was tested against the results of $H_2/O_2/Ar$ experiments, and the results were found to compare well with those of the similar work of ref. 4. The absorption values obtained were used to calculate the OH concentrations in the $CH_4/O_2/N_2/Ar$ experiments.

The light source for this work was a xenon arc-lamp, which was pulsed to provide an output of the form shown in Figure 1 (top). The pulse was triggered, via a delay line, from one of the pressure transducers, to allow the light output to reach the linear portion of the waveform before shock wave arrival at the observation station. The light passed through the shock tube and into a Monospec 600 grating monochromator, with reciprocal dispersion of 0.82 nm/mm, and slit width set at 0.02 mm. The radiation at the exit slit illuminated an EMI 9789 QB phototube, and the resultant signal was stored in a Datalab DL 905 Digital recorder.

The use of infra-red emission and absorption measurements to provide information on the post-shock temperatures in shock-waves has been described previously.[5,6] In this work, measurements were made of emission and absorption behind reflected shock waves, in mixtures of up to 3% CO_2 in argon. This permitted assessment of the validity of the one-dimensional ideal gas calculations of temperature and observation time for the $CH_4/N_2/O_2/Ar$ experiments. The measurements were carried out within a 0.11µm bandwidth, centred on 4.575µm, in the 4.3µm band of CO_2. A high radiance continuous source was chopped at 15kHz, the chopped beam being passed through sapphire windows on the shock tube, and monitored by an indium antimonide detector (Mullard ORP 13) cooled with liquid nitrogen. The same detector also monitored the emission from the shock-heated gas, producing a combined signal. The transmissivity of the window on the detector side of the tube was measured carefully as this value is required for gas emissivity calculation. The transmitted signal is obtained as a ratio, before and after shock wave passage, and requires no

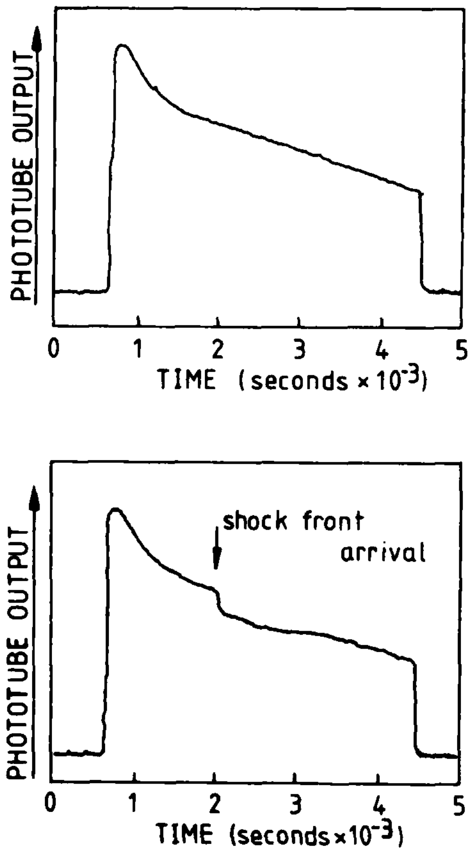

Figure 1.
The recorded phototube output voltage showing, at the top, the flash lamp output, and below, the changed trace resulting from absorption in the reacting gases.

calibration. The detector was calibrated using a separate standardised source before each run, as these devices show considerable long-term variability.

RESULTS

Concentration Measurements

The measurements presented here were carried out at two nominal temperatures, 3140 K and 2200 K, with five methane/oxygen ratios at the higher temperature, and only one at the lower temperature. The complete series of measurements carried out, and the comparison of the results obtained with values calculated using several chemical kinetic schemes are to be published shortly.[7] The mixtures used were typically 7% N_2, 2% O_2, 1% CH_4, 90% Ar, and were made up by partial pressures, in a quantity sufficient for several runs, in a stainless steel mixing vessel. In the case of the measurements at 3140 K, the minimum quantity of NO which could be measured with reasonable accuracy was shown to be 2×10^{-8} moles cm^{-3}, and the accuracy obtainable improved considerably with increasing concentration. Figure 2 presents results calculated from typical experiments measuring NO and OH concentrations. The concentrations of NO and OH at times from 0.0 to 0.6×10^{-3} seconds after reflected shock passage are shown by the circles and squares respectively, with bars representing estimated measurement error. The solid and dotted lines represent concentrations calculated using the computer program of Bittker and Scullin[8] and the kinetic scheme and rate data of Bowman and Seery.[1] Figure 3 presents a summary of the results of several further high temperature experiments for a range of methane/oxygen ratios at 0.4 x 10^{-3} seconds after reflected shock passage. In all the experiments, NO and OH concentrations were steady by this time.

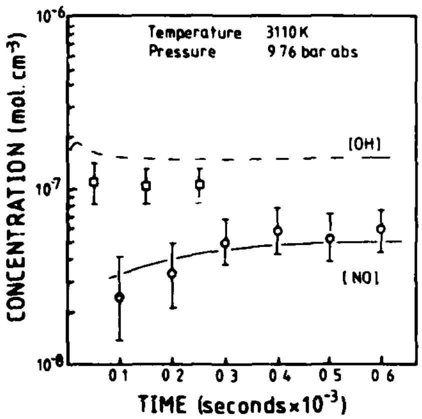

Figure 2.
Change of concentration with time for a typical experiment. The initial concentrations were, in units of moles %:

CH_4	1.4
O_2	2.0
N_2	6.6
Ar	90.0

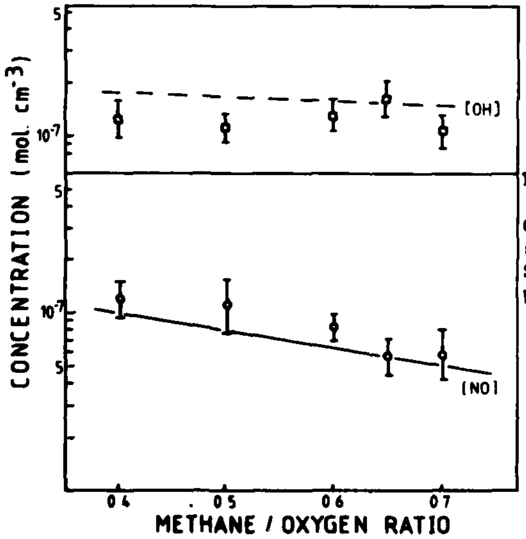

Figure 3.
Concentration at 0.4x10^{-3} sec after reflected shock arrival, of NO and OH. Solid and broken lines are predicted values.

For all these experiments, P ~ 9.7 bar, T ~ 3140 K. The solid and broken lines again represent the results of calculations of the concentrations of NO and OH by the program. At the temperatures of the incident wave experiments, the extended calibration work, with associated errors, led to a minimum measurable concentration of NO of 5 x 10^{-9} moles cm^{-3}. In the event, for the stoichiometric mixture considered, at 2200 K, the concentration of NO was not in excess of the measurable limit. This again agrees well with the predicted values using the Bowman-Seery reaction mechanism and rates, the calculated concentration for these conditions being 3.8 x 10^{-9} moles cm^{-3}, at 8.2 x 10^{-4} seconds after reflected shock passage. Additional computational kinetic work carried out by the authors,[7] involving a more complex reaction scheme, suggests slightly higher concentrations, but still less than 5×10^{-9} moles cm^{-3}. Thus this incident shock work confirms that the predictive methods employed adequately predict upper limits to the NO concentration formed.

Temperature Measurements

The temperatures were calculated from the emission/absorption measurements according to :

$$T = \frac{C_2}{\lambda \log_e \left[1 + \frac{C_1}{\lambda^5} \cdot \frac{(1 - I/I_o)}{e_s} \cdot \frac{V_s}{V} \cdot \tau_w \right]}$$

where C_1, C_2 are Plancks constants $C_1 = 2\pi hc^2$.
$C_2 = hc/k$.
λ is wavelength employed.
I_o, I are the measured intensities before and after shock arrival.
$e_s V/V_s$ emissive power of the gas, where V_s and V are measured detector voltages due to calibration source and gas emission.
τ_w window transmissivity.

The output obtained was in the form of figure 4, where the measured values are *indicated*.

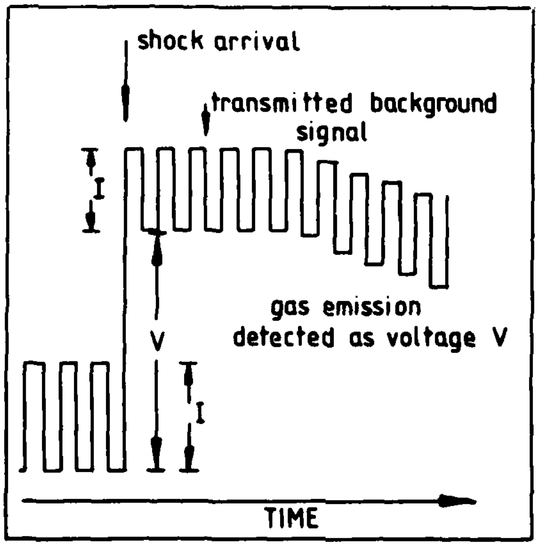

Figure 4.
General form of IMRA output showing values used in temperature calculation.

The temperature could be calculated from the output, at intervals of around 67μs. Two typical results calculated from such experiments are shown in Figure 5. A total of 55 such experiments were carried out on reflected shock waves, for temperatures as predicted from the shock Mach numbers, from 1500-4500 K. The mixtures used for these measurements ranged from 0.5-3.0% CO_2 in argon. For the sub-set of these results where $2850\ K < T < 3350\ K$, which is the range of temperatures employed in the NO formation experiments, the following statistics were obtained on 11 measurements at 4.575μm.

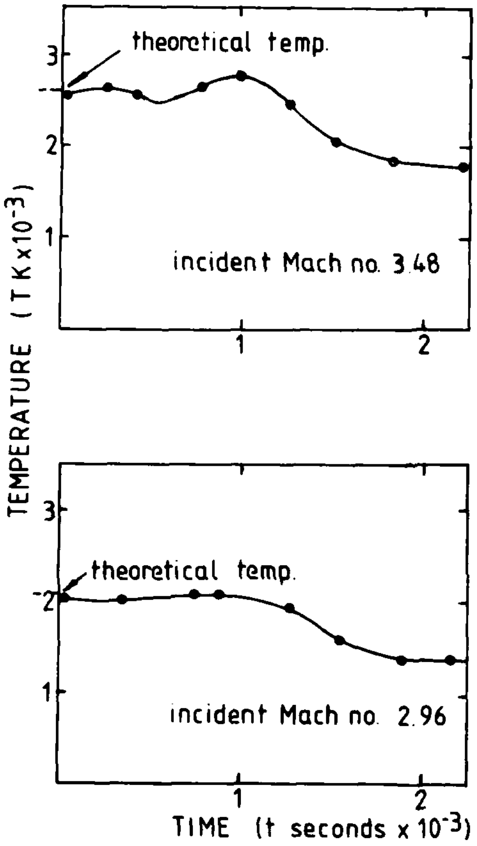

Figure 5. Variation of temperature with time behind reflected shock waves for two initial conditions.

T_{IMRA}/T_{IDEAL} mean value = 0.953

Standard deviation of results = 0.098

Standard error of mean = 0.029

For all 25 measurements at this wavelength, the equivalent results were:

T_{IMRA}/T_{IDEAL} mean value = 1.032

Standard deviation of results = 0.127

Standard error of mean value = 0.025

On the basis of the emission/transmission measurements, and the pressure traces for the observation position, the durations of both steady temperature and steady pressure were plotted as a function of the incident Mach number of the shocks (Figure 6). An analysis of the effect of measurement and calibration errors for the IMRA system employed has been carried out, and indicates that errors in temperature of order 2-7% should be expected. The agreement between ideal one-dimensional predictions and measurements is thus seen to be quite good for the initial post-shock conditions. The duration of steady temperature and pressure is considerably less than ideal calculations predict (1.2×10^{-3} secs for these conditions. For the incident shock Mach numbers employed in the

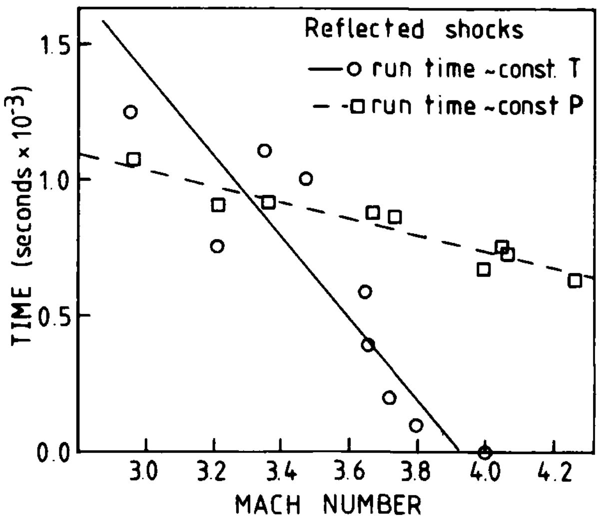

Figure 6. A plot of the duration of steady post reflected shock conditions against incident shock Mach number.

nitric oxide formation experiments, the duration of steady temperature could be expected to be ~ 375μs.

CONCLUSIONS

1. Experimental data for the formation of NO from $CH_4/O_2/N_2/Ar$ mixtures have been obtained for several mixtures at around 3000 K, extending the range of previous measurements in this temperature range.[1] The rate data of Bowman and Seery, together with their 17 reaction chemical kinetic scheme were found to predict adequately the quantities of nitric oxide formed at this temperature.

2. The one-dimensional ideal-gas calculations, by means of which the post-shock temperatures were calculated, were checked by the application of an infrared emission/absorption technique. The results of the measurements suggested that the initial temperatures were as calculated, within the limits of calculation and shock velocity measurement, but also suggested that the steady-temperature durations were no greater than 375μs, for the conditions of interest. However, the experimental measurements of concentration generally showed that concentrations had become steady by this time, so that this fact does not greatly affect the results obtained.

3. The total NO formation predicted for a stoichiometric mixture of 2200 K was approximately 5×10^{-9} moles cm^{-3}. The limit of measurement of NO in the incident wave tube, after allowing for the reduced precision due to the additional calibration procedures, was of the same order. In the event, the experimental measurements showed that the limit of measurement was not exceeded, up to the observation time limit of 0.8×10^{-3} seconds.

ACKNOWLEDGEMENTS

The authors are grateful for the financial support of the Science Research Council in this work, and also wish to thank Rolls-Royce Ltd., for the loan of

the infra-red temperature measurement apparatus.

REFERENCES

1. C.T. Bowman and D.T. Seery in "Emissions from continuous combustion systems". Ed. Cornelius and Agnew, Plenum Press, 123 (1972).
2. E. Tschuikow-Roux, Phys. Fluids 8 (1965).
3. F.A. Hewitt and D.E. Fussey, AIAA Journal, 16, 1102 (1978).
4. G.L. Schott and R.W. Getzinger in "Physical Chemistry of Gas Reactions", Vol. 1, Ed. B.P. Levitt, Plenum Press (1973), pp 81-160.
5. K.C. Lapworth, L.A. Allnutt and J.R. Pendelbury, J. Phys. D. Appl. Phys. 4, 759 (1971).
6. N.T. Jewell, MSc Thesis, University of Wales, "Temperature studies of detonations and other combustion systems" (1972).
7. M.J. Guinee, et al, to be published shortly.
8. D.A. Bittker and V.J. Scullin, NASA Rept No TN-D-6586 (1977).

HIGH TEMPERATURE METHYL RADICAL REACTIONS WITH ATOMIC AND MOLECULAR OXYGEN

K. A. BHASKARAN, P. FRANK, TH. JUST

Institut für Physikalische Chemie der Verbrennung, DFVLR
7000 Stuttgart 80, West Germany

A shock tube together with atomic resonance absorption spectrometry(ARAS) was used to record H-and O-atom concentration profiles at shock temperatures ranging within 1700 - 2300 K and total concentrations of about 1 to $1.5 \cdot 10^{-5}$ mole/ccm. Two sets of experiments were performed.

The first set, under excess O-atom conditions enabled selective study of the reaction: $CH_3 + O = CH_2O + H$. The rate constant suggested by [1,3,22-25] for this reaction is more or less compatible with our results.

The second batch of experiments were undertaken to study the relative importance of the two channels discussed in literature for the reaction of the methyl radical with O_2, namely:

$$CH_3 + O_2 = CH_2O + OH \qquad \text{I}$$

$$\left.\begin{array}{ll} CH_3 + O_2 & = CH_3O + O \\ CH_3O & = CH_2O + H \end{array}\right\} \qquad \text{II}$$

From our results, CH_3 seems to prefer the second route. This could be clearly deduced from measurements under excess O_2 conditions. From the experimental results, a rate constant $k= 7 \cdot 10^{12} \exp(-12910/T)$ ccm/mole·sec for this reaction was obtained. Incidentally, our results at lower O_2 conditions indicated strongly that contribution of $CH_3 + OH = CH_3O + H$ and fast decay of CH_3O to $CH_2O + H$ was indispensable to get a match with the measured profiles. An Arrhenius plot for this reaction produced a rate constant $k = 2 \cdot 10^{16} \exp(-13860/T)$ ccm/mole·sec. The above mentioned results are analysed and discussed.

INTRODUCTION

In the high temperature oxidation of simple hydrocarbons such as methane the reaction of CH_3 with O-atoms plays a leading role[1-4], whereas the reaction with O_2 might be of minor importance, if the reported relatively small rate constants for this reaction are correct. Though the basic framework of the methyl radical mechanism seems to be clear, satisfactory kinetic data for its oxidation reactions at high temperature are not available. Very little direct information is available about the reaction $CH_3 + O = CH_2O + H$. Flow reactor experiments at low temperatures (T = 300 K)[17 18] gave a rate constant of $6 - 11 \cdot 10^{13}$ ccm/mole·sec. The reported values in literature evaluated by shock tube and flame experiments covered the range of $10^{13} - 10^{14}$ ccm/mol·sec at high temperatures[1 3 22-25], but all these measurements allowed only to infer the rate coefficients for $CH_3 + O = CH_2O + H$ in a more or less indirect manner from the data. As this reaction is very significant in the oxidation scheme of the methyl radical, we wanted to study it in greater detail and to perform ect measurements at elevated temperatures and hence the first set of experiments reported in this paper.

Oxidation of methyl radical with molecular oxygen was studied previously by Brabbs and Brokaw[13]. While the primary reaction in their scheme is $CH_3 + O_2 = CH_2O + O + H$, e.g. Tsuboi[3] suggested an alternative route: $CH_3+O_2 = CH_2O+OH$. Though both these reactions may run parallel, their relative importance was not established. The present work explores the possibility of fixing the experimental conditions under which these reactions play significant roles.

Ethane, because of its rapid decay under the present experimental conditions[8 10 15] served as an ideal source for the methyl radical. For the study of the methyl radical reaction with atomic oxygen, N_2O was chosen to supply the required O-atoms, as it is reported to have a very fast decomposition rate [6 16]. Atomic resonance absorption spectrometry[5] was used in the investigations to record H-and O-atom concentration profiles at shock temperatures ranging within 1700 - 2300 K and total concentrations of about $1 - 1.5 \cdot 10^{-5}$ mole/ccm. Due to the high sensitivity of the ARAS method with respect to the detection of H-and O-atoms, experiments can be performed with extremely diluted mixtures of hydrocarbons/oxygen species. In many cases, as studied in this work, it is therefore possible to tailor the reaction conditions, so that the reaction under consideration has an overwhelming influence on the time dependent H-and O-atom concentration profiles. Evidently reliable conclusions on mechanisms and rate constants can be drawn straight away.

EXPERIMENTAL ASPECTS

Details of the shock tube are given elsewhere[7]. The test gases used in the experiments were supplied by L'Air Liquide, West Germany, with the following purities: $C_2H_6 \geq 99.95\%$, $N_2O \geq 99.99\%$, $O_2 \geq 99.998\%$, Ar $\geq 99.9999\%$. The range of gas mixtures used in the investigations is given in Table I.

Table I. Range of test gas mixtures in argon

C_2H_6	(ppm)	1	5	5	10	5	10
N_2O	(ppm)	100	2.5	-	-	-	-
O_2	(ppm)	-	-	5000	2000	500	250

EXPERIMENTAL RESULTS

Under certain experimental conditions, underlying absorption by N_2O resp. O_2 had to be considered. The necessary absorption cross sections were determined in separate experiments.

For $X_{N_2O} \geq 2 \cdot 10^{-5}$ and $T \leq 1900$ K, the correct time dependent absorption of N_2O at 1302 Å had to be taken into account. The value found for this absorption cross section corresponds to $4 \cdot 10^7 cm^2$/mole at room temperature and to $3.6 \cdot 10^7$ cm^2/mole for $T \approx 1200$ K, whereas Watenabe et al[19] report a slightly higher value of $4.6 \cdot 10^7$ cm^2/mole at room temperature. The background absorption of O_2 at 1215 Å and 1302 Å for $X_{O_2} = 10^{-3}$ was not negligible but could be considered constant during the observation time. For 1302 Å only negligible temperature dependence of the absorption cross section was found. The value determined: $3 \cdot 10^5$ cm^2/mole is in good agreement with the published one[19] of $2.9 \cdot 10^5$ cm^2/mole at room temperature. However, the absorption due to O_2 at 1215 Å is strongly temperature dependent. At room temperature, a value of about 1000 cm^2/mole was found for the cross section, which corresponds within 20% of the reported one[19]. In the range 1100 - 2400 K, the absorption cross section σ_{O_2} (in cm^2/mole, base e) is approximately represented by the analytical expression: $\sigma_{O_2} = 452 \cdot T - 4.07 \cdot 10^5$. The strong increase in the absorption cross section at elevated temperatures in contrast with that at room temperature is easily explained by the assumption that with rising temperature the bands which form a small transmission window in the Lyman-α-line[19 20] extend farther and overlap. Thus the absorption increases rapidly.

In figs 3-7 typical results of the numerical simulation of the experiments are presented and compared with the measured data. A comparison between the measured and computed profiles shows that the assumed reaction mechanism is capable of reproducing not only the induction period but also the position and magnitude of the peaks in the C_2H_6/O and C_2H_6/O_2-experiments.

DISCUSSION

The overall reaction scheme adapted for computer simulation of experimental results is presented in Table II. The experimental conditions were tailored in such a way, that only a few reactions of Table II which may be different for each case were necessary for describing an individual set of experiments. Since the experimental uncertainties are in the order of ±20% of the concentrations of H- and O-atoms, a computer match was regarded satisfactory, when computed concentrations were within these limits. The methyl radical necessary for the subsequent reactions is produced in the first step (reaction 1).

1. Methyl Radical Reaction with Atomic Oxygen

Due to the very low initial concentrations of 1 ppm C_2H_6, reactions of methyl radicals with themselves (Table II, 2,3) may be safely neglected. At high temperatures, we have a very fast decay of C_2H_6 and N_2O so that for the H-atom profile reaction 7 is of primary importance. The rate constant reported in literature was compatible straight away with our results in the temperature range 2000 K and above. In the case of lower temperatures, where C_2H_6-decomposition is not instantaneous, we could achieve agreement with our results by reducing k_7 progressively with decreasing temperature. But, this would lead to conflicting results with the reported ones at room temperature[17 18]. Therefore, it seems much more reasonable to lower k_1.

The necessity of reducing k_1 was independently verified in additional experiments with a much higher initial mole fraction of ethane ($X_{C_2H_6} = 5 \cdot 10^{-4}$). The total molecular absorption at 1497 Å was measured for temperatures between 1570 and 1850 K. The absorption cross sections for CH_3, C_2H_6, C_2H_4 and C_2H_2 were determined by separate experiments (the cross section for CH_3 was evaluated by producing methyl radicals via fast thermal decay of azomethane[21]).

Table II

Rate Coefficients Valid for the Temperature Range 1700-2300 K

$k = A \cdot T^{n} \cdot \exp(-E/RT)$ ccm/mole·sec

No	REACTION	A	n	E/R K	ΔH^{o}_{o} kcal	REFERENCE
1	$C_2H_6 = CH_3 + CH_3$	$8 \cdot 10^{12}$	0	35400	90	this work^{+}
2	$CH_3 + CH_3 = C_2H_4 + 2H$	$8 \cdot 10^{14}$	0	13400	46.6	8
3	$CH_3 + CH_3 = C_2H_4 + H_2$	$1 \cdot 10^{16}$	0	16100	-56.6	evaluated-3,8
4	$N_2O + M = N_2 + O + M$	$1.45 \cdot 10^{15}$	0	30800	38.6	6,16
5	$CH_3 + N_2O = CH_2O + H + N_2$	$5 \cdot 10^{11}$	0	0	-31.2	estimated
6	$N_2O + H = N_2 + OH$	$7.6 \cdot 10^{13}$	0	7600	-62.7	29
7	$CH_3 + O = CH_2O + H$	$(8 \pm 1) 10^{13}$	0	0	-69.8	22-25,this work
8	$CH_2O + O = HCO + OH$	$5 \cdot 10^{13}$	0	2310	-15.2^{++}	1
9	$CH_2O + M = H_2 + CO + M$	$8.2 \cdot 10^{15}$	0	35000	-0.4	26
10	$CH_2O + M = HCO + H + M$	$1.8 \cdot 10^{16}$	0	40400	86.1^{++}	26
11	$O + H_2 = OH + H$	$1.5 \cdot 10^{14}$	0	6900	1.9	27
12	$CH_3 + M = CH_2 + H + M$	$6.1 \cdot 10^{15}$	0	44900	108.3	our work
13	$CH_3 + O_2 = CH_2O + OH$	$5.2 \cdot 10^{13}$	0	17400	-53.1	this work^{+++}
14	$CH_3 + O_2 = CH_2O + O + H$	$7 \cdot 10^{12}$	0	12900	48.2	this work
15	$CH_3 + OH = CH_2O + H_2$	$8 \cdot 10^{12}$	0	0	-71.7	9
16	$CH_3 + OH = CH_2O + 2H$	$2 \cdot 10^{16}$	0	13800	31.5	this work
17	$CH_3 + H = CH_2 + H_2$	$1.8 \cdot 10^{14}$	0	7600	5.1	11
18	$CH_3 + CH_2 = C_2H_4 + H$	$2 \cdot 10^{13}$	0	0	-61.7	estimated
19	$CH_2O + OH = HCO + H_2O$	$5 \cdot 10^{14}$	0	3170	-31.9^{++}	1
20	$HCO + M = H + CO + M$	$1 \cdot 10^{15}$	0	15000	16.7^{++}	12
21	$H + O_2 = OH + O$	$1.2 \cdot 10^{17}$	-0.907	8370	16.7	14
22	$OH + C_2H_4 = CH_2O + CH_3$	$5 \cdot 10^{12}$	0	0	-15.1	9
23	$OH + H_2 = H_2O + H$	$5.2 \cdot 10^{13}$	0	3270	-14.8	28
24	$OH + OH = H_2O + O$	$3.3 \cdot 10^{13}$	0	3520	-16.7	28

$^{+}$units: sec^{-1}, valid for the density range 1 to $1.5 \cdot 10^{-5}$ mol/ccm

$^{++}$based on recent data for $\Delta H^{o}_{f}(HCO) = 7.7 \pm 1.9$ kcal/mole, Reference 33.

$^{+++}$these are preliminary upper limits - see text

Within the limits of error for the individual absorption cross sections, agreement with the measured profiles (fig. 1) could be achieved only when the rate coefficient for reaction 1 as given by Roth and Just[8] was lowered by a factor of about 0.5. Particularly the maxima in fig. 1 depend strongly on the chosen value for k_1. It could also be shown in contrast to the conditions in ref. 8 that the possible follow up reaction $CH_3 + C_2H_6 = CH_4 + C_2H_5$ (1a) has here little influence on the profiles. The result for k_1 is not in conflict with ref. 8, since these authors were not able to measure k_1 independently from the relatively fast secondary step (reaction 1a). Lowering k_1 by a certain factor means simply an increase by the same factor of the rate coefficient for the mentioned reaction in order to obtain a good simulation of the H-atom profiles in ref. 8. With $k_1 = 0.5 \cdot k_1{}^8$, the extrapolation of k_7 to the low temperature range gave good agreement with the results of[17, 18]. Extending our experiments to T ≈ 2300 K, we found a slight decrease of k_7 with increasing temperature (see fig. 2). From the available evidence at this stage, it is not possible to confirm whether this is really due to "non-Arrhenius" behaviour of this rate constant or due to experimental reasons. Further experimentation should be carried out to clarify this. In the following we give a short description of the contributions of other reactions than 7 to the H- and O-atom profiles.

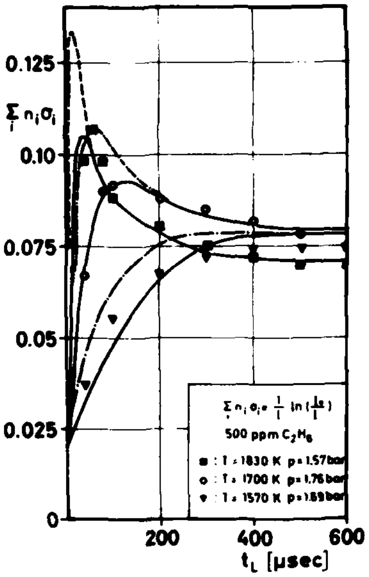

Fig. 1 Measured and computed total absorption profiles for C_2H_6 decomposition.

- - - computed $\Sigma n_i\sigma_i$ for 1830 K, $k_1 = k_1$

_____ computed $\Sigma n_i\sigma_i$ for 1830 K, $k_1 = 0.5\ k_1$

— · — computed $\Sigma n_i\sigma_i$ for 1700 K, $k_1 = k_1$

——— computed $\Sigma n_i\sigma_i$ for 1700 K, $k_1 = 0.5\ k_1$

— · — comp. $\Sigma n_i\sigma_i$ for 1570 K, $k_1 = k_1$

——— computed $\Sigma n_i\sigma_i$ for 1570 K, $k_1 = 0.5\ k_1$

1.1 T >2200 K

C_2H_6 and N_2O decompose very rapidly. After 200 μsec more than 90% of the initial concentrations have decomposed. Therefore, the H-atom profile is determined mainly by the reaction 7. Typical H-and O-atom profiles are shown in fig. 3. The nearly linear rise of the H-atom concentration shows that the H-atoms must be formed according to the reaction 7. Considering a primary step like $CH_3 + O = CH_2 + OH$, computer simulation showed quite a different

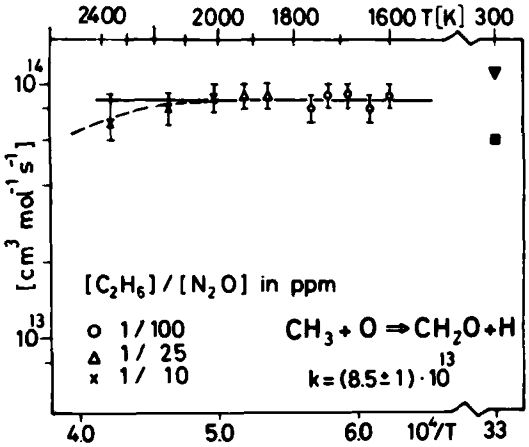

Fig. 2 Arrhenius plot for the reaction $CH_3+O=CH_2O+H$
▼ Low Temperature Data of Ref. 18
■ Low Temperature Data of Ref. 17

shape of the H-atom profiles (non-linear rise). The influence of the follow up reactions 9 and 10 is noticeable after about 200 µsec (relative deviation of the H-atom profile is about 20% for setting them zero). The chosen experimental conditions in the current investigation point clearly to these conclusions. Due to the excess of O-atoms, reactions with H and OH are of minor importance. All evaluated data are shown in fig. 2. As already mentioned, we are not sure, whether the slight decrease in k_7 at high temperatures is caused perhaps by the peculiar decay of intermediate CH_3O, see e.g.Golden[30] or is an artifact caused by an unlucky combination of several experimental errors.

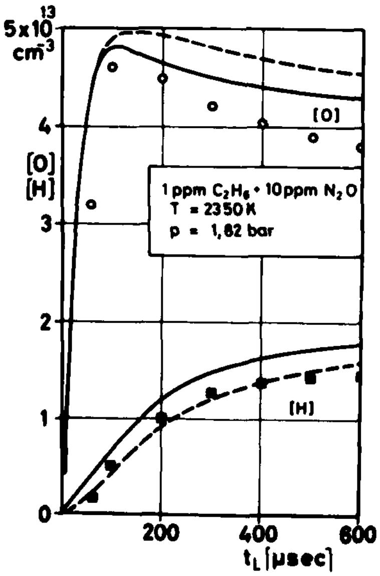

Fig. 3 H-and O-atom concentration profiles during the reaction CH_3+N_2O at high temperatures.

—— computed H and O- with $k_7=1\cdot10^{14}$
---- computed H and O- with $k_7=6\cdot10^{13}$
■ measured H ○ measured O-

1.2 T = 1900 - 2200 K

Reaction 1 has practically no influence. A slight induction period for H-atoms was observed and it is mainly due to the relatively slow decomposition of N_2O. Reactions 9 and 10 play a somewhat bigger role compared to the case 1.1. Reactions 15, 16 and 17 are of minor importance.

1.3 T < 190C K

The interpretation of the experiments with N_2O becomes more difficult because, under the chosen experimental conditions, both C_2H_6 and N_2O decompositions play an important role during the measuring time. At low temperatures (around 1600 to 1800 K) C_2H_6 decay is responsible for the marked induction times which appear in the H-atom profiles (fig. 4). For the first 200 μsec the H-atom profile is mainly determined by reactions 1,4 and 7. The influence of reaction 5: $CH_3 + N_2O = CH_2O + H + N_2$ can be neglected. If k_5 is made $\geq$ $5 \cdot 10^{12}$ ccm/mole·sec the computed H-atom profiles show a totally different shape (linear rise) compared with the measured ones. At temperatures where N_2O decomposition is relatively slow, the H-atom consuming reaction 6:

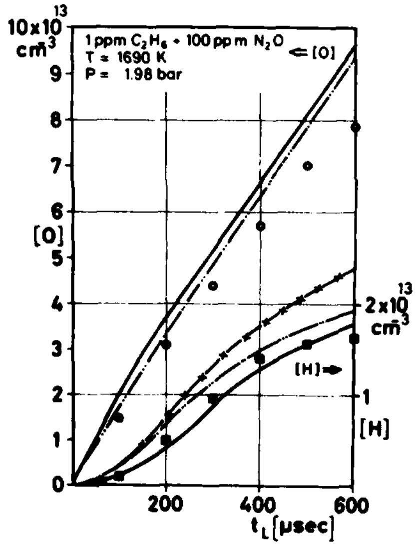

Fig. 4 H-and O-atom concentration profiles during the reaction C_2H_6+N_2O at low temperatures

— ·· — computed H-and O- with k_1=k_1, k_7=$1 \cdot 10^{14}$

———— computed H-and O- with k_1=$0.5k_1$and k_7=0.8 k_7

— x — computed H- with k_6=0

■ measured H ○ measured O

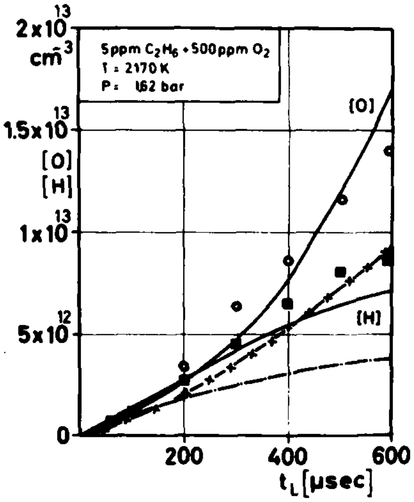

Fig. 5 H-and O-atom concentration profiles during the reaction CH_3+O_2

—— computed H-and O- with normal scheme

— x — computed O- with k_{16}= 0

— . — computed H- with k_{16}= 0

■ measured H ○ measured O

$N_2O + H = OH + N_2$ has a considerable influence on the H-atom profiles, as can be seen in fig. 4. At later stages of the reaction, contribution from the formaldehyde oxidation through reaction 8 becomes appreciable.

2. Methyl Radical Reaction with Molecular Oxygen

2.1 $O_2 \leq 500$ ppm

Generally we have for all experiments with O_2 a very strong influence of reaction 21. Any inaccuracy of this rate coefficient would affect the coefficients determined in this work. We based our evaluations on a recent survey by Schott et al[14]. Reactions 13 and 14 were found of very little significance. The H-atom profile is determined mainly by reactions 2, 7 in particular by 21 and the follow up reactions involving CH_3 and OH. The reaction 15: $CH_3 + OH = CH_2O + H_2$ alone, as discussed in literature[9], is incapable of reproducing the measured H-atom profiles. This fact was further confirmed by the computer simulation (elimination of this reaction produced only 8% reduction in H at 1800 K).

The formaldehyde decomposition proceeds mainly along the route: $CH_2O + M = H_2 + CO + M$ and influences the H-atom profile only indirectly. The effect of the H-producing channel: $CH_2O + M = HCO + H + M$ on the H-atom profile, is relatively small. Rimpel and Just[26] obtained recently exactly for the conditions of the present experiments (temperature and pressure) rate coefficient of the channels 9 and 10 (see Table II). Our simulation would be quite incompatible with our experimental results, if we would adapt for reaction 10 the value given by Schecker and Jost[12], but the simulation is improved, if the coefficient for 10 as given recently by Dean et al[31] is used.

The contribution of the reactions: $CH_3 + OH = CH_2 + H_2O$ ($k = 4 \cdot 10^{13}$, estimated) and $CH_2 + O_2 = CH_2O + O$ ($k = 10^{13} \cdot \exp(-5000/T)$, estimated) on H-and O-atom profiles is practically negligible. Only when the last rate constant is increased by an order of magnitude, do they have some 15% effect on O- but still no effect on H-atom profiles. So we conclude that just a step $CH_3 + OH =$ products is essential which produces immediately H-atoms. This forces us to consider the sequence of reactions: $CH_3 + OH = CH_3O + H$ and $CH_3O = CH_2O + H$ as the key steps in the production of H. The necessity of this step is clearly seen in fig. 5. A further confirmation about the importance of this step became obvious when the computer simulation showed that the reaction $CH_3 + OH = CH_4 + O$ has practically no influence, since the reverse was measured with satisfactory accuracy by Roth and Just[6] .

The decomposition of the CH_3O-radical under our experimental conditions is probably very rapid so that the rate constant for reaction 16 will in effect be the rate constant of $CH_3 + OH = CH_3O + H$. From the Arrhenius plot (fig. 7) a rate constant $k = 2 \cdot 10^{16} \exp(-13860/T)$ was evaluated. The activation energy obtained seems to be somewhat high, but then, this can be traced back to a probably strong non-Arrhenius behaviour of this reaction in the investigated temperature range. An investigation into the transition state ($HOCH_3$) would be very interesting.

The theoretical interpretation of the measurements of Roth and Just on $CH_4 + O = CH_3 + OH$ by Golden[30] led him to a typical threshold for this route of about 8 to 9 kcal/mole. This in turn leads at 2000 K to a contribution of about 7 to 6 kcal/mole by the temperature dependent partition functions for that case. We assume that this contribution is in the same order for the route 16, however, this needs a threshold energy in the order of about 20 kcal/mole which seems somewhat high when the endothermicity of about 10 kcal/mole for $CH_3 + OH = CH_3O + H$, Benson[32] is accepted. So we might at present not quite exclude that the rate parameters for 16 may be somewhat affected by uncertainties of other rate coefficients necessary for the evaluation of the H- and O-profiles under our conditions. The parameters of k_{16} have to be compared with those of k_{14}. If we make the same crude considerations concerning activation energy and probable threshold energy we can state that for $CH_3 + O_2 = CH_3O + O$ $\Delta H_o^o \approx 28$ kcal/mole the evaluated activation energy seems somewhat low. Thus without detailed theoretical considerations which have to be performed in future,we must admit,that at present we are confronted with some inconsistencies regarding the proper explanation of the routes 16 and 14.

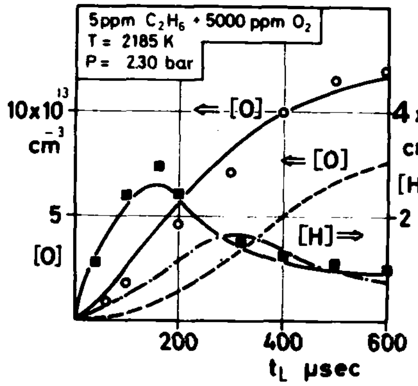

Fig. 6 H-and O-atom concentration profiles during CH_3+O_2

—— computed H-and O- with normal scheme

– – – computed O-with $k_{13}=k_{14}=0$

– · – computed H- with $k_{13}=k_{14}=0$

■ measured H

○ measured O

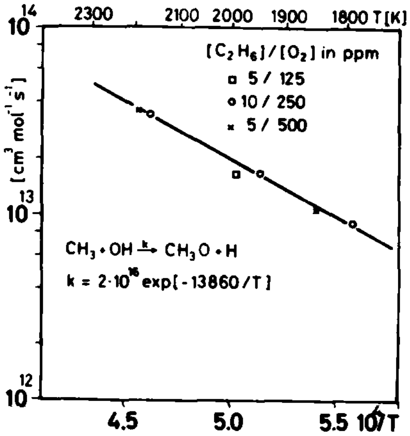

Fig. 7 Arrhenius plot for the reaction $CH_3+OH=CH_3O+H$

2.2 O_2= 5000 ppm

Experiments with smaller O_2-concentrations showed, as expected, little contributions from reactions 13 and 14. In order to study the individual contributions of these two reactions in detail, it was necessary to go to very high O_2 concentration range. Due to the high temperature k_1 is unimportant here. Due to the low initial C_2H_6 concentration reactions 2 and 3 play minor roles. At lower temperatures we saw again an induction period in the H-atom profile which could be simulated best by a lower k_1 (by 0.5) in comparison to ref. 8. Under these conditions reaction 14 together with 16 appears most important. All attempts to reproduce the measured H-and O-atom profiles through computer simulation with reactions 13 and 16 were unsuccessful. If the initial part of the profiles were matched through doubling the value of k_{13}, as reported by[3] the latter part could not be and vica versa. As against this, a slightly lower k_{14} than that reported by[13], produced satisfactory matching over the entire profile (fig. 6). This was found to hold for the entire temperature range as well. When reaction 13 and 14 are both eliminated, the computed H-and O-profiles are, as expected, very flat with small slopes, as shown in fig. 6. This leads us to the fact, that one of these reactions is absolutely necessary for the proper simulation of H-and O-profiles and from the earlier evidence it must be reaction 14. Our experimental results lead to a rate constant of $7\cdot10^{12}$ exp(-12910/T) ccm/mole·sec for this reaction. The oxygen profile turned out to be most sensitive to variations in k_{14}. The data scatter of the values for k_{14} is within ± 20%. Having chosen the best value for k_{14} we could show, that the alternative channel 13 can have only a rate constant of the order of $3.5\cdot10^9$ at 1800 K and 2.10^{10} at 2200 K. These values have to be considered as upper limits, since any further increase in these values make the agreement with the measured profiles unsatisfactory. With these data we can roughly ascribe to k_{13} an activation energy of the same order as we have found for k_{14}, which seems a reasonable result.

2.3 O_2 = 2000 ppm

Experiments in this range are of intermediate nature. The conclusions already drawn under 2.1 and 2.2. are found equally valid here. The measured H- and O-atom profiles are reproduced satisfactorily with reactions 14 and 16. Elimination of reaction 13 does in no way alter the situation.

CONCLUSIONS

omparing our results for

$CH_3 + O = CH_2O + H$ (7)

$CH_3 + OH = CH_3O + H$ (16)

$CH_3 + O_2 = CH_3O + O$ (14)

under a chemical aspect, we are led to the conjecture that in these reactions an important primary step is the formation of the C=O bondvia complexes which produce in 16 and 14 preferentially the intermediate species CH_3O, and that alternative routes like

$CH_3 + O = CH_2 + OH$ (7a)

$CH_3 + OH = CH_2O + H_2$ (15)

$= CH_2 + H_2O$ (15a)

$CH_3 + O_2 = CH_2O + OH$ (13)

are of lesser or negligible importance at least when simulation of H-and O-profiles of our experiments are considered. According to our results there is, in fact, much evidence that 7a and 15a may be excluded, whereas in 15 and 13 a CO bond is formed, but the further reaction of the respective complex is perhaps less straightforward by the specific way of H_2-and OH-formation. Reaction 15 may have a rate coefficient as discussed in the literature, however, reaction 13 turned out to have quite different Arrhenius parameter as e.g. given by Tsuboi[3]. Both reactions as given in Table II are of little importance for the generation of H-and O-atom profiles under our experimental conditions. So we may state that for proper modelling of CH_4 and C_2H_6 oxidation at elevated temperatures, in addition to the already used reaction 15, the route 16 is of great importance. As expected, route 13 and 14 are in real combustion situations practically unimportant, but they may be of occasional importance under particular circumstances, e.g. when experiments for the measurement of elementary reactions in CH_4/O_2, CH_3/O_2 and C_2H_6/O_2 systems are undertaken.

ACKNOWLEDGEMENT

We thank Dr. F. Bachmaier for the preparation of azomethane and E. Britzl for technical assistance. The financial support of the Deutsche Forschungsgemeinschaft is gratefully acknowledged.

REFERENCES

1. C.T. Bowman, 15th Symp. (Int.) on Comb., 869 (197[illegible])
2. D.B. Olson and W.C. Gardiner Jr., Combustion and Flame 32, 151 (1978)
3. T.Tsuboi, Jap. J. Appl. Phys. 15, 159 (1976) and 15th Symp. (Int.) on Comb., 883 (1974)
4. C.J. Jachimowski, Combustion and Flame 23, 233 (1974)
5. A.L. Myerson and W.S. Watt, J. Chem. Phys. 49, 425 (1966)
6. P. Roth and Th. Just, Ber. Bunsenges. physik. Chemie, 81, 572 (1977)
7. P. Roth and Th. Just, Ber. Bunsenges. physik. Chemie, 79, 682 (1975)
8. P. Roth and Th. Just, Ber. Bunsenges. physik. Chemie, 83, 577 (1979)
9. D.B. Olson, Univ. of Texas, Austin, Texas, CB 12/14 W Report 22
10. K. Glänzer, M. Quack and J. Troe, Chem.Phys. Letters, 39, 304 (1976) and 16th Symp. (Int.) on Comb., 949 (1976)
11. K.A. Bhaskaran, P. Frank and Th. Just, unpublished work on CH_4 decomposition
12. H.G. Schecker and W. Jost, Ber. Bunsenges. physik. Chemie, 73,521 (1969)
13. T.A. Brabbs and R.S. Brokaw, 15th Symp. (Int.) on Comb., 893 (1974)
14. G.L. Schott, Combustion and Flame 21, 457 (1973)
15. D.B. Olson, T. Tanzawa and W.C. Gardiner Jr., Int. J. Chem. Kinetics , 11, 23 (1979)
16. H.A. Olschewski, J. Troe and H.G. Wagner, Ber. Bunsenges. physik. Chem. 70, 450 (1966)
17. N. Washida and K.D. Bayes, Int. J. Chem. Kinetics, 777 (1976)
18. J. R. Slagle, F.J. Pruss Jr. and D. Gutman, Int. J. Chem. Kinetics, 6, 11 (1974)
19. K. Watanabe, N. Zelikoff and E.C.Y. Inn, AFCRC Techn.Rep. No. 53-23 Geophys. Res. Paper No. 21 (1953 b)
20. D. Appel and J.P. Appelton, 15th Symp. (Int.) on Combust., 701 (1974)
21. K. Glänzer, M. Qack and J. Troe, Chem. Phys. Letters, 39, 304 (1976)
22. J. Peeters and G. Mahnen, 14th Symp. (Int.) on Combust., 133 (1973)
23. A.M. Dean and G.B. Kistiakowsky, J. Chem. Phys., 54, 1718 (1970)
24. C.P. Fennimore and G.W. Jones, J.Phys. Chem., 65, 1532 (1961)
25. J.C. Biordi, C.P. Lazzara and J.F. Papp, Combustion and Flame 26, 57 (1967)
26. G. Rimpel and Th. Just, to be published
27. G.L. Schott, R.W. Getzinger and W.A. Seitz, Int. J. Chem. Kinetics, 6, 921 (1974)
28. D.L. Baulch, D.D. Drysdale and D.G. Horne, Kinetic Data for High Temp. Reactions, vol. 1 (1972)
29. D.L. Baulch, D.D. Drysdale and D.G. Horne, Kinetic Data for High Temp. Reactions, vol. 2 (1972)
30. D.M. Golden, J. Phys. Chem., 83, 108 (1979)
31. A.M. Dean, to be published in 17th Symp. (Int.) on Comb.(1978)
32. S.W. Benson, Thermochemical Kinetics Wiley and Sons, (1976) Second Edn.
33. D.M. Golden, S.W. Benson, Chem. Rev. 69, 125/34, 131 (1969)

SHOCK TUBE IGNITION OF NITROCELLULOSE

ARTHUR COHEN and LEON DECKER

Ignition and Combustion Branch, Propulsion Division
Ballistic Research Laboratory, ARRADCOM, APG, Maryland 21005, USA

A reflected shock technique has been used to measure ignition delays of nitrocellulose particles in N_2 at gas temperatures between 600-1200 K and pressures between .1-1.5 MPa. Delays are independent of pressure. The temperature dependence of the delays changes markedly at 750 K. Activation energies of 19.6 and 4.4 kcal/mole have been found for data at low and high temperatures, respectively. Calculations based on the low temperature results indicate ignition should occur in the incident shock region of the high temperature experiments which, at present, has not been observed. Calculations using a single ignition temperature or a rate constant derived from radiative ignition experiments will not adequately describe the data. A mechanism consisting of two consecutive condensed phase reactions each controlling ignition in a different temperature range is proposed.

INTRODUCTION

Recent efforts to model flame propagations in propellant beds have generated interest in determining ignition characteristics of explosive materials at elevated temperatures where heat transfer rates are large. At temperatures < 500 K, radiative[1] and conductive[2] heat transfer methods have been used to study NC ignition. Techniques for studying ignition at higher temperatures are limited by fast reaction times. Friedman[3] used a reflected shock technique, in which both convective and conductive heat transfer takes place, to study explosion delays at high temperatures in aerosols formed by small particles of explosive materials in air and oxygen. This technique has been applied to study ignition of similar materials in an inert environment. Ignition has been observed for nitrocellulose (NC), PETN, HMX and RDX in N_2 and Ar. The results of the experiments with NC in N_2 will be discussed. In these experiments it is difficult to distinguish between explosion and deflagration. Since either process can be initiated by the same stimulus, depending primarily on the amount of confinement and energy dissipation in the system, it has been assumed that the same energy production mechanism and activation energy apply to both induction periods. For explosive materials, particle temperatures can increase through heat transfer from the shocked gas and from initiation of exothermic reactions which can lead to ignition and to particle temperatures (T) > gas temperatures. Ignition is characterized by a rapid increase in T which results in an increase in particle emissive power above its gas temperature value.

Ignition is assumed to occur at this time. By determining the dependence of this time on particle temperatures, an activation energy appropriate to the ignition processes can be determined.

EXPERIMENTAL TECHNIQUE

The 4" I.D. shock tube has been described previously[4]. A schematic of the present test section is shown in Figure 1.

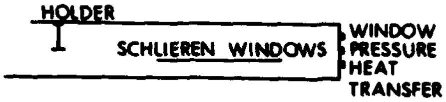

Figure 1. Schematic of test section.

The holder was either a 1" diameter disc or a 4" x .4" blade, both 1/16" thick and feathered at their edges to minimize flow disturbances. A 1/16" diameter rod supports the holders at the shock tube axis. The distance from the end wall (H) could be fixed at 6.21, 25.67 or 77.74 cm. Mounted in the end wall are a piezoelectric pressure transducer, a thin film heat transfer gage and a quartz window (diameter $\sim$ 1 cm) through which a photomultiplier tube (PMT) views the inside of the shock tube. The PMT is sensitive to radiation in the 3000-8000 Å region (S-20 response). For $\overline{T} > 650$ K, most of the emission measurements were made with a Hamamatsu R136 PMT. At lower temperatures an EMI 9558 was used. Shock velocities were obtained from time of arrival measurements at pressure transducers located upstream from the test section. In order to characterize the emission from NC, experiments were performed with several inert materials which included boron and carbon, solids with high emissivities, and cellulose acetate (CA), a cellulose polymer with molecular structure and physical properties similar to NC. Amorphous boron, activated charcoal, graphite and CA (39.8% acetyl) were obtained from Fisher, Merck, Joseph Dixon (New Jersey) and Eastman Kodak Companies, respectively. NC (12.2% N) was obtained from Hercules Powder Company. Samples with different size distributions were obtained by sieving. NC samples were heated in an oven at $T \simeq 400$ K for one hour to get rid of solvent, kept overnight at $T = 380$ K and then stored in a vacuum dessicator. Carbon and boron were heated at $T \sim 430$ K and then stored at $T \sim 370$ K. CA was heated at $T \simeq 413$ K for three hours and stored in a vacuum dessicator.

The experimental procedure consisted of (1) weighing the required sample ($\leq$ 150 mg), and placing it on the holder in the shock tube; (2) evacuating the tube to about 2.5 Pa; (3) filling the tube to the desired pressure with high purity N_2; and (4) adjusting driver pressure and composition (He, air) to give the desired shock strength. Signals from the end wall pressure transducer and PMT were recorded on an oscilloscope. Figure 2 represents one of these records.

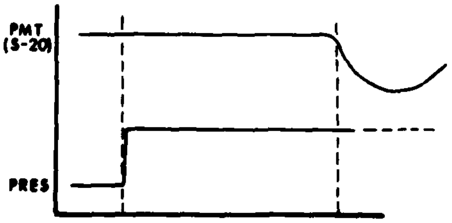

Figure 2. End wall oscilloscope records showing pressure jump at shock reflection and delay to emission.

The technique uses the incident shock and gas flow to disperse and accelerate particles from the holder. Ignition occurs after shock reflection except for experiments with the strongest shocks and with H = 77.74 cm. A sketch of the wave dynamics in the shock tube is shown in Figure 3.

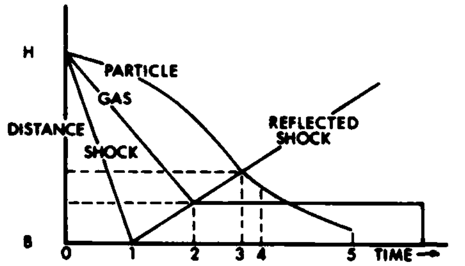

Figure 3. Sketch of the trajectories of the incident and reflected shocks and of a gas and condensed particle located initially at the holder (H). The designated times refer to the following: (0,1) - incident shock arrival at the holder and end wall; (2,3) - the gas and condensed particle intersections with the reflected shock; (4) - completion of the condensed particle temperature relaxation period; (5) detection of emission.

The gas particle is assumed to stagnate and relax instantaneously to the equilibrium reflected shock temperature ($\overline{T}$). The particle relaxation time depends on the thermodynamic properties of gas and particle, their relative velocity, and the particle size. The emission time (t_e) is defined as the time between shock reflection and detection of emission (t_{15} in Figure 3). Detection depends on particle temperature, size and emissivity and the PMT sensitivity. The ignition delay (t_i) is defined as the time the particle spends in the reflected shock region prior to igniting (t_{35} in Figure 3). For propellant particles the experimental t_e value is used to calculate t_i. For inert particles t_e is used to estimate the size of particles responsible for the initial emission. In order to obtain t_i from t_e, the incident and reflected shock velocities and the particle velocity behind the incident shock must be determined. Particle velocity is obtained from solution of the time dependent particle momentum equation. This requires knowledge of the gas shock parameters which are calculated from the steady state 1D gas conservation equations by using measured incident shock velocities, and neglecting the presence of particles. The procedure by which the activation energy (E) is derived from the variation of t_i with T depends on the relative values of the temperature relaxation time (t_f, t_{34} in Figure 3) and t_i. For $t_f << t_i$, the analysis used by Friedman[3] is applicable. It assumes that reactions occur in the solid and that ignition delays are due to particles with diameters (D) equal to Semenoff's "critical" value (D*). For D < D*, ignition does not occur due to rapid heat transfer from the particle which prevents particle temperature from exceeding the gas temperature. For $D \geq D^*$, ignition occurs after the critical size particle ignites. Using $(T-\overline{T}) = 2R\overline{T}^2/E$ as the ignition criterion and assuming first order kinetics for the energy production mechanism, an equation for t_i, in terms of $\overline{T}$, was obtained and is given by

$$t_i = 1.23\ CR\overline{T}^2/(EQAe^{-E/R\overline{T}}), \qquad (1)$$

with the critical diameter

$$D^* \approx [4.4\ \overline{k}\ R\overline{T}^2/(\rho EAQe^{-E/R\overline{T}})]^{1/2}. \qquad (2)$$

If the particle heat capacity (C) is known then by determining t_i and $\overline{T}$, values for E and the product of the heat of reaction (Q) and preexponential factor (A) can be determined. For $t_i \sim t_f$, a direct comparison between calculated and experimental delays through solution of the time dependent particle conservation equations is required. These equations are listed below together with the Drag and Nusselt number correlations suggested by Rudinger[5] which were used for calculating particle velocity and temperature. The particle temperature is assumed uniform and reactant consumption is neglected. (Bar refers to gas properties).

$$\text{Momentum:}\quad \frac{dU}{dt} = \frac{3}{4}\,\frac{C_D}{D}\,\frac{\bar{\rho}}{\rho}\,|\bar{U}-U|(\bar{U}-U);\; C_D = \frac{24}{Re} + \frac{4}{Re^{1/3}}\;;\; Re = \frac{\bar{\rho}D|\bar{U}-U|}{\bar{\mu}}$$

$$\text{Energy:}\quad \frac{dT}{dt} = \frac{6\bar{h}(\bar{T}-T)}{C\rho D} - \frac{6\varepsilon\sigma T^4}{C\rho D} + \frac{QAe^{-E/RT}}{C}\;;\; \bar{h} = \frac{Nu\bar{k}}{D}\;;$$

$$Nu = 2 + .46Pr^{.33}Re^{.55};\; t_f = \frac{C\rho D^2}{6\bar{k}Nu}$$

EXPERIMENTAL RESULTS

Shock velocities were obtained from time of arrival measurements at three piezoelectric transducers. End wall pressure measurements indicate that the presence of the holder with or without particles had little effect on the magnitude of the pressure rise at shock reflection or on the pressure behavior afterwards. Figure 4 shows the results of the shock reflection measurements.

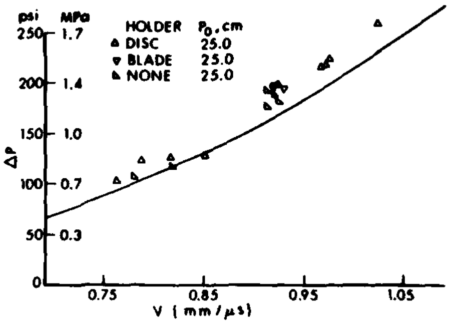

Figure 4. Plot of pressure jump at shock reflection vs shock velocity for disc and blade holders located 25.67 cm from end wall with initial pressure equal to 33.3 KPa. Solid line is the calculated value.

Although there is about a 10% deviation from theory at higher shock velocities, the presence of the holders is not the cause of the discrepancy. It is believed that the use of 1D gas conservation equations to calculate gas properties is still valid.

Emission from boron and carbon particles has been observed in the reflected shock region at $\bar{T} > 800$ K. The boron data for two sample weights and two sample sizes are shown in Figure 5. The background radiation responsible for the blank data is probably due to the presence of a small number of particles in the shock tube which are difficult to remove. Fortunately it is not difficult to distinguish between background radiation and emission from test particles of boron, carbon and NC when placed on the holder. For $\bar{T} <$ 1000 K, emission with these test particles occur much earlier than blank emission therefore background $t_e \gg$ test t_e. For $\bar{T} > 1000$ K, when t_e become comparable, the initial slope of the PMT signal due to as little as 2.5 mg of test particles >> initial slope due to the background. The data with D = 25-37 μm, lie below the I_{25} line which suggests that in these experiments initial emission is detected from particles with D < 25 μm which is the minimum diameter expected in the sample, based on screen-size measurements. For the given PMT sensitivity, $\bar{T} > 800$ K was required in order to detect emission. If it is assumed that T = 800 K is the minimum particle temperature necessary to detect emission then the calculations in Figure 5 indicate that the initial emission is due to particles with D = 1-10 μm. It is possible that the presence of such small particles in the sample is due to their adherence to larger particles during the sieving process. Separation may then occur during the shock dispersal process. Data with carbon also fail to reveal a particle size effect and it has been assumed that in these experiments the measured t_e are due to inert particles with $D \leq 10$ μm.

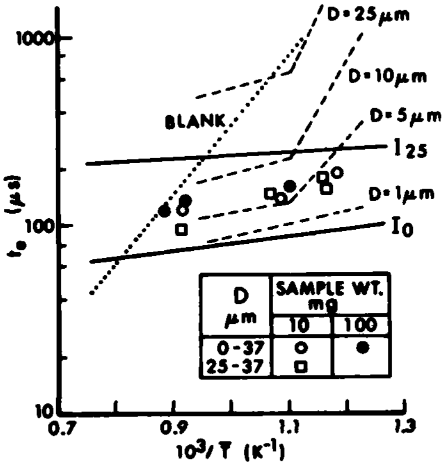

Figure 5. Semi-log plot of t_e vs $10^3/\overline{T}$ for boron particles (ρ = 2.35 g/cm^3, C = .30 cal/g-K) located initially on the holder with H = 25.67 cm and P_0 = 33.3 kPa showing the absence of effects of particle size and sample weight on t_e.

..... BLANK: Least square fit of t_e data without particles on holder.

——— I_D: Calculated time between shock reflection and reflected shock intersection of particle of diameter in μm indicated by subscript D. (I_0 refers to gas particle).

----- D: Calculated time for particle with diameter = D to reach T = 800 K.

A comparison of emission signals at $\overline{T}$ > 800 K in NC and carbon is shown in Figure 6.

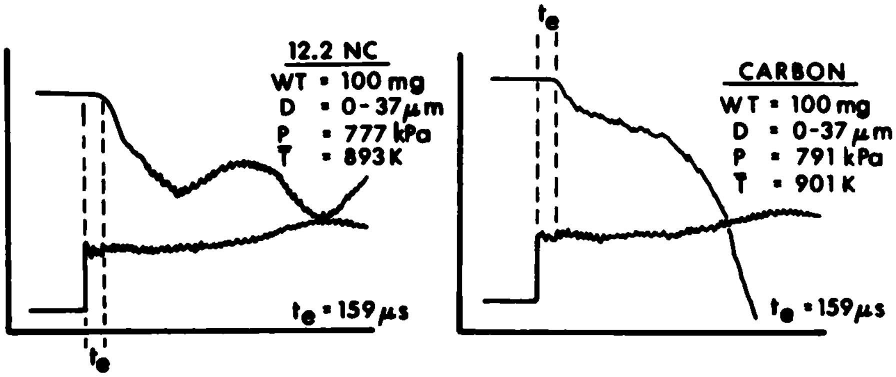

Figure 6. Traces of the end wall pressure and emission records taken with the same oscilloscope settings, under similar shock conditions, for similar particle distributions of NC and carbon showing difficulties in determining when ignition occurs.

The pressure signals are quite similar. The increase in pressure which occurs approximately 1100 μs after shock reflections leads to an increase in emission intensity associated with flow disturbances and not ignition. The emission times (t_e) are similar and from these records it would be difficult to tell if and when NC ignites. It is not difficult to tell after the shot that ignition has occurred. When the tube is opened one observes smoke and very few NC particles. Spectrograms taken at $\overline{T}$ = 1000 K indicate that the emission is continuous over the wavelength interval 4000-8000 Å and is attributed to thermal radiation. To determine when ignition occurs, experiments with CA were performed. Expecting that the emissivities (ε) and thermal properties of CA and NC would be similar it was thought that comparisons of the emission intensities under similar shock conditions would indicate the time of ignition. However, emission was not observed in the experiments with CA even at $\bar{T} \simeq 1100$ K.

The results of many experiments, using the Hamamatsu R 136 PMT, show that for data taken with 100 mg samples and with the same size distribution, emission from boron, carbon and NC occurs at $\bar{T} > 800$ K but not from CA. Within the experimental error, t_e are equal with boron and carbon but slightly longer with NC. At $\bar{T} < 800$ K emission is observed only with NC. Detection occurs at gas temperatures as low as $\bar{T} = 650$ K (600 K with the EMI 9558 PMT). It would appear that under present experimental conditions $T > 800$ K are required to detect emission from boron and carbon ($\varepsilon \simeq .8$), and somewhat higher from NC whose emissivity $< .8$. This implies that during the experiments where $\bar{T} < 800$ K, in which NC emission is observed, particle temperatures are greater than gas temperatures ($T > \bar{T}$). This is attributed to self-heating due to ignition. For $\bar{T} > 800$ K, the results with CA similarly imply that NC emission is due to self-heating and not to convective heating from the gas. Based on these conclusions, it has been assumed that the initial emission signal corresponds to ignition in the NC experiments. Since particle emissive power depends exponentially on T, it is probable that the size of the NC particles responsible for initial emission is smaller than those in the boron experiments (i.e., $D < 10$ μm).

The results of experiments with NC are shown in Figure 7.

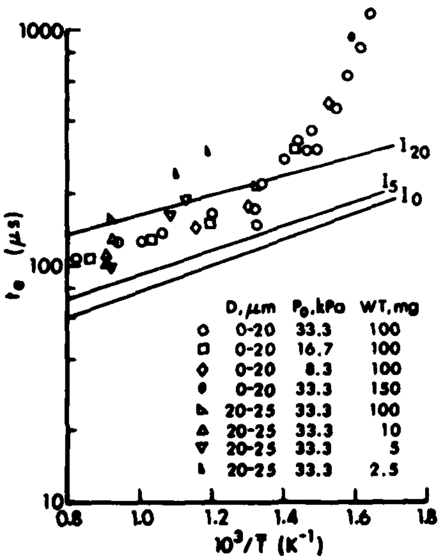

Figure 7. A semi-log plot of t_e vs $10^3/\bar{T}$ for NC particles with the holder at a distance of 25.67 cm from the end wall showing the effect of particle size, sample weight, and initial pressure (P_o). The lines labeled I_D ($D = 0, 5, 20$) are the calculated time after shock reflection for the arrival into the reflected shock region of gas particles and NC particles ($\rho = 1.5$ g/cm^3) of 5 and 20 μm diameters, respectively, located initially on the holder.

If ignition is assumed to take place in the reflected shock region, then these calculations indicate that for $\bar{T} > 750$ K $D^* < 5$ μm. For $D = 0\text{-}20$ μm, a four-fold change in pressure does not affect t_e which suggests that under these conditions ignition is controlled by condensed phase reactions.

The apparent increase in t_e with sample weight for the $D = 20\text{-}25$ μm data at $\bar{T} \simeq 1100$ K is attributed to increased scatter in data at high temperatures.

The decrease at $\overline{T} < 900$ K is attributed to the increased difficulty in detecting smaller (and therefore earlier) particle emission due to the combined effect of a smaller number of these particles and to their lower emissive power. The effects of changing the nominal size distributions from D = 0-20 μm to D = 20-25 μm on t_e is not great and, similar to the results with boron, is attributed to the presence and ignition of particles with D < 20 μm in both samples. Emission was never observed in any of these experiments before shock reflection. Experimental emission times (t_e) were converted to ignition delays (t_i) by assuming that the igniting NC particles were small enough so that the difference in time between their intersection and a gas particle's intersection with the reflected shock (I_D-I_O) is small compared to t_i ($t_{23} << t_{35}$ in Figure 3). Under these conditions $t_i = t_e - t_o$, where t_o (t_{12} in Figure 3) is obtained from the calculated I_O line. Figure 8 contains data for different holder distances.

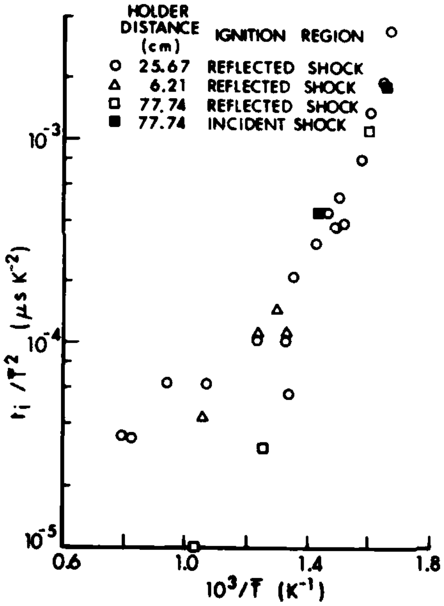

Figure 8. A semi-log plot of $t_i/\overline{T}^2$ vs $10^3/\overline{T}$ showing the effects of incident shock heating time and the particle-reflected shock intersection on t_i. The data was taken with 100 mg samples of 0-20 μm particles at P_o = 33.3 kPa.

Increasing H from 6.21 to 25.67 cm which corresponds to approximately a four-fold increase in incident shock heating time (t_{03} in Figure 3) has little effect on t_i. Increasing $\underline{H}$ to 77.4 cm leads to a decrease in t_i from expected values for $\overline{T} > 800$ K. At $\overline{T} > 935$ K (incident shock gas temperature ($\overline{S}$) > 600 K) ignition occurs prior to shock reflection in the incident shock region. The solid points are plotted using this incident gas temperature and are consistent with data taken in the reflected shock region indicating that the particle-reflected shock intersection does not greatly affect ignition behavior.

The data in Figure 7 suggest that a change in behavior occurs at T ≈ 750 K. The data for D = 0-20 μm were divided into two groups, $10^3/\overline{T} \lessgtr 1.34$, and fit to equation (1) by a linear least squares analysis. The data and results are shown in Figure 9.

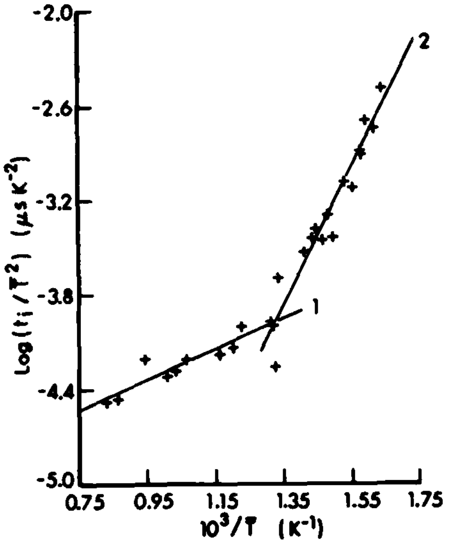

Figure 9. Plot of log $(t_i/\overline{T}^2)$ vs $10^3/\overline{T}$ from which values for E and QA are derived. Solid lines are the results of least squares fit to equation (1) of data shown in Figure 7 for D = 0-20 μm.

1: $10^3/\overline{T} < 1.34$, $E \simeq 4.4$ kcal/mole, $QA \simeq 3.7\text{x}10^7$ cal/g-sec

2: $10^3/\overline{T} > 1.34$, $E \simeq 19.6$ kcal/mole, $QA \simeq 1.1\text{x}10^{11}$ cal/g-sec

Using equation (2), the corresponding estimate for D* is approximately 2.5 μm at high temperatures and 5.2 μm at low temperatures. Corrections to the derived t_i values for particles of this size would not affect the results of the analysis appreciably.

Calculations were performed to determine if these results were consistent with the observations that, in these experiments, ignition does not occur before shock reflection. Taking into account changes in D* for the incident and reflected shock regions, particle trajectories were calculated from solution of the momentum equation and ignition delays were determined from the results of the least squares analysis. These calculations predict ignition before shock reflection for $\overline{S} > 660$ K ($10^3/\overline{T} < .94$). At present, it is difficult to account for this discrepancy but it appears to be due to the use of the less sensitive PMT for data taken with $\overline{S} > 660$ K.

COMPARISON WITH PREVIOUS RESULTS

Lenchitz, et al.[1], has studied radiative ignition of thin (10 μm) NC films using an arc image furnace and found that the radiant energy required for ignition in N_2 at one atmosphere were consistent with a calculated ignition temperature of 573 K. Thompson and Suh[6], by measuring surface temperature and comparing theoretical and experimental radiant ignition delay measurements for M2 propellant (∿ 77% NC, 20% nitroglycerine), derived a set of values for A, E and Q describing chemical reaction in the solid. These values ($A = 10^{17}$ s^{-1}, E = 40 kcal/mole, Q = 62.5 cal/g-sec) were used to calculate the trajectories and temperatures of NC ($\rho = 1.5$ g/cm³, C = .37 cal/g-K) particles through the incident and reflected shock regions. The results for 1 and 20 μm diameter particles located initially 25.67 cm from the end wall with $P_0 = 33.3$ kPa are shown in Figure 10.

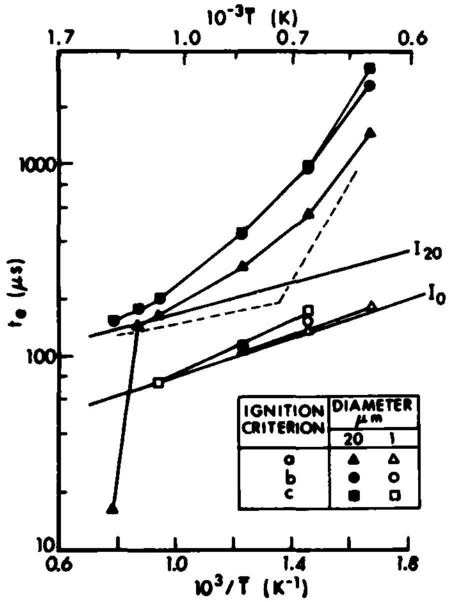

Figure 10. Semi-log plot of calculated emission times (t_e) vs $10^3/\overline{T}$ for three ignition criterion: a) T = 563 K; b) T - gas temperature > 1 K; and c) T - gas temperature > Q/C (K).

holder distance = 25.67 cm; P_o = 33.3 kPa

----- results of least squares analysis shown in Figure 9

——— I_D defined in Figure 7

Calculations performed at $\overline{T}$ = 599, 684, 811, 1059 and 1298 K. Absence of calculated results indicates either ignition occurs prior to shock reflection or not at all. Absence of least squares results indicates absence of experimental data.

For D = 20 μm, the calculations predict the general shape of the delay data. They also show that ignition based on criterion a) ($\overline{T}$ = 563 K) is not appreciably affected by allowing Q = 0. For D = 1 μm, at $\overline{T}$ > 1056 K, using criteria a) and b) leads to ignition prior to shock reflection (t_e < 0) while at $\overline{T}$ < 599 K, using criteria b) and c) leads to infinite delays. The latter implies that D* > 1 μm. For D = 20 μm, at low temperature ($\overline{T}$ < 684 K), using criterion a) calculated delays are slightly larger and their temperature dependence slightly smaller than experimental values. As $\overline{T}$ increases to 1060 K, the agreement with experiments decreases. At T ≈ 1140 K the calculations do agree with experiments but as $\overline{T}$ increases further, they predict a sharp increase in temperature dependence and delays much smaller than those observed. For D = 20 μm using criteria b) and c) leads to predicted delays much larger than those measured. For D between 1 and 20 μm calculations for D = 20 μm, give the best agreement with experimental data. However, the experimental data indicate that particles with D < 5 μm are responsible for the ignition delays. Calculations for particles with D < 5 μm give considerably less agreement with experimental data since at high temperatures it predicts ignition before shock reflection and at low temperatures delays much smaller than those observed.

CONCLUSION

It appears that at $\overline{T}$ > 600 K convective and conductive ignition of NC cannot be predicted by using a single ignition temperature nor by using an exothermic reaction described by a single Arrhenius rate constant with parameters determined from radiative ignition measurements. A qualitative description of the delay data can be obtained by a mechanism involving two consecutive condensed phase processes -- $A \longrightarrow B \longrightarrow C$ -- each controlling ignition in different temperature ranges. The first has a low activation energy (E_1) and is rate controlling at high temperatures while the second has a high activation energy (E_2) and is rate controlling at low temperatures. Statistical analysis of the ignition delay data give values of 4.4 and 19.6 kcal/mole for E_1 and E_2, respectively. The relation of these values to activation energies for molecular reactions is at present unknown. Calculations, using the kinetic and thermodynamic parameters derived from the statistical analysis, give the expected agreement with data at $\overline{T} < 750$ K but at higher temperatures, as was noted when using the ignition delay values directly, predict ignition before shock reflection. Efforts to resolve this discrepancy are now underway.

REFERENCES

1. C. Lenchitz, E. Hayes, R. W. Velicky, L. Schlosberg, and N. P. Suh, Comb. Sci. and Tech., 7, 1 (1973).
2. A. S. Shteynberg, V. B. Ulybiss, V. V. Barzykin, and A. G. Merzhanov, Eng. Phys. J., USSR 10, 4, 482 (1966).
3. M. H. Friedman, Comb. and Flame 10, 112 (1966).
4. A. Cohen, BRL Report No. 1673, September 1973.
5. G. Rudinger, "Nonequilibrium Flows", P. P. Wegener, ed. (Marcel Dekker, New York and London, 1969), Chap. 3.
6. C. L. Thompson and N. P. Suh, Comb. Sci. and Tech., 2, 59 (1970).

LIST OF SYMBOLS

(Bar over symbol refers to reflected shock gas property)

Symbol	Property
A	preexponential factor
C	heat capacity
C_D	drag coefficient
D	diameter
D*	critical diameter
E	activation energy
ε	emissivity
H	distance from end wall
h	heat transfer coefficient
k	thermal conductivity
Nu	Nusselt number
Pr	Prandtl number
Q	heat of reaction
R	gas constant
Re	Reynolds number
ρ	density
$\overline{S}$	incident gas temperature
σ	Stefan-Boltzmann constant
T	temperature
t	time
t_e	emission time
t_f	temperature relaxation time
t_i	ignition delay time
t_o	incident shock gas heating time
t_p	incident shock particle heating time
U	velocity

THE EFFECT OF REACTION EXOTHERMICITY ON SHOCK PROPAGATION

J. N. Bradley, W. D. Capey and F. Faraji

Department of Chemistry, University of Essex, Colchester, England

The effect of reaction exothermicity on shock propagation has been investigated by measuring shock velocities and induction times for mixtures of hydrogen and oxygen in argon over a range of compositions and pressures. Coupling between the reaction and the shock wave is only observed above a minimum shock strength, characteristic of the initial pressure and composition. The onset of coupling is quite sharp and corresponds to the simultaneous arrival at the first detector station of the incident shock wave and of an acoustic wave originating from the contact surface at the termination of the induction period.

For higher pressures and richer mixtures, the wave rapidly accelerates to the theoretical Chapman-Jouguet detonation velocity but for lower pressures and weaker mixtures, a ***chemically-enhanced shock wave*** is observed. In the latter case, the reaction adds a constant velocity increment to the shock wave irrespective of the strength of the driving shock. Between the two limiting cases, marginal detonation is observed.

The measured induction times are in good agreement with previous work and fit the relation

$$\tau = 7.39 \times 10^{-11} \exp(15.7 \text{ kcal}/RT)\ [H_2]^{-\frac{1}{2}}\ [O_2]^{-\frac{1}{2}}$$

where concentrations are in moles/litre.

INTRODUCTION

In recent years, there has been a renewed interest in the initiation of detonation stimulated, at least in part, by concern over the hazards associated with the accidental release of inflammable gases and liquids which are stored at high pressure. The present investigation is concerned with the nature of the coupling between the chemical reaction and the propagation of a shock wave under limiting conditions. It is anticipated that a greater knowledge of the physical and chemical processes involved will lead to a better understanding of the mechanism by which detonation is initiated and eventually to a greater degree of control, for example by the addition of chemical promoters or inhibitors.

EXPERIMENTAL

The shock tube used in the present investigation was fabricated from $\frac{1}{4}$" thick brass sheet and is of rectangular cross-section with internal dimensions, 153 mm by 83 mm. The driver and experimental sections are respectively 1.22 m and 2.43 m long. The experimental section is evacuated by an Edwards 3" mercury diffusion pump, backed by a 170 l/min rotary pump, and the combined leak/outgassing rate is below 4 μ/min. Melinex sheet, manufactured by I.C.I. Ltd., is employed for the diaphragms, combinations of appropriate thicknesses being used to ensure that mechanical bursting is achieved close to the spontaneous bursting pressure.

The propagation of the shock is monitored by a laser schlieren technique. The light from a Spectra Physics 156 laser passes through a sequence of partially-silvered mirrors to give six separate beams normal to the shock tube. These then pass through six pairs of flush-mounted, optical quality windows, situated at 150 mm intervals along the tube. Further mirrors recombine the beams on a knife edge placed on the vertical diameter of an E.M.I. 9526B photomultiplier. The output from the photomultiplier is fed into an exponential amplifier with low-level noise rejection and displayed on one beam of a Tektronix 555 oscilloscope. The signals are also used to operate a six-channel sequential timer with a 10 MHz response. The technique provides five independent velocity measurements with an accuracy of ± 0.1%. The complete system is illustrated schematically in Figure 1.

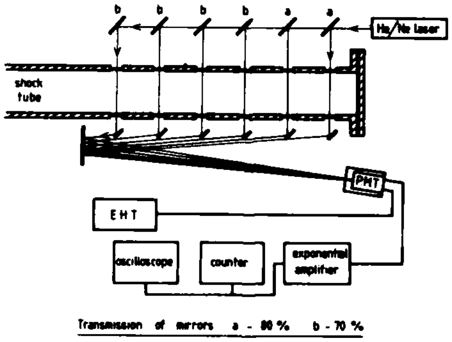

Figure 1. Schematic diagram of schlieren system

The light output from the reaction zone is monitored by an E.M.I. 6256 photomultiplier located at the third detector station and provides measurements of the induction delay for the reaction.

Experiments were carried out on compositions of hydrogen (1 to 22.5%) and oxygen (1.5 to 23%) in argon over the pressure range 10-50 torr.

In this investigation, the quantity under observation is the shock velocity and an alternative parameter must therefore be employed to characterize the strength of the shock. The bursting pressure ratio itself is unsuitable and a more obvious quantity is the incident shock temperature. In conventional shock tube experiments, the temperature is calculated from the shock velocity and the known thermodynamic properties of the gas but this approach clearly cannot be adopted here. However, the properties behind the shock wave can be calculated theoretically from the physical conditions at the time of diaphragm rupture by assuming that the shock wave obeys the Rankine-Hugoiot relations, that the expansion takes place adiabatically, and that the pressures and flow velocities on each side of the contact surface can be equated. This calculation normally over-estimates the strength of the shock because diaphragm rupture is not instantaneous, throttling of the flow occurs, and energy is lost. This difficulty has been overcome in the present work by applying an empirical correction factor which reduces the theoretical flow velocity out of the driver section. This correction factor is determined by studying shock waves in pure argon under conditions as close as possible to those of the reactive systems. Its value is typically in the range 0.6 - 0.8 but depends critically on such factors as the proximity to spontaneous bursting, the number and thickness of the diaphragms, and even the immediate pre-history of the diaphragm material. The ***nil-reaction*** temperature selected to characterize the strength of the shock is obtained assuming complete rotational and vibrational relaxation but no chemical reaction. The simple computer program which performs these calculations also allows for the introduction of an additional contribution to the total energy, when required.

RESULTS AND DISCUSSION

The first feature of note is that there is no evidence of coupling at low shock strengths but as the shock strength is raised the onset of coupling is quite rapid. The value of the nil-reaction temperature at which this occurs, termed the ***coupling temperature*** T_c, can be determined to ± 10° without difficulty. A previous paper[1] has shown that the value of T_c depends on the chemical nature of the reactants, the composition and the pressure. For hydrogen-oxygen-argon systems, the current work shows that T_c can be related to the composition by

$$T_c = (10.95 \text{ kcal}/R) \times \ln (1.19 \times 10^{-6} [H_2]^{-\frac{1}{2}} [O_2]^{-\frac{1}{2}})$$

where concentrations are expressed in moles/litre.

Above T_c, three regions of behaviour can be identified:-

(i) At high mixture strengths/pressures, an increase in shock strength leads to a rapidly-accelerating shock wave and at temperatures greater than $T_c + 50^{\circ}$, the shock wave has stabilized at a velocity close to the theoretical value for a one-dimensional Chapman-Jouguet detonation. This behaviour is illustrated in Figure 2.

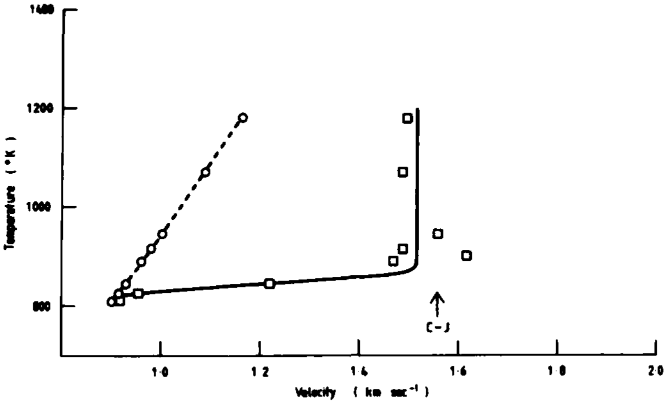

a) mean velocities

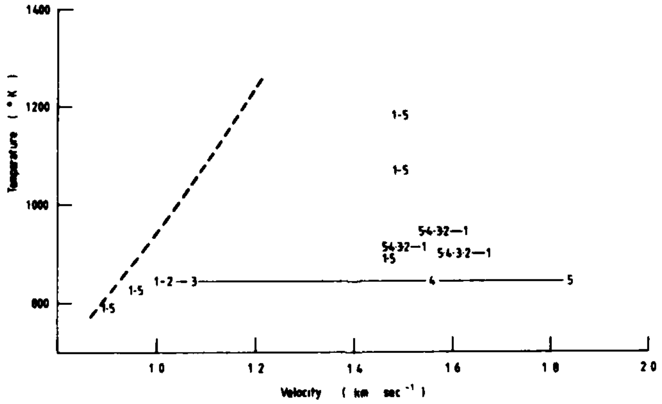

b) sequential velocities

Figure 2. Dependence of shock velocity on *nil-reaction* temperature for 25%($2H_2$ + O_2) in Ar at 50 torr pressure.

(ii) With weak mixtures/low pressures, the shock velocity soon settles down at a value higher than that predicted in the absence of reaction but well below the C-J velocity. As the shock strength is increased, the velocity increment remains roughly constant even through the C-J value. The shock velocity shows small fluctuations about the mean value but no regularity can be detected. A typical example of this behaviour is shown in Figure 3.

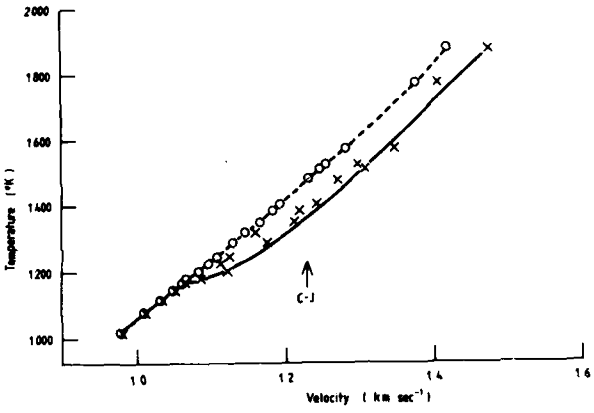

a) mean velocities

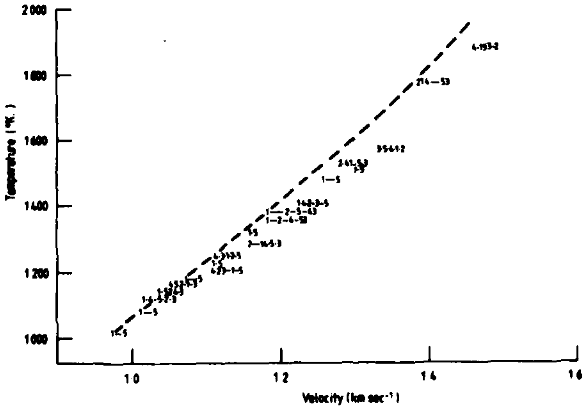

b) sequential velocities

Figure 3. Dependence of shock velocity on *nil-reaction* temperature for 10%($2H_2 + O_2$) in Ar at 10 torr.

This form of coupling between the reaction exothermicity and the shock wave to give a *chemically enhanced shock wave* has received little mention in the literature.

(iii) Between the two limiting cases, the situation becomes rather less clear-cut. A plot of mean velocities still indicates a distinction between the chemically-enhanced wave and the detonation. However examination of the individual velocity records shows that the shock velocity makes quite wide excursions from the mean, in the case of the chemically-enhanced wave often approaching the theoretical value. An example of this transitional behaviour is shown in Figure 4.

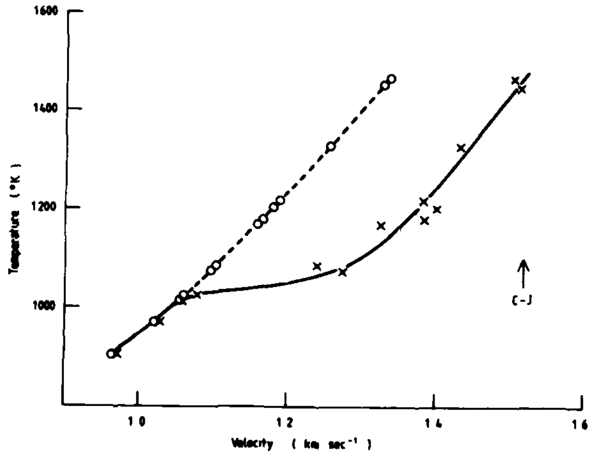

a) mean velocities

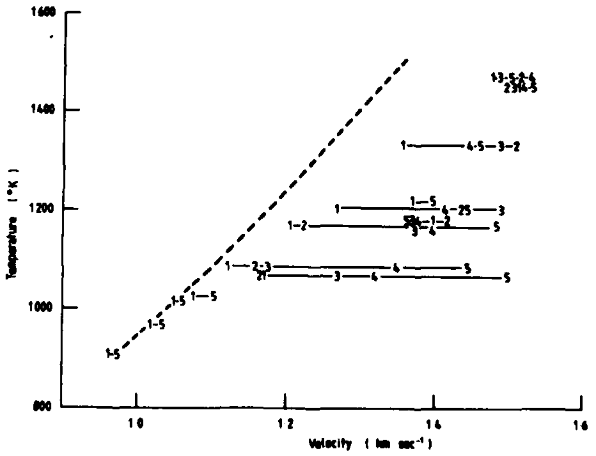

b) sequential velocities

Figure 4. Dependence of shock velocity on nil-reaction temperature for 25%($2H_2 + O_2$) to Ar at 10 torr pressure

Measurements of the induction delay show the expected exponential dependence on temperature. If the nil-reaction temperature is used, the delays observed above the onset of coupling are markedly shorter than expected, particularly in the case of detonation. However, the use of a nil-reaction temperature calculated from the measured velocity allows all the data points to be described by a single relationship.

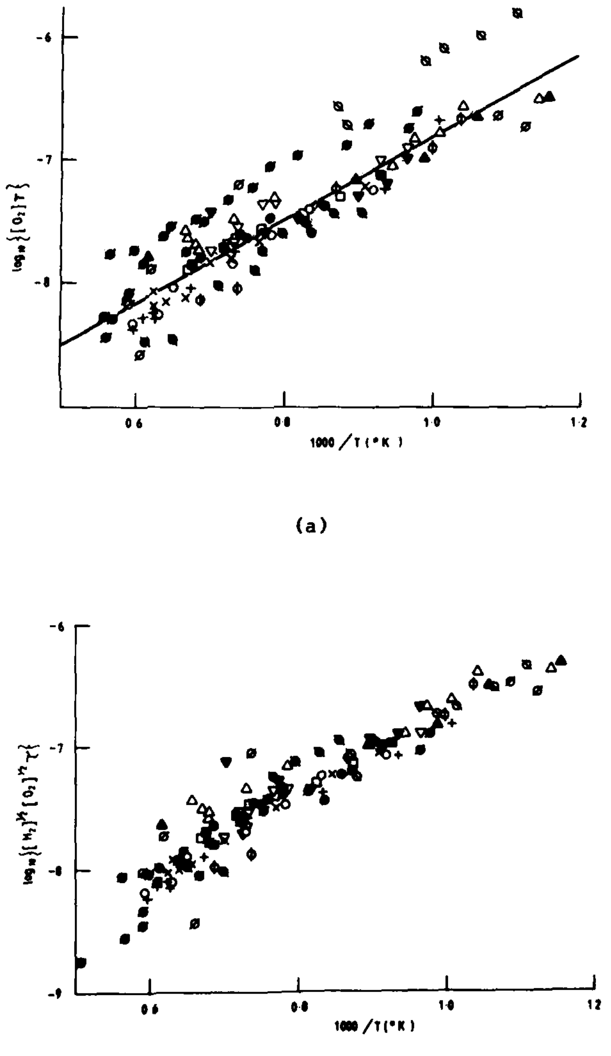

(a)

(b)

Figure 5. Plots of log (concentration x induction time) versus reciprocal temperature. The line in Figure 5a represents Schott's relationship.

Figure 5a shows that the results are in excellent agreement with Schott's relationship[2] but Figure 5b demonstrates that a dependence on $[H_2]^{\frac{1}{2}}$ $[O_2]^{\frac{1}{2}}$ is more satisfactory and leads to

$$\tau = 7.39 \times 10^{-11} \exp(15.7 \text{ kcal}/RT)\ [H_2]^{-\frac{1}{2}}[O_2]^{-\frac{1}{2}} \text{ sec}$$

This relationship can be used to show that the onset of coupling, as defined by the coupling temperature T_c, corresponds to the case when a pressure wave, originating from the contact surface at the termination of the induction period, coincides with the shock wave at the first detector (Figure 6). The observations therefore provide very convincing support for the general picture of coupling between energy release and shock propagation. It is perhaps surprising that the maximum attainable effect of the reaction exothermicity is observed so soon after the first onset of coupling and that the position of the contact surface, where reaction first occurs, coincides with predictions based on ideal shock tube behaviour.

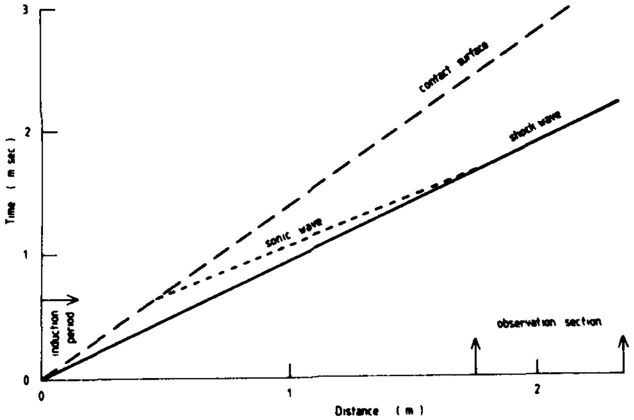

Figure 6. x,t plot for wave behaviour in for 10%($2H_2$ + O_2) in Ar at 10 torr

A more interesting aspect of the work concerns the reaction-enhanced shock wave. The results illustrated in Figure 3 and those on other weak mixtures show that the question of whether an enhanced shock or a detonation occurs is not significantly influenced by the strength of the initial shock and at high temperature, when the induction delay is short, an enhanced wave can still occur. Calculations show that only 20 per cent of the available energy is involved in the enhancement of the shock velocity.

ACKNOWLEDGEMENT

The authors wish to express their gratitude to Dr. D. H. Edwards for his many helpful comments and advice and Dr. D. C. Bull for performing the detonation calculations.

REFERENCES

1. J. N. Bradley, W. D. Capey and F. Farajii, Archive of Thermodynamics and Combustion, Warsaw, vol. 1 (1979).
2. G. L. Schott and J. H. Kinsey, J. Chem. Phys. 29, 1177 (1958).

A SPECTROSCOPIC TEMPERATURE MEASUREMENT OF CONVERGING DETONATIONS

TADAYOSHI SUGIMURA

Department of Transport Machine Engineering, Meijo University, Nagoya, Japan

TOSHITAKA FUJIWARA

Department of Aeronautical Engineering, Nagoya University, Nagoya, Japan

In view of obtaining a high-temperature plasmas, and application to a high-power gasdynamic pulse laser, several experimental investigations have been reported on converging gaseous detonations. In the present experiment, the emission of CN violet band from the converging point was analyzed using a microdensitometer. In order to determine the temperature at the converging point of a detonation, a method of matching the entire emission spectra was utilized. A combination of the gasdynamic quantities (temperature, number density of CN molecules, and Lorentian broadening width) can theoretically provide the anticipated emission spectra of the observed band, assuming Boltzmann distributions for rotational, vibrational and electronic energy levels. After several trial-and-error processes, the best fit was obtained for $T \simeq 11{,}000$ K, $N \simeq 7.5 \times 10^{16}$/cc, and the Lorentian broadening width $W_{\ell} = 0.03$ A: The detonation was produced using equimolar oxyacetylene mixtures at $P_1 = 60$ Torr and $T_1 =$ room temperature in a 80-cm-dia. double-disc-type detonation chamber with 3∿13 mm channel depth. It was found, as a result, that unavoidable doppler broadening inherent to high temperature experiments and a wide slit function could be handled with no essential difficulty and a correct rotational/vibrational temperature could be obtained.

INTRODUCTION

The experimental investigations of converging gaseous detonations have been aimed at establishing very high temperature plasmas or very high pressures from the viewpoint of imploding shock wave theory, or, more recently, applications to high-power gasdynamic pulse lasers. The present authors have been engaged in measuring the rotational temperatures[3,4] at the collapsing center of converging detonation waves using the multi-line method. Although the multiline method was rather simple, the associated disadvantages have already been pointed out: The effects of line overlapping caused by Doppler broadenings due to the high temperature, anticipated pressure broadenings, self-absorption due to the large path length (3 mm at about 60 atm), and instrumental broadenings by wide slit functions (even when a 0.42 A slit was used, five-shot exposure was necessary to obtain sufficient light amount).

In the present investigation, such effects turn out to be not obscuring any more in yielding a temperature as correctly as possible. Instead, each rotational line profile partaining to a particular band was theoretically calculated taking account of the above-mentioned broadenings and self-absorption, and was added up to provide an entire band profile, which was compared with the observed band spectra. Searching of the associated parameters including the temperature of the emitting gas was performed until the best fit was obtained between the observed and calculated band spectra.

EXPERIMENTS

A schematic diagram of the experimental apparatus along with the measurement equipments is illustrated in Fig.1. Prior to the experiment, the entire system is evacuated down to below 0.3 Torr and then the test section is filled with an equi-molar oxyacetylene mixture at P_1 = 60 Torr and T_1 = 300 K. In the pre-run tube with 10 mm i.d. and 450 mm length the detonation is initiated by the discharge at an automobile spark plug using an ignition coil. The detonation propagates vertically upwards, and then enters into the diverging section (800 mm dia. and 12.9 mm depth) of the double-disc type chamber. Following the passage through the smoothly-shaped annular corner, converging starts and ends up in the constant-depth (3 mm) cylinder of 122 mm radius.

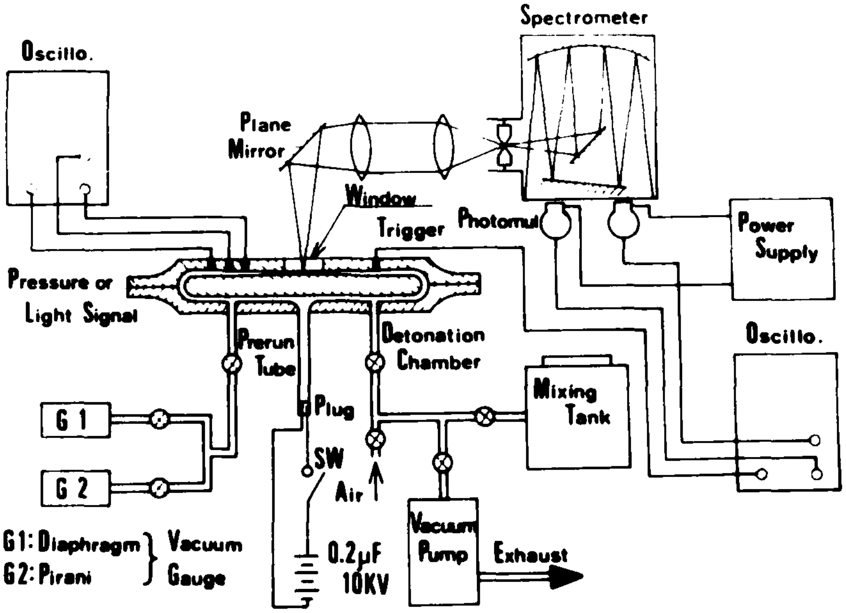

Fig.1. Schematic diagram of experimental apparatus and measuring system. The detonation chamber is of double-disc type having 80 cm dia. and 3 mm channel width within 244 mm dia. in the converging section.

The detonation collapse was reproduced within 1 mm dia. at the geometrical center of the chamber, where a quartz window of 16 mm dia. was allocated for observation. The emission during the collapsing process from the 4 mm dia. center region was introduced into the entrance slit (50 ∿ 200 μ) of a Shimazu GE-100 spectrometer (f = 100 cm, grating 1200 groove/mm, dispersion 120μ/A) and was photographed on a Kodak TRI-X400 film.

In addition, several pressure transducers (Toyoda PMS-5M, and 8M; 80 ∿ 100 KHz, 5 ∿ 8 mm ϕ) were mounted along the passage of converging detonations to elucidate monitoring of the unsteady propagation velocity as well as the highest pressure realized at the instant of collapse.

RESULTS AND DISCUSSIONS

Photometrical monitoring of OH emission spectra from the collapsing center, typically shown in Fig.2, shows a few microsec rise time corresponding to the establishment of a high temperature and pressure, followed by steep decay taking place in less than 10 microsec caused by the cylindrical expansion. Therefore, it was assumed that the recording of the emission spectrum on the film was performed by the radiation produced at the instant of highest temperature. This could also be justified by the strong dependence of radiation on temperature. In view of the wavelength resolution, the entrance slit width of the spectrometer was selected as 50 μ (0.42 A) typically, necessitating five-shot exposure and increased-sensitivity development of TRI-X400 up to about ASA 2500 to obtain a spectroscopic photograph.

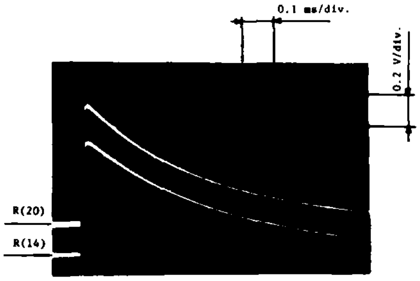

Fig.2. Oscillogram of OH emission from the point of detonation collapse. R_2 branch of OH A $^2\Sigma$- X $^2\Pi$(0,0) band system was observed. Slit widths; 50μ (entrance) and 100 μ (exit), mixture; C_2H_2+O_2 at P_1 = 60 Torr and T_1 = 300 K, photomul.; RCA-1P28.

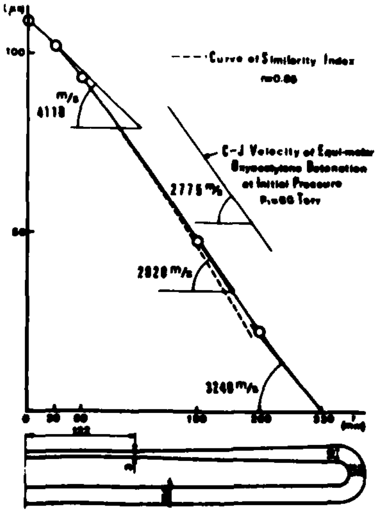

Fig.3. Distance-time diagram of converging detonation. Mixture gas; C_2H_2+O_2, initial pressure; P_1 = 60 Torr, t; time (microsec), r; distance from center of detonation chamber (mm), open circles; observation by pressure transducer.

The pressure transducer records revealed, as shown in Fig.3, that immediately after the entrance into the converging section the detonation accelerated to an overdriven state as a result of re-establishment of the front, then decelerated down close to the C-J velocity 2,775 m/s at P_1 = 60 Torr, and again started accelerating up to 4,110 m/s in the close vicinity of collapsing center. This converging process showed a good agreement with a cylindrically converging shock wave, which was analyzed by Guderley, in a gas with the adiabatic index $\gamma = 1.28$ and yielded the similarity index $n = 0.85$.

Fig.4 shows an emission spectrogram from the point of detonation collapse. As pointed out by Huni[2], the CN violet emission was the strongest among various observed bands in equi-molar oxyacetylene detonations. Although nitrogen was not artificially given to the oxyacetylene mixture, the initially insufficient vacuum contributed as a source of nitrogen to form CN rather in abundance. Although the emission OH A $^2\Sigma$ - X $^2\Pi$ (0,0) band system is not strong enough to appear in Fig.4, it is well within the performance of the photomultiplier, as shown in Fig.2. In the case of acetylene concentration less than 50 %, it would be preferable to observe OH or CH emissions. The emission spectrogram shown in Fig.5 gives CN violet band systems in more detail, by using a 50μ width slit.

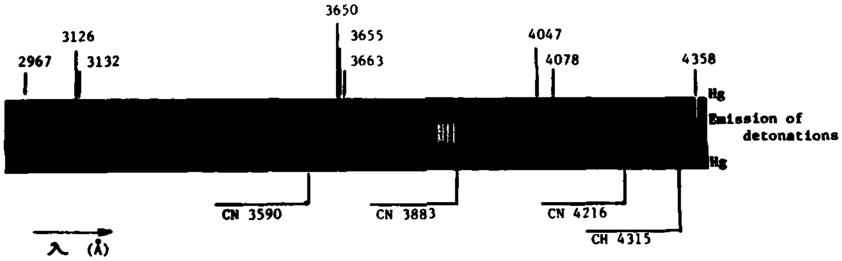

Fig.4. Emission spectrogram from the point of detonation collapse. Entrance slit of spectrometer; 200μ x 6 mm, mixture; C_2H_2+O_2 at 60 Torr, number of superpositions; 5, film; TRI-X400.

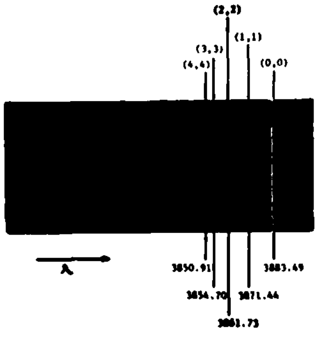

Fig.5. Emission spectrogram of CN violet B $^2\Sigma$ - X $^2\Sigma$ (0,0) ∿ (4,4) band system. Entrance slit of spectrometer; 50 μ x 6 mm, mixture; C_2H_2+O_2 at 60 Torr, number of superpositions; 5, film; TRI-X400.

A typical example of the microdensitometer trace shown in Fig.6 indicates the emission of CN B $^2\Sigma$ - X $^2\Sigma$ (0,0) ∿ (4,4) bands (P and R branches) for the following case: Initial pressure P_1 = 60 Torr, initial temperature T_1 = 300 K, slit width 50 μ (0.42 A), and channel depth 3 mm.

A theoretical calculation of th emission spectra using the identical values for the thickness of radiating layer 3 mm and the rectangular slit function of width 0.42 A was carried out, assuming a Voigt profile for each rotational line taking account of Gaussian Doppler and Lorentian pressure broadenings. The number density of the radiator CN, the rotational/vibrational/electronic temperature and the Lorentian broadening width were adjusted to provide the closest fit between the observed and calculated spectra. A typical example of the calculated spectra is shown in Fig.7. It is noted that in the CN violet B $^2\Sigma$ - X $^2\Sigma$ transition the main bands degrade toward shorter wavelength while the tail bands toward longer. Thus, in principle, the wavelength range of interest λ = 3801 ∿ 3885 A is influenced by the main bands located on the longer wavelength side and the tail bands on the shorter. However, it was confirmed that such effects were negligibly small in the present temperature range, since the bands were distant from the range of interest and had small Franck-Condon factors.

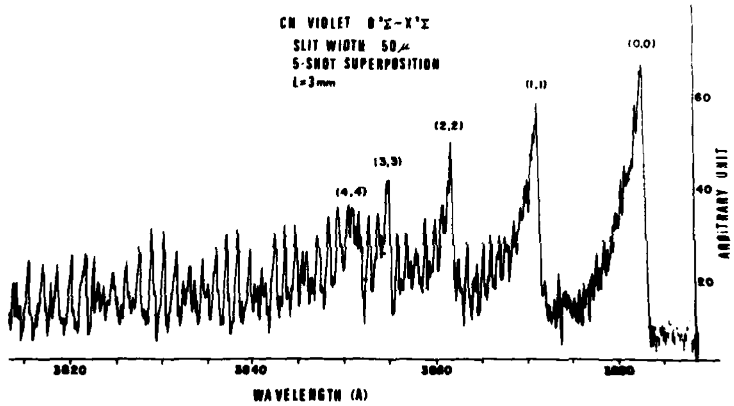

Fig.6. Densitogram of CN violet emission from the point of detonation collapse.
Entrance slit of spectrometer; 50 μ x 6 mm, mixture; C_2H_2+O_2 at 60 Torr and 300 K, number of superpositions; 5, depth of gas layer; 3 mm.

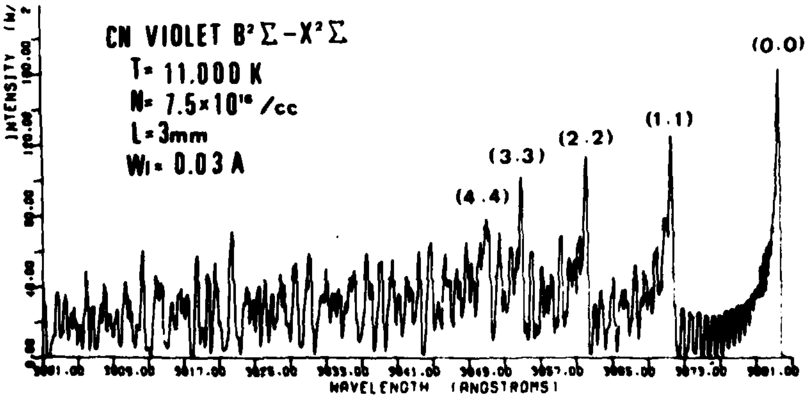

Fig.7. Computer simulation of CN violet emission: Synthetic spectra. N; number density of radiator CN, L; thickness of radiating layer = 3 mm, W_{ℓ} ; pressure broadening half width.

Regarding the pressure broadening, anticipated strong effects due to the high pressure $P \simeq 60$ atm were considerably compensated by the high temperature, yielding $W_\ell \simeq 0.03$ A which could virtually be approximated zero in comparison with the other broadenings (Doppler 0.05 A at 10,000 K). As shown in Fig.7 and other unlisted synthetic spectra, however, a finite pressure broadening ~ 0.03 A provided a microscopically closer fit with the observed one. The effect of the number density N of the radiator was straightforward: Increasing it gave rise to stronger emission and increased absorption and, as a result, relative intensity of each rotational line became closer to unity providing nearly continuous emissions. Incidentally, the number density $N = 7.5 \times 10^{16}$/cc which gave a close fit between Figs.6 and 7 was of the order of the number of nitrogen atoms assuming that the initial nitrogen molecules as impurity existed entirely in the form of CN at P = 60 atm and T = 11,000 K. The influence of the temperature was two-fold: Through the Boltzmann distribution in energy levels and the Doppler broadening width. Since the Boltzmann distribution was assumed in rotational, vibrational and electronic levels, a higher temperature produced a more flattened spectral distribution with a larger broadening.

As a result of searching, it was found that the closest fit could be obtained by setting T (rotational, vibrational and electronic) = 10,000 $\sim$ 13,000 K, $N = (0.75 \sim 1.5) \times 10^{17}$/cc, and $W_\ell \leq 0.03$ A. A more careful comparison between Fig.6 and numerous synthetic spectra reveals that the line locations had to be adjusted more accurately by positioning each band origin more appropriately. As a result, further fitting in the more detailed part of the spectra was realized by setting T = 11,000 K, $N = 7.5 \times 10^{16}$/cc and $W_\ell = 0.03$ A.

It may be noteworthy, however, that there are essentially two more parameters included in real experiments. First, the assumption of thermal equilibrium, i.e., use of the same rotational, vibrational and electronic temperatures can be questioned. Using a different vibrational temperature may be necessary in such a process of short time (< 10 μsec). Second, since the temperature and the number density of the radiator and, as a result, the emission from the collapsing center are strong functions of time, the microdensitogram illustrated in Fig.6 is in fact the integrated intensity during such a nonsteady process. However, if such nonsteady effects have to be taken into account, simultaneous use of photometrical measurements based upon the two-line method and theoretical calculation of emission spectra seems simpler and preferable.

REFERENCES

1. R. Knystautas, B.H.K. Lee and J.H. Lee, Phys. Fluids 12, I-165 (1969).
2. J.R. Huni, Ph.D.Thesis, Univ. British Columbia (1970).
3. T. Fujiwara, S. Taki and T. Sugimura, Acta Astronautica, 1, 7/8 (1974).
4. T. Sugimura, K. Hayashi and T. Fujiwara, AIAA PAPER 76-130 (1976).
5. E.E. Whiting, J.O. Arnold and G.C. Lyle, NASA TN-D5088 (1969).
6. C. Park and T. Fujiwara, Proc. 11th Intern. Shock Tube Symp. 148 (1977).

ON THE DETONATION OF UNCONFINED ALUMINUM PARTICLES DISPERSED IN AIR

ALLEN J. TULIS

IIT Research Institute
Chicago, Illinois 60616, USA

The unconfined detonation of aluminum particles dispersed in air and the mechanism whereby such detonation is achieved were investigated. Experiments were conducted using linear aluminum-air clouds produced by the shock-dissemination method. Attempts to detonate unconfined spherical atomized aluminum dispersed in air failed. The particles were too large. Attempts to detonate unconfined but highly fuel-rich flake aluminum particles dispersed in air resulted in rapid decay of an initiated 600 m/sec detonation wave. Attempts to detonate unconfined near-stoichiometric flake aluminum particles dispersed in air were successful and resulted in a detonation velocity propagating at about 1900 m/sec. It was determined that initiation was critical and required matching the incident shock from the initiation source to the aluminum-air detonation velocity. It is concluded that the detonation of unconfined aluminum powder dispersed in air requires (1) a sufficiently large surface-to-mass ratio, (2) near-stoichiometric concentration, and (3) an initiation shock velocity slightly greater than the Chapman-Jouguet detonation velocity of the aluminum-air cloud. We were not able to achieve detonation in unconfined aluminum-air dispersions by ignition means other than sufficiently strong shock waves. The aluminum flake powder used had a surface-to-mass ratio of 3 to 4 m^2/g. The detonation velocity that we observed is remarkably close to the shock strength needed to obtain a sufficiently high temperature in the compressed convective flow region behind the shock wave to melt the aluminum oxide coating that invariably exists on aluminum.

INTRODUCTION

Although the detonation of gaseous and condensed single-phase systems has been known and extensively studied for over a century, the detonation of two-phase systems has gained attention only relatively recently. In the early 1950s studies reported upon the confined detonation of liquid aerosols[1] and liquid films[2] in an oxidizing gaseous environment. The early 1960s saw the appearance of systematic shock-tube studies of the detonation mechanism of two-phase liquid fuels in gaseous oxidizers.[3] It was not until the late 1960s that the unconfined detonation of two-phase systems was achieved and became the subject of intense investigations. Since then much has been learned about the physical and chemical mechanisms involved in the detonation of unconfined two-phase liquid-fuel-in-air systems, referred to as fuel-air explosives (FAE). Little progress has been made, however, in achieving detonation with other than a few select liquid fuels.

More recently, interest in FAE technology has centered on the unconfined detonation of solid fuel particles dispersed in air, particularly aluminum particles. The detonation of confined two-phase aluminum particles dispersed in oxygen was reported in 1968.[4] Strong, but not conclusive, evidence for the detonation of aluminum particles in air in shock-tube experiments was reported in 1975.[5] The unconfined detonation of aluminum particles dispersed in air, however, has not been reported in the open literature. It is the purpose of this paper to report the results of experiments in which the unconfined detonation of aluminum particles dispersed in air was achieved and, furthermore, to consider the mechanism whereby such detonation was achieved.

HETEROGENEOUS DETONATION

Certain criteria for heterogeneous two-phase detonation are manifest, whether the fuel particles are a liquid or a solid. The primary criteria is that the concentration of fuel in oxidizer be correct, which generally implies a near-stoichiometric concentration. The second criteria is that the fuel particles be sufficiently small, or more correctly of sufficiently large surface-to-mass ratio, so that chemical reaction can take place within the time frame of the Chapman-Jouguet zone of the detonation. Although important and perhaps influencing under some constraints,[6] fuel vaporization is not considered a necessary event for two-phase heterogeneous detonation and may in fact preclude detonation.[7]

The detonation of unconfined two-phase liquid-fuel-in-air dispersions is a unique combination of physical and chemical mechanisms and has been postulated to occur as follows.

The liquid fuel is initially dispersed in air to form an aerosol, the requisite two-phase fuel dispersed in air. This is generally achieved very quickly; i.e., in a fraction of a second, by using explosive central burster dissemination. The resultant two-phase cloud that is formed is not homogeneous and the droplet sizes vary by many orders of magnitude. If ignited in this state, with a spark, flame, or thermal source, the fuel will deflagrate and result in a huge fireball. A major reason why detonation does not occur is that the droplets are too large. It has been estimated that in order to react sufficiently fast for a detonation to propagate the droplets would have to be smaller than 10 μm.[8] There are, certainly, droplets smaller than 10 μm formed, but they vaporize very rapidly. Such premature vaporization has been postulated[9] and demonstrated[7] to be detrimental to the heterogeneous detonation mechanism requisite for two-phase detonation.

In order to detonate such two-phase fuel dispersed in air, use is made of so-called second-event (SE) explosives. These SE explosives are propelled into the fuel-air cloud, at an appropriate time and location, and detonated. The resultant shock wave shatters the larger liquid droplets, as it systematically passes over them, forming a micromist of particles in the wake of each droplet. This orders-of-magnitude reduction in particle size results in a sufficiently large surface-to-mass ratio to allow the propagation of a detonation. The mechanism of this detonation is by the adiabatic heating of the micromist droplets to temperatures wherein the autoignition induction time is less than the transit time of the compression wave. The adiabatic heating is also accompanied by high pressure within the compression wave. It is this author's opinion that this high pressure is also needed as it prevents flash vaporization of the micromist particles, a process that would preclude detonation.[7]

In the detonation of unconfined solid fuel particles dispersed in air, particularly metals such as aluminum, entirely different mechanistic concepts must be considered. For instance, the solid particles are preformed and will not shatter or strip into micromist particles as in the case of liquid fuels. After the initial dissemination of a solid particle aerosol the solid particles can be considered stationary. Therefore, if detonation is to proceed, the solid particles must be sufficiently small (have a large surface-to-mass ratio) and be dispersed in a satisfactory concentration in air.

Satisfaction of the above two criteria of surface-to-mass ratio and concentration, although being a necessary condition, is evidently not a sufficient condition for the detonation of unconfined aluminum powder dispersed in air. Shock wave energy of substantial magnitude is also necessary. The convective gaseous flow behind a shock wave, however, makes the detonation of unconfined aluminum and other solid microparticles of fuel dispersed in air difficult to initiate. Calculations show that momentum imparted to microparticles by the convective gas flow behind an attenuating shock wave enables the microparticles to eventually attain a velocity greater than that of the local convective gas flow. Hence these particles cannot be assumed to be without inertia. It is the distribution of particles in the region behind the shock waves, whether of spherical, cylindrical, or planar geometry, that becomes paramount in achieving or precluding detonation in unconfined solid fuel particles dispersed in air by shock waves.

The state behind a shock wave can be calculated by the following equations:

$$\text{pressure:} \quad P_s = P_o(7M_s{}^2-1)/6 \qquad \text{I}$$

$$\text{density:} \quad \rho_s = \rho_o(6M_s{}^2)/(5+M_s{}^2) \qquad \text{II}$$

$$\text{velocity:} \quad V_s = a_o\ 5(M_s{}^2-1)/6M_s \qquad \text{III}$$

where:

subscript o is the state ahead of the shock wave
subscript s is the state behind the shock wave
a is the sonic velocity in the undisturbed gas
M_s is the shock Mach number.

Assuming standard conditions ahead of the shock wave and the standard equation of state, Table I illustrates conditions behind the shock wave at various shock velocities. (Sonic velocity of 330 m/sec was assumed for these calculations.)

Table I. Conditions Behind a Shock Wave Propagating in Ambient Air at Standard Conditions

M_s	D* m/sec	P at	T_s °K	$\frac{\rho_s}{\rho_o}$	V_s m/sec
1	330	1.0	298	1.0	0
2	660	4.5	497	2.7	412
3	990	10.3	787	3.9	783
4	1320	18.5	1198	4.6	1031
5	1650	29.0	1728	5.0	1320
6	1980	41.8	2350	6.3	1604
7	2310	57.0	3146	5.4	1886
8	2640	74.5	3964	5.6	2166
9	2970	94.3	4930	5.7	2444
10	3300	116.4	6091	5.7	2722

*D is the shock wave velocity, or the detonation velocity when present

Studies on the relaxation distance of powder particles behind shock waves have demonstrated the dramatic effect of particle size. Typical relaxation distances of 1 m for 50 μm particles and of a few cm for 10 μm particles have been reported.[10] This assumes spherical particles. As mass is reduced and geometry changes from a sphere to a flat plate - as in the case of flake aluminum - the relaxation distance approaches zero; i.e., the particles acquire the convective flow velocity instantly. Figure 1 illustrates the distribution of dust particles when subjected to a spherical blast wave. Initially homogeneous, the particles affected are shown to be accumulated directly behind the attenuating shock wave leaving an inner dust-free core of gas. The conclusion has been made[11] that there is nearly always a velocity lag between the dust particles and the gas flow. Hence, unless a steady-state shock wave is propagating; i.e., Chapman-Jouguet detonation, the dust-particle-to-gas concentration will be altered, often dramatically.

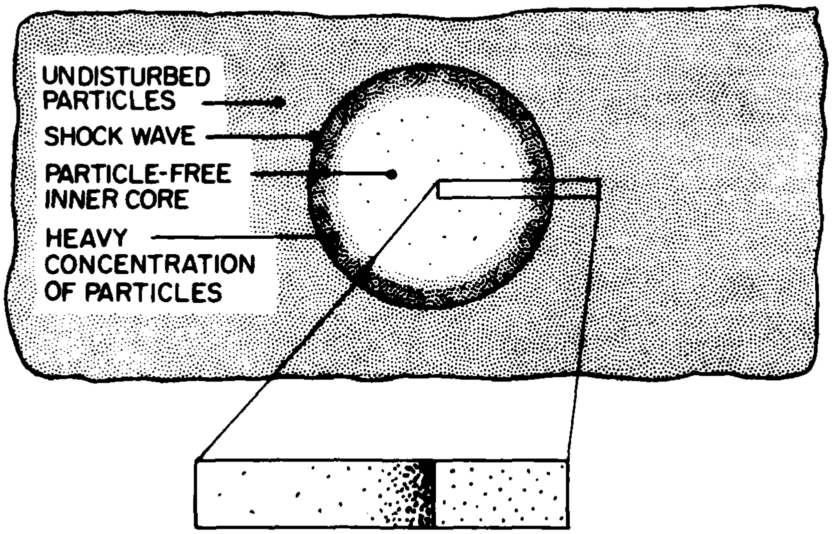

Figure 1. Eff‿ ‿ of a strong shock wave on redistribution of solid microparticles homogeneously dispersed in air.

It is our contention that this disproportionate redistribution of solid particles in the air medium is the major cause of detonation propagation failure in the case of unconfined aluminum particles dispersed in air - as well as most other solid-fuel dispersals in air - when initiation is attempted with the use of high explosives. When such SE high explosives are detonated in a near-stoichiometric aluminum powder dispersal in air, the result is a shock wave and associated convective gas velocity that is 4 to 5 times greater than the expected detonation velocity of the aluminum-air system. The resultant shock wave and its attendant convective gas flow, to be sure, will rapidly degrade to sonic velocity - but it would be most fortuitous that adequate coupling between the incipient flame front and the diverging and attenuating shock wave could be achieved. It is believed that this extensive overdrive causes too severe a depletion of fuel particles in the zone where the flame front is required for appropriate coupling to the shock front, and an excessive concentration of fuel particles in the compression wave, where detonation propagation would need be sustained. Our approach, then, was to attempt to match the initiation characteristics of the SE to that of the expected detonation characteristics of the aluminum-air system. Inadequate SE energy, on the other hand, would also result in failure because the aluminum particles would not be heated to autoignition temperatures within the time frame of the detonation.

COMBUSTION OF ALUMINUM

The combustion of aluminum particles in air and other oxidizing gases has some unique characteristics that have to date prevented comprehensive understanding of the mechanisms involved. The primary factor is the oxide film that invariably forms on the aluminum surface whenever exposed to oxygen. This alumina film, Al_2O_3, melts at 2318°K compared to the 923°K melting point of aluminum itself. Early investigations[12,13] established that a prerequisite for combustion was a sufficiently high temperature to melt the alumina film. Later studies[14] proved that ignition could be achieved at temperatures substantially below the alumina melting temperature. Other researchers have investigated the ignition mechanism of aluminum oxidation and have identified numerous conditional factors for ignition such as film abrasion and cracking, aluminum vapor diffusion through the alumina film, changes in film crystalline structure, and aluminum particle explosion. Although we are investigating these, and other, factors regarding their influence on the mechanism of unconfined aluminum powder detonation when dispersed in air, this work has not been completed. Publication of these results is anticipated in the near future.

Table II lists the results of IITRI's EQUIL chemical equilibrium computer program for the detonation of various aluminum powder concentrations in dry air. Based on a product of alumina only, the stoichiometric concentration of aluminum in air would be 331 mg/l.

Table II. Aluminum-Air Equilibrium Calculations

C_{Al} mg/l	T_{CJ} °K	P_{CJ} psi	Weight Percent Products											
			Al^l	Al^g	$Al_2O_3^s$	$Al_2O_3^l$	Al_2O	AlO	AlO_2	N_2	O_2	NO	N	O
50	1673	167	0.00	0.00	7.14	0.00	0.00	0.00	0.00	73.86	18.81	0.18	0.00	0.00
100	2450	242	0.00	0.00	0.00	13.77	0.00	0.00	0.00	70.51	14.07	1.58	0.00	0.07
150	3120	300	0.00	0.00	0.00	19.92	0.00	0.00	0.00	67.27	8.96	3.15	0.00	0.68
200	3666	344	0.00	0.02	0.00	25.54	0.01	0.03	0.04	64.78	4.30	3.48	0.00	1.79
250	3993	372	0.00	0.58	0.00	28.72	0.46	0.23	0.32	62.92	1.85	2.77	0.02	2.14
300	4082	384	0.00	1.63	0.00	29.45	1.79	0.36	0.50	61.16	1.05	2.15	0.02	1.84
331*	4101	388	0.00	2.30	0.00	29.60	2.82	0.40	0.55	60.10	0.77	1.84	0.02	1.61
350	4108	391	0.00	2.76	0.00	29.69	3.37	0.40	0.55	59.48	0.63	1.65	0.02	1.46
400	4102	396	0.00	3.81	0.00	29.50	5.21	0.38	0.52	57.87	0.37	1.23	0.02	1.09
700	3021	350	0.04	18.65	0.00	31.71	0.00	0.00	0.00	49.58	0.00	0.00	0.00	0.00
1000	2948	319	17.01	12.42	0.00	27.54	0.00	0.00	0.00	43.04	0.00	0.00	0.00	0.00
2000	2620	234	48.84	2.15	0.00	19.13	0.00	0.00	0.00	29.89	0.00	0.00	0.00	0.00
3000	2282	192	62.22	0.23	14.65	0.00	0.00	0.00	0.00	22.89	0.00	0.00	0.00	0.00

*Stoichiometric based on Al_2O_3 product

Figure 2 illustrates the Chapman-Jouguet temperature and pressure resulting from the detonation of aluminum powder in air as a function of aluminum concentration. Note the critical effect of the lean limit on temperature compared to the rich limit. Concentrations below the lean limit of about 100 mg/l or above the rich limit of about 2600 mg/l result in a reaction temperature below the melting point of alumina. It is most reasonable to assume that the detonation limits on aluminum concentration would be within this range. This, of course, assumes that the detonation mechanism is similar to the combustion mechanism. Detonation limits are generally considerably narrower than combustion limits.

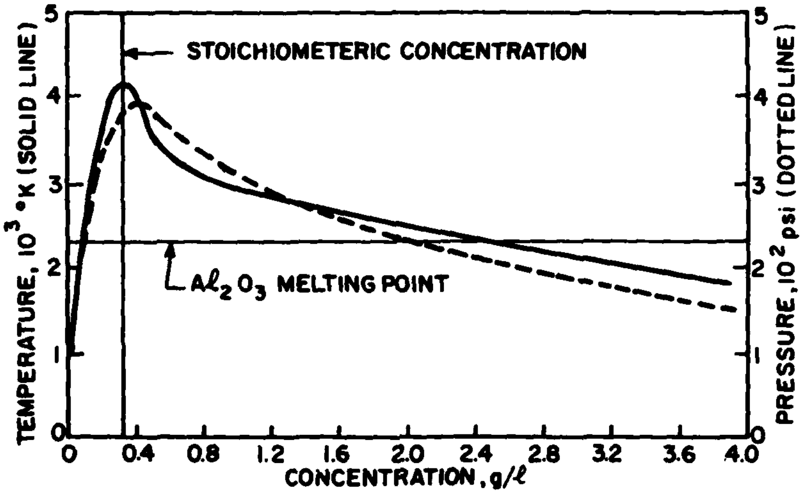

Figure 2. Chapman-Jouguet temperature and pressure for aluminum powder detonation in air as a function of aluminum concentration as determined by IITRI's EQUIL equilibrium code.

EXPERIMENTAL PROCEDURE

FAE experiments generally utilize a central explosive burster charge to disperse liquid or solid particles into an aerosol cloud. This is an expedient and results in a cloud generated in a fraction of a second. It does, however, result in a very inhomogeneous cloud that is additionally contaminated with the products of the explosive charge.

Figure 3 illustrates a diagnostic experimental apparatus we developed for the study of solid particle dispersions in air. As illustrated, a downward dissemination was used for the experiments to be described in this paper. The steel channel was nearly 5 m long and 0.4 m wide so as to provide a linear cloud of adequate length to assess detonation velocity. Prior to dissemination the aluminum powder was held in place on the underside of the steel channel by very thin picture frame glass. Very thin sheet explosive was used to transmit a powderful shock through the steel channel into the aluminum powder while withholding the explosive product gases. Initial experiments determined that a thin plywood attenuator was necessary between the sheet explosive and the steel channel to provide a more uniform shock transfer into the steel channel and hence a more uniform dissemination of the powder. The thick pine slab above the sheet explosive minimized the flame output from the detonation, and in turn largely precluded disturbance of the aluminum powder dissemination process and allowed clearer and more definitive cine coverage.

The shock dispersal velocity of the aluminum powder was about 30 m/sec, surprisingly similar to that obtained in our previous studies on the shock dispersal of liquids.[15] This dispersal velocity is adequately fast to prevent significant effect of wind and gravity on particle fallout. The shock-pulverized glass particles remain but neither affect the dissemination process nor interfere with the subsequent detonation of the aluminum powder.

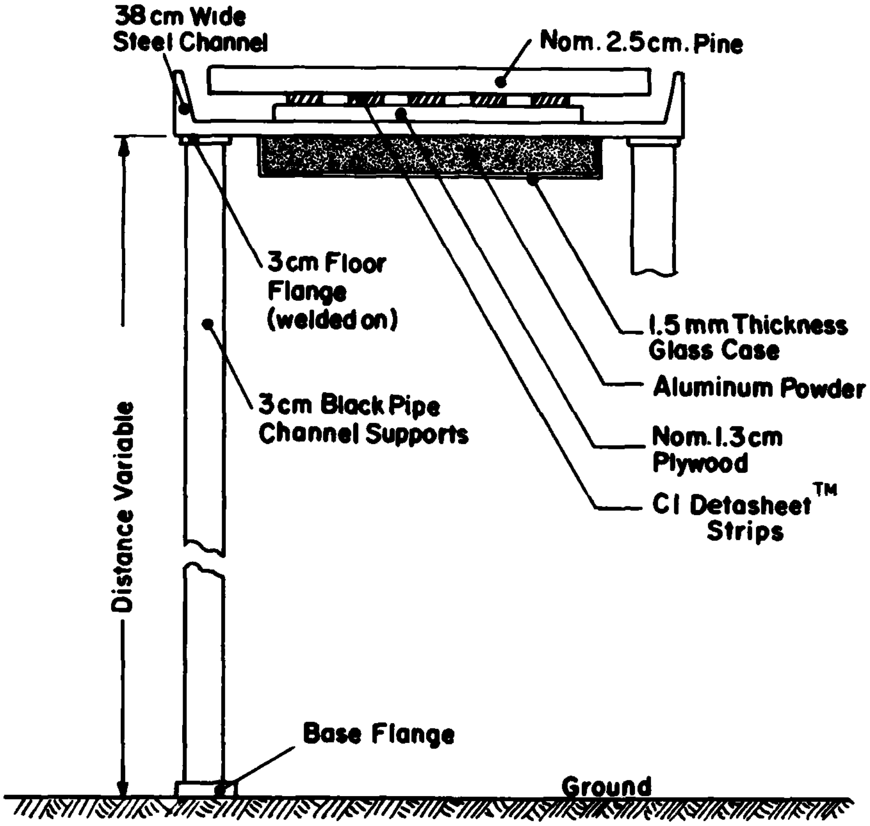

Figure 3. IITRI shock dispersal apparatus for obtaining highly homogeneous aluminum, and other, solid-particle unconfined dispersions in air. (End view of 4.6 m length steel channel. Note: for vertical upward dispersals, the powder does not have to be contained in the glass case.)

(By turning the apparatus upside down, an upward dissemination is achieved which does not require initial containment of the powder.) A typical experiment proceeded as follows (refer to Figures 3 and 4).

(1) Based on the anticipated dissemination cloud size and concentration desired, an appropriate amount of aluminum powder was secured to the underside of the steel channel using thin picture frame glass.

(2) Strips of C1 Detasheet™ explosive were glued to the upper surface of the plywood attenuator, which was then placed on the upper surface of the steel channel. The pine covering slabs were then placed on top of the sheet explosive.

(3) The SE system was secured and the sheet explosive initiator charge was also emplaced.

(4) Upon firing, the sheet explosive transmitted a strong shock through the steel channel into the glass-constrained aluminum powder. The sheet ex-

plosive flame, product gases, and all debris were blown upward from the channel and were prevented from contaminating the aluminum powder-air dispersion, which progressed downward and, with the apparatus utilized, required about 100 msec to achieve complete and relatively uniform dispersal. Figure 4 illustrates the test condition at this point.

(5) The SE system was initiated and, in successful cases, coupled to the aluminum-air aerosol and caused its detonation.

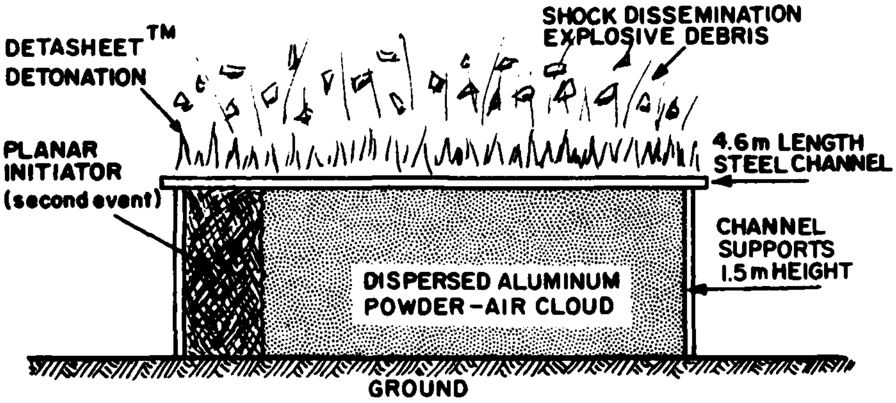

Figure 4. IITRI diagnostic apparatus and technique for dispersing unconfined aluminum into a linear cloud in air and evaluating aluminum-air detonation. (Frontal view.)

Instrumentation consisted chiefly of high-speed Fastax cameras; i.e., framing rates of about 4000 frames/sec, and passive pressure gauges. The sole objective of these experiments was to demonstrate that an unconfined aluminum dispersion in air could detonate. Evidence of such detonation was obtained from the flame front velocity through the aluminum-air cloud and evidence of over-pressure recorded on the passive pressure gauges.

The aluminum powders used in this study were of two general types: (1) atomized aluminum particles of 15 to 25 μm size that were relatively spherical and (2) flake aluminum with a surface area of 3 to 4 m^2/g.

RESULTS AND CONCLUSIONS

The following observations are made from the experiments conducted to date.

(1) Attempts to detonate unconfined spherical atomized aluminum dispersed in air failed. The spherical particles, about 15 to 25 μm, were evidently too large.

(2) Attempts to detonate unconfined but highly fuel-rich flake aluminum particles dispersed in air resulted in a decaying detonation which initiated in the aluminum-air cloud at a detonation velocity of about 600 m/sec before degrading to a deflagration.

(3) An approximately stoichiometric unconfined flake aluminum-air cloud, when properly initiated, achieved a steady propagating detonation velocity of

about 1900 m/sec.

Thus, the detonation of unconfined aluminum powder dispersed in air depends on (1) a sufficiently large surface-to-mass ratio, (2) near stoichiometric concentration, and (3) an initiation shock velocity slightly greater than the Chapman-Jouguet detonation velocity of the aluminum-air cloud. Excessively strong initiation shock waves will distort the aluminum particle distribution and decouple the incipient detonation front from the rapidly decaying incident shock wave. Note that in our experiments we utilized linear aluminum aerosol clouds and planar SE initiation. Other geometries, particularly with a point SE initiation, could be expected to be more complex and difficult to initiate.

To summarize, for a solid-particle FAE, the solid particles have to be of sufficiently small particle size or, as in the case of the flake aluminum, of adequate surface-to-mass ratio. If such particles are dispersed into an appropriate concentration in air, then detonation is feasible. A simple flame or spark ignition, however, will result in a deflagration that may, under some conditions, build up to a detonation. We could not achieve detonation in our experiments with linear aluminum-air clouds about 4 m long unless we used shock wave initiation. Furthermore, very strong shock waves such as those that result from the detonation of condensed high explosives would not produce detonation - at least not directly and in the limited size aluminum-air clouds we investigated.

We did achieve the unconfined detonation of solid aluminum particles dispersed in air by utilizing appropriate SE systems that provided shock wave initiation characteristics close to those of the subsequent aluminum-air detonation. A particularly interesting aspect of this work is that the 1850 to 1950 m/sec detonation velocity is remarkably close to the shock strength needed to obtain a sufficiently high temperature in the compressed region behind the shock wave to melt the alumina film on the aluminum particles. It is not known, at this time, whether this is coincidental or a requirement for the detonation of aluminum particles dispersed in air.

ACKNOWLEDGEMENT

This work was conducted as part of an Internal Research and Development program sponsored by the IIT Research Institute.

REFERENCES

1. J.H. Burgoyne and L. Cohen, Proc. Roy. Soc. A225, 375 (1954).
2. R. Loison, Comptes. Rendus. 234, 512 (1952).
3. F.B. Cramer, Ninth Symp. on Comb., Academic Press, New York, 482 (1963).
4. W.A. Strauss, AIAA J. 6, No. 9, 1753 (1968).
5. P. Lu, W. Ugn, O. Sandus and N. Slagg, Picatinny Arsenal Technical Report 4825, (1975).
6. J.T. Zung, J. of Chem. Physics 46, No. 6, 2064 (1967).
7. A.J. Tulis, Astronautica Acta 17, No. 4,5, 435 (1972).
8. J.H. Burgoyne and O. Cohen, J. Coll. Sci. 8, 364 (1953).
9. M.V. Sullivan, J.K. Wolfe and W.A. Zisman, Ind. and Engr. Chem. 39, 1607 (1947).
10. M. Donato, M.A. Bergeron and J.H. Lee, Shock Tube and Shock Wave Research, University of Washington Press, 459 (1977).
11. N. Gerber and J.M. Bartos, AIAA J. 2, No. 1, 120 (1973).
12. R. Friedman and A. Macek, Combustion and Flame 6, 9 (1962).
13. R. Friedman and A. Macek, Ninth Symp. on Comb., Academic Press, New York, 703 (1963).
14. M.A. Gurevich, E.S. Ozerov and K.I. Lapkina, Fiz. Goreniya Vzryva 6,2(1970).
15. A.J. Tulis, Shock Tube and Shock Wave Research, U. Wash. Press, 91 (1977).

TEMPERATURE MEASUREMENT IN DETONATION WAVES BY USING LIGHT EMISSION FROM SHOCK HEATED ARGON

KUNIO TERAO, KEI IMAMURA and NOBUYOSHI TAKASU

Department of Mechanical Engineering,
Yokohama National University, Yokohama, Japan

The gas temperature in the detonation wave in a stoichiometric propane-oxygen mixture was measured by using the light reversal method in which the light emission from the argon gas heated behind reflected shock waves in a shock tube was used as a light source. The measured gas temperature agrees fairly well with the electron temperature which was measured in the same detonation wave by the laser scattering method. The experimental results suggest that the local temperature in the detonation wave is much higher than the theoretical gasdynamic temperature.

INTRODUCTION

The spectrum line reversal method[1,2] is well known as the most convenient method for measuring a high temperature during a very short time of a few microseconds. It is, however, difficult to establish a stable light source of a temperature higher than 3000 K as required for this method. Most frequently the sodium lines are used for this method, but since sodium is solid at room temperature, it is difficult to mix it with gas and to heat it quickly. Besides, because of its vaporization delay this method does not permit to measure the temperature of gas at non-steady state instantaneously rising from room temperature to more than several thousand degrees.

With the intention of using as a high temperature light source, we investigated the light emission of shock heated argon gas whose temperature can be regulated at an arbitrary value according to the initial shock generating conditions, and applied it to measure the temperature in detonation waves.

In this paper the measuring method and results are reported, and compared with the electron temperature in the same detonation wave which was measured by the laser light scattering method.

TEMPERATURE OF ARGON BEHIND REFLECTED SHOCK WAVES

In order to generate a light source for the reversal method an argon gas of 99.99 % purity was heated behind reflected shock waves in a shock tube of stainless steel having 50 mm inner-diameter and 8 m length. The shock waves were driven by H_e or H_2 gas in a 1 m long tube of high pressure section.

The gas temperature behind the reflected shock waves can be theoretically calculated from the initial state of the gas and the Mach number of the incident shock waves. At first, however, it should be examined if the gas temperature really agrees with the theoretically calculated one. The propagation velocity of the incident shock waves was measured by three piezoelectrical pressure transducers, placed at positions separated from each other by 50 cm distance. The intensity of spectrum lines of the light emitted from the shock heated argon gas was measured by a monochromator through a photomultiplier (R 446 made by Hamamatsu T-V Co.).

In our experiments the incident shock waves having the Mach number of 5.83, 6.39 and 6.93 were investigated. The theoretical temperature behind the reflected shock waves for these three cases are 7 640 K, 9 120 K and 10 700 K, respectively.

The intensity of a spectrum line I_λ at the transition from n-level to m-level at an equilibrium state is expressed as the equation (1)[3],

$$I_\lambda = \frac{hc}{4\pi\lambda} g_n A_{nm} \frac{N(T)}{U(T)} \exp\left(-\frac{E_n}{kT}\right), \tag{1}$$

from which we further obtain the relation

$$\ln\left(\frac{\lambda I_\lambda}{g_n A_{nm}}\right) = -\frac{E_n}{kT} + constant, \tag{2}$$

where h is Planck's constant, c light velocity, λ wave length, g_n statistical weight, A_{nm} transition probability of the line, $N(T)$ gas density, $U(T)$ partition function, E_n energy of the n-level of the line and k Boltzmann's constant. According to the equation (2), the gas temperature T can be estimated from the relation of the intensity I_λ to the energy E_n, if g_n and A_{nm} are known and the intensities corresponding to two or more different spectrum lines in the same gas are obtained.

We measured the intensities of the spectrum lines of 5912.1 Å and that of

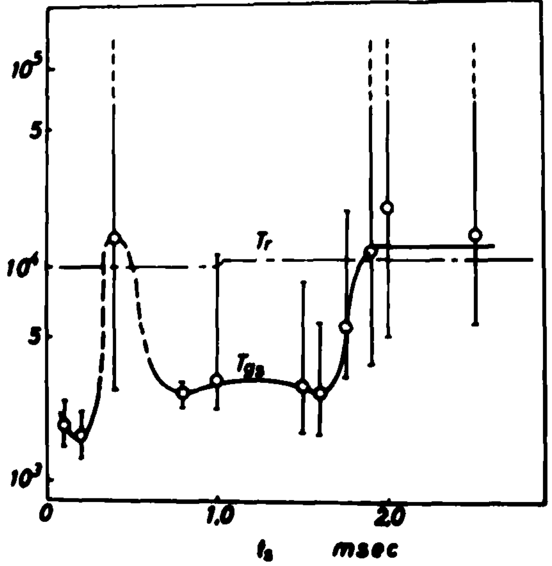

Fig.1. Measured gas temperature T_{gs} and theoretical gasdynamic temperature T_r behind reflected shock waves with respect to the time t_s after the reflected shock front passed the measuring point.

6043.2 Å wave length, whose transition probabilities A_{nm} were $15.24\cdot10^{-5}sec^{-1}$ and $30.6\cdot10^{-5}sec^{-1}$, statistical weight g_n 3 and 7 and energy levels E_n 121011.98 cm^{-1} and 123832.50 cm^{-1}; respectively[4]. We repeated the same measurement more than 5 times and estimated the temperature from the mean values.

The estimated gas temperature T_{gs} with respect to the time after the reflected shock front passed the measuring point is represented in Figure 1. The results show that the temperature of argon during the first 2 msec after the passing of the reflected shock front is very unstable and usually much lower than the theoretical one. The temperature after this first period agrees well with the theoretical one. This observation indicates that the shock reflects a few more times on the contact surface. In a shorter shock tube having 4 m length we obtained much shorter relaxation time of about 200 μsec. The reason for this unstable phenomenon is not clear, it probably may be attributed to a non-equilibrium state of ionization. In any way, it is confirmed that the light of argon emitted more than 2 msec after the passing of the reflected shock front is available as a high temperature light source. The temperature of the argon in this period, therefore, should be 7 000 K for the Mach number of 5.85, 8 500 K for 6.39 and 11 500 K for 6.39.

TEMPERATURE IN DETONATION WAVES

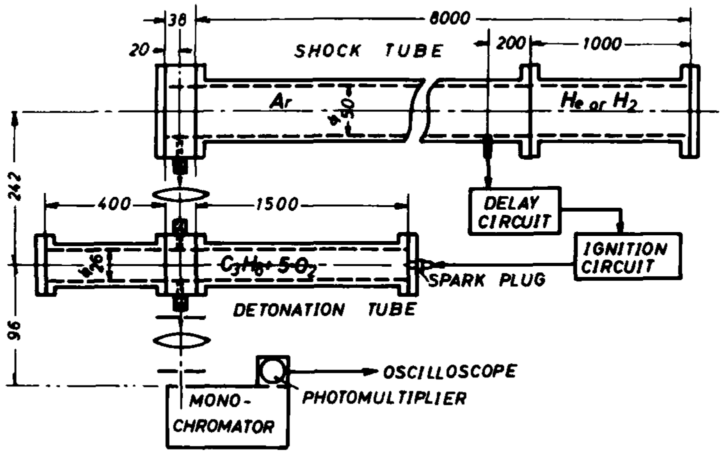

Fig.2. Scheme of the arrangement of the experimental apparatus. Scale in mm.

The experiments were carried out, as shown schematically in Figure 2, by using a detonation tube of stainless steel having 26 mm inner-diameter and 2 m length together with the same shock tube which was used for the measurement of the argon temperature behind reflected shock waves. Both the tubes were arranged in parallel with each other, keeping a distance of 242 mm. The detonation was initiated by a spark ignition whose timing was regulated by the incident shock waves in the argon through a piezoelectric pressure transducer and a delay-circuit so that the reflected shock wave and the detonation wave should pass the measuring point on the same optical path at the same moment. The detonation wave propagated in a stoichiometric propane-oxygen mixture having 2 % argon gas at the initial pressure of 200 torr and room temperature of 22 °C with a velocity of 2310 m/sec, while the shock wave propagated in argon with the Mach number of 5.85, 6.39 and 6.93 and reflected at the end wall of the shock tube.

The spectrum lines of 5912.1 Å and 6043.2 Å wave length from argon behind the reflected shock waves and those in the detonation wave were measured at the same time on the same optical path with a monochromator through a photomultiplier(R 446). The temperature in the detonation wave can be estimated by observing the reversing instants of the spectrum lines from the argon behind the reflected shock waves. We adjusted the measuring timing of the detonation emission to the period more than 2 msec after the reflected shock front passed, as explained previously.

The measurements were carried out at three different temperatures behind the reflected shocks, i.e. 7 000 K, 8 500 K and 11 500 K by regulating the propagation velocity of the incident shock waves. Thus, it is possible to know where the temperature in the detonation wave is higher than 11 500 K, or between 11 500 K and 8 500 K, or between 8 500 K and 7 000 K, or below 7 000 K. The results are illustrated in Figure 3. From the overlapped region of two results, i.e. the results obtained by observing the spectrum line of 5912.1 Å wave length and that of 6043.2 Å, the most probable temperature with respect to the time after the detonation front passed the measuring point, i.e. to the distance behind the detonation front is expressed by a thick solid line in the Figure 3. The temperature behind the detonation front is much higher than that estimated from the Chapman-Jouget condition T_d.

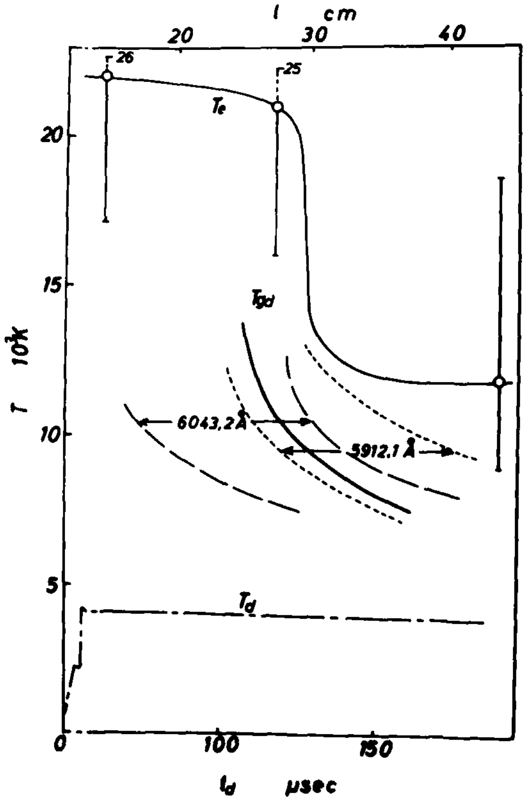

Fig.3. Gas temperature T_{gd} measured by the light reversal method, theoretical gasdynamic temperature T_d and electron temperature T_e in the detonation wave in a stoichiometric propane-oxygen mixture with respect to the time t_d after the detonation front passed the measuring point, eventl. to the distance ℓ from the detonation front.

MEASUREMENT OF THE ELECTRON TEMPERATURE IN DETONATION WAVES BY LASER LIGHT SCATTERING

In order to examine if the temperature in the detonation wave measured by the spectrum line reversal method is correct, we also measured the electron temperature in the same detonation wave by the laser light scattering method [5].

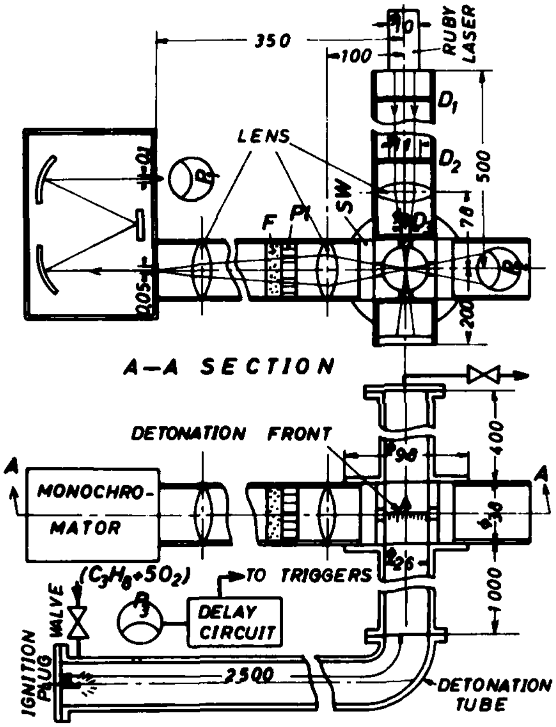

Fig.4. Scheme of the experimental apparatus for measurement of the electron temperature in detonation wave by laser light scattering method. Scale in mm.

Figure 4 illustrates a scheme of the experimental apparatus. A tube of stainless steel having 26 mm inner-diameter and about 4 m length was filled with a stoichiometric propane-oxygen mixture. A detonation initiated by a spark plug propagated through this tube, at first horizontally and then vertically upwards and passed over a measuring point.

We used in this experiment a Q-switched ruby giant pulse laser beam having 20 MW ±2MW, 20 nsec duration of half value intensity and 6943 Å wave length. Its optical system was arranged so that the laser beam was focussed on the center line of the detonation tube. The emission of the laser beam was triggered by the luminescence of the detonation through a photomultiplier P_3 (Toshiba MS9S) and its triggering time was regulated by a delay-circuit so that the laser beam could be emitted at an arbitrary instant after the passing of the detonation front at the measuring point. Thus, it was possible to emit the beam to an arbitrary position behind the detonation front. At the same time, the light of an arbitrary wave length scattered by the charged particles in the detonation waves in the direction of angle 90^o against the incident laser beam direction was measured with a monochromator through a photomultiplier P_1(R 446) and oscilloscope.

Both the laser light and the detonation luminescence were recorded on the same oscilloscope through a photomultiplier P_2 (Toshiba MS9S) and so it was possible to estimate the measurement position behind the detonation front, which could be varied by regulating the triggering time with the delay-circuit. As each experiment permits us to measure only one fixed wave length, it was necessary to repeat several times the measurement at the same position by changing the measured wave length to obtain the spectrum of the scattered light. Three light trap diaphragms D_1, D_2 and D_3, a filter F and a polarizer Pl were set on the light path in order to eliminate the stray light and the luminescence of the detonation.

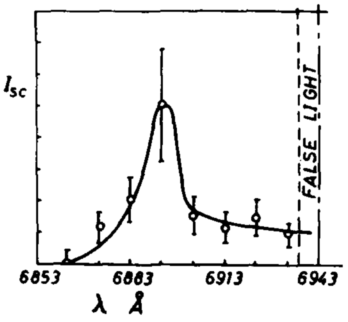

Fig.5. Spectrum of the scattered light at 30 mm behind the detonation front. Intensity I_{SC} is in an arbitrary unit.

Thus, we could obtain the spectra of the scattered light in the detonation wave as shown in Figure 5. The fluctuation of the laser beam was taken into consideration and the intensity of the scattered light was corrected in each case according to the laser power. The measurement error range is also indicated.

The laser light scattered in an ionized gas consists of two components, that is, electron component and ion component[6]. The electron component depends on the fluctuation of electrons which move freely, while the ion component depends on the fluctuation of electrons which correlated with the motion of ions. The profile of the ion component, however, had so small frequency range that we could not obtain it. The spectra as shown in Figure 5 are those of the electron component, while the ion component is hidden in the false light region.

The form of the component is essentially determined by a characteristic parameter α, which is defined by

$$\alpha \simeq \frac{\lambda_o}{2\pi D\, \sin\frac{\theta}{2}}\,, \qquad (3)$$

where D is Debye length, λ_o the wave length of the incident laser beam and θ the scattering angle. Comparing the spectra experimentally obtained with those theoretically obtained by W.H.Kegel[7], it is possible to obtain the characteristic parameter α. From α and the spectra of the scattered light we could obtain the electron temperature and the electron density.

COMPARISON WITH ELECTRON TEMPERATURE

The measured electron temperature also is represented in Figure 3 in comparison with the gas temperature obtained by the spectrum line reversal method. During the first period of about 120 μsec after the detonation front passes the measuring point, the electron temperature is estimated to be about 20 000 K. Then, it rapidly decreases to about 12 000 K. The gas temperature measured by the spectrum line reversal method also has the same tendency, although it is about 5 000 K lower than the electron temperature in the whole region. Considering the measurement errors, both the temperatures of the electrons and the gas agree with each other fairly well and are much higher than the theoretical gas temperature. Figure 6 illustrates the electron temperature and ion density in the same detonation wave measured by the double probe method using multistep pulse potential[8]. The results also suggest the same, if we consider the cooling effect of the probe surfaces. Thus, we can conclude that the gas temperature in the detonation wave measured by the spectrum line reversal method is approximately correct and has a value much higher than the theoretical gasdynamic temperature.

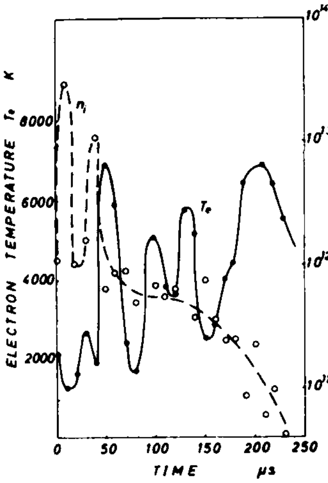

Fig.6. Electron temperature T_e and ion density n_i in the detonation wave in a stoichiometric propane-oxygen mixture with respect to the time after the detonation front passes. Measured by the double probe method using multistep pulse potential.

DISCUSSION

Considering the formation of so-called triple shocks[9] in the detonation waves, the temperature must never be uniform in the detonation waves. The light reversal method permits us to measure only the highest temperature in the gas on the optical path. The measured temperature, therefore, may be that of the triple shocks in which the pressure as well as the temperature should be much higher than those in their surrounding region. If an isochoric combustion takes place in the tripls shocks, the temperature should be about 14 000 K.

CONCLUSIONS

The light emission of argon heated behind reflected shock waves was investigated by measuring the spectrum line intensities. The obtained results show that the spectrum lines emitted from argon in a certain region behind the reflected shock waves can be used as a light source having an arbitrary temperature corresponding to the shock condition. And, two spectrum lines of argon behind the reflected shock waves were used to measure the gas temperature in the detonation wave in a stoichiometric propane-oxygen mixture by the light reversal method. The experimental results indicate that the gas temperature behind the detonation front agrees fairly well with the electron temperature measured by the laser light scattering method and that it has values much higher than those calculated from the Chapman-Jouget condition.

If we could use as a light source a more stable gas having much shorter relaxation time at the temperature in a wider range with a finer scale division, it is possible to obtain more accurate results.

REFERENCES

1. A.G.Gaydon & H.G.Wolfhard, Flames, Chapman & Hall Ltd.(1970) Ch.X.
2. S.S.Penner, Quantitative Molecular Spectroscopy and Gas Emissivities, Addison-Wesley Publ.Co.(1959) Ch.16.
3. W.Lochte-Holtgreven, Plasma Diagnostics, North Holland (1968),Ch.3.
4. S.V.Desai & W.H.Corcoran, J.Quant.Radiat.Transfer 8,1721(1968).
5. K.Terao & N.Takasu, Japan.J.Appl.Phys. 15, 2027 (1976).
6. H.J.Kunze, Plasma Diagnostics, North Holland (1968),Ch.9.
7. W.H.Kegel, IPP 6/34, Institut f. Plasmaphysik (1965).
8. K.Terao, T.Neda, K.Nakao & T.Sato, Japan.J.Appl.Phys. 8, 834 (1969).
9. R.I.Solouhkin, Shock Waves and Detonations in Gases, Mono Book Corp.(1966). Ch.VI.

LASER SCHLIEREN DEFLECTION IN INCIDENT SHOCK FLOW

T. TANZAWA, Y. HIDAKA and W. C. GARDINER, JR.

Department of Chemistry
University of Texas at Austin, Texas, USA

Initial laser schlieren deflections behind incident shock waves were recorded and compared with presently available theories. It is found that using a quadrant photodiode detector permits accurate assignment of time zero. High-sensitivity laser schlieren data were collected to determine the deflection due to wall boundary layer growth. When the observed deflections are compared with presently available flow models, it is found that laminar boundary layer growth only accounts for about half of the observed signal in non-relaxing test gas. Averaging local beam deflections over the finite beam profile, weighting by the gaussian power distribution of the laser beam, was found to be a necessary correction if one attempts to study very high speed relaxation processes.

INTRODUCTION

The study of chemical or physical relaxation processes behind incident shock waves can be effectively carried out by the laser-schlieren method if one knows the connection between the change in the refractive index gradient of the test gas and the progress of the relaxation, the time origin of the observed signal, and the relationship between the observed signal and the refractive index gradient in the test gas. In the very simplest situation one assumes the specific refractivity of the test gas to remain constant, that the laser beam is deflected as a unit, and that the gas flow is ideal and steady.[1] For more refined experiments, one can also take into account a changing specific refractivity,[2] possible absorption of the beam and integration of the beam deflection over its finite beam profile,[3] and more realistic flow models. The latter would include allowance for the axial density gradient due to mass loss to the wall boundary layer,[4,5] attenuation of the shock speed[6] and curvature and/or tilt of the shock front.[7] All of these allowances turn out to be small corrections to the connection between modulation of the detected beam intensity and the rate of the relaxation process as long as the density gradient generated by the relaxation is larger than about 10^{-5}g/cm^4 and one avoids trying to probe close to the shock front with a very narrow laser beam. If one does have to be concerned with small modulations or to extend observations as close as possible to the shock front, then one is forced to consider very carefully how to relate the modulation to the relaxation profile. Additional uncertainties arise if an attempt is made to integrate the modulation trace over the whole relaxation zone without independent means to locate the time origin with respect to shock passage through the laser beam.

In this paper we report experiments directed toward understanding the behavior of the probe beam right at the shock front and the degree to which the best available theories describing the small (about 1 x 10^{-6}g/cm^4 density gradient or density gradient equivalent) modulations match the observations in absence of relaxation.

EXPERIMENTAL

The shock tube in which the experiments were done has been described in detail.[8] Briefly, it had a circular cross-section with i.d. = 7.62 cm; the interior was honed to a mirror finish and all windows and shock detectors matched the internal surface to better than ±0.01 mm. The He-Ne laser beam, from a highly stabilized 30-cm oscillator cavity, was found to have a maximum total width of 1.3 mm inside the shock tube when used without telescopes and 0.4 mm when telescopes were employed. It passed through schlieren-grade $\lambda/4$ windows on the shock tube and was detected by a UDT Pin-Spot 8/D quadrant photodiode located, usually, 4 m from the shock tube. The detector electronics were found by pulsed LED experiments to have a response time of less than 20 ns.

In auxiliary experiments, the curvature and tilt of the shock front were measured by a thin film resistance gauge technique. Gauges were placed at appropriate spacings to detect the arrival of the incident shock at stations on the shock tube end wall. Very high speed electronics and recording were used to record arrival times simultaneously at several stations.

RESULTS AND DISCUSSIONS

Representative modulation profiles for small and normal beam runs in pure argon test gas are shown in Figure 1; the characteristic widths and modulations from such traces are shown as a function of initial test gas pressure in Figure 2. From the magnitude, sign, and pressure dependence of the M_1 modulation we first inferred, incorrectly, that it is to be attributed simply to removal of part of the beam away from the downstream segment of the detector by refraction and/or reflection of part of the beam onto the upstream segment as the shock enters the beam. We subsequently realized that this modulation is instead an extremely complex phenomenon; the detected signal does not distinguish whether diffraction and/or reflection are taking place when the laser beam is focused on the center of the photodiode detector, since the gaussian distribution of the power changes mostly in intensity, hardly at all in shape,

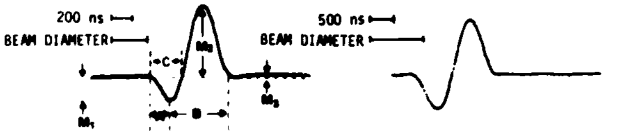

(a) SMALL-BEAM EXPERIMENTS IN ARGON (b) NORMAL-BEAM EXPERIMENTS IN ARGON

Figure 1. Representative laser-schlieren oscilloscope records.

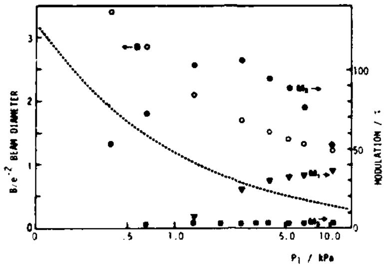

Figure 2 (a). Characteristic widths and modulations from small-beam-diameter experiments in argon. Open symbols refer to widths, solid symbols to modulations, and the dashed line to the theoretical bulge calculation of de Boer (ref. 7).

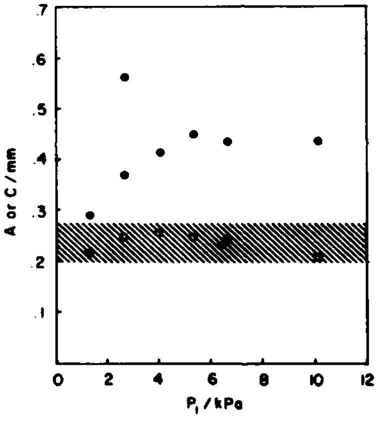

Figure 2(b). Comparison of "A" and "C" widths (Figure 1) to radius of small beam in shock tube. Upper limit of shaded area is 1.8% $(1/e^4)$ modulation width, an approximation to minimum observable signal at amplification shown in Figure 1.

when a portion of the beam far from the detector (i.e. within the shock tube) is deflected. We did learn by separate experiments that the initial deflection signal is indeed mainly due to refractive deflection of part of the beam away from the downstream segment of the detector: The laser beam was focused slightly outside of the photodiode detector, i.e. just off its downstream or upstream sides, and the distance from shock tube to detector was reduced. It was found that the detector caught laser beam power from the initial transient only when the beam was focused off the downstream side of the detector. Reflection is therefore insignificant for the test gas densities used.

Dove and Tietelbaum[9] suggested on theoretical arguments an identification of the time origin for shock front arrival, assuming various models and a distant split detector, and Tanzawa and Gardiner[10] found experimentally that the time origin for shock front arrival at the center of the beam corresponds to the first signal minimum prior to the large positive deflection. Figure 2 shows a comparison of half the small-beam laser width with measured values of

"A", the distance between the first observable negative signal and the first minimum, and of "C", the distance to the zero-crossing point. It can be seen that the values of "A" are essentially independent of initial pressure and correspond to the laser beam radius. The "C"-values, on the other hand, correspond to distances notably larger than the laser beam radius. For the narrow-beam configuration, therefore, the minimum signal appears to result when the shock front arrives at the center of the laser beam because maximum negative signal occurs at the time half of the beam is refracted in the downstream direction.

The main modulation M_2 is then attributable to refraction by the curved shock front as it traverses the laser beam. The residual modulation M_3 manifests the dfflection of the beam due to the net effect of mass loss to the wall boundary layer, density gradients within the two boundary layers traversed, and attenuation of the shock speed. The width of the main modulation, B, should then correspond to the sum of the beam radius and the axial extent of the shock front. Using the theoretical value of the axial extent due to de Boer[7] one sees in Figure 2a that the B-values are larger than this. In the experiments with the thin film gauges, however, it was found that the axial extents were in good agreement with those computed from de Boer's theory. We have no explanation for the discrepancy evidenced by the B-values shown in Figure 2a.

Refractive index gradient profiles were calculated in the following manner. Using numerical integration of the flow equations, local refractive index profiles were computed.[11] To average them over the beam width, a spatial integration of the local deflections generated in each profile integration step was performed over twice the laser beam $1/e^2$ diameter by Simpson's Rule, using a weighting function for the laser beam power distribution $I(x) = A \exp(-8x^2/B^2)$, where x is the flow axis, B is the $1/e^2$ laser beam diameter, and A is the normalization factor. For this integration the local refractive index gradients were fitted over twice the laser beam diameter to a second order polynomial form, and then the integration of $[A \exp(-8x^2/B^2)] \cdot \{\alpha x^2 + \beta x + \gamma\}$ was performed numerically.[12] The refractive index at 633 nm was computed through a non-linear least square analysis to fit the Cauchy dispersion equation[13] to experimental refractivity data. In Figure 3 we

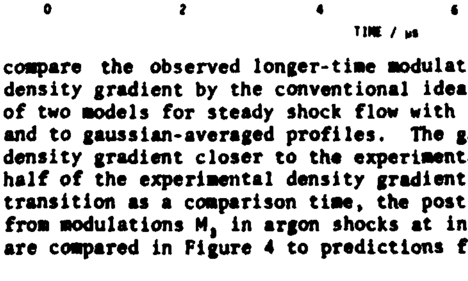

Figure 3. Comparison of experimental density gradient with predictions: Symbols, our experiments; solid line, Mirel's variable-area flow model, local deflection (ref. 4); short-dashed line, averaged deflection for Mirels' model; long-dashed line, local deflection for our variable-area flow model (ref. 5). The same notations are used in Figure 4.

compare the observed longer-time modulation in an argon shock, converted to density gradient by the conventional ideal-flow equation,[1] to the predictions of two models for steady shock flow with laminar boundary layer formation and to gaussian-averaged profiles. The gaussian-averaged profile gave a density gradient closer to the experimental values. It is still only about half of the experimental density gradient, however. Taking 2 μs after the A/B transition as a comparison time, the post-shock density gradients computed from modulations M_3 in argon shocks at initial pressures from 0.4 to 34 kPa are compared in Figure 4 to predictions from laminar boundary layer theory.

Again one sees that the theory predicts only half of the observed deflection.

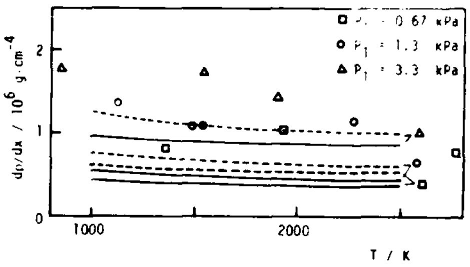

Figure 4. Experimental density gradients at 2 μs. Solid and dashed lines were computed for each starting pressure as indicated in the caption for Figure 3.

We attempted to see whether real gas effects contributed to the more substantial boundary layer effect. These should be more pronounced in lower-γ gases than in pure Ar. A 10% C_2H_2 in Ar mixture was used. As seen in Figure 5,

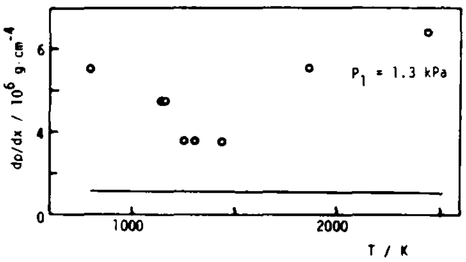

Figure 5. Density gradients at 2 μs in 10% C_2H_2 in Ar. Solid line is our variable-area flow model, assuming no relaxation and no reaction.

the density gradient at below 1400 K is due mainly to the vibrational relaxation of C_2H_2, while above 1500 K the density gradient begins to increase because of chemical reactions. As we have seen for Ar in Figures 3-5, both Mirels' uniform free stream mode' and the variable free stream, flat plate model of Bertin et al. fail to account for even half of the observed deflections. The discrepancy may be larger than for pure Ar.

It is possible that some of the discrepancy could be due to limitations of the Bertin et al. model, in particular to the fact that the wall of the shock tube is actually curved rather than flat. It seems more likely to us, however, that the major source of it is to be found in optical effects of the growing boundary layer upon the beam. The effect of attenuation of the shock speed has been predicted to be small negative contribution to the density gradient.[6] For higher starting pressures, it is possible that the wall boundary layer flow is no longer laminar.

One is then faced with the question of how best to interpret laser-schlieren experiments in which relaxation occurs. It is clearly better to take the boundary layer into account somehow rather than simply to ignore it; presumably there is no better way to do this at present than to use a variable-area flow model rather than a constant-area one, and to choose the parameters of the variable-area model to give the best continuity equation for the test gas conditions used. In this way at least the time base of the model should be closer to reality than the ideal, constant area model. Then, however, we believe that correcting the density gradient inferred from an experiment in a relaxing gas should best be done by subtracting the difference between the theoretical and observed modulations in non-relaxing shocks (Figures 3-5) from the modulations in relaxing shocks. As seen in the C_2H_2 situation shown in Figure 5, the correction for boundary layer effects may give substantially different measures of relaxation or reaction rates than the uncorrected values.

Most early applications of the laser schlieren technique were to relaxation processes that were shown experimentally to be nearly exponential decays to equilibrium, as judged from semilogarithmic graphs of deflection signals. Deflection signals from this kind of experiment are larger and faster than in the above examples. For modeling comparisons we selected such an experiment in H_2:Ar = 30:70, T_2 = 2673 K, P_1 = 16.1 torr, corresponding to a published experimental record.[14] The experimental relaxation time for these conditions is τ_{app} = 0.323 μs laboratory time, or an apparent relaxation distance of 0.65 mm. In a two-level approximation this corresponds to a rate constant of $8.5 \times 10^5 s^{-1}$ for $H_2(v=0) \rightarrow H_2(v=1)$. Thermochemical data for these two species were generated from molecular properties and used to compute deflection signals.

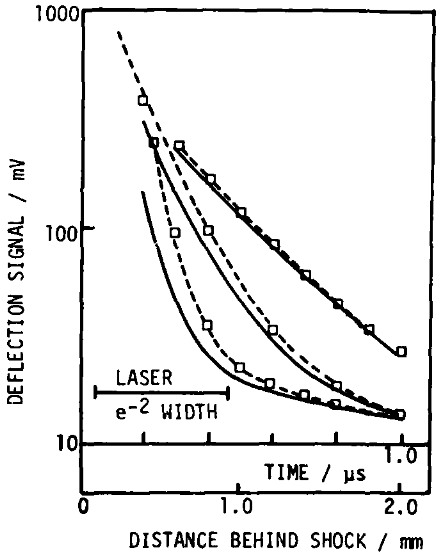

Figure 6. —— Local and ---- gaussian-averaged signals for a relaxation process. The upper pair of lines corresponds to the observed relaxation rate of an experiment in H_2:Ar = 30:7. The lower pairs of lines are for twice and four times this rate.

Figure 6 shows profiles of the local and the quadratically-fitted (over twice the laser $1/e^2$ width), spatially-averaged deflection signal for the actual experimental relaxation time and also for two hypothetical experiments in which the same relaxation process occurs at twice or four times the actual rate. One sees that the local and averaged profiles appear equally exponential. The deviation is appreciable for the experimental relaxation rate and becomes severe for the faster rates. Since these faster rates are readily observable experimentally, it is clear that assigning observed signals to local deflections may be seriously wrong.

The primary conclusion of this investigation is that for experimental situations where the laser-schlieren method is used to probe density gradients that are not much greater than 1×10^{-6} g/cm^4, one should employ variable-area flow models for simulations of the relaxation process but correct the observed beam modulations by subtracting the experimentally observed residual modulation in nonrelaxing gas, despite the inconsistency thus implied in the data reduction. A second conclusion is that by using a quadrant photodiode it is possible to assign the narrow-beam time origin as the first minimum prior to

the main positive deflection, in agreement with conclusions drawn before by theoretical arguments. A third conclusion is that spatial averaging may introduce appreciable corrections to the deflection for rapidly changing refractive index gradient profiles.

ACKNOWLEDGEMENT

This research was supported by the Robert A. Welch Foundation and the U. S. Army Research Office.

REFERENCES

1. J. H. Kiefer and R. W. Lutz, J. Chem. Phys. *44*, 658 (1966).
2. B. F. Walker and W. C. Gardiner, Jr., J. Chem. Phys. *48*, 5279 (1968); D. B. Olson, T. Tanzawa and W. C. Gardiner, Jr., Int. J. Chem. Kin. *11*, 23 (1979).
3. R. G. Macdonald, G. Burns, and R. K. Boyd, J. Chem. Phys. *66*, 3598 (1977).
4. H. Mirels,in Shock Tube Research, Proceedings of the Eighth International Shock Tube Symposium, London, 1971, p. 6, and references therein to earlier work.
5. J. J. Bertin, E. S. Ehrhardt, W. C. Gardiner, Jr. and T. Tanzawa, in Modern Developments in Shock Tube Research, Proceedings of the Tenth International Shock Tube Symposium, Kyoto, 1975, p. 595.
6. P. C. T. de Boer and J. A. Miller, in Modern Developments in Shock Tube Research, Proceedings of the Tenth International Shock Tube Symposium, Kyoto, 1975, p. 397.
7. P. C. T. de Boer, Phys. Fluids *6*, 962 (1963).
8. J. E. Hardy and W. C. Gardiner, Jr., Sixteenth Symposium (International) on Combustion, p. 985, The Combustion Institute, 1977.
9. J. E. Dove and H. Teitelbaum, Proceedings of the Eleventh International Shock Tube Symposium, Seattle, 1977, p. 474.
10. T. Tanzawa and W. C. Gardiner, Jr., Seventeenth Symposium (International) on Combustion, in press, The Combustion Institute, 1979.
11. W. C. Gardiner, Jr., B. F. Walker, and C. B. Wakefield, in Shock Waves in Chemistry, A. Lifshitz, Ed., Marcel Dekker, New York, 1979.
12. W. C. Gardiner, Jr. and T. Tanzawa, J. Chem. Phys., submitted, 1979.
13. W. C. Gardiner, Jr. and T. Tanzawa, Combustion & Flame, in press, 1979.
14. J. H. Kiefer and R. W. Lutz, J. Chem. Phys. *44*, 668 (1966).

ION-MOLECULE REACTION MEASUREMENTS BY A SHOCK-TUBE PULSED-FLOW PULSED-AFTERGLOW TECHNIQUE

JEN-SHIH CHANG*, S. JOSHI, G. L. OGRAM and R. M. HOBSON

Department of Physics and Centre for Research in Experimental Space Science,
York University, Toronto, Canada

An experimental technique, the shock-tube pulsed-flow pulse-afterglow technique (STPFPA), has been developed for measuring ion-molecule reaction rates and dissociative volume recombination coefficients in a low temperature gas (gas temperature $T_g < 300$°K). The cooled gas in the expansion flow of the STPFPA method enables one to measure the gas temperature dependences of the rate coefficients of ion molecule reactions and dissociative volume recombination in the range of 100°K to 300°K. The theory of the medium pressure plasma afterglow has been developed for Helium-reactant gas mixtures taking into account diffusion, volume recombination, charge transfer and other ion-molecule reactions to obtain reaction rates using the STPFPA method. In the $He\text{-}N_2$ and He-CO gas mixture, the charge transfer reaction $He_2^+ + XY \xrightarrow{k} XY^+ + 2He$ and volume recombination $XY^+ + e \xrightarrow{\beta} X + Y$ are considered, where XY represents CO or N_2. From the comparisons between numerical theoretical and experimental results, we obtain $k = 2.1 \pm 0.3$ and $1.5 \pm 0.3 \times 10^{-9}$ cm^3 $molecule^{-1}$ sec^{-1} for $He - N_2$ and He - CO gas mixture, respectively, at 208°K. In the case of $He - O_2$ gas mixtures, charge transfer reactions $He_2^+ + O_2 \xrightarrow{k_1} O_2^+ + 2He$, $He_2^+ + O_2 \xrightarrow{k_2} O + O^+ + 2He$, $O^+ + O_2 \xrightarrow{k_3} O_2^+ + O$ and volume recombination $O_2^+ + e \xrightarrow{\beta} O + O$ are considered. Correlating theory and experimental results, we obtain $k_1/k_2 = 3.5$ and $k_1 + k_2 = 1.05 \times 10^{-9}$ cm^3 $molecule^{-1}$ sec^{-1} at a gas pressure of 11 torr at a calculated temperature of 208°K in the expansion flow of the flow tube. The charge transfer rates of CH_4 with He_2^+ is discussed in detail.

I. INTRODUCTION

Many measurements have been made of ion-molecule reaction rate coefficients, due mainly to their importance in ionospheric research, flames, gaseous electronics and in many plasmas of laboratory interest. All previous measurements by flowing afterglow technique FA, stationary pulsed afterglow technique SPA, and selected ion flow tube SIFT techniques have been made over a restricted range of gas temperatures close to room temperature, 300°K. The measurement of the gas temperature dependence of ion-molecule reaction rates has, in the past, been done either by the complete heating (or cooling) of a flowing

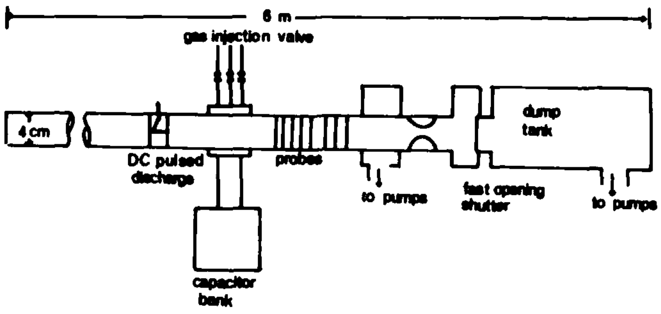

Figure 1 Schematic of shock-tube pulsed-flow pulsed-afterglow apparatus

afterglow system[1] or by a drift tube technique. The range of gas temperatures covered by the flowing afterglow system is restricted to between 88°K and 600°K. Difficulty also arises from the effect of the thermal boundary layer on the correction factors of the basic flowing afterglow data analysis in the slip flow condition[2]. In the case of the drift tube experiments it is difficult to obtain an ionic velocity distribution which is Maxwellian[9]. The shock tube pulsed-flow pulsed-afterglow technique STPFPA enables the investigation of reaction rates over a wide range of gas temperatures, firstly in the range from 100°K to 300°K by expansion cooling, and secondly in the range from 700°K to 4000°K by shock heating. The ionic velocity distribution will be Maxwellian in both cases, and the operating conditions can be chosen such that the thermal boundary layer is thin[3].

In this paper the gas cooling features of the STPFPA technique are discussed in Sec. II. In Sec. III, the theoretical analysis used in the determination of the reaction rates from the experimental data will be outlined. The preliminary reaction rate measurements at 208°K obtained by the investigation of the effect of injection of N_2, CO, O_2 and CH_4 gases into a helium afterglow are discussed in Sec. IV.

II. EXPERIMENTAL APPARATUS

The basic apparatus is a pressure-driven glass shock tube of the type developed in this laboratory and employed for many years[14] (inner diameter 4 cm). It was adapted by the addition of D.C. discharge electrodes, a mixture gas injection valve, an expansion nozzle and a fast-open shutter. The present version of the shock-tube is shown schematically in figure 1.

The high-pressure section was evacuated to below 10^{-6} torr, then filled with research-grade helium to a pressure in the range 5-20 torr. The rupture of the diaphragm by the fast opening shutter triggered a D.C. pulsed discharge of approximately 100 μs duration which ionized a section of the test gas. As soon as the expansion fan reached the resultant plasma the plasma moved downstream. The reactant gas was injected into the plasma slice when it passed the injection valve. The gas temperature of the expansion fan T can be controlled by the size and shape of the expansion nozzle which changes the gas velocity u. The flow properties behind expansion waves in a perfect gas are expressed as follows:

(a) flow temperature ratio

$$T/T_4 = [1 - u(\gamma - 1)/2a_4]^2 \qquad (2.1)$$

(b) flow density ratio

$$\rho/\rho_4 = [1 - u(\gamma - 1)/2a_4]^{2/(\gamma - 1)} \qquad (2.2)$$

(c) pressure ratio

$$P/P_4 = [1 - u(\gamma - 1)/2a_4]^{2\gamma/(\gamma - 1)} \qquad (2.3)$$

(d) sound speed ratio

$$a/a_4 = 1 - u(\gamma - 1)/2a_4 \qquad (2.4)$$

where γ is the ratio of special heat and the subscript 4 refers to the region in front of the expansion fan.

The flow velocity was determined by measuring the time interval between double-probe responses in the diagnostic section[4]. The gas temperature was determined by measuring the electron temperature by a direct plasma parameter display electrostatic triple-probe method[4,5] in the diagnostic section. The probes consisted of stainless-steel wires of radius $R_p = 0.0115$ cm mounted, under tension, transversly to the flow. Each probe arm was mounted about 0.7 cm apart in the same cross-sectional plane, the separation between double probes being 10 cm. The triple probes were mounted alternately with the double probes.

The reactant gas was injected perpendicular to the flow using a jet injection technique similar to that used by Morgenthaler[6], and Smoot and Allred[7]. The reactant gas was stored in a small tank which was separated from the shock tube by a Teflon valve and the injection nozzle. The valve was opened by discharging a 40 μF condenser bank (charged to 4 kV) through it. The opening time of the valve was measured and found to be 3 msec.

A hollow cathode discharge was generated between a cylindrical cathode and a central anode pin. The cylindrical cathode and anode pin were made from stainless steel with a diameter of 4 cm and 0.1 cm, respectively. Discharge pulse lengths between 50 and 500 μs have been used.

III. THEORY OF He-X MIXTURE PLASMA AFTERGLOW

The theory of the charge density decay in a gas mixture afterglow plasma has been developed by Bolden et al[8], Ferguson et al[2], Jarvis[10], Adams et al[11] and Scaccia and Kennedy[12]. Most of these treatments assume that the plasma loss due to volume ion-electron recombination is small compared to the loss by ambipolar diffusion. In this section, the theoretical analysis used in the determination of the reaction rates from the experimental data will be discussed for the case of injection of various gases into a helium afterglow.

We assume a weakly ionized plasma with no imposed electric or magnetic field. We also assume that the characteristic tube dimension d >> the Debye length λ_D >> the charged particle mean free path, so that plasma diffusion is ambipolar. We neglect metastable-metastable and super-elastic collisions and therefore assume that the electron and gas temperatures are the same during the afterglow period. At the pressures considered essentially all the helium ions will be converted to the dimer ions. The types of reactions considered here are:

(1) Charge transfer

$$He_2^+ + X_2 \overset{k_1}{\rightarrow} X_2^+ + 2He$$

$$\overset{k_2}{\rightarrow} X^+ + X + 2He$$

(2) The Ion-molecular reaction

$$X^+ + X_2 \overset{k_3}{\rightarrow} X_2^+ + X$$

(3) Volume recombination of the product molecular ion

$$X_2^+ + e \overset{\rho_1}{\rightarrow} 2X$$

Here, we have neglected the volume recombination between the molecular Helium ions and electrons, since the reaction rate coefficient is many orders of magnitude smaller then ρ_1. We have also assumed that the diffusion coefficients of atomic and molecular ions for the reactant gas X are approximately equal. The nondimensional governing equations are then:

(i) electron

$$\frac{\partial n_e}{\partial \tau} = C_1\left(\frac{\partial^2 n_e}{\partial r} + \frac{1}{r}\frac{\partial n_e}{\partial r}\right) - \beta n_e n_2 \qquad (3.1)$$

(ii) Helium ion

$$\frac{\partial n_1}{\partial \tau} = \left(\frac{\partial^2 n_1}{\partial r^2} + \frac{1}{r}\frac{\partial n_1}{\partial r^2}\right) - (\delta_1 + \delta_2)\, n_1 + c_0 n_1 \ln n_e \qquad (3.2)$$

(iii) X_2^+ ion

$$\frac{\partial n_2}{\partial \tau} = \left(\frac{\partial^2 n_2}{\partial r^2}\right) + \frac{1}{r}\frac{\partial n_2}{\partial r}) + \delta_1 n_1 + \delta_3 n_3 - \beta n_e n_2 + c_0 n_2 \ln n_e$$

(3.3)

(iv) X^+ ion

$$\frac{\partial n_3}{\partial \tau} = \left(\frac{\partial^2 n_3}{\partial r^2} + \frac{1}{r}\frac{\partial n_3}{\partial r}\right) + \delta_2 n_1 - \delta_3 n_3 + c_0 n_3 \ln n_e \qquad (3.4)$$

where $n_e = n_1 + n_2$ and the nondimensional variables are:

$$\begin{aligned}
n_1 &= N_1/N_e(t=0), \quad \tau = tD_0/R_p^2, \; r = R/R_p, \\
\delta &= k[X]R_p^2/D_0, \quad n_2 = N_1/N_e(t=0), \; n_e = N_e/N_e(t=0) \\
\beta &= \rho[N_e(t=0)]R_p^2/D_0, \quad c_0 = (\mu_0/D_0)(D_e - D_0)/(\mu_e + \mu_0) \qquad (3.5) \\
c_1 &= (\mu_e D_0 + \mu_0 D_e)/D_0(\mu_e + \mu_0)
\end{aligned}$$

Three types of charge transfer reaction channels will be discussed.

(i) one channel reaction ($k_2 \equiv 0$)

To a first order approximation, we can replace the diffusion term by a first order density loss term[15], i.e. $\nabla^2 n \approx -qn$, in equations (3.1) - (3.3). Then, the following analytical solutions may be obtained

$$n_1 = \exp[-(q + \delta_1)\tau] \qquad (3.6)$$

$$n_e = \frac{\exp\{-q\tau - [\beta/(q + \delta_1)]\exp[-(q + \delta_1)\tau]\}}{\exp\{-\beta/(q + \delta_1)\} + \beta \int_0^{\tau} \exp\{-q\tau' - [\beta/(q + \delta_1)]\exp[-(q+\delta_1)\tau']\}d\tau'} \qquad (3.7)$$

Typical numerical solutions of equations (3.1) - (3.4) are compared with approximate solutions of equations (3.6) and (3.7) in figure 2 for $\beta = 2000$, $\delta = 1000$. Here finite difference methods have been used to solve equations (3.1 - 3.3). Figure 2 shows that the plasma density decay is dominated by the charge transfer reaction and volume recombination for early and late afterglow times respectively. Hence the rate coefficients for charge transfer and volume recombination may be obtained by fitting the experimentally measured charge density decay to theoretically generated curves.

Typical reactant gases for this case would be Nitrogen and Carbon monoxide. The exact numerical solutions agree well with the approximate solutions except for very late afterglow times.

(ii) two channel reactions

The approximate solutions for equations (3.1) - (3.5) for the two channel cases are:

$$n_1 = \exp[-(q + \delta_1 + \delta_2)\tau] \qquad (3.8)$$

$$n_3 = [\delta_1/(\delta_3 - \delta_1 - \delta_2)]\{\exp(-q-\delta_3)\tau - \exp(-q-\delta_1-\delta_2)\tau\} \qquad (3.9)$$

$$n_e = \exp f(\tau)/\{\exp f(\tau) + \beta\int_0^\tau \exp f(\tau')\,d\tau'\} \qquad (3.10)$$

$$f(\tau) = q\tau + \beta n_1/(q + \delta_1 + \delta_2) + [\beta\delta_2/(\delta_1 + \delta_2 - \delta_3)]\{\exp(-q-\delta_3)\tau/(q + \delta_3) - n_1/q + \delta_1 + \delta_2)\} \qquad (3.11)$$

where the electron density decay can be obtained by a simple numerical integration. A typical reactant gas for this type of reaction is Oxygen.

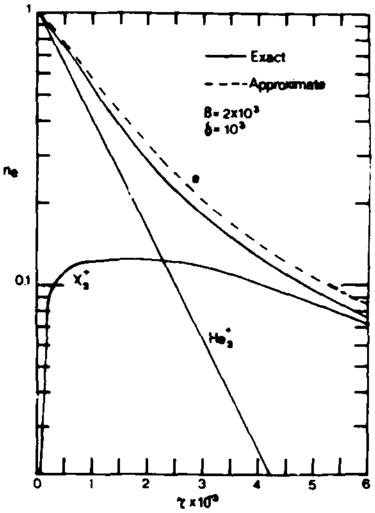

Figure 2 Comparisons between approximate and exact theoretical values for the plasma decay.

(iii) Multi-channel reaction

For a polyatomic gas, such as NH_3 or CH_4, a multi-channel charge transfer reaction can be expected. For example, we obtain for CH_4;

$$He_2^+ + CH_4 \begin{array}{l} \xrightarrow{k_1} CH_4^+ + 2He \\ \xrightarrow{k_2} CH_3^+ + H + 2He \\ \xrightarrow{k_3} CH_2^+ + H_2 + 2He \\ \xrightarrow{k_4} CH^+ + H + H_2 + 2He \end{array}$$

The theory for such a reaction is complicated since it has four channels. There are five different ion species involved in the sytem and all the product ions recombine rapidly. However, if we can assume that the volume recombination coefficients for the species CH_n^+ are similar, we can obtain a solution of the same form as equation (3.7) except that k_1 is replaced by $k_0 = \sum_{n=1}^{m} k_n$. Recent volume recombination rate measurements by McGowan et al[13] show that this approximation is valid for ions such as CH_n^+.

4. EXPERIMENTAL RESULTS AND DISCUSSIONS

(i) Single-channel reactions

The single-channel reaction with He_2^+ ions has been measured for N_2 and CO gases. The reaction schemes are $He_2^+ + N_2^+ + 2He$ and $He_2^+ + CO \xrightarrow{k} CO^+ + 2He$. Figure 3 shows the measured charge density decay in the tube for the case of CO as the injected gas at 208°K. The charge density has been normalized to the density at the injection point. The family of curves shown are obtained from the theory of section 3 with the charge transfer reaction rate as the variable parameter. A value of $k = 1.5 \pm 0.3 \times 10^{-9}$ cm^3/sec gave a best fit with the measured results. These results also can be confirmed by changing

AD-A091 010 HEBREW UNIV JERUSALEM (ISRAEL) F/G 20/4
PROCEEDINGS OF THE INTERNATIONAL SYMPOSIUM ON SHOCK TUBES AND W--ETC(
FEB 80 A LIFSHITZ, J ROM AFOSR-78-3679
UNCLASSIFIED AFOSR-TR-80-1141 NL

7 of 8
AD
A091010

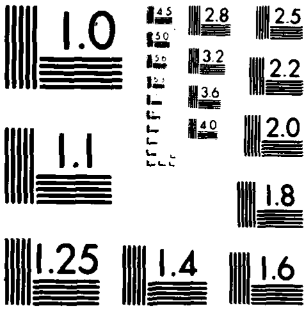

MICROCOPY RESOLUTION TEST CHART
NATIONAL BUREAU OF STANDARDS 1963 A

the concentration of the injection gas. The values for the dissociative recombination coefficient and diffusion coefficient used in the theoretical calculations are listed in table I together with their temperature dependences.

A similar analysis carried out for N_2 gives a value for the charge transfer reaction rate of 2.1 ± 0.3 × 10^{-9} cm^3/sec at 208°K.

(ii) two-channel reactions

The reactions for O_2 injected into the He_2^+ plasma are

$$He_2^+ + O_2 \xrightarrow{k_1} O_2^+ + 2He$$

$$\xrightarrow{k_2} O^+ + O + 2He$$

$$O^+ + O_2 \xrightarrow{k_3} O_2^+ + O$$

The numerical charge density decay results from section 3 are shown in figure 4 for various specified values of the ratio k_1/k_2, at a certain specified value of $(k_1 + k_2)$, which was obtained by fitting to the experimental values. The values of $k_1 + k_2 = 1.05 \times 10^{-9}$ cm^3/sec and $k_1/k_2 = 3.5$ respectively gave a best fit to the experimental results.

(iii) multi-channel reactions

The reaction of He_2^+ with CH_4 is a multi-channel reaction. The calculations were performed for the exothermic channels which lead to the production of CH_4^+, CH_3^+, CH_2^+ and CH^+. A plot of charge density decay is shown in the figure 5. The value of $k = k_1 + k_2 + k_3 + k_4 = 0.58 \pm 0.1 \times 10^{-9}$ cm^3/sec gave a best fit with the theoretical curve.

The previous results for the charge transfer reaction rate coefficients of helium molecular ions are summarized in table II together with the present results.

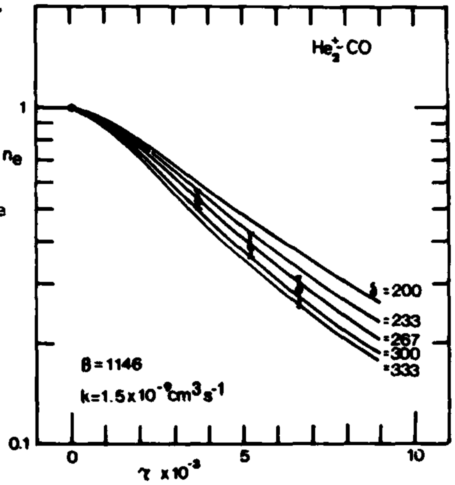

Figure 3 Plasma density decay following the injection of CO into a helium afterglow. The experimental measurements are shown together with the theoretically derived curves. t = 0 refer to the time of injection of the CO.

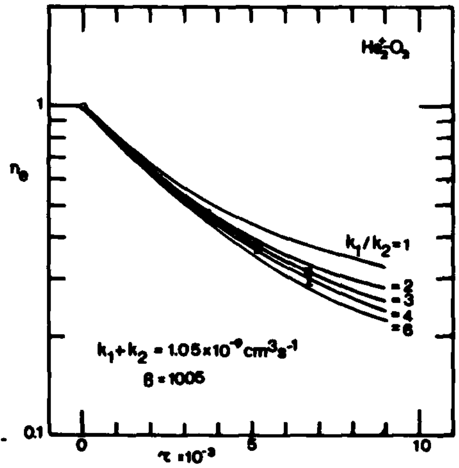

Figure 4 Plasma density decay following the injection of O_2 into helium afterglow. Theoretical curves for various values of branching ratio are also shown.

TABLE I. Volume Recombination Coefficient

Gas	ρ_1 (cm^3/sec)	$\alpha(T_e^{-\alpha})$	Ref.
N_2^+	2.5×10^{-7}	0.37	[20]
CO^+	3.9×10^{-7}	0.57	[21]
CH_4^+	3.0×10^{-7}	0.4	[13]
O_2^+	2.1×10^{-7} $2.0 \times 10^{-10}(k_3)$	0.63	[20] [17]

TABLE II. Reaction rates for He_2^+ with CO, N_2, O_2, CH_4

Injected Gas	Reaction Rate x $10^9 cm^3/s$		
	This Study	Others	(Ref)
CO	1.5 ± 0.3	0.53 ±0.05 1.4 ±0.4 1.08 ±0.3	[18] [16] [19]
N_2	2.1 ± 03	1.3 ± 0.4 0.6 0.6 ± 0.05 1.06± 0.1	[16] [17] [18] [19]
O_2	$k_1+k_2=1.05 \pm 0.1$ $k_1/k_2=3.5$	$k_1+k_2= 1.05 \pm 0.1$ $=0.7 \pm 0.05$	[16] [18]
CH_4	$k_1+k_2+k_3+k_4$ $=0.71 \pm 0.1$	$k_1+k_2+k_3+k_4$ $=0.55 \pm 0.1$ $=0.5 \pm 0.1$	 [18] [19]

The authors wish to express their appreciation to J.G. Laframboise, D.K. Bohme, A.J. Cunningham, R.H. Prince and B. Evans for valuable discussions and comments. They also wish to express their gratitude to K. Keskinen and A. Salem for design and constraction of the apparatus. This work was supported by the National Research Council of Canada.

* present address: Department of Engineering Physics, McMaster University, Hamilton, Ontario Canada

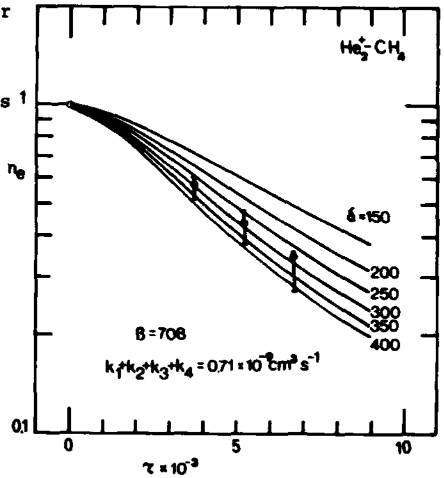

Figure 5 Plasma density decay on injection a helium afterglow. Theoretically derived curves for various values of the total charge transfer rate coefficient are also shown.

References

1. D.B. Dunkin, F.C. Fehsenfeld, A.L. Schmetrekopf and E.E. Ferguson, J. Chem. Phys. 49, 1365 (1968)
2. E.E. Ferguson, F.C. Feshenfeld and A.L. Schmeltekopf, Adv. At. Mol. Phys. 5, 1 (1969)
3. H. Mirels, Phys. Fluids 6, 1201 (1963)
4. G.L. Ogram, J.S. Chang and R.M. Hobson, J. Appl. Phys. 50, 726 (1979)
5. S.L. Chen and T. Sekiguchi, J. Appl. Phys. 36, 2362 (1965)
6. J.H. Morgenthaler, NASA CR-747 (1967)
7. L.D. Smoot and L.D. Allred AIAA J. 13, 721 (1975)
8. R.C. Bolden, R.S. Hemsworth, M.J. Shaw and N.D. Twiddy, J. Phys. B: At. Mol. Phys. 3, 45 (1970)
9. F.C. Fehsenfeld, Int. J. Mass. Spec. & Ion Phys. 16, 151 (1975)
10. S. Jarvis Jr., J. Res. Nation. Bur. Stand. B: Math Sci. 72B, 135 (1968)
11. N.G. Adams, M.J. Church and D. Smith, J. Phys. D: Appl. Phys. 8, 1409 (1975)
12. C. Scaccia and L.A. Kennedy, AIAA J. 12, 1268 (1974)
13. J.B.A. Mitchell, P. Mul. V.S. D'Angelo and J.W. McGowan, Bull. Canad. Phys. Asso. 34, 35 (1978)
14. R.M. Hobson in "Recent developments in Shock Tube Research" ed. D. Bersharder and W. Griffith (1974)
15. J.S. Chang, Phys. Lett. 63A, 304 (1977)
16. D.K. Bohme, N.G. Adams, Moseman, D.B. Dunkin and E.E. Ferguson, J. Chem. Phys. 52, 5094 (1970)
17. F.C. Fehsenfeld, A.L. Schemetekopf, P.D. Goldan, H.I. Schiff and E.E. Ferguson, J. Chem. Phys. 44, 4087 (1965)
18. M. Bourene and J. LeCalve, J. Phys. (Paris) 32, 29 (1971)
19. F.W. Lee, C.B. Collins and R.A. Waller, J. Chem. Phys. 65, 1605 (1976)
20. A.J. Cunningham and R.M. Hobson, J. Phys. B: Mol. Phys. 5, 2320 and 2328 (1972)
21. M.H. Mentzoni and J. Donohoe, Canad. J. Phys. 47, 1789 (1969)

PLASMA PROPERTIES IN A SHOCK HEATED ARGON ATOMIC BEAM

B. EVANS, R. M. HOBSON

Department of Physics, York University, Toronto, Canada

JEN-SHIH CHANG

Department of Engineering Physics, McMaster University, Hamilton, Canada

K. TESHIMA

Department of Aeronautical Engineering, Kyoto University, Japan

Plasma properties of shock-heated argon atomic beams generated from the reflected region and expanded through a nozzle-skimmer system, have been studied experimentally and theoretically. The experimental range of the present work covers a reflected shock temperature range from 9000 K to 12,500°K, hence leading to beam velocities from 2.5 to 5 km/sec, electron temperatures from 450°K to 1,200°K and plasma densities from 10^5 to 10^8 cm^{-3}. Experimental and theoretical results show that: (1) only Ar^+ ions have been observed in the present experiment; (2) the electron temperature in the atomic beam is much higher than that of the gas(or ion) temperature, and agrees well with the new theoretical values; (3) the radial ion and electron density profiles show that the plasma beam is much wider than the predicted neutral beam; (4) the ion and electron densities increase with increasing reflected region temperature. However, the absolute magnitude is a few orders of magnitude less than the theory. The possible mechanism for this difference is discussed; (5) the present theory predicts accurately the beam velocity; (6) the shape of the beam is very elongated, but a relatively uniform plasma can be produced; (7) the radial and axial profiles of electric field shows a good correlation with ion and electron density profiles.

INTRODUCTION

For many years oven source molecular beams have been used in a variety of research areas such as gas kinetics[8], molecular scattering[8] and space simulation[9]. However molecular beams produced by shock heating have been slow to become productive since, due primarily to their intermittent nature, their properties are rather poorly understood[8,20]. On the other hand they do produce beams of particles in the range of energies 1 - 10eV and, along with this very high intensities (about 10^{21} molecules/sec). This makes them of great interest since this is the energy range which covers the dissociation energies of chemical bonds and the activation energies of many chemical reactions[5, 19]. However, in the case of shock-heated molecular beams with large enthalpies (> 10^6 J/kg), the behaviour of charged particles plays an important role in the subsequent development of the beams. Therefore, in this paper, the plasma properties in a molecular beam that is developed from the expansion of a reflected shock heated gas have been investigated both experimentally and theoretically for argon gas.

2. EXPERIMENTAL APPARATUS

The shock-heated molecular beam apparatus (SHMB) is shown in figure 1. The beam is formed by a high pressure-driven shock tube (I.D. 8.9 cm) using the gas heated in the reflected shock region, then expanded into the low pressure chamber ($p \simeq 10^{-7}$ torr, I.D. 65 cm) through a convergent-divergent conical nozzle and a skimmer. The throat diameter and half angles for nozzle and skimmer are 1 cm - 30° and 0.75 cm - 35°, respectively. The collimator (I.D. 15 cm) is located in the middle of the low pressure chamber to sample this beam. The entrance diameter of the sampling orifice and the half angle of the collimator head are 0.75 cm and 25°, respectively. The cylindrical stainless steel wire probes (radius $R_p = 0.115$ mm and length $\ell = 14$ cm) are located at four parallel positions axially and in one case at five locations radially inside the collimator. Argon gas was used in the experiment together with hydrogen as the driver gas. The ion and neutral composition of the beam have been measured by the mass spectrometer located at an angle 45° from the axis at the end of the collimator. Only Ar^+ ions have been observed in the present experiment.

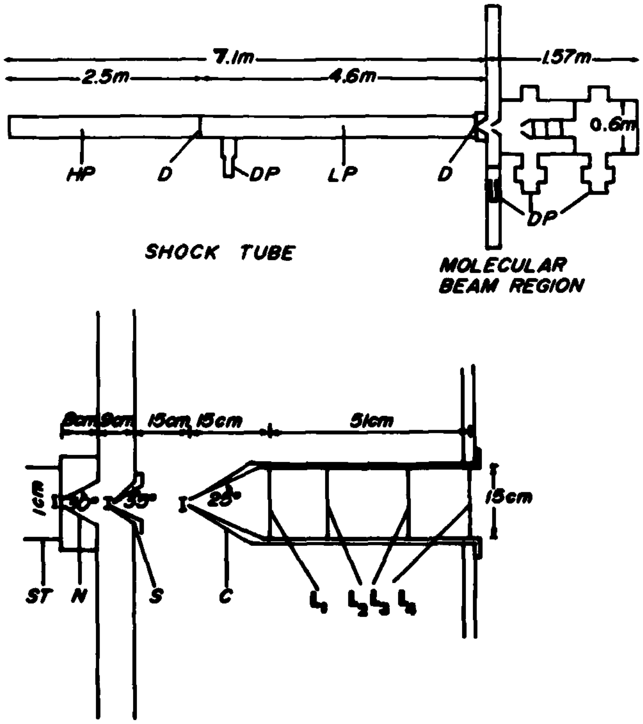

Figure 1. Schematic of the shock tube and associated expansion nozzles.

HP-High pressure driver
D-Diaphram
DP-Diffusion pump
LP-Low pressure section
ST-Shock Tube
N-Nozzle
S-Skimmer
C-Collimator
L_1-L_4-Probe Locations

3. PLASMA DIAGNOSTICS BY AN ELECTROSTATIC PROBE

(i) beam velocity and duration measurement

The beam velocity was measured from the time difference between the current signal of two single probes situated about 51 cm apart. A typical result obtained from the single probes is shown in figure 2a. Figure 2a shows the uniform plasma that can be produced by the present SHMB apparatus. The probe sheath and circuit response time in the collisionless plasma under the present range of conditions is of the order of 10^{-6} sec[17]. Therefore, the shape of the signal response can be taken to represent the shape of the plasma in the beam.

(ii) plasma density measurement

The theory of cylindrical electrostatic probes in a collisionless flowing plasma has been developed by Mott-Smith and Langmuir[16] and Hoegy and Wharton[11] for orbital motion limited condition, i.e. probe radius Rp << Debye length λ_D. The approximate formula for a cylinder in a cross flow in the case of attracting and retarding potentials and associated currents are;

$$I_{at.} \simeq I_o \frac{2}{\sqrt{\pi}} \{\phi_p/\varepsilon + S_i^2 + (\phi_p/\varepsilon + \tfrac{1}{2} S_i^2)/(\phi_p/\varepsilon + S_i^2)\}^{\frac{1}{2}} \qquad (3.1)$$

$$\text{for } (\phi_p/\varepsilon + S_i^2) > 1$$

and

$$I_{ret.} \simeq I_o \exp(-\phi_p)\,[1 + (\tfrac{1}{2} + \phi_p) S_e^2 + (\phi_p^2/4 - \phi_p/4 - 1/16) S_e^4 + \ldots.] \qquad (3.2)$$

respectively, where I_o is the random motion current $\frac{1}{4} Ne(8kT/\pi m)^{\frac{1}{2}}$, e is the electric charge, k is Boltzmann's constant, m is the mass, N is the number density, ϕ_p is the nondimensional potential eV_p/kT, T is the temperature, V_p is the surface potential, S is the speed ratio $U/(2kT/m)^{1/2}$, ε is the ion-to-electron temperature ratio (T_i/T_e), and U is the plasma velocity.

From the recent numerical prediction of the probe current using a symmetrical potential profile model in a collisionless flowing plasma and developed by Godard[10], the orbital motion limited attracting current expression (eq. 3.1) can be applied to any value of the Debye ratio (R_p/λ_D) for $S_i \gg 1$ when the effect of the wake[7,15] can be neglected. These results are also confirmed experimentally by Evans et al[7] for the range of R_p/λ_D from 0.5 to 4. For the present beam condition, the range of the ion and electron speed ratio is approximately between 10 and 0.1, respectively. Therefore, equation 3.1 is used for both electron and ion density determination; at the same time the ion temperature is determined from the theory developed in the next section.

(iii) electron temperature and electric field measurement

The electron temperature has been determined by the triple probe method[3], since the reproduceability of both the plasma and the smaller electron-to-ion current ratio predicted by equations 3.1 and 3.2 does not permit an accurate determination of electron temperature when $T_e \lesssim 0.1$ eV[2].

The triple-probe method has particular merit in the present case, since no voltage sweep is required. In the triple-probe method, three identical probes P_1, P_2 and P_3 with different probe potentials V_1, V_2 and V_3 are used together in the plasma to be measured. V_{13} $(=V_3 - V_1)$ is the externally applied voltage between probe P_1 and P_3, P_2 is by nature always at the floating potential, and $V_{12}(=V_2 - V_1)$ is measured by a high input impedance technique. The currents to each probe become $I_2 = 0$ and $I_1 - I_3 = I$. Therefore, the relations between N_e, T_e, V_{13} and V_{12} can be generalized as follows[22]:

$$\frac{1}{1 + h_1(\phi_{12}, \phi_{13})} = \frac{1 - \exp(-\phi_{12}) + h_2(\phi_{12})}{1 - \exp(-\phi_{13}) + h_3(\phi_{12}, \phi_{13})} \tag{3.3}$$

and

$$N_e = I_3 h_4(\phi_{12}) \frac{4}{aA_p} \left(\frac{2\pi m_e}{kT_e}\right)^{\frac{1}{2}} \tag{3.4}$$

where A_p is the area of probe, h_1, h_2 and h_3 are correction factors due to the difference between the ideal nondimensional probe current[16] $i_p = -\exp(-\phi_p) + a$, and actual current $i_p = -g_1(\phi_p)\exp(-\phi_p) + a g_2(\phi_p)$, i.e. eqs. (3.1) and (3.2) for this case, and a is a constant equal to the ratio between ion and electron current at space potential. For the ideal triple probe case[3] h_1, h_2, h_3 and h_4 have the values unity, zero, zero and unity, respectively. Equation (3.3) serves to determine Te from the measured voltage V_{12}, and equation (3.4) serves to determine Ne from the measured I_3 and V_{12}. We can obtain the local electric field E_{12} between P_1 and P_2 when $V_{13} = 0$ and electron temperature when V_{13} is constant. Therefore, a more accurate electron temperature can be measured after we subtract E_{12} from the signal of V_{12}.

A typical response of the triple probe, V_{12} and the electric field are shown in figures 2a to 2c for $T_5 = 11{,}230$°K. Figure 2 also shows the uniformity of the plasma that can be obtained from the SHMB.

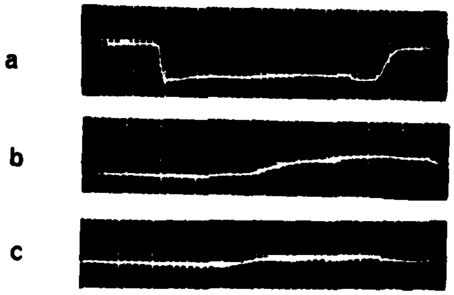

Figure 2. Typical oscilloscope trace from (a) single probe showing ion current density (at ion attracting potential), (b) triple probe V_{12} for $V_{13} = 0.1$V (electron temperature), and (c) triple probe V_{12} for $V_{13} = 0$ V (electric field) for $T_5 = 11230$°K. The horizontal scale is 0.2 msec/cm.

4. THEORETICAL MODEL OF PLASMA DECAY AND ELECTRON TEMPERATURE RELAXATION IN A SHOCK HEATED MOLECULAR BEAM

The theoretical model of SHMB was first proposed by Jones[13] for small reflected temperature conditions ($T_5 < 8000$°K). In the present model, two different regions are considered; namely a nozzle expansion region and a skimmer expansion region. In the above two regions both the energy equations for gas and electrons, and the momentum and continuity equations for gas and plasma have been solved. Here we assumed that the net charge density is zero (i.e. a plasma exists) throughout the model. We also assumed that the plasma is optically thin and has a Maxwellian distribution of energy.

In the shock reflected region, the JPL Thermo-chemistry Program[12] has been used. In the expansion nozzle, the one-dimensional inviscid adiabatic model developed by Talbot[21] has been modified. Three-body and radiative volume recombination, electron-ion and electron-neutral elastic collisions are considered for the nozzle region. In describing the skimmer expansion, the latter model is employed as far as it concerns electron energy and plasma density conservation. However for the neutral gas particles the theory of Mirels and Mullen[14] is used. Here we assumed that the effect of the collimator can be neglected, since the mean free path of the particles is much larger than the dimension of the collimator.

Typical theoretical electron and gas temperature, and gas plasma number density decay along the axis of SHMB, calculated by this model, are shown in figure 3 for $T_5 = 11230$°K. The slower electron temperature and faster plasma density decay are due to the energy conversion taking place during the electron-ion volume recombination reactions.

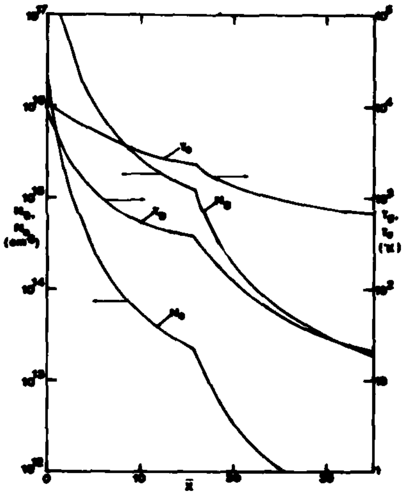

Figure 3. Theoretical gas and plasma densities, and gas and electron temperature as a function of nondimensional distance from nozzle entrance

$$\bar{x} = \frac{x \tan\theta}{r} = \frac{x}{0.866} .$$

5. EXPERIMENTAL RESULTS

Beam velocity V_b, electron temperature T_e, electron and ion density versus shock tube reflected region temperature T_5 are shown in figures 4 (a), (b), (c) and (d), respectively at a distance 66cm downstream from the collimator orifice L_4; solid lines represent the theoretical curves which were calculated by the present theoretical model described in sec. 4. Fig. 5 shows similar dependences at a distance of 15 cm downstream from the collimator orifice L_1; (a) electron temperature, (b) electron density, and (c) ion density. Figure 4a shows that the theoretical neutral gas beam velocity agrees well with that of the measured plasma beam velocity. This indicates that the neutral beam coincides with the plasma beam, and the calculated gas (or ion) temperature is confirmed to be correct, which implies that most of thermal kinetic energy is converted into directed flow.

Figures 4b and 5a shows that the electron temperature agrees well with the theoretical values, where T_{max} is the electron temperature at the collimator orifice, and T_{min} isthe electron temperature at each measuring point. Figures 4b and 4c show that the electron and ion densities have an order of magnitude difference at the entrance region of the collimator (L_1), where both N_e and N_i are four orders of magnitude lower than the theoretical values. However, figures 5c and 5d shows that this difference becomes smaller downstream of collimator (L_4). Figures 5c and 5d also show that the net charge density (N_e-N_i), becomes smaller when T_5 is small. This phenomena of charge separation can also be found from axial electron temperature, electron density, ion density and electric field profiles as shown in figures 6 (a), (b), (c) and (d), respectively for $T_5 = 11230$°K, where theoretical axial profiles calculated employing the model described in sec. 4 are represented by solid lines. An order of 0.1 V/cm axial electric field E_x has been observed in the entrance region of collimator, and this axial electric

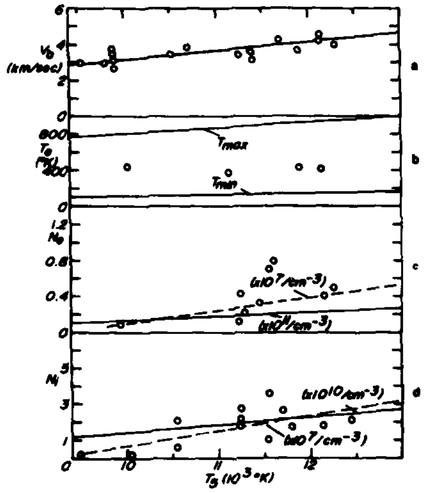

Figure 4. Beam velocity, electron temperature, electron and ion density as a function of the reflected temperature of the shock tube, at 66 cm downstream of collimator orifice.

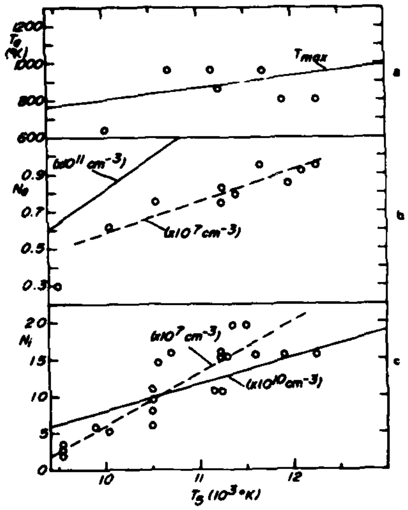

Figure 5. Electron temperature, electron and ion density as functions of the shock tube reflected temperature at 15 cm downstream of the collimator orifice.

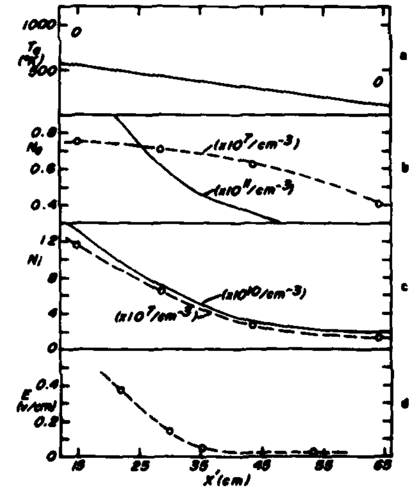

Figure 6. Axial dependencies of electron temperature, electron and ion densities, and axial electric field for T_5 = 11,230°K. Here x' = 0 at the collimator orifice.

field decreases with increasing x′. The order of magnitude calculations of space charge field caused by the net charge (N_i-N_e) using Poissons equation, figures 6b and 6c agree well with present observations.

A possible mechanism describing this charge separation may be due to the effect on the plasma by the collimator. In the front of collimator a sheath is formed when the plasma beam arrives from the skimmer thus driving the collimator negative w.r.t. plasma potential; since the collimator potential is floating with respect to the plasma potential[6]. In the floating potential plasma sampling, i.e. electron current flux $\equiv$ ion current flux, only part of the electrons can pass the sheath which is at a retarding potential for electrons while the ions are attracted by this potential. Therefore, in the entrance region, inside the collimator, the ion density is much larger than that of the electrons. In the next stage, the electric field formed by this space charge gradually disappears downstream of the collimator, since the Debye ratio (collimator

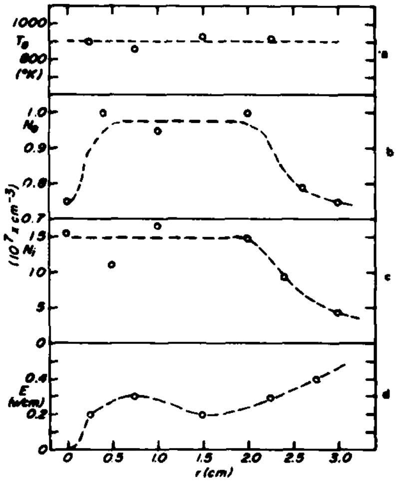

Figure 7. Radial dependencies of electron temperature, electron and ion densities, and radial electric field E_r, 15 cm downstream of collimator orifice; at $T_5 = 11{,}230$°K.

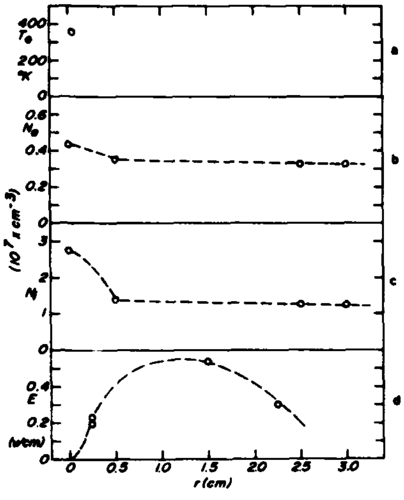

Figure 8. Radial dependencies of electron temperature, electron and ion densities, and radial electric field at 66 cm downstream of collimator orifice at $T_5 = 11{,}230$°K

radius/Debye length) is large enough to result in a quasi-neutralized beam.

Electron temperature, electron density, ion density and radial electric field profiles are shown in figures 7(a), (b), (c) and (d), respectively for $T_5 = 11{,}230$°K at L_4. No radial electron temperature dependence has been observed from figure 7a. Figures 7b and c demonstrate the abnormal charge depletion in the centre region of the collimator. This phenomena becomes opposite at the downstream location L_4 as shown in the figure 8. However, the electric field profile measured and displayed in figure 7d agrees in qualitative behaviour with the electric field calculated from the Poisson equation and employing the net charge (N_e-N_i) from figures 7b and 7c. This can be taken to imply that the potential profile created by the collimator geometry has a significant influence on the charged particle profiles. Figures 2, 7 and 8 show that the plasma beam is much wider than the predicted and measured[20] neutral beam, and the overall length is very elongated.

Acknowledgements

We wish to express our appreciation to J.G. Laframboise, R. Godard, R.H. Prince and G.L. Ogram for valuable discussions and comments. This work was supported by the National Research Council of Canada.

References

1. J.S. Chang, M. Kamitsuma and Sin-Li Chen, Planet. Space Sci. <u>25</u>, 973 (1977)
2. J.S. Chang, K. Keskinen and R.M. Hobson, Jpn. J. Appl. Phys. <u>18</u>,7005 (1979)
3. Sin-Li Chen and T. Sekiguichi, J. Appl. Phys. <u>36</u>, 2263 (1965)
4. C.J. Chen. J. Chem. Phys. <u>50</u>, 1560 (1969).
5. K.C.A. Crane and R.J. Stalker, J. Phys. D: Appl. Phys. <u>10</u>, 679 (1977)
6. H.W. Drawin "Mass spectrometry of plasmas" in "Plasma Diagnostics" Ch. 13, North Holland (1968)
7. B. Evans, J.S. Chang and R.M. Hobson, Trans. Amer. Geophys. <u>59</u>, 337 (1978)
8. M.A.D. Fluendy and K.P. Lawley "Chemical Applications of Molecular Beam Scattering", Chapman and Hall Ed. p.85 (1973)
9. B. French, AIAA Journal <u>3</u>, 993 (1965)
10. R. Godard, Ph.D. Thesis, York University (1975)
11. W.R. Hoegy and L.E. Wharton, J. Appl. Phys. <u>44</u>, 5365 (1973)
12. T.E. Horton and W.A. Menard, Jet Propulsion Laboratory, Technical Report 32-1350 (1969)
13. T.V. Jones, Proceedings of the 7th AGARD Meeting "Selected Topics in Aerothermochemistry" Oslo, I. Glassman Ed. (1966)
14. H. Mirels and J.F. Mullen, AIAA Journal <u>1</u>, 596 (1963)
15. M. Makita and K. Kuriki, Phys. Fluid <u>21</u>, 1279 (1978)
16. H. Mott-Smith and I. Langmuir, Phys. Rev. <u>28</u>, 727 (1926)
17. T. Okuda, J. IEE Japan, <u>83</u> ,1922 (1963)
18. G.T. Skinner, Cornell Technical Report CAL No. RM-2028-A-1, Cornell Aeronautical Laboratory Inc. (1969)
19. D. Spence and K.T. Dolder, Phys. Fluids <u>13</u>, 88 (1970)
20. K. Teshima and N. Takahashi, In this proceedings (1979)
21. L. Talbot, University of California at Berkley, Report No. AS-65-14 (1965)
22. G.L. Ogram, J.S. Chang and R.M. Hobson, J. Appl. Phys. <u>50</u>, 726 (1979)

NOVEL LASER DOPPLER VELOCIMETER ENABLING FAST INSTANTANEOUS RECORDINGS

GÜNTER SMEETS and ALFRED GEORGE

German-French Research Institute of Saint-Louis
68-Saint-Louis, France

A new species of a laser Doppler velocimeter is presented based on wavelength detection with a two beam interferometer. The sensitivity to small Doppler shifts of the monochromatic laser light is obtained using an optical path difference, $\Delta\phi$, which is large as compared to the light wavelength λ. By means of a fast feedback system, the phase, $\Delta\phi/\lambda$ is kept constant. Wavelength changes are immediately answered by changes of $\Delta\phi$ generated with a Pockels cell. The Pockels cell voltage is a signal proportional to the instantaneous wavelength changes of the scattered light enabling a direct recording of the corresponding velocity component of the scattering object. With a slight seeding of the flow, a continuous recording can be obtained having a time resolution of 1 μs or less. The technique is therefore specially well suited for local and non-intrusive velocity measurements in highly unsteady flows. Its application to shock tube experiments will be discussed and demonstrated by a number of examples.

INTRODUCTION

This Doppler velocimeter can be regarded as a rather special type of spectrometer. At its entrance it receives the scattered and Doppler shifted light of a continuous monochromatic laser. As the output a continuous electrical signal is generated that proportionally follows the wavelength changes of the light. Thus a direct velocity signal is available with a possible time resolution of one μs or even less.

The instrument is basically a two-beam (Michelson) interferometer. The sensitivity to small Doppler shifts of the monochromatic laser light is obtained using an optical path difference $\Delta\phi$, which is large as compared to the light wavelength λ. Michelson-spectrometers have been described by Ring and Schofield and Elsworth, James and Sternberg[2]. Barker and Hollenbach[3] and Munson and May[4] applied them to velocity measurements of moving surfaces by directly recording the interferometric radiant flux modulations, which are of course not linearly related to the wavelength changes and also vary according to the scattering intensity modulations.

The velocimeter described in this article uses a fast feedback system maintaining a constant phase $\Delta\phi/\lambda$. Doppler shifts of the wavelength λ are immediately answered by changes of $\Delta\phi$ generated with a Pockels cell. The

Pockels cell voltage can be directly recorded as the velocity signal.

DESCRIPTION OF THE SYSTEM

The operating principle of the system is illustrated in Fig. 1. A portion of the scattered Doppler-shifted laser light is fed into the Michelson interferometer. The entering beam is divided by means of a polarizing beamsplitter cube separating the two modes of linear polarization. A glass block in the longer leg matches the wave fronts of the two bundles and allows for finite bundle angles so that a high light gathering power of the instrument is achieved.

After recombination, the two modes are mixed in a second polarizing beamsplitter of 45° orientation. This leads to the following complementary radiant flux modulation at the photocathodes of the two photomultipliers:

$$P_1 = P_0\cos^2(\pi\Delta\phi/\lambda) \qquad (1)$$

$$P_2 = P_0\sin^2(\pi\Delta\phi/\lambda). \qquad (2)$$

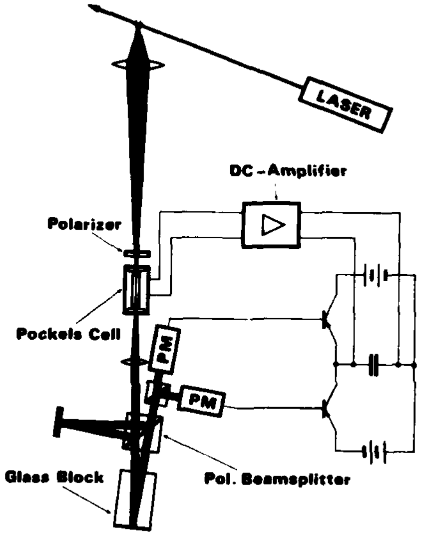

Fig. 1 Fast wavelength tracking system

Using a simple electronic system, a current is generated which is proportional to the difference of the photomultiplier signals. This difference current is transmitted to a capacitor. The voltage of the capacitor is amplified and applied to a Pockels cell located at the entrance of the Michelson.

The scattered laser light, prior to entering the Pockels cell, is previously polarized at 45° with respect to its crystal axes. In this case two coherent polarization modes polarized in the direction of the crystal axes are generated in the Pockels cell. A voltage applied to the Pockels cell, U_{PC}, introduces an optical path difference $\Delta\phi_{PC}$ between the two modes according to:

$$\Delta\phi_{PC} = \alpha U_{PC}. \qquad (3)$$

The polarization modes produced in the Pockels cell keep their identity in the Michelson interferometer and are sent through the different legs. Therefore, the Pockels cell acts on the overall optical path difference of the system as though it were integrated in the Michelson interferometer affecting the path length of one of its legs.

The feedback system is in equilibrium for equal radiant power on both photomultipliers. In this case, an equal current passes through both transistors and there is no difference current altering the voltage of the capacitor as well as that of the Pockels cell. According to Eqs. (1) and (2), an equilibrium situation is given if the total optical path difference is

$$\Delta\phi/\lambda = 1/4 \pm n/2. \qquad (4)$$

n is an integer of the order 10^5 to 10^6. The equilibrium is stable if

$$\Delta\phi/\lambda = 1/4 \pm n \qquad (5)$$

In this case a wavelength shift $d\lambda$ (due to a velocity change in the scattering region) is immediately compensated for by a change of the optical path difference in the Pockels cell, $d\Delta\phi_{PC}$,

$$d\Delta\phi_{PC} = (\Delta\phi/\lambda)\cdot d\lambda \qquad (6)$$

so that the equilibrium condition (5) is retained. According to Eqs (3) and (6) there is a linear relation between $d\lambda$ and the Pockels cell voltage change, dU_{PC},

$$dU_{PC} = (\Delta\phi/\alpha\cdot\lambda)\cdot d\lambda \qquad (7)$$

Recording of the Pockels cell voltage variations $dU_{PC}(t)$ results, therefore, in a continuous recording of the Doppler shift $d\lambda(t)$ (and of the corresponding velocity component in the scattering region). The sensitivity of the system can be adapted to the velocity range by the choice of $\Delta\phi$ (size of the glass block). Since relation (7) is independent of the radiant power amplitude P_0, variations in scattering intensity over a wide range can be allowed for.

The time constant of the system τ, however, does depend on P_0. In order to obtain the quantitative expression for τ, the differential equation governing the feedback system will be derived.

The currents I_1 and I_2 passing through the two transistors are controlled by the radiant powers at the photomultipliers, P_1 and P_2:

$$\begin{aligned} I_1 &= \beta P_1, \\ I_2 &= \beta P_2. \end{aligned} \qquad (8)$$

Equal sensitivity β is assumed. For slightly unequal sensitivities, the basic results of the following calculations remain valid. The voltage U of the capacitance C is modified by the difference current $I_1 - I_2$ according to

$$U = (1/C) \int (I_1 - I_2)dt \qquad (9)$$

As the capacitor is coupled with the Pockels cell via an amplifier having an amplification factor V, U leads to an additional optical path difference in the Pockels cell, $\Delta\phi_{PC}$,

$$\Delta\phi_{PC} = V\alpha U, \qquad (10)$$

which adds to the optical path difference of the Michelson interferometer, $\Delta\phi_I$. The total optical path difference is given by

$$\Delta\phi = \Delta\phi_I + \Delta\phi_{PC}. \qquad (11)$$

By combining Eqs (1), (2), and (8)-(11), the differential equation for the feedback system is found to be

$$\frac{d}{dt}\Delta\phi_{PC} = \frac{V\alpha\beta P_0}{C}\cos(2\pi\Delta\phi/\lambda). \qquad (12)$$

This proves Eq. (5) to give the conditions of stable equilibrium corresponding to the central points of the negative slopes of the cosine. For small deviations from equilibrium, that is, within the straight portion of the slope, Eq. (12) can be linearized. If

$$\Delta\phi_e = (1/4 \pm n)\lambda \qquad (13)$$

is an equilibrium value of $\Delta\phi$, and if

$$d\Delta\phi = \Delta\phi - \Delta\phi_e = \Delta\phi_{PC} - \Delta\phi_{PC_e} \qquad (14)$$

is a deviation from the equilibrium value within the straight portion of the slope, Eq. (12) can be replaced by the linear differential equation

$$\frac{d}{dt}\,\Delta\phi_{PC} = -\,\frac{2\pi V\alpha\beta P_0}{\lambda C}\,(\Delta\phi_{PC} - \Delta\phi_{PC_e}). \qquad (15)$$

The equilibrium value $\Delta\phi_{PC_e}$ depends on the instantaneous wavelength of the scattered light and is, therefore, a function of time depending on the velocity variation in the scattering region.

From Eq. (15) the time constant for the response of the system is found to be

$$\tau = \frac{\lambda C}{2\pi V\alpha\beta P_0}\,. \qquad (16)$$

From Eqs. (1), (2) and (8) it is apparent that βP_0 is equal to the current amplitude I_0 passing through the transistors. It is, therefore, twice the mean current $\bar{I}$ in an equilibrium state,

$$\beta P_0 = 2\,\bar{I}. \qquad (17)$$

$\bar{I}$ can easily be recorded by inserting a low impedance resistor R into the transistor circuit. As the other constants in (16) are known, τ can be monitored by recording $\bar{I}$,

$$\tau = \lambda\cdot C/4\pi\cdot V\cdot\alpha\cdot\bar{I}\,. \qquad (18)$$

An overall view of the optical arrangement is given in Fig. 2. For greater clarity, the scattered laser light bundles are represented by their axes only. The Michelson interferometer includes the central polarizing beamsplitter cube, a surface mirror, and the glass block with a back surface mirror. These components are incorporated in a compact steel block minimizing the vibrational sensitivity of the interferometer and shielding it from the ambient light and from both the acoustic and turbulent perturbations of the optical path difference. The block also contains a 9o^{o}-prism and the second beamsplitter cube turned by 45^{o}. For the adjustment of the interferometer, the glass block

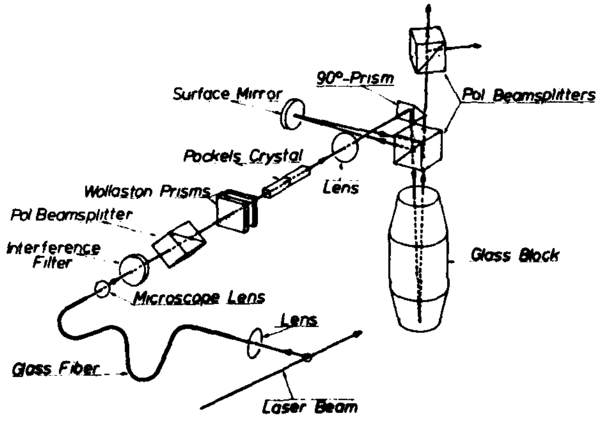

Fig. 2 Optical arrangement

can be translated and the surface mirror is rotatable around two axes.

The photomultipliers are flanged directly to the exit side of the steel block. At its entrance, a tube is mounted containing the additional optical components which are in sequence: an interference filter (used only in special cases), a polarizer, a pair of Wollaston prisms, the Pockels cell, and a lens. The entering scattered light bundle is first polarized at 45° with respect to the optical axes of the subsequent Wollaston prisms, Pockels cell crystals, as well as to the incidence plane of the central polarizing beamsplitter. Thus, two modes of perpendicular polarization having equal intensity are generated. They are separated by the central beamsplitter and sent into the different legs of the Michelson. The Pockels cell crystals and the pair of Wollaston prisms are both equivalent to phase plates introducing additional retardations between the polarization modes. The retardation in the Pockels cell is proportional to the applied voltage, whereas the retardation by the Wollaston prisms depends on their relative position. Shifting of one of the Wollaston prisms in the lateral direction enables a fine adjustment of the optical path difference. The lens is applied to keep the bundle diameter to a minimum within the Michelson. Its focal plane coincides approximately with the reflector surfaces.

The optical path difference in the Pockels cell slightly depends on the light direction, a fact which limits the allowable light bundle aperture in the Pockels cell to about 2°. Aslo in the Michelson interferometer, the optical path difference is not entirely independent of position and light direction because of the inevitable imperfections of the beamsplitter and the reflectors. Finally also the sensitivity of the photocathodes varies considerably over the area. This may lead to uncertainties in the velocity recordings, if there is no guarantee that the geometry of the scattered light bundle remains completely unchanged.

In order to avoid this possible source of error, the receiving optics are coupled to the measuring unit via a glass monofiber. In this case, the geometry of the light bundle entering the interferometer from the fiber exit is almost independent of the original scattered light distribution. The fiber optics coupling also considerably facilitates the adjustment and affords the possibility of a remote measurement which is of importance in case of noisy objects.

A receiving objective transforms the scattered laser light bundle into the small diameter and large numerical aperture of a glass monofiber having a core diameter 25oμm. A microscope objective images the exit plane of the fiber into the Pockels cell. With polished fiber ends and suitably matched bundle angles, the radiation loss can be kept small.

The capacitor voltage is transformed into an optical path shift by means of the Pockels cell PC 19 and the high voltage DC amplifier LA 1o A, both from Electro Optic Developments. The bandwidth limitation of this amplifier allows for a minimum time constant of about one μs of the actual system.

A more detailed description of the Doppler velocimeter, its mechanical, optical and electronic components as well as its performance characteristics are given by Smeets and George[5,6].

CALIBRATION

The calibration factor in Eq. (7), $\Delta\phi/\alpha\cdot\lambda$, can be determined experimentally using the arrangement shown in Fig. 3. By means of a polarizing beamsplitter or a Foster prism, a laser beam is split into its polarization modes. They fall on separate locations at the periphery of a fast turning disk leading to opposite Doppler shifts. The scattered light is depolarized so that part of it in the back scattered direction passes through the Foster prism leaving it in a new direction.

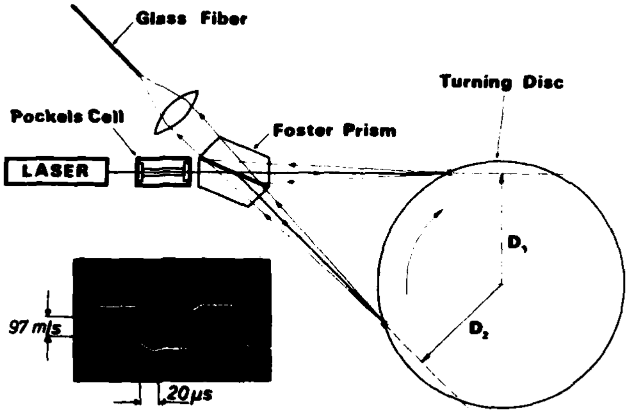

Fig. 3 Arrangement for calibration

A square-wave voltage applied to a Pockels cell of 45° orientation placed immediately behind the laser causes switching of the polarization mode and of the corresponding direction of the initial laser beam. Thus, the Doppler shift of the backscattered light bundle transmitted to the system also shows a square-wave variation. The wavelength jump, $\Delta\lambda$ depends on the velocity component in the light direction, Δu and is given by:

$$\frac{\Delta\lambda}{\lambda} = 2\,\frac{\Delta u}{c} = 2\,\frac{\omega(D_1 + D_2)}{c} \tag{19}$$

where c is the light velocity, ω the angular velocity of the disk, and D_1 and D_2 the spacings between the disk axis and the prolongations of the two partial laser beams.

An example of a calibration signal is shown in Fig. 3. The disk radius was 50 mm and ω was approximately $2\pi\cdot 500\ s^{-1}$. By means of a groove in the periphery of the disk, scattered light is interrupted once every turn allowing for an accurate determination of ω from a frequency measurement.

An experimental determination of the calibration factor offers the advantage that knowledge of the Pockels cell constant as well as of the refractive index and dispersion of the optical components is no longer necessary.

The signal in Fig. 3 also shows the time constant of the system. As the switching Pockels cell, a Lasermetrics 3032 was used driven by an Optimation PA - 25 A amplifier. This combination attains a switching time constant of the order 0.1 μs. The finite rise time in the calibration signal indicates, therefore, the time resolution of the velocimeter.

APPLICATION TO SHOCK TUBE EXPERIMENTS

In gas flow measurements, the scattered light is due to tracer particles. In unseeded flows, the concentration of "natural" dust particles is so low that the scattered light flux originating from a test volume of one millimeter cube or smaller is very discontinuous. The capability of the instrument for resolving velocity changes in microseconds can only be used if there is at any time at least one particle present in the test volume so that the velocity information is continuously transmitted to the velocimeter. This requires - except for the case of two-phase flows - a certain degree of seeding. The desirable seeding for the application of the velocimeter consists of a relatively high number density of rather small particles. In this case, the scattered radiation entering the velocimeter will be uniform and of sufficient intensity. The particle relaxation and the mass loading by the particles can be ignored.

It has been found that filtered cigarette smoke with a concentration of one or two cigarettes for 1 m^3 is quite convenient. For the shock tube experiments described in the following, the driven section was filled with atmospheric pressure air seeded with cigarette smoke. The illuminating laser was a Spetra Physics Model 165 Argon laser used with an internal etalon for single frequency operation having an output of about 1 W.

Figure 4 demonstrates the arrangement used for recording the normal flow velocity behind a shock wave (of shock Mach number 1.6) along the axis of a shock tube. The orientation of the effective velocity component is given by the bisector of the angle between incidence and observation direction. The recorded signals show the expected step function of the velocity followed by a slight increase due to boundary layer action (see Mirels[7]).

The negative velocity jump after 1100 µs is due to an obstacle some centimeters downstream of the measuring point. The fast displayed signal demonstrates that the rise time is not essentially in excess of 1 µs. This is a proof that the particle relaxation time does not exceed one µs. The upper signal is a monitor for the instantaneous current amplitude in the transistor circuit. The voltage across a resistor in the circuit is applied to a logarithmic amplifier and its output is recorded as the monitor signal. The upper signal indicates that the scattering intensity falls off by nearly a factor ten during the registration time. This has no effect at all on the velocity signal.

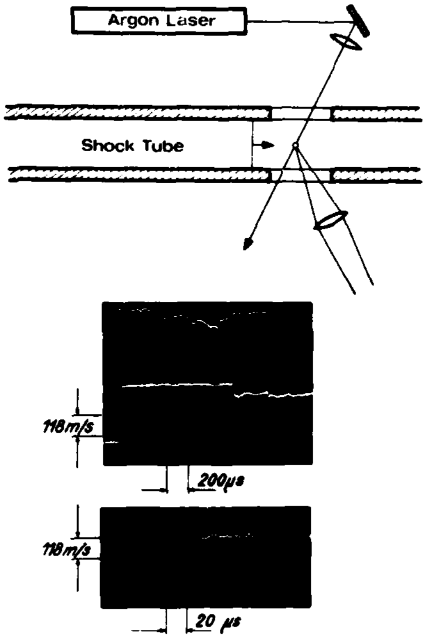

Fig. 4 Velocity recording behind the incident shock.

The magnitude of the recorded velocity is in good agreement with the value calculated from the measured shock speed using the simple shock relations for ideal gases.

The same arrangement used in this test experiment to record the trivial flow behind the primary shock wave can be applied to a great variety of real flow situations in shock tube research. In the following, the investigation of a shock tube generated supersonic jet will be reported.

As is shown in Fig. 5, the jet emanates from a nozzle located in the end wall of the shock tube after reflection of the shock wave from the end of the tube. With a shock Mach number of about $M_s = 1.7$, a supersonic jet having a Mach number $M_j = 2$ is generated. At this relatively low shock Mach number, the air in the shock tube is compressed nearly isentropically by the incident and the reflected shock. The subsequent expansion in the nozzle leading to the initial atmospheric pressure of the gas also brings the gas back to room temperature so that the sound speeds inside and outside the jet are nearly identical: $a_j \approx a_\infty$. The nozzle has an exit diameter D = 10 mm and is contoured to generate a parallel supersonic jet.

Fig. 5 shows a recording of the velocity in the main flow direction, v_x. The chosen measuring point was on the jet axis $r = 0$ at a distance $x =$ 60 mm from the nozzle exit. Already 300 µs after the arrival of the first shock wave at the test position, the jet has attained its stationary state at this section. The monitor signal indicates that the scattered light level was at any time sufficiently high to guarantee a time resolution $\tau \leq 10$ µs. Only small velocity variations appear on the jet axis, probably due to a strong ultrasonic field consisting of a series of Mach waves. When the measuring point is moved away from the axis and approaches the turbulent mixing layer of the jet, the velocity fluctuations increase. This is demonstrated in Fig. 6, which shows a set of v_x-records of the same jet at $x = 40$ mm for various distances r from the axis. In the mixing layer from $r = 5$ mm up to $r = 7$ mm the velocity variations Δv_x are very strong, their peak to peak values reach about half the jet speed. The average velocity shows a plateau in the interior jet and drops continuously in the mixing layer with increasing r. At $r =$ 9 mm the average velocity is not far from zero. Now and then a burst appears. In addition, velocity fluctuations associated to an emitted strong Mach wave field occur. Quantitative data concerning these Mach waves in the near field of supersonic jets were obtained using an optical microphone developped by Smeets and George[8].

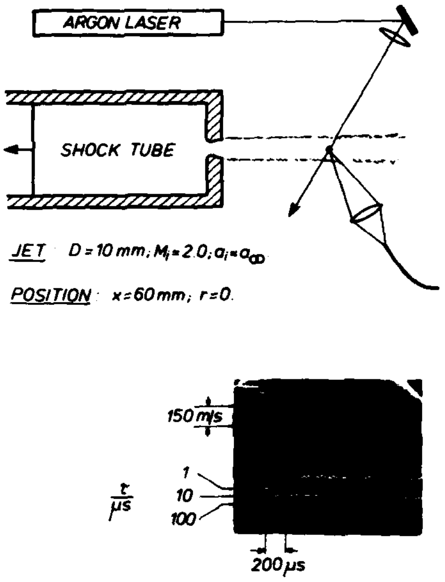

Fig. 5 Velocity recording in a shock tube generated supersonic jet

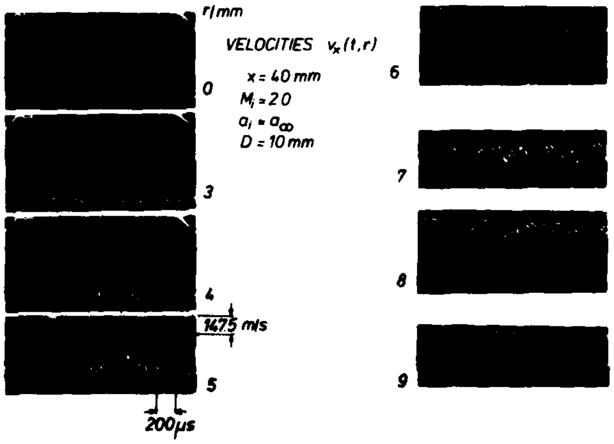

Fig. 6 Velocities at various positions of the jet

In order to achieve a continuous signal from the mixing region, the gas atmosphere surrounding the jet must also be seeded with cigarette smoke as is the gas in the shock tube. For this, a reservoir containing the smoke atmosphere was flanged to the end of the shock tube.

From several series of velocity records, time averaged velocity profiles were plotted. Fig. 7 shows $\bar{v}_x$ (r) - profiles for x = 2o mm, 4o mm and 8o mm. It is of course an open question, whether there is a physical meaning of an average velocity in a shear layer in view of extremely large fluctuations. On the other hand the velocity fluctuations are of special interest as they can give some information about the turbulence structure of the shear layer.

By simply changing the observation direction, the two additional velocity components v_r and v_ϕ can be recorded. This is indicated in Fig. 8.

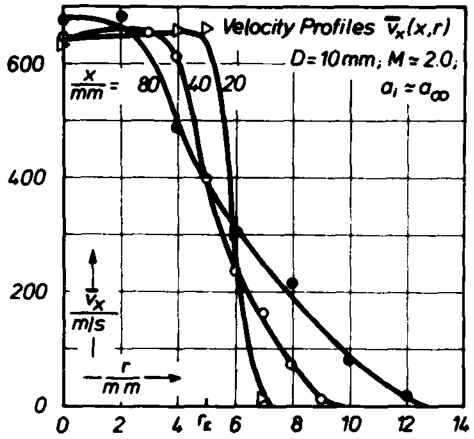

Fig. 7 Time averaged velocity profiles of the jet

The circumferential component vϕ, for instance, is obtained if the laser beam passes off axis through the jet and if the test volume is chosen in the plane of symmetry. In Fig. 8 the three velocity fluctuations Δv_x, Δv_r, Δv_ϕ received for the same coordinates x = 4o mm, r = 6 mm are compared. The three components show comparable frequencies. The amplitude of the transversal fluctuations Δv_r and Δv_ϕ is smaller by a factor 4 as compared to Δv_x.

The signals in Fig. 8 were recorded subsequently with the same instrument. A more crucial information on the turbulence structure could be of course achieved with coherent signals. A second velocimeter is in preparation which will offer the possibility of recording simultaneously two signals related to two components at the same point or to velocities at two different points.

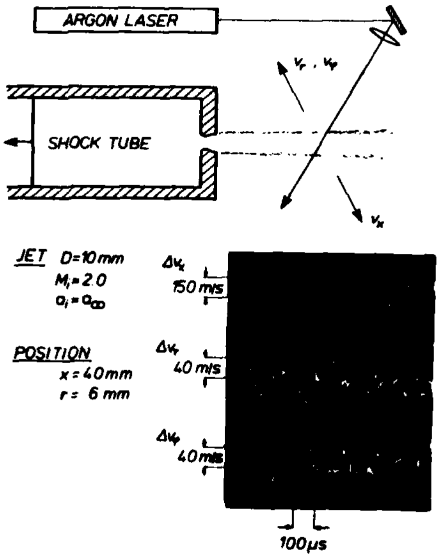

Fig. 8 Recording of the three components of velocity fluctuations.

CONCLUDING REMARKS

The velocimeter described in this article opens new possibilities in shock tube diagnostics: the velocity variations of the highly unsteady flows typical of shock tube experiments can now be recorded in real time. The measurement is local and non-intrusive. The range of velocities has in principle no upper limit except for the light velocity. On the other hand, the sensitivity of the system can be made high enough to resolve velocity variations of a fraction of a m/s. The record in Fig. 9 shows the velocity variation associated with an N-wave-like pressure perturbance from a spark. The high sensitivity was achieved by replacing the glass block by a multiple pass system consisting of a plane mirror and a spherical mirror resulting in an optical path difference of 2.4 m.

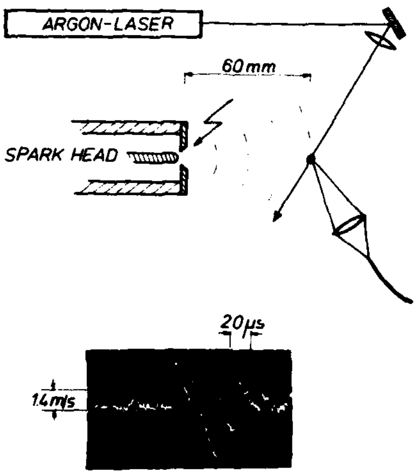

Fig. 9 Velocity variation from a spark gap generated pressure wave.

REFERENCES

1. J. Ring, J.W. Schofield, Appl. Opt. 11, 5o7 (1972)
2. Y. Elsworth, J.F. James, R.S. Sternberg, J. Phys. E 7, 813 (1974)
3. L.M. Barker, R.E. Hollenbach, J. Appl. Phys. 43, 4669 (1972)
4. D.E. Munson, R.P. May, AIAA J. 14, 235 (1976)
5. G. Smeets, A. George, Rev. Sci Instrum 49, 1589 (1978)
6. G. Smeets, A. George: Laser-Doppler-Velozimetrie mithilfe eines Michelson-Interferometers mit schneller Phasennachführung. German-French Research Institute of Saint-Louis rep. R 124/78 (1978)
7. H. Mirels, Phys. Fluids, 9,1o, 19o7 (1966)
8. G. Smeets, A. George, JASA 63, 3, 872 (1977)

MOLECULAR BEAMS FROM SHOCK HEATED SOURCE

KOJI TESHIMA and NORIO TAKAHASHI

Department of Aeronautical Engineering
Kyoto University, Kyoto, Japan

Properties of argon beams produced by a simple shock-tube-driven molecular beam apparatus are examined. As measured by platinum thin film gauges, intensities of $4\text{-}9\times10^{20}$ particles $\text{ster}^{-1}\text{sec}^{-1}$ for times ranging from 1-3 msec are achieved, much smaller than those predicted by theory. The discrepancy is explained by skimmer interactions, the extent of which has been correlated with the ratio of Knudsen number to Mach number at the skimmer, Kn_S/M_S, for molecular beams with room temperature sources. The present results are about 10 times higher for a given Kn_S/M_S than the earlier results. This is explained by mainly higher source temperature.

INTRODUCTION

Molecular beams have proved to be extremely powerful and versatile experimental tools in a wide range of problems in physics and chemistry, including studies of gas-surface interactions and molecular energy transfer mechanisms as well as of expansion processes by which the molecular beams are produced. Conventional steady flow nozzle beams with resistance heated nozzles have two limitations. In the first place the source temperature cannot greatly exceed 3000°K. In the second place steady flow requires high capacity vacuum pumps or the complications of staging. Beams from the shock-heated source gas, on the other hand, first proposed by Skinner,[1] can take advantage of very high effective source temperatures, much above the melting point of walls. This advantage has been utilized to produce high energy atomic beams of 1-3 e.v. for studies of gas-surface interactions by Jones,[2] Skinner,[3] and Calia and Oman.[4] Because shock-heating means that flows are intermittent, high intensities can be easily obtained with much smaller vacuum pump capacity than would be required for steady flow sources of equivalent intensity. Moreover, because internal energies are often frozen during hypersonic expansion, beams of highly excited (vibrationally and electronically) species can be obtained. Therefore, shock-heated molecular beam sources could be attractive in studies of reaction dynamics, especially when internal energy plays an important role. Spence and Dolder[5] have reported that fragmentation patterns for vibrationally excited O_2 molecules in shock-heated beams differ from those obtained at room temperature. Ions and electrons can also occur in such beams and because of their high speed ratio provide simulation of plasma flow encountered by upper atmosphere satellites.[6] The direct mass sampling of species from shock tubes in the form of molecular beams has been attempted by several authors.[5-7] Therefore, development and understanding of techniques for using shock-heated gas as a beam source may advance the art of molecular beam sampling of shock tube reactors so that mass spectrometric analysis can be more effectively used and interpreted.

In this paper, we report on properties of argon beams produced by a simple shock-tube-driven molecular beam apparatus, which has a nozzle-skimmer arrangement similar to that of Jones.[8] Intensities of the beams have been measured by platinum thin film gauges. Difference between measured intensities and those predicted by theory is discussed in terms of skimmer interactions, the extent of which can be correlated with the ratio of Knudsen number to Mach number at the skimmer, Kn_S/M_S, as reported by Fenn and Deckers[9] and Anderson *et al.*.[10]

THEORETICAL PREDICTION OF BEAM INTENSITY

The important components of a typical nozzle beam system are a nozzle, a skimmer and a collimator. The gas from a reservoir expands through the nozzle to form a supersonic stream from which a small sample flows through a collimating "skimmer" to form a beam. The nozzle expansion can be treated as a one-dimensional inviscid and adiabatic flow with real gas effects. For such flows of ionized gas, the governing equations i.e. the global continuity, momentum and energy conservation and the electron species and energy conservation equations, have been well established. In the present calculation the expressions by Talbot *et al.*[11] have been used and for numerical integrations at the nozzle throat the technique by Hall and Russo[12] has been used. Typical results of flow properties along a conical nozzle with a half angle of 30° are shown in Fig.1. Conditions at the skimmer entrance have been calculated assuming that the nozzle extends to the skimmer entrance.

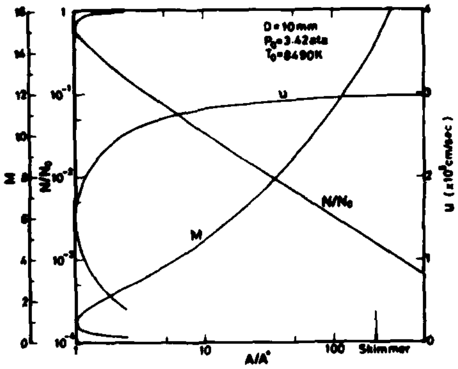

Fig.1 Flow velocity u, Mach number M, and number density ratio N/N_0 against the area ratio A/A^*. Three body recombination and optically thick conditions are assumed.

For analytical treatments of the skimmer flow, both free molecular theory and continuum theory can be applied. The nozzle beam theory first proposed by Kantrowitz and Grey[13] is based on free molecular theory, which gives number density, N(x), of a molecular beam at an axial distance x from the skimmer entrance on axis;

$$N(x)/N_S = (\gamma/2)M_S^2(r_S/x)^2, \qquad \mathrm{I}$$

where γ is the specific heat ratio of the gas, N_S the number density at the skimmer entrance and r_S the skimmer orifice radius.

Under most present experimental conditions flows are not entirely free molecular at the skimmer, but in the transition regime. The skimmer has a conical shape with a sharp lip at the entrance of which the external angle is small enough so that the shock wave produced on the outside of the cone is attached. The internal angle is large enough so that the inner wall of the skimmer does not limit further expansion. Therefore, the skimmer flow can be treated as a hypersonic expansion into a vacuum through an orifice. Several analytical expressions have been obtained. Thornhill[14] has given a steady solution for large axial distance, which is given by

$$N(x)/N_S = \{(\gamma^2/2)(\gamma-1)/(2\gamma-1)\}M_S^2\,(r_S/x)^2\,. \qquad \text{II}$$

The problem can be treated as a two-dimensional unsteady expansion of initially uniform gas. From the analysis of Greifinger and Cole[15] the density can be expressed by

$$N(x)/N_S = C(\gamma)M_S^2\,(r_S/x)^2\,, \qquad \text{III}$$

where $C(\gamma)$ is a function of γ and given graphically by them. A similar treatment by Mirels and Mullen[16] gives the same expression with different values of $C(\gamma)$. All the theoretical expressions including the free molecular model have the same functional form except for $C(\gamma)$. The values of $C(\gamma)$ are compared for $\gamma=5/3$ in Table 1. The free molecular theory predicts values 1.9-2.6 times larger than the continuum theories. This problem can also be treated as an axisymmetric Prandtle-Meyer expansion and the flow properties can be calculated by the method of characteristics, which gives an exact solution. Our calculation was started from 33 equally spaced initial points on the primary Mach line at the orifice and was done on a sufficient number of Mach lines at intervals of 0.05 to values large enough so that solutions for any desired axial distance can be obtained. The calculated density on axis is compared with the Thornhill solution in Fig.2. There is quite good agreement between them except at small values of x/r_S where the latter is not really applicable.

Table 1. Comparison of values of $C(\gamma)$ for $\gamma=5/3$

	Kantrowitz & Grey	Thornhill	Greifinger & Cole	Mirels & Mullen
$C(\gamma)$	0.833	0.397	0.32	0.444

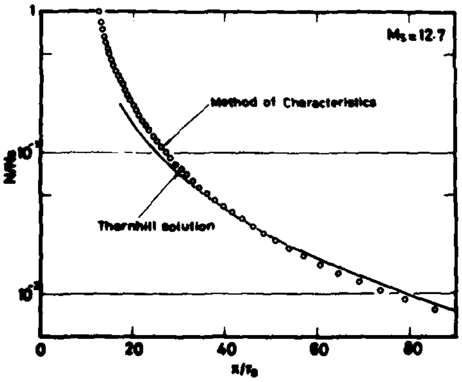

Fig.2 Comparison of the density on the skimmer axis obtained by the method of characteristics with the Thornhill solution for skimmer Mach number of 12.7.

EXPERIMENTAL

Apparatus

As shown in Fig.3, the apparatus consisted of a shock tube and a vacuum tank containing a skimmer and a collimator. The shock tube was connected with the vacuum tank by a convergent-divergent conical nozzle. The tube was initially isolated from the vacuum tank by a polyethylene diaphragm close to the nozzle with thickness of either 4 or 8 μm. The diaphragm was ruptured by the high pressure gas behind the reflected shock so that the hot gas in the shock

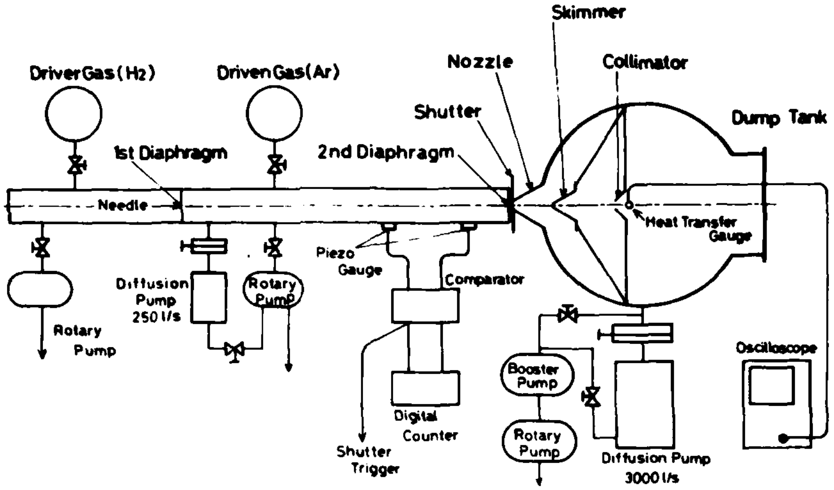

Fig.3. Schematic of the apparatus.

tube could expand through the nozzle into the vacuum tank. A small portion of the expanded gas passed successively through the skimmer and the collimator to form the shock-heated molecular beam.

The shock tube consisted of a 2.5 m driver section and a 4.7 m driven section. Both were made of stainless steel pipes having an inside diameter of 12.8 cm and were separated by a diaphragm. Several layers of polycarbonate film ranging from 100 to 250 μm in thickness were used. The driver gas was hydrogen and the test gas was pure(99.995% at the bottle) argon. The diaphragm was ruptured by an electromagnetically driven needle in order to keep shock conditions constant. The measured shock velocity varied within 1% at the same initial pressures across the diaphragm.

The arrangement of the nozzle-skimmer-collimator system in the vacuum tank is shown in Fig.4. It would be desirable to isolate three chambers, i.e. the chambers between nozzle and skimmer, and skimmer and collimator, and the experimental chamber, from each one other in order to prevent molecules reflected from the walls from interfering with the beam. Because in our apparatus they were in the same chamber, whose volume was 0.6 m^3 with a 10 inches oil diffusion pump, we could not avoid such interaction. Experimental results showed

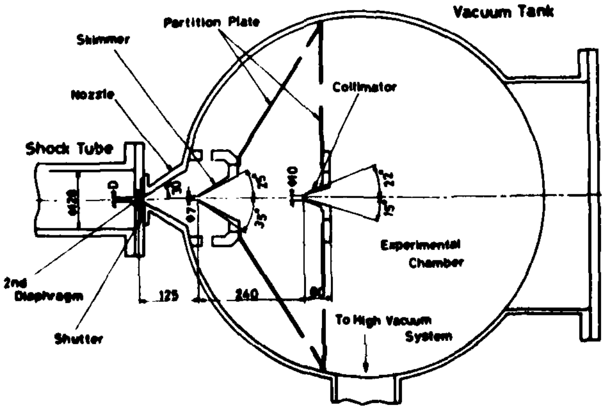

Fig.4 Details of the nozzle-skimmer-collimator system.

this effect limited the beam duration times. Before the shock tube was fired, the background pressure was in the range between 1×10^{-5} and 5×10^{-6} Torr. A sliding shutter was incorporated in the nozzle just downstream of the diaphragm to stop the flow into the vacuum tank shortly after the expansion started. The shutter was operated by a spring-rotary solenoid system and triggered by a pressure gauge signal. This mechanism permitted gas flow for 30-50 msec and prevented pressure rises higher than a few Torr after a shot. Therefore, the vacuum tank did not need to be exposed to atmosphere for replacement of the diaphragm and could be re-evacuated within a few minutes to high vacuum.

Divergent-convergent conical nozzles were used with a 30° half angle divergent section from any of three different throat diameters, 3.2, 5 and 10 mm. The axial length was 10 cm. The skimmer was located 12.5 cm downstream from the nozzle throat. It had a 7 mm orifice diameter and external and internal half angles of 35° and 25°, respectively. Thus any external shock should have been attached and internal flow should have been free from wall effects. The lip of the skimmer orifice was machined to as sharp an edge as possible to minimize its effects on the beam intensity. The collimator was located 23.9 cm downstream of the skimmer orifice. Two collimators with different geometries were used; the external and the internal half angles of 65° and 45°, respectively, with 15 mm orifice diameter (collimator 1) and 22° and 15° with 10 mm orifice diameter (collimator 2).

Intensity Measurments

Thin film heat transfer gauges were used to measure the molecular beam intensity. In a free molecular flow, the heat transfer rate, $\dot{q}(t)$, to a body can be expressed by

$$\dot{q}(t) = (1/2)\ C\ m\ N\ u^3, \qquad \text{IV}$$

Table 2. Experimental conditions. P_4 and P_1 are the pressures across the diaphragm and T_0 and P_0 are the stagnation temperature and pressure, respectively.

P_4 ata	P_1 Torr	M_1	T_0 °K	P_0 ata	D mm	M_S	N_S 10^{15} cm^{-3}	Kn_S
9.0	10	6.44	9020	3.71	10	13.9	4.74	0.0512
					5	21.5	1.18	0.205
					3.2	28.0	0.468	0.499
	8	6.81	9630	3.30	10	12.9	3.89	0.0624
					5	19.3	0.974	0.249
					3.2	24.5	0.399	0.608
	5	7.68	10560	2.55	10	10.7	2.63	0.0922
					5	15.0	0.662	0.367
					3.2	18.2	0.272	0.892
	1	9.26	11090	0.70	10	7.92	0.634	0.383
					5	10.6	0.160	1.52
					3.2	12.5	0.0656	3.70
7.0	20	5.21	6250	4.73	10	14.7	8.84	0.0275
	15	5.58	7115	4.12	10	14.7	6.76	0.0359
	10	6.18	8490	3.42	10	14.3	4.66	0.0521
	8	6.43	8970	2.95	10	13.8	3.79	0.0640
					5	21.4	0.945	0.257
					3.2	27.9	0.388	0.626
	5	7.02	9810	2.18	10	12.1	2.50	0.0972
	2	8.06	10560	1.10	10	9.60	1.11	0.218
	1	8.55	10590	0.61	10	8.87	0.604	0.402
6.0	3	7.37	10040	1.42	10	11.2	1.57	0.155
	2	7.80	10330	1.04	10	10.1	1.09	0.222
3.0	3	6.53	8940	1.13	10	13.6	1.45	0.167
	2	6.98	9480	0.85	10	12.2	1.01	0.240

where m is the mass of the beam molecule, N is the number density of the beam and C includes the accommodation coefficient which is here assumed to be unity. Here, the beam velocity, u, can be taken as the asymptotic value obtained from the nozzle flow calculation. Measurements were made at three points, i.e. on axis, 7 and 14 mm off axis at several different places downstream of the skimmer. The properties of the gas in the reflected shock region are shown in Table 2 along with conditions at the skimmer entrance obtained from the nozzle flow calculation.

RESULTS AND DISCUSSIONS

Typical signals of the heat transfer gauges are shown in Fig.5. Fig.5a shows that the surface temperature increases gradually after the beam arrival at the gauge for about 1.2 msec until it reaches to a plateau, then begins to fall. The period of the signal increase corresponds to that of constant $\dot{q}(t)$ or duration of beam, as can be seen from Fig.5b, which compares the signal with one using an analog network. After about 1 msec beam duration, the gas reflected from the walls begins to affect the beam, then after 1-2 msec the beam has decayed.

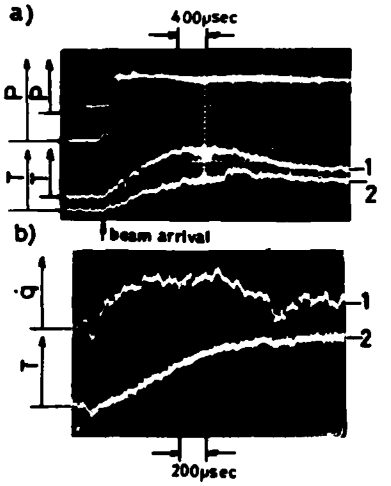

Fig.5 Typical signals of heat transfer gauges. Fig.5a includes two pressure histories at the reflected shock region and two heat transfer gauge signals on axis; 1 and 7 mm off axis; 2 downstream from collimator. Fig.5b shows heat transfer gauge signals with; 1 and without; 2 the analog network.

Measured intensities on axis at 5 cm downstream of the collimator for three different nozzles and for various shock conditions are shown in Fig.6 compared with the theoretical values. If Knudsen numbers at the skimmer entrance are greater than unity, they can be considered to follow the Kantrowitz-Grey solution. As can be seen from the values of Kn_S listed in Table 2, in cases of P_1=1 Torr, D=3.2 and 5 mm, this solution can be applicable, but in other cases continuum theories should be applied. However, measured values are much less than either theory would predict. Contributions of the interference between beam molecules and the collimator to this difference were examined. Intensities observed at the same point with the collimator 1 or 2 and without it for the 10 mm throat nozzle are shown in Fig.7 compared with the theoretical values. Differences of intensities with two different shape collimator are not significant for all conditions. Smaller intensities with a collimator than those without it can be explained by a reduction of solid angle spanned by the heat transfer gauge. Thus the main departure from theory may result from the interaction between the expanded gas and the skimmer. Fenn and Deckers[9] have reported that under steady flow conditions the ratio of observed to theoretical

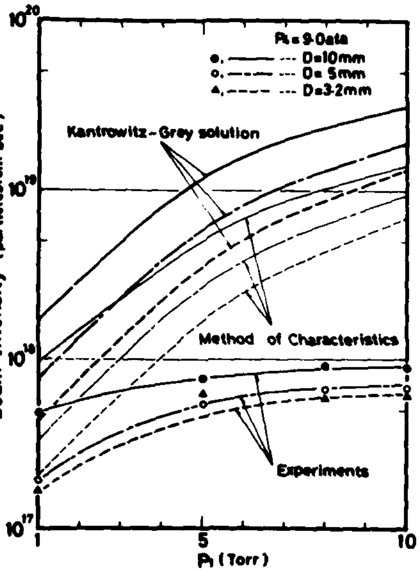

Fig.6 Comparison of the measured beam intensity with theories.

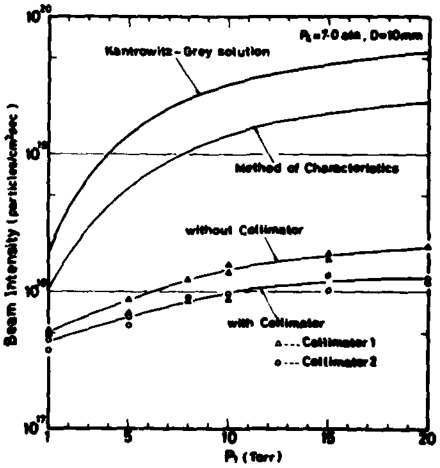

Fig.7 Effects of collimators on the beam intensity.

intensity can be correlated with a dimensionless quantity, Kn_S/M_S, and Anderson *et al.*[10] have extended this correlation over a wide range of experimental conditions. In Fig.8 the ratio of the observed intensity without the collimator to the Kantrowitz-Grey prediction is plotted against Kn_S/M_S compared with their room temperature source beam result. Because there may exist a thick boundary layer along the nozzle wall at very low pressure, the boundary layer displacement thickness has been taken into account in calculations of the conditions at the skimmer for 10 mm throat nozzle. Data both with and without this correction are shown in the figure and show the same correlation. No correction has been made for other nozzles, but the data with the boundary layer correction would approach to 10 mm nozzle correlation curve. The trend of our data is very

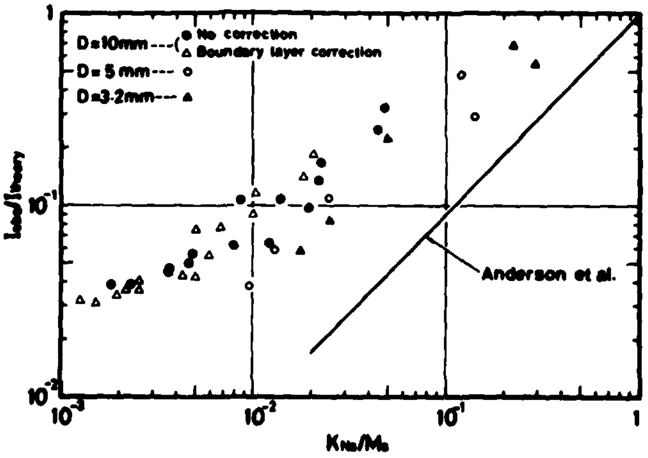

Fig.8 Correlation of the beam intensity with skimmer parameter Kn_s/M_s.

similar to that of Anderson *et al.*, but about 10 times larger for a given value of Kn_S/M_S in the case of 10 mm nozzle.

Because Kn_S is less than unity for most of the present experimental conditions, there may exist a gas cloud around the orifice due to a viscous layer at the lip.[10,17,18] The velocity distribution of the molecules in the cloud may be considered as resulting from almost complete accommodation with the wall. A Knudsen number is an inverse measure of the number of collisions which occur between free stream molecules and those wall accommodated molecules. Therefore, the approach to theoretical intensity should be directly proportional to the value of this parameter. The Mach number in the denominator seems to be a measure of the sensitivity of the system to disturbance by collisions. At higher Mach numbers a relatively slight change in the trajectories passing through the skimmer can significantly affect the measured intensity because of the high degree of collimation due to flow. At lower Mach numbers a relatively greater trajectory change is required for the same proportional reduction in the beam intensity. Therefore, Kn_S/M_S is inversely proportional to the degree of the scattering given by collisions between beam molecules and those in the cloud, i.e. in hard sphere molecules the probability of a collision between a beam molecule and a wall accommodated molecule. Because the extent of the skimmer interference, which relates inversely to the observed to theoretical intensity ratio, increases with this probability, then the correlation of this ratio against Kn_S/M_S can be well explained.

The difference between the present and earlier results is obviously due in part at least the large difference in the source temperature. Considering the scatter of the beam as a result of momentum transfer by collisions between beam molecules and wall accommodated molecules, for the same Mach number in both cases the ratio of the degree of scattering can be estimated as being directly proportional to the probability of such a collision. In terms of momentum transfer or viscosity cross section, this probability is essentially inversely proportional to the relative velocity of free stream and the wall accommodated molecules or the square root of the source temperature. In comparing our results with those of Anderson *et al.* we note that our source temperature is about 20-30 times higher. Therefore, the skimmer interference should be about 4.6-5.9 times less in our case. The remaining discrepancy is very probably due to geometrical differences, our system being somewhat less highly collimated than theirs and therefore less sensitive to small angle scattering.

In Fig.9 are shown beam intensities along x for each nozzle, along with the predictions by Thornhill. It can be seen that downstream of the skimmer there is an axial dependence of x^{-2}, consistent with theories. In Fig.10 are shown radial intensity profiles at four different positions with 3.2 mm nozzle. In terms of a self-similar relation on the radial distribution, the spreading angle of the beam was estimated to be 4.6-6.8° half angle, which are reasonably consistent with theories. Fig.11 shows radial intensity profiles for three nozzles measure at 5 cm downstream of the collimator 1. It can be seen that the beams are well collimated. In Fig.12 are shown beam duration times for the three nozzles. They vary from 1 to 3 msec and become shorter with increasing nozzle throat diameter. Larger throat diameter results in more gas flow into the vacuum tank, so the consequent increase in background pressure causes a proportional attenuation of the beams.

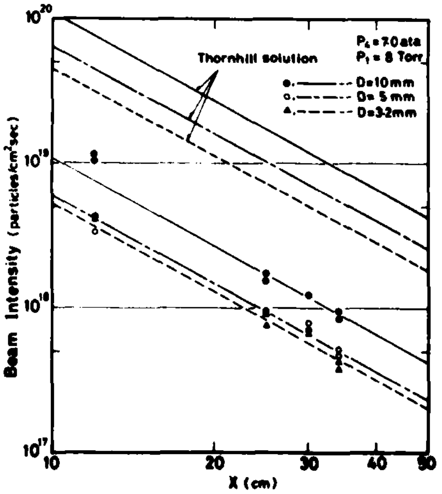

Fig.9 Beam intensity along the distance from the skimmer entrance, x.

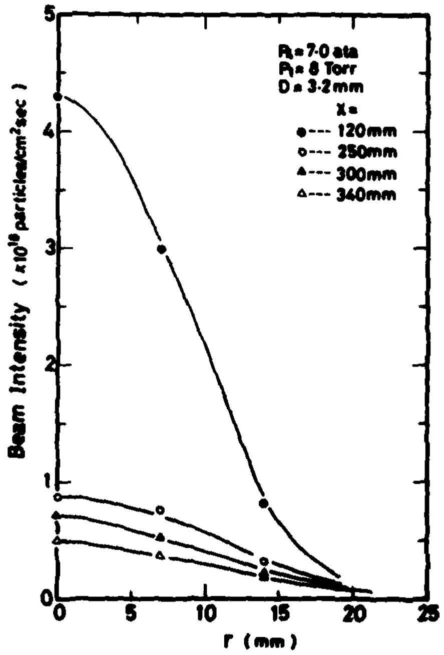

Fig.10 Radial beam intensity profiles at various x.

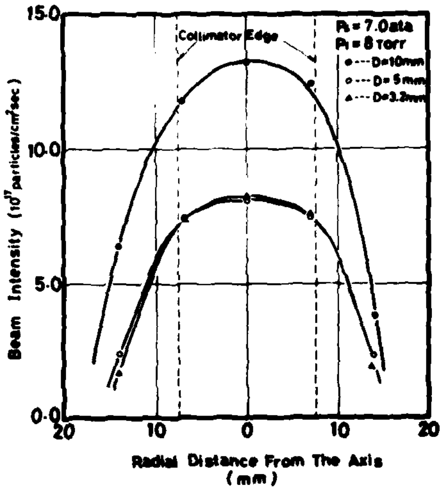

Fig.11 Radial beam intensity profiles downstream of the collimator 1.

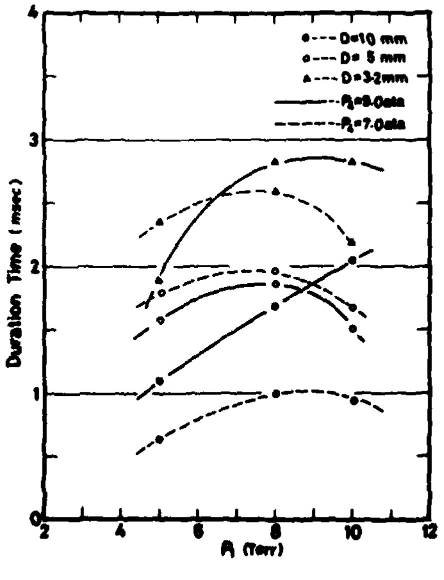

Fig.12 Duration time of beams.

ACKNOWLEDGEMENTS

This study was supported in part by the Hatakeyama Culture Foundation. The calculations of the method of characteristics were carried out using a computer program made by M. Deguchi.

REFERENCES

1. G.T. Skinner, Phys. Fluids *4*, 1172 (1961).
2. T.V. Jones and M.A. Byrne, *6th Rarefied Gas Dynamics*, 1311 (1969).
3. G.T. Skinner, *ibid.*, 1325 (1969).
4. V.S. Calia and R.A. Oman, J. Chem. Physics *52*, 6184 (1970).
5. D. Spence and K.T. Dolder, Phys. Fluids *13*, 88 (1970).
6. B. Evans, J.S. Chang, R.M. Hobson and K. Teshima, in this Proceeding.
7. K.C.A. Crane and R.J. Stalker, J. Phys. D: Appl. Phys., *10*, 679 (1977).
8. T.V. Jones, AGARD CP *12*, 379 (1967).
9. J.B. Fenn and J. Deckers, *3rd Rarefied Gas Dynamics*, 497 (1963).
10. J.B. Anderson, R.P. Andres and J.B. Fenn, *Adv. in Chem. Physics 10*, 275 (1966).
11. L. Talbot, Y.S. Chou and F. Robben, Univ. California Rept.AS-65-14, (1965).
12. J.G. Hall and A.L. Russo, CAL Report No.AD-118-A-6, (1959).
13. A. Kantrowitz and J. Grey, Rev. Sci. Instr. *22*, 328 (1951).
14. K.C. Thornhill, Royal Armament Res. and Dev. Est., Rept.6/65 (1965).
15. C. Greifinger and J.D. Cole, AIAA J. *3*, 1200 (1965).
16. H. Mirels and J.F. Mullen, AIAA J. *1*, 596 (1963).
17. G.E. McMichael and J.B. French, Phys. Fluids *9*, 1419 (1966).
18. K. Bier and O. Hagena, *5th Rarefied Gas Dynamics*, 260 (1966).

"GAIM" — GAS-ADDITION, IMPEDANCE-MATCHED ARC DRIVER

ROBERT E. DANNENBERG

Ames Research Center, NASA,
Moffett Field, California 94035, USA

A conceptual view for a GAIM energy/driver system to maximize shock-tube performance through efficient interfacing of the energy source with the gas dynamics of the arc driver is presented. Electrical and arc-chamber requirements are evaluated utilizing two new computer codes. One code calculates the shock wave generated for a selected time rate and magnitude of arc-energy input; the other computes the values of external circuit elements required to produce the selected energy input, with the driver represented as the load element of the electrical discharge circuit. Results indicate that the energy-storage capability and the driver arrangement needed to produce the highest shock Mach number can be achieved by means of driver gas addition and by impedance matching (GAIM). Design criteria are presented for arc energy requirements necessary to produce given shock-wave speeds. Shock velocities as high as the 70 km/sec required for simulating Jovian entry now seem possible in shock-tube operation. Practical implementation of a GAIM system is discussed.

INTRODUCTION

In view of the potential shock-speed capability of arc-driven shock tubes, which far exceeds the performance demonstrated by most operational facilities, a mathematical effort has been conducted to study the energy/driver system requirements necessary to produce the highest possible shock speed for the least expenditure of energy. Two new computer codes were utilized to calculate the gas-dynamic behavior of an arc-heated shock tube and to determine the energy source requirements to optimize the energy discharged in the driver. Results of the study showed that the attainment of the potential performance was possible, in part, through efficient interfacing of the electrical impedance of the energy source with that of the energetic plasma developed during gas heating. In addition, the input time for a given maximum energy and the arc-chamber size are factors that must be balanced so that the energy input is completed before the mass of the gas in the chamber falls to zero.

A powerful arc-driver incorporating driver gas addition and impedance matching (GAIM) is under study at Ames Research Center; the objective is to achieve near-potential shock-speed performance for the shock-tube operation.[1] With the GAIM concept, the energy/driver system is designed to incorporate (1) tailoring of the electrical properties of the capacitive energy system with the circuit load to deliver energy to the load at a prescribed rate for a prescribed interval of time; (2) tailoring of the volume of the driver chamber, gas, and preset pressure so that the electrical resistance of the subsequent arc discharge will be properly matched to the impedance of the other components; and (3) provision for driver gas addition to be properly programmed to start gas injection into the chamber during the first-quarter cycle of the circuit current. The purpose of this paper is to examine pertinent gas-dynamic and discharge-circuit parameters and to indicate their sensitivity in effecting the generation of the final shock Mach number of a GAIM system with an arc energy input of 1000 kJ.

NUMERICAL PROCEDURES

A review of high-performance arc-driven shock tubes was presented at the 1977 International Shock Tube Symposium.[2] Shortly thereafter, two new analytical codes were developed. They addressed arc-driver operation from the point of view of modeling two of the driver functions independently: (1) as a shock wave generator; and (2) as a load element in the electrical discharge circuit. The first code (EGEN) models the unsteady gas dynamic characteristics of arc-driven shock tubes.[3] The code computes the driver gas properties during energy input, the gas mass flow from the driver, and the generated shock-wave speed. The EGEN code requires as input data the gas load conditions of the driver and driven tube, chamber dimensions, and the time rate and magnitude of the energy input. This program provided criteria for analyzing performance limitations to shock velocity based on the reduction of gas mass in the driver chamber as a function of time during the energy input period.

The second code (ERES) allows the designer to determine the energy system requirements needed to duplicate a particular driver energy input distribution derived from EGEN computations. The energy storage, cabling, and arc-driver system represents a series electrical circuit. The ERES code models the release of energy for a megajoule discharge in an R-L-C series circuit with an R-L load.[4] The system components are delineated as equivalent elements in the model circuit. Both the resistance and the inductance of the load (driver) are represented by effective values that characterize their behavior during arc heating. The ERES code computes the instantaneous load voltage, load energy, and circuit current characteristics, based on the load and external circuit impedances.

Load impedance for use in the preceding program is evaluated on the basis of results obtained by means of a third program, SPARK. SPARK models the transient electrical discharge performance of a capacitive energy storage and arc-driver network.[5] It computes the instantaneous energy absorption (and other) characteristics for all of the resistive components of the circuit elements from a description of only the external elements, the bank potential, and the time history (oscillogram) of the circuit current. The electrical characteristics of many different arc-driven facilities were determined using the SPARK program. The range of systems examined encompassed energy storage units of tens to hundreds of kilojoules with capacitor banks with operating voltages to 40 kV, and currents in the hundreds of kiloamperes with rise times of tens to several hundred microseconds. Analysis of the results showed that the electrical response of a driver with its arc-discharge was aptly characterized by an effective load resistance. The value of the effective resistance (and to a lesser extent the effective inductance) is a useful measure in relating preset chamber variables to their electrical counterparts as well as to generated (measured) shock speed. The application of SPARK calculations for the design of an arc-chamber to achieve the appropriate resistance during the electrical discharge has been discussed and reported in Ref. 2. Although using the three independent programs was perhaps a complex way to proceed, their combined calculations are believed to give good agreement with experimental results.

The calculations and designs presented herein were made for a constant-area shock tube, 10.16 cm diam. The driver and driven gases were hydrogen with initial loading pressures of 10 atm and 1 Torr, respectively. The diaphragm separating the driver and driven tubes is assumed to be of sufficient strength to hold the preset pressure difference and to burst at the moment the heating occurs. The time distribution of the energy addition to the arc chamber for EGEN computations was chosen from the data in Ref. 5, which is representative of the highest shock Mach number obtained experimentally (i.e., M_S = 36 moving into hydrogen at 1 Torr). Curves for different maximum energy transfer in a given time period, or the same energy input over different times, were developed as affine transformations of the base curve. All the arc energy was assumed to be transferred to the gas by joule heating. Most of the calculations were made for 1000 kJ total energy input, a value required for the achievement of polar or retrograde entry velocities into the Jovian atmosphere.

GAS-DYNAMIC CONSIDERATIONS

EGEN computations indicate that the final shock-wave speed produced by a designated energy input continued to increase during gas heating until either of two conditions occurred with respect to the driver gas. One was that the energy input was completed before the driver gas was depleted within the chamber; the other was that the gas was exhausted prior to the completion of the total energy input. The mass efflux determination distinguishes EGEN from other methods, which in fact do not attempt to determine any change in driver gas mass through the shock generation process. For the mathematical model, total gas depletion prior to complete energy input limits generation of maximum shock speed. A similar condition may inhibit the performance capability of arc-heated drivers.

An important result to emerge from EGEN calculations was that driver length is critical in determining maximum shock Mach number. This is illustrated in Figure 1 for the 1000 kJ energy input with a deposition time of 50 μsec. As the length was reduced, the shock Mach number increased to a maximum, after which it declined toward zero as the length approached zero. The latter would be anticipated, of course, because a shock cannot be driven without driver gas. The increase in Mach number as the driver length decreased appeared to be a higher energy density at first, offsetting the tendency to run out of gas. Similar characteristics were observed for curves derived for a practical range of gas load pressures and total energies compatible with that of contemporary arc-driven shock tubes.

EGEN calculations were made to determine what effect varying the time over which the 1000 kJ energy input is discharged into the driver gas would have on shock-wave Mach number for a number of different driver lengths. Results of these calculations are shown in Figure 2. Clearly, discharge periods that are either too short or too long are detrimental to generation of shock speed. The highest shock speeds were produced with very short energy input times in

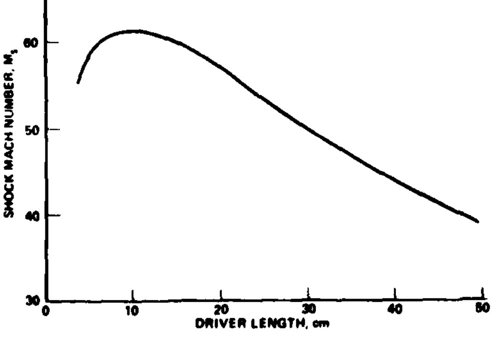

Figure 1. Shock speed sensitivity to driver length for energy of 1000 kJ deposited in a 50 μsec input period; driver diam 10.16 cm.

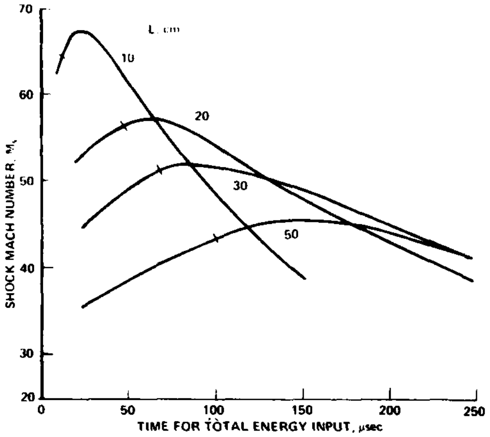

Figure 2. Shock speed sensitivity to total time of energy input for 1000 kJ deposition; driver diam 10.16 cm.

minimal length chambers, as typified by the 10-cm driver in Figure 2. The high rate of energy input dictated by a short input time presents severe problems to the design of the electrical circuit to develop the prerequisite energy characteristics. Also, the steepness of the curve is indicative of potentially large changes in performance arising from normal test variations encountered in daily operation. As the chamber length increased, the maximum shock Mach number decreased and the corresponding total energy input time increased. The longer energy input time periods are within the capabilities of present day capacitive discharge circuitry.

For the shortest total energy input times shown by the curves in Figure 2, the energy input was completed before all of the driver gas was exhausted from the chamber. The shock speeds are slightly higher than those for an instantaneous energy addition (representative of constant volume operation using a heavy metal diaphragm and the same total energy input). As the total input period increases, it approaches the time when the energy input was completed at the same instant when the mass of gas in the driver was reduced to zero. Times corresponding to this dual condition are indicated by tick marks on the curves. It can be noted that the indicated time points are slightly less than those for the maximum Mach number. These differences may be exaggerated with the EGEN model as a result of neglect of the rarefaction wave system in the driver. They do, however, indicate a correlation between the time period of energy transfer to the driver gas for maximum shock Mach number with the time for the driver chamber to be depleted of gas. As the total energy input times became longer, the gas was exhausted from the driver prior to the complete introduction of the available energy. The generated shock Mach number decreased as progressively smaller portions of the total energy were being discharged into the gas. The remaining portions of the 1000 kJ did not contribute toward shock generation.

Initially, it might appear that an easy solution to higher performance with a given energy input would be to increase the initial gas mass in the driver. With the use of light plastic diaphragms, initial load pressures are limited to a maximum of several atmospheres, and operation is at that level. Furthermore, increasing the initial gas pressure would adversely affect the rate of energy input and consequently, the shock speed. Also, although a low-load pressure tends to induce a more rapid initial rate of energy input, experience has shown that a gas pressure that is too low results in excessive voltage oscillations caused by circuit ringing. Driver gas addition offers an attractive approach to supplementing the mass flow of gas within the driver during the total period of energy input. Potential advantages of gas addition are that chamber pressure would be raised and maintained during the latter half of the heating cycle, and circuit damping would be increased. The foregoing would permit the practical use of short arc chambers operating over longer total energy input times to produce higher shock speeds.

The results from the EGEN model also provide design criteria regarding the arc energy requirement to produce a given shock-wave speed. The energy capability of the total system would be greater due to other resistive losses in the circuit. The curve designated "optimized energy input" in Figure 3 shows the variation of shock Mach number with maximum arc energy discharged into the driver gas in its "best" time and chamber length. When consideration is given to prescribing the ratings for components of discharge circuits to develop the prerequisite energy/time features in the load (driver), it is easily demonstrated that electrical duplication is quite impractical and that it might be impossible for certain energy/driver formats. Those formats include short arcs or very fast rise rates as noted earlier. The realistically achievable performance based on EGEN derived energy/time properties with a tenable capacitive discharge circuit is indicated by the shaded area in Figure 3. Shock Mach numbers as high as 56 for simulating Jovian entry speeds are predicted with efficient performance for an energy input of about 1000 kJ.

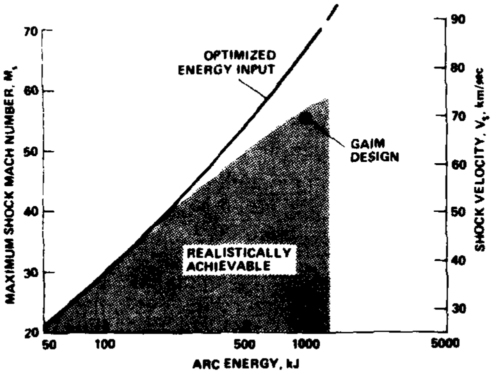

Figure 3. Mach number sensitivity to arc energy input; P_1 = 1 Torr hydrogen; driver diam 10.16 cm.

ELECTRICAL CONSIDERATIONS

The achievement of potential performance dictates that maximum available electrical energy be converted into kinetic energy in the shock-heated gas and that the arc heating of the driver gas be as rapid and as efficient as possible. This is accomplished by matching the capacitor bank and the high-voltage cabling to the driver-arc resistance and inductance in such a way that the energy input is not only rapid and complete as possible, but that a minimum amount of energy is dissipated external to the arc chamber.

Fast-energy-transfer times dictate that the combined external circuit and load (driver) inductances in the electrical discharge network be low.[6] Good design practices used in building large capacitive storage systems generally achieve a "low" external inductance, of the order of 0.1 to 0.3 μH. A lower value for the external inductance cannot be realized without considerable technical effort and very high cost. The load inductance is a different matter. The effective inductances developed by arc formations within driver chambers are significantly larger than the low values of well-developed energy-storage systems. Typically, load inductances for short chambers are 2 or 3 times that of the external value and several times larger for longer drivers. For high-performance operation, it is important that careful attention be given to driver details in order to arrive at the lowest practical load inductance. Parameters that act to reduce load inductance include lower chamber pressure, shorter arc length, higher arc voltage, or a discharge of greater specific energy. Positioning the arc chamber within, or as close as possible, to the current collector or cable termination assembly is another prerequisite for a low-inductive installation.

Parametric analysis of capacitive discharge circuits by ERES computations highlighted the limitation imposed by the maximum or rated voltage of a particular capacitor bank on the rate of energy delivery to the load. For the purposes of this discussion, it is assumed (based on experimental results) that the strength of the shock wave generated in the driven tube increases as energy is transferred to the load at a more rapid rate. Load energy curves are presented in Figure 4 for representative combinations of capacitance and voltage tc produce a 1000-kJ total energy input. The impedance values used in the calculations were representative of those encountered in practice. Although not presented, the circuit current and voltage across the load corresponding to each case in the figure were also determined from code calculations. The results of the sample calculations illustrate the improvement in rise-time of the load energy with higher voltage and lowered capacitance.

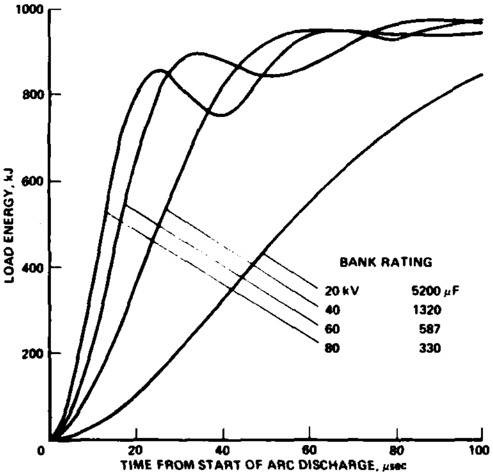

Figure 4. Load energy waveforms for a series R-L-C circuit with varying bank voltage and capacitance.

The energy input represented by the 60 kV curve in Figure 4 represents a close match with the energy distribution realized from EGEN calculations to achieve potential shock-speed performance. To develop the energy input with a capacitive energy-storage system would require an intricacy of electrical design and operation at the limit of existing capabilities (dashed line in Fig. 3). It can be observed that the shape of the energy input curve changes with increasing voltage (Fig. 4) in a manner reflecting an increasingly oscillatory type of discharge performance. At 80 kV, the severity of the voltage oscillation (overshoot) precludes acceptable operation.

The preceding discussion has been concerned with capacitive energy-storage systems. A new type of power supply, a compensating, pulsed alternator,[7] offers promise of a capability for developing voltages to 100 kV with pulsed energies of a few thousand kilojoules within the prerequisite input times. The alternator converts mechanical, rotational energy directly into electrical energy, utilizing the principles of magnetic induction and flux compression. Analysis of an alternator driving a matched impedance load is in progress. Until such times as alternators are available as replacements to capacitive power supplies, the GAIM driver would be powered by arc energy storage system equipped with an extra-high voltage capacitor bank.

GAIM DRIVER

A schematic assembly of a GAIM driver designed for operation with arc discharges to 1000 kJ is shown in Figure 5. The arc chamber would be 26 cm long. A number of the parts indicated on the figure have been selected based on experience gained from their use with other drivers at the Ames facility. Without doubt, many variations in hardware assembly are possible that could produce similar operation. Certainly, new ideas will germinate during work toward the next performance level.

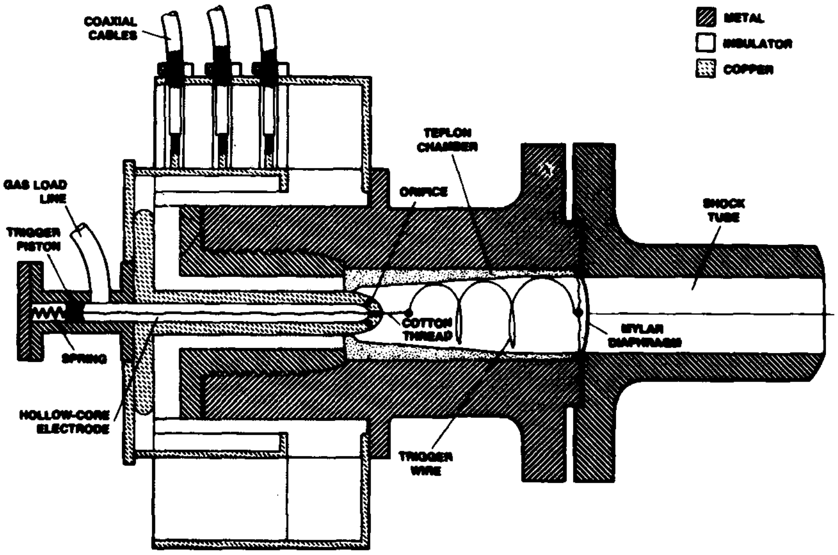

Figure 5. Assembly of GAIM driver with 10.16-cm diam shock tube.

In GAIM operation, the run cycle begins by purging and filling the arc-chamber with several atmospheres of hydrogen. The capacitor bank, cabling, and electrode are charged to the preset voltage. In a programmed sequence, high-pressure driver gas stored in an external reservoir is fed into the gas load line by opening a remotely controlled valve. The pressure increases in the hollow core of the high-voltage electrode, causing the piston to actuate. The trigger wire is pulled toward the electrode, inducing voltage breakdown between the electrode and trigger wire, and the wire explodes and initiates the arc strike. Gas enters the arc chamber through the electrode to augment the rate of mass flow of heated gas from the chamber. Orifices in the tip of the electrode control the rate of the gas addition.

To enhance shock generation, injection of driver gas must begin shortly after arc heating starts and continue through the energy input period. Because the total energy transfer is essentially completed at approximately the end of the first half-cycle of the circuit current, gas that continued to enter the chamber would serve to improve circuit damping by acting as an additional load resistance. EGEN calculations show that with only the normal gas load in the driver, the chamber pressures rise, peak, and fall off as energy input nears completion. Gas addition would raise the chamber pressure during the latter portion of the energy cycle. It is estimated that an added quantity of gas between 2 and 3 times that of the normal initial load mass in the chamber would be adequate during the heating period.

The length and shape of the arc chamber have been designed for the arc plasma to develop the appropriate resistance during the electrical discharge to provide for the proper impedance match between the driver and the external circuit components. Energy for the arc would be supplied by a 733 μF capacitor bank, which would be capable of storing approximately 1.3 MJ when charged to a maximum of 60 kV. With this energy storage arrangement powering the arc driver assembly shown in Figure 5, the projected performance into 1 Torr of hydrogen is a Mach number of 56.

CONCLUDING REMARKS

It has been shown that computer codes now available provide mathematical tools for the design of arc-drivers to maximize their shock generating capabilities and to define their electrical circuits in order to achieve the selected energy transference to the arc chambers. Results reveal that the production of the highest shock Mach number for a given maximum energy requires optimizing the input time of the energy for the arc-chamber size together with a harmonious matching of energy and driver components. The GAIM system maximizes shock tube performance through efficient interfacing of the energy source with the gas dynamics of the driver utilizing driver gas addition and electrical impedance matching.

REFERENCES

1. R.E. Dannenberg, "GAIM" — An Advanced Arc Driver Concept, Proceedings of the First Nonideal Plasma Workshop, Pasadena, California, Nov. 14-15, 1978.
2. R.E. Dannenberg, A New Look at Performance Capabilities of Arc Driven Shock Tubes, Proceedings of the 11th International Symposium on Shock Tubes and Waves, B. Ahlborn, A. Hertzberg, and D. Russell, eds., University of Washington Press, Seattle, Washington, 416-31 (1978).
3. B.E. Milton and R.E. Dannenberg, Unsteady Gas Dynamic Model of an Arc Heated Shock Tube, submitted for publication, AIAA Journal, 1979.
4. G. Barnes and R.E. Dannenberg, Transient Solution for Megajoule Energy Release in a Lumped Parameter Series R-L-C Circuit, submitted for publication, Journal of Applied Physics, 1979.
5. P.I. Slapnicar and R.E. Dannenberg, Development of Dynamic Discharge Arc Driver with Computer-Aided Circuit Simulation, AIAA Journal, *14*, 9, 1183-88, (1976).
6. F.R. Livingston and W.A. Menard, Toward Understanding the Conical Arc-Chamber Driver, Recent Developments in Shock Tube Research, Proceedings of the Ninth International Shock Tube Symposium, D. Bershader and W. Griffith, eds., Stanford University Press, Stanford, California, 664-7 (1973).
7. B.M. Carder, W.L. Gagnon, and W.F. Weldon, Compensated Pulsed Alternator, Lawrence Livermore Laboratory, Livermore, California (1978).

THERMAL ISOMERIZATION REACTIONS OF SUBSTITUTED CYCLOHEPTATRIENES IN SHOCK WAVES

D. C. ASTHOLZ, J. TROE and W. WIETERS

Institut für Physikalische Chemie, Universität Göttingen
Tammannstrasse 6, D — 3400 Göttingen, West-Germany

The thermal unimolecular isomerization of cycloheptatriene, and of methyl-, ethyl-, and isopropyl-cycloheptatriene, to the corresponding aromatic products have been investigated in the temperature range 900-1400 K in shock wave experiments. Even for these large molecules fall-off behaviour has to be taken into account mainly due to weak collision effects. By the use of a full weak collision theory reduced fall-off curves have been calculated. From the limiting high pressure rate constants a very reliable set of specific rate constants, k(E), is derived.

INTRODUCTION

It is generally assumed that unimolecular dissociation or isomerization reactions of "large" polyatomic molecules (more than 30 oscillators) under normal experimental conditions occur very close to the high pressure, first order limit of the reaction. However, due to fall-off effects, this assumption becomes invalid under shock wave conditions1). This effect has often been overlooked when shock wave experiments have been combined with low temperature data in order to derive more precise Arrhenius parameters or thermodynamic values.

EXPERIMENTAL

We therefore intended to study four model isomerization reactions in shock waves to demonstrate quantitatively this effect. We have investigated the aromatization reactions of cycloheptatriene (CHT), 7-methyl-cycloheptatriene (Me-CHT), 7-ethyl-cycloheptatriene (Et-CHT), and 7-isopropyl-cycloheptatriene (isoPr-CHT) in the temperature range 900-1400 K and at concentrations of the bath gas Ar in the range $8 \cdot 10^{-7} \leqslant [\mathrm{Ar}] \leqslant 2 \cdot 10^{-4}$ mol cm^{-3}. The reactions are particularly clean unimolecular isomerization reactions following relatively simple mechanisms2). The products are toluene from CHT, ethylbenzene, o-, m-, p-xylene and styrene from Me-CHT3), independent of the position of the methyl group. From Et-CHT and isoPr-CHT, the analogous higher substituted aromatization products are formed4). The reactions behind incident or reflected shock waves could conveniently be monitored by UV light absorption, in the 280-310 nm range, of the disappearing seven-membered ring parent molecules. Details of the experimental technique have been described previously, see in particular ref. (1).

RESULTS

The measured strictly first order rate constants were well represented by Arrhenius plots which in all cases were perfectly linear. The following Arrhenius expressions for the thermal isomerization reactions were obtained:

CHT: $k_1 = 10^{13.43 \pm 0.25} \exp(-208.5 \pm 6.0 \text{ kJ mol}^{-1}/RT) \text{ s}^{-1}$ (1)

between 900 and 1300 K and at $[\text{Ar}] \simeq 7 \cdot 10^{-5}$ mol cm^{-3} in best agreement with our earlier results 5),

Me-CHT: $k_2 = 10^{13.25 \pm 0.23} \exp(-203.5 \pm 5.0 \text{ kJ mol}^{-1}/RT) \text{ s}^{-1}$ (2)

between 900 and 1400 K at $[\text{Ar}] \simeq 3 \cdot 10^{-5}$ mol cm^{-3},

Et-CHT: $k_3 = 10^{13.14 \pm 0.22} \exp(-200.7 \pm 5.0 \text{ kJ mol}^{-1}/RT) \text{ s}^{-1}$ (3)

between 940 and 1350 K at $[\text{Ar}] \simeq 3 \cdot 10^{-5}$ mol cm^{-3},

isoPr-CHT: $k_4 = 10^{12.93 \pm 0.35} \exp(-196.6 \pm 8.2 \text{ kJ mol}^{-1}/RT) \text{ s}^{-1}$ (4)

between 960 and 1340 K at $[\text{Ar}] \simeq 3 \cdot 10^{-5}$ mol cm^{-3}.

For CHT 2) and Me-CHT 3), low temperature experiments near 600 K from static systems are available which are well consistent with the present data. Fig. 1 compares our results for the thermal isomerization of Me-CHT with the low temperature data from ref. (3). The Arrhenius plot over 12 orders of magnitude appears to be impressively straight.

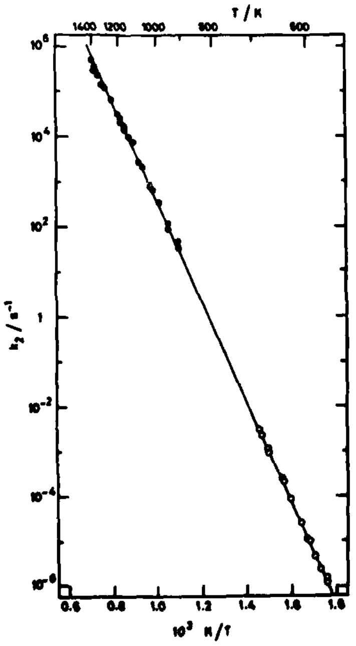

Figure 1. First-order rate constant of the thermal isomerization of 7-methyl-cycloheptatriene (Me-CHT)
[(o) from ref. (3),
(●) from this work]

At first sight the reaction rates did not seem to depend on the total pressure. However, with more careful experiments, over the large pressure range studied ($8 \cdot 10^{-7} \leq [Ar] \leq 2 \cdot 10^{-4}$ mol cm^{-3}, small pressure effects (less than a factor of two) became apparent indicating that under the present conditions the reaction was not, as assumed before, at its high pressure limit. Therefore, the measured points of Fig. 1 do not directly correspond to the limiting high pressure rate constant $k_{2\infty}$. Fig. 2 shows for Me-CHT the detected minor dependence of k_2 on the Ar-concentration at temperatures above 1000 K. Since the effect is too small for an experimental extrapolation toward the high pressure limit, a careful fall-off analysis has to be applied. This can only be done by the use of a full weak collision theory of unimolecular reactions.

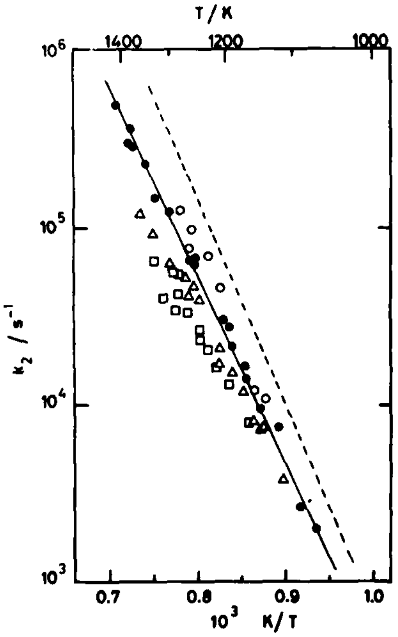

Figure 2. Thermal isomerization of Me-CHT in shock waves above 1000 K.
(□):[Ar]≃ $8 \cdot 10^{-7}$ mol · cm^{-3}
(△):[Ar]≃ $3 \cdot 10^{-6}$ mol · cm^{-3}
(●):[Ar]≃ $3 \cdot 10^{-5}$ mol · cm^{-3}
(○):[Ar]≃ $2 \cdot 10^{-4}$ mol · cm^{-3}
The dashed line represents the high pressure limit $k_{2\infty}$

DISCUSSION

Fall-off Corrections and High Pressure Rate Constants

The dominant quantities of a fall-off curve are the pressure-proportional low pressure rate constant k_0 and the pressure-independent limiting high pressure rate constant k_{∞} , and they have to be calculated first. Performing our calculations according to ref. (6), at first the weak collision efficiency β_c at the low pressure limit has to be estimated. In the present cases, from photoactivation experiments (ref. 4,7) values of the average energy $-\langle \Delta E \rangle$ transferred per collision have been deduced from which β_c values near 0.04 at 1200 K were calculated. The limiting high pressure rate constants were obtained following usual transition state theory (ref. 6). The interpolating fall-off curves are of fairly universal shape, if they are represented by

k/k_∞ as a function of the dimensionless pressure scale k_0/k_∞ in factorized form[6)]

$$k/k_\infty = F^{LH}(k_0/k_\infty) \cdot F^{SC}(k_0/k_\infty) \cdot F^{WC}(k_0/k_\infty) \qquad (1)$$

with the Lindemann - Hinshelwood factor $(k_0/k_\infty)/(1 + k_0/k_\infty)$, the strong collision ($F^{SC}$) and the weak collision broadening factors (F^{WC}).
The strong collision broadening factors were obtained from an exact counting of states procedure. In addition to this quantity, the weak collision broadening of the fall-off curve has to be considered. Solutions of the weak collision master equation have been calculated indicating an appreciable weak collision broadening of these fall-off curves. At the center of the fall-off curve the broadening is mainly caused by strong collision broadening while at the pressures applied in this work, the larger width of the weak collision broadening factor dominates. The analysis showed that, under the shock wave conditions, the fall-off was entirely due to weak collision effects (both shift and broadening) whereas the usual strong collision unimolecular rate theory would have predicted that the reaction was practically at its high pressure limit. In Fig. 3 the measurements for Me-CHT at 1200 K have been compared with both the full weak collision fall-off curve and the pure strong collision curve. The experimental points in Fig. 3 indicate the extent of the fall-off corrections required. The small experimentally detectable increase in the rate constants with pressure agrees well with the predictions of the weak collision unimolecular rate theory applied. However, it has to be emphasized that the discussed weak collision fall-off corrections, although by far too small to allow for an experimental extrapolation toward the high pressure limit, cannot be neglected. Therefore, such an analysis in the future will become obligatory for shock wave studies of any unimolecular reaction of a polyatomic molecule.

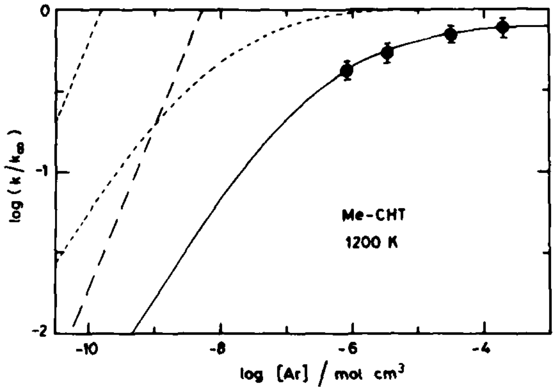

Figure 3. Calculated weak collision fall-off curve of the thermal isomerization of Me-CHT in Ar at 1200 K. [(●): measurements from this work, see text}. The dotted curve represents the pure strong collision fall-off curve.

After the correction of the fall-off effects, the following limiting high pressure rate constants were obtained:

CHT : $k_{1\infty} = 10^{14.10} \exp(-220.5 \text{ kJ mol}^{-1}/RT) \text{ s}^{-1}$ (5)

Me-CHT : $k_{2\infty} = 10^{13.99} \exp(-216.4 \text{ kJ mol}^{-1}/RT) \text{ s}^{-1}$ (6)

Et-CHT : $k_{3\infty} = 10^{13.65} \exp(-208.9 \text{ kJ mol}^{-1}/RT) \text{ s}^{-1}$ (7)

isoPr-CHT : $k_{4\infty} = 10^{13.44} \exp(-204.8 \text{ kJ mol}^{-1}/RT) \text{ s}^{-1}$ (8)

where $k_{1\infty}$ and $k_{2\infty}$ apply to temperatures between 600 and 1400 K, whereas $k_{3\infty}$ and $k_{4\infty}$ apply to 900 - 1400 K.

Specific Rate Constants k(E)

We have also simulated these high pressure rate constants by suitable threshold energies and activated complex frequencies. This analysis was by no means unique and different models could reproduce the data. However, these models all predict nearly the same specific rate constants k(E) in the thermal average$^{1)}$.

$$k_\infty = \int_{E_0}^{\infty} k(E)\, f(E)\, dE \qquad \text{(II)}$$

Hence, this ambiguity is of no practical relevance. The specific rate constants obtained in this way by statistical calculations, agree very well with recent steady state$^{4)}$ and laser flash isomerization experiments$^{8)}$ of the same reactions. Therefore, the present systems may perhaps serve as the best exemplary prototype for unimolecular reactions which have until now been accessible.

It might be mentioned that the present experiments report fall-off effects for the largest molecules for which fall-off behaviour has experimentally been detected so far. However, even for molecules of this size [with 39 (CHT), 47 (+1) (Me-CHT), 55(+2) (Et-CHT), 63(+3) (isoPr-CHT) oscillators (+ internal rotors)] , fall-off effects are always present in shock waves and should not be overlooked.

ACKNOWLEDGEMENT

This work has been supported by the Deutsche Forschungsgemeinschaft Discussions with Drs. K. Glänzer, H. Hippler, K. Luther, M. Quack and Prof. R. Walsh are gratefully acknowledged.

REFERENCES

(1) D. C. Astholz, J. Troe and W. Wieters, J. Chem. Phys., 70, 5107 (1979)

(2a) R. Atkinson and B. A. Thrush, Proc. Roy. Soc. Lond., A 316, 123, 131, 143 (1970)

(2b) S. W. Orchard and B. A. Thrush, Proc. Roy. Soc. Lond., A 329, 273 (1972)

(3) K. W. Egger, J. Am. Chem. Soc., 90, 6 (1968)

(4) J. Troe and W. Wieters, J. Chem. Phys., to be published

(5) K. Glänzer, S. H. Luu and J. Troe, Ber. Bunsenges. Physik. Chem., 79, 855 (1975), and references therein

(6) J. Troe, J. Phys. Chem., 83, 114 (1979)

(7) S. H. Luu and J. Troe, Ber. Bunsenges. Physik. Chem., 77, 325 (1973); 78, 766 (1974)

(8) H. Hippler, K. Luther, J. Troe and R. Walsh, J. Chem. Phys., 68, 323 (1978); see also Disc. Far. Soc., 67, 000 (1979).

OXIDATION OF CYANOGEN III. SHOCK INITIATED IGNITION IN C_2N_2-O_2-H_2-Ar MIXTURES

ASSA LIFSHITZ and MENASHE BIDANI

Department of Physical Chemistry, The Hebrew University, Jerusalem, Israel

The ignition of cyanogen in mixtures containing oxygen and hydrogen diluted in argon was studied behind reflected shock waves in a 2 in. i.d. single pulse shock tube. The measurements covered the temperature range 1100-1800 K at pressures (p_5) varying from approximately 2 to 7 atmospheres. The ignition delay times ranged between 80 and 1500 μsec. The experimental results of close to two hundred and fifty tests can be correlated by the relationship:

$$\tau = \lambda[C_2N_2]^{-0.67}[O_2]^{-0.59}[H_2]^{-0.81}[Ar]^{+1.32} \text{ sec.},$$

where $\lambda = 2.27 \times 10^{-14}\exp(22.0\text{x}10^3/RT)$ and concentrations are expressed in mole per cubic centimeter.

In the presence of hydrogen, the ignition of cyanogen is faster than in its absence, it has a much weaker temperature dependence and shows considerable different concentration dependence.

The above relationship can serve as a basis for a comparison between computer and laboratory experiments. Two reaction schemes, one for the C_2N_2+O_2+Ar and the other for H_2+O_2+Ar were coupled through O, H, OH and CN radicals and the effect of this coupling on the parametric relation was examined.

INTRODUCTION

We have recently studied the ignition of cyanogen behind reflected shocks in mixtures containing cyanogen, oxygen and argon[1]. The parametric relation which described the induction times showed a very strong dependence on the cyanogen concentration and a very weak dependence on the oxygen concentration:

$$\tau = 10^{\alpha}\exp(E/RT)[C_2N_2]^{\beta_1}[O_2]^{\beta_2}[Ar]^{\beta_3} \text{ sec}$$

where
$$\alpha = -13.97 \pm 0.15$$

$$E = 34.7 \pm 0.8 \text{ (kcal/mole)}$$

$$\beta_1 = -1.01 \pm 0.04$$

$$\beta_2 = -0.21 \pm 0.04$$

$$\beta_3 = 0.22 \pm 0.05$$

and concentration are expressed in mole per cubic centimeter.

Modeling of the oxidation process[2] gave a very good agreement between the computer and laboratory experiments when fifteen elementary steps composed the reaction scheme. The examination of the sensitivity spectrum showed that the overall oxidation was determined almost uniquely by the thermal chain:

$$O + C_2N_2 \rightarrow NCO + CN$$

$$CN + O_2 \rightarrow NCO + O$$

Since in this cycle the rate constant of the second step is considerably bigger than that of the first steps[3,4] the latter determins the propagation rate of the cycle. The rate is therefore almost independent of the O_2 concentration but strongly dependent on the C_2N_2 concentration, as has been observed experimentally.

The oxidation of cyanogen attracted a lot of attention in recent years in particular in view of its potential as a source for chemically pumping CO. This non hydrogen fuel will not produce OH radicals in its oxidation and will thus prevent the shortening of the vibrational relaxation time of CO via the very fast $CO+OH \rightarrow CO_2+H$ reaction. Now when the mechanism of the C_2N_2 oxidation is fairly well established[2] it is of great interest to examine the influence of small quantities of hydrogen on its oxidation.

In this article, experimental results of ignition delays in $C_2N_2+O_2+H_2+Ar$ mixtures taken over a wide range of conditions will be presented. The coupling between the $C_2N_2+O_2$ and the H_2+O_2 systems will be discussed.

EXPERIMENTAL

Apparatus

The ignition was studied in a 2-in. i.d. single pulse shock tube. Its driven section, 10 ft long was made of "double tough" Pyrex tubing and was separated from the driver section by Mylar polyester diaphragms of varying thickness. The driver section was adjustable in small steps in order to achieve the best running conditions; its maximum length was 10 ft. Before each test, the shock tube was pumped down to 0.1 mtorr. The description of the tube and the mode of its operation has already been given in earlier publications[5].

Incident shock velocities were recorded in order to calculate the reflected shock parameters. These were measured with two miniature high frequency pressure transducers placed 244 mm apart. The signals produced by the shock waves passing over the transducers were fed into a Hewlett Packard Model 5302A universal counter. Time intervals were read to 0.1 μsec.

Reflected shock temperatures (T_5) and density ratios (ρ_5/ρ_1) were calculated from the measured incident shock velocities using the steady shock equations and the ideal gas equation of state. No chemical reaction was assumed in these calculations. The temperatures (T_5) and densities (ρ_5) listed in the various tables are those immediately following the shock reflection from the end plate and before any chemical reaction took place. These temperatures are not necessarily equal to the ones at the instant of ignition.

The progress of the reaction was followed by pressure observations. The output of another miniature high frequency pressure transducer, located at the end plate of the driven section, was fed into a biomation Model 805 transient recorder, and the ignition was signified by a sudden rise from a plateau value, caused by the onset of combustion. The ignition delay time was taken as the time interval between the reflection of the shock from the end plate and the sudden rise in pressure. A representative trace is shown in Figure 1.

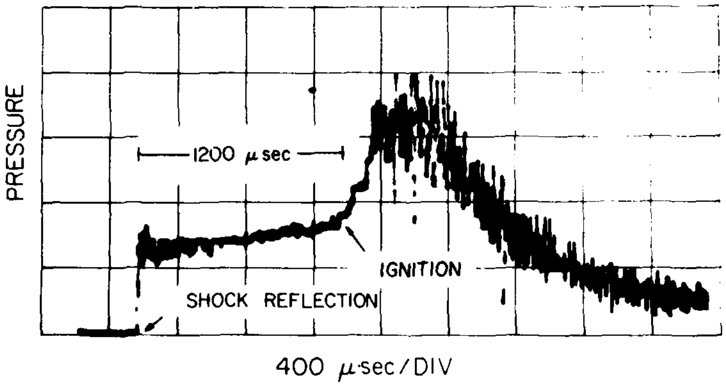

Figure 1: A pressure record. The induction time is shown as the time interval between the reflection of the shock wave from the end plate of the driven section and the ignition point.

Materials and Analysis

Seven reaction mixtures were prepared on a high pressure line and stored at high pressure (~50 psig) in stainless steel cylinders. Both the line and the cylinders were baked to ~100°C and later pumped down to bettern than 0.1 millitorr. The experimental conditions of nine groups of experiments are listed in Table I.

The cyanogen used in this study was C.P. grade listed as 98.5% pure. The oxygen ultra high pure was 99.99%, the hydrogen prepurified grade was 99.95% and the argon high purity grade was 99.995% pure. Driver gas helium was of high purity grade listed as 99.995% pure. All the gases were obtained from the Matheson Gas Co. and were used directly from the cylinders without further purification.

RESULTS

Derivation of the Experimental Parameters α, E and β_is

For the purpose of the modeling of ignition delay times by computer experiments,one must perform enough laboratory experiments and summarize the experimental results in a simple parametric relation suitable for this purpose. In a number of ignition studies in the past the collection of the data was successfully summarized in an equation of the type [6-9]

$$\tau = 10^{\alpha} \exp[E/RT] \prod_i C_i^{\beta_i} \qquad 1$$

where T is the reflected shock temperature upon reflection from the driven end and C_i is the concentration of a component i after being processes by the reflected shock wave but before any chemical reaction took place. In this study, as has been done in the past, we have designed our experiments in such a manner that the β_i could be independently derived. Refined values of these parameters as well as α and E were obtained later by regression analysis of all the data.

Table I. Summary of the Experimental Conditions of the Nine Groups of Experiments

Group	% C_2N_2	% O_2	% H_2	$\sim$ p1 torr	$\sim C_5 \times 10^5$ mole/cc	τ(μsec) at 1300K	T5 K (Range)	symbol
A	7	7	0.5	100	4.0	400	1115-1505	○
B	7	7	0.5	50	2.2	700	1225-1705	△
C	7	7	1	100	3.9	225	1050-1385	□
D	7	3.5	0.5	100	4.0	700	1200-1475	▼
E	3.5	3.5	0.5	100	3.6	1350	1430-1915	◇
F	3.5	3.5	0.5	200	7.0	680	1225-1695	●
G	3.5	3.5	0.25	100	3.9	2000	1360-1745	■
H	3.5	3.5	0.25	200	7.0	1320	1280-1550	◒
I	7	3.5	1	100	4.0	340	1110-1430	▽

In order to determine the four β_is, α and E, nine groups of experiments totalling approximately 250 shocks were performed. Table II shows details of three representative tests from each of the five groups.

Preliminary values of each of the four parameters β_1 β_2 β_3 and β_4 in the equation

$$\tau = \lambda\ [C_2N_2]^{\beta_1}\ [O_2]^{\beta_2}\ [H_2]^{\beta_3}\ [Ar]^{\beta_4} \qquad \text{II}$$

were evaluated by an intercomparison of runs from two groups of experiments. Figure 2 shows an intercomparison of tests from groups A, D and E plotted as log τ vs 1/T. The distance between the lines corresponding to groups A and D gives β_2 and that between E and D gives β_1. The distance between A and D is somewhat smaller than that between E and D, $\beta_1 \sim -0.9$ and $\beta_2 \sim -0.7$. Figure 3 shows a comparison between the induction times of groups A and C plotted again as log τ vs 1/T. The distance between the two lines on this figure, -0.27 gives a value -0.9 for β_3. A strong dependence on the hydrogen concentration is obvious from this plot. The effect of argon on the induction times is shown in Figure 4 where data from groups A and H are compared. The big distance between the two parallel lines indicates a strong inhibiting effect of the argon; $\beta_4 \sim 1.3$. The exact values of the four power dependencies as well as that of λ (eq. II) was obtained by a least squares analysis of the entire collection of the data. The values are:

$$\beta_1 = -0.67$$

$$\beta_2 = -0.59$$

$$\beta_3 = -0.81$$

$$\beta_4 = 1.32$$

$$\lambda = 2.27 \times 10^{-14} \exp(22.0 \times 10^3/RT)$$

Figure 5 shows a plot of log λ vs 1/T where all the data points scatter along one line with a slope corresponding to 22.0 kcal/mole.

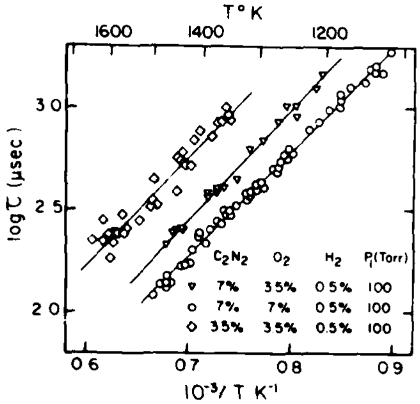

Figure 2. A plot of log τ vs 1/T for groups of shocks A(○), D(▽) and E(◇). The distance between A and D gives an indication of β_2 (Eq. II) and that between E and D is a measure for β_1.β_1 is somewhat bigger than β_2.

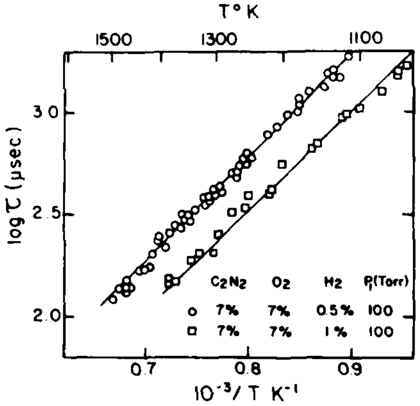

Figure 3. A plot of log τ vs 1/T for groups of shocks A(○) and C(□). The distance between the two parallel lines, -0.27 gives a value of -0.9 for β_3.

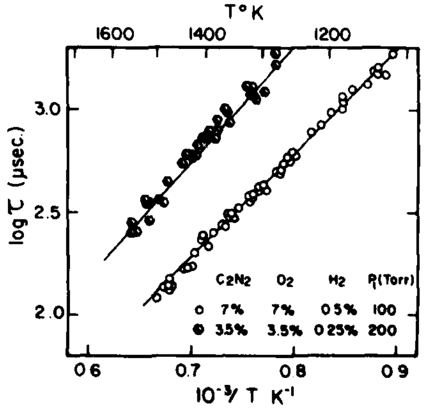

Figure 4. A plot of log τ vs 1/T for groups of shocks A(○) and H(●). The distance between the two parallel lines shows a very strong inhibiting effect of argon.β_4 $\sim$ 1.3.

Table II: Details of the Experimental Conditions for Representative Tests

Group	% C_2N_2	% O_2	% H_2	$C_5 \times 10^5$ mole/cc	T_5 (°K)	τ μsec
A	7	7	½	3.55	1114	1900
				3.97	1276	490
				4.23	1384	250
B	7	7	½	1.92	1226	1100
				2.25	1511	212
				2.44	1707	72
C	7	7	1	3.53	1101	1045
				3.98	1274	320
				4.24	1383	146
D	7	3.5	½	3.72	1215	1200
				3.21	1298	680
				4.28	1468	210
E	3.5	3.5	½	3.44	1353	900
				3.70	1506	336
				3.91	1648	222
F	3.5	3.5	½	6.75	1315	800
				7.22	1451	275
				7.53	1551	176
G	3.5	3.5	¼	3.45	1358	1440
				3.59	1444	960
				3.74	1540	580
H	3.5	3.5	¼	6.68	1297	1200
				7.12	1425	600
				7.52	1553	256
I	7	3.5	1	3.48	1118	1280
				3.70	1202	720
				4.21	1426	190

CONCLUSIONS

The experimental results clearly indicate that the addition of hydrogen to the reaction mixtures in quantities of the order of $H_2/O_2 \sim 1/25 - 1/10$ has a very great influence on the progress of the oxidation reaction. The induction times are on the average 5 times shorter, moreover, the parametric relation which describes the ignition delays is considerably different than the one corresponding to the O_2-C_2N_2-Ar system without added hydrogen. The induction times become very strongly dependent on the argon concentration, the higher its concentration the longer the induction times get, $\tau \propto [Ar]^{+1.32}$. The very strong dependence on the C_2N_2 concentration and the very weak dependence on the O_2 concentration which was found in the absence of hydrogen now disappear and the induction times are affected by changes in $[O_2]$ and $[C_2N_2]$ approximately to the same extent. The temperature dependence is considerably smaller, 22.0 as compared to 34.7 kcal/mole in the absence of hydrogen. A strong dependence on the H_2; $\tau \propto [H_2]^{-0.81}$ is also observed.

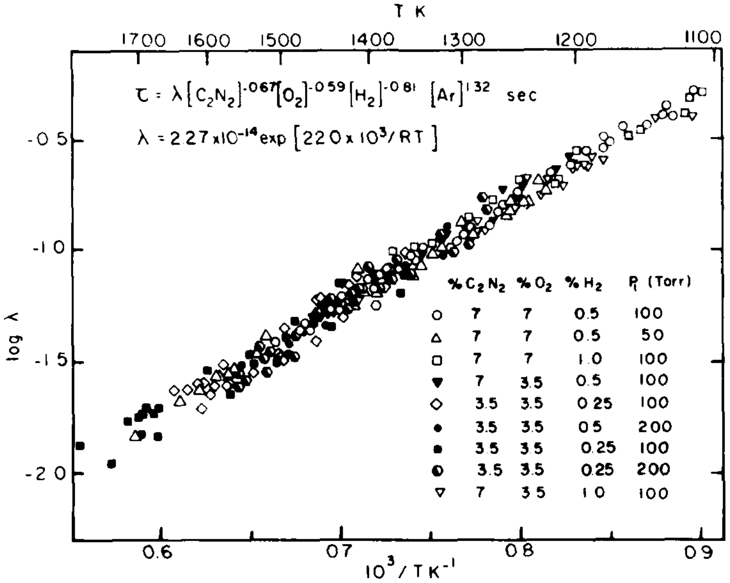

Figure 5. A plot of log $\{\tau/([C_2N_2]^{-0.67}[O_2]^{-0.59}[H_2]^{-0.81}[Ar]^{+1.32})\}$ vs. 1/T for the entire collection of the data. With this correlation all the points scatter along one line with a slope corresponding to 22.0 kcal/mole.

In order to examine the influence of hydrogen on the oxidation reaction we have first constructed a reaction scheme of 25 elementary steps which contained the $C_2N_2+O_2$ scheme (15 steps)[2] and the H_2+O_2 scheme (11 steps)[10]. If the two schemes are combined to one scheme, they are coupled by oxygen atoms *only*. A computer modeling of these systems showed the following features. The induction times were shorter by a factor ~ 5 compared to the $O_2+C_2N_2$ without hydrogen as has been observed experimentally, it showed a very strong dependence on the hydrogen concentration; $\tau \propto [H_2]^{-1.53}$, and a strong dependence on the argon; $\tau \propto [Ar]^{+1.25}$. However, the dependence on the O_2 and C_2N_2 was very similar to what has been calculated in the $O_2+C_2N_2$ system alone. The temperature dependence was also very close to the one in the $C_2N_2+O_2$ scheme namely, 37.5 kcal/mole vs. 34.7 kcal/mole.

It has been shown in a previous study[2] that in the cyanogen oxygen system without hydrogen the oxidation rate was determined almost uniquely by the $O+C_2N_2\rightarrow NCO+CN$ reaction, and the strong dependence of the ignition delay on the C_2N_2 concentration was the result of this behavior. The question to ask is to what extent this step looses its dominant influence as coupling between the two systems is introduced. It so appears that when the coupling is carried out by O atoms *only*, the $C_2N_2+O_2$ system is almost unaffected in the sense of its mechanism by the introduction of small quantities of hydrogen. The only difference is the addition of an external supply of oxygen atoms by the H_2+O_2 scheme.

We have arbitrarily increased the rate constant of the $O+C_2N_2\rightarrow NCO+CN$ step by a factor of 2 and found τ to be shortened by 40%. This result is very simi-

lar to what has been calculated for the 15 step $C_2N_2+O_2$ scheme.

The strong dependence on the hydrogen concentration is explained by its function in supplying oxygen atoms from the O_2+H_2 scheme.

The inhibiting effect of argon on the ignition delay is very strong compared to studies without hydrogen. The effect of argon is usually the result of two phenomena. Since most of the free radicals reach concentrations much higher than their equilibrium concentrations, any increase in the third body concentration will enhance radical recombinations and thus increase the ignition delay. A still stronger effect is caused by the increase in the heat capacity/heat released, a fact which will tend to supress temperature increase during the induction period and thus slow down the progress of the reaction.

In order to examine the reasons for the strong effect of the argon on the induction period we have arbitrarily increased the heat capacity of argon by 1 cal/deg·mole. We first ran a computer experiment with the 15 step $C_2N_2+O_2$ scheme and then an experiment with the combined 25 step $C_2N_2+O_2+H_2$ scheme. The induction period in the latter increased from 960 to 1415 μsec (∿ 47%) whereas in the system without the hydrogen, from 5240 to 6200 μsec (∿ 18%). This difference gives a good explanation for the very high inhibiting effect of the argon in the $C_2N_2+O_2+H_2$ system compared to the $C_2N_2+O_2$ alone. Much more heat is released during the induction period when hydrogen is added to the reaction mixture. Since the H_2+O_2 is a very reactive system it reaches its post ignition conditions at the early stages of the reaction with considerable heat release, and behaves as if the $C_2N_2+O_2$ system does not exist.

As the second stage of examining the influence of hydrogen we have coupled the two systems via H, OH and CN radicals introducing the reactions:

$$OH + CO \rightarrow CO_2 + H \qquad 1$$

$$H + C_2N_2 \rightarrow HCN + CN \qquad 2$$

$$CN + H_2 \rightarrow HCN + H \qquad 3$$

$$HCN + O \rightarrow CN + OH \qquad 4$$

one by one where rate constants were taken from various literature sources. By the introduction of these elementary steps one could observe the following features. All the steps in which H atoms were consumed inhibited the progress of the reaction. Reaction 2 for example increased the induction time by more than a factor of 3. Reaction 1 shortened τ factor of 2. The competition on H atoms decreases the rate of the $H+O_2$ branching step and thus slows down the oxidation. In addition to the influence on the ignition delay itself, the temperature dependence and the effect of C_2N_2 weaken when additional coupling is applied.

We were unable to find the set of reactions that will reproduce the experimental power dependencies and the temperature dependence. The effect of the cyanogen and oxygen comes out too small as compared to the experimental observation. We hope to present a detailed modeling study at a later stage.

REFERENCES

1. A. Lifshitz, K. Scheller, and D. Bass, J. Chem. Phys., *60*, 3678 (1974).
2. A. Lifshitz and M. Frenklach, Int. J. Chem. Kinet., submitted for publication.
3. J.C. Boden and B.A. Trush, Proc. Roy. Soc., *A305*, 107 (1968).
4. J.C. Boden and B.A. Trush, Proc. Roy. Soc., *A305*, 107 (1968).
5. A. Bar-Nun and A. Lifshitz, J. Chem. Phys., *47*, 2878 (1967).

6. A. Lifshitz, M. Frenklach, P. Schechner and H.F. Carroll, Int. J. Chem. Kinet., 7, 753 (1975).
7. A. Lifshitz and P. Kahana, *Shock Tube and Shock Wave Research*, Proc. 11th Symp. (Int.) on Shock Tubes and Waves, University of Washington Press, Seattle, p 398 (1977).
8. A. Lifshitz and P. Schechner, Int. J. Chem. Kinet., 7, 125 (1975).
9. A. Burcat, A. Lifshitz, K. Scheller and G.B. Skinner, Proc. 13th Symp. (Int.) on Combustion (1970), The Combustion Inst. p 745 (1971).
10. T. Fugiwara, Proc. 15th Symp. (Int.) on Combustion 1974, The Combustion Inst. p 1515 (1975).

THERMAL DECOMPOSITION OF CH_3

P. ROTH, U. BARNER, R. LOHR

Fachgebiet Strömungstechnik
University of Duisburg, Duisburg, W. Germany

At temperatures $T > 1700$ K and pressures $p \approx 1.5$ bar the decomposition of C_2H_6 (0.5 ÷ 4 ppm in Ar) behind shock waves into CH_3-radicals is very fast, so that CH_3 can be regarded as the initial concentration. By direct measurement of the time dependent H-atom concentrations in the reaction zone behind shock waves the rate constant of the reaction

$$CH_3 + M \xrightarrow{k} CH_2 + H + M$$

$$k = 3.23\times10^{-8} \exp(-46.1\times10^{3}\ K/T)\ cm^3\ s^{-1}$$

in the temperature range $2150 \leq T \leq 2850$ K was measured. The experiments were performed at total densities of about $4\times10^{18} cm^{-3}$. By computer simulations with a set of five or eight chemical reactions we were able to show, that the H-atom production is basicly determined by the given reaction. Under our experimental conditions secondary reactions are unimportant.

INTRODUCTION

In hydrocarbon oxidation processes reactions of CH_3 -radicals are very important. Normally they are part of a complex overall reaction system; their individual reaction behaviour under high temperature conditions is not separable in detail and not fully understood. The treatment of complex coupled systems for the interpretation of measurements is a characteristic task in reaction kinetics. Our concept in studying hydrocarbon reactions is to use very low concentrations of the reactants and to measure the H-atom (or O-atom) production in such systems. The detection technique is the atomic resonance absorption spectrophotometry (ARAS) in shock tube experiments, which has successfully been applied to the investigation of the reaction behaviour of small molecules. The recombination of CH_3 to form C_2H_6 at temperatures $T \approx 1500$ K has been studied by GLÄNZER, QUACK and TROE [1]. ROTH and JUST [2] investigated the reaction CH_3 + CH_3 by means of the ARAS-technique. Measurements of the high temperature pyrolytical decomposition of CH_3 are not known.

Under energetical aspects the reaction channels

$$CH_3 + M \xrightarrow{1} CH_2 + H + M \qquad \Delta^R h = 457.5 \text{ kJ/mol}$$

$$\xrightarrow{1a} CH + H_2 + M \qquad \Delta^R h = 448.6 \text{ kJ/mol}$$

are very similar; with regards to kinetics, however, the first reaction path seems more probable. This reaction channel has been considered by OLSON and GARDINER [3] in the methane oxidation system.

In order to clarify this problem we performed H-atom measurements behind shock waves. The CH_3-radicals were generated by decomposition of highly diluted C_2H_6. Under our conditions the decay of ethane is so fast that CH_3 may be regarded as the initial substance. Because of the very low concentrations a simple kinetic interpretation of the measured time dependent H-atom profiles is possible.

EXPERIMENTAL

The experimental study was carried out in a new stainless steel cylindrical shock tube which had an internal diameter of 7.9 cm. It had been constructed as an UHV-apparatus with a special inner surface and a very low leak- and outgassing rate. A schematic general view is given in fig. 1. A careful experimental procedure allows us to evacuate the tube by a liquid nitrogen-cooled Ti-sublimation pump and a turbomolecular pump with forepump via a special end plate valve down to about 10^{-8} mbar. The residual gas, which is practically free of hydrocarbon compounds, is controlled by a quadrupol mass-spectrometer. The gas mixing system and the storage bottle for the mixture are controlled in a similar way.

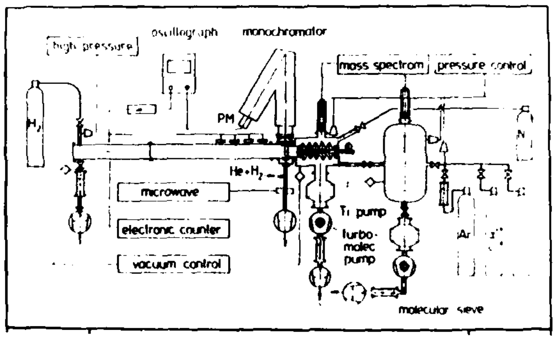

Figure 1. Schematic general view of the UHV shock tube.

The optical setup and details of the experimental technique have been described previously [4] and are included in fig. 1. The arrangement consists of a microwave-excited discharge lamp for the emission of the H-doublet at 121.6 nm, a 1-m-McPherson vacuum-UV-monochromator and a special solar blind photomultiplier. The opto-electrical setup has a time constant of about 15 µs.

Because of the high sensitivity of the optical measurement technique all gases used were of ultrahigh purity (Ar: 99.9999, C_2H_6: 99.95). Test gas mixtures were prepared manometrically with calibrated diaphragm-type pressure gauges (see fig. 1). The whole mixing system can be heated to about 300 °C. Test runs in argon showed almost negligible absorption signals of H-atoms behind reflected shock waves up to temperatures $T \approx 3000$ K. Thus the unrestricted usefulness of the shock tube and the measurement technique up to these temperatures is proved. Reflected shock conditions were computed in the conventional way from incident shock velocities, which were measured in the standard manner with thin-film resistances and three 10 MHz electronic counters. Experimental profiles were recorded photographically from a Tektronix oscilloscope and hand-digitized for computer processing.

CALIBRATION

The ARAS-technique is an optical line-emission/line-absorntion method with different spectral contours of the radiation and absorption lines. The shocked gas can be considered as a homogeneous isothermal absorber of length l and concentration [H] with an absorption coefficient $k_{\nu,a}$, which is mainly doppler-broadened. The relation between the measured absorption and the H-atom concentration in the reaction zone inside the shock tube is given by

$$A = \frac{\int_{-\infty}^{+\infty} I_\nu \{1-\exp(-k_{\nu,a}[H]l)\}d\nu}{\int_{-\infty}^{+\infty} I_\nu d\nu}$$

$$k_{\nu,a} = k_0(T)\ \exp\{-\frac{4\ \ln 2\ (\nu - \nu_0)^2}{\Delta\nu_D^2(T)}\}$$

$$k_0(T) = \frac{1.17\text{x}10^{-11}}{\sqrt{T}}\ \text{cm}^2 \qquad (T\ \text{in K})$$

The integral relation between A and [H] contains the unknown spectral radiation intensity I_ν of the microwave-excited resonance lamp. Dominantly it is a function of the temperature T_e and the concentration $[H]_e$ of the emitter gas and both variables vary with the length x_e of the discharge flow

$$I_\nu = I_\nu\{T_e(x_e), [H]_e(x_e)\}$$

Neither $T_e(x_e)$ nor $[H]_e(x_e)$ are known and therefore the given integral relation cannot be evaluated. A simple correlation between measured absorption and H-atom concentration does not exist.

For this reason calibration measurements using mixtures of H_2/Ar have been performed. The rate coefficient of the dissociation reaction is well known. This is why computed time dependent H-atom concentrations can be correlated to measured time dependent absorption signals. The calibration data are shown in fig. 2. A weak temperature dependence is observed. The absolute accuracy of all measured H-atom concentrations and their interpretation in terms of rate coefficients naturally depend on the accuracy of the kinetic calibration data.

A comparison between measured calibration data and computations using different simple models for the unknown spectral radiation intensity I_ν is given in fig. 3. The lowest curve is the solution for an infinitesimal sharp emission line. The dotted lines were computed under the assumption of an optically thin emission gas of uniform temperature T_e, which is doppler-broadened. The lower curve with $\alpha = \sqrt{(T_e/T)} = 2$ belongs to the higher shocked gas temperature T.

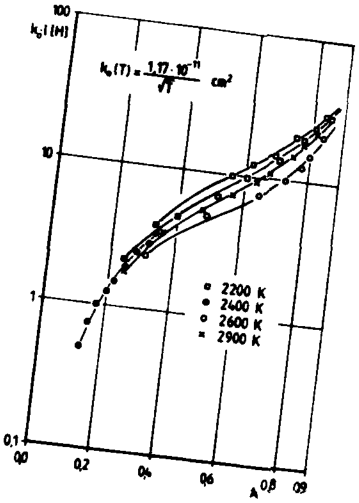

Figure 2. Calibration data of H-atom measurements

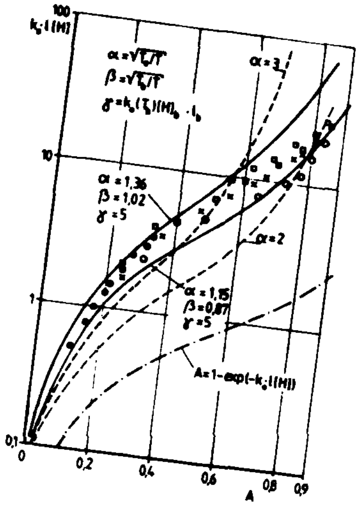

Figure 3. Different models for the spectral emission intensity I_ν

A remarkably better agreement with the calibration measurements is possible with a two-layer emission gas model of different but uniform temperatures T_e and T_b with $T_b < T_e$. The optical thickness of the colder layer near the shock tube window is characterized by $\gamma = k_0(T_b)\,[H]_b\,l_b$. The two curves of fig. 3 were computed with identical values of the optical thickness and temperature ratio T_e/T_b but different temperatures T of the shocked gas, which correspond to the highest and lowest experimental values. Within the limits of the simple model the agreement between the computation and the experimental data is satisfactory. A quite similar three parameter model has been used by APPLE and APPLETON [5] in their D_2-dissociation study. A better agreement may be obtained using a more realistic multi-layer model for the radiation of the H-atom resonance lamp.

RESULTS AND DISCUSSION

Using the calibrated optical system described in the previous section the time dependent concentration of H-atoms was measured during the thermal decomposition of CH_3 behind reflected shock waves. Five different mixtures of ultrahigh purity with initial C_2H_6-concentrations of 0.5 ÷ 4 ppm were used. The range of reflected-shock temperatures was 2150 ÷ 2850 K, and the initial reflected-shock total concentrations were of the order of 10^{19} cm^{-3}. Under these conditions the decomposition of C_2H_6 into CH_3 is very fast [2] and CH_3 can be regarded as "quasi-initial concentration". A representative record of the H_α-absorption profile obtained by shock-heating a test gas mixture of 4 ppm CH_3 diluted in argon is given in fig. 4.

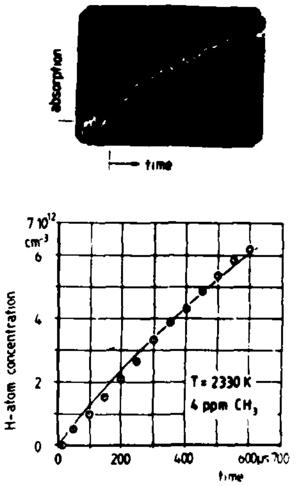

Figure 4. Example of measured time dependent absorption and H-atom profile

The H-atom profile was constructed simply by using the calibration characteristic shown in fig. 2. The first linear increase of the H-atom concentration, which was found in nearly all experiments, is remarkable; measurements with lower concentrations of reactants and higher temperatures showed a deviation towards a more stationary value after the initial linear increase, which is about half the maximum equilibrium concentration. By measuring the slope of the linear increase of such atom concentrations a reaction rate

$$k_{exp} = \left(\frac{d\,[H]\,/dt}{[CH_3]\,[Ar]} \right)_{t \simeq 0}$$

was determined. Results presented in the usual Arrhenius form are shown in fig. 5. A low temperature correction with respect to the initial bimolecular parallel reaction channel [2]

$$CH_3 + CH_3 \longrightarrow C_2H_5 + H \longrightarrow C_2H_4 + 2\,H$$

is included. An initial concentration dependence is not discernible. The data shown in fig. 5 are quite accurately represented by the simple Arrhenius expression

$$k_{exp} = 3.23\times10^{-8}\ \exp(\ -46\ 100\ K/T)\ cm^3\ s^{-1}$$

The apparent activation temperature T_a = 46 100 K is of a magnitude which would be expected for a unimolecular decomposition of CH_3 according to reaction 1.

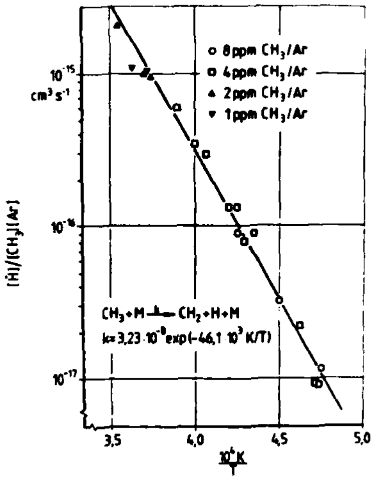

Figure 5. Arrhenius plot of the measured initial H-atom slope

A first interpretaion of the experimental results was carried out using the following kinetic mechanism:

$$CH_3 + M \xrightarrow{1} CH_2 + H + M$$

$$\xrightarrow{1a} CH + H_2 + M$$

$$CH_3 + H \xrightarrow{2} CH_2 + H_2$$

$$CH_3 + CH_2 \xrightarrow{3} C_2H_4 + H$$

Only the initial decomposition and two subsequent reaction steps are included. At lower temperatures the bimolecular channel [2] and the first subsequent reaction must be regarded.

$$CH_3 + CH_3 \xrightarrow{4} C_2H_4 + 2\ H$$

$$C_2H_4 + M \xrightarrow{5} C_2H_3 + H + M$$

The following discussion of the computational results has to show whether or not secondary reactions influence the initial H-atom production and falsify the interpretation $k_{exp} = k_1$. The H-atom measurements are not sufficient to explain the reaction behaviour of the overall system and to determine additional rate coefficients of subsequent reactions. Computer simulations of the given mechanism were carried out for the conditions of the experiments and compared with the measured H-atom profiles. Setting $k_{exp} = k_1$ the used rate coefficients are

$k_1 = 3.23\times10^{-8} \exp(-46\,100\ K/T)$ $cm^3\ s^{-1}$

$k_{1_a} = 0$ or $k_{1_a} = k_1$

$k_2 = 1.2\times10^{-9} \exp(-7600\ K/T)$ $cm^3\ s^{-1}$ 3

$k_3 = 3.3\times10^{-11}$ $cm^3\ s^{-1}$ 3

$k_4 = 1.33\times10^{-9} \exp(-13\,400\ K/T)$ $cm^3\ s^{-1}$ 2

$k_5 = 6.3\times10^{-7} \exp(-49\,400\ K/T)$ $cm^3\ s^{-1}$ 6

Some results are presented in fig. 6. It is impossible to explain the experimental results without reaction 1. If channel 1a was the only initial step (neglecting the known reaction 4), the H-atoms would have to be products of secondary reactions. This is not in agreement with the experimental fact of linear increase. It is clear that the initial behaviour of the highly diluted reaction system is dominantly determined by reaction 1 and is given quite correctly by the computer model. With increasing reaction time the computed H-atom concentrations are lower than the more linear experimental values. The reaction channel 1a enlarges the deviation. It seems to be unimportant under our experimental conditions.

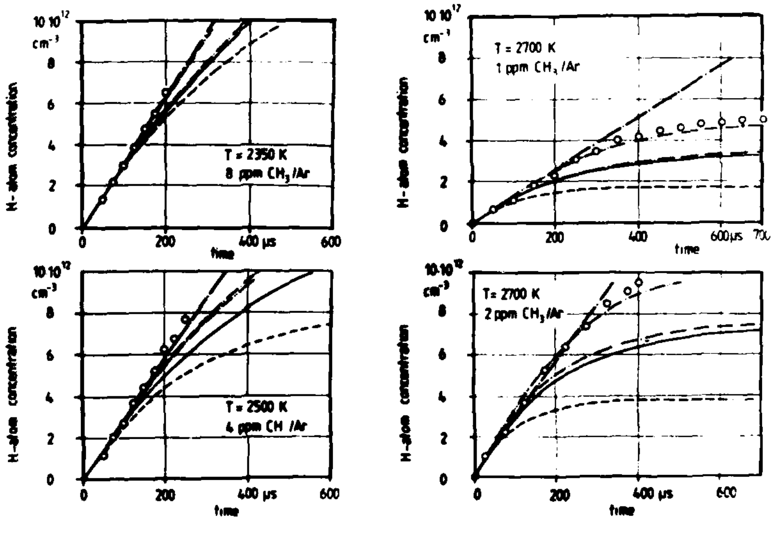

Figure 6.
Examples of measured and computed H-atom profiles

—— $k_1 \div k_5$, $k_{1_a} = 0$

– – $k_1 \div k_5$, $k_{1_a} = k_1$

–.– $k_1 \div k_5$, $k_3 \to 3.0 \times k_3$

–..– $k_1 \div k_8$, $k_{1_a} = 0$

For better agreement between the experimental and analytical results, the formation of H-atoms by secondary reactions must be enlarged. Two different ways are possible:

a) variation of the relatively unknown rate coefficients k_2 and k_3,

b) completion of the reaction system by further CH_2-reactions.

A greater value of k_3 improves the computed concentration but the effect is low at higher temperatures. More realistic are additional CH_2-reactions.

$$CH_2 + M \xrightarrow{6} CH + H + M$$

$$\xrightarrow{6a} C + H_2 + M$$

$$CH_2 + H \xrightarrow{7} CH + H_2$$

$$CH_2 + CH \xrightarrow{8} C_2H_2 + H$$

Computed profiles using rate coefficients

$$k_6 = k_{6_a} = k_1$$

$$k_7 = k_8 = k_3$$

are included in fig. 6. By variation of the rate coefficients the differences between the measured and computed profiles can be brought to a minimum value. A unique set of coefficients k_2 to k_8 cannot be given. Uncertainties as to the rate coefficients of reactions 2 to 8 do not seem to influence the determination of the rate expression for reaction 1. For the conditions investigated, the primary apparent rate coefficient of fig. 5 can be identified with the rate coefficient of reaction 1. The present value of k_1 is in agreement with estimates obtained from weak-collision unimolecular reaction rate theory for the low pressure region. The collision efficiency [7]

$$\beta_c = \frac{k_1}{k_1^{sc}} \approx 0.04 \quad , \qquad T = 2600\ K$$

is consistent with other values for reactions of simple polyatomic molecules.

Acknowledgment

The financial support of the Deutsche Forschungsgemeinschaft is gratefully acknowledged.

REFERENCES

1. K. Glänzer, M. Quack, J. Troe, Chem. Phys. Letters 39, 304 (1976)
2. P. Roth, Th. Just, Ber. d. Bunsenges. f. Phys. Chem.,to be published
3. D.B. Olson, W.C. Gardiner, Comb. and Flame 32, 151 (1978)
4. P. Roth, Th. Just, Ber. d. Bunsenges. f. Phys. Chem. 81, 572 (1977)
5. D. Apple, J.P. Appleton, 15th Symp. (Int.) on Comb., Tokyo 1974
6. Th. Just, P. Roth, R. Damm, 16th Symp. (Int.) on Comb., Boston 1976
7. J. Troe, J. Chem. Phys. 66, 4758 (1977)

RESONANCE ABSORPTION MEASUREMENTS OF ATOM CONCENTRATIONS IN REACTING GAS MIXTURES.

4. MEASUREMENTS OF H AND D ATOMS IN OXIDATION OF H_2, D_2 and CD_4.

CHI-CHANG CHIANG and GORDON B. SKINNER

Department of Chemistry, Wright State University
Dayton, Ohio 45435, USA

Resonance absorption spectroscopy has been used to measure H and D concentrations in shock-heated H_2-O_2-Ar, D_2-O_2-Ar, and CD_4-O_2-Ar mixtures. In all, ten different compositions were studied over the range of 925-1825K for the first two mixtures, and 1700-2200K for the last. Under the conditions studied relatively few elementary reactions were involved, so that rate coefficients could be deduced. We find

$H + O_2 \rightarrow OH + O$ $k_3 = 1.1$ E14 exp(-67.4 kJ/RT) $mole^{-1} cm^3 s^{-1}$
$H + O_2 + Ar \rightarrow HO_2 + Ar$ $k_5 = 7$ E14 $mole^{-2} cm^6\ s^{-1}$ at 1000K
$D + O_2 \rightarrow OD + O$ $k_{3D} = 1.6$E13 exp(-62.8 kJ/RT) $mole^{-1} cm^3 s^{-1}$
$D + O_2 + Ar \rightarrow DO_2 + Ar$ $k_{5D} = 1.6$E14 $mole^{-2} cm^6 s^{-1}$ at 1000K
$CD_3 + O_2 \rightarrow DCDO + OD$ $k_6 = 6.8$E11 exp(-38 kJ/RT) $mole^{-1} cm^3 s^{-1}$

The isotope effect in reaction 3 is larger than one would normally expect for this type of reaction.

INTRODUCTION

Although the reaction between hydrogen and oxygen is one of the most-studied combustion systems, there have been only a few experiments[1,2] in which H atom concentrations (or D concentrations for the D_2-O_2 reaction) have been measured. The progress of the reaction has more often (for example,[3,4]) been studied by measurements of OH radical concentrations, from which H concentrations have been calculated using assumed reaction mechanisms.

Similarly, the CH_4-O_2 reaction has been extensively studied (for example,[5,6]), and elaborate kinetic models have been developed that contain reactions involving H atoms, yet no measurements of H or D atom concentrations have been reported. The formation of H atoms in methane pyrolysis, however, has been investigated by Roth and Just[7].

EXPERIMENTAL

For making these measurements we have used a 7.6 cm diameter stainless steel shock tube which has been described in detail elsewhere[8]. This reference also describes the optical system used to detect H and D atoms by resonance absorption spectroscopy, and the methods of calibrating the system. For the research described here we used light source B of reference 8, with 0.1% H_2 or D_2 in helium as light source gas. Calibration curves for H applicable to the experiments described in this paper are shown in Figure 1. Similar curves applied for D atoms.

Measurements were made behind reflected shock waves at a distance of 2 cm from the end plate, but close enough so that side wall effects were minimal. Observed reaction times varied from 50 microseconds to 2 milliseconds, depending on the temperature and gas mixture being studied.

Gas mixtures were made up by pressure within 2% of the nominal composition, except for those low concentration mixtures that required two or three dilutions, for which the uncertainty could be 4%. For making up a dilute mixture, such as 100 ppm CD_4 in Ar, we first evacuated a gas cylinder, then added 2 PSI (1 PSI = 6.895×10^3 Pa) of argon, then 1 PSI of CD_4, then 97 PSI of argon, the latter fairly rapidly so as to produce mixing. After allowing at least 16 hours for further mixing, sometimes with mild heating of one side of the cylinder to produce convection currents, the above procedure was repeated to dilute 1 PSI of the 1% mixture by a factor of 100 to produce the 100 ppm mixture. Concentrations below 50 ppm required an additional dilution.

MATERIALS

For making up sample gas mixtures we used Airco Grade 5.8 argon, containing 0.5 ppm CO + CO_2, 0.5 ppm hydrocarbons reported as methane, 1 ppm O_2 and 0.5 ppm H_2, with a dew point of -105°F. Matheson Ultra High Purity hydrogen (99.999%) and oxygen (99.99%) were used, each containing less than 1 ppm hydrocarbons. Deuterium was also from Matheson, 99.5 atom % pure. CD_4 was obtained from Merck, Sharp and Dohme of Canada, and was stated to have a minimum isotopic purity of 99%. For driver gas we used Airco helium (99.995%) and argon (99.995%), while for the discharge lamp gas we used Airco Grade 5 helium (99.999%) and the H_2 and D_2 listed above. No further purification of the gases was attempted.

RESULTS

The gas mixtures studied are listed in Tables 1 and 2. For each experiment we obtained an incident shock speed, a pressure record at the observation station (the pressure transducer was at the same axial position as the observation ports, but on the top rather than the sides of the tube), and a Lyman-α absorption curve. The incident shock speed was used to calculate the reflected shock temperature and pressure. Shock tube driver concentrations were "tailored" by adding argon to the helium driver gas, and the pressure records were used only to check on this point. The reflected shock pressure remained constant within 2%, our limit of measurement, throughout the period during which atom concentrations are reported. It may also be mentioned that, due to the sensitivity of the method of analysis, the extent of reaction during the measurement period was never enough to bring about a significant temperature change due to energy release or absorption.

The temperature range studied for each mixture was limited at the lower end by the detection limit. We considered that there should be at least a 10% decrease of intensity over a time of 1.5 to 2 milliseconds for a significant measurement. From Figure 1, a 10% decrease of intensity corresponds to about 10^{-12} mole cm^{-3} of H atoms. At the high concentration end, we limited our data to absorptions less than 90%, corresponding to 2-5 x 10^{-11} mole cm^{-3}, depending on the temperature. Also, the 90% absorption had to occur at times greater than 20 microseconds, since our measurement time constant was about 3 microseconds.

For the H_2 and D_2 oxidation reactions it was found, as expected, that the atom concentrations increased exponentially with time. Sometimes the first point fell below the exponential curve, but not enough detail was observable to show how the exponential curve was approached. A typical set of data is

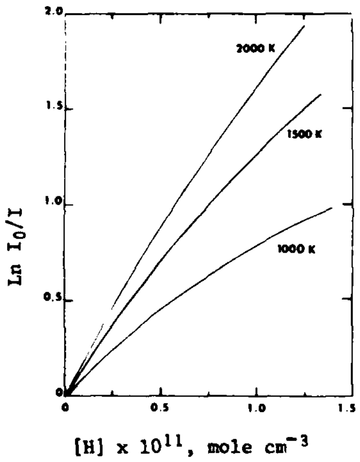

Figure 1. Calibration curves for H atoms.

shown in Figure 2. In Table 1 we give the experimental results in terms of the slope of the graph of ln [H] or [D] versus 1/T, and the intercept at time zero.

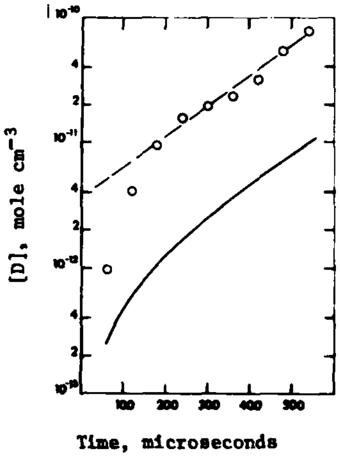

Figure 2. Measured and calculated D concentrations for mixture of 2% D_2 and 0.2% O_2 in argon, 1321 K, 2.63 atm total pressure. O, measured concentrations; – – , Line drawn through data to obtain slope of graph; ——, Curve calculated using data of Table 3.

For methane oxidation, the concentration of D usually increased linearly at first, then tended to level off at the two lower oxygen concentrations. Two typical curves are shown in Figures 3 and 4. These data are more difficult to present concisely. We have attempted to do so in Table 2 by giving the initial slope of the curve and also two points, one near the middle and one near the end of the measurement time. In comparing modeling calculations with experiment, we actually used six to ten points along the curve.

Table 1. Experimental Data and Calculations for Formation of H and D Atoms in H_2-O_2-Ar and D_2- O_2-Ar Mixtures

Temp, K.	Pressure, Atm	Expt. Slope, s^{-1}*	[H] or [D] as t → o mole cm^{-3}	$\frac{\text{Expt}}{\text{Calc}}$ Slope	k_1, Calc., $mole^{-1}$ cm^3 s^{-1}
Mixture 1 5% H_2, 2.5% O_2					
925	1.98	1.22E04	-	1.32	-
933	1.83	1.69E04	-	1.58	-
949	1.99	1.44E04	-	1.01	-
949	1.89	1.52E04	-	1.09	-
986	1.77	1.64E04	4.4E-13	.77	1.2E04
1032	1.93	2.52E04	9.8E-13	.70	3.8E04
1042	1.96	3.02E04	5.1E-13	.77	2.1E04
1117	2.21	5.80E04	1.5E-13	.76	1.0E05
Mixture 2 1% H_2, 0.5% O_2					
1000	2.22	4.24E03	1.8E-12	.73	2.3E05
1037	2.37	8.25E03	1.0E-12	.95	1.6E05
1103	2.35	1.55E04	1.0E-12	1.08	2.8E05
1154	2.53	1.95E04	1.0E-12	.94	3.8E05
1304	2.71	4.05E04	6.3E-12	.90	5.6E06
Mixture 3 0.1% H_2, 0.05% O_2					
1069	2.19	1.42E03	2.8E-13	.86	6.5E05
1192	2.51	2.68E03	3.4E-13	.98	1.7E06
1204	2.48	2.74E03	4.4E-13	.96	2.4E06
1232	1.40	2.15E03	3.1E-13	1.00	3.5E06
1244	2.89	3.98E03	6.1E-13	.99	3.7E06
1245	2.48	3.76E03	4.3E-13	1.02	3.0E06
1320	2.76	5.65E03	6.3E-13	1.05	6.0E06
1414	2.64	7.19E03	8.8E-13	1.02	1.4E07
1618	2.70	1.32E04	1.5E-12	1.07	5.6E07
1826	2.58	1.80E04	1.2E-12	1.00	9.3E07
Average ratio for all H_2-O_2-Ar experiments				.98	
Mixture 4 5% D_2, 2.5% O_2					
992	2.03	8.66E03	1.2E-13	1.22	7.6E02
995	1.99	8.97E03	4.5E-14	1.25	3.0E02
1022	1.88	6.00E03	3.3E-12	.60	2.9E03
1028	1.90	8.56E03	1.5E-12	.89	1.4E03
1072	2.04	1.43E04	2.2E-12	.95	2.7E03
1099	2.13	2.20E04	1.5E-12	1.22	2.1E04
Mixture 5 1% D_2, 0.5% O_2					
966	2.08	2.55E03	7.8E-14	1.77	1.9E03
1012	2.25	2.40E03	1.0E-12	1.21	3.6E04
1045	2.39	2.96E03	1.4E-12	.90	5.8E04
1097	2.60	3.70E03	3.0E-12	.86	1.7E05
1142	2.47	6.41E03	1.6E-12	1.12	1.3E05
1234	2.82	8.57E03	2.8E-12	.87	3.5E05
Mixture 6 0.1% D_2, 0.05% O_2					
1194	3.25	1.68E03	1.1E-12	.73	9.5E05
1319	3.66	2.84E03	2.9E-12	.97	4.5E06
1402	3.51	3.35E03	2.5E-12	1.05	6.0E06
1490	3.37	3.78E03	3.6E-12	.97	1.3E07
1617	3.28	4.16E03	3.4E-12	.82	2.1E07

1734	3.03	4.70E03	2.8E-12	.84	2.7E07
Mixture 7 2% D_2, 0.2% O_2					
974	1.87	8.70E02	9.5E-13	.75	1.4E04
1015	2.16	1.74E03	2.8E-12	1.30	5.1E04
1033	1.81	1.92E03	1.4E-12	1.42	3.5E04
1036	2.19	1.75E03	1.9E-12	1.21	4.0E04
1039	2.04	2.37E03	1.0E-12	.95	2.3E04
1064	2.24	2.26E03	3.0E-12	1.41	7.8E04
1111	2.41	1.69E03	5.4E-12	.76	1.8E05
1118	2.43	1.70E03	4.2E-12	.83	1.5E05
1132	2.37	3.19E03	2.5E-12	1.00	1.1E05
1146	1.67	4.00E03	1.5E-12	1.25	9.3E04
1161	2.47	3.23E03	3.2F-12	1.09	1.5E05
1264	2.70	6.02E03	3.6E-12	1.17	2.8E05
1321	2.79	5.31E03	5.8E-12	.84	5.9E05
1321	2.63	5.62E03	3.5E-12	1.03	4.8E05
1344	2.54	6.52E03	3.6E-12	1.04	4.5E05
1359	2.40	7.14E03	3.5E-12	1.11	5.0E05
1402	2.39	7.93E03	4.4E-12	1.04	7.8E05
1419	2.38	9.24E03	5.4E-12	.98	1.0E06
1444	2.28	7.75E03	4.8E-12	.91	1.1E06
1483	2.55	8.60E03	4.8E-12	.84	1.1E06
1612	2.16	1.32E04	5.4E-12	1.02	2.4E06

Average ratio for all D_2-O_2-Ar experiments 1.03

*Slope is dln [H]/dt

Table 2 Experimental Data for Formation of D Atoms in CD_4-O_2-Ar Mixtures

Temp, K.	Pressure Atm	Initial Slope, mole cm^{-3}/sec	$Time_1$ μsec	$[D]_1$ mole cm^{-3}	$Time_2$ μsec	$[D]_2$ mole cm^{-3}
Mixture 8 20ppm CD_4, 40 ppm O_2						
1763	3.33	4.2E-09	400	1.4E-12	800	2.0E-12
1807	3.32	1.0E-08	400	2.7E-12	800	3.7E-12
1830	3.38	1.0E-08	200	2.0E-12	360	3.7E-12
1877	3.24	1.8E-08	200	3.3E-12	400	4.7E-12
1927	3.36	2.7E-08	200	5.2E-12	360	8.1E-12
1943	3.26	4.0E-08	150	5.8E-12	300	8.9E-12
2004	3.26	6.6E-08	150	8.8E-12	300	1.4E-11
2022	3.00	1.0E-07	100	9.3E-12	230	1.6E-11
2050	3.21	1.0E-07	100	8.3E-12	200	1.3E-11
2165	2.97	3.0E-07	50	1.4E-11	100	1.9E-11
Mixture 9 100 ppm CD_4, 200 ppm O_2						
1720	3.09	2.1E-08	200	3.3E-12	400	4.5E-12
1734	3.13	3.0E-08	150	2.3E-12	300	2.6E-12
1799	3.30	1.4E-08	100	1.4E-12	200	2.2E-12
1830	3.12	5.0E-08	150	6.1E-12	300	8.0E-12
1861	2.94	1.1E-07	150	1.2E-11	300	1.9E-11
1901	2.61	7.0E-08	150	7.3E-12	300	9.6E-12
1926	3.22	1.3E-07	100	9.0E-12	180	1.1E-11
1943	2.84	2.4E-07	100	2.0E-11	180	3.0E-11
1986	3.07	3.3E-07	50	1.7E-11	100	3.4E-11
2195	3.03	4.9E-07	30	1.5E-11	60	2.5E-11
Mixture 10 50 ppm CD_4, 1000 ppm O_2						
1719	3.50	2.1E-09	1000	2.4E-12	1800	1.2E-11

Table 2 cont.

1777	3.31	2.7E-09	400	1.1E-12	800	4.4E-12
1784	3.33	5.7E-09	600	3.6E-12	1200	1.4E-11
1823	3.30	6.6E-09	600	4.7E-12	1200	1.7E-11
1903	3.38	2.6E-08	200	3.0E-12	360	4.6E-12
1919	3.29	3.5E-08	200	5.2E-12	360	7.8E-12
1971	3.27	6.0E-08	200	7.7E-12	360	1.1E-11
2024	3.25	8.6E-08	70	6.0E-12	140	1.0E-11
2110	3.13	1.8E-07	70	8.2E-12	140	1.1E-11

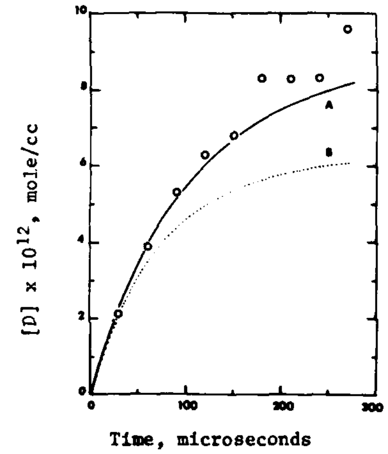

Figure 3.
Measured and calculated D concentrations for mixture of 100 ppm CD_4, 200 ppm O_2 in argon, 1901 K, 2.61 atm total pressure. O, measured concentrations; Curve A, calculated using data of Table 4; Curve B, calculated using reaction 3 (for H) rather than 3D from Table 3.

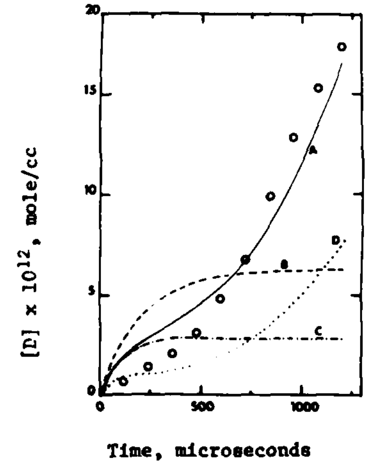

Figure 4.
Measured and calculated D concentrations for mixture of 50 ppm CD_4, 1000 ppm O_2 in argon, 1823 K, 3.30 atm total pressure. O, Measured concentrations; Curve A, calculated using data of Table 4; Curve B, calculated using only reactions 1 and 2 from Table 4; Curve C, calculated using only reactions 1 to 5 from Table 4; Curve D, calculated using reaction 3 (for H) rather than 3D from Table 3.

DISCUSSION

Since our detection method is sensitive, we measured atom concentrations quite near the beginning of the reactions, before any appreciable fractions of reactants were used up. Moreover, three-body atom combinations are unimportant because of the low atom concentrations. For the hydrogen-oxygen reaction, the only important steps are:

$$\mathrm{H_2 + O_2 \rightarrow 2\ OH} \tag{1}$$
$$\mathrm{H + HO_2} \tag{1a}$$
$$\mathrm{OH + H_2 \rightarrow H_2O + H} \tag{2}$$
$$\mathrm{H + O_2 \rightarrow OH + O} \tag{3}$$
$$\mathrm{O + H_2 \rightarrow OH + H} \tag{4}$$
$$\mathrm{H + O_2 + Ar \rightarrow HO_2 + Ar} \tag{5}$$

There is still uncertainty about the relative importance of reactions (1) and (1a). As Jachimowski and Houghton[4] pointed out, they are very hard to distinguish experimentally and lead to almost identical kinetic behavior after a brief initial period. We had hoped to distinguish between them because the high sensitivity of our method allowed us to make measurements at smaller extents of reaction than can be done with OH, but we were not able to.

Given the above five reactions, it can be shown[3,4] that after a brief initial period, reactions 2 to 5 reach a steady state in which concentrations of H, OH and O maintain a constant ratio to one another. Under these conditions,

$$[\mathrm{H}] = [\mathrm{H}]_0 \exp \frac{(2k_3 - k_5\,[\mathrm{Ar}])\,[\mathrm{O_2}]\,t}{c} \tag{I}$$

$$\text{where}\quad [\mathrm{H}]_0 = \frac{k_1\,[\mathrm{H_2}]}{k_3} \quad \text{or} \quad [\mathrm{H}]_0 = \frac{k_{1a}[\mathrm{H_2}]}{k_2} \tag{II}$$

$$c = \frac{k_3\,[\mathrm{O_2}]}{k_4\,[\mathrm{H_2}]} + \frac{2k_3\,[\mathrm{O_2}]}{k_2\,[\mathrm{H_2}]} + 1 \tag{III}$$

In these equations, concentrations of H_2 and O_2 are the initial values, for the beginning of this section.

For stoichiometric and richer mixtures at moderate temperatures (1200 - 1500 K) the slope of the graph of log [H] versus time is determined mainly by k_3, since k_5 [Ar], k_2 and k_4 are large compared to k_3, and c is therefore close to 1. A graph of ln (d ln [H]/dt)/ [O_2] versus the reciprocal of the temperature produces a nearly straight line at the higher temperatures, with a slope closely related to the Arrhenius activation energy of reaction 3. At lower temperatures reaction 5 becomes significant, and the graph curves downward.

Essentially then, the experimental values of d ln [H]/dt are most sensitive to k_3 and k_5, and not very sensitive to k_1, k_2 and k_4. None of the reverse reactions are significant. Accordingly, we have carried out a simple numerical integration of the above equations, using literature data for rate constants for reactions 1, 2 and 4, and adjusting k_3 and k_5 to give the best fit to the experimental data. The rate constant expressions we used are given in Table 3. We calculated the rate constant for reaction 4D using the activated complex theory model of Schott, Getzinger and Seitz[10] allowing for the mass change, and then assumed that the same isotope effect would be found for reaction 2, since the chemical change is essentially the same. The calculated isotope effect was close to a factor of 2 in our temperature range. For reaction 1, for which the mechanism is not well known, we simply estimated an isotope effect of a factor of 0.65. These calculations should be satisfactory because of the low sensitivity of k_3 and k_5 to the values of the other rate constants.

Table 3. Kinetic Data for H_2-O_2 and D_2-O_2 Reactions

Reaction	Arrhenius Parameters A*	E, kJ	Reference
1. $H_2 + O_2 \rightarrow 2OH$	1.7E 13	205.6	4
2. $OH + H_2 \rightarrow H_2O + H$	5.2E 13	27.2	9
3. $H + O_2 \rightarrow OH + O$	1.1E 14	67.4	this work
4. $O + H_2 \rightarrow OH + H$	2.2E 14	57.5	10
5. $H + O_2 + Ar \rightarrow HO_2 + Ar$	4.4E 14	-4.2	this work
1D $D_2 + O_2 \rightarrow 2OD$	1.1E 13	205.6	see text
2D $OD + D_2 \rightarrow D_2O + D$	3.3E 13	29.3	see text
3D $D + O_2 \rightarrow OD + O$	1.6E 13	62.8	this work
4D $O + D_2 \rightarrow OD + D$	1.4E 14	59.6	see text
5D $D + O_2 + Ar \rightarrow DO_2 + Ar$	1.0E 14	-4.2	this work

*Units of A, $mole^{-1}$ cm^3 s^{-1} for Reactions 1-4; $mole^{-2}$ cm^6 s^{-1} for Reaction 5

The derived rate constants for reactions 3 and 5 tend to be somewhat lower than recent literature values. For reaction 3 at 1300K, we obtain 2.2E11 $mole^{-1}$ cm^3 s^{-1}, while Baulch et al (11) give 3.3E11 and Schott (12) obtained 2.9E11. This agreement is probably within the experimental errors of the methods used. For reaction 5 at 1000 K, we obtain 7E14, $mole^{-1}$ cm^3 s^{-1}, while Baulch et al give 2.5E15. Our lower-temperature results are quite sensitive to k_5, and use of the Baulch value causes a large reduction in the calculated slope, d ln [H]/dt, and a large increase in the ratio of expt/calc slope below 1050K. The calculated rate constants for k_3 and k_5 are coupled, in that at a low temperature the two rate constants can be increased or decreased together without change in calculated slope. The values of Table 3 gave the best fit to the data over the entire temperature range.

For the deuterium reactions we again found rate constants somewhat lower than expected. At 1300 K the isotope effect for reaction 3 is a factor of 4.5, while that for reaction 5 over the entire range is 4.4. Actually, as we indicated above, since reaction 5 is important only over the 900-1050 K range, we were not able to determine its temperature dependence, and simply adopted that suggested by Baulch et al. Such a large isotope effect would not normally be expected, since no bonds involving H or D are broken in the reaction. Kurzius and Boudart[13], from static ignition studies, deduced that there is essentially no kinetic isotope effect for reaction 3 near 900 K. In a study rather like ours, but at higher temperatures where the influence of reactions 2 and 4 is greater, Appel and Appleton[2] also found a moderately small isotope effect. We have no simple explanation for the discrepancy, but would like to point out that the H + O_2 reaction is an unusual one, in that the HO_2 intermediate is a stable species. If, in the lower temperature end of our range, the chemical mechanisms of reactions 3 and 5 are similar, so that reaction 3 involves a long-lived complex, then an unusual isotope effect could result.

It seems that in spite of our precautions there were some H atom-producing impurities that initiated H_2 and D_2 oxidation. This is probably the reason why our estimates of k_1, listed in Table 1, are erratic, as shown in Figure 5. Calculations show that even unmeasurably low concentrations of H would cause substantial changes in the initiation rate. The effect would be to increase the absolute levels of [H] and [D], and hence the apparent values of k_1 and k_{1D}, but make very little difference in the slope, d ln [H]/dt. If this is so, then the dashed line of Figure 5, which has the equation k = 5.4E12 exp(-171kJ/RT) $mole^{-1}$ cm^3 s^{-1}, represents an upper limit for the rate constant for reaction 1. The solid line is Jachimowski and Houghton's expression which we quoted in Table 1. The data of Table 3, therefore, typically produce calculated curves of [H] or [D] versus time which, when plotted on a logarithmic scale, are parallel to the experimental curves, but displaced downward, as in Figure 2. From the deuterium data our upper limit for k_{1D} is 4.0E12 exp(-154kJ/RT) $mole^{-1}$ cm^3 s^{-1}.

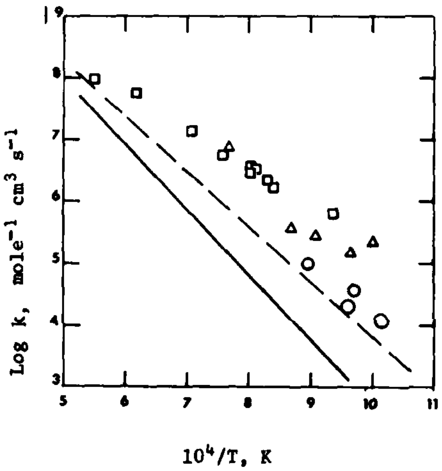

Figure 5.

Rate constants for $H_2 + O_2 \rightarrow 2\ OH$ calculated from experimental data. O, 5% H_2, 2.5% O_2; Δ, 1% H_2, 0.5% O_2; □, 0.1% H_2, 0.05% O_2; ——, equation of Jachimowski and Houghton[4]; - - -, upper limit deduced as described in text.

For the CD_4 - O_2 calculations we used earlier data as far as possible. The seven reactions considered are listed in Table 4. Modeling showed that at these low concentrations combination of CH_3 radicals would not occur to a significant extent, and other C_2 molecules would not tend to form. Rate constants for reactions 6D and 7D of Table 4 were determined by Lyman-α spectroscopy in our laboratory. They are in good agreement with Roth and Just's data[7] when isotope effects are calculated using RRKM and Activated Complex Theory methods. Rate coefficients for reaction 3D were transferred directly from Table 3 to Table 4. Reactions 8D and 9D are important, but they are relatively fast and the rate of appearance of D is not sensitive to their rate constants. We have used recent literature values, adjusted by a factor of 0.6 for the isotope effect for a simple H atom transfer in the 1700-2200 K range.

Table 4. Kinetic Data for CD_4-O_2 Reaction

	Reaction	Arrhenius Parameters		Reference
		A*	E,kJ	
6D.	$CD_4 + Ar \rightarrow CD_3 + D + Ar$	5.4E15	336	14
7D.	$D + CD_4 \rightarrow D_2 + CD_3$	2.1E15	93	14
3D.	$D + O_2 \rightarrow OD + O$	1.6E14	63	this work
8D.	$O + CD_4 \rightarrow OD + CD_3$	2.4E14	58	15**
9D.	$OD + CD_4 \rightarrow D_2O + CD_3$	5.2E13	32	16***
10D.	$CD_3 + O_2 \rightarrow DCDO + OD$	6.8E11	38	this work
11D.	$DCDO + Ar \rightarrow 2D + CO + Ar$	4.5E16	301	this work

Table 4 cont.

*Units of mole^{-1} cm^3 s^{-1}

**An isotope effect of 0.6 has been assumed

***This is not the equation recommended by the authors, since their data were below 1000 K. Our rate coefficients are an extrapolation of theirs to the 1700-2200 K range, taking into consideration higher temperature data which they discuss in their paper, and also assuming an isotope effect of 0.6.

Rate coefficients for reactions 10D and 11D have been given for hydrogen analogs by Olson and Gardiner[6], $k_{10} = 6.9E12 \exp(-38kJ/RT)$ mole^{-1} cm^3 s^{-1}, and by Schecker and Jost[17], $k_{11} = 5.0E16 \exp(-301\ kJ/RT)$ mole^{-1} cm^3 s^{-1}.

We have written reaction 11D as a global reaction involving first dissociation to formyl radical and then dissociation of the radical. At our low concentrations and relatively high temperatures, all formyl radicals will rapidly dissociate to D + CO, so that each formaldehyde dissociation leads to two D atoms.

With these rate coefficients as the only variables in the modeling, we found the best agreement with our experimental [D] measurements with coefficients only slightly less (Table 4) than those above for H reactions. Reduction by a factor of 0.5 led to low [D] values for the 50/1000 mixtures, although the difference was not much more than the experimental scatter. We conclude that reactions 10D and 11D are important in the reaction, since no other process we can think of would lead to the D concentrations we found for the 50/1000 mixtures, and we consider that our data are consistent with the values of Olson and Gardiner and of Schecker and Jost, provided the isotope effects are 0.5 or more. This would be expected for formaldehyde dissociation in this range, but the mechanism of the $CH_3 + O_2$ reaction is too uncertain to estimate an isotope effect.

We have examined the effects of the various elementary reactions on the overall production of D atoms for each reaction mixture. For the 20/40 and 100/200 mixtures pyrolysis is the main reaction occurring. Setting some or all of the other rate constants to zero makes changes of less than 10% in D concentration. If the rate constant for reaction 3D is increased to that of reaction 3, that is, assuming no isotope effect, the calculated D concentration drops due to greater loss of atoms by that reaction as shown in Figure 3. Our data for the 100/200 mixture can be correlated somewhat better with the value we quote for reaction 3D than for that for reaction 3.

For the 50/2000 mixture, reactions 3 and 8-11 have a greater effect, as shown by the calculated curves of Figure 4. The D concentration does not level off as it does in pyrolysis or with low O_2 concentrations, but rises, apparently due to the effect of reactions 10 and 11, which produce D atoms from CD_3. The data cannot be well modeled with the rate constant for reaction 3 in place of that for reaction 3D. We conclude, therefore, that the CD_4 data tend to confirm our large kinetic isotope effect for reaction 3.

ACKNOWLEDGEMENTS

This research was supported by the United States Department of Energy under Contract EY-76-S-02-2944. The authors wish to thank Mr. Scot Pencil for assistance with some of the experimental work, calculations and figures.

REFERENCES

1. A.L. Myerson and W.S. Watt, J. Chem. Phys., 49, 425(1968).
2. D. Appel and J.P. Appleton, Symposium (Int.) on Combustion, 15, 701(1975).
3. G.L. Schott and J.L. Kinsey, J. Chem. Phys., 29, 1177(1958).
4. C.J. Jachimowski and W.M. Houghton, Comb. Flame, 17, 25(1971).
5. D.B. Olson and W.C. Gardiner, Jr., J. Phys. Chem., 81, 2414(1977).
6. D.B. Olson and W.C. Gardiner, Jr., Comb. Flame, 32, 151(1978).
7. P. Roth and T. Just, Ber. Buns. Ges. Phys. Chem., 79, 682(1975).
8. C.-C. Chiang, A. Lifshitz, G.B. Skinner and D.R. Wood, J. Chem. Phys., 70, 5614 (1979).
9. W.C. Gardiner, W.G. Mallard, M. Morinaga, J.H. Owen, W.T. Rawlins, T. Takeyama and B.F. Walker, Symposium (Int.) on Combustion 14, 61(1973).
10. G.L. Schott, R.W. Getzinger and W.A. Seitz, Int. J. Chem. Kinet., 6, 921 (1974).
11. D.L. Baulch, D.D. Drysdale, D.G. Horne and A.C. Lloyd, Evaluated Kinetic Data for High Temperature Reactions. Volume 1. Homogeneous gas phase reactions of the H_2-O_2 system. CRC Press, Cleveland, Ohio, 1972.
12. G.L. Schott, Comb. Flame, 21, 357(1973).
13. S.C. Kurzius and M. Boudart, Comb. Flame, 12, 477(1968).
14. C.C. Chiang, J.A. Baker and G.B. Skinner, Paper presented at American Chemical Society National Meeting, Honolulu, Hawaii, 1979; to be published.
15. P. Roth and T. Just, Ber. Buns. Ges. Phys. Chem., 81, 572(1977).
16. R. Zellner and W. Steinert, Int. J. Chem. Kinet., 8, 397(1976).
17. H.C. Schecker and W. Jost, Ber. Buns. Ges. Phys. Chem., 73, 521(1969).

SHOCK WAVES IN INTERSTELLAR SPACE

MOSHE ELITZUR

Astronomy Department, University of Illinois, Urbana, IL 61801, USA
and Physics Department, Weizmann Institute, Rehovot, Israel

Some mechanisms which lead to the formation of shock waves in interstellar clouds and the effects of their propagation are presented.

INTRODUCTION

The space between stars (the interstellar medium) has two components to it: a rarefied (densities ~ 1 cm^{-3}) hot medium and denser clouds (densities in the range of $\sim 10^2$-10^6 cm^{-3}). The clouds are quite cold with temperatures which are typically below 100°K and the speed of sound in a cloud is therefore only of order 0.5 km/sec. At the same time, motions of order a few km/sec are quite common and manifest themselves in the doppler shifts of molecular lines. Shock waves should therefore be a common phenomenon in interstellar clouds. Since the conditions behind shock fronts are very different from those which exist elsewhere in the clouds (in particular, the temperatures are much higher), the propagation of a shock should lead to observable effects. Some of these effects and mechanisms which lead to shock production in interstellar clouds are presented here.

SHOCK FORMATION MECHANISMS

HII Regions[1]

Young and massive stars (masses about 30 times the mass of the sun) have high surface temperatures, in the range of 20,000-50,000°K. Their radiation is thus capable of fully ionizing the surrounding gas and producing a sphere of ionized hydrogen, known as an "HII Region" (the term HII corresponds to ionized hydrogen which contributes two free particles to the gas). The radius r_s of the HII region is determined from the global equilibrium between the number of ionizations and recombinations, namely

$$\frac{4\pi}{3} r_s^3 n_H^2 \alpha = S \qquad \text{I}$$

where n_H is the density, α is the recombination coefficient and S is the number of ionizing ultraviolet photons emitted per second by the star. Typical radii obtained are of order

$$r_s \simeq 10^{20}/n_H^{2/3} \text{ cm} \qquad \text{II}$$

where n_H is typically in the range 10^2-10^6 cm^{-3}. For comparison - the earth distance from the sun is of order 10^{13}cm.

Since the mean free path of an ionizing photon is very large in the fully ionized gas and very small in the neutral gas, the transition between the two phases is sharp. The HII region radio emission which results from electron-ion recombinations and from free-free processes is detected with the aid of radio telescopes.

The photoionization heats up the material and the equilibrium temperature of the HII region is typically $\sim 10^4$ °K, compared with temperatures of $\lesssim 100$°K in the surrounding medium. Since the density in the two regions is roughly the same, a pressure jump of two orders of magnitude exists across the ionization front. The HII region will therefore begin to expand at a velocity which is characterised by the speed of sound in the ionized matter and super-sonic with regard to the surrounding medium. A shock wave will develop, in exact analogy to a shock tube.

As the HII region is expanding, its density decreases and r_s increases (eq. I). The ionization front is therefore moving outward and acts as a spherical piston which keeps pushing the shock, as long as the pressure inside the HII region exceeds that in the ambient gas. The surface structure of HII region in steady state expansion (which may last a few million years) is that of an ionization front preceded by a shock front which are moving together at a velocity of about 10 km/sec. In between them there is a shell of compressed material at a high density, due to the cooling (at approximately constant pressure) from the high post-shock temperature.

Stars are formed many times in associations and a group of young and bright stars may form together. Their combined radiation leads to the formation of very big ionization fronts which eat their way into clouds and push ahead of them large shock waves with typical dimensions of about 10^{20} cm.

Supernova Explosion

Stars maintain hydrostatic equilibrium during the main phase of their life-time by counteracting the pull of self gravity with thermal pressure. The thermal energy is supplied by thermo-nuclear reactions. When the nuclear fuel is exhausted, the gravitational pull leads to a collapse and a supernova explosion with the release of about 10^{51} ergs. A supernova shell is expanding with an initial velocity of order 1000 km/sec, typically. The shell can expand by many orders of magnitude before it is dissipated by the pressure of the interstellar medium and by radiative losses. In fact, the shell life-time is long enough that with the currently accepted rate of a supernova explosion in the galaxy every 50 years, approximately, the shells run into each other and may fill the entire galaxy. A three-component picture for the interstellar medium has therefore been advocated recently[2,3]. It involves the clouds, the intercloud medium and the supernova remnants which run into both. It is thus claimed that most interstellar clouds will contain at least one shock of modest strength (velocity of a few km/sec) at any time[4].

Mass Motions

Mass motions of a few km/sec are widespread in interstellar clouds. The cause for the motions is not always clear and the entire subject of cloud collapse and the role of turbulence is not yet well understood. Most numerical calculations of collapse, which are not too sophisticated at this stage, lead to supersonic velocities and the formation of a standing shock at a distance of 10^{15}-10^{16}cm from the center of the collapse.

SHOCK MANIFESTATIONS

The first suggestion for a specific manifestation of a shock in an interstellar cloud was made by Kwan and Scoville[5]. They observed radio line emission of the CO molecule from the Orion Nebula (a dense molecular cloud) and noticed that the frequency (or equivalent velocity) profile had a narrow core ($\Delta V \sim 1$ km/sec) and very broad wings ($\Delta V \sim 50$ km/sec). They suggested that the broad component was due to a spherical shock wave expanding around an active part of the nebula. This proposal received quick support from the detection of H_2 vibration emission in Orion[6] which can be convincingly interpreted as due to shock excitation[7-9] since the required temperature is much higher than that which exists elsewhere in the cloud.

Another manifestation of the same shock comes from molecular abundancies. The abundance of certain species in the hot post shock gas is quite different from that in the cold cloud phase. Observationally, the SiO molecule shows a regular abundance in the narrow core component of the Orion Nebula and a significant enhancement in the broad component. Since it can be shown that SiO production is greatly enhanced behind interstellar shocks, this lends support to the picture of the shock in Orion[10].

Another molecule whose abundance is greatly enhanced behind shocks in dense clouds is H_2O [11]. Not surprisingly, a high H_2O abundance has been detected in Orion[12].

When H_2O is produced behind the shock interface of an HII region, the strong UV flux of the bright star will photodissociate the H_2O and lead to a high OH abundance. The OH lives long enough to provide an explanation for the OH maser emission which is detected in the direction of compact HII regions[13].

Shock waves may also provide an explanation for what has been the longest standing problem in interstellar chemistry - the CH^+ abundance. All the steady state calculations which tried to explain the observed abundance of CH^+ in clouds fell short by about two orders of magnitude. Due to the low temperatures in clouds, the chemical schemes always considered only reactions which are either exothermic or have no activation energy at all. The reaction

$$C^+ + H_2 \rightarrow CH^+ + H \qquad (1)$$

which is endothermic by 0.4 ev was thus left out. However, the reaction does proceed behind shock fronts which run into diffuse clouds and the amount of CH^+ produced this way is sufficient to explain the observations[14,15]. If the CH^+ is indeed produced in the narrow hot component behind the shock, the doppler velocity of its lines should be shifted from those of other molecules which are abundant in the bulk of the large, cool component. Such a velocity shift has been known to exist for some time[16] and its explanation was thus an immediate and natural consequence of the shock model. In addition, the shock explanation can work only if the shock runs into material which has its density above a certain value which allows for molecule formation. The shock therefore defines three velocity components which should be observable in molecular line emission: a cool pre-shock gas, a hot immediate post-shock and a cool distant post-shock gas. All three have now been identified in the direction of Zeta Ophiuchi (a star which shows a high CH^+ abundance) and the separations between the components are of the sense and size which are predicted by the shock model[17].

It is evident that phenomena behind shock fronts are becoming an important subject in the study of interstellar clouds. Since it is quite certain that various stages of star formation are associated with shock fronts, the significance of interstellar shocks is likely to increase even further

REFERENCES

1. L. Spitzer, Physical Processes in the Interstellar Medium, New York: Wiley (1978).
2. D.P. Cox and B.W. Smith, Ap. J. *189*, L105 (1974).
3. C.F. McKee and J.P. Ostriker, Ap. J. *218*, 148 (1977).
4. D.P. Cox, Ap. J. (in press).
5. J. Kwan and N.Z. Scoville, Ap. J. Lett. *210*, L39 (1976).
6. T.N. Gautier, U. Fink, R.P. Treffers and H.P. Larson, Ap. J. Lett. *207*, L129 (1976).
7. D.J. Hollenbach and J.M. Shull, Ap. J. *216*, 419 (1977).
8. J. Kwan, Ap. J. *216*, 713 (1977).
9. R. London, R. McCray and S.I. Chu, Ap. J. *217*, 442 (1977).
10. C.J. Lada, M. Oppenheimer and T.W. Hartquist, Ap. J. Lett. *226*, L153 (1978).
11. M. Elitzur, Ap. J. *229*, 560 (1979).
12. T.G. Phillips, N.Z. Scoville, J. Kwan, P.J. Huggins and P.G. Wannier, Ap. J. Lett. *222*, L59 (1978).
13. M. Elitzur and T. de Jong, Astr. Ap. *67*, 323 (1978).
14. M. Elitzur and W.D. Watson, Ap. J. Lett. *222*, L141 (1978).
15. M. Elitzur and W.D. Watson, Ap. J. (submitted).
16. F.H. Chaffee, Ap. J. *199*, 379 (1975).
17. R.M. Crutcher, Ap. J. Lett. (in press).

This work was supported by NSF grant AST-7823648.

CO GASDYNAMIC LASER MEASUREMENTS IN A SHOCK TUNNEL

MICHAEL TILLEMAN*, JOSEF STRICKER and ALEXANDER BURCAT

Department of Aeronautical Engineering,
Technion — Israel Institute of Technology, Haifa, Israel

The small signal gain measurements of a CO gasdynamic shock tube driven laser (GDL) is presented in this work. The low signal TEM_{00} single frequency continuous wave laser beam is passed through the nozzle of a shock tunnel, and its intensity is amplified by the radiative properties of the $CO/N_2/Ar$ expanding mixture.

The various mixtures were brought to stagnation temperatures of 1850-3500°K and pressures of 17-50 atm which supplied the expanding gas for the measured amplification of the EDL's beam.

Maximum small signal gain normalized to the stagnation pressure is found between 2500-2800°K, and the highest values were obtained with a 10% CO / 90% Ar mixture (0.055% $cm^{-1}atm^{-1}$).

The experimental data were correlated with numerical calculations based on a model that describes the vibrational energy level population in the CO and N_2 molecules. Good agreement was obtained.

INTRODUCTION

A CO gasdynamic laser (GDL) was reported previously by McKenzie[1] and Watt[2] who measured the laser power output in a shock tunnel where the expansion of high enthalpy CO-N_2-Ar mixtures was used for power measurements. The result was a quasi cw laser radiation in the wavelength range of 4.8-5.4μ, originating from a multitude of partially inverted vibrational states of CO.

For a theoretical comparison of the GDL power measurements, McKenzie[1] computed the small signal gain in the expansion by a model based on the SSH theory,[3] and compared it with spectral laser power measurements. An improved numerical model was later reported by Center and Caledonia[4] and then by Zielinski,[5] and both based the calculations of the vibrational energy levels population exchange constants on the semi-classical theory[6] (long range collisions by classical treatment and short range collisions by quantum mechanics). Many of the vibra-

---

* In Partial fulfilment of a D.Sc. Thesis to be submitted to the Senate of the Technion - Israel Institute of Technology.

tional constants computed by Center et al.[4], and by Zielinski,[5] as well as the small signal gain and the laser power values were not compared to experimental data.

In the present study the small signal gain of CO-N_2-Ar mixtures was measured, following a rapid supersonic expansion, which, along with the modeling of the non-equilibrium flow, would yield insight into the GDL's mechanism in a way which was not possible with the former power measurements. Good agreement between the experimental data and computation was obtained.

EXPERIMENTAL

a. The Shock-Tube

An 8 cm ID shock tube ends with a thin Mylar diaphragm beyond which a convergent divergent nozzle of an axysimmetric configuration with a 20° angle opens into a 500 liter dump tank. Two optical paths are adjusted through the nozzle at A/A^* 1500 and 2500. Through the first optical path a CO laser beam from a CO electrical discharge laser (EDL) is passed through two KCl windows. The other optical path is equipped with two mirrors, one gold coated for maximum reflectivity and the other germanium coated with a 2% transmissivity in the 4.8-6μ range.

The first path is used for small signal gain amplification while the other is used for total power output. In both cases a gold-doped germanium IR detector is used, and the signals are recorded on 805 Biomation transient signal recorders. The optical arrangements and the detecting devices are shown schematically in Figure 1.

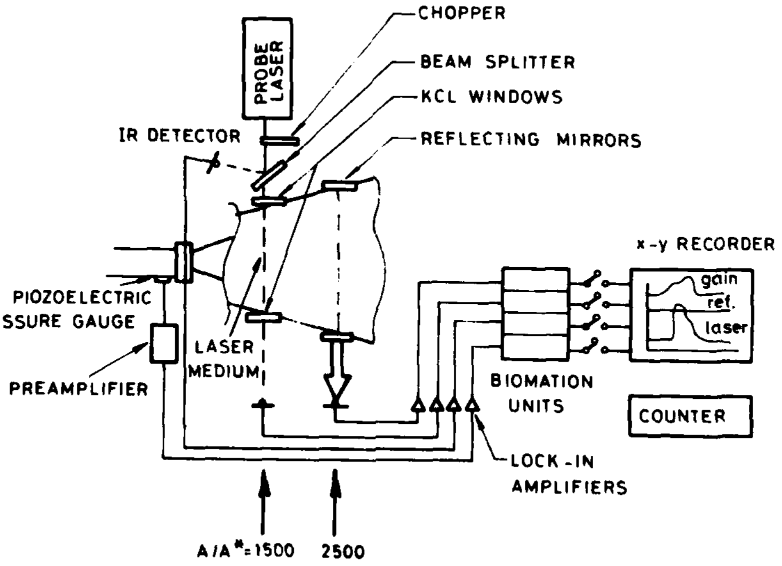

FIG. 1. The experimental set-up in the shock tunnel nozzle.

The incident shock speed in the shock tube is measured via two thin platinum films located 0.1 and 0.5 m from the end Mylar diaphragm. Their signal starts and stops a Beckman counter with ±1 μsec measuring capability. The stagnation pressure is measured with a calibrated Kistler 603A piezoelectric transducer and the measurement is compared with the calculated P_5 values obtained from the shock conservation equations. The agreement is within 2%. The stagnation temperature and all the other parameters (density ratio, etc.) are also calculated from the shock conservation equations.

The main diaphragm of the shock tube is a thin copper plate. The shock tube is evacuated, the driver to ~1 torr, the driven to $\sim10^{-5}$ torr and the dump tank together with the nozzle to 0.07 torr.

b. The CO Electrical Discharge Laser (EDL)

The EDL was built according to Brechignac et al.[7] A mixture of $CO/N_2/He$ with a relationship of 0.3/0.3/9 torr flows through a 1.8 cm pyrex tube immersed in liquid nitrogen. A voltage of 6 KV at 30 mA discharges between a cathode and two anodes 80 cm apart, produces a plasma in the slowly flowing CO mixture. A multiline laser power of 4 W is extracted from the cavity obtained along the discharge path in the pyrex tube. One of the cavity mirrors has a 100% reflectance and the other a 3% transmittance at about 5 μm. A TEM_{00} single line laser of 20-50 mW is obtained by replacing the flat reflecting mirror with a Bausch & Lomb replica difraction grating. The grating has 100 lines/mm blazed at 6 μm and is mounted on a rotating stand. An iris is placed between the 3% transmitting mirror and the tube's brewster window. The mirror is linearly adjusted by differential screws. The output beam stability of the EDL is within 4%.

The frequency used in the EDL was 5.0744 μm ($v=7\rightarrow6, P(3)$).

The probe beam when passed through the nozzle was of low intensity (less than 30 mW/cm^2) in order to avoid saturation effects.

c. Materials

The materials used for the experiments were C.P. Matheson CO 99.5% pure, I.B. Miller N_2 99.7% pure and Herzelia Gas Products Ar 99.5% pure. Airco pure helium served as driver gas. The only impurities were N_2 and O_2 in atmospheric proportions. Separate mixtures were made manometrically for each experiment in a tank and mixed with a hand stirrer. They were then introduced into the shock tube, building a driven pressure of ~1/4 atm.

Table 1 summarizes the mixtures used in this research.

TABLE 1. Composition of the mixtures used in the research.

#	CO	N_2	Ar	# of Shocks
1	5	0	95	4
2	10	0	90	5
3	5	15	80	11
4	8	24	68	8
5	10	30	60	11

CALCULATIONS

a. Vibrational Kinetics Theory

The flow of the expanding CO-N_2-Ar mixture from a high enthalpy stagnation chamber is described by nonlinear conservation equations together with rate equations of the population in a given vibrational level.

The latter represents the following vibrational energy transfer mechanism:

$$\mathrm{CO}(v) + \mathrm{M} \rightleftharpoons \mathrm{CO}(v-1) + \mathrm{M} + \Delta E_{\mathrm{VT}} \tag{1}$$

$$\mathrm{N_2}(v) + \mathrm{M} \rightleftharpoons \mathrm{N_2}(v-1) + \mathrm{M} + \Delta E_{\mathrm{VT}} \tag{2}$$

$$\mathrm{CO}(v) + \mathrm{CO}(n) \rightleftharpoons \mathrm{CO}(v\pm1) + \mathrm{CO}(n\mp1) \pm \Delta E_{\mathrm{VV}} \tag{3}$$

$$\mathrm{CO}(v) + \mathrm{N_2}(n) \rightleftharpoons \mathrm{CO}(v\pm1) + \mathrm{N_2}(n\mp1) \pm \Delta E_{\mathrm{VV}} \tag{4}$$

$$\mathrm{N_2}(v) + \mathrm{N_2}(n) \rightleftharpoons \mathrm{N_2}(v\pm1) + \mathrm{N_2}(n\mp1) \pm \Delta E_{\mathrm{VV}} \tag{5}$$

$$\mathrm{CO}(v) \rightleftharpoons \mathrm{CO}(v-s) + sh\nu \qquad s=1,2 \tag{6}$$

where v, n and s denote different vibrational levels of the molecules and M is any colliding molecule causing a V-T energy transfer. Reactions (1)-(2) are V-T collisions while reactions (3)-(5) are V-V energy transfer. If the vibrational level transfers are non-resonant then the energy difference ΔE_{VV} is contributed to the kinetic energy of the molecule. Typically $\Delta E_{\mathrm{VV}} \ll \Delta E_{\mathrm{VT}}$, the result is therefore that the V-T collisions are much less probable than the V-V and thus only a small amount of translational energy is added to the gas. Equation (6) represents the radiative transition which is significantly slower than the collisional, and is included here for the sake of completeness only. $s=1,2$ denotes the fundamental and overtone transitions.

The rate equations of a certain vibrational level population, due to the transition mechanism listed in Eqs.(1)-(6), can be expressed in the following way

$$\left(\frac{dN_n}{dt}\right)_{\mathrm{CO}} = \sum_{i=1}^{2}\left(\frac{dN_n}{dt}\right)_i^{\mathrm{V-V}} + \sum_{j=1}^{3}\left(\frac{dN_n}{dt}\right)_j^{\mathrm{V-T}} + \sum_{m=1}^{2} N_{n+m}a_{n+m,n} - \sum_{m=1}^{2} N_n a_{n,n-m} \tag{I}$$

where i and j denote CO, N_2 or Ar; N is the concentration of the molecules of each component (CO, N_2, Ar) and a is the Einstein spontaneous emission coefficient; $\sum_{i=1}^{2}\left(\frac{dN_n}{dt}\right)_i^{\mathrm{V-V}}$ denotes the net collision population rate contribution by CO and N_2 molecules to the n-th vibrational level of CO; $\sum_{j=1}^{3}\left(\frac{dN_n}{dt}\right)_j^{\mathrm{V-T}}$ is the V-T collision contribution of all molecules, i.e., CO, N_2 and Ar; the third and the fourth members in the Eq.(I) are the spontaneous decay expressions for populating and depopulating the CO n-th level.

The equation for the N_2 molecule can be expressed similarly to the CO molecule except that the spontaneous decay expressions are deleted because N_2 is a homonuclear molecule and has a zero dipole moment.

The detailed rate time expression is

$$\left(\frac{dN_n}{dt}\right)_i^{\text{V-V}} = \left[P_{v+1,v_i}^{n,n+1_{\text{CO}}} N_{v+1}^i N_n^{\text{CO}} + P_{v,v+1_i}^{n+1,n_{\text{CO}}} N_v^i N_{n+1}^{\text{CO}} - \right.$$

$$\left. - P_{v,v+1_i}^{n,n-1_{\text{CO}}} N_v^i N_n^{\text{CO}} + P_{v+1,v_i}^{n-1,n_{\text{CO}}} N_{v+1}^i N_{n-1}^{\text{CO}} \right] Z_{\text{CO-}i} \qquad \text{(II)}$$

where the index i denotes the colliding partner of either CO or N_2, P is the transition probability and $Z_{\text{CO-}i}$ is the collision frequency at unit density. The V-T rate is

$$\left(\frac{dN_n}{dt}\right)_j^{\text{V-T}} = \left[P_{n+1,n}^{\text{CO-}j} \left(N_{n+1} - N_n \exp(-h\nu/kT) \right) N^j - \right.$$

$$\left. - P_{n,n-1}^{\text{CO-}j} \left(N_n - N_{n-1} \exp(-h\nu/kT) \right) N^j \right] Z_{\text{CO-}j} \qquad \text{(III)}$$

where ν is the transition frequency. Hence the complete vibrational state of the gas is determined by employing an equation of the form of (I) for each vibration level of CO and N_2, resulting in a coupled set of rate conservation equations.

A major problem is the evaluation of the transition probabilities for the calculation of the density rates. Early works in the field[8] used the Landau-Teller model[9] which is based on a harmonic vibrational energy structure relaxation towards equilibrium through V-T collisions and the V-T transition probability being proportional to the molecule's quantum number. This model predicted satisfactorily experimental data for low quantum numbers but failed where the V-V mechanism became significant.

A model presented by Treanor et al.[10] showed the deviation of an anharmonic molecule's behavior from the harmonic model. This model uses the V-V mechanism and neglects the V-T and radiative effects. Accordingly the molecule's population obtains a non-Boltzman vibrational distribution.

McKenzie[1] used in his model V-V and V-T probability values calculated by the SSH theory, which is based on the usual assumption of an harmonic oscillator repulsive potential and a one dimensional collisional model. This model is adequate for low vibrational levels but not for the high ones. The calculations were not referred to any experimental data.

Zielinski[5] correlated some of his computed parameters to data obtained by Hancock and Smith.[11]

The present study uses the last model of long range and short range interactions with correlation to available experimental results. In this manner the V-V transition probabilities were compared as follows: CO-CO[11, 12]; CO-N_2[13, 14]; and the V-T probabilities; CO-CO[15]; N_2-N_2[15, 16]; CO-N_2[17]; N_2-CO[16]; CO-Ar[15].

Following the rapid temperature decrease, the V-V transition probabilities are exceeding the V-T by several orders of magnitude at the lower vibrational levels. Since the spacing between the upper levels decreases, transferring molecules into the upper levels requires transferring some vibrational energy to translation, and hence the V-V pumping occurs. The pumping to high levels is limited by the V-T mechanism which is fast enough at the high levels.

The described process results in a non-Boltzman distribution predicted by the earlier investigators[1, 4, 10] and is shown in Figure 2. Figure 2 represents the normalized population with respect to the zero level concentration distribution for three of our mixtures calculated for the experimental conditions encountered in our study.

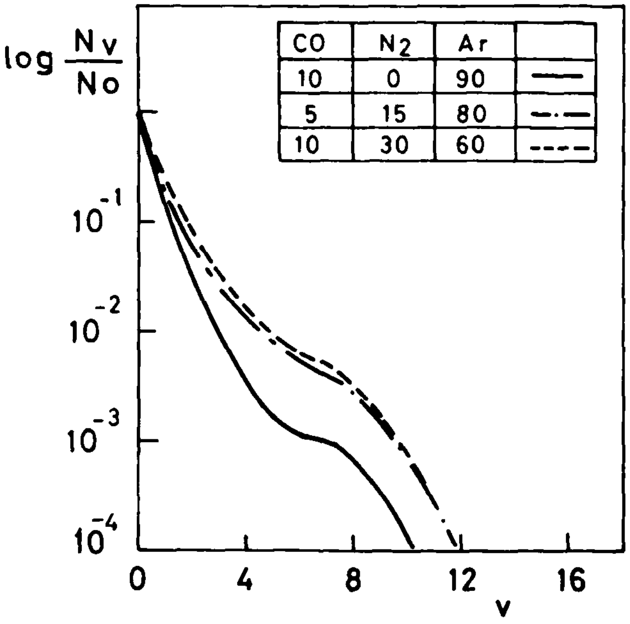

FIG. 2. Calculated results at $A/A^* = 1500$, $T_0 = 2500°K$ and $P_0 = 30$ atm of the population distribution for different vibrational levels for three of the mixtures investigated.

b. The Numerical Model

The numerical model that was translated to a computer algorithm consists of a set of simultaneous equations which include the following gasdynamic nonlinear conservation equations:

$\frac{d}{dx}(\rho A u) = 0$ continuity equation (IV)

$\rho u \frac{du}{dx} = -\frac{dp}{dx}$ momentum equation (V)

$\frac{d}{dx}\left[\frac{7}{2} RT(X_{CO}+X_{N_2}) + \frac{5}{2} RT X_{Ar} + M \frac{u^2}{2} + E_v\right] = 0$ energy equation (VI)

$P = \rho RT$ equation of state (VII)

where X is the mole percent of the species, M is the average molecular weight of the mixture, E_v is the vibrational energy in the system, u is the velocity of the gas, and A is the flow cross section area in the nozzle.

To these equations the density rate equations of the participating species, i.e., the various vibrational level populations of CO and N_2 were added. The rotational levels population distribution is assumed to be in equilibrium with the translational temperature.

The vibrational structure of CO contains about 75 levels, but the redistribution of energy in the expansion flow leaves all levels above 20 with a negligible population. Therefore only the first 20 CO vibrational levels were taken into consideration and 18 of N_2, resulting in a total of 39 rate equations. The system of equations was integrated with the conditions occurring in the expansion nozzle (by the Adams predictor corrector technique[18]), for the mixtures mentioned in Table 1, stagnation temperatures of 1850-3500°K and pressures of 17-30 atm.

The momentum transfer was described by the Euler equation which excludes the boundary layer from the vibrationally excited gas. As already mentioned typical results of the population distribution where the small signal gain was measured are presented in Fig. 2.

The transition broadening between the vibration rotation levels that may obtain a Doppler and a Lorentz shape must also be taken into account. Since the dominant line shape is formed by the values of static pressure and temperature that vary with the parameters, a general shape was chosen according to

$$g(0) = \frac{4}{4\Delta\nu_c}\chi \exp \chi^2 \int_t^{\infty} \exp(-\xi^2)d\xi \qquad \text{(VIII)}$$

where $\chi = [\Delta\nu_c/(\ln 2)^{\frac{1}{2}}]/\Delta\nu_D$, $\Delta\nu_c$ and $\Delta\nu_D$ are the full half widths associated with the collision broadening (Lorentz) and Doppler broadening, respectively.

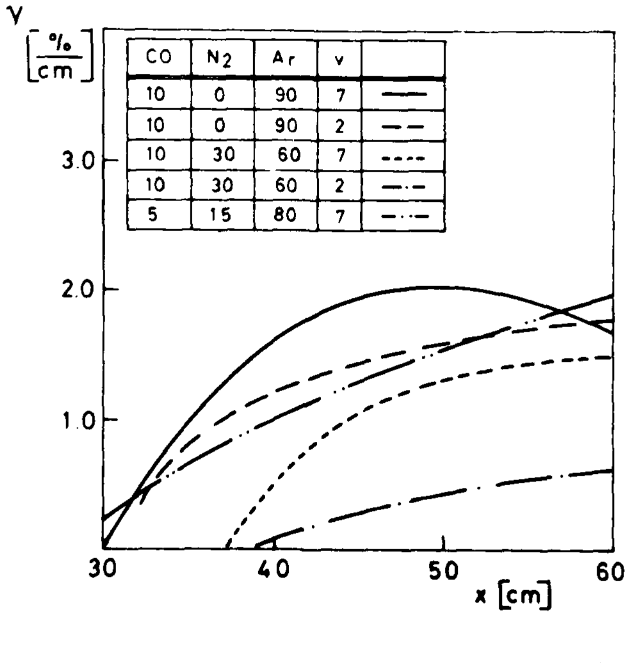

FIG. 3. Calculated small signal gain values γ vs the downstream distance in the nozzle for several transitions showing optima at different points. T_0 = 2500°K, P_0 = 30 atm.

Figure 3 presents the changes of the small signal gain values of several transitions with the downstream distance, showing optima at different points for different transitions.

RESULTS

Before starting an experiment the EDL probe is turned on at the chosen frequency. Only some of the EDL's available frequencies are mutual with the GDL due to different CO vibrational distribution and translation temperature. A frequency of the GDL that was predicted to amplify efficiently the probe laser beam was found to be 5.0744 μm ($v=7 \rightarrow 6, P(3)$).

The small signal gain was determined according to

$$\gamma_0 = \frac{1}{L}\left(\ln \frac{V_{signal}}{V_{ref}}\right) = \frac{1}{L}\left(\ln \frac{I_2}{I_1}\right) \qquad \text{(IX)}$$

where V_{signal} and V_{ref} are the measured and reference voltages obtained from the detectors, and I_1 and I_2 are the reference and amplified laser beam intensities. The maximum error of the small signal gain measurement was ± 10%.

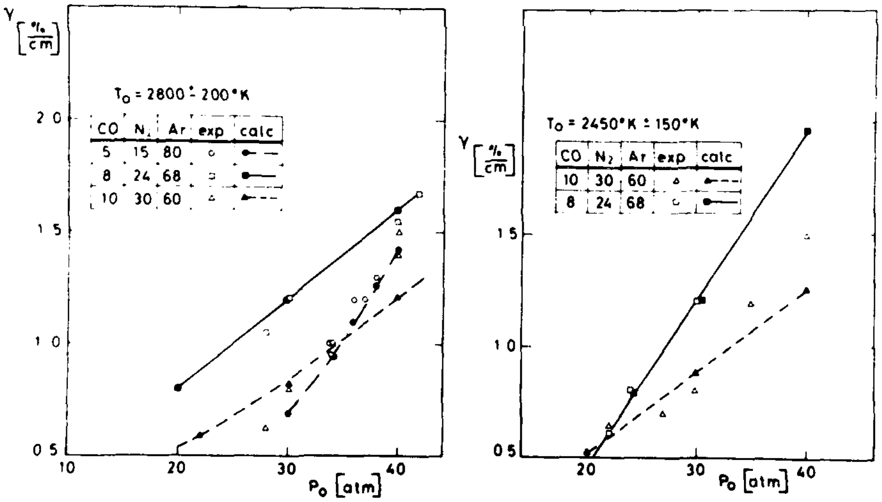

FIG. 4. Small signal gain of measured and calculated points (open and black symbols) vs the stagnation pressure for two stagnation temperatures.

Figure 4 represents a plot of the small signal gain vs the stagnation pressure at the stagnation temperature of 2800 ± 200°K and 2450 ± 150°K. This shows the small signal gain to change with the stagnation pressure by a power slightly greater than 1. It served as a justification to normalize the small signal gain by the stagnation pressure.

Figure 5 represents the small signal gain measurements, normalized by the stagnation pressure vs the stagnation temperature. On the same figure the computed values are also presented: the computed points are represented by

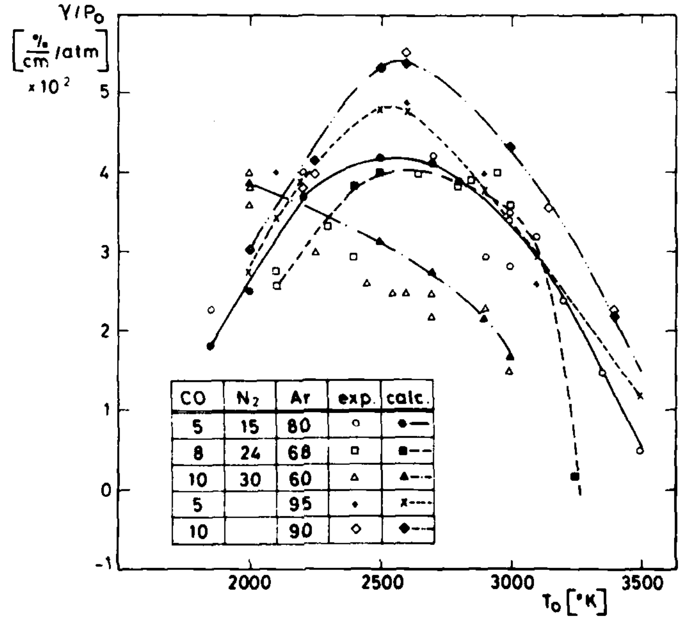

FIG. 5. Small signal gain measurements and calculations normalized by the stagnation pressure vs the stagnation temperature.

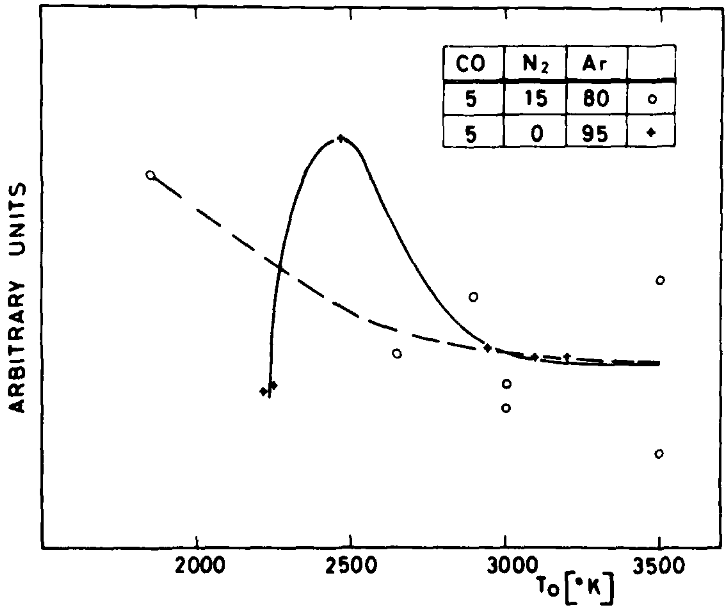

FIG. 6. Total output lasing power vs stagnation temperature, measured at $A/A^* = 2500$.

black symbols and the experimental ones by open symbols. The maxima of all the mixtures except #5 are around 2600°K.

Figure 6 represents total output lasing power. These values were taken as qualitative references and no effort was made to get the maximum output available by using better output coupling and better mirror quality. Thus these values were only a third of the output measured by McKenzie[1] and cannot be compared on the same scale.

DISCUSSION AND CONCLUSIONS

In Figure 5 the maxima of all mixtures are around 2600°K except mixture #5. This one has a maxima below 2000°K and in our temperature range we get only its shoulder. All experimental results are backed up by computer simulations which show a very good agreement. The shifted maxima of mixture #5 is explained by the relatively large amount of light diatomic molecules (40%) and the relatively small amount (only 60%) of heavy monoatomic species (Ar). The presence of a diatomic molecule in the expansion results in a slower cooling of the gas mixture. Henceforth, an increase in the amount of diatomic molecules is followed by an increase in the downstream temperature. The latter exerts negative influence on the small signal gain by moving the optimal rotation-vibration transfer band to higher rotation levels (thus decreasing the partial population inversion) and by forming a wider doppler broadening, i.e., decreasing the shape function.

During the high temperature period the V-T relaxation mechanism is very effective since the V-T diatomic-diatomic collisions are faster than the diatomic-Ar collisions. If the amount of Ar atoms is reduced, a faster relaxation of the CO molecules to their equilibrium state is caused, increasing the translational temperature. The other compositions where the CO does not relax so fast, because the amount of Ar is greater, will encounter the same process later on when the stagnation temperature passes the 2900°K range.

CO is known to decompose above 3000°K but apparently not to a high extent since the agreement between calculated and experimental points appears to be very good although no decomposition processes were accounted for in the kinetic mechanism.

The mixtures including N_2 show a lesser agreement than the other and this amounts up to a 15% difference, as seen in Figures 4 and 5. A probable source of error is the V-V transition probabilities in the N_2-N_2 collisions where no experimental data are available and thus the calculated values could not be checked. Unfortunately, the vibrational population distribution is very sensitive to V-V transition probabilities.

The total power measurements were made for qualitative purposes, since it can be shown that it is very difficult to match a multiline power measurement to a theoretical model. The three main assumptions on which these calculations are based (a - full cavity radiation; b - known diffraction losses and no mirror imperfections; c - no boundary layer losses) are not matched by experimental reality. Hence our investigation is a first attempt to measure directly the small signal gain and show by the good agreement the validity of the model.

The following conclusions should be mentioned:

a. Under the experimental conditions mentioned, the optimal stagnation temperature was found to be 2600°K.

b. The results were found to have a linear dependency on stagnation pressure.

c. N_2 has a contradictory influence on the CO GDL. On one hand it facilitates the CO population inversion as seen in Figure 2, and on the other hand it increases the static temperature. Thus, as seen in Figure 5, it is not essential to include nitrogen in the expanding mixtures.

d. The rapid small signal gain decrease after 2600°K is due to the increase of the static temperature and the increase of the V-T transfer probabilities.

e. The CO decomposition in the experimental temperature range is negligible and has no effect on the lasing properties.

f. The sensitivity of the calculated values on the rate constants is very high. Therefore the knowledge of the rate constants is essential.

g. The system is sensitive to H_2 and H_2O impurities only. N_2 and especially O_2 impurities are not harmful and may even be helpful.

ACKNOWLEDGEMENTS

The authors would like to thank Mr. E. Verdnikov for his devoted technical assistance and to Dr. H. Keren from the Hebrew University of Jerusalem for his guidance on the EDL CO construction.

REFERENCES

1. R. McKenzie, 5 μm Laser Radiation from a Carbon Monoxide Gasdynamic Expansion, NASA TM X-62,006 (1970).
2. W.S. Watt, *App. Phys. Lett.*, *18* (1971), 487.
3. R.N. Schwartz, Z.I. Slawsky, K.F. Herzfeld, *J. Chem. Phys.*, *20* (1952), 1591.
4. R.E. Center, G.E. Caledonia, *App. Opt.*, *10* (1971), 1795.
5. A. Zielinsky, Continuous Wave Gasdynamic CO Laser, IMP PAN 10/889/77 (in Polish).
6. R.D. Sharma, C.A. Brau, *J. Chem. Phys.*, *50* (1969), 924.
7. P. Brechignac, J.P. Martin, G. Taieb, *IEEE J. Quant. Elec.*, *QE-10* (1974), 797.
8. N.G. Basov, V.G. Mikhaylov, A.N. Orayevsky, V.A. Shcheglov, *Soviet Phys.-Tech. Phys.*, *13* (1969), 1630.
9. L. Landau, E. Teller, *Z. Phys. Sov. Union*, *10* (1936), 34.
10. C.E. Treanor, J.W. Rich, R.G. Rehm, *J. Chem. Phys.*, *48* (1968), 1798.
11. G. Hancock, W.M. Smith, *App. Opt.*, *10* (1971), 1827.
12. R.L. Taylor, M. Camac, R.M. Reinberg, *11th Symp. Combust.* (1967), 1966.
13. Y. Sato, S. Tsuchiya, K. Kuratani, *J. Chem. Phys.*, *50* (1969), 1911.
14. W.H. Green, J.K. Hancock, *J. Chem. Phys.*, *59* (1973), 4326.
15. R.C. Millikan, D.R. White, *J. Chem. Phys.*, *39* (1963), 3209.
16. H.K. Sheen, *J. Chem. Phys.*, *60* (1974), 1064.
17. W.J. Hooker, R.C. Millikan, *J. Chem. Phys.*, *38* (1963), 214.
18. C.W. Gear, *Numerical Initial Value Problems in Ordinary Differential Equations*, Prentice-Hall Inc. (1971).

FLUID PROCESSES IN SUPERSONIC DIFFUSION LASERS

GEORGE W. BUTLER and DAVID A. RUSSELL

Aerospace and Energetics Research Program,
University of Washington, Seattle, Washington 98195, USA

The pressure distribution was measured downstream of two different screen nozzles in a combination shock-Ludwieg tube facility that mixes pure A or a 5% F_2/A oxidizer with H_2 fuel. A quasi 1-D coupled fluid-chemistry model is developed which is used to systematically isolate prominent fluid processes. Nozzle geometries, non ideal expansions, overall and relative entrainments, base entrainment, and base pressure are explored and reference conditions selected. With these choices the model was found to be in general agreement with the experimental results. It was then used to predict HF laser performance for a particular set of conditions. Significant fluid process sensitivity is predicted.

INTRODUCTION

The performance of high-energy continuous-wave lasers is fundamentally tied to fluid processes. This is particularly true for the chemical or supersonic diffusion laser where molecular mixing and reaction of two reagent streams creates population inversions in the product species. Supersonic flow produces a high non-equilibrium mass flux, limits the upstream extent of the exothermic reaction, provides necessary cooling for gain, and rapidly removes the deactivated reaction product. Normally,only the first stages of the mixing layers are useful, since deactivation by the spent reaction product soon competes with excited state production. Thus, multi-nozzle arrays are used with small scale fuel and oxidizer expansions. These are in many cases interconnected by substantial base regions.

The first models of the successful HF supersonic laser assumed that the reagents were premixed to a constant fluid state before chemistry began.[1] An improvement accounted for the heat release as the reactions progressed, thereby modifying the fluid state and the reaction rates. More sophisticated models followed, in which the premixed assumption was replaced by "flame sheet" or "scheduled mixing" assumptions.[2,3] These introduce, in effect, an axial fluid mixing scale.

The details of the mixing process are important: the layers are unstable and transitional, taking distances of at least 300 nozzle-exit boundary layer momentum-thicknesses to become fully turbulent (i.e., Ref. 1). Trips have been tried to hasten the transition, and inert gas injection or large base regions used to delay reagent mixing until the turbulent state had been attained. Small nozzles produce relatively thick boundary layers, and simple large-angle wedge or conical expansions are often used for both ease of construction and loss minimization.[4]

The simple expansions produce a recurring wave pattern downstream as each flow is turned and confined to a channel by its neighbors. An entropy field is created through which the gas is processed.[5] As the adjacent streams come together in the mixing region and react, local heating causes a displacement effect which also creates waves. These "reaction shocks"[6] change the properties of the incoming streams and the subsequent reaction rates in the mixing layer. Such coupling effects can be substantial. Indeed, HF laser performance is limited by ability to convect heat away, and both oxidizer diluent and excess fuel are used to insure that the cavity does not choke. Some progress has now been made in full Navier-Stokes modeling of HF laser nozzle pairs with turbulence and coupled chemistry. However, in view of the complication of the process there is much to be done with simpler models guided by experiment. This is the approach taken here. Experiments are first described, followed by development of a new quasi 1-D model, comparison of it with experiments, and predictions of HF laser sensitivity to fluid processes.

EXPERIMENTS

Facility and Operating Conditions

Figure 1 shows the shock-Ludwieg tube facility constructed for the present study. The oxidizer gas is shock heated in the 5x20x75C cm driven tube. Reflection of this shock ruptures a thin Al diaphragm and the partially dissociated gas expands through alternate nozzle columns in the screen nozzle to a

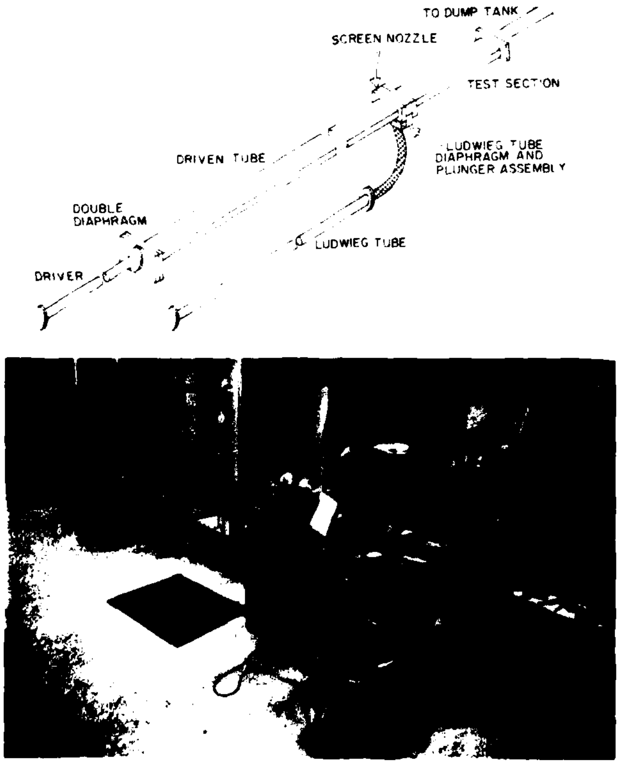

Figure 1.
Shock-Ludwieg Tube Facility

5x20x100 cm long test section. Unheated fuel is simultaneously supplied to the companion nozzle columns from the 7.5 i.d.x600 cm Ludwieg tube. Timing is accomplished by using a double diaphragm to start the shock tube and an electronically delayed, solenoid operated cutter to break a Mylar diaphragm in the Ludwieg tube. The supersonic fuel and oxidizer streams mix and react downstream of the nozzle and exit to a 2.5 m^3 dump tank. The test section top and bottom walls are diverged at ¼° to compensate for turbulent boundary layer growth, and various viewing windows and pressure ports fitted.

5% F_2 in A was used as the oxidizer. While no direct check of F_2 content was available, runs with 3 separately ordered bottles showed no mixture trends over a two-year period. The facility was carefully passivated to insure against F_2 depletion to the walls. During a run, the oxidizer was shock heated to a nominal 2.5 atm and 1000° K (15% dissociated) with an N_2 driver. The incident shock wave speed and reflected shock pressure (P_5) were used with equilibrium calculations to obtain specific conditions. Use of the A diluent enhanced the test time, made driving easier, and led to cavity mixing losses comparable to those brought about by chemistry. Comparison runs were made with the F_2 removed in order to study this process and check for the effects of reaction. Pure unheated H_2 was used in the Ludwieg tube with measured upstream P_0 values ranging from 4.5 to 1.5 atm. Corresponding fuel to oxidizer nozzle-exit static pressure rations (P_{H_2}/P_F) were calculated to be 3.04 to 1.06. The first Ludwieg tube pressure step of 10 msec was set to encompass the 5 msec of shock tube test time.

Two mixing screen nozzles were used, both involving supersonic expansion through a conical half angle (α_n) of 10° with exit dimension (d) of 0.5 cm and area ratio of 10. Conical subsonic relief left throats one throat-diameter long. The ten oxidizer expansions in each column are fed directly by the shock tube, whereas the nine fuel expansions in each adjacent column are connected through a manifold to the Ludwieg tube. In the small base case the expansions were close packed, leaving a base area ratio h/H=0.14, where h is the equivalent 2-D base width and H is the column spacing. The large base case had an h/H = 0.71. H was 0.44 cm for the small base and 1.25 cm for the wide base. Both screen nozzles had an extra fuel column next to the side walls to prevent etching.

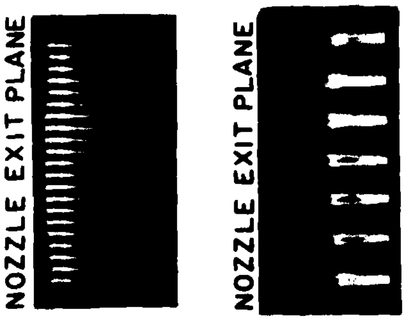

0.14		h/H	0.71	
F_2/A	H_2	GAS	F_2/A	H_2
1000	300	T_0(°K)	1050	300
2.31	3.35	P_0(atm)	3.03	2.18
3.04		P_{H_2}/P_F	1.40	

Figure 2. Emission Photographs of Reacting Flow

Representative Data

While the densities were low for standard optical techniques, open-shutter emission photographs looking down on the cavity flow revealed flow features. That on the left of Fig. 2 shows light coming from upper level HF* production. There is an over-abundance of H_2, which appears as the dark regions. The F_2/A is just barely visible in the center of the start of each band of light. The bright band ending 3H downstream may have been enhanced by reflections. The large base case on the right of Fig. 2 shows much more structure: islands of oxidizer appear as the burning layers grow and are driven together by the high pressure fuel. There is also evidence of recompression/reaction shocks.

A parameter study indicated that pressure would be particularly sensitive to process assumptions. Thus, piezoelectric transducers were located in the center of the top wall at various axial stations down the cavity. Adequate signal-to-noise was obtained by potting the gages in a silicon rubber epoxy and using 30 khz low-pass filters. Fig. 3 presents two representative cavity traces, together with a P_5 trace taken during the same run. The initial step signals the beginning of the fuel flow, and is followed by a second step as the oxidizer is mixed. The cavity traces show 4 msec of this flow, with a gradual climb coinciding with increases in P_5. Pressure irregularities attributed to choking waves were observed for $P_{H_2}/P_F < 1.75$ for the small base case and for $P_{H_2}/P_F < 1.1$ for the large base case. For traces that showed uniform flow, the pressure was read at a selected point and divided by the corresponding P_5. The resulting ratio could be read to ±5%.

MODELING

Model Development

The fluid process is represented schematically on Fig. 4. Radial oxidizer and fuel streams with substantial boundary layers expand to the full H through a complex system of expansion and compression waves. The corner stream lines

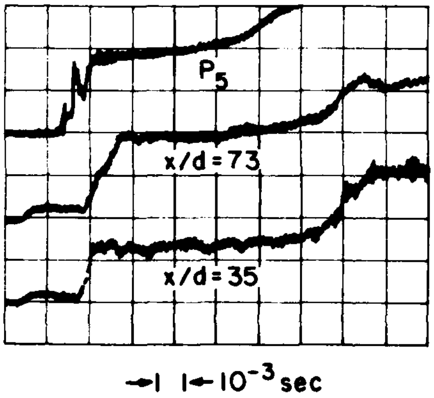

Figure 3. Pressure Histories, $h/H = 0.71$, conditions similar to case of Figure 2 (ordinate ≈ 10^3 torr/div for P_5, ≈ 10 torr/div for cavity gages)

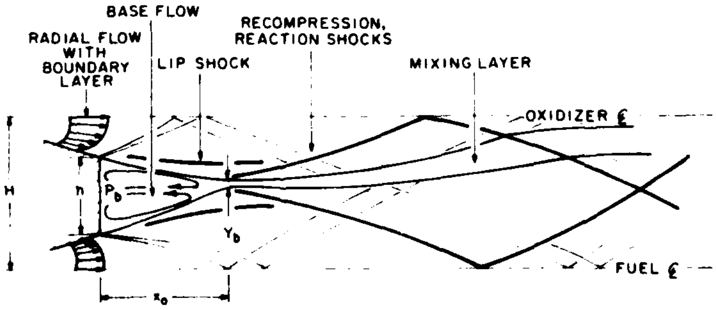

Figure 4. Schematic of 2-D Flow Field

approximately bound a base zone characterized by low speed recirculating fluid at pressure P_b. This zone narrows from h to a neck (Y_b) at a distance X_0 from the base wall. Gas from each free stream turns through the recompression/reaction shock system to be ultimately entrained and burned within the growing free shear layer.

Fig. 5 depicts a quasi 1-D model for this process. Assuming perfect gases and frozen chemistry, the expanding streams are brought to uniform states at the nozzle exit plane. These states (subscript e) are found by solving the conservation equations[4]:

$$\rho u \delta^{**} = \rho_e u_e \qquad \text{with} \quad \delta^{**} \equiv \frac{2}{1+\cos(\alpha_n)} - 4\frac{\delta^*}{d} \quad ,$$

$$P + \rho u^2 \theta^* = P_e + \rho_e u_e^2 \qquad \text{with} \quad \theta^* \equiv 1-4\cos(\alpha_n)\left(\frac{\theta}{d} + \frac{\delta^*}{d}\right) \quad ,$$

$$\text{and} \quad \rho u h_o \varepsilon^* = \rho_e u_e h_{o_e} \qquad \text{with} \quad \varepsilon^* \equiv \frac{2}{1+\cos(\alpha_n)} - 4\left(\frac{\delta^*}{d} - \frac{\varepsilon}{d}\right) .$$

Here ρ, u, P and h_o are evaluated in the radial isentropic core at the nozzle exit, while δ*, θ, and ε are the laminar boundary layer integral defects at the same location. δ*/d and θ/d have general magnitudes of 4% and 0.5% respectively. The entrained mass in the Y_b region is assumed to have come from equal width layers of the uniform gas states and mixed in a 1-D fashion with a fraction of the total base area (A_b) to P_b. Possible reaction of this gas will be addressed later. Each free stream minus the entrained mass then expands into the remaining base region to a uniform, chemically frozen state at X_0. The algebraic equations describing this process form an iterative set for $P_1 = P_2$. If a pressure matching condition cannot be determined, the highest pressure stream is assumed to dominate and expand to fill the entire base region. Thus the mixing/reaction process begins with a cavity flow field consisting of Y_b surrounded by uniform fuel and oxidizer streams turned to the axial direction.

The process continues with fluid from each free stream entrained at constant rates (α_i) to be mixed uniformly within the developing layer. A simplified HF chemistry is used which has 3 primary levels (v=1,2,3) pumped mainly by the cold reaction ($F + H_2 \rightleftarrows HF^* + H$), and a lumped upper level (v=4,5,6) pumped by the hot reaction ($H + F_2 \rightleftarrows HF^* + F$).[1] Energy transfer due to production and deactivation of HF, and H recombination is directly coupled with the fluid state in a move-mix fashion. Reaction within each cell proceeds at constant fluid conditions for Δx. Energy is added to the translational/rotational modes at the beginning of each subsequent cell, incoming fluid elements uniformly mixed and the flow parameters calculated at the cell exit. When both fuel and oxidizer streams have been consumed by the mixing process, the reaction continues one dimensionally with adjustments to the fluid state at each Δx.

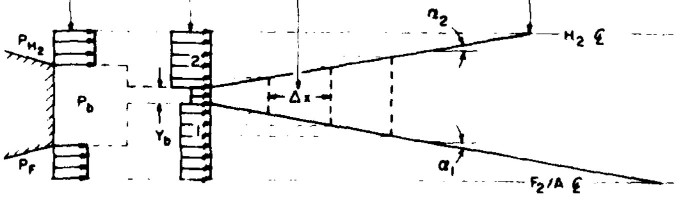

Figure 5. Flow Model

Sensitivity to Flow Parameters

Fig. 6 examines the sensitivity of the cavity pressure distribution to primary fluid parameters: the entrainment half angle (α), α_2/α_1, Y_b/h, and P_b for the wide base geometry and plenum conditions of Fig. 2. A reference parameter set with $\alpha = \alpha_1=\alpha_2=\frac{1}{2}°$, $Y_b/h=0.1$, and $P_b=0.15$ is indicated on each graph by a dashed line. The four graphs explore the independent variation of each parameter. The upper left hand graph shows the effects of varying α which should be substantially smaller than classical turbulent boundary growth rates. Values of ¼, ½, 1 and 90 are shown, the latter being an absolute upper mixing limit. α influences the mixing pressure profile by determining the relative influence of incoming gas to that already present within the layer. With chemistry, decreasing α reduces F atom consumption. Since for these conditions HF production is F atom driven, the lower energy coupled to the fluid brings about smaller changes in P. α_2/α_1 is more difficult to determine and greatly influences P. The upper right graph demonstrates this for various α_2/α_1. When $\alpha_2/\alpha_1<1$, P shows a rapid rate of change due not only to the increase of F, but also to the decrease in H_2 available as a high heat capacity bath.

The lower left graph illustrates the sensitivity of the pressure profile to the entrained base gas characterized by Y_b/h. As Y_b/h increases from zero, more of each free stream becomes involved in the recirculation zone, which by assumption is at P_b. For a fixed α it thus takes longer distances for the shear layer pressure to reach a given level. When $Y_b/h=1$, nearly 20% of the mass is confined to the shear layer core, whereas with $Y_b/h=0.1$, only 2% is involved. The latter is chosen as a reasonable value considering entrainment

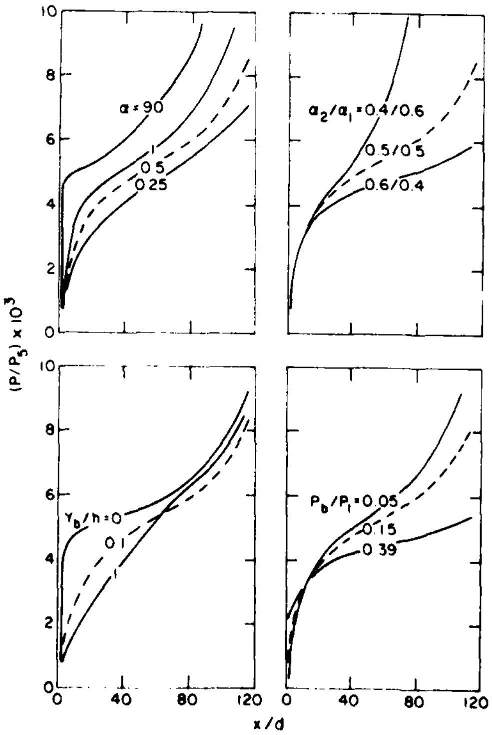

Figure 6. Pressure Sensitivity to Fluid Dynamic Parameters, Large Base Case of Fig. 2. (--- reference case: $\alpha=0.5°$; $\alpha_2/\alpha_1=1$; $Y_b/h=0.1$; $P_b/P_1=0.15$)

rates, mass flux levels, and base geometries.[7] The lower right graph on the figure indicates the sensitivity of the pressure history to P_b. The upper curve represents a minimum P_b found by expanding each uniform nozzle exit state independently and isentropically to the full cavity area and picking the lower of the two pressures. The lowest of the three curves represents a maximum P_b estimate, for which each mixed exit flow is expanded isentropically to match the pressure of its companion stream and then mixed to a uniform chemically frozen state. An equivalent 1-D problem is then posed in which both initial flows are mixed with the base and P_b iterated until the chemically frozen state is reached. The dashed reference line is based on experimental observations[8] where simple Prandtl-Meyer turns from each nozzle wall to the measured P_b agree to first order with measured X_o. X_o was chosen to be equal h[7,8] and the resulting curve falls between the limiting extremes.

All the curves of Fig. 6 are, of course, directly affected by the choice of chemical kinetics. For $x/d \leq 20$, the relatively fast cold reaction is the principal chemical process and energy contributor. At larger x/d, the slower, more energetic hot reaction dominates as a result of H atom production and entrained F_2. The slope changes observed at larger x/d reflect this shift in principal reaction. For the present conditions recombination has a negligible influence on P. Prereaction of the Y_b gas has been considered and is expected to have a small effect on this figure.

DISCUSSION

Comparison between Theory and Experiment

Normalized cavity pressures are plotted on Fig. 7 vs. x/d for representative experimental conditions and the reference theory of the previous section used for comparison. Pure A data are shown as filled-in symbols while those in which F_2 was present are open. Each run produced 3-4 points at different x/d; the symbol scatter is representative of differences in the individual run conditions.

The left-hand figure is for h/H=0.14 with $P_{H_2}/P_F=3.04$. All traces start at $P_b \simeq 10^{-3}P_5$ and climb rapidly due to the dissimilar gas mixing entropy rise in the shear layer. This rise is an important feature of the near flow, and appears to be completed within ≃ 20 x/d for runs with and without chemistry.

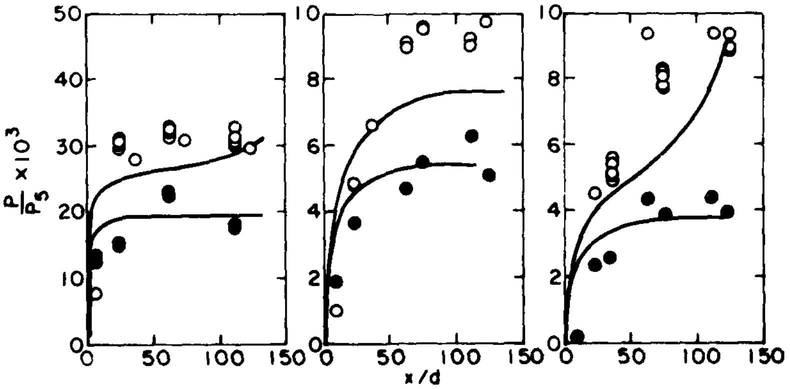

Figure 7. Pressure Profiles Comparisons between Experiment and Model Prediction; (left-hand figure: h/H=0.14, P_{H_2}/P_F=3.04; middle h/H=0.71, P_{H_2}/P_F=2.56; right: h/H=0.71, P_{H_2}/P_F=1.43).

The data support the rapid climb and subsequent leveling. Data with chemistry fall well below the calculated final state levels, and some 50% higher than that without chemistry. Considering the complexity of the phenomena, the theory provides a reasonable near field profile consistent with far field P levels.

The runs for h/H=0.71 show good agreement with theory for the pure A cases, now exhibiting a pressure rise drawn out to approximately 60 x/d, because of the larger H. For x/d < 50 the agreement for the chemistry runs is also good; however, there is a tendency for the data to be high at layer x/d. Runs with nominal P_{H_2}/P_F of 1.74 and 2.02 showed similar trends.

From Fig. 6 an increased α at high x/d or decreased entrainment of fuel would be necessary to bring about better agreement with the chemistry runs. While the mixing layer changes character as discussed in the Introduction, this occurs quickly and is unlikely to explain the present results. The detailed entropy field developed due to the nozzle turning waves, recompression waves, and reaction shocks is, of course, modeled here only in an average sense. The initial regions of the layer are actually shocked by stronger than average waves, to which the reaction shocks would add a contribution. These should cause a sharper initial climb to a higher reaction level. In addition, the possibility of disturbances from the walls must be considered. Although the walls were boundary layer corrected and the pure A runs indicated no particular difficulties, horizontal axis shadowgraphs and interferograms suggest the possibility of wall-originated waves. While these would need only a fraction of a degree turning strength to significantly increase P, they should influence the flow on a scale dependent on cavity height. Both small and large base data show similar profile trends at greatly different x/d, supporting a process description scaled by H.

Laser Performance

The temperature and pressure sensitivity of the rate processes and the short length scales lead to considerably increased sensitivity of HF laser performance to the flow variables and models. Calculations of power output were carried out for a representative laser operating with h/H=0.2 with present expansion geometry and 100 mixing layers. A Fabry-Perot resonator, variable upper and lower lasing levels, and a constant gain window were assumed. Mirror reflections of 1.0 and .99 were chosen with absorption coefficients set to 0. 5% F_2 in He at T_0=1500°K and P_5=3 atm was mixed with 100% H_2 at matched static exit pressures. The ordinate on Fig. 8 is the rate of change of power (P_w) with distance in relative units. Integrating this over x gives the total closed cavity power per unit height of individual shear layer. Multiplying P_w by 0.05 gives an approximate output power in W/cm^2 of flow cross-sectional area, and by

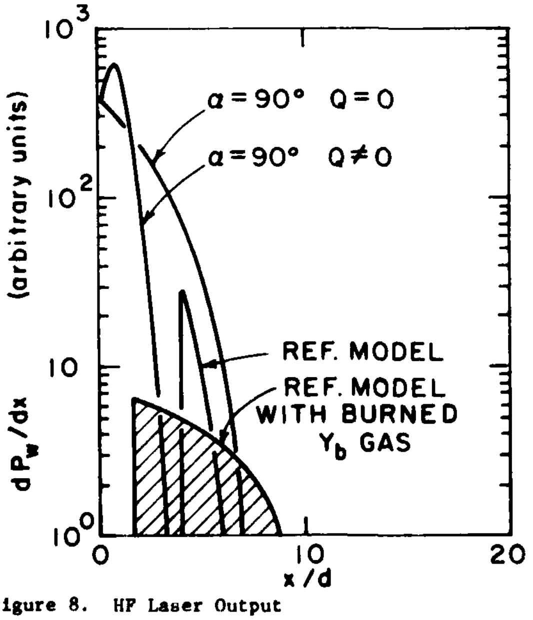

Figure 8. HF Laser Output

1.0 gives the output power in W/[gm(F+F_2)/sec].

The premixed case is shown on Fig. 8 as a reference, with and without heat coupling (Q) to the flow. $Q \neq 0$ reduces the output P_w of this laser and distributes it over 1/2 the axial distance. The reference model shows an order of magnitude smaller output, delayed in initiation. Furthermore, the cross hatched area shows the substantial effect caused by complete prereaction of the base feed gas. Referring to Fig. 6, the peak dP_w/dx of the laser is found to double with α increased to 1° because of the increased F atom entrainment. However, the length of the lasing zone is approximately halved. Decreasing α_2/α_1 has a similar effect. It appears that total P_w reaches a limit with increasing F entrainment. Increasing Y_b/h enhances the near flow lasing conditions by diminishing the relative influence of downstream mixing. Increasing P_b has little effect on peak dP_w/dx, but does increase the length of the lasing zone.

It is concluded that even modest base regions can dominate laser performance, and that the new model offers a way of exploring these and other fluid processes in a consistent manner. Further, modeling of the effects of the base and of the complex coupled wave system awaits improved understanding of the parameters used in the present model with verification by more direct measurement of the chemical and energy state of the gas.

ACKNOWLEDGEMENTS

This research was supported by the United States Air Force Office of Scientific Research (Grants 73-2512 and 77-3450; Contract F49620-79-C-0020). Much of the work will be contained in a Ph.D. dissertation by the first author.

REFERENCES

1. R.W.F. Gross and J.F. Bott, Handbook of Chemical Lasers, Wiley, N.Y.(1976).
2. H. Mirels, AIAA J. 14, 7, 930 (1976).
3. J.E. Broadwell, Applied Optics 13, 962 (1974).
4. D.A. Russell, S.E. Neice, and P.H. Rose, AIAA J. 13, 5, 593 (1975).
5. T.S. Vaidyanathan, Ph.D. dissertation, University of Washington (1979).
6. W.R. Warren, Acta Astronautica 1, 813 (1974).
7. F.R. Hama, NASA TR No. 32-1033 (1976).
8. A. Roshko and G.J. Thomke, AIAA J. 4, 6, 975 (1966).

AD-A091 010   HEBREW UNIV JERUSALEM (ISRAEL)   F/G 20/4
PROCEEDINGS OF THE INTERNATIONAL SYMPOSIUM ON SHOCK TUBES AND W--ETC(
FEB 80   A LIFSHITZ, J ROM   AFOSR-78-3679
UNCLASSIFIED   AFOSR-TR-80-1141   NL

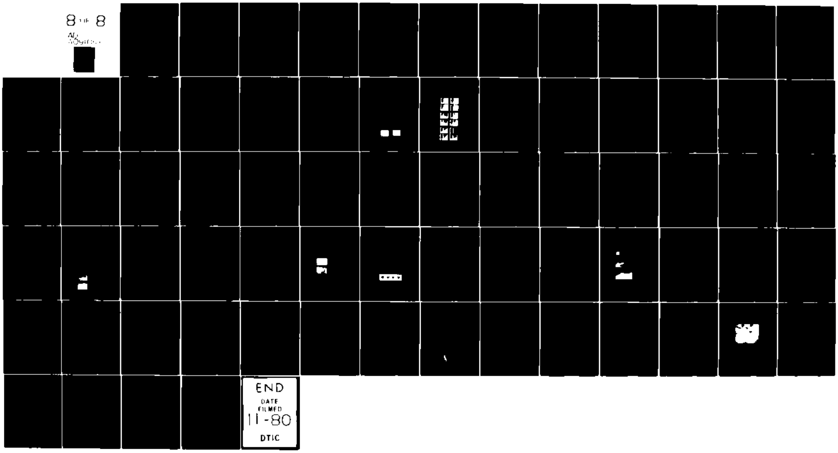

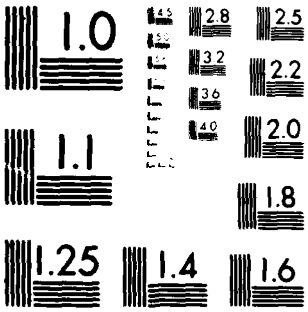
1.0
4.5
5.0
5.6
2.8
2.5
3.2
2.2
3.6
4.0
2.0
1.1
1.8
1.25
1.4
1.6

LASER-INDUCED-FUSION EXPERIMENTS AT KMS FUSION

STEPHEN B. SEGALL

KMS Fusion, Inc.
Ann Arbor, Michigan USA

Laser-induced-implosion experiments have been performed at both 1.06 μm and 0.53 μm. Using gas-filled glass-shell targets irradiated with 1.06 μm light, neutron yield scaled with the 3.7 power of the incident laser power. Peak fuel densities of up to 7 g/cm^3 have been obtained when the fuel in the target was cryogenically cooled to a thin solid or liquid layer on the inside surface of the glass shell. Absorption of laser light has been found to increase with increasing laser wavelength and decreasing laser intensity. Fractional absorption of about 50 percent has been obtained for spherical shell targets illuminated with 1.06 μm light at an intensity of 2x10^{13} W/cm^2 with a pulse duration of 1 nsec.

INTRODUCTION

The KMSF program has been engaged in the development of laser fusion physics by studying, experimentally and theoretically, the irradiation and implosion of spherical-shell, fuel-filled targets. Experiments have been done to quantify the conditions of the imploded target core, to measure the amount of laser energy absorbed, and to examine the transport of the absorbed energy.

IMPLOSION STUDIES

Experiments are performed using a high power (0.5 TW) Nd: glass laser which emits light with a wavelength of 1.06 μm. The laser beam illuminating the target is made up of a series of individual 30-psec mode-locked pulses stacked to produce an overall pulse length variable from 30 to several hundred picoseconds[1]. The light is focused onto the target using a lens-ellipsodial-mirror illumination system[2] which produces nearly uniform illumination at near-normal incidence[3]. The targets are generally DT-filled glass microshells ranging in diameter from about 55 to 85 μm with wall thickness on the order of 1 μm. Measurements of neutron yield, alpha-particle energy spectra, and x-ray pinhole camera images, together with numerical simulations, are used to provide a description of the laser-driven implosion process[4].

The energy spectrum of alpha particles from the DT fusion reaction provides an upper limit to the fuel-ion temperature at peak compression[5]. The energy lost by the alpha particles as they traverse the compressed fuel and shell can provide a measure of $\int \rho dr$. The magnetic spectrograph used to measure the alpha-particle spectra is described in Reference (6).

The time-integrated x-ray emission from the target is imaged using two pinhole cameras[7,8]. Each camera has an array of four 5 μm pinholes, which are covered with beryllium-foil filters of various thicknesses. The inner region of intense x-ray emission occurs when the imploding tamper material is stopped by the back pressure of the compressed DT gas. If the compressed core is larger than the resolution of the pinhole camera, the inner feature will appear as a ring from which the volume compression can be estimated. In some instances, the inner feature of the image appears as a solid core (a central peak on the microdensitometer trace) rather than a ring. Computer simulations described in Reference (8) show that this could result if the compressed-core radius were less than the camera resolution. The peak could also be produced by mixing of the glass into the fuel. Thus reliable compression measurements cannot be obtained from these centrally peaked x-ray photographs.

Maximum neutron yield as a function of laser power is plotted in Figure 1. The data are for glass microshell targets filled with 2 mg/cm^3 of DT gas. A straight-line fit through the data shows that the yield scales as the 3.7 power of the laser power.

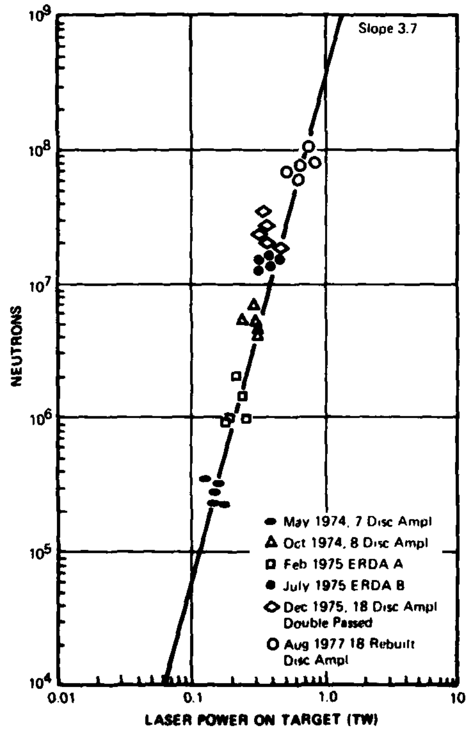

Figure 1. Neutron yield verses laser power on target. The five highest yields obtained with each of six different laser configurations are plotted on the graph.

This scaling can be understood using a similarity model of the adiabatic compression-expansion cycle of a DT-filled target developed by Mayer, et. al[9]. In this reference the neutron yield N is given by

$$N = \lambda(1-\lambda)p^2D^4C^{2/3}\ F_{DT}(\theta) \qquad \text{I}$$

where λ is the tritium fraction of the fill gas, p is the fill pressure in atmospheres, D is the initial target diameter in 100 μm units, and C is the volume compression of the target. F_{DT}, which is a function related to the DT reaction rate, is plotted in Figure 2 as a function of peak fuel-ion temperature θ. For the temperature range $0.7 < \theta < 2.5$ keV, which includes the range of fuel temperatures measured in our experiments,

$$F_{DT}(\theta) \propto \theta^{\frac{11}{2}} \qquad \text{II}$$

The scaling of the neutron yield with laser power P_L can be found by determining the dependence of peak fuel temperature on laser power, taking compression to be independent of laser power when the pulse length is matched to the implosion time τ.

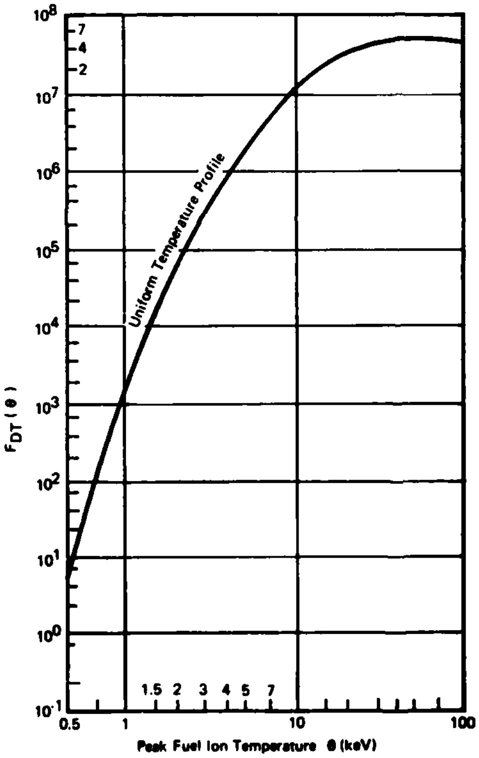

Figure 2. The function $F_{DT}(\theta)$ from Reference (9).

Assuming that at the instant of peak compression the imploded tamper and compressed fuel are at the same temperature, that the ions and electrons also have the same temperature in the dense tamper and fuel, and that the tamper and fuel are fully ionized, the energy deposited in the imploding mass is given by

$$\alpha\, \epsilon\, P_L\, \tau = 3/2[(1 + Z_T)\, N_T + (1 + Z_f)\, N_f]\theta \qquad III$$

where ε is the fraction of the incident power absorbed by the target, α is the fraction of this absorbed power transmitted by electron thermal conduction from the hot target corona to the imploding tamper material, N_T and N_f are the number of tamper and fuel ions respectively and Z_T and Z_f are the average atomic numbers of the tamper and fuel.

If we assume the implosion velocity is given by the isothermal sound speed then

$$\tau \propto D/\theta^{\frac{1}{2}} \qquad \text{IV}$$

since the sound speed is proportional to the square root of the electron temperature. Substituting (IV) in (III) we obtain

$$\theta \propto P_L^{2/3} \qquad \text{V}$$

Using (V) and (II) in equation (I) we obtain a dependence of the neutron yield on the 3.7 power of P_L, which is the experimental result.

Since the slope of F_{DT} (θ) decreases as θ increases, we expect the rate of increase of neutron yield with laser power to decrease as laser power is further increased.

Neutron yield scaling with absorbed energy per unit target mass provides another source of information on the implosion process. At fixed values of absorbed energy per unit mass, the ion temperature is approximately fixed, so that yield variations would most likely be due to variations in compressed fuel density. Figure 3 shows normalized neutron yields as a function of absorbed energy per unit mass[10]. We have added the KMSF data to this plot, which was prepared at the Lawrence Livermore Laboratory (LLL). At the lower values of absorbed energy, many of the KMSF yields are significantly higher. These higher values probably result from greater fuel density during compression of the target. This result suggests that the ellipsoidal-mirror illumination system used at KMSF can produce more symmetric, higher density compressions than a two-lens illumination system (like that used at LLL for example).

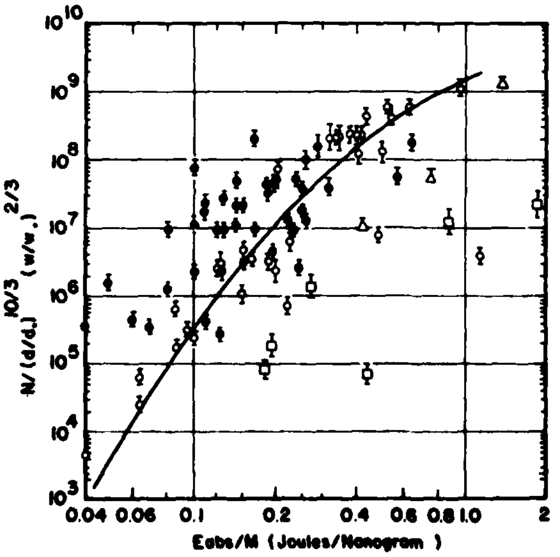

Figure 3. Normalized neutron yield verses laser energy absorbed divided by target mass. Recent KMSF data (solid circles) have been added to this figure, which was taken from Reference (10). Open symbols represent LLL data. d is the target diameter, w its wall thickness. $d_* = 85\mu m$, $w_* = 0.8\ \mu m$.

Another method that is being investigated to increase fuel density at peak compression is the use of cryogenically cooled targets in which the gaseous fuel is condensed out to form a thin layer on the inside surface of the tamper shell. Higher densities should be achieved because the back pressure of the fuel on the tamper during the implosion process should be reduced.

In the first series of experiments a liquid fuel layer was produced. The liquid layer was rarely uniform, displaying a typical asymmetry in thickness of two to one. This asymmetry persisted during compression, with the compressed region in the x-ray pinhole photographs displaced from the target center an amount corresponding to the initial asymmetry. Compressions from 50 to 350 have been measured, corresponding to fuel densities from 0.8 g/cm^3 to 7 g/cm^3. Neutron yields were $\sim$ 2-to-7 x 10^7 and fuel-ion temperatures $\sim$ 1 to 2 keV. Additional evidence of increased fuel densitites for liquid-layer targets comes from alpha-particle energy spectra, which are downshifted from 3.52 MeV by as much as 300 keV for liquid-layer targets, but not more than 100 keV for gas-filled targets. This downshift is shown in Figure 4a, with the experimental uncertainty approximately 70 keV. The alpha-particle spectrum from a typical gas-filled target is shown in Figure 4b for comparison.

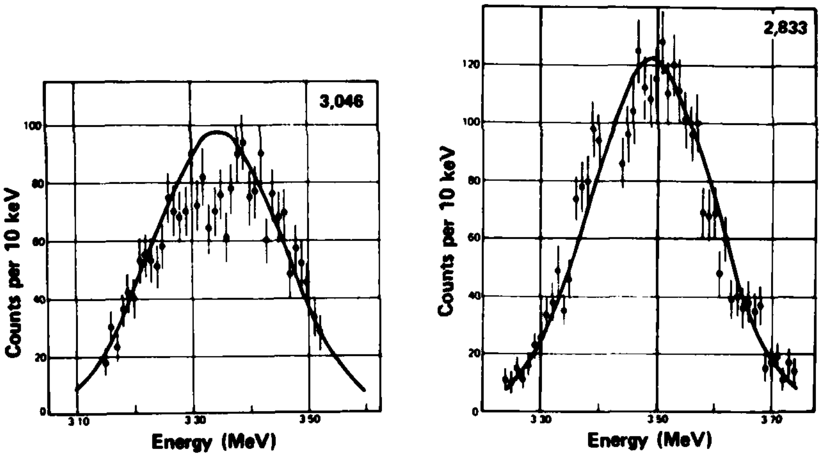

Figure 4. Alpha particle energy spectrum for (a) cryogenic liquid layer target shot and (b) gas filled target. In 4a the fitted gaussian (solid line) has a mean energy of 3.33±.07 MeV and FWHM of 265±20 keV corresponding to a fuel ion temperature of 2.2±0.4 keV. In 4b the mean energy is 3.49±.07 MeV and the FWHM is 250±.05 keV corresponding to a temperature of 2.0±0.3 keV.

There have been additional experiments in which the fuel was condensed in a solid layer on the inner surface of the shell. The asymmetry in the fuel distribution was significantly reduced in comparison with the liquid-layer targets. The x-ray pinhole photographs showed a more symmetrical implosion; and as a result a more accurate measurement of the compressed-fuel density was obtained. The neutron yields were comparable with those of the liquid-layer targets at equivalent laser power on target. The highest compression for a solid-layer target, as inferred from the x-ray pinhole photograph, was 370, corresponding to a maximum fuel density of 7 g/cm^3. The original target diameter was 88 μm, from which one calculates a <ρR> of approximately 4.3 mg/cm^2 in the compressed fuel. This value for <ρR> is consistent with the observed 10% downshift in the measured alpha spectrum.

FAST IONS AND TRANSPORT

Most of the laser-light energy is absorbed near the critical-density surface. Much of this energy ultimately appears as kinetic energy of the ions in the blowoff plasma. The study of the evolution of energy partitioning involves the interrelated questions of how the absorbed energy is transported to the remaining electrons, and how this energy is converted into ion kinetic energy.

Ion spectral measurements have been obtained with biased charge collectors, a magnetic spectrograph, and a Thomson parabola spectrograph[6]. The Thomson parabola spectrograph measures the charge-to-mass ratio in addition to the ion velocity and so provides the most detailed information about the fast ions.

The velocity distribution of these ions shows the well-known two-component shape[11], consisting of a small number of fast ions with velocities in excess of 10^8 cm/sec followed by a larger group of ions whose velocities are a few times 10^7 cm/sec. The fast ions constitute about 8% of the original target mass, but carry off a sizable amount (∿ 40%) of the absorbed laser energy. If this two-component ion spectrum results from a two-temperature electron distribution, then by studying the ion spectrum in detail we may be able to draw inferences about the electrons and, therefore, about the absorption and transport processes at the target. A straightforward interpretation of the two-component ion distribution can be obtained from the isothermal rarefaction model[12,13]. Using this simple model, a measurement of the scale velocity of the ion spectrum gives the electron temperature of the corona.

The fast ions with a distribution characteristic of electron temperatures near 10 keV, presumably come from the hot corona, and represent material that has passed through the laser-light-absorption region. The slow ions originate in the cooler (∿ 1 keV) interior of the target wall. The sharp thermal gradient implied by this interpretation cannot be understood on the basis of classical transport coefficients, but it is consistent with the inhibited transport suggested in other experiments on planar targets[14] with a flux limiter $f \simeq 6\,(Zm_e/2m_i)^{1/2} \simeq 1/15$.

ABSORPTION EXPERIMENTS

Absorption of laser light by spherical shell targets has been measured as a function of a number of parameters including laser wavelength, bandwidth, intensity, and pulse length, and target composition. A differential calorimeter positioned in the annular gap between the ellipsoidal mirrors is the primary diagnostic used to determine absorbed energy. Total absorbed energy values are obtained by assuming a uniform plasma blowoff and extrapolating the energy measured in the acceptance angle of the detector to 4π solid angle. Plasma blowoff energy has been found to vary as a function of detector position for spherical shell targets illuminated at intensities of the order of $5\text{x}10^{16}$ watts/cm^2 using f/1 focusing lenses[15]. However, in our experiments, using the lens-ellipsoidal-mirror focusing system at from one to three orders of magnitude lower laser intensity, the illumination pattern and the plasma blowoff appear to be considerably more symmetric[16]. Absorbed energy values obtained using a bubble calorimeter[17], which collects all of the plasma blowoff, were consistent with the extrapolated energy values obtained using the thermopile calorimeter.

Target absorption has been studied for a number of different experimental conditions[18]. At a power level of about 0.5 TW with normal-incidence focusing for which the focal positions of the two beams were coincident with the center of the target, fractional absorption of 80-μm-diameter targets was 17.1 ± 0.6%. This increased to 18.9±0.7% when the laser power was reduced to ∿ 0.1 TW. When the 1.06 μm laser light was frequency-doubled by means of KDP crystals, the fractional absorption further increased to 22.8 ± 2.3%. The laser power in the 0.53 μm beam incident on the target was also about 0.1 TW. Absorption did not appear to be strongly dependent on laser pulse length, which varied between 30 and 400 psec in these experiments. The small changes in absorption with relatively large changes in laser power and wavelength indicate that classical inverse bremsstrahlung, which should be strongly dependent on laser intensity and wavelength, is making only a small contribution to the absorbed energy. It is believed that most of the absorption is a consequence of resonance absorption[19-21], although other mechanisms such as enhanced collisional absorption due to ion acoustic turbulance[22] and absorption due to parametric instabilities may also be contributing.

Absorption of laser energy by resonance absorption is less desirable than absorption by collisional processes. Energy is absorbed by resonance absorption primarily in a very thin zone at the critical density surface in a process which accelerates electrons to high energies, producing a suprathermal tail on the electron energy distribution. At laser intensities of about 10^{15} W/cm^2 and above the mean free path of these electrons may be longer than the shell thickness causing preheating of the fuel inside the shell. In addition, the high energy electrons accelerate ions in the corona to higher velocities than would be the case if the same absorption were produced by inverse bremsstrahlung alone. This reduces the momentum per unit absorbed energy needed to drive the target implosion.

The most dramatic changes in target absorption were obtained when a plasma spatial filter (PSF) was used in the laser system[23]. The plasma spatial filter is a beam-smoothing component of the laser system consisting essentially of a planar target and lens interposed in the path of the laser beam at an early stage in the sequence of laser amplifiers (Figure 5). The plasma that forms on the target at the focus of the lens behaves as an active mirror, reflecting a portion of the beam back along the incident path to be amplified by subsequent amplifiers before being focused onto the fusion pellet. The result is a spatially more homogeneous laser beam with a bandwidth of approximately 40 Å as compared with the normal 4 Å bandwidth. Using the PSF with 1.06 μm light, fractional absorption increased from 17.1% to 25.5%. The increase in fractional absorption for green light was even greater (Figure 6).

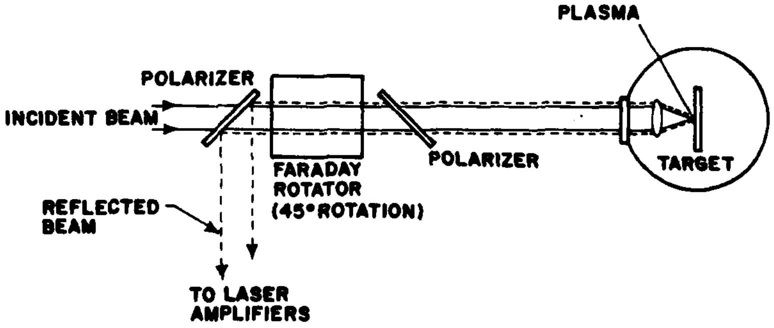

Figure 5. Schematic diagram of plasma spatial filter.

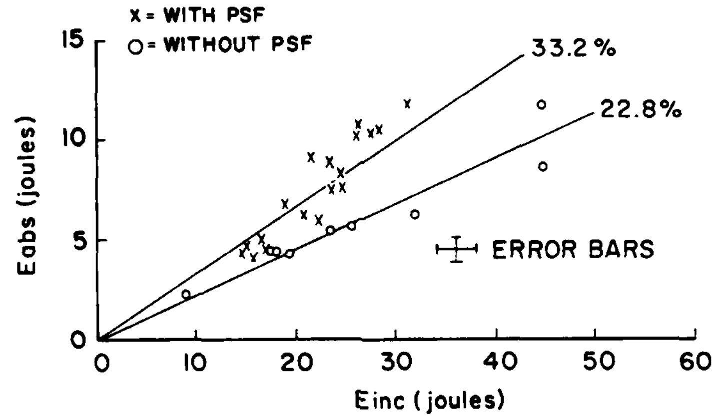

Figure 6. Absorption of laser energy at 0.53 μm with and without the plasma spatial filter. Targets were nominal 80 μm diameter glass shells and laser power was about 0.1 TW.

One possible explanation for the increase in absorption on target shots for which the PSF was used is that the wider bandwidth of the laser light reduced the fraction of the laser energy scattered by stimulated Brillouin scattering (SBS)[24-27]. A signature of SBS is that the reflected light should be redshifted[28]. Since the spectrum of the reflected light is already Doppler blue shifted, one would expect a larger blue shift with the PSF than without. Table I shows data on spectral shifts for targets irradiated with 1.06 μm light. On the average, target shots for which the PSF was on line produced larger blue shifts than target shots without the PSF, indicating that some of the laser light is being lost due to SBS and that use of the plasma spatial filter reduces this loss. Data for the absorption experiments described above is summarized in Table II.

TABLE I

SPECTRAL SHIFT OF 1.06 μm RADIATION RETURNED THROUGH FOCUSING OPTICS

With Plasma Filter		Without Plasma Filter	
Shot	Δλ(Å)	Shot	Δλ(Å)
3582	-16	3613	-9.6
3584	-13	3617	-4.8
3597	-16	3614	0.0
3599	-13	3618	-3.2
3560	- 8	3622	-6.4
		3623	-3.0

TABLE II

SUMMARY OF ABSORPTION MEASUREMENTS FOR SPHERICAL SHELLS

λ(μm)	Target Material	Plasma Filter	Pulse Length Psec	Intensity (10^{15} W/cm^2)	Absorption (%)
1.06	Glass	Out	24-84	1.8 -5.2	17.1±0.6
1.06	Glass	Out	112-190	0.3 -0.7	18.9±0.7
1.06	Glass	In	74-178	0.6 -2.2	25.5±1.9

Table II (Continued)

λ(μm)	Target Material	Plasma Filter	Pulse Length Psec	Intensity (10^{15} W/cm^2)	Absorption (%)
1.06	PVA	In	63-175	0.6 -2.5	21.5±2.8
0.352	Glass	Out	149-328	0.4 -0.6	22.8±2.3
0.532	Glass	In	191-380	0.25-0.5	33.2±4.8

Experiments have also been carried out with 1.06 μm laser light using longer laser pulses (∿ 1 nsec) on larger spherical shell targets (109 - 290 μm diameter). For these experiments two thermopile differential calorimeters located at different positions in the annular gap as well as an unfiltered TLD chip were used to measure the absorbed energy. Energy absorption for target shots with and without the PSF as a function of laser intensity are shown in Figure 7.

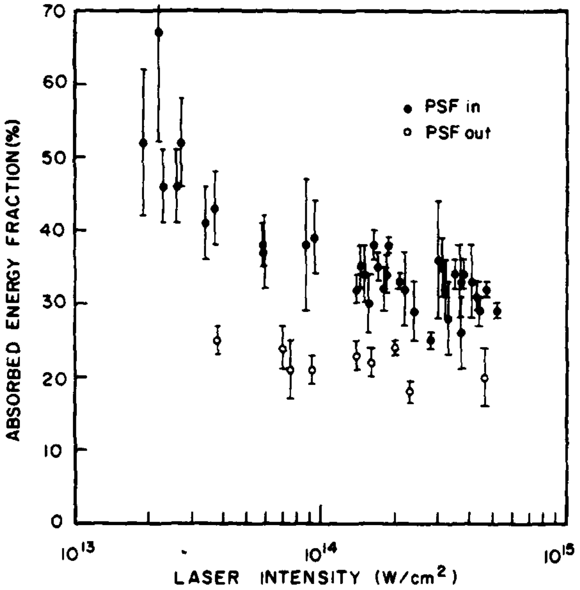

Figure 7. Measured energy absorption fractions verses laser intensity with and without the plasma spatial filter. The error bars are the standard deviation of a weighted average of three detector measurements.

In the long pulse experiments a thicker plasma corona could form around the target permitting enhanced inverse bremsstrahlung for laser light entering the corona, but also enhancing stimulated Brillouin scatter. From Figure 7 the absorbed energy fraction appears to be slightly higher than for the shorter pulse experiment at comparable intensities indicating some increase due to the thicker corona. Without the plasma spatial filter, however, fractional absorption remains below 30% on all target shots. Fractional absorption is significantly higher with the PSF on line, increasing to over 50% at intensities of about 2 x 10^{13} W/cm^2.

The absorption experiments that have been carried out at KMS Fusion clearly indicate the need for broad bandwidth laser light to obtain high fractional absorption. Absorption is also increased by increasing the laser pulse length, reducing the laser intensity, and reducing the laser wavelength, all of which serve to increase collisional absorption and, hence, decrease the fraction of the laser energy absorbed by the resonance absorption process.

In general, if laser intensity is lower, longer implosion times are required to reach a given implosion velocity. To attain implosion velocities required for thermonuclear burn, larger or thinner-walled targets are therefore needed. Large aspect ratio (ratio of target radius to wall thickness) shells, however, are more likely to develop hydrodynamic instabilities which would degrade the implosion symmetry. In experiments that have been performed to date, we have seen no evidence of instabilities in the x-ray pinhole pictures for aspect ratios of up to 50, and neutron yields are consistent with those that would be expected for symmetric implosions.

On three target shots the neutron yield obtained in the long pulse experiments fell on the line for maximum neutron yield given in Figure 1. The highest neutron yield in the green light experiments was over an order of magnitude greater than the value given by the line in Figure 1. Neutron yields obtained on these shots are shown in Table III.

TABLE III

PEAK NEUTRON YIELDS IN LONG PULSE AND GREEN LIGHT EXPERIMENTS

Shot Number	Laser Wavelength (μm)	Target Diameter (μm)	Wall Thickness (μm)	Laser Power (TW)	Pulse Length (psec)	Neutron Yield
3986	1.06	115	1.6	.537	759	3.7×10^7
3990	1.06	154	1.5	.373	1086	1.0×10^7
3987	1.06	128	1.9	.317	953	4.6×10^6
3431	0.53	85	1.2	.084	346	1.7×10^6

At the present time an upgrade of our laser system is being completed which will raise peak laser power from 0.5 TW to about 2 TW at one micrometer wavelength and to about 0.6 TW at half a micrometer. As higher laser power becomes available, it is expected that extension of these studies will lead to a better understanding of the target implosion process and result in continued increases in the ratio of nuclear energy produced to incident laser energy.

ACKNOWLEDGEMENT

The work reported on in this paper is the result of the efforts of the entire KMSF experimental staff. In particular, credit should be given to F.J. Mayer, D.C. Slater, G. Charatis, and R.R. Johnson.

This work was supported by the United States Department of Energy under contract ED-78-08-1598.

REFERENCES

1. C.E. Thomas and L.D. Siebert, Appl. Opt. 15, 462 (1976).
2. C.E. Thomas, Appl. Opt. 13, 1267 (1975).
3. K.A. Brueckner, J.E. Howard, Appl. Opt. 14, 1274 (1975).
4. P.M. Campbell, P. Hammerling, R.R. Johnson, J.J. Kubis, F.J. Mayer, and D.C. Slater, Plasma Physics and Controlled Nuclear Fusion Research, (Proc. Int. Conf., Berchtesgaden, 1976) IAEA, Vienna (1977) Vol. 1, p.227.
5. V.W. Slivinsky, H.G. Ahlstrom, K.G. Tirsell, J. Larsen, S. Glaros, G. Zimmerman, and H. Shay, Phys. Rev. Lett. 35 1083 (1975); R.R. Goforth, F.J. Mayer, H. Brysk, and R.A. Cover, J. Appl. Phys. 47 2850 (1976).
6. D.C. Slater and F.J. Mayer, Laser Interaction and Related Plasma Phenomena, Vol. 4B, H.J. Schwarz and H. Hora, eds. (Plenum, NY, 1977) p. 603.

7. G. Charatis, J. Downward, R. Goforth, B. Guscott, T. Henderson, S. Hildum, R. Johnson, K. Moncur, T. Leonard, F. Mayer, S. Segall, L. Siebert, D. Solomon, and C. Thomas, Plasma Physics and Controlled Nuclear Fusion Research, (Proc. Int. Conf., Tokyo, 1974) IAEA, Vienna (1975) Vol. II, p. 314.
8. P.M. Campbell, G. Charatis, and G.R. Montry, Phys. Rev. Lett. 34 74 (1975).
9. F.J. Mayer, R.R. Johnson, and D.J. Tanner, Phys. Fluids 19, 2049 (1976).
10. H.G. Ahlstrom, Lawrence Livermore Laboratory Report UCRL-79819 (1977).
11. C. Yamanaka, T. Yamanaka, T. Sasaki, K. Yoshida, M. Waki, H.B. Kang, Phys. Rev. A6 2335 (1972); A.W. Ehler, J. Appl. Phys. 46 2464 (1975); G. Charatis, J. Downward, R. Goforth, B. Guscott, T. Henderson, S. Hildum, R. Johnson, K. Moncur, T. Leonard, F. Mayer, S. Segall, L. Siebert, D. Solomon, and C. Thomas, Plasma Physics and Controlled Nuclear Fusion Research (Proc. Int. Conf., Tokyo, 1974) IAEA, Vienna (1975) Vol. II, p. 317.
12. L.D. Landau, E.M. Lifshitz, Fluid Mechanics (Pergamon, London, 1959), p. 359.
13. K.A. Brueckner in Laser Induced Fusion and X-Ray Laser Studies, S.F. Jacobs, M.O. Scully, M. Sargent, and C.D. Cantrell, eds. (Addison-Wesley, Reading, Mass., 1976).
14. F. Young, R. Whitlock, R. Decoste, B. Ripin, D. Nagel, J. Stamper, J. McMahon, and S. Bodner, Appl. Phys. Lett. 30 45 (1977); B. Yaakobi and T. Bristow, Phys. Rev. Lett. 38 350 (1977); J. Pearlman and J. Anthes, Appl. Phys. Lett. 27 581 (1975); A.W. Ehler, D.V. Giovanielli, R.P. Godwin, G.H. McCall, R.L. Morse, and S.D. Rockwood, Los Alamos Scientific Laboratory Report La-5611-MS (1974).
15. V.C. Rupert, S.R. Gunn and J.F. Holzrichter, J. Appl. Phys. 49 132 (1978).
16. G.E. Busch, "Holographic Interferometry", KMS Fusion 1978 Annual Report.
17. J.D. Simpson, KMS Fusion 1977 Annual Report, p. 2-37.
18. S.B. Segall, KMSF Report No. U787 (1978).
19. J.P. Friedberg, R.W. Mitchell, R.L. Morse, and L.I. Rudsinski, Phys. Rev. Lett. 28 795 (1972).
20. K.G. Estabrook, E.J. Valeo, and W.L. Kruer, Phys. Fluids 18 1151 (1975).
21. K.R. Manes, V.C. Rupert, J.M. Auerbach, P. Lee, and E. Swain, Phys. Rev. Lett. 39 281 (1977).
22. R.J. Faehl and W.L. Kruer, Phys. Fluids 20, 55 (1977).
23. N.K. Moncur, Appl. Opt. 16, 1449 (1977).
24. D.W. Forslund, J.M. Kindel, and E.L. Lindman, Phys. Rev. Lett. 30 739 (1973).
25. W.L. Kruer, E.J. Valeo, and K.G. Estabrook, Phys. Rev. Lett. 35, 1076 (1975).
26. B.H. Ripin, F.C. Young, J.A. Stamper, C.M. Armstrong, R. Decoste, E.A. McLean, and S.E. Bodner, Phys. Rev. Lett. 39, 611 (1977).
27. K. Mizuno and J.S. DeGroot, Phys. Rev. Lett. 39, 608 (1977).
28. D.W. Phillion, W.L. Kruer, and V.C. Rupert, Phys. Rev. Lett. 39, 1529 (1977).

PRESSURE WAVE ATTENUATION IN REPETITIVELY PULSED FUSION LASERS

J. SHWARTZ, V. A. KULKARNY and D. A. AUSHERMAN

TRW Defense and Space Systems Group
Redondo Beach, California 90278, USA

A one-dimensional finite-difference code developed to analyze pressure wave attenuation in vented-duct acoustic absorbers is presented. Code calculations were compared with experimental results obtained with a modified shock tube, in which the conventional driven section was replaced by a vented duct. For the initial rapid attenuation of strong waves the code and experimental results are generally in good agreement. The code failed to predict, however, the residual high frequency pressure fluctuations which persisted for time scales of 100 ms and longer, at amplitudes of the order of 10^{-3} times the initial driver overpressure. It is shown that these residual oscillations can be attributed to two-dimensional effects in the duct. Their presence indicates that a simple vented duct cannot produce the level of pressure wave attenuation required for most fusion laser applications.

INTRODUCTION

Repetitively pulsed flowing gas lasers are currently being considered as prime candidates for driving Inertial Confinement Fusion Reactors (ICFR)[1, 2]. As presently envisioned, the laser drivers will have to generate about 10^6 joules of energy per pulse at a repetition rate of the order of 10 pulses per second. The pulsed energy is to be focused on small pelets, filled with deuterium and tritium and falling in succession through a reactor chamber, to produce thermonuclear reactions and net power gain.

To reduce the size and cost of laser drivers for ICFR, the radiation energy density generated in the laser cavity must be fairly high, i.e. - 10 or more joules per liter of cavity volume. Since laser efficiencies are typically less than 10%, energy at a density of one to a few hundred joules per liter-atm. must be deposited in the laser cavity to initiate the lasing process. The fraction of the deposited energy which is not extracted by lasing will typically be converted into translational energy (or heat) on a microsecond time scale. This will result in a substantial, nearly instantaneous, temperature and pressure rise in the laser cavity after each lasing pulse. A sudden pressure rise generates compression and rarefaction waves which can reverberate in the laser cavity for times which are long compared to the interpulse time - which is typically of the order of 100 m sec. The density (or optical) homogeneity of the lasing media is thus clearly destroyed after each lasing pulse.

For the laser energy to be focusable onto the small fusion targets, typically of 1 mm diameter, the density of the lasing media must be uniform to within 10^{-3} to 10^{-4} of the average cavity density just prior to the extraction of any lasing pulse. To achieve such conditions, the heated and optically distorted gas left over in the cavity from a previous pulse must be convected out of the laser cavity by establishing a continuous flow of gas through the cavity. This continuous flow will fill the cavity with a fresh charge of gas after each pulse. The more persistent pressure fluctuations cannot be convected, however, out of the laser cavity and insteady they must be attenuated and damped out by other means.

This paper describes an attempt to test and evaluate a pressure wave suppressor which appeared to be suitable for ICFR gas laser drivers.

To achieve the required density uniformity stated above the relative pressure fluctuations in the cavity must be confined to the same range of 10^{-3} to 10^{-4} prior to the initiation of any lasing pulse. Since the over-pressure generated in fusion-type pulsed lasers is of the order of the base pressure (namely, the energy deposition typically doubles the cavity pressure), the pressure attenuation required is also in the range of 10^{-3} to 10^{-4}. Another requirement imposed on the pressure wave attenuator is that the pressure drop it produces be kept to a minimum so that the power required to drive the gas through the laser flow-loop will not be large compared to the time averaged laser power.

A class of pressure wave absorbers which can potentially meet the above two requirements is shown in Figure 1. The first two, (a) and (b), we call "passive absorbers" since they do not act on the mean flow and they become activated and dissipateive only when the gas pressure in the duct changes with time. Similar devices are in use in other pulsed laser systems; i.e. - in the repetitively pulsed chemical^3 and CO$_2^4$ lasers. Such devices are very effective in reducing the initially high over-pressure by a factor of about 10^2 within a few milliseconds. However, the effectiveness of passive devices in reducing pressure fluctuations to the range of 10^{-3} to 10^{-4} remains questionalbe. Some active suppression devices, such as depicted in Figure 1(c), may be required to reduce the pressure fluctuations to a level which is compatible with the ICF laser applications. This and similar issues are addressed in the present paper.

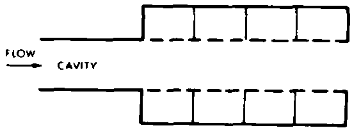

(a) VENTED SIDE WALL ABSORBER

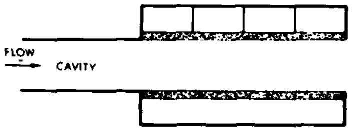

(b) POROUS SIDE WALL ABSORBER

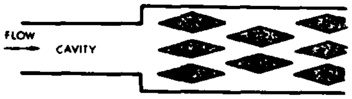

(c) DIAMOND SHAPED POROUS ABSORBERS

Figure 1. Examples of Pressure Wave Suppressors used in Repetitively Pulsed Lasers^{3,4}.

A model which was previously developed^3 for a vented (passive) duct absorber is first discussed. This model has been presently modified to better account for the effect of the vents on the duct flow, particularly in the presence of a mean ("grazing") flow and very small duct pressure perturbations which are of interest for fusion-type lasers.

A series of experiments, designed to test the effectiveness of simple vented duct absorbers, is then presented. A shock tube with a conventional driver, activated by a pressure-burst diaphragm and connected to a long vented driven section was used for these experiments. Pressure histories were recorded in the driver and along the vented driven section, starting with the diaphragm burst. These pressure traces were compared with the model predictions and found to be generally in good agreement.

The experiments show that the vented duct typically reduces the initial over-pressure in the driver by a factor of 10^2 on a time scale equal roughly to ten times the acoustic transit time through the driver. Further reductions in pressure fluctuations are hard to come-by with this vented duct absorber. Small pressure fluctuations, at the 10^{-3} level, persist for times longer than 100 times the driver's acoustic transit time. Improvements in the performance of vented duct absorbers are clearly needed to make such absorbers suitable for the laser fusion applications.

ANALYSIS

The unsteady flow in a vented duct can be described approximately by the time-dependent, one-dimensional flow conservation equations:

$$\frac{\partial}{\partial t}(\rho) + \frac{\partial}{\partial x}(\rho u) + \sigma_1 = 0 \qquad \text{I}$$

$$\frac{\partial}{\partial t}(\rho u) + \frac{\partial}{\partial x}(\rho u^2) + \frac{\partial p}{\partial x} + \sigma_2 = 0 \qquad \text{II}$$

$$\frac{\partial}{\partial t}\left[\rho\left(e + \frac{u^2}{2}\right)\right] + \frac{\partial}{\partial x}\left[\rho u\left(e + \frac{u^2}{2} + \frac{p}{\rho}\right)\right] + \sigma_3 = 0 \qquad \text{III}$$

with the effects of the vents represented by the volumetrically distributed source/sink terms, σ. We assume further that the gas is ideal and calorically perfect and therefore

$$p = \rho RT \quad \text{and} \quad e = C_v T = \frac{1}{\gamma - 1}\left(\frac{p}{\rho}\right) \qquad \text{IV}$$

The conditions for outflow and inflow through the vents are shown schematically in Figure 2. Subscript "a" designates the given stationary conditions outside the duct. For <u>outflow</u>, when $p > p_a$, the sink terms can be written as:

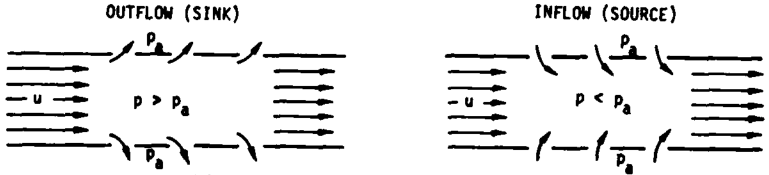

Figure 2. Schematic Representation of the Effect of Side-Wall Vents on One-Dimensional Duct Flow.

$$\sigma_1 = \frac{a\dot{m}^-}{A} = \frac{4\alpha\dot{m}^-}{D},\ \sigma_2^- = u\sigma_1^- \text{ and } \sigma_3^- = C_p T_o \sigma_1^- \qquad \text{V}$$

whereas for <u>inflow</u>, when $p < p_a$, the source terms are given by

$$\sigma_1{}^{+} = \frac{-a\dot{m}^{+}}{A} = \frac{-4\alpha\dot{m}^{-}}{D}\ ,\ \sigma_2{}^{+} = 0 \text{ and } \sigma_3{}^{+} = C_pT_a\sigma_1{}^{+} \qquad \text{VI}$$

Here a is the vent area per unit duct length, A is the duct cross-section, D its hydraulic diameter and α the percent-open-area of the duct wall. T_o is the stagnation temperature of the gas inside the duct and $\dot{m}$ is the mass flow per unit vent area.

The determination of the mass flow per unit area through the vent orifices, $\dot{m}$, as a function of the gas denisty, the two pressures, p and p_a, and the "grazing" velocity in the duct, u, is clearly the key to a proper evaluation of the effect of the vents on the duct flow and the pressure suppression characteristics of a vented duct.

The mass flow per unit vent area can be written as $\dot{m} = C_D\dot{m}_i$, where C_D, the vent discharge coefficient, is a function of the pressures p and p_a and the grazing velocity u, and m_i, the ideal mass flux through the vents, is defined as the mass that would be flowing out of the vent (per unit area) under isentropic flow conditions.

$$\dot{m}_i{}^{-} = \begin{cases} \dfrac{p}{\sqrt{RT}}\left[\left(\dfrac{2\gamma}{\gamma-1}\right)\left(\dfrac{p_a}{p}\right)^{2/\gamma}\left[1-\left(\dfrac{p_a}{p}\right)^{\frac{\gamma-1}{\gamma}}\right]\right]^{\frac{1}{2}} & \text{if } \dfrac{p_a}{p} > \left(\dfrac{2}{\gamma+1}\right)^{\frac{\gamma}{\gamma-1}} \\[2ex] \dfrac{p}{\sqrt{RT}}\left[\gamma\left(\dfrac{2}{\gamma+1}\right)^{\frac{\gamma+1}{\gamma-1}}\right]^{\frac{1}{2}} & \text{if } \dfrac{p_a}{p} < \left(\dfrac{2}{\gamma+1}\right)^{\frac{\gamma}{\gamma-1}} \end{cases} \qquad \text{VII}$$

for outflow (i.e. - when $p > p_a$). A similar expression would apply for inflow (when $p < p_a$) with the roles of p and p_a reversed.

For zero grazing velocity (u=0) the discharge coefficient, designated here by C_D^0, was extensively measured and documented (see, e.g., Ref. 5). The effect of a grazing velocity (u≠0) has also been measured, mainly be researchers interested in shock attenuation and vented duct acoustics[6-10]. There is howver, no analytical model which is uniformly valid for a wide range of duct (or grazing) velocities and pressure differences across the vents.

One promising approach for modeling the effect of grazing flow on the vent discharge coefficient was recently proposed by B. Sturtevant[11]. In this approach the well known solution for an incompressible two-dimensional duct flow near a line sink of finite strength placed across one wall is first used to calculate the force acting on the mass discharged through the sink, in a direction perpendicular to the duct, as a function of the sink strength (or mass outflux). A momentum balance is then applied in the same direction with the ideal sink replaced by a finite slit. From this momentum balance, the actual mass flow through the slit, as a function of the pressure difference across the slit, $|p-p_a|$, and the grazing velocity, u, can be determined. The result is

$$C_D \equiv \frac{\dot{m}}{\dot{m}_i} = \left|\frac{u}{V_i}\right| \left[\sqrt{K_1^2 + K_2^2\left(\frac{V_i}{u}\right)^2} - K_1\right] \qquad \text{VIII}$$

where V_i, the ideal jet velocity through the slit, is defined by

$$V_i \equiv \frac{2|p-p_a|}{\rho} \qquad \text{IX}$$

Both K_1 and K_2 are constants associated with the pressure integration over a control volume which contains the mass discharged through the side-wall slit.

They were left here as indeterminate constants, to be selected so as to fit a wide range of available experimental data and thereby account, in an approximate fashion, for departures from the ideal incompressible flow assumed in this model.

For a zero grazing velocity (or $u/V_i << 1$), Eq. VIII yields $C_D=C_D^0=K_2$, and K_2 should therefore be taken from Perry's[5] experimental data for C_D. In the range where $V_i/u << 1$, Eq. VIII should be compared with the experimental data obtained by Rogers and Hersh[10] for the same flow regime. They found $C_D \simeq 0.65 (V_i/u)^{0.9}$ for outflow and $C_D \simeq 0.94 (V_i/u)^{1.1}$ for inflow. Eq. VIII predicts a linear dependence of C_D on (V_i/u) for this regime. Neglecting the small difference in power of V_i/u, the comparison yields $K_1=0.31$ for outflow and $K_1=0.21$ for inflow. $K_2 = C_D^0 \doteq 0.63$ was used for this comparison since the data[10] was taken under essentially incompressible flow conditions.

A comparison of experimental data and model predictions for C_D as a function of v_i/u is presented in Figure 3. Although the agreement is less than perfect it is compatible with our vented duct flow model, considering other approximations made in deriving this model. The duct flow model as used in this study is then formulated in terms of Equations I through IX, which can be solved numerically for a variety of initial and boundary conditions. Solutions were obtained using the Lax-Wendorf differencing scheme with Flux Corrected Transport[3,12]. Typical results are presented in the next section and compared with experiments.

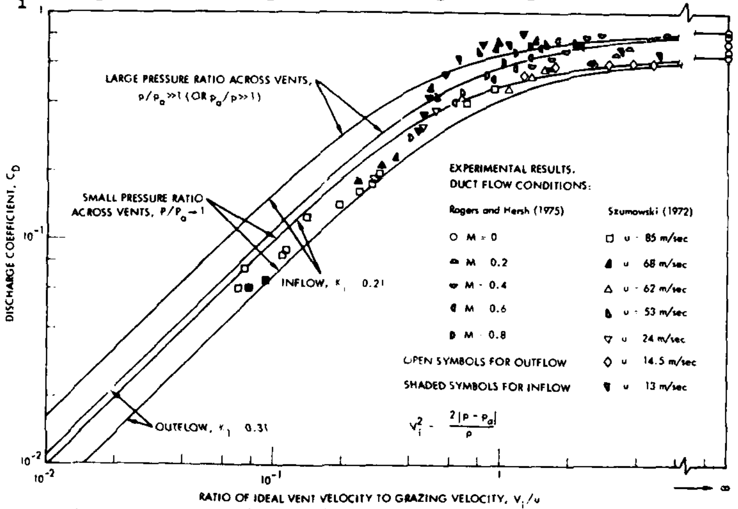

Figure 3. Vent Discharge Coefficients vs. Normalized Ideal Jet Velocities.

EXPERIMENTS

The experiments performed had two major objectives. One was to check and validate the code described in the previous section, and the other to test the effectiveness of vented duct absorbers under conditions which simulate the operation of pulsed lasers.

For the first set of experiments we have used a conventional shock tube, depicted schematically in Figure 4. A 24" driver section was used to generate shocks which were propagated into a 78" solid-wall (unvented) tube. Both had a square internal cross-section of 3.5 x 3.5". Air was the working fluid with pressure in the driven section fixed at 1 atm while driving pressure was varied

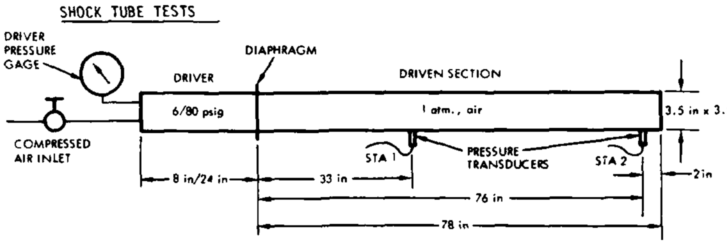

Figure 4. Shock Tube Used for Preliminary Code Verifications Tests.

between 6 and 80 psig. Pressure traces were recorded near the mid point and near the closed, downstream end of the driven section. Both short time (0 to 10 ms) and long time (0 to 100 ms) traces were recorded. These experiments were very useful in checking out the basic 1-D transient code, without the sink and source terms, and the numerical procedure used.

Results of a test with 80 psig driver pressure are first shown in Figure 5 and compared with the code predictions. For the first 10 ms the code appears to be in excellent agreement with the experimental results. The magnitude of the incident wave as well as the first wave reflected from the closed end of the driven section are properly predicted both at the center of the driven section (Station 1) and near it's closed and (Station 2). The time of arrival and temporal variation of these first pressure pulses is also properly predicted. On a longer time scale, from 0 to 100 ms, a discrepancy developes between the measured and calculated pressure traces. First there are secondary waves which show up in the experiments but are not predicted by the code. The experiments show also a faster decay in the amplitude of the pressure pulses and a gradual delay in their time of arrival, as compared to the calculations. We believe that all these effects can be attributed to non-ideal processes in the shock tube, such as wave interactions with the diaphragm petals and with boundary layers, effects which were not considered in the code development. This conclusion is supported by the observation that as the driver pressure and the strength of the initial wave were reduced, the agreement between experiments and code predictions has improved. An experiment with 6 psig initial driver overpressure is shown in Figure 6. A 0.00025" Mylar diaphragm was used for this later case whereas a 0.012" aluminum diaphragm had to be used for the 80 psig case. The decay of the primary waves and the strength of the secondary waves both diminish significantly as the diaphragm thickness (and mass) and the strength of the initial waves are decreased. The results of the code calculation are very close now to the experimental results.

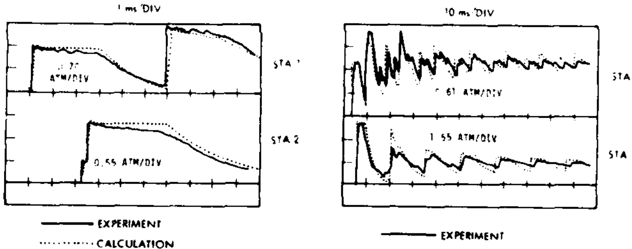

Figure 5. Pressure Pulse Traces in the Conventional Shock Tube (of Fig. 5) for 80 psig Driver Pressure; Comparison of Code Calculations and Experiments.

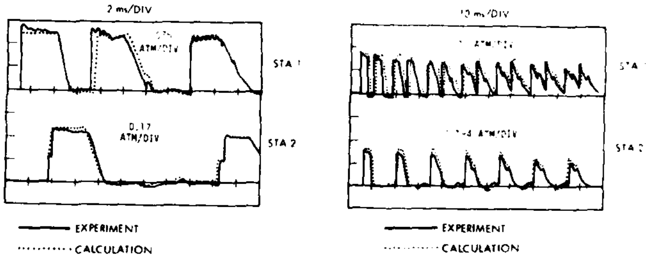

Figure 6. Same as Figure 5, for 6 psig Driver Pressure.

The analytical model and code were developed mainly to predict the interaction of pressure waves with vented-duct acoustic suppressors. When a vented duct is used, the initially strong pressure waves are expected to be suppressed by a factor of about 100 on a time scale of 10 ms or less. We have concluded therefore that the basic code would be adequate for our purposes, despite the discrepancies which showed up over the long test periods, when compared with experiments in which high driver overpressures were used.

For the main series of experiments the solid wall driven section was replaced by a similar duct which was vented on one side, as depicted in Figure 7.

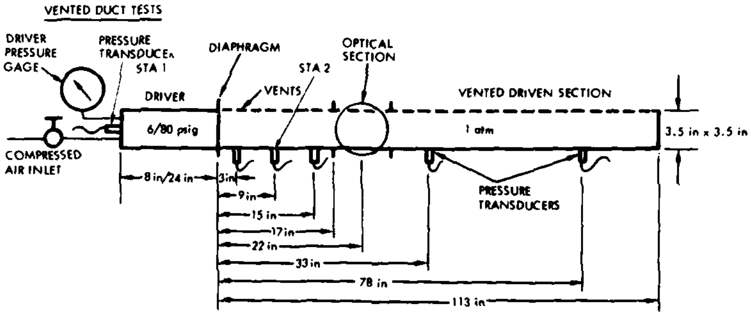

Figure 7. Shock Tube With Vented Duct Used for Pressure Suppression Experiments.

The top wall of the new driver section was perforated, with three holes of 23/64" drilled in symmetric rows across the top wall, 1.2" apart, to give a net 7.2% open area for this wall. An optical section with Schlieren grade windows was also incorporated in this duct to permit the application of optical diagnostics for the flow field generated after the diaphragm burst.

Results for the vented tube with a 24" driver and 7 psig initial overpressure are first shown in Figure 8. The first two traces on the left show the complete pressure histories at the two selected stations, one in the driver end wall and the other placed 9" downstream of the diaphragm up to 20 ms after the diaphragm burst. The figure on the right shows the same two traces with a higher resolution. The code calculations and the experimental results are in good agreement to within 20% of the initial overpressure. The code fails to predict, however, a wave which is reflected from the closed end of the vented tube and shows up at about 18 ms at station 2. It also fails to predict the

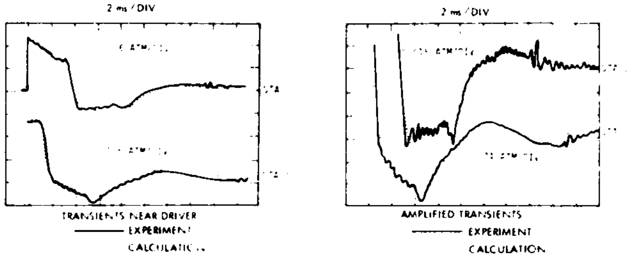

Figure 8. **Experimental Results and Code Calculations for a Vented Duct with 7.2% Open Area Connected to a 24" Driver with 7 psig Initial Overpressure.**

observed high frequency pressure oscillations, which appear to be amplified by this reflected wave.

Results for an 8" driver with 7 psig initial overpressure are shown in Figure 9. Similar discrepancies were found here between the code predictions and the experimental results. The observed high frequency oscillations, which were not predicted by the code, are particularly bothersome, since they have an amplitude of about 8 x 10^{-3} of the initial driver overpressure, a result

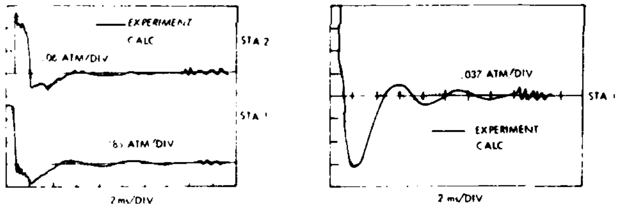

Figure 9. Same as Figure 8, for an 8" Driver with 7 psig Initial Over-Pressure.

which would not be admissible for most pulsed laser applications. We have observed these pressure fluctuations to persist on a longer time scale, at a level of 1.5 x 10^{-3} times the initial overpressure, up to 100 ms after the diaphragm burst, as is shown in Figure 10.

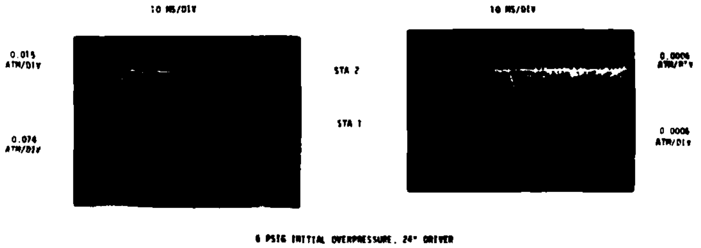

Figure 10. Long-Term Pressure Oscillations in a Vented Duct.

We have taken shadowgraph pictures of the shock and pressure wave interactions with the vented top wall of the shock tubes driven section. Some results are shown in Figure 11. The shock is moving from right to left. The jets coming out of the vents in the top wall are clearly visible up to about 5.5 ms after the diaphragm burst. The diffraction of waves from the vents can

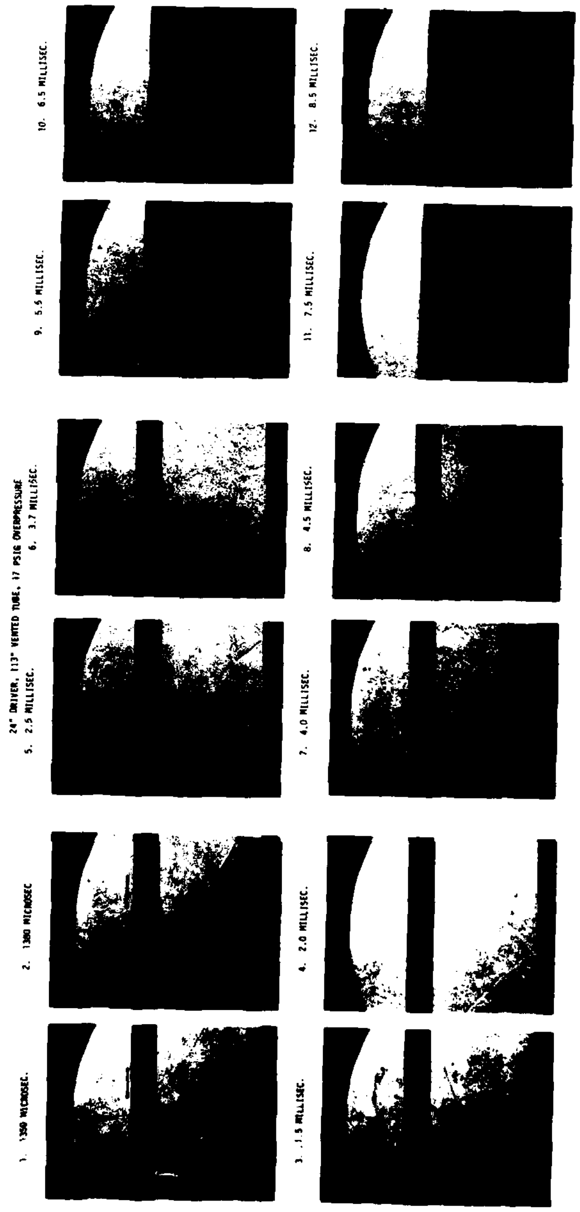

Figure 11. Shadowgraphs of Wave Interactions with a Vented Duct.

also be seen up to 4.0 ms. At this time the turbulent head of the driver gas fills up the field of view and it becomes difficult to detect any details of the flow field. Even so, we were able to see that at about 6.5 ms, when the pressure undershoot reaches the optical section, the flow through the vent is reversed. The transverse flow and pressure fields associated with the vent flow reversal is presumably responsible for the high frequency pressure oscillations detected in the experiments. It is interesting to note that the dominant frequency of the long-term oscillations is about 900 Hz, which corresponds roughly to a "quarter-wave" pressure oscillation across the short (transverse) dimension of the vented tube. A transverse pressure oscillation thus appears to be superimposed on the initially strong longitudinal mode. When these oscillations have a sufficiently low amplitude, no jets are generated and the vents are no longer dissipative. This can explain the persistance of the high frequency oscillations.

CONCLUSIONS

The one-dimensional model presented here can properly predict the short term (∿10 ms) interactions of pressure waves with a perforated duct, but it fails to predict the longer term effects. Further code modifications will be required to account for the long-term pressure oscillations observed in the experiments. A linearized model should be appropriate for the long term behavior and amenable to analytical solutions. Such solutions can then be incorporated into the one-dimensional numerical code to improve its predictive capabilities.

As far as the performance of the vented duct is concerned, it is quite clear that a vented duct alone can not produce the pressure attenuation required for fusion-type laser. Some additional dissipative devices are needed to affect the small, long term, pressure fluctuations. This could be done by placing flow-through porous absorbers inside the perforated duct or along the duct walls, either on top or instead of the perforations. Such modifications of the vented tube may also obviate the need for any major modifications of our model, other than adding proper dissipative (drag and heat transfer) components to the source/sink terms.

REFERENCES

1. R. Hofstadter, IEEE Transactions on Nuclear Science, 18, 33 (1977).
2. D. B. Henderson, Proceedings of the XIth International Symposium on Shock Tubes and Waves, 542 (1977).
3. D. R. Ausherman, E. I. Alber and E. Baum, AIAA 16th Aerospace Science Meeting, Huntsville, Al., Paper No. 78-237 (1978).
4. K. O. Tong, C. J. Knight and B. N. Srivastava, AIAA 5th Aeroacoustics Conference, Seattle, Wa., Paper No. 79-0602 (1979).
5. J. A. Perry, Jr., Transactions of the ASME, Paper No. 48-A-146 (1949).
6. G. M. Stokes, D. D. Davis, Jr., and T. B. Sellers, NACA TN-3085 (1954).
7. A. P. Szumowski, Proceedings of the VIIIth International Shock Tube Symposium, 14 (1971).
8. J. H. T. Wu and P. P. Ostrowski, Proceedings of the VIIIth International Shock Tube Symposium, 15 (1971).
9. A. P. Szumowski, Archieve of Mechanical Engineering-Poland ("Archiwum Budowy Maszyn") 14, 4, 559 (1972).
10. T. Rogers and A. S. Hersh, AIAA 2nd Aeroacoustics Conference, Hampton, VA., Paper No. 75-493 (1975).
11. B. Sturtevant, Private Communication.
12. D. L. Book, J. P. Boris and K. Hain, NRL Mem. Rept. No. 3021, Naval Research Laboratory, Washington D.C. (1975)

ENERGY AND POWER REQUIREMENTS FOR DIRECT INITIATION OF SPRAY DETONATIONS

ELI K. DABORA

Department of Mechanical Engineering
The University of Connecticut, Storrs, CT 06268, USA

A method for determining the critical energy and power requirements for the direct initiation of detonation in spray detonations is described. The method is based on a model of the reaction zone in which blast waves due to the energy release from each drop play a significant role. It is shown that the critical energy and power are dependent on the drop diameter, the ignition delay, the energy deposition time and an energy parameter that describes the energy time variation. In particular it is shown that the ignition delay plays a more pronounced role in the spray detonation than in all gaseous detonations. An approximate method for determining the effect of equivalence ratio on the critical energy and power is also presented and the results indicate that when the ignition delay is chemically controlled the trends are similar to those observed in gaseous detonations.

INTRODUCTION

Direct or blast initiation of gaseous detonations has been the subject of many articles. In a recent review[1], Lee describes the theoretical models used for determining the minimum or the critical blast energy necessary for a continued detonation. Sichel[2] developed a method for calculating critical energies for a particular fuel-oxidizer mixture at different equivalence ratios provided ignition data is available. Knystautas and Lee[3] indicated on the basis of their experiments in acetylene-oxygen that detonation initiation depends not only on an energy criterion but on the rate of energy deposition (power) as well.

The purpose of this paper is to describe a method for determining both energy and power requirements for spray detonations. Such detonations are now well documented[4-6]. Although they are similar to gaseous detonations, they exhibit enough differences under certain conditions, to warrant a different analysis. The key to this analysis is the reaction zone behind the front of the detonation wave. An idealized model of this zone has been suggested by the author[7]. This model will be briefly described first and then used in the analysis of energy and power requirements.

REACTION ZONE MODEL

The reaction zone model is based on photographic observations of the detonation phenomenon[4,8] in a medium consisting of fuel drops in a gaseous oxidizer. When a detonation takes place, the passage of the front induces a convective flow over the drops which because of their inertia, remain practically stationary. The convective flow serves to break up the drops and after a suitable time delay, t_{ig}, the partially or totally disintegrated drop ignites, resulting in heat release. Under certain conditions, this heat release is rapid enough to induce a blast wave around each drop within the reaction zone. The blast wave propagates towards the front reinforcing it after interaction.

In the idealized model the drops are assumed to be uniform in size and uniformly spaced, and the blast waves to originate at the center of the drops which remain stationary. Except for distortion due to the convective flow behind the front, the blast waves are considered spherical, with time dependent heat release in the form:

$$E = Wt^{\beta} \qquad \text{I}$$

with a duration $t = t_i$. In addition to being reasonable, this form of energy deposition has been used in self-similar[9] and perturbation solutions[10] of blast wave trajectories.

As the front propagates between drops it tends to decelerate; however, when it is overtaken by the blast waves from the drops it is strengthened. A steady detonation is then assumed possible when a balance between these two considerations is reached. It is shown by Dabora[7] that provided t_{ig}, t_i and β are known the Mach number, M_{bw} of the blast wave when it overtakes the front can be determined from the following equation:

$$t_{ig}/t_b = \{Z(\theta_2/\theta_1)^{\frac{1}{2}}/M - (\rho_1/\rho_2)w\}\ (R_0/a_2 t_b)^{3/(3-\beta)}(t_i/t_b)^{-\beta/(3-\beta)} \qquad \text{II}$$

where:

$$Z = R/R_0 = Z(M_{bw},\ \beta) \qquad \text{III}$$

$$w = a_2 t/R_0 = w(M_{bw},\ \beta) \qquad \text{IV}$$

$$R_0 = D\bar{Q}(p_1/p_2)^{1/3}(\rho_\ell/\rho_1)^{1/3} = R_0(M,\ \gamma,\ \bar{Q},\ \rho_\ell) \qquad \text{V}$$

and

$$t_b = T_b D/u_2(\rho_2/\rho_\ell)^{\frac{1}{2}} = t_b(M,\ D, \rho_\ell\ ) \qquad \text{VI}$$

Further, since M_{bw} is usually close to unity, the change in M can be approximated by

$$\Delta M/M \cong M_{bw} - 1 \qquad \text{VII}$$

Figure 1 shows typical calculations for $\Delta M/M$ which can be related to t_{ig} as:

$$\Delta M/M = k(t_{ig}/t_b)^{-m} \qquad \text{VIII}$$

Considering planar cylindrical or spherical geometry for the detonation front, the Mach number decrement as the front passes through a distance S is

$$\Delta M/M \cong -\ (\alpha+1)(S/R)/2 \qquad \text{IX}$$

Addition of IX to either VII or VIII and setting the net $\Delta M = 0$ give the

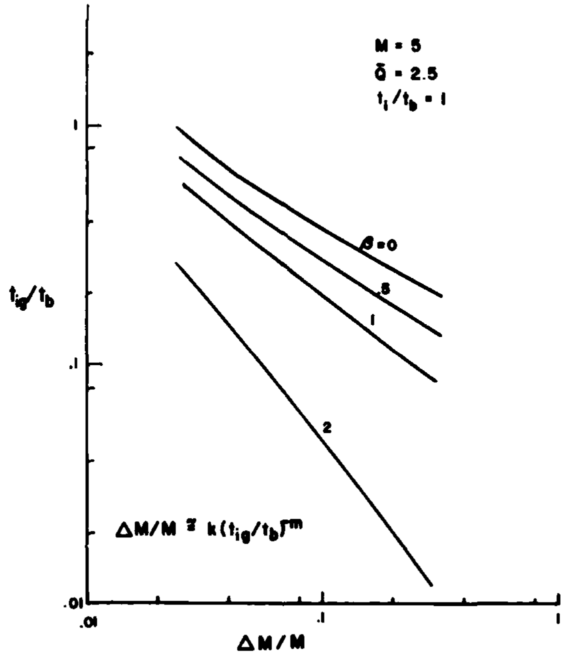

Figure 1. The Increment of the Frontal Mach Number

condition necessary for a steady detonation.

CRITICAL RADIUS AND MINIMUM INITIATION ENERGY

The condition for a steady detonation as described in the previous section corresponds to a critical detonation radius R* above which detonation continues without deceleration. If blast initiation is considered the blast energy must be such that a critical Mach number is achieved at R*. Although the critical Mach number in gaseous detonations has been observed to be somewhat lower than the Chapman-Jouguet Mach number, in this paper, it will be assumed that the latter is the critical Mach number. Since the classical constant energy blast wave shows that:

$$E = J_\alpha K_\alpha p_1 R^{\alpha+1} M^2 \qquad \text{X}$$

substituting R by R* and M by M_{CJ}, the critical energy for initiation can be determined. The procedure is as follows: for a given fuel oxidizer mixture M_{CJ} can be calculated (e.g. Gordon and McBride[11]); with t_{ig}, t_i and β known or assumed M_{bw} can be determined by trial and error from II; with S known, R* can be determined from IX and the critical energy E* determined from X. However, for better insight into the effect of the important parameters on E*, the approximation VIII can be used. Thus, combination of VIII, IX and X gives:

$$E^*/D^{\alpha+1} = J_\alpha K_\alpha p_1 [(\alpha+1)(t_{ig}/t_b)^m (S/D)/2k]^{\alpha+1} M^2 \qquad \text{XI}$$

In this equation S/D is a function of the fuel oxidizer ratio and E* can be scaled to the drop diameter. Comparison of this equation with its counterpart for a gaseous detonation shows that the dependence of E* on t_{ig} is much more pronounced for the spray case because m is usually greater than unity. This may be due to the discrete manner in which the heat is released. It should be noted from Figure 1 however, that as β increases m approaches unity.

To see the effects of t_{ig}/t_b, t_i/t_b and β, a reference critical energy E^*_{ref} corresponding to $t_{ig}/t_b = t_i/t_b = 1$ and $\beta = 0$ can be used as a reference parameter. It can then be shown that for sprays with the same drop diameter and composition:

$$E^*/E^*_{ref} = \{(k_{ref}/k_{\beta 1})[(t_{ig}/t_b)(t_i/t_b)^{\beta/(3-\beta)}]^{m_{\beta 1}}\}^{(\alpha+1)} \qquad \text{XII}$$

where k_{ref}, $k_{\beta 1}$ and $m_{\beta 1}$ can be determined from plots similar to Figure 1. For the spherical case ($\alpha = 2$), this equation is plotted in Figure 2 when M and $\overline{Q}$ are 5 and 2.5 respectively. It can be seen that t_{ig}/t_b has a pronounced effect at all values of β whereas the effect of t_i/t_b becomes more pronounced as β increases. The effect of β however is influenced by the value of t_i/t_b and apparently can go in either direction. As t_{ig}/t_b or t_i/t_b increase it becomes obvious that the initiation energy requirement can become so high that no practical source can be adequate for initiation.

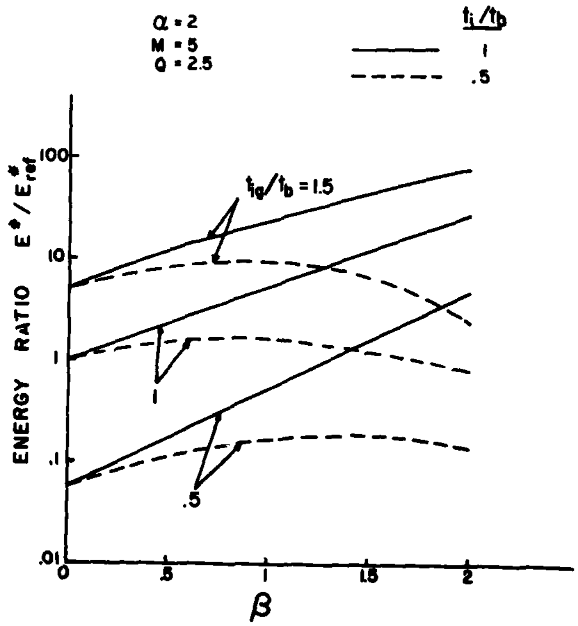

Figure 2. Effect of β and t_i/t_b on the Critical Energy

POWER REQUIREMENT

As was mentioned earlier, there is evidence that not only a critical energy is necessary for detonation initiation but a critical power as well. If the initiating blast energy is also in the form of equation I, it can be shown from the self-similar solution of variable energy blast waves[9] that

$$E = K_{\alpha}p_{1}J_{\alpha\beta}\left(\frac{\alpha+3}{\beta+2}\right)^{\beta} R^{(\alpha+1-\beta)} M^{(2+\beta)} (a_{1}t)^{\beta} \qquad \text{XIII}$$

With β = 1, and replacing R by R* and M by M*, differentiation of E with respect to time gives the energy rate necessary to produce the requisite critical conditions. To verify this, the data of Knystautas and Lee[3] were examined. First, the critical radius as a function of M is determined on the basis of the ignition delay equation and the method outlined by Lee and Ramamurthi[12]. Then applying XIII with β = 0 and using the experimentally determined critical energy of .11J/cm the corresponding R* and M* are found to be .27 cm and 4.64 respectively. The latter gave an induction time of .09 μsec. Further using XIII with β = 1, and the calculated values of R* and M*, the power is found to be .055Mw/cm which is within a factor of about two from the simply calculated power:

$$P^* = E^*/t_{ig} \qquad \text{XIV}$$

suggested by Lee and Ramamurthi. Because of its simplicity this equation is adopted in this paper. It follows then from XI that

$$P^*/D^{\alpha+1} = J_{\alpha}K_{\alpha}p_{1}(\alpha+1)^{\alpha+1} (S/D)^{\alpha+1} (t_{ig}/t_{b})^{(\alpha+1)m-1}M^{2}t_{b} \qquad \text{XV}$$

Table 1 shows some representative values of E* and P* for the conditions listed in the table which correspond to liquid hydrocarbon-air mixtures.

Table 1. Representative Values of E* and P*

$M = 5$, $p = 1$ atm., $\overline{Q} = 2.5$, $S/D = 20$, $t_{ig}/t_{b} = 1$, $\beta = 0$, $k = .0235$, $m = 1.35$

α	R*/D	$E^*/D^{\alpha+1}$(J/cm³)	E*	D(μ)	P*
0	425.5	1.78×10^{3}	1.78×10^{2}	1000	5.89
			1.78×10	100	5.89
			(J/cm²)		(Mw/cm²)
1	851	9.98×10^{6}	9.98×10^{4}	1000	3.30×10^{3}
			9.98×10^{2}	100	3.30×10^{2}
			(J/cm)		(Mw/cm)
2	1276.5	3.88×10^{10}	3.88×10^{7}(J)	1000	1.32×10^{6}(Mw)
			3.88×10^{4}	100	1.32×10^{4}

For comparison a planar shock at M = 5 produced in air by a 1m He driver can be calculated to be caused by 418 J/cm² energy input at a rate of .43 Mw/cm², and a dense explosive like tetryl releases 4.7 KJ/gm. Table 1 can be used in conjunction with XII or Figure 2 to obtain E* and P* at the desired values of β, t_{ig}/t_{b} and t_{i}/t_{b}.

EFFECT OF EQUIVALENCE RATIO

Sichel[2] has shown that if ignition delay times for a given fuel-oxidizer mixture at different stoichiometry can be related to the ignition delay at a given equivalence ratio for which the critical energy is known, then the critical energy at other equivalence ratios can be predicted analytically. His analysis for acetylene-oxygen and MAPP-air showed good agreement with experiment. In order to use Sichel's method in spray detonation, the variation of ignition delay with equivalence ratio need to be known. The equivalence ratio of course affects the propagation Mach number and this influences the ignition delay. Pierce et al.[13] advanced the idea that the ignition in spray detonation can be made up of two parts namely, a mechanical portion due to partial breakup of the drops and a chemical portion which is related to the type of fuel and oxidizer used, the mixing and evaporation that take place in the wake of the droplet and the temperature. Thus:

$$t_{ig} = t_m + t_{ch} \qquad \text{XVI}$$

where the mechanical time, t_m is estimated to be 1/3 the breakup time, t_b. For diethyl-cyclohexane (DECH) oxygen a chemical time can be deduced from their work. The mechanical and chemical times are plotted in Figure 3 against the reciprocal of the stagnation temperature behind the shock. The chemical time is little affected by the drop size and is shown as one line. One can see that there are regimes in which the mechanical time dominates and others in which the chemical time dominates. For example at M = 5 for droplets larger than 1000 μ the mechanical time is controlling whereas at M = 4 the chemical time is controlling for droplets lower than 100 μ.

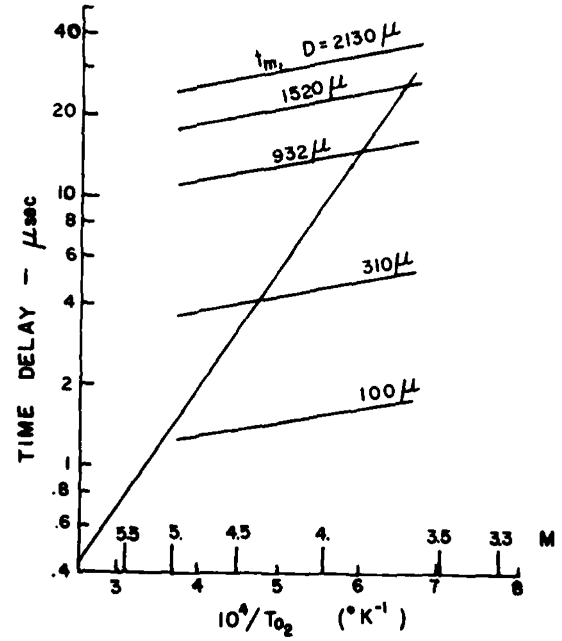

Figure 3. Mechanical and Chemical Time Delays for DECH in Oxygen

If Figure 3 can be generalized to other mixtures, it is possible to make predictions for E* and P* at different equivalence ratios. Incidently, data on heptane-air presented by Lu et al.[6] show a steeper line than the chemical time line shown in Figure 3.

To get a feel for the effect of equivalence ratio some reasonable approximations are made first. If an Arrhenius expression exists for t_{ch} it can be shown that

$$t_{ch} \propto 1/M^n \qquad \text{XVII}$$

where $11 < n < 17$ for an activation energy of 20-30 Kcal/mole in the temperature range corresponding to a shock at $4 < M < 6$. Also

$$t_m \propto t_b \propto 1/M \qquad \text{XIX}$$

and the Mach number of propagation

$$M^2 \propto q \qquad \text{XX}$$

where q is the heat release per unit mass of mixture. Further,

$$q/q_s \cong \phi(\mu_s+1)/(\mu_s+\phi) \qquad \phi \le 1 \qquad \text{XXI}$$

$$\cong (\mu_s+1)/(\mu_s+\phi) \qquad \phi > 1 \qquad \text{XXII}$$

and

$$(S/D)/(S/D)_s = 1/\phi^{1/3} \qquad \text{XXIII}$$

Using equation IX (normalized with respect to the stoichiometric case) in conjunction with relations XVII - XXIII, after noting that when t_m is controlling t_{ig}/t_b is not a function of M, one can show that for t_m controlling (i.e., large drops)

$$E^*/E^*_s = [(S/D)/(S/D)_s]^{\alpha+1}(M^2/M^2_s)(k_s/k)^{\alpha+1} \qquad \text{XXIV}$$

and since $k_s/k = 1$ for $\phi \le 1$ and $\phi^{1/3}$ for $\phi > 1$:

$$E^*/E^*_s = (1/\phi^{1/3})^{\alpha+1}\frac{(\mu_s+1)\phi}{\mu_s+\phi} \qquad \phi \le 1 \qquad \text{XXV}$$

$$= (\mu_s+1)/(\mu_s+\phi) \qquad \phi > 1 \qquad \text{XXVI}$$

Similarly for t_{ch} controlling (i.e., small drops)

$$E^*/E^*_s = [\frac{\mu_s+\phi}{(\mu_s+1)\phi}]^{\frac{m(n-1)(\alpha+1)-2}{2}} (1/\phi)^{(\alpha+1)/3} \qquad \phi \le 1 \qquad \text{XXVII}$$

$$= (\frac{\mu_s+\phi}{\mu_s+1})^{\frac{m(n-1)(\alpha+1)-2}{2}} \phi^{(m-1)(\alpha+1)/3} \qquad \phi > 1 \qquad \text{XXVIII}$$

The effect of ϕ on P* can be found by using equation XV from which it can be shown, after using the same approximation above that, for t_m controlling:

$$P^*/P^*_s = (1/\phi^{1/3})^{\alpha+1}[\frac{(\mu_s+1)\phi}{\mu_s+\phi}]^{1/2} \qquad \phi \le 1 \qquad \text{XXIX}$$

$$= (\frac{\mu_s+1}{\mu_s+\phi})^{1/2} \qquad \phi > 1 \qquad \text{XXX}$$

and for t_{ch} controlling

$$P^*/P^*_s = [\frac{1}{\phi^{1/3}}]^{\alpha+1} [\frac{(\mu_s+1)\phi}{\mu_s+\phi}]^{\frac{(n-1)[(\alpha+1)m-1]-1}{2}} \qquad \phi \le 1 \qquad \text{XXXI}$$

$$P^*/P_s^* = \left(\frac{\mu_s+\phi}{\mu_s+1}\right)^{\frac{(n-1)[(\alpha+1)m-1]-1}{2}} \phi^{\frac{m-1}{3}(\alpha+1)} \qquad \phi > 1 \qquad \text{XXXII}$$

From the above equations for E^*/E_s^* and P^*/P_s^*, it can be seen that when t_m is controlling the effect of ϕ is rather small for mixtures with $\mu_s \cong 16$. On the other hand when t_{ch} is controlling the effect of ϕ is very large because of the usually large value of n. Plots of the effect of ϕ when n = 15 are shown in Figures 4 and 5. Figure 4 exhibits the same kind of trends given by Sichel for the gaseous detonations in that lean mixtures require considerably higher critical energy than the stoichiometric or rich mixtures.

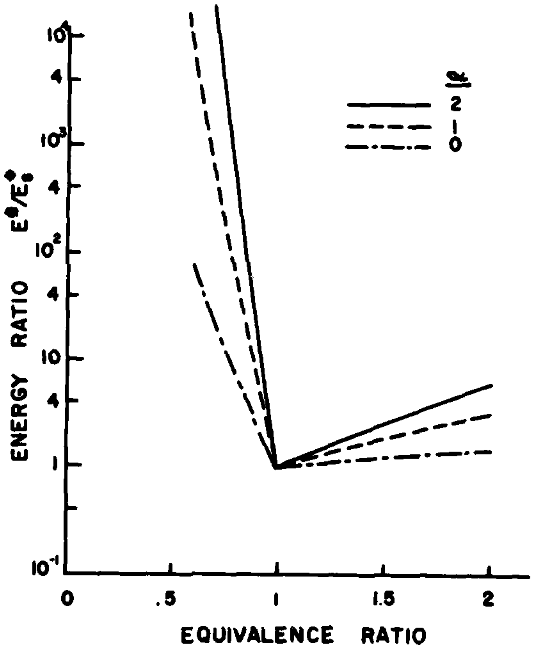

Figure 4. Effect of Equivalence Ratio on Critical Energy (Chemical Time Controlling, n = 15)

CONCLUSIONS

A method for evaluating the critical initiation energy and power for spray detonation has been developed. The basic data needed to make use of the method are the ignition delay and the temporal variation of the heat release from each drop, which points out the need of such data. A simplified analysis on the effect of equivalence ratio is also made. However, in principle, detailed calculations of that effect could equally be performed.

The similarity between the spray detonations and the gaseous detonations is pointed out. However, it would be interesting to determine analytically the conditions necessary for identical behavior.

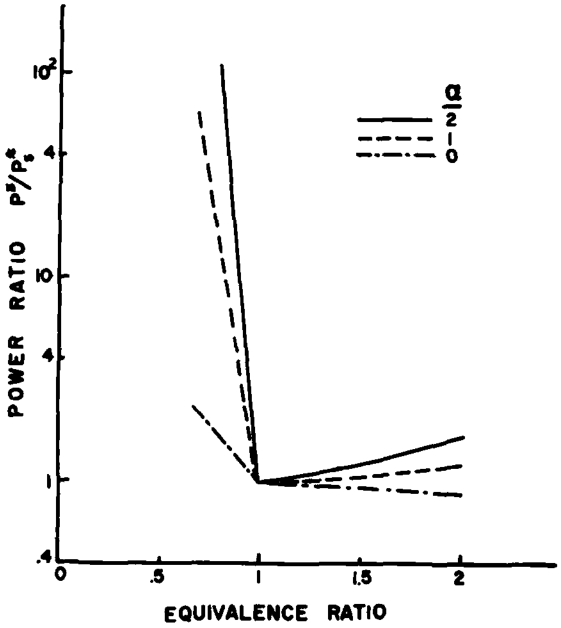

Figure 5. Effect of Equivalence Ratio on Critical Power
(Chemical Time Controlling, n = 15)

NOMENCLATURE

a = Velocity of sound
D = Drop diameter
E = Energy
E^* = Critical energy, energy/unit length or energy/unit area for $\alpha = 2,1$ or 0 respectively.
J_α, $J_{\alpha\beta}$ = Nondimensional blast wave energy integral for constant energy or variable energy blast wave
K_α = 4π, 2π or 1 for $\alpha = 2$, 1 or 0 respectively
k = Value of $\Delta M/M$ at $t_{ig}/t_b = 1$
M = Chapman Jouguet Mach number
M_{bw} = Blast wave Mach number
m = Exponent in equation VIII
n = Exponent in relation XVII
P = Power
P^* = Critical power
p = Pressure
Q = Heat per unit mass of liquid fuel
$\bar{Q}$ = $(Q/24R_g\theta_1)^{1/3}$ for $\phi \leq 1$ or $(Q/24R_g\theta_1\phi)^{1/3}$ for $\phi > 1$
q = Heat release per unit mass of mixture
R = Detonation or blast radius
R^* = Critical radius
R_0 = Explosion radius defined in equation V
R_g = Oxidizer gas constant
S = Spacing between drops

T_b = Nondimensional breakup time $\cong$ 4
t = Time
t_b = Breakup time
t_{ch} = Chemical time delay
t_i = Energy input time
t_{ig} = Ignition delay
t_m = Mechanical time delay
u = Convective flow velocity
W = Proportionality constant
w = Nondimensional time defined in equation IV
Z = Nondimensional radius defined in equation III
α = Geometric factor = 0, 1, 2 for planar, cylindrical or spherical waves respectively.
β = Time exponent in equation I
γ = Ratio of specific heats
θ = Gas temperature
μ = Oxidizer-fuel mass ratio
ρ_ℓ = Gas density
ρ = Liquid density
ϕ = Equivalence ratio

Subscripts:

1	Free stream condition
2	Condition behind shock wave
s	Stoichiometric condition
ref	Reference conditions
β_1	Condition for $\beta \neq 0$ at $t_i/t_b = 1$

ACKNOWLEDGEMENT

This work was sponsored by the U.S. Army Research Office under Grant No. DAAG-29-77-G-0112.

REFERENCES

1. Lee, J. H., Ann. Rev. Phys. Chem., 28, 75-104 (1977).
2. Sichel, M., Acta Astron., 4, 409-424 (1977).
3. Knystautas, R. and Lee, J. H., Comb. and Flame 27, 221-228 (1976).
4. Dabora, E. K., Ragland, K. W. and Nicholls, J. A., 12th Symp. (Inter.) on Comb., 19-26 (1969).
5. Nicholls, J. A., Sichel, M., Fry, R. and Glass, D. R., Acta Astron. 1, 385-404 (1974).
6. Lu, P. L., Slagg, N., Fishburn, B. D. and Ostrowski, P. P. "Relation of Chemical and Physical Processes in Two-Phase Detonations", Acta Astron., in press.
7. Dabora, E. K., Acta Astron., 6, 269-280 (1979).
8. Ragland, K. W., Dabora, E. K., and Nicholls, J. A., Phys. of Fluids, 11, 2377-88 (1968).
9. Dabora, E. K., AIAA J. 10, 1384-86 (1972).
10. Pitkin, E. T., Acta Astron. 4, 1137-58 (1977).
11. Gordon, S. and McBride, B., "Computer Program for Calculation of Complex Equilibrium Compositions, Rocket Performance, Incident and Reflected Shocks and Chapman-Jouguet Detonations," NASA SP-273 (1971).
12. Lee, J. H. and Ramamurthi, K., Comb. and Flame 27, 331-340 (1976).
13. Pierce, T. H., Kauffman, C. W. and Nicholls, J. A., AIAA Paper No. 75-163 (1975).

MEASUREMENTS OF ENERGY DENSITY IN SHOCK AND BLAST WAVES

J. M. Dewey and D. J. McMillin

University of Victoria, Victoria, B.C., Canada

A technique is described which enables the energy density in blast waves and shock tube flows to be computed from experimentally measured particle trajectories. This new technique is applied to a theoretical result describing the blast wave from a spherical TNT explosion, to experimental measurements of blast waves from spherical and hemispherical charges, and to measurements of reflected flow in a one-dimensional shock tube. Total energy values obtained by volume integration of computed energy profiles are compared to estimates of source energy yield in each case. Consistent results are obtained.

INTRODUCTION

Blast waves in air are produced by the rapid release of energy from sources such as nuclear explosions, chemical detonations and the rupture of pressurized vessels. In the case of most explosions, even those which are carefully controlled, the exact amount of energy deposited in the blast wave is not known. For example, in the case of an oxygen-deficient explosive such as TNT, the detonation products will continue to burn for some time after detonation, using atmospheric oxygen. It has been shown by Dewey[1] that this "after burning" has a measureable effect on the blast wave. For most chemical explosions some energy is released as radiant heat, and for nuclear explosions approximately 50% of the released energy is in the form of thermal and nuclear radiation. The amount of energy released to a shock wave probably can be calculated most accurately for the case of the rupture of a pressurized vessel, or a shock tube flow. Even here, however, it is difficult to determine the amount of energy expended in rupturing the vessel or the diaphragm and the amount carried by the debris from the vessel.

The problem of determining the energy in any shock wave is further complicated when interaction occurs with a solid or liquid interface. For an explosion close to, on, or below the ground surface a significant amount of energy is transmitted by seismic waves, or is dissipated by the process of producing a crater. Shock waves reflected normally or obliquely from a solid surface, or passing over a rough surface, will experience some energy loss and redistribution. There is particular interest in the redistribution of energy in shock waves passing through a branched tunnel system. A knowledge of the energy residing in a shock wave would be particularly valuable to studies of shock wave attenuation.

DETERMINATION OF ENERGY DENSITY AND TOTAL ENERGY

The internal energy per unit mass of an ideal gas is $C_V T$, where C_V is the specific heat at constant volume and T the absolute temperature. When the gas moves with a velocity u, its total energy per unit mass is

$$E_m = C_v T + \tfrac{1}{2}u^2 = \frac{1}{\gamma-1} RT + \tfrac{1}{2}u^2 = \frac{1}{\gamma-1} PV + \tfrac{1}{2}u^2,$$

using standard thermodynamic relationships (γ is the ratio of specific heats, P is the pressure, and V is the specific volume, or reciprocal of the density ρ). The total energy per unit volume of the gas is therefore

$$E_v = \frac{1}{\gamma-1} P + \tfrac{1}{2}\rho u^2.$$

Hence, for a shock wave moving into a gas which was initially at rest under ambient pressure P_a, the excess energy per unit volume due to the wave is

$$E = \frac{1}{\gamma-1} (P - P_a) + \tfrac{1}{2}\rho u^2.$$

If the excess energy per unit volume is known as a function of position throughout a shock wave, the total energy within the wave may be obtained by volume integration. For example, in the case of a spherical blast from a centred explosion, the total energy in the blast wave is

$$E_{TOT} = 4\pi \int_0^R r^2\, E(r)\, dr\ ,$$

where R is the radius of the shock at the leading edge of the blast wave.

To determine experimentally the energy in a shock wave it is necessary, therefore, to have an independent measure of the spatial profiles of the pressure, density and particle velocity throughout the wave. The most commonly measured physical property in blast waves is the hydrostatic pressure-time history obtained using high-frequency-response electronic transducers at fixed locations. In order to determine the spatial distribution of pressure throughout a blast wave it is necessary to have an extensive array of such transducers. The density in a shock tube flow can be measured with an interferometer, but instruments for measuring the density in blast waves are not readily available. The total pressure can be measured, but to extract the dynamic pressure ($\tfrac{1}{2}\rho u^2$) from the total pressure it is necessary to apply a compressibility factor which requires a knowledge of the local Mach number in the flow. A determination of the energy profile in a shock wave using gauges does not seem feasible.

An alternative method has been developed by which the physical properties required to compute energy in shock waves may be obtained by analyzing particle trajectories within the flow, measured by the high speed photography of smoke tracers introduced into the air just prior to the arrival of the shock wave. This particle trajectory analysis, as applied to the blast waves produced by chemical explosions, has been described by Dewey et al[2,3,4], and by Anderson and Deckker[5], and as applied to shock tube flows, by Dewey et al[6,7]. The method is summarized below, as applied to a generalized two-dimensional flow.

A grid of smoke tracers with initial positions (x_o, y_o) is established in the ambient gas before the arrival of the shock wave and the movement of the tracers by the wave is recorded by high speed photography. The positions (x,y) of the tracers at any time, t, can be determined, as well as both components of particle velocity, $\partial x/\partial t$ and $\partial y/\partial t$. Gas density, ρ, relative to its ambient value, ρ_a, is given by

$$\frac{\rho}{\rho_a} = \begin{vmatrix} \frac{\partial x}{\partial x_o} & \frac{\partial y}{\partial x_o} \\ \frac{\partial x}{\partial y_o} & \frac{\partial y}{\partial y_o} \end{vmatrix}^{-1} .$$

As a gas element is traversed by the shock at the leading edge of the wave, it undergoes a change of entropy, after which the flow is isentropic and adiabatic until the element is traversed by a subsequent shock. Pressure, P, in the gas element is therefore given by

$$\frac{P}{P_s} = \left(\frac{\rho}{\rho_s}\right)^{\gamma},$$

where P_s and ρ_s are the pressure and density immediately behind the shock, as determined from measurements of shock velocity. It should be noted that since the strength of a shock wave normally varies with position, the gas is left in a state of varying entropy and, hence, the final equation above is valid only in a Lagrangian co-ordinate system which follows the individual gas elements, and not in the Eulerian system of transducer measurements made at fixed locations.

The particle trajectory analysis method of studying shock waves thus provides information sufficient to determine the energy density and total energy in the waves.

APPLICATION TO NUMERICAL RESULTS

In order to validate the calculations described above for determining the energy density and total energy within blast waves, a set of energy density vs. distance curves was prepared for a centred explosion using data computed by Brode[8] for TNT. Brode computed particle velocity, hydrostatic pressure, and gas density as functions of reduced radius, λ, at reduced times, τ, for a spherical blast wave produced by a centred TNT explosion in a standard atmosphere at sea level at 0°C. Brode's results and a value of $\gamma = 1.4$ were used to compute excess energy density, and a scaling factor of $\alpha = 3.966$ m was applied to Brode's reduced radius values λ to obtain results describing the detonation of a 1 kg charge of TNT in a standard atmosphere at 15°C. The scaling factor α was determined earlier by Dewey[1], by matching Brode's computed variation of shock strength with distance to its measured variation in the blast waves produced by a large number of spherical TNT charges. The resulting energy density profiles are shown in Figure 1 at a number of selected times. The profiles were integrated and the resulting values of total energy are listed in Table 1. The energy values shown in parentheses in Table 1 do not represent total energy because the energy density was not defined over the full range of radii between the explosion centre and the primary shock front.

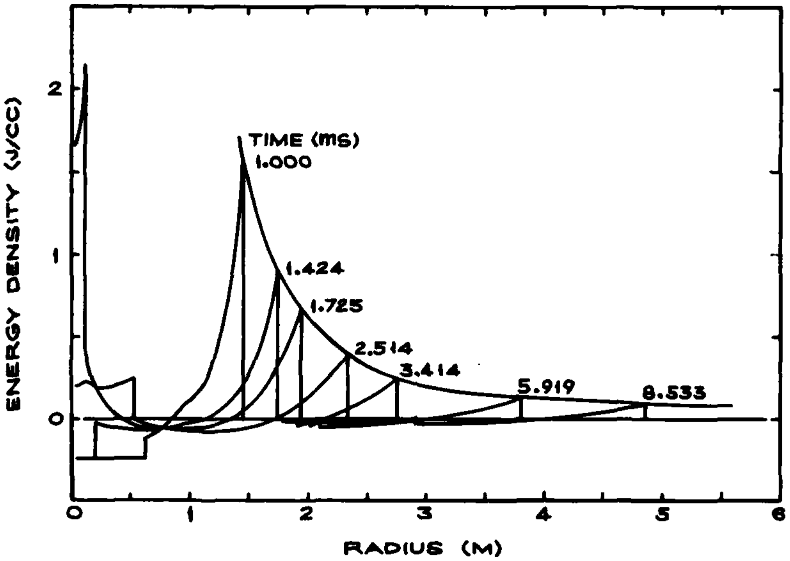

Figure 1. Energy density vs. radius curves computed using the data of Brode, scaled to a 1 kg TNT charge.

Table 1. Total energy from 1 kg TNT using the data of Brode.

Time (ms)	Energy (MJ)
0.4405	4.811
0.5384	5.301
0.7239	5.073
1.000	5.090
1.424	4.841
1.725	5.343
2.514	4.212
3.414	(5.3)
5.919	(3.9)
8.533	(2.8)

The mean value of the total energy for those times at which data were available over the full range of radii, is 4.95 MJ. This result may be compared to the total energy yield of 1 kg TNT which is thought to be approximately 4.85 MJ using data from Cook[9] for TNT with a loading density of 1.57 g/cc. The agreement between these two results validates the energy density calculation to within 2 per cent.

BLAST WAVE MEASUREMENTS

Energy density profiles have been computed from data measured experimentally using the techniques described above, for both a spherical and hemispherical blast. The spherical blast wave was produced by a 490 kg charge of TNT detonated at a height of 18.2 m (DRES Canada FE589/6, 17 October 1969). The large height of burst and the positioning of the smoke puff grid in this experiment yielded a relatively large amount of particle trajectory data in the primary blast wave. Results were scaled to represent a one kilogram charge detonated in a standard atmosphere. A profile of the energy density in the wave computed at a scaled time of 8.5 ms is shown in Figure 2. Also shown is the energy profile calculated from Brode's results at the same scaled time. The scatter of the experimental points arises partly from a lack of spatial resolution in the measurement of density and pressure, and partly because the data were not measured along a single radius vector, but throughout the region covered by the smoke puff grid.

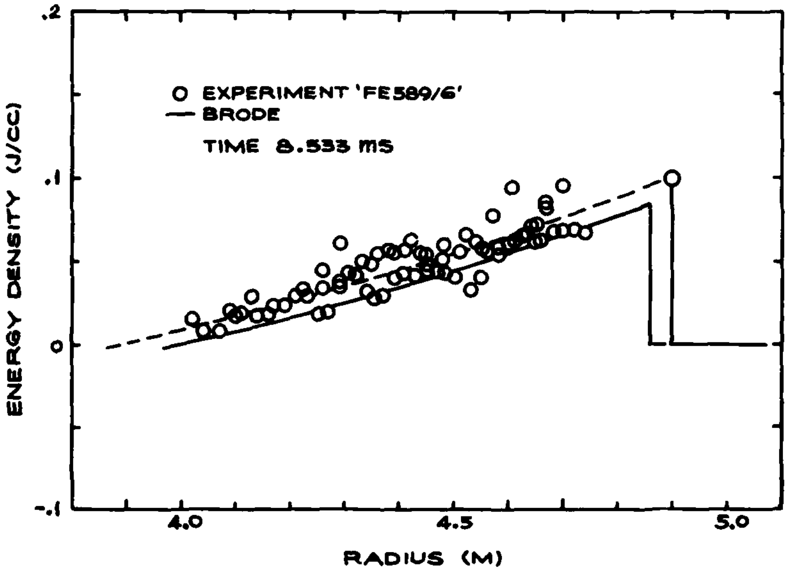

Figure 2. Energy density in the spherical primary wave of experiment FE589/6, scaled to a 1 kg TNT charge. Also shown is the curve computed using the data of Brode at the same scaled time.

The two profiles appear to be similar in shape and, had Brode's results been scaled to match the experimentally observed shock position and strength, the Brode curve would have been an excellent descriptor of the experimental points. The positive phase of the experimental energy density profile (indicated by the broken curve in Figure 2) was integrated over a full sphere to obtain an energy of approximately 13.3 MJ. The corresponding integral for the positive phase of the Brode curve is 8.0 MJ. Both of these figures place the available energy in the positive phase of the blast waves well in excess of the total energy released by the charge, namely 4.85 MJ. The excess positive phase energy is, of course, balanced by a deficit of energy in the negative region of the blast wave, a region of expanded and cooled gas.

As a result of this observation, Brode's results were re-integrated over the positive phases only, at times for which data were available. Integrated positive phase energy is plotted in Figure 3 as a function of time. The energy integral appears to remain approximately constant until a time of about 3.5 ms, after which it increases almost linearly with time. Also shown are the data from Table 1, that is, the total energy in the blast wave at those times for which the complete energy profile was known, and the mean of those values.

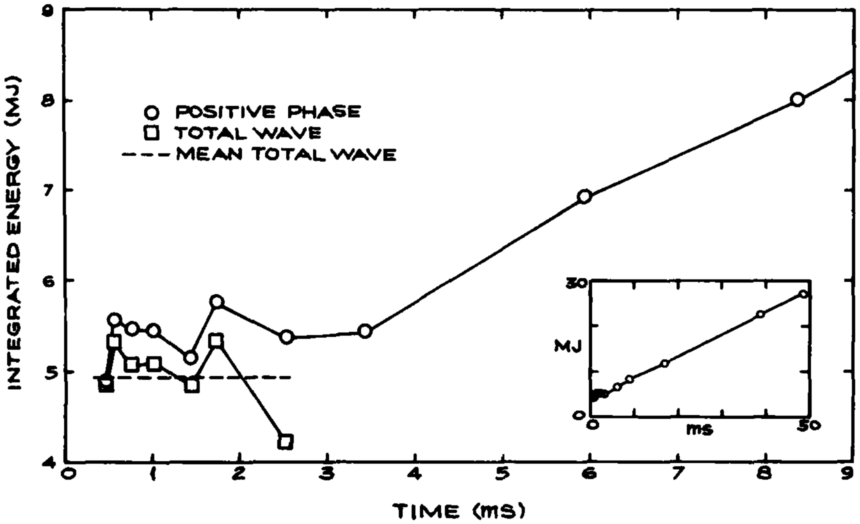

Figure 3. Integrated energy in the waves computed using the data of Brode, as a function of time, scaled to a 1 kg TNT charge.

The increase with time of the positive phase energy may be compared to a result of Thornhill[10], who showed on the basis of a purely theoretical analysis that the blast wave from a central source is divided into two regions. There is an inner sphere, the radius of which is defined by the first positive characteristic which fails to overtake the shock in a finite distance, so that flow within the inner sphere can have no influence on the decay of the shock. The excess energy in the blast wave exterior to this inner sphere increases indefinitely in proportion to the shock radius. Since the characteristic which determines the two regions defined by Thornhill is very close to the end of the positive phase, the result shown in Figure 3 might have been expected.

Energy density profiles were also determined in the blast wave from a 454 thousand kg TNT explosion (DRES Canada FE548, July 1964). Results in this case were scaled to represent a 0.656 kg hemisphere detonated at ground level in a standard atmosphere, to match the experimentally derived shock strength vs. distance curve to that of Brode's 1 kg free charge. The energy density profile along a radius vector at a scaled time of 3.4 ms is shown in Figure 4, together with the matching profile from Brode's results. Again, agreement between the experimental results and those of Brode is good. The integrated positive phase energy for the experimental profile shown in Figure 4 is 3.53 MJ, greater than the total energy released from the explosion (3.18 MJ in this case) by almost exactly the same relative amount as in the case of Brode (about 9%). It is approximately at this time of 3.4 ms that the positive phase energy begins to increase with time. Again, in Figure 4 as in Figure 3, had Brode's curve been scaled to match the experimental shock position and strength, it would have been an excellent descriptor of the experimental points. The main difference between the two curves shown in Figure 4 is in time.

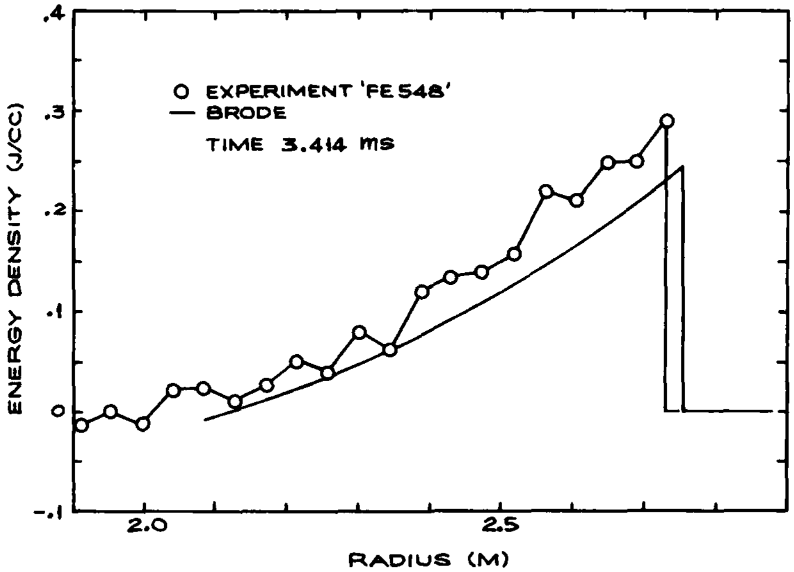

Figure 4. Energy density in the hemispherical wave of experiment FE548. Here the data were scaled so that the peak energy vs. radius curve matched the one computed using the data of Brode scaled to a 1 kg TNT charge.

SHOCK TUBE MEASUREMENTS

Measurements of pressure, density and particle velocity in a shock tube, obtained by the analysis of the experimentally observed particle trajectories, were reported by Dewey and Whitten[5]. These results have been used to determine the energy density in the flow at times of 14 ms and 20 ms after the diaphragm was ruptured. The rectangular shock tube used in these experiments was 7.6 cm by 25.4 cm in cross-section and 9.25 m long, including a 1.0 m compression chamber. The Mach number of the shock was 1.34. At 14 ms the shock front was approaching the closed end of the tube, and at 20 ms it had been reflected, as shown by the energy density profiles in Figure 5. The internal energy of the compressed air before the diaphragm was ruptured was 16.5 kJ. The integrated energy in the leading 3.8 m of the shock wave at 14 ms is 18.8 kJ, and in the observed part of the reflected wave it is 22.5 kJ.

It is difficult to compare the integrated energy in two waves because energy is transported both by gas particles at velocity u and by compression waves at velocity $u+a$, where a is the local sound speed. Both u and a vary with position and time. The energy in the wave ahead of the particle marked PB at 14 ms is 17.8 kJ. The energy in the wave ahead of the same particle at 20 ms is 22.5 kJ, indicating a net sound wave transport of 4.7 kJ between these times. The broken curve in Figure 5 represents the 14 ms wave folded back on itself and matched to the 20 ms wave. The energy in the same length of the 20 ms wave (ahead of the point LA) is 19.9 kJ. The total energy in the 14 ms wave is carried by a shorter length of wave at 20 ms (ahead of the point marked EA). The positive characteristic through the point PA at 14 ms is the point CA at 20 ms, so that flow behind PA at 14 ms cannot have affected the wave ahead of CA at 20 ms. The integrated energy ahead of CA at 20 ms is 17.5 kJ.

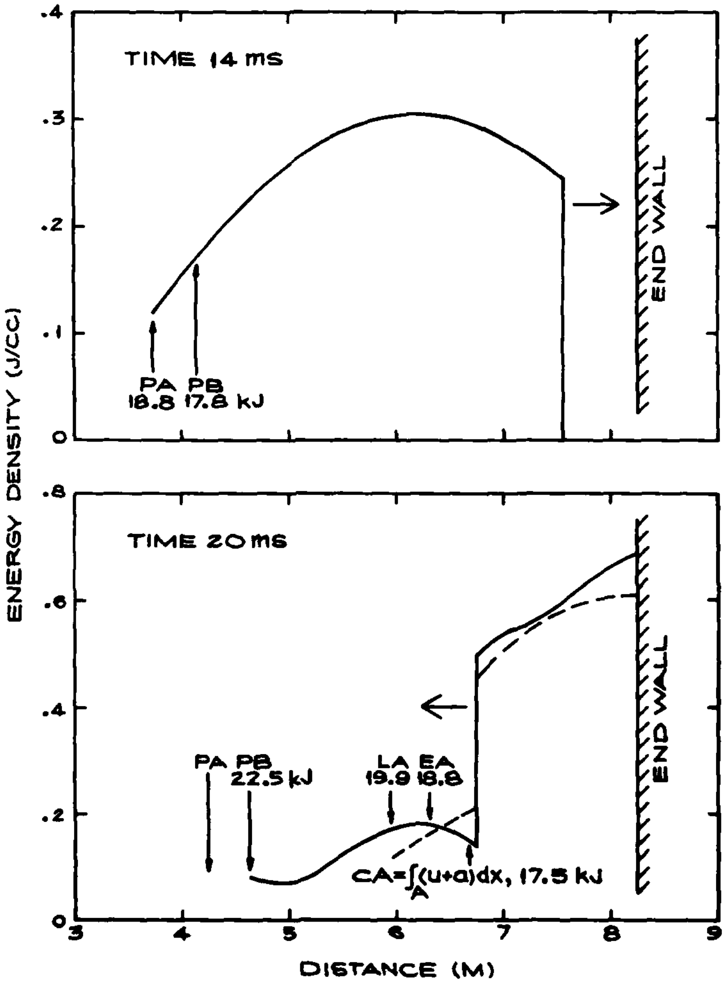

Figure 5. Energy density in a one-dimensional shock tube flow at two times, before and after reflection of the wave by an end wall. Annotation gives total energy values ahead of points shown.

An exact comparison between two waves to determine, for example, the energy loss at a reflecting wall in a shock tube, could only be made by performing two separate experiments (one with and one without the wall). Energy values could then be integrated for the same point in time in each experiment.

CONCLUSIONS

The technique for determining the energy density within blast waves and shock tube flows is at an early stage of development and it is difficult to draw firm conclusions from the results presented in this paper. Nevertheless, it has been possible, for the first time, to determine the energy density profiles in shock waves using the measured physical properties of the waves. Consistent results were obtained when the method was applied to the numerical calculations of Brode, to measurements of the blast waves produced by a free spherical charge and a hemispherical charge at the ground surface, and to measurements in a one-dimensional shock tube flow. It is interesting to note that for all of the blast waves studied the integrated energy in the positive phase is greater than the total energy released by the explosion, and that it continues to grow as the blast wave expands. Total energy, of course, must be conserved and the excess energy in the positive phase is balanced by an energy deficit to be found in the central region of expanded gas.

ACKNOWLEDGEMENTS

The authors gratefully acknowledge the opportunity offered by the Defence Research Establishment Suffield and the Defense Nuclear Agency to participate in and to have access to the results from the experiments discussed in this paper. The analyses were carried out with the assistance of contracts from the Ballistic Research Laboratories and the General Electric Company, with additional financial support by the Natural Science and Engineering Research Council of Canada and the University of Victoria. The assistance and encouragement of J. Keefer are gratefully acknowledged.

REFERENCES

1. Dewey, J.M., Proc. Roy. Soc. *A 279*, 366 (1964).
2. Dewey, J.M., Proc. Roy. Soc. *A 324*, 275 (1971).
3. Dewey, J.M., McMillin, D.J. and Classen, D.F., J. Fluid Mech. *81*, 701 (1977).
4. Anderson, J.H.B. and Deckker, B.E.L., Proc. Roy. Soc. *A 358*, 31 (1977).
5. Dewey, J.M. and McMillin, D.J., in preparation.
6. Dewey, J.M. and Whitten, B.T., Phys. Fluids *18*, 437 (1975).
7. Dewey, J.M. and Walker, D.K., J. Appl. Phys. *46*, 3454 (1975).
8. Brode, H.L., Phys. Fluids *2*, 217 (1959).
9. Cook, M.A., The Science of High Explosives, Reinhold Publ. Corp., New York (1958).
10. Thornhill, C.K., A.R.D.E. Report (B) 27/57 (1957).

SHOCK WAVE GENERATION IN LIQUID BY A HIGH ENERGY CO_2 LASER PULSE

D. DUFRESNE, J. P. CARESSA, P. GIOVANNESCHI, M. AUTRIC, PH. BOURNOT

Institut de Mécanique des Fluides Marseille
1, rue Honnorat, 13003, Marseille, France

The interaction of high power laser radiation focused on the surface of a liquid provides new interesting possibilities for the production of high pressure, shock waves andacoustic waves in a liquid. This phenomenon can provide many important applications such as welding by shock wave, study of sea bottom emulsification and photochemistry.

When a powerful laser pulse is focused on the surface of a liquid a breakdown occurs, the laser energy is divided in acoustic and luminous energy. Generally a shock wave propagates inside the liquid and vapor is ejected off the surface.

The present paper describes some experiments of the interaction between a CO_2 laser beam and water using of 10^7 W cm^{-2} to several 10^8 W cm^{-2}. Fast quartz and piezoresistive pressure gauges are used to study the shock waves induced in the water.

The time evolution of the pressure depends on the thickness of the water and of the intensity of the laser flux. When the thickness is very small, less than 1 mm, the time evolution of the pressure follows the laser pulse. When the intensity of the laser pulse is low the pressure signal exhibits two peaks, the former is due to a thermoelastic mechanism and the latter to a vaporisation mechanism.

INTRODUCTION

The interaction of laser radiation with liquid provides new interesting possibilities for the production of high pressure and intense acoustic waves. According to the absorption coefficient of the liquid and the laser flux, the stress is due to several mechanisms. These different mechanisms have been studied both theoretically and experimentally[1] . There are four principal processes : dielectric breakdown, electrostriction, advanced evaporation and thermoelastic or thermal expansion. In the interaction of CO_2 laser with water, the absorption of the laser energy is very high and only the two last processes are present.

The thermoelastic process is due to the thermal expansion of a rapid heated volume by the laser energy. If the light energy absorbed by the liquid is above the vaporisation threshold, the liquid will evaporate and the vapor is ejected from the surface and the recoil momentum produces a pressure pulse in the liquid.

The interaction of CO_2 laser pulses with water have been performed first by Bunkin et al[2] who have shown that very high pressure can be obtained. Bushanam and Barnes[3] have made a model which describes the thermoelastic process. Feiock and Goodwin[4] have developped a numerical code for the pure evaporation process. Recently Sigrist and Kneubühl[5] have studied in detail the thermoelastic and evaporation process.

These experimental works have been made with a low energy (some Joule) and short laser pulse (about 100 ns). In this paper we reported an experimental investigation of interaction of a high energy (100 J) and long pulse laser (2μs). In this case there is a breakdown above the surface of the water and the laser induced stress wave is controlled by the properties of the plasma located near the surface[6].

The pressure induced by the laser energy is measured with piezoresistive carbon and piezoelectric quartz jauge for different thickness of water.

Theschlieren pictures showed that the stress wave is spherical.

EXPERIMENTS

a) CO_2 laser and experimental arrangement

The experiments of interaction laser-radiation with liquid are performed with a CO_2 cold cathode electron-beam type laser : this system used in an instable oscillator mode is capable of emetting 100 J of laser energy in a gain switched pulse. The shape, the duration and the energy of the laser pulse depends upon the decharge parameter (E/p : ratio of the electric field to the laser gaz pressure) and the gas mixture. Two typical laser pulses are shown in fig. (1). With $E/p = 3$ KV cm^{-1} bar^{-1} and with a nitrogen free mixture

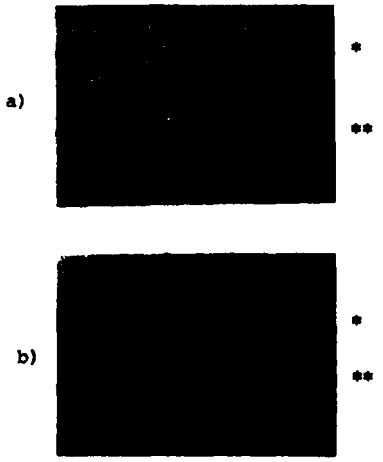

Fig. 1 Laser pulses and pressure signals

a) $\frac{E}{p} = 3$ KV cm^{-1} bar^{-1}

b) $\frac{E}{p} = 5$ KV cm^{-1} bar^{-1}

a) 500 ns/c b) 500 ns/c

*Laser pulse

**Pressure signal

($He - N_2 - CO_2$; 3-0-1) the laser pulse consists only of a single peak with a FWHM of 100 ns. The laser pulse obtained with a gaz mixture ($He-N_2-CO_2$; 3-2-1) and with E/p = 5 KV cm^{-1} bar^{-1} contains an initial high power peak followed by a high energy low power tail.

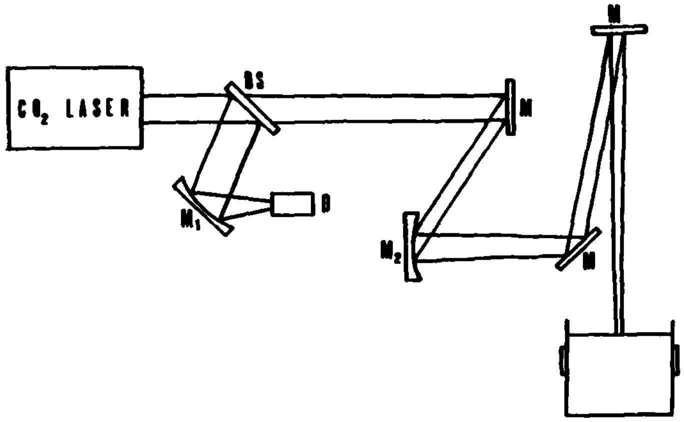

Fig. 2 Experimental apparatus

B.S. Beam splitter ; M Plane mirror ; M_1 Spherical mirror ;

M_2 Spherical mirror (focal length 5 m)

In the experimental apparatus fig. (2) the laser beam is focused on the water surface by a spherical mirror (focal length 5 m). The diameter of the laser beam at the surface is about 1 cm. The spatial distribution of the energy determined by burning on Kalvar film is uniform. With this experimental arrangement the spike flux is about 3.25 10^8 W cm^{-2} and during the tail it is about 10^7 W cm^{-2} the shape and the intensity of the laser pulse are monitored by a photon drag detector.

b) Devices for stress measurements

The pressure measurements are performed with carbon piezoresistive gauge (Dynasen model 15.300.E) with a sensitive surface of 1.57 x 1.27 mm^2 . These gauges used in conjonction with a pulsed power supply have a rise time of 10ns and the sensivity depends on the voltage of the power supply. The piezoresistive pressure transducer and holder assembly are shown fig. (3).

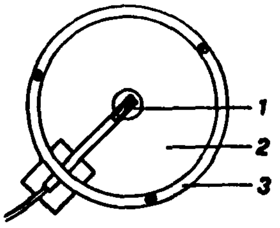

Fig. 3 Carbon gauge holder assembly

1. Piezoresistive gauge
2. Terphane foils
3. Holder

Different configurations of the holder assembly are used
. gauge located between two pieces of glass
. gauge without backing material and directly immersed into water.

The latter configuration gives a better result with a shock transient time which records the true propagating pressure wave.

Quartz gauges are also used for recording pressure close to the surface of the liquid.

MEASUREMENTS AND RESULTS

In the production of high pressure in water with a CO_2 laser pulse there are two important parameters : the thickness of water and the laser flux.

The influence of the thickness of water has been studied by measuring the pressure wave for several laser energy (16.5 to 72 J) and for a distance h from the impact varying from 0 to 100 mm. The results obtained are presented fig. (4). The dependance of the maximum pressure with h is in a good agreement with the law of spherical wave propagation. The decrease is proportionnal to 1/h for h higher than 6 mm. When the thickness of water is small, the time evolution of pressure follows the laser pulse. This evolution is comparable with pressure induced by the interaction of a powerful laser beam with a solid target covered with a thin layer of paint. Without water the measured pressure is 245 bar corresponding of the pressure induced by the laser on a solid. There is a maximum for h = 4.5 mm. A pressure as high as 1 kbar is measured.

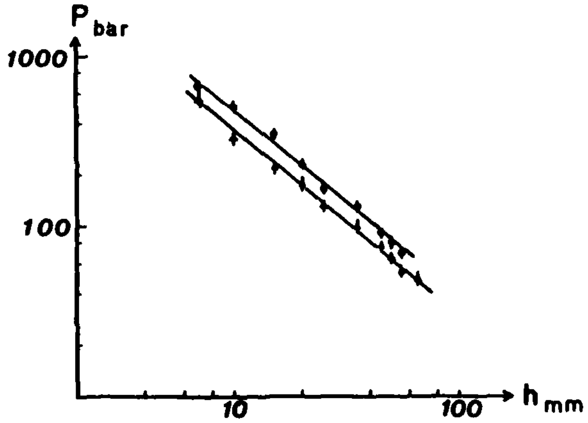

Fig. 4 Peak pressure versus distance h

● E = 72 J
▲ E = 16.5 J

In fig. (5) are shown the delay times of shock wave on the pressure gauge. From these results the velocity of the shock wave is determined, which is 1540 $m\ s^{-1}$. The figure (5) showed also that the shock wave induced by the laser beam is not immediate. The time of formation of the shock is about 1 μs. This result is consistent with other experiments which have determined this time with fast framing camera[7].

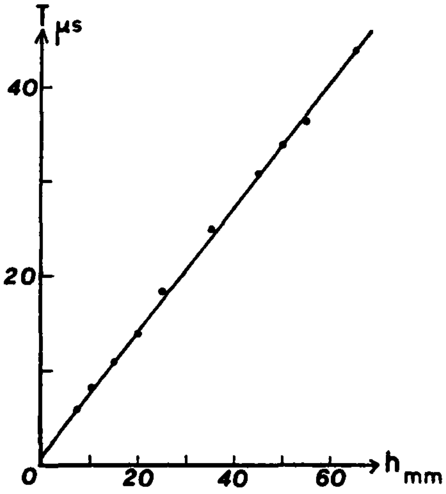

Fig. 5 Delay time versus distance h

As the pressure wave is propagating the steeper portion of the pressure is attenuated corresponding to the attenuation of the high frequencies components of the signal.

The evolution of a pressure wave versus the laser power is studied for h = 10 mm and for laser flux varying between 3,25 10^8 W cm^{-2} to 10^7 W cm^{-2}. The attenuation of the power is made by inserting in the laser beam known attenuators (foil of terphane). With this method the shape and the duration of the laser pulses are constant.

The evolution of pressure signals versus laser flux is plotted fig. (6).

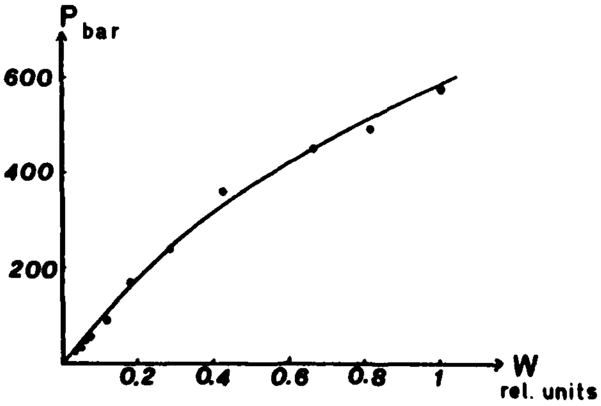

Fig. 6 Peak pressure versus laser flux

(W = 1 ⟹ 3,25 10^8 W cm^{-2})

For the lower laser flux the pressure wave exhibits two peaks, a rapid first one lasting about 100 ns, followed by a second large pressure signal. The total duration of the pressure signal increases when the laser flux decreases fig. (7).

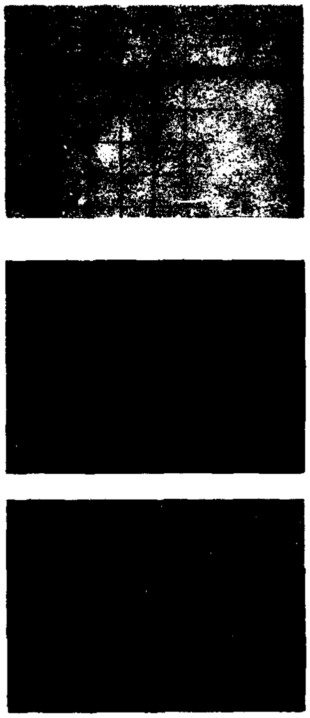

a) Below breakdown threshold

b) Near breakdown threshold

c) Above breakdown threshold

Fig. 7 Pressure signals

The time evolution of the pressure signal is comparable with those obtained by Sigrist et al, near vaporisation threshold. But because the long duration of the laser used in our experiments, the pressure always exhibits the two pulses. The first pulse is due to a thermoelastic process. The maximum experimental values of the pressure are in good agreement with the theorical values calculated with Hu's formula.

The evolution of time between the two peaks versus the laser flux is plotted fig. (8). In the same figure is shown the time required to obtain the vaporisation threshold of water (2,6 J cm^{-2}). There is good agreement when the laser flux is low in this case no breakdown occurs at the surface of the liquid . For lower values of the laser flux the main pressure pulse is attributed to a direct vaporisation of water by the laser.

As the laser flux becomes higher the delay time between the two peaks decreases and when the plasma above the surface is well established the pressure fig. 7 consists of a single peak with a duration nearly constant (750 - 800 ns). The width of the pulse pressure is independant of the shape of the laser pulse. In this case the thermoelastic process exits but it is immediately overlapped by the vaporisation process.

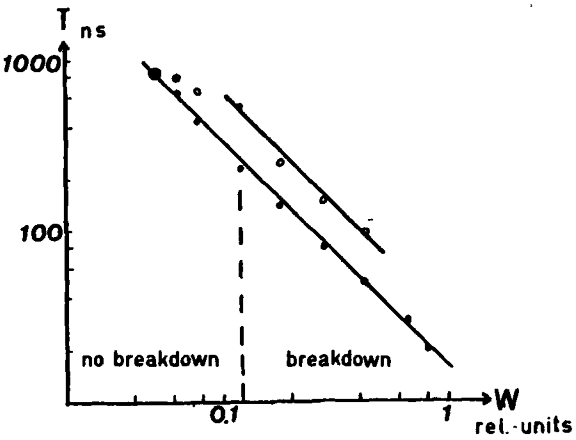

Fig. 8 Time between the two peaks versus laser flux

● Time required to obtain 2,6 J cm^{-2}

○ Measured time

In our experiments the breakdown threshold is found to be 3 10^7 W cm^{-2} . The formation of plasma above the surface of water is very fast and it screens[8] the water. In this case the vaporisation process is not due to the direct heating of the water by the laser energy. Pirri[9] et al have demonstrated that the transfert of the energy from the plasma to a solid target is effective and the dominant transfert mechanism is radiative.

Fig. 9 showed the pictures of the shock wave. Fast framing camera and flash are used. The time between two pictures is 5 µs.

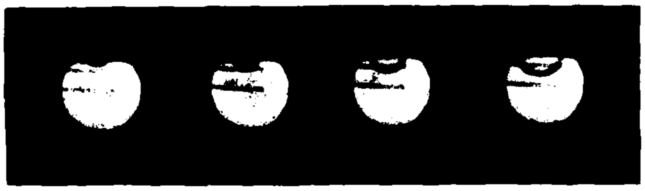

Fig. 9 Time sequential photographs of the shock wave in water

CONCLUSION

An experimental investigation of the production of high pressure in a liquid by powerful laser pulses has been performed. Below the breakdown threshold the pressure is due to thermoelastic or vaporisation process by direct absorption of the laser energy. With a plasma above the water the two precedent mechanisms are controlled by absorption of the plasma radiation.

ACKNOWKEDGMENTS

The authors would like to acknowledge the able assistance of Mr. J. David and Mr. Bosca (HDE/CEA Limeil France) for the stress measurements and to Mr. J.P. Fragassi and Mr. M. Sarrazin in assisting with the laser experiments.

REFERENCES

1. C.L. HU, J. Acoust. Soc. Am. 46, 728 (1969)

2. F.V. BUNKIN, N.V. KARLOV, V.M. KOMISSAROV and G.P. KUZ'MIN J.E.T.P. Letters 13, 341 (1971)

3. G.S. BUSHANAM, F.S. BARNES, J. Appl. Phys. 46, 2074 (1975)

4. F.D. FEIOCK and L.K. GOODWIN, J. Appl. Phys. 43, 5061 (1972)

5. M.W. SIGRIST and F.K. KNEUBUHL, J. Acoust. Soc. Am. 64, 1652 (1978)

6. B.P. FAIRAUD and A.H. CLAUER, J. Appl. Phys. 50, 1497 (1979)

7. M. HUGENSCHMIDT, K. VOLLRATH, 12th Congress oh High Speed Photography, Toronto (August 1976)

8. Ph. BOURNOT, P.A. PINCOSY, G. INGLESAKIS, M. AUTRIC, D. DUFRESNE and J.P. CARESSA, Acta Astronautica 6, 257 (1979)

9. A.N. PIRRI, R.G. ROOT and P.K.S. WU, A.I.A.AJournal 16, 1296 (1978)

ENTRAINMENT OF DUST BY AN AIR SHOCK WAVE: INFLUENCE OF SHOCK DIFFRACTION AROUND AN OBSTACLE

K. BRACHT* and W. MERZKIRCH

Institut für Thermo- und Fluiddynamik
Ruhr-Universität, D-4630 Bochum, Germany

Dust from a layer on the floor of a shock tube is entrained by the air flow behind the unsteady shock wave. The development of the dust mass concentration profiles is measured by means of an optical extinction method. Prior to the erosion of the dust the shock is diffracted around an obstacle. The large scale vortex shedded from the obstacle dominates the mass transfer and dust entrainment which is more intense than in the case without obstacle.

INTRODUCTION

Dust explosions are a severe source of danger in underground coal mines. Prior to the initiation of such an explosion there occurs the formation of an air-dust mixture. The unsteady air flow behind a pressure wave or shock wave moving along the gallery of a mine may entrain the coal dust covering the floor and the walls of the gallery, thus forming the dangerous dust cloud. Since the mixture is explosive only within a certain range of values of the dust concentration in air [1], one is generally interested in knowing and understanding the development of the dust concentration as a function of time in the described flow.

This process has been investigated by a series of shock tube experiments and compared with model calculations [2]. In these experiments, the dust from a plane layer on the floor of a shock tube was entrained by the (two-dimensional) air flow behind the unsteady, normal shock wave. At fixed cross-sections of the tube, x = const, the development of the dust mass concentration profiles was measured by means of an optical extinction method. For positions x far enough downstream of the leading edge of the dust deposit, the concentration profiles are independent of x and can

---

* K. Bracht is now with Gesellschaft für Reaktorsicherheit, D-5000 Köln, Germany

be described by the following exponential law (x is the coordinate along the axis of the tube):

$$c(y,t) \;/\; c_0(t) = \exp[\,-\alpha(t)\cdot y\,], \qquad (1)$$

where c is the dust mass concentration as a function of the height y above the channel floor and the time t after the arrival of the shock at the position of x = 0 (leading edge of the dust deposit); $c_0(t)$ is the dust concentration in an infinitesimal height ($y \to 0$), and $\alpha(t)$ is a measure for the distribution of dust across the air stream. Both c_0 and α are extrapolated from the measurements, they depend on the shock strength and on the properties of the dust material. For large values of time, c_0 and α approach stationary limits, and $c(y,t\to\infty)$ agrees with the concentration profiles derived by the theory of stationary pneumatic transport.

The experiments described in [2] have been performed in a shock tube of rectangular, constant cross-section. This situation is not very realistic when applied to the galleries of underground coal mines where obstructions may change the cross-section of a gallery. The shock wave is reflected and diffracted from such obstructions, and the rate of dust entrainment and dust cloud formation must be different than in the case of plane, parallel flow behind the undisturbed, normal shock wave. Therefore, further experiments have been performed in which the shock wave diffracts around a rectangular body before reaching the dust layer (Figure 1). The interaction of the dust layer with a curved shock and the existance of large-scale vortices in the air flow result in a more rapid entrainment process. These experiments are described in this paper and compared with the earlier results produced in the shock tube with constant cross-section [2].

EXPERIMENTAL PROCEDURE

The experimental facility and the properties of the dust are the same as described in [2,3]. The strength of the initially plane shock is constant in all experiments, with the shock Mach number $M_s = 1.18$ and the velocity of the (undisturbed) air flow $U_2 = 95$m/s. The flow in the test chamber of rectangular cross section is, to high a degree of accuracy, plane or two-dimensional. It is assumed therefore that the gross properties of the developing two-phase flow are also two-dimensional, i.e. they do not depend on the z-coordinate in the direction of the transmitted laser beam.

The extinction of the laser beam recorded as a function of time (Figure 2) is a measure of the instantaneous dust concentration. A special calibration procedure [2] permitts to convert the measured light intensity into values of mean dust concentration $\bar{c}$ (measured in milligramme per liter, mg/l). These values are averaged over the particular size distribution of the used dust, over the depth (in z-direction) of the test section where the flow is, of course, not perfectly two-dimensional, and over a number of individual measurements which show fairly good reproducibility. Taking the measurements for various positions y of the laser beam above the channel floor permitts to record the dust concentration profile $\bar{c}$ (y,t) at a fixed cross section x = const of the shock tube.

The process of dust entrainment and formation of the dust cloud is illustrated by a series of high-speed shadowgraphs (Figure 1). The first of these three photographs shows the shock wave dif-

Figure 1. Series of 3 shadowgraphs showing the erosion and entrainment of dust by a shock wave diffracting around a rectangular obstacle. The horizontal line is in a distance y = 30mm from the floor and designates half of the height of the test section. The shock seen in the first shadowgraph propagates from left to right. The pictures are taken 100µs, 500µs and 1500µs after the arrival of the shock at the leading edge of the obstacle.

fracted over the rectangular obstacle. The initial stage of dust entrainment is dominated by the unsteady vortex shedded from the obstacle. The dust cloud forms and grows much faster than it has been observed in the case without an obstacle in the shock tube [2,3].

EVALUATION OF EXPERIMENTS AND DISCUSSION

Dust concentration profiles $\bar{c}$ (y,t) for the position x = 80 mm downstream of the rearward edge of the obstacle are shown in Figure 3. The time coordinate t is measured from the arrival of the shock wave at the obstacle. The curves start the later from $\bar{c}$ = 0, the higher the position y of the laser beam above the channel floor. The measured curves end when the degree of light extinction exceeds 90% (y = 1 and 2.5 mm), or when the shock wave reflected from the closed end of the shock tube again reaches the test section.

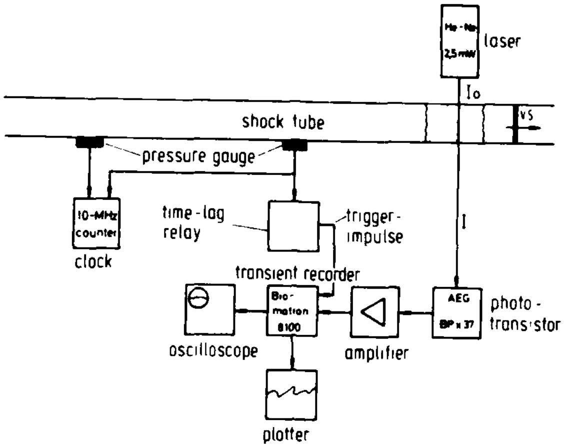

Figure 2. Optical extinction technique adopted to the shock tube.

The profiles for the lower test positions (y < 10 mm) exhibit a characteristic maximum and minimum which were not observed in the experiments without obstacle. It is thought that this pattern is caused by the interaction of the dust deposit with the vortex shedded from the obstacle. The vortex moves with the velocity of the air flow behind the shock. Its time of arrival at the test position x = 80 mm is in agreement with the appearance of the maximum in the dust profiles. The vortex superposes a motion which first is directed downward, thus acting opposite to the raising motion of the dust particles and therefore causing the maximum and the subsequent decrease of $\bar{c}$. The following upward flow induced by the vortex supports the raising motion of the dust and causes the $\bar{c}$-profiles to increase again. At the higher test positions the dust concentration is too low yet that the action of the vortex could be observed.

Further downstream of the obstacle the disturbances produced by the vortex are smoothed out since the vortex decays. At x = 260mm (Figure 4) the dust profiles appear very similar to the pattern which has been measured without obstacle. However, the curves for the lower test positions (y < 10 mm) are less steep here. This can be explained with the former observation that the flow behind the diffracted shock wave and the shedded vortex increase the rate of dust entrainment, so that the dust is distributed more uniformly over the cross section of the channel.

The data of Figure 4 can be cross-plotted by exchanging the parameter (height y above the channel floor) with the abscissa (time). From the new representation of these data (Figure 5) one recognizes the same functional behavior of the experimental results as in the case without obstacle, i.e. the data follow the exponential law of equation (1). The quantity $\alpha(t)$ is the negative slope of the curves in Figure 5, and $\bar{c}_0(t)$ is found by intersecting the straight curves with the abscissa ($\bar{c}$ - axis). The latter results are shown in Figure 6 for the two test positions

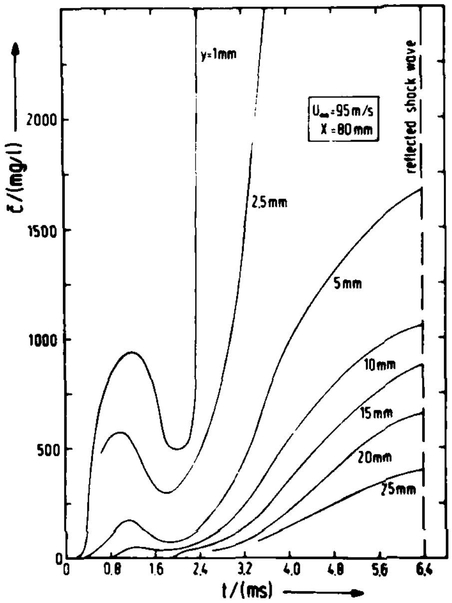

Figure 3. Mean dust concentration $\bar{c}$ as function of time for various values of the height y above the channel floor. Test position x = 80 mm downstream of the osstacle.

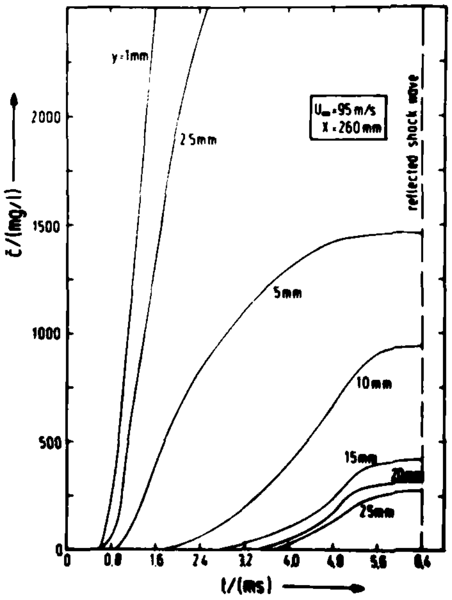

Figure 4. Mean dust concentration $\bar{c}$ as function of time for various values of the height y above the channel floor. Test position x = 260mm.

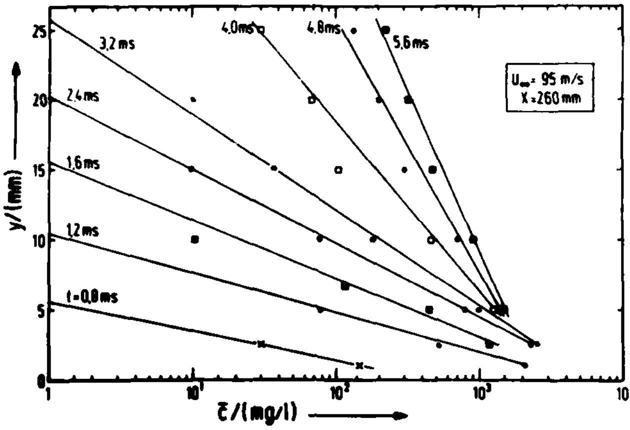

Figure 5. Mean dust concentration $\bar{c}$ as function of the height y above the channel floor as obtained by cross-plotting the data of Figure 4. The parameter t is the time after the arrival of the shock at the leading edge of the obstacle.

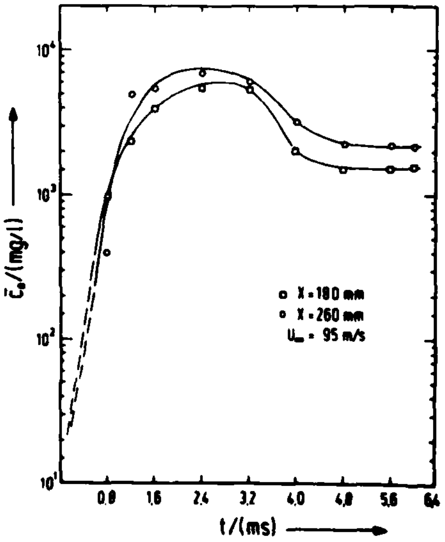

Figure 6. Extrapolated values $\bar{c}_0$ according to equation (9) as function of time for two different test positions x.

x = 180 mm and x = 260 mm. In [2] the values of $\bar{c}_0(t)$ are interpreted to be the dust mass concentration in an infinitesimal height ($y \to 0$ but $y > 0$) above the floor. From this assumption it follows that the fitting curves in Figure 6 must originate from the point $\bar{c}_0 = 0$, $t = 0$: no dust is raised at $t = 0$.
The following pattern of the curves can be explained with the different mechanisms being responsible for the dust erosion in the laminar and in the turbulent stage of the shock tube flow. The interaction of the dust deposit with the initially thin, laminar shock tube boundary layer [3] causes a strong lift force acting on the particles in the dust layer so that they raise by a small amount, but they cannot be entrained at the same rate by the (still) laminar air flow. With increasing degree of turbulence the dust can be distributed at a higher rate in the air flow. At the same time the intense erosion of dust as caused in the laminar phase decreases, i.e. $\bar{c}_0$ decreases after having passed the maximum. Finally a stage of equilibrium is reached when all the dust raised due to an interaction with the turbulent boundary layer can be entrained by the turbulent channel flow.

The values in Figure 6 are about half an order of magnitude smaller than in the case without obstacle (see Figure 25 in [2]). This again confirms the earlier assumption that the large scale vortices promote the distribution of the eroded dust across the channel flow. Both $\bar{c}_0$ and α approach constant values for $t \to \infty$, and therefore also $\bar{c}$ apparently has a stationary limit for large values of time. This limit has been shown to be in agreement with the results of the stationary pneumatic transport theory. Furthermore one may conclude that the experimental data of Figure 5 also are in agreement with the theory of Hwang, Singer and Hartz [4]; this theory has been evaluated and compared with the experiments without obstacle in [2]. The diffusion coefficients used in [4] will have greater values here, thus accounting for the action of the vortices.

The summarized result of these investigations is that the entrainment of the dust by the shock tube flow is promoted by the presence of an obstacle in the flow channel. The fluid mechanical reason for this rapid entrainment is the formation and shedding of a large scale vortex from the obstacle. This vortex determines the flow structure behind the diffracted shock wave and it intensifies the mass transfer in this flow regime. This result is of particular interest for the study of the dust explosions in coal mines, as mentioned in the beginning, since such obstacles usually are present in the galleries of underground coal mines.

ACKNOWLEDGEMENT

This research has been supported by a grant from Minister für Wissenschaft und Forschung des Landes Nordrhein-Westfalen. The authors are grateful for the assistance of H. Eudenbach, E. Hellbrügge and E. Ronkholz in performing the experiments.

REFERENCES

1. K.N. Palmer, Dust Explosions and Fires, Chapman & Hall, London (1973).
2. W. Merzkirch and K. Bracht, Aufwirbelung von Staub durch Druckwellen in Luft, Forschungsbericht des Landes Nordrhein-Westfalen Nr. 2785, Westdeutscher Verlag, Opladen (1978).

3. W. Merzkirch and K. Bracht, Int. J. Multiphase Flow 4, 89 (1978)
4. C.C. Hwang, J.M. Singer and T.N. Hartz, Dispersion of Dust in a Channel by a Turbulent Gas Stream, US Bureau of Mines, Pittsburgh, Pa., Rept. Invest. 7854 (1974)

THE FLUID DYNAMIC ASPECTS OF AN EFFICIENT POINT DESIGN ENERGY EXCHANGER

J. F. Zumdieck, T. S. Vaidyanathan, E. L. Klosterman,
R. T. Taussig, P. E. Cassady and W. J. Thayer

Mathematical Sciences Northwest, Inc., Bellevue, Washington 98009 USA

W. H. Christiansen

University of Washington, Seattle, Washington 98195 USA

Examination of wave compression-expansion machinery in light of increased demands for efficient energy conversion reveals a number of potentially useful applications. The energy exchanger is a wave machine which transfers work from one gas stream to another by unsteady gas dynamic compression and expansion through waves. Energy exchangers have been suggested which utilize a tailored gas interface together with staged compression to obtain efficient, high pressure ratio energy exchange between dissimilar working fluids. Interface tailoring prevents wave reflection from the contact surface between gases and may be imposed by maintaining the product of the density and the speed of sound at the same value on each side of the fluid-fluid interface. Staged multi-shock compression must be used to reduce losses in a high pressure ratio wave machine.

Further progress toward substantiating these ideas has awaited experimental demonstration of an efficient high compression ratio wave machine. A device to meet this need is currently under development. This machine has a compression ratio of 5.6 and an overall power transfer of 0.3 MW. A machine of this general description was chosen because it permits demonstration of the desired effects in an experimentally manageable operating regime. Of particular concern in the design and test phases are control and documentation of losses due to throttling, friction, heat transfer, leakage, interface mixing and shock waves.

INTRODUCTION

The use of an energy exchanger to increase the thermal efficiency of a power cycle has often been proposed.[1,2] Its unique operating characteristics permit operation and work extraction on high temperature streams that would be unobtainable with conventional axial flow turbines of the same inlet conditions and throughput. Although this idea shows promise for specific cycles, up to now no attempt has been made to develop scaling laws which describe the performance of energy exchangers over a broad range of operating conditions or to demonstrate a very efficient device. Such an effort is currently in progress at Mathematical Sciences Northwest, Inc. (MSNW).

Energy Exchanger

The energy exchanger is a device which continuously transfers work from an expanding primary gas stream to a secondary gas which in turn absorbs work while being continuously compressed. This transfer is accomplished by unsteady gas dynamic processes which are transformed into spatially steady positions by means of a set of axial tubes arranged on a rotating drum. The tubes rotate into confluence with properly phased stationary supply and exhaust manifolds arranged at opposite ends of the tubes on the periphery of the drum. Figure 1 is an idealized representation of energy exchanger operating principles. Driven gas is introduced at the right hand boundary and is compressed and scavenged by driver gas introduced along the left hand side. The driver gas is subsequently exhausted along the left hand boundary inducing an inflow of fresh driven gas charge for a new wave cycle.

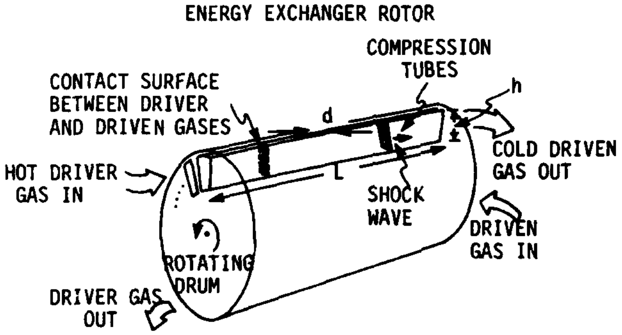

Figure 1. Energy Exchanger Drum and Tubes.

As a work extraction element in a topping cycle application, the energy exchanger has a fundamental advantage over a gas turbine because of the continuous cooling provided by the secondary driven gas stream. This application was first proposed by Claude Seippel, the inventor of the energy exchanger, in 1942 as a method for improving the thermal efficiency of a power cycle by raising the peak operating temperature. The idea was improved upon by Weatherston and Hertzberg,[3] who proposed using separate, appropriately matched fluids with staged systems of compression and expansion waves to obtain high efficiency, high-pressure-ratio work transfer. An energy exchanger which utilizes these latter principles can be employed as an element in a topping cycle, as shown in Figure 2, to augment any one of a number of thermal power conversion cycles with significant improvements in overall efficiency for moderate operating conditions and conservative component efficiency requirements. Figure 3 shows the energy exchanger efficiency and peak conditions required to produce a particular overall thermal efficiency for a 38 percent efficient bottoming cycle. For example, an 83 percent efficient energy exchanger with an inlet temperature of 1800°K and a pressure ratio of 3.3 will increase the overall thermal efficiency of a 38 percent efficient plant by nearly 10 percent.

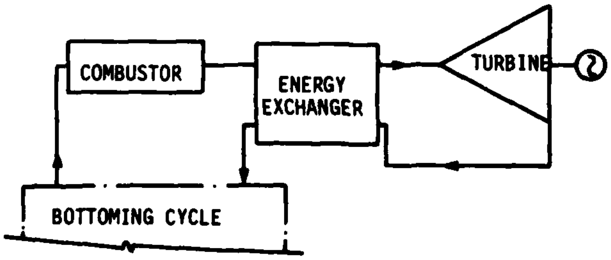

Figure 2. Energy Exchanger in Topping Cycle Application

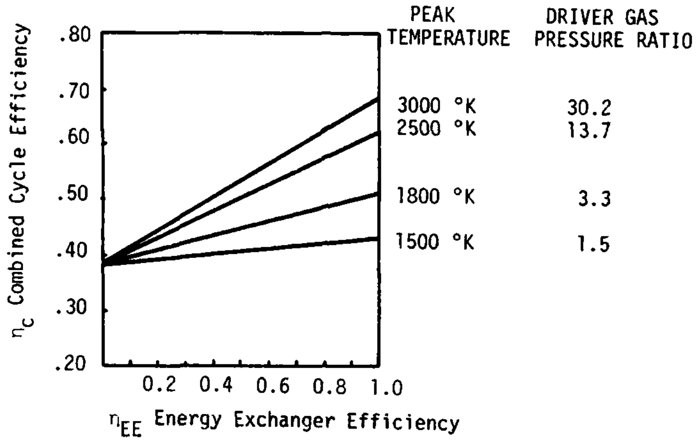

Figure 3. Effect of Energy Exchanger on Combined Cycle Efficiency

A high performance two fluid point design device is currently under development at MSNW. The object in developing this experimental device is to establish the viability of the two fluid principle in the pressure ratio range of present generation machines; that is, up to 2.5. Then, by addition of a second driver gas stage and suitable transfer passages, the device can be extended to the pressure ratios up to 5.6. This latter pressure ratio is in the range of interest for energy exchanger application to advanced power system cycles. Understanding and controlling the highly interactive steady and unsteady fluid mechanical effects is central to the problem of obtaining efficient operation.

The criteria used in developing an efficient fluid mechanical design for this proof-of-concept experiment is presented herein. The fluid modeling techniques used to establish and refine the experimental wave cycles are discussed. Methods used to characterize and estimate losses are given. Also included is a description of the design of a high mass and enthalpy flow, short duration blowdown facility which allows quasi-continuous wave testing of energy exchangers with power transfer rates up to 0.3 MW.

Motivation For A Two Fluid Energy Exchanger

Interest in a two fluid energy exchanger stems from the Weatherston and Hertzberg wave system in which perfect energy transfer can, in principle, be achieved. The conditions required for perfect transfer in a two fluid device are 1) the matching of the product of the speed of sound and the density at the contact surface between gases and 2) the use of staged systems of compression waves. The former condition, referred to as impedance matching or interface tailoring, permits perfect transmission of pressure waves across the contact surface without reflection. The second condition approximates isentropic processes through a series of weak compression waves.

A simple wave diagram which illustrates this ideal cycle is shown in Figure 4. A uniform driver stream is entrained onto the rotor in region ① as it scavenges a spent driven gas stream. In non-uniform region ② a focused set of waves, generated by incoming driven gas, compresses the driven stream and the last remnant of the spent driver. This compression continues through part of uniform region ③. In the central part of region ③ a uniform driver stream is used to scavenge the compressed driven stream. In the latter part of region ③ and the non-uniform region ④, driver gas is expelled through centered expansion waves, thus completing the cycle. In an impedance matched system the mass flows of the driver and driven streams are identical. Recirculation of the gas in the non-uniform regions is necessary to achieve perfect efficiency. Here two ports are shown in each fan to approximate the infinite number of recirculation ports required for ideal operation.

The fundamental advantage of a two fluid impedance matched device over its single fluid or two fluid mismatched counterpart is the simplicity of the wave patterns required to initialize the wave cycle. An orderly cycle closure and uniform steady manifold flows are essential to obtaining high performance in a two fluid machine. Flow disturbances during the low pressure scavenging process promote mixing of the gases at the fluid-fluid contact surface and will result in efficiency penalties, particularly in closed systems where it is necessary to separate and reprocess the contaminated effluent driver and driven streams. Although stricter requirements for efficient cycle closure prevail in the two fluid machine, a compensating feature is that greater design latitude is afforded in choosing a practical means of utilizing available energy. As will be seen, this advantage is maximum near the impedance matched condition.

Energy Exchanger Efficiency

The performance of an energy exchanger operating between given pressure states may be measured in terms of the actual work extracted by the machine. The maximum work extractable by any process operating between two given pressure states is an ideal isentropic work extraction process. The efficiency of an energy exchanger may therefore be defined as the ratio of the actual work transferred to the driven stream to the maximum work that can be transferred by an ideal isentropic process that takes all of the driver to the low pressure state. Formally the efficiency is

$$\eta = \frac{Wd}{W_{D_{ideal}}}$$

The wave phenomena dictates that during the operational cycle some fluid elements enter or exit the energy exchanger at pressures intermediate between the operating pressures. These forced operations at varying intermediate pressures impose a penalty on the actual work extracted by a given energy exchanger, thus influencing its performance.

A perfect energy exchanger is one which delivers the driven stream at the highest possible availability state while extracting the maximum possible work from the driver stream. An energy exchanger which delivers only a portion of the driver at the ambient pressure and the rest at some higher intermediate state, though isentropic, has performed poorly compared to a perfect thermodynamic process. By this criterion two isentropic energy exchangers are not identical in performance if one of them extracts 90% of maximum possible work as compared to 80% of another. While it may be argued that the latter machine delivers part of the driver at a higher availability state from which work can be extracted in principle, it must be realized that the less efficient machine requires additional gadgets to extract equal amounts of work and is hence less desirable.

In terms of the above definition the relationship between isentropic operation and the performance of the energy exchanger is clear. For a prescribed driver and driven inlet condition, the more non-isentropic the machine processes are the less efficient the energy exchanger is. Isentropy is, therefore, a necessary condition for high efficiency. It is, however, not a sufficient condition for peak performance. The efficiency of an isentropic machine with a given compression ratio depends on the ratio of acoustic impedance across the contact surface. We shall refer to this ratio as the mismatch parameter K and define it to be the speed of sound in the driver stream divided by the speed of sound in the driven stream along the contact surface. The mismatch parameter is equal to unity if the acoustic impedances are matched across the contact surface.

The general relationship between the efficiency of an energy exchanger and the mismatch parameter can be illustrated by considering a specific example. Let us consider the wave diagram shown in Figure 5. The compression is achieved by two equal shocks while the expansion is completed in four stages. If the state of the driver gas and the mismatch parameter are chosen, the strength and location of all the waves become uniquely determined for a closed cycle of operation.

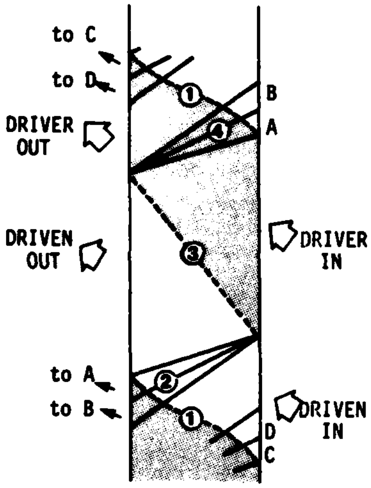

Figure 4. Ideal Impedance Matched Wave Cycle.

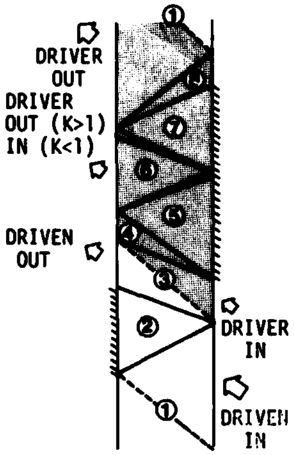

Figure 5. Modified Ideal Wave Cycle.

On the driver side the first and fourth waves are always expansion waves whereas the second and third waves are compression or expansion waves depending on whether the mismatch parameter is less than or greater than unity. On the driven side the flow is uniform along the inlet and exit manifolds for the wave arrangement considered. Shock compression results in losses in the given stream due to entropy production which is not significant at small pressure ratios.

The efficiency of an energy exchanger which operates according to the wave diagram of Figure 5 can now be calculated. In Figure 6 the calculated efficiency for a compression ratio of 2.5 is plotted as a function of the mismatch parameter. Since the non-isentropy is sufficiently small for the pressure ratio considered, the calculated efficiency is a close approximation to isentropic efficiency. The peak efficiency of about 96% is achieved when the impedances are matched. The peak efficiency is less than unity because part of the driver is not expanded to ambient pressure inside of the machine.

In a single fluid device the mismatch is equal to the square root of the temperature ratio across the contact surface. This value ranges between 1.5 and 2.0 for machines of practical interest. For this pressure ratio the efficiency penalty for mismatch is almost 10%. Since only two fluid devices can

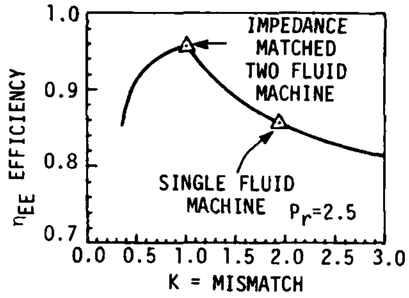

Figure 6. Energy Exchanger Efficiency vs Mismatch Parameter.

be designed to have matched impedance under meaningful operating conditions, they are seen to enjoy a fundamental efficiency advantage over single fluid devices. For high K, excess total availability is contained in the primary driver stream, some of which must be jettisoned at intermediate conditions to close the wave cycle. In contrast, the availability of the primary driver stream is too low at low K and makeup driver must be provided at intermediate conditions to accomplish closure.

Initial experiments at MSNW are being conducted on a pressure ratio 2.5 device with a system of waves identical to that shown in Figure 5. The performance of energy exchangers built and operated to date has fallen off sharply as the pressure ratio has increased beyond 2.5. In order to extend the concept to the higher range of pressure ratios which are of interest in topping cycle applications, the use of multiple driver stages with transfer passages becomes necessary. A promising recirculation scheme is shown in Figure 7. It is particularly advantageous for two fluid impedance matched machines since the mass flow and fluid conditions in exhaust region ⑦ are identical to those in the first stage driver region ③. This approach has been utilized in the design of the MSNW Pr 5.6 two fluid energy exchanger.

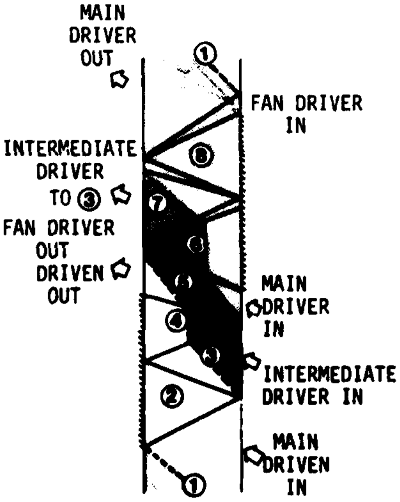

Figure 7. Energy Exchanger with Two Stage Driver and Transfer Passage.

Pressure ratios of 5 to 6 would extend energy exchanger operation to a regime beyond the range of turbine inlet temperatures currently being contemplated for the most advanced power systems. Discussions thus far have dealt with ideal energy exchanger performance and it is clear that there are definite efficiency advantages to be gained from operating a two fluid impedance matched device. However, to realize these benefits, losses must be understood and minimized.

Characterizing Loss Mechanisms

While the ideal wave diagram provides an appropriate baseline case for assessing wave machinery potential, the performance of these devices is severely impacted by real processes not indicated on the diagram. These loss mechanisms are largely surface to volume effects which become dominant for small devices. The importance of these loss mechanisms and how they scale with dimension parameters cannot be underestimated in choosing an efficient point design.

Table I summarizes the loss mechanisms considered and their scaling relationship where known. The first losses are total pressure losses due to shock waves. This effect depends on the strength, $\Delta p/p$, of the wave with weak waves more nearly approximating isentropic compression. For a given overall pressure ratio, π , a large number of weak waves, n , may be used instead of a single shock, thus increasing the efficiency of compression. In the limit of $n \rightarrow \infty$ the wave system becomes isentropic.[3] Boundary layers in the tubes are a source of pressure losses due to friction and energy losses due to heat transfer. In this instance it is important to keep the Mach number, M , of the flow in the tubes low while at the same time keeping the Reynolds number based on tube hydraulic diameter, Re_d, as large as possible. The length of the rotor, ℓ, should be made as short as possible in relation to the tube dimension, d. In addition, the flow in the machine may be made more adiabatic by raising the rotor temperature to more nearly approximate the appropriately averaged recovery temperature, T_r, of the flow. There is a clearance, t , required between the rotor and manifolds. At the same time this gap acts like a labyrinth seal. The relative amount of mass that is lost through this seal, $\dot{m}_L$, to the amount of fluid being processed, $\dot{m}$, is proportional to $M(t/d)$. The most suitable method for reducing this fraction is to reduce the clearance between the manifold and rotor without, of course, taking undue risks of material contact. Of course, if the gap were to be made very small, then windage friction would become important. This could be reduced by reducing the rotor speed. The means of reducing the losses are not necessarily independent of one another. In fact, optimizing the design involves finding a balance between the competing loss mechanisms.

A large class of losses may be grouped together under the title of mixing effects. In these effects different fluids are mixed with one another, or differently processed fluids of the same variety are mixed together. In either case the mixing of the identity of the fluid through composition, momentum, or energy reduces the performance of the machine. The main interface between the driver and driven fluid is subject to surface instability whenever different density fluids are accelerated through expansion or compression fans. This classic instability mechanism is minimized or eliminated by impedance matching the fluids. In addition, this contact surface is never plane because of the presence of the boundary layer. As such, at the exit plane of the rotor, there will be the presence of gas due to the core flow (undisturbed by the boundary layer) and gas under different conditions in the boundary layer on the wetted surface of the tube. The ratio of these two gases collected in the manifold system is a function of boundary layer thickness, δ , to the tube dimension, d. Choosing a large R_e and small ℓ/d reduces the mixing loss. Even if one were fortunate enough to have an essentially plane contact surface there is still a potential loss which can be visualized using Figure 8. Imagine a finite number of tubes on a rotor, each one displaced in time by d/V_m from its

Table I. Loss Mechanisms in Energy Exchangers

Loss Mechanism	Functional Dependence	Means of Reducing Loss
1. Shock Wave Pressure Losses	$\ln p_0/p_0' = \frac{\Delta s}{R} \approx \sum_m \left(\frac{\Delta p}{p}\right)^3$	Increase number of waves for given π so $\frac{\Delta p}{p} \to 0$.
2. Boundary Layer Pressure Losses	$\frac{\Delta p}{p} \sim \frac{1}{Re_d^{1/2}} \left(\frac{\ell}{d}\right) M^2$	Reduce Mach number of flow. Keep Reynolds number large.
3. Boundary Layer Heat Losses	$\frac{\dot{Q}}{\dot{H}} \sim \frac{1}{Re_d^{1/2}} \left(\frac{\ell}{d}\right) \left(\frac{T_r - T_w}{T_o - T_i}\right)$	In addition to above, make machine near adiabatic by heating wall temperature to recovery temperature.
4. Leakage Mass Loss	$\frac{\dot{m}_L}{\dot{m}_{in}} \sim M \left(\frac{t}{d}\right)$	Reduce clearance between manifold and rotor.
5. Windage, etc.	$\frac{P_w}{\dot{H}} \sim \frac{U_m^2}{a^2 Re_t}$	Reduce rotor velocity.
6. Mixing Effects:		
Contact Surface Instability	fn $\frac{(\rho a)_1}{(\rho a)_2}$	Impedance match interface.
Contact Surface B.L. Mix	fn (δ/d)	Make $\delta/d \ll 1$ by making Re large and ℓ/d small.
Collection Efficiency	$\frac{\dot{m}}{\dot{m}_p} = \frac{N-1}{N}$	Increase number of tubes/collection nozzle, increase rotor speed.
Throttling of Driver Gas	fn $\left(\frac{\Delta p}{p}\right)$ & d/U_m	Reduce Δp & same as above.
Manifold Mixing		Increase number of manifolds.
7. Inlet and Diffuser	$\frac{\Delta p}{p} \sim M^2$	

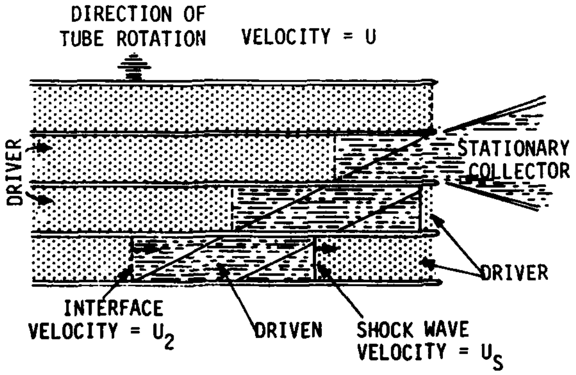

Figure 8. Energy Exchanger Collection Efficiency.

$$\eta_C = \frac{\text{MASS COLLECTED}}{\text{PROCESSED MASS}} = 1 - \frac{1}{\frac{L}{D}\left(\frac{U}{U_2} - \frac{U}{U_s}\right)}$$

$$= \frac{N-1}{N}$$

neighbor, V_m being the rotor tangential velocity. Because of the finite particle speed, U_2, the contact surface of each tube is displaced in an axial direction from its neighbor by d/V_mU_2. A stationary collector or manifold collects the processed gas. Only part of this gas can be collected if contamination of the driver gas is to be avoided. The general result for the ratio of collected gas to processed gas is $\frac{N-1}{N}$ where N is the ratio of manifold width divided by tube width. The collected fraction may be improved by increasing the number of tubes and increasing the tube length, both of which are in direct opposition to earlier improvements suggested for boundary layer control. Mixing effects become noticeable not only at the collection ports, but at the entrance manifold through losses in the driver stream. As each low pressure tube is first exposed to the driver nozzle, a jetting of the driver gas occurs causing mixing and pressure losses. A little later the tube is fully opened to the system and this effect stops. While the exact functional dependence of the loss is not known, it depends on the relative pressure difference, $\Delta p/p$, between the driver and driven gas at the point of opening and the duration of opening. Thus reducing the pressure jump across the wave reduces throttling of the driver gas and if $a/V_m >> \ell/d$, then the duration of the throttling is short.

The last and very important mixing effect is termed manifold mixing. Expansion and compression fans place non-uniform conditions at the exit plane of the rotor. If these conditions are not properly imposed, this flow can undergo additional entropy production, mixing in the manifold or unwanted wave reflections into the machine. Optimal placement of ports and adjustment of port flow conditions provides a means of controlling these losses. In order to fully realize the potential of the energy exchanger, the kinetic energy invested in the flow streams must be efficiently managed and recovered. Nozzles and diffusers should be designed to provide smooth acceleration of inlet flows to match the proper axial gas velocity and the rotor tangential velocity at the junction between the manifolds and the rotor face. An overspeed rotor will act as an impulse compressor extracting power from the rotor driving motor. An underspeed rotor will act as an impulse turbine delivering power to the rotor driving mechanism. Both of these latter effects adversely influence efficiency since a difference in tangential velocity at the entrance or exit interface will produce waves in the rotor tubes.

Fluid Modeling

In order to design an efficient energy exchanger and to predict its performance correctly, we have developed two major numerical codes. The first, a method-of-characteristics code, solves the ideal compressible fluid equations to obtain a self-consistent pattern of unsteady waves representing the gas flow in one tube of an energy exchanger. The second code employs a flux corrected transport method of solving the fully dissipative fluid equations to take account of finite width shockwaves, shock wave formation times, heat transfer and viscous boundary layer drag.

The method-of-characteristics code is used primarily as an aid to design intuition, to check the precise wave pattern produced in a tube when a variety of open and closed port sequences are postulated. The precise location of these ports and gas exhaust conditions can be computed so that manifold placement in the rotor design can be established. The results can also be used to determine appropriate entrance and exit manifold gas conditions, duration of the complete gas dynamic cycle and operating efficiency under ideal gas conditions. To predict the flow under real operating conditions, gas dynamic losses must be analyzed with the complete fluid equations. In particular the pressure drop in tubes with a length-to-diameter ratio of 50 to 100 and finite Mach number flow speeds can be substantial. Choked flow can also occur if the heat transfer is too large. Both of these effects are encompassed by the flux corrected transport or FCT code which is a recent finite difference scheme developed by Boris and Book.[4] The FCT technique is chosen instead of the Lax-Wendroff techniques[5] because the latter is highly diffusive and unstable near sharp discontinuities like a shock front or a contact surface, which are commonly encountered in an energy exchanger. The FCT method has the further advantage of reducing the numerically induced shock width to just one or two grids on the numerical space mesh used to represent the finite difference approximation to the fluid differential equations. The implementation of this code is based on a numerical scheme originated by Coakley[6] to treat energy exchanger flow systems. Coakley's unique contribution was an algorithm to treat two different adjacent gases (e.g., driver and driven gases). His technique carefully tracks the interface between the gases and breaks the solution space into two distinct regions where the interface forms a moving boundary between them. In this way even impedance mismatched flow behavior can be computed including the wealth of wave reflections which may occur at the interface. We have used this code sparingly, because of its greater expense, to quantify various aspects of the losses associated with real energy exchanger performance. The FCT approach has permitted considerable accuracy in predicting the change in wave patterns (e.g., delays in wave exits, increased transit times, etc.) associated with the fully dissipative flows.

The preceding fluid modeling, strictly speaking, is applicable just to one-dimensional fluid flows. Additional analytic quasi-two and -three dimensional modeling of the manifold flows was necessary in order to reduce the aerodynamic losses due to high velocities, flow turning, flow non-uniformities and diffuser losses (e.g., flow separation). Simple constraints were also derived as design guides to limit the amount of mixing at the gas interface due to finite tube opening times; the rule used is to keep the opening time short compared to the acoustic transit time down the length of the tube.

Design of Experimental Device

The goal of the experimental program is to demonstrate the concept of an efficient energy exchanger at pressure ratios at and beyond the range of present day devices. Central to this problem is the development of a machine which combines the ideas of impedance matching and staged compression in an optimal, low loss configuration.

To emphasize the ideal and the real effects of interest the experiment was designed using monatomic gases with modest temperatures, pressures and rotor velocities, while at the same time maintaining physical dimensions and mass throughputs sufficiently large so as to minimize surface to volume effects. A machine has been built which is capable of operating in the impedance matched or mismatched mode at a pressure ratio of 2.5 and a work transfer rate of 100 KW. By adding a second driver gas stage impedance matched performance can be demonstrated at a pressure ratio of 5.6 and transfer rate of 300 KW. The physical parameters for this device are listed in Table II.

Table II. Machine Parameters

Pressure Ratio	2.5 [5.6]
Work Transfer	100 KW [300 KW]
Rotor Length	42 cm
Rotor Diameter	42 cm
Rotor Tube Speed	4130 cm/sec
Tube Dimensions	$h=4cm$, $d=1cm$ ($d_H=2.67cm$)
Driven Gas (Matched Case)	80 Ar, 20 He
Driver Gas	100 Ar
Driver Inlet Temperature	525°K [725°K]
Driven Inlet Temperature	295°K
Driver Mass Flowrate	1500 g/sec
Driven Mass Flowrate	1500 g/sec
Collector Efficiency	.9
Run Time	4 sec

Values in Table II refer to the pressure ratio 2.5 design and values in brackets refer to the pressure ratio 5.6 configuration. Figure 9 is a photograph of the MSNW pressure ratio 2.5 design showing the rotor, manifolds and

Figure 9. Photograph of MSNW Pressure Ratio 2.5 Energy Exchanger.

Estimates were made of the losses in the experimental device using the functional dependencies given in Table I. These are shown in Table III.

Table III. Estimated Losses for Experimental Device

Loss Source	% Loss
1. Shock Wave Pressure Losses	~0
2. Heat Transfer in Tubes	1.0
3. Boundary Layer	4.0
4. Leakage	4.0
5. Windage and Friction	2.0
6. Mixing Effects including Collection Efficiency	5.0
7. Inlet and Diffuser Losses	3.0

Losses are given in percent of maximum work of expansion of the driver stream. Item 6 represents the largest anticipated loss and at the same time the most difficult to evaluate analytically. As such it is a major topic of the experimental investigation. The second largest source of loss is the leakage from rotor-manifold face seals through gaps of .15 mm. The third major loss source is due to boundary layer pressure drop which has been minimized by maintaining tube Mach numbers below .4. Manifold and diffuser losses are expected to account for a three percent loss. Friction and heat transfer account for the remaining inefficiency, leading to an estimated device efficiency of 75 to 80%.

Two important features of the design are the rotor geometry and the manifold configurations. The rotor length to hydraulic diameter of 28 was chosen to minimize boundary layer pressure loss and heat transfer effects while maintaining the tube opening and closing times necessary for a .9 collection efficiency.

The physical arrangement of energy exchanger components required a complex design for these helicoidal nozzle and diffuser manifolds. The driver inlet flow was expanded from Mach 0.1 plenum tube conditions through smoothly contracting helicoidal nozzles to Mach 0.4 at the rotor-manifold interface. The tangential components of these velocities match the rotational speed of the rotor tubes at this interface. In this manner both the driver and driven gases are provided to the individual energy exchanger tubes with a minimum amount of flow disturbance.

The manner in which the processed gases are removed from the rotor also significantly affects the overall efficiency of device operation. Diffusers with total divergence angles of 7 degrees were incorporated in these helicoidal exhaust manifolds to decelerate the exhaust flows to Mach 0.1 and efficiently recover total pressure.

Design of Experimental Facility

Figure 10 shows the layout of the gas supply system required for initial tests on the 100 KW, pressure ratio 2.5, energy exchanger. The energy exchanger is shown schematically as a stationary system of waves with supply and exhaust lines leading to and from the appropriate flow regions. Also pictured are the various tanks, valves, heaters and flow meters required to supply steady flow conditions during a six second blowdown episode. Control of the system during blowdown is provided by a minicomputer. The programmed opening of control valves provides an interval of quasi-steady flow conditions during which experimental data is taken. The rotor manifolds and individual flow lines are maintained at predetermined temperatures corresponding to gas flow temperatures during testing.

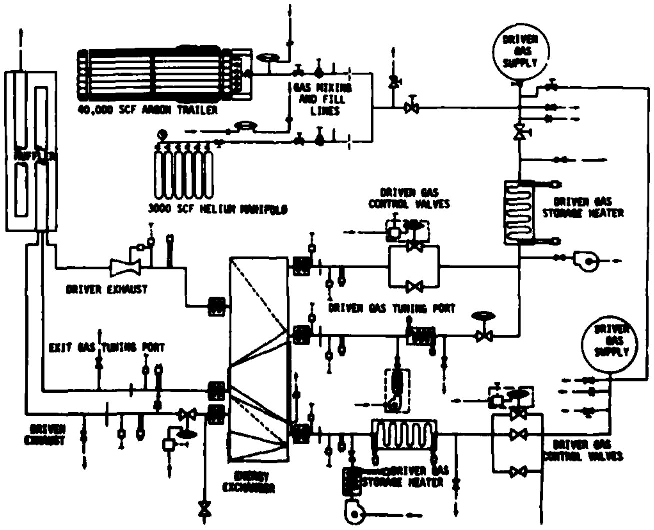

Figure 10. Energy Exchanger Gas Blowdown Facility

Experimental Program

The experimental program has multiple objectives of (1) verifying power transfer and efficiency, (2) providing data on sensitivity to off-design operation, (3) providing rates of driver and driven gas mixing and (4) providing detailed characterizations of the principle loss mechanisms.

Standard orifice and venturi type flow meters, pressure probes, and thermocouples are used to measure mass flow, pressure, and temperature of the driver and driven gas inlet and outlet streams for calculation of the power transfer and efficiency. Total pressure and temperature measurements are made in low velocity duct sections up and downstream of the manifolds and rotor so that diffuser pressure losses are included in the power transfer and efficiency. Gas sampling probes are located at critical inlet and outlet duct regions near the rotor to provide data for determination of mixing rates across driver/driven gas interfaces. Gas samples are analyzed off line, using a gas chromatograph. Multiple static pressure taps and pressure transducers are located at critical wave reflection points between manifolds to evaluate the effects of finite tube opening and closing times on pressure wave location, strength, and waveform.

SUMMARY

The rationale used in the design of an efficient energy exchanger is presented. Methods used to estimate ideal and real behavior over a range of conditions are discussed. The design configuration is given for an experimental device which has been built and will operate at pressure ratios of 2.5 and 5.6 with power levels of 100 and 300 KW respectively. Methods of energizing the device and measuring its actual performance are also included.

ACKNOWLEDGEMENTS

The authors would like to express their thanks and appreciation to Professor Abraham Hertzberg for his help and guidance throughout the many phases of this work. This work was supported by the United States Department of Energy Basic Energy Sciences Division under Contract No. ER-78-C-06-1084.

REFERENCES

1. C. Seippel, "Pressure Exchanger," U.S. Patent No. 2,399,394, 1946.
2. A. Kantrowitz et al., "Heat Engines Based on Wave Processes", Graduate School of Aeronautical Engineering, Cornell University, Ithaca, New York, March 21, 1949.
3. R.C. Weatherston and A. Hertzberg, "The Energy Exchanger, A New Concept for High Efficiency Gas Turbine Cycles," *Journal of Engineering for Power*, 1966.
4. J.P. Boris and D.L. Book, "Solution of Continuity Equations by the Method of Flux-Corrected Transport", Chapter 11, Vol. 16, *Methods of Computational Physics*, Academic Press, New York, 1976.
5. R.D. Richtmyer and K.W. Morton, "Difference Methods for Initial Value Problems," 2nd Edition, Sections 12.9 and 13.9, *Interscience*, New York, 1967.
6. T. Coakley, Private Communication, NASA Ames Research Center, California, June, 1978.

INDEX

Ahlborn, B. 366
Akamatsu, T. 169, 187
Anderson, J. D. 386
Astholz, D. C. 607
Ausherman, D. R. 675
Autric, M. 704

Barner, U. 621
Bar-Nun, A. 457
Bauer, S. H. 409
Baum, D. W. 242
Ben-Dor, G. 288
Bershader, D. 258
Betser, A. 341
Bhaskaran, K. A. 503
Bidani, M. 612
Blendstrup, G. 258
Bournot, Ph. 704
Bracht, K. 712
Bradley, J. N. 524
Brimelow, P. I. 232
Brocher, E. 161
Brode, H. L. 31
Bro, K. 429
Brun, R. 180
Bull, G. V. 82
Burcat, A. 644
Butler, G. W. 655

Capey, W. D. 524
Caressa, J. P. 704
Cassady, P. E. 446, 720
Chang, J. S. 562, 571
Chapman, G. T. 127
Chiang, C. C. 629
Christiansen, W. H. 379, 720
Cohen, A. 514
Colasurdo, G. 386
Cook, W. J. 127
Craig, J. E. 248
Czerwinski, W. 276

Dabora, E. K. 685
Dannenberg, R. E. 599
Decker, L. 514
Demmig, F. 197
Dewey, J. M. 695
Dove, J. E. 457
Dufresne, D. 704
Dumitrescu, L. Z. 137

Eliezer, S. 66
Elitzur, M. 640
Evans, B. 571

Farajii, F. 524
Fontaine, B. 147
Forestier, B. 147
Frank, P. 503
Fujikawa, S. 169
Fujiwara, T. 533
Fussey, D. E. 495

Gardiner, W. C. 555
Garen, W. 155
George, A. 579
Gill, S. P. 242
Giovanneschi, P. 704
Glass, I. I. 232, 288
Gnoyke, R. E. 276
Gottlieb, J. J. 276
Grillo, A. 486
Grimshaw, J. F. 349
Groenig, H. 207
Guinee, M. J. 495

Haas, J. F. 359
Hahne, G. 222
Haines, K. A. 248
Hajduk, J. C. 97
Hanson, R. K. 476
Henderson, L F. 334
Hesselink, L. 359
Hewitt, F. A. 495
Hidaka, Y. 555
Hobson, R. M. 562, 571
Honma, H. 215
Hornung, H. 298

Imamura, K. 548
Itaya, M. 314
Itoh, S. 314

Jones, E. 386
Joshi, S. 562
Just, Th. 503

Kekez, M. M. 396

Kiefer, J. H. 97
Kim, S. S. 437
Kivity, Y. 341
Kline, J. M. 465
Klosterman, E. L. 446, 720
Kruger, C. H. 476
Kulkarny, V. A. 675
Kwan, J. 366

Langhoff, P. 258
Lau, J. H. 396
Lederman, S. 48
Leitch, A. 298
Lensch, G. 155
Levine, R. D. 111
Lifshitz, A. 612
Löhr, R. 621
Lougheed, G. D. 396
Lozzi, A. 308

Margalith, E. 376
Marmor, E. 341
McMillin, D. J. 695
Merzkirch, W. 712
Meyer-Prüssner, R. 197
Milton, B. E. 495
Miyoshi, S. 187

Neemeh, R. A. 324

Oertel, H. 266
Oggiano, M. S. 386
Ogram, G. L. 562
Onorato, M. 386
Ostrowski, P. P. 324

Palmer, T. F. 495
Park, C. 419
Parthasarathy, K. N. 386
Pearson, J. 366
Pennelegion, L. 349
Penner, S. S. 465
Presley, L. L. 127

Reed, R. 486
Roose, T. R. 476
Rose, P. H. 3
Roth, P. 621
Russell, D. A. 655

Sandeman, J. 298
Savic, P. 396
Schneider, C. P. 222
Segall, S. B. 664
Shimmin, W. L. 242
Shirai, H. 419
Shirazian, M. 446
Shiun Liu, W. 232
Shwartz, J. 675
Siegenthaler, A. 334
Skinner, G. B. 629
Slack, M. W. 486
Smeets, G. 579
Steinhauer, L. 446
Stricker, J. 644
Sturtevant, B. 359
Sugimura, T. 533
Sulzmann, K. G. P. 465
Sweeney, D. W. 429

Tabayashi, K. 409
Takahashi, N. 589
Takano, Y. 187
Takasu, N. 548
Takayama, K. 232
Tanzawa, T. 555
Taussig, R. T. 446, 720
Terao, K. 548
Teshima, K. 571, 589
Thayer, W. J. 720
Thor, H. J. 207
Tilleman, M. 644
Troe, J. 607
Tulis, A. J. 539

Vaidyanathan, T S. 446, 720
Valensi, J. 147
Valetta, M. J. 180

Wahba, N. N. 276
Wieters, W. 607
Wittig, S. L. K. 429, 437
Wu, J. H. T. 324
Wurz, D. E. 437

Yoshida, H. 215
Yu, T. S. H. 324

Zahoransky, R. A. 437
Zeitoun, D. 180
Zmora, H. 66
Zumdieck, J. F. 720

PREVIOUS PROCEEDINGS OF THE SHOCK TUBE SYMPOSIA

Proceedings of the V International Shock Tube Symposium, published by the U.S. Naval Ordnance Laboratory, White Oaks, Silver Spring, Maryland, May 1966 (a loose-leaf publication).

High Temperature and Short Duration Flows. Proceedings of the VI International Shock Tube Symposium, R.J. Emrich, O. Laporte and H. Reichenbach, eds., The Physics of Fluids Supplement I, 1969.

Shock Tubes. Proceedings of the VII International Shock Tube Symposium, I. I. Glass, editor, University of Toronto Press, Toronto 1970.

Shock Tube Research. Proceedings of the VIII International Shock Tube Symposium, J.L. Stollery, A.G. Gaydon and P.R. Owen, eds. Chapman and Hall, London, 1971.

Recent Developments in Shock Tube Research. Proceedings of the IX International Shock Tube Symposium, D. Bershader and W. Griffith, eds. Stanford University Press, Stanford, 1973.

Modern Developments in Shock Tube Research. Proceedings of the X International Shock Tube Symposium, G. Kamimoto, editor, Shock Tube Research Society, Japan, 1975.

Shock Tube and Shock Wave Research. Proceedings of the XI International Symposium on Shock Tubes and Waves. B. Ahlborn, A. Hertzberg and D. Russell, eds., University of Washington Press, Seattle, 1978.

END

DATE

FILMED

11-80

DTIC